Weisheng Wang · Guanghui Li · Guoqing He

Analysis and Mitigation of Broadband Oscillation in Renewable Energy Generation and AC/DC Transmission Systems

中国电力出版社
CHINA ELECTRIC POWER PRESS
Springer

Analysis and Mitigation of Broadband Oscillation in Renewable Energy Generation and AC/DC Transmission Systems

Weisheng Wang · Guanghui Li · Guoqing He

Analysis and Mitigation of Broadband Oscillation in Renewable Energy Generation and AC/DC Transmission Systems

中国电力出版社
CHINA ELECTRIC POWER PRESS

Springer

Weisheng Wang
China Electric Power Research Institute
Beijing, China

Guanghui Li
China Electric Power Research Institute
Beijing, China

Guoqing He
China Electric Power Research Institute
Beijing, China

ISBN 978-981-99-1567-5 ISBN 978-981-99-1568-2 (eBook)
https://doi.org/10.1007/978-981-99-1568-2

Jointly published with China Electric Power Press.
The print edition is not for sale in China (Mainland). Customers from China (Mainland) please order the print book from: China Electric Power Press.
ISBN of the mainland of China edition: 978-7-5198-8109-2

© China Electric Power Press 2023
This work is subject to copyright. All rights are solely and exclusively licensed by the Publisher, whether the whole or part of the material is concerned, specifically the rights of reprinting, reuse of illustrations, recitation, broadcasting, reproduction on microfilms or in any other physical way, and transmission or information storage and retrieval, electronic adaptation, computer software, or by similar or dissimilar methodology now known or hereafter developed.
The use of general descriptive names, registered names, trademarks, service marks, etc. in this publication does not imply, even in the absence of a specific statement, that such names are exempt from the relevant protective laws and regulations and therefore free for general use.
The publishers, the authors, and the editors are safe to assume that the advice and information in this book are believed to be true and accurate at the date of publication. Neither the publishers nor the authors or the editors give a warranty, expressed or implied, with respect to the material contained herein or for any errors or omissions that may have been made. The publishers remain neutral with regard to jurisdictional claims in published maps and institutional affiliations.

This Springer imprint is published by the registered company Springer Nature Singapore Pte Ltd.
The registered company address is: 152 Beach Road, #21-01/04 Gateway East, Singapore 189721, Singapore

Foreword by Jianbo Guo

China is a country with abundant renewable energy resources, such as wind energy and solar energy. Vigorously developing renewable energy is a strategic measure to construct a new type energy system and achieve carbon peaking and carbon neutrality. By 2030, the electric production proportion of renewable energy generation in China will reach 20%, and by 2060, the proportion will exceed 50%.

A major challenge for the safe and stable operation of high-proportion renewable energy power systems is broadband oscillation. Since 2009, broadband oscillation accidents of renewable energy grid-connected systems have encountered frequent domestically and internationally, threatening the safe and stable operation of power systems and leading to the abandonment of wind and solar energy. In recent years, broadband oscillation has become the focus of academic and industrial research. With the rapid development of renewable energy bases in deserts, Gobi, desertification areas, and distant sea areas in China, the high-proportion renewable energy power systems have interwoven multi-time scales, intensified nonlinear characteristics, and complex dynamic characteristics. The safety and stability problem, especially the oscillation problem, is more prominent. Therefore, a book is urgently needed to systematically and comprehensively introduce the analysis methods, suppression measures, and practical applications of broadband oscillation, help readers fully understand the oscillation problems, guide the development and construction of renewable energy bases, and ensure the stable operation of large-scale renewable energy grid-connected systems in China.

Based on the national research and development projects, the scientific projects of the State Grid Corporation of China, and based on ten years of collaborative research with relevant universities, renewable energy equipment manufacturers, and power generation enterprises, the Renewable Energy Research Center of China Electric Power Research Institute has made breakthroughs in the research of broadband oscillation mechanism, analysis methods, and suppression technology. In addition, the research achievements have been applied to multiple practical projects and achieved significant oscillation suppression effects. I have participated many times in their symposiums on the analysis and mitigation of broadband oscillation in renewable energy grid-connected systems. I think their theoretical achievements and practical

experience are worth further refining and sharing with everyone as soon as possible. It can be said that the publication of this book is at the right time.

The sharpness of a sword results from repeated grinding, while the fragrance of plum blossoms comes from frigid weather. This book comprehensively summarizes the theoretical methods and practical experience for the analysis and mitigation of broadband oscillation in renewable energy grid-connected systems by the New Energy Research Center. Its content covers the modeling of the renewable energy grid-connected system, analysis and mitigation of broadband oscillation, and engineering applications. It has a rich theoretical basis and innovation, as well as a large amount of practical data and project cases. It embodies the blood and sweat of frontline scientific and technological workers and shows the latest research results in broadband oscillation of renewable energy grid-connected systems.

I recommend this book, *Analysis and Mitigation of Broadband Oscillation in Renewable Energy Generation and AC/DC Transmission Systems*, to everyone. I believe the publication of this book will provide a valuable reference for engineers of power and renewable energy engineering design, technology research and development, and operation management, as well as teachers and students of electrical engineering.

Beijing, China
October 2022

Jianbo Guo
Academician of Chinese Academy of Engineering
Honorary President of China Electric Power
Research Institute

Foreword by An Luo

The onshore wind and solar energy resources of China are mainly located in the north, northwest, and northeast regions, while the load centers are mainly located in the central, and eastern regions. The reverse distribution of resources and loads determines the necessity of long-distance AC/DC transmission of bulk power electricity. In addition, MMC-HVDC transmission has become the main way of offshore wind power development and utilization in China. With the development of large-scale renewable energy, the sending-end of the AC/DC transmission system gradually formed a local "double-high" power system of high-penetration renewable energy and high-penetration power electronics. The operation characteristics of such systems are dominated by the power electronic device control and have undergone profound changes compared with traditional power systems. In recent years, many renewable energy generation and AC/DC transmission systems have experienced oscillations leading to tripping-off accidents domestically and internationally, seriously affecting the safe and stable operation of power systems.

For the oscillation problem of renewable energy under multiple transmission scenarios, there is a lack of systematic research and summary domestically and internationally, as well as a lack of works covering the basic theory of oscillation, analysis methods, research methods, and multi-scenario engineering applications. The writing team of this book is composed of well-known experts and scholars in the field of renewable energy generation, as well as engineers with rich practical experience. This book integrates theory with practice and summarizes the experience of the Renewable Energy Research Center in solving engineering oscillation problems. There are many engineering lessons and insights in this book that can only be obtained through personal experience.

This book, *Analysis and Mitigation of Broadband Oscillation in Renewable Energy Generation and AC/DC Transmission Systems* is divided into four parts and 19 chapters, which is a highly condensed summary of years of research by the author and team. Part I introduces the small-signal modeling methods for various types of converters, which lay a foundation for the smallsignal modeling for complex power electronic devices. Part II introduces the small-signal modeling methods for wind turbines, PV units, SVG, LCC-HVDC, and MMC-HVDC, moreover, it

reveals the mechanism of negative damping effect in different frequency bands for different power electronic devices. Part III introduces the small-signal modeling method of renewable energy generation plants, and analyzes the broadband oscillation mechanism of renewable energy generation connected into HVAC, LCC-HVDC, and MMC-HVDC systems. Part IV introduces the impedance reshaping methods for renewable energy generation units, SVG, LCC-HVDC, and MMC-HVDC, and presents multiple practical cases of broadband oscillation mitigation in gridconnected renewable energy systems.

This book has strong innovation, comprehensive and rich content, and clear organization. It is a high-level academic work that comprehensively and systematically introduces the oscillation problem of renewable energy grid-connected systems and has significant academic value and practical guidance significance. I believe this book will provide great theoretical guidance and valuable practical reference for the current and future solutions to the oscillation problems of renewable energy grid-connected systems.

Changsha, China
October 2022

An Luo
Academician of Chinese Academy of Engineering
Professor of Hunan University

Foreword by Guangfu Tang

To achieve carbon peaking and carbon neutrality, energy is the main battlefield, and electricity is the main force. In the clean and low-carbon transformation of energy and electricity, the proportion of new energy in the power grid continues to increase, and the "doublehigh" feature of the high proportion of new energy and the high proportion of power electronics is becoming increasingly prominent. The stability characteristics of the power system have undergone profound changes compared to traditional power systems. Large-scale renewable energy tripping-off accidents caused by broadband oscillations in China have brought new technological challenges to the operation of large-scale renewable energy bases in the north, northwest, and northeast regions, and will affect the future development and construction of renewable energy bases in deserts, Gobi, desertification areas, and distant sea offshore wind power bases.

The Renewable Energy Research Center of China Electric Power Research Institute has made a comprehensive breakthrough in the analysis and mitigation of broadband oscillation in renewable energy grid-connected systems. Firstly, the frequency coupling impedance models for power electronic devices are established, including wind turbines, PV units, SVG, LCC-HVDC, and MMC-HVDC, and the mechanism of broadband oscillation for renewable energy generation bases connected into HVAC, LCC-HVDC, and MMC-HVDC systems is revealed. Then, the electromagnetic transient simulation platform for ten million kilowatts level renewable energy bases under multiple transmission scenarios is constructed, which can be used for the oscillation recurrence, mechanism analysis, and verification of oscillation mitigation strategy. Finally, the theoretical analysis and simulation results are applied to solve the practical oscillations in Hami Xinjiang, Zhangbei Hebei, and Xilin Gol Inner Mongolia. This book systematically and comprehensively introduces the modeling method, analysis methods, suppression measures, and practical applications of broadband oscillation, which is an impressive achievement for the scientific research and practice of the Renewable Energy Research Center in the past decade. This book is of great significance for ensuring the stable operation of large-scale renewable energy generation in China and achieving carbon peaking and carbon neutrality.

This book has distinct academic innovation and application guidance, in which the content is detailed and practical. In addition to introducing the basic theory and

analysis methods of renewable energy grid-connected system oscillation, this book also analyzes the project cases of broadband oscillation in China in recent years. This book can be used by research and development engineers or operation management engineers of electric power and renewable energy, and as a reference for teachers and students of electric power majors in universities and colleges.

In the future, the development of global energy will continue the trend of low carbon. I believe the publication of this book, *Analysis and Mitigation of Broadband Oscillation in Renewable Energy Generation and AC/DC Transmission Systems*, will provide important technical instructions for the construction and operation of the new type power system.

Beijing, China
October 2022

Guangfu Tang
Academician of Chinese Academy of Engineering
Honorary President of State Grid Smart Grid
Research Institute

Preface

Vigorously developing renewable energy generation (REG) is an important measure for countries worldwide to promote low-carbon energy transformation and ensure energy security. With the continuous increase of the installed capacity and proportion of REG, mainly including wind power and photovoltaic (PV) power generation, the stable operation of REG and AC/DC transmission systems has become a technical bottleneck for the sustainable development of REG. Since 2009, broadband oscillation accidents of REG and AC/DC transmission systems have encountered frequent domestically and internationally, resulting in severe consequences such as large-scale REG tripping-off grids, equipment damage, and an increase in the abandonment of wind and solar energy. The analysis and mitigation of broadband oscillation is a great challenge.

Dr. Jian Sun, IEEE Fellow and professor at Rensselaer Polytechnic Institute, first proposed a sequence impedance analysis method based on harmonic linearization at the 23rd IEEE Applied Power Electronics Conference and Exposition (APEC 2008) in February 2008, which promoted the impedance-based stability analysis method proposed by R. D. Middlebrook in 1976 from DC systems to AC systems. Since then, domestic and foreign academics have carried out much research and extension work on this method.

In recent years, the Renewable Energy Research Center of China Electric Power Research Institute (CEPRI) has made multiple major breakthroughs in the analysis and mitigation of broadband oscillations in REG and AC/DC transmission systems based on the sequence impedance analysis method. The technical challenges related to the oscillations in REG clusters connected into different transmission systems, including HVAC, line commutated converter- based high voltage direct current (LCC-HVDC), and modular multilevel converter-based high voltage direct current (MMC-HVDC), have been overcome. A comprehensive solution with clear mechanism, precise analysis, and effective mitigation has been formed. In terms of the theoretical models, the frequency coupling impedance models of power electronic devices applied in the wind and PV power generation, static var generator (SVG), LCC-HVDC, and MMC-HVDC have been established to reveal the broadband oscillation mechanism of REG and AC/DC transmission systems. In terms of platform

construction, a full electromagnetic transient (EMT) simulation platform for the simulation of ten million kilowatts level REG under multiple transmission scenarios is constructed, which can be used for the oscillation recurrence, mechanism analysis, and verification of oscillation mitigation strategy. In terms of engineering applications, the oscillation issues encountered in REG and AC/DC transmission systems such as Hami Xinjiang (HVAC transmission), Zhangbei Hebei (MMC-HVDC transmission), and Xilin Gol Inner Mongolia (LCC-HVDC transmission) have been successfully solved. This book is a cohesive summary of the research results and practical experiences.

This book highlights the fundamentality and practicability in content and explains the profound in simple terms, including both the theoretical methods and project cases. The book with topic-oriented broadband oscillation in REG and AC/DC transmission systems is divided into four parts. Part I is Small-Signal Modeling of Converters, which contains four chapters and introduce the frequency-domain small-signal modeling method, and introduces impedance modeling of three types of basic converters commonly used in power electronic devices, including two-level converter, modular multilevel converter, and thyristor converter. Part II is Impedance Model and Characteristic Analysis of REG and HVDC Transmission, which contains six chapters and introduces the impedance modeling and characteristic analysis of the full power conversion wind turbine, doubly-fed induction generator (DFIG)-based wind turbine, PV unit, SVG, LCC-HVDC, and MMC-HVDC. Part III is Broadband Oscillation Analysis of REG and AC/DC Transmission System, which contains three chapters and introduces the impedance modeling and characteristic analysis of REG plants and introduces oscillation analysis of REG connected into HVAC and HVDC transmission systems. Part IV is Broadband Oscillation Mitigation of REG and AC/DC Transmission Systems, which contains five chapters and introduces the impedance reshaping of different types of REG units, SVG, LCC-HVDC, and MMC-HVDC as well as project cases.

I overall designed and finalized this book and wrote the introduction. The division of labor for each chapter is as follows.

Part I is finally compiled by Guanghui Li, of which Chap. 2 is written by Guanghui Li, Chap. 3 is written by Yuqi Duan, Chaps. 4 and 5 are written by Yuntao Xiao.

Part II is finally compiled by Guanghui Li, of which Chaps. 6 and 11 are written by Guanghui Li, Chaps. 7 and 8 are written by Yu Lei, Chap. 9 is written by Yuntao Xiao, Chap. 10 is written by Yuntao Xiao and Ni Zhen.

Part III is finally compiled by Guoqing He, of which Chap. 12 is written by Haijiao Wang, Chap. 13 is written by Yuntao Xiao and Haijiao Wang, Chap. 14 is written by Guoqing He and Ni Zhen.

Part IV is finally compiled by Weisheng Wang, of which Chap. 15 is written by Yu Lei, Chaps. 16 and 17 are written by Guoqing He, Chap. 18 is written by Guanghui Li, Chap. 19 is written by Chun Liu and Yuqi Duan.

The Appendix is written by Guoqing He and Guanghui Li.

Liping Gao, Keke Liu, Junhua Ma, Caiyun Gao, Zixuan Guo, Yuye Li, Fangfang Yu, Xing Zhang, Yanxia Sun and Yue Zhang from the Renewable Energy Research

Center of CEPRI made active contributions to the theoretical research, technology development, and engineering practice in this book.

The authors sincerely appreciate Prof. Jianbo Guo, academician of the Chinese Academy of Engineering and professorate senior engineer of CEPRI, Prof. An Luo, academician of the Chinese Academy of Engineering and professor of Hunan University, and Prof. Tang Guangfu, academician of the Chinese Academy of Engineering and Honorary President of State Grid Smart Grid Research Institute, for their guidance in technology development, engineering application, and book writing. Moreover, thanks to them for writing the prefaces of this book.

Prof. Geng Yang of Tsinghua University, Prof. Yutian Liu of Shandong University, Prof. Yue Yuan of Hohai University, Prof. Chengyong Zhao of North China Electric Power University, Prof. Xiong Du of Chongqing University and Prof. Yuehui Huang of CEPRI have reviewed the draft of this book and made many valuable comments and suggestions, from which the authors benefit greatly and are grateful.

With regard to the authors' level, there are inevitably shortcomings or omissions in the book so that the authors would appreciate readers' criticism and comments.

Beijing, China
November 2022

Weisheng Wang

Contents

1 Introduction 1
1.1 Background 1
1.2 Analysis Method of Oscillation 4
1.3 Mitigation Method of Oscillation 8
References 10

Part I Small-Signal Modeling of Converters

2 Frequency-Domain Small-Signal Modeling Method 15
2.1 Linearization of Power Electronic Nonlinear System 16
2.1.1 Nonlinear Model 16
2.1.2 Linearized Model 17
2.2 Frequency-Domain Linearization 19
2.2.1 Steady-State Operating Point in Frequency Domain 19
2.2.2 Linearization Analysis in Frequency Domain 22
2.3 Frequency-Domain Linearization of Typical Nonlinearity 25
2.3.1 Linearization of Switching Process 25
2.3.2 Linearization of Modulation Process 28
2.3.3 Linearization of Park Transformation and PLL 29
References 33

3 Impedance Modeling of Two-Level Converter 35
3.1 Operation Principle 35
3.1.1 Topology 35
3.1.2 Averaged Model 36
3.1.3 Control Strategy 37
3.2 Frequency-Domain Modeling of Steady-State Operation 38
3.2.1 Frequency-Domain Characteristic Analysis of Steady-State Operating Point 38
3.2.2 Frequency-Domain Steady-State Model of Main Circuit 41

3.3 Small-Signal Impedance Modeling in Frequency Domain 42
3.3.1 Small-Signal Frequency-Domain Characteristic Analysis 43
3.3.2 Frequency-Domain Small-Signal Model of Main Circuit 46
3.3.3 Frequency-Domain Small-Signal Model of Control Loops 48
3.3.4 AC Port Impedance Model 53
References 57

4 Impedance Modeling of Modular Multilevel Converter 59
4.1 Averaged Modeling of MMC Arm 59
4.1.1 Topology 60
4.1.2 Operation Principle of Submodules 60
4.1.3 Equivalent Model of MMC Arm 64
4.2 Time-Domain Modeling of Main Circuit 66
4.2.1 Time-Domain Characteristic Analysis of Arm Voltage and Current 66
4.2.2 Time-Domain Model of Arm Circuit 73
4.3 Frequency-Domain Modeling of Steady-State Operation 74
4.3.1 Frequency-Domain Characteristic Analysis of Steady-State Operating Point 74
4.3.2 Frequency-Domain Steady-State Model of Main Circuit 79
4.4 Small-Signal Impedance Modeling in Frequency Domain 82
4.4.1 Small-Signal Frequency-Domain Characteristic Analysis 82
4.4.2 Frequency-Domain Small-Signal Model of Main Circuit 87
4.4.3 Frequency-Domain Small-Signal Model of Control Loops 90
4.4.4 AC Port Impedance Model 102
Reference 104

5 Impedance Modeling of Thyristor Converter 105
5.1 Operation Principle 105
5.1.1 Topology 106
5.1.2 Conduction Principle 106
5.2 Time-Domain Modeling of Main Circuit 108
5.2.1 Time-Domain Model Without Considering Commutation Overlap 109
5.2.2 Time-Domain Model Considering Commutation Overlap 110
5.3 Frequency-Domain Modeling of Steady-State Operation 114
5.3.1 Frequency-Domain Characteristic Analysis of Steady-State Operating Point 115

5.3.2 Frequency-Domain Steady-State Model of Main Circuit 118
5.4 Small-Signal Impedance Modeling in Frequency Domain 121
5.4.1 Small-Signal Frequency-Domain Characteristic Analysis 121
5.4.2 Frequency-Domain Small-Signal Model of Main Circuit 127
5.4.3 Frequency-Domain Small-Signal Model of Switching Functions 128
5.4.4 AC Port Impedance Model 141

Part II Impedance Model and Characteristic Analysis of REG and HVDC Transmission

6 Impedance Model and Characteristic Analysis of Full Power Converter-Based Wind Turbine 147
6.1 Operation Principle and Control Strategy 147
6.1.1 Operation Principle 148
6.1.2 Time-Domain Model of PMSG-Based Wind Turbine 150
6.1.3 Control Strategy 155
6.2 Frequency-Domain Modeling of Steady-State Operation 158
6.2.1 Frequency-Domain Characteristic Analysis of Steady-State Operating Point 158
6.2.2 Frequency-Domain Steady-State Model of Main Circuit 161
6.3 Small-Signal Impedance Modeling in Frequency Domain 162
6.3.1 Small-Signal Frequency-Domain Characteristic Analysis 163
6.3.2 Frequency-Domain Small-Signal Model 168
6.3.3 AC Port Impedance Model 173
6.4 Analysis of Broadband Impedance Characteristics 176
6.4.1 Frequency-Band Division of Broadband Impedance 177
6.4.2 Analysis of Negative Damping Characteristics 182
References 195

7 Impedance Model and Characteristics Analysis of DFIG-Based Wind Turbines 197
7.1 Operation Principle and Control Strategy 197
7.1.1 Operation Principle 197
7.1.2 Time-Domain Model of DFIG-Based Wind Turbines 200
7.1.3 Control Strategy 207
7.2 Frequency-Domain Modeling of Steady-State Operation 210

7.2.1 Frequency-Domain Characteristics Analysis of Steady-State Operating Point 210
7.2.2 Frequency-Domain Steady-State Model of Main Circuit 214
7.3 Small-Signal Impedance Modeling in Frequency Domain 215
7.3.1 Small-Signal Frequency-Domain Characteristics Analysis 215
7.3.2 Frequency-Domain Small-Signal Model 220
7.3.3 AC Port Impedance Model 227
7.4 Analysis of Broadband Impedance Characteristics 229
7.4.1 Stator-GSC Decoupling Model 229
7.4.2 Frequency-Band Division of Broadband Impedance 232
7.4.3 Analysis of Negative Damping Characteristics 239
References 252

8 Impedance Model and Characteristic Analysis of PV Unit 253
8.1 Operation Principle and Time-Domain Model 253
8.1.1 Operation Principle 253
8.1.2 Time-Domain Model 256
8.2 Frequency-Domain Modeling of Steady-State Operation 256
8.2.1 Frequency-Domain Characteristic Analysis of Steady-State Operating Point 256
8.2.2 Frequency-Domain Steady-State Model of Main Circuit 259
8.3 Small-Signal Impedance Modeling in Frequency Domain 260
8.3.1 Small-Signal Frequency-Domain Characteristic Analysis 260
8.3.2 Frequency-Domain Small-Signal Model 263
8.3.3 AC Port Impedance Model 266
8.4 Analysis of Broadband Impedance Characteristics 268
8.4.1 Frequency-Band Division of Broadband Impedance 269
8.4.2 Analysis of Negative Damping Characteristics 273

9 Impedance Model and Characteristic Analysis of SVG 283
9.1 Operation Principle and Control Strategy 283
9.1.1 Topology 283
9.1.2 Operation Principle 284
9.1.3 Control Strategy 285
9.2 Frequency-Domain Modeling of Steady-State Operation 287
9.2.1 Frequency-Domain Characteristic Analysis of Steady-State Operating Point 288
9.2.2 Frequency-Domain Steady-State Model of Main Circuit 289

9.3 Small-Signal Impedance Modeling in Frequency Domain 290
9.3.1 Small-Signal Frequency-Domain Characteristic Analysis 291
9.3.2 Frequency-Domain Small-Signal Model 293
9.3.3 AC Port Impedance Model 298
9.4 Impedance Characteristic Analysis of Reactive Power Control Mode SVG 300
9.4.1 Frequency-Band Division of Broadband Impedance 302
9.4.2 Analysis of Negative Damping Characteristics 308
9.5 Impedance Characteristic Analysis of AC Voltage Control Mode SVG 315
9.5.1 Frequency-Band Division of Broadband Impedance 315
9.5.2 Analysis of Negative Damping Characteristics 319

10 Impedance Model and Characteristic Analysis of LCC-HVDC 325
10.1 Operation Principle and Control Strategy 325
10.1.1 Topology 325
10.1.2 Operation Principle 327
10.1.3 Control Strategy 332
10.2 Frequency-Domain Modeling of Steady-State Operation 334
10.2.1 Frequency-Domain Characteristic Analysis of Steady-State Operating Point 334
10.2.2 Frequency-Domain Steady-State Model of Main Circuit 340
10.3 Small-Signal Impedance Modeling in Frequency Domain 341
10.3.1 Small-Signal Frequency-Domain Characteristic Analysis 341
10.3.2 Frequency-Domain Small-Signal Model 345
10.3.3 AC Port Impedance Model 350
10.4 Analysis of Broadband Impedance Characteristics 353
10.4.1 Frequency-Band Division of Broadband Impedance 353
10.4.2 Analysis of Negative Damping Characteristics 360
Reference 365

11 Impedance Model and Characteristic Analysis of MMC-HVDC 367
11.1 Operation Principle and Control Strategy 368
11.1.1 Topology 368
11.1.2 Operation Principle 369
11.1.3 Control Strategy 375
11.2 Frequency-Domain Modeling of Steady-State Operation 379
11.2.1 Frequency-Domain Characteristic Analysis of Steady-State Operating Point 379

11.2.2 Frequency-Domain Steady-State Model of Main Circuit 382
11.3 Small-Signal Impedance Modeling in Frequency Domain 385
11.3.1 Small-Signal Frequency-Domain Characteristic Analysis 385
11.3.2 Frequency-Domain Small-Signal Model 388
11.3.3 AC Port Impedance Model 401
11.4 Impedance Characteristic Analysis of Passive Islanding Mode MMC-HVDC 405
11.4.1 Frequency-Band Division of Broadband Impedance 406
11.4.2 Analysis of Negative Damping Characteristics 416
11.5 Impedance Characteristic Analysis of Grid-Connected Mode MMC-HVDC 425
11.5.1 Frequency-Band Division of Broadband Impedance 425
11.5.2 Analysis of Negative Damping Characteristics 432
Reference 439

Part III Broadband Oscillation Analysis of REG and AC/DC Transmission System

12 Impedance Modeling and Analysis of REG Plant 443
12.1 Structure of REG Plant and Model of Collecting Network 443
12.1.1 Typical Structure of REG Plant 443
12.1.2 Collecting Line Model 446
12.1.3 Transformer Model 450
12.2 Impedance Modeling of REG Plant 455
12.2.1 Small-Signal Circuit Model Involving Frequency Coupling Effect 455
12.2.2 Impedance Network Model of Multi-Unit System Involving Frequency Coupling Effect 458
12.2.3 Equivalent Impedance Model of REG Plant Involving Frequency Coupling Effect 461
12.2.4 Calculation of Equivalent Impedance of REG Plant 466
12.3 Impedance Characteristic Analysis of REG Plant 469
12.3.1 Influence of Collecting Lines on the Impedance Characteristics 469
12.3.2 Influence of Transformer Levels on the Impedance Characteristics 471
12.3.3 Influence of Operation Mode on Impedance Characteristics 472
References 473

13 Analysis of Broadband Oscillation for REG Connected into HVAC System 475
13.1 Stability Criteria 475
13.2 Frequency-Band Division and Oscillation Analysis 478
13.2.1 Frequency-Band Division 478
13.2.2 Oscillation Risk Evaluation for PMSG/PV Plant Connected into Weak Grid 478
13.2.3 Oscillation Risk Evaluation for DFIG Plant Connected into Weak Grid 480
13.3 Frequency Coupling Effect Analysis 481
13.4 Simulation Verification 483
13.4.1 Oscillation Verification for PMSG/PV Plant Connected into Weak Grid 483
13.4.2 Oscillation Verification for DFIG Plant Connected into Weak Grid 490
13.5 Field Test Verification 493
13.5.1 Oscillation Verification for PMSG/PV Plant Connected into Weak Grid 494
13.5.2 Oscillation Verification for DFIG Plant Connected into Weak Grid 496
References 500

14 Analysis of Broadband Oscillation for REG Connected into HVDC System 501
14.1 Analysis of Oscillation for REG Connected into LCC-HVDC System 502
14.1.1 Stability Criteria 502
14.1.2 Frequency-Band Division and Oscillation Analysis 504
14.1.3 Simulation Verification 508
14.2 Analysis of Oscillation for REG Connected into MMC-HVDC System 516
14.2.1 Stability Criteria 516
14.2.2 Frequency-Band Division and Oscillation Analysis 520
14.2.3 Simulation Verification 523
Reference 528

Part IV Broadband Oscillation Mitigation of REG and AC/DC Transmission Systems

15 Oscillation Mitigation Based on Impedance Reshaping of REG Unit 531
15.1 Impedance Reshaping of PMSG-Based Wind Turbine 532
15.1.1 Impedance Reshaping Strategy 532
15.1.2 Reshaped Impedance Model 534
15.1.3 Impedance Reshaping Design 536
15.1.4 Simulation Verification 543
15.1.5 Field Test Verification 547

15.2 Impedance Reshaping of DFIG-Based Wind Turbine 548
15.2.1 Impedance Reshaping Strategy 549
15.2.2 Reshaped Impedance Model 551
15.2.3 Impedance Reshaping Design 553
15.2.4 Simulation Verification 561
15.2.5 Field Test Verification 565
References 567

16 Oscillation Mitigation Based on the Impedance Reshaping of SVG 569
16.1 Impedance Reshaping of PMSG-Based Wind Plants 569
16.1.1 Impedance Reshaping Strategy of SVG 570
16.1.2 Reshaped Impedance Model of SVG 572
16.1.3 Impedance Reshaping Design 573
16.1.4 Simulation Verification 577
16.2 Impedance Reshaping of DFIG-Based Wind Plant 578
16.2.1 Impedance Reshaping Strategy of SVG 579
16.2.2 Reshaped Impedance Model of SVG 584
16.2.3 Impedance Reshaping Design 585
16.2.4 Simulation Verification 590

17 Oscillation Mitigation Based on Impedance Reshaping of LCC-HVDC 593
17.1 Impedance Reshaping Strategy of LCC-HVDC 593
17.2 Reshaped Impedance Model of LCC-HVDC 594
17.3 Impedance Reshaping Design of LCC-HVDC 598
17.3.1 Influence of PLL of the Sending-End LCC on Impedance Characteristics 599
17.3.2 Influence of Control Loops of the Receiving-End LCC on Impedance Characteristics 600
17.3.3 Influence of Main Circuit Parameters on Impedance Characteristics 602
17.4 Simulation Verification 603
17.4.1 Oscillation Mitigation of PMSG-Based Wind Plants Connected into LCC-HVDC System 603
17.4.2 Oscillation Mitigation of DFIG-Based Wind Plants Connected into LCC-HVDC System 604
17.4.3 Oscillation Mitigation of PV Plants Connected into LCC-HVDC System 605

18 Oscillation Mitigation Based on Impedance Reshaping of MMC-HVDC 609
18.1 Impedance Reshaping Strategy of MMC-HVDC 609
18.1.1 Impedance Reshaping Method of Band I_{MMC} 610
18.1.2 Impedance Reshaping Method of Band III_{MMC} 610
18.1.3 Impedance Reshaping Method of Band IV_{MMC} 610
18.2 Reshaped Impedance Model of MMC-HVDC 611

18.3 Impedance Reshaping Design of MMC-HVDC 612
18.3.1 Impedance Reshaping Design of Band I_{MMC} 612
18.3.2 Impedance Reshaping Design of Band III_{MMC} 614
18.3.3 Impedance Reshaping Design of Band IV_{MMC} 615
18.4 Simulation Verification 617
18.4.1 Oscillation Mitigation of PMSG-Based Wind Plants Connected into MMC-HVDC System 618
18.4.2 Oscillation Mitigation of DFIG-Based Wind Plants Connected into MMC-HVDC System 622
18.4.3 Oscillation Mitigation of Overhead Lines Connected into MMC-HVDC System 624
References 626

19 Project Cases of REG and AC/DC Transmission System Oscillation 627
19.1 Sub- and Super-Synchronous Oscillations of PMSG-Based Wind Plants Connected into Weak Grid 627
19.1.1 Project Overview 628
19.1.2 Oscillation Analysis 629
19.1.3 Oscillation Mitigation 633
19.2 Sub- and Super-Synchronous Oscillations of DFIG-Based Wind Plants Connected into Weak Grid 634
19.2.1 Project Overview 634
19.2.2 Oscillation Analysis 634
19.2.3 Oscillation Mitigation 638
19.3 High-Frequency Oscillation of REG Connected into MMC-HVDC 639
19.3.1 Project Overview 639
19.3.2 Oscillation Analysis 641
19.3.3 Oscillation Mitigation 643
19.4 High-Frequency Oscillation of REG Connected into MMC-HVDC 646
19.4.1 Project Overview 646
19.4.2 Oscillation Analysis 647
19.4.3 Oscillation Mitigation 649
19.5 Broadband Oscillation of REG Connected into LCC-HVDC 650
19.5.1 Project Overview 650
19.5.2 Oscillation Analysis 651
19.5.3 Oscillation Mitigation 658

Appendix A: Test and Experimental Verification Platform of REG and AC/DC Transmission Systems 663

Appendix B: Full Electromagnetic Transient Simulation Platform for REG and AC/DC Transmission Systems 669

Index 675

Abbreviations

AC	Alternating current
CHIL	Controller hardware-in-the-loop
CM	Common mode
CPS	Carrier phase shift
DC	Direct current
DFIG	Doubly-fed induction generator
DLL	Dynamic link library
DM	Differential mode
FACTS	Flexible alternating current transmission system
FBSM	Full-bridge submodule
FFT	Fast Fourier transform
FTT	Field type test
GCSC	Gate-controlled series capacitor
GM	Gain margin
GSC	Grid-side converter
HBSM	Half-bridge submodule
HVAC	High-voltage alternating current
HVDC	High-voltage direct current
IGBT	Insulated-gate bipolar transistor
LCC	Line-commutated converter
LCC-HVDC	Line-commutated converter-based high voltage direct current
LVRT	Low-voltage ride-through
MMC	Modular multilevel converter
MMC-HVDC	Modular multilevel converter-based high voltage direct current
MPPT	Maximum power point tracking
MSC	Machine-side converter
MTDC	Multi-terminal direct current
NLM	Nearest-level modulation
PCC	Point of common coupling
PI	Proportional integral
PLL	Phase lock loop

PM	Phase margin
PMSG	Permanent magnet synchronous generator
PV	Photovoltaic
PWM	Pulse width modulation
REG	Renewable energy generation
RSC	Rotor-side converter
SCF	Stationary coordinate frame
SCR	Short circuit ratio
SM	Submodule
SMES	Superconducting magnetic energy storage
SPWM	Sinusoidal pulse width modulation
SRF	Synchronous rotating frame
SSCI	Subsynchronous control interaction
SSO	Subsynchronous oscillation
SSSC	Static series synchronous compensator
SVC	Static var compensator
SVG	Static var generator
TCSC	Thyristor-controlled series compensation
UHVDC	Ultra-high-voltage direct current
UPFC	Unified power flow controller
VCCS	Voltage controlled current source
VSC	Voltage source converter
WTGS	Wind turbine generator system

Main Physical Quantity Symbols

Description:

1. The main symbols in this book are divided into four categories: electrical and signal variables, frequency-domain steady-state vectors and matrices, frequency-domain small-signal vectors, transfer functions and coefficients of controllers.
2. Each type of physical quantity is sorted alphabetically, with uppercase letters after lowercase letters and the Greek alphabet after English letters.
3. The physical quantities of the same letter are sorted by their subscripts, starting with numbers and then letters.
4. Individual physical quantities that appear less frequently are explained along with the text in the book.

Electrical and Signal Variables

a	Constant complex vector operator
a_0, c_0	Fourier series DC component
a_k	Fourier series coefficient of cosine component
A, φ	Amplitude and phase of small-signal component of combined angle at $f_\mathrm{p} - f_1$
A_α, φ_α	Amplitude and phase of small-signal component of trigger angle at $f_\mathrm{p} - f_1$
A_θ, φ_θ	Amplitude and phase of small-signal component of PLL output angle at $f_\mathrm{p} - f_1$
b_k	Fourier series coefficient of sine component
$B_\mathrm{au}^{(1)}$, $B_\mathrm{au}^{(2)}$, …, $B_\mathrm{au}^{(N)}$	Switching function of the ith SM in the phase-a upper arm ($i = 1 \sim N$)
$B_\mathrm{av}^{(1)}$, $B_\mathrm{av}^{(2)}$, …, $B_\mathrm{av}^{(N)}$	Switching function of the ith SM in the phase-a lower arm ($i = 1 \sim N$)

$B_{\mathrm{bu}}^{(1)}, B_{\mathrm{bu}}^{(2)}, \ldots, B_{\mathrm{bu}}^{(N)}$	Switching function of the ith SM in the phase-b upper arm ($i = 1 \sim N$)
$B_{\mathrm{bv}}^{(1)}, B_{\mathrm{bv}}^{(2)}, \ldots, B_{\mathrm{bv}}^{(N)}$	Switching function of the ith SM in the phase-b lower arm ($i = 1 \sim N$)
$B_{\mathrm{cu}}^{(1)}, B_{\mathrm{cu}}^{(2)}, \ldots, B_{\mathrm{cu}}^{(N)}$	Switching function of the ith SM in the phase-c upper arm ($i = 1 \sim N$)
$B_{\mathrm{cv}}^{(1)}, B_{\mathrm{cv}}^{(2)}, \ldots, B_{\mathrm{cv}}^{(N)}$	Switching function of the ith SM in the phase-c lower arm ($i = 1 \sim N$)
C_{dc}	DC bus capacitance
C_{dcL}	Line capacitor in a single $\prod$-line segment
C_{eeq}	Arm capacitor of receiving-end MMC
C_{eq}	Arm capacitor
C_{esm}	SM capacitor of receiving-end MMC
C_{f}	AC filter capacitance
C_{feq}	Arm capacitor of sending-end MMC
C_{fsm}	SM capacitor of sending-end MMC
C_{sm}	SM capacitor
$\boldsymbol{C}_{\mathrm{x}}(t)$	Time-domain transfer function matrix from state vector to output vector
D_{dr}	Duty cycle
$\boldsymbol{D}_{\mathrm{u}}(t)$	Time-domain transfer function matrix from input vector to output vector
$f(t)$	Periodic signal
$\hat{f}(t)$	Small-signal vector of periodical signal
f_1	Fundamental frequency
f_+, f_-, f_{z}	The positive-sequence, the negative-sequence and the zero-sequence components of the three-phase AC signals
$f_{\mathrm{a}}, f_{\mathrm{b}}, f_{\mathrm{c}}$	Three-phase AC signals
f_{abc}	Frequencies of small-signal components of arm DM currents
f_{car}	Frequency of the carrier wave
f_{cdq}	Frequencies of small-signal components of dq-axis circulating currents
f_{com}	Frequencies of small-signal components of arm CM currents
f_{dq}	Frequencies of small-signal components of dq-axis currents
f_{etc}	PLL bandwidth in receiving-end converter station
f_{fiac}	AC current loop bandwidth in sending-end MMC
f_{ftc}	PLL bandwidth in sending-end converter station
f_{gic}	GSC current loop bandwidth
f_{iac}	AC current loop bandwidth
f_{idc}	DC current loop bandwidth
f_{mcom}	Frequencies of small-signal components of arm CM modulation signals

f_{mdif}	Frequencies of small-signal components of arm DM modulation signal
f_{osc}	Oscillation frequency
f_{p}	Perturbation frequency
f_{pc}	Active power loop bandwidth
f_{qc}	Reactive power loop bandwidth
f_{r}	Rotor electrical frequency
f_{ric}	RSC current loop bandwidth
f_{rma}	Frequency of the modulation wave
f_{sic}	MSC current loop bandwidth
f_{tc}	PLL bandwidth
f_{vac}	AC voltage loop bandwidth
f_{vdc}	DC voltage loop bandwidth
f_{vs}	Overall voltage loop bandwidth
F_{k+}, F_{k-}, F_{k0}	The amplitude of the positive-sequence, the negative-sequence and the zero-sequence components at kf_1
i_{a}, i_{b}, i_{c}	Three-phase AC currents
i_{adc}, i_{bdc}, i_{cdc}	Three-phase current compensation quantities
i_{au}, i_{bu}, i_{cu}	Three-phase upper arm currents
i_{av}, i_{bv}, i_{cv}	Three-phase lower arm currents
i_{cd}, i_{cq}	d- and q-axis circulating currents
i_{cdref}, i_{cqref}	d- and q-axis circulating current references
i_{cira}, i_{cirb}, i_{circ}	Three-phase arm circulating currents
i_{coma}, i_{comb}, i_{comc}	Three-phase arm CM currents
i_{Cfa}, i_{Cfb}, i_{Cfc}	Three-phase AC currents of the filter capacitors
i_{Cfd}, i_{Cfq}	d- and q-axis capacitor currents
i_{d}, i_{q}	d- and q-axis currents
i_{dc}	DC current
i_{difa}, i_{difb}, i_{difc}	Three-phase arm DM currents
i_{dref}, i_{qref}	d- and q-axis current references
i_{ea}, i_{eb}, i_{ec}	Receiving-end three-phase AC currents
i_{ea1}, i_{eb1}, i_{ec1}	Three-phase AC currents of Converter I in the receiving-end LCC
i_{ea2}, i_{eb2}, i_{ec2}	Three-phase AC currents of Converter II in the receiving-end LCC
i_{eau}, i_{ebu}, i_{ecu}	Three-phase upper arm currents of receiving-end MMC
i_{eav}, i_{ebv}, i_{ecv}	Three-phase lower arm currents of receiving-end MMC
i_{ecd}, i_{ecq}	The d- and q-axis circulating currents of receiving-end MMC
i_{ecoma}, i_{ecomb}, i_{ecomc}	Three-phase arm CM currents of receiving-end MMC
i_{ed}, i_{eq}	The d- and q-axis currents of receiving-end MMC
i_{edc}	DC current of the receiving-end converter station
i_{edifa}, i_{edifb}, i_{edifc}	Three-phase arm DM currents of receiving-end MMC
i_{edref}, i_{eqref}	The d- and q-axis current references of receiving-end MMC

i_{fa}, i_{fb}, i_{fc}	Sending-end three-phase AC currents
i_{fa1}, i_{fb1}, i_{fc1}	Three-phase AC currents of Converter I in the sending-end LCC
i_{fa2}, i_{fb2}, i_{fc2}	Three-phase AC currents of Converter II in the sending-end LCC
i_{fau}, i_{fbu}, i_{fcu}	Three-phase upper arm currents of sending-end MMC
i_{fav}, i_{fbv}, i_{fcv}	Three-phase lower arm currents of sending-end MMC
i_{fcd}, i_{fcq}	The d- and q-axis circulating currents of sending-end MMC
i_{fcoma}, i_{fcomb}, i_{fcomc}	Three-phase arm CM currents of sending-end MMC
i_{fd}, i_{fq}	The d- and q-axis currents of sending-end MMC
i_{fdc}	DC current of the sending-end converter station
i_{fdifa}, i_{fdifb}, i_{fdifc}	Three-phase arm DM currents of sending-end MMC
i_{fdref}, i_{fqref}	The d- and q-axis current references of sending-end MMC
i_{ga}, i_{gb}, i_{gc}	Three-phase GSC AC currents
i_{gd}, i_{gq}	The d- and q-axis GSC currents
i_{gdref}, i_{gqref}	The d- and q-axis GSC current references
i_{pv}	PV array output current
i_{ra}, i_{rb}, i_{rc}	Three-phase rotor AC currents
i_{rd}, i_{rq}	The d- and q-axis rotor currents
i_{rp}, i_{rn}	Positive- and negative-sequence components of the rotor currents
i_{sa}, i_{sb}, i_{sc}	Three-phase stator AC currents
i_{sd}, i_{sq}	The d- and q-axis stator currents
i_{sdref}, i_{sqref}	The d- and q-axis stator current references
i_{sm}	SM input current
i_{sp}, i_{sn}	Positive- and negative-sequence components of the stator currents
I_1, φ_{i1}	Amplitude and phase of the fundamental frequency component of AC current
I_{dc}	Steady-state vector of DC current
I_{dcref}	DC current reference
I_k, $\varphi_{\mathrm{i}k}$	Amplitude and phase of the arm current harmonic component at kf_1
I_{m}	Maximum power point current under the standard condition
I'_{m}	Maximum power point current under the non-standard condition
I_{sc}	Short circuit current under the standard condition
I'_{sc}	Short circuit current under the non-standard condition
J	Mechanical inertia
k_{eT}	Transformer voltage ratio at the receiving end
k_{fT}	Transformer voltage ratio at the sending end
K_{e}	Turn ratio of stator and rotor windings

K_{m}	Modulation gain
l_{line}	DC transmission line length
L_{arm}	Arm inductor
L_{dc}	DC smoothing reactor
L_{dcL}	Line inductor in a single $\prod$-line segment
L_{earm}	Arm inductor of receiving-end MMC
L_{eg}	Inductor of receiving-end AC grid
L_{eT}	Transformer leakage inductance at the receiving end
L_{f}	AC filter inductance
L_{farm}	Arm inductor of sending-end MMC
L_{fT}	Transformer leakage inductance at the sending end
$L_{1\mathrm{s}}$, $L_{1\mathrm{r}}$	DFIG stator and rotor leakage inductance
L_{m}	Excitation inductance
L_{ms}, L_{mr}	DFIG stator and rotor mutual inductance
L_{s}, L_{r}	DFIG stator and rotor inductance
L_{s0}	Average value of PMSG stator self-inductance
L_{s2}	Second harmonic amplitude of PMSG stator self-inductance
L_{sd}, L_{sq}	PMSG stator dq-axis inductances
L_{T}	Equivalent commutation inductor
m_{a}, m_{b}, m_{c}	Three-phase modulation signals
m_{am}, m_{bm}, m_{cm}	Three-phase arm modulation signals
m_{au}, m_{bu}, m_{cu}	Three-phase upper arm modulation signals
m_{av}, m_{bv}, m_{cv}	Three-phase lower arm modulation signals
m_{cd}, m_{cq}	The d- and q-axis circulating modulation signals
m_{coma}, m_{comb}, m_{comc}	Three-phase arm CM modulation signals
m_{d}, m_{q}	The d- and q-axis modulation signals
m_{difa}, m_{difb}, m_{difc}	Three-phase arm DM modulation signals
m_{eau}, m_{ebu}, m_{ecu}	Three-phase upper arm modulation signals of receiving-end MMC
m_{eav}, m_{ebv}, m_{ecv}	Three-phase lower arm modulation signals of receiving-end MMC
m_{ecoma}, m_{ecomb}, m_{ecomc}	Three-phase arm CM modulation signals of receiving-end MMC
m_{ed}, m_{eq}	The d- and q-axis modulation signals of receiving-end MMC
m_{edifa}, m_{edifb}, m_{edifc}	Three-phase arm DM modulation signals of receiving-end MMC
m_{fau}, m_{fbu}, m_{fcu}	Three-phase upper arm modulation signals of sending-end MMC
m_{fav}, m_{fbv}, m_{fcv}	Three-phase lower arm modulation signals of sending-end MMC
m_{fcd}, m_{fcq}	The d- and q-axis circulating modulation signals of sending-end MMC

m_{fcoma}, m_{fcomb}, m_{fcomc}	Three-phase arm CM modulation signals of sending-end MMC
m_{fdifa}, m_{fdifb}, m_{fdifc}	Three-phase arm DM modulation signals of sending-end MMC
m_{fd}, m_{fq}	The d- and q-axis modulation signals of sending-end MMC
m_{ga}, m_{gb}, m_{gc}	Three-phase modulation signals of GSC
m_{gd}, m_{gq}	The d- and q-axis modulation signals of GSC
m_{ra}, m_{rb}, m_{rc}	Three-phase modulation signals of RSC
m_{sa}, m_{sb}, m_{sc}	Three-phase modulation signals of MSC
m_{vca}, m_{vcb}, m_{vcc}	Three-phase voltage balancing modulation signals
M_1	Fundamental modulation index
M_{s0}	Average value of PMSG stator mutual inductance
M_{s2}	Second harmonic amplitude of PMSG stator mutual inductance
n_{au}, n_{bu}, n_{cu}	Number of inserted SMs in three-phase upper arms
n_{av}, n_{bv}, n_{cv}	Number of inserted SMs in three-phase lower arms
n_r	Rotor mechanical speed
n_{s}	Stator magnetic field speed
n_{slip}	Rotor magnetic field speed relative to the rotor
N	Arm SM number
N_{DFIG}	Number of DFIG-based wind turbines
N_{e}	Arm SM number of receiving-end MMC
N_{f}	Arm SM number of sending-end MMC
N_{par}	Number of PV modules in parallel
N_{PMSG}	Number of PMSG-based wind turbines
N_{PV}	Number of PV units
N_{ser}	Number of PV modules in series
p	Pole pairs
P_{er}, Q_{er}	Output active and reactive power of DFIG rotor
P_{es}, Q_{es}	Output active and reactive power of DFIG stator
P_{g}, Q_{g}	Output active and reactive power of GSC
P_{load}, Q_{load}	Active and reactive power of sending-end MMC
P_{m}	Maximum power point output power under the standard condition
P'_{m}	Maximum power point output power under the non-standard condition
P_{N}	Rated power
P_{ref}, Q_{ref}	Active and reactive power references
R_{arm}	Arm resistor
R_{dcL}	Line resistor in a single $\prod$-line segment
R_{earm}	Arm resistor of receiving-end MMC
R_{farm}	Arm resistor of sending-end MMC
R_{min}	Radius of Nyquist forbidden area
R_{s}, R_{r}	Stator, rotor resistance

s_a, s_b, s_c	Three-phase switching function
s_{a0}, s_{b0}, s_{c0}	Three-phase ideal switching function
s_{ea1}, s_{eb1}, s_{ec1}	Three-phase switching functions of Converter I in receiving-end LCC
s_{ea2}, s_{eb2}, s_{ec2}	Three-phase switching functions of Converter I and Converter II in receiving-end LCC
s_{fa1}, s_{fb1}, s_{fc1}	Three-phase switching functions of Converter I in sending-end LCC
s_{fa2}, s_{fb2}, s_{fc2}	Three-phase switching functions of Converter I and Converter II in sending-end LCC
s_{ia}, s_{ib}, s_{ic}	Three-phase current switching functions
s_n	Slip
s_{va}, s_{vb}, s_{vc}	Three-phase voltage switching functions
S	Irradiance
S_{ref}	Irradiance under the standard condition
S_{SVG}	Rated capacity of SVG
t	Time
T	Temperature
T_1	Fundamental wave period
T_c	Control period
T_{car}	Carrier wave period
T_e	Electromagnetic torque
T_{eiac}	Filter time delay of AC current in receiving-end MMC
T_{eic}	Filter time delay of circulating current in receiving-end MMC
T_{evac}	Filter time delay of AC voltage in receiving-end MMC
T_{eval}	Control period of receiving-end MMC valve control
T_{evdc}	Filter time dalay of DC voltage in receiving-end MMC
T_{fiac}	Filter time delay of AC current in sending-end MMC
T_{fic}	Filter time delay of circulating current in sending-end MMC
T_{fpol}	Control period of sending-end MMC pole control
T_{fvac}	Filter time delay of AC voltage in sending-end MMC
T_{fval}	Control period of sending-end MMC valve control
T_{iac}	Filter time delay of AC current
T_{idcf}	Filter time delay of DC current
T_m	Mechanical torque
T_{ref}	Temperature under the standard condition
T_{rma}	Modulation period
T_s	Time delay
T_{vac}	Filter time delay of AC voltage
T_{vc}	Filter time delay of arm capacitor voltage
T_{vdcf}	Filter time delay of DC voltage
$\boldsymbol{u}$	Input vector
$\hat{\boldsymbol{u}}$	Small-signal input vector

$\boldsymbol{u}_0$	Input vector in equilibrium
$u_1, u_2, \ldots, u_r$	Input signals
$v_{\mathrm{a}}, v_{\mathrm{b}}, v_{\mathrm{c}}$	Three-phase AC voltages
$v_{\mathrm{ab}}, v_{\mathrm{ba}}, v_{\mathrm{bc}}, v_{\mathrm{cb}}, v_{\mathrm{ac}}, v_{\mathrm{ca}}$	ab, ba, bc, cb, ac, ca line voltages
$v_{\mathrm{am}}, v_{\mathrm{bm}}, v_{\mathrm{cm}}$	Three-phase arm voltages
v_{ao}	Output AC voltage of phase a
$v_{\mathrm{au}}, v_{\mathrm{bu}}, v_{\mathrm{cu}}$	Three-phase upper arm voltages
$v_{\mathrm{av}}, v_{\mathrm{bv}}, v_{\mathrm{cv}}$	Three-phase lower arm voltages
v_{C}	SM capacitor voltage
$v_{\mathrm{Cam}}, v_{\mathrm{Cbm}}, v_{\mathrm{Ccm}}$	Three-phase arm capacitor voltages
v_{car}	Carrier wave
$v_{\mathrm{Cau}}, v_{\mathrm{Cbu}}, v_{\mathrm{Ccu}}$	Three-phase upper arm capacitor voltages
$v_{\mathrm{Cau}}^{(1)}, v_{\mathrm{Cau}}^{(2)}, \ldots, v_{\mathrm{Cau}}^{(N)}$	Capacitor voltage of the ith SM in the phase-a upper arm ($i = 1 \sim N$)
$v_{\mathrm{Cav}}, v_{\mathrm{Cbv}}, v_{\mathrm{Ccv}}$	Three-phase lower arm capacitor voltages
$v_{\mathrm{Cav}}^{(1)}, v_{\mathrm{Cav}}^{(2)}, \ldots, v_{\mathrm{Cav}}^{(N)}$	Capacitor voltage of the ith SM in the phase-a lower arm ($i = 1 \sim N$)
$v_{\mathrm{Cbu}}^{(1)}, v_{\mathrm{Cbu}}^{(2)}, \ldots, v_{\mathrm{Cbu}}^{(N)}$	Capacitor voltage of the ith SM in the phase-b upper arm ($i = 1 \sim N$)
$v_{\mathrm{Cbv}}^{(1)}, v_{\mathrm{Cbv}}^{(2)}, \ldots, v_{\mathrm{Cbv}}^{(N)}$	Capacitor voltage of the ith SM in the phase-b lower arm ($i = 1 \sim N$)
$v_{\mathrm{Ccu}}^{(1)}, v_{\mathrm{Ccu}}^{(2)}, \ldots, v_{\mathrm{Ccu}}^{(N)}$	Capacitor voltage of the ith SM in the phase-c upper arm ($i = 1 \sim N$)
$v_{\mathrm{Ccv}}^{(1)}, v_{\mathrm{Ccv}}^{(2)}, \ldots, v_{\mathrm{Ccv}}^{(N)}$	Capacitor voltage of the ith SM in the phase-c lower arm ($i = 1 \sim N$)
$v_{\mathrm{coma}}, v_{\mathrm{comb}}, v_{\mathrm{comc}}$	Three-phase arm CM voltages
$v_{\mathrm{d}}, v_{\mathrm{q}}$	The d- and q-axis voltages
v_{dc}	DC voltage
v_{dcL}	DC output voltage
$v_{\mathrm{difa}}, v_{\mathrm{difb}}, v_{\mathrm{difc}}$	Three-phase arm DM voltages
$v_{\mathrm{ea}}, v_{\mathrm{eb}}, v_{\mathrm{ec}}$	Receiving-end three-phase AC voltages
$v_{\mathrm{ea1}}, v_{\mathrm{eb1}}, v_{\mathrm{ec1}}$	Three-phase AC voltages of Converter I in receiving-end LCC
$v_{\mathrm{ea2}}, v_{\mathrm{eb2}}, v_{\mathrm{ec2}}$	Three-phase AC voltages of Converter II in receiving-end LCC
$v_{\mathrm{eCau}}, v_{\mathrm{eCbu}}, v_{\mathrm{eCcu}}$	Three-phase upper arm capacitor voltages of receiving-end MMC
$v_{\mathrm{eCav}}, v_{\mathrm{eCbv}}, v_{\mathrm{eCcv}}$	Three-phase lower arm capacitor voltages of receiving-end MMC
$v_{\mathrm{ed}}, v_{\mathrm{eq}}$	The d- and q-axis voltages of receiving-end MMC
v_{edc}	DC voltage of receiving-end converter station
$v_{\mathrm{edifa}}, v_{\mathrm{edifb}}, v_{\mathrm{edifc}}$	Three-phase arm DM voltages of receiving-end MMC
v_{eO}	Receiving-end AC neutral voltage
$v_{\mathrm{eTa}}, v_{\mathrm{eTb}}, v_{\mathrm{eTc}}$	Line-side three-phase AC voltages at receiving end
$v_{\mathrm{fa}}, v_{\mathrm{fb}}, v_{\mathrm{fc}}$	Sending-end three-phase AC voltages

v_{fa1}, v_{fb1}, v_{fc1}	Three-phase AC voltages of Converter I in sending-end LCC
v_{fa2}, v_{fb2}, v_{fc2}	Three-phase AC voltages of Converter II in sending-end LCC
v_{fcoma}, v_{fcomb}, v_{fcomc}	Three-phase arm CM voltages of sending-end MMC
v_{fd}, v_{fq}	The d- and q-axis voltages of sending-end MMC
v_{fdc}	DC voltage of sending-end converter station
v_{fdifa}, v_{fdifb}, v_{fdifc}	Three-phase arm DM voltages of sending-end MMC
v_{fCau}, v_{fCbu}, v_{fCcu}	Three-phase upper arm capacitor voltages of sending-end MMC
v_{fCav}, v_{fCbv}, v_{fCcv}	Three-phase lower arm capacitor voltages of sending-end MMC
v_{fO}	Sending-end AC neutral voltage
v_{fTa}, v_{fTb}, v_{fTc}	Line-side three-phase AC voltages at the sending end
v_{ga}, v_{gb}, v_{gc}	Three-phase modulation voltages of GSC
v_{ia}, v_{ib}, v_{ic}	Three-phase modulation voltages
v_{NO}	DC negative port voltage
v_{O}	AC neutral voltage
v_{PO}	DC positive port voltage
v_{ra}, v_{rb}, v_{rc}	Three-phase AC voltages of the rotor
v_{rd}, v_{rq}	The d- and q-axis rotor voltages
v_{rma}	Modulation wave
v_{rp}, v_{rn}	Positive- and negative-sequence components of the rotor voltage
v_{sa}, v_{sb}, v_{sc}	Three-phase AC voltages of the stator
v_{sd}, v_{sq}	The d- and q-axis stator voltages
v_{sm}	SM output voltage
$v_{\mathrm{sm_au}}^{(1)}$, $v_{\mathrm{sm_au}}^{(2)}$, …, $v_{\mathrm{sm_au}}^{(N)}$	Output voltage of the ith SM in the phase-a upper arm ($i = 1 \sim N$)
$v_{sm_av}^{(1)}$, $v_{\mathrm{sm_av}}^{(2)}$, …, $v_{\mathrm{sm_av}}^{(N)}$	Output voltage of the ith SM in the phase-a lower arm ($i = 1 \sim N$)
$v_{\mathrm{sm_bu}}^{(1)}$, $v_{\mathrm{sm_bu}}^{(2)}$, …, $v_{\mathrm{sm_bu}}^{(N)}$	Output voltage of the ith SM in the phase-b upper arm ($i = 1 \sim N$)
$v_{\mathrm{sm_bv}}^{(1)}$, $v_{\mathrm{sm_bv}}^{(2)}$, …, $v_{\mathrm{sm_bv}}^{(N)}$	Output voltage of the ith SM in the phase-b lower arm ($i = 1 \sim N$)
$v_{\mathrm{sm_cu}}^{(1)}$, $v_{\mathrm{sm_cu}}^{(2)}$, …, $v_{\mathrm{sm_cu}}^{(N)}$	Output voltage of the ith SM in the phase-c upper arm ($i = 1 \sim N$)
$v_{\mathrm{sm_cv}}^{(1)}$, $v_{\mathrm{sm_cv}}^{(2)}$, …, $v_{\mathrm{sm_cv}}^{(N)}$	Output voltage of the ith SM in the phase-c lower arm ($i = 1 \sim N$)
v_{sp}, v_{sn}	Positive- and negative-sequence components of the stator voltage
v_{Ta}, v_{Tb}, v_{Tc}	Three-phase AC input voltages
V_1, φ_{v1}	Amplitude and phase of the fundamental frequency component of AC voltage
V_{acref}	AC voltage reference

V_{car}	Amplitude of the carrier wave
V_C	Rated SM capacitor voltage
V_{dc}	Steady-state value of DC voltage
V_{dcref}	DC voltage reference
V_{e1}, φ_{ev1}	Amplitude and phase of the fundamental frequency component of receiving-end AC voltage
V_{f1}, φ_{fv1}	Amplitude and phase of the fundamental frequency component of sending-end AC voltage
V_{fdc}	Steady-state value of DC voltage in sending-end converter station
V_m	Maximum power point voltage under the standard condition
V_{oc}	Open circuit voltage under the standard condition
V'_{oc}	Open circuit voltage under the non-standard condition
W_m	Stored energy and magnetic coenergy of the magnetic field
$\boldsymbol{x}$	State vector
$\hat{\boldsymbol{x}}$	Small-signal state vector
$\boldsymbol{x}_0$	State vector in equilibrium
$x_1, x_2, \ldots, x_n$	State variables
$\dot{x}_1, \dot{x}_2, \ldots, \dot{x}_n$	Derivative of state variables to time
$\boldsymbol{y}$	Output vector
$Z_{load}(s)$	Sending-end AC load impedance
Δs_{ia}, Δs_{ib}, Δs_{ic}	Three-phase current switching functions variations
Δs_{va}, Δs_{vb}, Δs_{vc}	Three-phase voltage switching function variations
ΔS	Irradiance difference between the non-standard and standard conditions
ΔT	Temperature difference between the non-standard and standard conditions
α	Trigger angle
α_0	Steady-state trigger angle
α_e	Trigger angle of receiving-end LCC
α_{e0}	Steady-state trigger angle of receiving-end LCC
α_f	Trigger angle of sending-end LCC
α_{f0}	Steady-state trigger angle of sending-end LCC
α_{fmin}	Minimum trigger angle of sending-end LCC
β_a, β_b, β_c	Phase-shift angles between three phases
γ	Propagation characteristic of the overhead line
$\gamma_1, \gamma_2, \gamma_3, \gamma_4, \gamma_5, \gamma_6$	Phase-shift angles of the six natural commutation points
$\gamma_{e1}, \gamma_{e2}, \ldots, \gamma_{e12}$	Phase-shift angles of the twelve natural commutation points in receiving-end LCC
$\gamma_{f1}, \gamma_{f2}, \ldots, \gamma_{f12}$	Phase-shift angles of the twelve natural commutation points in sending-end LCC
μ	Overlap angle
μ_e	Overlap angle of receiving-end LCC

μ_{ei}	Equivalent current overlap angle of receiving-end LCC
μ_f	Overlap angle of sending-end LCC
μ_{fi}	Equivalent current overlap angle of sending-end LCC
μ_i	Equivalent current overlap angle
$\theta_1, \theta_2, \theta_3, \theta_4, \theta_5, \theta_6$	Reference angle of six thyristors
$\theta_{e1}, \theta_{e2}, \ldots, \theta_{e12}$	Reference angles of twelve thyristors in receiving-end LCC
θ_{ePLL}	PLL output angle of receiving-end converter station
θ_{etc}	PLL PM in receiving-end converter station
θ_f	Rotation reference angle of sending-end MMC
$\theta_{f1}, \theta_{f2}, \ldots, \theta_{f12}$	Reference angles of twelve thyristors in sending-end LCC
θ_{fiac}	AC current loop PM in sending-end MMC
θ_{fPLL}	PLL output angle of sending-end converter station
θ_{ftc}	PLL PM in sending-end converter station
θ_{gic}	GSC current loop PM
θ_{iac}	AC current loop PM
θ_{idc}	DC current loop PM
θ_{pc}	Active power loop PM
θ_{PLL}	PLL output angle
θ_{qc}	Reactive power loop PM
θ_r	Electrical angle of rotor rotating coordinate frame
θ_{ric}	RSC current loop PM
θ_s	Electrical angle of SRF
θ_{sic}	MSC current loop PM
θ_{slip}	Relative electrical angle of rotor rotating coordinate frame and SRF
θ_{tc}	PLL PM
θ_{vac}	AC voltage loop PM
θ_{vdc}	DC voltage loop PM
θ_{vs}	Overall voltage loop PM
ω_1	Angular velocity at f_1
ω_p	Angular velocity at f_p
ω_r	Rotor electrical angular frequency
ω_s	Electrical angular frequency of SRF
$\psi_{fa}, \psi_{fb}, \psi_{fc}$	PMSG rotor flux linkage
ψ_{fd}, ψ_{fq}	The d- and q-axis PMSG rotor flux linkage
ψ_{fp}, ψ_{fn}	Positive- and negative-sequence components of PMSG rotor flux linkage
$\psi_{ra}, \psi_{rb}, \psi_{rc}$	DFIG rotor flux linkage
ψ_{rd}, ψ_{rq}	The d- and q-axis DFIG rotor flux linkage
ψ_{rp}, ψ_{rn}	Positive- and negative-sequence components of DFIG rotor flux linkage
$\psi_{sa}, \psi_{sb}, \psi_{sc}$	Stator flux linkage
ψ_{sd}, ψ_{sq}	The d- and q-axis the stator flux linkage

ψ_{sp}, ψ_{sn}	Positive- and negative-sequence components of the stator flux linkage
ψ_{f}	PMSG rotor flux linkage
σ	Leakage coefficient
φ_{k+}, φ_{k-}, φ_{k0}	The phase of the positive-sequence, the negative-sequence and the zero-sequence components at kf_1

Frequency-Domain Steady-State Vectors and Matrices

$\boldsymbol{A}$	Transformation matrix of arm steady-state vectors
$\boldsymbol{A}_{\mathrm{c}}$	CM matrix of arm steady-state vectors
$\boldsymbol{A}_{\mathrm{c0}}$	Zero-sequence CM matrix of arm steady-state vectors
$\boldsymbol{A}_{\mathrm{d}}$	DM matrix of arm steady-state vectors
$\boldsymbol{A}_{\mathrm{p}}$	Transformation matrix of arm small-signal vector
$\boldsymbol{A}_{\mathrm{pc}}$	CM matrix of arm small-signal vectors
$\boldsymbol{A}_{\mathrm{pc0}}$	Zero-sequence CM matrix of the arm small-signal vectors
$\boldsymbol{A}_{\mathrm{pd}}$	DM matrix of arm small-signal vectors
$\boldsymbol{A}_{\mathrm{pd0}}$	Modified admittance matrix of arm inductor
$\boldsymbol{A}_{\mathrm{x}}(s)$	Frequency-domain transfer function matrix from state vector to the derivative of state vector
$\boldsymbol{B}$	Transformation matrix
$\boldsymbol{B}_{\mathrm{u}}(s)$	Frequency-domain transfer function matrix from input vector to the derivative of state vector
$\boldsymbol{C}$	Transformation coefficient matrix of switching functions
$\boldsymbol{C}_{\mathrm{x}}(s)$	Frequency-domain transfer function matrix from state vector to output vector
$\boldsymbol{D}$	Phase-sequence coefficient matrix of steady-state vectors
$\boldsymbol{D}_{\mathrm{ad}}$	AC/DC conversion matrix
$\boldsymbol{D}_{\mathrm{p}}$	Phase-sequence coefficient matrix of small-signal vectors

$\boldsymbol{D}_{\mathrm{u}}(s)$	Frequency-domain transfer function matrix from input vector to output vector
$\boldsymbol{F}(s)$	Steady-state vector of the periodic signal
$\boldsymbol{F}_{\mathrm{c\theta a}}(s)$, $\boldsymbol{F}_{\mathrm{c\theta b}}(s)$, $\boldsymbol{F}_{\mathrm{c\theta c}}(s)$	Frequency-domain vectors of $\cos\theta_{\mathrm{PLL}}$, $\cos(\theta_{\mathrm{PLL}} - 2\pi/3)$, $\cos(\theta_{\mathrm{PLL}} + 2\pi/3)$
$\boldsymbol{F}_k$	Steady-state component of the periodic signal at kf_1
$\boldsymbol{F}_{\mathrm{s\theta a}}(s)$, $\boldsymbol{F}_{\mathrm{s\theta b}}(s)$, $\boldsymbol{F}_{\mathrm{s\theta c}}(s)$	Frequency-domain vectors of $\sin\theta_{\mathrm{PLL}}$, $\sin(\theta_{\mathrm{PLL}} - 2\pi/3)$, $\sin(\theta_{\mathrm{PLL}} + 2\pi/3)$
$\boldsymbol{G}$	Frequency-domain transfer function vectors of the nonlinear equations $\boldsymbol{g}$
$\boldsymbol{H}$	Frequency-domain transfer function vectors of the nonlinear equations $\boldsymbol{h}$
$\boldsymbol{I}_1$	Steady-state component of AC current at f_1
$\boldsymbol{I}_{\mathrm{a}}$, $\boldsymbol{I}_{\mathrm{b}}$, $\boldsymbol{I}_{\mathrm{c}}$	Steady-state vectors of three-phase AC currents
$\boldsymbol{I}_{\mathrm{a}}(s)$, $\boldsymbol{I}_{\mathrm{b}}(s)$, $\boldsymbol{I}_{\mathrm{c}}(s)$	Frequency-domain steady-state vectors of three-phase AC currents
$\boldsymbol{I}_{\mathrm{au}}$, $\boldsymbol{I}_{\mathrm{bu}}$, $\boldsymbol{I}_{\mathrm{cu}}$	Steady-state vectors of three-phase upper arm currents
$\boldsymbol{I}_{\mathrm{av}}$, $\boldsymbol{I}_{\mathrm{bv}}$, $\boldsymbol{I}_{\mathrm{cv}}$	Steady-state vectors of three-phase lower arm currents
$\boldsymbol{I}_{\mathrm{coma}}$, $\boldsymbol{I}_{\mathrm{comb}}$, $\boldsymbol{I}_{\mathrm{comc}}$	Three-phase arm CM currents
$\boldsymbol{I}_{\mathrm{Cf1}}$	Steady-state fundamental component of AC currents of filter capacitors
$\boldsymbol{I}_{\mathrm{dc}}$	Steady-state vector of DC current
$\boldsymbol{I}_{\mathrm{ea}}$, $\boldsymbol{I}_{\mathrm{eb}}$, $\boldsymbol{I}_{\mathrm{ec}}$	Steady-state vectors of receiving-end three-phase AC currents
$\boldsymbol{I}_{\mathrm{eau}}$, $\boldsymbol{I}_{\mathrm{ebu}}$, $\boldsymbol{I}_{\mathrm{ecu}}$	Steady-state vectors of three-phase upper arm currents in receiving-end MMC
$\boldsymbol{I}_{\mathrm{eav}}$, $\boldsymbol{I}_{\mathrm{ebv}}$, $\boldsymbol{I}_{\mathrm{ecv}}$	Steady-state vectors of three-phase lower arm currents in receiving-end MMC
$\boldsymbol{I}_{\mathrm{edc}}$	Steady-state vector of DC current in receiving-end converter station
$\boldsymbol{I}_{\mathrm{fa}}$, $\boldsymbol{I}_{\mathrm{fb}}$, $\boldsymbol{I}_{\mathrm{fc}}$	Steady-state vectors of sending-end three-phase AC currents

$\boldsymbol{I}_{\mathrm{fa},6n_1\pm1+12n_2}$, $\boldsymbol{I}_{\mathrm{fb},6n_1\pm1+12n_2}$, $\boldsymbol{I}_{\mathrm{fc},6n_1\pm1+12n_2}$	Steady-state harmonic components of sending-end three-phase AC currents at $(6n_1 \pm 1 + 12n_2) f_1$
$\boldsymbol{I}_{\mathrm{fa1},6n_1\pm1+12n_2}$, $\boldsymbol{I}_{\mathrm{fb1},6n_1\pm1+12n_2}$, $\boldsymbol{I}_{\mathrm{fc1},6n_1\pm1+12n_2}$	Steady-state harmonic components of three-phase AC currents of Converter I at $(6n_1 \pm 1 + 12n_2) f_1$ in sending-end LCC
$\boldsymbol{I}_{\mathrm{fa2},6n_1\pm1+12n_2}$, $\boldsymbol{I}_{\mathrm{fb2},6n_1\pm1+12n_2}$, $\boldsymbol{I}_{\mathrm{fc2},6n_1\pm1+12n_2}$	Steady-state harmonic components of three-phase AC currents of Converter II at $(6n_1 \pm 1 + 12n_2) f_1$ in sending-end LCC
$\boldsymbol{I}_{\mathrm{fau}}$, $\boldsymbol{I}_{\mathrm{fbu}}$, $\boldsymbol{I}_{\mathrm{fcu}}$	Steady-state vectors of three-phase upper arm currents in sending-end MMC
$\boldsymbol{I}_{\mathrm{fav}}$, $\boldsymbol{I}_{\mathrm{fbv}}$, $\boldsymbol{I}_{\mathrm{fcv}}$	Steady-state vectors of three-phase lower arm currents in sending-end MMC
$\boldsymbol{I}_{\mathrm{fcoma}}$, $\boldsymbol{I}_{\mathrm{fcomb}}$, $\boldsymbol{I}_{\mathrm{fcomc}}$	Steady-state vectors of three-phase arm circulating currents in sending-end MMC
$\boldsymbol{I}_{\mathrm{fdc}}$	Steady-state vector of DC current in sending-end converter station
$\boldsymbol{I}_{\mathrm{fdc},12n_2}$	Steady-state harmonic components of DC current in sending-end LCC at $12n_2 f_1$
$\boldsymbol{I}_{\mathrm{g}}$	Current of AC grid
$\boldsymbol{I}_{\mathrm{g1}}$	Steady-state component of GSC AC current at f_1
$\boldsymbol{I}_{\mathrm{ga}}$, $\boldsymbol{I}_{\mathrm{gb}}$, $\boldsymbol{I}_{\mathrm{gc}}$	Steady-state vectors of three-phase GSC AC currents
$\boldsymbol{I}_{\mathrm{ideal}}$	Current of REG port connected into ideal AC grid
$\boldsymbol{I}_{\mathrm{LCC}}$	LCC-HVDC current source
$\boldsymbol{I}_{\mathrm{out}}$	Current of REG port
$\boldsymbol{I}_{\mathrm{pv}}$	Steady-state vector of PV output current
$\boldsymbol{I}_{\mathrm{r1}}$	Steady-state component of rotor current at f_1
$\boldsymbol{I}_{\mathrm{ra}}$, $\boldsymbol{I}_{\mathrm{sb}}$, $\boldsymbol{I}_{\mathrm{sc}}$	Steady-state vectors of three-phase rotor currents
$\boldsymbol{I}_{\mathrm{RE}}$	Equivalent current source of REG plants
$\boldsymbol{I}_{\mathrm{s1}}$	Steady-state component of stator current at f_1

$\boldsymbol{I}_{\mathrm{sa}}$, $\boldsymbol{I}_{\mathrm{sb}}$, $\boldsymbol{I}_{\mathrm{sc}}$	Steady-state vectors of three-phase stator currents
$\boldsymbol{I}_{\mathrm{trans}}$	Current of HVDC
$\boldsymbol{M}_{1}$	Steady-state component of modulation signal at f_1
$\boldsymbol{M}_{\mathrm{a}}$, $\boldsymbol{M}_{\mathrm{b}}$, $\boldsymbol{M}_{\mathrm{c}}$	Steady-state vectors of three-phase modulation signals
$\boldsymbol{M}_{\mathrm{a}}(s)$, $\boldsymbol{M}_{\mathrm{b}}(s)$, $\boldsymbol{M}_{\mathrm{c}}(s)$	Frequency-domain steady-state vectors of three-phase AC modulation signals
$\boldsymbol{M}_{\mathrm{am}}$, $\boldsymbol{M}_{\mathrm{bm}}$, $\boldsymbol{M}_{\mathrm{cm}}$	Steady-state vectors of three-phase arm modulation signals
$\boldsymbol{M}_{\mathrm{au}}$, $\boldsymbol{M}_{\mathrm{bu}}$, $\boldsymbol{M}_{\mathrm{cu}}$	Steady-state vectors of three-phase upper arm modulation signals
$\boldsymbol{M}_{\mathrm{av}}$, $\boldsymbol{M}_{\mathrm{bv}}$, $\boldsymbol{M}_{\mathrm{cv}}$	Steady-state vectors of three-phase lower arm modulation signals
$\boldsymbol{M}_{\mathrm{eau}}$, $\boldsymbol{M}_{\mathrm{ebu}}$, $\boldsymbol{M}_{\mathrm{ecu}}$	Steady-state vectors of three-phase upper arm modulation signals in receiving-end MMC
$\boldsymbol{M}_{\mathrm{eav}}$, $\boldsymbol{M}_{\mathrm{ebv}}$, $\boldsymbol{M}_{\mathrm{ecv}}$	Steady-state vectors of three-phase lower arm modulation signals in receiving-end MMC
$\boldsymbol{M}_{\mathrm{fau}}$, $\boldsymbol{M}_{\mathrm{fbu}}$, $\boldsymbol{M}_{\mathrm{fcu}}$	Steady-state vectors of three-phase upper arm modulation signals in sending-end MMC
$\boldsymbol{M}_{\mathrm{fav}}$, $\boldsymbol{M}_{\mathrm{fbv}}$, $\boldsymbol{M}_{\mathrm{fcv}}$	Steady-state vectors of three-phase lower arm modulation signals in sending-end MMC
$\boldsymbol{M}_{\mathrm{g1}}$	Steady-state component of GSC modulation signal at f_1
$\boldsymbol{M}_{\mathrm{ga}}$, $\boldsymbol{M}_{\mathrm{gb}}$, $\boldsymbol{M}_{\mathrm{gc}}$	Steady-state vectors of three-phase GSC modulation signals
$\boldsymbol{M}_{\mathrm{r1}}$	Steady-state component of RSC modulation signal at f_1
$\boldsymbol{M}_{\mathrm{ra}}$, $\boldsymbol{M}_{\mathrm{rb}}$, $\boldsymbol{M}_{\mathrm{rc}}$	Steady-state vectors of three-phase RSC modulation signals
$\boldsymbol{M}_{\mathrm{s1}}$	Steady-state component of MSC modulation signal at f_1
$\boldsymbol{M}_{\mathrm{sa}}$, $\boldsymbol{M}_{\mathrm{sb}}$, $\boldsymbol{M}_{\mathrm{sc}}$	Steady-state vectors of three-phase MSC modulation signals
$\boldsymbol{S}_{\mathrm{a}}[k,m]$, $\boldsymbol{S}_{\mathrm{b}}[k,m]$, $\boldsymbol{S}_{\mathrm{c}}[k,m]$	Complex Fourier coefficients of three-phase switching functions at $kf_1 + m(f_{\mathrm{p}} - f_1)$

$\boldsymbol{S}_{\mathrm{eia}}$, $\boldsymbol{S}_{\mathrm{eib}}$, $\boldsymbol{S}_{\mathrm{eic}}$	Steady-state vectors of three-phase current switching functions in receiving-end LCC
$\boldsymbol{S}_{\mathrm{eva}}$, $\boldsymbol{S}_{\mathrm{evb}}$, $\boldsymbol{S}_{\mathrm{evc}}$	Steady-state vectors of three-phase voltage switching functions in receiving-end LCC
$\boldsymbol{S}_{\mathrm{fa1},6n\pm1}$, $\boldsymbol{S}_{\mathrm{fb1},6n\pm1}$, $\boldsymbol{S}_{\mathrm{fc1},6n\pm1}$	Steady-state components of three-phase switching functions of Converter I at $(6n \pm 1)f_1$ in sending-end LCC
$\boldsymbol{S}_{\mathrm{fa2},6n\pm1}$, $\boldsymbol{S}_{\mathrm{fb2},6n\pm1}$, $\boldsymbol{S}_{\mathrm{fc2},6n\pm1}$	Steady-state components of three-phase switching functions of Converter II at $(6n \pm 1)f_1$ in sending-end LCC
$\boldsymbol{S}_{\mathrm{fia}}$, $\boldsymbol{S}_{\mathrm{fib}}$, $\boldsymbol{S}_{\mathrm{fic}}$	Steady-state vectors of three-phase current switching functions in sending-end LCC
$\boldsymbol{S}_{\mathrm{fi}k}$	Steady-state components of current switching function at kf_1 in sending-end LCC
$\boldsymbol{S}_{\mathrm{fva}}$, $\boldsymbol{S}_{\mathrm{fvb}}$, $\boldsymbol{S}_{\mathrm{fvc}}$	Steady-state vectors of three-phase voltage switching functions in sending-end LCC
$\boldsymbol{S}_{\mathrm{fv}k}$	Steady-state components of voltage switching function at kf_1 in sending-end LCC
$\boldsymbol{S}_{\mathrm{ia}}$, $\boldsymbol{S}_{\mathrm{ib}}$, $\boldsymbol{S}_{\mathrm{ic}}$	Steady-state vectors of three-phase current switching functions
$\boldsymbol{S}_{\mathrm{ia}}[k,m]$, $\boldsymbol{S}_{\mathrm{ib}}[k,m]$, $\boldsymbol{S}_{\mathrm{ic}}[k,m]$	Complex Fourier coefficients of three-phase current switching functions at $kf_1 + m(f_{\mathrm{p}} - f_1)$
$\boldsymbol{S}_{\mathrm{va}}$, $\boldsymbol{S}_{\mathrm{vb}}$, $\boldsymbol{S}_{\mathrm{vc}}$	Steady-state vectors of three-phase voltage switching functions
$\boldsymbol{S}_{\mathrm{va}}[k,m]$, $\boldsymbol{S}_{\mathrm{vb}}[k,m]$, $\boldsymbol{S}_{\mathrm{vc}}[k,m]$	Complex Fourier coefficients of three-phase voltage switching functions at $kf_1 + m(f_{\mathrm{p}} - f_1)$
$\boldsymbol{T}_{\mathrm{O}}$	Zero-sequence DM matrix of steady-state vector
$\boldsymbol{T}_{\mathrm{p}}$	Zero-sequence DM matrix of arm small-signal vector
$\boldsymbol{U}$	Identity matrix
$\boldsymbol{U}(s)$	Frequency-domain steady-state vector of input signals
$\boldsymbol{U}_{\mathrm{p}}$	Complex exponential of the original input signals at f_{p}

$\boldsymbol{V}_1$	Steady-state component of AC voltage at f_1
$\boldsymbol{V}_{-1}$	Steady-state component of AC voltage at $-f_1$
$\boldsymbol{V}_\mathrm{a}$, $\boldsymbol{V}_\mathrm{b}$, $\boldsymbol{V}_\mathrm{c}$	Steady-state vectors of three-phase AC voltages
$\boldsymbol{V}_\mathrm{a}(s)$, $\boldsymbol{V}_\mathrm{b}(s)$, $\boldsymbol{V}_\mathrm{c}(s)$	frequency-domain steady-state vectors of three-phase AC voltages
$\boldsymbol{V}_\mathrm{Cam}$, $\boldsymbol{V}_\mathrm{Cbm}$, $\boldsymbol{V}_\mathrm{Ccm}$	Steady-state vectors of three-phase arm capacitor voltages
$\boldsymbol{V}_\mathrm{Cau}$, $\boldsymbol{V}_\mathrm{Cbu}$, $\boldsymbol{V}_\mathrm{Ccu}$	Steady-state vectors of three-phase upper arm capacitor voltages
$\boldsymbol{V}_\mathrm{Cav}$, $\boldsymbol{V}_\mathrm{Cbv}$, $\boldsymbol{V}_\mathrm{Ccv}$	Steady-state vectors of three-phase lower arm capacitor voltages
$\boldsymbol{V}_\mathrm{dc}$	Steady-state vector of DC voltage
$\boldsymbol{V}_\mathrm{dc}(s)$	Frequency-domain steady-state vector of DC voltage
$\boldsymbol{V}_\mathrm{ea}$, $\boldsymbol{V}_\mathrm{eb}$, $\boldsymbol{V}_\mathrm{ec}$	Steady-state vector of receiving-end three-phase AC voltages
$\boldsymbol{V}_\mathrm{ea1}$, $\boldsymbol{V}_\mathrm{eb1}$, $\boldsymbol{V}_\mathrm{ec1}$	Steady-state vectors of three-phase AC voltages of Converter I in receiving-end LCC
$\boldsymbol{V}_\mathrm{ea2}$, $\boldsymbol{V}_\mathrm{eb2}$, $\boldsymbol{V}_\mathrm{ec2}$	Steady-state vectors of three-phase AC voltages of Converter II in receiving-end LCC
$\boldsymbol{V}_\mathrm{eCau}$, $\boldsymbol{V}_\mathrm{eCbu}$, $\boldsymbol{V}_\mathrm{eCcu}$	Steady-state vectors of three-phase upper arm capacitor voltages in receiving-end MMC
$\boldsymbol{V}_\mathrm{eCav}$, $\boldsymbol{V}_\mathrm{eCbv}$, $\boldsymbol{V}_\mathrm{eCcv}$	Steady-state vectors of three-phase lower arm capacitor voltages in receiving-end MMC
$\boldsymbol{V}_\mathrm{edc}$	Steady-state vector of DC voltage in receiving-end converter station
$\boldsymbol{V}_\mathrm{eO}$	Steady-state vector of receiving-end AC neutral voltage
$\boldsymbol{V}_\mathrm{eTa}$, $\boldsymbol{V}_\mathrm{eTb}$, $\boldsymbol{V}_\mathrm{eTc}$	Steady-state vectors of line-side three-phase AC voltages at the receiving end
$\boldsymbol{V}_\mathrm{fa}$, $\boldsymbol{V}_\mathrm{fb}$, $\boldsymbol{V}_\mathrm{fc}$	Steady-state vector of sending-end three-phase AC voltages
$\boldsymbol{V}_\mathrm{fa1}$, $\boldsymbol{V}_\mathrm{fb1}$, $\boldsymbol{V}_\mathrm{fc1}$	Steady-state vectors of three-phase AC voltages of Converter I in sending-end LCC
$\boldsymbol{V}_{\mathrm{fa1},6n\pm1}$, $\boldsymbol{V}_{\mathrm{fb1},6n\pm1}$, $\boldsymbol{V}_{\mathrm{fc1},6n\pm1}$	Steady-state harmonic components of three-phase AC voltages of Converter I at $(6n \pm 1) f_1$ in sending-end LCC

$\boldsymbol{V}_{\mathrm{fa2}}$, $\boldsymbol{V}_{\mathrm{fb2}}$, $\boldsymbol{V}_{\mathrm{fc2}}$	Steady-state vectors of three-phase AC voltages of Converter II in sending-end LCC
$\boldsymbol{V}_{\mathrm{fa2},n\pm1}$, $\boldsymbol{V}_{\mathrm{fb2},6n\pm1}$, $\boldsymbol{V}_{\mathrm{fc2},6n\pm1}$	Steady-state harmonic components of three-phase AC voltages of Converter II at $(6n \pm 1) f_1$ in sending-end LCC
$\boldsymbol{V}_{\mathrm{fCau}}$, $\boldsymbol{V}_{\mathrm{fCbu}}$, $\boldsymbol{V}_{\mathrm{fCcu}}$	Steady-state vectors of three-phase upper arm capacitor voltages in sending-end MMC
$\boldsymbol{V}_{\mathrm{fCav}}$, $\boldsymbol{V}_{\mathrm{fCbv}}$, $\boldsymbol{V}_{\mathrm{fCcv}}$	Steady-state vectors of three-phase lower arm capacitor voltages in sending-end MMC
$\boldsymbol{V}_{\mathrm{fdc}}$	Steady-state vector of DC voltage in sending-end converter station
$\boldsymbol{V}_{\mathrm{fdc},6(n_1+n_2)}$	Steady-state harmonic components of DC voltage at $6(n_1+n_2) f_1$ in sending-end LCC
$\boldsymbol{V}_{\mathrm{fdc1},6(n_1+n_2)}$	Steady-state harmonic components of DC voltages of Converter I at $6(n_1 + n_2) f_1$ in sending-end LCC
$\boldsymbol{V}_{\mathrm{fdc2},6(n_1+n_2)}$	Steady-state harmonic components of DC voltages of Converter II at $6(n_1 + n_2) f_1$ in sending-end LCC
$\boldsymbol{V}_{\mathrm{fO}}$	Steady-state vector of sending-end AC neutral voltage
$\boldsymbol{V}_{\mathrm{fTa}}$, $\boldsymbol{V}_{\mathrm{fTb}}$, $\boldsymbol{V}_{\mathrm{fTc}}$	Steady-state vectors of line-side three-phase AC voltages at the sending end
$\boldsymbol{V}_{\mathrm{g}}$	AC grid voltage source
$\boldsymbol{V}_{\mathrm{g1}}$	Steady-state component of GSC voltage at f_1
$\boldsymbol{V}_{\mathrm{ga}}$, $\boldsymbol{V}_{\mathrm{gb}}$, $\boldsymbol{V}_{\mathrm{gc}}$	Steady-state vectors of three-phase GSC voltages
$\boldsymbol{V}_{\mathrm{i1}}$	Steady-state component of modulation voltage at f_1
$\boldsymbol{V}_{\mathrm{ia}}$, $\boldsymbol{V}_{\mathrm{ib}}$, $\boldsymbol{V}_{\mathrm{ic}}$	Steady-state vectors of three-phase modulation voltages
$\boldsymbol{V}_{\mathrm{L1}}$, $\boldsymbol{I}_{\mathrm{L1}}$	Steady-state voltage and current vectors at the beginning of overhead line or high voltage side of double winding transformer
$\boldsymbol{V}_{\mathrm{L2}}$, $\boldsymbol{I}_{\mathrm{L2}}$	Steady state voltage and current vectors at the end of overhead line or low-voltage side of double winding transformer
$\boldsymbol{V}_{\mathrm{MMC}}$	MMC-HVDC voltage source

$\boldsymbol{V}_{\mathrm{O}}$	Steady-state vector of AC neutral voltage
$\boldsymbol{V}_{\mathrm{r1}}$	Steady-state component of rotor voltage at f_1
$\boldsymbol{V}_{\mathrm{ra}}$, $\boldsymbol{V}_{\mathrm{rb}}$, $\boldsymbol{V}_{\mathrm{rc}}$	Steady-state vectors of three-phase rotor voltages
$\boldsymbol{V}_{\mathrm{s1}}$	Steady-state component of stator voltage at f_1
$\boldsymbol{V}_{\mathrm{sa}}$, $\boldsymbol{V}_{\mathrm{sb}}$, $\boldsymbol{V}_{\mathrm{sc}}$	Steady-state vectors of three-phase stator voltages
$\boldsymbol{V}_{\mathrm{sys}}$	Open-circuit voltage of the REG port
$\boldsymbol{V}_{\mathrm{Ta}}$, $\boldsymbol{V}_{\mathrm{Tb}}$, $\boldsymbol{V}_{\mathrm{Tc}}$	Steady-state vectors of three-phase AC input voltages
$\boldsymbol{X}(s)$	Steady-state vector of state variables
$\boldsymbol{Y}$	AC port admittance
$\boldsymbol{Y}_0$	Admittance of overhead line per unit length
$\boldsymbol{Y}_{\mathrm{B}}$	Admittance of the Π-type equivalent circuit for overhead line
$\boldsymbol{Y}_{\mathrm{Bpn}}$	Admittance matrix of overhead line
$\boldsymbol{Y}_{\mathrm{Cdc}}$	Small-signal admittance of DC-bus capacitor
$\boldsymbol{Y}_{\mathrm{Ceeq0}}$	Admittance of arm capacitor of receiving-end MMC in steady-state frequency order
$\boldsymbol{Y}_{\mathrm{Ceq0}}$	Admittance of arm capacitor in steady-state frequency order
$\boldsymbol{Y}_{\mathrm{Cfeq0}}$	Admittance of arm capacitor of sending-end MMC in steady-state frequency order
$\boldsymbol{Y}_{\mathrm{DFIG}}$	AC port admittance of DFIG-based wind turbines
$\boldsymbol{Y}_{\mathrm{DFIG}}^{\mathrm{nn}}$	Negative-sequence coupling admittance of PMSG-based wind turbines
$\boldsymbol{Y}_{\mathrm{DFIG}}^{\mathrm{np}}$	Negative-sequence coupling admittance of PMSG-based wind turbines
$\boldsymbol{Y}_{\mathrm{DFIG}}^{\mathrm{pn}}$	Positive-sequence coupling admittance of PMSG-based wind turbines
$\boldsymbol{Y}_{\mathrm{DFIG}}^{\mathrm{pp}}$	Positive-sequence admittance of PMSG-based wind turbines
$\boldsymbol{Y}_{\mathrm{edc}}$	DC port admittance of receiving-end converter station
$\boldsymbol{Y}_{\mathrm{Larm}}$	Admittance of arm inductor of receiving-end MMC in small-signal frequency order

$\boldsymbol{Y}_{\mathrm{LCC}}$	AC port admittance of LCC-HVDC at the sending end
$\boldsymbol{Y}'_{\mathrm{LCC}}$	AC port admittance of LCC-HVDC at the sending end after impedance reshaping
$\boldsymbol{Y}_{\mathrm{LCC}}^{\mathrm{nn}}$	Negative-sequence admittance of LCC-HVDC at the sending end
$\boldsymbol{Y}_{\mathrm{LCC}}^{\mathrm{np}}$	Negative-sequence coupling admittance of LCC-HVDC at the sending end
$\boldsymbol{Y}_{\mathrm{LCC}}^{\mathrm{pn}}$	Positive-sequence coupling admittance of MMC-HVDC at the sending end
$\boldsymbol{Y}_{\mathrm{LCC}}^{\mathrm{pp}}$	Positive-sequence admittance of MMC-HVDC at the sending end
$\boldsymbol{Y}_{\mathrm{Learm}}$	Admittance of arm inductor of receiving-end MMC in small-signal frequency order
$\boldsymbol{Y}_{\mathrm{Lfarm}}$	Admittance of arm inductor of sending-end MMC in small-signal frequency order
$\boldsymbol{Y}_{\mathrm{L}ij}$	Admittance matrix of the collecting line of turbine j of collecting line i
$\boldsymbol{Y}_{\mathrm{MMC}}$	AC port admittance of MMC-HVDC at the sending end
$\boldsymbol{Y}_{\mathrm{MT}}$	Admittance matrix of the main transformer of the wind farm
$\boldsymbol{Y}_{\mathrm{nn}}$	Negative-sequence admittance
$\boldsymbol{Y}_{\mathrm{np}}$	Negative-sequence coupling admittance
$\boldsymbol{Y}_{\mathrm{N}}^{\mathrm{nn}}$	Nodal admittance matrix of negative-sequence impedance network
$\boldsymbol{Y}_{\mathrm{N}}^{\mathrm{np}}$	Diagonal matrix composed of the negative-sequence coupling admittance of each turbine
$\boldsymbol{Y}_{\mathrm{N}}^{\mathrm{pn}}$	Diagonal matrix composed of the positive-sequence coupling admittance of each turbine
$\boldsymbol{Y}_{\mathrm{N}}^{\mathrm{pp}}$	Nodal admittance matrix of positive-sequence impedance network
$\boldsymbol{Y}_{\mathrm{pn}}$	Positive-sequence coupling admittance
$\boldsymbol{Y}_{\mathrm{pp}}$	Positive-sequence admittance
$\boldsymbol{Y}_{\mathrm{pv}}$	AC port admittance of PV units

$\boldsymbol{Y}_{\mathrm{PMSG}}$	AC port admittance of PMSG-based wind turbines
$\boldsymbol{Y}_{\mathrm{PMSG}}^{\mathrm{nn}}$	Negative-sequence coupling admittance of PMSG-based wind turbines
$\boldsymbol{Y}_{\mathrm{PMSG}}^{\mathrm{np}}$	Negative-sequence coupling admittance of PMSG-based wind turbines
$\boldsymbol{Y}_{\mathrm{PMSG}}^{\mathrm{pn}}$	Positive-sequence coupling admittance of PMSG-based wind turbine
$\boldsymbol{Y}_{\mathrm{PMSG}}^{\mathrm{pp}}$	Positive-sequence admittance of PMSG-based wind turbines
$\boldsymbol{Y}_{\mathrm{PV}}^{\mathrm{nn}}$	Negative-sequence admittance of PV units
$\boldsymbol{Y}_{\mathrm{PV}}^{\mathrm{np}}$	Negative-sequence coupling admittance of PV units
$\boldsymbol{Y}_{\mathrm{PV}}^{\mathrm{pn}}$	Positive-sequence coupling admittance of PV units
$\boldsymbol{Y}_{\mathrm{PV}}^{\mathrm{pp}}$	Positive-sequence admittance of PV units
$\boldsymbol{Y}_{\mathrm{self}}$	Sending-end LCC admittance
$\boldsymbol{Y}_{\mathrm{SVG}}$	AC port admittance of SVG
$\boldsymbol{Y}_{\mathrm{SVG}}^{\mathrm{nn}}$	Negative-sequence coupling admittance of SVG
$\boldsymbol{Y}_{\mathrm{SVG}}^{\mathrm{np}}$	Negative-sequence admittance of SVG
$\boldsymbol{Y}_{\mathrm{SVG}}^{\mathrm{pn}}$	Positive-sequence coupling admittance of SVG
$\boldsymbol{Y}_{\mathrm{SVG}}^{\mathrm{pp}}$	Positive-sequence admittance of SVG
$\boldsymbol{Y}_{\mathrm{T}}$	Admittance of the Γ-type equivalent circuit for double wing transformer
$\boldsymbol{Y}_{\mathrm{T}ij}$	Admittance matrix of the box transformer of turbine j of collecting line i
$\boldsymbol{Y}_{\mathrm{Tpn}}$	Admittance matrix of double wing transformer
$\boldsymbol{Y}_{\mathrm{WF}}$	Admittance matrix of wind farm
$\boldsymbol{Y}_{\mathrm{WF}}^{\mathrm{nn}}$	Negative-sequence admittance of wind farm
$\boldsymbol{Y}_{\mathrm{WF}}^{\mathrm{np}}$	Negative-sequence coupling admittance of wind farm
$\boldsymbol{Y}_{\mathrm{WF}}^{\mathrm{pn}}$	Positive-sequence coupling admittance of wind farm
$\boldsymbol{Y}_{\mathrm{WF}}^{\mathrm{pp}}$	Nodal admittance matrix of positive-sequence impedance network
$\boldsymbol{Y}_{\mathrm{W}ij}$	Admittance matrix of turbine j of collecting line i

$\boldsymbol{Z}$	AC port impedance
$\boldsymbol{Z}_0$	Impedance of overhead line per unit length
$\boldsymbol{Z}_{\text{array}}$	Impedance of PV array
$\boldsymbol{Z}_{\text{C}}$	Characteristic impedance of the overhead line
$\boldsymbol{Z}_{\text{CdcL}}$	Impedance of line capacitor in a single $\prod$-line segment
$\boldsymbol{Z}_{\text{Ceeq}}$	Admittance of arm capacitor of receiving-end MMC in small-signal frequency order
$\boldsymbol{Z}_{\text{Ceq}}$	Impedance of arm capacitor in small-signal frequency order
$\boldsymbol{Z}_{\text{Cfeq}}$	Admittance of arm capacitor of sending-end MMC in small-signal frequency order
$\boldsymbol{Z}_{\text{CN}}$	Equivalent impedance of transformers
$\boldsymbol{Z}_{\text{DFIG}}$	AC port impedance of DFIG-based wind turbines
$\boldsymbol{Z}_{\text{DFIG}}^{\text{nn}}$	Negative-sequence impedance of DFIG-based wind turbines
$\boldsymbol{Z}_{\text{DFIG}}^{\text{np}}$	Negative-sequence coupling impedance of DFIG-based wind turbines
$\boldsymbol{Z}_{\text{DFIG}}^{\text{pn}}$	Positive-sequence coupling impedance of DFIG-based wind turbines
$\boldsymbol{Z}_{\text{DFIG}}^{\text{pp}}$	Positive-sequence impedance of DFIG-based wind turbines
$\boldsymbol{Z}_{\text{eac}}$	AC-side impedance at the receiving end
$\boldsymbol{Z}_{\text{edc}}$	DC port impedance of receiving-end converter station
$\boldsymbol{Z}'_{\text{edc}}$	DC port admittance of receiving-end station after impedance reshaping
$\boldsymbol{Z}_{\text{eflt}}$	Receiving-end AC filter impedance in the small-signal frequency order
$\boldsymbol{Z}_{\text{eg}}$	Receiving-end AC grid impedance in small-signal frequency order
$\boldsymbol{Z}_{\text{eT}}$	Impedance of transformer leakage inductance at the receiving end in small-signal frequency order
$\boldsymbol{Z}_{\text{eT0}}$	Impedance of transformer leakage inductance at the receiving end in steady-state frequency order

$\boldsymbol{Z}_{\mathrm{fdc}}$	DC-side impedance of sending-end converter station
$\boldsymbol{Z}'_{\mathrm{fdc}}$	DC-side impedance of sending-end converter station after impedance reshaping
$\boldsymbol{Z}_{\mathrm{fflt}}$	Sending-end AC filter impedance
$\boldsymbol{Z}_{\mathrm{fT}}$	Impedance of transformer leakage inductance at the sending end in small-signal frequency order
$\boldsymbol{Z}_{\mathrm{fT0}}$	Impedance of transformer leakage inductance at the sending end in steady-state frequency order
$\boldsymbol{Z}_{\mathrm{g}}$	AC grid impedance
$\boldsymbol{Z}_{\mathrm{GSC}}$	GSC-side impedance of DFIG-based wind turbines
$\boldsymbol{Z}_{\mathrm{L}}$	Impedance of the Π-type equivalent circuit for overhead line
$\boldsymbol{Z}_{\mathrm{Larm0}}$	Impedance of arm inductor in steady-state frequency order
$\boldsymbol{Z}_{\mathrm{LCC}}$	AC port impedance of LCC-HVDC at the sending end
$\boldsymbol{Z}_{\mathrm{LCC}}^{\mathrm{nn}}$	Negative-sequence impedance of LCC-HVDC at the sending end
$\boldsymbol{Z}_{\mathrm{LCC}}^{\mathrm{np}}$	Negative-sequence coupling impedance of LCC-HVDC at the sending end
$\boldsymbol{Z}_{\mathrm{LCC}}^{\mathrm{pn}}$	Positive-sequence coupling impedance of LCC-HVDC at the sending end
$\boldsymbol{Z}_{\mathrm{LCC}}^{\mathrm{pp}}$	Positive-sequence impedance of LCC-HVDC at the sending end
$\boldsymbol{Z}_{\mathrm{Ldc}}$	Impedance of DC smoothing reactor
$\boldsymbol{Z}_{\mathrm{LdcL}}$	Impedance of line inductor in a single ∏-line segment
$\boldsymbol{Z}_{\mathrm{Learm0}}$	Impedance of arm inductor of sending-end MMC in steady-state frequency order
$\boldsymbol{Z}_{\mathrm{Lf}}$	Impedance of AC filter inductor in small-signal frequency order
$\boldsymbol{Z}_{\mathrm{Lf0}}$	Impedance of AC filter inductor in steady-state frequency order
$\boldsymbol{Z}_{\mathrm{Lfarm0}}$	Impedance of arm inductor of sending-end MMC in steady-state frequency order
$\boldsymbol{Z}_{\mathrm{Lpn}}$	Impedance matrix of overhead line

$\boldsymbol{Z}_{\mathrm{MMC}}$	AC port impedance of MMC-HVDC
$\boldsymbol{Z}_{\mathrm{MMC}}^{\mathrm{nn}}$	Negative-sequence impedance of MMC-HVDC at the sending end
$\boldsymbol{Z}_{\mathrm{MMC}}^{\mathrm{np}}$	Negative-sequence coupling impedance of MMC-HVDC at the sending end
$\boldsymbol{Z}_{\mathrm{MMC}}^{\mathrm{pn}}$	Positive-sequence coupling impedance of MMC-HVDC at the sending end
$\boldsymbol{Z}_{\mathrm{MMC}}^{\mathrm{pp}}$	Positive-sequence impedance of MMC-HVDC at the sending end
$\boldsymbol{Z}_{n}$	Equivalent impedance of $\prod$-line segments with receiving-end LCC considered
$\boldsymbol{Z}_{\mathrm{nn}}$	Negative-sequence impedance
$\boldsymbol{Z}_{\mathrm{np}}$	Negative-sequence coupling impedance
$\boldsymbol{Z}_{\mathrm{pn}}$	Positive-sequence coupling impedance
$\boldsymbol{Z}_{\mathrm{pp}}$	Positive-sequence impedance
$\boldsymbol{Z}_{\mathrm{PMSG}}$	AC port impedance of PMSG-based wind turbines
$\boldsymbol{Z}_{\mathrm{PMSG}}^{\mathrm{nn}}$	Negative-sequence impedance of PMSG-based wind turbines
$\boldsymbol{Z}_{\mathrm{PMSG}}^{\mathrm{np}}$	Negative-sequence coupling impedance of PMSG-based wind turbines
$\boldsymbol{Z}_{\mathrm{PMSG}}^{\mathrm{pn}}$	Positive-sequence coupling impedance of PMSG-based wind turbines
$\boldsymbol{Z}_{\mathrm{PMSG}}^{\mathrm{pp}}$	Positive-sequence impedance of PMSG-based wind turbines
$\boldsymbol{Z}_{\mathrm{PV}}$	AC port impedance of PV units
$\boldsymbol{Z}_{\mathrm{PV}}^{\mathrm{nn}}$	Negative-sequence impedance of PV units
$\boldsymbol{Z}_{\mathrm{PV}}^{\mathrm{np}}$	Negative-sequence coupling impedance of PV units
$\boldsymbol{Z}_{\mathrm{PV}}^{\mathrm{pn}}$	Positive-sequence coupling impedance of PV units
$\boldsymbol{Z}_{\mathrm{PV}}^{\mathrm{pp}}$	Positive-sequence impedance of PV units
$\boldsymbol{Z}_{\mathrm{RdcL}}$	Impedance of line resistor in a single $\prod$-line segment
$\boldsymbol{Z}_{\mathrm{RE}}$	REG port impedance
$\boldsymbol{Z}_{\mathrm{RSC}}^{\mathrm{pp}}$	Outer impedance of rotor winding

$\boldsymbol{Z}_{\text{self}}$	Sending-end LCC impedance
$\boldsymbol{Z}_{\text{stator}}$	Stator-side impedance of DFIG-based wind turbines
$\boldsymbol{Z}_{\text{stator}}^{\text{pp}}$	Stator impedance of DFIG-based wind turbines
$\boldsymbol{Z}_{\text{sys}}$	System impedance seen from REG plants
$\boldsymbol{Z}_{\text{SVG}}^{\text{nn}}$	Negative-sequence impedance of SVG
$\boldsymbol{Z}_{\text{SVG}}^{\text{np}}$	Negative-sequence coupling impedance of SVG
$\boldsymbol{Z}_{\text{SVG}}^{\text{pn}}$	Positive-sequence coupling impedance of SVG
$\boldsymbol{Z}_{\text{SVG}}^{\text{pp}}$	Positive-sequence impedance of SVG
$\boldsymbol{Z}_{\text{SVG}}^{\text{Q}}$	Impedance of SVG in reactive power mode
$\boldsymbol{Z}_{\text{SVG}}^{\text{V}}$	Impedance of SVG in AC voltage mode
$\boldsymbol{Z}_{\text{T}}$	Impedance of equivalent commutation inductor in small-signal frequency order
$\boldsymbol{Z}_{\text{T0}}$	Impedance of equivalent commutation inductor in steady-state frequency order
$\boldsymbol{Z}_{\text{Tpn}}$	Impedance matrix of double wing transformer
$\boldsymbol{Z}_{\text{W-T}}$, $\boldsymbol{Y}_{\text{W-T}}$	Impedance and admittance matrices of single wind turbine with transformer
$\boldsymbol{Z}_{\text{W//W}}$, $\boldsymbol{Y}_{\text{W//W}}$	Impedance and admittance matrixes of two paralleled wind turbines with transformers
$\Delta\boldsymbol{S}_{\text{va}}[k,m]$, $\Delta\boldsymbol{S}_{\text{vb}}[k,m]$, $\Delta\boldsymbol{S}_{\text{vc}}[k,m]$	Complex Fourier coefficients of three-phase voltage switching function variations at $kf_1 + m(f_\text{p} - f_1)$
$\Delta\boldsymbol{S}_{\text{ia}}[k,m]$, $\Delta\boldsymbol{S}_{\text{ib}}[k,m]$, $\Delta\boldsymbol{S}_{\text{ic}}[k,m]$	Complex Fourier coefficients of three-phase current switching function variations at $kf_1 + m(f_\text{p} - f_1)$

Frequency-Domain Small-Signal Vectors

$\hat{\boldsymbol{f}}(s)$	Small-signal vector of the periodic perturbation signal

$\hat{\boldsymbol{i}}^{\mathrm{pn}}, \hat{\boldsymbol{i}}^{\mathrm{np}}$	Small-signal controlled current sources vectors of the positive- and negative-sequence impedance networks
$\hat{\boldsymbol{i}}_0^{\mathrm{p}}, \hat{\boldsymbol{i}}_0^{\mathrm{n}}$	Small-signal positive- and negative-sequence current vectors at the PCC of wind farm
$\hat{\boldsymbol{i}}_{\mathrm{a}}, \hat{\boldsymbol{i}}_{\mathrm{b}}, \hat{\boldsymbol{i}}_{\mathrm{c}}$	Small-signal vectors of three-phase AC currents
$\hat{\boldsymbol{i}}_{\mathrm{a}}(s), \hat{\boldsymbol{i}}_{\mathrm{b}}(s), \hat{\boldsymbol{i}}_{\mathrm{c}}(s)$	Frequency-domain small-signal vectors of three-phase AC currents
$\hat{\boldsymbol{i}}_{\mathrm{adc}}, \hat{\boldsymbol{i}}_{\mathrm{bdc}}, \hat{\boldsymbol{i}}_{\mathrm{cdc}}$	Small-signal vectors of three-phase current compensation quantities
$\hat{\boldsymbol{i}}_{\mathrm{au}}, \hat{\boldsymbol{i}}_{\mathrm{bu}}, \hat{\boldsymbol{i}}_{\mathrm{cu}}$	Small-signal vectors of three-phase upper arm currents
$\hat{\boldsymbol{i}}_{\mathrm{av}}, \hat{\boldsymbol{i}}_{\mathrm{bv}}, \hat{\boldsymbol{i}}_{\mathrm{cv}}$	Small-signal vectors of three-phase lower arm currents
$\hat{\boldsymbol{i}}_{\mathrm{cd}}, \hat{\boldsymbol{i}}_{\mathrm{cq}}$	Small-signal vectors of d- and q-axis circulating currents
$\hat{\boldsymbol{i}}_{\mathrm{coma}}, \hat{\boldsymbol{i}}_{\mathrm{comb}}, \hat{\boldsymbol{i}}_{\mathrm{comc}}$	Small-signal vectors of three-phase arm CM currents
$\hat{\boldsymbol{i}}_{\mathrm{d}}, \hat{\boldsymbol{i}}_{\mathrm{q}}$	Small-signal vectors of d- and q-axis currents
$\hat{\boldsymbol{i}}_{\mathrm{dc}}(s)$	Frequency-domain small-signal vectors of DC current
$\hat{\boldsymbol{i}}_{\mathrm{dc}}$	Small-signal vector of DC current
$\hat{\boldsymbol{i}}_{\mathrm{dref}}, \hat{\boldsymbol{i}}_{\mathrm{qref}}$	Small-signal vectors of d- and q-axis current references
$\hat{\boldsymbol{i}}_{\mathrm{DFIG}}$	Small-signal component of AC current of DFIG wind plant at f_{osc}
$\hat{\boldsymbol{i}}_{\mathrm{DFIG2}}$	Small-signal component of AC current of DFIG wind plant at $f_{\mathrm{osc}} - 2f_1$
$\hat{\boldsymbol{i}}_{\mathrm{ea}}, \hat{\boldsymbol{i}}_{\mathrm{eb}}, \hat{\boldsymbol{i}}_{\mathrm{ec}}$	Small-signal vectors of receiving-end three-phase AC currents
$\hat{\boldsymbol{i}}_{\mathrm{ea1}}, \hat{\boldsymbol{i}}_{\mathrm{eb1}}, \hat{\boldsymbol{i}}_{\mathrm{ec1}}$	Small-signal vectors of three-phase AC currents of Converter I in receiving-end LCC
$\hat{\boldsymbol{i}}_{\mathrm{ea2}}, \hat{\boldsymbol{i}}_{\mathrm{eb2}}, \hat{\boldsymbol{i}}_{\mathrm{ec2}}$	Small-signal vectors of three-phase AC currents of Converter II in receiving-end LCC
$\hat{\boldsymbol{i}}_{\mathrm{eau}}, \hat{\boldsymbol{i}}_{\mathrm{ebu}}, \hat{\boldsymbol{i}}_{\mathrm{ecu}}$	Small-signal vectors of three-phase upper arm currents in receiving-end MMC
$\hat{\boldsymbol{i}}_{\mathrm{eav}}, \hat{\boldsymbol{i}}_{\mathrm{ebv}}, \hat{\boldsymbol{i}}_{\mathrm{ecv}}$	Small-signal vectors of three-phase lower arm currents in receiving-end MMC
$\hat{\boldsymbol{i}}_{\mathrm{ecoma}}, \hat{\boldsymbol{i}}_{\mathrm{ecomb}}, \hat{\boldsymbol{i}}_{\mathrm{ecomc}}$	Small-signal vectors of three-phase arm circulating currents in sending-end MMC
$\hat{\boldsymbol{i}}_{\mathrm{ed}}, \hat{\boldsymbol{i}}_{\mathrm{eq}}$	Small-signal vectors of d- and q-axis currents in receiving-end MMC
$\hat{\boldsymbol{i}}_{\mathrm{edc}}$	Small-signal vector of DC current in receiving-end converter station
$\hat{\boldsymbol{i}}_{\mathrm{edref}}, \hat{\boldsymbol{i}}_{\mathrm{eqref}}$	Small-signal vectors of d- and q-axis current references in receiving-end MMC
$\hat{\boldsymbol{i}}_{\mathrm{fa}}, \hat{\boldsymbol{i}}_{\mathrm{fb}}, \hat{\boldsymbol{i}}_{\mathrm{fc}}$	Small-signal vectors of sending-end three-phase AC currents
$\hat{\boldsymbol{i}}_{\mathrm{fa1}}, \hat{\boldsymbol{i}}_{\mathrm{fb1}}, \hat{\boldsymbol{i}}_{\mathrm{fc1}}$	Small-signal vectors of three-phase AC currents of Converter I in sending-end LCC

$\hat{\boldsymbol{i}}_{\mathrm{fa2}}, \hat{\boldsymbol{i}}_{\mathrm{fb2}}, \hat{\boldsymbol{i}}_{\mathrm{fc2}}$	Small-signal vectors of three-phase AC currents of Converter II in sending-end LCC
$\hat{\boldsymbol{i}}_{\mathrm{fau}}, \hat{\boldsymbol{i}}_{\mathrm{fbu}}, \hat{\boldsymbol{i}}_{\mathrm{fcu}}$	Small-signal vectors of three-phase upper arm currents in sending-end MMC
$\hat{\boldsymbol{i}}_{\mathrm{fav}}, \hat{\boldsymbol{i}}_{\mathrm{fbv}}, \hat{\boldsymbol{i}}_{\mathrm{fcv}}$	Small-signal vectors of three-phase lower arm currents in sending-end MMC
$\hat{\boldsymbol{i}}_{\mathrm{fcoma}}, \hat{\boldsymbol{i}}_{\mathrm{fcomb}}, \hat{\boldsymbol{i}}_{\mathrm{fcomc}}$	Small-signal vectors of three-phase arm circulating currents in sending-end MMC
$\hat{\boldsymbol{i}}_{\mathrm{fd}}, \hat{\boldsymbol{i}}_{\mathrm{fq}}$	Small-signal vectors of d- and q-axis currents in sending-end MMC
$\hat{\boldsymbol{i}}_{\mathrm{fdc}}$	Small-signal vector of DC current in sending-end converter station
$\hat{\boldsymbol{i}}_{\mathrm{fdref}}, \hat{\boldsymbol{i}}_{\mathrm{fqref}}$	Small-signal vectors of d- and q-axis current references in sending-end MMC
$\hat{\boldsymbol{i}}_{\mathrm{ga}}, \hat{\boldsymbol{i}}_{\mathrm{gb}}, \hat{\boldsymbol{i}}_{\mathrm{gc}}$	Small-signal vectors of three-phase GSC AC currents
$\hat{\boldsymbol{i}}_{\mathrm{gp}}$	Small-signal component of GSC AC current at f_{p}
$\hat{\boldsymbol{i}}_{\mathrm{gp-2}}$	Small-signal component of GSC AC current at $f_{\mathrm{p}} - 2f_{\mathrm{l}}$
$\hat{\boldsymbol{i}}_{\mathrm{p}}$	Small-signal component of AC current at f_{p}
$\hat{\boldsymbol{i}}_{\mathrm{p-2}}$	Small-signal component of AC current at $f_{\mathrm{p}} - 2f_{\mathrm{l}}$
$\hat{\boldsymbol{i}}_{\mathrm{PMSG}}$	Small-signal component of AC current of PMSG wind plant at f_{osc}
$\hat{\boldsymbol{i}}_{\mathrm{PMSG2}}$	Small-signal component of AC current of PMSG wind plant at $f_{\mathrm{osc}} - 2f_{\mathrm{l}}$
$\hat{\boldsymbol{i}}_{\mathrm{PV}}$	Small-signal component of AC current of PV plant at f_{osc}
$\hat{\boldsymbol{i}}_{\mathrm{PV2}}$	Small-signal component of AC current of PV plant at $f_{\mathrm{osc}} - 2f_{\mathrm{l}}$
$\hat{\boldsymbol{i}}_{\mathrm{ra}}, \hat{\boldsymbol{i}}_{\mathrm{rb}}, \hat{\boldsymbol{i}}_{\mathrm{rc}}$	Small-signal vectors of three-phase rotor and RSC AC currents
$\hat{\boldsymbol{i}}_{\mathrm{rp}}$	Small-signal component of the rotor current at f_{p}
$\hat{\boldsymbol{i}}_{\mathrm{rp-2}}$	Small-signal component of the rotor current at $f_{\mathrm{p}} - 2f_{\mathrm{l}}$
$\hat{\boldsymbol{i}}_{\mathrm{sa}}, \hat{\boldsymbol{i}}_{\mathrm{sb}}, \hat{\boldsymbol{i}}_{\mathrm{sc}}$	Small-signal vectors of three-phase stator currents
$\hat{\boldsymbol{i}}_{\mathrm{sp}}$	Small-signal component of the stator current at f_{p}
$\hat{\boldsymbol{i}}_{\mathrm{sp-2}}$	Small-signal component of the stator current at $f_{\mathrm{p}} - 2f_{\mathrm{l}}$
$\hat{\boldsymbol{m}}_{\mathrm{a}}, \hat{\boldsymbol{m}}_{\mathrm{b}}, \hat{\boldsymbol{m}}_{\mathrm{c}}$	Small-signal vectors of three-phase modulation signals
$\hat{\boldsymbol{m}}_{\mathrm{a}}(s), \hat{\boldsymbol{m}}_{\mathrm{b}}(s), \hat{\boldsymbol{m}}_{\mathrm{c}}(s)$	Frequency-domain small-signal vectors of three-phase AC modulation signals
$\hat{\boldsymbol{m}}_{\mathrm{abc}}$	Rotation vector of modulation signal in three-phase SCF
$\hat{\boldsymbol{m}}_{\mathrm{am}}, \hat{\boldsymbol{m}}_{\mathrm{bm}}, \hat{\boldsymbol{m}}_{\mathrm{cm}}$	Small-signal vectors of three-phase arm modulation signals
$\hat{\boldsymbol{m}}_{\mathrm{au}}, \hat{\boldsymbol{m}}_{\mathrm{bu}}, \hat{\boldsymbol{m}}_{\mathrm{cu}}$	Small-signal vectors of three-phase upper arm modulation signals
$\hat{\boldsymbol{m}}_{\mathrm{av}}, \hat{\boldsymbol{m}}_{\mathrm{bv}}, \hat{\boldsymbol{m}}_{\mathrm{cv}}$	Small-signal vectors of three-phase lower arm modulation signals

$\hat{\boldsymbol{m}}_{\mathrm{cd}}$, $\hat{\boldsymbol{m}}_{\mathrm{cq}}$	Small-signal vectors of d- and q-axis circulating modulation signals
$\hat{\boldsymbol{m}}_{\mathrm{coma}}$, $\hat{\boldsymbol{m}}_{\mathrm{comb}}$, $\hat{\boldsymbol{m}}_{\mathrm{comc}}$	Small-signal vectors of three-phase arm CM modulation signals
$\hat{\boldsymbol{m}}_{\mathrm{d}}$, $\hat{\boldsymbol{m}}_{\mathrm{q}}$	Small-signal vectors of d- and q-axis modulation signals
$\hat{\boldsymbol{m}}_{\mathrm{difa}}$, $\hat{\boldsymbol{m}}_{\mathrm{difb}}$, $\hat{\boldsymbol{m}}_{\mathrm{difc}}$	Small-signal vectors of three-phase arm DM modulation signals
$\hat{\boldsymbol{m}}_{\mathrm{dq}}$	Rotation vector of modulation signal in SRF
$\hat{\boldsymbol{m}}_{\mathrm{eau}}$, $\hat{\boldsymbol{m}}_{\mathrm{ebu}}$, $\hat{\boldsymbol{m}}_{\mathrm{ecu}}$	Small-signal vectors of three-phase upper arm modulation signals in receiving-end MMC
$\hat{\boldsymbol{m}}_{\mathrm{eav}}$, $\hat{\boldsymbol{m}}_{\mathrm{ebv}}$, $\hat{\boldsymbol{m}}_{\mathrm{ecv}}$	Small-signal vectors of three-phase lower arm modulation signals in receiving-end MMC
$\hat{\boldsymbol{m}}_{\mathrm{ecd}}$, $\hat{\boldsymbol{m}}_{\mathrm{ecq}}$	Small-signal vectors of d- and q-axis circulating modulation signal in receiving-end MMC
$\hat{\boldsymbol{m}}_{\mathrm{ecoma}}$, $\hat{\boldsymbol{m}}_{\mathrm{ecomb}}$, $\hat{\boldsymbol{m}}_{\mathrm{ecomc}}$	Small-signal vectors of three-phase arm CM modulation signals in receiving-end MMC
$\hat{\boldsymbol{m}}_{\mathrm{ed}}$, $\hat{\boldsymbol{m}}_{\mathrm{eq}}$	Small-signal vectors of d- and q-axis AC modulation signal in receiving-end MMC
$\hat{\boldsymbol{m}}_{\mathrm{edifa}}$, $\hat{\boldsymbol{m}}_{\mathrm{edifb}}$, $\hat{\boldsymbol{m}}_{\mathrm{edifc}}$	Small-signal vectors of three-phase arm DM modulation signals in receiving-end MMC
$\hat{\boldsymbol{m}}_{\mathrm{fau}}$, $\hat{\boldsymbol{m}}_{\mathrm{fbu}}$, $\hat{\boldsymbol{m}}_{\mathrm{fcu}}$	Small-signal vectors of three-phase upper arm modulation signals in sending-end MMC
$\hat{\boldsymbol{m}}_{\mathrm{fav}}$, $\hat{\boldsymbol{m}}_{\mathrm{fbv}}$, $\hat{\boldsymbol{m}}_{\mathrm{fcv}}$	Small-signal vectors of three-phase lower arm modulation signals in sending-end MMC
$\hat{\boldsymbol{m}}_{\mathrm{fcd}}$, $\hat{\boldsymbol{m}}_{\mathrm{fcq}}$	Small-signal vectors of d- and q-axis circulating modulation signal in sending-end MMC
$\hat{\boldsymbol{m}}_{\mathrm{fcoma}}$, $\hat{\boldsymbol{m}}_{\mathrm{fcomb}}$, $\hat{\boldsymbol{m}}_{\mathrm{fcomc}}$	Small-signal vectors of three-phase arm CM modulation signals in sending-end MMC
$\hat{\boldsymbol{m}}_{\mathrm{fd}}$, $\hat{\boldsymbol{m}}_{\mathrm{fq}}$	Small-signal vectors of dq-axis AC modulation signal in sending-end MMC
$\hat{\boldsymbol{m}}_{\mathrm{fdifa}}$, $\hat{\boldsymbol{m}}_{\mathrm{fdifb}}$, $\hat{\boldsymbol{m}}_{\mathrm{fdifc}}$	Small-signal vectors of three-phase arm DM modulation signals in sending-end MMC
$\hat{\boldsymbol{m}}_{\mathrm{ga}}$, $\hat{\boldsymbol{m}}_{\mathrm{gb}}$, $\hat{\boldsymbol{m}}_{\mathrm{gc}}$	Small-signal vectors of three-phase GSC modulation signals
$\hat{\boldsymbol{m}}_{\mathrm{gp}}$	Small-signal component of GSC modulation signal at f_{p}
$\hat{\boldsymbol{m}}_{\mathrm{gp-2}}$	Small-signal component of GSC modulation signal at $f_{\mathrm{p}} - 2f_1$
$\hat{\boldsymbol{m}}_{\mathrm{p}}$	Small-signal component of modulation signal at f_{p}
$\hat{\boldsymbol{m}}_{\mathrm{p-2}}$	Small-signal component of modulation signal at $f_{\mathrm{p}} - 2f_1$
$\hat{\boldsymbol{m}}_{\mathrm{ra}}$, $\hat{\boldsymbol{m}}_{\mathrm{rb}}$, $\hat{\boldsymbol{m}}_{\mathrm{rc}}$	Small-signal vectors of three-phase RSC modulation signals
$\hat{\boldsymbol{m}}_{\mathrm{rp}}$	Small-signal component of RSC modulation signal at f_{p}
$\hat{\boldsymbol{m}}_{\mathrm{rp-2}}$	Small-signal component of RSC modulation signal at $f_{\mathrm{p}} - 2f_1$

$\hat{\boldsymbol{m}}_{\mathrm{sa}}$, $\hat{\boldsymbol{m}}_{\mathrm{sb}}$, $\hat{\boldsymbol{m}}_{\mathrm{sc}}$	Small-signal vectors of three-phase MSC modulation signals
$\hat{\boldsymbol{m}}_{\mathrm{sp}}$	Small-signal component of MSC modulation signal at f_{p}
$\hat{\boldsymbol{m}}_{\mathrm{sp-2}}$	Small-signal component of MSC modulation signal at $f_{\mathrm{p}} - 2f_1$
$\hat{\boldsymbol{m}}_{\mathrm{vca}}$, $\hat{\boldsymbol{m}}_{\mathrm{vcb}}$, $\hat{\boldsymbol{m}}_{\mathrm{vcc}}$	Small-signal vectors of three-phase voltage balancing modulation signals
$\hat{\boldsymbol{p}}_{\mathrm{e}}$, $\hat{\boldsymbol{q}}_{\mathrm{e}}$	Small-signal vectors of active and reactive power
$\hat{\boldsymbol{p}}_{\mathrm{es}}$, $\hat{\boldsymbol{q}}_{\mathrm{es}}$	Small-signal vectors of stator active and reactive power
$\hat{\boldsymbol{s}}_{\mathrm{eia}}$, $\hat{\boldsymbol{s}}_{\mathrm{eib}}$, $\hat{\boldsymbol{s}}_{\mathrm{eic}}$	Small-signal vectors of three-phase current switching functions in receiving-end LCC
$\hat{\boldsymbol{s}}_{\mathrm{eva}}$, $\hat{\boldsymbol{s}}_{\mathrm{evb}}$, $\hat{\boldsymbol{s}}_{\mathrm{evc}}$	Small-signal vectors of three-phase voltage switching functions in receiving-end LCC
$\hat{\boldsymbol{s}}_{\mathrm{fia}}$, $\hat{\boldsymbol{s}}_{\mathrm{fib}}$, $\hat{\boldsymbol{s}}_{\mathrm{fic}}$	Small-signal vectors of three-phase current switching functions in sending-end LCC
$\hat{\boldsymbol{s}}_{\mathrm{fva}}$, $\hat{\boldsymbol{s}}_{\mathrm{fvb}}$, $\hat{\boldsymbol{s}}_{\mathrm{fvc}}$	Small-signal vectors of three-phase voltage switching functions in sending-end LCC
$\hat{\boldsymbol{s}}_{\mathrm{ia}}$, $\hat{\boldsymbol{s}}_{\mathrm{ib}}$, $\hat{\boldsymbol{s}}_{\mathrm{ic}}$	Small-signal vectors of three-phase current switching functions
$\hat{\boldsymbol{s}}_{\mathrm{va}}$, $\hat{\boldsymbol{s}}_{\mathrm{vb}}$, $\hat{\boldsymbol{s}}_{\mathrm{vc}}$	Small-signal vectors of three-phase voltage switching functions
$\hat{\boldsymbol{u}}(s)$	Frequency-domain small-signal vector of input signals
$\hat{\boldsymbol{u}}_{\mathrm{a}}$, $\hat{\boldsymbol{u}}_{\mathrm{b}}$, $\hat{\boldsymbol{u}}_{\mathrm{c}}$	Small-signal vectors of three-phase input signals
$\hat{\boldsymbol{u}}_{\mathrm{abc}}$	Rotation vector of input signal in three-phase SCF
$\hat{\boldsymbol{u}}_{\mathrm{d}}$, $\hat{\boldsymbol{u}}_{\mathrm{q}}$	Small-signal vectors of input signals in SRF
$\hat{\boldsymbol{u}}_{\mathrm{dq}}$	Small-signal rotation vector of input signal in SRF
$\hat{\boldsymbol{v}}^{\mathrm{p}}$, $\hat{\boldsymbol{v}}^{\mathrm{n}}$	Small-signal nodal voltage vectors of the positive- and negative- sequence impedance networks
$\hat{\boldsymbol{v}}_0^{\mathrm{p}}$, $\hat{\boldsymbol{v}}_0^{\mathrm{n}}$	Small-signal positive- and negative- sequence voltage vectors at the PCC of wind farm
$\hat{\boldsymbol{v}}_{\mathrm{a}}$, $\hat{\boldsymbol{v}}_{\mathrm{b}}$, $\hat{\boldsymbol{v}}_{\mathrm{c}}$	Small-signal vectors of three-phase AC voltages
$\hat{\boldsymbol{v}}_{\mathrm{a}}(s)$, $\hat{\boldsymbol{v}}_{\mathrm{b}}(s)$, $\hat{\boldsymbol{v}}_{\mathrm{c}}(s)$	Frequency-domain small-signal vectors of three-phase AC voltages
$\hat{\boldsymbol{v}}_{\mathrm{am}}$, $\hat{\boldsymbol{v}}_{\mathrm{bm}}$, $\hat{\boldsymbol{v}}_{\mathrm{cm}}$	Small-signal vectors of three-phase arm voltages
$\hat{\boldsymbol{v}}_{\mathrm{Cam}}$, $\hat{\boldsymbol{v}}_{\mathrm{Cbm}}$, $\hat{\boldsymbol{v}}_{\mathrm{Ccm}}$	Small-signal vectors of three-phase arm capacitor voltages
$\hat{\boldsymbol{v}}_{\mathrm{Cau}}$, $\hat{\boldsymbol{v}}_{\mathrm{Cbu}}$, $\hat{\boldsymbol{v}}_{\mathrm{Ccu}}$	Small-signal vectors of three-phase upper arm capacitor voltages
$\hat{\boldsymbol{v}}_{\mathrm{Cav}}$, $\hat{\boldsymbol{v}}_{\mathrm{Cbv}}$, $\hat{\boldsymbol{v}}_{\mathrm{Ccv}}$	Small-signal vectors of three-phase lower arm capacitor voltages
$\hat{\boldsymbol{v}}_{\mathrm{d}}$, $\hat{\boldsymbol{v}}_{\mathrm{q}}$	Small-signal vectors of d- and q-axis voltages
$\hat{\boldsymbol{v}}_{\mathrm{dc}}$	Small-signal vector of DC voltage
$\hat{\boldsymbol{v}}_{\mathrm{dc}}(s)$	Frequency-domain small-signal vector of DC voltage
$\hat{\boldsymbol{v}}_{\mathrm{DFIG}}$	Small-signal component of AC voltage of DFIG wind plant at f_{osc}

$\hat{\boldsymbol{v}}_{\mathrm{DFIG2}}$	Small-signal component of AC voltage of DFIG wind plant at $f_{\mathrm{osc}} - 2f_1$
$\hat{\boldsymbol{v}}_{\mathrm{ea}}$, $\hat{\boldsymbol{v}}_{\mathrm{eb}}$, $\hat{\boldsymbol{v}}_{\mathrm{ec}}$	Small-signal vectors of receiving-end three-phase AC voltages
$\hat{\boldsymbol{v}}_{\mathrm{ea1}}$, $\hat{\boldsymbol{v}}_{\mathrm{eb1}}$, $\hat{\boldsymbol{v}}_{\mathrm{ec1}}$	Small-signal vectors of three-phase AC voltages of Converter I in receiving-end LCC
$\hat{\boldsymbol{v}}_{\mathrm{ea2}}$, $\hat{\boldsymbol{v}}_{\mathrm{eb2}}$, $\hat{\boldsymbol{v}}_{\mathrm{ec2}}$	Small-signal vectors of three-phase AC voltages of Converter II in receiving-end LCC
$\hat{\boldsymbol{v}}_{\mathrm{ecoma}}$, $\hat{\boldsymbol{v}}_{\mathrm{ecomb}}$, $\hat{\boldsymbol{v}}_{\mathrm{ecomc}}$	Small-signal vectors of three-phase arm CM voltages in receiving-end MMC
$\hat{\boldsymbol{v}}_{\mathrm{eCau}}$, $\hat{\boldsymbol{v}}_{\mathrm{eCbu}}$, $\hat{\boldsymbol{v}}_{\mathrm{eCcu}}$	Small-signal vectors of three-phase upper arm capacitor voltages in receiving-end MMC
$\hat{\boldsymbol{v}}_{\mathrm{eCav}}$, $\hat{\boldsymbol{v}}_{\mathrm{eCbv}}$, $\hat{\boldsymbol{v}}_{\mathrm{eCcv}}$	Small-signal vectors of three-phase lower arm capacitor voltages in receiving-end MMC
$\hat{\boldsymbol{v}}_{\mathrm{edc}}$	Small-signal vector of DC voltage in receiving-end converter station
$\hat{\boldsymbol{v}}_{\mathrm{edifa}}$, $\hat{\boldsymbol{v}}_{\mathrm{edifb}}$, $\hat{\boldsymbol{v}}_{\mathrm{edifc}}$	Small-signal vectors of three-phase arm DM voltages in receiving-end MMC
$\hat{\boldsymbol{v}}_{\mathrm{eO}}$	Small-signal vector of receiving-end AC neutral voltage
$\hat{\boldsymbol{v}}_{\mathrm{eTa}}$, $\hat{\boldsymbol{v}}_{\mathrm{eTb}}$, $\hat{\boldsymbol{v}}_{\mathrm{eTc}}$	Small-signal vectors of line-side three-phase AC voltages at the receiving end
$\hat{\boldsymbol{v}}_{\mathrm{fa}}$, $\hat{\boldsymbol{v}}_{\mathrm{fb}}$, $\hat{\boldsymbol{v}}_{\mathrm{fc}}$	Small-signal vectors of sending-end three-phase AC voltages
$\hat{\boldsymbol{v}}_{\mathrm{fa1}}$, $\hat{\boldsymbol{v}}_{\mathrm{fb1}}$, $\hat{\boldsymbol{v}}_{\mathrm{fc1}}$	Small-signal vectors of three-phase AC voltages of Converter I in sending-end LCC
$\hat{\boldsymbol{v}}_{\mathrm{fa2}}$, $\hat{\boldsymbol{v}}_{\mathrm{fb2}}$, $\hat{\boldsymbol{v}}_{\mathrm{fc2}}$	Small-signal vectors of three-phase AC voltages of Converter II in sending-end LCC
$\hat{\boldsymbol{v}}_{\mathrm{fcoma}}$, $\hat{\boldsymbol{v}}_{\mathrm{fcomb}}$, $\hat{\boldsymbol{v}}_{\mathrm{fcomc}}$	Small-signal vectors of three-phase arm CM voltages in sending-end MMC
$\hat{\boldsymbol{v}}_{\mathrm{fCau}}$, $\hat{\boldsymbol{v}}_{\mathrm{fCbu}}$, $\hat{\boldsymbol{v}}_{\mathrm{fCcu}}$	Small-signal vectors of three-phase upper arm capacitor voltages in sending-end MMC
$\hat{\boldsymbol{v}}_{\mathrm{fCav}}$, $\hat{\boldsymbol{v}}_{\mathrm{fCbv}}$, $\hat{\boldsymbol{v}}_{\mathrm{fCcv}}$	Small-signal vectors of three-phase lower arm capacitor voltages in sending-end MMC
$\hat{\boldsymbol{v}}_{\mathrm{fd}}$, $\hat{\boldsymbol{v}}_{\mathrm{fq}}$	Small-signal vectors of d- and q-axis voltages in sending-end MMC
$\hat{\boldsymbol{v}}_{\mathrm{fdc}}$	Small-signal vector of DC voltage in sending-end converter station
$\hat{\boldsymbol{v}}_{\mathrm{fdifa}}$, $\hat{\boldsymbol{v}}_{\mathrm{fdifb}}$, $\hat{\boldsymbol{v}}_{\mathrm{fdifc}}$	Small-signal vectors of three-phase arm DM voltages in sending-end MMC
$\hat{\boldsymbol{v}}_{\mathrm{fO}}$	Small-signal vector of sending-end AC neutral voltage
$\hat{\boldsymbol{v}}_{\mathrm{fTa}}$, $\hat{\boldsymbol{v}}_{\mathrm{fTb}}$, $\hat{\boldsymbol{v}}_{\mathrm{fTc}}$	Small-signal vectors of line-side three-phase AC voltages at the sending end
$\hat{\boldsymbol{v}}_{\mathrm{g}}$	Small-signal component of AC grid voltage at f_{p}
$\hat{\boldsymbol{v}}_{\mathrm{g2}}$	Small-signal component of AC grid voltage at $f_{\mathrm{p}} - 2f_1$

$\hat{\boldsymbol{v}}_{\mathrm{ga}}, \hat{\boldsymbol{v}}_{\mathrm{gb}}, \hat{\boldsymbol{v}}_{\mathrm{gc}}$	Small-signal vectors of three-phase GSC modulation voltages
$\hat{\boldsymbol{v}}_{\mathrm{gp}}$	Small-signal component of GSC AC voltage at f_{p}
$\hat{\boldsymbol{v}}_{\mathrm{gp-2}}$	Small-signal component of GSC AC voltage at $f_{\mathrm{p}} - 2f_{\mathrm{l}}$
$\hat{\boldsymbol{v}}_{\mathrm{ia}}, \hat{\boldsymbol{v}}_{\mathrm{ib}}, \hat{\boldsymbol{v}}_{\mathrm{ic}}$	Small-signal vectors of three-phase modulation voltages
$\hat{\boldsymbol{v}}_{\mathrm{ip}}$	Small-signal component of modulation voltage at f_{p}
$\hat{\boldsymbol{v}}_{\mathrm{ip-2}}$	Small-signal component of modulation voltage at $f_{\mathrm{p}} - 2f_{\mathrm{l}}$
$\hat{\boldsymbol{v}}_{\mathrm{L1}}, \hat{\boldsymbol{i}}_{\mathrm{L1}}$	Small-signal voltage and current vectors at the beginning of overhead line or high voltage side of double winding transformer
$\hat{\boldsymbol{v}}_{\mathrm{L2}}, \hat{\boldsymbol{i}}_{\mathrm{L2}}$	Small-signal voltage and current vectors at the end of overhead line or low-voltage side of double winding transformer
$\hat{\boldsymbol{v}}_{\mathrm{O}}$	Small-signal vector of AC neutral voltage
$\hat{\boldsymbol{v}}_{\mathrm{p}}$	Small-signal component of AC voltage at f_{p}
$\hat{\boldsymbol{v}}_{\mathrm{p-2}}$	Small-signal component of AC voltage at $f_{\mathrm{p}} - 2f_{\mathrm{l}}$
$\hat{\boldsymbol{v}}_{\mathrm{PMSG}}$	Small-signal component of AC voltage of PMSG wind plant at f_{osc}
$\hat{\boldsymbol{v}}_{\mathrm{PMSG2}}$	Small-signal component of AC voltage of PMSG wind plant at $f_{\mathrm{osc}} - 2f_{\mathrm{l}}$
$\hat{\boldsymbol{v}}_{\mathrm{PV}}$	Small-signal component of AC voltage of PV plant at f_{osc}
$\hat{\boldsymbol{v}}_{\mathrm{PV2}}$	Small-signal component of AC voltage of PV plant at $f_{\mathrm{osc}} - 2f_{\mathrm{l}}$
$\hat{\boldsymbol{v}}_{\mathrm{ra}}, \hat{\boldsymbol{v}}_{\mathrm{rb}}, \hat{\boldsymbol{v}}_{\mathrm{rc}}$	Small-signal vectors of three-phase rotor voltages
$\hat{\boldsymbol{v}}_{\mathrm{rp}}$	Small-signal component of the rotor voltage at f_{p}
$\hat{\boldsymbol{v}}_{\mathrm{rp-2}}$	Small-signal component of the rotor voltage at $f_{\mathrm{p}} - 2f_{\mathrm{l}}$
$\hat{\boldsymbol{v}}_{\mathrm{sa}}, \hat{\boldsymbol{v}}_{\mathrm{sb}}, \hat{\boldsymbol{v}}_{\mathrm{sc}}$	Small-signal vectors of three-phase stator voltages
$\hat{\boldsymbol{v}}_{\mathrm{sp}}$	Small-signal component of the stator voltage at f_{p}
$\hat{\boldsymbol{v}}_{\mathrm{sp-2}}$	Small-signal component of the stator voltage at $f_{\mathrm{p}} - 2f_{\mathrm{l}}$
$\hat{\boldsymbol{v}}_{\mathrm{Ta}}, \hat{\boldsymbol{v}}_{\mathrm{Tb}}, \hat{\boldsymbol{v}}_{\mathrm{Tc}}$	Small-signal vectors of three-phase AC input voltage
$\hat{\boldsymbol{x}}(s)$	Small-signal vector of state variables
$\hat{\boldsymbol{\alpha}}_{\mathrm{f}}$	Small-signal vector of trigger angle in sending-end LCC
$\hat{\boldsymbol{\delta}}$	Small-signal vector of combined angle
$\hat{\boldsymbol{\delta}}_{\mathrm{e}}$	Small-signal vector of combined angle in receiving-end LCC
$\hat{\boldsymbol{\delta}}_{\mathrm{f}}$	Small-signal vector of combined angle in sending-end LCC
$\hat{\boldsymbol{\theta}}_{\mathrm{ePLL}}$	Small-signal vector of PLL output angle in receiving-end converter station
$\hat{\boldsymbol{\theta}}_{\mathrm{fPLL}}$	Small-signal vector of PLL output angle in sending-end converter station
$\hat{\boldsymbol{\theta}}_{\mathrm{PLL}}$	Small-signal vector of PLL output angle
$\hat{\boldsymbol{\theta}}_{\mathrm{PLL}}(s)$	Frequency-domain small-signal vector of PLL output angle

Transfer Functions and Coefficients of Controllers

B_{d}	Bandwidth of the virtual impedance controller band-pass filter
$G_{\mathrm{dd}}(s)$	Transfer function from $\hat{\boldsymbol{u}}_{\mathrm{d}}$ to $\hat{\boldsymbol{m}}_{\mathrm{d}}$
$G_{\mathrm{dq}}(s)$	Transfer function from $\hat{\boldsymbol{u}}_{\mathrm{q}}$ to $\hat{\boldsymbol{m}}_{\mathrm{d}}$
$G_{\mathrm{qd}}(s)$	Transfer function from $\hat{\boldsymbol{u}}_{\mathrm{d}}$ to $\hat{\boldsymbol{m}}_{\mathrm{q}}$
$G_{\mathrm{qq}}(s)$	Transfer function from $\hat{\boldsymbol{u}}_{\mathrm{q}}$ to $\hat{\boldsymbol{m}}_{\mathrm{q}}$
$H_{\mathrm{c}}(s)$	Transfer function of active damping controller
$H_{\mathrm{d}}(s)$	Transfer function of virtual impedance controller
$H_{\mathrm{eiac}}(s)$	Transfer function of AC current controller in receiving-end MMC
$H_{\mathrm{eic}}(s)$	Transfer function of circulating current controller in receiving-end MMC
$H_{\mathrm{ePLL}}(s)$	Transfer function of PLL controller in receiving-end converter station
$H_{\mathrm{f}}(s)$	Transfer function of voltage feedforward controller
$H_{\mathrm{fiac}}(s)$	Transfer function of AC current controller in sending-end MMC
$H_{\mathrm{fic}}(s)$	Transfer function of circulating current controller in sending-end MMC
$H_{\mathrm{fPLL}}(s)$	Transfer function of PLL controller in sending-end converter station
$H_{\mathrm{gi}}(s)$	Transfer function of GSC current controller
$H_{\mathrm{iac}}(s)$	Transfer function of AC current controller
$H_{\mathrm{ic}}(s)$	Transfer function of circulating current controller
$H_{\mathrm{idc}}(s)$	Transfer function of DC current controller
$H_{\mathrm{p}}(s)$	Transfer function of active power controller
$H_{\mathrm{PLL}}(s)$	Transfer function of PLL controller
$H_{\mathrm{q}}(s)$	Transfer function of reactive power controller
$H_{\mathrm{ri}}(s)$	Transfer function of RSC current controller
$H_{\mathrm{s}}(s)$	Type-S voltage feedforward controller
$H_{\mathrm{si}}(s)$	Transfer function of MSC current controller
$H_{\mathrm{vac}}(s)$	Transfer function of AC voltage controller
$H_{\mathrm{vc}}(s)$	Transfer function of phase voltage balancing controller
$H_{\mathrm{vdc}}(s)$	Transfer function of DC voltage controller
$H_{\mathrm{vs}}(s)$	Transfer function of overall voltage controller
$H_{\mathrm{y}}(s)$	Transfer function of virtual admittance controller
k_{c}	Active damping coefficient
k_{d}	Virtual impedance coefficient
k_{ev}	Voltage feedforward coefficient of receiving-end MMC
k_{f}	Voltage feedforward coefficient
k_{fv}	Voltage feedforward coefficient of sending-end MMC
k_{s}	Voltage feedforward coefficient in SCF
k_{y}	Virtual admittance coefficient
K_{c}	Decoupling coefficient of circulating current control
K_{d}	Decoupling coefficient of AC current controller
K_{ed}	Decoupling coefficient of AC current control in receiving-end MMC

K_{eiacp}, K_{eiaci} Proportional and integral coefficients of AC current controller in receiving-end MMC

K_{eic} Decoupling coefficient of circulating current control in receiving-end MMC

K_{eicp}, K_{eici} Proportional and integral coefficients of circulating current controller in receiving-end MMC

K_{epp}, K_{epi} Proportional and integral coefficients of PLL controller in receiving-end converter station

K_{fd} Decoupling coefficient of AC current control in sending-end MMC

K_{fiacp}, K_{fiaci} Proportional and integral coefficients of AC current controller in sending-end MMC

K_{fic} Decoupling coefficient of circulating current control in sending-end MMC

K_{ficp}, K_{fici} Proportional and integral coefficients of circulating current controller in sending-end MMC

K_{fpp}, K_{fpi} Proportional and integral coefficients of PLL controller in sending-end converter station

K_{gd} Decoupling coefficient of GSC current control

K_{gip}, K_{gii} Proportional and integral coefficients of GSC current controller

K_{iacp}, K_{iaci} Proportional and integral coefficients of AC current controller

K_{ic} Current proportional factor

K_{icp}, K_{ici} Proportional and integral coefficients of circulating current controller

K_{idcp}, K_{idci} Proportional and integral coefficients of DC current controller

K_{pep}, K_{pei} Proportional and integral coefficients of active power controller

K_{pp}, K_{pi} Proportional and integral coefficients of PLL controller

K_{qep}, K_{qei} Proportional and integral coefficients of reactive power controller

K_{r} Virtual impedance gain

K_{rd} Decoupling coefficient of RSC current control

K_{rip}, K_{rii} Proportional and integral coefficients of RSC current controller

K_{sd} Decoupling coefficient of MSC current control

K_{sip}, K_{sii} Proportional and integral coefficients of MSC current controller

K_{vacp}, K_{vaci} Proportional and integral coefficients of AC voltage controller

K_{vcp}, K_{vci} Proportional and integral coefficients of phase voltage balancing controller

K_{vdcp}, K_{vdci} Proportional and integral coefficients of DC voltage controller

K_{vsp}, K_{vsi} Proportional and integral coefficients of overall voltage controller

Q_{c} Quality factor of band-pass filter in active damping control

Q_{d} Quality factor of virtual impedance controller band-pass filter

Q_{f} Quality factor of band-pass filter in voltage feedforward control

Q_{s} Quality factor of low-pass filter in voltage feedforward control

R_{d} Virtual resistance

$T_{\mathrm{ePLL}}(s)$ Closed-loop transfer function of PLL controller in receiving-end converter station

$T_{\mathrm{fPLL}}(s)$ Closed-loop transfer function of PLL controller in sending-end converter station

$T_{\mathrm{idc}}(s)$	Transfer function of DC current filter
$T_{\mathrm{PLL}}(s)$	Closed-loop transfer function of PLL controller
$T_{\mathrm{vdc}}(s)$	Transfer function of DC voltage filter
ω_{c0}	Center angular frequency of the active damping band-pass filter
ω_{c1}	The lower limit of the active damping controller band-pass filter angular frequency
ω_{c2}	The upper limit of the active damping controller band-pass filter angular frequency
ω_{d0}	Center angular frequency of the virtual impedance controller band-pass filter
ω_{dh}	The upper limit of the virtual impedance controller band-pass filter angular frequency
ω_{dl}	The lower limit of the virtual impedance controller band-pass filter angular frequency
ω_{f0}	Center angular frequency of band-pass filter in voltage feedforward control
ω_{s0}	Center angular frequency of low-pass filter in voltage feedforward control
ω_{s1}	Cut-off angular frequency of low-pass filter in voltage feedforward control
ω_{y1}	The lower limit of the virtual admittance controller band-pass filter angular frequency
ω_{y2}	The upper limit of the virtual admittance controller band-pass filter angular frequency

Chapter 1
Introduction

1.1 Background

Energy is the basis for the survival and development of human society. The exploitation and utilization of energy have extensively promoted the development of the world economy and society. The key to achieving carbon peaking and carbon neutrality is to drive energy transition through innovation. With the green transformation of the power industry, wind power, photovoltaic (PV), and other renewable energy generation (REG) is developing rapidly worldwide. By the end of 2021, the cumulative world capacity of the installed wind power and PV generation amounted to 849 GW and 825 GW. In China, REG has been developing rapidly in the past two decades. By the end of 2021, the cumulative capacity of the installed wind power and PV generation amounted to 328 GW and 307 GW respectively, accounting for approximately 26.7% of the total installed power generation capacity in China [1]. REG (wind power and PV generation) has become the second-largest power source in China. To achieve carbon peaking and carbon neutrality and ensure the security of energy supply, China will accelerate the planning and construction of large-scale wind power and PV base projects in the deserts, Gobi, desertification areas, vigorously develop distributed REG, and promote the construction.

With the continuous increase of the installed capacity of REG, the stability problem of the REG grid-connected system is prominent, restricting the transmission and consumption of renewable energy. The wind and solar energy resources of China are mainly located in the north, northwest, and northeast regions, while the load centers are mainly located in the central and eastern regions. Due to the reverse distribution of resources and load, bulk power long-distance transmission is necessary. Line-commutated converter-based high voltage direct current (LCC-HVDC) transmission over long distances has become the dominant form of large-scale utilization of onshore renewable energy in China.

The Hami-Zhengzhou LCC-HVDC project is the first LCC-HVDC project mainly for REG transmission in China. The project starts in Hami of Xinjiang and ends in

© China Electric Power Press 2023

W. Wang et al., *Analysis and Mitigation of Broadband Oscillation in Renewable Energy Generation and AC/DC Transmission Systems*,
https://doi.org/10.1007/978-981-99-1568-2_1

Table 1.1 LCC-HVDC projects mainly for REG transmission in China

Project Name	DC Voltage (kV)	Capacity (MW)	Transmission Line Length (km)	Operation Year
Hami-Zhengzhou	±800	8000	2210	2014
Jiuquan-Hunan	±800	8000	2383	2017
Ximeng-Taizhou	±800	10,000	1628	2017
Zhalute-Qingzhou	±800	10,000	1234	2017
Shanghaimiao-Shandong	±800	10,000	1238	2019
Zhundong-Wannan	±1100	12,000	3324	2019
Qinghai-Henan	±800	8000	1587	2020
Shanbei-Hubei	±800	8000	1137	2021

Zhengzhou of Henan. The total length of the direct current (DC) transmission line is 2210 km, the nominal DC voltage is ±800 kV, and the transmission capacity is 8 GW. By the end of 2021, a total of 23 LCC-HVDC projects had been put into operation or under construction in China, and 8 of them are mainly for the transmission of REG, as shown in Table 1.1 [2].

In recent years, the development of offshore wind power in China has been accelerated, and the total planned installed capacity of offshore wind power in all provinces has exceeded 124 GW, exhibiting the characteristics of large scale, clustering, and extending to the deep and distant sea [3]. At the same time, the REG development strategy in China's Gobi Desert and other desertification regions has been promoted in an orderly manner.

The modular multilevel converter-based high voltage direct current (MMC-HVDC) and multi-terminal direct current (MMC-MTDC) grid have become crucial technologies for the transmission and grid connection of large-scale REG. The MMC-HVDC projects for REG transmission in China and other countries are shown in Table 1.2.

The REG, line with series compensation, LCC-HVDC, and MMC-HVDC all contain power electronic devices, making the large-scale REG grid-connected system to be local "double-high" power system [4]. "Double-high" means a high proportion of REG and a high proportion of power electronic devices. The operation characteristics of the local "double-high" power system are dominated by power electronic device control, which is significantly different from conventional power systems. In recent years, large-scale broadband oscillation incidents and tripping-off incidents of REG occurred in many regions of China and other countries, seriously affecting the safe and stable operation of the power system.

In 2009, oscillations occurred in a doubly-fed induction generator (DFIG)-based wind plant in South Texas, the United States. The DFIG-based wind plant was transmitted by the line with series compensation at the time. The oscillation voltage and current both had the subsynchronous oscillation components of about 20Hz, which finally triggered the crowbar protection of the wind turbine generator system (WTGS), causing large-scale tripping-off of WTGSs, and the overcurrent also caused

Table 1.2 MMC-HVDC projects for REG transmission in China and other countries

Project Name	DC Voltage (kV)	Capacity (MW)	Operation Year
BorWin1	±150	400	2010
Shanghai Nanhui	±30	20	2011
Guangdong Nan'ao	±160	200	2013
BorWin2	±300	800	2015
HelWin1	±250	576	2015
SylWin1	±320	864	2015
HelWin2	±320	690	2015
DolWin1	±320	800	2015
DolWin2	±320	916	2016
DolWin3	±320	900	2018
BorWin3	±320	900	2019
Zhangbei MMC-MTDC	±500	4500	2020
Jiangsu Rudong	±400	1100	2021

damage to the WTGS [5]. In 2010, continuous oscillations of 10~13 Hz occurred in a DFIG-based wind plant of the Xcel Energy in southwestern Minnesota, the United States, during normal switching of the series compensation devices, some WTGSs were damaged due to the accident [6]. In 2014, oscillations of 250~350 Hz occurred in the Borwin1 project in the North Sea of Germany, causing the filter capacitor of the HVDC offshore platform to be burnt down. The system had been shut down for half a year, causing huge economic losses to the local power company, which aroused wide attention in the industry [7].

In 2010, oscillations occurred in the Shanghai Nanhui wind plant connected to the MMC-HVDC transmission system (Shanghai Nanhui project) during its commissioning. The oscillations of 20~30 Hz were observed several times during the gradual increase of the wind plant's output power [8]. In 2012, several oscillations caused by the DIFG-based wind plant and the line with series compensation occurred in Guyuan, Hebei, China. The frequency range is 4~9 Hz [9]. In 2013, oscillations of about 30 Hz occurred in the Nan'ao MMC-MTDC system in China (Guangdong Nan'ao project) during the gradual increase of wind plant output power, which caused the tripping-off of the WTGSs [10]. In 2015, oscillations of 23/77 Hz occurred in the permanent magnet synchronous generators (PMSG)-based wind plant connected to the AC grid system (Hami-Zhengzhou project) in Hami, Xinjiang, China. On July 1, 2015, the oscillation excited the torsional vibration of the shaft system of the thermal power units, finally leading to the tripping-off of the thermal power generating units more than 300 km away and the DC power dip of the LCC-HVDC system [11]. In June 2020, the Zhangbei MMC-MTDC grid (Zhangbei MMC-MTDC project) was put into operation. With the gradual increase of REG grid connection capacity,

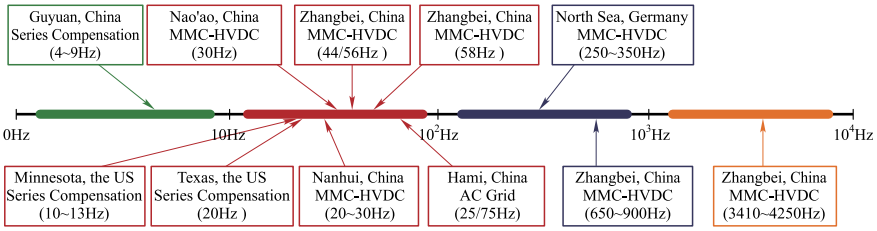

Fig. 1.1 Broadband oscillation occurred in China and other countries

broadband oscillations of 44/56, 58, 650–900, and 3410–4250 Hz have occurred in the system, which seriously affects the safe and stable operation of the system [12]. The broadband oscillation occurred in China and other countries are shown in Fig. 1.1.

1.2 Analysis Method of Oscillation

The broadband oscillation problem of REG and AC/DC transmission systems is a typical small-signal stability problem. Various analysis methods have been proposed, such as the eigenvalue analysis method, complex torque coefficient analysis method, time-domain simulation analysis method, impedance-based analysis method, etc.

1. Eigenvalue Analysis Method

The eigenvalue analysis method is widely used to analyze the small-signal stability of power systems. The system is first linearized on a certain operating point, and the state-space model can be established. The system is first linearized on a certain operating point, and the state-space model can be established. For the eigenvalue analysis method, first, the system linearization model is established, then the system stability can be determined by solving the eigenvalues, eigenvectors, and participation factors of the system state-space matrix.

In addition to analyzing stability, by using eigenvalue analysis, the risk factors of oscillations can be determined. For example, by calculating the participation factors of the oscillation modals, the influence of each state variable on each modal of the system can be analyzed. Or, by calculating the eigenvalue sensitivity matrix, the sensitivity of some key parameters to the eigenvalue can be analyzed.

The eigenvalue analysis method is based on rigorous scientific theory and has clear physical concepts and accuracy. It can be used to optimize the controller design to mitigate broadband oscillations. The REG and AC/DC transmission systems contain the power electronic devices of WTGS, PV unit, static var generator (SVG), LCC-HVDC, MMC-HVDC, etc. The control systems are “grey box/black box” and difficult to obtain parameters for the eigenvalue analysis. In addition, the REG base generally contains hundreds or even thousands of generation units. The dimension

of the corresponding linearized state-space matrix could be extremely high, leading to the problem of "dimension disaster" in the eigenvalue analysis.

2. Complex Torque Coefficient Analysis Method

The Complex torque coefficient analysis method is specially used to analyze subsynchronous oscillation problems caused by the interaction of electromechanical torsional vibration. The basic idea is to superimpose small disturbances of different frequencies on the generator rotor angle to obtain the generator's electrical and mechanical complex torque response by solving the system linearized model or analyzing the test curves of the time-domain simulation or real physical system. The ratios of electrical and mechanical complex torque responses to the rotor angle small disturbance are the equivalent electrical and mechanical complex torque coefficient, respectively. The real part of the complex torque coefficient is the elastic coefficient, and the imaginary part is the damping coefficient. By analyzing the relationship between electrical and mechanical elastic coefficients and damping coefficients of different frequencies, the system subsynchronous oscillation risk can be determined.

The complex torque coefficient analysis method is based on the system linearized model and can be considered as a combination of the frequency scanning method and eigenvalue analysis method. It has certain advantages over the eigenvalue analysis method if the parameters of the studied generator shaft system are incomplete. On the other hand, the curve of damping coefficient changing with disturbances frequency can be obtained by frequency scanning, which is conducive to intuitively analyzing the influence of parameter changes on the subsynchronous oscillation risk. This method is only applicable to analysis the oscillation problems related to the dynamic characteristics of generators. The applicability is inadequate for the analysis of the REG and AC/DC transmission systems which contain the power electronic devices of WTGS, PV unit, SVG, LCC-HVDC, MMC-HVDC, etc.

3. Time-Domain Simulation Analysis Method

By establishing equivalent models of REG and AC/DC transmission systems and solving differential and algebraic equations using electromagnetic transient (EMT) simulation, time-varying response curve of system variables can be obtained, and dynamic characteristics of the system can be analyzed. The EMT and electromechanical transient process of power electronic devices from several hundred nanoseconds to several seconds can be simulated in time-domain simulation. Different factors can be considered in the time-domain simulation process, including control characteristics of the power electronic device, nonlinear characteristics of the grid devices such as lightning arrester, transformer, reactor, etc., and the distributed parameters of the transmission lines. Various types of grid faults and line switching can also be simulated.

Using controller hardware-in-the-loop (CHIL) simulation, the time-domain simulation analysis of the "gray box/black box" control system can be realized. The CHIL simulation platform uses simulation model to substitute other actual equipment except for the controller under test. Then, the simulation model is connected with the real controller to form a closed loop test system. The software and hardware

of the system are required to operate according to the time scale of the actual system, so as to achieve the simulation of the operating state of the whole system under different conditions, and verify the control strategies of the actual controller.

The time-domain simulation analysis method can characterize the nonlinear factors of power electronic devices in REG and HVDC transmission, and characterize the logic switching between steady-state operation and fault ride through. It can accurately recur the broadband oscillation frequency, but also the oscillation amplitude.

4. Impedance-Based Analysis Method

The impedance-based analysis method was first used in the input filter design of DC systems, and then gradually applied to the small-signal stability analysis of single-phase and three-phase AC systems and AC/DC hybrid systems.

For REG and AC/DC transmission systems, the impedance-based analysis method divides the system into two subsystems to evaluate the broadband oscillation risk. The REG subsystem is equivalent to an ideal current source I_{i} paralleled with an equivalent impedance Z_{i}, and the grid subsystem is equivalent to an ideal voltage source V_{g} in series with an equivalent impedance Z_{g}. The simplified equivalent model of the REG and AC/DC transmission systems is shown in Fig. 1.2. V_{out} and I_{out} represent the small-signal voltage and current components of the point of common coupling (PCC) respectively.

The stability of REG and AC/DC transmission system can be determined by analyzing the stability of $\boldsymbol{V}_{\mathrm{out}}$ and $\boldsymbol{I}_{\mathrm{out}}$. According to Fig. 1.2, it can be obtained as

$$\boldsymbol{I}_{\mathrm{out}} = \left(\boldsymbol{I}_{\mathrm{i}} - \boldsymbol{V}_{\mathrm{g}}/\boldsymbol{Z}_{\mathrm{i}}\right)\frac{1}{1+\boldsymbol{Z}_{\mathrm{g}}/\boldsymbol{Z}_{\mathrm{i}}} \tag{1.1}$$

Under reasonable design, the REG and the grid subsystem are considered stable, i.e., $(\boldsymbol{I}_{\mathrm{i}} - \boldsymbol{V}_{\mathrm{g}}/\boldsymbol{Z}_{\mathrm{i}})$ in Eq. (1.1) is stable. Thus the stability of the REG and AC/DC transmission systems depends on

$$\boldsymbol{G}(s) = \frac{1}{1+\boldsymbol{Z}_{\mathrm{g}}/\boldsymbol{Z}_{\mathrm{i}}} \tag{1.2}$$

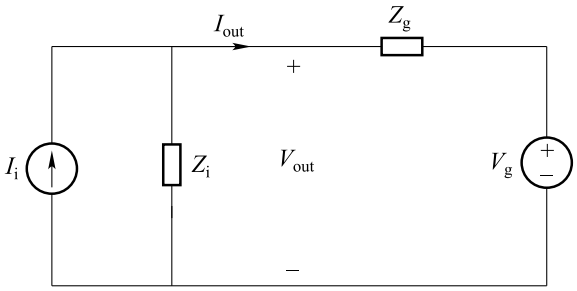

Fig. 1.2 Simplified equivalent model of the REG and AC/DC transmission systems

If, and only if the ratio of grid to REG impedance $\mathbf{Z}_g/\mathbf{Z}_i$ meets the Nyquist stability criterion, the system is stable.

The impedance modeling, impedance measurement, stability analysis, and oscillation mitigation of the REG and AC/DC transmission systems have been studied extensively and deeply, and a series of research results have been obtained. According to the different coordinate frames, the impedance model can be divided into the dq-axis impedance in the synchronous rotation frame (SRF) and the sequence impedance in the stationary coordinate frame (SCF).

1. dq-axis impedance

For three-phase AC systems, the AC periodic signal in the stationary coordinate system can be transformed into the DC signal in SRF. Thus, the system can be linearized on the DC steady-state operating points. The impedance model obtained by this linearization method is the dq-axis impedance model.

It should be noted that obtaining DC steady-state operating points by transforming the AC periodic signals to SRF is only applicable to three-phase symmetric systems. The dq-axis impedance modeling method has certain limitations to be used in the REG connected to the unbalanced grid or contains harmonic components in the steady-state operating trajectories. The dq-axis impedance model is based on the local grid connection point. Because the dq-axis impedance model of each REG unit is established in its own SRF, when modeling the impedance of REG plants, it is necessary to rotate the impedance model of each REG unit to a unified SRF, which is difficult to achieve. Therefore, the dq-axis impedance modeling method has certain limitations in the stability analysis of large-scale REG plants.

2. Sequence impedance

For three-phase circuits and systems, any group of three-phase small disturbances can be decomposed into a group of symmetrical positive-sequence, negative-sequence, and zero-sequence disturbances using the symmetrical component method. The sequence impedance can be obtained by calculating the response to each sequence disturbance of the circuit or system. In general, positive-sequence disturbance voltage leads to both positive- and negative-sequence current responses. Negative-sequence disturbance voltage may also lead to negative-sequence and positive-sequence disturbance current responses. And zero-sequence current cannot exist in the three-phase system without the neutral line. Therefore, the impedance of the three-phase system can be described as a positive and negative sequence impedance matrix of two rows and two columns.

The harmonic linearization method can directly linearize the nonlinear time-varying systems in SCF and is often used to model the sequence impedance. The small sinusoidal voltage or current disturbances of different frequencies are superimposed on the steady-state sinusoidal operating trajectories of the system, and the response components of each segment of the system can be analyzed by fast Fourier transform (FFT) or double Fourier transform. Then the mathematical relationship

between the responses and the disturbances is derived, and the positive and negative sequence impedance models of the system can be obtained.

The impedance-based analysis method can not only determine the stability of the REG and AC/DC transmission systems under specific operating conditions, but also quantitatively analyze the system stability margin. This method can reveal the oscillation mechanism of the system, optimize the control characteristics of power electronic devices, and provide guidance for improving system stability.

The impedance-based analysis method is a linearization method at a specific operating point, which is difficult to analyze the switching process of power electronic devices from steady-state operation to fault ride through. The time-domain simulation method can analyze the switching process of power electronic devices from steady-state operation to fault ride through. However, it can not reveal the oscillation mechanism of the system. This book combines these two methods to carry out impedance modeling, model verification, mechanism analysis, oscillation mitigation strategy verification, and solve the broadband oscillation problems in the engineering site.

1.3 Mitigation Method of Oscillation

To solve the broadband oscillation problems of REG and AC/DC transmission systems, a series of oscillation mitigation methods have been proposed. The methods mainly include optimizing existing devices and adding auxiliary devices.

1. Optimizing Existing Devices

The REG and AC/DC transmission systems contain many power electronic devices, and device control is an important factor affecting the system oscillation. By optimizing the control parameters or improving the control structures of the power electronic devices, the impedance of the devices can be reshaped to mitigate the oscillation.

(a) Optimizing control parameters

Impedance reshaping based on control parameter optimization is easy to realize. By tuning the control parameters of power electronic devices, the impedance characteristics of the devices in specific frequency bands can be optimized to mitigate oscillation. In [13], the sub- and super-synchronous oscillations mitigation of PMSG-based wind plants is achieved by impedance reshaping based on PLL parameter optimization.

(b) Improving control structures

It is difficult to achieve oscillation mitigation of some frequency bands only depending on optimizing control parameters, for the tunning range of control

parameters is limited. By introducing additional controllers such as virtual admittance or active damping, impedance reshaping and oscillation mitigation of specific frequency bands can be realized.

In [14], a supplementary damping control strategy for the grid-side converter (GSC) is proposed, to mitigate the sub- and super- synchronous oscillations of the PMSG-based wind plants connected to the MMC-HVDC transmission system. In [15], an active damping control strategy suitable for the GSC with an LCL filter is proposed, to mitigate the high-frequency oscillation of PMSG-based wind plants.

For the high-frequency mitigation of DFIG-based wind plants, the impedance reshaping methods based on the Chebyshev filter [16], stator current feedforward active damping control [17], virtual impedance [18, 19], phase advance compensation active damping control [20] are proposed.

2. Adding Auxiliary Devices

Adding auxiliary devices is mainly adding series and parallel flexible alternating current transmission system (FACTS) devices.

(1) Series FACTS devices. The series FACTS devices for oscillation mitigation of REG plants mainly include thyristor-controlled series compensator (TCSC), gate-controlled series capacitor (GCSC), static series synchronous compensator (SSSC), etc.

In [21], the mitigation strategy of TCSC and SVC on the subsynchronous oscillation of wind plants is proposed, and the damping effect of subsynchronous control interaction (SSCI) under large disturbance is verified by simulation. The series FACTS devices can achieve good mitigation effects if they are reasonably designed, but they are not flexible in structure and lack reliability for being connected in series in the system. (2) Parallel FACTS devices. The parallel FACTS devices for oscillation mitigation of the REG plants mainly include static var compensator (SVC), SVG, unified power flow controller (UPFC), superconducting magnetic energy storage (SMES), etc. In [22], the interaction mode of REG and SVG is analyzed using participation factors, and a mitigation strategy of SVC based on additional damping is proposed. In [23], an additional damping method to mitigate subsynchronous oscillation based on series side and parallel side converters of UPFC is proposed.

In [24], a subsynchronous damper with simultaneous injection of sub- and super-synchronous current is proposed. In [25], a single frequency modulation damping control strategy that only generates sub- or super-synchronous current is proposed. In [26], a new type of generator terminal subsynchronous damper consisting of a multi-mode compensated current calculator and a compensated current generator is proposed. In [27], an active damping method based on SVG to mitigate oscillation is proposed.

Compared with the series FACTS devices, parallel FACTS devices are flexible and reliable in structure. However, they generally cannot fundamentally solve the broadband oscillation problem because of the limitation of mitigation capability.

References

1. China Electric Power Planning & Engineering Insititute. Report on China electric power development 2022 [M]. Beijing: People's Daily Press, 2022. (Chinese)
2. XIN B A, GUO M Q, WANG S W, et al. Friendly HVDC transmission technologies for large-scale renewable energy and their engineering practice [J]. Automation of Electric Power Systems, 2021, 45(22): 1–8. (Chinese)
3. CHEN L N. Development status and prospect analysis of offshore wind power [J]. China's High-Tech, 2020, (13): 75–76. (Chinese)
4. WANG W S, LI G H, GUO J B. Large-scale renewable energy transmission by HVDC: challenges and proposals [J/OL]. Engineering, [2022–09–16]. https://doi.org/10.1016/j.eng.2022.04.017.10.1016/j.eng.2022.04.017
5. IEEE Power & Energy Society. Wind energy systems sub-synchronous oscillations: events and modeling (TR80) [R]. Piscataway, NJ: IEEE PES, 2020.
6. NARENDRA K, FEDIRCHUK D, MIDENCE R. New microprocessor based relay to monitor and protect power systems against sub-harmonics: 2011 IEEE Electrical Power and Energy Conference, Winnipeg, MB, Canada, October 3–5, 2011 [C]. Piscataway, NJ: IEEE, 2011.
7. BUCHHAGEN C, RAUSCHER C, MENZE A, et al. BorWin1-first experiences with harmonic interactions in converter dominated grids: International ETG Congress 2015; Die Energiewende-Blueprints for the new energy age, Bonn, Germany, November 17–18, 2015 [C]. Berlin: VDE, 2015.
8. YIN C Q, XIE X R, LIU H, et al. Analysis and control of the oscillation phenomenon in VSC-HVDC transmission system [J]. Power System Technology, 2018, 42(4): 1117–1123.
9. XIE X R, ZHANG X, LIU H K, et al. Characteristic analysis of subsynchronous resonance in practical wind farms connected to series-compensated transmissions [J]. IEEE Transactions on Energy Conversion, 2017, 32(3): 1117–1126. (Chinese)
10. WEI W, XU S K, LI Y, et al. The system commissioning of Nan'ao VSC-MTDC demonstration project [J]. Southern Power System Technology, 2015, 9(1): 73–77. (Chinese)
11. LIU H K, XIE X R, HE J B, et al. Subsynchronous interaction between direct-drive PMSG based wind farms and weak AC networks [J]. IEEE Transactions on Power Systems, 2017, 32(6): 4708–4720.
12. DU Z Y, YANG Y X, JI K, et al. High frequency harmonic resonance and suppression in Zhangbei project [J]. Power System Technology, 2022, 46(8): 3066–3075. (Chinese)
13. ZHANG C, WANG W S, HE G Q, et al. Analysis of sub-synchronous oscillation of full-converter wind farm based on sequence impedance and an optimized design method for PLL parameters [J]. Proceedings of the CSEE, 2017, 37(23): 6757–6767.
14. WANG H X, GUO J M, XIE Z W, et al. Grid-side supplementary damping suppression method of sub-& super-synchronous oscillation in offshore wind farms [J]. Southern Power System Technology, 2021, 15(11): 49–55. (Chinese)
15. ZHANG Z H, WU W M, SHUAI Z K, et al. Principle and robust impedance-based design of grid-tied inverter with LLCL-filter under wide variation of grid-reactance [J]. IEEE Transactions on Power Electronics, 2019, 34(5): 4362–4374.
16. VIETO I, LI G H, SUN J. Behavior, modeling and damping of a new type of resonance involving type-III wind turbines: 2018 IEEE 19th Workshop on Control and Modeling for Power Electronics (COMPEL), Padua, Italy, June 25–28, 2018 [C]. Piscataway, NJ: IEEE, 2018.
17. SONG Y P, WANG X F, BLAABJERG F. Doubly fed induction generator system resonance active damping through stator virtual impedance [J]. IEEE Transactions on Industrial Electronics, 2017, 64(1): 125–137.
18. HU B, NIAN H, YANG J, et al. High-frequency resonance analysis and reshaping control strategy of DFIG system based on DPC [J]. IEEE Transactions on Power Electronics, 2021, 36(7): 7810–7819.

19. NIAN H, TONG H, HU B, et al. High frequency resonance suppression of doubly fed induction generator connected to VSC-HVDC system based on direct power control without phase-locked loop [J]. Power System Technology, 2022, 46(7): 2492–2500.
20. SONG Y P, BLAABJERG F, WANG X F. Analysis and active damping of multiple high frequency resonances in DFIG system [J]. IEEE Transactions on Energy Conversion, 2017, 32(1): 369–381.
21. VARMA R K, AUDDY S, SEMSEDINI Y. Mitigation of subsynchronous resonance in a series-compensated wind farm using FACTS controllers [J]. IEEE Transactions on Power Delivery, 2008, 23(3): 1645–1654.
22. BIAN X Y, SHI L, ZHOU Q B, et al. Sub-synchronous interaction and its suppression measurement caused by grid-integration of DFIG-based wind farms using probabilistic method [J]. High Voltage Engineering, 2016, 42(9): 2740–2747. (Chinese)
23. ZHU X Y, JIN M, LI J S, et al. Auxiliary equipment based processing strategy for MMC-HVDC DC faults [J]. Automation of Electric Power Systems, 2016, 40(16): 44–48+97. (Chinese)
24. WANG L, XIE X R, JIANG Q R, et al. Mitigation of multimodal subsynchronous resonance via controlled injection of supersynchronous and subsynchronous currents [J]. IEEE Transactions on Power Systems, 2014, 29(3): 1335–1344.
25. LUO C, XIAO X N, ZHANG J, et al. The optimal damping control strategy design of parallel active subsynchronous oscillation Suppressor [J]. Transaction of China Electrotechnical Society, 2016, 31(21): 150–158. (Chinese)
26. XIE X R, WANG L, GUO X J, et al. Development and field experiments of a generator terminal subsynchronous damper [J]. IEEE Transactions on Power Electronics, 2014, 29(4): 1693–1671.
27. BOOPATHI V P, MUZAMIL A R, KUMUDINI DEVI R P, et al. Analysis and mitigation of subsynchronous oscillations in a radially-connected wind farm: 2014 Power and Energy Systems: Towards Sustainable Energy, Bangalore, India, March 13–15, 2014 [C]. Piscataway, NJ: IEEE, 2014.

Part I
Small-Signal Modeling of Converters

Renewable energy generation (REG) [1–5] and alternating current (AC)/direct current (DC) transmission systems [6–11] include REG-side power electronic devices, such as wind turbine generator system (WTGS), photovoltaic (PV) units, and static var generators (SVG). It also includes system-side power electronic devices, such as line commutated converter-based high voltage direct current (LCC-HVDC) and modular multilevel converter-based high voltage direct current (MMC-HVDC). The DC/AC converters in these devices can be classified into three basic categories: two-level converters, modular multilevel converters (MMC), and thyristor converters. This part focuses on the impedance modeling of these three basic converters, including the following chapters:

Chapter 2: Frequency-Domain Small-Signal Modeling Method. For the nonlinear system composed of power electronic devices, the frequency-domain steady-state model is established. The small-signal linearization of the nonlinear parts of the system is carried out to obtain the relationships between voltage and current small-signal responses. Finally, the frequency-domain small-signal impedance model of the system is established.

Chapter 3: Impedance Modeling of Two-Level Converter. Based on the averaged model of switching devices, the frequency-domain relationship between the AC and DC voltages is obtained, and the small-signal frequency conversion relationship is analyzed. Considering phase-lock loop (PLL), AC current control, DC voltage control, and other typical control loops, the small-signal AC port impedance model of the two-level converter is established.

Chapter 4: Impedance Modeling of Modular Multilevel Converter. Based on the MMC averaged model, the steady-state harmonic characteristics of the arm currents, capacitor voltages, and modulation signals are analyzed, and the frequencydomain steady-state model of MMC is established. Then, the frequency-domain small-signal distribution characteristics of the MMC main circuit and control loops are analyzed. Finally, the small-signal AC port impedance model of the MMC is established, including PLL, AC current control, and circulating current control.

Chapter 5: Impedance Modeling of Thyristor Converter. The time-domain model of the switching function of the thyristor converter considering the commutation

overlapping process is established. The harmonic characteristics of the voltages and currents at the AC and DC ports are analyzed. The frequency-domain steady-state model of the main circuit is established. Based on the steady-state and small-signal models of the switching functions, the small-signal AC port impedance model of the thyristor converter is established, including PLL, AC current control and phase control.

The impedance models of the two-level converter, MMC, and thyristor converter established in this part will be used as the basic models for impedance modeling of wind turbines, PV units, SVG/ MMC-HVDC, and LCC-HVDC in this book.

References

1. WANG W S, LIU C, QIN S Y, et al. Renewable energy grid connection and dispatching operation technology series [M]. Beijing: China Electric Power Press, 2020. (Chinese)
2. WANG Z A, LIU J J. Power Electronics [M]. 5th Edition. Beijing: China Machine Press, 2009.(Chinese)
3. ZHANG X, ZHANG C W. PWM rectifier and its control [M]. Beijing: China Machine Press, 2012. (Chinese)
4. RUAN X B, et al. Control techniques for LCL-type grid-connected inverters [M]. Beijing: Science Press, 2022. (Chinese)
5. SHU Y B, CHEN G P, HE J B, et al. Building a new electric power system based on new energy Sources [J]. Strategic Study of CAE, 2021, 23(06): 61-69. (Chinese)
6. XU Z, et al. Modular multilevel converter-based high voltage DC power transmission systems [M]. Beijing: China Machine Press, 2013. (Chinese)
7. TANG G F. HVDC transmission technology based on voltage source converter [M]. Beijing: China Electric Power Press, 2010. (Chinese)
8. SONG Q, RAO H. Analysis and design of the converters in VSC-HVDC system [M]. Beijing: Tsinghua University Press, 2015. (Chinese)
9. TAO Y. Analysis and application of HVDC transmission control and protection system [M]. Beijing: China Electric Power Press, 2015. (Chinese)
10. RAO H, LENG X B, PAN Y X, et al. Analysis of the global HVDC power transmission development and the suggestion of the HVDC export [J]. Southern Power System Technology, 2019, 13(10): 1-7. (Chinese)
11. LIU J Z, MA L F, WANG Q H, et al. Offshore Wind power supports China's energy transition [J]. Strategic Study of CAE, 2021, 23(1): 149-159. (Chinese)

Chapter 2
Frequency-Domain Small-Signal Modeling Method

Power electronic devices are widely used in renewable energy generation and AC/DC transmission systems. These systems are nonlinear due to the switching process and active control of power electronic devices. Since the theories of classical stability analysis are suitable for linear models, the linearization of the power electronic devices should be figured out to access system stability [1–3].

Power electronic devices are widely used in single-phase, three-phase balanced, and three-phase unbalanced AC systems. In addition, the diode circuit, thyristor circuit and MMC system all exhibit multi-harmonic characteristics. Time-domain linearization is not capable for these AC systems, as they are nonlinear with periodic time-varying operating points.

For the nonlinear AC system composed of power electronic devices, if the minimum period is taken as the unit, the system operating point will not change from the perspective of the averaged value of the period. Thus, frequency-domain linearization is a preferable solution. By converting the nonlinear AC system to the frequency domain and linearizing it near the frequency-domain equilibrium point, a frequency-domain linearized model can be obtained to conduct system stability analysis.

To establish the frequency-domain linearization model of the nonlinear system: (1) superpose a small-signal perturbation on the system's steady-state voltage or current trajectory; (2) Establish the linearized model by using Taylor expansion, Fourier transform, or Double Fourier transform for each nonlinear part; (3) Calculate the relationship of the response to the perturbation, i.e., the impedance model; (4) Change the frequency of small-signal perturbation to obtain the broadband impedance model. The linearization modeling process of the nonlinear system is shown in Fig. 2.1.

© China Electric Power Press 2023

W. Wang et al., *Analysis and Mitigation of Broadband Oscillation in Renewable Energy Generation and AC/DC Transmission Systems*,
https://doi.org/10.1007/978-981-99-1568-2_2

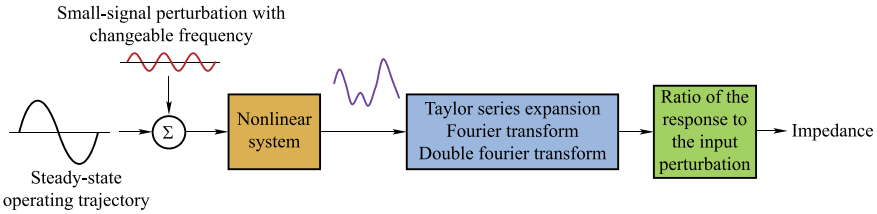

Fig. 2.1 Frequency-domain linearization for nonlinear system

2.1 Linearization of Power Electronic Nonlinear System

2.1.1 Nonlinear Model

The dynamic characteristics of nonlinear power electronic devices can be described by a set of first-order ordinary differential equations, expressed as

$$\begin{cases} \dot{x}_i = g_i(x_1, x_2, \ldots, x_n; u_1, u_2, \ldots, u_r; t) & i = 1, 2, \ldots, n \\ y_j = h_i(x_1, x_2, \ldots, x_n; u_1, u_2, \ldots, u_r; t) & j = 1, 2, \ldots, m \end{cases} \tag{2.1}$$

where $u_1, u_2, \cdots, u_r$ are the input signals; $x_1, x_2, \cdots, x_n$ are the state variables; $\dot{x}_i$ is the derivative of x_i to time t; $y_1, y_2, \cdots, y_m$ are the output signals.

The state and output equations of the system can be written in the state space equation form, which can be used to describe the dynamic characteristics of the state variables and output signals with the change of input variables, expressed as

$$\begin{cases} \dot{\boldsymbol{x}} = \boldsymbol{g}(\boldsymbol{x}, \boldsymbol{u}, t) \\ \boldsymbol{y} = \boldsymbol{h}(\boldsymbol{x}, \boldsymbol{u}, t) \end{cases} \tag{2.2}$$

where $\boldsymbol{u}$ is the input vector containing all independent inputs; $\boldsymbol{x}$ is the state vector containing all state variables, $\boldsymbol{y}$ is the output vector containing all outputs, $\boldsymbol{g}$ represent the nonlinear equations with state variables; $\boldsymbol{h}$ represent the nonlinear equations with output signals.

$$\boldsymbol{x} = \begin{bmatrix} x_1 \\ x_2 \\ \vdots \\ x_n \end{bmatrix}, \boldsymbol{u} = \begin{bmatrix} u_1 \\ u_2 \\ \vdots \\ u_r \end{bmatrix}, \boldsymbol{g} = \begin{bmatrix} g_1 \\ g_2 \\ \vdots \\ g_n \end{bmatrix}, \boldsymbol{y} = \begin{bmatrix} y_1 \\ y_2 \\ \vdots \\ y_m \end{bmatrix}, \boldsymbol{h} = \begin{bmatrix} h_1 \\ h_2 \\ \vdots \\ h_m \end{bmatrix} \tag{2.3}$$

2.1.2 Linearized Model

The small-signal stability is generally a concern when analyzing the stability of nonlinear systems composed of power electronic devices. To obtain a linear model for which the classic stability analysis can be applied, a small-signal model that has been linearized around a equilibrium point need to be constructed.

The linearization of the above nonlinear system is implemented at the system's equilibrium point, where all the derivatives of the state variables $\dot{x}_1, \dot{x}_2, \ldots, \dot{x}_n$ equal to zero. The state equation in equilibrium can be expressed as

$$\dot{\boldsymbol{x}} = \boldsymbol{g}(\boldsymbol{x}_0, \boldsymbol{u}_0, t) = 0 \tag{2.4}$$

where $\boldsymbol{x}_0$ and $\boldsymbol{u}_0$ are the state vector and the input vector in equilibrium respectively.

Then, a small-signal perturbation is superimposed about the equilibrium point, that is

$$\begin{cases} \boldsymbol{x} = \boldsymbol{x}_0 + \hat{\boldsymbol{x}} \\ \boldsymbol{u} = \boldsymbol{u}_0 + \hat{\boldsymbol{u}} \end{cases} \tag{2.5}$$

where the superscript "^" represents small signals of state variables and input variables.

Hence, the state equation can be expressed as

$$\dot{\boldsymbol{x}} = \boldsymbol{g}\left[(\boldsymbol{x}_0 + \hat{\boldsymbol{x}}), (\boldsymbol{u}_0 + \hat{\boldsymbol{u}}), t\right] \tag{2.6}$$

When the perturbation is small enough, the system can be linearized. The Taylor series expansion of the state equation can be carried out at the equilibrium point $(\boldsymbol{x}_0, \boldsymbol{u}_0)$, expressed as

$$\begin{aligned} \dot{x}_i = {} & g_i(\boldsymbol{x}_0, \boldsymbol{u}_0, t) + \left.\frac{\partial g_i(\boldsymbol{x}, \boldsymbol{u}, t)}{\partial x_1}\right|_{\boldsymbol{x}=\boldsymbol{x}_0, \boldsymbol{u}=\boldsymbol{u}_0} \cdot \hat{x}_1 + \cdots + \left.\frac{\partial g_i(\boldsymbol{x}, \boldsymbol{u}, t)}{\partial x_n}\right|_{\boldsymbol{x}=\boldsymbol{x}_0, \boldsymbol{u}=\boldsymbol{u}_0} \cdot \hat{x}_n \\ & + \left.\frac{\partial g_i(\boldsymbol{x}, \boldsymbol{u}, t)}{\partial u_1}\right|_{\boldsymbol{x}=\boldsymbol{x}_0, \boldsymbol{u}=\boldsymbol{u}_0} \cdot \hat{u}_1 + \cdots + \left.\frac{\partial g_i(\boldsymbol{x}, \boldsymbol{u}, t)}{\partial u_r}\right|_{\boldsymbol{x}=\boldsymbol{x}_0, \boldsymbol{u}=\boldsymbol{u}_0} \cdot \hat{u}_r \\ & + R_{2i}(\boldsymbol{x}, \boldsymbol{u}, t) \end{aligned} \tag{2.7}$$

where $i = 1, 2, \ldots, n$ and $R_{2i}(\boldsymbol{x}, \boldsymbol{u}, t)$ is the remainder of the Taylor series expansion of second and above order, which can be negligible in linearization analysis.

According to Eq. (2.7), the Taylor series contains the constant term, the first-order linear terms and the high-order nonlinear terms. In linearization steps, those high-order nonlinear terms are firstly neglected. Then, according to Eq. (2.4), there is $\dot{\boldsymbol{x}}_{i0} = g_i(\boldsymbol{x}_0, \boldsymbol{u}_0, t) = 0$. Therefore, only the first-order linear terms are retained, expressed as

$$\dot{\hat{x}}_i = \left.\frac{\partial g_i(\boldsymbol{x},\boldsymbol{u},t)}{\partial x_1}\right|_{\boldsymbol{x}=\boldsymbol{x}_0,\boldsymbol{u}=\boldsymbol{u}_0} \cdot \hat{x}_1 + \cdots + \left.\frac{\partial g_i(\boldsymbol{x},\boldsymbol{u},t)}{\partial x_n}\right|_{\boldsymbol{x}=\boldsymbol{x}_0,\boldsymbol{u}=\boldsymbol{u}_0} \cdot \hat{x}_n + \left.\frac{\partial g_i(\boldsymbol{x},\boldsymbol{u},t)}{\partial u_1}\right|_{\boldsymbol{x}=\boldsymbol{x}_0,\boldsymbol{u}=\boldsymbol{u}_0} \cdot \hat{u}_1 + \cdots + \left.\frac{\partial g_i(\boldsymbol{x},\boldsymbol{u},t)}{\partial u_r}\right|_{\boldsymbol{x}=\boldsymbol{x}_0,\boldsymbol{u}=\boldsymbol{u}_0} \cdot \hat{u}_r \tag{2.8}$$

Similarly, the small-signal of output signals can be derived as

$$\hat{y}_j = \left.\frac{\partial h_j(\boldsymbol{x},\boldsymbol{u},t)}{\partial x_1}\right|_{\boldsymbol{x}=\boldsymbol{x}_0,\boldsymbol{u}=\boldsymbol{u}_0} \cdot \hat{x}_1 + \cdots + \left.\frac{\partial h_j(\boldsymbol{x},\boldsymbol{u},t)}{\partial x_n}\right|_{\boldsymbol{x}=\boldsymbol{x}_0,\boldsymbol{u}=\boldsymbol{u}_0} \cdot \hat{x}_n + \left.\frac{\partial h_j(\boldsymbol{x},\boldsymbol{u},t)}{\partial u_1}\right|_{\boldsymbol{x}=\boldsymbol{x}_0,\boldsymbol{u}=\boldsymbol{u}_0} \cdot \hat{u}_1 + \cdots + \left.\frac{\partial h_j(\boldsymbol{x},\boldsymbol{u},t)}{\partial u_r}\right|_{\boldsymbol{x}=\boldsymbol{x}_0,\boldsymbol{u}=\boldsymbol{u}_0} \cdot \hat{u}_r \tag{2.9}$$

where $j = 1, 2, \ldots, m$

By reformulating Eqs. (2.8) and (2.9) in the vector form, the state equations of the system around the equilibrium point can be described as

$$\begin{cases} \dot{\hat{\boldsymbol{x}}} = \boldsymbol{A}_{\mathrm{x}}(t)\hat{\boldsymbol{x}} + \boldsymbol{B}_{\mathrm{u}}(t)\hat{\boldsymbol{u}} \\ \hat{\boldsymbol{y}} = \boldsymbol{C}_{\mathrm{x}}(t)\hat{\boldsymbol{x}} + \boldsymbol{D}_{\mathrm{u}}(t)\hat{\boldsymbol{u}} \end{cases} \tag{2.10}$$

where $\boldsymbol{A}_{\mathrm{x}}(t)$ is the time-domain transfer function matrix from state vector to the derivative of state vector; $\boldsymbol{B}_{\mathrm{u}}(t)$ is the time-domain transfer function matrix from input vector to the derivative of state vector; $\boldsymbol{C}_{\mathrm{x}}(t)$ is the time-domain transfer function matrix from state vector to output vector; and $\boldsymbol{D}_{\mathrm{u}}(t)$ is time-domain transfer function matrix from input vector to output vector. They can be expressed as

$$\boldsymbol{A}_{\mathrm{x}}(t) = \begin{bmatrix} \frac{\partial g_1}{\partial x_1} & \cdots & \frac{\partial g_1}{\partial x_n} \\ \vdots & \vdots & \vdots \\ \frac{\partial g_n}{\partial x_1} & \cdots & \frac{\partial g_n}{\partial x_n} \end{bmatrix}, \quad \boldsymbol{B}_{\mathrm{u}}(t) = \begin{bmatrix} \frac{\partial g_1}{\partial u_1} & \cdots & \frac{\partial g_1}{\partial u_r} \\ \vdots & \vdots & \vdots \\ \frac{\partial g_n}{\partial u_1} & \cdots & \frac{\partial g_n}{\partial u_r} \end{bmatrix},$$
$$\boldsymbol{C}_{\mathrm{x}}(t) = \begin{bmatrix} \frac{\partial h_1}{\partial x_1} & \cdots & \frac{\partial h_1}{\partial x_n} \\ \vdots & \vdots & \vdots \\ \frac{\partial h_m}{\partial x_1} & \cdots & \frac{\partial h_m}{\partial x_n} \end{bmatrix}, \quad \boldsymbol{D}_{\mathrm{u}}(t) = \begin{bmatrix} \frac{\partial h_1}{\partial u_1} & \cdots & \frac{\partial h_1}{\partial u_r} \\ \vdots & \vdots & \vdots \\ \frac{\partial h_m}{\partial u_1} & \cdots & \frac{\partial h_m}{\partial u_r} \end{bmatrix} \tag{2.11}$$

2.2 Frequency-Domain Linearization

For the power electronic devices used in REG and AC/DC transmission system, their operating points are sinusoidal and periodic in time domain. Since there is no equilibrium point the aforementioned linearization method cannot be conducted in time domain. In this section, the input/output signals and the state variables are first transformed in the frequency domain to obtain steady-state operating point. Then, the power electronic devices can be linearized around the steady-state operating point in frequency domain.

2.2.1 Steady-State Operating Point in Frequency Domain

For the nonlinear systems of REG and AC/DC transmission, the input/output signals and the state variables can be uniformly described as

$$\begin{cases} f_{\mathrm{a}} = \sum\limits_{k=0}^{\infty} F_{k+}\cos(2k\pi f_1 t + \varphi_{k+}) + \sum\limits_{k=0}^{\infty} F_{k-}\cos(2k\pi f_1 t + \varphi_{k-}) \\ \qquad + \sum\limits_{k=0}^{\infty} F_{k0}\cos(2k\pi f_1 t + \varphi_{k0}) \\ f_{\mathrm{b}} = \sum\limits_{k=0}^{\infty} F_{k+}\cos(2k\pi f_1 t - 2\pi/3 + \varphi_{k+}) + \sum\limits_{k=0}^{\infty} F_{k-}\cos(2k\pi f_1 t + 2\pi/3 + \varphi_{k-}) \\ \qquad + \sum\limits_{k=0}^{\infty} F_{k0}\cos(2k\pi f_1 t + \varphi_{k0}) \\ f_{\mathrm{c}} = \sum\limits_{k=0}^{\infty} F_{k+}\cos(2k\pi f_1 t + 2\pi/3 + \varphi_{k+}) + \sum\limits_{k=0}^{\infty} F_{k-}\cos(2k\pi f_1 t - 2\pi/3 + \varphi_{k-}) \\ \qquad + \sum\limits_{k=0}^{\infty} F_{k0}\cos(2k\pi f_1 t + \varphi_{k0}) \end{cases} \tag{2.12}$$

where f_{a}, f_{b}, f_{c} denote the three-phase AC signals; f_1 is the fundamental frequency; k is a positive integer; F_{k+}, F_{k-}, F_{k0} are the amplitudes of the positive-sequence, negative-sequence and zero-sequence components of the three-phase AC signals at kf_1; φ_{k+}, φ_{k-}, φ_{k0} are the phases of the positive-sequence, negative-sequence and the zero-sequence components of the three-phase AC signals at kf_1.

The positive-sequence, negative-sequence, and zero-sequence components can be decomposed from the three-phase AC signals based on the symmetrical component theory, that is,

$$\begin{bmatrix} f_+ \\ f_- \\ f_z \end{bmatrix} = \frac{1}{3}\begin{bmatrix} 1 & a & a^2 \\ 1 & a^2 & a \\ 1 & 1 & 1 \end{bmatrix}\begin{bmatrix} f_a \\ f_b \\ f_c \end{bmatrix} \tag{2.13}$$

where f_+, f_-, f_z are the positive-sequence, negative-sequence, and zero-sequence components of the three-phase AC signals; $a = e^{j2\pi/3}$ is the constant complex vector operator.

If the three-phase signals are periodic time-varying, the decomposed positive-sequence, negative-sequence, and zero-sequence components are periodic time-varying as well. Particularly, the three-phase signals of the diode converter, thyristor converter, and modular multilevel converter contain multiple harmonic components besides the fundamental component. Their positive-sequence, negative-sequence and zero-sequence components will contain periodic time-varying sinusoidal signals with multiple frequencies. Since the signals in Eq. (2.13) are periodic signals, they can be represented using Fourier series as a linear combination of sinusoids, if each periodic signal $f(t)$ satisfies the Dirichlet conditions as follows:

1. The periodic signal $f(t)$ is continous over a period, or has only a finite number of the first kind of discontinuities points.
2. There are only a finite number of extreme points in a period, then the Fourier series of $f(t)$ is convergent.
3. If t is a continuous point of $f(t)$, the series converges to $f(t)$, otherwise if t is a discontinuous point of $f(t)$, the series converges to $[f(t-0) + f(t+0)]/2$.

In general, a periodic signal is represented by $f(t)$ with period T_1. So the angular frequency is $\omega_1 = 2\pi/T_1$ and the frequency is $f_1 = 1/T_1$. Its Fourier series can be expressed as

$$f(t) = a_0 + \sum_{k=1}^{\infty} [a_k \cos(2k\pi f_1 t) + b_k \sin(2k\pi f_1 t)] \tag{2.14}$$

where k is positive integer; the coefficient of each harmonic components can be calculated by the following equations.

The DC component of the Fourier series a_0 can be obtained by

$$a_0 = \frac{1}{T_1}\int_{t_0}^{t_0+T_1} f(t)\mathrm{d}t \tag{2.15}$$

The cosine component a_k can be obtained by

$$a_k = \frac{2}{T_1}\int_{t_0}^{t_0+T_1} f(t)\cos(2k\pi f_1 t)\mathrm{d}t \tag{2.16}$$

The sinusoidal component b_k can be obtained by

$$b_k = \frac{2}{T_1}\int_{t_0}^{t_0+T_1} f(t)\sin(2k\pi f_1 t)\mathrm{d}t \tag{2.17}$$

The Fourier series in Eq. (2.14) can be further simplified by combining the cosine and sinusoidal components, expressed as

$$f(t) = c_0 + \sum_{k=1}^{\infty} c_k \cos(2k\pi f_1 t + \varphi_k) \tag{2.18}$$

where c_0 is the DC component of the Fourier series; c_k and φ_k are the amplitude and phase of the harmonic component at kf_1 respectively.

$$\begin{cases} c_0 = a_0 \\ c_k = \sqrt{a_k^2 + b_k^2} \\ \tan\varphi_k = -\dfrac{b_k}{a_k} \end{cases} \tag{2.19}$$

According to Eq. (2.18), the periodic signals satisfying Dirichlet conditions can be decomposed into a DC component and harmonic components at different frequencies.

According to Euler's formula, the Fourier series in Eq. (2.18) can be written in the complex exponential form, expressed as

$$f(t) = c_0 + \sum_{k=1}^{\infty}\left(\frac{c_k}{2}\mathrm{e}^{\mathrm{j}2k\pi f_1 t}\mathrm{e}^{\mathrm{j}\varphi_k} + \frac{c_k}{2}\mathrm{e}^{-\mathrm{j}2k\pi f_1 t}\mathrm{e}^{-\mathrm{j}\varphi_k}\right) \tag{2.20}$$

According to Eq. (2.20), the periodic signal contains not only the harmonic components at kf_1 but also the harmonic components at $-kf_1$.

Take the Fourier series coefficients as

$$\boldsymbol{F}_k = \frac{c_k}{2}\mathrm{e}^{\mathrm{j}\varphi_k} \tag{2.21}$$

$\boldsymbol{F}_k$ denotes the complex exponential form for the coefficients of the harmonic components at kf_1 and $\boldsymbol{F}_{-k}$ denotes the coefficient of the harmonic components at $-kf_1$. The relationship can be expressed as

$$\boldsymbol{F}_{-k} = \boldsymbol{F}_k^* \tag{2.22}$$

where the superscript "*" donates the conjugate operation.

Taking $\boldsymbol{F}_0 = c_0$, the complex exponential form of the Fourier series for periodic signal $f(t)$ can be expressed as

$$f(t) = \sum_{k=-\infty}^{\infty} \boldsymbol{F}_k \mathrm{e}^{\mathrm{j}2k\pi f_1 t} \tag{2.23}$$

where $\boldsymbol{F}_k$ ($k = \pm 1, \pm 2, \ldots$) represents the amplitude and phase of the harmonic components at kf_1 in the frequency domain.

For the periodic signal $f(t)$, its operating trajectory is periodic time-varying in time domain. According to Eq. (2.23), its states are time-invariant in frequency domain, as the coefficients of the harmonic components at kf_1 remain constant.

In order to describe the harmonic components at different frequencies in the frequency domain, their coefficients are arranged with the frequency order $[-kf_1, \ldots, -f_1, 0, f_1, \ldots, kf_1]^{\mathrm{T}}$ as the following vector.

$$\boldsymbol{F}(s) = \left[\boldsymbol{F}_{-k}, \ldots, \boldsymbol{F}_{-1}, \boldsymbol{F}_0, \boldsymbol{F}_1, \ldots, \boldsymbol{F}_k\right]^{\mathrm{T}} \tag{2.24}$$

where the superscript "T" donates the transposition operation and the "0" element in the frequency order denotes the DC component.

$\boldsymbol{F}(s)$ is the frequency-domain expression of the periodic signal $f(t)$ at the steady-state operating point, defined as the steady-state vector of the periodic signal. The Fourier coefficient $\boldsymbol{F}_k$ can be defined as the steady-state component of the periodic signal at kf_1.

2.2.2 *Linearization Analysis in Frequency Domain*

When the input/output signals and state variables of a nonlinear system are periodic time-varying, the steady-state operating point can be obtained through the aforementioned Fourier series. Accordingly, the linearization can be implemented in frequency domain to establish a small-signal model.

Similarly, as in time domain, a small-signal periodic perturbation is superimposed at the steady-state operating point in frequency domain, that is

$$\begin{cases} \boldsymbol{x}(s) = \boldsymbol{X}(s) + \hat{\boldsymbol{x}}(s) \\ \boldsymbol{u}(s) = \boldsymbol{U}(s) + \hat{\boldsymbol{u}}(s) \end{cases} \tag{2.25}$$

where $\boldsymbol{X}(s)$ and $\boldsymbol{U}(s)$ are the stead-state vectors of state variables and input signals in frequency domain respectively; $\hat{\boldsymbol{x}}(s)$ and $\hat{\boldsymbol{u}}(s)$ are the small-signal vectors of state variables and input signals in frequency domain respectively.

According to Eq. (2.3), the state vector and input vector in time domain contain multiple periodic signals. Correspondingly, according to Eq. (2.24), each periodic signal contains multiple harmonic components in frequency domain. Thus, the state variables and input signals at the stead-state operating point in frequency domain can be expressed as

$$\boldsymbol{X}(s) = \begin{bmatrix} \boldsymbol{X}_1(s) \\ \boldsymbol{X}_2(s) \\ \cdots \\ \boldsymbol{X}_n(s) \end{bmatrix}, \quad \boldsymbol{U}(s) = \begin{bmatrix} \boldsymbol{U}_1(s) \\ \boldsymbol{U}_2(s) \\ \cdots \\ \boldsymbol{U}_r(s) \end{bmatrix} \tag{2.26}$$

where $\boldsymbol{X}_1(s) \sim \boldsymbol{X}_n(s)$ and $\boldsymbol{U}_1(s) \sim \boldsymbol{U}_r(s)$ are the frequency-domain expressions of each periodic state variable and input signal respectively, similar as that in Eq. (2.24).

Correspondingly, the frequency-domain expressions of the small-signal state variables and input signals are both in vector form, as follows

$$\hat{\boldsymbol{x}}(s) = \begin{bmatrix} \hat{\boldsymbol{x}}_1(s) \\ \hat{\boldsymbol{x}}_2(s) \\ \cdots \\ \hat{\boldsymbol{x}}_n(s) \end{bmatrix}, \quad \hat{\boldsymbol{u}}(s) = \begin{bmatrix} \hat{\boldsymbol{u}}_1(s) \\ \hat{\boldsymbol{u}}_2(s) \\ \cdots \\ \hat{\boldsymbol{u}}_r(s) \end{bmatrix} \tag{2.27}$$

Since the period of the small-signal perturbation can be different from that of the steady-state operating point, the small-signal perturbation may contain different frequency harmonics from the steady-state operating point. In general, the frequency-domain expression of the small-signal $\hat{f}(t)$ can be arranged as a vector with the frequency order $[f_\mathrm{p} - kf_1, \ldots, f_\mathrm{p} - f_1, f_\mathrm{p}, f_\mathrm{p} + f_1, \ldots, f_\mathrm{p} + kf_1]^\mathrm{T}$.

$$\hat{\boldsymbol{f}}(s) = \left[\hat{\boldsymbol{f}}_{\mathrm{p}-k}, \ldots, \hat{\boldsymbol{f}}_{\mathrm{p}-1}, \hat{\boldsymbol{f}}_\mathrm{p}, \hat{\boldsymbol{f}}_{\mathrm{p}+1}, \ldots, \hat{\boldsymbol{f}}_{\mathrm{p}+k}\right]^\mathrm{T} \tag{2.28}$$

where f_p can be any frequency; k is the positive integer; $\hat{\boldsymbol{f}}_\mathrm{p}$ is the Fourier coefficient and can be defined as the small-signal component at f_p.

The frequency-domain small-signal state variables $\hat{\boldsymbol{x}}_1(s) \sim \hat{\boldsymbol{x}}_n(s)$ and input signals $\hat{\boldsymbol{u}}_1(s) \sim \hat{\boldsymbol{u}}_r(s)$ in Eq. (2.27) can be represented by the small-signal column vector shown in Eq. (2.28).

With the small-signal perturbation, the state equation in frequency domain can be expressed as

$$\dot{\boldsymbol{x}}(s) = \boldsymbol{G}\left[\left(\boldsymbol{X}(s) + \hat{\boldsymbol{x}}(s)\right), \left(\boldsymbol{U}(s) + \hat{\boldsymbol{u}}(s)\right)\right] \tag{2.29}$$

where $\boldsymbol{G}$ is the frequency-domain transfer functions of state variables $\boldsymbol{g}$.

Similarly, as that in the time domain, the Taylor expansion of these nonlinear relations can be carried out at the steady-state operating point $(\boldsymbol{X}(s), \boldsymbol{U}(s))$. The high-order nonlinear terms of $\left(\hat{\boldsymbol{x}}(s), \hat{\boldsymbol{u}}(s)\right)$ are neglected, thus the linearized expression is

$$\begin{aligned}\dot{\hat{\boldsymbol{x}}}_i(s) = & \left.\frac{\partial \boldsymbol{G}_i(\boldsymbol{x}(s), \boldsymbol{u}(s))}{\partial \boldsymbol{x}_1}\right|_{\boldsymbol{X}(s),\boldsymbol{U}(s)} \otimes \hat{\boldsymbol{x}}_1(s) + \cdots \\ & + \left.\frac{\partial \boldsymbol{G}_i(\boldsymbol{x}(s), \boldsymbol{u}(s))}{\partial \boldsymbol{x}_n}\right|_{\boldsymbol{X}(s),\boldsymbol{U}(s)} \otimes \hat{\boldsymbol{x}}_n(s) \\ & + \left.\frac{\partial \boldsymbol{G}_i(\boldsymbol{x}(s), \boldsymbol{u}(s))}{\partial \boldsymbol{u}_1}\right|_{\boldsymbol{X}(s),\boldsymbol{U}(s)} \otimes \hat{\boldsymbol{u}}_1(s) + \cdots \\ & + \left.\frac{\partial \boldsymbol{G}_i(\boldsymbol{x}(s), \boldsymbol{u}(s))}{\partial \boldsymbol{u}_r}\right|_{\boldsymbol{X}(s),\boldsymbol{U}(s)} \otimes \hat{\boldsymbol{u}}_r(s)\end{aligned} \tag{2.30}$$

where "⊗" denotes the convergence in frequency domain and $i = 1, 2, \ldots, n$.

Correspondingly, the linearized expression of output signals in frequency domain can be derived as

$$\begin{aligned}\hat{\boldsymbol{y}}_j(s) = & \left.\frac{\partial \boldsymbol{H}_j(\boldsymbol{x}(s), \boldsymbol{u}(s))}{\partial \boldsymbol{x}_1}\right|_{\boldsymbol{X}(s),\boldsymbol{U}(s)} \otimes \hat{\boldsymbol{x}}_1(s) + \cdots \\ & + \left.\frac{\partial \boldsymbol{H}_j(\boldsymbol{x}(s), \boldsymbol{u}(s))}{\partial \boldsymbol{x}_n}\right|_{\boldsymbol{X}(s),\boldsymbol{U}(s)} \otimes \hat{\boldsymbol{x}}_n(s) \\ & + \left.\frac{\partial \boldsymbol{H}_j(\boldsymbol{x}(s), \boldsymbol{u}(s))}{\partial \boldsymbol{u}_1}\right|_{\boldsymbol{X}(s),\boldsymbol{U}(s)} \otimes \hat{\boldsymbol{u}}_1(s) + \cdots \\ & + \left.\frac{\partial \boldsymbol{H}_j(\boldsymbol{x}(s), \boldsymbol{u}(s))}{\partial \boldsymbol{u}_r}\right|_{\boldsymbol{X}(s),\boldsymbol{U}(s)} \otimes \hat{\boldsymbol{u}}_r(s)\end{aligned} \tag{2.31}$$

where $\boldsymbol{H}$ is the frequency-domain transfer functions of output signals $\boldsymbol{h}$ and $j = 1, 2, \ldots, m$.

By reformulating Eqs. (2.30) and (2.31) in the vector form, the state equations of the linearized system at the steady-state operating point in frequency domain can be described as

$$\begin{cases}\dot{\hat{\boldsymbol{x}}}(s) = \boldsymbol{A}_{\mathrm{x}}(s) \otimes \hat{\boldsymbol{x}}(s) + \boldsymbol{B}_{\mathrm{u}}(s) \otimes \hat{\boldsymbol{u}}(s) \\ \hat{\boldsymbol{y}}(s) = \boldsymbol{C}_{\mathrm{x}}(s) \otimes \hat{\boldsymbol{x}}(s) + \boldsymbol{D}_{\mathrm{u}}(s) \otimes \hat{\boldsymbol{u}}(s)\end{cases} \tag{2.32}$$

where $\boldsymbol{A}_{\mathrm{x}}(s)$ is the frequency-domain transfer function matrix from state vector to the derivative of state vector, $\boldsymbol{B}_{\mathrm{u}}(s)$ is the frequency-domain transfer function matrix from input vector to the derivative of state vector, $\boldsymbol{C}_{\mathrm{x}}(s)$ is the frequency-domain transfer function matrix from state vector to output vector; $\boldsymbol{D}_{\mathrm{u}}(s)$ is the frequency-domain transfer function matrix from input vector to output vector. They can be expressed as

$$\begin{aligned}
\boldsymbol{A}_{\mathrm{x}}(s) &= \begin{bmatrix} \dfrac{\partial \boldsymbol{G}_1}{\partial \boldsymbol{x}_1} & \cdots & \dfrac{\partial \boldsymbol{G}_1}{\partial \boldsymbol{x}_n} \\ \cdots & \cdots & \cdots \\ \dfrac{\partial \boldsymbol{G}_n}{\partial \boldsymbol{x}_1} & \cdots & \dfrac{\partial \boldsymbol{G}_n}{\partial \boldsymbol{x}_n} \end{bmatrix}, \quad \boldsymbol{B}_{\mathrm{u}}(s) = \begin{bmatrix} \dfrac{\partial \boldsymbol{G}_1}{\partial \boldsymbol{u}_1} & \cdots & \dfrac{\partial \boldsymbol{G}_1}{\partial \boldsymbol{u}_r} \\ \cdots & \cdots & \cdots \\ \dfrac{\partial \boldsymbol{G}_n}{\partial \boldsymbol{u}_1} & \cdots & \dfrac{\partial \boldsymbol{G}_n}{\partial \boldsymbol{u}_r} \end{bmatrix} \\
\boldsymbol{C}_{\mathrm{x}}(s) &= \begin{bmatrix} \dfrac{\partial \boldsymbol{H}_1}{\partial \boldsymbol{x}_1} & \cdots & \dfrac{\partial \boldsymbol{H}_1}{\partial \boldsymbol{x}_n} \\ \cdots & \cdots & \cdots \\ \dfrac{\partial \boldsymbol{H}_m}{\partial \boldsymbol{x}_1} & \cdots & \dfrac{\partial \boldsymbol{H}_m}{\partial \boldsymbol{x}_n} \end{bmatrix}, \quad \boldsymbol{D}_{\mathrm{u}}(s) = \begin{bmatrix} \dfrac{\partial \boldsymbol{H}_1}{\partial \boldsymbol{u}_1} & \cdots & \dfrac{\partial \boldsymbol{H}_1}{\partial \boldsymbol{u}_r} \\ \cdots & \cdots & \cdots \\ \dfrac{\partial \boldsymbol{H}_m}{\partial \boldsymbol{u}_1} & \cdots & \dfrac{\partial \boldsymbol{H}_m}{\partial \boldsymbol{u}_r} \end{bmatrix}
\end{aligned} \tag{2.33}$$

The aforementioned linearization method in frequency domain is based on the averaged model over one minimum periodic T_1. The frequency-domain expressions of the periodic signals and the small-signal perturbation contain multiple harmonic components at different frequencies. Hence, this method is called frequency-domain linearization.

2.3 Frequency-Domain Linearization of Typical Nonlinearity

In this section, the frequency-domain linearization for the typical nonlinear process in the power electronic devices for REG and AC/DC transmission is explained in detail, including the switching process, the modulation process and the Park transformation.

2.3.1 Linearization of Switching Process

The conversion of electrical energy, including DC/DC conversion, DC/AC conversion, AC/DC conversion and AC/AC conversion, can be realized by the switching process of power electronic converters. The switching process is typically nonlinear. In this section, an averaged model is established for the switching process. Thus, the converter switches can be linearized and replaced with controlled voltage sources.

Take DC/AC converter as an example, in which high-frequency sinusoidal pulse width modulation (SPWM) techniques are used to improve the power quality and to remove the undesirable harmonics at the switching frequency. The topology and the waveforms of the single-phase inverter are shown in Fig. 2.2, where T1–T4 are the switches, V_{dc} is the DC voltage, v_{ao} is the output AC voltage, v_{car} is the high-frequency triangular carrier wave and v_{rma} is the sinusoidal modulation wave.

The SPWM switch voltage waveform is generated by the comparison between the modulation wave v_{rma} and the triangular carrier wave v_{car}. The detailed SPWM principle is explained as

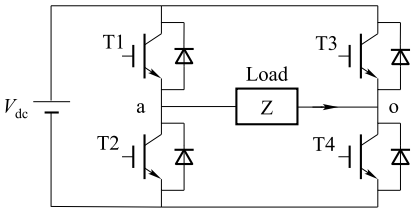

(a) Topology of the single-phase inverter circuit

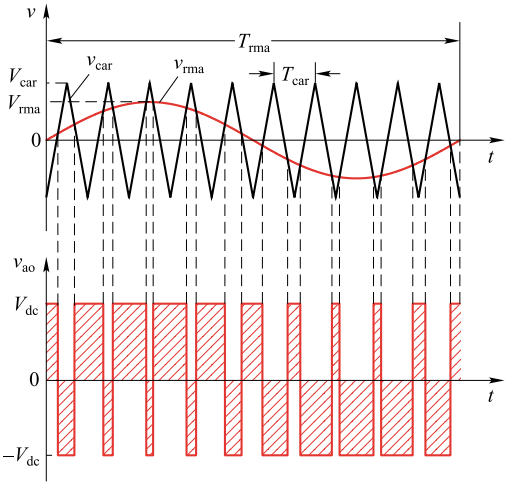

(b) Voltage waveform

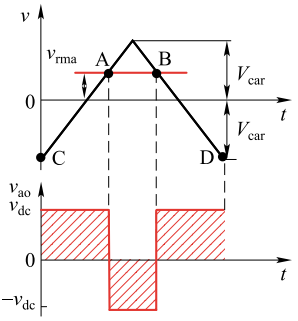

(c) Duty cycle

Fig. 2.2 Topology and waveforms of the single-phase inverter circuit

1. If $v_{rma} \geq v_{car}$, switches T1 and T4 turn on, and switches T2 and T3 turn off. In this period, the output AC voltage equals to $v_{ao} = V_{dc}$.
2. If $v_{rma} < v_{car}$, switches T2 and T3 turn on, and switches T1 and T4 turn off. In this period, the output AC voltage equals to $v_{ao} = -V_{dc}$.

This switching process produces a rectangular waveform for the output AC voltage v_{ao}, as shown in Fig. 2.2b. Thus, v_{ao} can be formulated as

$$v_{ao} = s_a \cdot V_{dc} \tag{2.34}$$

where s_a is the switching function. It is a piecewise function, expressed as

$$s_a = \begin{cases} 1, & v_{rma} \geq v_{car} \\ -1, & v_{rma} < v_{car} \end{cases} \tag{2.35}$$

The sinusoidal modulation wave v_{rma} can be expressed as $v_{rma} = V_{rma} \sin(2\pi f_{rma} t)$, where V_{rma} and f_{rma} are its amplitude and frequency, respectively. The amplitude and phase of the carrier wave v_{car} are V_{car} and f_{car} respectively,

thus the carrier period equals to $T_{\text{car}}=1/f_{\text{car}}$. If the frequency of the carrier wave is much higher than that of the modulation wave, the switching process can be averaged over one carrier period, that is, v_{rma} remains approximately unchanged in T_{car}. As seen from Fig. 2.2c, in one carrier period, when $v_{\text{rma}} > v_{\text{car}}$, T1 and T4 turn on. Conversely, T1 and T4 turn off. The duty cycle D_{dr} of T1 and T4 is defined as the fraction of time in which the switches turn on. Geometrically, D_{dr} can be derived by

$$D_{\text{dr}} = \frac{CD - AB}{CD} = \frac{1}{2}\left(1 + \frac{v_{\text{rma}}}{V_{\text{car}}}\right) \tag{2.36}$$

The average of output voltage over one carrier period is

$$v_{\text{ao}} = (2D_{\text{dr}} - 1)V_{\text{dc}} \tag{2.37}$$

Substituting Eq. (2.36) into Eq. (2.37), the averaged output voltage over one carrier period is

$$v_{\text{ao}} = \frac{V_{\text{dc}}}{V_{\text{car}}} v_{\text{rma}} \tag{2.38}$$

Hence, if the frequency of the carrier wave is enough high, the output AC voltage v_{ao} can be expressed as

$$v_{\text{ao}} = m_{\text{a}} V_{\text{dc}} \tag{2.39}$$

where m_{a} is the modulation signal of phase a, expressed as

$$m_{\text{a}} = \frac{V_{\text{rma}}}{V_{\text{car}}} \sin(2\pi f_{\text{rma}} t) \tag{2.40}$$

In conclusion, the switching process can be linearized as the averaged model in Eq. (2.39). Specifically, the piecewise non-linear function s_{a} in Eq. (2.34) is replaced by the continuous modulation signal m_{a}, based on the condition that the frequency of the carrier wave is much higher than that of the modulation wave. According to the averaged switching model, the single-phase inverter circuit can be equivalent to the averaged circuit in Fig. 2.3, where the switches are replaced by a controlled voltage source $m_{\text{a}} V_{\text{dc}}$.

Similarly, the averaged switching model of the three-phase inverter circuit or other converters can be obtained.

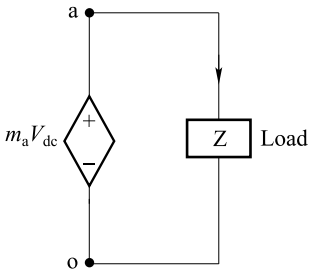

Fig. 2.3 Averaged switching model of the single-phase inverter circuit

2.3.2 *Linearization of Modulation Process*

In Sect. 2.3.1, the DC side of the inverter is set as an ideal voltage source, then the averaged model is obtained by the linearizing of the switching process. However, the averaged model will be nonlinear if the DC-side voltage is not constant, as the output AC voltage in Eq. (2.39) is the multiplication of two variant signals. The frequency-domain linearization is used to obtain a linear small-signal model of the modulation process in this Section.

Take the three-phase inverter circuit in Fig. 2.4 as an example, the DC side is set as a DC bus capacitor C_{dc} instead of the ideal voltage source. According to the averaged model, the relationship between the AC side and DC side is expressed as

$$\begin{cases} v_l = K_m m_l v_{dc} \\ i_{dc} = \sum\limits_{l=a,b,c} m_l i_l \end{cases} \tag{2.41}$$

where K_m is the modulation gain, v_l, i_l, $m_l (l = a, b, c)$ are the three-phase AC voltages, three-phase AC currents, and three-phase modulation signals respectively; $l = a, b, c$ represent a, b and c three phase, v_{dc}, i_{dc} are the DC voltage and DC current respectively.

Confirmed by Eq. (2.41), the DC/AC conversion is nonlinear due to the modulation process. In order to establish a linear model, v_{dc}, i_l and m_l are firstly transformed in

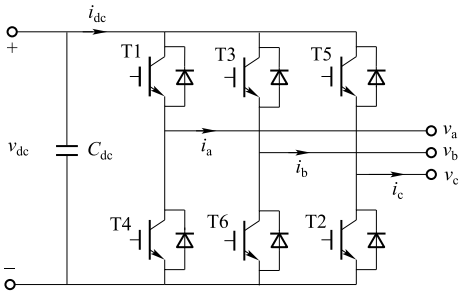

Fig. 2.4 Topology of the three-phase inverter circuit

frequency domain to obtain the steady-state operating points, denoted by frequency-domain steady-state vector of DC voltage $\boldsymbol{V}_{\mathrm{dc}}(s)$, frequency-domain steady-state vector of AC current $\boldsymbol{I}_l(s)$ and frequency-domain steady-state vector of modulation signal $\boldsymbol{M}_l(s)$.

A small-signal periodic perturbation is superimposed on the steady-state operating point in the frequency domain, that is

$$\begin{cases} \boldsymbol{v}_{\mathrm{dc}}(s) = \boldsymbol{V}_{\mathrm{dc}}(s) + \hat{\boldsymbol{v}}_{\mathrm{dc}}(s) \\ \boldsymbol{i}_l(s) = \boldsymbol{I}_l(s) + \hat{\boldsymbol{i}}_l(s) \\ \boldsymbol{m}_l(s) = \boldsymbol{M}_l(s) + \hat{\boldsymbol{m}}_l(s) \end{cases} \tag{2.42}$$

where $\boldsymbol{v}_{\mathrm{dc}}(s)$ is the frequency-domain small-signal vector of DC voltage; $\boldsymbol{i}_l(s)$ is the frequency-domain small-signal vector of AC current; $\boldsymbol{m}_l(s)$ is the frequency-domain small-signal vector of modulation signal. Equation (2.41) is transformed into frequency domain and linearized by neglecting the high-order nonlinear terms of the Taylor series expansion. The frequency-domain linearization model of the modulation process can be expressed as

$$\begin{cases} \hat{\boldsymbol{v}}_l(s) = K_{\mathrm{m}}\left(\boldsymbol{M}_l(s) \otimes \hat{\boldsymbol{v}}_{\mathrm{dc}}(s) + \boldsymbol{V}_{\mathrm{dc}}(s) \otimes \hat{\boldsymbol{m}}_l(s)\right) \\ \hat{\boldsymbol{i}}_{\mathrm{dc}}(s) = \sum\limits_{l=\mathrm{a,b,c}} \left(\boldsymbol{M}_l(s) \otimes \hat{\boldsymbol{i}}_l(s) + \boldsymbol{I}_l(s) \otimes \hat{\boldsymbol{m}}_l(s)\right) \end{cases} \tag{2.43}$$

where $\hat{\boldsymbol{v}}_l(s)$ is the frequency-domain small-signal vector of three-phase AC voltage; $\hat{\boldsymbol{i}}_{\mathrm{dc}}(s)$ is the frequency-domain small-signal of DC current.

2.3.3 *Linearization of Park Transformation and PLL*

In general, a phase-lock loop (PLL) is used in grid-connected converters to synchronize with the grid voltages. Since the PLL and current control loop typically employ Park transformation, which is nonlinear, the frequency-domain linearization method needs to be adopted to obtain a linear small-signal model.

Figure 2.5 depicts the block diagram of PLL.

With the phase-locked angle obtained by PLL, the d-axis voltage v_{d} and q-axis voltage v_{q} can be derived from the three-phase AC voltages by Park transformation, expressed as

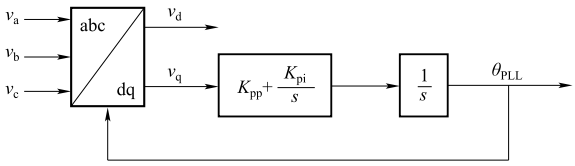

Fig. 2.5 Block diagram of PLL controller

$$\begin{cases} v_{\mathrm{d}} = \dfrac{2}{3}[\cos\theta_{\mathrm{PLL}} \cdot v_{\mathrm{a}} + \cos(\theta_{\mathrm{PLL}} - 2\pi/3) \cdot v_{\mathrm{b}} + \cos(\theta_{\mathrm{PLL}} + 2\pi/3) \cdot v_{\mathrm{c}}] \\ v_{\mathrm{q}} = -\dfrac{2}{3}[\sin\theta_{\mathrm{PLL}} \cdot v_{\mathrm{a}} + \sin(\theta_{\mathrm{PLL}} - 2\pi/3) \cdot v_{\mathrm{b}} + \sin(\theta_{\mathrm{PLL}} + 2\pi/3) \cdot v_{\mathrm{c}}] \end{cases} \tag{2.44}$$

where v_{a}, v_{b}, v_{c} are the three-phase AC voltages with period T_1 and fundamental frequency $f_1 = 1/T_1$, $\theta_{\mathrm{PLL}} = 2\pi f_1 t$ is the phase-lock angle (PLL output angle).

According to Eq. (2.44), it can be seen that Park's transformation is nonlinear due to the multiplication with cosine or sine functions. In order to establish a linear model, v_{a}, v_{b} and v_{c} are firstly transformed in frequency domain to obtain the steady-state operating points, denoted by $\boldsymbol{V}_{\mathrm{a}}(s)$, $\boldsymbol{V}_{\mathrm{b}}(s)$ and $\boldsymbol{V}_{\mathrm{c}}(s)$, similar to the expression in Eq. (2.24).

$$\begin{cases} \boldsymbol{V}_{\mathrm{a}}(s) = \left[\, \boldsymbol{V}_{-1},\ 0,\ \boldsymbol{V}_1 \,\right]^{\mathrm{T}} \\ \boldsymbol{V}_{\mathrm{b}}(s) = \left[\, \boldsymbol{V}_{-1}\mathrm{e}^{\mathrm{j}2\pi/3},\ 0,\ \boldsymbol{V}_1\mathrm{e}^{-\mathrm{j}2\pi/3} \,\right]^{\mathrm{T}} \\ \boldsymbol{V}_{\mathrm{c}}(s) = \left[\, \boldsymbol{V}_{-1}\mathrm{e}^{-\mathrm{j}2\pi/3},\ 0,\ \boldsymbol{V}_1\mathrm{e}^{\mathrm{j}2\pi/3} \,\right]^{\mathrm{T}} \end{cases} \tag{2.45}$$

where $\boldsymbol{V}_1$ is the steady-state component of $\boldsymbol{V}_{\mathrm{a}}$ at f_1; $\boldsymbol{V}_{-1}$ is the steady-state component at $-f_1$, satisfying $\boldsymbol{V}_{-1} = \boldsymbol{V}_1^*$.

According to Euler's formula, it can be obtained that

$$\begin{cases} \cos\theta_{\mathrm{PLL}} = \left(\mathrm{e}^{\mathrm{j}2\pi f_1 t} + \mathrm{e}^{-\mathrm{j}2\pi f_1 t}\right)/2 \\ \sin\theta_{\mathrm{PLL}} = -\mathrm{j}\left(\mathrm{e}^{\mathrm{j}2\pi f_1 t} - \mathrm{e}^{-\mathrm{j}2\pi f_1 t}\right)/2 \end{cases} \tag{2.46}$$

The Fourier series coefficients can be directly obtained from Eq. (2.46), Thus the frequency-domain vectors of the cosine and sine functions in Eq. (2.44) can be expressed as

$$\begin{cases} \boldsymbol{F}_{\mathrm{c}\theta\mathrm{a}}(s) = \dfrac{1}{2}\left[\, 1,\ 0,\ 1 \,\right]^{\mathrm{T}} \\ \boldsymbol{F}_{\mathrm{c}\theta\mathrm{b}}(s) = \dfrac{1}{2}\left[\, \mathrm{e}^{\mathrm{j}2\pi/3},\ 0,\ \mathrm{e}^{-\mathrm{j}2\pi/3} \,\right]^{\mathrm{T}} \\ \boldsymbol{F}_{\mathrm{c}\theta\mathrm{c}}(s) = \dfrac{1}{2}\left[\, \mathrm{e}^{-\mathrm{j}2\pi/3},\ 0,\ \mathrm{e}^{\mathrm{j}2\pi/3} \,\right]^{\mathrm{T}} \end{cases} \tag{2.47}$$

$$\begin{cases} \boldsymbol{F}_{\mathrm{s}\theta\mathrm{a}}(s) = \dfrac{\mathrm{j}}{2}\left[\, 1,\ 0,\ -1 \,\right]^{\mathrm{T}} \\ \boldsymbol{F}_{\mathrm{s}\theta\mathrm{b}}(s) = \dfrac{\mathrm{j}}{2}\left[\, \mathrm{e}^{\mathrm{j}2\pi/3},\ 0,\ -\mathrm{e}^{-\mathrm{j}2\pi/3} \,\right]^{\mathrm{T}} \\ \boldsymbol{F}_{\mathrm{s}\theta\mathrm{c}}(s) = \dfrac{\mathrm{j}}{2}\left[\, \mathrm{e}^{-\mathrm{j}2\pi/3},\ 0,\ -\mathrm{e}^{\mathrm{j}2\pi/3} \,\right]^{\mathrm{T}} \end{cases} \tag{2.48}$$

where $\boldsymbol{F}_{\mathrm{c}\theta\mathrm{a}}(s)$, $\boldsymbol{F}_{\mathrm{c}\theta\mathrm{b}}(s)$, $\boldsymbol{F}_{\mathrm{c}\theta\mathrm{c}}(s)$ are the frequency-domain vectors of $\cos\theta_{\mathrm{PLL}}$, $\cos(\theta_{\mathrm{PLL}} - 2\pi/3)$, $\cos(\theta_{\mathrm{PLL}}+2\pi/3)$ respectively $\boldsymbol{F}_{\mathrm{s}\theta\mathrm{a}}(s)$, $\boldsymbol{F}_{\mathrm{s}\theta\mathrm{b}}(s)$, $\boldsymbol{F}_{\mathrm{s}\theta\mathrm{c}}(s)$ are the

frequency-domain vectors of $\sin\theta_{\mathrm{PLL}}$, $\sin(\theta_{\mathrm{PLL}}-2\pi/3)$, $\sin(\theta_{\mathrm{PLL}}+2\pi/3)$ respectively.

The small-signal perturbations at f_{p} in positive sequence is superimposed on the three-phase AC voltages, denoted by $\hat{\boldsymbol{v}}_{\mathrm{a}}(s)$, $\hat{\boldsymbol{v}}_{\mathrm{b}}(s)$ and $\hat{\boldsymbol{v}}_{\mathrm{c}}(s)$, similar to Eq. (2.28).

$$\begin{cases} \hat{\boldsymbol{v}}_{\mathrm{a}}(s) = \left[0,\ \hat{\boldsymbol{v}}_{\mathrm{p}},\ 0\right]^{\mathrm{T}} \\ \hat{\boldsymbol{v}}_{\mathrm{b}}(s) = \left[0,\ \hat{\boldsymbol{v}}_{\mathrm{p}}\mathrm{e}^{-\mathrm{j}2\pi/3},\ 0\right]^{\mathrm{T}} \\ \hat{\boldsymbol{v}}_{\mathrm{c}}(s) = \left[0,\ \hat{\boldsymbol{v}}_{\mathrm{p}}\mathrm{e}^{\mathrm{j}2\pi/3},\ 0\right]^{\mathrm{T}} \end{cases} \tag{2.49}$$

where is the small-signal component of AC voltage at. Moreover, these small-signal perturbations also introduce small-signal response to the PLL output angle, denoted by $\hat{\boldsymbol{\theta}}_{\mathrm{PLL}}(s)$.

Based on the steady-state operating point, Eq. (2.44) is transformed into frequency domain and linearized by neglecting the high-order nonlinear terms in the Taylor expansion. The small-signal vectors of the d- and q-axis voltages can be respectively expressed as

$$\begin{cases} \hat{\boldsymbol{v}}_{\mathrm{d}}(s) = \dfrac{2}{3}\left[\boldsymbol{F}_{\mathrm{c}\theta\mathrm{a}}(s)\otimes\hat{\boldsymbol{v}}_{\mathrm{a}}(s) + \boldsymbol{F}_{\mathrm{c}\theta\mathrm{b}}(s)\otimes\hat{\boldsymbol{v}}_{\mathrm{b}}(s) + \boldsymbol{F}_{\mathrm{c}\theta\mathrm{c}}(s)\otimes\hat{\boldsymbol{v}}_{\mathrm{c}}(s)\right] \\ \qquad -\dfrac{2}{3}\left[\boldsymbol{F}_{\mathrm{s}\theta\mathrm{a}}(s)\otimes\boldsymbol{V}_{\mathrm{a}}(s) + \boldsymbol{F}_{\mathrm{s}\theta\mathrm{b}}(s)\otimes\boldsymbol{V}_{\mathrm{b}}(s) + \boldsymbol{F}_{\mathrm{s}\theta\mathrm{c}}(s)\otimes\boldsymbol{V}_{\mathrm{c}}(s)\right]\cdot\hat{\boldsymbol{\theta}}_{\mathrm{PLL}}(s) \\ \hat{\boldsymbol{v}}_{\mathrm{q}}(s) = -\dfrac{2}{3}\left[\boldsymbol{F}_{\mathrm{s}\theta\mathrm{a}}(s)\otimes\hat{\boldsymbol{v}}_{\mathrm{a}}(s) + \boldsymbol{F}_{\mathrm{s}\theta\mathrm{b}}(s)\ \otimes\ \hat{\boldsymbol{v}}_{\mathrm{b}}(s) + \boldsymbol{F}_{\mathrm{s}\theta\mathrm{c}}(s)\otimes\ \hat{\boldsymbol{v}}_{\mathrm{c}}(s)\right] \\ \qquad -\dfrac{2}{3}\left[\boldsymbol{F}_{\mathrm{c}\theta\mathrm{a}}(s)\otimes\boldsymbol{V}_{\mathrm{a}}(s) + \boldsymbol{F}_{\mathrm{c}\theta\mathrm{b}}(s)\otimes\boldsymbol{V}_{\mathrm{b}}(s) + \boldsymbol{F}_{\mathrm{c}\theta\mathrm{c}}(s)\otimes\boldsymbol{V}_{\mathrm{c}}(s)\right]\cdot\hat{\boldsymbol{\theta}}_{\mathrm{PLL}}(s) \end{cases} \tag{2.50}$$

As shown in Eq. (2.50), the multiplication in time domain is turned into the convolution in frequency domain. The computation of the convolution involves four steps: reversing, shifting, multiplying and integrating. The convolution of frequency-domain vectors can be simplified by expanding the vector into a matrix. Take $\boldsymbol{F}_{\mathrm{c}\theta\mathrm{a}}(s)\otimes\hat{\boldsymbol{v}}_{\mathrm{a}}(s)$ as an example, $\boldsymbol{F}_{\mathrm{c}\theta\mathrm{a}}(s)$ can be extended to a matrix, expressed as

$$\boldsymbol{F}_{\mathrm{c}\theta\mathrm{a}}(s) = \frac{1}{2}\begin{bmatrix} 0 & 1 & 0 \\ 1 & 0 & 1 \\ 0 & 1 & 0 \end{bmatrix} \tag{2.51}$$

The extension steps include:

1. The steady-state vector is transposed into a row vector and arranged in a reverse order, as the center row of the steady-state matrix.
2. The kth row above the center row is obtained by shifting the center row by k elements into the left, with the last k elements filled by 0.

3. The kth row below the center row is obtained by shifting the center row by k elements into the right, with the first k elements filled by 0.

Thus, the convolution $\boldsymbol{F}_{c\theta a}(s) \otimes \hat{\boldsymbol{v}}_a(s)$ can be simplified to the scalar product, that is, the multiplication of a matrix and a vector. Similarly, this method can be used to compute other convolutions in Eq. (2.50). The small-signal vectors of d- and q-axis voltages can be obtained as

$$\begin{cases} \hat{\boldsymbol{v}}_d(s) = \left[\hat{\boldsymbol{v}}_p,\ 0,\ 0\right]^T \\ \hat{\boldsymbol{v}}_q(s) = \left[-j\hat{\boldsymbol{v}}_p,\ 0,\ 0\right]^T - V_1\hat{\boldsymbol{\theta}}_{PLL}(s) \end{cases} \tag{2.52}$$

where V_1 is the amplitude of the AC voltage and composed of the harmonic components at $\pm f_1$, satisfying $V_1 = 2|\boldsymbol{V}_1|$.

According to the block diagram of the PLL, the frequency-domain relationship between $\hat{\boldsymbol{v}}_q(s)$ and $\hat{\boldsymbol{\theta}}_{PLL}(s)$ is

$$\hat{\boldsymbol{\theta}}_{PLL}(s) = H_{PLL}(s)\hat{\boldsymbol{v}}_q(s) \tag{2.53}$$

$$H_{PLL}(s) = \left(K_{pp} + \frac{K_{pi}}{s}\right)\frac{1}{s} \tag{2.54}$$

where $H_{PLL}(s)$ is the transfer function of PLL, and K_{pp}, K_{pi} are proportional and integral coefficients of PLL respectively.

Substituting Eq. (2.52) into Eq. (2.54), the linearized expression between $\hat{\boldsymbol{\theta}}_{PLL}(s)$ and $\hat{\boldsymbol{v}}_p$ can be derived as

$$\hat{\boldsymbol{\theta}}_{PLL}(s) = \left[-jT_{PLL}[j2\pi(f_p - f_1)] \cdot \hat{\boldsymbol{v}}_p,\ 0,\ 0\right]^T \tag{2.55}$$

where "s" equals to $j2\pi(f_p\text{-}f_1)$; $T_{PLL}(s)$ is the closed-loop transfer function of PLL, expressed as

$$T_{PLL}(s) = \frac{H_{PLL}(s)}{1 + V_1 H_{PLL}(s)} \tag{2.56}$$

Substituting Eq. (2.55) into Eq. (2.52), the linearized expression between $\hat{\boldsymbol{v}}_q(s)$ and $\hat{\boldsymbol{v}}_p$ can be derived as

$$\hat{\boldsymbol{v}}_q(s) = \left[j\left(V_1 T_{PLL}[j2\pi(f_p - f_1)] - 1\right)\hat{\boldsymbol{v}}_p,\ 0,\ 0\right]^T \tag{2.57}$$

According to Eqs. (2.49), (2.52), (2.55) and (2.57), small-signal perturbations at f_p in positive sequence are superimposed on the AC voltages, thus the small-signal response of $\hat{\boldsymbol{v}}_d(s)$, $\hat{\boldsymbol{v}}_q(s)$, and $\hat{\boldsymbol{\theta}}_{PLL}(s)$ at $f_p - f_1$ will be generated, which is consistent with the rotation direction of Park transformation. Similarly, small-signal

perturbations at f_p in negative sequence will generate the small-signal response of $\hat{\boldsymbol{v}}_d(s)$, $\hat{\boldsymbol{v}}_q(s)$, and small-signal response of $\hat{\boldsymbol{\theta}}_{PLL}(s)$ at $f_p + f_1$.

Furthermore, the dq-axis components will be transformed into three-phase modulation signals through inverse Park transformation. Since it also involves the multiplication of cosine and sine functions, the frequency-domain linearization for inverse Park transformation can be obtained in similar approaches.

References

1. CESPEDES M, SUN J. Impedance modeling and analysis of grid-connected voltage-source converters [J]. IEEE Transactions on Power Electronics, 2014, 29(3): 1254–1261.
2. SUN J. Two-port characterization and transfer immittances of AC-DC converters-part I: modeling [J]. IEEE Open Journal of Power Electronics, 2021, 2: 440–462.
3. SUN J. Two-port characterization and transfer immittances of AC-DC converters-part II: applications [J]. IEEE Open Journal of Power Electronics, 2021, 2: 483–510.

Chapter 3
Impedance Modeling of Two-Level Converter

The mathematical model of two-level converter includes several non-linear parts such as insulated-gate bipolar transistor (IGBT) switching, pulse width modulation (PWM), Park transformation, and PLL[1, 2]. Besides, the dynamic characteristics of the DC bus, which shows as a non-ideal voltage source, will also affect the frequency coupling in a broad frequency band an the accuracy of Nyquist stability criterion. Some oscillations may be missed in the oscillation evaluation with the traditional two-level converter model, which neglects the dynamics of DC bus [3–5].

In this chapter, the influence on frequency coupling of the DC voltage controller of two-level converter is firstly studied. With the frequency-domain linearization method, the expression of the relationship between the modulation voltage and the DC voltage is established based on the averaged model. In addition, the small-signal response relationships in frequency domain are analyzed. Then the small-signal AC port impedance model considering PLL, AC current loop, and DC voltage loop is established. The established model in this chapter lays a foundation for the impedance modeling and stability analysis of wind turbines and PV units.

3.1 Operation Principle

3.1.1 Topology

The two-level converter mainly adopts the three-phase half-bridge topology, as shown in Fig. 3.1. Since the DC-side is paralleled with capacitor, this topology is voltage source converter (VSC). In the figure, V_a, V_b, V_c are three-phase AC voltages, i_a, i_b, i_c are three-phase AC currents, and V_{ia}, V_{ib}, V_{ic} are three-phase AC modulation voltages. L_f is the AC filter inductor. C_{dc} is the DC bus capacitor. V_{dc} and i_{dc}

© China Electric Power Press 2023

W. Wang et al., *Analysis and Mitigation of Broadband Oscillation in Renewable Energy Generation and AC/DC Transmission Systems*,
https://doi.org/10.1007/978-981-99-1568-2_3

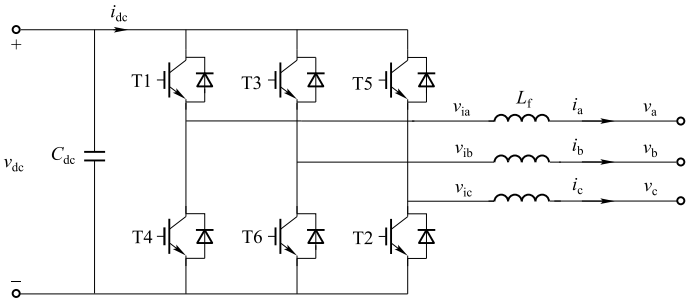

Fig. 3.1 Topology of two-level converter

are the DC voltage and current respectively. T1–T6 are the IGBT switches. $l = $ a, b, c represent phase a, phase b, and phase c respectively.

3.1.2 Averaged Model

According to the linearization method of the switches, the influence of harmonics with the carrier frequency can be neglected when the frequency of PWM carrier is much higher than that of the modulation wave. Hence, the averaged model of two-level converter is shown in Fig. 3.2.

According to Fig. 3.2, the relationship of voltages and currents between the AC port and DC port of two-level converter satisfies

$$\begin{cases} v_{il} = K_{\mathrm{m}} m_l v_{\mathrm{dc}} \\ i_{\mathrm{dc}} = \sum\limits_{l=\mathrm{a,b,c}} m_l i_l \end{cases} \tag{3.1}$$

where K_{m} is the modulation gain, m_l is the three-phase modulation signal.

According to the relationship between i_l, V_{il}, and V_l, the current of the AC filter inductor can be obtained by

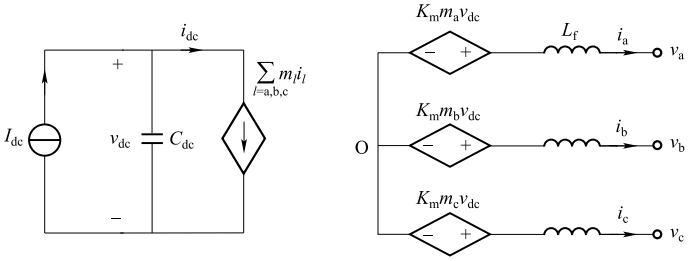

Fig. 3.2 The averaged model of two-level converter

$$v_{il} = v_l + L_f \frac{di_l}{dt} \tag{3.2}$$

Assuming that the input of the DC port of the converter is an ideal current source, based on the instantaneous power balance principle between the input and the output, the following equation can be obtained as

$$v_{dc}\left(I_{dc} - C_{dc}\frac{dv_{dc}}{dt}\right) = \sum_{l=a,b,c} v_{il} i_l \tag{3.3}$$

where l_{dc} is the steady-state value of DC current.

3.1.3 Control Strategy

Figure 3.3 shows the control diagram of the two-level converter, including PLL, DC voltage control and AC current control.

PLL is generally used to obtain the phase of grid voltage, which is also called the grid-connected synchronization control. Proportional integral (PI) controller is generally used in the PLL which transfer function can be expressed as

$$H_{PLL}(s) = \left(K_{pp} + \frac{K_{pi}}{s}\right)\frac{1}{s} \tag{3.4}$$

where K_{pp} and K_{pi} are proportional and integral coefficients respectively.

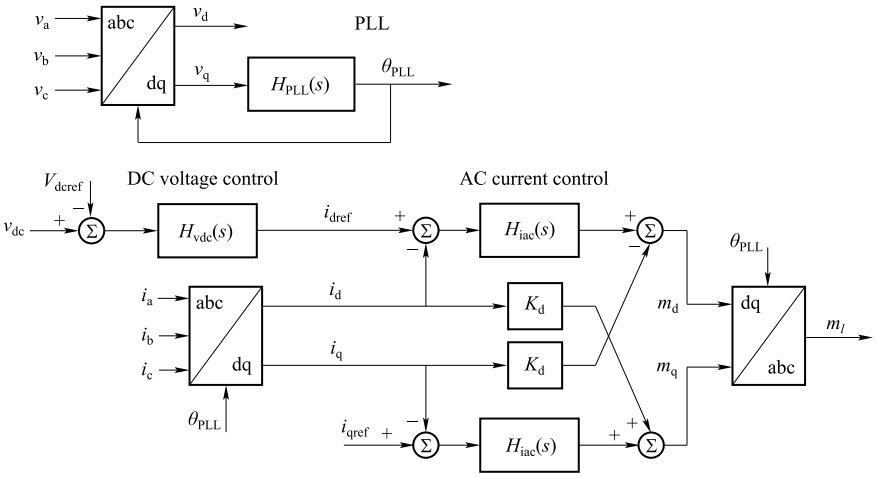

Fig. 3.3 Control diagram of two-level converter

With the phase-locked angle θ_{PLL} obtained by PLL, the three-phase AC voltage v_l in stationary coordinate frame (SCF) can be transformed to the dq-axis components in synchronous rotating frame (SRF) by Park transformation. The two-level converter are generally controlled in the SRF, using a dual-loop control structure with a DC voltage outer loop and AC current inner loop.

The objective of the DC voltage loop is to regulate the DC voltage according to the DC voltage reference V_{dcref}, which generates the d-axis current reference i_{dref} for the AC current loop. PI controller is generally used in the DC voltage loop, which transfer function can be expressed as

$$H_{\mathrm{vdc}}(s) = K_{\mathrm{vdcp}} + \frac{K_{\mathrm{vdci}}}{s} \tag{3.5}$$

where K_{vdcp} and K_{vdci} are the proportional and integral coefficients of the DC voltage loop respectively.

The objective of the AC current loop is to regulate the d- and q-axis current i_{d} and i_{q} according to the d- and q- axis current references i_{dref} and i_{qref}. PI controller is generally used in the AC current loop, whose transfer function can be expressed as

$$H_{\mathrm{iac}}(s) = K_{\mathrm{iacp}} + \frac{K_{\mathrm{iaci}}}{s} \tag{3.6}$$

where K_{iacp} and K_{iaci} are the proportional and integral coefficients of the AC current loop respectively.

3.2 Frequency-Domain Modeling of Steady-State Operation

The steady-state operating point of the two-level converter is periodical time-varying. In this section, the steady-state voltages and currents of the two-level converter are first transformed to frequency domain through FFT to obtain the steady-state operating point. Then, the frequency-domain steady-state model of the main circuit is established.

3.2.1 Frequency-Domain Characteristic Analysis of Steady-State Operating Point

Table 3.1 shows the parameters of the main circuit and controllers of a two-level converter. Based on these parameters, Fig. 3.4 shows the steady-state waveforms in time domain and the operating point in frequency domain. It can be seen that the AC

Table 3.1 Parameters of the main circuit and controllers of two-level converter

Parameter	Definition	Value
P_{N}	Rated power	1.5 MW
V_1	Amplitude of the fundamental component of AC voltage	563 V
V_{dc}	Steady-state value of DC voltage	1150 V
C_{dc}	DC bus capacitance	129.6 mF
C_{f}	AC filter capacitance	600 μF
L_{f}	AC filter inductance	75 μH
K_{pp}, K_{pi}	Proportional and integral coefficients of PLL controller	0.0385, 60
K_{iacp}, K_{iaci}	Proportional and integral coefficients of AC current controller	2×10^{-4}, 0.5000
K_{d}	Decoupling coefficient of AC current controller	4.0977×10^{-5}
K_{vdcp}, K_{vdci}	Proportional and integral coefficients of DC voltage controller	96,603

voltages, AC currents, and modulation signals only contain components at $\pm f_1$, and the DC voltage only contains DC component.

The time-domain expression of three-phase AC voltages can be expressed as

$$\begin{cases} v_{\mathrm{a}} = V_1 \cos(2\pi f_1 t + \varphi_{\mathrm{v1}}) \\ v_{\mathrm{b}} = V_1 \cos\left(2\pi f_1 t + \varphi_{\mathrm{v1}} - \dfrac{2\pi}{3}\right) \\ v_{\mathrm{c}} = V_1 \cos\left(2\pi f_1 t + \varphi_{\mathrm{v1}} + \dfrac{2\pi}{3}\right) \end{cases} \tag{3.7}$$

where V_1 and φ_{v1} are the amplitude and phase of the fundamental component of AC voltage respectively.

The steady-state components of AC voltages, AC currents, modulation signals can be arranged in the following frequency order.

$$\left[-f_1,\ 0,\ f_1\right]^{\mathrm{T}} \tag{3.8}$$

For example, the steady-state vector of the phasea AC voltage in frequency domain can be expressed as

$$\boldsymbol{V}_{\mathrm{a}} = \left[\boldsymbol{V}_{-1},\ 0,\ \boldsymbol{V}_1\right]^{\mathrm{T}} \tag{3.9}$$

Each element in the vector is expressed in the complex vector form, where $\boldsymbol{V}_1 = V_1 e^{\mathrm{j}\varphi_{\mathrm{v1}}}/2$ and $\boldsymbol{V}_{-1} = V_1 e^{-\mathrm{j}\varphi_{\mathrm{v1}}}/2$; V_1 is the steady-state component of AC voltage at f_1, V_{-1} is the steady-state component of AC voltage at $-f_1$. It can be seen that $\boldsymbol{V}_{-1} = \boldsymbol{V}_1^*$, where the superscript * denotes the conjugate operation.

Similarly, the steady-state vectors of phase-a AC current $\boldsymbol{I}_{\mathrm{a}}$ and modulation signal $\boldsymbol{M}_{\mathrm{a}}$ can be expressed as

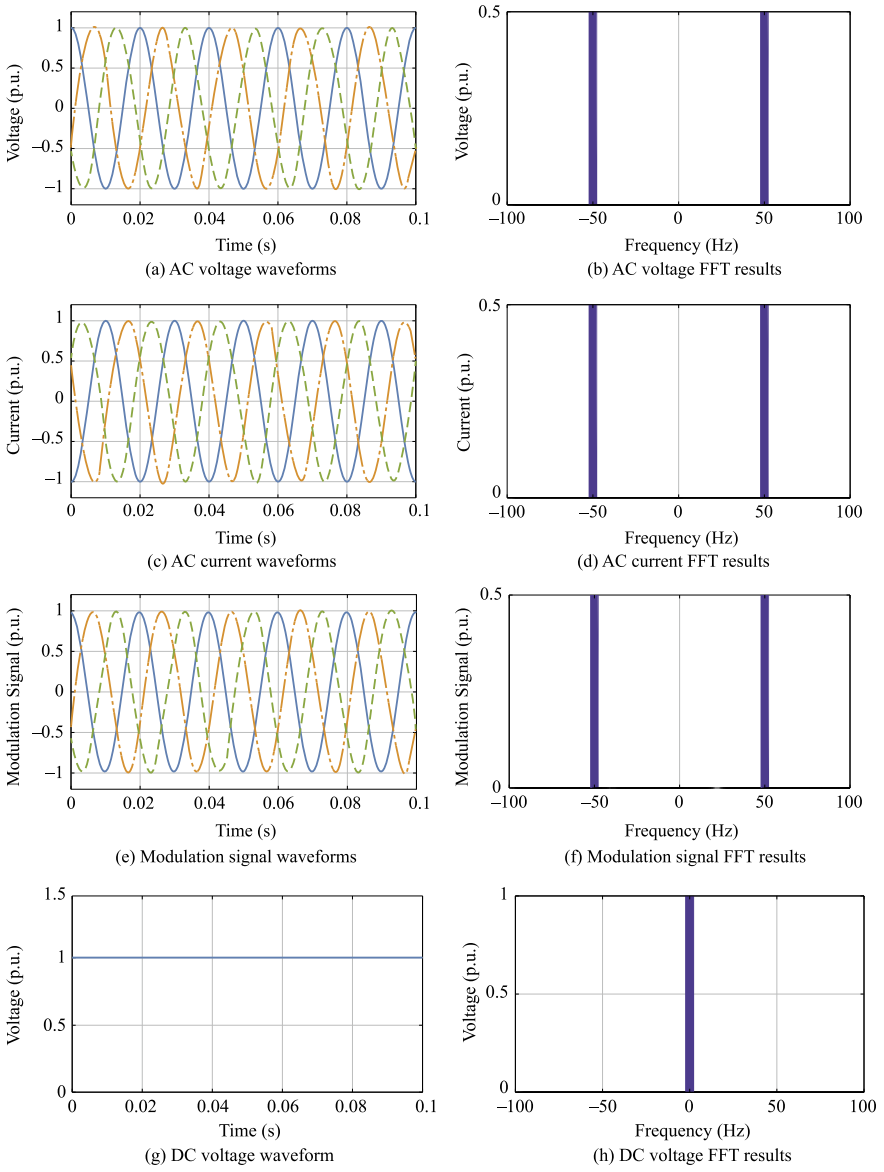

(a) AC voltage waveforms
(b) AC voltage FFT results
(c) AC current waveforms
(d) AC current FFT results
(e) Modulation signal waveforms
(f) Modulation signal FFT results
(g) DC voltage waveform
(h) DC voltage FFT results

Fig. 3.4 Steady-state waveforms and FFT results of the two-level converter

$$\begin{cases} \boldsymbol{I}_{\mathrm{a}} = \left[\boldsymbol{I}_1^*,\ 0,\ \boldsymbol{I}_1 \right]^{\mathrm{T}} \\ \boldsymbol{M}_{\mathrm{a}} = \left[\boldsymbol{M}_1^*,\ 0,\ \boldsymbol{M}_1 \right]^{\mathrm{T}} \end{cases} \tag{3.10}$$

where $\boldsymbol{I}_1$ and $\boldsymbol{M}_1$ are the steady-state components of AC current and modulation signal at f_1 respectively.

According to the phase-sequence relationship, the steady-state vectors of phase b and phase c can be obtained as

$$\begin{cases} \boldsymbol{V}_{\mathrm{b}} = \boldsymbol{D}\boldsymbol{V}_{\mathrm{a}}, & \boldsymbol{V}_{\mathrm{c}} = \boldsymbol{D}^{*}\boldsymbol{V}_{\mathrm{a}} \\ \boldsymbol{I}_{\mathrm{b}} = \boldsymbol{D}\boldsymbol{I}_{\mathrm{a}}, & \boldsymbol{I}_{\mathrm{c}} = \boldsymbol{D}^{*}\boldsymbol{I}_{\mathrm{a}} \\ \boldsymbol{M}_{\mathrm{b}} = \boldsymbol{D}\boldsymbol{M}_{\mathrm{a}}, & \boldsymbol{M}_{\mathrm{c}} = \boldsymbol{D}^{*}\boldsymbol{M}_{\mathrm{a}} \end{cases} \tag{3.11}$$

where $\boldsymbol{D}$ is the phase-sequence coefficient matrix of steady-state vectors, expressed as

$$\boldsymbol{D} = \mathrm{diag}\left[\left\{ \mathrm{e}^{-\mathrm{j}2k\pi/3} \right\}\Big|_{k=-1,0,1} \right] \tag{3.12}$$

In Eqs. (3.9)–(3.11), the components at f_1 are in positive sequence, and the corresponding ones lag $2\pi/3$ in turn in the three-phase vectors. The components at $-f_1$ are in negative sequence, and the corresponding ones lead $2\pi/3$ in turn in the three-phase vectors. In addition, the middle component is in zero sequence.

DC voltage only contains DC component, and its steady-state vector can be expressed as

$$\boldsymbol{V}_{\mathrm{dc}} = \left[0,\ V_{\mathrm{dc}},\ 0 \right]^{\mathrm{T}} \tag{3.13}$$

where V_{dc} is the steady-state value of DC voltage.

3.2.2 Frequency-Domain Steady-State Model of Main Circuit

The frequency-domain steady-state model of the main circuit can be obtained by transforming Eq. (3.2) into frequency-domain, which can be expressed as

$$\boldsymbol{V}_{\mathrm{i}l} = \boldsymbol{V}_{l} + \boldsymbol{Z}_{\mathrm{Lf0}}\boldsymbol{I}_{l} \tag{3.14}$$

where $\boldsymbol{V}_{\mathrm{i}l}$ is the steady-state vector of three-phase modulation voltage, $\boldsymbol{Z}_{\mathrm{Lf0}}$ is the impedance of AC filter inductor in steady-state frequency order. $\boldsymbol{Z}_{\mathrm{Lf0}}$ is a diagonal matrix, which can be expressed as

$$\boldsymbol{Z}_{\mathrm{Lf0}} = \mathrm{j}2\pi L_{\mathrm{f}} \cdot \mathrm{diag}\left[-f_1,\ 0,\ f_1 \right] \tag{3.15}$$

Based on above equations, the frequency order of $\boldsymbol{V}_{\mathrm{i}l}$ are consistent with that of $\boldsymbol{V}_{l}$ and $\boldsymbol{I}_{l}$. The difference between $\boldsymbol{V}_{\mathrm{i}l}$ and $\boldsymbol{V}_{l}$ at f_1 drops on the filter inductor, generating a response of $\boldsymbol{I}_{l}$ at f_1. The same is true for the components at $-f_1$.

By transforming Eq. (3.1) into the frequency domain, the steady-state vector of the three-phase AC modulation voltage can be obtained as

Table 3.2 The steady-state frequency response relationship of DC voltage, modulation signal, and modulation voltage

Steady-State Vectors	$\boldsymbol{V}_{\mathrm{dc}}$	$\boldsymbol{M}_l$	$\boldsymbol{V}_{il}$
Frequency	DC	f_1	f_1
		$-f_1$	$-f_1$

$$\boldsymbol{V}_{\mathrm{i}l} = K_{\mathrm{m}}\boldsymbol{M}_l \otimes \boldsymbol{V}_{\mathrm{dc}} \tag{3.16}$$

The convolution operation can be realized by scalar product. To use scalar product, $\boldsymbol{M}_l$ needs to be expanded into a matrix. Taking phase a as an example, the steady-state vector of the AC modulation voltage. $\boldsymbol{M}_{\mathrm{a}}$ in Eq. (3.10) can be extended to a 3×3 matrix, which can be expressed as

$$\boldsymbol{M}_{\mathrm{a}} = \begin{bmatrix} 0 & \boldsymbol{M}_1^* & 0 \\ \boldsymbol{M}_1 & 0 & \boldsymbol{M}_1^* \\ 0 & \boldsymbol{M}_1 & 0 \end{bmatrix} \tag{3.17}$$

The extension steps include:

1. The steady-state vector is transposed into a row vector and arranged in a reverse order, as the center row of the steady-state matrix $\boldsymbol{M}_{\mathrm{a}}$.
2. The Row 1 of the steady-state matrix $\boldsymbol{M}_{\mathrm{a}}$ is obtained by shifting the center row by one element into the left, with the last one element filled by 0.
3. The Row 3 of the steady-state matrix $\boldsymbol{M}_{\mathrm{a}}$ is obtained by shifting the center row by one element into the right, with the first one element filled by 0.

Based on Eq. (3.16), the steady-state relationship of DC voltage, modulation signal, and AC modulation voltage in frequency domain is shown in Table 3.2. It indicates that the component of $\boldsymbol{M}_l$ at f_1 multiples $\boldsymbol{V}_{\mathrm{dc}}$, generating a component in $\boldsymbol{V}_{il}$ at f_1. Meanwhile, the steady-state component of $\boldsymbol{M}_l$ at $-f_1$ multiples $\boldsymbol{V}_{\mathrm{dc}}$, generating a steady-state component in $\boldsymbol{V}_{il}$ at $-f_1$.

3.3 Small-Signal Impedance Modeling in Frequency Domain

In this section, the frequency-domain linearization method is used to establish the small-signal AC port impedance model of the two-level converter. First, the AC voltage, AC current, and modulation signals are transformed to the frequency domain to obtain the operating point. Then, the small-signal perturbation of different frequencies are injected to the AC voltage. Finally, the impedance model is established by calculating the responses of AC current to the AC voltage perturbation.

3.3.1 Small-Signal Frequency-Domain Characteristic Analysis

According to the instantaneous input/output power balance of the two-level converter, a small-signal DC voltage respone will be generated after the injecting a small-signal perturbation in AC voltage. A small-signal response in the AC modulation voltage will be generated by multiplying the steady-state vector of the modulation signal $\boldsymbol{M}_1$ and the small-signal vector of DC voltage. A small-signal response of AC current will be generated based on the difference between the modulation voltage and the AC voltage. The small-signal transfer path and frequency response relationship of the two-level converter are shown in Fig. 3.5.

In Fig. 3.5, a small-signal perturbation $\hat{\boldsymbol{v}}_l$ in the positive sequence at f_p is injected into the AC voltage at the steady-state operating point. Take phase a as an example, a small-signal response of active power at $f_\mathrm{p} - f_1$ will be generated in the AC port, since the small-signal vector of AC voltage $\hat{\boldsymbol{v}}_a$ multiplying the steady-state vector of AC current $\boldsymbol{I}_\mathrm{a}$. According to the instantaneous power balance, a small-signal response of active power at $f_\mathrm{p} - f_1$ will be generated in the DC port. Meanwhile, a small-signal DC voltage response $\hat{\boldsymbol{v}}_\mathrm{dc}$ will also be generated at $f_\mathrm{p} - f_1$.

According to Eq. (3.16), $\hat{\boldsymbol{v}}_\mathrm{dc}$ at $f_\mathrm{p} - f_1$ multiplying the steady-state component of $\boldsymbol{M}_\mathrm{a}$ at f_1 leads to a small-signal response of AC modulation voltage $\hat{\boldsymbol{v}}_\mathrm{ia}$ at f_p. Similarly, $\hat{\boldsymbol{v}}_\mathrm{dc}$ at $f_\mathrm{p} - f_1$ multiplying the steady-state component of $\boldsymbol{M}_\mathrm{a}$ at $-f_1$ leads to a small-signal response of $\hat{\boldsymbol{v}}_\mathrm{ia}$ at $f_\mathrm{p} - 2f_1$. Furthermore, the difference between $\hat{\boldsymbol{v}}_\mathrm{ia}$ and $\hat{\boldsymbol{v}}_\mathrm{a}$ at f_p on the filter inductor leads to a small-signal response of $\hat{\boldsymbol{i}}_\mathrm{a}$ at f_p. Similarly, $\hat{\boldsymbol{v}}_\mathrm{ia}$ at $f_\mathrm{p} - 2f_1$ leads to a small-signal response of $\hat{\boldsymbol{i}}_\mathrm{a}$ at $f_\mathrm{p} - 2f_1$.

In summary, the small-signal response of AC current $\hat{\boldsymbol{i}}_\mathrm{a}$ includes components at f_p and $f_\mathrm{p} - 2f_1$ under the small-signal positive-sequence AC voltage perturbation $\hat{\boldsymbol{v}}_\mathrm{a}$ at f_p. This frequency coupling effect is caused by DC bus dynamics, where f_p is the dominant frequency and $f_\mathrm{p} - 2f_1$ is the coupling frequency.

In addition, the small-signal response of the AC modulation signal $\hat{\boldsymbol{m}}_l$ is also generated due to the converter control. As seen in Fig. 3.3, the coordinate transformation is required for generating the modulation signals. Define the small-signal vector of the three-phase AC input signals as $\hat{\boldsymbol{u}}_\mathrm{abc}$, the small-signal vector of the three-phase AC modulation signasl as $\hat{\boldsymbol{m}}_\mathrm{abc}$. The corresponding vectors in SCF can be expressed as

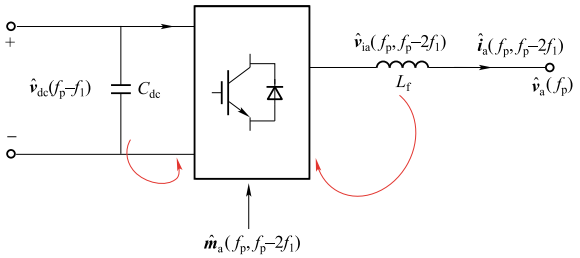

Fig. 3.5 The small-signal transfer path and frequency response relationship of the two-level converter

$$\begin{cases} \hat{\boldsymbol{u}}_{\mathrm{abc}} = 2/3\left(\hat{\boldsymbol{u}}_{\mathrm{a}} + \mathrm{e}^{\mathrm{j}2\pi/3}\hat{\boldsymbol{u}}_{\mathrm{b}} + \mathrm{e}^{-\mathrm{j}2\pi/3}\hat{\boldsymbol{u}}_{\mathrm{c}}\right) \\ \hat{\boldsymbol{m}}_{\mathrm{abc}} = 2/3\left(\hat{\boldsymbol{m}}_{\mathrm{a}} + \mathrm{e}^{\mathrm{j}2\pi/3}\hat{\boldsymbol{m}}_{\mathrm{b}} + \mathrm{e}^{-\mathrm{j}2\pi/3}\hat{\boldsymbol{m}}_{\mathrm{c}}\right) \end{cases}. \tag{3.18}$$

Accordingly, the small-signal vector in the SRF can be expressed as

$$\begin{cases} \hat{\boldsymbol{u}}_{\mathrm{dq}} = \hat{\boldsymbol{u}}_{\mathrm{d}} + \mathrm{j}\hat{\boldsymbol{u}}_{\mathrm{q}} \\ \hat{\boldsymbol{m}}_{\mathrm{dq}} = \hat{\boldsymbol{m}}_{\mathrm{d}} + \mathrm{j}\hat{\boldsymbol{m}}_{\mathrm{q}} \end{cases} \tag{3.19}$$

where $\hat{\boldsymbol{u}}_{\mathrm{d}}$, $\hat{\boldsymbol{u}}_{\mathrm{q}}$ are the d- and q-axis small-signal vectors of the input signals respectively; $\hat{\boldsymbol{m}}_{\mathrm{d}}$, $\hat{\boldsymbol{m}}_{\mathrm{q}}$ are the d- and q-axis small-signal vectors of the modulation signals respectively.

The relationship between vectors in the SCF and SRF satisfies

$$\begin{cases} \hat{\boldsymbol{u}}_{\mathrm{dq}} = \mathrm{e}^{-\mathrm{j}\theta_1}\hat{\boldsymbol{u}}_{\mathrm{abc}} \\ \hat{\boldsymbol{m}}_{\mathrm{abc}} = \mathrm{e}^{\mathrm{j}\theta_1}\hat{\boldsymbol{m}}_{\mathrm{dq}} \end{cases} \tag{3.20}$$

where θ_1 is the rotation reference angle in SRF, $\theta_1 = \omega_1 t$; ω_1 is the fundamental angular frequency.

Thus, the small-signal relationship between the modulation signal vectors and input signal vectors in SRF can be expressed by the transfer function matrix as

$$\begin{bmatrix} \hat{\boldsymbol{m}}_{\mathrm{d}} \\ \hat{\boldsymbol{m}}_{\mathrm{q}} \end{bmatrix} = \begin{bmatrix} G_{\mathrm{dd}}(s) & G_{\mathrm{dq}}(s) \\ G_{\mathrm{qd}}(s) & G_{\mathrm{qq}}(s) \end{bmatrix} \begin{bmatrix} \hat{\boldsymbol{u}}_{\mathrm{d}} \\ \hat{\boldsymbol{u}}_{\mathrm{q}} \end{bmatrix} \tag{3.21}$$

where $G_{\mathrm{dd}}(s)$ is the transfer function from $\hat{\boldsymbol{u}}_{\mathrm{d}}$ to $\hat{\boldsymbol{m}}_{\mathrm{d}}$, $G_{\mathrm{dq}}(s)$ is the transfer function from $\hat{\boldsymbol{u}}_{\mathrm{q}}$ to $\hat{\boldsymbol{m}}_{\mathrm{d}}$, $G_{\mathrm{qd}}(s)$ is the transfer function from $\hat{\boldsymbol{u}}_{\mathrm{d}}$ to $\hat{\boldsymbol{m}}_{\mathrm{q}}$; $G_{\mathrm{qq}}(s)$ is the transfer function from $\hat{\boldsymbol{u}}_{\mathrm{q}}$ to $\hat{\boldsymbol{m}}_{\mathrm{q}}$.

Substituting Eq. (3.19) into Eq. (3.21), $\hat{\boldsymbol{m}}_{\mathrm{dq}}$ can be rewritten as

$$\begin{aligned} \hat{\boldsymbol{m}}_{\mathrm{dq}} = &\left(\frac{G_{\mathrm{dd}}(s) + G_{\mathrm{qq}}(s)}{2} + \mathrm{j}\frac{G_{\mathrm{qd}}(s) - G_{\mathrm{dq}}(s)}{2}\right)\hat{\boldsymbol{u}}_{\mathrm{dq}} \\ &+ \left(\frac{G_{\mathrm{dd}}(s) - G_{\mathrm{qq}}(s)}{2} + \mathrm{j}\frac{G_{\mathrm{qd}}(s) + G_{\mathrm{dq}}(s)}{2}\right)\hat{\boldsymbol{u}}^{*}_{\mathrm{dq}} \end{aligned} \tag{3.22}$$

The input signals at f_{p} in positive sequence can be expressed as a vector that rotates in the forward direction (anticlockwise direction) in the SCF with angular velocity $\omega_{\mathrm{p}}(\omega_{\mathrm{p}} = 2\pi f_{\mathrm{p}})$, which can be expressed as

$$\hat{\boldsymbol{u}}_{\mathrm{abc}} = \boldsymbol{U}_{\mathrm{p}}\mathrm{e}^{\mathrm{j}\omega_{\mathrm{p}}t} \tag{3.23}$$

where $\boldsymbol{U}_{\mathrm{p}}$ is the complex Fourier coefficient of the original input signal at $\hat{\boldsymbol{u}}_l f_{\mathrm{p}}$.

Substituting Eq. (3.23) into Eq. (3.20), $\hat{\boldsymbol{u}}_{\mathrm{dq}}$ can be obtained as

$$\hat{\boldsymbol{u}}_{\mathrm{dq}} = \boldsymbol{U}_{\mathrm{p}} \mathrm{e}^{\mathrm{j}(\omega_{\mathrm{p}}-\omega_1)t} \tag{3.24}$$

Eq. (3.24) indicates that $\hat{\boldsymbol{u}}_{\mathrm{dq}}$ rotates in the forward direction at $\omega_{\mathrm{p}} - \omega_1$ in SRF. According to Eqs. (3.22) and (3.24), $\hat{\boldsymbol{m}}_{\mathrm{dq}}$ contains rotation vectors both in the forward and backward directions, referring to $\hat{\boldsymbol{u}}_{\mathrm{dq}}$ and $\hat{\boldsymbol{u}}^*_{\mathrm{dq}}$ respectively.

Substituting Eq. (3.22) into Eq. (3.20), $\hat{\boldsymbol{m}}_{\mathrm{abc}}$ can be rewritten as

$$\hat{\boldsymbol{m}}_{\mathrm{abc}} = \hat{\boldsymbol{m}}_{\mathrm{abc1}} + \hat{\boldsymbol{m}}_{\mathrm{abc2}} \tag{3.25}$$

where

$$\begin{cases} \hat{\boldsymbol{m}}_{\mathrm{abc1}} = \left(\dfrac{G_{\mathrm{dd}}(s) + G_{\mathrm{qq}}(s)}{2} + \mathrm{j}\dfrac{G_{\mathrm{qd}}(s) - G_{\mathrm{dq}}(s)}{2} \right) \boldsymbol{U}_{\mathrm{p}} \mathrm{e}^{\mathrm{j}\omega_{\mathrm{p}}t} \\ \hat{\boldsymbol{m}}_{\mathrm{abc2}} = \left(\dfrac{G_{\mathrm{dd}}(s) - G_{\mathrm{qq}}(s)}{2} + \mathrm{j}\dfrac{G_{\mathrm{qd}}(s) + G_{\mathrm{dq}}(s)}{2} \right) \boldsymbol{U}^*_{\mathrm{p}} \mathrm{e}^{-\mathrm{j}(\omega_{\mathrm{p}}-2\omega_1)t} \end{cases} \tag{3.26}$$

According to Eqs. (3.25) and (3.26), once $G_{\mathrm{dd}}(s) \neq G_{\mathrm{qq}}(s)$ or $G_{\mathrm{qd}}(s) \neq -G_{\mathrm{dq}}(s)$, there will be $\hat{\boldsymbol{m}}_{\mathrm{abc2}} \neq 0$. It means that, once the control in SRF is asymmetric in $\hat{\boldsymbol{m}}_{\mathrm{abc}}$, there will be not only the rotation vector $\hat{\boldsymbol{m}}_{\mathrm{abc1}}$ with angular velocity ω_{p} in the forward direction, but also the rotation vector $\hat{\boldsymbol{m}}_{\mathrm{abc2}}$ with angular velocity $\omega_{\mathrm{p}} - 2\omega_1$ in the backward direction. The transformation process of the relevant rotation vectors is shown in Fig. 3.6.

Therefore, the small-signal response of phase-a modulation signal $\hat{\boldsymbol{m}}_{\mathrm{a}}$ also includes components f_{p} and $f_{\mathrm{p}} - 2f_1$ under the small-signal AC voltage perturbation $\hat{\boldsymbol{v}}_l$ at f_{p}. According to Eq. (3.16), $\hat{\boldsymbol{m}}_{\mathrm{a}}$ at f_{p} multiplying the steady-state component of $\boldsymbol{V}_{\mathrm{dc}}$ leads to $\hat{\boldsymbol{v}}_{\mathrm{ia}}$ at f_{p}. Similarly, $\hat{\boldsymbol{m}}_{\mathrm{a}}$ at $f_{\mathrm{p}} - 2f_1$ multiplying $\boldsymbol{V}_{\mathrm{dc}}$ leads to $\hat{\boldsymbol{v}}_{\mathrm{ia}}$ at $f_{\mathrm{p}} - 2f_1$. Furthermore, $\hat{\boldsymbol{v}}_{\mathrm{ia}}$ $\hat{\boldsymbol{v}}_{\mathrm{a}}$ at f_{p} and f_{p}-$2f_1$ drop on the filter inductor leads to $\hat{\boldsymbol{i}}_{\mathrm{a}}$ at f_{p} and $\hat{\boldsymbol{v}}_{\mathrm{ia}}$ $f_{\mathrm{p}} - 2f_1$ respectively. $\hat{\boldsymbol{i}}_{\mathrm{a}}$ $f_{\mathrm{p}} - 2f_1$.

In conclusion, the DC bus dynamics and asymmetry control in dq-axis also lead to frequency coupling effect. Under the small-signal perturbation in the positive sequence at f_{p}, there are not only AC current response at f_{p} in positive sequence, but also the coupling AC current response at $f_{\mathrm{p}} - 2f_1$ in negative sequence in the two-level

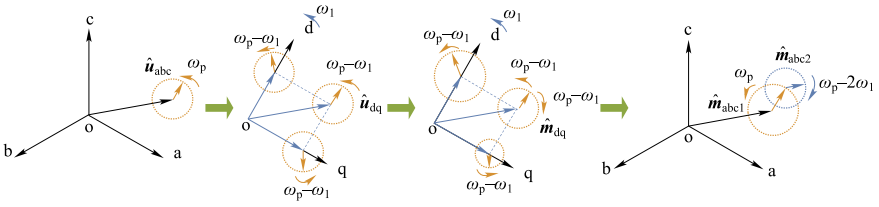

(a) Disturbance at ω_{p} on SCF (b) Disturbance at ω_{p}–ω_1 on SRF (c) Response at ω_{p}–ω_1 on SRF (d) Response at ω_{p} and ω_{p}–$2\omega_1$ on SCF

Fig. 3.6 Transformation process of rotation vectors in SCF and SRF

Table 3.3 The small-signal frequency responses of AC voltage, DC voltage and modulation signals

Small-Signal Vectors	Frequency
$\hat{\boldsymbol{v}}_{\mathrm{dc}}$	$f_{\mathrm{p}} - f_1$
$\hat{\boldsymbol{m}}_l$	f_{p}
	$f_{\mathrm{p}} - 2f_1$
$\hat{\boldsymbol{v}}_{\mathrm{i}l}$	f_{p}
	$f_{\mathrm{p}} - 2f_1$

converter. The small-signal frequencies of AC voltage, DC voltage, and modulation signals are shown in Table 3.3.

3.3.2 *Frequency-Domain Small-Signal Model of Main Circuit*

In order to describe the frequency-domain characteristics of voltages and currents of two-level converter, the small-signal components are arranged in the following frequency order.

$$\left[\, f_{\mathrm{p}} - 2f_1,\ f_{\mathrm{p}} - f_1,\ f_{\mathrm{p}},\ f_{\mathrm{p}} + f_1,\ f_{\mathrm{p}} + 2f_1 \,\right]^{\mathrm{T}} \tag{3.27}$$

The phase-a small-signal vector of the AC voltage, AC current, and modulation signal can be expressed as

$$\begin{cases} \hat{\boldsymbol{v}}_{\mathrm{a}} = \left[\hat{\boldsymbol{v}}_{\mathrm{p}-2},\ 0,\ \hat{\boldsymbol{v}}_{\mathrm{p}},\ 0,\ 0\right]^{\mathrm{T}} \\ \hat{\boldsymbol{i}}_{\mathrm{a}} = \left[\hat{\boldsymbol{i}}_{\mathrm{p}-2},\ 0,\ \hat{\boldsymbol{i}}_{\mathrm{p}},\ 0,\ 0\right]^{\mathrm{T}} \\ \hat{\boldsymbol{m}}_{\mathrm{a}} = \left[\hat{\boldsymbol{m}}_{\mathrm{p}-2},\ 0,\ \hat{\boldsymbol{m}}_{\mathrm{p}},\ 0,\ 0\right]^{\mathrm{T}} \end{cases} \tag{3.28}$$

where the subscript p and $\mathrm{p}-2$ represent to the small-signal components at f_{p} and $f_{\mathrm{p}} - 2f_1$ respectively.

According to Eq. (3.28), based on the phase-sequence relationship, the small-signal vectors of phase b and phase c in frequency domain can be obtained as

$$\begin{cases} \hat{\boldsymbol{v}}_{\mathrm{b}} = \boldsymbol{D}_{\mathrm{p}}\hat{\boldsymbol{v}}_{\mathrm{a}}, \quad \hat{\boldsymbol{v}}_{\mathrm{c}} = \boldsymbol{D}_{\mathrm{p}}^{*}\hat{\boldsymbol{v}}_{\mathrm{a}} \\ \hat{\boldsymbol{i}}_{\mathrm{b}} = \boldsymbol{D}_{\mathrm{p}}\hat{\boldsymbol{i}}_{\mathrm{a}}, \quad \hat{\boldsymbol{i}}_{\mathrm{c}} = \boldsymbol{D}_{\mathrm{p}}^{*}\hat{\boldsymbol{i}}_{\mathrm{a}} \\ \hat{\boldsymbol{m}}_{\mathrm{b}} = \boldsymbol{D}_{\mathrm{p}}\hat{\boldsymbol{m}}_{\mathrm{a}}, \ \hat{\boldsymbol{m}}_{\mathrm{c}} = \boldsymbol{D}_{\mathrm{p}}^{*}\hat{\boldsymbol{m}}_{\mathrm{a}} \end{cases} \tag{3.29}$$

where $\boldsymbol{D}_{\mathrm{p}}$ is the phase sequence coefficient matrix of small-signal vectors, expressed as

$$\boldsymbol{D}_{\mathrm{p}} = \boldsymbol{D}\mathrm{e}^{-\mathrm{j}2\pi/3} = \mathrm{diag}\left[\left\{\mathrm{e}^{-\mathrm{j}2(k+1)\pi/3}\right\}\Big|_{k=-2,-1,0,1,2}\right] \tag{3.30}$$

According to Table 3.3, the small-signal vector of DC voltage $\hat{\boldsymbol{v}}_{\mathrm{dc}}$ only contains small-signal component at $f_{\mathrm{p}} - f_1$, expressed as

$$\hat{\boldsymbol{v}}_{\mathrm{dc}} = \left[0,\ \hat{\boldsymbol{v}}_{\mathrm{dc}-1},\ 0,\ 0,\ 0\right]^{\mathrm{T}} \tag{3.31}$$

According to Eq. (3.3) the frequency-domain model of the DC bus can be obtained as.

$$I_{\mathrm{dc}}\hat{\boldsymbol{v}}_{\mathrm{dc}} - V_{\mathrm{dc}}\boldsymbol{Y}_{\mathrm{Cdc}}\hat{\boldsymbol{v}}_{\mathrm{dc}} = \sum_{l=\mathrm{a,b,c}} \left(\boldsymbol{I}_l \otimes \hat{\boldsymbol{v}}_{\mathrm{i}l} + \boldsymbol{V}_{\mathrm{i}l} \otimes \hat{\boldsymbol{i}}_l\right) \tag{3.32}$$

where $\boldsymbol{Y}_{\mathrm{Cdc}}$ is the admittance of DC-bus capacitor. It can be arranged in the following frequency order.

$$\boldsymbol{Y}_{\mathrm{Cdc}} = \mathrm{j}2\pi C_{\mathrm{dc}} \cdot \mathrm{diag}\left[f_{\mathrm{p}} - 2f_1,\ f_{\mathrm{p}} - f_1,\ f_{\mathrm{p}},\ f_{\mathrm{p}} + f_1,\ f_{\mathrm{p}} + 2f_1\right] \tag{3.33}$$

According to Eq. (3.8), to achieve the convolution between the steady-state vectors and the small-signal vectors, the steady-state frequency order needs to be expanded based on Eq. (3.27).

$$\left[-2f_1,\ -f_1,\ 0,\ f_1,\ 2f_1\right]^{\mathrm{T}} \tag{3.34}$$

In order to apply the scalar product, $\boldsymbol{I}_l$ and $\boldsymbol{V}_{\mathrm{i}l}$ are firstly extended to fifth-order matrices. Then, the frequency-domain steady-state vector in Sect. 3.2 is substituted into Eq. (3.32). The frequency-domain relationship between $\hat{\boldsymbol{v}}_{\mathrm{dc}}$, $\hat{\boldsymbol{v}}_{\mathrm{ia}}$, and $\hat{\boldsymbol{i}}_{\mathrm{a}}$ can be expressed as

$$\hat{\boldsymbol{v}}_{\mathrm{dc}} = \boldsymbol{B}_1\hat{\boldsymbol{v}}_{\mathrm{ia}} + \boldsymbol{B}_2\hat{\boldsymbol{i}}_{\mathrm{a}} \tag{3.35}$$

where $\boldsymbol{B}_1$ and $\boldsymbol{B}_2$ are fifth-order matrices. All the other elements in the matrices are zero except for

$$\begin{cases} \boldsymbol{B}_1(2,1) = 3\boldsymbol{I}_1/\left[I_{\mathrm{dc}} - \mathrm{j}2\pi(f_{\mathrm{p}} - f_1)C_{\mathrm{dc}}V_{\mathrm{dc}}\right] \\ \boldsymbol{B}_1(2,3) = 3\boldsymbol{I}_1^*/\left[I_{\mathrm{dc}} - \mathrm{j}2\pi(f_{\mathrm{p}} - f_1)C_{\mathrm{dc}}V_{\mathrm{dc}}\right] \end{cases} \tag{3.36}$$

$$\begin{cases} \boldsymbol{B}_2(2,1) = 3\boldsymbol{V}_{\mathrm{i}1}/\left[I_{\mathrm{dc}} - \mathrm{j}2\pi(f_{\mathrm{p}} - f_1)C_{\mathrm{dc}}V_{\mathrm{dc}}\right] \\ \boldsymbol{B}_2(2,3) = 3\boldsymbol{V}_{\mathrm{i}1}^*/\left[I_{\mathrm{dc}} - \mathrm{j}2\pi(f_{\mathrm{p}} - f_1)C_{\mathrm{dc}}V_{\mathrm{dc}}\right] \end{cases} \tag{3.37}$$

According to Eq. (3.16), the frequency-domain small-signal model of DC bus can be obtained as

$$\hat{\boldsymbol{v}}_{\mathrm{i}l} = K_{\mathrm{m}}\left(\boldsymbol{M}_l \otimes \hat{\boldsymbol{v}}_{\mathrm{dc}} + \boldsymbol{V}_{\mathrm{dc}} \otimes \hat{\boldsymbol{m}}_l\right) \tag{3.38}$$

Based on Eq. (3.14), the frequency-domain small-signal model of main circuit can be obtained as

$$\hat{\boldsymbol{v}}_{il} = \hat{\boldsymbol{v}}_l + \boldsymbol{Z}_{\mathrm{Lf}}\hat{\boldsymbol{i}}_l \tag{3.39}$$

where $\boldsymbol{Z}_{\mathrm{Lf}}$ is the impedance of AC filter inductor. It can be expressed in the following small-signal frequency order.

$$\boldsymbol{Z}_{\mathrm{Lf}} = \mathrm{j}2\pi L_{\mathrm{f}} \cdot \mathrm{diag}\left[f_{\mathrm{p}} - 2f_1,\, f_{\mathrm{p}} - f_1,\, f_{\mathrm{p}},\, f_{\mathrm{p}} + f_1,\, f_{\mathrm{p}} + 2f_1\right] \tag{3.40}$$

3.3.3 *Frequency-Domain Small-Signal Model of Control Loops*

As shown in Fig. 3.3, PLL is used to track the phase angle of AC voltage. DC voltage control module is used to maintain the constant DC voltage and to generate d-axis AC current reference. AC current control is used to generate the modulation signals. The small-signal models of control loops can be established by deducing the transfer function among the small-signals.

3.3.3.1 Small-Signal Model of PLL

The structure of PLL is shown in Fig. 3.7.

The voltage perturbation $\hat{\boldsymbol{v}}_{\mathrm{a}}$ leads to a small-signal response $\hat{\boldsymbol{\theta}}_{\mathrm{PLL}}$ in the phase-locked angle. The relationship between $\hat{\boldsymbol{v}}_{\mathrm{a}}$ and $\hat{\boldsymbol{\theta}}_{\mathrm{PLL}}$ can be expressed as

$$\hat{\boldsymbol{\theta}}_{\mathrm{PLL}} = \boldsymbol{G}_{\theta}\hat{\boldsymbol{v}}_{\mathrm{a}} \tag{3.41}$$

where $\boldsymbol{G}_{\theta}$ is the transfer function matrix of PLL. It is a fifth-order matrix. All the other elements in $\boldsymbol{G}_{\theta}$ are zero except for

$$\boldsymbol{G}_{\theta}(2,1) = -\boldsymbol{G}_{\theta}(2,3) = \mathrm{j}T_{\mathrm{PLL}}[\mathrm{j}2\pi(f_{\mathrm{p}} - f_1)] \tag{3.42}$$

where $T_{\mathrm{PLL}}(s)$ is the closed-loop transfer function of PLL, expressed as

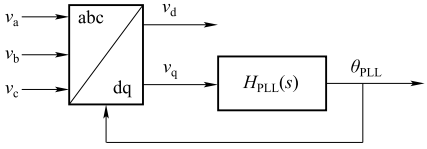

Fig. 3.7 Control diagram of PLL

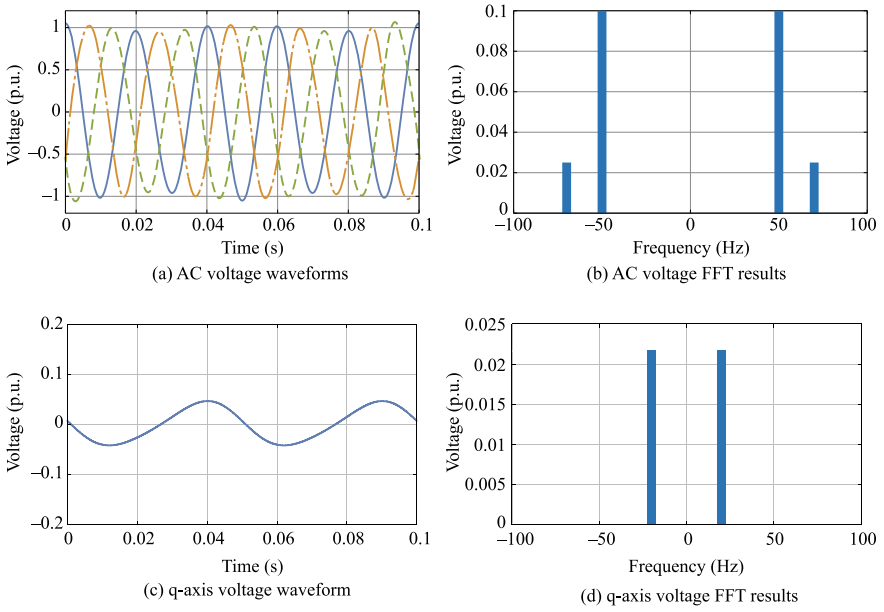

Fig. 3.8 Waveforms and FFT results of AC voltage and q-axis voltage

$$T_{\mathrm{PLL}}(s) = \frac{H_{\mathrm{PLL}}(s)}{1 + V_1 H_{\mathrm{PLL}}(s)} \tag{3.43}$$

According to Eq. (3.28), the AC voltage may contain small-signal components both at f_p and $f_\mathrm{p} - 2f_1$. However, under PLL control of Eq. (3.42), there will only be a small-signal component at $f_\mathrm{p} - f_1$ in $\hat{\boldsymbol{\theta}}_{\mathrm{PLL}}$. The waveforms and FFT results of AC voltage and q-axis voltage are shown in Fig. 3.8.

As seen from Fig. 3.8, if the AC voltage is superposed with a small-signal perturbation of 70 Hz, after the Park transformation, there will be only a small-signal response at 20 Hz in the q-axis voltage.

3.3.3.2 Small-Signal Model of DC Voltage Control

DC voltage controller is used to maintain a constant DC voltage, whose structure is shown in Fig. 3.9.

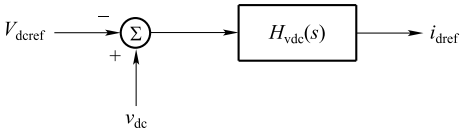

Fig. 3.9 Control diagram of DC voltage controller

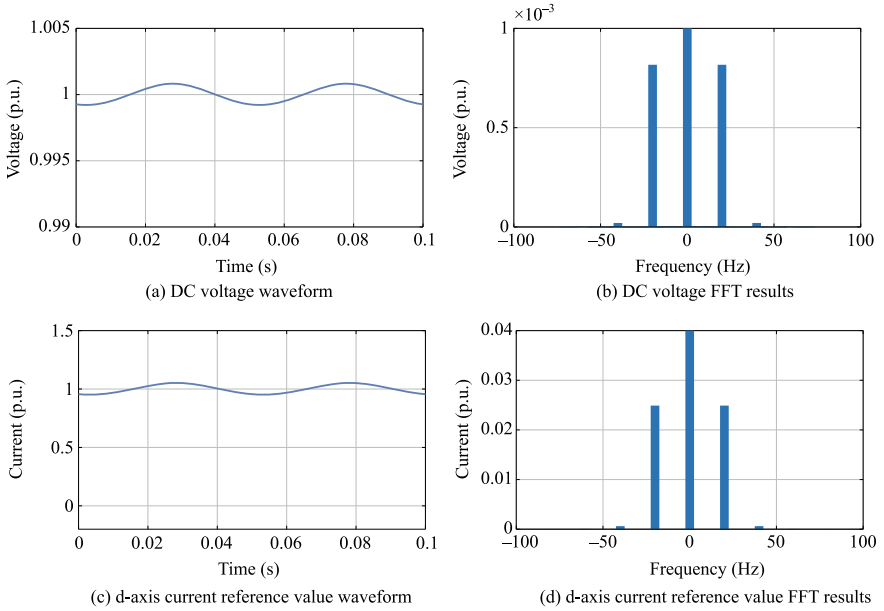

Fig. 3.10 Waveforms and FFT results of DC voltage and d-axis current reference

According to Fig. 3.9, the relationship between the small-signal vector of d-axis current reference $\hat{\boldsymbol{i}}_{\text{dref}}$ and $\hat{\boldsymbol{v}}_{\text{dc}}$ can be expressed as

$$\hat{\boldsymbol{i}}_{\text{dref}} = \boldsymbol{H}_{\text{vdc}} \cdot \hat{\boldsymbol{v}}_{\text{dc}} \tag{3.44}$$

where $\boldsymbol{H}_{\text{vdc}}$ is a fifth-order matrix. All the other elements in $\boldsymbol{G}_{\theta}$ are zero except for

$$\boldsymbol{H}_{\text{vdc}} = \text{diag}\Big[\left\{H_{\text{vdc}}[\text{j}2\pi(f_{\text{p}} + kf_1)]\right\}\big|_{k=-2,-1,0,1,2}\Big] \tag{3.45}$$

According to Eq. (3.44), a small-signal component at $f_{\text{p}} - f_1$ will be superposed into $\hat{\boldsymbol{i}}_{\text{dref}}$. The waveforms and FFT results of DC voltage and d-axis current reference are shown in Fig. 3.10. It can be seen that if the DC voltage v_{dc} is superposed with a small-signal perturbation of 20 Hz, after the DC voltage control, there will be a small-signal response at 20 Hz in i_{dref}.

3.3.3.3 Small-Signal Model of AC Current Control

AC current controller is used to generate modulation signals, whose structure is shown in Fig. 3.11.

According to Fig. 3.11, the relationship between the small-signal vectors $\hat{\boldsymbol{i}}_{\text{d}}$, $\hat{\boldsymbol{i}}_{\text{q}}$ and $\hat{\boldsymbol{v}}_{\text{a}}$, $\hat{\boldsymbol{i}}_{\text{a}}$ can be expressed as

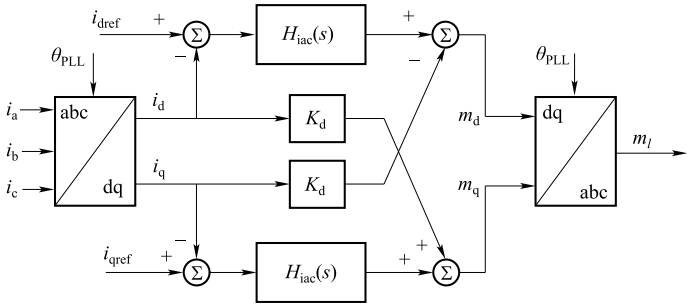

Fig. 3.11 Block diagram of DC voltage controller

$$\begin{cases} \hat{\boldsymbol{i}}_{\mathrm{d}} = \boldsymbol{C}_1\hat{\boldsymbol{v}}_{\mathrm{a}} + \boldsymbol{C}_2\hat{\boldsymbol{i}}_{\mathrm{a}} \\ \hat{\boldsymbol{i}}_{\mathrm{q}} = \boldsymbol{C}_3\hat{\boldsymbol{v}}_{\mathrm{a}} + \boldsymbol{C}_4\hat{\boldsymbol{i}}_{\mathrm{a}} \end{cases} \tag{3.46}$$

where $\boldsymbol{C}_1$, $\boldsymbol{C}_2$, $\boldsymbol{C}_3$ and $\boldsymbol{C}_4$ are all fifth-order matrices. All the other elements are zero except for

$$\begin{cases} \boldsymbol{C}_1(2,1) = T_{\mathrm{PLL}}[\mathrm{j}2\pi(f_{\mathrm{p}} - f_1)]\left(\boldsymbol{I}_1 - \boldsymbol{I}_1^*\right) \\ \boldsymbol{C}_1(2,3) = -T_{\mathrm{PLL}}[\mathrm{j}2\pi(f_{\mathrm{p}} - f_1)]\left(\boldsymbol{I}_1 - \boldsymbol{I}_1^*\right) \end{cases} \tag{3.47}$$

$$\begin{cases} \boldsymbol{C}_2(2,1) = 1 \\ \boldsymbol{C}_2(2,3) = 1 \end{cases} \tag{3.48}$$

$$\begin{cases} \boldsymbol{C}_3(2,1) = -\mathrm{j}T_{\mathrm{PLL}}[\mathrm{j}2\pi(f_{\mathrm{p}} - f_1)]\left(\boldsymbol{I}_1 + \boldsymbol{I}_1^*\right) \\ \boldsymbol{C}_3(2,3) = \mathrm{j}T_{\mathrm{PLL}}[\mathrm{j}2\pi(f_{\mathrm{p}} - f_1)]\left(\boldsymbol{I}_1 + \boldsymbol{I}_1^*\right) \end{cases} \tag{3.49}$$

$$\begin{cases} \boldsymbol{C}_4(2,1) = \mathrm{j} \\ \boldsymbol{C}_4(2,3) = -\mathrm{j} \end{cases} \tag{3.50}$$

As mentioned above, there are small-signal components at f_{p} and $f_{\mathrm{p}} - 2f_1$ in the AC current small-signal vector $\hat{\boldsymbol{i}}_{\mathrm{a}}$. However, after the Park transformation, there will be only the small-signal components at $f_{\mathrm{p}} - f_1$ in $\hat{\boldsymbol{i}}_{\mathrm{d}}$ and $\hat{\boldsymbol{i}}_{\mathrm{q}}$. The waveforms and FFT results of AC current before and after the Park transformation are shown in Fig. 3.12.

The small-signal vectors of d- and q-axis modulation signals $\hat{\boldsymbol{m}}_{\mathrm{d}}$ and $\hat{\boldsymbol{m}}_{\mathrm{q}}$ are expressed as

$$\begin{cases} \hat{\boldsymbol{m}}_{\mathrm{d}} = H_{\mathrm{iac}}[\mathrm{j}2\pi(f_{\mathrm{p}} - f_1)]\left(\hat{\boldsymbol{i}}_{\mathrm{dref}} - \hat{\boldsymbol{i}}_{\mathrm{d}}\right) - K_{\mathrm{d}}\hat{\boldsymbol{i}}_{\mathrm{q}} \\ \hat{\boldsymbol{m}}_{\mathrm{q}} = H_{\mathrm{iac}}[\mathrm{j}2\pi(f_{\mathrm{p}} - f_1)]\left(\hat{\boldsymbol{i}}_{\mathrm{qref}} - \hat{\boldsymbol{i}}_{\mathrm{q}}\right) + K_{\mathrm{d}}\hat{\boldsymbol{i}}_{\mathrm{d}} \end{cases} \tag{3.51}$$

where the small-signal vector of q-axis current reference $\hat{\boldsymbol{i}}_{\mathrm{qref}} = 0$.

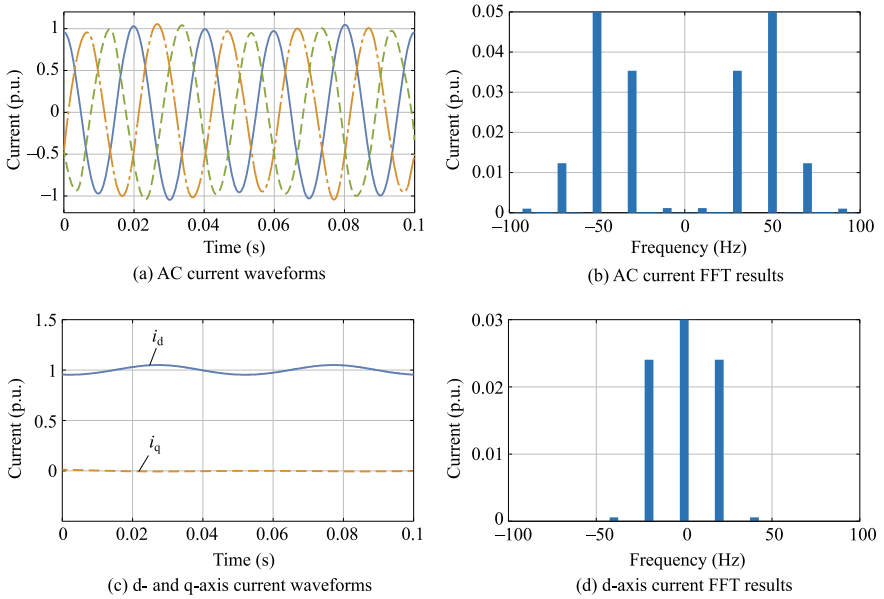

(a) AC current waveforms (b) AC current FFT results

(c) d- and q-axis current waveforms (d) d-axis current FFT results

Fig. 3.12 Waveforms and FFT results of the AC current before and after Park transformation

Substituting Eqs. (3.44) and (3.46) into Eq. (3.51), the small-signal vectors of $\hat{\boldsymbol{m}}_\mathrm{d}$ and $\hat{\boldsymbol{m}}_\mathrm{q}$ can be obtained as

$$\begin{cases} \hat{\boldsymbol{m}}_\mathrm{d} = \boldsymbol{D}_1\hat{\boldsymbol{v}}_\mathrm{ia} + \boldsymbol{D}_2\hat{\boldsymbol{i}}_\mathrm{a} + \boldsymbol{D}_3\hat{\boldsymbol{v}}_\mathrm{dc} \\ \hat{\boldsymbol{m}}_\mathrm{q} = \boldsymbol{D}_4\hat{\boldsymbol{v}}_\mathrm{ia} + \boldsymbol{D}_5\hat{\boldsymbol{i}}_\mathrm{a} \end{cases} \tag{3.52}$$

where $\boldsymbol{D}_1, \boldsymbol{D}_2, \boldsymbol{D}_3, \boldsymbol{D}_4$ and $\boldsymbol{D}_5$ are all fifth-order matrices. All the other elements are zero except for

$$\begin{cases} \boldsymbol{D}_1(2,1) = T_\mathrm{PLL}[\mathrm{j}2\pi(f_\mathrm{p}-f_1)] \cdot \left[\left\{-H_\mathrm{iac}[\mathrm{j}2\pi(f_\mathrm{p}-f_1)] + \mathrm{j}K_\mathrm{d}\right\}I_1 \right. \\ \qquad\qquad \left. + \left\{H_\mathrm{iac}[\mathrm{j}2\pi(f_\mathrm{p}-f_1)] + \mathrm{j}K_\mathrm{d}\right\}\boldsymbol{I}_1^*\right] \\ \boldsymbol{D}_1(2,3) = -T_\mathrm{PLL}[\mathrm{j}2\pi(f_\mathrm{p}-f_1)] \cdot \left[\left\{-H_\mathrm{iac}[\mathrm{j}2\pi(f_\mathrm{p}-f_1)] + \mathrm{j}K_\mathrm{d}\right\}I_1 \right. \\ \qquad\qquad \left. + \left\{H_\mathrm{iac}[\mathrm{j}2\pi(f_\mathrm{p}-f_1)] + \mathrm{j}K_\mathrm{d}\right\}\boldsymbol{I}_1^*\right] \end{cases} \tag{3.53}$$

$$\begin{cases} \boldsymbol{D}_2(2,1) = -H_\mathrm{iac}[\mathrm{j}2\pi(f_\mathrm{p}-f_1)] - \mathrm{j}K_\mathrm{d} \\ \boldsymbol{D}_2(2,3) = -H_\mathrm{iac}[\mathrm{j}2\pi(f_\mathrm{p}-f_1)] + \mathrm{j}K_\mathrm{d} \end{cases} \tag{3.54}$$

$$\boldsymbol{D}_3(2,2) = H_\mathrm{iac}[\mathrm{j}2\pi(f_\mathrm{p}-f_1)]H_\mathrm{vdc}[\mathrm{j}2\pi(f_\mathrm{p}-f_1)] \tag{3.55}$$

$$\begin{cases} \boldsymbol{D}_4(2,1) = T_{\mathrm{PLL}}[\mathrm{j}2\pi(f_\mathrm{p}-f_1)] \cdot \left[\left\{\mathrm{j}H_{\mathrm{iac}}[\mathrm{j}2\pi(f_\mathrm{p}-f_1)]+K_\mathrm{d}\right\}\boldsymbol{I}_1\right. \\ \qquad\qquad \left. + \left\{\mathrm{j}H_{\mathrm{iac}}[\mathrm{j}2\pi(f_\mathrm{p}-f_1)]-K_\mathrm{d}\right\}\boldsymbol{I}_1^*\right] \\ \boldsymbol{D}_4(2,3) = -T_{\mathrm{PLL}}[\mathrm{j}2\pi(f_\mathrm{p}-f_1)] \cdot \left[\left\{\mathrm{j}H_{\mathrm{iac}}[\mathrm{j}2\pi(f_\mathrm{p}-f_1)]+K_\mathrm{d}\right\}\boldsymbol{I}_1\right. \\ \qquad\qquad \left. + \left\{\mathrm{j}H_{\mathrm{iac}}[\mathrm{j}2\pi(f_\mathrm{p}-f_1)]-K_\mathrm{d}\right\}\boldsymbol{I}_1^*\right] \end{cases} \tag{3.56}$$

$$\begin{cases} \boldsymbol{D}_5(2,1) = -\mathrm{j}H_{\mathrm{iac}}[\mathrm{j}2\pi(f_\mathrm{p}-f_1)]+K_\mathrm{d} \\ \boldsymbol{D}_5(2,3) = \mathrm{j}H_{\mathrm{iac}}[\mathrm{j}2\pi(f_\mathrm{p}-f_1)]+K_\mathrm{d} \end{cases} \tag{3.57}$$

The d- and q-axis modulation signals are transformed into three-phase modulation signals through inverse Park transformation. Taking phase a as an example, the small-signal vector of the modulation signal $\hat{\boldsymbol{m}}_\mathrm{a}$ can be expressed as

$$\hat{\boldsymbol{m}}_\mathrm{a} = \boldsymbol{E}_1 \cdot \hat{\boldsymbol{v}}_\mathrm{dc} + \boldsymbol{E}_2 \cdot \hat{\boldsymbol{v}}_\mathrm{a} + \boldsymbol{E}_3 \cdot \hat{\boldsymbol{i}}_\mathrm{a} \tag{3.58}$$

where $\boldsymbol{E}_1$, $\boldsymbol{E}_2$ and $\boldsymbol{E}_3$ are all fifth-order matrices. All the other elements are zero except for

$$\begin{cases} \boldsymbol{E}_1(1,2) = H_{\mathrm{iac}}[\mathrm{j}2\pi(f_\mathrm{p}-f_1)]H_{\mathrm{vdc}}[\mathrm{j}2\pi(f_\mathrm{p}-f_1)]/2 \\ \boldsymbol{E}_1(3,2) = H_{\mathrm{iac}}[\mathrm{j}2\pi(f_\mathrm{p}-f_1)]H_{\mathrm{vdc}}[\mathrm{j}2\pi(f_\mathrm{p}-f_1)]/2 \end{cases} \tag{3.59}$$

$$\begin{cases} \boldsymbol{E}_2(1,1) = -\boldsymbol{E}_2(1,3) = T_{\mathrm{PLL}}[\mathrm{j}2\pi(f_\mathrm{p}-f_1)] \\ \qquad\qquad \cdot \left[\left\{H_{\mathrm{iac}}[\mathrm{j}2\pi(f_\mathrm{p}-f_1)]+\mathrm{j}K_\mathrm{d}\right\}\boldsymbol{I}_1^* + \boldsymbol{M}_1^*\right] \\ \boldsymbol{E}_2(3,1) = -\boldsymbol{E}_2(3,3) = T_{\mathrm{PLL}}[\mathrm{j}2\pi(f_\mathrm{p}-f_1)] \\ \qquad\qquad \cdot \left[\left\{-H_{\mathrm{iac}}[\mathrm{j}2\pi(f_\mathrm{p}-f_1)]+\mathrm{j}K_\mathrm{d}\right\}\boldsymbol{I}_1 - \boldsymbol{M}_1\right] \end{cases} \tag{3.60}$$

$$\begin{cases} \boldsymbol{E}_3(1,1) = -H_{\mathrm{iac}}[\mathrm{j}2\pi(f_\mathrm{p}-f_1)]-\mathrm{j}K_\mathrm{d} \\ \boldsymbol{E}_3(3,3) = -H_{\mathrm{iac}}[\mathrm{j}2\pi(f_\mathrm{p}-f_1)]+\mathrm{j}K_\mathrm{d} \end{cases} \tag{3.61}$$

Based on the above Equations, there are small-signal component at $f_\mathrm{p}-f_1$ in $\hat{\boldsymbol{m}}_\mathrm{d}$ and $\hat{\boldsymbol{m}}_\mathrm{q}$. After the inverse Park transformation, there will be not only the small-signal component at f_p, but also component at $f_\mathrm{p}-2f_1$ in $\hat{\boldsymbol{m}}_\mathrm{a}$, $\hat{\boldsymbol{m}}_\mathrm{b}$, $\hat{\boldsymbol{m}}_\mathrm{c}$. The waveforms and FFT results of the modulation signal before and after inverse Park transformation are shown in Fig. 3.13.

3.3.4 AC Port Impedance Model

Defining the AC current flowing to the grid as the forward direction, the AC port admittance matrix of two-level converter can be expressed as

$$\boldsymbol{Y} = -\frac{\hat{\boldsymbol{i}}_l}{\hat{\boldsymbol{v}}_l} \tag{3.62}$$

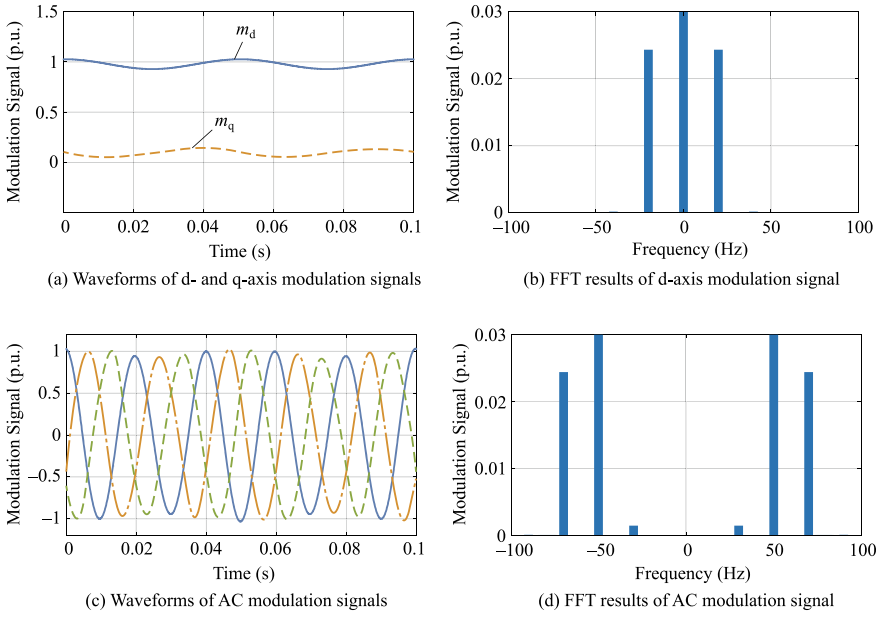

(a) Waveforms of d- and q-axis modulation signals

(b) FFT results of d-axis modulation signal

(c) Waveforms of AC modulation signals

(d) FFT results of AC modulation signal

Fig. 3.13 Waveforms and FFT results of the modulation signal before and after inverse Park transformation

Taking phase a as an example, according to Eqs. (3.35), (3.38), and (3.58), the small-signal vector of modulation voltage can be obtained by

$$\hat{\boldsymbol{v}}_{\mathrm{ia}} = \boldsymbol{F}_1\hat{\boldsymbol{v}}_{\mathrm{dc}} + \boldsymbol{F}_2\hat{\boldsymbol{v}}_{\mathrm{a}} + \boldsymbol{F}_3\hat{\boldsymbol{i}}_{\mathrm{a}} \tag{3.63}$$

where $\boldsymbol{F}_1$, $\boldsymbol{F}_2$ and $\boldsymbol{F}_3$ are all fifth-order matrices. All the other elements are zero except for

$$\begin{cases} \boldsymbol{F}_1(1,2) = K_{\mathrm{m}}V_{\mathrm{dc}}/2 \cdot H_{\mathrm{iac}}[\mathrm{j}2\pi(f_{\mathrm{p}} - f_1)]H_{\mathrm{vdc}}[\mathrm{j}2\pi(f_{\mathrm{p}} - f_1)] + K_{\mathrm{m}}\boldsymbol{M}_1^* \\ \boldsymbol{F}_1(3,2) = K_{\mathrm{m}}V_{\mathrm{dc}}/2 \cdot H_{\mathrm{iac}}[\mathrm{j}2\pi(f_{\mathrm{p}} - f_1)]H_{\mathrm{vdc}}[\mathrm{j}2\pi(f_{\mathrm{p}} - f_1)] + K_{\mathrm{m}}\boldsymbol{M}_1 \end{cases} \tag{3.64}$$

$$\begin{cases} \boldsymbol{F}_2(1,1) = -\boldsymbol{F}_2(1,3) = K_{\mathrm{m}}V_{\mathrm{dc}}T_{\mathrm{PLL}}[\mathrm{j}2\pi(f_{\mathrm{p}} - f_1)] \\ \qquad\qquad \cdot \left[\left\{H_{\mathrm{iac}}[\mathrm{j}2\pi(f_{\mathrm{p}} - f_1)] + \mathrm{j}K_{\mathrm{d}}\right\}\boldsymbol{I}_1^* + \boldsymbol{M}_1^*\right] \\ \boldsymbol{F}_2(3,1) = -\boldsymbol{F}_2(3,3) = K_{\mathrm{m}}V_{\mathrm{dc}}T_{\mathrm{PLL}}[\mathrm{j}2\pi(f_{\mathrm{p}} - f_1)] \\ \qquad\qquad \cdot \left[\left\{-H_{\mathrm{iac}}[\mathrm{j}2\pi(f_{\mathrm{p}} - f_1)] + \mathrm{j}K_{\mathrm{d}}\right\}\boldsymbol{I}_1 - \boldsymbol{M}_1\right] \end{cases} \tag{3.65}$$

$$\begin{cases} \boldsymbol{F}_3(1,1) = K_{\mathrm{m}}V_{\mathrm{dc}} \cdot \left[-H_{\mathrm{iac}}[\mathrm{j}2\pi(f_{\mathrm{p}} - f_1)] - \mathrm{j}K_{\mathrm{d}}\right] \\ \boldsymbol{F}_3(3,3) = K_{\mathrm{m}}V_{\mathrm{dc}} \cdot \left[-H_{\mathrm{iac}}[\mathrm{j}2\pi(f_{\mathrm{p}} - f_1)] + \mathrm{j}K_{\mathrm{d}}\right] \end{cases} \tag{3.66}$$

Substituting Eq. (3.63) into Eq. (3.39), the AC port admittance matrix expression is obtained by

$$\boldsymbol{Y} = -\frac{\hat{\boldsymbol{i}}_{\mathrm{a}}}{\hat{\boldsymbol{v}}_{\mathrm{a}}} = -[\boldsymbol{F}_1\boldsymbol{B}_2 + \boldsymbol{F}_3 - \boldsymbol{Z}_{\mathrm{Lf}}(\boldsymbol{U} - \boldsymbol{F}_1\boldsymbol{B}_1)]^{-1}(\boldsymbol{U} - \boldsymbol{F}_1\boldsymbol{B}_1 - \boldsymbol{F}_2) \tag{3.67}$$

where $\boldsymbol{U}$ is the identity matrix.

Since the small-signal vectors $\hat{\boldsymbol{v}}_{\mathrm{a}}$ and $\hat{\boldsymbol{i}}_{\mathrm{a}}$ only contain the components at f_{p} and $f_{\mathrm{p}} - 2f_1$, zero elements in $\boldsymbol{Y}$ can be neglected. Thus, $\boldsymbol{Y}$ can be expressed as

$$\begin{bmatrix} -\hat{\boldsymbol{i}}_{\mathrm{p}} \\ -\hat{\boldsymbol{i}}_{\mathrm{p-2}} \end{bmatrix} = \begin{bmatrix} \boldsymbol{Y}_{\mathrm{pp}} & \boldsymbol{Y}_{\mathrm{np}} \\ \boldsymbol{Y}_{\mathrm{pn}} & \boldsymbol{Y}_{\mathrm{nn}} \end{bmatrix} \begin{bmatrix} \hat{\boldsymbol{v}}_{\mathrm{p}} \\ \hat{\boldsymbol{v}}_{\mathrm{p-2}} \end{bmatrix} \tag{3.68}$$

where $\boldsymbol{Y}_{\mathrm{pp}}$ is the positive-sequence admittance, representing the response of $-\hat{\boldsymbol{i}}_{\mathrm{p}}$ at f_{p} under $\hat{\boldsymbol{v}}_{\mathrm{p}}$ at f_{p}. $\boldsymbol{Y}_{\mathrm{pn}}$ is the positive-sequence coupled admittance, representing the response of $-\hat{\boldsymbol{i}}_{\mathrm{p-2}}$ at $f_{\mathrm{p}} - 2f_1$ under $\hat{\boldsymbol{v}}_{\mathrm{p}}$ at f_{p}. $\boldsymbol{Y}_{\mathrm{nn}}$ is the negative-sequence admittance, representing the response of $-\hat{\boldsymbol{i}}_{\mathrm{p-2}}$ at $f_{\mathrm{p}} - 2f_1$ under $\hat{\boldsymbol{v}}_{\mathrm{p-2}}$ at $f_{\mathrm{p}} - 2f_1$. $\boldsymbol{Y}_{\mathrm{np}}$ is the negative-sequence coupled admittance, representing the response of $-\hat{\boldsymbol{i}}_{\mathrm{p}}$ at f_{p} under $\hat{\boldsymbol{v}}_{\mathrm{p-2}}$ at $f_{\mathrm{p}} - 2f_1$; $\boldsymbol{Y}_{\mathrm{pp}} = \boldsymbol{Y}$ (3,3) is the element in the 3rd row and 3rd column of $\boldsymbol{Y}$. $\boldsymbol{Y}_{\mathrm{np}} = \boldsymbol{Y}$ (3,1) is the element in the 3rd row and 1st column of $\boldsymbol{Y}$. $\boldsymbol{Y}_{\mathrm{pn}} = \boldsymbol{Y}$ (1,3) is the element in the 1st row and 3rd column of $\boldsymbol{Y}$. $\boldsymbol{Y}_{\mathrm{nn}} = \boldsymbol{Y}$ (1,1) is the element in the 1st row and 1st column of $\boldsymbol{Y}$.

According to Eq. (3.68), the impedance matrix of two-level converter can be obtained by

$$\begin{bmatrix} \boldsymbol{Z}_{\mathrm{pp}} & \boldsymbol{Z}_{\mathrm{pn}} \\ \boldsymbol{Z}_{\mathrm{np}} & \boldsymbol{Z}_{\mathrm{nn}} \end{bmatrix} = \begin{bmatrix} \boldsymbol{Y}_{\mathrm{pp}} & \boldsymbol{Y}_{\mathrm{np}} \\ \boldsymbol{Y}_{\mathrm{pn}} & \boldsymbol{Y}_{\mathrm{nn}} \end{bmatrix}^{-1} \tag{3.69}$$

where $\boldsymbol{Z}_{\mathrm{pp}}$ is the positive-sequence impedance, $\boldsymbol{Z}_{\mathrm{pn}}$ is the positive-sequence coupled impedance, $\boldsymbol{Z}_{\mathrm{nn}}$ is the negative-sequence impedance, $\boldsymbol{Z}_{\mathrm{np}}$ is the negative-sequence coupled impedance.

Besides, the relationship between $\boldsymbol{Z}_{\mathrm{pp}}$ and $\boldsymbol{Z}_{\mathrm{nn}}$ satisfies $\boldsymbol{Z}_{\mathrm{nn}} = \boldsymbol{Z}_{\mathrm{pp}}^{*}(\mathrm{j}2\omega_1 - s)$, and the relationship between $\boldsymbol{Z}_{\mathrm{pn}}$ and $\boldsymbol{Z}_{\mathrm{np}}$ satisfies $\boldsymbol{Z}_{\mathrm{np}} = \boldsymbol{Z}_{\mathrm{pn}}^{*}(\mathrm{j}2\omega_1 - s)$.

After the small-signal perturbation is superposed on the steady-state operating point, the small-signal relationship in the two-level converter can be summarized as follows.

1. The two-level converter employs PLL to synchronize with the grid voltages. The voltage perturbation leads to a small-signal response of phase-locked angle $\hat{\boldsymbol{\theta}}_{\mathrm{PLL}}$ at $f_{\mathrm{p}} - f_1$.
2. The small-signal response of AC power is generated at $f_{\mathrm{p}} - f_1$ by multiplying the AC voltage small-signal vector and the AC current steady-state vector, or multiplying the AC current small-signal vector and the AC voltage steady-state vector. Then, the small-signal response of AC power at $f_{\mathrm{p}} - f_1$ is transferred to the DC port and leads to DC voltage small-signal response $\hat{\boldsymbol{v}}_{\mathrm{dc}}$ at $f_{\mathrm{p}} - f_1$.
3. The AC current control involves the phase-locked angle and d- and q-axis current reference. With the phase-locked angle, the dq-axis currents are derived from the

three-phase AC currents through Park transformation. The d- and q-axis modulation signals are then generated by AC current control. Eventually, the three-phase modulation signals are obtained by inverse Park transformation. Thus, the small-signal responses of modulation signal $\hat{\boldsymbol{m}}_l$ contains components both at f_p and $f_\mathrm{p} - 2f_1$.

4. According to the modulation process of the two-level converter, there are small-signal responses of three-phase modulation voltages $\hat{\boldsymbol{v}}_{\mathrm{i}l}$ at f_p and $f_\mathrm{p} - 2f_1$ by multiplying the small-signal vector of modulation signal and the steady-state vector of the DC voltage, or multiplying the small-signal vector of DC voltage and the steady-state vector of the modulation signal.
5. Since the difference between the modulation voltage and the AC voltage drops on the inductor, small-signal responses of three-phase AC current $\hat{\boldsymbol{i}}_l$ are generated at f_p and $f_\mathrm{p} - 2f_1$.

In summary, under $\hat{\boldsymbol{v}}_\mathrm{p}$ at f_p (positive-sequence), a small-signal component of AC current $-\hat{\boldsymbol{i}}_\mathrm{p}$ at f_p (positive-sequence) is generated due to the positive-sequence admittance $\boldsymbol{Y}_\mathrm{pp}$. Meanwhile, another small-signal component of AC current $-\hat{\boldsymbol{i}}_{\mathrm{p}-2}$ at $f_\mathrm{p} - 2f_1$ (negative-sequence) is generated due to the positive-sequence coupling admittance $\boldsymbol{Y}_\mathrm{pn}$. Under $\hat{\boldsymbol{v}}_{\mathrm{p}-2}$ at $f_\mathrm{p} - 2f_1$ (negative-sequence), a small-signal component of AC current $-\hat{\boldsymbol{i}}_{\mathrm{p}-2}$ at $f_\mathrm{p} - 2f_1$ (negative-sequence) is generated due to negative-sequence admittance $\boldsymbol{Y}_\mathrm{nn}$. Meanwhile, another small-signal component of AC current $-\hat{\boldsymbol{i}}_\mathrm{p}$ at f_p (positive-sequence) is generated due to the negative-sequence coupling admittance $\boldsymbol{Y}_\mathrm{np}$. The relationship between positive and negative-sequence voltages and currents of two-level converter is shown in Fig. 3.14.

In order to verify the accuracy of the established impedance model, impedance scanning based on the simulation model of two-level converter is implemented. A small-signal perturbation of a specific frequency is injected into the AC voltage and the current response of AC current is then measured. Based on the FFT analysis, the AC port impedance can be derived by the ratio between the frequency-domain components of the injected voltage and the obtained current. Finally, the impedance curve can be obtained by repeating the above process within certain frequency range. Figure 3.15 shows the comparison between analytical impedance (in solid lines) and scanning impedance (in discrete points). As seen from the figure, all the discrete points fall on the solid lines, which verify the accuracy of the established impedance model of the two-level converter.

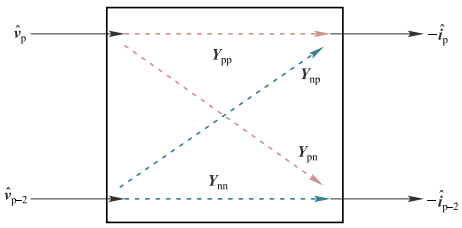

Fig. 3.14 The relationship between positive and negative-sequence voltages and currents of two-level converter

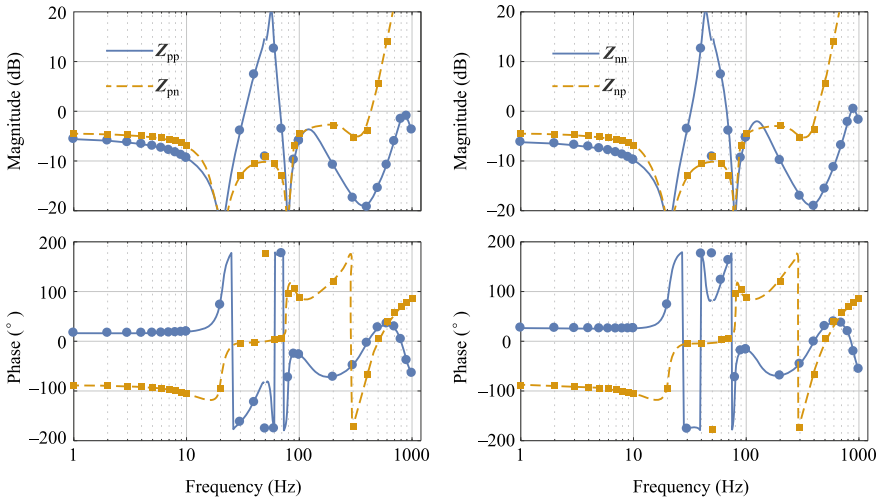

(a) Positive-sequence impedance and positive-sequence coupling impedance

(b) Negative-sequence impedance and negative-sequence coupling impedance

Fig. 3.15 Analytical and scanning results of the AC port impedance of two-level converter

References

1. ZENG Q R, CHANG L C. An advanced SVPWM-based predictive current controller for three-phase Inverters in distributed generation systems [J]. IEEE Transactions on Industrial Electronics, 2008, 55(3): 1235–1246.
2. XIN Z, WANG X F, QIN Z, et al. An improved second-order generalized integrator based quadrature signal generator [J]. IEEE Transactions on Power Electronics, 2016, 31(12): 8068–8073.
3. WU X Q, WANG Y C, CHEN X, et al. Sequence impedance model and interaction stability research of three-phase grid-connected inverters with considering coupling effects [J]. Proceedings of the CSEE, 2020, 40(5): 1605–1617. (Chinese)
4. WANG X F, HARNEFORS L, BLAABJERG F. Unified impedance model of grid-connected voltage-source converters [J]. IEEE Transactions on Power Electronics, 2018, 33(2): 1775–1787.
5. WANG G N, DU X, ZOU X M, et al. Self and accompanying admittance model for three-phase grid-tied inverter stability analysis [J]. Proceedings of the CSEE, 2017, 37(14): 3973–3981+4275. (Chinese)

Chapter 4
Impedance Modeling of Modular Multilevel Converter

Different from two-level converter, each arm of MMC is composed of dozens to hundreds of identical submodules (SM) and multilevel output voltage can be formed by the switching cooperation of SMs. Due to the particular topology of the MMC main circuit, the arm current, capacitor voltage, and modulation signal contain DC, fundamental, second, and other harmonic components [1]. The harmonic components lead to increases in power loss and capacitor voltage fluctuation. In addition to the fundamental current control, additional circulating current control is also introduced in MMC.

This chapter is to establish the small-signal impedance model of MMC considering multiple steady-state harmonics. First, the main-circuit topology and operation principle of SMs are presented, and the arm averaged model is established based on the consistency of the input-output characteristics. Then, the steady-state harmonic characteristics of the arm current, capacitor voltage, and modulation signal are analyzed. The time-domain modeling of the main circuit and the frequency-domain modeling of the steady-state operation are carried out. Furthermore, the small-signal distribution characteristics of the main circuit and control loops in the frequency domain are elaborated. Finally, the small-signal impedance model of MMC considering PLL, inner current control, and circulating current control is established and verified. The established model in this chapter lays a foundation for the impedance modeling and characteristic analysis of SVG and MMC-HVDC in the coming chapters.

4.1 Averaged Modeling of MMC Arm

Since each arm of MMC contains dozens to hundreds of SMs, the modeling of MMC including the dynamic characteristics of the switching process is complicated. According to the consistency principle of the arm input–output characteristics and

© China Electric Power Press 2023

W. Wang et al., *Analysis and Mitigation of Broadband Oscillation in Renewable Energy Generation and AC/DC Transmission Systems*,
https://doi.org/10.1007/978-981-99-1568-2_4

the operation principle of SMs, this section establishes the arm averaged model of MMC to simplify the complexity of the mathematical modeling and analysis.

4.1.1 Topology

Each arm is composed of multiple identical SMs in series, and the connection types between the arms each other are different due to various application scenarios. The typical topology of MMC is shown in Fig. 4.1. The star connection and delta connection, as shown in Fig. 4.1(a, b) respectively, are mainly applied in SVG. The double-star connection shown in Fig. 4.1(c) is mainly applied in high voltage direct current (HVDC) for AC/DC power conversion. The connection points P and N at the DC port are respectively connected to the positive and negative poles of the DC transmission line, and long-distance power transmission can be realized.

The double-star connection shown in Fig. 4.1(c) is taken as an example in this section to present the operation principle of MMC. The MMC consists of two arms per phase leg, where each arm comprises N SMs and an arm inductor L_{arm}. The arm resistor R_{arm} represents the power loss of the switching devices in each arm. v_l and i_l (l = a, b, c) are the three-phase AC voltages and currents respectively. v_{dc} and i_{dc} are the DC voltage and current respectively. $v_{l\text{u}}$ and $v_{l\text{v}}$ are the three-phase upper and lower arm voltages respectively. $i_{l\text{u}}$ and $i_{l\text{v}}$ are the three-phase upper and lower arm currents respectively. The subscript "u" denotes the upper arm and "v" denotes the lower arm.

Multiple SM topologies have been developed, among which the most typical and widespread applications are half-bridge submodule (HBSM) and full-bridge submodule (FBSM), as shown in Fig. 4.2. The HBSM consists of two IGBTs (T1, T2), two antiparallel diodes (D1, D2), and an SM capacitor C_{sm}. The FBSM consists of four IGBTs (T1, T2, T3, T4), four antiparallel diodes (D1, D2, D3, D4) and an SM capacitor C_{sm}. v_{C} is the SM capacitor voltage, i_{sm} is the SM input current, and v_{sm} is the SM output voltage. By comparing the topologies of HBSM and FBSM, the HBSM has fewer switches, lower cost, and less power loss, while the FBSM possesses the output capability of the negative level.

4.1.2 Operation Principle of Submodules

In this section, the current flowing circuits, charging and discharging states, and output voltages of the HBSM and FBSM are analyzed, respectively, according to the switching states of SMs.

The HBSM has three operation modes, i.e., inserting, bypassing, and blocking. The current flowing circuits of the HBSM in the three operating modes are given in Table 4.1. When T1 is on and T2 is off, the HBSM is in the inserting mode and the SM output voltage $v_{\text{sm}} = v_{\text{c}}$. If the SM input current i_{sm} is positive, the SM capacitor is charged; otherwise, it is discharged. When T1 is off and T2 is on, the HBSM is

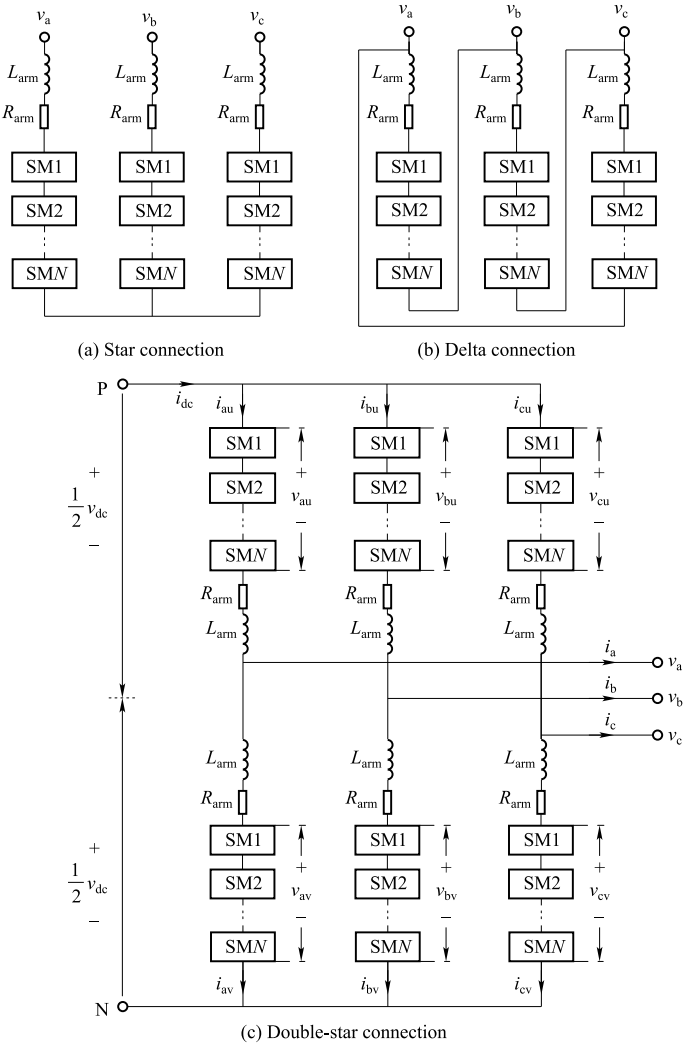

Fig. 4.1 The typical topology of MMC

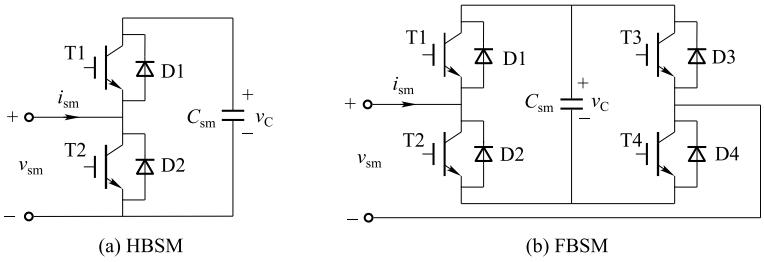

Fig. 4.2 The typical topology of SM

Table 4.1 The current flowing circuits of the HBSM

Operation Modes	Switching States	$i_{sm} > 0$	$i_{sm} < 0$
Inserting	T1 on T2 off	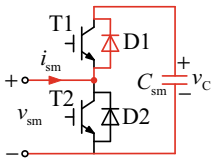	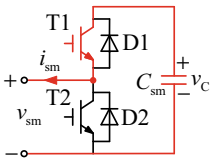
Bypassing	T2 on T1 off	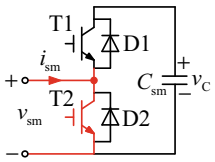	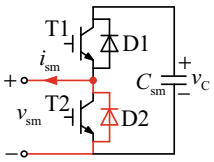
Blocking	T1 off T2 off	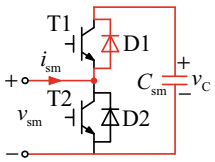	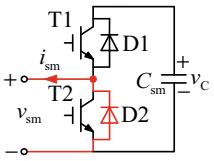

in the bypassing mode, and $v_{sm} = 0$. The SM capacitor voltage remains unchanged. When both T1 and T2 are off, the HBSM is in the blocking mode. If i_{sm} is positive, $v_{sm} = v_C$ and the SM capacitor is charged; otherwise, $v_{sm} = 0$ and the SM capacitor is discharged.

The operation states of the HBSM are summarized in Table 4.2. In the table, "1" means the driving signal is high and the switch is turned on, while "0" means the driving signal is low and the switch is turned off.

The FBSM has four operation modes, i.e., inserting, bypassing, reverse inserting, and blocking. The current flowing circuits of the FBSM in the four operation modes are given in Table 4.3. When T1, T4 are on and T2, T3 are off, the FBSM is in the inserting mode and the SM output voltage $v_{sm} = v_C$. If the SM input current i_{sm} is positive, the SM capacitor is charged; otherwise, it is discharged. When T1,

Table 4.2 Operation states of the HBSM

Operation Modes	T1	T2	v_{sm}	i_{sm}	C_{sm}
Inserting	1	0	v_C	>0	Charged
				<0	Discharged
Bypassing	0	1	0	>0	Bypassed
				<0	Bypassed
Blocking	0	0	v_C	>0	Charged
			0	<0	Bypassed

Table 4.3 The current flowing circuits of the FBSM

Operating Modes	Switching States	$i_{sm} > 0$	$i_{sm} < 0$
Inserting	T1 on T2 off T3 off T4 on	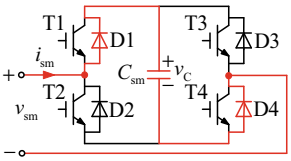	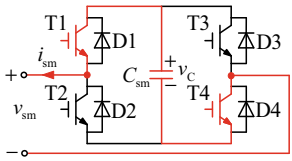
Bypassing	T1 on T2 off T3 on T4 off	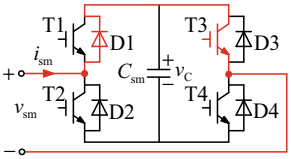	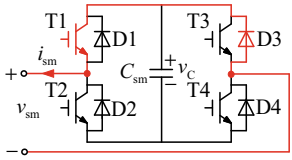
	T1 off T2 on T3 off T4 on	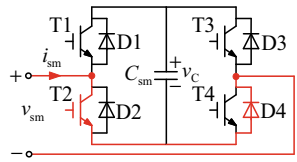	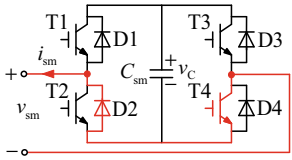
Reverse inserting	T1 off T2 on T3 on T4 off	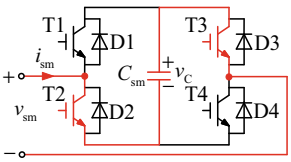	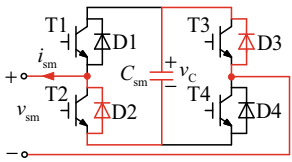
Blocking	T1 off T2 off T3 off T4 off	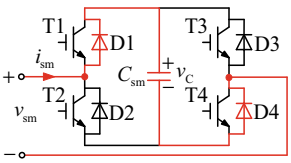	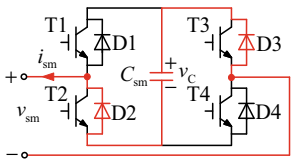

T3 are on and T2, T4 are off, or T2, T4 are on and T1, T3 are off, the FBSM is in the bypassing mode, and $v_{sm} = 0$. The SM capacitor voltage remains unchanged. When T2, T3 are on and T1, T4 are off, the FBSM is in the reverse inserting mode and $v_{sm} = -v_C$. If i_{sm} is positive, the SM capacitor is discharged; otherwise, it is charged. When T1, T2, T3, and T4 are off, the FBSM is in the blocking mode. If i_{sm} is positive, $v_{sm} = v_C$; otherwise, $v_{sm} = -v_C$. The SM capacitor is charged in both cases. The reverse inserting mode and the blocking mode of the FBSM are mainly used to clear the fault current of MMC under the DC-side short-circuit fault, or to charge SM capacitors when the MMC starts up. During normal operation, the FBSM

Table 4.4 Operation states of the FBSM

Operation Modes	T1	T2	T3	T4	V_{sm}	i_{sm}	C_{sm}
Inserting	1	0	0	1	v_C	>0	Charged
						<0	Discharged
Bypassing	1	0	1	0	0	>0	Bypassed
	0	1	0	1		<0	Bypassed
Reverse inserting	0	1	1	0	$-v_C$	>0	Discharged
						<0	Charged
Blocking	0	0	0	0	v_C	>0	Charged
					$-v_C$	<0	Charged

operates in two modes: inserting and bypassing. The operation states of the FBSM are summarized in Table 4.4.

By comparing the operating states of the HBSM and FBSM, under normal operation conditions, the operating characteristics of the HBSM and FBSM are nearly the same, except that FBSM has an additional switching combination in the bypassing mode.

4.1.3 Equivalent Model of MMC Arm

Each SM can be inserted or bypassed by controlling the switching states (on or off) of the IGBTs. When the SM is inserted, the arm current flows through the SM capacitor, and the SM output voltage is equal to the SM capacitor voltage. The SM capacitor is charged or discharged according to the direction of the arm current. When the SM is bypassed, the SM output voltage is zero, and the SM capacitor voltage remains unchanged. By numbering the SMs from 1 to N in each arm, the capacitor voltage and output voltage of the ith SM ($i = 1, 2, \ldots, N$) are respectively

$$\begin{cases} C_{\mathrm{sm}} \dfrac{\mathrm{d}v_{Cl\mathrm{u}}^{(i)}}{\mathrm{d}t} = B_{l\mathrm{u}}^{(i)} i_{l\mathrm{u}} \\ C_{\mathrm{sm}} \dfrac{\mathrm{d}v_{Cl\mathrm{v}}^{(i)}}{\mathrm{d}t} = B_{l\mathrm{v}}^{(i)} i_{l\mathrm{v}} \end{cases} \tag{4.1}$$

$$\begin{cases} v_{\mathrm{sm}_l\mathrm{u}}^{(i)} = B_{l\mathrm{u}}^{(i)} v_{Cl\mathrm{u}}^{(i)} \\ v_{\mathrm{sm}_l\mathrm{v}}^{(i)} = B_{l\mathrm{v}}^{(i)} v_{Cl\mathrm{v}}^{(i)} \end{cases} \tag{4.2}$$

where $B_{l\mathrm{u}}^{(i)}$, $B_{l\mathrm{v}}^{(i)}$ are the switching functions of the ith SM in three-phase upper and lower arms respectively. If the ith SM is inserted, the corresponding switching function is 1; otherwise, the switching function is 0. $v_{C l\mathrm{u}}^{(i)}$, $v_{C l\mathrm{v}}^{(i)}$ are the capacitor voltages of the ith SM in three-phase upper and lower arms respectively. $v_{\mathrm{sm}_l\mathrm{u}}^{(i)}$, $v_{\mathrm{sm}_l\mathrm{v}}^{(i)}$ are the output voltages of the ith SM in three-phase upper and lower arms respectively.

The capacitor voltage balancing algorithm is usually adopted to maintain SM capacitor voltage balancing in each arm. In brief, the SMs with the lowest capacitor voltages in each arm are given priority to be charged, while the SMs with the highest capacitor voltages in each arm are given priority to be discharged. Thus, the capacitor voltage of each SM satisfies

$$\begin{cases} v_{C l\mathrm{u}}^{(1)} = v_{C l\mathrm{u}}^{(2)} = \cdots = v_{C l\mathrm{u}}^{(N)} = \dfrac{v_{C l\mathrm{u}}}{N} \\ v_{C l\mathrm{v}}^{(1)} = v_{C l\mathrm{v}}^{(2)} = \cdots = v_{C l\mathrm{v}}^{(N)} = \dfrac{v_{C l\mathrm{v}}}{N} \end{cases} \tag{4.3}$$

where $v_{C l\mathrm{u}}$, $v_{C l\mathrm{v}}$ denote the three-phase upper and lower arm capacitor voltages respectively, equaling the sum of the capacitor voltages of N SMs in the corresponding arm.

Combing with Eq. (4.3), the summations of the capacitor voltages and output voltages of N SMs in Eqs. (4.1) and (4.2) are respectively shown as

$$\begin{cases} \dfrac{C_{\mathrm{sm}}}{N} \dfrac{\mathrm{d}v_{C l\mathrm{u}}}{\mathrm{d}t} = m_{l\mathrm{u}} i_{l\mathrm{u}} \\ \dfrac{C_{\mathrm{sm}}}{N} \dfrac{\mathrm{d}v_{C l\mathrm{v}}}{\mathrm{d}t} = m_{l\mathrm{v}} i_{l\mathrm{v}} \end{cases} \tag{4.4}$$

$$\begin{cases} v_{l\mathrm{u}} = m_{l\mathrm{u}} v_{C l\mathrm{u}} \\ v_{l\mathrm{v}} = m_{l\mathrm{v}} v_{C l\mathrm{v}} \end{cases} \tag{4.5}$$

where $m_{l\mathrm{u}}$, $m_{l\mathrm{v}}$ are the three-phase upper and lower arm modulation signals respectively, equaling the percentage of the inserted SMs in the corresponding arm.

The number of the inserted SMs in each arm is always an integer, i.e., $m_{l\mathrm{u}}N$ or $m_{l\mathrm{v}}N$ is rounded to the nearest integer. Since the number of SMs in each arm is dozens to hundreds, $m_{l\mathrm{u}}$ and $m_{l\mathrm{v}}$ can be regarded as continuous quantities during the modeling and analysis.

According to Eqs. (4.4) and (4.5), the operation of N SMs in each arm can be equivalent to a controlled source circuit based on the consistency principle of the arm input–output characteristics. The MMC averaged model is obtained, as shown in Fig. 4.3. In the figure, C_{eq} is the arm capacitor and satisfies $C_{\mathrm{eq}} = C_{\mathrm{sm}}/N$. The controlled voltage sources $m_{l\mathrm{u}} v_{C l\mathrm{u}}$, $m_{l\mathrm{v}} v_{C l\mathrm{v}}$ are used to represent the three-phase upper and lower arm voltages, and the controlled current sources $m_{l\mathrm{u}} i_{l\mathrm{u}}$, $m_{l\mathrm{v}} i_{l\mathrm{v}}$ are used to represent the capacitor currents in the three-phase upper and lower arms.

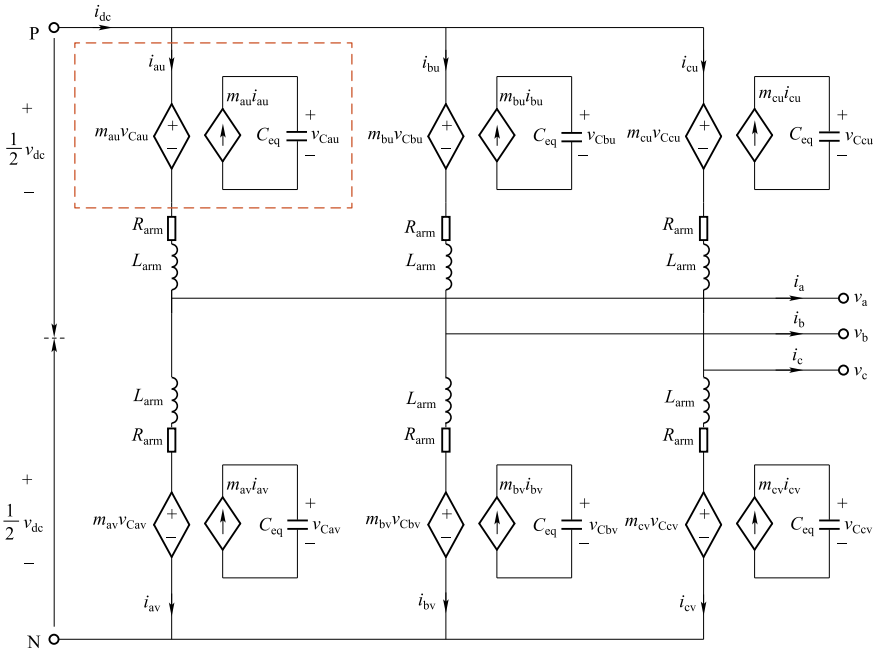

Fig. 4.3 MMC averaged model

4.2 Time-Domain Modeling of Main Circuit

This section first analyzes the operating characteristics of arm voltages and currents according to the MMC averaged model. Then, the relationships between AC currents, arm currents and circulating currents are derived. Finally, the time-domain analytical model of the main circuit is established.

4.2.1 Time-Domain Characteristic Analysis of Arm Voltage and Current

During normal operation, MMC operates at the steady-state operating point. Three-phase AC voltages and AC currents are expressed as

$$\begin{cases} v_l = V_1 \cos(\omega_1 t + \varphi_{v1} + \beta_l) \\ i_l = I_1 \cos(\omega_1 t + \varphi_{i1} + \beta_l) \end{cases} \tag{4.6}$$

where V_1, φ_{v1} are the amplitude and phase of the fundamental component of AC voltage respectively. I_1, φ_{i1} are the amplitude and phase of the fundamental component of AC current respectively. β_l are the phase-shift angles between three phases, equaling 0, $-2\pi/3$, $2\pi/3$ respectively.

The schematic diagram of the MMC operation principle is shown in Fig. 4.4. The sum of the upper and lower arm voltages in each phase constitutes the DC voltage, and half of the difference between the upper and lower arm voltages in each phase constitutes the AC voltage, which can be expressed as

$$\begin{cases} v_{\mathrm{dc}} = m_{l\mathrm{u}} v_{Cl\mathrm{u}} + m_{l\mathrm{v}} v_{Cl\mathrm{v}} \\ v_l = \dfrac{1}{2}(m_{l\mathrm{v}} v_{Cl\mathrm{v}} - m_{l\mathrm{u}} v_{Cl\mathrm{u}}) \end{cases} \tag{4.7}$$

The voltage drop of the arm inductor and resistor is neglected in Eq. (4.7) for introducing the operation principle in brief.

According to Eqs. (4.6) and (4.7), the three-phase arm voltages can be obtained

$$\begin{cases} m_{l\mathrm{u}} v_{Cl\mathrm{u}} = \dfrac{1}{2} v_{\mathrm{dc}} - V_1 \cos(\omega_1 t + \varphi_{v1} + \beta_l) \\ m_{l\mathrm{v}} v_{Cl\mathrm{v}} = \dfrac{1}{2} v_{\mathrm{dc}} + V_1 \cos(\omega_1 t + \varphi_{v1} + \beta_l) \end{cases} \tag{4.8}$$

The upper and lower arm voltages in each phase contain the DC and fundamental components. The DC components of the upper and lower arm voltages equally divide

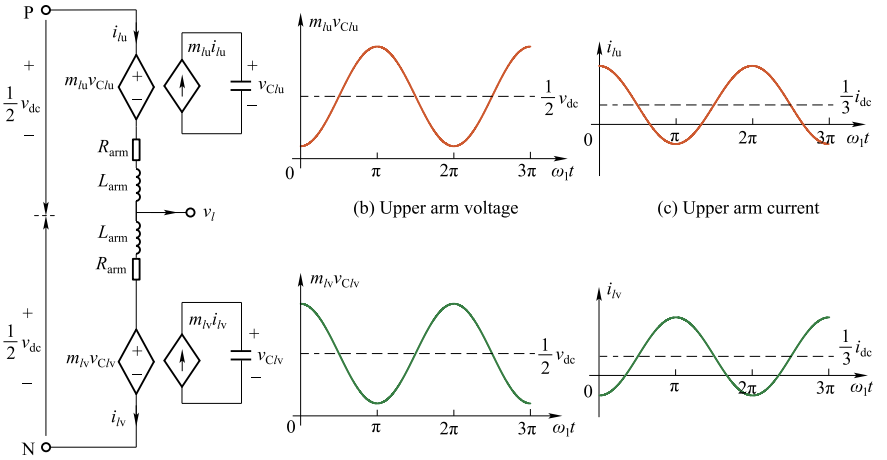

Fig. 4.4 The schematic diagram of the MMC operating principle

the DC voltage, and the fundamental components have the same amplitude but opposite phase. Besides, the sequence relationship of the fundamental components in the upper or lower arms among three phases is positive sequence.

Since the three-phase upper and lower arm voltages $v_{C/u}$, $v_{C/v}$ operate around v_{dc}, the modulation signals of three-phase upper and lower arms can be obtained according to Eq. (4.8).

$$\begin{cases} m_{lu} = \dfrac{1}{2}[1 - M_1 \cos(\omega_1 t + \varphi_{v1} + \beta_l)] \\ m_{lv} = \dfrac{1}{2}[1 + M_1 \cos(\omega_1 t + \varphi_{v1} + \beta_l)] \end{cases} \tag{4.9}$$

where M_1 is denoted as the fundamental modulation index, and the expression is

$$M_1 = \frac{2V_1}{v_{dc}} \tag{4.10}$$

According to the relationship of arm currents, the sum of the three-phase upper or lower arm currents constitutes the DC current, while the difference between the upper and lower arm currents in each phase constitutes the AC current. The following equation can be obtained

$$\begin{cases} i_{dc} = \sum\limits_{l=a,b,c} i_{lu} = \sum\limits_{l=a,b,c} i_{lv} \\ i_l = i_{lu} - i_{lv} \end{cases} \tag{4.11}$$

The expressions of the upper and lower arm current are

$$\begin{cases} i_{lu} = \dfrac{1}{3} i_{dc} + \dfrac{1}{2} I_1 \cos(\omega_1 t + \varphi_{i1} + \beta_l) \\ i_{lv} = \dfrac{1}{3} i_{dc} - \dfrac{1}{2} I_1 \cos(\omega_1 t + \varphi_{i1} + \beta_l) \end{cases} \tag{4.12}$$

Due to the three-phase symmetry of MMC, the DC current i_{dc} is distributed equally among three phases, and $i_{dc}/3$ flows through both the upper and lower arms in each phase.

According to the modulation signals in Eq. (4.9), the number of the inserted SMs in each arm satisfies

$$\begin{cases} n_{lu} = m_{lu} N = \dfrac{N}{2}[1 - M_1 \cos(\omega_1 t + \varphi_{v1} + \beta_l)] \\ n_{lv} = m_{lv} N = \dfrac{N}{2}[1 + M_1 \cos(\omega_1 t + \varphi_{v1} + \beta_l)] \end{cases} \tag{4.13}$$

Based on Eq. (4.13), the drive signals of the switches in each SM can be generated by modulation strategies, such as nearest-level modulation (NLM) or carrier phase shift (CPS) modulation.

By substituting Eq. (4.9) into Eq. (4.4) and then integrating Eq. (4.4), the expressions of three-phase upper and lower arm capacitor voltages $v_{C/u}$ and $v_{C/v}$ can be derived.

$$\begin{cases} v_{C/u} = v_{dc} + \dfrac{1}{6C_{eq}}\left[i_{dc} - \dfrac{3}{4}M_1 I_1 \cos(\varphi_{v1} - \varphi_{i1})\right]t \\ \qquad + \dfrac{I_1}{4\omega_1 C_{eq}}\sin(\omega_1 t + \varphi_{i1} + \beta_l) - \dfrac{M_1 i_{dc}}{6\omega_1 C_{eq}}\sin(\omega_1 t + \varphi_{v1} + \beta_l) \\ \qquad - \dfrac{M_1 I_1}{16\omega_1 C_{eq}}\sin(2\omega_1 t + \varphi_{v1} + \varphi_{i1} + 2\beta_l) \\ v_{C/v} = v_{dc} + \dfrac{1}{6C_{eq}}\left[i_{dc} - \dfrac{3}{4}M_1 I_1 \cos(\varphi_{v1} - \varphi_{i1})\right]t \\ \qquad - \dfrac{I_1}{4\omega_1 C_{eq}}\sin(\omega_1 t + \varphi_{i1} + \beta_l) + \dfrac{M_1 i_{dc}}{6\omega_1 C_{eq}}\sin(\omega_1 t + \varphi_{v1} + \beta_l) \\ \qquad - \dfrac{M_1 I_1}{16\omega_1 C_{eq}}\sin(2\omega_1 t + \varphi_{v1} + \varphi_{i1} + 2\beta_l) \end{cases} \tag{4.14}$$

To ensure the stable operation of MMC, the active power of AC and DC sides should be maintained in balance, which satisfies

$$v_{dc} i_{dc} = \frac{3}{2} V_1 I_1 \cos(\varphi_{v1} - \varphi_{i1}) \tag{4.15}$$

According to Eq. (4.15), the terms relative to time t in the upper and lower subequations of Eq. (4.14) are zero, indicating that the net energy absorbed by each arm in a fundamental period is zero. The capacitor voltage in each arm is thus maintained near the rated value.

According to Eq. (4.14), the arm capacitor voltage contains the DC, fundamental, and second harmonic components. The fundamental components of the upper and lower arm capacitor voltages in each phase have the same amplitude but opposite phase, which are the differential mode (DM) components. The second harmonic components have the same amplitude and phase, which are the common mode (CM) components.

According to Eq. (4.5), multiple harmonic components are also introduced into the arm voltage in each arm due to the multiplication of the arm modulation signal and capacitor voltage, which can be derived as

$$
\begin{cases}
m_{l\mathrm{u}} v_{C l\mathrm{u}} = \dfrac{1}{2} v_{\mathrm{dc}} + \dfrac{M_1 I_1}{16\omega_1 C_{\mathrm{eq}}} \sin(\varphi_{\mathrm{v1}} - \varphi_{\mathrm{i1}}) - \dfrac{1}{2} M_1 v_{\mathrm{dc}} \cos(\omega_1 t + \varphi_{\mathrm{v1}} + \beta_l) \\
\qquad - \dfrac{M_1 i_{\mathrm{dc}}}{12\omega_1 C_{\mathrm{eq}}} \sin(\omega_1 t + \varphi_{\mathrm{v1}} + \beta_l) + \dfrac{\left(8 + M_1^2\right) I_1}{64\omega_1 C_{\mathrm{eq}}} \sin(\omega_1 t + \varphi_{\mathrm{i1}} + \beta_l) \\
\qquad - \dfrac{3 M_1 I_1}{32\omega_1 C_{\mathrm{eq}}} \sin(2\omega_1 t + \varphi_{\mathrm{v1}} + \varphi_{\mathrm{i1}} + 2\beta_l) \\
\qquad + \dfrac{M_1^2 i_{\mathrm{dc}}}{24\omega_1 C_{\mathrm{eq}}} \sin(2\omega_1 t + 2\varphi_{\mathrm{v1}} + 2\beta_l) \\
\qquad + \dfrac{M_1^2 I_1}{64\omega_1 C_{\mathrm{eq}}} \sin(3\omega_1 t + 2\varphi_{\mathrm{v1}} + \varphi_{\mathrm{i1}} + 3\beta_l) \\
m_{l\mathrm{v}} v_{C l\mathrm{v}} = \dfrac{1}{2} v_{\mathrm{dc}} + \dfrac{M_1 I_1}{16\omega_1 C_{\mathrm{eq}}} \sin(\varphi_{\mathrm{v1}} - \varphi_{\mathrm{i1}}) + \dfrac{1}{2} M_1 v_{\mathrm{dc}} \cos(\omega_1 t + \varphi_{\mathrm{v1}} + \beta_l) \\
\qquad + \dfrac{M_1 i_{\mathrm{dc}}}{12\omega_1 C_{\mathrm{eq}}} \sin(\omega_1 t + \varphi_{\mathrm{v1}} + \beta_l) - \dfrac{\left(8 + M_1^2\right) I_1}{64\omega_1 C_{\mathrm{eq}}} \sin(\omega_1 t + \varphi_{\mathrm{i1}} + \beta_l) \\
\qquad - \dfrac{3 M_1 I_1}{32\omega_1 C_{\mathrm{eq}}} \sin(2\omega_1 t + \varphi_{\mathrm{v1}} + \varphi_{\mathrm{i1}} + 2\beta_l) \\
\qquad + \dfrac{M_1^2 i_{\mathrm{dc}}}{24\omega_1 C_{\mathrm{eq}}} \sin(2\omega_1 t + 2\varphi_{\mathrm{v1}} + 2\beta_l) \\
\qquad - \dfrac{M_1^2 I_1}{64\omega_1 C_{\mathrm{eq}}} \sin(3\omega_1 t + 2\varphi_{\mathrm{v1}} + \varphi_{\mathrm{i1}} + 3\beta_l)
\end{cases}
\tag{4.16}
$$

As shown in Eq. (4.16), the DC and second harmonic components of the upper and lower arm voltages in each phase have the same amplitude and phase, which are the CM components. The fundamental and third harmonic components have the same amplitude but opposite phase, which are the DM components. The sum and difference of the upper and lower sub-equations in Eq. (4.16) can be calculated as

$$\begin{cases} m_{l\mathrm{u}}v_{C l\mathrm{u}} + m_{l\mathrm{v}}v_{C l\mathrm{v}} = v_{\mathrm{dc}} + \dfrac{M_1 I_1}{8\omega_1 C_{\mathrm{eq}}}\sin(\varphi_{\mathrm{v}1} - \varphi_{\mathrm{i}1}) \\ \qquad\qquad - \dfrac{3M_1 I_1}{16\omega_1 C_{\mathrm{eq}}}\sin(2\omega_1 t + \varphi_{\mathrm{v}1} + \varphi_{\mathrm{i}1} + 2\beta_l) \\ \qquad\qquad + \dfrac{M_1^2 i_{\mathrm{dc}}}{12\omega_1 C_{\mathrm{eq}}}\sin(2\omega_1 t + 2\varphi_{\mathrm{v}1} + 2\beta_l) \\ \dfrac{1}{2}(m_{l\mathrm{v}}v_{C l\mathrm{v}} - m_{l\mathrm{u}}v_{C l\mathrm{u}}) = V_1\cos(\omega_1 t + \varphi_{\mathrm{v}1} + \beta_l) \\ \qquad\qquad + \dfrac{M_1 i_{\mathrm{dc}}}{12\omega_1 C_{\mathrm{eq}}}\sin(\omega_1 t + \varphi_{\mathrm{v}1} + \beta_l) \\ \qquad\qquad - \dfrac{\left(8 + M_1^2\right) I_1}{64\omega_1 C_{\mathrm{eq}}}\sin(\omega_1 t + \varphi_{\mathrm{i}1} + \beta_l) \\ \qquad\qquad - \dfrac{M_1^2 I_1}{64\omega_1 C_{\mathrm{eq}}}\sin(3\omega_1 t + 2\varphi_{\mathrm{v}1} + \varphi_{\mathrm{i}1} + 3\beta_l) \end{cases} \tag{4.17}$$

It can be concluded from Eq. (4.17) that the sum of the upper and lower arm voltages in each phase constitutes the DC port voltage. The DC port voltage also contains the second harmonic component, which is in negative sequence among three phases. Besides, half of the difference between the upper and lower arm voltages in each phase constitutes the AC port voltage. Apart from the fundamental component, the AC port voltage also contains the third harmonic component, which is in zero sequence among three phases. Since the AC port of MMC is usually connected to the three-wire system, a third harmonic response of AC current will not be produced.

The difference between DC voltage and the sum of the upper and lower arm voltages in each phase drops on the arm inductor and resistor, which yields

$$\begin{aligned} L_{\mathrm{arm}}\frac{\mathrm{d}i_{\mathrm{cir}l}}{\mathrm{d}t} + R_{\mathrm{arm}}i_{\mathrm{cir}l} = &-\frac{M_1 I_1}{16\omega_1 C_{\mathrm{eq}}}\sin(\varphi_{\mathrm{v}1} - \varphi_{\mathrm{i}1}) \\ &+ \frac{3M_1 I_1}{32\omega_1 C_{\mathrm{eq}}}\sin(2\omega_1 t + \varphi_{\mathrm{v}1} + \varphi_{\mathrm{i}1} + 2\beta_l) \\ &- \frac{M_1^2 i_{\mathrm{dc}}}{24\omega_1 C_{\mathrm{eq}}}\sin(2\omega_1 t + 2\varphi_{\mathrm{v}1} + 2\beta_l) \end{aligned} \tag{4.18}$$

where the DC component on the right hand of the equation is the equivalent voltage drop of the arm resistor. The second harmonic voltage components among three phases are in negative sequence, and will cause additional negative-sequence second harmonic currents flowing through the upper and lower arms. Since the negative-sequence second harmonic currents among three phases cancel each other, the currents will not flow into both the AC and DC sides of MMC, only circulating within the arms. Therefore, $i_{\mathrm{cir}l}$ is the three-phase arm circulating currents.

According to Eq. (4.4), the arm circulating current (second harmonic) multiplying the arm modulation signal (DC and fundamental components) leads to fundamental,

second and additional third harmonic components in the arm capacitor voltage. Then, the arm capacitor voltage multiplying the arm modulation signal leads to fundamental, second, third and fourth harmonic components in the arm voltage. Furthermore, the difference between the DC voltage and the sum of the upper and lower arm voltages causes the fourth harmonic response in the arm circulating current, apart from the second harmonic component.

The repeat multiplication of the arm current and modulation signal, or the arm capacitor voltage and modulation signal, the arm current and capacitor voltage will contain, in theory, infinite number of steady-state harmonic components at $kf_1(k = 0,1,2,...)$. The amplitudes of these harmonic components gradually become smaller as the frequency increases due to the filtering effect of the SM capacitors and arm inductors.

In particular, the odd-order $[(2n+1)f_1, n = \pm 0, \pm 1, \pm 2, \ldots]$ harmonic components are DM components with the same amplitude but opposite phase, while the even-order $(2nf_1)$ harmonic components of the upper and lower arms are CM components with the same amplitude and phase. The DM components of the arm currents constitute half of the AC current, and the zero-sequence components at $(6n+3)f_1$ are excluded, since there is no zero-sequence AC current path. The CM components of the arm currents constitute the arm circulating current, in which the second harmonic is the main component. The bridge arm circulating current flowing through the submodule will increase the switching loss and cause capacitor voltage fluctuations. In this case, MMC generally suppresses the arm circulating current through a PI controller.

Considering the DM and CM harmonic components, the expressions of the three-phase upper and lower arm currents in Eq. (4.12) can be refined as

$$\begin{cases} i_{l\mathrm{u}} = I_k \cos(k\omega_1 t + \varphi_{\mathrm{i}k} + k\beta_l) \\ i_{l\mathrm{v}} = (-1)^k I_k \cos(k\omega_1 t + \varphi_{\mathrm{i}k} + k\beta_l) \end{cases} \tag{4.19}$$

where I_k, $\varphi_{\mathrm{i}k}$ are the amplitude and phase of the arm current harmonic component at kf_1 respectively.

The three-phase arm DM and CM currents can be expressed as

$$\begin{cases} i_{\mathrm{dif}l} = \dfrac{i_{l\mathrm{u}} - i_{l\mathrm{v}}}{2} \\ i_{\mathrm{com}l} = \dfrac{i_{l\mathrm{u}} + i_{l\mathrm{v}}}{2} \end{cases} \tag{4.20}$$

where three-phase arm DM currents $i_{\mathrm{dif}l}$ constitutes half of the AC currents, containing the components at kf_1 with $k = 2n+1$ and $k \neq 3n$ $(n = 0, 1, 2, \ldots)$. Three-phase arm CM currents $i_{\mathrm{com}l}$ form the arm circulating currents, containing the components at kf_1 with $k = 2n$. In addition, the DC component of $i_{\mathrm{com}l}$ is $i_{\mathrm{dc}}/3$.

4.2.2 Time-Domain Model of Arm Circuit

According to the arm voltage and current relationship in Sect. 4.2.1, the time-domain model of the three-phase upper and lower arm circuits can be developed as Eqs. (4.21) and (4.22), considering the voltage drop across the arm inductor and resistor.

$$v_{l\mathrm{u}} + L_{\mathrm{arm}}\frac{\mathrm{d}i_{l\mathrm{u}}}{\mathrm{d}t} + R_{\mathrm{arm}}i_{l\mathrm{u}} = \frac{v_{\mathrm{dc}}}{2} - v_l - v_{\mathrm{O}} \tag{4.21}$$

$$v_{l\mathrm{v}} + L_{\mathrm{arm}}\frac{\mathrm{d}i_{l\mathrm{v}}}{\mathrm{d}t} + R_{\mathrm{arm}}i_{l\mathrm{v}} = \frac{v_{\mathrm{dc}}}{2} + v_l + v_{\mathrm{O}} \tag{4.22}$$

where v_{O} is the AC neutral voltage.

The sum and difference of Eqs. (4.21) and (4.22) are calculated as

$$L_{\mathrm{arm}}\frac{\mathrm{d}i_{\mathrm{dif}l}}{\mathrm{d}t} + R_{\mathrm{arm}}i_{\mathrm{dif}l} = -v_{\mathrm{dif}l} - v_l - v_{\mathrm{O}} \tag{4.23}$$

$$L_{\mathrm{arm}}\frac{\mathrm{d}i_{\mathrm{com}l}}{\mathrm{d}t} + R_{\mathrm{arm}}i_{\mathrm{com}l} = \frac{v_{\mathrm{dc}}}{2} - v_{\mathrm{com}l} \tag{4.24}$$

where $v_{\mathrm{dif}l}$, $v_{\mathrm{com}l}$ are the three-phase arm DM and CM voltages respectively, and expressed as

$$\begin{cases} v_{\mathrm{dif}l} = \dfrac{v_{l\mathrm{u}} - v_{l\mathrm{v}}}{2} \\ v_{\mathrm{com}l} = \dfrac{v_{l\mathrm{u}} + v_{l\mathrm{v}}}{2} \end{cases} \tag{4.25}$$

According to Eq. (4.23), the three-phase arm DM currents $i_{\mathrm{dif}l}$ flow into the AC side of MMC, and the AC equivalent circuit can be obtained, as shown in Fig. 4.5(a). According to Eq. (4.24), the three-phase arm CM currents $i_{\mathrm{com}l}$ circulate within three-phase arms, and the circulating current circuit can be obtained, as shown in Fig. 4.5(b). Based on the equivalent circuits, the decoupled control of AC currents and circulating currents can be achieved by adjusting the three-phase arm DM and CM voltages respectively.

The sum of the three-phase voltages or currents is zero for a symmetric three-phase AC system. Based on the AC equivalent circuit, the expression of the AC neutral voltage v_{O} can be derived as

$$v_{\mathrm{O}} = -\frac{1}{3}\sum_{l=\mathrm{a,\,b,\,c}} v_{\mathrm{dif}l} \tag{4.26}$$

It can be concluded that the AC neutral voltage v_{O} is the zero-sequence component of the three-phase arm DM voltages $v_{\mathrm{dif}l}$.

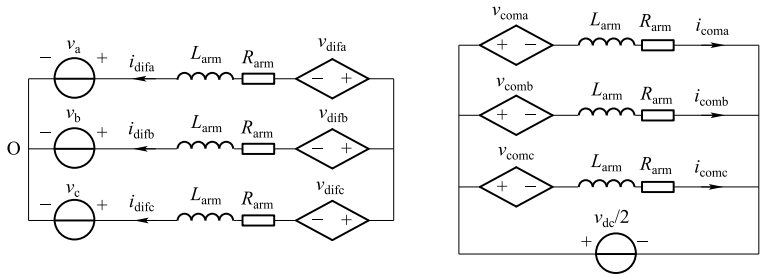

(a) AC equivalent circuit (b) Circulating current equivalent circuit

Fig. 4.5 The AC and circulating current equivalent circuits of MMC

4.3 Frequency-Domain Modeling of Steady-State Operation

According to the time-domain model of the main circuit, this section first analyzes the steady-state harmonic characteristics of MMC arm currents, capacitor voltages, and modulation signals in frequency domain. Then, the DM, CM, and phase-sequence relationships of the electrical quantities among three-phase upper and lower arms are studied. Finally, the frequency-domain steady-state model of the main circuit is established, which provides the steady-state operating point for small-signal impedance modeling.

4.3.1 Frequency-Domain Characteristic Analysis of Steady-State Operating Point

According to Sect. 4.2, the arm current, capacitor voltage, and circulating current contain multiple steady-state harmonic components. The harmonic components in the arm circulating current will cause the increase of the power loss and arm capacitor voltage ripple. The circulating current control can be used to eliminate the arm circulating current, and will introduce multiple harmonic components in the modulation signal, correspondingly. The frequency-domain characteristics at the steady-state operating point with and without circulating current control are analyzed as follows.

Figure 4.6 shows the waveforms and FFT results of the steady-state quantities in the phase-a upper arm without circulating current control. The main circuit and controller parameters are listed in Table 4.5. In the figure, the DC components of the phase-a upper arm current i_{au} and capacitor voltage v_{Cau} are taken as the base values respectively. The waveforms and FFT results show that the phase-a upper arm modulation signal m_{au} contains only DC and fundamental components without the circulating current control. Due to the interaction of the arm current, capacitor voltage and modulation signal, the arm current and capacitor voltage contain DC, fundamental,

second harmonic, third harmonic, fourth harmonic, and even higher-order harmonic components. The second harmonic is the dominant among the multiple harmonic components, since their amplitudes gradually become smaller as the frequency increases. Certainly, the amplitudes of the steady-state harmonic components in the arm current and capacitor voltage depend are mainly dependent on the size of the arm inductance and capacitance. Notably, there is no $3nf_1$ ($n = 0, 1, 2, \ldots$) harmonic component in the arm current, since there is no zero-sequence current path on the AC side of MMC.

Figure 4.7 shows the waveforms and FFT results of the steady-state quantities in the phase-a upper arm with the circulating current control. As seen from the figure, the dominant second harmonic component in the arm current is effectively eliminated

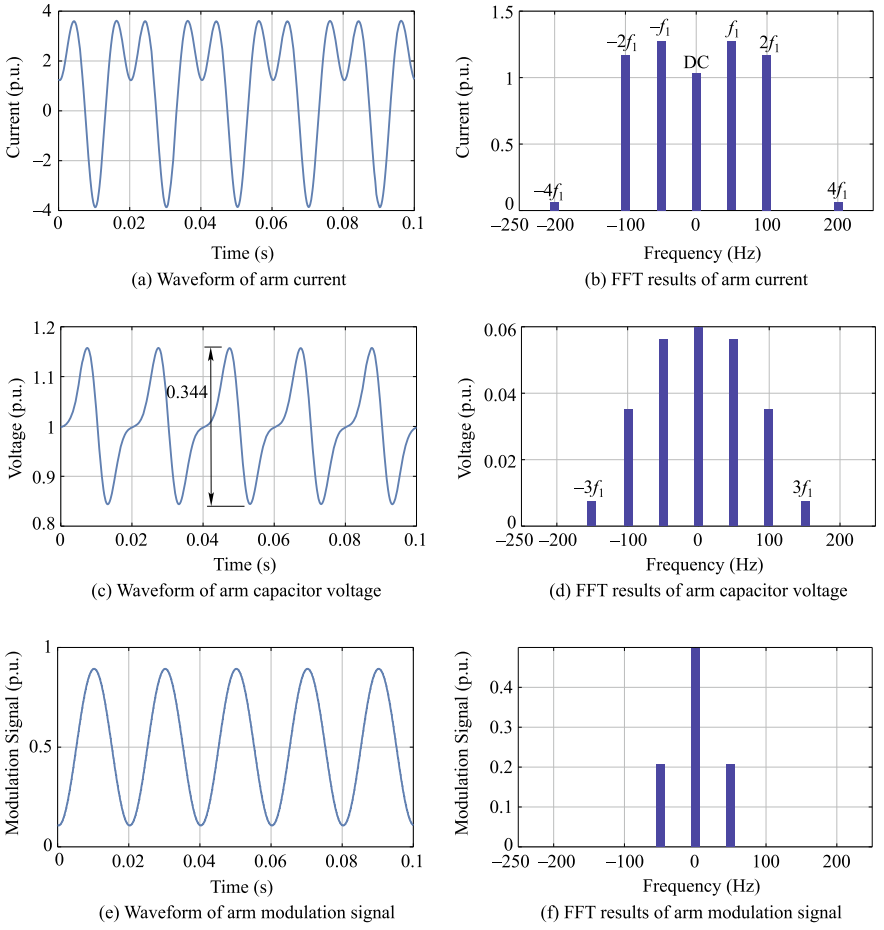

(a) Waveform of arm current
(b) FFT results of arm current
(c) Waveform of arm capacitor voltage
(d) FFT results of arm capacitor voltage
(e) Waveform of arm modulation signal
(f) FFT results of arm modulation signal

Fig. 4.6 The waveforms and FFT results of the steady-state quantities in the phase-a upper arm without circulating current control

Table 4.5 Main circuit and controller parameters of MMC

Parameter	Definition	Value
P_{N}	Rated power	1000 MW
V_1	Fundamental component amplitude of AC voltage	253.1 kV
V_{dc}	Steady-state value of DC voltage	640 kV
N	Arm SM number	256
V_{C}	Rated SM capacitor voltage	2.5 kV
C_{sm}	SM capacitance	8 mF
L_{arm}	Arm inductance	50 mH
K_{pp}, K_{pi}	Proportional and integral coefficients of the PLL controller	3.5106×10^{-4}, 0.0441
K_{iacp}, K_{iaci}	Proportional and integral coefficients of the AC current controller	1.2149×10^{-5}, 0.0053
K_{d}	Decoupling coefficient of the of the AC current control	1.2272×10^{-5}
K_{icp}, K_{ici}	Proportional and integral coefficients of the circulating current controller	3.4710×10^{-5}, 0.0218
K_{c}	Decoupling coefficient of the of the circulating current control	4.9088×10^{-5}

with the circulating current control. In addition, the arm capacitor voltage ripple is also reduced, and the peak-to-peak value of the voltage ripple is reduced from 34.4% to 16.4%, compared with Fig. 4.6(c). In consequence, the circulating current control is beneficial to the reduction of power loss and capacitance requirement in MMC.

As shown in Fig. 4.7, the amplitudes of the third and higher-order harmonic components are small, but each quantity of MMC contains, in theory, infinite number of steady-state harmonic components. Without loss of generality, the steady-state harmonic components at any frequency kf_1 in the arm current, capacitor voltage and modulation signal are considered. In this section, the frequency-domain column vector is used to describe the steady-state harmonic characteristics. The steady-state harmonic components of MMC quantities at kf_1 ($k = 0, \pm 1, \ldots, \pm g$) are arranged in the following steady-state frequency order

$$\left[-gf_1, \ldots, -f_1, 0, f_1, \ldots, gf_1\right]^{\mathrm{T}} \tag{4.27}$$

Taking the phase-a upper arm as an example, the steady-state vectors of the arm current, capacitor voltage and modulation signal can be expressed as

$$\begin{cases} \boldsymbol{I}_{\mathrm{au}} = [\ldots, \boldsymbol{I}^*_{\mathrm{au3}}, \boldsymbol{I}^*_{\mathrm{au2}}, \boldsymbol{I}^*_{\mathrm{au1}}, \boldsymbol{I}_{\mathrm{au0}}, \boldsymbol{I}_{\mathrm{au1}}, \boldsymbol{I}_{\mathrm{au2}}, \boldsymbol{I}_{\mathrm{au3}}, \ldots]^{\mathrm{T}} \\ \boldsymbol{V}_{\mathrm{Cau}} = [\ldots, \boldsymbol{V}^*_{\mathrm{Cau3}}, \boldsymbol{V}^*_{\mathrm{Cau2}}, \boldsymbol{V}^*_{\mathrm{Cau1}}, \boldsymbol{V}_{\mathrm{Cau0}}, \boldsymbol{V}_{\mathrm{Cau1}}, \boldsymbol{V}_{\mathrm{Cau2}}, \boldsymbol{V}_{\mathrm{Cau3}}, \ldots]^{\mathrm{T}} \\ \boldsymbol{M}_{\mathrm{au}} = [\ldots, \boldsymbol{M}^*_{\mathrm{au3}}, \boldsymbol{M}^*_{\mathrm{au2}}, \boldsymbol{M}^*_{\mathrm{au1}}, \boldsymbol{M}_{\mathrm{au0}}, \boldsymbol{M}_{\mathrm{au1}}, \boldsymbol{M}_{\mathrm{au2}}, \boldsymbol{M}_{\mathrm{au3}}, \ldots]^{\mathrm{T}} \end{cases} \tag{4.28}$$

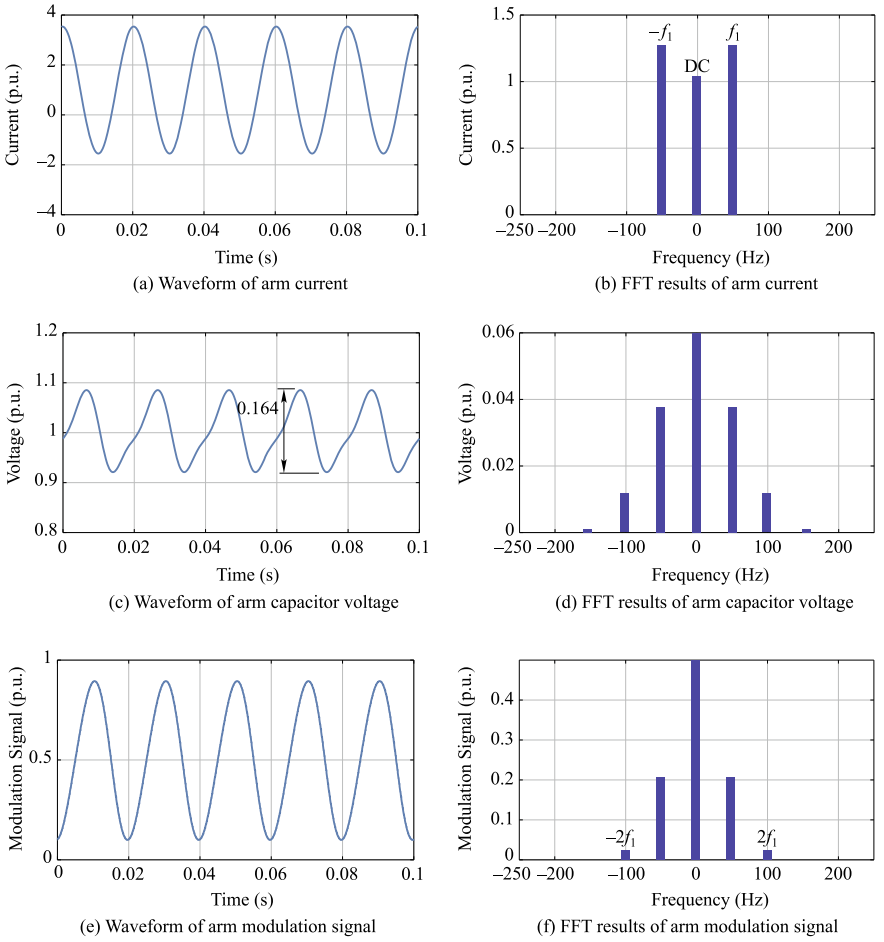

Fig. 4.7 The waveforms and FFT results of the steady-state quantities in the phase-a upper arm with circulating current control

where each component in the vectors is represented in the form of complex vector, representing its amplitude and phase at the corresponding frequency, such as $\boldsymbol{I}_{\mathrm{au}k} = I_k \mathrm{e}^{\mathrm{j}\varphi_{\mathrm{i}k}}$, $\boldsymbol{V}_{\mathrm{Cau}k} = V_k \mathrm{e}^{\mathrm{j}\varphi_{\mathrm{v}k}}$, and $\boldsymbol{M}_{\mathrm{au}k} = M_k \mathrm{e}^{\mathrm{j}\varphi_{\mathrm{m}k}}$. The subscript number of each component $k = 0, \pm1, \pm2, \ldots, \pm\mathrm{g}$ indicates the harmonic order, corresponding to the frequency kf_1.

Both the steady-state components at kf_1 and $-kf_1$ for each actual harmonic component at frequency kf_1 is considered in the steady-state vector. This is necessary for steady-state modeling of MMC. Specifically, the component at $-k_1 f_1$ multiplying the component at kf_1 produces a response at $(k_2 - k_1) f_1$, such as $k_2 - k_1 = 2$, which still belongs to the frequencies that need to be considered in the steady-state vector. Besides, the component at $-kf_1$ is equal to the conjugate of the component at kf_1,

such as $\boldsymbol{I}_{\mathrm{au}(-k)} = \boldsymbol{I}^*_{\mathrm{au}k}$, $\boldsymbol{V}_{\mathrm{au}(-k)} = \boldsymbol{V}^*_{\mathrm{au}k}$, and $\boldsymbol{M}_{\mathrm{au}(-k)} = \boldsymbol{M}^*_{\mathrm{au}k}$. The amplitude of the harmonic component at kf_1 or $-kf_1$ is equal to half of each actual harmonic component at frequency kf_1.

Besides, the odd-order harmonic components of the upper and lower arm quantities in each arm are DM components, while the even-order harmonic components are CM components. According to Eq. (4.28), the steady-state vectors of the phase-a lower arm current, capacitor voltage, and modulation signal can be obtained as

$$\boldsymbol{I}_{\mathrm{av}} = \boldsymbol{A}\boldsymbol{I}_{\mathrm{au}},\ \boldsymbol{V}_{\mathrm{Cav}} = \boldsymbol{A}\boldsymbol{V}_{\mathrm{Cau}},\ \boldsymbol{M}_{\mathrm{av}} = \boldsymbol{A}\boldsymbol{M}_{\mathrm{au}} \tag{4.29}$$

where $\boldsymbol{A}$ is the transformation matrix of the arm steady-state vectors, expressed as

$$\boldsymbol{A} = \mathrm{diag}\left[\left\{(-1)^k\right\}\big|_{k=-g,\ldots,0,\ldots,g}\right] \tag{4.30}$$

The DM components of the upper and lower arm currents in each phase constitute half of the AC current, and the CM components constitute the arm circulating current. The steady-state vectors of the AC current and arm circulating current in phase a can be obtained.

$$\begin{cases} \boldsymbol{I}_{\mathrm{a}} = 2\boldsymbol{A}_{\mathrm{d}}\boldsymbol{I}_{\mathrm{au}} \\ \boldsymbol{I}_{\mathrm{coma}} = \boldsymbol{A}_{\mathrm{c}}\boldsymbol{I}_{\mathrm{au}} \end{cases} \tag{4.31}$$

where $\boldsymbol{A}_{\mathrm{d}}$ is the DM matrix of the arm steady-state vectors, and $\boldsymbol{A}_{\mathrm{c}}$ is the CM matrix of the arm steady-state vectors. Their expressions are

$$\begin{cases} \boldsymbol{A}_{\mathrm{d}} = \dfrac{1}{2}\mathrm{diag}\left[\left\{1-(-1)^k\right\}\big|_{k=-g,\ldots,0,\ldots,g}\right] \\ \boldsymbol{A}_{\mathrm{c}} = \dfrac{1}{2}\mathrm{diag}\left[\left\{1+(-1)^k\right\}\big|_{k=-g,\ldots,0,\ldots,g}\right] \end{cases} \tag{4.32}$$

Furthermore, according to the phase-sequence relationship, for the steady-state component at kf_1, the phase-shift angle between two adjacent phases is

$$-\frac{2k\pi}{3} = \begin{cases} -2\pi/3, & k = 3n+1 \\ 2\pi/3, & k = 3n+2\ (n = 0, \pm1, \pm2, \ldots) \\ 0, & k = 3n \end{cases} \tag{4.33}$$

where, $-2\pi/3$ indicates a positive-sequence relationship among three phases, $2\pi/3$ indicates negative-sequence relationship; 0 indicates a zero-sequence relationship.

The phase-sequence relationship among three phases can be expressed by defining the following modulo-3 function

$$\mathrm{mod}(k,3)=\begin{cases}+1, & k=3n+1\\ -1, & k=3n+2\ (n=0,\pm1,\pm2,\ldots)\\ 0, & k=3n\end{cases} \tag{4.34}$$

where $+1$ indicates positive sequence, i.e., the component at $(3n+1)f_1$ is in positive sequence. -1 indicates negative sequence, i.e., the component at $(3n+2)f_1$ is in negative sequence. 0 indicates zero sequence, i.e., the component at $3nf_1$ is in zero sequence.

According to the DM, CM, and phase-sequence relationships shown in Eqs. (4.29) and (4.34), the steady-state vectors of the arm currents, capacitor voltages, and modulation signals in each arm of phase b and phase c can be obtained.

$$\begin{cases}\boldsymbol{I}_{\mathrm{bu}}=\boldsymbol{D}\boldsymbol{I}_{\mathrm{au}}, & \boldsymbol{V}_{\mathrm{Cbu}}=\boldsymbol{D}\boldsymbol{V}_{\mathrm{Cau}}, & \boldsymbol{M}_{\mathrm{bu}}=\boldsymbol{D}\boldsymbol{M}_{\mathrm{au}}\\ \boldsymbol{I}_{\mathrm{bv}}=\boldsymbol{D}\boldsymbol{A}\boldsymbol{I}_{\mathrm{au}}, & \boldsymbol{V}_{\mathrm{Cbv}}=\boldsymbol{D}\boldsymbol{A}\boldsymbol{V}_{\mathrm{Cau}}, & \boldsymbol{M}_{\mathrm{bv}}=\boldsymbol{D}\boldsymbol{A}\boldsymbol{M}_{\mathrm{au}}\end{cases} \tag{4.35}$$

$$\begin{cases}\boldsymbol{I}_{\mathrm{cu}}=\boldsymbol{D}^{*}\boldsymbol{I}_{\mathrm{au}}, & \boldsymbol{V}_{\mathrm{Ccu}}=\boldsymbol{D}^{*}\boldsymbol{V}_{\mathrm{Cau}}, & \boldsymbol{M}_{\mathrm{cu}}=\boldsymbol{D}^{*}\boldsymbol{M}_{\mathrm{au}}\\ \boldsymbol{I}_{\mathrm{cv}}=\boldsymbol{D}^{*}\boldsymbol{A}\boldsymbol{I}_{\mathrm{au}}, & \boldsymbol{V}_{\mathrm{Ccv}}=\boldsymbol{D}^{*}\boldsymbol{A}\boldsymbol{V}_{\mathrm{Cau}}, & \boldsymbol{M}_{\mathrm{cv}}=\boldsymbol{D}^{*}\boldsymbol{A}\boldsymbol{M}_{\mathrm{au}}\end{cases} \tag{4.36}$$

where $\boldsymbol{D}$ is the phase-sequence coefficient matrix of the steady-state vectors, expressed as

$$\boldsymbol{D}=\mathrm{diag}\left[\left\{\mathrm{e}^{-\mathrm{j}2k\pi/3}\right\}\Big|_{k=-g,\ldots,0,\ldots,g}\right] \tag{4.37}$$

4.3.2 Frequency-Domain Steady-State Model of Main Circuit

Based on the steady-state vectors of the arm current, capacitor voltage and modulation signal, the frequency-domain steady-state model of arm circuit in the phase-a upper arm can be obtained by transforming Eqs. (4.4) and (4.21) from the time domain to the frequency domain, which can be expressed as

$$\boldsymbol{Y}_{\mathrm{Ceq0}}\boldsymbol{V}_{\mathrm{Cau}}=\boldsymbol{M}_{\mathrm{au}}\otimes\boldsymbol{I}_{\mathrm{au}} \tag{4.38}$$

$$\boldsymbol{Z}_{\mathrm{Larm0}}\boldsymbol{I}_{\mathrm{au}}=\frac{1}{2}\boldsymbol{V}_{\mathrm{dc}}-\boldsymbol{V}_{\mathrm{a}}-\boldsymbol{M}_{\mathrm{au}}\otimes\boldsymbol{V}_{\mathrm{Cau}}-\boldsymbol{V}_{\mathrm{O}} \tag{4.39}$$

$\boldsymbol{V}_{\mathrm{dc}}$ and $\boldsymbol{V}_{\mathrm{a}}$ are the steady-state vectors of the DC voltage and phase-a AC voltage respectively, and the expressions are given as

$$\boldsymbol{V}_{\mathrm{dc}}=\left[\ldots,\ 0,\ \ldots,\ 0,\ V_{\mathrm{dc}},\ 0,\ \ldots,\ 0,\ \ldots\right]^{\mathrm{T}} \tag{4.40}$$

$$\boldsymbol{V}_{\mathrm{a}} = \left[\ldots,\ 0,\ \ldots,\ V_1/2,\ 0,\ V_1/2,\ \ldots,\ 0,\ \ldots\right]^{\mathrm{T}} \tag{4.41}$$

$\boldsymbol{Z}_{\mathrm{Lam0}}$ and $\boldsymbol{Y}_{\mathrm{Ceq0}}$ are the impedance of the arm inductor and admittance of the arm capacitor in the steady-state frequency order respectively, which are

$$\boldsymbol{Z}_{\mathrm{Larm0}} = R_{\mathrm{arm}}\boldsymbol{U} + \mathrm{j}2\pi L_{\mathrm{arm}} \cdot \mathrm{diag}\left[-gf_1,\ \ldots,\ -f_1,\ 0,\ f_1,\ \ldots,\ gf_1\right] \tag{4.42}$$

$$\boldsymbol{Y}_{\mathrm{Ceq0}} = \mathrm{j}2\pi C_{\mathrm{eq}} \cdot \mathrm{diag}\left[-gf_1,\ \ldots,\ -f_1,\ 0,\ f_1,\ \ldots,\ gf_1\right] \tag{4.43}$$

where $\boldsymbol{U}$ is identity matrix of $(2g+1) \times (2g+1)$.

In order to use scalar product instead of convolution in Eqs. (4.38) and (4.39), the steady-state vectors of the arm modulation signals need to be expanded into matrices. Using the vector $\boldsymbol{M}_{\mathrm{au}}$ as an example, the expression of the expanded steady-state matrix with $g = 3$ is given here for explaining the expansion principle.

$$\boldsymbol{M}_{\mathrm{au}} = \begin{bmatrix}
\boldsymbol{M}_{\mathrm{au0}} & \boldsymbol{M}^*_{\mathrm{au1}} & \boldsymbol{M}^*_{\mathrm{au2}} & \boldsymbol{M}^*_{\mathrm{au3}} & \cdots & & & & \\
\boldsymbol{M}_{\mathrm{au1}} & \boldsymbol{M}_{\mathrm{au0}} & \boldsymbol{M}^*_{\mathrm{au1}} & \boldsymbol{M}^*_{\mathrm{au2}} & \boldsymbol{M}^*_{\mathrm{au3}} & \cdots & & & \\
\boldsymbol{M}_{\mathrm{au2}} & \boldsymbol{M}_{\mathrm{au1}} & \boldsymbol{M}_{\mathrm{au0}} & \boldsymbol{M}^*_{\mathrm{au1}} & \boldsymbol{M}^*_{\mathrm{au2}} & \boldsymbol{M}^*_{\mathrm{au3}} & \cdots & & \\
\boldsymbol{M}_{\mathrm{au3}} & \boldsymbol{M}_{\mathrm{au2}} & \boldsymbol{M}_{\mathrm{au1}} & \boldsymbol{M}_{\mathrm{au0}} & \boldsymbol{M}^*_{\mathrm{au1}} & \boldsymbol{M}^*_{\mathrm{au2}} & \boldsymbol{M}^*_{\mathrm{au3}} & \cdots & \\
\cdots & \boldsymbol{M}_{\mathrm{au3}} & \boldsymbol{M}_{\mathrm{au2}} & \boldsymbol{M}_{\mathrm{au1}} & \boldsymbol{M}_{\mathrm{au0}} & \boldsymbol{M}^*_{\mathrm{au1}} & \boldsymbol{M}^*_{\mathrm{au2}} & \boldsymbol{M}^*_{\mathrm{au3}} & \cdots \\
 & \cdots & \boldsymbol{M}_{\mathrm{au3}} & \boldsymbol{M}_{\mathrm{au2}} & \boldsymbol{M}_{\mathrm{au1}} & \boldsymbol{M}_{\mathrm{au0}} & \boldsymbol{M}^*_{\mathrm{au1}} & \boldsymbol{M}^*_{\mathrm{au2}} & \boldsymbol{M}^*_{\mathrm{au3}} \\
 & & \cdots & \boldsymbol{M}_{\mathrm{au3}} & \boldsymbol{M}_{\mathrm{au2}} & \boldsymbol{M}_{\mathrm{au1}} & \boldsymbol{M}_{\mathrm{au0}} & \boldsymbol{M}^*_{\mathrm{au1}} & \boldsymbol{M}^*_{\mathrm{au2}} \\
 & & & \cdots & \boldsymbol{M}_{\mathrm{au3}} & \boldsymbol{M}_{\mathrm{au2}} & \boldsymbol{M}_{\mathrm{au1}} & \boldsymbol{M}_{\mathrm{au0}} & \boldsymbol{M}^*_{\mathrm{au1}} \\
 & & & & \cdots & \boldsymbol{M}_{\mathrm{au3}} & \boldsymbol{M}_{\mathrm{au2}} & \boldsymbol{M}_{\mathrm{au1}} & \boldsymbol{M}_{\mathrm{au0}}
\end{bmatrix} \tag{4.44}$$

where

1. The steady-state vector is transposed into a row vector and arranged in a reverse order, as the $(g+1)$th (center) row of the steady-state matrix.
2. The kth row ($k = 1, 2, ..., g$) above the center row is obtained by shifting the center row by k elements into the left, with the last k elements filled by 0.
3. The kth row ($k = 1, 2, ..., g$) below the center row is obtained by shifting the center row by k elements into the right, with the first k elements filled by 0.

According to the DM, CM, and phase-sequence relationships of the steady-state vectors in the three-phase upper and lower arms, the frequency-domain steady-state model of the other arm circuits can also be obtained according to Eqs. (4.38) and (4.39).

In Eq. (4.39), $\boldsymbol{V}_{\mathrm{O}}$ is the steady-state vector of AC neutral voltage, and can be obtained by transforming Eq. (4.26) to the frequency domain

$$\boldsymbol{V}_{\mathrm{O}} = -\frac{1}{6}\sum_{l=\mathrm{a,b,c}} \left(\boldsymbol{M}_{l\mathrm{u}}\boldsymbol{V}_{\mathrm{C}l\mathrm{u}} - \boldsymbol{M}_{l\mathrm{v}}\boldsymbol{V}_{\mathrm{C}l\mathrm{v}}\right) \tag{4.45}$$

Table 4.6 The frequency-domain characteristics of the steady-state vectors in MMC

Steady-State Vectors	Frequency
$\boldsymbol{V}_{\mathrm{C}l\mathrm{u}}, \boldsymbol{V}_{\mathrm{C}l\mathrm{v}}$	kf_1
$\boldsymbol{I}_{l\mathrm{u}}, \boldsymbol{I}_{l\mathrm{v}}$	kf_1 $(k \neq 6n+3)$
$\boldsymbol{M}_{l\mathrm{u}}, \boldsymbol{M}_{l\mathrm{v}}$	kf_1 $(k \neq 6n+3)$
$\boldsymbol{I}_l$	$(6n+1)f_1$
	$(6n+5)f_1$
$\boldsymbol{I}_{\mathrm{com}l}$	$6nf_1$
	$(6n+2)f_1$
	$(6n+4)f_1$

As known from Eq. (4.45), the AC neutral voltage is the zero-sequence DM component of the three-phase upper and lower arm voltages, and Eq. (4.45) can thus be simplified to

$$\boldsymbol{V}_{\mathrm{O}} = \boldsymbol{T}_{\mathrm{O}} \boldsymbol{M}_{\mathrm{au}} \boldsymbol{V}_{\mathrm{Cau}} \tag{4.46}$$

where $\boldsymbol{T}_{\mathrm{O}}$ is the zero-sequence DM matrix of the steady-state vectors, expressed as

$$\boldsymbol{T}_{\mathrm{O}} = \mathrm{diag}\left[\{T_k\}|_{k=-g,\ldots,0,\ldots,g} \right] \tag{4.47}$$

where $T_k = -1$ if and only if k is an integer multiple of 3 and not divisible by 2, i.e., $\mathrm{mod}(k, 3) = 0$ and $\mathrm{mod}(k, 2) = 1$, corresponding to $k = 6n + 3$. Otherwise, $T_k = 0$. It is worth noting that the modulo-2 function $\mathrm{mod}(k, 2)$ gives 0 and 1 for $k = 2n$ (CM) and $k = 2n + 1$ (DM) respectively, $n = 0, 1, 2, \ldots$.

$\boldsymbol{V}_{\mathrm{O}}$ cancels the zero-sequence DM voltage of the three-phase upper and lower arms in Eq. (4.39), so the corresponding zero-sequence DM current is zero, i.e., there is no zero-sequence current path on the AC side of MMC.

In summary, the frequency-domain characteristics of the steady-state vectors in MMC are listed in Table 4.6. The steady-state vectors of the three-phase upper and lower arm capacitor voltages ($\boldsymbol{V}_{\mathrm{C}l\mathrm{u}}$, $\boldsymbol{V}_{\mathrm{C}l\mathrm{v}}$) contain infinite number of steady-state harmonic components at kf_1. The steady-state vectors of the arm currents and modulation signals ($\boldsymbol{I}_{l\mathrm{u}}$, $\boldsymbol{I}_{l\mathrm{v}}$, $\boldsymbol{M}_{l\mathrm{u}}$, $\boldsymbol{M}_{l\mathrm{v}}$) contain all harmonic components at kf_1 $(k \neq 6n + 3)$, with the zero-sequence DM components excluded. The steady-state vectors of the AC currents $\boldsymbol{I}_l$ contain the DM harmonic components at $(6n + 1)f_1$ and $(6n + 5)f_1$, with the zero sequence excluded. The steady-state vectors of the arm circulating currents contain the CM components at $6nf_1$, $(6n + 2)f_1$, and $(6n + 4)f_1$.

4.4 Small-Signal Impedance Modeling in Frequency Domain

This section carries out the small-signal impedance modeling of MMC in the frequency domain. First, a small-signal perturbation is superimposed on the AC voltage at the steady-state operating point, and the frequency-domain distribution characteristics of the voltage, current and modulation signal are elaborated. Then, the frequency-domain small-signal models of the main circuit and control loops are developed, respectively. Finally, the small-signal impedance model of MMC is established by calculating the response of the AC current to the AC voltage perturbation.

4.4.1 Small-Signal Frequency-Domain Characteristic Analysis

As mentioned in Sect. 4.3.1, the arm current, capacitor voltage and modulation signal of MMC contain multiple steady-state harmonic components, such as DC, fundamental, second and so on, which altogether form the steady-state operating point of the MMC. After injecting a small-signal perturbation of AC voltage at the steady-state operation point, the multiplication between the arm current or arm capacitor voltage and the arm modulation signal will produce small-signal responses at the sidebands around steady-state harmonic frequencies. Besides, a small-signal response will be also introduced into the modulation signal under the effect of the control loops in MMC.

The small-signal transfer path and frequency response relationship of MMC are shown in Fig. 4.8. The frequency-domain small-signal characteristics will be analyzed in terms of ignoring and considering the small-signal vector of the modulation signal, respectively.

First, the case ignoring the small-signal vector of the modulation signal is analyzed. The positive-sequence small-signal perturbation at f_p is superimposed on the AC voltage at the steady-state operating point. The difference between the small-signal component of the AC voltage $\hat{\boldsymbol{v}}_l$ at f_p and the DM component of the upper and lower arm voltages drops on the arm inductor, which leads to a small-signal response of the AC current $\hat{\boldsymbol{i}}_l$ at f_p. Subsequently, the small-signal responses of the arm current $\hat{\boldsymbol{i}}_{l\mathrm{u}}$, $\hat{\boldsymbol{i}}_{l\mathrm{v}}$ at f_p are produced.

The small-signal responses of $\hat{\boldsymbol{i}}_{l\mathrm{u}}, \hat{\boldsymbol{i}}_{l\mathrm{v}}$ at f_p multiplying the steady-state components of the modulation signal $\boldsymbol{M}_{l\mathrm{u}}, \boldsymbol{M}_{l\mathrm{v}}$ at $k_1 f_1$ ($k_1 = 0, \pm 1, \ldots, \pm g$) leads to small-signal responses of the arm capacitor voltage $\hat{\boldsymbol{v}}_{Cl\mathrm{u}}$, $\hat{\boldsymbol{v}}_{Cl\mathrm{v}}$ at $f_\mathrm{p} + k_1 f_1$.

The small-signal components of $\hat{\boldsymbol{v}}_{Cl\mathrm{u}}$, $\hat{\boldsymbol{v}}_{Cl\mathrm{v}}$ multiplying the steady-state components of $\boldsymbol{M}_{l\mathrm{u}}$, $\boldsymbol{M}_{l\mathrm{v}}$ at $k_2 f_2$ ($k_2 = 0, \pm 1, \ldots, \pm g$) leads to small-signal responses of the arm voltage at $f_\mathrm{p} + (k_1 + k_2) f_1$. k_1, k_2 are arbitrary integers that can be equal or different, so they are uniformly denoted by k hereafter to simplify the description,

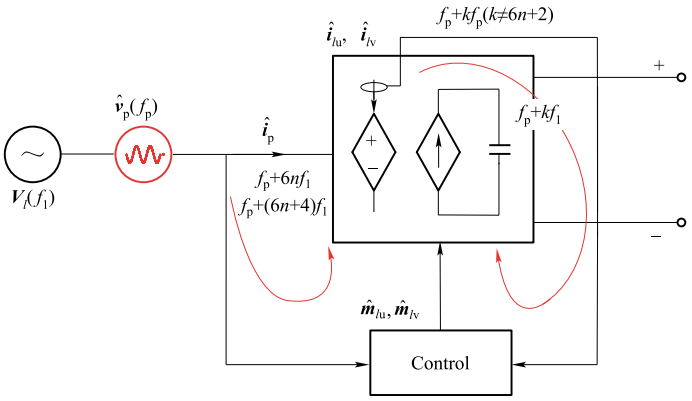

Fig. 4.8 The small-signal transfer path and frequency response relationship of MMC

i.e., small-signal components of the arm voltage at $f_p + kf_1$ are produced. The difference between the small-signal components of the arm voltage and the AC voltage or DC voltage dropping on the arm inductor leads to small-signal responses of $\hat{\boldsymbol{i}}_{lu}$, $\hat{\boldsymbol{i}}_{lv}$ at $f_p + kf_1$.

Furthermore, the small-signal characteristics considering the small-signal vector of the modulation signal are analyzed. Since the arm current $\hat{\boldsymbol{i}}_{lu}$, $\hat{\boldsymbol{i}}_{lv}$ contains small-signal components at $f_p + kf_1$, the small-signal responses of the modulation signal $\hat{\boldsymbol{m}}_{lu}$, $\hat{\boldsymbol{m}}_{lv}$ at $f_p + kf_1$ are generated correspondingly under the effects of AC current control and circulating current control. Besides, PLL is used to track the phase angle of AC voltage in MMC. After injecting the positive-sequence small-signal perturbation at f_p on the AC voltage, the small-signal component of the PLL output angle at $f_p - f_1$ is generated, which also leads to the small-signal responses of the modulation signal $\hat{\boldsymbol{m}}_{lu}$, $\hat{\boldsymbol{m}}_{lv}$ at $f_p + kf_1$.

The small-signal components of $\hat{\boldsymbol{m}}_{lu}$, $\hat{\boldsymbol{m}}_{lv}$ at $f_p + kf_1$ multiplying the steady-state components of the arm current $\boldsymbol{I}_{lu}$, $\boldsymbol{I}_{lv}$ at kf_1 leads to the small-signal responses of the arm capacitor voltage $\hat{\boldsymbol{v}}_{Clu}$, $\hat{\boldsymbol{v}}_{Clv}$ at $f_p + kf_1$. In addition, the small-signal components of $\hat{\boldsymbol{m}}_{lu}$, $\hat{\boldsymbol{m}}_{lv}$ at $f_p + kf_1$ multiplying the steady-state components of the arm capacitor voltage $\boldsymbol{V}_{Clu}$, $\boldsymbol{V}_{Clv}$ at kf_1 leads to the small-signal responses of the arm current $\hat{\boldsymbol{i}}_{lu}$, $\hat{\boldsymbol{i}}_{lv}$ at $f_p + kf_1$.

To sum up, the small-signal components of an electrical quantity multiplying the steady-state components of the modulation signal leads to small-signal responses of the other electrical quantities. Meanwhile, the small-signal components of the modulation signal multiplying the steady-state components of an electrical quantity also leads to small-signal responses of the other electrical quantities. The balance will be finally achieved after repeating the above process.

Besides, the multiplication between small-signal components leads to responses at $2f_p + kf_1$, $3f_p + kf_1$ and even higher-order small-signal frequencies. Since their

amplitudes are proportional to the square or higher order of the small-signal perturbation, these small-signal responses can be ignored in the linearization modeling process.

For instance, a positive-sequence small-signal voltage perturbation, 0.05p.u. at $f_p = 30$ Hz, is superimposed on the AC voltage. After reaching the steady state, the waveforms and the FFT results of the small-signal quantities in the phase-a upper arm are shown in Fig. 4.9. The main circuit and controller parameters are listed in Table 4.5. As seen from the figure, the small-signal responses at $f_p + kf_1$ are introduced into the arm current, capacitor voltage, and modulation signal, and the amplitudes of the higher-frequency components are relatively small.

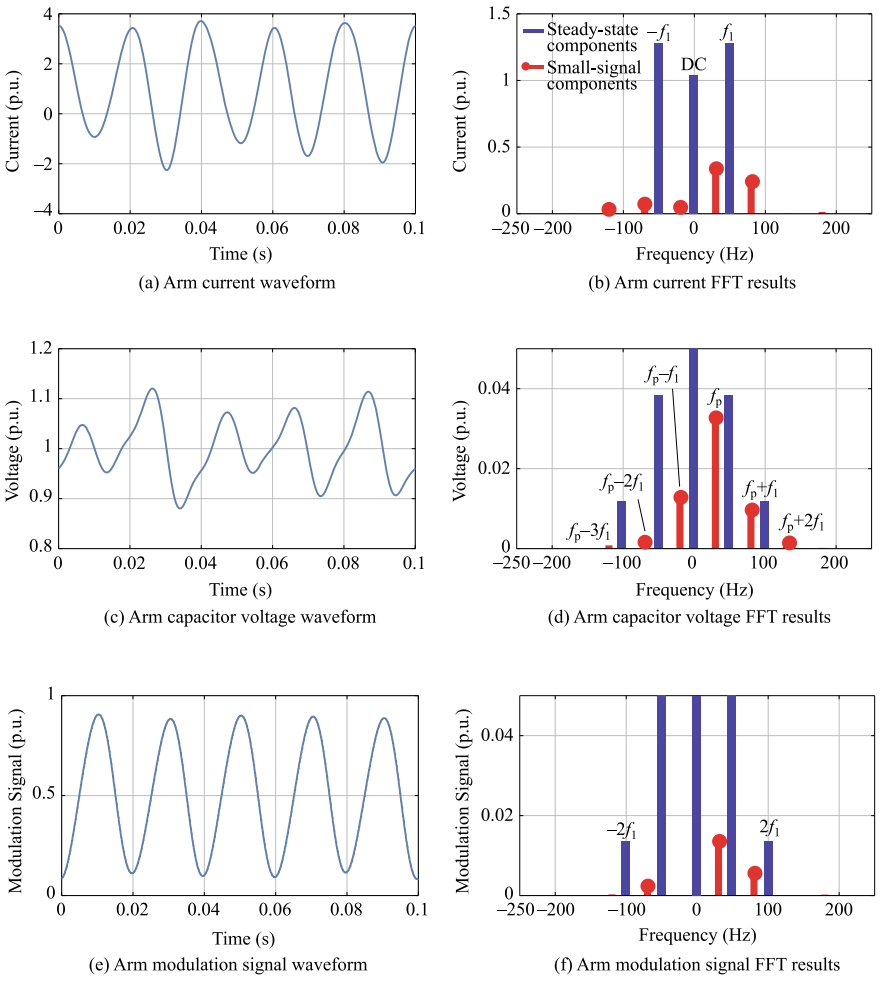

(a) Arm current waveform

(b) Arm current FFT results

(c) Arm capacitor voltage waveform

(d) Arm capacitor voltage FFT results

(e) Arm modulation signal waveform

(f) Arm modulation signal FFT results

Fig. 4.9 The waveforms and FFT results of the small-signal quantities in the phase-a upper arm with circulating current control

In order to describe the frequency-domain small-signal characteristics, the small-signal components of MMC quantities at $f_\mathrm{p} + kf_1$ are arranged in the following small-signal frequency order.

$$\left[f_\mathrm{p} - gf_1, \ldots, f_\mathrm{p} - f_1, f_\mathrm{p}, f_\mathrm{p} + f_1, \ldots, f_\mathrm{p} + gf_1 \right]^\mathrm{T} \tag{4.48}$$

Taking the phase-a upper arm as an example, the small-signal vectors of the arm current, capacitor voltage, and modulation signal can be expressed as

$$\begin{cases} \hat{\boldsymbol{i}}_\mathrm{au} = [\ldots, \hat{\boldsymbol{i}}_{\mathrm{au}-3}, \hat{\boldsymbol{i}}_{\mathrm{au}-2}, \hat{\boldsymbol{i}}_{\mathrm{au}-1}, \hat{\boldsymbol{i}}_{\mathrm{au}0}, \hat{\boldsymbol{i}}_{\mathrm{au}+1}, \hat{\boldsymbol{i}}_{\mathrm{au}+2}, \hat{\boldsymbol{i}}_{\mathrm{au}+3}, \ldots]^\mathrm{T} \\ \hat{\boldsymbol{v}}_\mathrm{Cau} = [\ldots, \hat{\boldsymbol{v}}_{\mathrm{Cau}-3}, \hat{\boldsymbol{v}}_{\mathrm{Cau}-2}, \hat{\boldsymbol{v}}_{\mathrm{Cau}-1}, \hat{\boldsymbol{v}}_{\mathrm{Cau}0}, \hat{\boldsymbol{v}}_{\mathrm{Cau}+1}, \hat{\boldsymbol{v}}_{\mathrm{Cau}+2}, \hat{\boldsymbol{v}}_{\mathrm{Cau}+3}, \ldots]^\mathrm{T} \\ \hat{\boldsymbol{m}}_\mathrm{au} = [\ldots, \hat{\boldsymbol{m}}_{\mathrm{au}-3}, \hat{\boldsymbol{m}}_{\mathrm{au}-2}, \hat{\boldsymbol{m}}_{\mathrm{au}-1}, \hat{\boldsymbol{m}}_{\mathrm{au}0}, \hat{\boldsymbol{m}}_{\mathrm{au}+1}, \hat{\boldsymbol{m}}_{\mathrm{au}+2}, \hat{\boldsymbol{m}}_{\mathrm{au}+3}, \ldots]^\mathrm{T} \end{cases} \tag{4.49}$$

where each component $\hat{\boldsymbol{i}}_{\mathrm{au}k}, \hat{\boldsymbol{v}}_{\mathrm{Cau}k}, \hat{\boldsymbol{m}}_{\mathrm{au}k}$ represents the small-signal component at the frequency $f_\mathrm{p} + kf_1$.

For the positive-sequence perturbation, the angle is delayed by $2\pi/3$ among three phases. Combined with the phases of the steady-state components at kf_1, the phase-shift angle between adjacent phases for a small-signal component at $f_\mathrm{p}+kf_1$ becomes

$$-\frac{2(k+1)\pi}{3} = \begin{cases} -2\pi/3, & k = 3n \\ 2\pi/3, & k = 3n+1 \\ 0, & k = 3n+2 \end{cases} \tag{4.50}$$

The phase-sequence relationship among three phases for small-signal components can be expressed by defining the following modulo-3 function

$$\mathrm{mod}(k+1, 3) = \begin{cases} +1, & k = 3n \\ -1, & k = 3n+1 \\ 0, & k = 3n+2 \end{cases} \tag{4.51}$$

The small-signal component at $f_\mathrm{p} + 3nf_1$ is in positive sequence, the small-signal component at $f_\mathrm{p}+(3n+1)f_1$ is in negative sequence, and the small-signal component at $f_\mathrm{p} + (3n+2)f_1$ is in zero sequence.

According to the phase-sequence relationship shown in Eq. (4.51), the small-signal vectors of the arm currents, capacitor voltages, and modulation signals in the upper arms of phase b and phase c can be obtained.

$$\begin{cases} \hat{\boldsymbol{i}}_\mathrm{bu} = \boldsymbol{D}_\mathrm{p}\hat{\boldsymbol{i}}_\mathrm{au}, \hat{\boldsymbol{v}}_\mathrm{Cbu} = \boldsymbol{D}_\mathrm{p}\hat{\boldsymbol{v}}_\mathrm{Cau}, \hat{\boldsymbol{m}}_\mathrm{bu} = \boldsymbol{D}_\mathrm{p}\hat{\boldsymbol{m}}_\mathrm{au} \\ \hat{\boldsymbol{i}}_\mathrm{cu} = \boldsymbol{D}_\mathrm{p}^*\hat{\boldsymbol{i}}_\mathrm{au}, \hat{\boldsymbol{v}}_\mathrm{Ccu} = \boldsymbol{D}_\mathrm{p}^*\hat{\boldsymbol{v}}_\mathrm{Cau}, \hat{\boldsymbol{m}}_\mathrm{cu} = \boldsymbol{D}_\mathrm{p}^*\hat{\boldsymbol{m}}_\mathrm{au} \end{cases} \tag{4.52}$$

where $\boldsymbol{D}_\mathrm{p}$ is the phase-sequence coefficient matrix of the small-signal vectors, expressed as

$$\boldsymbol{D}_{\mathrm{p}} = \mathrm{diag}\left[\{\mathrm{e}^{-\mathrm{j}2(k+1)\pi/3}\}\big|_{k=-g,\ldots,0,\ldots,g} \right] \tag{4.53}$$

Similarly, after injecting the positive-sequence perturbation, the DM and CM characteristics of the small-signal components at $f_{\mathrm{p}} + kf_1$ in the upper and lower arms satisfy the following relationship. If $k = 2n$, i.e., $\mathrm{mod}(k+1, 2) = 1$, the small-signal component at $f_{\mathrm{p}} + 2nf_1$ is the DM component. If $k = 2n+1$, i.e., $\mathrm{mod}(k+1, 2) = 0$, the small-signal component at $f_{\mathrm{p}} + (2n+1)f_1$ is the CM component.

Based on the DM and CM relationships of the small-signal components, the small-signal vectors of the arm currents, capacitor voltages, and modulation signals in the three-phase lower arms can be obtained according to Eqs. (4.49) and (4.52).

$$\begin{cases} \hat{\boldsymbol{i}}_{\mathrm{av}} = \boldsymbol{A}_{\mathrm{p}}\hat{\boldsymbol{i}}_{\mathrm{au}}, & \hat{\boldsymbol{v}}_{\mathrm{Cav}} = \boldsymbol{A}_{\mathrm{p}}\hat{\boldsymbol{v}}_{\mathrm{Cau}}, & \hat{\boldsymbol{m}}_{\mathrm{av}} = \boldsymbol{A}_{\mathrm{p}}\hat{\boldsymbol{m}}_{\mathrm{au}} \\ \hat{\boldsymbol{i}}_{\mathrm{bv}} = \boldsymbol{D}_{\mathrm{p}}\boldsymbol{A}_{\mathrm{p}}\hat{\boldsymbol{i}}_{\mathrm{au}}, & \hat{\boldsymbol{v}}_{\mathrm{Cbv}} = \boldsymbol{D}_{\mathrm{p}}\boldsymbol{A}_{\mathrm{p}}\hat{\boldsymbol{v}}_{\mathrm{Cau}}, & \hat{\boldsymbol{m}}_{\mathrm{bv}} = \boldsymbol{D}_{\mathrm{p}}\boldsymbol{A}_{\mathrm{p}}\hat{\boldsymbol{m}}_{\mathrm{au}} \\ \hat{\boldsymbol{i}}_{\mathrm{cv}} = \boldsymbol{D}_{\mathrm{p}}^{*}\boldsymbol{A}_{\mathrm{p}}\hat{\boldsymbol{i}}_{\mathrm{au}}, & \hat{\boldsymbol{v}}_{\mathrm{Ccv}} = \boldsymbol{D}_{\mathrm{p}}^{*}\boldsymbol{A}_{\mathrm{p}}\hat{\boldsymbol{v}}_{\mathrm{Cau}}, & \hat{\boldsymbol{m}}_{\mathrm{cv}} = \boldsymbol{D}_{\mathrm{p}}^{*}\boldsymbol{A}_{\mathrm{p}}\hat{\boldsymbol{m}}_{\mathrm{au}} \end{cases} \tag{4.54}$$

where $\boldsymbol{A}_{\mathrm{p}}$ is the transformation matrix of the arm small-signal vectors, expressed as

$$\boldsymbol{A}_{\mathrm{p}} = \mathrm{diag}\left[\{(-1)^{k+1}\}\big|_{k=-g,\ldots,0,\ldots,g} \right] \tag{4.55}$$

The DM components of the upper and lower arm currents in each phase constitute half of the AC current, and the CM components constitute the arm circulating current. The small-signal vectors of the three-phase AC currents and arm circulating currents can be obtained.

$$\begin{cases} \hat{\boldsymbol{i}}_{l} = 2\boldsymbol{A}_{\mathrm{pd}}\hat{\boldsymbol{i}}_{l\mathrm{u}} \\ \hat{\boldsymbol{i}}_{\mathrm{com}l} = \boldsymbol{A}_{\mathrm{pc}}\hat{\boldsymbol{i}}_{l\mathrm{u}} \end{cases} \tag{4.56}$$

where $\boldsymbol{A}_{\mathrm{pd}}$ is the DM matrix of the arm small-signal vectors, and $\boldsymbol{A}_{\mathrm{pc}}$ is the CM matrix of the arm small-signal vectors. Their expressions are

$$\begin{cases} \boldsymbol{A}_{\mathrm{pd}} = \dfrac{1}{2}\mathrm{diag}\left[\{1 + (-1)^{k}\}\big|_{k=-g,\ldots,0,\ldots,g} \right] \\ \boldsymbol{A}_{\mathrm{pc}} = \dfrac{1}{2}\mathrm{diag}\left[\{1 - (-1)^{k}\}\big|_{k=-g,\ldots,0,\ldots,g} \right] \end{cases} \tag{4.57}$$

According to the relationship of CM, DM, and phase sequence among three-phase arms, the small-signal vector of the other arms can be obtained from the small-signal vector of one arm. In summary, the frequency-domain characteristics of the small-signal vectors in MMC are listed in Table 4.7. The small-signal vectors of the three-phase upper and lower arm capacitor voltages ($\hat{\boldsymbol{v}}_{Cl\mathrm{u}}$, $\hat{\boldsymbol{v}}_{Cl\mathrm{v}}$) contain infinite number of small-signal components at $f_{\mathrm{p}} + kf_1$. The small-signal vectors of the arm currents and modulation signals ($\hat{\boldsymbol{i}}_{l\mathrm{u}}$, $\hat{\boldsymbol{i}}_{l\mathrm{v}}$, $\hat{\boldsymbol{m}}_{l\mathrm{u}}$, $\hat{\boldsymbol{m}}_{l\mathrm{v}}$) contain all components at

Table 4.7 The frequency-domain characteristics of the small-signal vectors in MMC

Steady-Sstate Vectors	Frequency
$\hat{\boldsymbol{v}}_{Clu}$, $\hat{\boldsymbol{v}}_{Clv}$	$f_p + kf_1$
$\hat{\boldsymbol{i}}_{lu}$, $\hat{\boldsymbol{i}}_{lv}$	$f_p + kf_1$ $(k \neq 6n+2)$
$\hat{\boldsymbol{m}}_{lu}$, $\hat{\boldsymbol{m}}_{lv}$	$f_p + kf_1$ $(k \neq 6n+2)$
$\hat{\boldsymbol{i}}_l$	$f_p + 6nf_1$
	$f_p + (6n+4)f_1$
$\hat{\boldsymbol{i}}_{coml}$	$f_p + (6n+1)f_1$
	$f_p + (6n+3)f_1$
	$f_p + (6n+5)f_1$

$f_p + kf_1$ $(k \neq 6n+2)$, with the zero-sequence DM components excluded. The small-signal vectors of the AC currents ($\hat{\boldsymbol{i}}_l$) contain the DM components at $f_p + 6nf_1$ and $f_p + (6n+4)f_1$, with the zero sequence excluded. The small-signal vectors of the arm circulating currents contain the CM components at $f_p + (6n+1)f_1$, $f_p + (6n+3)f_1$, and $f_p + (6n+5)f_1$.

4.4.2 *Frequency-Domain Small-Signal Model of Main Circuit*

Based on the small-signal vectors of the arm current, capacitor voltage, and modulation signal, this section establishes the frequency-domain small-signal model of the main circuit.

By transforming Eqs. (4.4) and (4.21) to the frequency domain, the small-signal model of the arm circuit in the phase-a upper arm can be obtained.

$$\begin{cases} \hat{\boldsymbol{v}}_{Cau} = \boldsymbol{Z}_{Ceq}\left(\boldsymbol{I}_{au} \otimes \hat{\boldsymbol{m}}_{au} + \boldsymbol{M}_{au} \otimes \hat{\boldsymbol{i}}_{au}\right) \\ \hat{\boldsymbol{i}}_{au} = -\boldsymbol{Y}_{Larm}\left(\hat{\boldsymbol{v}}_a + \boldsymbol{V}_{Cau} \otimes \hat{\boldsymbol{m}}_{au} + \boldsymbol{M}_{au} \otimes \hat{\boldsymbol{v}}_{Cau} + \hat{\boldsymbol{v}}_O\right) \end{cases} \tag{4.58}$$

where $\hat{\boldsymbol{v}}_a$ is the small-signal vector of the phase-a AC voltage, expressed as

$$\hat{\boldsymbol{v}}_a = [\ldots, 0, \hat{\boldsymbol{v}}_{p-2}, 0, \hat{\boldsymbol{v}}_p, 0, 0, 0, \ldots]^T \tag{4.59}$$

Correspondingly, $\hat{\boldsymbol{v}}_p$ and $\hat{\boldsymbol{v}}_{p-2}$ are the small-signal components of AC voltages at f_p and $f_p - 2f_1$ resepectively.

$\boldsymbol{Y}_{Larm}$ and $\boldsymbol{Z}_{Ceq}$ are the admittance of the arm inductor and impedance of the arm capacitor in the small-signal frequency order respectively, which are

$$\boldsymbol{Y}_{\mathrm{Larm}} = \mathrm{diag}\Bigg[\cdots, \frac{1}{R_{\mathrm{arm}} + \mathrm{j}2\pi(f_{\mathrm{p}} - kf_1)L_{\mathrm{arm}}}, \cdots, \frac{1}{R_{\mathrm{arm}} + \mathrm{j}2\pi(f_{\mathrm{p}} - f_1)L_{\mathrm{arm}}}, \frac{1}{R_{\mathrm{arm}} + \mathrm{j}2\pi f_{\mathrm{p}}L_{\mathrm{arm}}}, \frac{1}{R_{\mathrm{arm}} + \mathrm{j}2\pi(f_{\mathrm{p}} + f_1)L_{\mathrm{arm}}}, \cdots, \frac{1}{R_{\mathrm{arm}} + \mathrm{j}2\pi(f_{\mathrm{p}} + kf_1)L_{\mathrm{arm}}}, \cdots\Bigg] \tag{4.60}$$

$$\boldsymbol{Z}_{\mathrm{Ceq}} = \frac{1}{\mathrm{j}2\pi C_{\mathrm{eq}}} \cdot \mathrm{diag}\Bigg[\cdots, \frac{1}{f_{\mathrm{p}} - kf_1}, \cdots, \frac{1}{f_{\mathrm{p}} - f_1}, \frac{1}{f_{\mathrm{p}}}, \frac{1}{f_{\mathrm{p}} + f_1}, \cdots, \frac{1}{f_{\mathrm{p}} + kf_1}, \cdots\Bigg] \tag{4.61}$$

According to the DM, CM, and phase-sequence relationships of the small-signal vectors in the three-phase upper and lower arms, the frequency-domain small-signal model of the other arm circuits can also be obtained according to Eq. (4.58).

$\hat{\boldsymbol{v}}_{\mathrm{O}}$ is the small-signal vector of AC neutral voltage, which can be obtained by transforming Eq. (4.26) to the frequency domain and combining the DM, CM, and phase-sequence relationships.

$$\hat{\boldsymbol{v}}_{\mathrm{O}} = \boldsymbol{T}_{\mathrm{p}}(\boldsymbol{M}_{\mathrm{au}} \otimes \hat{\boldsymbol{v}}_{\mathrm{Cau}} + \boldsymbol{V}_{\mathrm{Cau}} \otimes \hat{\boldsymbol{m}}_{\mathrm{au}}) \tag{4.62}$$

where $\boldsymbol{T}_{\mathrm{p}}$ is the zero-sequence DM matrix of the arm small-signal vectors, expressed as

$$\boldsymbol{T}_{\mathrm{p}} = \mathrm{diag}\Big[\{T_{\mathrm{p}k}\}\big|_{k=-g,\ldots,0,\ldots,g}\Big] \tag{4.63}$$

where $T_{\mathrm{p}k} = -1$ if and only if $k+1$ is an integer multiple of 3 and not divisible by 2, i.e., $\mathrm{mod}(k+1, 3) = 0$ and $\mathrm{mod}(k+1, 2) = 1$, corresponding to $k = 6n+2$. Otherwise, $T_{\mathrm{p}k} = 0$.

$\hat{\boldsymbol{v}}_{\mathrm{O}}$ cancels the zero-sequence DM components of the three-phase upper and lower arm voltages in Eq. (4.58), so the small-signal vectors of the corresponding arm currents exclude the zero-sequence DM components, i.e., there is no zero-sequence current path on the AC side of MMC. The function of $\hat{\boldsymbol{v}}_{\mathrm{O}}$ can be replaced by modifying $\boldsymbol{Y}_{\mathrm{Larm}}$, which is given as

$$\boldsymbol{Y}_{\mathrm{Larm}} = \boldsymbol{A}_{\mathrm{pd0}} \cdot \mathrm{diag}\Bigg[\cdots, \frac{1}{R_{\mathrm{arm}} + \mathrm{j}2\pi(f_{\mathrm{p}} - kf_1)L_{\mathrm{arm}}}, \cdots, \frac{1}{R_{\mathrm{arm}} + \mathrm{j}2\pi(f_{\mathrm{p}} - f_1)L_{\mathrm{arm}}}, \frac{1}{R_{\mathrm{arm}} + \mathrm{j}2\pi f_{\mathrm{p}}L_{\mathrm{arm}}}, \frac{1}{R_{\mathrm{arm}} + \mathrm{j}2\pi(f_{\mathrm{p}} + f_1)L_{\mathrm{arm}}}, \cdots, \frac{1}{R_{\mathrm{arm}} + \mathrm{j}2\pi(f_{\mathrm{p}} + kf_1)L_{\mathrm{arm}}}, \cdots\Bigg] \tag{4.64}$$

where $\boldsymbol{A}_{\mathrm{pd0}}$ is the modified admittance matrix of arm inductor, and $\boldsymbol{A}_{\mathrm{pd0}} = \boldsymbol{T}_{\mathrm{p}} + \boldsymbol{U}$. If and only if $\mathrm{mod}(k+1,3) = 0$ and $\mathrm{mod}(k+1,2) = 1$, corresponding to $k = 6n+2$, the diagonal element in $\boldsymbol{Y}_{\mathrm{Larm}}$ is zero; otherwise, the diagonal element remains unchanged.

The modified $\boldsymbol{Y}_{\mathrm{Larm}}$ forces the zero-sequence DM components of the arm currents to be zero, such that $\hat{\boldsymbol{v}}_{\mathrm{O}}$ can be dropped from Eq. (4.58). Therefore, the frequency-domain small-signal model of the arm circuit can be simplified as

$$\begin{cases} \hat{\boldsymbol{v}}_{\mathrm{Cau}} = \boldsymbol{Z}_{\mathrm{Ceq}}\left(\boldsymbol{I}_{\mathrm{au}} \otimes \hat{\boldsymbol{m}}_{\mathrm{au}} + \boldsymbol{M}_{\mathrm{au}} \otimes \hat{\boldsymbol{i}}_{\mathrm{au}}\right) \\ \hat{\boldsymbol{i}}_{\mathrm{au}} = -\boldsymbol{Y}_{\mathrm{Larm}}\left(\hat{\boldsymbol{v}}_{\mathrm{a}} + \boldsymbol{V}_{\mathrm{Cau}} \otimes \hat{\boldsymbol{m}}_{\mathrm{au}} + \boldsymbol{M}_{\mathrm{au}} \otimes \hat{\boldsymbol{v}}_{\mathrm{Cau}}\right) \end{cases} \tag{4.65}$$

In order to use the scalar product instead of convolution in Eq. (4.65), the steady-state vectors $\boldsymbol{I}_{\mathrm{au}}$, $\boldsymbol{V}_{\mathrm{Cau}}$, $\boldsymbol{M}_{\mathrm{au}}$ shown in Eq. (4.28) need to be expanded into matrices. According to the expansion principle in Eq. (4.44), the steady-state matrices of the phase-a upper arm current and capacitor voltage are given as

$$\boldsymbol{I}_{\mathrm{au}} = \begin{bmatrix} \boldsymbol{I}_{\mathrm{au0}} & \boldsymbol{I}^*_{\mathrm{au1}} & \boldsymbol{I}^*_{\mathrm{au2}} & \boldsymbol{I}^*_{\mathrm{au3}} & \cdots & & & & \\ \boldsymbol{I}_{\mathrm{au1}} & \boldsymbol{I}_{\mathrm{au0}} & \boldsymbol{I}^*_{\mathrm{au1}} & \boldsymbol{I}^*_{\mathrm{au2}} & \boldsymbol{I}^*_{\mathrm{au3}} & \cdots & & & \\ \boldsymbol{I}_{\mathrm{au2}} & \boldsymbol{I}_{\mathrm{au1}} & \boldsymbol{I}_{\mathrm{au0}} & \boldsymbol{I}^*_{\mathrm{au1}} & \boldsymbol{I}^*_{\mathrm{au2}} & \boldsymbol{I}^*_{\mathrm{au3}} & \cdots & & \\ \boldsymbol{I}_{\mathrm{au3}} & \boldsymbol{I}_{\mathrm{au2}} & \boldsymbol{I}_{\mathrm{au1}} & \boldsymbol{I}_{\mathrm{au0}} & \boldsymbol{I}^*_{\mathrm{au1}} & \boldsymbol{I}^*_{\mathrm{au2}} & \boldsymbol{I}^*_{\mathrm{au3}} & \cdots & \\ \cdots & \boldsymbol{I}_{\mathrm{au3}} & \boldsymbol{I}_{\mathrm{au2}} & \boldsymbol{I}_{\mathrm{au1}} & \boldsymbol{I}_{\mathrm{au0}} & \boldsymbol{I}^*_{\mathrm{au1}} & \boldsymbol{I}^*_{\mathrm{au2}} & \boldsymbol{I}^*_{\mathrm{au3}} & \cdots \\ & \cdots & \boldsymbol{I}_{\mathrm{au3}} & \boldsymbol{I}_{\mathrm{au2}} & \boldsymbol{I}_{\mathrm{au1}} & \boldsymbol{I}_{\mathrm{au0}} & \boldsymbol{I}^*_{\mathrm{au1}} & \boldsymbol{I}^*_{\mathrm{au2}} & \boldsymbol{I}^*_{\mathrm{au3}} \\ & & \cdots & \boldsymbol{I}_{\mathrm{au3}} & \boldsymbol{I}_{\mathrm{au2}} & \boldsymbol{I}_{\mathrm{au1}} & \boldsymbol{I}_{\mathrm{au0}} & \boldsymbol{I}^*_{\mathrm{au1}} & \boldsymbol{I}^*_{\mathrm{au2}} \\ & & & \cdots & \boldsymbol{I}_{\mathrm{au3}} & \boldsymbol{I}_{\mathrm{au2}} & \boldsymbol{I}_{\mathrm{au1}} & \boldsymbol{I}_{\mathrm{au0}} & \boldsymbol{I}^*_{\mathrm{au1}} \\ & & & & \cdots & \boldsymbol{I}_{\mathrm{au3}} & \boldsymbol{I}_{\mathrm{au2}} & \boldsymbol{I}_{\mathrm{au1}} & \boldsymbol{I}_{\mathrm{au0}} \end{bmatrix} \tag{4.66}$$

$$\boldsymbol{V}_{\mathrm{Cau}} = \begin{bmatrix} \boldsymbol{V}_{\mathrm{Cau0}} & \boldsymbol{V}^*_{\mathrm{Cau1}} & \boldsymbol{V}^*_{\mathrm{Cau2}} & \boldsymbol{V}^*_{\mathrm{Cau3}} & \cdots & & & & & \\ \boldsymbol{V}_{\mathrm{Cau1}} & \boldsymbol{V}_{\mathrm{Cau0}} & \boldsymbol{V}^*_{\mathrm{Cau1}} & \boldsymbol{V}^*_{\mathrm{Cau2}} & \boldsymbol{V}^*_{\mathrm{Cau3}} & \cdots & & & & \\ \boldsymbol{V}_{\mathrm{Cau2}} & \boldsymbol{V}_{\mathrm{Cau1}} & \boldsymbol{V}_{\mathrm{Cau0}} & \boldsymbol{V}^*_{\mathrm{Cau1}} & \boldsymbol{V}^*_{\mathrm{Cau2}} & \boldsymbol{V}^*_{\mathrm{Cau3}} & \cdots & & & \\ \boldsymbol{V}_{\mathrm{Cau3}} & \boldsymbol{V}_{\mathrm{Cau2}} & \boldsymbol{V}_{\mathrm{Cau1}} & \boldsymbol{V}_{\mathrm{Cau0}} & \boldsymbol{V}^*_{\mathrm{Cau1}} & \boldsymbol{V}^*_{\mathrm{Cau2}} & \boldsymbol{V}^*_{\mathrm{Cau3}} & \cdots & & \\ \cdots & \boldsymbol{V}_{\mathrm{Cau3}} & \boldsymbol{V}_{\mathrm{Cau2}} & \boldsymbol{V}_{\mathrm{Cau1}} & \boldsymbol{V}_{\mathrm{Cau0}} & \boldsymbol{V}^*_{\mathrm{Cau1}} & \boldsymbol{V}^*_{\mathrm{Cau2}} & \boldsymbol{V}^*_{\mathrm{Cau3}} & \cdots \\ & \cdots & \boldsymbol{V}_{\mathrm{Cau3}} & \boldsymbol{V}_{\mathrm{Cau2}} & \boldsymbol{V}_{\mathrm{Cau1}} & \boldsymbol{V}_{\mathrm{Cau0}} & \boldsymbol{V}^*_{\mathrm{Cau1}} & \boldsymbol{V}^*_{\mathrm{Cau2}} & \boldsymbol{V}^*_{\mathrm{Cau3}} \\ & & \cdots & \boldsymbol{V}_{\mathrm{Cau3}} & \boldsymbol{V}_{\mathrm{Cau2}} & \boldsymbol{V}_{\mathrm{Cau1}} & \boldsymbol{V}_{\mathrm{Cau0}} & \boldsymbol{V}^*_{\mathrm{Cau1}} & \boldsymbol{V}^*_{\mathrm{Cau2}} \\ & & & \cdots & \boldsymbol{V}_{\mathrm{Cau3}} & \boldsymbol{V}_{\mathrm{Cau2}} & \boldsymbol{V}_{\mathrm{Cau1}} & \boldsymbol{V}_{\mathrm{Cau0}} & \boldsymbol{V}^*_{\mathrm{Cau1}} \\ & & & & \cdots & \boldsymbol{V}_{\mathrm{Cau3}} & \boldsymbol{V}_{\mathrm{Cau2}} & \boldsymbol{V}_{\mathrm{Cau1}} & \boldsymbol{V}_{\mathrm{Cau0}} \end{bmatrix} \tag{4.67}$$

$\boldsymbol{I}_{\mathrm{au}}$, $\boldsymbol{V}_{\mathrm{Cau}}$, $\boldsymbol{M}_{\mathrm{au}}$ in the following parts of this chapter denote the corresponding steady-state matrices, and convolution is replaced by scalar product.

4.4.3 Frequency-Domain Small-Signal Model of Control Loops

According to the frequency-domain small-signal model of the arm circuit, both the arm current and arm capacitor voltage are related to the arm modulation signal, and are coupled to each other via the arm modulation signal. In this section, based on the control strategy of MMC, the frequency-domain small-signal model of the control loops, including PLL, AC current loop, and circulating current loop, is established. Then, the small-signal vectors of the arm modulation signal are obtained, which can be related to the small-signal model of the main circuit.

4.4.3.1 Control Strategy

The control of MMC includes PLL, AC current control, circulating current control, and SM capacitor voltage balancing control. PLL is used in MMC to obtain the voltage phase of the grid, which provides the reference angle for the Park transformation and inverse Park transformation. Besides, based on the equivalent circuits shown in Fig. 4.5, AC current control and circulating current control can be decoupled by adjusting the three-phase arm DM and CM voltages, respectively. Since the SM capacitor voltage balancing control is usually implemented at the switching level of about several kilohertz, the voltage imbalance among SM capacitors is relatively small, and the assumption made in Eq. (4.3) is justified. Therefore, the SM capacitor voltage balancing control can be ignored in the MMC control. The typical control diagram of MMC is shown in Fig. 4.10.

In Fig. 4.10, $H_{\mathrm{iac}}(s)$ is the transfer function of the AC current controller, expressed as $H_{\mathrm{iac}}(s) = K_{\mathrm{iacp}} + K_{\mathrm{iaci}}/s$. K_{iacp}, K_{iaci} are the corresponding proportional and integral coefficients respectively. i_{dref}, i_{qref} are the dq-axis current references, which are given as constants in this chapter. i_{d}, i_{q} are the dq-axis currents, and K_{d} is the decoupled coefficient of the AC current control. m_{d}, m_{q} are the dq-axis modulation signals, which are the outputs of AC current controllers. m_{difl} are the three-phase arm DM modulation signals generated by the inverse Park transformation.

The circulating current control is performed in the negative-sequence second-harmonic SRF. $H_{\mathrm{ic}}(s)$ is the transfer function of the circulating current controller, expressed as $H_{\mathrm{ic}}(s) = K_{\mathrm{icp}} + K_{\mathrm{ici}}/s$. K_{icp}, K_{ici} are the corresponding proportional and integral coefficients respectively. i_{cdref}, i_{cqref} are the dq-axis circulating current references, which are both set as zero. i_{cd}, i_{cq} are the dq-axis circulating currents, and K_{c} is the decoupled coefficient of the circulating current control. m_{cd}, m_{cq} are the dq-axis circulating modulation signals, which are the outputs of circulating current controllers. m_{coml} are the three-phase arm CM modulation signals generated by the inverse Park transformation.

The three-phase upper and lower arm modulation signals can be obtained according to m_{difl} and m_{coml}.

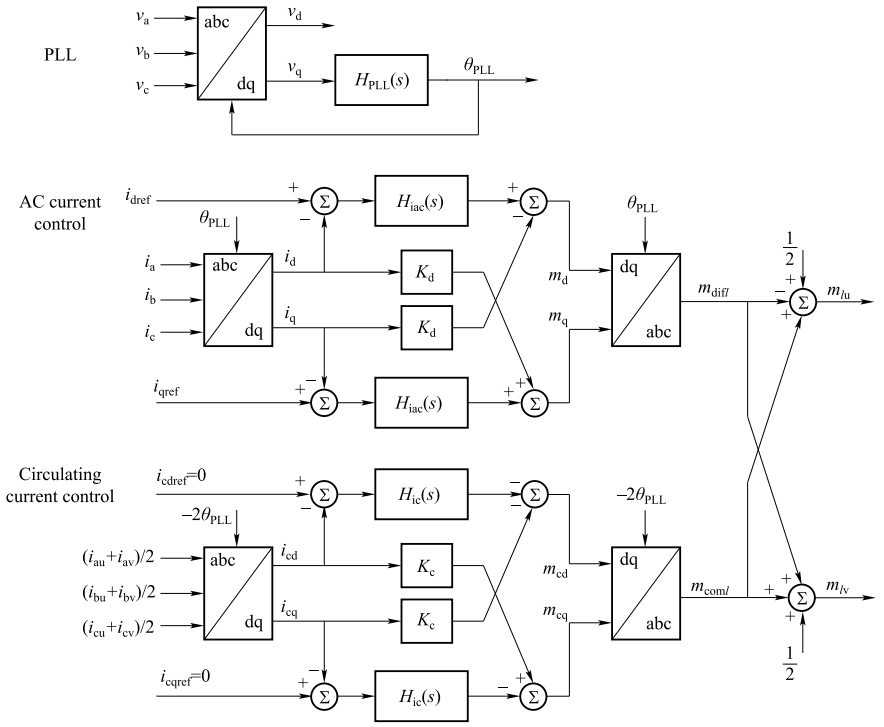

Fig. 4.10 The typical control diagram of MMC

$$\begin{cases} m_{lu} = \dfrac{1}{2} - m_{difl} + m_{coml} \\ m_{lv} = \dfrac{1}{2} + m_{difl} + m_{coml} \end{cases} \tag{4.68}$$

4.4.3.2 Small-Signal Model of Control Loop

1. Small-Signal Model of PLL

Based on the small-signal model of PLL as mentioned in Chap. 2, the small-signal vectors of the PLL output angle can be expressed as

$$\hat{\boldsymbol{\theta}}_{PLL} = \boldsymbol{G}_{\theta}\hat{\boldsymbol{v}}_{a} \tag{4.69}$$

where $\boldsymbol{G}_{\theta}$ is the $(2g+1) \times (2g+1)$ transfer function matrix of PLL with the frequency coupling considered, and all the other elements in the matrix are zero except for Eq. (4.70).

$$\begin{cases} \boldsymbol{G}_\theta(g, g-1) = \mathrm{j}T_{\mathrm{PLL}}[\mathrm{j}2\pi(f_\mathrm{p} - f_1)] \\ \boldsymbol{G}_\theta(g, g+1) = -\mathrm{j}T_{\mathrm{PLL}}[\mathrm{j}2\pi(f_\mathrm{p} - f_1)] \end{cases} \tag{4.70}$$

where $\boldsymbol{G}_\theta(g, g-1)$ is the $(g, g-1)$ th element of $\boldsymbol{G}_\theta$; $\boldsymbol{G}_\theta(g, g+1)$ is the $(g, g+1)$ th element of $\boldsymbol{G}_\theta$.

2. **Small-Signal Model of AC Current Control**

Since the DM components of the upper and lower arm currents in each phase constitute half of the AC current, the small-signal vectors of the three-phase AC currents $\hat{\boldsymbol{i}}_l$ can be obtained according to Eqs. (4.52) and (4.56).

$$\begin{cases} \hat{\boldsymbol{i}}_\mathrm{a} = 2\boldsymbol{A}_\mathrm{pd}\hat{\boldsymbol{i}}_\mathrm{au} \\ \hat{\boldsymbol{i}}_\mathrm{b} = 2\boldsymbol{A}_\mathrm{pd}\boldsymbol{D}_\mathrm{p}\hat{\boldsymbol{i}}_\mathrm{au} \\ \hat{\boldsymbol{i}}_\mathrm{c} = 2\boldsymbol{A}_\mathrm{pd}\boldsymbol{D}_\mathrm{p}^*\hat{\boldsymbol{i}}_\mathrm{au} \end{cases} \tag{4.71}$$

The vector $\hat{\boldsymbol{i}}_l$ contains the DM small-signal components except for the zero sequence, and the corresponding frequencies are

$$f_\mathrm{abc} = \frac{1 + (-1)^k}{2} \cdot |\mathrm{mod}(k+1, 3)| \cdot (f_\mathrm{p} + kf_1) \tag{4.72}$$

where the zero frequency is not included.

As shown in Fig. 4.10, the AC current control is performed in SRF, involving the Park transformation, PI control, and inverse Park transformation.

According to the small-signal model of the Park transformation as mentioned in Chap. 2, the small-signal components of the AC currents and PLL output angle lead to small-signal responses in the dq-axis currents. Substituting $\boldsymbol{I}_l$, $\hat{\boldsymbol{i}}_l$, and $\hat{\boldsymbol{\theta}}_\mathrm{PLL}$ into the small-signal model of the Park transformation, the small-signal vectors of the dq-axis currents can be derived as

$$\begin{cases} \hat{\boldsymbol{i}}_\mathrm{d} = \boldsymbol{E}_\mathrm{id}\hat{\boldsymbol{i}}_\mathrm{au} + \boldsymbol{E}_\mathrm{vd}\hat{\boldsymbol{v}}_\mathrm{a} \\ \hat{\boldsymbol{i}}_\mathrm{q} = \boldsymbol{E}_\mathrm{iq}\hat{\boldsymbol{i}}_\mathrm{au} + \boldsymbol{E}_\mathrm{vq}\hat{\boldsymbol{v}}_\mathrm{a} \end{cases} \tag{4.73}$$

where $\boldsymbol{E}_\mathrm{id}$, $\boldsymbol{E}_\mathrm{vd}$, $\boldsymbol{E}_\mathrm{iq}$, $\boldsymbol{E}_\mathrm{vq}$ are $(2g+1) \times (2g+1)$ matrices, and all other elements in the matrices are zero except for Eqs. (4.74)–(4.77).

$$\begin{cases} \boldsymbol{E}_\mathrm{id}(g+k+1, g+k) = (1 - |\mathrm{mod}(k+1, 3)|) \cdot [1 - (-1)^k] \\ \boldsymbol{E}_\mathrm{id}(g+k+1, g+k+2) = (1 - |\mathrm{mod}(k+1, 3)|) \cdot [1 - (-1)^k] \end{cases} \tag{4.74}$$

$$\begin{cases} \boldsymbol{E}_\mathrm{vd}(g, g-1) = T_{\mathrm{PLL}}[\mathrm{j}2\pi(f_\mathrm{p} - f_1)] \cdot 2(\boldsymbol{I}_\mathrm{au1} - \boldsymbol{I}_\mathrm{au1}^*) \\ \boldsymbol{E}_\mathrm{vd}(g, g+1) = -T_{\mathrm{PLL}}[\mathrm{j}2\pi(f_\mathrm{p} - f_1)] \cdot 2(\boldsymbol{I}_\mathrm{au1} - \boldsymbol{I}_\mathrm{au1}^*) \end{cases} \tag{4.75}$$

$$\begin{cases} \boldsymbol{E}_\mathrm{iq}(g+k+1, g+k) = \mathrm{j}(1 - |\mathrm{mod}(k+1, 3)|) \cdot [1 - (-1)^k] \\ \boldsymbol{E}_\mathrm{iq}(g+k+1, g+k+2) = -\mathrm{j}(1 - |\mathrm{mod}(k+1, 3)|) \cdot [1 - (-1)^k] \end{cases} \tag{4.76}$$

$$\begin{cases} \boldsymbol{E}_{\mathrm{vq}}(g, g-1) = -\mathrm{j}T_{\mathrm{PLL}}[\mathrm{j}2\pi(f_{\mathrm{p}} - f_1)] \cdot 2(\boldsymbol{I}_{\mathrm{au1}} + \boldsymbol{I}_{\mathrm{au1}}^*) \\ \boldsymbol{E}_{\mathrm{vq}}(g, g+1) = \mathrm{j}T_{\mathrm{PLL}}[\mathrm{j}2\pi(f_{\mathrm{p}} - f_1)] \cdot 2(\boldsymbol{I}_{\mathrm{au1}} + \boldsymbol{I}_{\mathrm{au1}}^*) \end{cases} \tag{4.77}$$

After the Park transformation, $\hat{\boldsymbol{i}}_{\mathrm{d}}, \hat{\boldsymbol{i}}_{\mathrm{q}}$ contain only zero-sequence components, and the corresponding frequencies are

$$f_{\mathrm{dq}} = \frac{1 - (-1)^k}{2} \cdot (1 - |\mathrm{mod}(k+1, 3)|) \cdot (f_{\mathrm{p}} + kf_1) \tag{4.78}$$

where the zero frequency is also not included.

The waveforms and FFT results of $\hat{\boldsymbol{i}}_{\mathrm{d}}, \hat{\boldsymbol{i}}_{\mathrm{q}}$ are shown in Fig. 4.11 when the small-signal perturbation is superimposed at $t = 0.05$s. Figure 4.11(a, c) show the time-domain waveforms with the base value is taken as the DC component of the steady-state d-axis current. Figure 4.11(b, d) show the corresponding FFT results, in which only the spectrum results of the small-signal components are illustrated. As seen from Fig. 4.11, the small-signal component at $f_{\mathrm{p}} - f_1$ is dominant in $\hat{\boldsymbol{i}}_{\mathrm{d}}, \hat{\boldsymbol{i}}_{\mathrm{q}}$, and the amplitudes of other components at $f_{\mathrm{p}} - 7f_1$ and $f_{\mathrm{p}} + 5f_1$ are relatively small.

According to Fig. 4.10, the AC current control includes the PI controller and dq-axis decoupled control. The small-signal vectors of the dq-axis modulation signals can be obtained based on the AC current control.

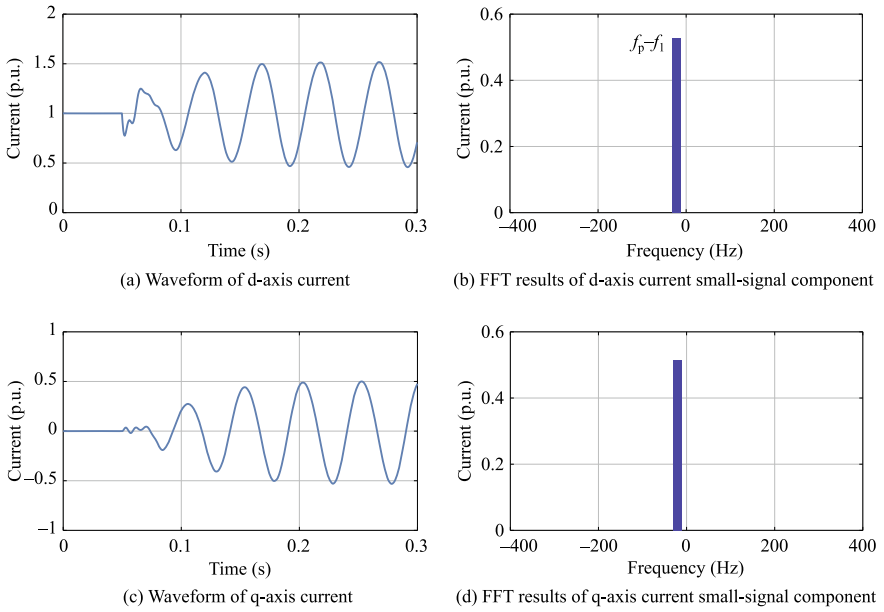

(a) Waveform of d-axis current

(b) FFT results of d-axis current small-signal component

(c) Waveform of q-axis current

(d) FFT results of q-axis current small-signal component

Fig. 4.11 The waveforms and FFT results of the dq-axis small-signal vectors of AC currents

$$\begin{cases} \hat{\boldsymbol{m}}_{\mathrm{d}} = -\boldsymbol{H}_{\mathrm{iac}}\hat{\boldsymbol{i}}_{\mathrm{d}} - K_{\mathrm{d}}\hat{\boldsymbol{i}}_{\mathrm{q}} \\ \hat{\boldsymbol{m}}_{\mathrm{q}} = -\boldsymbol{H}_{\mathrm{iac}}\hat{\boldsymbol{i}}_{\mathrm{q}} + K_{\mathrm{d}}\hat{\boldsymbol{i}}_{\mathrm{d}} \end{cases} \tag{4.79}$$

where $\boldsymbol{H}_{\mathrm{iac}}$ is the transfer function matrix of the AC current controller, expressed as

$$\boldsymbol{H}_{\mathrm{iac}} = \mathrm{diag}\Big[\left\{H_{\mathrm{iac}}[\mathrm{j}2\pi(f_{\mathrm{p}} + kf_1)]\right\}\big|_{k=-g,\ldots,0,\ldots,g}\Big] \tag{4.80}$$

Substituting $\hat{\boldsymbol{i}}_{\mathrm{d}}$, $\hat{\boldsymbol{i}}_{\mathrm{q}}$ in Eq. (4.73) into Eq. (4.79), the expressions of the dq-axis small-signal vectors of the AC modulation signals can be obtained.

$$\begin{cases} \hat{\boldsymbol{m}}_{\mathrm{d}} = \boldsymbol{F}_{\mathrm{id}}\hat{\boldsymbol{i}}_{\mathrm{au}} + \boldsymbol{F}_{\mathrm{vd}}\hat{\boldsymbol{v}}_{\mathrm{a}} \\ \hat{\boldsymbol{m}}_{\mathrm{q}} = \boldsymbol{F}_{\mathrm{iq}}\hat{\boldsymbol{i}}_{\mathrm{au}} + \boldsymbol{F}_{\mathrm{vq}}\hat{\boldsymbol{v}}_{\mathrm{a}} \end{cases} \tag{4.81}$$

where $\boldsymbol{F}_{\mathrm{id}}$, $\boldsymbol{F}_{\mathrm{vd}}$, $\boldsymbol{F}_{\mathrm{iq}}$, $\boldsymbol{F}_{\mathrm{vq}}$ are $(2g+1)\times(2g+1)$ matrices, and all the other elements in the matrices are zero except for Eqs. (4.82)–(4.85).

$$\begin{cases} \boldsymbol{F}_{\mathrm{id}}(g+k+1, g+k) = -(1-|\mathrm{mod}(k+1,3)|)\cdot[1-(-1)^k] \\ \qquad\qquad \cdot\{H_{\mathrm{iac}}[\mathrm{j}2\pi(f_{\mathrm{p}}+kf_1)] - \mathrm{mod}(k,3)\mathrm{j}K_{\mathrm{d}}\} \\ \boldsymbol{F}_{\mathrm{id}}(g+k+1, g+k+2) = -(1-|\mathrm{mod}(k+1,3)|)\cdot[1-(-1)^k] \\ \qquad\qquad \cdot\{H_{\mathrm{iac}}[\mathrm{j}2\pi(f_{\mathrm{p}}+kf_1)] + \mathrm{mod}(k,3)\mathrm{j}K_{\mathrm{d}}\} \end{cases} \tag{4.82}$$

$$\begin{cases} \boldsymbol{F}_{\mathrm{vd}}(g, g-1) = -2T_{\mathrm{PLL}}[\mathrm{j}2\pi(f_{\mathrm{p}}-f_1)] \\ \qquad\qquad \cdot\left[\left\{H_{\mathrm{iac}}[\mathrm{j}2\pi(f_{\mathrm{p}}-f_1)] - \mathrm{j}K_{\mathrm{d}}\right\}\boldsymbol{I}_{\mathrm{au1}}\right. \\ \qquad\qquad \left. - \left\{H_{\mathrm{iac}}[\mathrm{j}2\pi(f_{\mathrm{p}}-f_1)] + \mathrm{j}K_{\mathrm{d}}\right\}\boldsymbol{I}_{\mathrm{au1}}^*\right] \\ \boldsymbol{F}_{\mathrm{vd}}(g, g+1) = 2T_{\mathrm{PLL}}[\mathrm{j}2\pi(f_{\mathrm{p}}-f_1)] \\ \qquad\qquad \cdot\left[\left\{H_{\mathrm{iac}}[\mathrm{j}2\pi(f_{\mathrm{p}}-f_1)] - \mathrm{j}K_{\mathrm{d}}\right\}\boldsymbol{I}_{\mathrm{au1}}\right. \\ \qquad\qquad \left. - \left\{H_{\mathrm{iac}}[\mathrm{j}2\pi(f_{\mathrm{p}}-f_1)] + \mathrm{j}K_{\mathrm{d}}\right\}\boldsymbol{I}_{\mathrm{au1}}^*\right] \end{cases} \tag{4.83}$$

$$\begin{cases} \boldsymbol{F}_{\mathrm{iq}}(g+k+1, g+k) = (1-|\mathrm{mod}(k+1,3)|)\cdot[1-(-1)^k] \\ \qquad\qquad \cdot\{\mathrm{mod}(k,3)\mathrm{j}H_{\mathrm{iac}}[\mathrm{j}2\pi(f_{\mathrm{p}}+kf_1)] + K_{\mathrm{d}}\} \\ \boldsymbol{F}_{\mathrm{iq}}(g+k+1, g+k+2) = (1-|\mathrm{mod}(k+1,3)|)\cdot[1-(-1)^k] \\ \qquad\qquad \cdot\{-\mathrm{mod}\ (k,3)\mathrm{j}H_{\mathrm{iac}}[\mathrm{j}2\pi(f_{\mathrm{p}}+kf_1)] + K_{\mathrm{d}}\} \end{cases} \tag{4.84}$$

$$\begin{cases} \boldsymbol{F}_{\mathrm{vq}}(g, g-1) = -2T_{\mathrm{PLL}}[\mathrm{j}2\pi(f_{\mathrm{p}}-f_1)] \\ \qquad\qquad \cdot\left[\left\{K_{\mathrm{d}} - \mathrm{j}H_{\mathrm{iac}}[\mathrm{j}2\pi(f_{\mathrm{p}}-f_1)]\right\}\boldsymbol{I}_{\mathrm{au1}}^*\right. \\ \qquad\qquad \left. - \left\{K_{\mathrm{d}} + \mathrm{j}H_{\mathrm{iac}}[\mathrm{j}2\pi(f_{\mathrm{p}}-f_1)]\right\}\boldsymbol{I}_{\mathrm{au1}}\right] \\ \boldsymbol{F}_{\mathrm{vq}}(g, g+1) = 2T_{\mathrm{PLL}}[\mathrm{j}2\pi(f_{\mathrm{p}}-f_1)] \\ \qquad\qquad \cdot\left[\left\{K_{\mathrm{d}} - \mathrm{j}H_{\mathrm{iac}}[\mathrm{j}2\pi(f_{\mathrm{p}}-f_1)]\right\}\boldsymbol{I}_{\mathrm{au1}}^*\right. \\ \qquad\qquad \left. - \left\{K_{\mathrm{d}} + \mathrm{j}H_{\mathrm{iac}}[\mathrm{j}2\pi(f_{\mathrm{p}}-f_1)]\right\}\boldsymbol{I}_{\mathrm{au1}}\right] \end{cases} \tag{4.85}$$

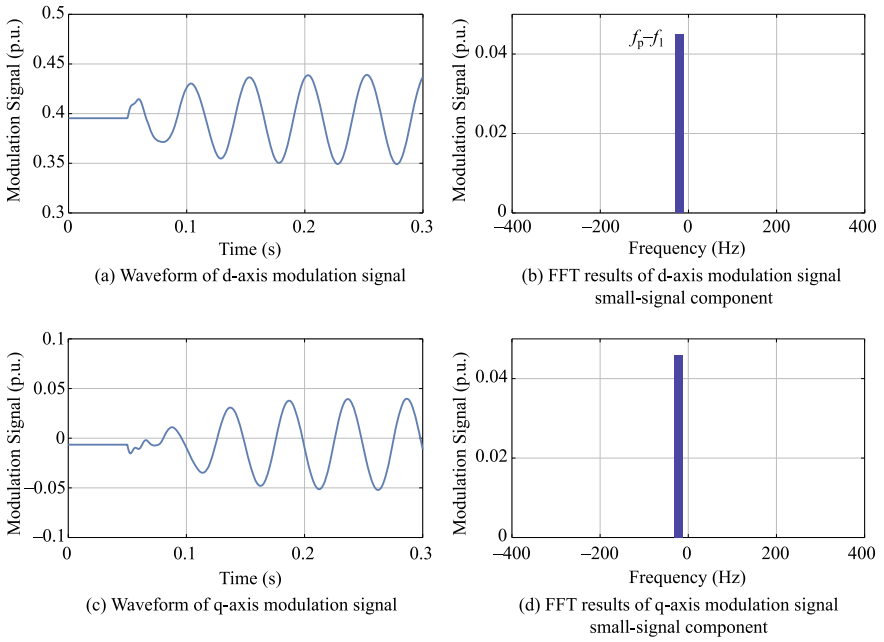

(a) Waveform of d-axis modulation signal

(b) FFT results of d-axis modulation signal small-signal component

(c) Waveform of q-axis modulation signal

(d) FFT results of q-axis modulation signal small-signal component

Fig. 4.12 The waveforms and FFT results of the dq-axis small-signal vectors of AC modulation signals

The waveforms and FFT results of $\hat{\boldsymbol{m}}_{\mathrm{d}}$, $\hat{\boldsymbol{m}}_{\mathrm{q}}$ are shown in Fig. 4.12 after the small-signal perturbation superimposed. As seen from the figure, the frequencies of the small-signal components of $\hat{\boldsymbol{m}}_{\mathrm{d}}$, $\hat{\boldsymbol{m}}_{\mathrm{q}}$ are the same as those of $\hat{\boldsymbol{i}}_{\mathrm{d}}$, $\hat{\boldsymbol{i}}_{\mathrm{q}}$. Besides, the frequency of the dominant component in $\hat{\boldsymbol{m}}_{\mathrm{d}}$, $\hat{\boldsymbol{m}}_{\mathrm{q}}$ is also $f_{\mathrm{p}} - f_1$, and the amplitudes of other components are relatively small.

The small-signal vector of the phase-a arm DM modulation signal $\hat{\boldsymbol{m}}_{\mathrm{difa}}$ can be obtained by applying inverse Park transformation to $\hat{\boldsymbol{m}}_{\mathrm{d}}$, $\hat{\boldsymbol{m}}_{\mathrm{q}}$.

$$\hat{\boldsymbol{m}}_{\mathrm{difa}} = \boldsymbol{G}_1 \hat{\boldsymbol{i}}_{\mathrm{au}} + \boldsymbol{G}_2 \hat{\boldsymbol{v}}_{\mathrm{a}} \tag{4.86}$$

where $\boldsymbol{G}_1$, $\boldsymbol{G}_2$ are $(2g+1) \times (2g+1)$ matrices, and all the other elements in the matrices are zero except for Eqs. (4.87) and (4.88).

$$\begin{aligned} \boldsymbol{G}_1(g+k+1, g+k+1) = {} & |\mathrm{mod}(k+1, 3)| \cdot [1 + (-1)^k] \\ & \cdot \{-H_{\mathrm{iac}}[\mathrm{j}2\pi(f_{\mathrm{p}} + kf_1 - \mathrm{mod}(k+1, 3) f_1)] \\ & + \mathrm{mod}(k+1, 3)\mathrm{j}K_{\mathrm{d}}\} \end{aligned} \tag{4.87}$$

$$\begin{cases} \boldsymbol{G}_2(g-1,g-1) = -\boldsymbol{G}_2(g-1,g+1) \\ \qquad\qquad = T_{\mathrm{PLL}}[\mathrm{j}2\pi(f_\mathrm{p}-f_1)] \\ \qquad\qquad \cdot \left[2\left\{H_{\mathrm{iac}}[\mathrm{j}2\pi(f_\mathrm{p}-f_1)]+\mathrm{j}K_\mathrm{d}\right\}\boldsymbol{I}_{\mathrm{au1}}^{*}-\boldsymbol{M}_{\mathrm{au1}}^{*}\right] \\ \boldsymbol{G}_2(g+1,g-1) = -\boldsymbol{G}_2(g+1,g+1) \\ \qquad\qquad = -T_{\mathrm{PLL}}[\mathrm{j}2\pi(f_\mathrm{p}-f_1)] \\ \qquad\qquad \cdot \left[2\left\{H_{\mathrm{iac}}[\mathrm{j}2\pi(f_\mathrm{p}-f_1)]-\mathrm{j}K_\mathrm{d}\right\}\boldsymbol{I}_{\mathrm{au1}}-\boldsymbol{M}_{\mathrm{au1}}\right] \end{cases} \tag{4.88}$$

Under the effect of the dq-axis asymmetric control as mentioned in Chap. 3, the coupled components at $f_{\mathrm{abc}}-2f_1$ are also introduced into $\hat{\boldsymbol{m}}_{\mathrm{difa}}$ after the inverse Park transformation, in addition to the components at the frequencies f_{abc} shown in Eq. (4.72). The frequencies of the small-signal components of $\hat{\boldsymbol{m}}_{\mathrm{difa}}$ are expressed as

$$f_{\mathrm{mdif}} = |\mathrm{mod}(k+1,3)| \cdot (f_\mathrm{p}+kf_1) \tag{4.89}$$

where the zero frequency is not included.

The waveforms and FFT results of $\hat{\boldsymbol{m}}_{\mathrm{difa}}$ are shown in Fig. 4.13 after the small-signal perturbation superimposed. As seen from the figure, the coupled component at $f_\mathrm{p}-2f_1$ is also introduced into $\hat{\boldsymbol{m}}_{\mathrm{difa}}$, in addition to the small-signal response at f_p.

3. Small-Signal Model of Circulating Current Control

The small-signal vectors of the three-phase arm CM currents $\hat{\boldsymbol{i}}_{\mathrm{com}l}$ can be obtained according to Eqs. (4.52) and (4.56).

$$\begin{cases} \hat{\boldsymbol{i}}_{\mathrm{coma}} = \boldsymbol{A}_{\mathrm{pc}}\hat{\boldsymbol{i}}_{\mathrm{au}} \\ \hat{\boldsymbol{i}}_{\mathrm{comb}} = \boldsymbol{A}_{\mathrm{pc}}\boldsymbol{D}_\mathrm{p}\hat{\boldsymbol{i}}_{\mathrm{au}} \\ \hat{\boldsymbol{i}}_{\mathrm{comc}} = \boldsymbol{A}_{\mathrm{pc}}\boldsymbol{D}_\mathrm{p}^{*}\hat{\boldsymbol{i}}_{\mathrm{au}} \end{cases} \tag{4.90}$$

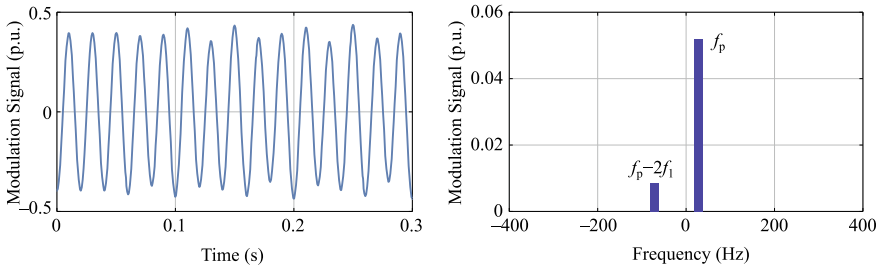

(a) Waveform of DM modulation signal

(b) FFT results of DM modulation signal small-signal component

Fig. 4.13 The waveforms and FFT results of the small-signal vector of the phase-a arm DM modulation signal

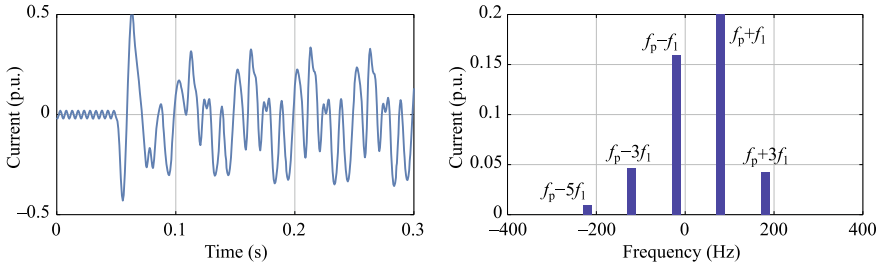

(a) Waveform of arm CM current

(b) FFT results of arm CM current small-signal component

Fig. 4.14 The waveforms and FFT results of the small-signal vector of the phase-a arm CM current

The small-signal vectors $\hat{\boldsymbol{i}}_{\mathrm{com}l}$ contain the CM components, and the corresponding frequencies are

$$f_{\mathrm{com}} = \frac{1-(-1)^k}{2} \cdot (f_{\mathrm{p}} + kf_1) \tag{4.91}$$

where the zero frequency is not included.

Taking phase a as an example, the waveforms and FFT results of $\hat{\boldsymbol{i}}_{\mathrm{coma}}$ are shown in Fig. 4.14 after the small-signal perturbation superimposed. In the figure, the base value is taken as one-third of the steady-state DC current. The significant small-signal components at $f_{\mathrm{p}} \pm f_1$, $f_{\mathrm{p}} \pm 3f_1$, and $f_{\mathrm{p}} - 5f_1$ are produced in $\hat{\boldsymbol{i}}_{\mathrm{coma}}$. The zero-sequence component at $f_{\mathrm{p}} - f_1$ will flow into the DC side, leading to a small-signal response of the DC current at $f_{\mathrm{p}} - f_1$.

Since the arm CM current in each phase constitutes the arm circulating current, small-signal components will also be introduced into the quantities involved in the circulating current loop.

After the negative-sequence second-harmonic Park transformation, the small-signal components of the arm circulating currents and PLL output angle lead to small-signal responses in the dq-axis circulating currents. The corresponding small-signal vectors $\hat{\boldsymbol{i}}_{\mathrm{cd}}$, $\hat{\boldsymbol{i}}_{\mathrm{cq}}$ can be derived as

$$\begin{cases} \hat{\boldsymbol{i}}_{\mathrm{cd}} = \boldsymbol{E}_{\mathrm{icd}}\hat{\boldsymbol{i}}_{\mathrm{au}} + \boldsymbol{E}_{\mathrm{vcd}}\hat{\boldsymbol{v}}_{\mathrm{a}} \\ \hat{\boldsymbol{i}}_{\mathrm{cq}} = \boldsymbol{E}_{\mathrm{icq}}\hat{\boldsymbol{i}}_{\mathrm{au}} + \boldsymbol{E}_{\mathrm{vcq}}\hat{\boldsymbol{v}}_{\mathrm{a}} \end{cases} \tag{4.92}$$

where $\boldsymbol{E}_{\mathrm{icd}}$, $\boldsymbol{E}_{\mathrm{vcd}}$, $\boldsymbol{E}_{\mathrm{icq}}$, $\boldsymbol{E}_{\mathrm{vcq}}$ are $(2g+1) \times (2g+1)$ matrices, and all other elements in the matrices are zero except for Eqs. (4.93)–(4.96).

$$\begin{cases} \boldsymbol{E}_{\mathrm{icd}}(g+k+1, g+k-1) = (1-|\mathrm{mod}(k+1,3)|) \cdot [1-(-1)^k] \\ \boldsymbol{E}_{\mathrm{icd}}(g+k+1, g+k+3) = (1-|\mathrm{mod}(k+1,3)|) \cdot [1-(-1)^k] \end{cases} \tag{4.93}$$

$$\begin{cases} \boldsymbol{E}_{\mathrm{vcd}}(g, g-1) = T_{\mathrm{PLL}}[\mathrm{j}2\pi(f_{\mathrm{p}} - f_1)] \cdot 2(\boldsymbol{I}_{\mathrm{au2}} - \boldsymbol{I}_{\mathrm{au2}}^*) \\ \boldsymbol{E}_{\mathrm{vcd}}(g, g+1) = -T_{\mathrm{PLL}}[\mathrm{j}2\pi(f_{\mathrm{p}} - f_1)] \cdot 2(\boldsymbol{I}_{\mathrm{au2}} - \boldsymbol{I}_{\mathrm{au2}}^*) \end{cases} \tag{4.94}$$

$$\begin{cases} \boldsymbol{E}_{\mathrm{icq}}(g+k+1, g+k) = \mathrm{j}(1 - |\mathrm{mod}(k+1, 3)|) \cdot [1 - (-1)^k] \\ \boldsymbol{E}_{\mathrm{icq}}(g+k+1, g+k+2) = -\mathrm{j}(1 - |\mathrm{mod}(k+1, 3)|) \cdot [1 - (-1)^k] \end{cases} \tag{4.95}$$

$$\begin{cases} \boldsymbol{E}_{\mathrm{vcq}}(g, g-1) = -\mathrm{j}T_{\mathrm{PLL}}[\mathrm{j}2\pi(f_{\mathrm{p}} - f_1)] \cdot 2(\boldsymbol{I}_{\mathrm{au2}} + \boldsymbol{I}_{\mathrm{au2}}^*) \\ \boldsymbol{E}_{\mathrm{vcq}}(g, g+1) = \mathrm{j}T_{\mathrm{PLL}}[\mathrm{j}2\pi(f_{\mathrm{p}} - f_1)] \cdot 2(\boldsymbol{I}_{\mathrm{au2}} + \boldsymbol{I}_{\mathrm{au2}}^*) \end{cases} \tag{4.96}$$

After the negative-sequence second-harmonic Park transformation, the dq-axis small-signal vectors $\hat{\boldsymbol{i}}_{\mathrm{cd}}$, $\hat{\boldsymbol{i}}_{\mathrm{cq}}$ contain zero-sequence components, and the corresponding frequencies are expressed as

$$f_{\mathrm{cdq}} = \frac{1 - (-1)^k}{2} \cdot (1 - |\mathrm{mod}(k+1, 3)|) \cdot (f_{\mathrm{p}} + kf_1) \tag{4.97}$$

where the zero frequency is not included.

The waveforms and FFT results of $\hat{\boldsymbol{i}}_{\mathrm{cd}}$, $\hat{\boldsymbol{i}}_{\mathrm{cq}}$ are shown in Fig. 4.15 after the small-signal perturbation is superimposed. As seen from the figure, the small-signal components at $f_{\mathrm{p}} - f_1$, $f_{\mathrm{p}} + 5f_1$, and $f_{\mathrm{p}} - 7f_1$ are produced in $\hat{\boldsymbol{i}}_{\mathrm{cd}}$, $\hat{\boldsymbol{i}}_{\mathrm{cq}}$. The component at $f_{\mathrm{p}} - f_1$ is dominant, and the amplitudes of other components are relatively small.

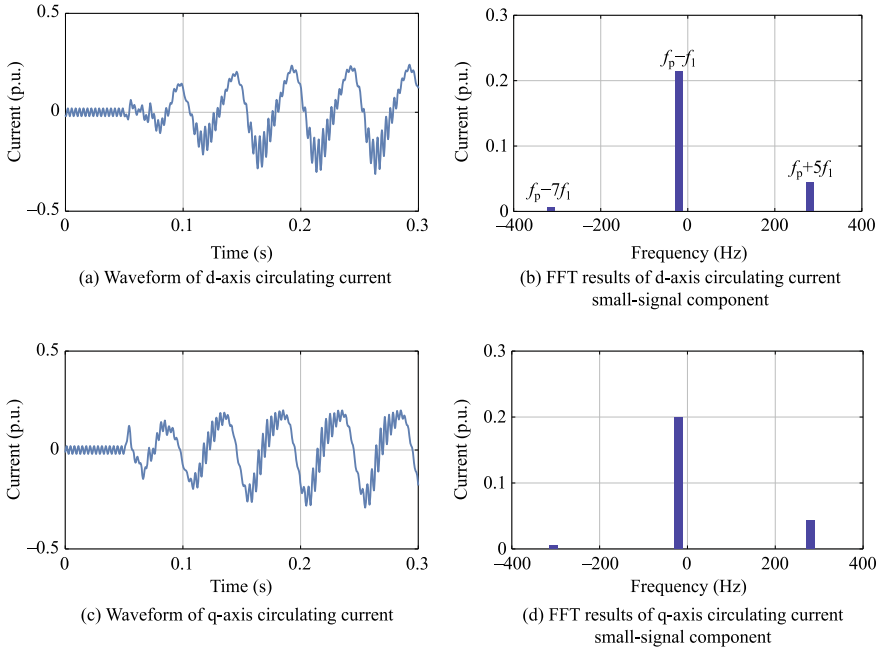

(a) Waveform of d-axis circulating current

(b) FFT results of d-axis circulating current small-signal component

(c) Waveform of q-axis circulating current

(d) FFT results of q-axis circulating current small-signal component

Fig. 4.15 The waveforms and FFT results of the dq-axis small-signal vectors of arm circulating currents

According to Fig. 4.10, the circulating current control includes the PI controller and dq-axis decoupled control. The small-signal vectors of the dq-axis circulating modulation signals can be obtained based on the circulating current control.

$$\begin{cases} \hat{\boldsymbol{m}}_{\mathrm{cd}} = \boldsymbol{H}_{\mathrm{ic}}\hat{\boldsymbol{i}}_{\mathrm{cd}} - K_{\mathrm{c}}\hat{\boldsymbol{i}}_{\mathrm{cq}} \\ \hat{\boldsymbol{m}}_{\mathrm{cq}} = \boldsymbol{H}_{\mathrm{ic}}\hat{\boldsymbol{i}}_{\mathrm{cq}} + K_{\mathrm{c}}\hat{\boldsymbol{i}}_{\mathrm{cd}} \end{cases} \tag{4.98}$$

where $\boldsymbol{H}_{\mathrm{ic}}$ is the transfer function matrix of the circulating current controller, expressed as

$$\boldsymbol{H}_{\mathrm{ic}} = \mathrm{diag}\Big[\left\{H_{\mathrm{ic}}[\mathrm{j}2\pi(f_{\mathrm{p}} + kf_1)]\right\}\big|_{k=-g,\ldots,0,\ldots,g}\Big] \tag{4.99}$$

Substituting $\hat{\boldsymbol{i}}_{\mathrm{cd}}$, $\hat{\boldsymbol{i}}_{\mathrm{cq}}$ in Eq. (4.92) into Eq. (4.98), the expressions of the small-signal vectors of the dq-axis circulating modulation signals can be obtained.

$$\begin{cases} \hat{\boldsymbol{m}}_{\mathrm{cd}} = \boldsymbol{F}_{\mathrm{icd}}\hat{\boldsymbol{i}}_{\mathrm{au}} + \boldsymbol{F}_{\mathrm{vcd}}\hat{\boldsymbol{v}}_{\mathrm{a}} \\ \hat{\boldsymbol{m}}_{\mathrm{cq}} = \boldsymbol{F}_{\mathrm{icq}}\hat{\boldsymbol{i}}_{\mathrm{au}} + \boldsymbol{F}_{\mathrm{vcq}}\hat{\boldsymbol{v}}_{\mathrm{a}} \end{cases} \tag{4.100}$$

where $\boldsymbol{F}_{\mathrm{icd}}$, $\boldsymbol{F}_{\mathrm{vcd}}$, $\boldsymbol{F}_{\mathrm{icq}}$, $\boldsymbol{F}_{\mathrm{vcq}}$ are $(2g+1)\times(2g+1)$ matrices, and all the other elements in the matrices are zero except for Eqs. (4.101) to (4.104).

$$\begin{cases} \boldsymbol{F}_{\mathrm{icd}}(g+k+1, g+k-1) = (1-|\mathrm{mod}(k+1,3)|)\cdot\dfrac{1-(-1)^k}{2} \\ \qquad\qquad \cdot\{H_{\mathrm{ic}}[\mathrm{j}2\pi(f_{\mathrm{p}}+kf_1)] + \mathrm{mod}(k,3)\mathrm{j}K_{\mathrm{c}}\} \\ \boldsymbol{F}_{\mathrm{icd}}(g+k+1, g+k+3) = (1-|\mathrm{mod}(k+1,3)|)\cdot\dfrac{1-(-1)^k}{2} \\ \qquad\qquad \cdot\{H_{\mathrm{ic}}[\mathrm{j}2\pi(f_{\mathrm{p}}+kf_1)] - \mathrm{mod}(k,3)\mathrm{j}K_{\mathrm{c}}\} \end{cases} \tag{4.101}$$

$$\begin{cases} \boldsymbol{F}_{\mathrm{vcd}}(g, g-1) = -2T_{\mathrm{PLL}}[\mathrm{j}2\pi(f_{\mathrm{p}}-f_1)] \\ \qquad\qquad \cdot\left[\left\{H_{\mathrm{ic}}[\mathrm{j}2\pi(f_{\mathrm{p}}-f_1)] - \mathrm{j}K_{\mathrm{c}}\right\}\boldsymbol{I}^*_{\mathrm{au2}}\right. \\ \qquad\qquad \left.-\left\{H_{\mathrm{ic}}[\mathrm{j}2\pi(f_{\mathrm{p}}-f_1)] + \mathrm{j}K_{\mathrm{c}}\right\}\boldsymbol{I}_{\mathrm{au2}}\right] \\ \boldsymbol{F}_{\mathrm{vcd}}(g, g+1) = 2T_{\mathrm{PLL}}[\mathrm{j}2\pi(f_{\mathrm{p}}-f_1)] \\ \qquad\qquad \cdot\left[\left\{H_{\mathrm{ic}}[\mathrm{j}2\pi(f_{\mathrm{p}}-f_1)] - \mathrm{j}K_{\mathrm{c}}\right\}\boldsymbol{I}^*_{\mathrm{au2}}\right. \\ \qquad\qquad \left.-\left\{H_{\mathrm{ic}}[\mathrm{j}2\pi(f_{\mathrm{p}}-f_1)] + \mathrm{j}K_{\mathrm{c}}\right\}\boldsymbol{I}_{\mathrm{au2}}\right] \end{cases} \tag{4.102}$$

$$\begin{cases} \boldsymbol{F}_{\mathrm{icq}}(g+1+k, g+1+k-1) = (1-|\mathrm{mod}(k+1,3)|)\cdot\dfrac{1-(-1)^k}{2} \\ \qquad\qquad \cdot\{-\mathrm{mod}\ (k,3)\mathrm{j}H_{\mathrm{ic}}[\mathrm{j}2\pi(f_{\mathrm{p}}+kf_1)] + K_{\mathrm{c}}\} \\ \boldsymbol{F}_{\mathrm{icq}}(g+1+k, g+1+k+1) = (1-|\mathrm{mod}(k+1,3)|)\cdot\dfrac{1-(-1)^k}{2} \\ \qquad\qquad \cdot\{\mathrm{mod}(k,3)\mathrm{j}H_{\mathrm{ic}}[\mathrm{j}2\pi(f_{\mathrm{p}}+kf_1)] + K_{\mathrm{c}}\} \end{cases} \tag{4.103}$$

$$\begin{cases} \boldsymbol{F}_{\mathrm{vcq}}(g, g-1) = -2T_{\mathrm{PLL}}[\mathrm{j}2\pi(f_{\mathrm{p}} - f_1)] \\ \qquad\qquad \cdot \left[\left\{\mathrm{j}H_{\mathrm{ic}}[\mathrm{j}2\pi(f_{\mathrm{p}} - f_1)] + K_{\mathrm{c}}\right\}\boldsymbol{I}_{\mathrm{au2}}^{*}\right. \\ \qquad\qquad \left. + \left\{\mathrm{j}H_{\mathrm{ic}}[\mathrm{j}2\pi(f_{\mathrm{p}} - f_1)] - K_{\mathrm{c}}\right\}\boldsymbol{I}_{\mathrm{au2}}\right] \\ \boldsymbol{F}_{\mathrm{vcq}}(g, g+1) = 2T_{\mathrm{PLL}}[\mathrm{j}2\pi(f_{\mathrm{p}} - f_1)] \\ \qquad\qquad \cdot \left[\left\{\mathrm{j}H_{\mathrm{ic}}[\mathrm{j}2\pi(f_{\mathrm{p}} - f_1)] + K_{\mathrm{c}}\right\}\boldsymbol{I}_{\mathrm{au2}}^{*}\right. \\ \qquad\qquad \left. + \left\{\mathrm{j}H_{\mathrm{ic}}[\mathrm{j}2\pi(f_{\mathrm{p}} - f_1)] - K_{\mathrm{c}}\right\}\boldsymbol{I}_{\mathrm{au2}}\right] \end{cases} \tag{4.104}$$

The waveforms and FFT results of $\hat{\boldsymbol{m}}_{\mathrm{cd}}$, $\hat{\boldsymbol{m}}_{\mathrm{cq}}$ are shown in Fig. 4.16 after the small-signal perturbation is superimposed. As seen from the figure, the frequencies of the small-signal components of $\hat{\boldsymbol{m}}_{\mathrm{cd}}$, $\hat{\boldsymbol{m}}_{\mathrm{cq}}$ are the same as those of $\hat{\boldsymbol{i}}_{\mathrm{cd}}$, $\hat{\boldsymbol{i}}_{\mathrm{cq}}$. Besides, the frequency of the dominant component in $\hat{\boldsymbol{m}}_{\mathrm{cd}}$, $\hat{\boldsymbol{m}}_{\mathrm{cq}}$ is also $f_{\mathrm{p}} - f_1$, and the amplitudes of other components are relatively small.

The small-signal vector of the phase-a arm CM modulation signal $\hat{\boldsymbol{m}}_{\mathrm{coma}}$ can be obtained by applying the corresponding inverse Park transformation (negative-sequence second-harmonic) to $\hat{\boldsymbol{m}}_{\mathrm{cd}}$, $\hat{\boldsymbol{m}}_{\mathrm{cq}}$.

$$\hat{\boldsymbol{m}}_{\mathrm{coma}} = \boldsymbol{G}_3\hat{\boldsymbol{i}}_{\mathrm{au}} + \boldsymbol{G}_4\hat{\boldsymbol{v}}_{\mathrm{a}} \tag{4.105}$$

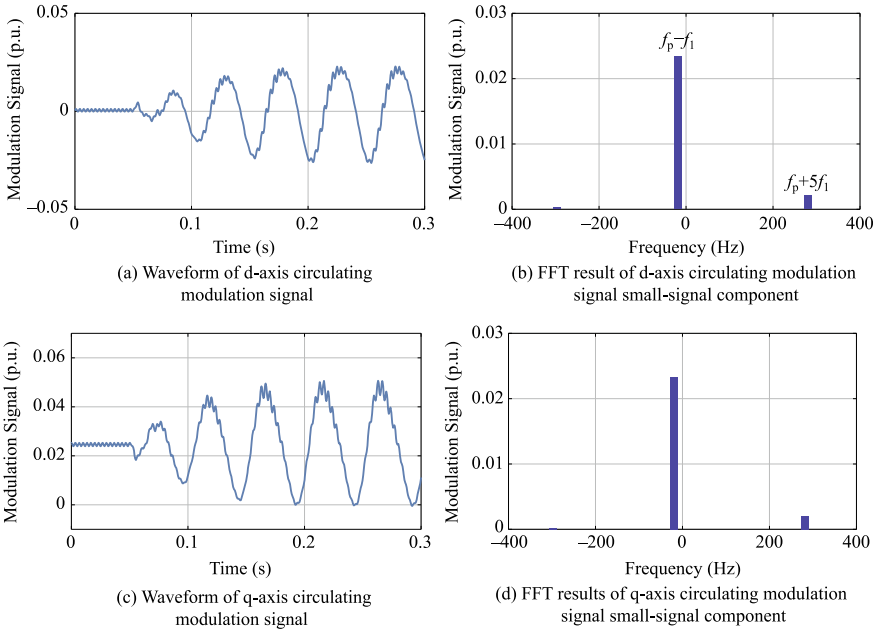

(a) Waveform of d-axis circulating modulation signal

(b) FFT result of d-axis circulating modulation signal small-signal component

(c) Waveform of q-axis circulating modulation signal

(d) FFT results of q-axis circulating modulation signal small-signal component

Fig. 4.16 The waveforms and FFT results of the dq-axis small-signal vectors of circulating modulation signals

where $\boldsymbol{G}_3$, $\boldsymbol{G}_4$ are $(2g+1)\times(2g+1)$ matrices, and all the other elements in the matrices are zero except for Eqs. (4.106) and (4.107).

$$\begin{aligned}\boldsymbol{G}_3(g+k+1,g+k+1)=&\frac{1-(-1)^k}{2}\cdot|\mathrm{mod}(k+1,3)|\cdot\\&\{H_{\mathrm{ic}}[\mathrm{j}2\pi(f_\mathrm{p}+kf_1+\mathrm{mod}(k+1,3)\cdot 2f_1)]-\mathrm{mod}(k+1,3)\mathrm{j}K_\mathrm{c}\}\end{aligned}\tag{4.106}$$

$$\begin{cases}\boldsymbol{G}_4(g-2,g-1)=-\boldsymbol{G}_4(g-2,g+1)\\\qquad\qquad=2T_{\mathrm{PLL}}[\mathrm{j}2\pi(f_\mathrm{p}-f_1)]\\\qquad\qquad\cdot\left[\left\{-H_{\mathrm{ic}}[\mathrm{j}2\pi(f_\mathrm{p}-f_1)]+\mathrm{j}K_\mathrm{c}\right\}\boldsymbol{I}_{\mathrm{au2}}^*+\boldsymbol{M}_{\mathrm{au2}}^*\right]\\\boldsymbol{G}_4(g+2,g-1)=-\boldsymbol{G}_4(g+2,g+1)\\\qquad\qquad=2T_{\mathrm{PLL}}[\mathrm{j}2\pi(f_\mathrm{p}-f_1)]\\\qquad\qquad\cdot\left[\left\{H_{\mathrm{ic}}[\mathrm{j}2\pi(f_\mathrm{p}-f_1)]+\mathrm{j}K_\mathrm{c}\right\}\boldsymbol{I}_{\mathrm{au2}}-\boldsymbol{M}_{\mathrm{au2}}\right]\end{cases}\tag{4.107}$$

Under the effect of the dq-axis asymmetric control, the coupled components at $f_{\mathrm{com}}-2f_1$ are also introduced into $\hat{\boldsymbol{m}}_{\mathrm{coma}}$ after the inverse Park transformation, in addition to the components at the frequencies f_{com} shown in Eq. (4.91). The frequencies of the small-signal components of $\hat{\boldsymbol{m}}_{\mathrm{coma}}$ are expressed as

$$f_{\mathrm{mcom}}=\frac{1-(-1)^k}{2}\cdot|\mathrm{mod}(k+1,3)|\cdot(f_\mathrm{p}+kf_1)\tag{4.108}$$

where the zero frequency is not included.

The waveforms and FFT results of $\hat{\boldsymbol{m}}_{\mathrm{coma}}$ are shown in Fig. 4.17 after the small-signal perturbation superimposed. As seen from the figure, the small-signal components at $f_\mathrm{p}+f_1$ and $f_\mathrm{p}\pm 3f_1$ are produced in $\hat{\boldsymbol{m}}_{\mathrm{coma}}$, in which the component at $f_\mathrm{p}+f_1$ is dominant.

4. **Small-Signal Model of Arm Modulation Signal**

Based on the relationship between the arm modulation signal and DM and CM modulation signals shown in Eq. (4.68), the small-signal vector of the phase-a upper

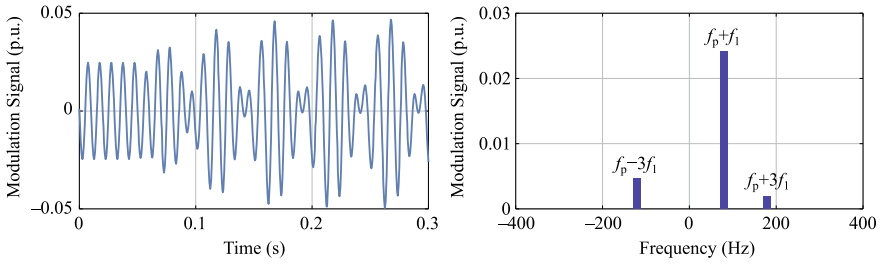

(a) Waveform of CM modulation signal

(b) FFT results of CM modulation signal small-signal component

Fig. 4.17 The waveforms and FFT results of the small-signal vector of the phase-a arm CM modulation signal

arm modulation signal $\hat{\boldsymbol{m}}_{\mathrm{au}}$ can be obtained according to Eqs. (4.86) and (4.105).

$$\hat{\boldsymbol{m}}_{\mathrm{au}} = \boldsymbol{G}_{\mathrm{i}}\hat{\boldsymbol{i}}_{\mathrm{au}} + \boldsymbol{G}_{\mathrm{v}}\hat{\boldsymbol{v}}_{\mathrm{a}} \tag{4.109}$$

where $\boldsymbol{G}_{\mathrm{i}}$, $\boldsymbol{G}_{\mathrm{v}}$ are expressed as

$$\begin{cases} \boldsymbol{G}_{\mathrm{i}} = -\boldsymbol{G}_1 + \boldsymbol{G}_3 \\ \boldsymbol{G}_{\mathrm{v}} = -\boldsymbol{G}_2 + \boldsymbol{G}_4 \end{cases} \tag{4.110}$$

According to the DM, CM, and phase-sequence relationships between the small-signal vectors shown in Eqs. (4.52) and (4.54), the small-signal vectors of the other arm modulation signals can also be obtained according to $\hat{\boldsymbol{m}}_{\mathrm{au}}$.

4.4.4 AC Port Impedance Model

The AC port impedance model of MMC is established in this section according to the frequency-domain small-signal models of the main circuit and control loops.

Firstly, based on the small-signal model of the arm circuit shown in Eq. (4.65), combining the two sub-equations and eliminating the small-signal vectors of the phase-a upper arm capacitor voltage $\hat{\boldsymbol{v}}_{\mathrm{Cau}}$ yields,

$$\begin{aligned} &(\boldsymbol{U} + \boldsymbol{Y}_{\mathrm{Larm}}\boldsymbol{M}_{\mathrm{au}}\boldsymbol{Z}_{\mathrm{Ceq}}\boldsymbol{M}_{\mathrm{au}})\hat{\boldsymbol{i}}_{\mathrm{au}} + \boldsymbol{Y}_{\mathrm{Larm}}\hat{\boldsymbol{v}}_{\mathrm{a}} \\ &\quad + \boldsymbol{Y}_{\mathrm{Larm}}(\boldsymbol{V}_{\mathrm{Cau}} + \boldsymbol{M}_{\mathrm{au}}\boldsymbol{Z}_{\mathrm{Ceq}}\boldsymbol{I}_{\mathrm{au}})\hat{\boldsymbol{m}}_{\mathrm{au}} = 0 \end{aligned} \tag{4.111}$$

Then, substituting $\hat{\boldsymbol{m}}_{\mathrm{au}}$ shown in Eq. (4.109) into Eq. (4.111), the following closed-loop small-signal model can be developed

$$\begin{aligned} &\left[\boldsymbol{U} + \boldsymbol{Y}_{\mathrm{Larm}}\boldsymbol{M}_{\mathrm{au}}\boldsymbol{Z}_{\mathrm{Ceq}}\boldsymbol{M}_{\mathrm{au}} + \boldsymbol{Y}_{\mathrm{Larm}}(\boldsymbol{V}_{\mathrm{Cau}} + \boldsymbol{M}_{\mathrm{au}}\boldsymbol{Z}_{\mathrm{Ceq}}\boldsymbol{I}_{\mathrm{au}})\boldsymbol{G}_{\mathrm{i}}\right]\hat{\boldsymbol{i}}_{\mathrm{au}} \\ &\quad + \boldsymbol{Y}_{\mathrm{Larm}}\left[\boldsymbol{U} + (\boldsymbol{V}_{\mathrm{Cau}} + \boldsymbol{M}_{\mathrm{au}}\boldsymbol{Z}_{\mathrm{Ceq}}\boldsymbol{I}_{\mathrm{au}})\boldsymbol{G}_{\mathrm{v}}\right]\hat{\boldsymbol{v}}_{\mathrm{a}} = 0 \end{aligned} \tag{4.112}$$

According to Eqs. (4.71) and (4.112), the AC port admittance of MMC can be established.

$$\boldsymbol{Y} = -\frac{\hat{\boldsymbol{i}}_{\mathrm{a}}}{\hat{\boldsymbol{v}}_{\mathrm{a}}} = -\frac{2\boldsymbol{Y}_{\mathrm{Larm}}\left[\boldsymbol{U} + (\boldsymbol{V}_{\mathrm{Cau}} + \boldsymbol{M}_{\mathrm{au}}\boldsymbol{Z}_{\mathrm{Ceq}}\boldsymbol{I}_{\mathrm{au}})\boldsymbol{G}_{\mathrm{v}}\right]\boldsymbol{A}_{\mathrm{pd}}}{\boldsymbol{U} + \boldsymbol{Y}_{\mathrm{Larm}}\boldsymbol{M}_{\mathrm{au}}\boldsymbol{Z}_{\mathrm{Ceq}}\boldsymbol{M}_{\mathrm{au}} + \boldsymbol{Y}_{\mathrm{Larm}}(\boldsymbol{V}_{\mathrm{Cau}} + \boldsymbol{M}_{\mathrm{au}}\boldsymbol{Z}_{\mathrm{Ceq}}\boldsymbol{I}_{\mathrm{au}})\boldsymbol{G}_{\mathrm{i}}} \tag{4.113}$$

where $\boldsymbol{Y}$ is a $(2g+1) \times (2g+1)$ matrix.

The small-signal components at f_p and $f_\mathrm{p} - 2f_1$ are the main components in the small-signal vectors of the AC voltage and current of MMC, while the amplitudes of the other components are relatively small. The characteristics of the AC port impedance or admittance at f_p and $f_\mathrm{p} - 2f_1$ are more significant. Only relevant elements at these two frequencies are extracted, and the relationship between the small-signal vectors of the AC voltage and current and AC port admittance is reformulated as

$$\begin{bmatrix} -\hat{\boldsymbol{i}}_\mathrm{p} \\ -\hat{\boldsymbol{i}}_{\mathrm{p}-2} \end{bmatrix} = \begin{bmatrix} \boldsymbol{Y}_\mathrm{pp} & \boldsymbol{Y}_\mathrm{np} \\ \boldsymbol{Y}_\mathrm{pn} & \boldsymbol{Y}_\mathrm{nn} \end{bmatrix} \begin{bmatrix} \hat{\boldsymbol{v}}_\mathrm{p} \\ \hat{\boldsymbol{v}}_{\mathrm{p}-2} \end{bmatrix} \tag{4.114}$$

where $\hat{\boldsymbol{i}}_\mathrm{p}$ and $\hat{\boldsymbol{i}}_{\mathrm{p}-2}$ are the small-signal components of AC currents at f_p and $f_\mathrm{p} - 2f_1$ resepectively. The expression of the 2×2 AC port admittance matrix is

$$\begin{bmatrix} \boldsymbol{Y}_\mathrm{pp} & \boldsymbol{Y}_\mathrm{np} \\ \boldsymbol{Y}_\mathrm{pn} & \boldsymbol{Y}_\mathrm{nn} \end{bmatrix} = \begin{bmatrix} \boldsymbol{Y}(g+1, g+1) & \boldsymbol{Y}(g+1, g-1) \\ \boldsymbol{Y}(g-1, g+1) & \boldsymbol{Y}(g-1, g-1) \end{bmatrix}$$

where

$\boldsymbol{Y}_\mathrm{pp}$ is the positive-sequence admittance, representing the small-signal response of AC current at f_p in positive sequence under per unit small-signal perturbation of AC voltage at f_p in positive sequence.
$\boldsymbol{Y}_\mathrm{pn}$ is the positive-sequence coupled admittance, representing the small-signal response of AC current at $f_\mathrm{p} - 2f_1$ in negative sequence under per unit small-signal perturbation of AC voltage at f_p in positive sequence.
$\boldsymbol{Y}_\mathrm{nn}$ is the negative-sequence admittance, representing the small-signal response of AC current at $f_\mathrm{p} - 2f_1$ in negative sequence under per unit small-signal perturbation of AC voltage at $f_\mathrm{p} - 2f_1$ in negative sequence.
$\boldsymbol{Y}_\mathrm{np}$ is the negative-sequence coupled admittance, representing the small-signal response of AC current at f_p in positive sequence under per unit small-signal perturbation of AC voltage at $f_\mathrm{p} - 2f_1$ in negative sequence.
$\boldsymbol{Y}(g+1, g+1)$ is the element in the $(g+1)$ th row and the $(g+1)$ th column of $\boldsymbol{Y}$.
$\boldsymbol{Y}(g+1, g-1)$ is the element in the $(g+1)$ th row and the $(g-1)$ th column of $\boldsymbol{Y}$.
$\boldsymbol{Y}(g-1, g+1)$ is the element in the $(g-1)$ th row and the $(g+1)$ th column of $\boldsymbol{Y}$.
$\boldsymbol{Y}(g-1, g-1)$ is the element in the $(g-1)$ th row and the $(g-1)$ th column of $\boldsymbol{Y}$.

The AC port impedance of MMC can be obtained by calculating the inverse matrix of the AC port admittance as

$$\begin{bmatrix} \boldsymbol{Z}_\mathrm{pp} & \boldsymbol{Z}_\mathrm{pn} \\ \boldsymbol{Z}_\mathrm{np} & \boldsymbol{Z}_\mathrm{nn} \end{bmatrix} = \begin{bmatrix} \boldsymbol{Y}_\mathrm{pp} & \boldsymbol{Y}_\mathrm{np} \\ \boldsymbol{Y}_\mathrm{pn} & \boldsymbol{Y}_\mathrm{nn} \end{bmatrix}^{-1} \tag{4.115}$$

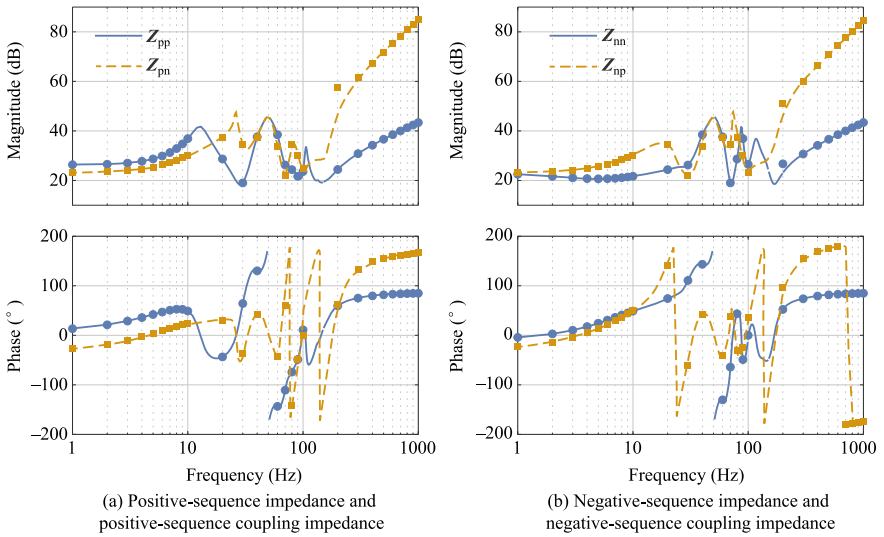

Fig. 4.18 The analytical and scanning results of the AC port impedance of MMC

where

$\boldsymbol{Z}_{pp}$ represents the positive-sequence impedance, which is the element in the first row and the first column of the AC port admittance inverse matrix.
$\boldsymbol{Z}_{pn}$ represents the positive-sequence coupled impedance, which is the element in the first row and the second column of the AC port admittance inverse matrix.
$\boldsymbol{Z}_{nn}$ represents the negative-sequence impedance, which is the element in the second row and the second column of the AC port admittance inverse matrix.
$\boldsymbol{Z}_{np}$ represents the negative-sequence coupled impedance, which is the element in the second row and the first column of the AC port admittance inverse matrix.

In addition, the frequency-domain relationship between the negative-sequence impedance and the positive-sequence impedance satisfies $\boldsymbol{Z}_{nn} = \boldsymbol{Z}_{pp}^{*}(j2\omega_1 - s)$, and the frequency-domain relationship between the negative-sequence coupled impedance and the positive-sequence coupled impedance satisfies $\boldsymbol{Z}_{np} = \boldsymbol{Z}_{pn}^{*}(j2\omega_1 - s)$.

The main circuit and controller parameters of MMC are listed in Table 4.5. Figure 4.18 shows the analytical (in solid lines) and scanning (in discrete points) results of the AC port impedance of MMC. As seen from the figure, all the discrete points fall on the solid lines, which verifies the accuracy of the established impedance model of MMC.

Reference

1. SUN J, LIU H C. Sequence impedance modeling of modular multilevel converters [J]. IEEE Journal of Emerging and Selected Topics in Power Electronics, 2017, 5(4): 1427–1443.

Chapter 5
Impedance Modeling of Thyristor Converter

Different from the two-level converter and MMC based on IGBTs, the thyristor converter using semi-controlled devices turns on and off following the AC grid voltage. The high-frequency PWM modulation technology cannot be applied. The nonlinear switching process of the thyristor converter is described by the piecewise switching function within a fundamental period, which cannot be equivalent to the continuous modulation signal under PWM modulation. Besides, the switching frequency of the thyristor converter is relatively low, and the AC/DC voltage and current contain multiple characteristic harmonics.

This chapter is to establish the small-signal impedance model of the thyristor converter, considering the piecewise switching function and characteristic harmonics. First, the main-circuit topology and operating principle of the thyristor converter are presented, and the time-domain model of the switching function including the overlap angle is derived. Then, the steady-state harmonic characteristics of the AC and DC voltages and currents are analyzed. The time-domain modeling of the main circuit and the frequency-domain modeling of the steady-state operation is carried out. Furthermore, the frequency-domain small-signal models of the main circuit and switching function are developed. Finally, the small-signal impedance model of the thyristor converter, considering PLL, DC current control, and phase control, is established and verified. The established model in this chapter lays a foundation for the impedance modeling and characteristic analysis of LCC-HVDC in the coming chapters.

5.1 Operation Principle

In this section, the topology and operating principle of the thyristor converter are introduced, and the AC/DC voltage and current conversions are analyzed.

© China Electric Power Press 2023

W. Wang et al., *Analysis and Mitigation of Broadband Oscillation in Renewable Energy Generation and AC/DC Transmission Systems*,
https://doi.org/10.1007/978-981-99-1568-2_5

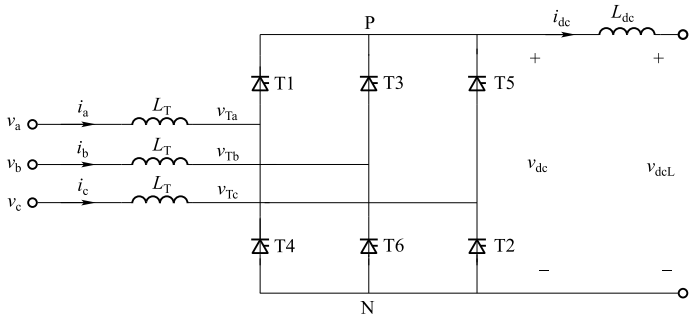

Fig. 5.1 The main circuit of the 6-pulse thyristor converter

5.1.1 Topology

The main circuit of the 6-pulse thyristor converter is shown in Fig. 5.1. This converter consists of six thyristors T1–T6. The common cathode of T1, T3, and T5 in the upper bridge is connected to the positive DC pole, and the anode of T2, T4, and T6 in the lower bridge is connected to the negative DC pole. v_l, i_l (l = a, b, c) are the three-phase AC voltages and currents respectively. v_{Tl} are the three-phase AC input voltages, and L_T is the equivalent commutation inductor. v_{dc}, i_{dc} are the DC voltage and current respectively. L_{dc} is a DC smoothing reactor, and v_{dcL} is the DC output voltage. The DC side of the thyristor converter can be connected to the load or the DC power grid.

5.1.2 Conduction Principle

The conduction of a semi-controlled thyristor (from the off-state to the on-state) should simultaneously satisfy: ① The positive voltage is applied between the anode and cathode; ② A firing pulse is applied to the gate.

When one thyristor is on in each of the upper and lower bridges, the corresponding line voltage is connected to the DC port through the two conducting thyristors and constitutes the DC voltage. The six thyristors turn on and off consecutively at the natural commutation points, i.e., the intersections of the three-phase voltages. The conduction order of the six thyristors is T1-T2-T3-T4-T5-T6.

Taking the positive zero-crossing of the line voltage v_{bc} as the reference point and ignoring the equivalent commutation inductor, the phase-shift angles of the six natural commutation points are $\gamma_1 = -\pi/3$, $\gamma_2 = 0$, $\gamma_3 = \pi/3$, $\gamma_4 = 2\pi/3$, $\gamma_5 = \pi$, $\gamma_6 = 4\pi/3$ respectively. The firing pulses are applied to T1, T2, T3, T4, T5, T6 respectively at each of the six natural commutation point, and the waveforms of the three-phase AC voltages, line voltages, and DC voltage are shown in Fig. 5.2.

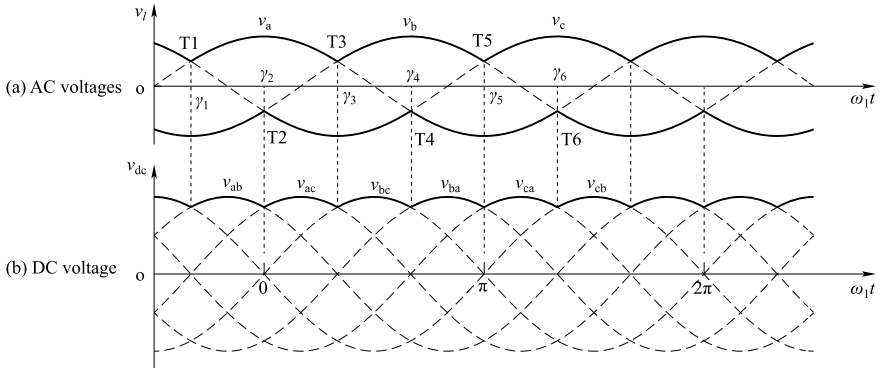

Fig. 5.2 The voltage waveforms when triggered at the natural commutation point

The DC voltage of the thyristor converter can be regulated by delaying the trigger angle at the natural commutation point. The trigger angle is given as α, and the instant at which the firing pulse of each thyristor is $\gamma_h + \alpha$ ($h = 1, 2, \ldots, 6$). The waveforms of the AC/DC voltages and currents are shown in Fig. 5.3.

As seen in Fig. 5.3, the one fundamental period ($\gamma_1 + \alpha \sim \gamma_1 + \alpha + 2\pi$) is divided into six intervals: I, II, III, IV, V, VI, with $\pi/3$ for each interval. Interval I ($\gamma_1 + \alpha \sim \gamma_2 + \alpha$) is analyzed as an example. Although the phase-a voltage is the maximum in the previous internal (VI: $\gamma_1 \sim \gamma_1 + \alpha$), T1 is not triggered and off under the trigger angle α, and the phase-a current is zero. T5 and T6 remain on, and the DC voltage is equal to the line voltage v_{cb}. The phase-b current is equal to $-i_{dc}$, and the phase-c current is equal to i_{dc}. When T1 is triggered at $\gamma_1 + \alpha$, T5 turns off, and T1 turns on. The DC voltage is equal to the line voltage v_{ab}. Three-phase AC currents are respectively: $i_a = i_{dc}$, $i_b = -i_{dc}$, $i_c = 0$. Similarly, the operating states of the thyristor converter in other intervals can be obtained. The thyristor conducting state, AC current, and DC voltage in each interval are listed in Table 5.1.

According to Fig. 5.3 and Table 5.1, each thyristor of T1–T6 conducts in turn for one-third of the fundamental period. In addition, only one thyristor in the upper bridges and only one thyristor in the lower bridges conduct at a time, and they belong to different phases. When the upper bridge thyristor is on, the DC current flows through the phase where the thyristor is, and the phase voltage constitutes the DC positive port voltage. Likewise, when the lower bridge thyristor is on, the DC current flows through the phase in the opposite direction, and the phase voltage constitutes the DC negative port voltage. The difference between the DC positive port voltage and DC negative port voltage forms the DC voltage. The waveforms of the DC voltage in the six intervals are the same. In other words, six pulses exist in the DC voltage waveform within a fundamental period, so the thyristor converter is also called a 6-pulse thyristor converter.

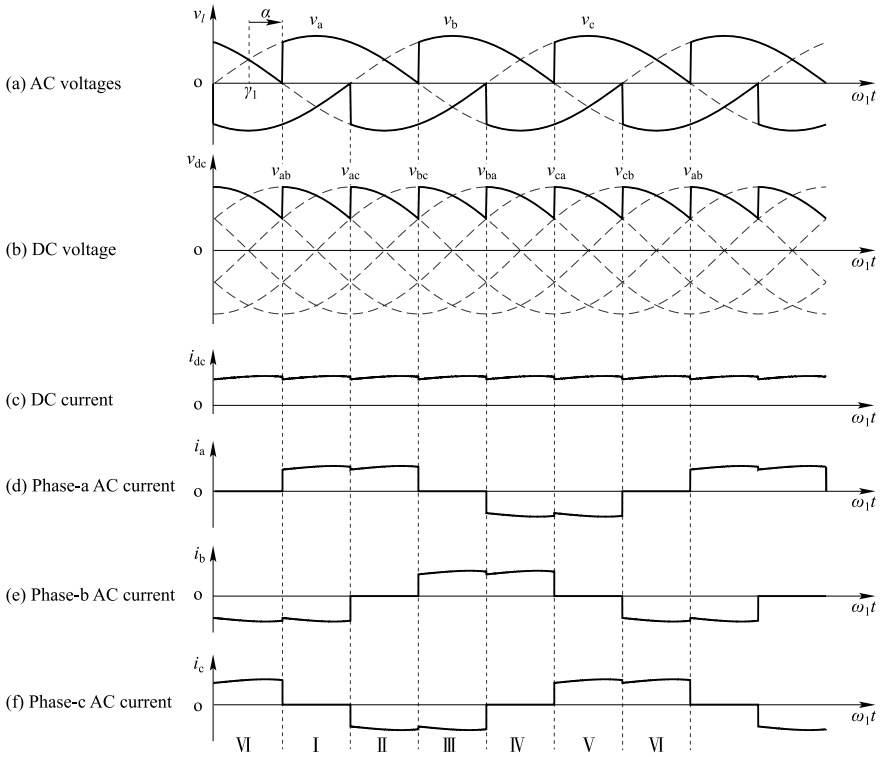

Fig. 5.3 The voltage and current waveforms when delaying the trigger angle α

Table 5.1 Operation state of the thyristor converter in each interval

Interval	I	II	III	IV	V	VI
Conducting thyristor in the upper bridge	T1	T1	T3	T3	T5	T5
Conducting thyristor in the lower bridge	T6	T2	T2	T4	T4	T6
i_a	i_{dc}	i_{dc}	0	$-i_{dc}$	$-i_{dc}$	0
i_b	$-i_{dc}$	0	i_{dc}	i_{dc}	0	$-i_{dc}$
i_c	0	$-i_{dc}$	$-i_{dc}$	0	i_{dc}	i_{dc}
v_{dc}	$v_a - v_b$	$v_a - v_c$	$v_b - v_c$	$v_b - v_a$	$v_c - v_a$	$v_c - v_b$

5.2 Time-Domain Modeling of Main Circuit

This section first derives the conversion relationship between AC/DC voltages and currents. Then, the influence of the equivalent commutation inductor on the voltage and current characteristics is analyzed. The voltage and current switching functions considering the commutation process are developed. Finally, the time-domain analytical model of the main circuit is established.

5.2.1 Time-Domain Model Without Considering Commutation Overlap

According to Sect. 5.1, the relationship between AC/DC voltages and currents can be described by defining the following three-phase switching function.

$$s_l = \begin{cases} 1, & \text{if upper bridge thyristor on, lower bridge thyristor off} \\ 0, & \text{if upper and lower bridge thyristors off} \\ -1, & \text{if upper bridge thyristor off, lower bridge thyristor on} \end{cases} \tag{5.1}$$

Based on Eq. (5.1) and Fig. 5.3, the three-phase switching functions in each interval are listed in Table 5.2, and the corresponding waveforms are shown in Fig. 5.4.

The conversion relationships of the AC/DC voltages and currents can be expressed as

$$v_{\mathrm{dc}} = \sum_{l=\mathrm{a,b,c}} s_l v_{\mathrm{T}l} \tag{5.2}$$

$$i_l = s_l i_{\mathrm{dc}} \tag{5.3}$$

Table 5.2 Three-phase switching functions in each interval

Interval	I	II	III	IV	V	VI
s_{a}	1	1	0	−1	−1	0
s_{b}	−1	0	1	1	0	−1
s_{c}	0	−1	−1	0	1	1

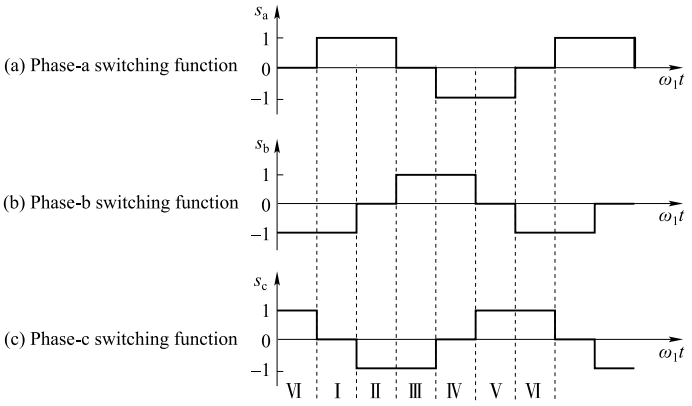

Fig. 5.4 The waveforms of three-phase switching function

As shown in Fig. 5.4, the switching function waveform presents a rectangular wave with a period of 2π, and the three-phase switching functions differ from each other by $2\pi/3$. The values of the three-phase switching functions vary with the intervals, and the switching functions can be expressed as

$$s_l = \begin{cases} 1, & \gamma_1 + \alpha + \beta_l + 2p\pi \le \omega_1 t < \gamma_3 + \alpha + \beta_l + 2p\pi \\ 0, & \gamma_3 + \alpha + \beta_l + 2p\pi \le \omega_1 t < \gamma_4 + \alpha + \beta_l + 2p\pi \\ -1, & \gamma_4 + \alpha + \beta_l + 2p\pi \le \omega_1 t < \gamma_6 + \alpha + \beta_l + 2p\pi \\ 0, & \gamma_6 + \alpha + \beta_l + 2p\pi \le \omega_1 t < \gamma_1 + \alpha + 2\pi + \beta_l + 2p\pi \end{cases} \tag{5.4}$$

where $2p\pi$ (p is an integer) represents the arbitrary period; β_l are the phase-shift angles between three phases. β_a, β_b, β_c equal to 0, $2\pi/3$, $-2\pi/3$ respectively.

5.2.2 *Time-Domain Model Considering Commutation Overlap*

Due to the transformer leakage inductance, AC line reactance, etc., there is an equivalent commutation inductance at the AC port of the thyristor converter. Considering the effect of the commutation inductance, the time-domain model of the AC-side circuit can be expressed as

$$v_{\mathrm{T}l} = v_l - L_{\mathrm{T}} \frac{\mathrm{d}i_l}{\mathrm{d}t} \tag{5.5}$$

Due to the commutation inductance, the AC current cannot change abruptly, and the commutation is non-instantaneous. The AC current contains a duration over which the current changes from zero to $\pm i_{\mathrm{dc}}$ or from $\pm i_{\mathrm{dc}}$ to zero, corresponding to the commutation period. The commutation process between T5 and T1 from Interval VI to Interval I is taken as an example. When T1 is triggered, T5, that is initially on, cannot be turned off instantaneously. Both T1 and T5 are on during the commutation process. The commutating phase a and phase b form a commutation circuit through T1 and T5, as shown in Fig. 5.5.

The waveforms of the AC and DC voltages and currents with the influence of the commutation are shown in Fig. 5.6. μ is the overlap angle, corresponding to the commutation period.

As seen in Fig. 5.6, during the commutation process ($\gamma_1 + \alpha \sim \gamma_1 + \alpha + \mu$), the phase-c current i_{c} flowing through T5 decreases from i_{dc} to zero gradually, while phase-a current i_{a} flowing through T1 increases from zero to i_{dc} gradually. The sum of the two phase currents constitutes the DC current, which is expressed as

$$i_{\mathrm{a}} + i_{\mathrm{c}} = i_{\mathrm{dc}} \tag{5.6}$$

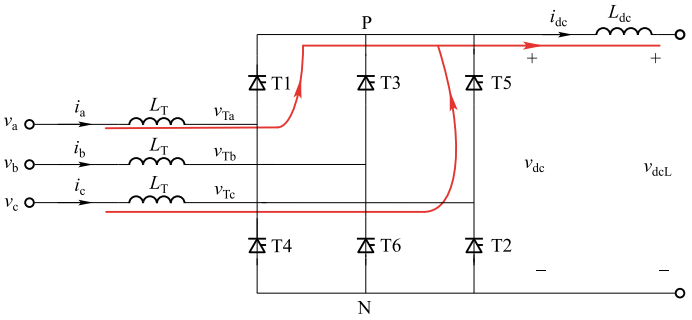

Fig. 5.5 The diagram of the commutation circuit

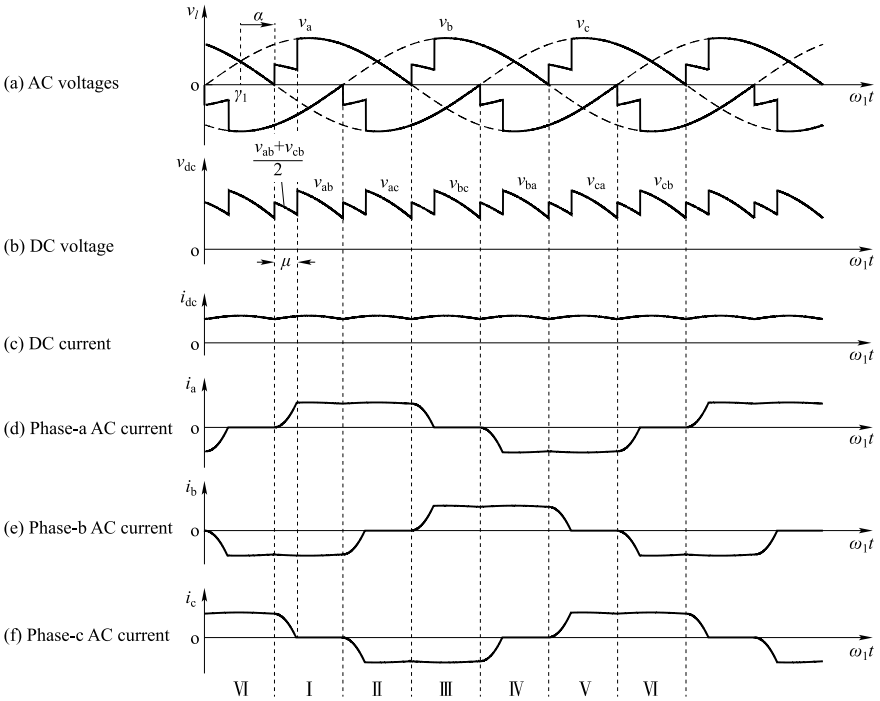

Fig. 5.6 The voltage and current waveforms with the influence of the commutation

Besides, the commutation circuit satisfies

$$L_T \frac{di_a}{dt} - L_T \frac{di_c}{dt} = v_{ac} \tag{5.7}$$

At the beginning of the commutation process $\omega_1 t = \gamma_1 + \alpha$, the initial values of v_{ac} and i_a are

$$\begin{cases} v_{\mathrm{ac}}|_{\omega_1 t=\gamma_1+\alpha} = \sqrt{3}V_1 \sin(\gamma_1 + \alpha + \pi/3) \\ i_{\mathrm{a}}|_{\omega_1 t=\gamma_1+\alpha} = 0 \end{cases} \tag{5.8}$$

where V_1 is the amplitude of the fundamental component of the AC voltage.

Substituting Eq. (5.8) to Eqs. (5.6) and (5.7), the expression of the phase-a current during the commutation process can be derived.

$$i_{\mathrm{a}} = \frac{\sqrt{3}V_1}{2\omega_1 L_{\mathrm{T}}}[\cos\alpha - \cos(\omega_1 t + \pi/3)] \tag{5.9}$$

At the end of the commutation process $\omega_1 t = \gamma_1 + \alpha + \mu$, i_{a} increases to the steady-state value of the DC current I_{dc}, which is expressed as

$$i_{\mathrm{a}}|_{\omega_1 t=\gamma_1+\alpha+\mu} = I_{\mathrm{dc}} \tag{5.10}$$

Substituting Eq. (5.10) to Eq. (5.9), the expression of the overlap angle μ can be obtained as

$$\mu = \arccos\left(\cos\alpha - \frac{2\omega_1 L_{\mathrm{T}} I_{\mathrm{dc}}}{\sqrt{3}V_1}\right) - \alpha \tag{5.11}$$

As seen from Eq. (5.11), the overlap angle μ is relevant to the trigger angle α, the amplitude of the fundamental component of the AC voltage V_1, and equivalent commutation inductor L_{T}.

Furthermore, the DC voltage during the commutation process is analyzed. For the DC positive port voltage, the phase-a voltage and phase-c voltage are connected to the DC positive pole, and the expression of the DC positive port voltage is

$$v_{\mathrm{PO}} = \frac{v_{\mathrm{a}} + v_{\mathrm{c}}}{2} \tag{5.12}$$

At the same time, the expression of the DC negative port voltage is

$$v_{\mathrm{NO}} = v_{\mathrm{b}} \tag{5.13}$$

According to Eqs. (5.12) and (5.13), the DC voltage can be calculated as

$$v_{\mathrm{dc}} = \frac{v_{\mathrm{ab}} + v_{\mathrm{cb}}}{2} \tag{5.14}$$

The commutation processes between other thyristors are similar, and the voltage and current changes during the commutation process can also be obtained. According to Figs. 5.3 and 5.6, considering the commutation process, the switching function does not present an ideal rectangular wave, and the voltage and current switching functions are inconsistent. The waveforms of the voltage and current switching functions under the influence of the commutation process are shown in Fig. 5.7.

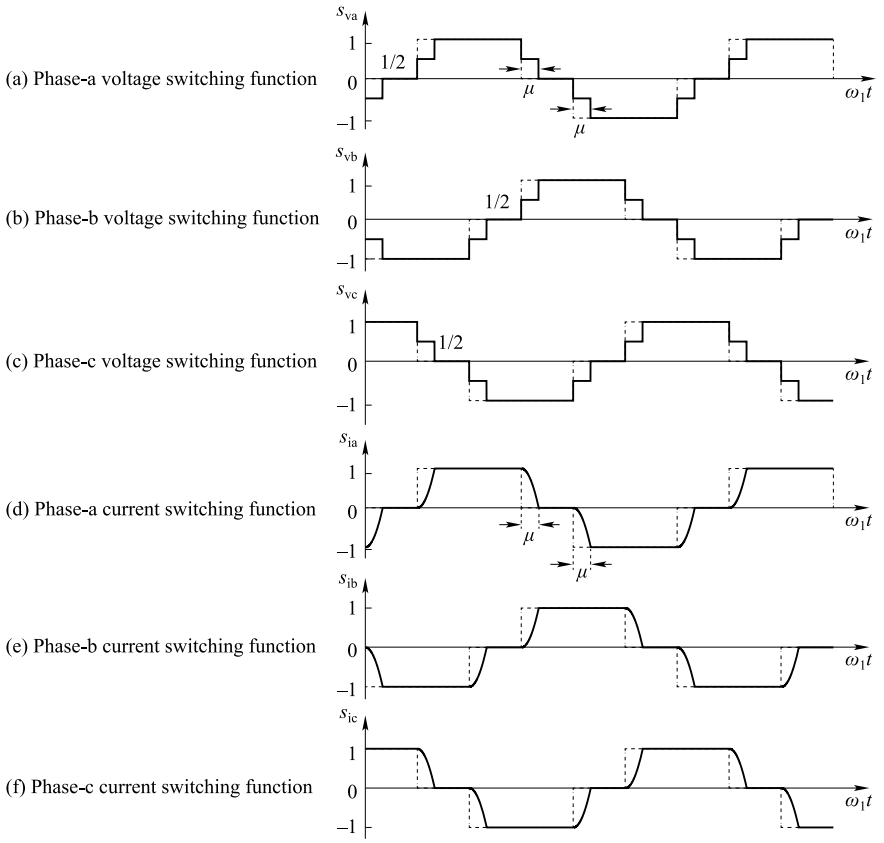

Fig. 5.7 The waveforms of the voltage and current switching functions with the influence of the commutation

Except for the commutation period, the voltage and current switching functions in other intervals are consistent with Eq. (5.1). During the commutation process, the commutation circuit forms the phase-to-phase short circuit, and the voltage switching function is equally divided between the two commutating phases. The voltage switching function of the thyristor that should be turned on instantaneously is one-half less with the pulse width μ, while the voltage switching function of the thyristor that should be turned off instantaneously is one-half more with the pulse width μ.

Besides, the AC current has a nonlinear transition during the commutation period. The commutation period from Interval VI to Interval I is taken as an example. Based on Eq. (5.9), the phase-a current switching function during the turning on of T1 can be calculated with dividing the commutating phase current by the DC current.

$$s_{\mathrm{ia}} = \frac{i_{\mathrm{a}}}{i_{\mathrm{dc}}} = \frac{\cos\alpha - \cos(\omega_1 t - \pi/3)}{\cos\alpha - \cos(\alpha + \mu)} \tag{5.15}$$

According to Eqs. (5.6), (5.9), and (5.15), the phase-c current switching function during the turning off of T5 can also be derived.

$$s_{\mathrm{ic}} = 1 - s_{\mathrm{ia}} = \frac{\cos(\omega_1 t - \pi/3) - \cos(\alpha + \mu)}{\cos\alpha - \cos(\alpha + \mu)} \tag{5.16}$$

Likewise, the expressions of the current switching functions in other commutation periods can be obtained.

Based on Eq. (5.4), the voltage and current switching functions at any time with the influence of the commutation can be expressed as

$$\begin{cases} s_{\mathrm{v}l} = s_l + \Delta s_{\mathrm{v}l} \\ s_{\mathrm{i}l} = s_l + \Delta s_{\mathrm{i}l} \end{cases} \tag{5.17}$$

where $\Delta s_{\mathrm{v}l}$, $\Delta s_{\mathrm{i}l}$ are the voltage and current switching function variations introduced by the commutation process respectively, and can be expressed as

$$\Delta s_{\mathrm{v}l} = \begin{cases} -\dfrac{1}{2}, & \gamma_1 + \alpha + \beta_l + 2p\pi \le \omega_1 t < \gamma_1 + \alpha + \mu + \beta_l + 2p\pi \\ \dfrac{1}{2}, & \gamma_3 + \alpha + \beta_l + 2p\pi \le \omega_1 t < \gamma_3 + \alpha + \mu + \beta_l + 2p\pi \\ \dfrac{1}{2}, & \gamma_4 + \alpha + \beta_l + 2p\pi \le \omega_1 t < \gamma_4 + \alpha + \mu + \beta_l + 2p\pi \\ -\dfrac{1}{2}, & \gamma_6 + \alpha + \beta_l + 2p\pi \le \omega_1 t < \gamma_6 + \alpha + \mu + \beta_l + 2p\pi \end{cases} \tag{5.18}$$

$$\Delta s_{\mathrm{i}l} = \begin{cases} -\dfrac{\cos(\omega_1 t + \pi/3) - \cos(\alpha + \mu)}{\cos\alpha - \cos(\alpha + \mu)}, & \gamma_1 + \alpha + \beta_l + 2p\pi \le \omega_1 t \\ & < \gamma_1 + \alpha + \mu + \beta_l + 2p\pi \\ \dfrac{\cos(\omega_1 t - \pi/3) - \cos(\alpha + \mu)}{\cos\alpha - \cos(\alpha + \mu)}, & \gamma_3 + \alpha + \beta_l + 2p\pi \le \omega_1 t \\ & < \gamma_3 + \alpha + \mu + \beta_l + 2p\pi \\ \dfrac{\cos(\omega_1 t - 2\pi/3) - \cos(\alpha + \mu)}{\cos\alpha - \cos(\alpha + \mu)}, & \gamma_4 + \alpha + \beta_l + 2p\pi \le \omega_1 t \\ & < \gamma_4 + \alpha + \mu + \beta_l + 2p\pi \\ -\dfrac{\cos(\omega_1 t - 4\pi/3) - \cos(\alpha + \mu)}{\cos\alpha - \cos(\alpha + \mu)}, & \gamma_6 + \alpha + \beta_l + 2p\pi \le \omega_1 t \\ & < \gamma_6 + \alpha + \mu + \beta_l + 2p\pi \end{cases} \tag{5.19}$$

5.3 Frequency-Domain Modeling of Steady-State Operation

According to the time-domain model of the main circuit, this section analyzes the steady-state harmonic characteristics of the AC/DC voltages, currents, and switching

functions in frequency domain. Then, the frequency-domain steady-state model of the main circuit is established, which provides the steady-state operating point for small-signal impedance modeling.

5.3.1 *Frequency-Domain Characteristic Analysis of Steady-State Operating Point*

It is well known that the DC voltage of the 6-pulse thyristor converter contains the characteristic harmonic components at $6nf_1 (n = 0, \pm1, \pm2, \pm3 \ldots)$, and the AC current contains the characteristic harmonic components at $(6n \pm 1) f_1$. For instance, the waveforms of the DC voltage, AC current, and voltage and current switching functions in the thyristor converter are shown in Fig. 5.8. In the figure, the DC voltage is referenced to its DC component, and the AC current and switching functions are referenced to their fundamental components respectively.

As seen in Fig. 5.8, the DC voltage contains not only the DC component but also the characteristic harmonic components at the multiple integers of 300 Hz, i.e., $6nf_1$. The AC current and the corresponding current switching function contain not only the fundamental component but also the characteristic harmonic components at $\pm5f_1, \pm7f_1, \pm11f_1, \pm13f_1$, etc., i.e., $(6n \pm 1) f_1$. According to Eq. (5.3), the AC current is equal to the multiplication of the current switching function and DC current. Since the DC current is constant to some extent, the waveforms of the AC current and current switching function are nearly identical. Besides, the waveform of the voltage switching function is different from that of the current switching function, but their harmonic orders are the same. The amplitudes of these harmonic components gradually become smaller as the harmonic order increases.

In this section, the frequency-domain column vector is used to describe the steady-state harmonic characteristics. The steady-state harmonic components of the thyristor converter quantities are arranged in the following steady-state frequency order.

$$[\,(-6g-1)f_1, \ldots, -2f_1, -f_1, 0, f_1, 2f_1, \ldots, (6g+1)f_1\,]^{\mathrm{T}} \tag{5.20}$$

where the frequency order is from $-(6g+1)f_1$ to $(6g+1)f_1$ ($12g+3$ in total).

The AC voltage and current contain the steady-state harmonic components at $(6n \pm 1) f_1$. Taking phase a as an example, the steady-state vectors of the AC voltage and current can be expressed as

$$\begin{cases} \boldsymbol{V}_{\mathrm{a}} = [\ldots, \boldsymbol{V}_7^*, 0, \boldsymbol{V}_5^*, 0, 0, 0, \boldsymbol{V}_1^*, 0, \boldsymbol{V}_1, 0, 0, 0, \boldsymbol{V}_5, 0, \boldsymbol{V}_7, \ldots]^{\mathrm{T}} \\ \boldsymbol{I}_{\mathrm{a}} = [\ldots, \boldsymbol{I}_7^*, 0, \boldsymbol{I}_5^*, 0, 0, 0, \boldsymbol{I}_1^*, 0, \boldsymbol{I}_1, 0, 0, 0, \boldsymbol{I}_5, 0, \boldsymbol{I}_7, \ldots]^{\mathrm{T}} \end{cases} \tag{5.21}$$

where each component is represented in the form of complex vector, such as $\boldsymbol{V}_k = V_k e^{j\varphi_{vk}}$, $\boldsymbol{I}_k = I_k e^{j\varphi_{ik}}$. The subscript number $k = 0, \pm1, \pm2, \ldots, \pm(6g+1)$ indicates the harmonic order, corresponding to the frequency kf_1. The component at $-kf_1$

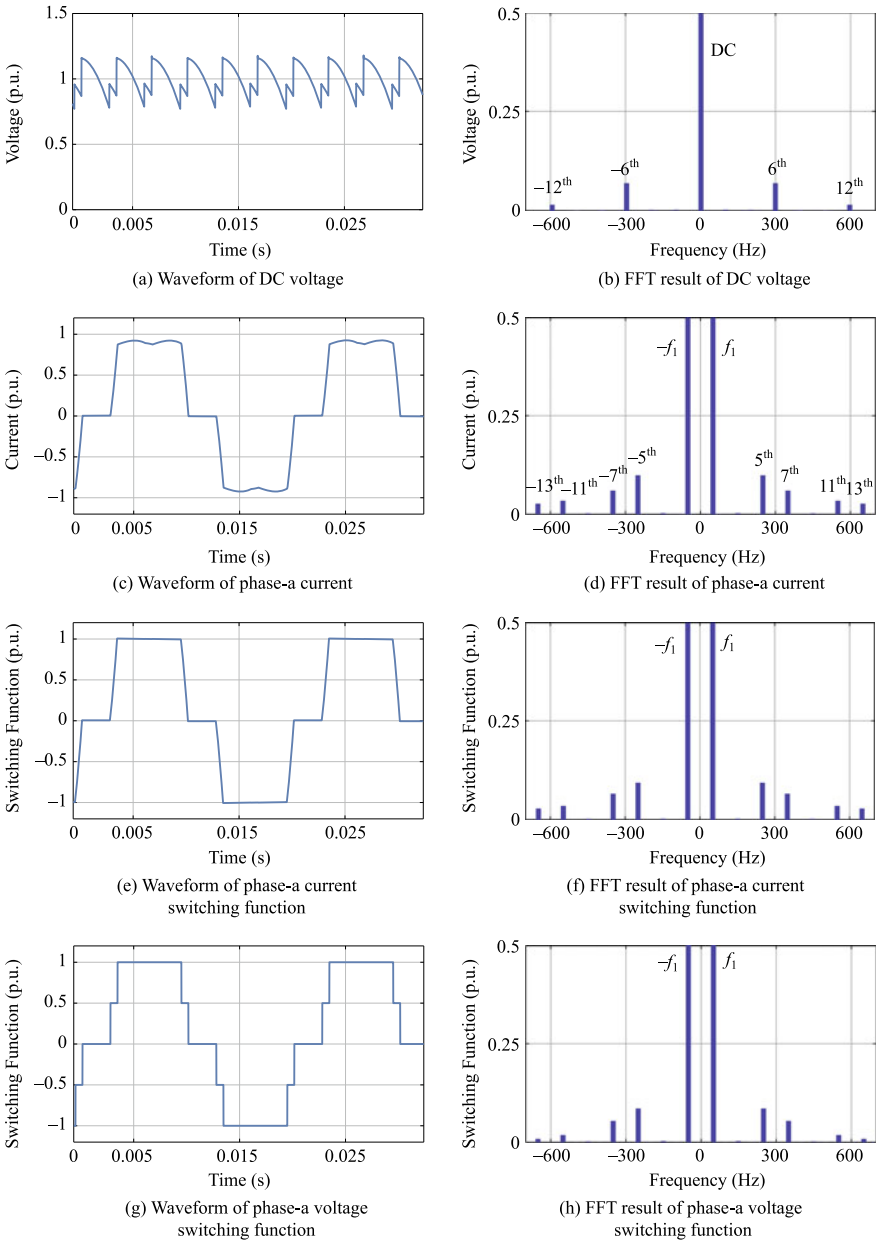

(a) Waveform of DC voltage

(b) FFT result of DC voltage

(c) Waveform of phase-a current

(d) FFT result of phase-a current

(e) Waveform of phase-a current switching function

(f) FFT result of phase-a current switching function

(g) Waveform of phase-a voltage switching function

(h) FFT result of phase-a voltage switching function

Fig. 5.8 The waveforms and FFT results of the steady-state quantities in the thyristor converter

is equal to the conjugate of the component at kf_1, such as $\boldsymbol{V}_{-k} = \boldsymbol{V}_k^*$, $\boldsymbol{I}_{-k} = \boldsymbol{I}_k^*$. The amplitude of the harmonic component at kf_1 or $-kf_1$ is equal to half of each actual harmonic component at frequency kf_1. For the AC voltage and current, and the components are non-zero if and only if $k = 6n \pm 1$.

The frequencies of the steady-state components contained in the voltage and current switching functions are consistent with the AC voltage and current. Considering the influence of the commutation, the steady-state vectors of the phase-a voltage and current switching functions can be expressed as

$$\begin{cases} \boldsymbol{S}_{\mathrm{va}} = [\ldots,\ \boldsymbol{S}_{\mathrm{v7}}^*,\ 0,\ \boldsymbol{S}_{\mathrm{v5}}^*,\ 0,\ 0,\ 0,\ \boldsymbol{S}_{\mathrm{v1}}^*,\ 0,\ \boldsymbol{S}_{\mathrm{v1}},\ 0,\ 0,\ 0,\ \boldsymbol{S}_{\mathrm{v5}},\ 0,\ \boldsymbol{S}_{\mathrm{v7}},\ \ldots]^{\mathrm{T}} \\ \boldsymbol{S}_{\mathrm{ia}} = [\ldots,\ \boldsymbol{S}_{\mathrm{i7}}^*,\ 0,\ \boldsymbol{S}_{\mathrm{i5}}^*,\ 0,\ 0,\ 0,\ \boldsymbol{S}_{\mathrm{i1}}^*,\ 0,\ \boldsymbol{S}_{\mathrm{i1}},\ 0,\ 0,\ 0,\ \boldsymbol{S}_{\mathrm{i5}},\ 0,\ \boldsymbol{S}_{\mathrm{i7}},\ \ldots]^{\mathrm{T}} \end{cases} \tag{5.22}$$

where $\boldsymbol{S}_{\mathrm{v}k}$ or $\boldsymbol{S}_{\mathrm{i}k}$ is the steady-state component at the frequency kf_1, and the element is non-zero if and only if $k = 6n \pm 1$.

According to the phase-sequence relationship of the steady-state component at kf_1, the phase-shift angle between two adjacent phases is

$$-\frac{2k\pi}{3} = \begin{cases} -2\pi/3, & k = 3n+1 \\ 0, & k = 3n \\ 2\pi/3, & k = 3n-1 \end{cases} \quad (n = 0, \pm 1, \pm 2, \ldots) \tag{5.23}$$

where $-2\pi/3$ indicates a positive-sequence relationship among three phases; $2\pi/3$ indicates negative-sequence relationship; 0 indicates a zero-sequence relationship.

The AC voltage, AC current, and switching function contain the steady-state harmonic components at $(6n \pm 1) f_1$, in which the component at $(6n + 1) f_1$ is in positive sequence, and the component at $(6n - 1) f_1$ is in negative sequence.

Based on the phase-sequence relationship of the steady-state component at each frequency, the steady-state vectors of the AC voltages and currents in phase b and phase c can be obtained according to Eq. (5.21).

$$\boldsymbol{V}_{\mathrm{b}} = \boldsymbol{D}\boldsymbol{V}_{\mathrm{a}}, \quad \boldsymbol{I}_{\mathrm{b}} = \boldsymbol{D}\boldsymbol{I}_{\mathrm{a}} \tag{5.24}$$

$$\boldsymbol{V}_{\mathrm{c}} = \boldsymbol{D}^*\boldsymbol{V}_{\mathrm{a}}, \quad \boldsymbol{I}_{\mathrm{c}} = \boldsymbol{D}^*\boldsymbol{I}_{\mathrm{a}} \tag{5.25}$$

where $\boldsymbol{D}$ is the phase-sequence coefficient matrix of the steady-state vectors, expressed as

$$\boldsymbol{D} = \mathrm{diag}\left[\{\mathrm{e}^{-\mathrm{j}2k\pi/3}\}\big|_{k=-6g-1,\ldots,0,\ldots,6g+1} \right] \tag{5.26}$$

Similarly, the steady-state vectors of the voltage and current switching functions in phase b and phase c can be expressed as

$$\begin{cases} \boldsymbol{S}_{\mathrm{vb}} = \boldsymbol{D}\boldsymbol{S}_{\mathrm{va}}, \quad \boldsymbol{S}_{\mathrm{ib}} = \boldsymbol{D}\boldsymbol{S}_{\mathrm{ia}} \\ \boldsymbol{S}_{\mathrm{vc}} = \boldsymbol{D}^{*}\boldsymbol{S}_{\mathrm{va}}, \ \boldsymbol{S}_{\mathrm{ic}} = \boldsymbol{D}^{*}\boldsymbol{S}_{\mathrm{ia}} \end{cases} \tag{5.27}$$

The DC voltage and current contain the steady-state harmonic components at $6nf_1$, and the other are zero. The steady-state vectors of the DC voltage and current can be expressed as

$$\begin{cases} \boldsymbol{V}_{\mathrm{dc}} = [\ldots, 0, \boldsymbol{V}^{*}_{\mathrm{dc6}}, 0, 0, 0, 0, 0, \boldsymbol{V}_{\mathrm{dc0}}, 0, 0, 0, 0, 0, \boldsymbol{V}_{\mathrm{dc6}}, 0, \ldots]^{\mathrm{T}} \\ \boldsymbol{I}_{\mathrm{dc}} = [\ldots, 0, \boldsymbol{I}^{*}_{\mathrm{dc6}}, 0, 0, 0, 0, 0, \boldsymbol{I}_{\mathrm{dc0}}, 0, 0, 0, 0, 0, \boldsymbol{V}_{\mathrm{dc6}}, 0, \ldots]^{\mathrm{T}} \end{cases} \tag{5.28}$$

5.3.2 *Frequency-Domain Steady-State Model of Main Circuit*

Based on the steady-state vectors of the AC/DC voltages and currents, the frequency-domain steady-state model of the main circuit is established in this section.

The steady-state model of the AC-side circuit can be obtained by transforming Eq. (5.5) to the frequency domain.

$$\boldsymbol{V}_{\mathrm{T}l} = \boldsymbol{V}_{l} - \boldsymbol{Z}_{\mathrm{T0}}\boldsymbol{I}_{l} \tag{5.29}$$

where $\boldsymbol{V}_{\mathrm{T}l}$ are the steady-state vectors of the three-phase AC input voltages respectively. $\boldsymbol{Z}_{\mathrm{T0}}$ is the impedance of the equivalent commutation inductor in the steady-state frequency order, expressed as

$$\begin{aligned} \boldsymbol{Z}_{\mathrm{T0}} = \mathrm{j}2\pi L_{\mathrm{T}} \cdot \mathrm{diag}\big[& (-6g-1)f_1, \ldots, -2f_1, -f_1, 0, \\ & f_1, 2f_1, \ldots, (6g+1)f_1 \big] \end{aligned} \tag{5.30}$$

The frequency-domain relationships of the AC/DC voltages and currents can be developed by transforming Eqs. (5.2) and (5.3) to the frequency domain.

$$\begin{cases} \boldsymbol{V}_{\mathrm{dc}} = \sum\limits_{l=\mathrm{a,b,c}} \boldsymbol{S}_{\mathrm{v}l} \otimes \boldsymbol{V}_{\mathrm{T}l} \\ \boldsymbol{I}_{l} = \boldsymbol{S}_{\mathrm{i}l} \otimes \boldsymbol{I}_{\mathrm{dc}} \end{cases} \tag{5.31}$$

In order to use the scalar product instead of the convolution in Eq. (5.31), the steady-state vectors of the switching functions need to be expanded into matrices. Using the vector $\boldsymbol{S}_{\mathrm{va}}$ as an example, the expression of the expanded steady-state matrix is given as

$$
S_{\mathrm{va}} = \begin{bmatrix}
\ddots & & & & & & & & & & & & & & \iddots \\
0 & \boldsymbol{S}^*_{\mathrm{v1}} & 0 & 0 & 0 & \boldsymbol{S}^*_{\mathrm{v5}} & 0 & \boldsymbol{S}^*_{\mathrm{v7}} & 0 & 0 & 0 & \boldsymbol{S}^*_{\mathrm{v11}} & 0 & \boldsymbol{S}^*_{\mathrm{v13}} & 0 \\
\boldsymbol{S}_{\mathrm{v1}} & 0 & \boldsymbol{S}^*_{\mathrm{v1}} & 0 & 0 & 0 & \boldsymbol{S}^*_{\mathrm{v5}} & 0 & \boldsymbol{S}^*_{\mathrm{v7}} & 0 & 0 & 0 & \boldsymbol{S}^*_{\mathrm{v11}} & 0 & \boldsymbol{S}^*_{\mathrm{v13}} \\
0 & \boldsymbol{S}_{\mathrm{v1}} & 0 & \boldsymbol{S}^*_{\mathrm{v1}} & 0 & 0 & 0 & \boldsymbol{S}^*_{\mathrm{v5}} & 0 & \boldsymbol{S}^*_{\mathrm{v7}} & 0 & 0 & 0 & \boldsymbol{S}^*_{\mathrm{v11}} & 0 \\
0 & 0 & \boldsymbol{S}_{\mathrm{v1}} & 0 & \boldsymbol{S}^*_{\mathrm{v1}} & 0 & 0 & 0 & \boldsymbol{S}^*_{\mathrm{v5}} & 0 & \boldsymbol{S}^*_{\mathrm{v7}} & 0 & 0 & 0 & \boldsymbol{S}^*_{\mathrm{v11}} \\
0 & 0 & 0 & \boldsymbol{S}_{\mathrm{v1}} & 0 & \boldsymbol{S}^*_{\mathrm{v1}} & 0 & 0 & 0 & \boldsymbol{S}^*_{\mathrm{v5}} & 0 & \boldsymbol{S}^*_{\mathrm{v7}} & 0 & 0 & 0 \\
\boldsymbol{S}_{\mathrm{v5}} & 0 & 0 & 0 & \boldsymbol{S}_{\mathrm{v1}} & 0 & \boldsymbol{S}^*_{\mathrm{v1}} & 0 & 0 & 0 & \boldsymbol{S}^*_{\mathrm{v5}} & 0 & \boldsymbol{S}^*_{\mathrm{v7}} & 0 & 0 \\
0 & \boldsymbol{S}_{\mathrm{v5}} & 0 & 0 & 0 & \boldsymbol{S}_{\mathrm{v1}} & 0 & \boldsymbol{S}^*_{\mathrm{v1}} & 0 & 0 & 0 & \boldsymbol{S}^*_{\mathrm{v5}} & 0 & \boldsymbol{S}^*_{\mathrm{v7}} & 0 \\
\boldsymbol{S}_{\mathrm{v7}} & 0 & \boldsymbol{S}_{\mathrm{v5}} & 0 & 0 & 0 & \boldsymbol{S}_{\mathrm{v1}} & 0 & \boldsymbol{S}^*_{\mathrm{v1}} & 0 & 0 & 0 & \boldsymbol{S}^*_{\mathrm{v5}} & 0 & \boldsymbol{S}^*_{\mathrm{v7}} \\
0 & \boldsymbol{S}_{\mathrm{v7}} & 0 & \boldsymbol{S}_{\mathrm{v5}} & 0 & 0 & 0 & \boldsymbol{S}_{\mathrm{v1}} & 0 & \boldsymbol{S}^*_{\mathrm{v1}} & 0 & 0 & 0 & \boldsymbol{S}^*_{\mathrm{v5}} & 0 \\
0 & 0 & \boldsymbol{S}_{\mathrm{v7}} & 0 & \boldsymbol{S}_{\mathrm{v5}} & 0 & 0 & 0 & \boldsymbol{S}_{\mathrm{v1}} & 0 & \boldsymbol{S}^*_{\mathrm{v1}} & 0 & 0 & 0 & \boldsymbol{S}^*_{\mathrm{v5}} \\
0 & 0 & 0 & \boldsymbol{S}_{\mathrm{v7}} & 0 & \boldsymbol{S}_{\mathrm{v5}} & 0 & 0 & 0 & \boldsymbol{S}_{\mathrm{v1}} & 0 & \boldsymbol{S}^*_{\mathrm{v1}} & 0 & 0 & 0 \\
\boldsymbol{S}_{\mathrm{v11}} & 0 & 0 & 0 & \boldsymbol{S}_{\mathrm{v7}} & 0 & \boldsymbol{S}_{\mathrm{v5}} & 0 & 0 & 0 & \boldsymbol{S}_{\mathrm{v1}} & 0 & \boldsymbol{S}^*_{\mathrm{v1}} & 0 & 0 \\
0 & \boldsymbol{S}_{\mathrm{v11}} & 0 & 0 & 0 & \boldsymbol{S}_{\mathrm{v7}} & 0 & \boldsymbol{S}_{\mathrm{v5}} & 0 & 0 & 0 & \boldsymbol{S}_{\mathrm{v1}} & 0 & \boldsymbol{S}^*_{\mathrm{v1}} & 0 \\
\boldsymbol{S}_{\mathrm{v13}} & 0 & \boldsymbol{S}_{\mathrm{v11}} & 0 & 0 & 0 & \boldsymbol{S}_{\mathrm{v7}} & 0 & \boldsymbol{S}_{\mathrm{v5}} & 0 & 0 & 0 & \boldsymbol{S}_{\mathrm{v1}} & 0 & \boldsymbol{S}^*_{\mathrm{v1}} \\
0 & \boldsymbol{S}_{\mathrm{v13}} & 0 & \boldsymbol{S}_{\mathrm{v11}} & 0 & 0 & 0 & \boldsymbol{S}_{\mathrm{v7}} & 0 & \boldsymbol{S}_{\mathrm{v5}} & 0 & 0 & 0 & \boldsymbol{S}_{\mathrm{v1}} & 0 \\
\iddots & & & & & & & & & & & & & & \ddots
\end{bmatrix} \tag{5.32}
$$

where

1. The steady-state vector is transposed into a row vector and arranged in a reverse order, as the $6g + 2$th (center) row of the steady-state matrix.
2. The kth row above the center row is obtained by shifting the center row by k elements into the left, with the last k elements filled by 0.
3. The kth row below the center row is obtained by shifting the center row by k elements into the right, with the first k elements filled by 0.

Similarly, the steady-state matrices of the three-phase AC voltage $\boldsymbol{V}_l$, input voltages $\boldsymbol{V}_{\mathrm{T}l}$, and current switching functions $\boldsymbol{S}_{\mathrm{i}l}$ can be obtained.

The characteristic harmonic frequencies of the AC- and DC-side quantities are different, and the steady-state matrix of the DC current, for example, can be expressed as

$$
\boldsymbol{I}_{\mathrm{dc}} = \begin{bmatrix}
\ddots & & & & & & & & & & & & & & & \iddots \\
\boldsymbol{I}_{\mathrm{dc0}} & 0 & 0 & 0 & 0 & 0 & \boldsymbol{I}^{*}_{\mathrm{dc6}} & 0 & 0 & 0 & 0 & 0 & \boldsymbol{I}^{*}_{\mathrm{dc12}} & 0 & 0 & \\
0 & \boldsymbol{I}_{\mathrm{dc0}} & 0 & 0 & 0 & 0 & 0 & \boldsymbol{I}^{*}_{\mathrm{dc6}} & 0 & 0 & 0 & 0 & 0 & \boldsymbol{I}^{*}_{\mathrm{dc12}} & 0 & \\
0 & 0 & \boldsymbol{I}_{\mathrm{dc0}} & 0 & 0 & 0 & 0 & 0 & \boldsymbol{I}^{*}_{\mathrm{dc6}} & 0 & 0 & 0 & 0 & 0 & \boldsymbol{I}^{*}_{\mathrm{dc12}} & \\
0 & 0 & 0 & \boldsymbol{I}_{\mathrm{dc0}} & 0 & 0 & 0 & 0 & 0 & \boldsymbol{I}^{*}_{\mathrm{dc6}} & 0 & 0 & 0 & 0 & 0 & \\
0 & 0 & 0 & 0 & \boldsymbol{I}_{\mathrm{dc0}} & 0 & 0 & 0 & 0 & 0 & \boldsymbol{I}^{*}_{\mathrm{dc6}} & 0 & 0 & 0 & 0 & \\
0 & 0 & 0 & 0 & 0 & \boldsymbol{I}_{\mathrm{dc0}} & 0 & 0 & 0 & 0 & 0 & \boldsymbol{I}^{*}_{\mathrm{dc6}} & 0 & 0 & 0 & \\
\boldsymbol{I}_{\mathrm{dc6}} & 0 & 0 & 0 & 0 & 0 & \boldsymbol{I}_{\mathrm{dc0}} & 0 & 0 & 0 & 0 & 0 & \boldsymbol{I}^{*}_{\mathrm{dc6}} & 0 & 0 & \\
0 & \boldsymbol{I}_{\mathrm{dc6}} & 0 & 0 & 0 & 0 & 0 & \boldsymbol{I}_{\mathrm{dc0}} & 0 & 0 & 0 & 0 & 0 & \boldsymbol{I}^{*}_{\mathrm{dc6}} & 0 & \\
0 & 0 & \boldsymbol{I}_{\mathrm{dc6}} & 0 & 0 & 0 & 0 & 0 & \boldsymbol{I}_{\mathrm{dc0}} & 0 & 0 & 0 & 0 & 0 & \boldsymbol{I}^{*}_{\mathrm{dc6}} & \\
0 & 0 & 0 & \boldsymbol{I}_{\mathrm{dc6}} & 0 & 0 & 0 & 0 & 0 & \boldsymbol{I}_{\mathrm{dc0}} & 0 & 0 & 0 & 0 & 0 & \\
0 & 0 & 0 & 0 & \boldsymbol{I}_{\mathrm{dc6}} & 0 & 0 & 0 & 0 & 0 & \boldsymbol{I}_{\mathrm{dc0}} & 0 & 0 & 0 & 0 & \\
0 & 0 & 0 & 0 & 0 & \boldsymbol{I}_{\mathrm{dc6}} & 0 & 0 & 0 & 0 & 0 & \boldsymbol{I}_{\mathrm{dc0}} & 0 & 0 & 0 & \\
\boldsymbol{I}_{\mathrm{dc12}} & 0 & 0 & 0 & 0 & 0 & \boldsymbol{I}_{\mathrm{dc6}} & 0 & 0 & 0 & 0 & 0 & \boldsymbol{I}_{\mathrm{dc0}} & 0 & 0 & \\
0 & \boldsymbol{I}_{\mathrm{dc12}} & 0 & 0 & 0 & 0 & 0 & \boldsymbol{I}_{\mathrm{dc6}} & 0 & 0 & 0 & 0 & 0 & \boldsymbol{I}_{\mathrm{dc0}} & 0 & \\
0 & 0 & \boldsymbol{I}_{\mathrm{dc12}} & 0 & 0 & 0 & 0 & 0 & \boldsymbol{I}_{\mathrm{dc6}} & 0 & 0 & 0 & 0 & 0 & \boldsymbol{I}_{\mathrm{dc0}} & \\
\iddots & & & & & & & & & & & & & & & \ddots
\end{bmatrix} \tag{5.33}
$$

For the AC/DC voltage conversion, the steady-state vector of the DC voltage $\boldsymbol{V}_{\mathrm{dc}}$ is equal to the sum of $\boldsymbol{V}_{\mathrm{T}l}$ multiplied by $\boldsymbol{S}_{\mathrm{v}l}$. In particular, the multiplication between the steady-state components of $\boldsymbol{S}_{\mathrm{v}l}$ at $(6n_1+1)f_1$ $(n_1 = 0, \pm1, \pm2, \ldots)$ with the steady-state components of $\boldsymbol{V}_{\mathrm{T}l}$ at $(6n_2-1)f_1$ $(n_2 = 0, \pm1, \pm2, \ldots)$, and the multiplication between the steady-state components of $\boldsymbol{S}_{\mathrm{v}l}$ at $(6n_1-1)f_1$ with the steady-state components of $\boldsymbol{V}_{\mathrm{T}l}$ at $(6n_2+1)f_1$, lead to the steady-state components of $\boldsymbol{V}_{\mathrm{dc}}$ at $6(n_1+n_2)f_1$.

In summary, the frequency-domain steady-state characteristics of the AC/DC voltages related to the voltage switching functions are listed in Table 5.3.

Similarly, the frequency-domain steady-state characteristics of the AC/DC currents related to the current switching functions are listed in Table 5.4.

The frequency-domain characteristics of the AC and DC steady-state components mentioned above are consistent with Fig. 5.8. n_1, n_2 are arbitrary integers that can be equal or different, so they are uniformly denoted by $n(n = 0, \pm1, \pm2, \ldots)$ hereafter

Table 5.3 The frequency-domain steady-state characteristics of the AC/DC voltages

Steady-State Vectors	$\boldsymbol{V}_{\mathrm{T}l}$	$\boldsymbol{S}_{\mathrm{v}l}$	$\boldsymbol{V}_{\mathrm{dc}}$
Frequency	$(6n_2-1)f_1$	$(6n_1+1)f_1$	$6(n_1+n_2)f_1$
	$(6n_2+1)f_1$	$(6n_1-1)f_1$	

Table 5.4 The frequency-domain steady-state characteristics of the AC/DC currents

Steady-State Vectors	$\boldsymbol{I}_{\mathrm{dc}}$	$\boldsymbol{S}_{\mathrm{i}l}$	$\boldsymbol{I}_l$
Frequency	$6n_2 f_1$	$(6n_1+1)f_1$	$[6(n_1+n_2)+1]f_1$
		$(6n_1-1)f_1$	$[6(n_1+n_2)-1]f_1$

to simplify the description, i.e., the AC voltage, current and switching functions contain the steady-state components at $(6n \pm 1) f_1$, and the DC voltage and current contain the steady-state components at $6nf_1$.

5.4 Small-Signal Impedance Modeling in Frequency Domain

This section carries out the small-signal impedance modeling of the thyristor converter in the frequency domain. First, a small-signal perturbation is superimposed on the AC voltage at the steady-state operating point, and the frequency-domain distribution characteristics of the voltage, current, and switching function are elaborated. Then, the frequency-domain small-signal models of the main circuit and switching function are developed, respectively. Finally, the small-signal impedance model of the thyristor converter is established by calculating the response of the AC current to the AC voltage perturbation.

5.4.1 Small-Signal Frequency-Domain Characteristic Analysis

After injecting a small-signal perturbation of AC voltage at the steady-state operation point, the small-signal responses of the DC voltage will be produced due to the turning on and off of the thyristors. Then, the small-signal components of the DC voltage drop on the DC smoothing reactor, leading to the small-signal components of the DC current. Furthermore, the small-signal responses of the AC current will be produced due to the turning on and off of the thyristor. The small-signal transfer path and frequency response relationship of the thyristor converter are shown in Fig. 5.9.

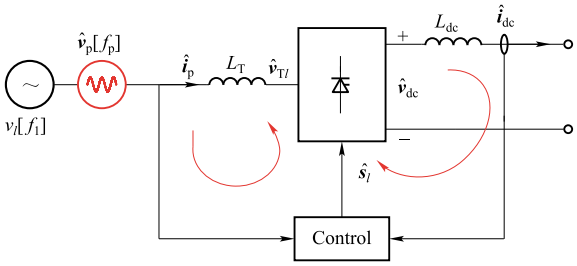

Fig. 5.9 The small-signal transfer path and frequency response relationship of the thyristor converter

Initially, a positive-sequence small-signal perturbation at f_p is superimposed on the AC voltage at the steady-state operating point. The difference between the small-signal component of the AC voltage $\hat{\boldsymbol{v}}_l$ at f_p and the input voltage drops on the equivalent commutation inductor, which leads to a small-signal response of the AC current $\hat{\boldsymbol{i}}_l$ at f_p. Subsequently, the small-signal response of the input voltage $\hat{\boldsymbol{v}}_{Tl}$ at f_p is also produced.

The small-signal component of the input voltage $\hat{\boldsymbol{v}}_{Tl}$ at f_p multiplying the steady-state components of the voltage switching function $\boldsymbol{S}_{vl}$ at $(6n-1)f_1$ leads to small-signal responses of the DC voltage $\hat{\boldsymbol{v}}_{dc}$ at $6nf_1+f_p-f_1$. The difference between the small-signal components of $\hat{\boldsymbol{v}}_{dc}$ at $6nf_1+f_p-f_1$ and the DC output voltage drops on the DC smoothing inductor, leading to the small-signal response of the DC current $\hat{\boldsymbol{i}}_{dc}$ at $6nf_1+f_p-f_1$.

The small-signal component of $\hat{\boldsymbol{i}}_{dc}$ at $6nf_1+f_p-f_1$ multiplying the steady-state components of the current switching function $\boldsymbol{S}_{il}$ at $(6n\pm1)f_1$ leads to small-signal responses of $\hat{\boldsymbol{i}}_l$ at $(6n\pm1)f_1+f_p-f_1$.

Furthermore, the small-signal components are also introduced into the voltage and current switching functions due to the control of the thyristor converter. Under the effects of PLL and DC current control, the small-signal responses of the voltage and current switching functions $\hat{\boldsymbol{s}}_{vl}$, $\hat{\boldsymbol{s}}_{il}$ are produced around the sideband of the steady-state components, i.e., at $(6n\pm1)f_1+f_p-f_1$. The small-signal components of $\hat{\boldsymbol{s}}_{vl}$ at $(6n\pm1)f_1+f_p-f_1$ multiplying the steady-state components of the AC input voltage $\boldsymbol{V}_{il}$ at $(6n\pm1)f_1$ leads to small-signal responses of $\hat{\boldsymbol{v}}_{dc}$ and $\hat{\boldsymbol{i}}_{dc}$ at $6nf_1+f_p-f_1$. The small-signal component of $\hat{\boldsymbol{s}}_{il}$ at $(6n\pm1)f_1+f_p-f_1$ multiplying the steady-state components of the DC current $\boldsymbol{I}_{dc}$ at $6nf_1$ leads to small-signal responses of $\hat{\boldsymbol{i}}_l$ at $(6n\pm1)f_1+f_p-f_1$. The balance will be finally achieved after repeating the above process. The frequency distribution characteristics of the small-signal quantities in the thyristor converter are shown in Fig. 5.10.

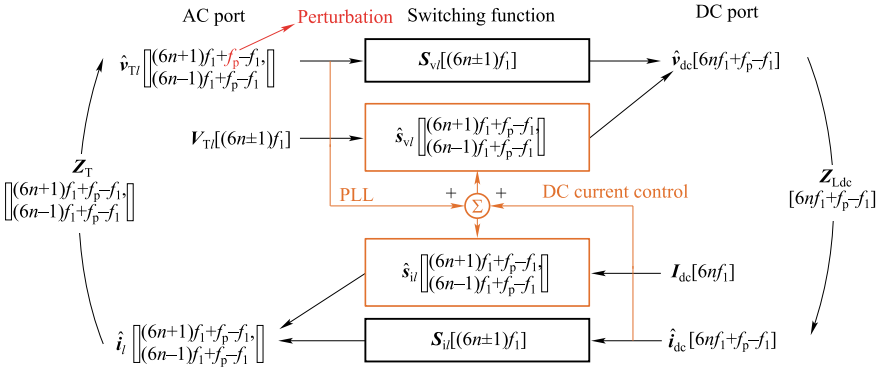

Fig. 5.10 The frequency distribution characteristics of the small-signal quantities in the thyristor converter

Table 5.5 Main circuit and controller parameters of the thyristor converter

Parameter	Definition	Value
P_N	Rated power	400 MW
V_1	Fundamental component amplitude of AC voltage	255 kV
f_1	Fundamental frequency	50 Hz
L_T	Equivalent commutation inductance	38.8 mH
L_{dc}	DC smoothing reactor inductance	300 mH
V_{dc}	Steady-state value of DC voltage	400 kV
K_{pp}, K_{pi}	Proportional and integral coefficients of the PLL controller	0.0105, 0.3333
K_{idcp}, K_{idci}	Proportional and integral coefficients of the DC current controller	0.0096, 0.4286
T_{idcf}	Filter time delay of the DC current	0.0012

Besides, the multiplication between small-signal components leads to responses at $2f_p + kf_1$, $3f_p + kf_1$ and even higher-order small-signal frequencies. Since their amplitudes are proportional to the square or higher order of the small-signal perturbation, these small-signal responses can be ignored in the linearization modeling process.

For instance, a positive-sequence small-signal voltage perturbation, 0.05 p.u. at $f_p = 30$ Hz, is superimposed on the AC voltage. The main circuit and controller parameters are listed in Table 5.5. After reaching the steady state, the waveforms and the FFT results of the small-signal quantities in the AC/DC voltages and voltage switching function are shown in Fig. 5.11.

Figure 5.11 shows the FFT results within -700 to 700 Hz. After injecting the small-signal voltage perturbation, the small-signal components at $(6n+1)f_1+f_p-f_1$ (-570, -270, 30, 330, 630 Hz) and $(6n-1)f_1+f_p-f_1$ (-670, -370, -70, 230, 530 Hz) are introduced into the AC input voltage and voltage switching function. The small-signal components at $6nf_1+f_p-f_1$ (-620, -320, -20, 280, 580 Hz) are introduced into the AC input voltage.

Similarly, the waveforms and the FFT results of the small-signal quantities in the AC/DC currents and current switching function are shown in Fig. 5.12.

Comparing Figs. 5.11 and 5.12, it can be seen that the frequencies of the small-signal components of the AC voltage, AC current, and voltage and current switching functions are the same, i.e., $(6n \pm 1)f_1 + f_p - f_1$. The frequencies of the small-signal components of the DC voltage and current are the same, i.e., $6nf_1 + f_p - f_1$.

In summary, the frequency-domain small-signal characteristics of the AC/DC voltages related to the voltage switching functions are listed in Table 5.6.

Similarly, the frequency-domain small-signal characteristics of the AC/DC currents related to the current switching functions are listed in Table 5.7.

In order to describe the frequency-domain small-signal characteristics, the small-signal components of the thyristor converter quantities are arranged in the following small-signal frequency order.

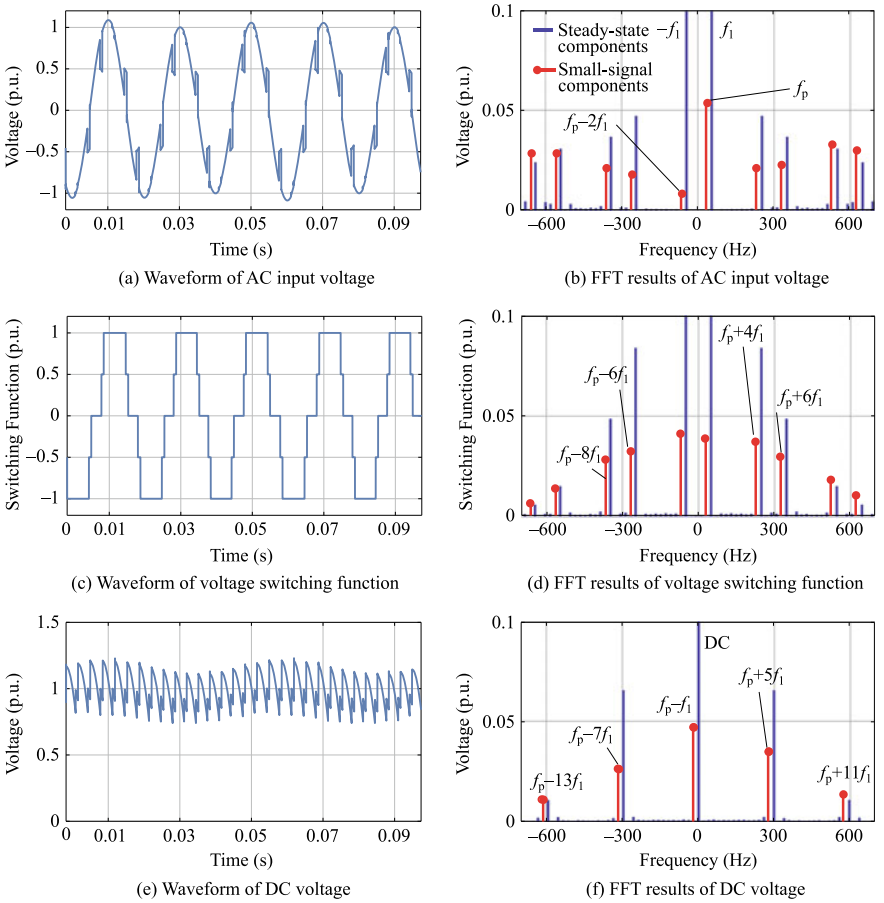

(a) Waveform of AC input voltage
(b) FFT results of AC input voltage
(c) Waveform of voltage switching function
(d) FFT results of voltage switching function
(e) Waveform of DC voltage
(f) FFT results of DC voltage

Fig. 5.11 The waveforms and FFT results of the small-signal quantities in the AC/DC voltages and voltage switching function

$$\begin{aligned}[\quad & f_\mathrm{p}-(6g+2)f_1,\ f_\mathrm{p}-(6g+1)f_1,\ f_\mathrm{p}-6gf_1,\ \ldots,\\ \ldots,\ & f_\mathrm{p}-2f_1,\quad f_\mathrm{p}-f_1,\quad f_\mathrm{p},\quad \ldots,\\ \ldots,\ & f_\mathrm{p}+(6g-2)f_1,\ f_\mathrm{p}+(6g-1)f_1,\ f_\mathrm{p}+6gf_1,\quad]^\mathrm{T}\end{aligned} \tag{5.34}$$

where the frequency order is from $f_\mathrm{p}-(6g+2)f_1$ to $f_\mathrm{p}+6gf_1$ ($12g+3$ in total).

The AC voltages and currents contain the small-signal components at $(6n\pm1)f_1+f_\mathrm{p}-f_1$. Taking the phase a as an example, the small-signal vectors of the AC voltage and current can be expressed as

$$\begin{cases}\hat{\boldsymbol{v}}_\mathrm{a}=[\ldots,\hat{\boldsymbol{v}}_{\mathrm{p}-8},0,\hat{\boldsymbol{v}}_{\mathrm{p}-6},0,0,0,\hat{\boldsymbol{v}}_{\mathrm{p}-2},0,\hat{\boldsymbol{v}}_\mathrm{p},0,0,0,\hat{\boldsymbol{v}}_{\mathrm{p}+4},0,\hat{\boldsymbol{v}}_{\mathrm{p}+6},\ldots]^\mathrm{T}\\ \hat{\boldsymbol{i}}_\mathrm{a}=[\ldots,\hat{\boldsymbol{i}}_{\mathrm{p}-8},0,\hat{\boldsymbol{i}}_{\mathrm{p}-6},0,0,0,\hat{\boldsymbol{i}}_{\mathrm{p}-2},0,\hat{\boldsymbol{i}}_\mathrm{p},0,0,0,\hat{\boldsymbol{i}}_{\mathrm{p}+4},0,\hat{\boldsymbol{i}}_{\mathrm{p}+6},\ldots]^\mathrm{T}\end{cases} \tag{5.35}$$

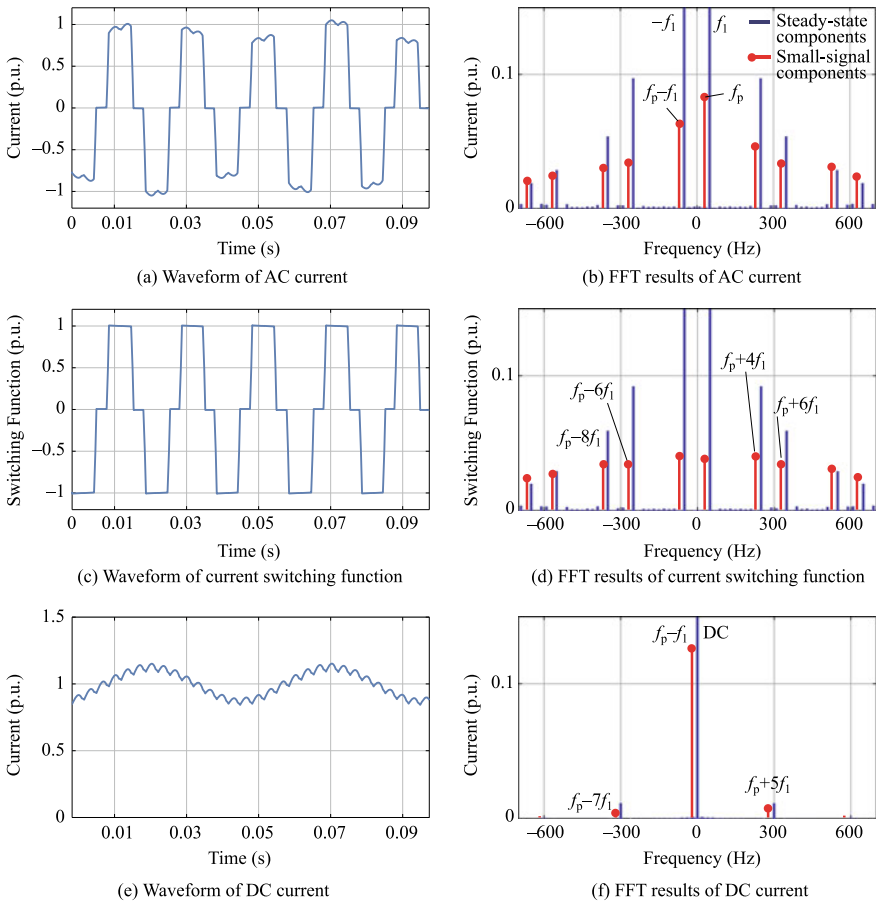

(a) Waveform of AC current
(b) FFT results of AC current
(c) Waveform of current switching function
(d) FFT results of current switching function
(e) Waveform of DC current
(f) FFT results of DC current

Fig. 5.12 The waveforms and FFT results of the small-signal quantities in the AC/DC currents and current switching function

Table 5.6 The frequency-domain small-signal characteristics of the AC/DC voltages

Small-Signal Vectors	Frequency
$\hat{\boldsymbol{v}}_{Tl}$	$(6n+1)f_1 + f_p - f_1$
	$(6n-1)f_1 + f_p - f_1$
$\hat{\boldsymbol{s}}_{vl}$	$(6n+1)f_1 + f_p - f_1$
	$(6n-1)f_1 + f_p - f_1$
$\hat{\boldsymbol{v}}_{dc}$	$6nf_1 + f_p - f_1$

Table 5.7 The frequency-domain small-signal characteristics of the AC/DC currents

Small-Signal Vectors	Frequency
$\hat{\boldsymbol{i}}_{\mathrm{dc}}$	$6nf_1 + f_\mathrm{p} - f_1$
$\hat{\boldsymbol{s}}_{il}$	$(6n+1)f_1 + f_\mathrm{p} - f_1$
	$(6n-1)f_1 + f_\mathrm{p} - f_1$
$\hat{\boldsymbol{i}}_l$	$(6n+1)f_1 + f_\mathrm{p} - f_1$
	$(6n-1)f_1 + f_\mathrm{p} - f_1$

where $\hat{\boldsymbol{v}}_{\mathrm{p}+k-1}$ or $\hat{\boldsymbol{i}}_{\mathrm{p}+k-1}$ is the small-signal component at the frequency $f_\mathrm{p}+(k-1)f_1$, and the element is non-zero if and only if $k = 6n \pm 1$.

The frequencies of the small-signal components of the voltage and current switching functions are the same as the AC voltage and current. The small-signal vectors of the voltage and current switching functions can be expressed as

$$\begin{cases} \hat{\boldsymbol{s}}_{\mathrm{va}} = [\ldots, \hat{\boldsymbol{s}}_{\mathrm{vp}-8}, 0, \hat{\boldsymbol{s}}_{\mathrm{vp}-6}, 0, 0, 0, \hat{\boldsymbol{s}}_{\mathrm{vp}-2}, 0, \hat{\boldsymbol{s}}_{\mathrm{vp}}, 0, 0, 0, \hat{\boldsymbol{s}}_{\mathrm{vp}+4}, 0, \hat{\boldsymbol{s}}_{\mathrm{vp}+6}, \ldots]^\mathrm{T} \\ \hat{\boldsymbol{s}}_{\mathrm{ia}} = [\ldots, \hat{\boldsymbol{s}}_{\mathrm{ip}-8}, 0, \hat{\boldsymbol{s}}_{\mathrm{ip}-6}, 0, 0, 0, \hat{\boldsymbol{s}}_{\mathrm{ip}-2}, 0, \hat{\boldsymbol{s}}_{\mathrm{ip}}, 0, 0, 0, \hat{\boldsymbol{s}}_{\mathrm{ip}+4}, 0, \hat{\boldsymbol{s}}_{\mathrm{ip}+6}, \ldots]^\mathrm{T} \end{cases} \tag{5.36}$$

where $\hat{\boldsymbol{s}}_{\mathrm{vp}+k-1}$ or $\hat{\boldsymbol{s}}_{\mathrm{ip}+k-1}$ is the small-signal component at the frequency $f_\mathrm{p} + (k-1)f_1$, and the element is non-zero if and only if $k = 6n \pm 1$.

The angle of the positive-sequence perturbation at f_p is delayed by $2\pi/3$ among three phases. For a small-signal component at $f_\mathrm{p} - f_1 + kf_1$ ($k = 0, \pm1, \pm2, \ldots, \pm(6g+1)$), the phase-shift angle between adjacent phases is

$$-\frac{2k\pi}{3} = \begin{cases} -2\pi/3, & k = 3n+1 \\ 0, & k = 3n \\ 2\pi/3, & k = 3n-1 \end{cases} \quad (n = 0, \pm1, \pm2, \ldots) \tag{5.37}$$

According to the phase-sequence relationship shown in Eq. (5.37), for the small-signal vectors, the component at $(6n+1)f_1 + f_\mathrm{p} - f_1$ is in positive sequence, the component at $(6n-1)f_1 + f_\mathrm{p} - f_1$ is in positive sequence, and the component at $6nf_1 + f_\mathrm{p} - f_1$ is in zero sequence. Therefore, the small-signal vectors of the AC voltages, AC currents, and switching functions in phase b and phase c can be obtained.

$$\begin{cases} \hat{\boldsymbol{v}}_\mathrm{b} = \boldsymbol{D}_\mathrm{p}\hat{\boldsymbol{v}}_\mathrm{a},\ \hat{\boldsymbol{i}}_\mathrm{b} = \boldsymbol{D}_\mathrm{p}\hat{\boldsymbol{i}}_\mathrm{a},\ \hat{\boldsymbol{s}}_\mathrm{vb} = \boldsymbol{D}_\mathrm{p}\hat{\boldsymbol{s}}_\mathrm{va},\ \hat{\boldsymbol{s}}_\mathrm{ib} = \boldsymbol{D}_\mathrm{p}\hat{\boldsymbol{s}}_\mathrm{ia} \\ \hat{\boldsymbol{v}}_\mathrm{c} = \boldsymbol{D}_\mathrm{p}^*\hat{\boldsymbol{v}}_\mathrm{a},\ \hat{\boldsymbol{i}}_\mathrm{c} = \boldsymbol{D}_\mathrm{p}^*\hat{\boldsymbol{i}}_\mathrm{a},\ \hat{\boldsymbol{s}}_\mathrm{vc} = \boldsymbol{D}_\mathrm{p}^*\hat{\boldsymbol{s}}_\mathrm{va},\ \hat{\boldsymbol{s}}_\mathrm{ic} = \boldsymbol{D}_\mathrm{p}^*\hat{\boldsymbol{s}}_\mathrm{ia} \end{cases} \tag{5.38}$$

where $\boldsymbol{D}_\mathrm{p}$ is the phase-sequence coefficient matrix of the small-signal vectors, expressed as

$$\boldsymbol{D}_\mathrm{p} = \mathrm{diag}\left[\{\mathrm{e}^{-\mathrm{j}2k\pi/3}\}\big|_{k=-6g-1,\ldots,0,\ldots,6g+1} \right] \tag{5.39}$$

The DC voltage and current contain the small-signal components at $6nf_1 + f_p - f_1$, and the corresponding small-signal vectors can be expressed as

$$\begin{cases} \hat{\boldsymbol{v}}_{dc} = [\ldots, 0, \hat{\boldsymbol{v}}_{dcp-7}, 0, 0, 0, 0, 0, \hat{\boldsymbol{v}}_{dcp-1}, 0, 0, 0, 0, 0, \hat{\boldsymbol{v}}_{dcp+5}, 0, \ldots]^T \\ \hat{\boldsymbol{i}}_{dc} = [\ldots, 0, \hat{\boldsymbol{i}}_{dcp-7}, 0, 0, 0, 0, 0, \hat{\boldsymbol{i}}_{dcp-1}, 0, 0, 0, 0, 0, \hat{\boldsymbol{i}}_{dcp+5}, 0, \ldots]^T \end{cases} \tag{5.40}$$

5.4.2 *Frequency-Domain Small-Signal Model of Main Circuit*

Based on the small-signal vectors of the AC/DC voltages, currents, and switching functions, this section establishes the frequency-domain small-signal model of the main circuit.

The small-signal model of the AC-side circuit can be obtained by transforming Eq. (5.5) to the frequency domain.

$$\hat{\boldsymbol{v}}_{Tl} = \hat{\boldsymbol{v}}_l - \boldsymbol{Z}_T \hat{\boldsymbol{i}}_l \tag{5.41}$$

where $\hat{\boldsymbol{v}}_{Tl}$ are the small-signal vectors of the three-phase AC input voltages. $\boldsymbol{Z}_T$ is the impedance of the equivalent commutation inductor in the small-signal frequency order, expressed as

$$\begin{aligned} \boldsymbol{Z}_T = \mathrm{j}2\pi L_T \cdot \mathrm{diag}\big[& f_p - (6g+2)f_1, \ldots f_p - 2f_1, \\ & f_p - f_1, f_p, \ldots, f_p + 6gf_1 \big] \end{aligned} \tag{5.42}$$

By transforming Eqs. (5.2) and (5.3) to the frequency domain, the frequency-domain relationships of the AC/DC voltages and currents can be developed.

$$\begin{cases} \hat{\boldsymbol{v}}_{dc} = \sum\limits_{l=a,b,c} \boldsymbol{S}_{vl} \hat{\boldsymbol{v}}_{Tl} + \sum\limits_{l=a,b,c} \boldsymbol{V}_{Tl} \hat{\boldsymbol{s}}_{vl} \\ \hat{\boldsymbol{i}}_l = \boldsymbol{I}_{dc} \hat{\boldsymbol{s}}_{il} + \boldsymbol{S}_{il} \hat{\boldsymbol{i}}_{dc} \end{cases} \tag{5.43}$$

where $\boldsymbol{V}_{Tl}$, $\boldsymbol{I}_{dc}$, $\boldsymbol{S}_{vl}$, $\boldsymbol{S}_{il}$ are the steady-state matrices of the AC input voltages, DC current, and voltage and current switching functions respectively for replacing the convolution with scalar product.

According to Eqs. (5.24), (5.25), and (5.38), the expression of the small-signal vector of the DC voltage can be simplified as

$$\hat{\boldsymbol{v}}_{dc} = \boldsymbol{D}_{ad}(\boldsymbol{V}_{Ta} \hat{\boldsymbol{s}}_{va} + \boldsymbol{S}_{va} \hat{\boldsymbol{v}}_{Ta}) \tag{5.44}$$

where $\boldsymbol{D}_{\mathrm{ad}}$ is the AC/DC conversion matrix, expressed as

$$\boldsymbol{D}_{\mathrm{ad}} = 3 \cdot \mathrm{diag}\left[\{1 - |\mathrm{mod}(k, 3)|\}|_{k=-6g-1,\ldots,0,\ldots,6g+1}\right] \tag{5.45}$$

The small-signal vectors of the DC voltage and current satisfy

$$\hat{\boldsymbol{i}}_{\mathrm{dc}} = \boldsymbol{Z}_{\mathrm{Ldc}}^{-1}\hat{\boldsymbol{v}}_{\mathrm{dc}} \tag{5.46}$$

where $\boldsymbol{Z}_{\mathrm{Ldc}}$ is the impedance of the DC smoothing reactor, expressed as

$$\begin{aligned}\boldsymbol{Z}_{\mathrm{Ldc}} = \mathrm{j}2\pi L_{\mathrm{dc}} \cdot \mathrm{diag}\big[&f_{\mathrm{p}} - (6g+2)f_1, \ldots, f_{\mathrm{p}} - 2f_1 \\ &f_{\mathrm{p}} - f_1, f_{\mathrm{p}}, \ldots, f_{\mathrm{p}} + 6gf_1\big]\end{aligned} \tag{5.47}$$

5.4.3 *Frequency-Domain Small-Signal Model of Switching Functions*

According to the frequency-domain small-signal model of the main circuit, both the conversion of the AC/DC voltages and currents are related to the switching functions, and are coupled to each other via the switching functions. In this section, based on the control strategy of the thyristor converter, the frequency-domain small-signal model of the voltage and current switching functions considering PLL and DC current control is established.

5.4.3.1 Control Strategy

The control of the thyristor converter includes PLL, DC current control, and phase control. PLL is used to acquire the voltage phase of the AC grid. The DC current control is used to determine the trigger angle α for regulating the active power. The phase control receives the PLL output angle θ_{PLL} and the trigger angle α, and then triggers the firing pulses to turn on the thyristors. The typical control diagram of the thyristor converter is shown in Fig. 5.13.

In the figure, I_{dcref} is the DC current reference. $H_{\mathrm{PLL}}(s)$, $H_{\mathrm{idc}}(s)$, $T_{\mathrm{idc}}(s)$ are the transfer functions of the PLL controller, DC current controller, and DC current filter respectively, expressed as

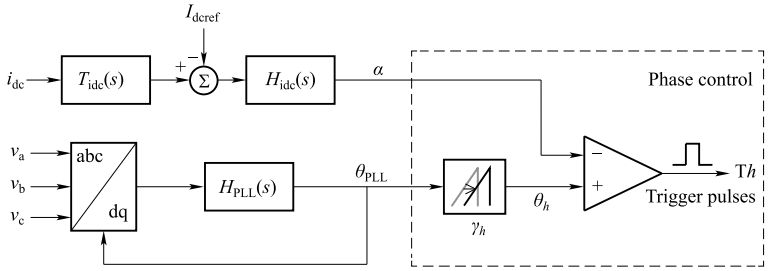

Fig. 5.13 The typical control diagram of the thyristor converter

$$\begin{cases} H_{\mathrm{PLL}}(s) = \left(K_{\mathrm{pp}} + \dfrac{K_{\mathrm{pi}}}{s}\right)\dfrac{1}{s} \\ H_{\mathrm{idc}}(s) = K_{\mathrm{idcp}} + \dfrac{K_{\mathrm{idci}}}{s} \\ T_{\mathrm{idc}}(s) = \dfrac{1}{1 + T_{\mathrm{idcf}}s} \end{cases} \tag{5.48}$$

where K_{pp}, K_{pi} are the proportional and integral coefficients of the PLL controller respectively. K_{idcp}, K_{idci} are the proportional and integral coefficients of the DC current controller respectively. T_{idcf} is the filter time delay of the DC current.

The reference angle of each thyristor θ_h can be obtained by equally delaying the PLL output angle θ_{PLL}, which can be expressed as

$$\begin{cases} \gamma_h = (h-2)\pi/3 \\ \theta_h = \theta_{\mathrm{PLL}} - \gamma_h \end{cases}, \quad h = 1, 2, \ldots, 6 \tag{5.49}$$

where h corresponds to each thyristor number. γ_h are the phase-shift angles of the six natural commutation points respectively, and the difference between two adjacent phase-shift angles is $\pi/3$. The PLL output angle can be also given as $\theta_{\mathrm{PLL}} = \omega_1 t$. The reference angle of each thyristor θ_h varies periodically with time in sawtooth waves, and $\theta_h \in [0, 2\pi)$.

At the initial moment, the thyristor Th is off. With the increase of θ_h, the firing pulse will be triggered to turn on Th once $\theta_h > \alpha$. The relationship between the switching function of the thyristor converter with θ_h and α is shown in Fig. 5.14.

In Fig. 5.14, the commutation process is not considered. When the reference angle θ_h and trigger angle α intersect, one thyristor will be turned on, and another one thyristor will be turned off. Meanwhile, the switching function will change its value, and the corresponding instant satisfies

$$\theta_h(t) = \alpha \tag{5.50}$$

According to Eqs. (5.49) and (5.50), representing the reference angle θ_h with the PLL output angle θ_{PLL}, the instant at which the switching function changes its value can be expressed as

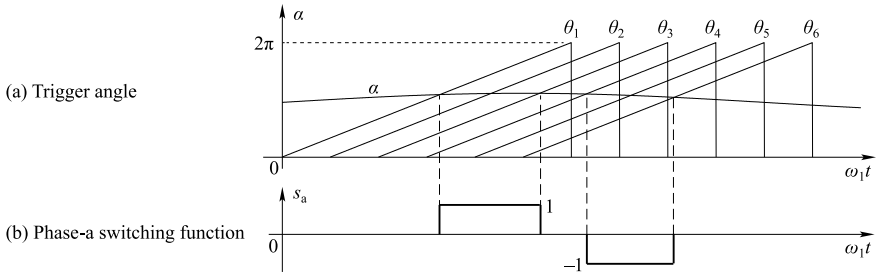

Fig. 5.14 The relationship between the switching function with the reference angle and trigger angle

$$\theta_{\mathrm{PLL}}(t) = \alpha + \gamma_h + 2p\pi \tag{5.51}$$

At the instants when $h = 1, 3, 4, 6$ in Eq. (5.51), the values of the phase-a switching function s_{a} change, as shown in Fig. 5.14. Likewise, the values of the phase-b switching function s_{b} change at the instants when $h = 3, 5, 6, 2$, the values of the phase-c switching function s_{c} change at the instants when $h = 5, 1, 2, 4$. The switching function lags $2\pi/3$ in order among three phases. The expression of the piecewise switching function is consistent with Eq. (5.4).

5.4.3.2 Small-Signal Components of PLL Output Angle and Trigger Angle

The AC voltage contains the small-signal components at $(6n \pm 1) f_1 + f_{\mathrm{p}} - f_1$. After the Park transformation, the small-signal components of the dq-axis voltages at $(6n-1) f_1 + f_{\mathrm{p}}$ are produced. Then, the small-signal components at $(6n-1) f_1 + f_{\mathrm{p}}$ are also introduced into the PLL output angle θ_{PLL} under the PLL control. Besides, the DC current contains the small-signal components at $(6n-1) f_1 + f_{\mathrm{p}}$. The small-signal components at $(6n-1) f_1 + f_{\mathrm{p}}$ are introduced into the trigger angle αunder the DC current control.

The amplitudes of the small-signal components in θ_{PLL} and α gradually become smaller as the frequency increases, and the component at $f_{\mathrm{p}} - f_1$ is the dominant. With the small-signal component at $f_{\mathrm{p}} - f_1$ considered, the PLL output angle θ_{PLL} and trigger angle α can be expressed as

$$\begin{cases} \theta_{\mathrm{PLL}}(t) = \omega_1 t + \varphi_{\mathrm{v1}} + A_\theta \cos\left[2\pi(f_{\mathrm{p}} - f_1) + \varphi_\theta\right] \\ \alpha(t) = \alpha_0 + A_\alpha \cos\left[2\pi(f_{\mathrm{p}} - f_1) + \varphi_\alpha\right] \end{cases} \tag{5.52}$$

where φ_{v1} is the phase of the fundamental component of the AC voltage; α_0 is the steady-state trigger angle; A_θ, φ_θ are the amplitude and phase of the small-signal component of the PLL output angle at $f_{\mathrm{p}} - f_1$ respectively; A_α, φ_α are the amplitude and phase of the small-signal component of the trigger angle at $f_{\mathrm{p}} - f_1$ respectively.

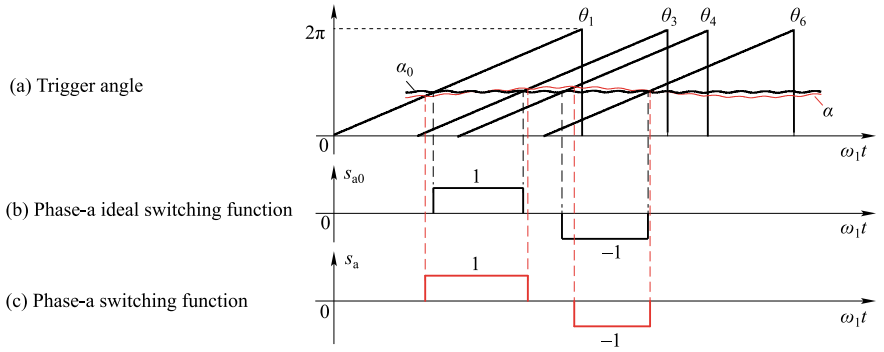

Fig. 5.15 The influence of the small-signal component of the trigger angle on the switching function

The influence of the small-signal component of the trigger angle on the switching function is shown in Fig. 5.15.

As seen in Fig. 5.15, during the normal operation, the switching function changes its value at the instants when the steady-state trigger angle α_0 and the reference angle of each thyristor (θ_1, θ_3, θ_4, θ_6) intersect, and the waveform of the corresponding switching function is s_{a0}. Under the influence of the small-signal component, the intersecting instants of the trigger angle α and reference angle θ_h change. The switching function also changes, and the waveform of the corresponding switching function is s_a. Similarly, the small-signal component of the PLL output angle also has an influence on the switching function.

According to Eqs. (5.51) and (5.52), the instants when there-phase switching functions change their values can be derived as

$$\omega_1 t = \alpha_0 - \varphi_{v1} + \gamma_h + A\cos\left[2\pi(f_p - f_1)t + \varphi\right] + 2p\pi \tag{5.53}$$

where A, φ are the amplitude and phase of the small-signal component of the combined angle, and can be expressed as

$$\begin{aligned} A\cos\left[2\pi(f_p - f_1)t + \varphi\right] = {} & A_\alpha \cos\left[2\pi(f_p - f_1)t + \varphi_\alpha\right] \\ & - A_\theta \cos\left[2\pi(f_p - f_1)t + \varphi_\theta\right] \end{aligned} \tag{5.54}$$

The frequency-domain expression of the small-signal component of the combined angle can be obtained by transforming Eq. (5.54) to the frequency domain.

$$A e^{j\varphi} = A_\alpha e^{j\varphi_\alpha} - A_\theta e^{j\varphi_\theta} \tag{5.55}$$

The analytical results of the small-signal components of the trigger angle and PLL output angle are developed as follows.

According to the DC current control diagram shown in Fig. 5.13, under the effect of the DC current filter $T_{\mathrm{idc}}(s)$ and DC current controller $H_{\mathrm{idc}}(s)$, the small-signal component of the DC current $\hat{\boldsymbol{i}}_{\mathrm{dcp}-1}$ at $f_{\mathrm{p}} - f_1$ leads to the small-signal response of the trigger angle $A_\alpha \mathrm{e}^{j\varphi_\alpha}$. The expression of $A_\alpha \mathrm{e}^{j\varphi_\alpha}$ is given as

$$A_\alpha \mathrm{e}^{j\varphi_\alpha} = T_{\mathrm{idc}}\left[\mathrm{j}2\pi\left(f_{\mathrm{p}} - f_1\right)\right] H_{\mathrm{idc}}\left[\mathrm{j}2\pi\left(f_{\mathrm{p}} - f_1\right)\right] \hat{\boldsymbol{i}}_{\mathrm{dcp}-1} \tag{5.56}$$

According to the PLL control diagram, the small-signal components of the AC voltage at f_{p} and $f_{\mathrm{p}} - 2f_1$ ($\hat{\boldsymbol{v}}_{\mathrm{p}}, \hat{\boldsymbol{v}}_{\mathrm{p}-2}$) lead to the small-signal responses of the dq-axis voltages at $f_{\mathrm{p}} - f_1$, after the Park transformation. Then, under the effect of the PLL control, the small-signal component of the PLL output angle at $f_{\mathrm{p}} - f_1$ ($A_\theta \mathrm{e}^{\mathrm{j}\varphi_\theta}$) is produced. The expression of $A_\theta \mathrm{e}^{\mathrm{j}\varphi_\theta}$ is given as

$$A_\theta \mathrm{e}^{\mathrm{j}\varphi_\theta} = -\mathrm{j}T_{\mathrm{PLL}}\left[\mathrm{j}2\pi\left(f_{\mathrm{p}} - f_1\right)\right]\left(\hat{\boldsymbol{v}}_{\mathrm{p}} - \hat{\boldsymbol{v}}_{\mathrm{p}-2}\right) \tag{5.57}$$

5.4.3.3 Small-Signal Model of Ideal Switching Function

According to Eq. (5.53), it can be seen that the instants when the switching functions change their values are related to the two frequencies: f_1 and $f_{\mathrm{p}} - f_1$. Letting

$$\begin{cases} x_{\omega\mathrm{t}} = 2\pi f_1 t \\ y_{\omega\mathrm{t}} = 2\pi(f_{\mathrm{p}} - f_1)t \end{cases} \tag{5.58}$$

The switching functions can be expressed as the functions of $x_{\omega\mathrm{t}}$ and $y_{\omega\mathrm{t}}$, $s_l = f[x_{\omega\mathrm{t}}, y_{\omega\mathrm{t}}]$. Taking phase a as an example, based on Eqs. (5.53) and (5.58), γ_h are taken as γ_1, γ_3, γ_4, γ_6, and the boundary conditions where the phase-a switching function changes its value are

$$\begin{cases} x_{\omega\mathrm{t}1} = A\cos(y_{\omega\mathrm{t}} + \varphi) + \alpha_0 - \varphi_{\mathrm{v}1} + \gamma_1 \\ x_{\omega\mathrm{t}3} = A\cos(y_{\omega\mathrm{t}} + \varphi) + \alpha_0 - \varphi_{\mathrm{v}1} + \gamma_3 \\ x_{\omega\mathrm{t}4} = A\cos(y_{\omega\mathrm{t}} + \varphi) + \alpha_0 - \varphi_{\mathrm{v}1} + \gamma_4 \\ x_{\omega\mathrm{t}6} = A\cos(y_{\omega\mathrm{t}} + \varphi) + \alpha_0 - \varphi_{\mathrm{v}1} + \gamma_6 \end{cases} \tag{5.59}$$

Ignoring the commutation process, the voltage and current switching functions are identical. The ideal switching function $s_{\mathrm{a}} = f[x_{\omega\mathrm{t}}, y_{\omega\mathrm{t}}]$ is shown in Fig. 5.16. In the figure, $s_{\mathrm{a}} = 1$ in the orange shaded area ($x_{\omega\mathrm{t}1} \le x_{\omega\mathrm{t}} \le x_{\omega\mathrm{t}3}$), $s_{\mathrm{a}} = -1$ in the blue shaded area ($x_{\omega\mathrm{t}4} \le x_{\omega\mathrm{t}} \le x_{\omega\mathrm{t}6}$), and $s_{\mathrm{a}} = 0$ outside the two shaded areas. The envelopes of $x_{\omega\mathrm{t}1}, x_{\omega\mathrm{t}3}, x_{\omega\mathrm{t}4}, x_{\omega\mathrm{t}6}$ vary periodically with $y_{\omega\mathrm{t}}$. The boundary conditions where the switching function changes its value are determined by Eqs. (5.58) and (5.59) together, corresponding to the intersect points between $y_{\omega\mathrm{t}} = \frac{f_{\mathrm{p}} - f_1}{f_1} x_{\omega\mathrm{t}}$ with $x_{\omega\mathrm{t}1}, x_{\omega\mathrm{t}3}, x_{\omega\mathrm{t}4}, x_{\omega\mathrm{t}6}$, as shown in Fig. 5.16.

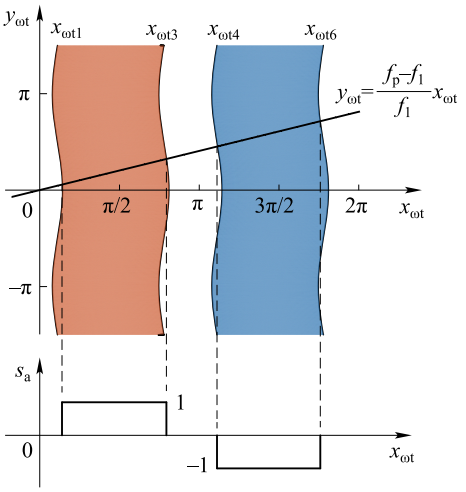

Fig. 5.16 The determination of the ideal switching function

The switching function $s_a = f[x_{\omega t}, y_{\omega t}]$ is a nonlinear piecewise function. Since s_a varies periodically with $x_{\omega t}$ and $y_{\omega t}$, and the frequency-domain expression of s_a can be obtained with the double Fourier series.

$$\boldsymbol{s}_a = \sum_{k=-\infty}^{\infty} \sum_{m=-\infty}^{\infty} \boldsymbol{S}_a[k, m] e^{jkx_{\omega t}} e^{jmy_{\omega t}} \tag{5.60}$$

where $\boldsymbol{S}_a[k, m]$ is the complex Fourier coefficient of the switching function $s_a = f[x_{\omega t}, y_{\omega t}]$ at the frequency $kf_1 + m(f_p - f_1)$.

The expression of $\boldsymbol{S}_a[k, m]$ can be calculated by integrating $s_a = f[x_{\omega t}, y_{\omega t}]$ over the unit cell area.

$$\boldsymbol{S}_a[k, m] = \frac{1}{4\pi^2} \int_{\tau-\pi}^{\tau+\pi} \int_{\sigma}^{\sigma+2\pi} f[x_{\omega t}, y_{\omega t}] e^{-jkx_{\omega t}} e^{-jmy_{\omega t}} dx_{\omega t} dy_{\omega t} \tag{5.61}$$

where σ, τ are arbitrary to satisfy $x_{\omega t} \in [\sigma, \sigma + 2\pi]$ and $y_{\omega t} \in [\tau - \pi, \tau + \pi]$.

Substituting Eq. (5.59) into Eq. (5.61) gives

$$\begin{aligned} \boldsymbol{S}_a[k, m] = & \frac{e^{-jk\alpha_0} e^{jk\varphi_{v1}} e^{jm\varphi} e^{-jm\pi/2} J_m(kA)}{-j2k\pi} \\ & \cdot \left(e^{-jk\pi/3} - e^{jk\pi/3} - e^{-j4k\pi/3} + e^{-j2k\pi/3} \right) \end{aligned} \tag{5.62}$$

where $J_m(kA)$ is the Bessel function of the first kind.

If the injected perturbation is small, the amplitude of the small-signal component of the combined angle A is small and $kA \to 0$. The following relationship is satisfied

$$\begin{cases} J_0(kA) \approx 1 \\ J_1(kA) = -J_{-1}(kA) \approx \dfrac{kA}{2} \\ \cdots \end{cases} \tag{5.63}$$

Simplifying Eq. (5.62), $\boldsymbol{S}_{\mathrm{a}}[k, m]$ can be expressed as

$$\begin{aligned} \boldsymbol{S}_{\mathrm{a}}[k, m] = & \frac{\sin(k\pi/3)\left(1 - \mathrm{e}^{-\mathrm{j}k\pi}\right)}{k\pi} J_m(kA) \\ & \mathrm{e}^{\mathrm{j}m\varphi} \mathrm{e}^{-\mathrm{j}m\pi/2} \mathrm{e}^{-\mathrm{j}k\alpha_0} \mathrm{e}^{\mathrm{j}k\varphi_{\mathrm{v1}}}, \quad k = 6n \pm 1 \end{aligned} \tag{5.64}$$

Based on the phase-sequence relationship of the steady-state vectors, the switching functions in phase b and phase c can be obtained.

$$\begin{cases} \boldsymbol{S}_{\mathrm{b}}[k, m] = \mathrm{e}^{-\mathrm{j}2k\pi/3} \boldsymbol{S}_{\mathrm{a}}[k, m] \\ \boldsymbol{S}_{\mathrm{c}}[k, m] = \mathrm{e}^{\mathrm{j}2k\pi/3} \boldsymbol{S}_{\mathrm{a}}[k, m] \end{cases} \tag{5.65}$$

Based on Eq. (5.64), the analytical results of the steady-state and small-signal vectors of the switching functions will be analyzed as follows.

According to Eq. (5.64), when $m = 0$, $\boldsymbol{S}_{\mathrm{a}}[k, 0]$ is the steady-state component of the switching function at kf_1, which corresponds to the element in the steady-state vectors $\boldsymbol{S}_{\mathrm{va}}$, $\boldsymbol{S}_{\mathrm{ia}}$ shown in Eq. (5.22). Without considering the commutation process, the expression of the steady-state components of the ideal switching function at kf_1 can be derived by substituting $m = 0$ into Eq. (5.64).

$$\begin{aligned} \boldsymbol{S}_{\mathrm{v}k} = \boldsymbol{S}_{\mathrm{i}k} &= \boldsymbol{S}_{\mathrm{a}}[k, 0] \\ &= \frac{\sin(k\pi/3)\left(1 - \mathrm{e}^{-\mathrm{j}k\pi}\right)}{k\pi} \mathrm{e}^{-\mathrm{j}k\alpha_0} \mathrm{e}^{\mathrm{j}k\varphi_{\mathrm{v1}}}, \quad k = 6n \pm 1 \end{aligned} \tag{5.66}$$

where the switching function contains the steady-state harmonic components at $(6n \pm 1) f_1$, and the other components are zero.

According to Eqs. (5.65) and (5.66), the frequency-domain steady-state components of the three-phase ideal switching functions are listed in Table 5.8. It can be seen that the steady-state components of the ideal switching function are related to α_0, φ_{v1}, and frequency order k ($k = 6n \pm 1$).

Besides, Table 5.9 lists the analytical and simulation results of the steady-state components of the three-phase ideal switching functions as $n = 0, 1, 2$. The main circuit parameters are listed in Table 5.5. The analytical results of the steady-state components at each frequency match with the simulation results well.

According to Eq. (5.64), when $m = \pm 1$, the following results can be derived.

Table 5.8 The frequency-domain steady-state components of the ideal switching function

Steady-State Components of Ideal Switching Function	Frequency-Domain Results at kf_1 ($k = 6n \pm 1$)
$\boldsymbol{S}_{\mathrm{a}}[k, 0]$	$\frac{\sin(k\pi/3)\left(1-\mathrm{e}^{-\mathrm{j}k\pi}\right)}{k\pi}\mathrm{e}^{-\mathrm{j}k\alpha_0}\mathrm{e}^{\mathrm{j}k\varphi_{\mathrm{v1}}}$
$\boldsymbol{S}_{\mathrm{b}}[k, 0]$	$\frac{\sin(k\pi/3)\left(1-\mathrm{e}^{-\mathrm{j}k\pi}\right)}{k\pi}\mathrm{e}^{-\mathrm{j}k\alpha_0}\mathrm{e}^{\mathrm{j}k\varphi_{\mathrm{v1}}}\mathrm{e}^{-\mathrm{j}2k\pi/3}$
$\boldsymbol{S}_{\mathrm{c}}[k, 0]$	$\frac{\sin(k\pi/3)\left(1-\mathrm{e}^{-\mathrm{j}k\pi}\right)}{k\pi}\mathrm{e}^{-\mathrm{j}k\alpha_0}\mathrm{e}^{\mathrm{j}k\varphi_{\mathrm{v1}}}\mathrm{e}^{\mathrm{j}2k\pi/3}$

Table 5.9 The analytical and simulation results of the steady-state components of the ideal switching function

Frequency	Analytical Results		Simulation Results	
$(6n \pm 1) f_1$	Amplitude	Phase	Amplitude	Phase
$\pm f_1$	0.5513	$\mp 26.98°$	0.5499	$\mp 27.08°$
$\pm 5f_1$	0.1103	$\pm 45.11°$	0.1115	$\pm 44.64°$
$\pm 7f_1$	0.0788	$\pm 171.15°$	0.0771	$\pm 170.33°$
$\pm 11f_1$	0.0501	$\mp 116.76°$	0.0511	$\mp 117.67°$
$\pm 13f_1$	0.0424	$\pm 9.28°$	0.0406	$\pm 7.59°$

$$\begin{cases} \boldsymbol{S}_{\mathrm{a}}[k, 1] = -\mathrm{j}\dfrac{\sin(k\pi/3)\left(1-\mathrm{e}^{-\mathrm{j}k\pi}\right)}{2\pi} A\mathrm{e}^{\mathrm{j}\varphi}\mathrm{e}^{-\mathrm{j}k\alpha_0}\mathrm{e}^{\mathrm{j}k\varphi_{\mathrm{v1}}} \\ \boldsymbol{S}_{\mathrm{a}}[k, -1] = -\mathrm{j}\dfrac{\sin(k\pi/3)\left(1-\mathrm{e}^{-\mathrm{j}k\pi}\right)}{2\pi} A\mathrm{e}^{-\mathrm{j}\varphi}\mathrm{e}^{-\mathrm{j}k\alpha_0}\mathrm{e}^{\mathrm{j}k\varphi_{\mathrm{v1}}} \end{cases} \tag{5.67}$$

where $\boldsymbol{S}_{\mathrm{a}}[k, 1]$ is the small-signal component of the switching function at $kf_1 + f_{\mathrm{p}} - f_1$; $\boldsymbol{S}_{\mathrm{a}}[k, -1]$ is the small-signal component of the switching function at $kf_1 - (f_{\mathrm{p}} - f_1)$.

The small-signal components at $kf_1 + f_{\mathrm{p}} - f_1$ and $-kf_1 - (f_{\mathrm{p}} - f_1)$, i.e., $\boldsymbol{S}_{\mathrm{a}}[k, 1]$ and $\boldsymbol{S}_{\mathrm{a}}[-k, -1]$, constitute the actual component at $kf_1 + f_{\mathrm{p}} - f_1$. Besides, according to Eq. (5.64), their relationship satisfies

$$\boldsymbol{S}_{\mathrm{a}}^{*}[-k, -1] = \boldsymbol{S}_{\mathrm{a}}[k, 1] \tag{5.68}$$

For the element in the small-signal vector of the ideal switching function shown in Eq. (5.36), the small-signal component of the ideal switching function at $f_{\mathrm{p}} - f_1 + kf_1$ can be derived as

$$\begin{aligned} \hat{\boldsymbol{s}}_{\mathrm{vp}+k-1} &= \hat{\boldsymbol{s}}_{\mathrm{ip}+k-1} = 2\boldsymbol{S}_{\mathrm{a}}[k, 1] \\ &= -\mathrm{j}\frac{\sin(k\pi/3)\left(1-\mathrm{e}^{-\mathrm{j}k\pi}\right)}{\pi} A\mathrm{e}^{\mathrm{j}\varphi}\mathrm{e}^{-\mathrm{j}k\alpha_0}\mathrm{e}^{\mathrm{j}k\varphi_{\mathrm{v1}}},\ k = 6n \pm 1 \end{aligned} \tag{5.69}$$

Table 5.10 The frequency-domain small-signal components of the ideal switching function

Small-Signal Components of Ideal Switching Function	Frequency-Domain Results at $kf_1 + f_p - f_1$ $(k = 6n \pm 1)$
$2\boldsymbol{S}_a[k, 1]$	$-\mathrm{j}\frac{\sin(k\pi/3)\left(1-\mathrm{e}^{-\mathrm{j}k\pi}\right)}{\pi} A\mathrm{e}^{\mathrm{j}\varphi}\mathrm{e}^{-\mathrm{j}k\alpha_0}\mathrm{e}^{\mathrm{j}k\varphi_{v1}}$
$2\boldsymbol{S}_b[k, 1]$	$-\mathrm{j}\frac{\sin(k\pi/3)\left(1-\mathrm{e}^{-\mathrm{j}k\pi}\right)}{\pi} A\mathrm{e}^{\mathrm{j}\varphi}\mathrm{e}^{-\mathrm{j}k\alpha_0}\mathrm{e}^{\mathrm{j}k\varphi_{v1}}\mathrm{e}^{-\mathrm{j}2k\pi/3}$
$2\boldsymbol{S}_c[k, 1]$	$-\mathrm{j}\frac{\sin(k\pi/3)\left(1-\mathrm{e}^{-\mathrm{j}k\pi}\right)}{\pi} A\mathrm{e}^{\mathrm{j}\varphi}\mathrm{e}^{-\mathrm{j}k\alpha_0}\mathrm{e}^{\mathrm{j}k\varphi_{v1}}\mathrm{e}^{\mathrm{j}2k\pi/3}$

where the switching function contains the small-signal components at $(6n \pm 1) f_1 + f_p - f_1$, and the other components are zero.

According to Eq. (5.69), the frequency-domain small-signal components of the three-phase ideal switching functions are listed in Table 5.10. It can be seen that the small-signal components of the ideal switching function are related to α_0, φ_{v1}, frequency order k ($k = 6n \pm 1$), and the small-signal component of the combined angle $A\mathrm{e}^{\mathrm{j}\varphi}$.

Comparing Eqs. (5.66) and (5.69), the relationship between the small-signal components of the ideal switching function with the steady-state components of the ideal switching function satisfies

$$\begin{cases} \hat{\boldsymbol{s}}_{vp+k-1} = -\mathrm{j}kA\mathrm{e}^{\mathrm{j}\varphi}\boldsymbol{S}_{vk} \\ \hat{\boldsymbol{s}}_{ip+k-1} = -\mathrm{j}kA\mathrm{e}^{\mathrm{j}\varphi}\boldsymbol{S}_{ik} \end{cases}, \quad k = 6n \pm 1 \tag{5.70}$$

It can be seen that the small-signal components of the switching function at $(6n \pm 1) f_1 + f_p - f_1$ are the sideband of the steady-state components at $(6n \pm 1) f_1$.

The second and higher-order ($|m| \geq 2$) small-signal components $\boldsymbol{S}_a[k, m]$ are ignored in the linearization modeling process.

5.4.3.4 Small-Signal Model of Switching Function with Commutation Influence

Considering the commutation process, the switching function does not present an ideal rectangular wave, and the voltage and current switching functions are inconsistent. The voltage and current switching functions are shown in Fig. 5.17.

Substituting the boundary conditions shown in Eq. (5.59) into Eq. (5.18) and Eq. (5.19), the variations of the voltage and current switching functions with the influence of the commutation can be expressed as

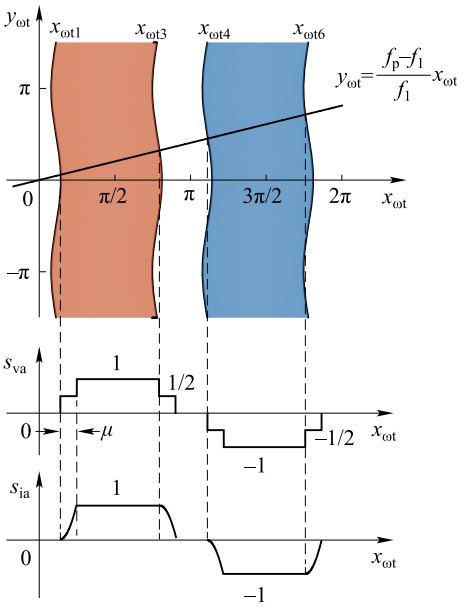

Fig. 5.17 The determination of the voltage and current switching function with the influence of the commutation

$$\Delta s_{va} = \begin{cases} -\dfrac{1}{2}, & x_{\omega t1} \le \omega_1 t < x_{\omega t1} + \mu \\ \dfrac{1}{2}, & x_{\omega t3} \le \omega_1 t < x_{\omega t3} + \mu \\ \dfrac{1}{2}, & x_{\omega t4} \le \omega_1 t < x_{\omega t4} + \mu \\ -\dfrac{1}{2}, & x_{\omega t6} \le \omega_1 t < x_{\omega t6} + \mu \end{cases} \tag{5.71}$$

$$\Delta s_{ia} = \begin{cases} -\dfrac{\cos(\omega_1 t + \pi/3) - \cos(\alpha + \mu)}{\cos\alpha - \cos(\alpha + \mu)}, & x_{\omega t1} \le \omega_1 t < x_{\omega t1} + \mu \\ \dfrac{\cos(\omega_1 t - \pi/3) - \cos(\alpha + \mu)}{\cos\alpha - \cos(\alpha + \mu)}, & x_{\omega t3} \le \omega_1 t < x_{\omega t3} + \mu \\ \dfrac{\cos(\omega_1 t - 2\pi/3) - \cos(\alpha + \mu)}{\cos\alpha - \cos(\alpha + \mu)}, & x_{\omega t4} \le \omega_1 t < x_{\omega t4} + \mu \\ -\dfrac{\cos(\omega_1 t - 4\pi/3) - \cos(\alpha + \mu)}{\cos\alpha - \cos(\alpha + \mu)}, & x_{\omega t6} \le \omega_1 t < x_{\omega t6} + \mu \end{cases} \tag{5.72}$$

According to Eq. (5.61), the complex Fourier coefficients of the voltage switching function variation can be obtained by applying the double Fourier series to Eq. (5.71).

$$\Delta \boldsymbol{S}_{\mathrm{va}}[k,m]=\frac{\mathrm{e}^{-\mathrm{j}k\mu}-1}{2}\boldsymbol{S}_{\mathrm{a}}[k,m] \tag{5.73}$$

The frequency-domain expression of the voltage switching function considering the commutation process is given as

$$\boldsymbol{S}_{\mathrm{va}}[k,m]=\frac{1+\mathrm{e}^{-\mathrm{j}k\mu}}{2}\boldsymbol{S}_{\mathrm{a}}[k,m] \tag{5.74}$$

Compared with the ideal switching function, the commutation process results in the amplitude and phase changes of the steady-state and small-signal components of the voltage switching function, without affecting the frequency distribution characteristics of the characteristic harmonic components.

The element at $(6n\pm 1)f_1$ in the steady-state vectors of the voltage switching function $\boldsymbol{S}_{\mathrm{va}}$ is derived as

$$\begin{aligned}\boldsymbol{S}_{\mathrm{v}k}=\boldsymbol{S}_{\mathrm{va}}[k,0]=&\frac{\sin(k\pi/3)\left(1-\mathrm{e}^{-\mathrm{j}k\pi}\right)\left(1+\mathrm{e}^{-\mathrm{j}k\mu}\right)}{2k\pi}\\&\mathrm{e}^{-\mathrm{j}k\alpha_0}\mathrm{e}^{\mathrm{j}k\varphi_{\mathrm{v}1}},\quad k=6n\pm 1\end{aligned} \tag{5.75}$$

The element at $(6n\pm 1)f_1+f_{\mathrm{p}}-f_1$ in the small-signal vectors of the voltage switching function $\hat{\boldsymbol{s}}_{\mathrm{va}}$ is derived as

$$\hat{\boldsymbol{s}}_{\mathrm{vp}+k-1}=2\boldsymbol{S}_{\mathrm{va}}[k,1]=-\mathrm{j}kA\mathrm{e}^{\mathrm{j}\varphi}\boldsymbol{S}_{\mathrm{v}k},\quad k=6n\pm 1 \tag{5.76}$$

The steady-state and small-signal components of the three-phase voltage switching functions are listed in Table 5.11. It can be seen that both the steady-state and small-signal components of the voltage switching functions are related to α_0, $\varphi_{\mathrm{v}1}$, and overlap angle μ. In addition, the small-signal components of the voltage switching functions are also related to $A\mathrm{e}^{\mathrm{j}\varphi}$.

As shown in Eq. (5.72), the changes of the current switching functions are nonlinear, so the frequency-domain results of the current switching functions are difficult to solve. It is necessary to linearize the current switching functions.

According to Eq. (5.72), integrating the current switching function variation between x_{h} and $x_{\mathrm{h}}+\mu$, and equating it to the area of the equivalent triangular pulse, gives the equivalent current overlap angle μ_{i}

$$\mu_{\mathrm{i}}=2\frac{\sin(\alpha_0+\mu)-\sin\alpha_0-\mu\cos(\alpha_0+\mu)}{\cos\alpha-\cos(\alpha_0+\mu)} \tag{5.77}$$

After the linearization, the expression of the current switching function variation is given as

Table 5.11 The frequency-domain results of the voltage switching function

Components	Voltage Switching Function	Frequency-Domain Results
Steady-state components at kf_1 ($k = 6n \pm 1$)	$\boldsymbol{S}_{\mathrm{va}}[k, 0]$	$\frac{\sin(k\pi/3)\left(1-\mathrm{e}^{-\mathrm{j}k\pi}\right)\left(1+\mathrm{e}^{-\mathrm{j}k\mu}\right)}{2k\pi}\mathrm{e}^{-\mathrm{j}k\alpha_0}\mathrm{e}^{\mathrm{j}k\varphi_{\mathrm{v}1}}$
	$\boldsymbol{S}_{\mathrm{vb}}[k, 0]$	$\frac{\sin(k\pi/3)\left(1-\mathrm{e}^{-\mathrm{j}k\pi}\right)\left(1+\mathrm{e}^{-\mathrm{j}k\mu}\right)}{2k\pi}\mathrm{e}^{-\mathrm{j}k\alpha_0}\mathrm{e}^{\mathrm{j}k\varphi_{\mathrm{v}1}}\mathrm{e}^{-\mathrm{j}2k\pi/3}$
	$\boldsymbol{S}_{\mathrm{vc}}[k, 0]$	$\frac{\sin(k\pi/3)\left(1-\mathrm{e}^{-\mathrm{j}k\pi}\right)\left(1+\mathrm{e}^{-\mathrm{j}k\mu}\right)}{2k\pi}\mathrm{e}^{-\mathrm{j}k\alpha_0}\mathrm{e}^{\mathrm{j}k\varphi_{\mathrm{v}1}}\mathrm{e}^{\mathrm{j}2k\pi/3}$
Small-signal components at $kf_1 + f_{\mathrm{p}} - f_1$ ($k = 6n \pm 1$)	$2\boldsymbol{S}_{\mathrm{va}}[k, 1]$	$-\mathrm{j}\frac{\sin(k\pi/3)\left(1-\mathrm{e}^{-\mathrm{j}k\pi}\right)\left(1+\mathrm{e}^{-\mathrm{j}k\mu}\right)}{2\pi}A\mathrm{e}^{\mathrm{j}\varphi}\mathrm{e}^{-\mathrm{j}k\alpha_0}\mathrm{e}^{\mathrm{j}k\varphi_{\mathrm{v}1}}$
	$2\boldsymbol{S}_{\mathrm{vb}}[k, 1]$	$-\mathrm{j}\frac{\sin(k\pi/3)\left(1-\mathrm{e}^{-\mathrm{j}k\pi}\right)\left(1+\mathrm{e}^{-\mathrm{j}k\mu}\right)}{2\pi}A\mathrm{e}^{\mathrm{j}\varphi}\mathrm{e}^{-\mathrm{j}k\alpha_0}\mathrm{e}^{\mathrm{j}k\varphi_{\mathrm{v}1}}\mathrm{e}^{-\mathrm{j}2k\pi/3}$
	$2\boldsymbol{S}_{\mathrm{vc}}[k, 1]$	$-\mathrm{j}\frac{\sin(k\pi/3)\left(1-\mathrm{e}^{-\mathrm{j}k\pi}\right)\left(1+\mathrm{e}^{-\mathrm{j}k\mu}\right)}{2\pi}A\mathrm{e}^{\mathrm{j}\varphi}\mathrm{e}^{-\mathrm{j}k\alpha_0}\mathrm{e}^{\mathrm{j}k\varphi_{\mathrm{v}1}}\mathrm{e}^{\mathrm{j}2k\pi/3}$

$$\Delta s_{\mathrm{ia}} = \begin{cases} \dfrac{1}{\mu_{\mathrm{i}}}(x_{\omega\mathrm{t}} - x_{\omega\mathrm{t}1}) - 1, & x_{\omega\mathrm{t}1} \le \omega_1 t \le x_{\omega\mathrm{t}1} + \mu_{\mathrm{i}} \\ -\dfrac{1}{\mu_{\mathrm{i}}}(x_{\omega\mathrm{t}} - x_{\omega\mathrm{t}3}) + 1, & x_{\omega\mathrm{t}3} \le \omega_1 t \le x_{\omega\mathrm{t}3} + \mu_{\mathrm{i}} \\ -\dfrac{1}{\mu_{\mathrm{i}}}(x_{\omega\mathrm{t}} - x_{\omega\mathrm{t}4}) + 1, & x_{\omega\mathrm{t}4} \le \omega_1 t \le x_{\omega\mathrm{t}4} + \mu_{\mathrm{i}} \\ \dfrac{1}{\mu_{\mathrm{i}}}(x_{\omega\mathrm{t}} - x_{\omega\mathrm{t}6}) - 1, & x_{\omega\mathrm{t}6} \le \omega_1 t \le x_{\omega\mathrm{t}6} + \mu_{\mathrm{i}} \end{cases} \tag{5.78}$$

According to Eq. (5.61), the complex Fourier coefficients of the current switching function variation can be obtained by applying the double Fourier series to Eq. (5.78).

$$\Delta \boldsymbol{S}_{\mathrm{ia}}[k, m] = \left(-1 + \mathrm{j}\frac{\mathrm{e}^{-\mathrm{j}k\mu_{\mathrm{i}}} - 1}{k\mu_{\mathrm{i}}}\right)\boldsymbol{S}_{\mathrm{a}}[k, m] \tag{5.79}$$

The frequency-domain expression of the voltage switching function considering the commutation process is given as

$$\boldsymbol{S}_{\mathrm{ia}}[k, m] = \left(\mathrm{j}\frac{\mathrm{e}^{-\mathrm{j}k\mu_{\mathrm{i}}} - 1}{k\mu_{\mathrm{i}}}\right)\boldsymbol{S}_{\mathrm{a}}[k, m] \tag{5.80}$$

Compared with the ideal switching function, the commutation process results in the amplitude and phase changes of the steady-state and small-signal components of the current switching function, without affecting the frequency distribution characteristics of the characteristic harmonic components.

The element at $(6n \pm 1) f_1$ in the steady-state vectors of the current switching function $\boldsymbol{S}_{ik}$ is derived as

$$\boldsymbol{S}_{ik} = \boldsymbol{S}_{ia}[k, 0] = \mathrm{j}\frac{\sin(k\pi/3)\left(1 - \mathrm{e}^{-\mathrm{j}k\pi}\right)\left(\mathrm{e}^{-\mathrm{j}k\mu_i} - 1\right)}{k^2\pi\mu_i} \mathrm{e}^{-\mathrm{j}k\alpha_0}\mathrm{e}^{\mathrm{j}k\varphi_{v1}}, \quad k = 6n \pm 1 \tag{5.81}$$

The element at $(6n \pm 1) f_1 + f_p - f_1$ in the small-signal vectors of the current switching function $\hat{\boldsymbol{s}}_{ia}$ is derived as

$$\hat{\boldsymbol{s}}_{ip+k-1} = 2\boldsymbol{S}_{ia}[k, 1] = -\mathrm{j}kA\mathrm{e}^{\mathrm{j}\varphi}\boldsymbol{S}_{ik}, \quad k = 6n \pm 1 \tag{5.82}$$

The steady-state and small-signal components of the three-phase current switching functions are listed in Table 5.12. It can be seen that both the steady-state and small-signal components of the current switching functions are related to α_0, φ_{v1}, and equivalent current overlap angle μ_i. In addition, the small-signal components of the current switching functions are also related to $A\mathrm{e}^{\mathrm{j}\varphi}$.

Under the control of PLL and DC current control, the small-signal vectors of the AC voltage $\hat{\boldsymbol{v}}_l$ and DC current $\hat{\boldsymbol{i}}_{dc}$ lead to the small-signal components of the combined angle $A\mathrm{e}^{\mathrm{j}\varphi}$. Then, the small-signal components of the voltage and current switching functions $\hat{\boldsymbol{s}}_{vl}$, $\hat{\boldsymbol{s}}_{il}$ are produced. Besides, $\hat{\boldsymbol{v}}_l$ and $\hat{\boldsymbol{i}}_{dc}$ are also influenced by $\hat{\boldsymbol{s}}_{vl}$ and $\hat{\boldsymbol{s}}_{il}$.

According to Eqs. (5.55), (5.56) and (5.57), the frequency-domain relationship between the small-signal vectors of combined angle $\hat{\boldsymbol{\delta}}$ with $\hat{\boldsymbol{i}}_{dc}$ and $\hat{\boldsymbol{v}}_a$ satisfies

Table 5.12 The frequency-domain results of the current switching function

Components	Voltage Switching Function	Frequency-Domain Results
Steady-state components at kf_1 $(k = 6n \pm 1)$	$\boldsymbol{S}_{ia}[k, 0]$	$\mathrm{j}\frac{\sin(k\pi/3)\left(1 - \mathrm{e}^{-\mathrm{j}k\pi}\right)\left(\mathrm{e}^{-\mathrm{j}k\mu_i} - 1\right)}{k^2\pi\mu_i}\mathrm{e}^{-\mathrm{j}k\alpha_0}\mathrm{e}^{\mathrm{j}k\varphi_{v1}}$
	$\boldsymbol{S}_{ib}[k, 0]$	$\mathrm{j}\frac{\sin(k\pi/3)\left(1 - \mathrm{e}^{-\mathrm{j}k\pi}\right)\left(\mathrm{e}^{-\mathrm{j}k\mu_i} - 1\right)}{k^2\pi\mu_i}\mathrm{e}^{-\mathrm{j}k\alpha_0}\mathrm{e}^{\mathrm{j}k\varphi_{v1}}\mathrm{e}^{-\mathrm{j}2k\pi/3}$
	$\boldsymbol{S}_{ic}[k, 0]$	$\mathrm{j}\frac{\sin(k\pi/3)\left(1 - \mathrm{e}^{-\mathrm{j}k\pi}\right)\left(\mathrm{e}^{-\mathrm{j}k\mu_i} - 1\right)}{k^2\pi\mu_i}\mathrm{e}^{-\mathrm{j}k\alpha_0}\mathrm{e}^{\mathrm{j}k\varphi_{v1}}\mathrm{e}^{\mathrm{j}2k\pi/3}$
Small-signal components at $kf_1 + f_p - f_1$ $(k = 6n \pm 1)$	$2\boldsymbol{S}_{ia}[k, 1]$	$\frac{\sin(k\pi/3)\left(1 - \mathrm{e}^{-\mathrm{j}k\pi}\right)\left(\mathrm{e}^{-\mathrm{j}k\mu_i} - 1\right)}{k\pi\mu_i}A\mathrm{e}^{\mathrm{j}\varphi}\mathrm{e}^{-\mathrm{j}k\alpha_0}\mathrm{e}^{\mathrm{j}k\varphi_{v1}}$
	$2\boldsymbol{S}_{ib}[k, 1]$	$\frac{\sin(k\pi/3)\left(1 - \mathrm{e}^{-\mathrm{j}k\pi}\right)\left(\mathrm{e}^{-\mathrm{j}k\mu_i} - 1\right)}{k\pi\mu_i}A\mathrm{e}^{\mathrm{j}\varphi}\mathrm{e}^{-\mathrm{j}k\alpha_0}\mathrm{e}^{\mathrm{j}k\varphi_{v1}}\mathrm{e}^{-\mathrm{j}2k\pi/3}$
	$2\boldsymbol{S}_{ic}[k, 1]$	$\frac{\sin(k\pi/3)\left(1 - \mathrm{e}^{-\mathrm{j}k\pi}\right)\left(\mathrm{e}^{-\mathrm{j}k\mu_i} - 1\right)}{k\pi\mu_i}A\mathrm{e}^{\mathrm{j}\varphi}\mathrm{e}^{-\mathrm{j}k\alpha_0}\mathrm{e}^{\mathrm{j}k\varphi_{v1}}\mathrm{e}^{\mathrm{j}2k\pi/3}$

$$\hat{\boldsymbol{\delta}} = \boldsymbol{Q}\hat{\boldsymbol{i}}_{\mathrm{dc}} + \boldsymbol{E}\hat{\boldsymbol{v}}_{\mathrm{a}} \tag{5.83}$$

where $\boldsymbol{Q}$, $\boldsymbol{E}$ are $(12g+3)\times(12g+3)$ matrices, and all other elements in the matrices are zero except for Eq. (5.84).

$$\begin{cases} \hat{\boldsymbol{\delta}}(6g+2) = A\mathrm{e}^{\mathrm{j}\varphi} \\ \boldsymbol{Q}(6g+2, 6g+2) = T_{\mathrm{idc}}\left[\mathrm{j}2\pi\left(f_{\mathrm{p}} - f_{\mathrm{l}}\right)\right]H_{\mathrm{idc}}\left[\mathrm{j}2\pi\left(f_{\mathrm{p}} - f_{\mathrm{l}}\right)\right] \\ \boldsymbol{E}(6g+2, 6g+1) = -\mathrm{j}T_{\mathrm{PLL}}\left[\mathrm{j}2\pi\left(f_{\mathrm{p}} - f_{\mathrm{l}}\right)\right] \\ \boldsymbol{E}(6g+2, 6g+3) = \mathrm{j}T_{\mathrm{PLL}}\left[\mathrm{j}2\pi\left(f_{\mathrm{p}} - f_{\mathrm{l}}\right)\right] \end{cases} \tag{5.84}$$

According to Eqs. (5.76) and (5.82), the relationship between $\hat{\boldsymbol{s}}_{\mathrm{va}}$, $\hat{\boldsymbol{s}}_{\mathrm{ia}}$ and $\hat{\boldsymbol{\delta}}$ can be derived as

$$\begin{cases} \hat{\boldsymbol{s}}_{\mathrm{va}} = \boldsymbol{C}\boldsymbol{S}_{\mathrm{va}}\hat{\boldsymbol{\delta}} \\ \hat{\boldsymbol{s}}_{\mathrm{ia}} = \boldsymbol{C}\boldsymbol{S}_{\mathrm{ia}}\hat{\boldsymbol{\delta}} \end{cases} \tag{5.85}$$

where $\boldsymbol{C}$ is the transformation coefficient matrix of the switching functions, expressed as

$$\boldsymbol{C} = -\mathrm{j}\cdot\mathrm{diag}\left[-6g-1, \ldots, 0 \ldots, 6g+1\right] \tag{5.86}$$

Based on the steady-state components of the voltage and current switching functions shown in Eqs. (5.75), and (5.81), the steady-state matrix of the voltage and current switching functions $\boldsymbol{S}_{\mathrm{va}}$, $\boldsymbol{S}_{\mathrm{ia}}$ can be obtained. Then, substituting Eq. (5.83) into Eq. (5.85), the small-signal components of the voltage and current switching functions can be derived.

5.4.4 AC Port Impedance Model

The AC port impedance model of the thyristor converter is established in this section according to the frequency-domain small-signal models of the main circuit and switching functions.

According to the frequency-domain relationship of the small-signal vectors of the AC/DC currents in Eq. (5.43), the relationship between the small-signal vector of the AC current $\hat{\boldsymbol{i}}_{\mathrm{a}}$ with the small-signal vectors of the AC voltage $\hat{\boldsymbol{v}}_{\mathrm{a}}$ and DC current $\hat{\boldsymbol{i}}_{\mathrm{dc}}$ satisfies

$$\hat{\boldsymbol{i}}_{\mathrm{a}} = \boldsymbol{I}_{\mathrm{dc}}\boldsymbol{C}\boldsymbol{S}_{\mathrm{ia}}\boldsymbol{E}\hat{\boldsymbol{v}}_{\mathrm{a}} + (\boldsymbol{I}_{\mathrm{dc}}\boldsymbol{C}\boldsymbol{S}_{\mathrm{ia}}\boldsymbol{Q} + \boldsymbol{S}_{\mathrm{ia}})\hat{\boldsymbol{i}}_{\mathrm{dc}} \tag{5.87}$$

Substituting Eqs. (5.41), (5.85), (5.87) into Eq. (5.44), the small-signal vector of the DC voltage is derived as

$$\begin{aligned}\hat{\boldsymbol{v}}_{\mathrm{dc}} &= \boldsymbol{D}_{\mathrm{ad}}[(\boldsymbol{V}_{\mathrm{Ta}}\boldsymbol{C}\boldsymbol{S}_{\mathrm{va}} - \boldsymbol{S}_{\mathrm{va}}\boldsymbol{Z}_{\mathrm{T}}\boldsymbol{I}_{\mathrm{dc}}\boldsymbol{C}\boldsymbol{S}_{\mathrm{ia}})\boldsymbol{E} + \boldsymbol{S}_{\mathrm{va}}]\hat{\boldsymbol{v}}_{\mathrm{a}} \\ &\quad + \boldsymbol{D}_{\mathrm{ad}}\left[(\boldsymbol{V}_{\mathrm{Ta}}\boldsymbol{C}\boldsymbol{S}_{\mathrm{va}} - \boldsymbol{S}_{\mathrm{va}}\boldsymbol{Z}_{\mathrm{T}}\boldsymbol{I}_{\mathrm{dc}}\boldsymbol{C}\boldsymbol{S}_{\mathrm{ia}})\boldsymbol{Q} - \boldsymbol{S}_{\mathrm{va}}\boldsymbol{Z}_{\mathrm{T}}\boldsymbol{S}_{\mathrm{ia}}\right]\hat{\boldsymbol{i}}_{\mathrm{dc}}\end{aligned} \tag{5.88}$$

According to Eqs. (5.46), (5.87), and (5.88), the AC port admittance of the thyristor converter can be established.

$$\begin{aligned}\boldsymbol{Y} = \frac{\hat{\boldsymbol{i}}_{\mathrm{a}}}{\hat{\boldsymbol{v}}_{\mathrm{a}}} &= \boldsymbol{I}_{\mathrm{dc}}\boldsymbol{C}_{\mathrm{s}}\boldsymbol{S}_{\mathrm{ia}}\boldsymbol{E} \\ &\quad + \frac{(\boldsymbol{I}_{\mathrm{dc}}\boldsymbol{C}\boldsymbol{S}_{\mathrm{ia}}\boldsymbol{Q} + \boldsymbol{S}_{\mathrm{ia}})\boldsymbol{D}_{\mathrm{ad}}\left[\begin{pmatrix}\boldsymbol{V}_{\mathrm{Ta}}\boldsymbol{C}\boldsymbol{S}_{\mathrm{va}} - \\ \boldsymbol{S}_{\mathrm{va}}\boldsymbol{Z}_{\mathrm{T}}\boldsymbol{I}_{\mathrm{dc}}\boldsymbol{C}\boldsymbol{S}_{\mathrm{ia}}\end{pmatrix}\boldsymbol{E} + \boldsymbol{S}_{\mathrm{va}}\right]}{\boldsymbol{Z}_{\mathrm{Ldc}} - \boldsymbol{D}_{\mathrm{ad}}\left[\begin{pmatrix}\boldsymbol{V}_{\mathrm{Ta}}\boldsymbol{C}\boldsymbol{S}_{\mathrm{va}} - \\ \boldsymbol{S}_{\mathrm{va}}\boldsymbol{Z}_{\mathrm{T}}\boldsymbol{I}_{\mathrm{dc}}\boldsymbol{C}\boldsymbol{S}_{\mathrm{ia}}\end{pmatrix}\boldsymbol{Q} - \boldsymbol{S}_{\mathrm{va}}\boldsymbol{Z}_{\mathrm{T}}\boldsymbol{S}_{\mathrm{ia}}\right]}\end{aligned} \tag{5.89}$$

where $\boldsymbol{Y}$ is a $(12g+1) \times (12g+3)$ matrix.

The small-signal components at f_{p} and $f_{\mathrm{p}} - 2f_1$ are the main components in the small-signal vectors of the AC voltage and current of the thyristor converter, while the amplitudes of the other components are relatively small. The characteristics of the AC port impedance or admittance at f_{p} and $f_{\mathrm{p}} - 2f_1$ are more significant. Only relevant elements at these two frequencies are extracted, and the relationship between the small-signal vectors of the AC voltage and current and AC port admittance is reformulated as

$$\begin{bmatrix}\hat{\boldsymbol{i}}_{\mathrm{p}} \\ \hat{\boldsymbol{i}}_{\mathrm{p-2}}\end{bmatrix} = \begin{bmatrix}\boldsymbol{Y}_{\mathrm{pp}} & \boldsymbol{Y}_{\mathrm{np}} \\ \boldsymbol{Y}_{\mathrm{pn}} & \boldsymbol{Y}_{\mathrm{nn}}\end{bmatrix}\begin{bmatrix}\hat{\boldsymbol{v}}_{\mathrm{p}} \\ \hat{\boldsymbol{v}}_{\mathrm{p-2}}\end{bmatrix} \tag{5.90}$$

where the expression of the 2×2 AC port admittance matrix is

$$\begin{bmatrix}\boldsymbol{Y}_{\mathrm{pp}} & \boldsymbol{Y}_{\mathrm{np}} \\ \boldsymbol{Y}_{\mathrm{pn}} & \boldsymbol{Y}_{\mathrm{nn}}\end{bmatrix} = \begin{bmatrix}\boldsymbol{Y}(6g+3, 6g+3) & \boldsymbol{Y}(6g+3, 6g+1) \\ \boldsymbol{Y}(6g+1, 6g+3) & \boldsymbol{Y}(6g+1, 6g+1)\end{bmatrix}$$

where

$\boldsymbol{Y}_{\mathrm{pp}}$ is the positive-sequence admittance, representing the small-signal response of AC current at f_{p} in positive sequence under per unit small-signal perturbation of AC voltage at f_{p} in positive sequence.

$\boldsymbol{Y}_{\mathrm{pn}}$ is the positive-sequence coupled admittance, representing the small-signal response of AC current at $f_{\mathrm{p}} - 2f_1$ in negative sequence under per unit small-signal perturbation of AC voltage at f_{p} in positive sequence.

$\boldsymbol{Y}_{\mathrm{nn}}$ is the negative-sequence admittance, representing the small-signal response of AC current at $f_{\mathrm{p}} - 2f_1$ in negative sequence under per unit small-signal perturbation of AC voltage at $f_{\mathrm{p}} - 2f_1$ in negative sequence.

$\boldsymbol{Y}_{\mathrm{np}}$ is the negative-sequence coupled admittance, representing the small-signal response of AC current at f_{p} in positive sequence under per unit small-signal perturbation of AC voltage at $f_{\mathrm{p}} - 2f_{\mathrm{l}}$ in negative sequence.
$\boldsymbol{Y}(6g+3, 6g+3)$ is the element in the $(6g+3)$th row and the $(6g+3)$th column of $\boldsymbol{Y}$.
$\boldsymbol{Y}(6g+3, 6g+1)$ is the element in the $(6g+3)$th row and the $(6g+1)$th column of $\boldsymbol{Y}$.
$\boldsymbol{Y}(6g+1, 6g+3)$ is the element in the $(6g+1)$th row and the $(6g+3)$th column of $\boldsymbol{Y}$.
$\boldsymbol{Y}(6g+1, 6g+1)$ is the element in the $(6g+1)$th row and the $(6g+1)$th column of $\boldsymbol{Y}$.

The AC port impedance of the thyristor can be obtained by calculating the inverse matrix of the AC port admittance as

$$\begin{bmatrix} \boldsymbol{Z}_{\mathrm{pp}} & \boldsymbol{Z}_{\mathrm{pn}} \\ \boldsymbol{Z}_{\mathrm{np}} & \boldsymbol{Z}_{\mathrm{nn}} \end{bmatrix} = \begin{bmatrix} \boldsymbol{Y}_{\mathrm{pp}} & \boldsymbol{Y}_{\mathrm{np}} \\ \boldsymbol{Y}_{\mathrm{pn}} & \boldsymbol{Y}_{\mathrm{nn}} \end{bmatrix}^{-1} \tag{5.91}$$

$\boldsymbol{Z}_{\mathrm{pp}}$ represents the positive-sequence impedance, which is the element in the first row and the first column of the AC port admittance inverse matrix.
$\boldsymbol{Z}_{\mathrm{pn}}$ represents the positive-sequence coupling impedance, which is the element in the first row and the second column of the AC port admittance inverse matrix.
$\boldsymbol{Z}_{\mathrm{nn}}$ represents the negative-sequence impedance, which is the element in the second row and the second column of the AC port admittance inverse matrix.
$\boldsymbol{Z}_{\mathrm{np}}$ represents the negative-sequence coupling impedance, which is the element in the second row and the first column of the AC port admittance inverse matrix.

In addition, the frequency-domain relationship between the negative-sequence impedance and the positive-sequence impedance satisfies $\boldsymbol{Z}_{\mathrm{nn}} = \boldsymbol{Z}_{\mathrm{pp}}^{*}(\mathrm{j}2\omega_{\mathrm{l}} - s)$, and the frequency-domain relationship between the negative-sequence coupled impedance and the positive-sequence coupling impedance satisfies $\boldsymbol{Z}_{\mathrm{np}} = \boldsymbol{Z}_{\mathrm{pn}}^{*}(\mathrm{j}2\omega_{\mathrm{l}} - s)$.

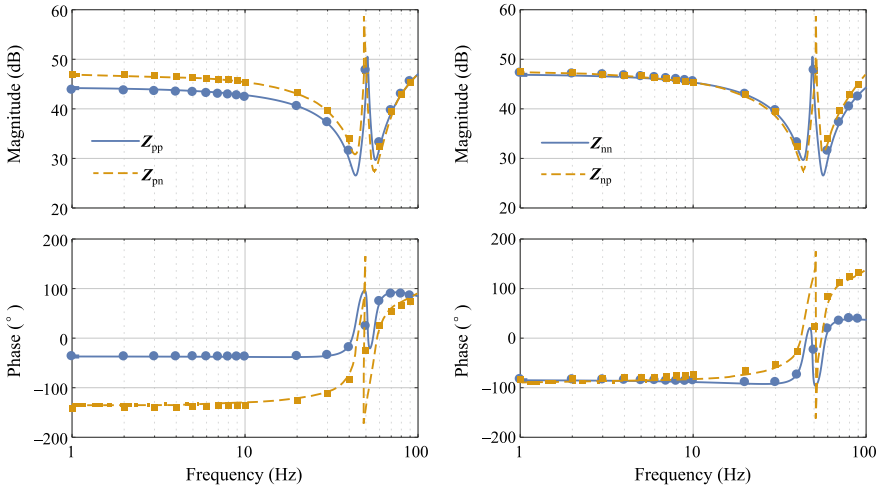

(a) Positive-sequence impedance and positive-sequence coupling impedance

(b) Negative-sequence impedance and negative-sequence coupling impedance

Fig. 5.18 The analytical and scanning results of the AC port impedance of the thyristor converter

The main circuit and controller parameters of the thyristor converter are listed in Table 5.5. Figure 5.18 shows the analytical (in solid lines) and scanning (in discrete points) results of the AC port impedance of the thyristor converter. As seen from the figure, all the discrete points fall on the solid lines, which verifies the accuracy of the established impedance model of the thyristor converter.

Part II
Impedance Model and Characteristic Analysis of REG and HVDC Transmission

The characteristic of the large-scale renewable energy generation (REG) base connected into high voltage direct current (HVDC) transmission system is dominated by the control of the power electronic devices. In order to further study the broadband oscillation problems at the sending end of the HVDC transmission system, this part conducts impedance modeling and characteristic analysis for this power electronic devices, including the wind turbine [1–3], photovoltaic (PV) unit [4], static var generators (SVG) [5], line commutated converter-based high-voltage direct current (LCC-HVDC) [6], and modular multilevel converter-based high-voltage direct current (MMC-HVDC) [7–9]. This part provides the basis for Part III of broadband oscillation analysis and Part IV of broadband oscillation suppression. This part includes the following chapters:

Chapter 6: Impedance Model and Characteristic Analysis of Full Power Converter-based Wind Turbine. The analytical impedance model of the full power conversion wind turbine is established. The main circuit of the full power conversion wind turbine includes the synchronous generator, machine-side converter (MSC), direct current (DC) bus and grid-side converter (GSC), and the control loop includes phase lock loop (PLL), inner alternating current (AC) current loop, DC voltage loop and outer power loop.

Chapter 7: Impedance Model and Characteristic Analysis of DFIG-Based Wind Turbine. The analytical impedance model of the doubly-fed induction generator (DFIG) wind turbine is established and verified. The main circuit of the DFIG wind turbine includes the asynchronous generator, rotor-side converter (RSC), DC bus and GSC, and the control loop includes PLL, AC current loop, DC voltage loop and outer power loop.

Chapter 8: Impedance Model and Characteristic Analysis of PV Unit. The analytical impedance model of the PV unit is established and verified. The main circuit includes the PV array, DC bus and grid-connected inverter, and the control loop includes PLL, AC current loop and DC voltage loop.

Chapter 9: Impedance Model and Characteristic Analysis of SVG. The analytical impedance model of the SVG is established. The main circuit uses cascaded H-bridge

topology, and there are two control modes: reactive power control and constant AC voltage control.

Chapter 10: Impedance Model and Characteristic Analysis of LCC-HVDC. The analytical impedance model of the LCC-HVDC is established. The main circuit includes the sending-end and receiving-end converter stations and DC transmission lines, and the control loop includes DC current control of the sending-end converter station and DC voltage control of the receiving-end converter station.

Chapter 11: Impedance Model and Characteristic Analysis of MMC-HVDC. The analytical impedance model of the MMC-HVDC is established. The main circuit includes the sending-end and receiving-end converter stations and DC transmission lines. The control loop includes AC voltage control/constant power control of the sending-end converter station and DC voltage control of the receiving-end converter station.

In Chaps. 6–11, the dominant factors affecting the impedance characteristics of the wind turbine, PV unit, SVG, LCC-HVDC, and MMC-HVDC are analyzed. Moreover, the frequency band division methods of broadband impedance characteristics are proposed, and the mechanism of the negative damping effect in each frequency band is revealed. Finally, based on the control hardware in the loop (CHIL) simulation platform, the broadband impedance curves of several types of devices are scanned, and the typical values of frequency band division are proposed.

References

1. YANG G, LUO Y L. Electrical machinery and motion control systems [M]. Beijing: Tsinghua University Press, 2006. (Chinese)
2. WU B, LANG Y Q, ZARGARI N, et al. Power conversion and control of wind energy systems [M]. Piscataway, NJ: Wiley-IEEE Press, 2011.
3. HE Y K, HU J B, XU L. Operation control of grid connected doubly fed induction wind turbine [M]. Beijing: China Electric Power Press, 2012. (Chinese)
4. ZHANG X, CAO R X. Solar photovoltaic grid connected power generation and its inverter control [M]. Beijing: China Machine Press, 2011. (Chinese)
5. ZHANG Y, SUN L T, CHEN X, et al. Sequence impedance network model and stability analysis for direct-drive wind farm with static var generator [J]. Proceedings of the CSEE, 2020, 40(9): 2877-2891. (Chinese)
6. JIANG K Z, ZHU J H, HU J B, et al. Small-signal modeling of LCC-HVDC systems with switching for electromagnetic timescale stability analyses of power systems [J]. Journal of Tsinghua University (Science and Technology), 2021, 61(5): 395-402. (Chinese)
7. JI K, TANG G F, PANG H, et al. Impedance modeling and analysis of MMC-HVDC for offshore wind farm integration [J]. IEEE Transactions on Power Delivery, 2020, 35(3): 1488-1501.
8. WU W H, CHEN Y D, LUO A, et al. DC impedance modeling, oscillation analysis and suppression method for VSC-HVDC system in the field of islands power supply [J]. Proceedings of the CSEE, 2018, 38(15): 4359-4368+4636. (Chinese)
9. ZHAO C Y, LIU W J, GUO C Y, et al. Topology of a hybrid transmission system for wind power grid connection [J]. Automation of Electric Power Systems, 2013, 37(15): 146-151. (Chinese)

Chapter 6
Impedance Model and Characteristic Analysis of Full Power Converter-Based Wind Turbine

Full power converter-based wind turbines are connected to the grid for power generation through two two-level converters: machine-side converter (MSC) and grid-side converter (GSC). The control objectives and strategies of MSC and GSC are different [1–3]. In addition, the DC bus connecting MSC and GSC presents non-ideal voltage source characteristic, introducing small-signal frequency coupling path between MSC and GSC.

In this chapter, permanent magnet synchronous generator (PMSG)-based wind turbines are taken as an example to carry out impedance modeling and characteristic analysis for full power converter-based wind turbines [4–6]. Firstly, the impedance model of the PMSG-based wind turbine is established and verified. The main circuit includes the synchronous generator, MSC, DC bus, and GSC. The AC control loops include PLL, AC current loop, DC voltage loop, and power loop. Then, the dominant factors of impedance characteristics in different frequency bands are analyzed. Furthermore, the frequency-band division method of broadband impedance is proposed, and the mechanism of negative damping characteristics in each frequency band is revealed. Finally, based on the CHIL simulation platform [7], the broadband impedances of several types of PMSG-based wind turbines are scanned, and the typical values of frequency-band division are given.

6.1 Operation Principle and Control Strategy

In accordance with the power level of the power electronic converter relative to the generator, wind turbines can be divided into full power converter-based wind turbines and partial power converter-based wind turbines (i.e. DFIG-based wind turbines). The classification of full power converter-based wind turbines is shown in Fig. 6.1. First, depending on the different types of generators, they can be divided into synchronous generator-based wind turbines and asynchronous generators based wind turbines.

© China Electric Power Press 2023

W. Wang et al., *Analysis and Mitigation of Broadband Oscillation in Renewable Energy Generation and AC/DC Transmission Systems*,
https://doi.org/10.1007/978-981-99-1568-2_6

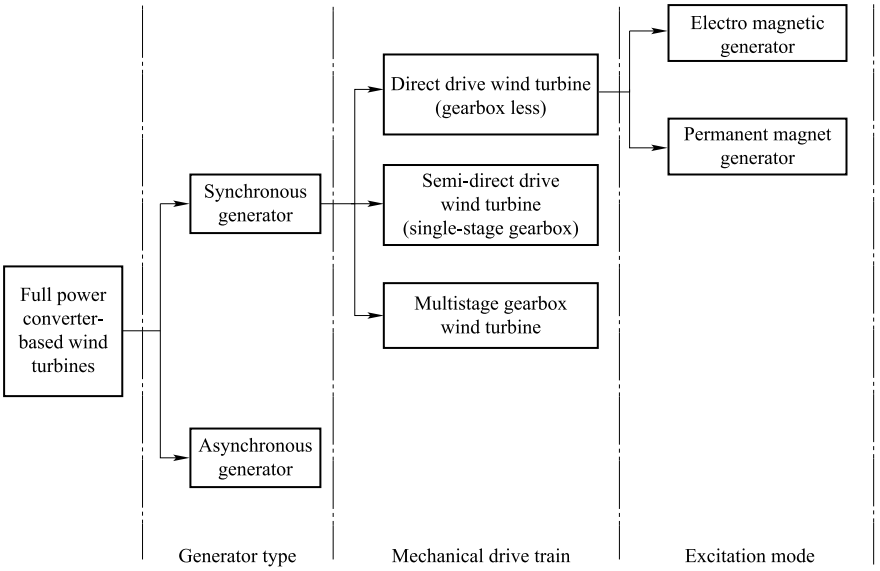

Fig. 6.1 Classification of full power converter-based wind turbines

For synchronous generator-based wind turbines, in accordance with the different mechanical drive trains, they can be further divided into direct drive wind turbines without gearboxes, semi-direct drive wind turbines with single-stage gearboxes, and wind turbines with multistage gearboxes. Direct drive wind turbines, which are the most commonly used type, can be divided into electro-magnetic synchronous generator-based wind turbines and PMSG-based wind turbines, in accordance with their different modes of rotor excitation.[1] In this book, PMSG-based wind turbines are taken as an example to carry out impedance modeling, characteristic analysis and oscillation mitigation for full power converter-based wind turbines.

6.1.1 Operation Principle

The stator of the PMSG-based wind turbine is connected to the grid through a back-to-back converter, and the structure is shown in Fig. 6.2. During the operation of the PMSG-based wind turbine, the wind drives the rotor to rotate, and the frequency of the stator voltage and current depends on the rotor's electrical speed. In order to ensure the output voltage and current of the PMSG-based wind turbine at the rated frequency, a back-to-back converter is required for frequency conversion.

[1] ENERCON, a German wind turbine manufacturer, is a well-known manufacturing enterprise that uses electromagnetic synchronous generators. The difference between the two magnetic methods does not affect the AC port impedance characteristics of the full power converter-based wind turbine.

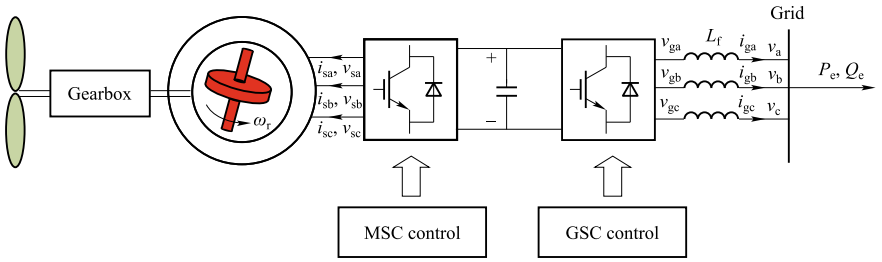

Fig. 6.2 Topology of the PMSG-based wind turbine

MSC is used to convert the voltage and current at the rotor electrical frequency from AC to DC, and GSC is used to convert the voltage and current from DC to AC so as to realize the variable-speed and constant-frequency operation of the PMSG-based wind turbine.

The wind turbine is the first stage of energy conversion, which is used to convert wind energy into mechanical energy. To maximize the utilization of wind energy while considering the power limitation of PMSG, the wind turbine can be controlled to operate in the maximum power point tracking (MPPT) zone, constant speed zone, and constant power zone, as shown in Fig. 6.3. In the MPPT zone, the wind speed is relatively low, the rotor speed and output power of the wind turbine are not reaching to their rated values, so the MPPT control is implemented. At this time, the pitch angle is kept at its minimum value and the wind energy utilization coefficient is kept at maximum and constant. In the constant speed zone, the rotor speed reaches the maximum value, but the output power is not reaching to the rated value. So the wind turbine will no longer operate in the MPPT zone, but maintain the maximum rotor speed. As the wind speed continues to increase, the output power of the wind turbine will increase to the rated value. In the constant power zone, the rotor speed is kept at the maximum value, and the output power will be maintained at the rated value through pitch angle adjustment.

There is a certain correspondence between wind speed, rotor speed and power reference value of the PMSG-based wind turbine. Accordingly, the power reference can be obtained from the wind speed or rotor speed. Taking a 2.0 MW PMSG-based wind turbine of a domestic manufacturer as an example, Fig. 6.4 shows the relationship between wind speed, rotor speed and output power. The cut-in wind speed is 3 m/s, and the cut-out wind speed is 20 m/s. When the wind speed is in the range of 3~9 m/s and the rotor speed is in the range of 5~14 r/min, the wind turbine operates in the MPPT zone, and the corresponding output power is between 70 kW~1.5 MW. With the increase of wind speed, the wind turbine enters the constant speed zone, in which the rotor speed is maintained at 14 r/min, and the output power continues to increase until it reaches 2.0 MW. Then, the wind turbine enters the constant power zone, its rotor speed is maintained at 14 r/min, and its output power is maintained at 2.0 MW.

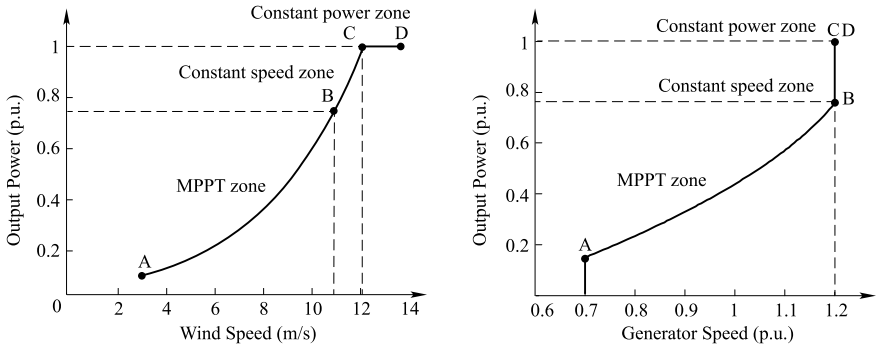

(a) Relationship between output power and wind speed

(b) Relationship between output power and rotor speed

Fig. 6.3 Operation zone of wind turbines

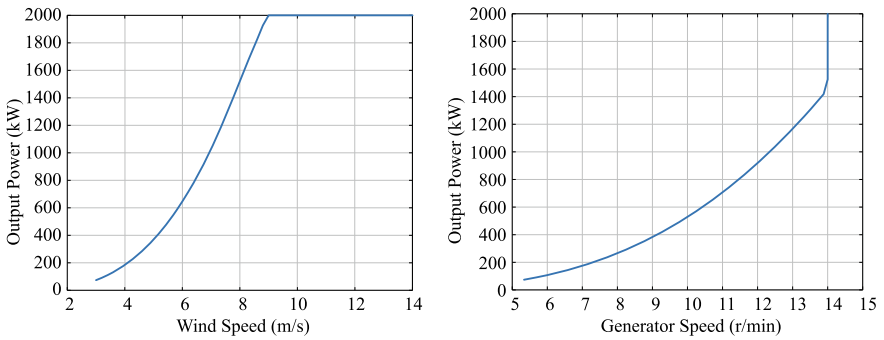

(a) Relationship between output power and wind speed

(b) Relationship between output power and rotor speed

Fig. 6.4 The relationship between output power, wind speed and rotor speed of a 2 MW PMSG-based wind turbine

6.1.2 Time-Domain Model of PMSG-Based Wind Turbine

6.1.2.1 Time-Domain Model in SCF

Since the dynamic mathematical model of PMSG exhibits high-order, nonlinear, strongly coupled characteristics, the following assumptions are adopted to facilitate analysis:

1. The stator three-phase winding is symmetrical, and the three-phase induced electromotive force is sinusoidal wave.
2. The influence of magnetic saturation, eddy current, hysteresis loss, and skin effect is neglected.
3. The conductivity of magnetically hard material is zero.

4. The magnetomotive force of the permanent magnet is constant, that is, the equivalent excitation current remains unchanged.
5. The effects of frequency and temperature variations on generator parameters are not considered.
6. There is no damping winding on the rotor.

Based on the above assumptions, PMSG can be equivalent to the model shown in Fig. 6.5. The stator three-phase winding axes A, B, and C are stationary in space and symmetrically distributed at an electrical angle of $2\pi/3$ with A-axis as the reference coordinate axis. The rotor rotates with an electrical angular velocity ω_r, and the electrical angle difference between the rotor and the A-axis is represented by θ_r. v_{sl} represent the three-phase AC voltages of the stator, i_{sl} represent the three-phase AC currents of the stator, l represents phase a, b, c.

The mathematical model of PMSG in SCF can be expressed by the voltage equation, flux linkage equation, torque equation and motion equation.

1. Voltage Equation

The voltage equation of three-phase stator windings can be given by

$$v_{sl} = R_s i_{sl} + \frac{d\psi_{sl}}{dt} \tag{6.1}$$

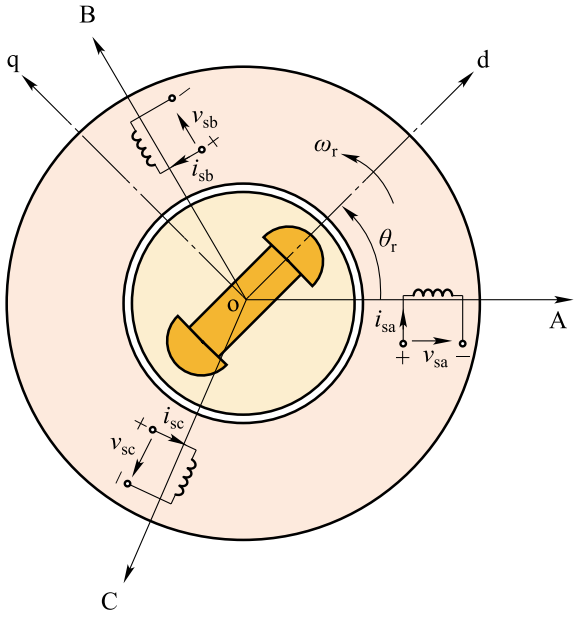

Fig. 6.5 Equivalent model of PMSG

where v_{sl} and i_{sl} $l = \mathrm{a}, \mathrm{b}, \mathrm{c}$ are the three-phase AC voltages and currents of the stator respectively; ψ_{sl} is the three-phase flux linkages of the stator; R_s is the stator resistance.

The voltage equation can be further expressed in the vector form as

$$\boldsymbol{v}_\mathrm{s} = \boldsymbol{R}_\mathrm{s}\boldsymbol{i}_\mathrm{s} + \frac{\mathrm{d}\boldsymbol{\Psi}_\mathrm{s}}{\mathrm{d}t} \tag{6.2}$$

where $\boldsymbol{v}_\mathrm{s} = [\,v_\mathrm{sa},\, v_\mathrm{sb},\, v_\mathrm{sc}\,]^\mathrm{T}$; $\boldsymbol{i}_\mathrm{s} = \left[\,i_\mathrm{sa},\, i_\mathrm{sb},\, i_\mathrm{sc}\,\right]^\mathrm{T}$; $\boldsymbol{\Psi}_\mathrm{s} = \left[\,\psi_\mathrm{sa},\, \psi_\mathrm{sb},\, \psi_\mathrm{sc}\,\right]^\mathrm{T}$; $\boldsymbol{R}_\mathrm{s} = \mathrm{diag}\left[\,R_\mathrm{s},\, R_\mathrm{s},\, R_\mathrm{s}\,\right]$.

2. Flux Linkage Equation

The flux linkage of each stator winding is the sum of its self-inductance flux linkage and the mutual inductance flux linkage with the permanent magnet and other windings. The flux linkage expression is

$$\boldsymbol{\Psi}_\mathrm{s} = \boldsymbol{L}_\mathrm{s}\boldsymbol{i}_\mathrm{s} + \boldsymbol{\Psi}_\mathrm{f} \tag{6.3}$$

with

$$\boldsymbol{L}_\mathrm{s} = \begin{bmatrix} L_\mathrm{s0} + L_\mathrm{s2a} & -M_\mathrm{s0} + M_\mathrm{s2c} & -M_\mathrm{s0} + M_\mathrm{s2b} \\ -M_\mathrm{s0} + M_\mathrm{s2c} & L_\mathrm{s0} + L_\mathrm{s2b} & -M_\mathrm{s0} + M_\mathrm{s2a} \\ -M_\mathrm{s0} + M_\mathrm{s2b} & -M_\mathrm{s0} + M_\mathrm{s2a} & L_\mathrm{s0} + L_\mathrm{s2c} \end{bmatrix}$$

$$\boldsymbol{\Psi}_\mathrm{f} = [\psi_\mathrm{fa}, \psi_\mathrm{fb}, \psi_\mathrm{fc}]^\mathrm{T}$$

where

$L_\mathrm{s2a} = L_\mathrm{s2}\cos 2\theta_\mathrm{r}$, $L_\mathrm{s2b} = L_\mathrm{s2}\cos 2(\theta_\mathrm{r} - 2\pi/3)$, $L_\mathrm{s2c} = L_\mathrm{s2}\cos 2(\theta_\mathrm{r} + 2\pi/3)$,$M_\mathrm{s2a} = M_\mathrm{s2}\cos 2\theta_\mathrm{r}$, $M_\mathrm{s2b} = M_\mathrm{s2}\cos 2(\theta_\mathrm{r} - 2\pi/3)$, $M_\mathrm{s2c} = M_\mathrm{s2}\cos 2(\theta_\mathrm{r} + 2\pi/3)$.

L_s0 and M_s0 are the average values of the self-inductance and mutual inductance of the stator respectively.

L_s2 and M_s2 are the second harmonic amplitudes of stator self-inductance and mutual inductance respectively.

$\boldsymbol{\Psi}_\mathrm{f}$ is the rotor flux linkage. ψ_fa, ψ_fb and ψ_fc are the components of $\boldsymbol{\Psi}_\mathrm{f}$ in three phases. $\psi_\mathrm{fa} = \psi_\mathrm{f}\cos\theta_\mathrm{r}$, $\psi_\mathrm{fb} = \psi_\mathrm{f}\cos(\theta_\mathrm{r} - 2\pi/3)$, $\psi_\mathrm{fc} = \psi_\mathrm{f}\cos(\theta_\mathrm{r} + 2\pi/3)$.$\psi_\mathrm{f}$ is the corresponding amplitude.

3. Torque Equation

According to the principle of electromechanical energy conversion, the stored energy and magnetic co-energy of the magnetic field under linear inductance conditions can be expressed as

$$W_{\mathrm{m}} = \frac{1}{2} \boldsymbol{i}_{\mathrm{s}}^{\mathrm{T}} \boldsymbol{\Psi}_{\mathrm{s}} \tag{6.4}$$

The electromagnetic torque equals to the change rate of magnetic co-energy when the mechanical angular changes. So the torque equation can be written as

$$T_{\mathrm{e}} = p \left. \frac{\partial W_{\mathrm{m}}}{\partial \theta_{\mathrm{r}}} \right|_{i=\text{constant}} \tag{6.5}$$

4. Motion Equation

Neglecting the viscous friction and torsional elasticity in PMSG, the motion equation can be written as

$$\begin{cases} T_{\mathrm{m}} - T_{\mathrm{e}} = \dfrac{J}{p} \dfrac{\mathrm{d}\omega_{\mathrm{r}}}{\mathrm{d}t} \\ \omega_{\mathrm{r}} = \dfrac{\mathrm{d}\theta_{\mathrm{r}}}{\mathrm{d}t} \end{cases} \tag{6.6}$$

where T_{m} is the mechanical torque, J is the mechanical inertia.

6.1.2.2 Time-Domain Model in SRF

Take the direction of the magnetic pole axis as the d-axis, and q-axis is ahead of the d-axis with an electrical angle of $\pi/2$ along the rotation direction. By Park transformation, the time-domain model of PMSG in SCF can be transformed to SRF as

$$\boldsymbol{v}_{\mathrm{sdq}} = \boldsymbol{R}_{\mathrm{sdq}} \boldsymbol{i}_{\mathrm{sdq}} + \frac{\mathrm{d}\boldsymbol{\psi}_{\mathrm{sdq}}}{\mathrm{d}t} + \begin{bmatrix} 0 & -\omega_{\mathrm{r}} \\ \omega_{\mathrm{r}} & 0 \end{bmatrix} \boldsymbol{\psi}_{\mathrm{sdq}} \tag{6.7}$$

$$\boldsymbol{\Psi}_{\mathrm{sdq}} = \boldsymbol{L}_{\mathrm{sdq}} \boldsymbol{i}_{\mathrm{sdq}} + \boldsymbol{\Psi}_{\mathrm{fdq}} \tag{6.8}$$

where

$\boldsymbol{v}_{\mathrm{sdq}} = [\, v_{\mathrm{sd}},\ v_{\mathrm{sq}} \,]^{\mathrm{T}}$, v_{sd} and v_{sq} are the d- and q-axis stator AC voltages respectively.
$\boldsymbol{i}_{\mathrm{sdq}} = \left[\, i_{\mathrm{sd}},\ i_{\mathrm{sq}} \,\right]^{\mathrm{T}}$, i_{sd} and i_{sq} are the d- and q-axis stator AC currents respectively.
$\boldsymbol{\Psi}_{\mathrm{sdq}} = [\, \psi_{\mathrm{sd}},\ \psi_{\mathrm{sq}} \,]^{\mathrm{T}}$, ψ_{sd} and ψ_{sq} are the d- and q-axis stator flux linkages respectively.
$\boldsymbol{\Psi}_{\mathrm{fdq}} = [\, \psi_{\mathrm{fd}},\ \psi_{\mathrm{fq}} \,]^{\mathrm{T}}$, ψ_{fd} and ψ_{fq} are the d- and q-axis rotor flux linkages respectively.
$\boldsymbol{L}_{\mathrm{sdq}} = \mathrm{diag}[\, L_{\mathrm{sd}},\ L_{\mathrm{sq}} \,]$, L_{sd} and L_{sq} are the d- and q-axis inductances respectively, expressed as $L_{\mathrm{sd}} = L_{\mathrm{s0}} + M_{\mathrm{s0}} + 3L_{\mathrm{s2}}/2$ and $L_{\mathrm{sq}} = L_{\mathrm{s0}} + M_{\mathrm{s0}} - 3L_{\mathrm{s2}}/2$.

$$\boldsymbol{R}_{\mathrm{sdq}} = \mathrm{diag}[\, R_{\mathrm{s}},\ R_{\mathrm{s}} \,].$$

In SCF, because of the inhomogeneity of the air gap, the equivalent inductance varies with θ_r. After Park transformation, the equivalent dq-axis winding of the stator is stationary relative to the rotor winding, making the equivalent dq-axis inductance a constant value. The dq-axis voltage, dq-axis current, and dq-axis flux linkage of the stator are also constant.

Substitute the flux linkage equation into the voltage equation, there is

$$\boldsymbol{v}_{\mathrm{sdq}} = \boldsymbol{R}_{\mathrm{sdq}}\boldsymbol{i}_{\mathrm{sdq}} + \boldsymbol{L}_{\mathrm{sdq}}\frac{\mathrm{d}\boldsymbol{i}_{\mathrm{sdq}}}{\mathrm{d}t} + \begin{bmatrix} 0 & -\omega_{\mathrm{r}} \\ \omega_{\mathrm{r}} & 0 \end{bmatrix}\left(\boldsymbol{L}_{\mathrm{sdq}}\boldsymbol{i}_{\mathrm{sdq}} + \boldsymbol{\Psi}_{\mathrm{fdq}}\right) \tag{6.9}$$

Furthermore, the output power expressions of PMSG in SRF can be deduced as

$$\begin{cases} P_{\mathrm{es}} = -\dfrac{3}{2}(v_{\mathrm{sd}}i_{\mathrm{sd}} + v_{\mathrm{sq}}i_{\mathrm{sq}}) \\ Q_{\mathrm{es}} = -\dfrac{3}{2}(v_{\mathrm{sq}}i_{\mathrm{sd}} - v_{\mathrm{sd}}i_{\mathrm{sq}}) \end{cases} \tag{6.10}$$

where P_{es} and Q_{es} are the output active power and reactive power of PMSG respectively.

6.1.2.3 Time-Domain Model under Asymmetric Conditions

Based on the time-domain model in SCF, symmetrical components method is adopted to separate the positive- and negative-sequence components of stator/rotor voltages and flux linkages. By multiplying the transformation matrix $\boldsymbol{B}$ on both sides of the equations, the transformed voltage equation can be obtained as

$$\boldsymbol{v}_{\mathrm{spn}} = \boldsymbol{R}_{\mathrm{s}}\boldsymbol{i}_{\mathrm{spn}} + \frac{\mathrm{d}\boldsymbol{\Psi}_{\mathrm{spn}}}{\mathrm{d}t} \tag{6.11}$$

The transformed flux linkage can be obtained as

$$\boldsymbol{\Psi}_{\mathrm{spn}} = \boldsymbol{B}\boldsymbol{L}_{\mathrm{s}}\boldsymbol{B}^{-1}\boldsymbol{i}_{\mathrm{spn}} + \boldsymbol{\Psi}_{\mathrm{fpn}} \tag{6.12}$$

where

$\boldsymbol{v}_{\mathrm{spn}} = [\, v_{\mathrm{sp}},\ v_{\mathrm{sn}} \,]^{\mathrm{T}}$, v_{sp} and v_{sn} are the positive- and negative-sequence components of the stator voltage respectively.
$\boldsymbol{i}_{\mathrm{spn}} = [\, i_{\mathrm{sp}},\ i_{\mathrm{sn}} \,]^{\mathrm{T}}$, i_{sp} and i_{sn} are the positive- and negative-sequence components of the stator current respectively.
$\boldsymbol{\Psi}_{\mathrm{spn}} = [\, \psi_{\mathrm{sp}},\ \psi_{\mathrm{sn}} \,]^{\mathrm{T}}$, ψ_{sp} and ψ_{sn} are the positive- and negative-sequence components of the stator flux linkage respectively.

$\boldsymbol{\Psi}_{\text{fpn}} = [\psi_{\text{fp}}, \psi_{\text{fn}}]^{\text{T}}$, ψ_{fp} and ψ_{fn} are the positive- and negative-sequence components of the rotor flux linkage respectively.

The expression of the transformation matrix $\boldsymbol{B}$ is

$$\boldsymbol{B} = \frac{1}{3}\begin{bmatrix} 1 & a & a^2 \\ 1 & a^2 & a \end{bmatrix}$$

where

$$a = \mathrm{e}^{\mathrm{j}\frac{2}{3}\pi}.$$

Moreover, it can be inferred that

$$\boldsymbol{B}\boldsymbol{L}_{\text{s}}\boldsymbol{B}^{-1} = \frac{1}{2}\begin{bmatrix} L_{\text{sd}} + L_{\text{sq}} & (L_{\text{sd}} - L_{\text{sq}})\mathrm{e}^{\mathrm{j}2\theta_{\text{r}}} \\ (L_{\text{sd}} - L_{\text{sq}})\mathrm{e}^{-\mathrm{j}2\theta_{\text{r}}} & L_{\text{sd}} + L_{\text{sq}} \end{bmatrix} \tag{6.13}$$

By substituting Eq. (6.12) into Eq. (6.11), there is

$$\begin{aligned} \boldsymbol{v}_{\text{spn}} = \boldsymbol{R}_{\text{s}}\boldsymbol{i}_{\text{spn}} + \frac{1}{2}\frac{\mathrm{d}}{\mathrm{d}t}\begin{bmatrix} L_{\text{sd}} + L_{\text{sq}} & (L_{\text{sd}} - L_{\text{sq}})\mathrm{e}^{\mathrm{j}2\theta_{\text{r}}} \\ (L_{\text{sd}} - L_{\text{sq}})\mathrm{e}^{-\mathrm{j}2\theta_{\text{r}}} & L_{\text{sd}} + L_{\text{sq}} \end{bmatrix}\boldsymbol{i}_{\text{spn}} \\ + \frac{\mathrm{d}}{\mathrm{d}t}\boldsymbol{\Psi}_{\text{fpn}} \end{aligned} \tag{6.14}$$

6.1.3 Control Strategy

The stator of PMSG-based wind turbine is connected to the grid through MSC and GSC to achieve variable-speed and constant-frequency operation and power control. The goal of GSC control is to maintain DC voltage stability and control the output reactive power of the PMSG-based wind turbine, while the goal of MSC control is to achieve MPPT.

6.1.3.1 GSC Control Strategy

The block diagram of typical GSC control is shown in Fig. 6.6. Since the DC voltage depends on the active power balance between the AC and DC ports, it can be maintained stable by regulating the AC port active power of GSC. Therefore, the DC voltage control is realized by the outer DC voltage loop and inner d-axis current control. The reactive power control can be realized by the outer reactive power loop

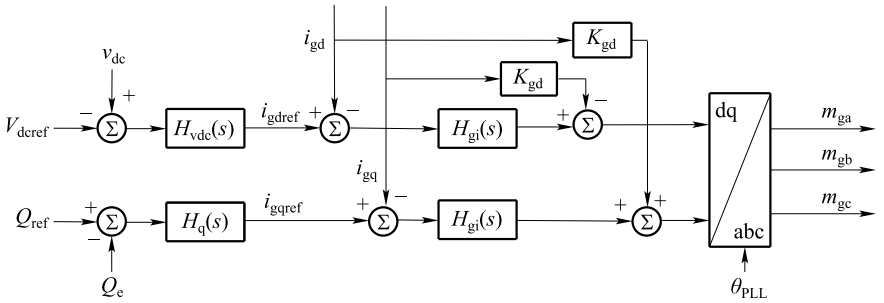

Fig. 6.6 Block diagram of typical GSC control

and the q-axis current control. Finally, the three-phase AC modulation signal of GSC can be obtained by inverse Park transformation.

The difference between the GSC modulation voltage and AC voltage drops on the filter inductor L_f, generating the AC current. Accordingly, the time-domain model of the main circuit of GSC can be expressed as

$$K_m v_{dc} m_{gl} = v_l + s L_f i_{gl} \tag{6.15}$$

where

K_m is the modulation gain.
v_{dc} is the DC voltage.
m_{gl} is the three-phase modulation signals of GSC.
v_l is the three-phase AC voltages.
i_{gl} is the three-phase AC currents of GSC.

6.1.3.2 MSC Control Strategy

MSC generally adopts d-axis stator current $i_{sd} = 0$ control. According to the time-domain model of PMSG, ignoring the influence of stator resistance, when PMSG operates in the steady state, its voltage equation can be obtained as

$$\begin{cases} v_{sd} = -\omega_r L_{sq} i_{sq} \\ v_{sq} \approx \omega_r \psi_f \end{cases} \tag{6.16}$$

Substituting Eq. (6.16) into Eq. (6.10), the expression of stator output active and reactive power can be derived as

$$\begin{cases} P_{es} = -\dfrac{3}{2}\omega_r \psi_f i_{sq} \\ Q_{es} = -\dfrac{3}{2}\omega_r L_{sq} i_{sq}^2 \end{cases} \tag{6.17}$$

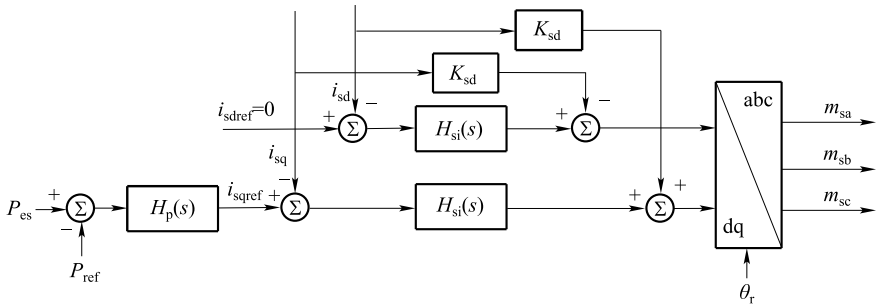

Fig. 6.7 Block diagram of typical MSC control

Then, the d- and q-axis current references of MSC can be obtained as

$$\begin{cases} i_{\text{sdref}} = 0 \\ i_{\text{sqref}} = -\dfrac{2P_{\text{ref}}}{3\omega_{\text{r}}\psi_{\text{f}}} \end{cases} \tag{6.18}$$

where P_{ref} is the active power reference, which is given by the main control system according to the actual wind speed.

Therefore, with $i_{\text{sd}} = 0$ control and the stator resistance ignored, the active power regulation can be realized by controlling the q-axis current of MSC. The block diagram of typical MSC control is shown in Fig. 6.7.

The AC side of MSC is directly connected to the stator, and the time-domain model of MSC main circuit can be expressed as

$$v_{sl} = K_{\text{m}} v_{\text{dc}} m_{sl} \tag{6.19}$$

where m_{sl} is the three-phase modulation signals of MSC; v_{sl} is the three-phase AC voltages of the stator, i.e., the three-phase modulation voltages of MSC.

6.1.3.3 Time-Domain Model of DC Bus

The DC voltage depends on the active power balance of MSC and GSC. The time-domain model of DC Bus can be expressed as

$$C_{\text{dc}} \frac{\text{d}v_{\text{dc}}}{\text{d}t} v_{\text{dc}} = -\sum_{l=\text{a,b,c}} v_{sl} i_{sl} - \sum_{l=\text{a,b,c}} v_{gl} i_{gl} \tag{6.20}$$

where

C_{dc} is the DC bus capacitor.

v_{sl} and i_{sl} are the three-phase modulation voltages and AC currents of MSC, respectively.
v_{gl} and i_{gl} are the three-phase modulation voltages and AC currents of GSC, respectively.

6.2 Frequency-Domain Modeling of Steady-State Operation

6.2.1 Frequency-Domain Characteristic Analysis of Steady-State Operating Point

At the steady-state operating point of PMSG-based wind turbine, the frequency of the stator voltages and currents is the rotor electrical frequency f_r, and so do the frequency of MSC AC voltages and currents. Meanwhile, The frequency of GSC AC voltages and currents is the rated frequency f_1.

Fig. 6.8 shows the waveforms and fast Fourier transform (FFT) results of the PMSG-based wind turbine at the steady-state operating point. When the rotor electrical frequency is 10Hz, the stator/MSC AC voltages, AC currents, and MSC modulation signals only contain components at ±10 Hz, while GSC AC voltages, AC currents, and modulation signals only contain components at $\pm f_1$. The DC voltage only contains the DC component.

The steady-state components of GSC can be arranged in the following order.

$$[-f_1,\ 0,\ f_1]^{\mathrm{T}} \tag{6.21}$$

The steady-state components of the stator and MSC can be arranged in the following order.

$$[-f_r,\ 0,\ f_r]^{\mathrm{T}} \tag{6.22}$$

Take phase a as an example, the steady-state vectors of GSC in frequency domain can be expressed as

$$\begin{cases} \boldsymbol{V}_{\mathrm{a}} &= [\boldsymbol{V}_1^*,\ 0,\ \boldsymbol{V}_1]^{\mathrm{T}} \\ \boldsymbol{I}_{\mathrm{ga}} &= [\boldsymbol{I}_{\mathrm{g1}}^*,\ 0,\ \boldsymbol{I}_{\mathrm{g1}}]^{\mathrm{T}} \\ \boldsymbol{M}_{\mathrm{ga}} &= [\boldsymbol{M}_{\mathrm{g1}}^*,\ 0,\ \boldsymbol{M}_{\mathrm{g1}}]^{\mathrm{T}} \end{cases} \tag{6.23}$$

The steady-state vectors of the stator and MSC in frequency domain can be expressed as

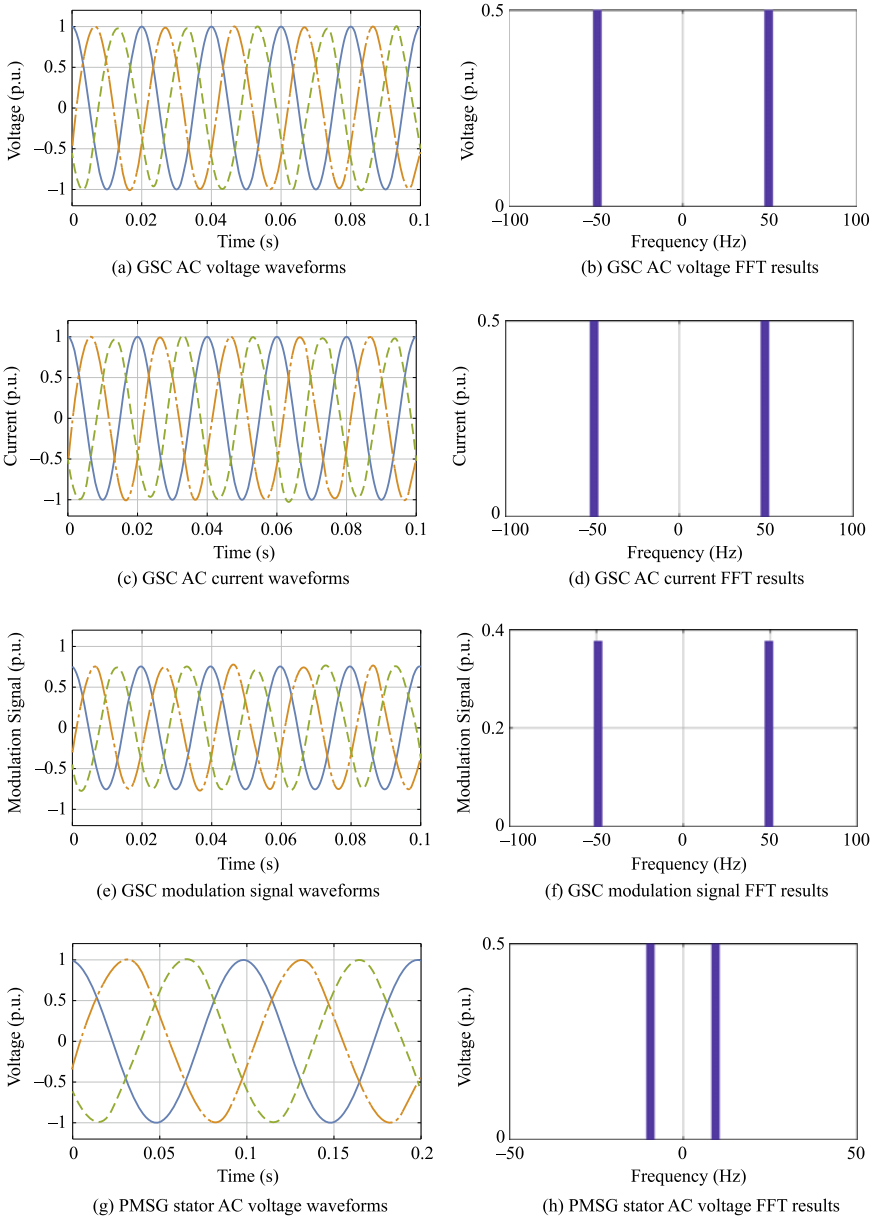

(a) GSC AC voltage waveforms
(b) GSC AC voltage FFT results
(c) GSC AC current waveforms
(d) GSC AC current FFT results
(e) GSC modulation signal waveforms
(f) GSC modulation signal FFT results
(g) PMSG stator AC voltage waveforms
(h) PMSG stator AC voltage FFT results

Fig. 6.8 Steady-state waveforms and FFT results of PMSG-based wind turbines

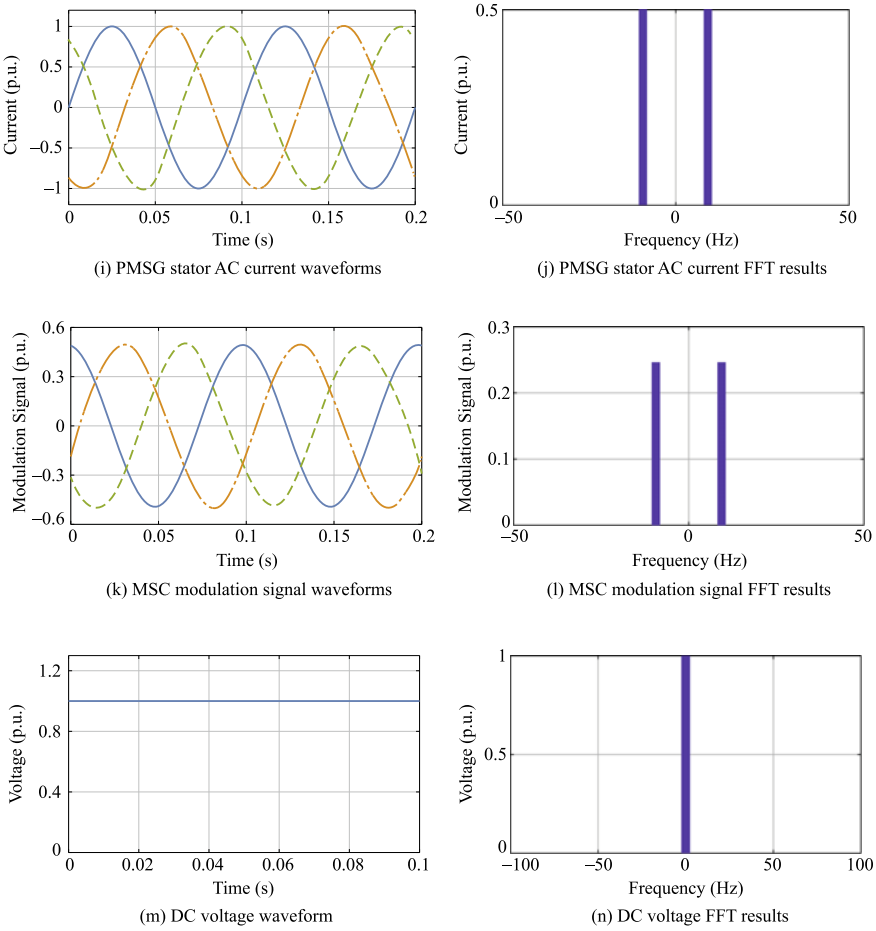

(i) PMSG stator AC current waveforms
(j) PMSG stator AC current FFT results
(k) MSC modulation signal waveforms
(l) MSC modulation signal FFT results
(m) DC voltage waveform
(n) DC voltage FFT results

Fig. 6.8 (continued)

$$\begin{cases} \boldsymbol{V}_{\mathrm{sa}} = [\,\boldsymbol{V}_{\mathrm{s1}}^{*},\ 0,\ \boldsymbol{V}_{\mathrm{s1}}\,]^{\mathrm{T}} \\ \boldsymbol{I}_{\mathrm{sa}} = [\,\boldsymbol{I}_{\mathrm{s1}}^{*},\ 0,\ \boldsymbol{I}_{\mathrm{s1}}\,]^{\mathrm{T}} \\ \boldsymbol{M}_{\mathrm{sa}} = [\,\boldsymbol{M}_{\mathrm{s1}}^{*},\ 0,\ \boldsymbol{M}_{\mathrm{s1}}\,]^{\mathrm{T}} \end{cases} \tag{6.24}$$

where

$\boldsymbol{V}_{\mathrm{a}}$ is the steady-state vector of GSC phase-a AC voltage.
$\boldsymbol{I}_{\mathrm{ga}}$ is the steady-state vector of GSC phase-a AC current.
$\boldsymbol{M}_{\mathrm{ga}}$ is the steady-state vector of GSC phase-a modulation signal.
$\boldsymbol{V}_{\mathrm{sa}}$ is the steady-state vector of the stator and MSC phase-a AC voltage.
$\boldsymbol{I}_{\mathrm{sa}}$ is the steady-state vector of the stator and MSC phase-a AC current.
$\boldsymbol{M}_{\mathrm{sa}}$ is the steady-state vector of MSC phase-a modulation signal.

Each element in the vector is expressed in the form of column complex vector, $\boldsymbol{V}_1 = V_1 e^{j\varphi_{v1}}/2$, $\boldsymbol{I}_{g1} = I_{g1} e^{j\varphi_{ig1}}/2$, $\boldsymbol{M}_{g1} = M_{g1} e^{j\varphi_{mg1}}/2$, $\boldsymbol{V}_{s1} = V_{s1} e^{j\varphi_{sv1}}/2$, $\boldsymbol{I}_{s1} = I_{s1} e^{j\varphi_{si1}}/2$, $\boldsymbol{M}_{s1} = M_{s1} e^{j\varphi_{ms1}}/2$, indicating the amplitude and phase of the steady-state components at corresponding frequency. Moreover, the negative- frequency component is equal to the conjugate of the positive-frequency component, which is indicated by the superscript "*".

The components at f_l and f_r are in positive sequence, and the corresponding elements lag $2\pi/3$ in turn in the three-phase vectors. The components at $-f_l$ and $-f_r$ are in negative sequence, and the corresponding elements lead $2\pi/3$ in turn in the three-phase vectors. In addition, the middle component is in zero sequence. According to the phase-sequence relationship, the steady-state vectors of phase b and phase c can be described as

$$\begin{cases} \boldsymbol{V}_b = \boldsymbol{D}\boldsymbol{V}_a,\ \boldsymbol{I}_{gb} = \boldsymbol{D}\boldsymbol{I}_{ga},\ \boldsymbol{M}_{gb} = \boldsymbol{D}\boldsymbol{M}_{ga} \\ \boldsymbol{V}_{sb} = \boldsymbol{D}\boldsymbol{V}_{sa},\ \boldsymbol{I}_{sb} = \boldsymbol{D}\boldsymbol{I}_{sa},\ \boldsymbol{M}_{sb} = \boldsymbol{D}\boldsymbol{M}_{sa} \end{cases} \tag{6.25}$$

$$\begin{cases} \boldsymbol{V}_c = \boldsymbol{D}^*\boldsymbol{V}_a,\ \boldsymbol{I}_{gc} = \boldsymbol{D}^*\boldsymbol{I}_{ga},\ \boldsymbol{M}_{gc} = \boldsymbol{D}^*\boldsymbol{M}_{ga} \\ \boldsymbol{V}_{sc} = \boldsymbol{D}^*\boldsymbol{V}_{sa},\ \boldsymbol{I}_{sc} = \boldsymbol{D}^*\boldsymbol{I}_{sa},\ \boldsymbol{M}_{sc} = \boldsymbol{D}^*\boldsymbol{M}_{sa} \end{cases} \tag{6.26}$$

where $\boldsymbol{D}$ is the phase-sequence coefficient matrix in the steady-state frequency order, expressed as

$$\boldsymbol{D} = \mathrm{diag}\left[\{e^{-j2k\pi/3}\}\big|_{k=-1,0,1} \right] \tag{6.27}$$

6.2.2 *Frequency-Domain Steady-State Model of Main Circuit*

6.2.2.1 PMSG Steady-State Model

Transforming the time-domain model of PMSG shown in Eq. (6.14) to the frequency domain, the steady-state model of PMSG can be obtained as

$$\boldsymbol{V}_{sl} = \left(R_s + s_0 \frac{L_{sd} + L_{sq}}{2} \right) \boldsymbol{I}_{sl} + s_0 \boldsymbol{\Psi}_{fl} \tag{6.28}$$

where $s_0 = 2\pi f_1$.

6.2.2.2 DC Bus Steady-State Model

Transforming the time-domain model of DC bus shown in Eq. (6.20) to the frequency domain, the steady-state model of DC bus can be obtained as

$$0 = -\sum_{l=\mathrm{a,b,c}} \boldsymbol{V}_{\mathrm{s}l} \otimes \boldsymbol{I}_{\mathrm{s}l} - \sum_{l=\mathrm{a,b,c}} \boldsymbol{V}_{\mathrm{g}l} \otimes \boldsymbol{I}_{\mathrm{g}l} \tag{6.29}$$

where $\boldsymbol{V}_{\mathrm{s}l}$ and $\boldsymbol{I}_{\mathrm{s}l}$ are the three-phase steady-state vectors of MSC modulation voltages and AC currents respectively; $\boldsymbol{V}_{\mathrm{g}l}$ and $\boldsymbol{I}_{\mathrm{g}l}$ are the three-phase steady-state vectors of GSC modulation voltages and AC currents respectively.

6.2.2.3 Steady-State Model of GSC

Transforming the time-domain model of GSC shown in Eq. (6.15) to frequency domain, the steady-state model of GSC can be obtained as

$$K_{\mathrm{m}} V_{\mathrm{dc}} \boldsymbol{M}_{\mathrm{g}l} = \boldsymbol{V}_l + \boldsymbol{Z}_{\mathrm{Lf0}} \boldsymbol{I}_{\mathrm{g}l} \tag{6.30}$$

where $\boldsymbol{Z}_{\mathrm{Lf0}}$ represents the impedance of the GSC AC filter inductor in the steady-state frequency order, which is a fifth-order diagonal matrix and can be expressed as

$$\boldsymbol{Z}_{\mathrm{Lf0}} = \mathrm{j}2\pi L_{\mathrm{f}} \cdot \mathrm{diag}[\,-2f_1,\ -f_1,\ 0,\ \ f_1,\ 2f_1\,]$$

6.2.2.4 Steady-State Model of RSC

Transforming the time-domain model of MSC shown in Eq. (6.19) to frequency domain, the steady-state model of MSC can be obtained as

$$K_{\mathrm{m}} V_{\mathrm{dc}} \boldsymbol{M}_{\mathrm{sa}} = \boldsymbol{V}_{\mathrm{sa}} \tag{6.31}$$

6.3 Small-Signal Impedance Modeling in Frequency Domain

In this section, the frequency-domain linearization method is used to establish the small-signal AC port impedance model of PMSG-based wind turbines. First, the AC voltages, AC currents, and modulation signals are transformed to the frequency domain to obtain the steady-state operating point. Then, a small-signal perturbation of a specific frequency is added to the AC voltages. Finally, the small-signal impedance model of PMSG-based wind turbines is established by calculating the response of AC currents to the small-signal perturbation in AC voltages.

6.3.1 Small-Signal Frequency-Domain Characteristic Analysis

Inject a small-signal positive-sequence perturbation at f_p into the AC voltage of PMSG-based wind turbines. The transfer path and frequency distribution of the small signals are shown in Fig. 6.9.

Take phase a as an example, the small-signal $\hat{\boldsymbol{v}}_l$ in the positive sequence at f_p is injected to the AC voltages of the PMSG-based wind turbine at the steady-state operating point. According to the small-signal frequency-domain characteristics of two-level converter in Sect. 3.3.1, small-signal responses at $\hat{\boldsymbol{v}}_{gl}$ f_p and $f_\mathrm{p}-2f_1$ will be generated in the GSC modulation voltage. The voltage difference between $\hat{\boldsymbol{v}}_{gl}$ and $\hat{\boldsymbol{v}}_l$ at f_p drops on the filter inductor leads to a small-signal response of GSC AC current $\hat{\boldsymbol{i}}_{gl}$ at f_p. Similarly, $\hat{\boldsymbol{v}}_{gl}$ at $f_\mathrm{p}-2f_1$ leads to a small-signal response of $\hat{\boldsymbol{i}}_{gl}$ at $f_\mathrm{p}-2f_1$.

For GSC, the small-signal component of $\hat{\boldsymbol{v}}_{gl}$ at f_p multiplying the steady-state component of GSC AC current $\boldsymbol{I}_{gl}$ at $-f_1$, the small-signal component of $\hat{\boldsymbol{v}}_{gl}$ at $f_\mathrm{p}-2f_1$ multiplying the steady-state component of GSC AC current $\boldsymbol{I}_{gl}$ at f_1, the small-signal component of $\hat{\boldsymbol{i}}_{gl}$ at f_p multiplying the steady-state component of GSC modulation voltage $\boldsymbol{V}_{gl}$ at $-f_1$, and the small-signal component of $\hat{\boldsymbol{i}}_{gl}$ at $f_\mathrm{p}-2f_1$ multiplying the steady-state component of GSC modulation voltage $\boldsymbol{V}_{gl}$ at f_1, both lead to small-signal responses of active power $\hat{\boldsymbol{p}}_\mathrm{e}$ at f_p-f_1, meanwhile leading to small-signal responses of DC voltage $\hat{\boldsymbol{v}}_\mathrm{dc}$ at f_p-f_1.

For MSC, the small-signal component of $\hat{\boldsymbol{v}}_\mathrm{dc}$ at $f_\mathrm{p}-f_1$ multiplying the steady-state component of MSC modulation signal $\boldsymbol{M}_{sl}$ at f_r leads to a small-signal response of MSC modulation voltage $\hat{\boldsymbol{v}}_{sl}$ at $f_\mathrm{p}-f_1+f_\mathrm{r}$. The small-signal component of $\hat{\boldsymbol{v}}_\mathrm{dc}$ at $f_\mathrm{p}-f_1$ multiplying the steady-state component of MSC modulation signal $\boldsymbol{M}_{sl}$ at $-f_\mathrm{r}$ leads to a small-signal response of $\hat{\boldsymbol{v}}_{sl}$ at $f_\mathrm{p}-f_1+f_\mathrm{r}$.

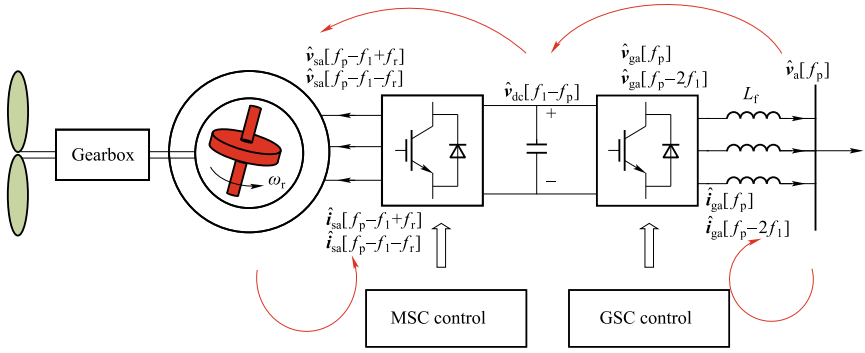

Fig. 6.9 Transfer path and frequency distribution of PMSG small signals

The small-signal components of $\hat{\boldsymbol{v}}_{sl}$ at $f_p - f_1 + f_r$ and $f_p - f_1 - f_r$ droping on the generator of PMSG-based wind turbine, leads to small-signal responses of the stator and MSC AC current $\hat{\boldsymbol{i}}_{sl}$ at $f_p - f_1 + f_r$ and $f_p - f_1 - f_r$ respectively.

Similarly, small-signal components of $\hat{\boldsymbol{v}}_{sl}$ at $f_p - f_1 + f_r$ and $f_p - f_1 - f_r$ multiplying the steady-state components of MSC AC current $\boldsymbol{I}_{sl}$ at $-f_r$ and f_r, and small-signal components of $\hat{\boldsymbol{i}}_{sl}$ at $f_p - f_1 - f_r$ and $f_p - f_1 - f_r$ multiplying the steady-state components of MSC AC voltage $\boldsymbol{V}_{sl}$ at $-f_r$ and f_r, also lead to small-signal responses of $\hat{\boldsymbol{v}}_{dc}$ at $f_p - f_1$, which are finally transferred to the AC port of the PMSG-based wind turbine through GSC modulation.

When the rotor electrical frequency of PMSG-based wind turbine is 10 Hz, and the injected small-signal perturbation is at 80 Hz, the waveforms and FFT results of GSC AC voltage, current and modulation signal are shown in Fig. 6.10. It can be seen that GSC AC voltage contains the small-signal components at 80 Hz, and GSC AC current and modulation signal contain small-signal components at 80 Hz and -20 Hz.The waveforms and FFT results of MSC AC voltage, current and modulation signal are shown in Fig. 6.11. It can be seen that they both contain components at 40 Hz and 20 Hz. The waveform and FFT result of DC voltage is shown in Fig. 6.12. It can be seen that it only contains the component at 30 Hz.

The frequency-domain characteristics of the small-signal vectors in PMSG-based wind turbine is shown in Table 6.1.

In order to describe the frequency-domain characteristics of voltages and currents of PMSG-based wind turbines, the small-signal components of GSC can be arranged into the following frequency order.

$$[\, f_p - 2f_1,\ f_p - f_1,\ f_p,\ f_p + f_1,\ f_p + 2f_1 \,]^T \tag{6.32}$$

The small-signal components of MSC can be arranged into the following frequency order.

$$[\, f_p - f_1 - f_r,\ f_p - f_1,\ f_p - f_1 + f_r,\ f_p - f_1 + 2f_r,\ f_p - f_1 + 3f_r \,]^T \tag{6.33}$$

In order to achieve the convolution between the steady-state vectors and small-signal vectors, the steady-state frequency orders in Eqs. (6.21) and (6.22) need to be expanded as

$$\begin{cases} [-2f_1,\ -f_1,\ 0,\ f_1,\ 2f_1\,]^T \\ [-2f_r,\ -f_r,\ 0,\ f_r,\ 2f_r\,]^T \end{cases} \tag{6.34}$$

where the steady-state components at $\pm 2f_1$ and $\pm 2f_r$ are zero.

Take phase a as an example, the small-signal vectors of GSC in frequency domain can be expressed as

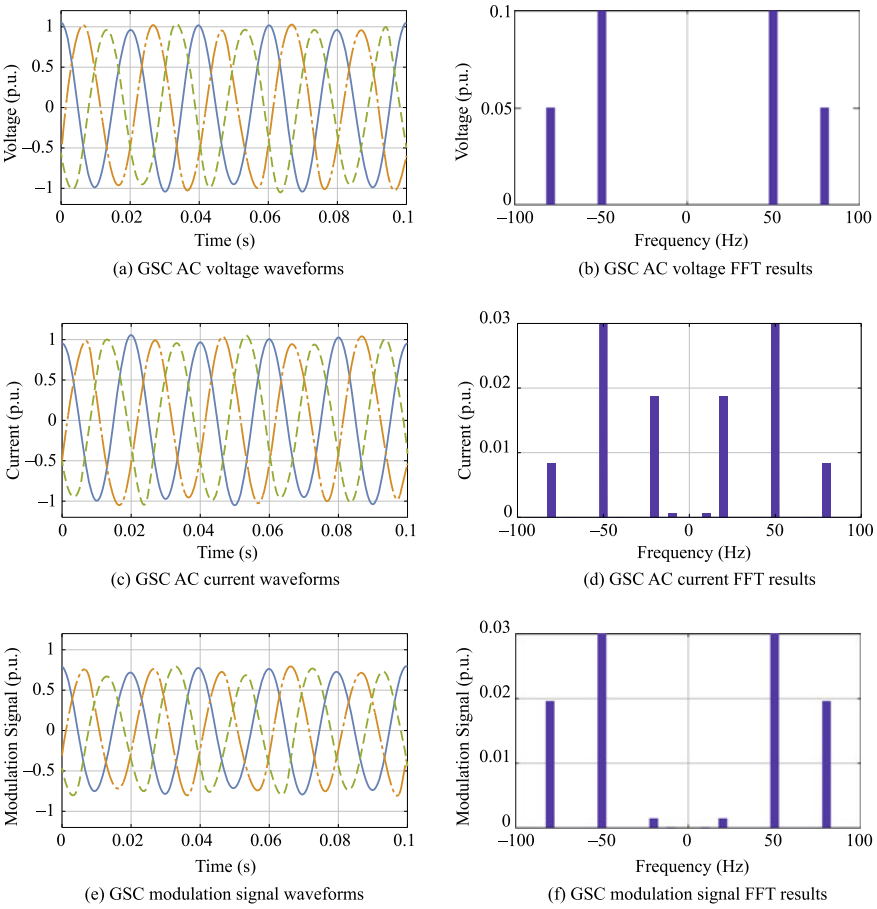

(a) GSC AC voltage waveforms
(b) GSC AC voltage FFT results
(c) GSC AC current waveforms
(d) GSC AC current FFT results
(e) GSC modulation signal waveforms
(f) GSC modulation signal FFT results

Fig. 6.10 Waveforms and FFT results of GSC AC voltage, current and modulation signal

$$\begin{cases} \hat{\boldsymbol{v}}_{\mathrm{a}} = [\,\hat{\boldsymbol{v}}_{\mathrm{p-2}},\ 0,\ \hat{\boldsymbol{v}}_{\mathrm{p}},\ 0,\ 0\,]^{\mathrm{T}} \\ \hat{\boldsymbol{i}}_{\mathrm{ga}} = [\,\hat{\boldsymbol{i}}_{\mathrm{gp-2}},\ 0,\ \hat{\boldsymbol{i}}_{\mathrm{gp}},\ 0,\ 0\,]^{\mathrm{T}} \\ \hat{\boldsymbol{m}}_{\mathrm{ga}} = [\,\hat{\boldsymbol{m}}_{\mathrm{gp-2}},\ 0,\ \hat{\boldsymbol{m}}_{\mathrm{gp}},\ 0,\ 0\,]^{\mathrm{T}} \end{cases} \tag{6.35}$$

The small-signal vectors of the stator and MSC in frequency domain can be expressed as

$$\begin{cases} \hat{\boldsymbol{v}}_{\mathrm{sa}} = [\,\hat{\boldsymbol{v}}_{\mathrm{sp-2}},\ 0,\ \hat{\boldsymbol{v}}_{\mathrm{sp}},\ 0,\ 0\,]^{\mathrm{T}} \\ \hat{\boldsymbol{i}}_{\mathrm{sa}} = [\,\hat{\boldsymbol{i}}_{\mathrm{sp-2}},\ 0,\ \hat{\boldsymbol{i}}_{\mathrm{sp}},\ 0,\ 0\,]^{\mathrm{T}} \\ \hat{\boldsymbol{m}}_{\mathrm{sa}} = [\,\hat{\boldsymbol{m}}_{\mathrm{sp-2}},\ 0,\ \hat{\boldsymbol{m}}_{\mathrm{sp}},\ 0,\ 0\,]^{\mathrm{T}} \end{cases} \tag{6.36}$$

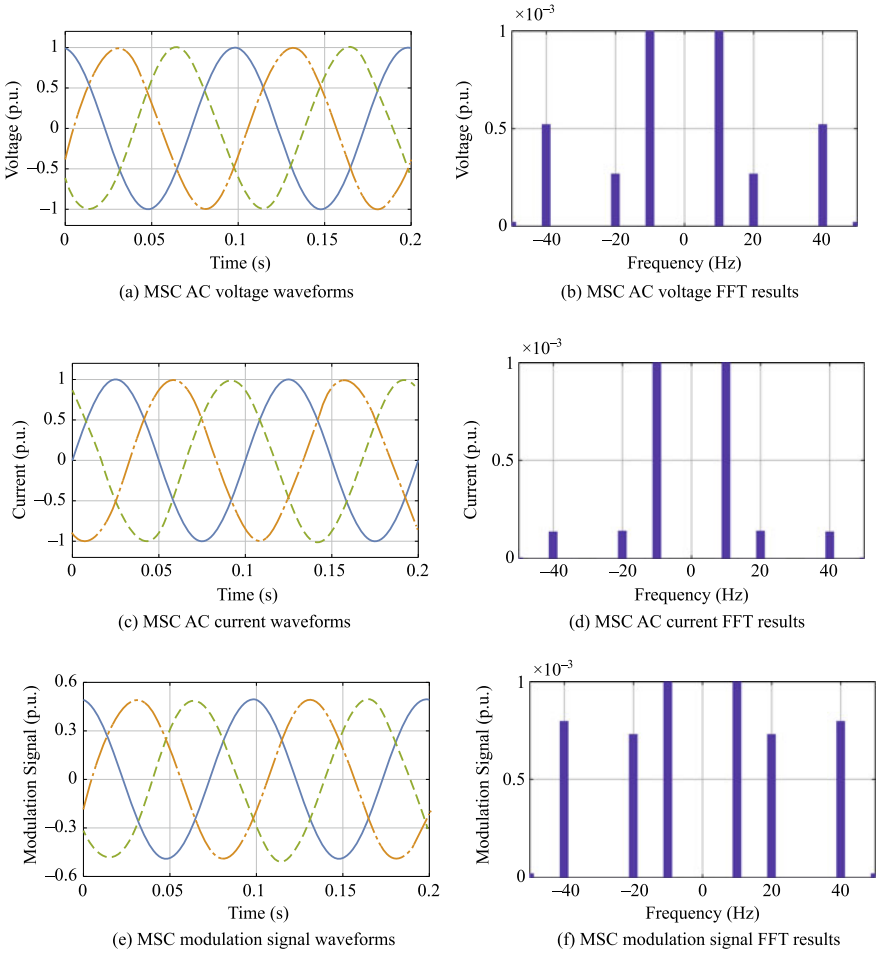

Fig. 6.11 Waveforms and FFT results of MSC AC voltage, current and modulation signal

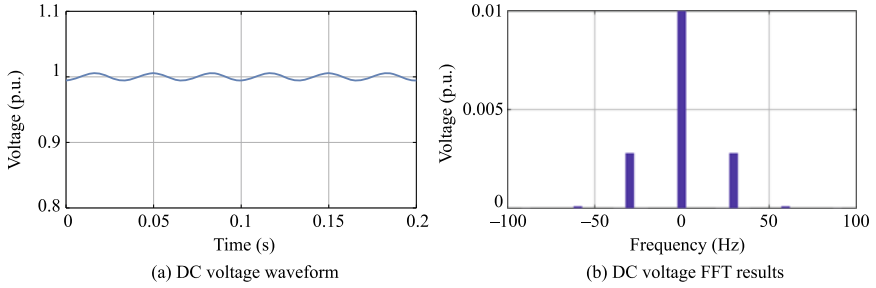

Fig. 6.12 Waveform and FFT result of DC voltage

Table 6.1 The frequency-domain characteristics of the small-signal vectors in PMSG-based wind turbine

PMSG-Based Wind Turbine	Small-Signal Vector	Frequency
GSC	$\hat{\boldsymbol{v}}_l$	f_p
	$\hat{\boldsymbol{i}}_{gl}$	f_p
		$f_\mathrm{p}-2f_\mathrm{1}$
	$\hat{\boldsymbol{m}}_{gl}$	f_p
		$f_\mathrm{p}-2f_\mathrm{1}$
MSC	$\hat{\boldsymbol{v}}_{sl}$	$f_\mathrm{p}-f_\mathrm{1}+f_\mathrm{r}$
		$f_\mathrm{p}-f_\mathrm{1}-f_\mathrm{r}$
	$\hat{\boldsymbol{i}}_{sl}$	$f_\mathrm{p}-f_\mathrm{1}+f_\mathrm{r}$
		$f_\mathrm{p}-f_\mathrm{1}-f_\mathrm{r}$
	$\hat{\boldsymbol{m}}_{sl}$	$f_\mathrm{p}-f_\mathrm{1}+f_\mathrm{r}$
		$f_\mathrm{p}-f_\mathrm{1}-f_\mathrm{r}$
DC Bus	$\hat{\boldsymbol{v}}_\mathrm{dc}$	$f_\mathrm{p}-f_\mathrm{1}$

where

$\hat{\boldsymbol{v}}_\mathrm{a}$ is the small-signal vector of GSC phase-a AC voltage.
$\hat{\boldsymbol{i}}_\mathrm{ga}$ is the small-signal vector of GSC phase-a AC current.
$\hat{\boldsymbol{m}}_\mathrm{ga}$ is the small-signal vector of GSC phase-a modulation signal.
$\hat{\boldsymbol{v}}_\mathrm{sa}$ is the small-signal vector of the stator and MSC phase-a AC voltage.
$\hat{\boldsymbol{i}}_\mathrm{sa}$ is the small-signal vector of the stator and MSC phase-a AC current.
$\hat{\boldsymbol{m}}_\mathrm{sa}$ is the small-signal vector of MSC phase-a modulation signal.

Each element in the vector is expressed in the form of complex vector, $\hat{\boldsymbol{v}}_\mathrm{p} = V_\mathrm{p}\mathrm{e}^{\mathrm{j}\varphi_\mathrm{vp}}/2$, $\hat{\boldsymbol{v}}_{\mathrm{p}-2} = V_{\mathrm{p}-2}\mathrm{e}^{\mathrm{j}\varphi_{\mathrm{vp}-2}}/2$, $\hat{\boldsymbol{i}}_\mathrm{gp} = I_\mathrm{gp}\mathrm{e}^{\mathrm{j}\varphi_\mathrm{igp}}/2$, $\hat{\boldsymbol{i}}_{\mathrm{gp}-2} = I_{\mathrm{gp}-2}\mathrm{e}^{\mathrm{j}\varphi_{\mathrm{igp}-2}}/2$, $\hat{\boldsymbol{m}}_\mathrm{gp} = M_\mathrm{gp}\mathrm{e}^{\mathrm{j}\varphi_\mathrm{mgp}}/2$, $\hat{\boldsymbol{m}}_{\mathrm{gp}-2} = M_{\mathrm{gp}-2}\mathrm{e}^{\mathrm{j}\varphi_{\mathrm{mgp}-2}}/2$, $\hat{\boldsymbol{v}}_\mathrm{sp} = V_\mathrm{sp}\mathrm{e}^{\mathrm{j}\varphi_\mathrm{vsp}}/2$, $\hat{\boldsymbol{v}}_{\mathrm{sp}-2} = V_{\mathrm{sp}-2}\mathrm{e}^{\mathrm{j}\varphi_{\mathrm{vsp}-2}}/2$, $\hat{\boldsymbol{i}}_\mathrm{sp} = I_\mathrm{sp}\mathrm{e}^{\mathrm{j}\varphi_\mathrm{isp}}/2$, $\hat{\boldsymbol{i}}_{\mathrm{sp}-2} = I_{\mathrm{sp}-2}\mathrm{e}^{\mathrm{j}\varphi_{\mathrm{isp}-2}}/2$, $\hat{\boldsymbol{m}}_\mathrm{sp} = M_\mathrm{sp}\mathrm{e}^{\mathrm{j}\varphi_\mathrm{msp}}/2$, $\hat{\boldsymbol{m}}_{\mathrm{sp}-2} = M_{\mathrm{sp}-2}\mathrm{e}^{\mathrm{j}\varphi_{\mathrm{msp}-2}}/2$, indicating the amplitude and phase of the small-signal components at the corresponding frequency. The negative-frequency component is equal to the conjugate of the positive-frequency component, indicated by the superscript "*".

The components at f_p and $f_\mathrm{p}-f_\mathrm{1}+f_\mathrm{r}$ are in positive sequence, and the corresponding elements lag $2\pi/3$ in turn in the three-phase vectors. The components at $f_\mathrm{p}-2f_\mathrm{1}$ and $f_\mathrm{p}-f_\mathrm{1}-f_\mathrm{r}$ are in negative sequence, and the corresponding elements lead $2\pi/3$ in turn in the three-phase vectors. In addition, the middle component is in zero sequence. According to the phase-sequence relationship, the small-signal vectors of phase b and phase c can be described as

$$\begin{cases} \hat{\boldsymbol{v}}_\mathrm{b} = \boldsymbol{D}_\mathrm{p}\hat{\boldsymbol{v}}_\mathrm{a},\ \hat{\boldsymbol{i}}_\mathrm{gb} = \boldsymbol{D}_\mathrm{p}\hat{\boldsymbol{i}}_\mathrm{ga},\ \hat{\boldsymbol{m}}_\mathrm{gb} = \boldsymbol{D}_\mathrm{p}\hat{\boldsymbol{m}}_\mathrm{ga} \\ \hat{\boldsymbol{v}}_\mathrm{sb} = \boldsymbol{D}_\mathrm{p}\hat{\boldsymbol{v}}_\mathrm{sa},\ \hat{\boldsymbol{i}}_\mathrm{sb} = \boldsymbol{D}_\mathrm{p}\hat{\boldsymbol{i}}_\mathrm{sa},\ \hat{\boldsymbol{m}}_\mathrm{sb} = \boldsymbol{D}_\mathrm{p}\hat{\boldsymbol{m}}_\mathrm{sa} \end{cases} \tag{6.37}$$

$$\begin{cases} \hat{\boldsymbol{v}}_{\mathrm{c}} = \boldsymbol{D}_{\mathrm{p}}^{*}\hat{\boldsymbol{v}}_{\mathrm{a}},\ \hat{\boldsymbol{i}}_{\mathrm{gc}} = \boldsymbol{D}_{\mathrm{p}}^{*}\hat{\boldsymbol{i}}_{\mathrm{ga}},\ \hat{\boldsymbol{m}}_{\mathrm{gc}} = \boldsymbol{D}_{\mathrm{p}}^{*}\hat{\boldsymbol{m}}_{\mathrm{ga}} \\ \hat{\boldsymbol{v}}_{\mathrm{sc}} = \boldsymbol{D}_{\mathrm{p}}^{*}\hat{\boldsymbol{v}}_{\mathrm{sa}},\ \hat{\boldsymbol{i}}_{\mathrm{sc}} = \boldsymbol{D}_{\mathrm{p}}^{*}\hat{\boldsymbol{i}}_{\mathrm{sa}},\ \hat{\boldsymbol{m}}_{\mathrm{sc}} = \boldsymbol{D}_{\mathrm{p}}^{*}\hat{\boldsymbol{m}}_{\mathrm{sa}} \end{cases} \tag{6.38}$$

where $\boldsymbol{D}_{\mathrm{p}}$ is the phase-sequence coefficient matrix in the small-signal frequency order, expressed as

$$\boldsymbol{D}_{\mathrm{p}} = \mathrm{diag}\left[\{\mathrm{e}^{-\mathrm{j}2(k+1)\pi/3}\}\big|_{k=-2,-1,0,1,2} \right] \tag{6.39}$$

6.3.2 Frequency-Domain Small-Signal Model

6.3.2.1 Small-Signal Model of PMSG

Based on Eq. (6.14), the small-signal components of the stator voltage at $f_{\mathrm{p}} - f_{\mathrm{l}} + f_{\mathrm{r}}$ and $f_{\mathrm{p}} - f_{\mathrm{l}} - f_{\mathrm{r}}$ can be calculated as

$$\begin{cases} \hat{\boldsymbol{v}}_{\mathrm{sp}} = \left(R_{\mathrm{s}} + \dfrac{L_{\mathrm{sd}} + L_{\mathrm{sq}}}{2} s_{\mathrm{sp}} \right) \hat{\boldsymbol{i}}_{\mathrm{sp}} + \dfrac{L_{\mathrm{sd}} - L_{\mathrm{sq}}}{2} s_{\mathrm{sp}} \hat{\boldsymbol{i}}_{\mathrm{sp}-2} \\ \hat{\boldsymbol{v}}_{\mathrm{sp}-2} = \dfrac{L_{\mathrm{sd}} - L_{\mathrm{sq}}}{2} s_{\mathrm{sp2}} \hat{\boldsymbol{i}}_{\mathrm{sp}} + \left(R_{\mathrm{s}} + \dfrac{L_{\mathrm{sd}} + L_{\mathrm{sq}}}{2} s_{\mathrm{sp2}} \right) \hat{\boldsymbol{i}}_{\mathrm{sp}-2} \end{cases} \tag{6.40}$$

where $s_{\mathrm{sp}} = \mathrm{j}2\pi(f_{\mathrm{p}} - f_{\mathrm{l}} + f_{\mathrm{r}})$, $s_{\mathrm{sp2}} = \mathrm{j}2\pi(f_{\mathrm{p}} - f_{\mathrm{l}} - f_{\mathrm{r}})$.

Transforming Eq. (6.40) in small-signal vector form, the small-signal model of PMSG can be obtained as

$$\hat{\boldsymbol{v}}_{\mathrm{sa}} = \boldsymbol{G}_{\mathrm{s}} \hat{\boldsymbol{i}}_{\mathrm{sa}} \tag{6.41}$$

where $\boldsymbol{G}_{\mathrm{s}}$ is fifth-order matrix. All other elements in the matrix are zero except for

$$\begin{cases} \boldsymbol{G}_{\mathrm{s}}(1,1) = R_{\mathrm{s}} + \frac{L_{\mathrm{sd}}+L_{\mathrm{sq}}}{2} s_{\mathrm{sp2}} \\ \boldsymbol{G}_{\mathrm{s}}(1,3) = \frac{L_{\mathrm{sd}}-L_{\mathrm{sq}}}{2} s_{\mathrm{sp2}} \\ \boldsymbol{G}_{\mathrm{s}}(3,1) = \frac{L_{\mathrm{sd}}-L_{\mathrm{sq}}}{2} s_{\mathrm{sp}} \\ \boldsymbol{G}_{\mathrm{s}}(3,3) = R_{\mathrm{s}} + \frac{L_{\mathrm{sd}}+L_{\mathrm{sq}}}{2} s_{\mathrm{sp}} \end{cases} \tag{6.42}$$

6.3.2.2 Small-Signal Model of DC Bus

Transforming Eq. (6.20) to frequency domain, the small-signal model of DC bus can be obtained as

$$s_1 C_{\mathrm{dc}} V_{\mathrm{dc}} \hat{\boldsymbol{v}}_{\mathrm{dc}} = -\sum_{l=\mathrm{a,b,c}} (\boldsymbol{I}_{sl} \otimes \hat{\boldsymbol{v}}_{sl} + \boldsymbol{V}_{sl} \otimes \hat{\boldsymbol{i}}_{sl}) - \sum_{l=\mathrm{a,b,c}} (\boldsymbol{I}_{gl} \otimes \hat{\boldsymbol{v}}_{gl} + \boldsymbol{V}_{gl} \otimes \hat{\boldsymbol{i}}_{gl}) \tag{6.43}$$

Furthermore, the small-signal vector of DC voltage can be expressed as

$$\hat{\boldsymbol{v}}_{\mathrm{dc}} = \boldsymbol{J}_{\mathrm{gi}} \hat{\boldsymbol{i}}_{\mathrm{ga}} + \boldsymbol{J}_{\mathrm{si}} \hat{\boldsymbol{i}}_{\mathrm{sa}} + \boldsymbol{J}_{\mathrm{gv}} \hat{\boldsymbol{v}}_{\mathrm{a}} + \boldsymbol{J}_{\mathrm{sv}} \hat{\boldsymbol{v}}_{\mathrm{sa}} \tag{6.44}$$

where $\boldsymbol{J}_{\mathrm{gi}}$, $\boldsymbol{J}_{\mathrm{si}}$, $\boldsymbol{J}_{\mathrm{gv}}$, $\boldsymbol{J}_{\mathrm{sv}}$ are fifth-order matrices. All other elements in the matrices are zero except for

$$\begin{cases} \boldsymbol{J}_{\mathrm{gi}}(2,1) = -\dfrac{3}{C_{\mathrm{dc}} V_{\mathrm{dc}} s_1} (\boldsymbol{V}_{\mathrm{g1}} + s_2 L_{\mathrm{f}} \boldsymbol{I}_{\mathrm{g1}}) \\ \boldsymbol{J}_{\mathrm{gi}}(2,3) = -\dfrac{3}{C_{\mathrm{dc}} V_{\mathrm{dc}} s_1} (\boldsymbol{V}^*_{\mathrm{g1}} + s L_{\mathrm{f}} \boldsymbol{I}^*_{\mathrm{g1}}) \end{cases} \tag{6.45}$$

$$\begin{cases} \boldsymbol{J}_{\mathrm{si}}(2,1) = -\dfrac{3}{C_{\mathrm{dc}} V_{\mathrm{dc}} s_1} \boldsymbol{V}_{\mathrm{s1}} \\ \boldsymbol{J}_{\mathrm{si}}(2,3) = -\dfrac{3}{C_{\mathrm{dc}} V_{\mathrm{dc}} s_1} \boldsymbol{V}^*_{\mathrm{s1}} \end{cases} \tag{6.46}$$

$$\begin{cases} \boldsymbol{J}_{\mathrm{gv}}(2,1) = -\dfrac{3}{C_{\mathrm{dc}} V_{\mathrm{dc}} s_1} \boldsymbol{I}_{\mathrm{g1}} \\ \boldsymbol{J}_{\mathrm{gv}}(2,3) = -\dfrac{3}{C_{\mathrm{dc}} V_{\mathrm{dc}} s_1} \boldsymbol{I}^*_{\mathrm{g1}} \end{cases} \tag{6.47}$$

$$\begin{cases} \boldsymbol{J}_{\mathrm{sv}}(2,1) = -\dfrac{3}{C_{\mathrm{dc}} V_{\mathrm{dc}} s_1} \boldsymbol{I}_{\mathrm{s1}} \\ \boldsymbol{J}_{\mathrm{sv}}(2,3) = -\dfrac{3}{C_{\mathrm{dc}} V_{\mathrm{dc}} s_1} \boldsymbol{I}^*_{\mathrm{s1}} \end{cases} \tag{6.48}$$

where $s = \mathrm{j}2\pi f_{\mathrm{p}}$, $s_1 = \mathrm{j}2\pi(f_{\mathrm{p}} - f_1)$, $s_2 = \mathrm{j}2\pi(f_{\mathrm{p}} - 2f_1)$.

6.3.2.3 Small-Signal Model of GSC

The small-signal modeling of GSC can be referred to Chap. 3. As shown in Fig. 6.6, GSC maintains the stability of DC voltage by controlling d-axis current through DC voltage loop, and controls the reactive power by regulating the q-axis current through the reactive power loop. The small-signal vectors of d- and q-axis current references of GSC can be expressed as

$$\begin{cases} \hat{\boldsymbol{i}}_{\mathrm{gdref}} = H_{\mathrm{vdc}}(s_1)\hat{\boldsymbol{v}}_{\mathrm{dc}} \\ \hat{\boldsymbol{i}}_{\mathrm{gqref}} = H_{\mathrm{q}}(s_1)\hat{\boldsymbol{q}}_{\mathrm{e}} \end{cases} \tag{6.49}$$

where $H_{\mathrm{vdc}}(s_1)$ is the transfer function of DC voltage controller, whose expression is $H_{\mathrm{vdc}}(s_1) = K_{\mathrm{vdcp}} + K_{\mathrm{vdci}}/s_1$; K_{vdcp} and K_{vdci} are proportional and integral coefficients respectively ; $H_{\mathrm{q}}(s_1)$ is the transfer function of reactive power controller, whose expression is$H_{\mathrm{q}}(s_1) = K_{\mathrm{qep}} + K_{\mathrm{qei}}/s_1$; K_{qep} and K_{qei} are proportional and integral coefficients respectively.

The small-signal vectors of PMSG-based wind turbine output reactive power can be calculated by

$$\hat{\boldsymbol{q}}_{\mathrm{e}} = \boldsymbol{Q}_{\mathrm{i}}\hat{\boldsymbol{i}}_{\mathrm{ga}} + \boldsymbol{Q}_{\mathrm{v}}\hat{\boldsymbol{v}}_{\mathrm{a}} \tag{6.50}$$

where $\boldsymbol{Q}_{\mathrm{i}}$ and $\boldsymbol{Q}_{\mathrm{v}}$ are fifth-order matrices. All other elements in the matrices are zero except for

$$\begin{cases} \boldsymbol{Q}_{\mathrm{i}}(2,1) = -\mathrm{j}3\boldsymbol{V}_1 \\ \boldsymbol{Q}_{\mathrm{i}}(2,3) = \mathrm{j}3\boldsymbol{V}_1^* \end{cases} \tag{6.51}$$

$$\begin{cases} \boldsymbol{Q}_{\mathrm{v}}(2,1) = \mathrm{j}3\boldsymbol{I}_{\mathrm{g1}} \\ \boldsymbol{Q}_{\mathrm{v}}(2,3) = -\mathrm{j}3\boldsymbol{I}_{\mathrm{g1}}^* \end{cases} \tag{6.52}$$

According to the structure of GSC, the small-signal vector of the GSC modulation signal can be derived as

$$\hat{\boldsymbol{m}}_{\mathrm{ga}} = \boldsymbol{E}_{\mathrm{dc}}\hat{\boldsymbol{v}}_{\mathrm{dc}} + \boldsymbol{E}_{\mathrm{gi}}\hat{\boldsymbol{i}}_{\mathrm{ga}} + \boldsymbol{E}_{\mathrm{gv}}\hat{\boldsymbol{v}}_{\mathrm{a}} \tag{6.53}$$

where $\boldsymbol{E}_{\mathrm{dc}}$, $\boldsymbol{E}_{\mathrm{gi}}$ and $\boldsymbol{E}_{\mathrm{gv}}$ are fifth-order matrices. All other elements in the matrices are zero except for

$$\begin{cases} \boldsymbol{E}_{\mathrm{dc}}(1,2) = \dfrac{1}{2}H_{\mathrm{gi}}(s_1)H_{\mathrm{vdc}}(s_1) \\ \boldsymbol{E}_{\mathrm{dc}}(3,2) = \dfrac{1}{2}H_{\mathrm{gi}}(s_1)H_{\mathrm{vdc}}(s_1) \end{cases} \tag{6.54}$$

$$\begin{cases} \boldsymbol{E}_{\mathrm{gi}}(1,1) = -\dfrac{3}{2}H_{\mathrm{gi}}(s_1)H_{\mathrm{q}}(s_1)\boldsymbol{V}_1 - H_{\mathrm{gi}}(s_1) - \mathrm{j}K_{\mathrm{gd}} \\ \boldsymbol{E}_{\mathrm{gi}}(1,3) = \dfrac{3}{2}H_{\mathrm{gi}}(s_1)H_{\mathrm{q}}(s_1)\boldsymbol{V}_1^* \\ \boldsymbol{E}_{\mathrm{gi}}(3,1) = \dfrac{3}{2}H_{\mathrm{gi}}(s_1)H_{\mathrm{q}}(s_1)\boldsymbol{V}_1 \\ \boldsymbol{E}_{\mathrm{gi}}(3,3) = -\dfrac{3}{2}H_{\mathrm{gi}}(s_1)H_{\mathrm{q}}(s_1)\boldsymbol{V}_1^* - H_{\mathrm{gi}}(s_1) + \mathrm{j}K_{\mathrm{gd}} \end{cases} \tag{6.55}$$

$$\begin{cases} \boldsymbol{E}_{\mathrm{gv}}(1,1) = \dfrac{3}{2} H_{\mathrm{gi}}(s_1) H_{\mathrm{q}}(s_1) \boldsymbol{I}_{\mathrm{g1}} \\ \qquad\qquad + T_{\mathrm{PLL}}(s_1)[\boldsymbol{M}_1^* + (H_{\mathrm{gi}}(s_1) + \mathrm{j}K_{\mathrm{gd}})\boldsymbol{I}_{\mathrm{g1}}^*] \\ \boldsymbol{E}_{\mathrm{gv}}(1,3) = -\dfrac{3}{2} H_{\mathrm{gi}}(s_1) H_{\mathrm{q}}(s_1) \boldsymbol{I}_{\mathrm{g1}}^* \\ \qquad\qquad - T_{\mathrm{PLL}}(s_1)[\boldsymbol{M}_1^* + (H_{\mathrm{gi}}(s_1) + \mathrm{j}K_{\mathrm{gd}})\boldsymbol{I}_{\mathrm{g1}}^*] \\ \boldsymbol{E}_{\mathrm{gv}}(3,1) = -\dfrac{3}{2} H_{\mathrm{gi}}(s_1) H_{\mathrm{q}}(s_1) \boldsymbol{I}_{\mathrm{g1}} \\ \qquad\qquad - T_{\mathrm{PLL}}(s_1)[\boldsymbol{M}_1 + (H_{\mathrm{gi}}(s_1) - \mathrm{j}K_{\mathrm{gd}})\boldsymbol{I}_{\mathrm{g1}}] \\ \boldsymbol{E}_{\mathrm{gv}}(3,3) = \dfrac{3}{2} H_{\mathrm{gi}}(s_1) H_{\mathrm{q}}(s_1) \boldsymbol{I}_{\mathrm{g1}}^* \\ \qquad\qquad + T_{\mathrm{PLL}}(s_1)[\boldsymbol{M}_1 + (H_{\mathrm{gi}}(s_1) - \mathrm{j}K_{\mathrm{gd}})\boldsymbol{I}_{\mathrm{g1}}] \end{cases} \tag{6.56}$$

Transforming Eq. (6.15) to frequency domain, the small-signal model of GSC main circuit can be obtained as

$$K_{\mathrm{m}}(V_{\mathrm{dc}}\hat{\boldsymbol{m}}_{\mathrm{ga}} + \boldsymbol{M}_{\mathrm{ga}}\hat{\boldsymbol{v}}_{\mathrm{dc}}) = \hat{\boldsymbol{v}}_{\mathrm{a}} + \boldsymbol{Z}_{\mathrm{Lf}}\hat{\boldsymbol{i}}_{\mathrm{ga}} \tag{6.57}$$

where $\boldsymbol{M}_{\mathrm{ga}}$ is the extended steady-state matrix of GSC modulation signal, whose expression is

$$\boldsymbol{M}_{\mathrm{ga}} = \begin{bmatrix} 0 & \boldsymbol{M}_{\mathrm{g1}}^* & 0 & 0 & 0 \\ \boldsymbol{M}_{\mathrm{g1}} & 0 & \boldsymbol{M}_{\mathrm{g1}}^* & 0 & 0 \\ 0 & \boldsymbol{M}_{\mathrm{g1}} & 0 & \boldsymbol{M}_{\mathrm{g1}}^* & 0 \\ 0 & 0 & \boldsymbol{M}_{\mathrm{g1}} & 0 & \boldsymbol{M}_{\mathrm{g1}}^* \\ 0 & 0 & 0 & \boldsymbol{M}_{\mathrm{g1}} & 0 \end{bmatrix}$$

$\boldsymbol{Z}_{\mathrm{Lf}}$ is a fifth-order diagonal matrix, representing the impedance of GSC AC filter inductor in the small-signal frequency order, expressed as

$$\boldsymbol{Z}_{\mathrm{Lf}} = \mathrm{j}2\pi L_{\mathrm{f}} \cdot \mathrm{diag}[\, f_{\mathrm{p}} - 2f_1,\ f_{\mathrm{p}} - f_1,\ f_{\mathrm{p}},\ f_{\mathrm{p}} + f_1,\ f_{\mathrm{p}} + 2f_1\,]$$

After simplification, the small-signal model of GSC can be expressed as

$$\hat{\boldsymbol{v}}_{\mathrm{a}} = \boldsymbol{F}_{\mathrm{dc}}\hat{\boldsymbol{v}}_{\mathrm{dc}} + \boldsymbol{F}_{\mathrm{gi}}\hat{\boldsymbol{i}}_{\mathrm{ga}} \tag{6.58}$$

in which $\boldsymbol{F}_{\mathrm{dc}}$ and $\boldsymbol{F}_{\mathrm{gi}}$ are fifth-order matrices, whose expression is

$$\begin{cases} \boldsymbol{F}_{\mathrm{dc}} = (\boldsymbol{U} - K_{\mathrm{m}}V_{\mathrm{dc}}\boldsymbol{E}_{\mathrm{gv}})^{-1}(K_{\mathrm{m}}\boldsymbol{M}_{\mathrm{ga}} + K_{\mathrm{m}}V_{\mathrm{dc}}\boldsymbol{E}_{\mathrm{dc}}) \\ \boldsymbol{F}_{\mathrm{gi}} = (\boldsymbol{U} - K_{\mathrm{m}}V_{\mathrm{dc}}\boldsymbol{E}_{\mathrm{gv}})^{-1}(K_{\mathrm{m}}V_{\mathrm{dc}}\boldsymbol{E}_{\mathrm{gi}} - \boldsymbol{Z}_{\mathrm{Lf}}) \end{cases} \tag{6.59}$$

$\boldsymbol{U}$ is fifth-order identity matrix.

6.3.2.4 Small-Signal Model of MSC

According to the typical control strategy of MSC in Fig. 6.7, the small-signal vectors of d- and q-axis current references of MSC can be expressed as

$$\begin{cases} \hat{\boldsymbol{i}}_{\text{sdref}} = 0 \\ \hat{\boldsymbol{i}}_{\text{sqref}} = H_{\text{p}}(s_1)\hat{\boldsymbol{p}}_{\text{es}} \end{cases} \tag{6.60}$$

where $H_{\text{p}}(s_1)$ is the transfer function of active power controller, whose expression is $H_{\text{p}}(s_1) = K_{\text{pep}} + K_{\text{pei}}/s_1$; K_{pep} and K_{pei} are the proportional and integral coefficients respectively.

The small-signal vectors of PMSG output active power can be calculated by

$$\hat{\boldsymbol{p}}_{\text{es}} = \boldsymbol{P}_{\text{i}}\hat{\boldsymbol{i}}_{\text{sa}} + \boldsymbol{P}_{\text{v}}\hat{\boldsymbol{v}}_{\text{sa}} \tag{6.61}$$

where $\boldsymbol{P}_{\text{i}}$ and $\boldsymbol{P}_{\text{v}}$ are fifth-order matrices. All other elements in the matrices are zero except for

$$\begin{cases} \boldsymbol{P}_{\text{i}}(2,1) = -3\boldsymbol{V}_{\text{s1}} \\ \boldsymbol{P}_{\text{i}}(2,3) = -3\boldsymbol{V}_{\text{s1}}^{*} \end{cases} \tag{6.62}$$

$$\begin{cases} \boldsymbol{P}_{\text{v}}(2,1) = -3\boldsymbol{I}_{\text{s1}} \\ \boldsymbol{P}_{\text{v}}(2,3) = -3\boldsymbol{I}_{\text{s1}}^{*} \end{cases} \tag{6.63}$$

According to the structure of MSC, the small-signal vector of the MSC modulation signal can be derived as

$$\hat{\boldsymbol{m}}_{\text{sa}} = \boldsymbol{E}_{\text{si}}\hat{\boldsymbol{i}}_{\text{sa}} + \boldsymbol{E}_{\text{sv}}\hat{\boldsymbol{v}}_{\text{sa}} \tag{6.64}$$

where $\boldsymbol{E}_{\text{si}}$ and $\boldsymbol{E}_{\text{sv}}$ are fifth-order matrices. All other elements in the matrices are zero except for

$$\begin{cases} \boldsymbol{E}_{\text{si}}(1,1) = -H_{\text{si}}(s_1) - \text{j}K_{\text{sd}} - \text{j}\dfrac{3}{2}H_{\text{p}}(s_1)H_{\text{si}}(s_1)\boldsymbol{V}_{\text{s1}} \\ \boldsymbol{E}_{\text{si}}(1,3) = -\text{j}\dfrac{3}{2}H_{\text{p}}(s_1)H_{\text{si}}(s_1)\boldsymbol{V}_{\text{s1}}^{*} \\ \boldsymbol{E}_{\text{si}}(3,1) = \text{j}\dfrac{3}{2}H_{\text{p}}(s_1)H_{\text{si}}(s_1)\boldsymbol{V}_{\text{s1}} \\ \boldsymbol{E}_{\text{si}}(3,3) = -H_{\text{si}}(s_1) + \text{j}K_{\text{sd}} + \text{j}\dfrac{3}{2}H_{\text{p}}(s_1)H_{\text{si}}(s_1)\boldsymbol{V}_{\text{s1}}^{*} \end{cases} \tag{6.65}$$

$$\begin{cases} \boldsymbol{E}_{\mathrm{sv}}(1,1) = -\mathrm{j}\dfrac{3}{2} H_{\mathrm{p}}(s_1) H_{\mathrm{si}}(s_1) \boldsymbol{I}_{\mathrm{s1}} \\ \boldsymbol{E}_{\mathrm{sv}}(1,3) = -\mathrm{j}\dfrac{3}{2} H_{\mathrm{p}}(s_1) H_{\mathrm{si}}(s_1) \boldsymbol{I}_{\mathrm{s1}}^{*} \\ \boldsymbol{E}_{\mathrm{sv}}(3,1) = \mathrm{j}\dfrac{3}{2} H_{\mathrm{p}}(s_1) H_{\mathrm{si}}(s_1) \boldsymbol{I}_{\mathrm{s1}} \\ \boldsymbol{E}_{\mathrm{sv}}(3,3) = \mathrm{j}\dfrac{3}{2} H_{\mathrm{p}}(s_1) H_{\mathrm{si}}(s_1) \boldsymbol{I}_{\mathrm{s1}}^{*} \end{cases} \tag{6.66}$$

Transforming Eq. (6.19) to frequency domain, the small-signal model of MSC main circuit can be obtained as

$$\hat{\boldsymbol{v}}_{\mathrm{sa}} = K_{\mathrm{m}}(V_{\mathrm{dc}} \hat{\boldsymbol{m}}_{\mathrm{sa}} + \boldsymbol{M}_{\mathrm{sa}} \hat{\boldsymbol{v}}_{\mathrm{dc}}) \tag{6.67}$$

After simplification, the small-signal model of MSC can be expressed as

$$\hat{\boldsymbol{v}}_{\mathrm{sa}} = \boldsymbol{B}_{\mathrm{dc}} \hat{\boldsymbol{v}}_{\mathrm{dc}} + \boldsymbol{B}_{\mathrm{si}} \hat{\boldsymbol{i}}_{\mathrm{sa}} \tag{6.68}$$

where $\boldsymbol{B}_{\mathrm{dc}}$ and $\boldsymbol{B}_{\mathrm{si}}$ are fifth-order matrices, whose expression is

$$\begin{cases} \boldsymbol{B}_{\mathrm{dc}} = (\boldsymbol{U} - K_{\mathrm{m}} V_{\mathrm{dc}} \boldsymbol{E}_{\mathrm{sv}})^{-1} K_{\mathrm{m}} \boldsymbol{M}_{\mathrm{sa}} \\ \boldsymbol{B}_{\mathrm{si}} = (\boldsymbol{U} - K_{\mathrm{m}} V_{\mathrm{dc}} \boldsymbol{E}_{\mathrm{sv}})^{-1} K_{\mathrm{m}} V_{\mathrm{dc}} \boldsymbol{E}_{\mathrm{si}} \end{cases} \tag{6.69}$$

$\boldsymbol{M}_{\mathrm{sa}}$ is the extended steady-state matrix of MSC modulation signal, which expression is

$$\boldsymbol{M}_{\mathrm{sa}} = \begin{bmatrix} 0 & \boldsymbol{M}_{\mathrm{s1}}^{*} & 0 & 0 & 0 \\ \boldsymbol{M}_{\mathrm{s1}} & 0 & \boldsymbol{M}_{\mathrm{s1}}^{*} & 0 & 0 \\ 0 & \boldsymbol{M}_{\mathrm{s1}} & 0 & \boldsymbol{M}_{\mathrm{s1}}^{*} & 0 \\ 0 & 0 & \boldsymbol{M}_{\mathrm{s1}} & 0 & \boldsymbol{M}_{\mathrm{s1}}^{*} \\ 0 & 0 & 0 & \boldsymbol{M}_{\mathrm{s1}} & 0 \end{bmatrix}$$

6.3.3 AC Port Impedance Model

The AC port admittance of PMSG-based wind turbines can be obtained as

$$\boldsymbol{Y}_{\mathrm{PMSG}} = -\frac{\hat{\boldsymbol{i}}_{\mathrm{ga}}}{\hat{\boldsymbol{v}}_{\mathrm{a}}} \tag{6.70}$$

Based on Eqs. (6.41), (6.44), (6.58) and (6.68), the relationship of each small-signal vector can be derived

$$\begin{cases} \boldsymbol{G}_{\mathrm{gg}}\hat{\boldsymbol{i}}_{\mathrm{ga}} + \boldsymbol{G}_{\mathrm{gs}}\hat{\boldsymbol{i}}_{\mathrm{sa}} + \boldsymbol{G}_{\mathrm{gv}}\hat{\boldsymbol{v}}_{\mathrm{a}} = 0 \\ \boldsymbol{G}_{\mathrm{sg}}\hat{\boldsymbol{i}}_{\mathrm{ga}} + \boldsymbol{G}_{\mathrm{ss}}\hat{\boldsymbol{i}}_{\mathrm{sa}} + \boldsymbol{G}_{\mathrm{sv}}\hat{\boldsymbol{v}}_{\mathrm{a}} = 0 \end{cases} \tag{6.71}$$

where

$$\begin{cases} \boldsymbol{G}_{\mathrm{gg}} = \boldsymbol{F}_{\mathrm{dc}}\boldsymbol{J}_{\mathrm{gi}} + \boldsymbol{F}_{\mathrm{gi}} \\ \boldsymbol{G}_{\mathrm{gs}} = \boldsymbol{F}_{\mathrm{dc}}\boldsymbol{J}_{\mathrm{si}} + \boldsymbol{F}_{\mathrm{dc}}\boldsymbol{J}_{\mathrm{sv}}\boldsymbol{G}_{\mathrm{s}} \\ \boldsymbol{G}_{\mathrm{gv}} = \boldsymbol{F}_{\mathrm{dc}}\boldsymbol{J}_{\mathrm{gv}} - \boldsymbol{U} \\ \boldsymbol{G}_{\mathrm{sg}} = \boldsymbol{B}_{\mathrm{dc}}\boldsymbol{J}_{\mathrm{gi}} \\ \boldsymbol{G}_{\mathrm{ss}} = \boldsymbol{B}_{\mathrm{dc}}\boldsymbol{J}_{\mathrm{si}} + (\boldsymbol{B}_{\mathrm{dc}}\boldsymbol{J}_{\mathrm{sv}} - \boldsymbol{U})\boldsymbol{G}_{\mathrm{s}} + \boldsymbol{B}_{\mathrm{si}} \\ \boldsymbol{G}_{\mathrm{sv}} = \boldsymbol{B}_{\mathrm{dc}}\boldsymbol{J}_{\mathrm{gv}} \end{cases} \tag{6.72}$$

By solving Eq. (6.71), there is

$$\hat{\boldsymbol{i}}_{\mathrm{ga}} = (\boldsymbol{G}_{\mathrm{gg}} - \boldsymbol{G}_{\mathrm{gs}}\boldsymbol{G}_{\mathrm{ss}}^{-1}\boldsymbol{G}_{\mathrm{sg}})^{-1}(\boldsymbol{G}_{\mathrm{gs}}\boldsymbol{G}_{\mathrm{ss}}^{-1}\boldsymbol{G}_{\mathrm{sv}} - \boldsymbol{G}_{\mathrm{gv}})\hat{\boldsymbol{v}}_{\mathrm{a}} \tag{6.73}$$

The AC port admittance of PMSG-based wind turbine can be obtained as

$$\boldsymbol{Y}_{\mathrm{PMSG}} = -(\boldsymbol{G}_{\mathrm{gg}} - \boldsymbol{G}_{\mathrm{gs}}\boldsymbol{G}_{\mathrm{ss}}^{-1}\boldsymbol{G}_{\mathrm{sg}})^{-1}(\boldsymbol{G}_{\mathrm{gs}}\boldsymbol{G}_{\mathrm{ss}}^{-1}\boldsymbol{G}_{\mathrm{sv}} - \boldsymbol{G}_{\mathrm{gv}}) \tag{6.74}$$

Since there are only components at f_{p} and $f_{\mathrm{p}} - 2f_{\mathrm{l}}$ in small-signal vectors of AC voltage and AC current of PMSG-based wind turbines, only relevant elements at these two frequencies are extracted, and the AC port admittance shown in Eq. (6.74) are rearranged as the following 2×2 matrix.

$$\begin{bmatrix} \boldsymbol{Y}_{\mathrm{PMSG}}^{\mathrm{pp}} & \boldsymbol{Y}_{\mathrm{PMSG}}^{\mathrm{np}} \\ \boldsymbol{Y}_{\mathrm{PMSG}}^{\mathrm{pn}} & \boldsymbol{Y}_{\mathrm{PMSG}}^{\mathrm{nn}} \end{bmatrix} = \begin{bmatrix} \boldsymbol{Y}_{\mathrm{PMSG}}(3,3) & \boldsymbol{Y}_{\mathrm{PMSG}}(3,1) \\ \boldsymbol{Y}_{\mathrm{PMSG}}(1,3) & \boldsymbol{Y}_{\mathrm{PMSG}}(1,1) \end{bmatrix} \tag{6.75}$$

where

$\boldsymbol{Y}_{\mathrm{PMSG}}(3,3)$ is the element in the third row and the third column of $\boldsymbol{Y}_{\mathrm{PMSG}}$;
$\boldsymbol{Y}_{\mathrm{PMSG}}(3,1)$ is the element in the third row and the first column of $\boldsymbol{Y}_{\mathrm{PMSG}}$;
$\boldsymbol{Y}_{\mathrm{PMSG}}(1,3)$ is the element in the first row and the third column of $\boldsymbol{Y}_{\mathrm{PMSG}}$;
$\boldsymbol{Y}_{\mathrm{PMSG}}(1,1)$ is the element in the first row and the first column of $\boldsymbol{Y}_{\mathrm{PMSG}}$.

The relationship between the small-signal components of AC voltage and AC current at the perturbation frequency and coupling frequency meets

$$\begin{bmatrix} -\hat{\boldsymbol{i}}_{\mathrm{p}} \\ -\hat{\boldsymbol{i}}_{\mathrm{p-2}} \end{bmatrix} = \begin{bmatrix} \boldsymbol{Y}_{\mathrm{PMSG}}^{\mathrm{pp}} & \boldsymbol{Y}_{\mathrm{PMSG}}^{\mathrm{np}} \\ \boldsymbol{Y}_{\mathrm{PMSG}}^{\mathrm{pn}} & \boldsymbol{Y}_{\mathrm{PMSG}}^{\mathrm{nn}} \end{bmatrix} \begin{bmatrix} \hat{\boldsymbol{v}}_{\mathrm{p}} \\ \hat{\boldsymbol{v}}_{\mathrm{p-2}} \end{bmatrix} \tag{6.76}$$

where

$\boldsymbol{Y}_{\mathrm{PMSG}}^{\mathrm{pp}}$ is the positive-sequence admittance of PMSG-based wind turbines, representing the small-signal response of AC current at f_{p} in positive sequence under per unit small-signal perturbation of AC voltage at f_{p} in positive sequence.
$\boldsymbol{Y}_{\mathrm{PMSG}}^{\mathrm{pn}}$ is the positive-sequence coupling admittance of PMSG-based wind turbines, representing the small-signal response of AC current at $f_{\mathrm{p}} - 2f_1$ in negative sequence under per unit small-signal perturbation of AC voltage at f_{p} in positive sequence.
$\boldsymbol{Y}_{\mathrm{PMSG}}^{\mathrm{nn}}$ is the negative-sequence admittance of PMSG-based wind turbines, representing the small-signal response of AC current at $f_{\mathrm{p}} - 2f_1$ in negative sequence under per unit small-signal perturbation of AC voltage at $f_{\mathrm{p}} - 2f_1$ in negative sequence.
$\boldsymbol{Y}_{\mathrm{PMSG}}^{\mathrm{np}}$ is the negative-sequence coupling admittance of PMSG-based wind turbines, representing the small-signal response of AC current at f_{p} in positive sequence under per unit small-signal perturbation of AC voltage at $f_{\mathrm{p}} - 2f_1$ in negative sequence.

The AC port impedance of PMSG-based wind turbine can be obtained by calculating the inverse matrix of the AC port admittance as

$$\begin{bmatrix} \boldsymbol{Z}_{\mathrm{PMSG}}^{\mathrm{pp}} & \boldsymbol{Z}_{\mathrm{PMSG}}^{\mathrm{pn}} \\ \boldsymbol{Z}_{\mathrm{PMSG}}^{\mathrm{np}} & \boldsymbol{Z}_{\mathrm{PMSG}}^{\mathrm{nn}} \end{bmatrix} = \begin{bmatrix} \boldsymbol{Y}_{\mathrm{PMSG}}^{\mathrm{pp}} & \boldsymbol{Y}_{\mathrm{PMSG}}^{\mathrm{np}} \\ \boldsymbol{Y}_{\mathrm{PMSG}}^{\mathrm{pn}} & \boldsymbol{Y}_{\mathrm{PMSG}}^{\mathrm{nn}} \end{bmatrix}^{-1} \tag{6.77}$$

$\boldsymbol{Z}_{\mathrm{PMSG}}^{\mathrm{pp}}$ represents the positive-sequence impedance of PMSG-based wind turbines, which is the element in the first row and the first column of the AC port admittance inverse matrix.
$\boldsymbol{Z}_{\mathrm{PMSG}}^{\mathrm{pn}}$ represents the positive-sequence coupling impedance of PMSG-based wind turbines, which is the element in the first row and the second column of the AC port admittance inverse matrix.
$\boldsymbol{Z}_{\mathrm{PMSG}}^{\mathrm{nn}}$ represents the negative-sequence impedance of PMSG-based wind turbines, which is the element in the second row and the second column of the AC port admittance inverse matrix.
$\boldsymbol{Z}_{\mathrm{PMSG}}^{\mathrm{np}}$ represents the negative-sequence coupling impedance of PMSG-based wind turbines, which is the element in the second row and the first column of the AC port admittance inverse matrix.

In addition, the frequency-domain relationship between the negative-sequence impedance and the positive-sequence impedance satisfies $\boldsymbol{Z}_{\mathrm{PMSG}}^{\mathrm{nn}} = \boldsymbol{Z}_{\mathrm{PMSG}}^{\mathrm{pp}^*}(\mathrm{j}2\omega_1 - s)$, and the frequency-domain relationship between the negative-sequence coupling impedance and the positive-sequence coupling impedance satisfies $\boldsymbol{Z}_{\mathrm{PMSG}}^{\mathrm{np}} = \boldsymbol{Z}_{\mathrm{PMSG}}^{\mathrm{pn}^*}(\mathrm{j}2\omega_1 - s)$.

Table 6.2 lists the main circuit and controller parameters of PMSG-based wind turbines. Figure 6.13 shows the comparison between analytical impedance (in solid lines) and scanning impedance (in discrete points). As seen from the figure, all the

Table 6.2 The main circuit and controller parameters of PMSG-based wind turbines

Parameter	Definition	Value
P_N	Rated power	1.5 MW
V_N	Rated AC voltage	563 V
f_1	Rated frequency	50 Hz
R_s	PMSG stator resistance	0.001 Ω
L_{sd}, L_{sq}	d- and q-axis inductance of the PMSG stator	2.7×10^{-4} H, 2.8×10^{-4} H
L_f	GSC filter inductance	0.0001 H
V_{dc}	DC voltage steady-state value	1200 V
K_{pp}, K_{pi}	Proportional and integral coefficients of PLL controller	0.0191, 1.6473
K_{gip}, K_{gii}	Proportional and integral coefficients of GSC AC current controller	1.8000×10^{-4}, 0.3386
K_{sip}, K_{sii}	Proportional and integral coefficients of MSC AC current controller	1.1000×10^{-5}, 6.3000×10^{-5}
K_{pep}, K_{pei}	Proportional and integral coefficients of MSC active power controller	6×10^{-5}, 1.1000×10^{-4}
K_{qep}, K_{qei}	Proportional and integral coefficients of GSC reactive power controller	5.900×10^{-4}, 0.0322
K_{vdcp}, K_{vdci}	Proportional and integral coefficients of DC voltage controller	9.5139, 1523
K_{sd}	Decoupling coefficient of MSC AC current control	4.2000×10^{-5}
K_{gd}	Decoupling coefficient of GSC AC current control	2.3000×10^{-5}

discrete points fall on the solid lines, which verify the accuracy of the established impedance model of PMSG-based wind turbines.

6.4 Analysis of Broadband Impedance Characteristics

In this section, based on the impedance model of PMSG-based wind turbines, the dominant factors of impedance characteristics in different frequency bands are analyzed, and the frequency-band division method of PMSG-based wind turbine impedance is proposed. Then, the frequency-band overlapping effects of multiple controllers are clarified and the negative damping characteristics of each frequency band are analyzed. Finally, based on CHIL impedance scanning results of different types of PMSG-based wind turbines, typical values of frequency band division are given.

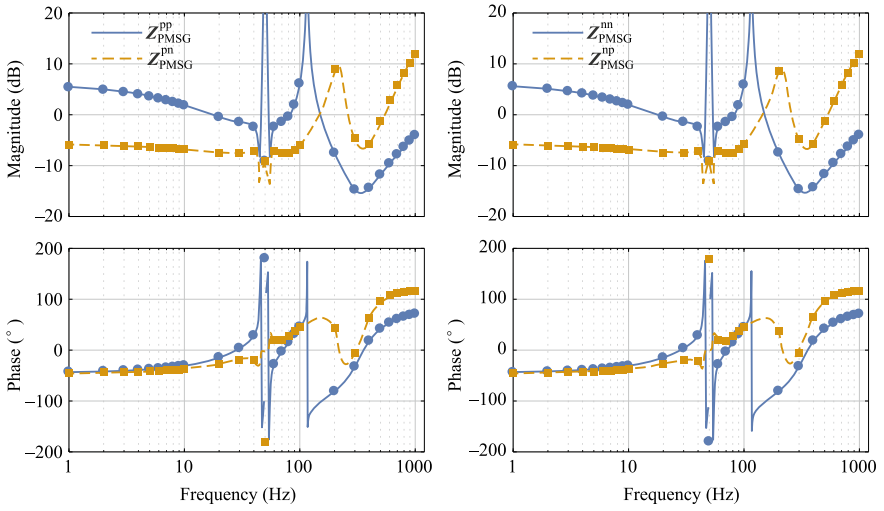

(a) Positive-sequence impedance and positive-sequence coupling impedance

(b) Negative-sequence impedance and negative-sequence coupling impedance

Fig. 6.13 Analytical and scanning results of PMSG-based wind turbine impedance

6.4.1 Frequency-Band Division of Broadband Impedance

In this section, the dominant factors of PMSG-based wind turbines impedance characteristics in each frequency band are analyzed, and the impedance frequency-band division method is proposed.

6.4.1.1 Influence of PLL on Impedance Characteristics

The block diagram of PLL is shown in Fig. 6.14, and the open-loop transfer function is shown in Eq. (6.78).

$$G_{\mathrm{PLL}}(s) = H_{\mathrm{PLL}}(s)V_1 \tag{6.78}$$

where $H_{\mathrm{PLL}}(s)$ is the transfer function of PLL.

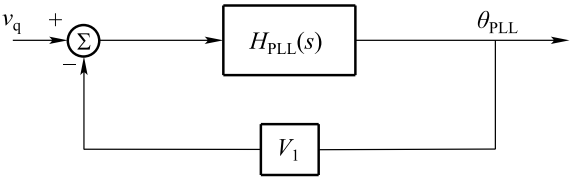

Fig. 6.14 Block diagram of PLL

Given PLL bandwidth f_{tc} and phase margin (PM) θ_{tc}, the proportional integral (PI) coefficients can be solved from Eq. (6.79).

$$\begin{cases} |V_1 H_{PLL}(s)|_{s=j2\pi f_{tc}} = 1 \\ \angle(V_1 H_{PLL}(s))_{s=j2\pi f_{tc}} = \theta_{tc} - 180^\circ \end{cases} \tag{6.79}$$

where the open-loop gain is 1 at f_{tc}, the corresponding PM is θ_{tc}.

The influence of PLL on impedance characteristics is shown in Fig. 6.15. On the one hand, the influence of PLL bandwidth can be obtained by setting f_{tc} to 5, 20 and 30 Hz respectively with a constant PM of 45°. On the other hand, the influence of PLL PM can be obtained by setting θ_{tc} to 20°, 45°and 70° respectively with a constant bandwidth of 5Hz.

As shown in Fig. 6.15, the bandwidth f_{tc} of PLL mainly affects the frequency of the impedance resonance peak $f_1 - f_{tc}$ and $f_1 + f_{tc}$. With the increase of f_{tc}, the difference between the resonance peak frequency and the fundamental frequency increases. At the frequency of the resonance peak, the phase of the impedance represents capacitive negative damping characteristics (the phase of the impedance less than −90°). The PM θ_{tc} of PLL mainly affects the impedance magnitude and phase at the frequency of the impedance resonance peak $f_1 - f_{tc}$ and $f_1 + f_{tc}$. With the increase of θ_{tc}, the level of the capacitive negative damping decreases. In conclusion, PLL mainly affects the impedance characteristics in $f_1 - f_{tc} < f < f_1 + f_{tc}$.

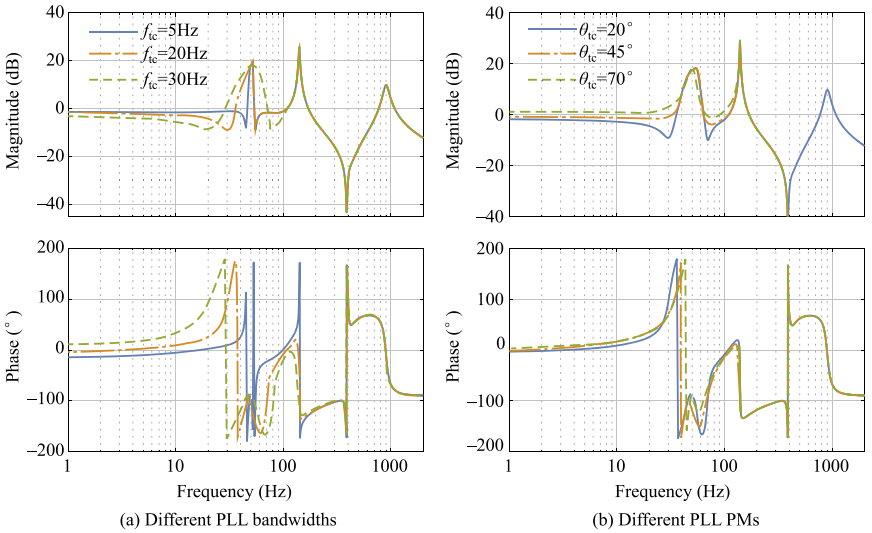

Fig. 6.15 Influence of PLL on impedance characteristics

6.4.1.2 Influence of GSC AC Current Loop on Impedance Characteristics

The block diagram of GSC AC current loop is shown in Fig. 6.16, and the open-loop transfer function is shown in Eq. (6.80).

$$G_{\mathrm{gi}}(s) = H_{\mathrm{gi}}(s)\frac{K_{\mathrm{m}}V_{\mathrm{dc}}}{sL_{\mathrm{f}}} \tag{6.80}$$

where $H_{\mathrm{gi}}(s)$ is the transfer function of GSC AC current loop.

Given GSC AC current loop bandwidth f_{gic} and PM θ_{gic}, the PI coefficients can be solved from Eq. (6.81).

$$\begin{cases} \left| H_{\mathrm{gi}}(s)\dfrac{K_{\mathrm{m}}V_{\mathrm{dc}}}{sL_{\mathrm{f}}} \right|_{s=\mathrm{j}2\pi f_{\mathrm{gic}}} = 1 \\ \angle\left(H_{\mathrm{gi}}(s)\dfrac{K_{\mathrm{m}}V_{\mathrm{dc}}}{sL_{\mathrm{f}}} \right)_{s=\mathrm{j}2\pi f_{\mathrm{gic}}} = \theta_{\mathrm{gic}} - 180^\circ \end{cases} \tag{6.81}$$

where the open-loop gain is 1 at f_{gic}, the corresponding PM is θ_{gic}.

The influence of GSC AC current loop on impedance characteristics is shown in Fig. 6.17. On the one hand, the influence of GSC AC current loop bandwidth can be obtained by setting f_{gic} to 100, 200 and 300 Hz respectively with a constant PM of 45°. On the other hand, the influence of GSC AC current loop PM can be obtained by setting θ_{gic} to 10°, 45° and 80° respectively with a constant bandwidth of 200Hz.

As shown in Fig. 6.17, GSC AC current loop mainly affects the impedance characteristics in $f < f_1 - f_{\mathrm{tc}}$ and $f_1 + f_{\mathrm{tc}} < f < f_1 + f_{\mathrm{gic}}$. At GSC AC current loop bandwidth $f_1 + f_{\mathrm{gic}}$ (in SCF), the magnitude of the impedance exhibits a resonant peak, the phase of the impedance changes from capacitive to inductive. With the increase of f_{gic}, the frequency of resonant peak increases. In addition, as GSC AC current loop PM θ_{gic} decreases, the resonant peak becomes steeper, the phase change becomes more intense, and the level of damping characteristics deepens.

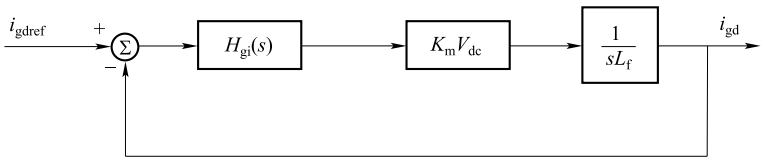

Fig. 6.16 Block diagram of GSC AC current loop

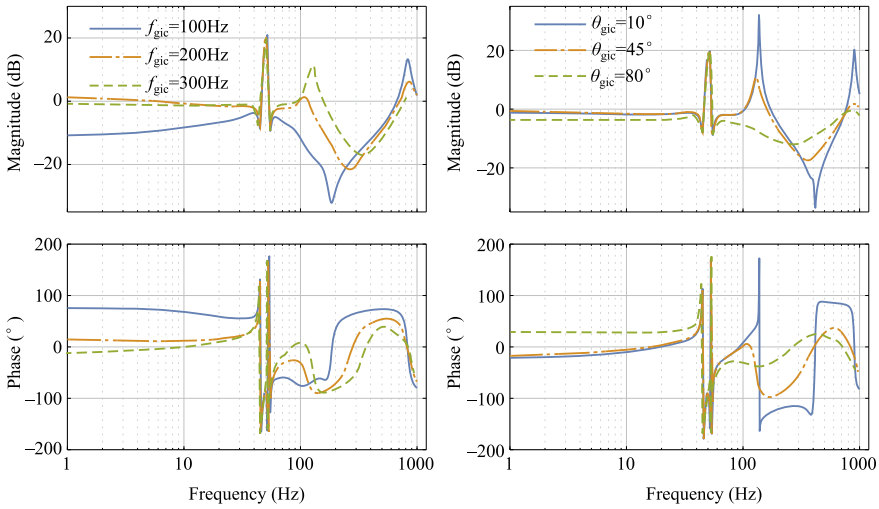

(a) Different GSC AC current loop bandwidths (b) Different GSC AC current loop PMs

Fig. 6.17 Influence of GSC current loop on impedance characteristics

6.4.1.3 Influence of LC Filter on Impedance Characteristics

According to the influence of GSC AC current loop on the impedance characteristics, when the frequency reaches GSC AC current loop bandwidth, the impedance characteristics change from capacitive to inductive. As the frequency further increases to the LC resonant frequency, the impedance characteristic changes from inductive to capacitive. The LC resonant frequency is related to the filter parameters. The influence of LC filter on impedance characteristics is shown in Fig. 6.18. The influence of the filter capacitor C_f is obtained by setting C_f to 0.3, 0.4 and 0.5 mF respectively with a constant filter inductance.

As shown in Fig. 6.18, LC filter mainly affects the impedance characteristics in $f > f_1 + f_{gic}$.The impedance is inductive at first, and at the LC resonant frequency, the phase changes from inductive to capacitive.

6.4.1.4 Influence of the Steady-State Operating Point on Impedance Characteristics

The impedance model of PMSG-based wind turbines is obtained by small-signal linearization based on the steady-state operating point. During the operation of PMSG-based wind turbines, the change of wind speed will lead to the variation of the steady-state operating point. Figure 6.19 shows the three-dimensional bode diagram of the influence of the steady-state operating point (active power) on impedance characteristics. It can be seen from the figure that the steady-state operating point mainly affects the impedance characteristics in $f < f_1 + f_{gic}$.

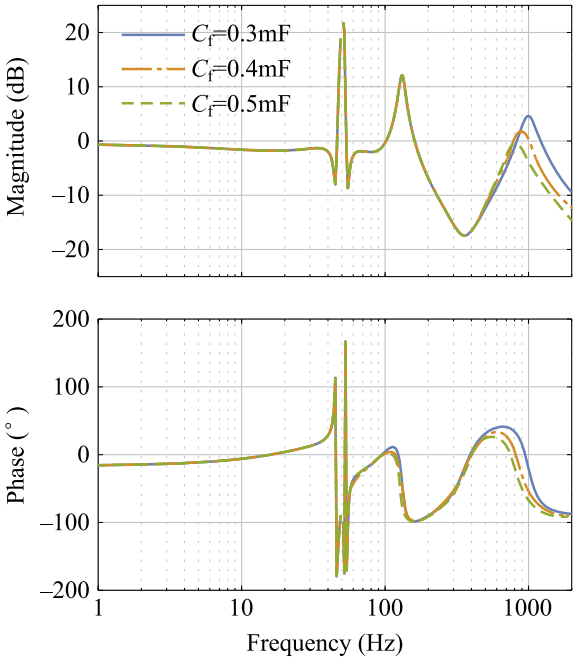

Fig. 6.18 Influence of LC filter on impedance characteristics

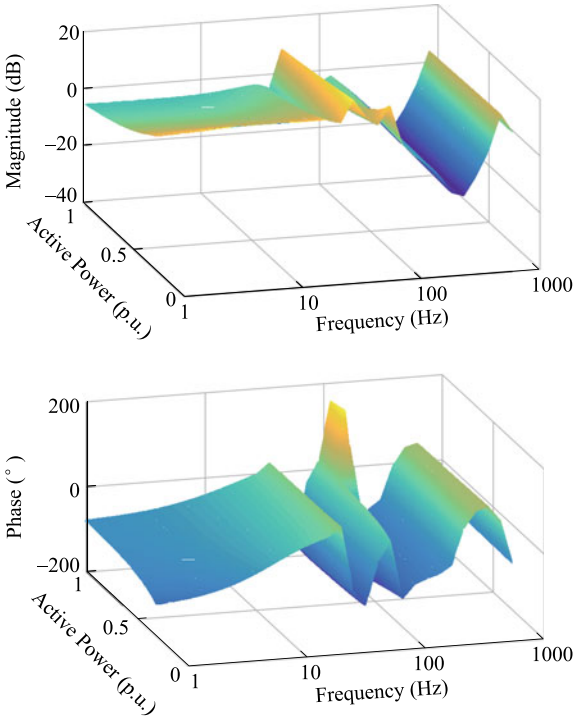

Fig. 6.19 Influence of the steady-state operating point on impedance characteristics

6.4.1.5 Frequency-Band Division Principle of Broadband Impedance

According to the dominant factors of PMSG-based wind turbines impedance characteristics in each frequency band, the following frequency bands can be divided:

1. Band $\mathrm{I}_{\mathrm{PMSG}}$ ($f < f_1 - f_{\mathrm{tc}}$): There is no dominant factors of PMSG-based wind turbines impedance characteristics. PLL, GSC AC current loop, and steady-state operating point all have an influence on the impedance characteristics in this band.
2. Band $\mathrm{II}_{\mathrm{PMSG}}$ ($f_1 - f_{\mathrm{tc}} < f < f_1 + f_{\mathrm{tc}}$): The impedance characteristics of PMSG-based wind turbines are dominated by PLL. As the bandwidth f_{tc} of PLL increases, the frequency range of Band $\mathrm{II}_{\mathrm{PMSG}}$ expands. As the PM θ_{tc} of PLL increases, the level of capacitive negative damping decreases.
3. Band $\mathrm{III}_{\mathrm{PMSG}}$ ($f_1 + f_{\mathrm{tc}} < f < f_1 + f_{\mathrm{gic}}$): The impedance characteristics of PMSG-based wind turbines are dominated by GSC AC current loop. With the increase of the bandwidth f_{gic}, the frequency range in which the impedance represents capacitive characteristics increases. With the increase of the PM θ_{gic}, the level of capacitive damping weakens.
4. Band $\mathrm{IV}_{\mathrm{PMSG}}$ ($f > f_1 + f_{\mathrm{gic}}$): The impedance characteristics of PMSG-based wind turbines are dominated by LC filter. As the frequency increases, the impedance changes from inductive to capacitive, and the resonance frequency is related to the main circuit LC filter parameters.

Impedance scanning is carried out based on CHIL platform of different types of PMSG-based wind turbines, and the scanning results are shown in Figs. 6.20, 6.21 and 6.22. It can be seen from the figure that the frequency range of Band $\mathrm{I}_{\mathrm{PMSG}}$ is around $f < 37$ Hz, the frequency range of Band $\mathrm{II}_{\mathrm{PMSG}}$ is around 37 Hz $< f <$ 63 Hz, the frequency range of Band $\mathrm{III}_{\mathrm{PMSG}}$ is around 63 Hz $< f <$ 420 Hz, and the frequency range of Band $\mathrm{IV}_{\mathrm{PMSG}}$ is around $f >$ 420 Hz.

6.4.2 Analysis of Negative Damping Characteristics

The frequency-band division principle of PMSG-based wind turbine impedance is proposed in Sect. 6.4.1. Considering the control system of PMSG-based wind turbine involves the coordination of multiple controllers, the impedance characteristics in each frequency band are affected not only by the dominant factors, but also by the frequency-band overlapping effects of other controllers. In this section, the frequency-band overlapping effects of MSC AC current loop, power loop, DC voltage loop and time delay will be analyzed to reveal the mechanism of the negative damping characteristics in each frequency band.

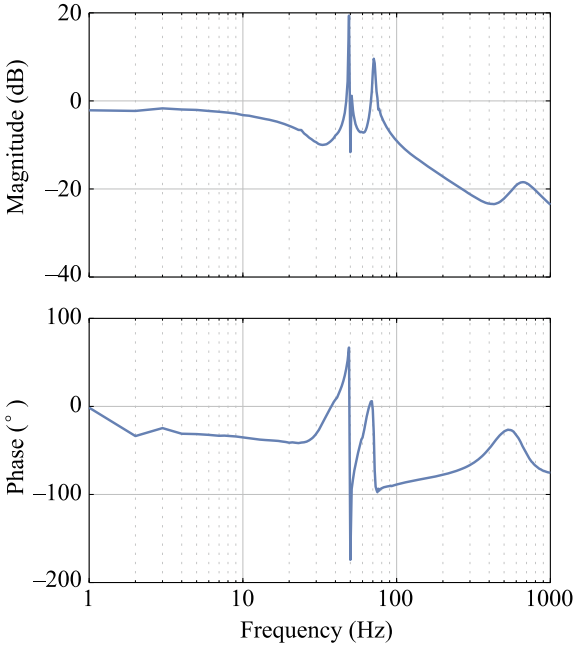

Fig. 6.20 Impedance of a 2.0 MWPMSG-based wind turbine (Type A)

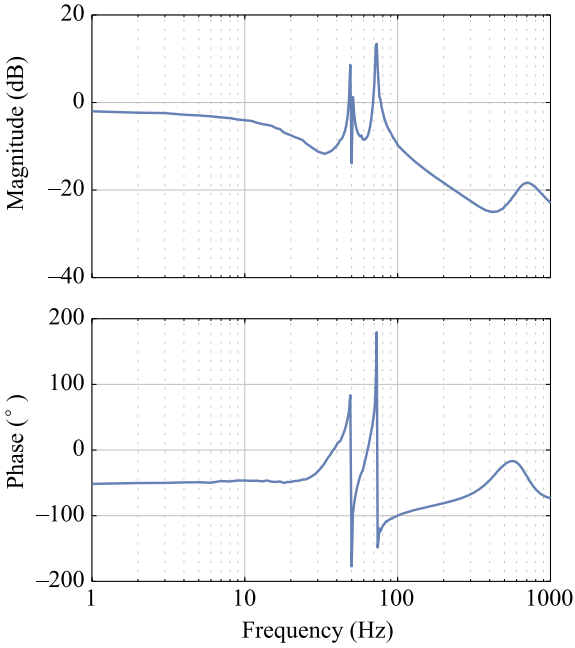

Fig. 6.21 Impedance of a 2.5 MWPMSG-based wind turbine (Type B)

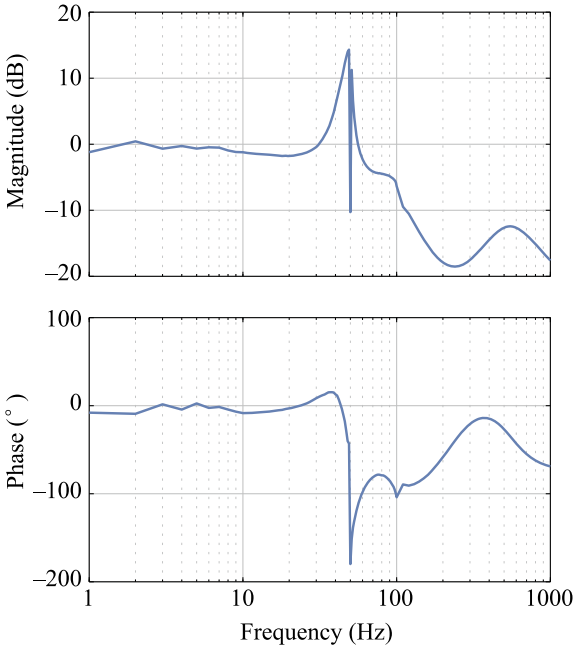

Fig. 6.22 Impedance of a 4.5 MWPMSG-based wind turbine (Type C)

6.4.2.1 Analysis of Negative Damping Characteristics in Band $\mathrm{II}_{\mathrm{PMSG}}$

In Band $\mathrm{II}_{\mathrm{PMSG}}$, the impedance characteristics of PMSG-based wind turbine are dominated by PLL. In addition, the impedance characteristics are also affected by DC voltage loop and GSC reactive power loop. In this section, the effects of DC voltage loop and reactive power loop on the impedance characteristics in Band $\mathrm{II}_{\mathrm{PMSG}}$ are analyzed to clarify the frequency-band overlapping effect.

1. Influence of DC Voltage Loop on Negative Damping Characteristics

The block diagram of DC voltage loop is shown in Fig. 6.23, and the open-loop transfer function is shown in Eq. (6.82).

$$G_{\mathrm{vdc}}(s) = \frac{3V_1}{2V_{\mathrm{dc}}C_{\mathrm{dc}}s} H_{\mathrm{vdc}}(s) \tag{6.82}$$

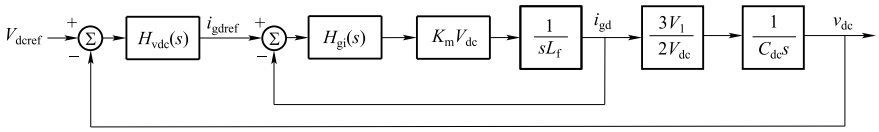

Fig. 6.23 Block diagram of DC power loop

Given the DC voltage loop bandwidth f_{vdc} and PM θ_{vdc}, the PI coefficients can be solved from

$$\begin{cases} \left| \dfrac{3V_1}{2V_{\mathrm{dc}}C_{\mathrm{dc}}s} H_{\mathrm{vdc}}(s) \right|_{s=\mathrm{j}2\pi f_{\mathrm{vdc}}} = 1 \\ \angle\left(\dfrac{3V_1}{2V_{\mathrm{dc}}C_{\mathrm{dc}}s} H_{\mathrm{vdc}}(s) \right)_{s=\mathrm{j}2\pi f_{\mathrm{vdc}}} = \theta_{\mathrm{vdc}} - 180^\circ \end{cases} \tag{6.83}$$

where the open-loop gain is 1 at f_{vdc}, the corresponding PM is θ_{vdc}.

The influence of DC voltage loop on the damping characteristics in Band $\mathrm{II}_{\mathrm{PMSG}}$ is shown in Fig. 6.24. The influence of DC voltage loop PM can be obtained by setting θ_{vdc} to 20°, 45° and 70° respectively with a constant bandwidth of 10 Hz.

As shown in Fig. 6.24, the frequency-band overlapping effect of PLL and DC voltage loop results in negative damping characteristics in this band. The PM of DC voltage loop affects the level of negative damping.

2. Influence of Reactive Power Loop on Negative Damping Characteristics

The block diagram of reactive power loop is shown in Fig. 6.25, and the open-loop transfer function is shown in Eq. (6.84).

$$G_{\mathrm{q}}(s) = \frac{3}{2} V_1 H_{\mathrm{q}}(s) \tag{6.84}$$

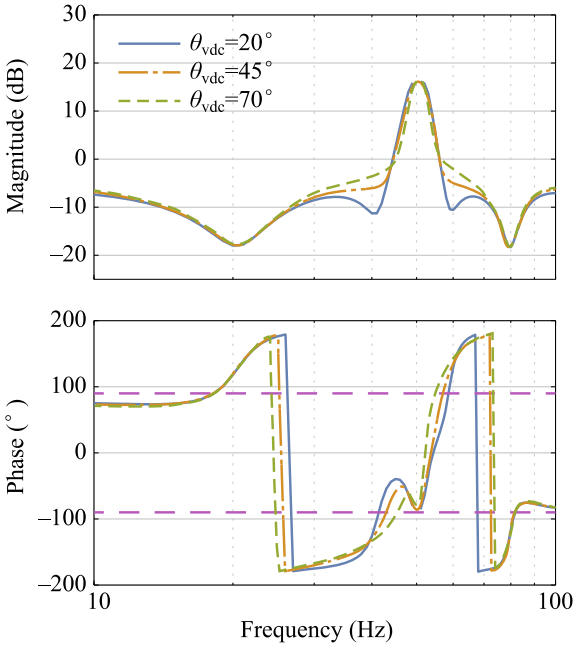

Fig. 6.24 Influence of GSC DC voltage loop PM on the damping characteristics in Band $\mathrm{II}_{\mathrm{PMSG}}$

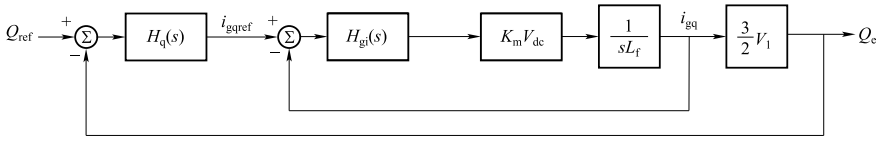

Fig. 6.25 Block diagram of GSC reactive power loop

Given the reactive power loop bandwidth f_{qc} and PM θ_{qc}, the PI coefficients can be solved from

$$\begin{cases} \left|\frac{3}{2}V_1 H_q(s)\right|_{s=j2\pi f_{qc}} = 1 \\ \angle\left(\frac{3}{2}V_1 H_q(s)\right)_{s=j2\pi f_{qc}} = \theta_{qc} - 180^\circ \end{cases} \tag{6.85}$$

where the open-loop gain is 1 at f_{qc}, the corresponding PM is θ_{qc}.

The influence of reactive power loop on the damping characteristics in Band II_{PMSG} is shown in Fig. 6.26. The influence of the reactive power loop PM can be obtained by setting θ_{qc} to 110°, 145° and 170° respectively with a constant bandwidth of 10 Hz.

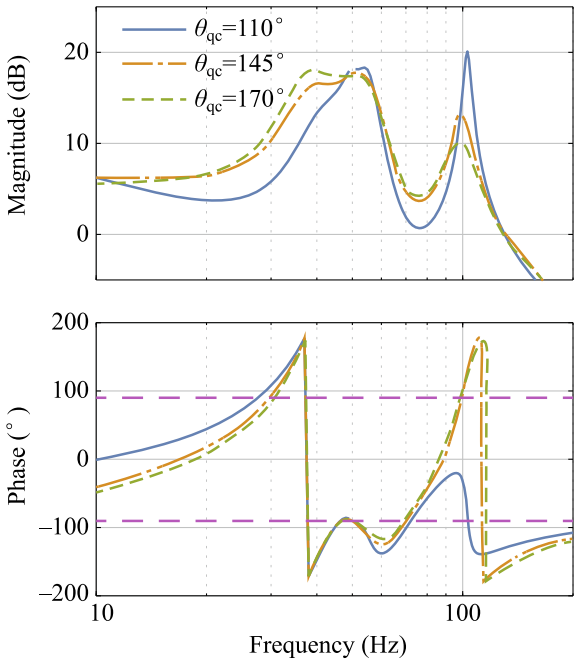

Fig. 6.26 Influence of reactive power loop PM on the damping characteristics in Band II_{PMSG}

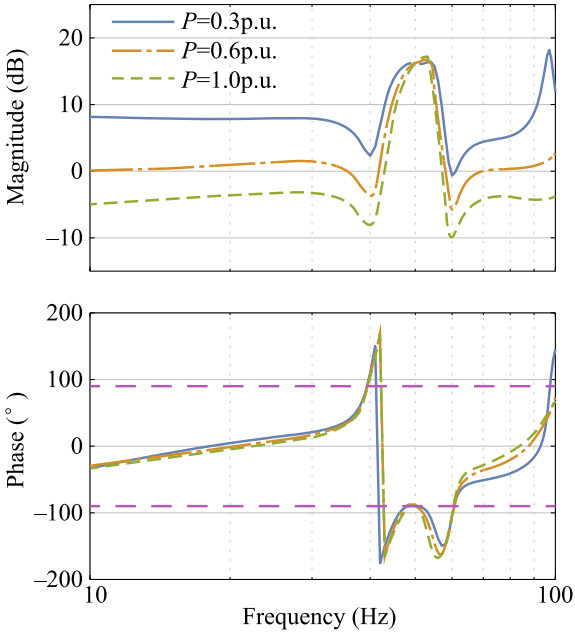

Fig. 6.27 Influence of the steady-state operating point on the damping characteristics in Band $\mathrm{II}_{\mathrm{PMSG}}$

As shown in Fig. 6.26, the frequency-band overlapping effect of PLL and reactive power loop affects the level of negative damping in this band. With the increase of the reactive power loop PM, the level of negative damping deepens.

3. Influence of the Steady-State Operating Point on Negative Damping Characteristics

Figure 6.27 shows the influence of the steady-state operating point on the damping characteristics in Band $\mathrm{II}_{\mathrm{PMSG}}$ when the active power changes from 0.3, 0.6 to 1.0 p.u. It can be seen that the magnitude of the impedance decreases with the increase of active power.

6.4.2.2 Analysis of Negative Damping Characteristics in Band $\mathrm{III}_{\mathrm{PMSG}}$

In Band $\mathrm{III}_{\mathrm{PMSG}}$, the impedance characteristics of PMSG-based wind turbine are dominated by GSC AC current loop. The impedance characteristics in the first half band are also affected by DC voltage loop, GSC AC current loop, MSC AC current loop, and active power loop at the same time. The impedance characteristics in the second half band are affected by time delay.

1. Influence of DC Voltage Loop on Negative Damping Characteristics

The influence of DC voltage loop on the damping characteristics in Band $\mathrm{III}_{\mathrm{PMSG}}$ is shown in Fig. 6.28. On the one hand, the influence of DC voltage loop bandwidth

can be obtained by setting f_{vdc} to 50, 70 and 100 Hz respectively with a constant PM of 60°. On the other hand, the influence of power loop PM can be obtained by setting θ_{vdc} to 10°, 45° and 80° respectively with a constant bandwidth of 70 Hz.

As shown in Fig. 6.28, the frequency-band overlapping effect of GSC current loop and DC voltage loop results in negative damping characteristics in this band. As the bandwidth and PM of DC voltage loop decreases, the level of negative damping deepens.

2. Influence of MSC Current Loop on Negative Damping Characteristics

The block diagram of MSC AC current loop is shown in Fig. 6.29, and the open-loop transfer function is shown in Eq. (6.86).

$$G_{\mathrm{si}}(s) = H_{\mathrm{si}}(s)\frac{K_{\mathrm{m}}V_{\mathrm{dc}}}{sL_{\mathrm{sq}}} \tag{6.86}$$

Given the MSC AC current loop bandwidth f_{sic} and PM θ_{sic}, the PI coefficients can be solved from

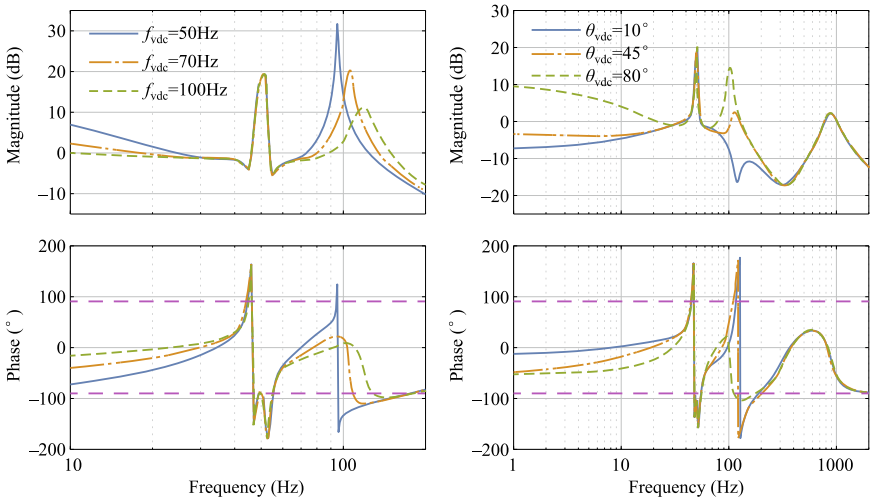

(a) Different DC voltage loop bandwidths (b) Different DC voltage loop PMs

Fig. 6.28 Influence of GSC DC voltage loop on the damping characteristics in Band III$_{\mathrm{PMSG}}$

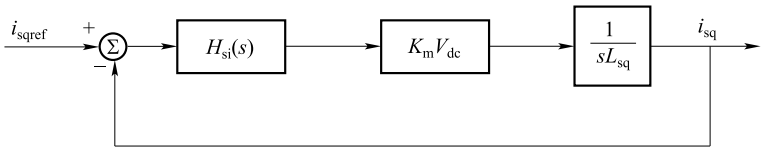

Fig. 6.29 Block diagram of MSC AC current loop

$$\begin{cases} \left| H_{\mathrm{si}}(s) \dfrac{K_{\mathrm{m}} V_{\mathrm{dc}}}{s L_{\mathrm{sq}}} \right|_{s=\mathrm{j}2\pi f_{\mathrm{sic}}} = 1 \\ \angle \left(H_{\mathrm{si}}(s) \dfrac{K_{\mathrm{m}} V_{\mathrm{dc}}}{s L_{\mathrm{sq}}} \right)_{s=\mathrm{j}2\pi f_{\mathrm{sic}}} = \theta_{\mathrm{sic}} - 180^{\circ} \end{cases} \tag{6.87}$$

where the open-loop gain is 1 at f_{sic}, the corresponding PM is θ_{sic}.

The influence of MSC AC current loop on the damping characteristics in Band $\mathrm{III}_{\mathrm{PMSG}}$ is shown in Fig. 6.30. On the one hand, the influence of MSC AC current loop bandwidth can be obtained by setting f_{sic} to 20, 40 and 60 Hz respectively with a constant PM of 45°. On the other hand, the influence of MSC AC current loop PM can be obtained by setting θ_{sic} to 10°, 45° and 70° respectively with a constant bandwidth of 60 Hz.

As shown in Fig. 6.30, there is a frequency-band overlapping effect of MSC AC current loop and GSC AC current loop in Band $\mathrm{III}_{\mathrm{PMSG}}$. As MSC AC current loop bandwidth increases, the level of negative damping decreases. MSC AC current loop PM has little effect on the level of negative damping. Since the DC bus provides a small-signal coupling path for MSC and GSC, the influence of MSC AC current loop on the damping characteristics is closely related to the DC bus capacitance and MSC AC current loop bandwidth. The larger the DC bus capacitance is, the smaller the effect of MSC AC current loop on damping characteristics is. The larger MSC AC current loop bandwidth is, the smaller the effect of MSC AC current loop on damping characteristics is. Especially, when MSC AC current loop bandwidth is higher than DC voltage loop bandwidth, the effect of MSC AC current loop on damping characteristics is significantly reduced.

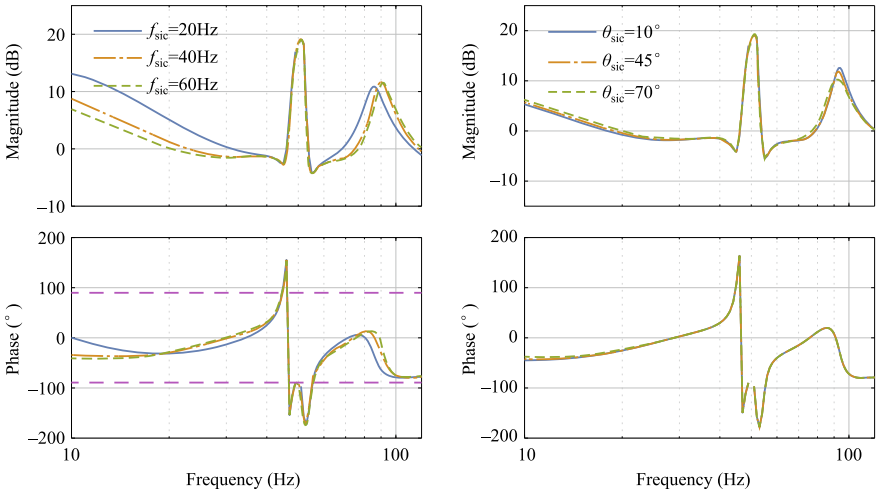

(a) Different MSC current loop bandwidths

(b) Different MSC current loop PMs

Fig. 6.30 Influence of MSC AC current loop on the damping characteristics in Band $\mathrm{III}_{\mathrm{PMSG}}$

3. Influence of Active Power Loop on Negative Damping Characteristics

The block diagram of active power loop is shown in Fig. 6.31, and the open-loop transfer function is shown in Eq. (6.88).

$$G_{\mathrm{p}}(s) = H_{\mathrm{p}}(s)\frac{3}{2}\omega_{\mathrm{r}}\psi_{\mathrm{f}} \tag{6.88}$$

Given the active power loop bandwidth f_{pc} and PM θ_{pc}, the PI coefficients can be solved from

$$\begin{cases} \left| H_{\mathrm{p}}(s)\frac{3}{2}\omega_{\mathrm{r}}\psi_{\mathrm{f}} \right|_{s=\mathrm{j}2\pi f_{\mathrm{pc}}} = 1 \\ \angle\left(H_{\mathrm{p}}(s)\frac{3}{2}\omega_{\mathrm{r}}\psi_{\mathrm{f}} \right)_{s=\mathrm{j}2\pi f_{\mathrm{pc}}} = \theta_{\mathrm{pc}} - 180^{\circ} \end{cases} \tag{6.89}$$

where the open-loop gain is 1 at f_{pc}, the corresponding PM is θ_{pc}.

The influence of active power loop on the damping characteristics in Band $\mathrm{III}_{\mathrm{PMSG}}$ is shown in Fig. 6.32. On the one hand, the influence of active power loop bandwidth can be obtained by setting f_{pc} to 0.5, 5 and 10 Hz respectively with a constant PM of 120°. On the other hand, the influence of active power loop PM can be obtained by setting θ_{pc} to 120°, 145° and 170° respectively with a constant bandwidth of 0.5 Hz.

As shown in Fig. 6.32, the active power loop bandwidth and PM have little effect on the damping characteristics in Band $\mathrm{III}_{\mathrm{PMSG}}$.

4. Influence of Time Delay on Negative Damping Characteristics

The influence of time delay on the damping characteristics in Band $\mathrm{III}_{\mathrm{PMSG}}$ is shown in Fig. 6.33. The influence of time delay can be obtained by changing it to 0, 50 and 100 μs respectively with a constant LC filter parameters. As shown in Fig. 6.33, the frequency-band overlapping effect of time delay and GSC AC current loop leads to negative damping characteristics in Band $\mathrm{III}_{\mathrm{PMSG}}$. In addition, with the increase of time delay, the level of negative damping deepens.

5. Influence of the Steady-State Operating Point on Negative Damping Characteristics

Figure 6.34 shows the influence of the steady-state operating point on the damping characteristics in Band $\mathrm{III}_{\mathrm{PMSG}}$ when the active power changes from 0.3, 0.6 to 1.0 p.u. It can be seen that the level of negative damping deepens with the increase of active power.

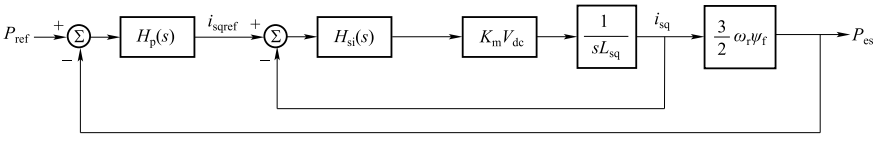

Fig. 6.31 Block diagram of active power loop

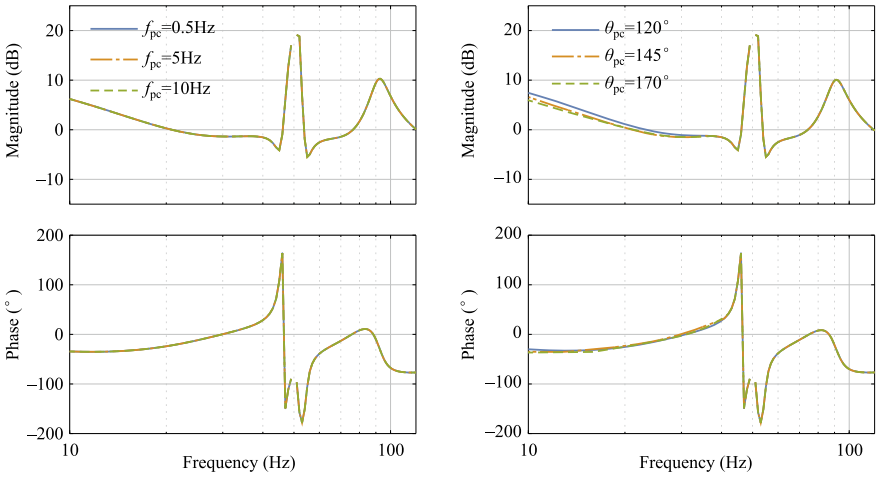

(a) Different MSC active power loop bandwidths (b) Different MSC active power loop PMs

Fig. 6.32 Influence of active power loop on the damping characteristics in Band III_{PMSG}

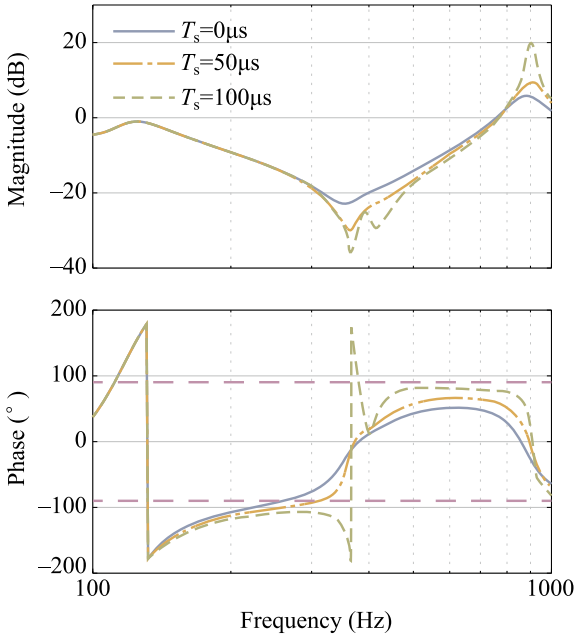

Fig. 6.33 Influence of time delay on the operating point on the damping Band III_{PMSG}

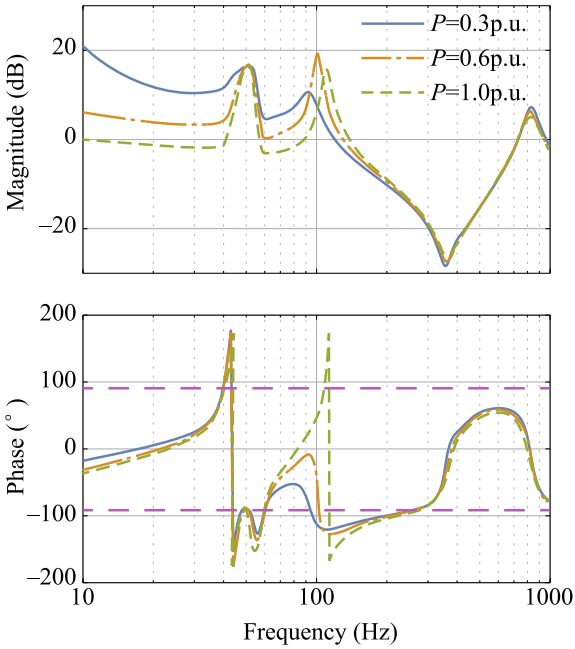

Fig. 6.34 Influence of steady-state operating point on the damping characteristics in Band III_{PMSG}

6.4.2.3 Analysis of Negative Damping Characteristics in Band IV_{PMSG}

In Band IV_{PMSG}, the impedance characteristics of PMSG-based wind turbine are dominated by LC filter and affected by time delay. The influence of time delay on the damping characteristics in Band IV_{PMSG} is shown in Fig. 6.35. The influence of time delay can be obtained by changing it from 0, 100 to 200 μs respectively with fixed LC filter parameters. As shown in Fig. 6.35, the frequency-band overlapping effect of time delay and LC filter leads to negative damping characteristics in Band IV_{PMSG}. In addition, with the increase of time delay, the level of negative damping deepens.

6.4.2.4 Summary of Negative Damping Characteristics in Each Frequency Band

Based on the analysis above, the following conclusions are obtained:

1. Band II_{PMSG}: The impedance characteristics are dominated by the PLL and affected by DC voltage loop, GSC reactive power loop and the steady-state operating point. When the bandwidth of DC voltage loop is lower than PLL, there is a frequency-band overlapping effect of DC voltage loop and PLL, resulting in negative damping characteristics in this band. The level of the negative damping deepens with the decrease of GSC reactive power loop PM and the increase of the active power.

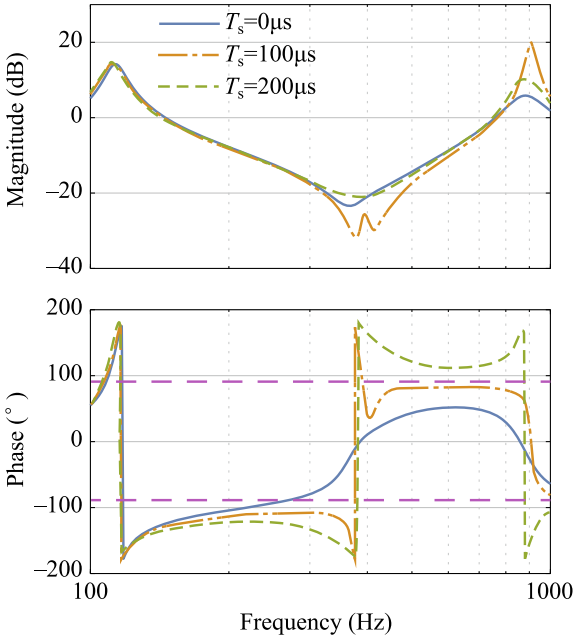

Fig. 6.35 Influence of time delay on the damping characteristics in Band IV_{PMSG}

2. Band III_{PMSG}: The impedance characteristics are dominated by GSC AC current loop and affected by MSC AC current loop, DC voltage loop and time delay. In the first half band of III_{PMSG}, there are frequency-band overlapping effects of DC voltage loop, MSC AC current loop and GSC AC current loop. The level of the negative damping deepens with the increase of active power. The level of the negative damping decreases with the increase of DC voltage loop PM and MSC AC current loop bandwidth. In the second half band of Band III_{PMSG}, the frequency-band overlapping effect of time delay and GSC AC current loop leads to negative damping characteristics near the bandwidth of GSC AC current loop, and the increase of time delay will aggravate the negative damping.
3. Band IV_{PMSG}: The impedance characteristics are dominated by LC filter. The frequency-band overlapping effect of time delay and LC filter leads to negative damping characteristics. The level of negative damping deepens with the increase of time delay.

Impedance scanning is carried out based on CHIL platform of different types of PMSG-based wind turbines, and the scanning results are shown in Figs. 6.36 and 6.37. In Fig. 6.36, the frequency-band overlapping effect of DC voltage loop and PLL leads to negative damping characteristics in Band II_{PMSG}. In Fig. 6.37, the frequency-band overlapping effect of DC voltage loop and GSC AC current loop leads to negative damping characteristics in Band III_{PMSG}.

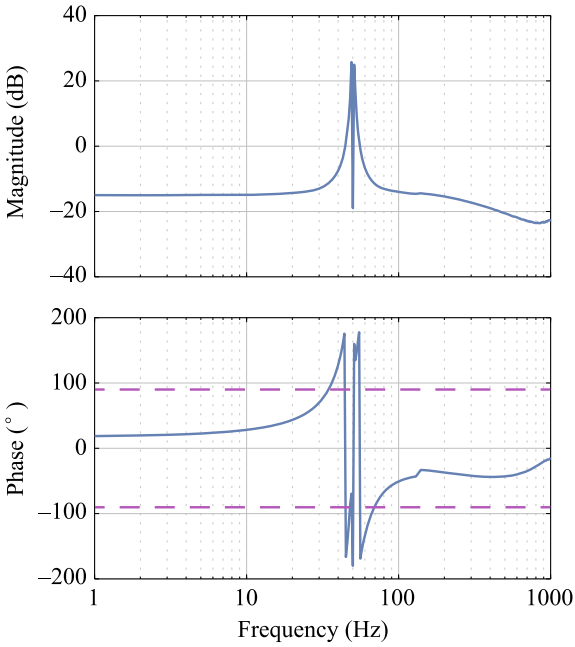

Fig. 6.36 Damping characteristics of a 4.5 MWPMSG-based wind turbine (Type D)

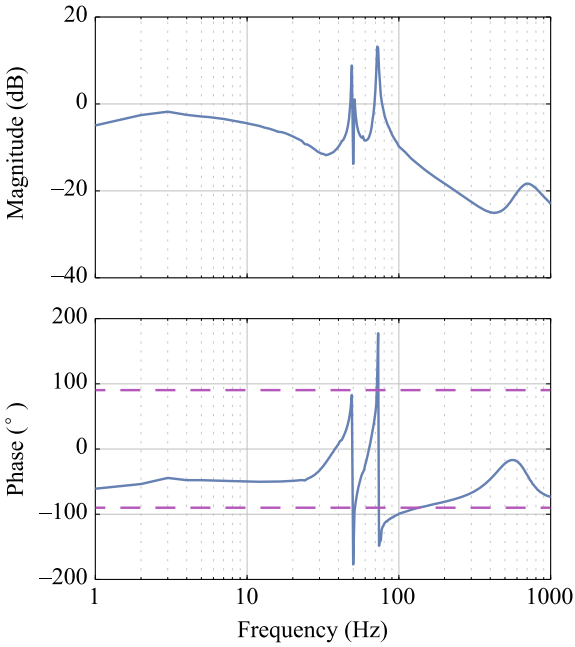

Fig. 6.37 Damping characteristics of a 2.5 MW PMSG-based wind turbine (Type E)

References

1. LIU F, LI Y, HE G Q, et al. Small signal modeling and stable operation strategy analysis of direct drive wind power grid-connected converter in extremely weak power grid [J]. Electric Power Automation Equipment, 2022, 42(8): 167–173. (Chinese)
2. WANG Z T, CHANG L C. A DC voltage monitoring and control method for three-phase grid-connected wind turbine inverters [J]. IEEE Transactions on Power Electronics, 2008, 23(3): 1118–1125.
3. LIU B, LI G H, WANG J J, et al. DC impedance of PMSG wind turbines machine-side model [J]. Electric Drive, 2020, 50(6): 109–114. (Chinese)
4. ZHANG C. Research on sub-synchronous oscillation of full-converter wind turbines integrated a weak AC grid based on impedance model [D]. Beijing: China Electric Power Research Institute, 2017. (Chinese)
5. LI G H, WANG W S, ZHANG X, et al. Sequence impedance modeling and analysis of permanent magnet synchronous generator considering machine side model [J]. Proceedings of the CSEE, 2019, 39(21): 6200–6212. (Chinese)
6. LI G H, WANG W S, LIU C, et al. Mechanism analysis and suppression method of wideband oscillation of PMSG wind farms connected to weak grid (Part I): analysis of wideband impedance characteristics and oscillation mechanism [J]. Proceedings of the CSEE, 2019, 39(22): 6547–6562. (Chinese)
7. LI G H, WANG W S, LIU C, et al. Impedance measurement and influence factors analysis for wind turbines based on control-hardware-in-the-loop [J]. Power System Technology, 2019, 43(5): 1624–1631. (Chinese)

Chapter 7
Impedance Model and Characteristics Analysis of DFIG-Based Wind Turbines

The stator winding of the DFIG-based wind turbine is directly connected to the grid, while the rotor winding is connected to the grid through two two-level converters: rotor-side converter (RSC) and GSC. The control objectives and strategies of RSC and GSC are both different [1]. The DC bus connecting the RSC and GSC presents non-ideal voltage source characteristics, introducing a small-signal frequency coupling path between RSC and GSC.

In this chapter, first, the analytical impedance model of DFIG-based wind turbines is established and verified [2, 3]. Its main circuit includes the asynchronous generator, RSC, DC bus, GSC and its control loops include PLL, inner current loop, DC voltage loop, and outer power loop. Then, the decoupling equivalent model of RSC-GSC is established, and the dominant factors affecting the impedance characteristics in different frequency bands are analyzed. Moreover, the frequency band division method of DFIG-based wind turbines is proposed, and the frequency-band overlapping effect of multiple controllers and the negative damping characteristics of each frequency band are clarified. Finally, based on CHIL simulation platform, the broadband impedances of different types of DFIG-based wind turbines are scanned, and typical values of frequency-band division are given.

7.1 Operation Principle and Control Strategy

7.1.1 Operation Principle

DFIG-based wind turbines are mainly composed of wind turbines, gearboxes and generators. The topology is shown in Fig. 7.1. First, the wind turbine converts wind energy into mechanical energy, and then the mechanical energy is transmitted to the

© China Electric Power Press 2023

W. Wang et al., *Analysis and Mitigation of Broadband Oscillation in Renewable Energy Generation and AC/DC Transmission Systems*,
https://doi.org/10.1007/978-981-99-1568-2_7

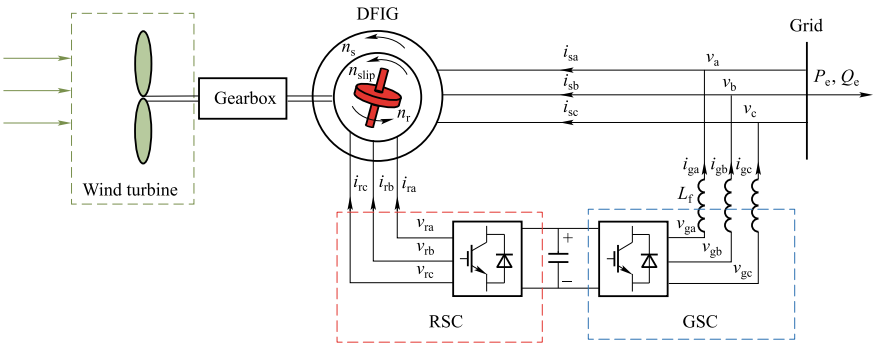

Fig. 7.1 Topology of PMSG-based wind turbines

generator through the gearbox. Finally, the generator converts the mechanical energy into electrical energy for power generation.

As shown in the figure, the stator winding of DFIG-based wind turbines is directly connected to the grid, and the rotor winding is connected to the grid through a three-phase back-to-back PWM converter. Usually, the converter close to the grid is called the grid-side converter (GSC), and the converter close to the rotor winding is called the rotor-side converter (RSC). During the operation of DFIG, the rotor speed changes with wind speed. In order to ensure the output AC voltage and current of DFIG-based wind turbines at the rated frequency, the three-phase back-to-back pulse width modulation (PWM) converter is needed to energize the rotor winding with AC current at frequency $f_1 - f_r$ for field excitation.

7.1.1.1 Wind Turbine Operation Principle

The operation zones of wind turbine can be divided into MPPT zone, constant speed zone and constant power zone according to the relationship between wind speed, rotor speed, and the output power. Taking a domestic manufacturer's 3 MW DFIG-based wind turbine as an example, Fig. 7.2 shows the relationship between its output power, wind speed, and rotor speed. The cut-in wind speed is 3m/s, and the cut-out wind speed is 20m/s. When the wind speed is in the range of 3~10m/s, and the rotor speed is in the range of 720~1200r/min, the wind turbine operates in the MPPT zone, and the corresponding output power is between 70kW~1.5MW. With the increase of wind speed, the wind turbine enters the constant speed zone, in which the rotor speed is maintained at 1200r/min, and the output power continues to increase until it reaches 3000kW. Then, the wind turbine enters the constant power zone, its rotor speed is maintained at 1200r/min, and its output power is maintained at 3000kW.

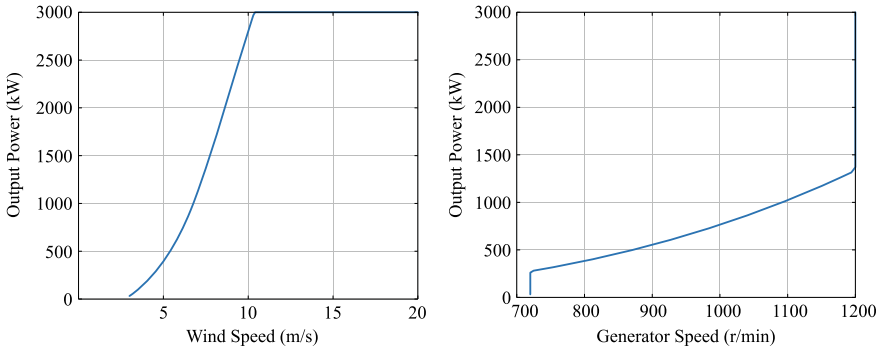

(a) Relationship between output power and wind speed

(b) Relationship between output power and rotor speed

Fig. 7.2 The relationship between output power, wind speed and rotor speed of a 3 MW DFIG-based wind turbine

7.1.1.2 Generator Operation Principle

The stator winding of DFIG is directly connected to the grid, and the rotor winding is connected to the grid through a back-to-back PWM converter. Since the DFIG air-gap magnetic field is established jointly by the magnetic fields generated by stator and rotor currents, the relative stationarity of the stator and rotor magnetic fields and the constant air-gap magnetic field are the two prerequisites for DFIG to realize electromechanical energy conversion stably. That is, the speed of the rotating magnetic field generated by the rotor current relative to the SCF (the sum of the rotor speed and the rotor magnetic field speed) is equal to the speed of the rotating magnetic field generated by the stator current.

In Fig. 7.1, n_s is the stator magnetic field speed, r/min; n_{slip} is the rotor magnetic field speed relative to the rotor, rpm; n_r is the rotor mechanical speed, r/min; f_s is the stator current frequency (fundamental frequency), Hz; f_{slip} is the rotor current frequency, Hz; f_r is the rotor electrical frequency, Hz; p is the pole pairs.

When DFIG is in stable operation, the following relationship exists between each rotational speed:

$$n_s = n_{slip} + n_r \tag{7.1}$$

According to the following relationship between frequency and rotational speed $f_s = pn_s/60$, $f_{slip} = pn_{slip}/60$, $f_r = pn_r/60$, there is

$$f_s = f_{slip} + f_r \tag{7.2}$$

When the rotor mechanical speed changes due to the variation of wind speed, the stator current frequency f_s can be kept constant by adjusting the rotor current frequency f_{slip}, so as to achieve the variable-speed constant-frequency operation of

DFIG. When the rotor speed is higher than synchronous speed, DFIG is in super-synchronous operation ($f_{\text{slip}} < 0$), the rotor magnetic field rotates in the opposite direction to the rotor, and the power flows from the rotor to the grid. When the rotor speed is lower than synchronous speed, DFIG is in sub-synchronous operation ($f_{\text{slip}} > 0$), the rotor magnetic field rotates in the same direction as the rotor, and the power flows from the grid to the rotor. When the rotor speed is equal to synchronous speed ($f_{\text{slip}} = 0$), there is no power exchange between the rotor and the grid.

7.1.2 Time-Domain Model of DFIG-Based Wind Turbines

7.1.2.1 Time-Domain Model in SCF

The dynamic mathematical model of DFIG is a high-order, nonlinear, strongly coupled multivariate system, and the following assumptions are often made to facilitate analysis:

1. The stator is connected to the grid with balanced three-phase AC voltage amplitude and frequency.
2. The magnetic circuit saturation is ignored, and the self and mutual inductances of each winding are considered to be constant values related to the magnetic circuit operating point.
3. The core loss is ignored.
4. The effects of frequency and temperature variations on DFIG parameters are not considered.
5. The rotor parameters are all converted to the stator side. After conversion, the number of turns of stator and rotor winding is equal.

Based on the above assumptions, DFIG can be equivalent to the model shown in Fig. 7.3. The stator three-phase winding axes A, B and C are stationary in space and symmetrically distributed at $2\pi/3$ electrical angle, with the A-axis as the reference coordinate axis. The rotor winding axes a, b and c rotate with the rotor at the electrical angular speed ω_{r}, and the electrical angle difference between the rotor a-axis and the stator A-axis is expressed by θ_{r}. v_{sl} represent the three-phase AC voltages of the stator. i_{sl} present the three-phase AC currents of the stator. v_{rl} represent the three-phase AC voltages of the DFIG rotor. i_{rl} represent the three-phase AC currents of the DFIG rotor. l representsrefers to phases a, b, c.

The time-domain model of DFIG in SCF can be expressed by voltage equation, flux linkage equation, torque equation and motion equation.

1. Voltage Equation

The voltage equation of each stator winding is given by

$$v_{\text{s}l} = R_{\text{s}} i_{\text{s}l} + \frac{\mathrm{d}\psi_{\text{s}l}}{\mathrm{d}t} \tag{7.3}$$

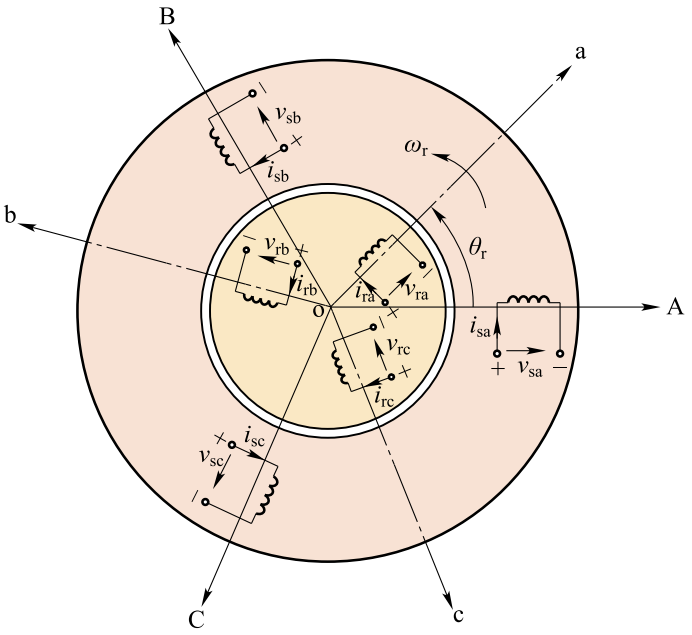

Fig. 7.3 Equivalent model of DFIG

where v_{sl} and i_{sl} (l = a, b, c) are the three-phase AC voltages and currents of the stator respectively; ψ_{sl} is the three-phase stator flux linkages;. R_s is the stator resistance.

And the voltage equation of each rotor winding is given by

$$v_{rl} = R_r i_{rl} + \frac{d\psi_{rl}}{dt} \tag{7.4}$$

where v_{rl} and i_{rl} are the three-phase AC voltages and currents of the rotor respectively; ψ_{rl} is the three-phase rotor flux linkages; R_r is the rotor resistance.

The above parameters are converted to the stator side, and for simplicity, the superscript "′" is omitted. It is worth noting that the frequency of the stator voltage, current and flux linkage is f_1 and the frequency of the rotor voltage, current and flux linkage is $f_1 - f_r$.

The voltage equation can be further expressed in vector form as

$$\boldsymbol{v}_s = \boldsymbol{R}_s \boldsymbol{i}_s + \frac{d\boldsymbol{\Psi}_s}{dt} \tag{7.5}$$

$$\boldsymbol{v}_r = \boldsymbol{R}_r \boldsymbol{i}_r + \frac{d\boldsymbol{\Psi}_r}{dt} \tag{7.6}$$

where $\boldsymbol{v}_s = [v_{sa}, v_{sb}, v_{sc}]^T$, $\boldsymbol{i}_s = [i_{sa}, i_{sb}, i_{sc}]^T$, $\boldsymbol{\Psi}_s = [\psi_{sa}, \psi_{sb}, \psi_{sc}]^T$, $\boldsymbol{R}_s = \text{diag}[R_s, R_s, R_s]^T$.

$\boldsymbol{v}_\mathrm{r} = [v_\mathrm{ra}, v_\mathrm{rb}, v_\mathrm{rc}]^\mathrm{T}$, $\boldsymbol{i}_\mathrm{r} = [i_\mathrm{ra}, i_\mathrm{rb}, i_\mathrm{rc}]^\mathrm{T}$, $\boldsymbol{\Psi}_\mathrm{r} = [\psi_\mathrm{ra}, \psi_\mathrm{rb}, \psi_\mathrm{rc}]^\mathrm{T}$, $\boldsymbol{R}_\mathrm{r} = \mathrm{diag}[R_\mathrm{r}, R_\mathrm{r}, R_\mathrm{r}]^\mathrm{T}$.

2. Flux Linkage Equation

The flux linkage of each winding is the sum of its own self-inductance flux linkage and the mutual inductance flux linkage of other windings to it, which can be expressed as

$$\begin{bmatrix} \boldsymbol{\Psi}_\mathrm{s} \\ \boldsymbol{\Psi}_\mathrm{r} \end{bmatrix} = \begin{bmatrix} \boldsymbol{L}_\mathrm{ss} & \boldsymbol{L}_\mathrm{sr} \\ \boldsymbol{L}_\mathrm{rs} & \boldsymbol{L}_\mathrm{rr} \end{bmatrix} \begin{bmatrix} \boldsymbol{i}_\mathrm{s} \\ \boldsymbol{i}_\mathrm{r} \end{bmatrix} \tag{7.7}$$

with

$$\boldsymbol{L}_\mathrm{ss} = \begin{bmatrix} L_\mathrm{ms} + L_\mathrm{1s} & -\frac{1}{2}L_\mathrm{ms} & -\frac{1}{2}L_\mathrm{ms} \\ -\frac{1}{2}L_\mathrm{ms} & L_\mathrm{ms} + L_\mathrm{1s} & -\frac{1}{2}L_\mathrm{ms} \\ -\frac{1}{2}L_\mathrm{ms} & -\frac{1}{2}L_\mathrm{ms} & L_\mathrm{ms} + L_\mathrm{1s} \end{bmatrix}$$

$$\boldsymbol{L}_\mathrm{rr} = \begin{bmatrix} L_\mathrm{mr} + L_\mathrm{1r} & -\frac{1}{2}L_\mathrm{mr} & -\frac{1}{2}L_\mathrm{mr} \\ -\frac{1}{2}L_\mathrm{mr} & L_\mathrm{mr} + L_\mathrm{1r} & -\frac{1}{2}L_\mathrm{mr} \\ -\frac{1}{2}L_\mathrm{mr} & -\frac{1}{2}L_\mathrm{mr} & L_\mathrm{mr} + L_\mathrm{1r} \end{bmatrix}$$

$$\boldsymbol{L}_\mathrm{rs} = \boldsymbol{L}_\mathrm{sr}^\mathrm{T} = L_\mathrm{ms} \begin{bmatrix} \cos\theta_\mathrm{r} & \cos(\theta_\mathrm{r} - 2\pi/3) & \cos(\theta_\mathrm{r} + 2\pi/3) \\ \cos(\theta_\mathrm{r} + 2\pi/3) & \cos\theta_\mathrm{r} & \cos(\theta_\mathrm{r} - 2\pi/3) \\ \cos(\theta_\mathrm{r} - 2\pi/3) & \cos(\theta_\mathrm{r} + 2\pi/3) & \cos\theta_\mathrm{r} \end{bmatrix}$$

where L_ms and L_mr are the mutual inductance of DFIG stator windings and rotor windings, respectively; L_1s and L_1r are the leakage inductance of DFIG stator windings and rotor windings, respectively. After the rotor parameters are turned to the stator side, there is $L_\mathrm{ms} = L_\mathrm{mr}$.

According to Eq. (7.7), $\boldsymbol{L}_\mathrm{rs}$ and $\boldsymbol{L}_\mathrm{sr}$ are two mutually transposed chunk matrices, both related to θ_r, and their elements are variable. In order to convert the variable-parameter matrix into a constant-parameter matrix, Park transformation is required.

3. Torque Equation

According to the principle of electromechanical energy conversion, the stored energy and magnetic co-energy of the magnetic field under linear inductance conditions are

$$W_\mathrm{m} = \frac{1}{2}\boldsymbol{i}^\mathrm{T}\boldsymbol{\Psi} \tag{7.8}$$

where $\boldsymbol{i} = [\boldsymbol{i}_\mathrm{s}, \boldsymbol{i}_\mathrm{r}]^\mathrm{T}$, $\boldsymbol{\Psi} = [\boldsymbol{\Psi}_\mathrm{s}, \boldsymbol{\Psi}_\mathrm{r}]$.

The electromagnetic torque is equal to the change rate of magnetic co-energy when the mechanical angular changes. So the torque expression can be written as

$$T_\mathrm{e} = p \left. \frac{\partial W_\mathrm{m}}{\partial \theta_\mathrm{r}} \right|_{i=\text{constant}} \tag{7.9}$$

4. Motion Equation

Neglecting the viscous friction and torsional elasticity in DFIG, the motion equation can be written as

$$\begin{cases} T_\mathrm{m} - T_\mathrm{e} = \dfrac{J}{p} \dfrac{\mathrm{d}\omega_r}{\mathrm{d}t} \\ \omega_\mathrm{r} = \dfrac{\mathrm{d}\theta_\mathrm{r}}{\mathrm{d}t} \end{cases} \tag{7.10}$$

where T_m is the mechanical torque; J is the mechanical inertia.

The above voltage equation, flux linkage equation, torque equation and motion equation constitute the time-domain model of DFIG in SCF. This is a nonlinear, strongly coupled multivariable system. In order to accommodate linear control strategies, the variables must be decoupled and simplified by Park transformation.

7.1.2.2 Time-Domain Model in SRF

Take the direction of grid voltage rotation vector as the d-axis, and the q-axis is ahead of d-axis π/2 electrical angle along the rotation direction. Through Park transformation, the time-domain model of DFIG in SCF can be transformed to SRF as

$$\boldsymbol{v}_\mathrm{sdq} = \boldsymbol{R}_\mathrm{sdq}\boldsymbol{i}_\mathrm{sdq} + \frac{\mathrm{d}\boldsymbol{\psi}_\mathrm{sdq}}{\mathrm{d}t} + \begin{bmatrix} 0 & -\omega_\mathrm{s} \\ \omega_\mathrm{s} & 0 \end{bmatrix} \boldsymbol{\psi}_\mathrm{sdq} \tag{7.11}$$

$$\boldsymbol{v}_\mathrm{rdq} = \boldsymbol{R}_\mathrm{rdq}\boldsymbol{i}_\mathrm{rdq} + \frac{\mathrm{d}\boldsymbol{\psi}_\mathrm{rdq}}{\mathrm{d}t} + \begin{bmatrix} 0 & -(\omega_\mathrm{s} - \omega_\mathrm{r}) \\ \omega_\mathrm{s} - \omega_\mathrm{r} & 0 \end{bmatrix} \boldsymbol{\psi}_\mathrm{rdq} \tag{7.12}$$

$$\begin{bmatrix} \boldsymbol{\Psi}_\mathrm{sdq} \\ \boldsymbol{\Psi}_\mathrm{rdq} \end{bmatrix} = \begin{bmatrix} \boldsymbol{L}_\mathrm{s} & \boldsymbol{L}_\mathrm{m} \\ \boldsymbol{L}_\mathrm{m} & \boldsymbol{L}_\mathrm{r} \end{bmatrix} \begin{bmatrix} \boldsymbol{i}_\mathrm{sdq} \\ \boldsymbol{i}_\mathrm{rdq} \end{bmatrix} \tag{7.13}$$

where ω_s and ω_r are the electrical angular frequencies of SRF and the rotor respectively.

$\boldsymbol{v}_\mathrm{sdq} = \left[v_\mathrm{sd}, v_\mathrm{sq}\right]^\mathrm{T}$, v_sd and v_sq are the d- and q-axis stator AC voltages respectively.
$\boldsymbol{v}_\mathrm{rdq} = \left[v_\mathrm{rd}, v_\mathrm{rq}\right]^\mathrm{T}$, v_rd and v_rq are the d- and q-axis rotor AC voltages respectively.

$\boldsymbol{i}_{sdq} = \left[i_{sd}, v_{sq}\right]^T$, i_{sd} and i_{sq} are the d- and q-axis stator AC currents respectively.
$\boldsymbol{i}_{rdq} = \left[i_{rd}, i_{rq}\right]^T$, i_{rd} and i_{rq} are the d- and q-axis rotor AC currents respectively.
$\boldsymbol{\Psi}_{sdq} = \left[\psi_{sd}, \psi_{sq}\right]^T$, ψ_{sd} and ψ_{sq} are the d- and q-axis stator flux linkages of DFIG respectively.
$\boldsymbol{\Psi}_{rdq} = \left[\psi_{rd}, \psi_{rq}\right]^T$, ψ_{rd} and ψ_{rq} are the d- and q-axis rotor flux linkages of DFIG respectively.
$\boldsymbol{R}_{sdq} = \mathrm{diag}[R_s, R_s]$, $\boldsymbol{R}_{rdq} = \mathrm{diag}[R_r, R_r]$.
$\boldsymbol{L}_m = \mathrm{diag}[L_m, L_m]$, L_m is excitation inductance, $L_m = 3L_{ms}/2$.
$\boldsymbol{L}_s = \mathrm{diag}[L_s, L_s]$, L_s is the stator inductance of DFIG, $L_s = L_{1s} + L_m$.
$\boldsymbol{L}_r = \mathrm{diag}\left[L_r, L_r\right]$, L_r is the rotor inductance of DFIG, $L_r = L_{1r} + L_m$.

The relationship between SRF, rotor rotation coordinate frame and SCF is shown in Fig. 7.4. In the figure, θ_s is the electrical angle of SRF, θ_r is the electrical angle of rotor rotating coordinate frame, θ_{slip} is the electrical angle difference of rotor rotating coordinate frame and SRF, and $\theta_{slip} = \theta_s - \theta_r$.

According to the time-domain model of DFIG in SRF, its equivalent circuit can be obtained as shown in Fig. 7.5.

The output power of DFIG in SRF can be further deduced as

$$\begin{cases} P_{es} = -\dfrac{3}{2}\left(v_{sd}i_{sd} + v_{sq}i_{sq}\right) \\ P_{er} = -\dfrac{3}{2}\left(v_{rd}i_{rd} + v_{rq}i_{rq}\right) \end{cases} \tag{7.14}$$

$$\begin{cases} Q_{es} = -\dfrac{3}{2}\left(v_{sq}i_{sd} - v_{sd}i_{sq}\right) \\ Q_{er} = -\dfrac{3}{2}\left(v_{rq}i_{rd} - v_{rd}i_{rq}\right) \end{cases} \tag{7.15}$$

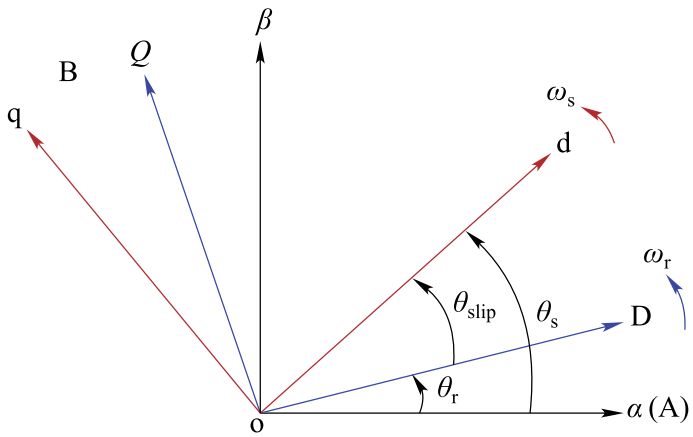

Fig. 7.4 The relationship between SRF, rotor rotation coordinate frame and SCF

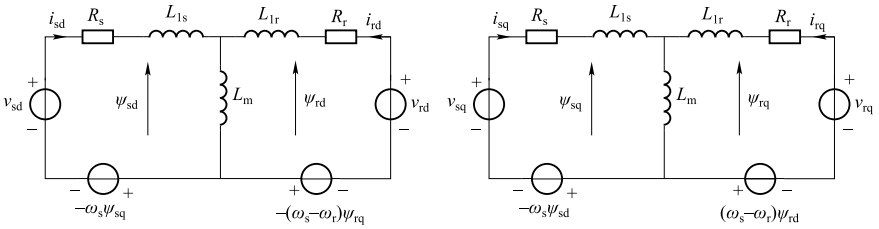

(a) d-axis equivalent circuit (b) q-axis equivalent circuit

Fig. 7.5 Equivalent circuit of DFIG in SRF

where P_{es} and Q_{es} are the output active power and reactive power of DFIG stator respectively;

P_{er} and Q_{er} are the output active power and reactive power of DFIG rotor respectively.

Ignoring the resistance of DFIG stator and rotor, the active power can be approximated to

$$\begin{cases} P_{es} \approx -\dfrac{3}{2}\omega_s L_m\left(i_{rd}i_{sq} - i_{rq}i_{sd}\right) \\ P_{er} \approx \dfrac{3}{2}(\omega_s - \omega_r)L_m\left(i_{rd}i_{sq} - i_{rq}i_{sd}\right) \end{cases} \tag{7.16}$$

Define the slip $s_n = (\omega_s - \omega_r)/\omega_s$, and the relationship between P_{es} and P_{er} is as follows

$$P_{er} \approx -s_n P_{es} \tag{7.17}$$

Therefore, the total active power output from DFIG to the grid is

$$P_e = (1 - s_n)P_{es}. \tag{7.18}$$

7.1.2.3 Time-Domain Model Under Asymmetric Conditions

Based on the time-domain model of DFIG in SCF, symmetrical components method is adopted to separate the positive and negative sequence components of DFIG voltage and flux linkage. The transformed voltage equations can be obtained by multiplying the transformation matrix $\boldsymbol{B}$ on both sides of the equation:

$$\begin{bmatrix} \boldsymbol{v}_{spn} \\ \boldsymbol{v}_{rpn} \end{bmatrix} = \begin{bmatrix} \boldsymbol{R}_s & 0 \\ 0 & \boldsymbol{R}_r \end{bmatrix}\begin{bmatrix} \boldsymbol{i}_{spn} \\ \boldsymbol{i}_{rpn} \end{bmatrix} + \frac{d}{dt}\begin{bmatrix} \boldsymbol{\Psi}_{spn} \\ \boldsymbol{\Psi}_{rpn} \end{bmatrix} \tag{7.19}$$

Correspondingly, the transformed flux linkage is given by

$$\begin{bmatrix} \boldsymbol{\Psi}_{\text{spn}} \\ \boldsymbol{\Psi}_{\text{rpn}} \end{bmatrix} = \boldsymbol{B} \begin{bmatrix} \boldsymbol{L}_{\text{ss}} & \boldsymbol{L}_{\text{sr}} \\ \boldsymbol{L}_{\text{rs}} & \boldsymbol{L}_{\text{rr}} \end{bmatrix} \boldsymbol{B}^{-1} \begin{bmatrix} \boldsymbol{i}_{\text{spn}} \\ \boldsymbol{i}_{\text{rpn}} \end{bmatrix} \tag{7.20}$$

where

$\boldsymbol{v}_{\text{spn}} = \left[v_{\text{sp}},\ v_{\text{sn}} \right]^{\text{T}}$, v_{sp} and v_{sn} are the positive- and negative-sequence components of the stator AC voltages respectively.
$\boldsymbol{v}_{\text{rpn}} = \left[v_{\text{rp}},\ v_{\text{rn}} \right]^{\text{T}}$, v_{rp} and v_{rn} are the positive- and negative-sequence components of the rotor AC voltages respectively.
$\boldsymbol{i}_{\text{spn}} = \left[i_{\text{sp}}, i_{\text{sn}} \right]^{\text{T}}$, i_{sp} and i_{sn} are the positive- and negative-sequence components of the stator AC currents respectively.
$\boldsymbol{i}_{\text{rpn}} = \left[i_{\text{rp}}, i_{\text{rn}} \right]^{\text{T}}$, i_{rp} and i_{rn} are the positive- and negative-sequence components of the rotor AC currents respectively.
$\boldsymbol{\Psi}_{\text{spn}} = \left[\psi_{\text{sp}}, \psi_{\text{sn}} \right]^{\text{T}}$, ψ_{sp} and ψ_{sn} are the positive-and negative-sequence components of the stator flux linkages respectively.
$\boldsymbol{\Psi}_{\text{rpn}} = \left[\psi_{\text{rp}}, \psi_{\text{rn}} \right]^{\text{T}}$, ψ_{rp} and ψ_{rn} are the positive- and negative-sequence components of the rotor flux linkages respectively.

All variables in the voltage and flux equations have been turned to the stator side. The transformation matrix $\boldsymbol{B}$ is as follows

$$\boldsymbol{B} = \frac{1}{3} \begin{bmatrix} 1 & a & a^2 \\ 1 & a^2 & a \end{bmatrix}$$

Simplify Eq. (7.20), yields

$$\begin{cases} \vec{\boldsymbol{\Psi}}^{\text{s}}_{\text{spn}} = \boldsymbol{L}_{\text{s}} \vec{\boldsymbol{i}}^{\text{s}}_{\text{spn}} + \boldsymbol{L}_{\text{m}} \begin{bmatrix} \text{e}^{\text{j}\theta_{\text{r}}} & 0 \\ 0 & \text{e}^{-\text{j}\theta_{\text{r}}} \end{bmatrix} \vec{\boldsymbol{i}}^{\text{r}}_{\text{rpn}} \\ \vec{\boldsymbol{\Psi}}^{\text{r}}_{\text{rpn}} = \boldsymbol{L}_{\text{r}} \vec{\boldsymbol{i}}^{\text{r}}_{\text{rpn}} + \boldsymbol{L}_{\text{m}} \begin{bmatrix} \text{e}^{-\text{j}\theta_{\text{r}}} & 0 \\ 0 & \text{e}^{\text{j}\theta_{\text{r}}} \end{bmatrix} \vec{\boldsymbol{i}}^{\text{s}}_{\text{spn}} \end{cases} \tag{7.21}$$

where the superscript "s" and "r" refer to the SCF and the rotor rotation coordinate frame respectively. Substitute Eq. (7.21) into Eq. (7.19), there is

$$\begin{cases} \vec{\boldsymbol{v}}^{\text{s}}_{\text{spn}} = \boldsymbol{R}_{\text{s}} \vec{\boldsymbol{i}}^{\text{s}}_{\text{spn}} + \boldsymbol{L}_{\text{s}} \dfrac{\text{d}\vec{\boldsymbol{i}}^{\text{s}}_{\text{spn}}}{\text{d}t} + \boldsymbol{L}_{\text{m}} \dfrac{\text{d}}{\text{d}t} \begin{bmatrix} \text{e}^{\text{j}\theta_{\text{r}}} & 0 \\ 0 & \text{e}^{-\text{j}\theta_{\text{r}}} \end{bmatrix} \vec{\boldsymbol{i}}^{\text{r}}_{\text{rpn}} \\ \vec{\boldsymbol{v}}^{\text{r}}_{\text{rpn}} = \boldsymbol{R}_{\text{r}} \vec{\boldsymbol{i}}^{\text{r}}_{\text{rpn}} + \boldsymbol{L}_{\text{r}} \dfrac{\text{d}\vec{\boldsymbol{i}}^{\text{r}}_{\text{rpn}}}{\text{d}t} + \boldsymbol{L}_{\text{m}} \dfrac{\text{d}}{\text{d}t} \begin{bmatrix} \text{e}^{-\text{j}\theta_{\text{r}}} & 0 \\ 0 & \text{e}^{\text{j}\theta_{\text{r}}} \end{bmatrix} \vec{\boldsymbol{i}}^{\text{s}}_{\text{spn}} \end{cases} \tag{7.22}$$

According to the relationship between the SCF and the rotor rotation coordinate frame, we can further obtain

$$\vec{\boldsymbol{i}}_{\mathrm{rpn}}^{\mathrm{s}} = \begin{bmatrix} \mathrm{e}^{\mathrm{j}\theta_{\mathrm{r}}} & 0 \\ 0 & \mathrm{e}^{-\mathrm{j}\theta_{\mathrm{r}}} \end{bmatrix} \vec{\boldsymbol{i}}_{\mathrm{rpn}}^{\mathrm{r}} \tag{7.23}$$

Based on Eq. (7.23), all electrical quantities in Eqs. (7.21) and (7.22) can be transformed into the SCF. Omitting the superscript "s", the voltage equation after positive and negative sequence decomposition is as follows

$$\begin{cases} \boldsymbol{v}_{\mathrm{spn}} = \boldsymbol{R}_{\mathrm{s}}\boldsymbol{i}_{\mathrm{spn}} + \boldsymbol{L}_{\mathrm{s}}\dfrac{\mathrm{d}\boldsymbol{i}_{\mathrm{spn}}}{\mathrm{d}t} + \boldsymbol{L}_{\mathrm{m}}\dfrac{\mathrm{d}\boldsymbol{i}_{\mathrm{rpn}}}{\mathrm{d}t} \\ \boldsymbol{v}_{\mathrm{rpn}} = \boldsymbol{R}_{\mathrm{r}}\boldsymbol{i}_{\mathrm{rpn}} + \boldsymbol{L}_{\mathrm{r}}\dfrac{\mathrm{d}\boldsymbol{i}_{\mathrm{rpn}}}{\mathrm{d}t} + \boldsymbol{L}_{\mathrm{m}}\dfrac{\mathrm{d}\boldsymbol{i}_{\mathrm{spn}}}{\mathrm{d}t} + \begin{bmatrix} -\mathrm{j}\omega_{\mathrm{r}} & 0 \\ 0 & \mathrm{j}\omega_{\mathrm{r}} \end{bmatrix}\boldsymbol{L}_{\mathrm{r}}\boldsymbol{i}_{\mathrm{rpn}} \\ \qquad + \begin{bmatrix} -\mathrm{j}\omega_{\mathrm{r}} & 0 \\ 0 & \mathrm{j}\omega_{\mathrm{r}} \end{bmatrix}\boldsymbol{L}_{\mathrm{m}}\boldsymbol{i}_{\mathrm{spn}} \end{cases} \tag{7.24}$$

The flux linkage equation after positive and negative sequence decomposition is

$$\begin{cases} \boldsymbol{\Psi}_{\mathrm{spn}} = \boldsymbol{L}_{\mathrm{s}}\boldsymbol{i}_{\mathrm{spn}} + \boldsymbol{L}_{\mathrm{m}}\boldsymbol{i}_{\mathrm{rpn}} \\ \boldsymbol{\Psi}_{\mathrm{rpn}} = \boldsymbol{L}_{\mathrm{r}}\boldsymbol{i}_{\mathrm{rpn}} + \boldsymbol{L}_{\mathrm{m}}\boldsymbol{i}_{\mathrm{spn}} \end{cases} \tag{7.25}$$

It should be emphasized that all quantities in Eqs. (7.24) and (7.25) are turned to the stator side and the SCF is used as the reference coordinate frame.

7.1.3 Control Strategy

The DFIG-based wind turbine adopts a pair of three-phase back-to-back voltage source converter (VSC), i.e., GSC and RSC, to achieve variable-speed and constant-frequency operation and power regulation. GSC is used to maintain the stability of DC voltage, and RSC is used to achieve MPPT control and reactive power control.

7.1.3.1 GSC Control Strategy

The block diagram of GSC typical control is shown in Fig. 7.6. It consists of two parts: the outer DC voltage loop and the inner AC current loop. Since the DC voltage depends on the active power balance of the AC and DC ports, the DC voltage control can be achieved by controlling the active component (d-axis component) of GSC AC current. The power factor control can be achieved by adjusting the reactive component (q-axis component) of the GSC AC current.

The difference between the three-phase modulation voltage of GSC and the AC voltage drops on the filter inductance L_{f}, generating the output current. Accordingly, the time-domain model of the main circuit can be expressed as

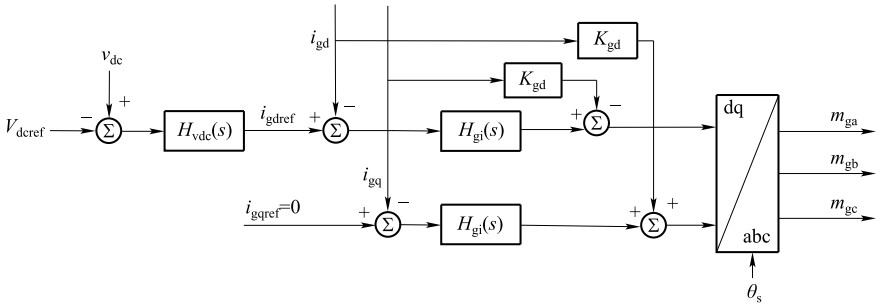

Fig. 7.6 The block diagram of GSC typical control

$$v_{gl} = K_m v_{dc} m_{gl} = v_l + sL_f i_{gl} \tag{7.26}$$

where

K_m is the modulation gain.
v_{dc} is the DC voltage.
v_{gl} (l = a, b, c) is the three-phase modulation voltage of GSC.
m_{gl} is the three-phase modulation signal of GSC.
v_l is the three-phase AC voltage of GSC.
i_{gl} is the three-phase AC current of GSC.

7.1.3.2 RSC control Strategy

According to the time-domain model of DFIG, when DFIG operates in steady state, its voltage equation can be written as follows with the influence of stator resistance ignored.

$$\boldsymbol{v}_{sdq} \approx \begin{bmatrix} 0 & -\omega_s \\ \omega_s & 0 \end{bmatrix} \boldsymbol{\psi}_{sdq} \tag{7.27}$$

Adopting the grid voltage orientation method, i.e., the d-axis of SRF is oriented to grid voltage vector, there is

$$\begin{cases} v_{sd} = V_s \approx -\omega_s \psi_{sq} \\ v_{sq} = 0 \approx \omega_s \psi_{sd} \end{cases} \tag{7.28}$$

where V_s is the stator voltage amplitude. Further we can get

$$\begin{cases} \psi_{sd} \approx 0 \\ \psi_{sq} \approx -\dfrac{V_s}{\omega_s} \end{cases} \tag{7.29}$$

According to Eq. (7.13), the d- and q-axis stator flux linkage can be expressed as

$$\begin{cases} \psi_{sd} = L_s i_{sd} + L_m i_{rd} \\ \psi_{sq} = L_s i_{sq} + L_m i_{rq} \end{cases} \tag{7.30}$$

Substituting Eq. (7.30) into Eq. (7.29), there is

$$\begin{cases} i_{sd} = -\dfrac{L_m}{L_s} i_{rd} \\ i_{sq} = -\dfrac{V_s}{L_s \omega_s} - \dfrac{L_m}{L_s} i_{rq} \end{cases} \tag{7.31}$$

Therefore, the output power of DFIG stator can be expressed as

$$\begin{cases} P_{es} \approx \dfrac{3 L_m V_s}{2 L_s} i_{rd} \\ Q_{es} \approx -\dfrac{3 V_s}{2 L_s} \left(\dfrac{V_s}{\omega_s} + L_m i_{rq} \right) \end{cases} \tag{7.32}$$

Based on Eq. (7.32), the output active power of DFIG stator can be controlled by the d-axis component of the rotor current, and the output reactive power of DFIG stator can be controlled by the q-axis component of the rotor current. Since the total output power of DFIG is the sum of the stator output power and the GSC output power, in order to control the total output power, it is necessary to add $1/(1 - s_n)$ to the rotor current control.

Figure 7.7 shows the block diagram of RSC typical control. $1/(1 - s_n)$ is added to the rotor current control. The outer power loop controls the total active and reactive power output of DFIG. The RSC AC current loop regulates the d-axis and q-axis components of the rotor current to achieve active and reactive power control, respectively.

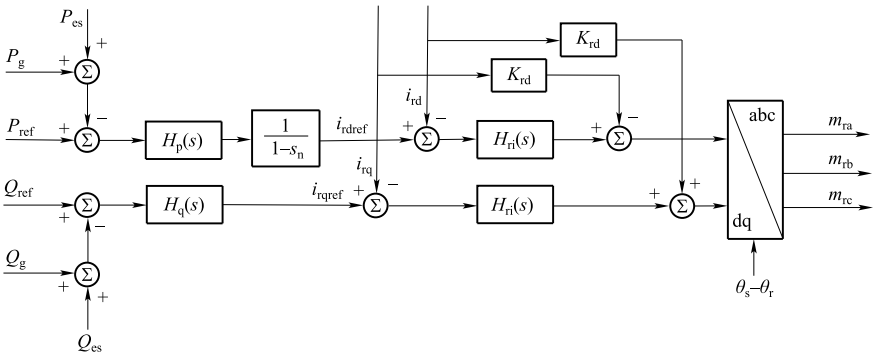

Fig. 7.7 The block diagram of RSC typical control

The AC side of RSC is directly connected to the rotor, and the time-domain model of RSC's main circuit can be expressed as

$$v_{rl} = K_e K_m v_{dc} m_{rl} \tag{7.33}$$

where K_e is the turn ratio of stator and rotor windings; m_{rl} are the three-phase modulation signals of RSC, which is referred to the rotor side; v_{rl} are the three-phase AC voltages of the rotor, which is referred to the stator side.

7.1.3.3 Time-Domain Model of DC Bus

As the DC voltage depends on the active power balance of AC and DC sides, the time domain model of DC bus can be expressed as follows.

$$C_{dc} \frac{dv_{dc}}{dt} v_{dc} = -\sum_{l=a,b,c} v_{rl} i_{rl} - \sum_{l=a,b,c} v_{gl} i_{gl} \tag{7.34}$$

where C_{dc} is the DC bus capacitance; i_{rl} are the three-phase AC currents of the rotor, i.e., the three-phase AC currents of RSC respectively.

7.2 Frequency-Domain Modeling of Steady-State Operation

7.2.1 Frequency-Domain Characteristics Analysis of Steady-State Operating Point

Since the stator winding and the AC-port of GSC are directly connected to the grid, the frequency of the stator voltage and current is f_1, as well as the frequency of GSC AC voltage and current. RSC is connected to the rotor winding for field excitation. According to the operation principle of DFIG, the frequency of the rotor voltage and current is $f_1 - f_r$, as well as the frequency of RSC AC voltage and current. In addition, the DC voltage only contains DC component at the steady-state operating point.

Figure 7.8 shows the waveforms and FFT results of voltage and current of the stator and GSC AC side at the steady-state operating point.It can be seen that they only contain components at $\pm f_1$.

Figure 7.9 shows the waveforms and FFT results of voltage and current of the rotor and RSC AC side at the steady-state operating point. It can be seen that they only contain components at $\pm(f_1 - f_r)$.

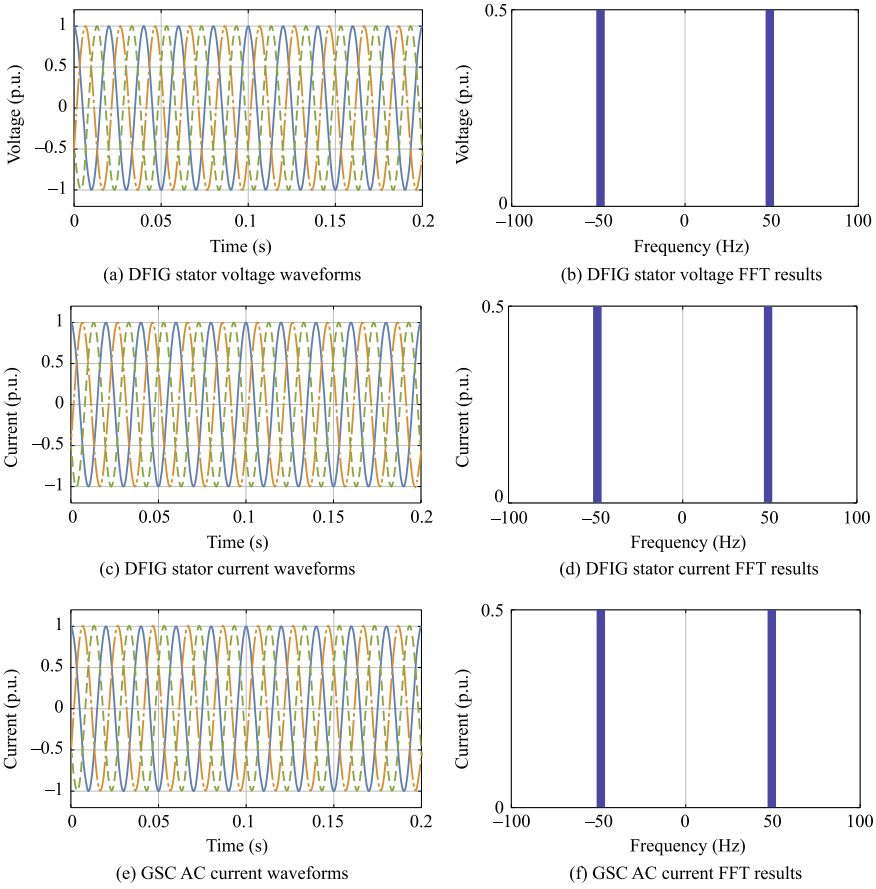

(a) DFIG stator voltage waveforms
(b) DFIG stator voltage FFT results
(c) DFIG stator current waveforms
(d) DFIG stator current FFT results
(e) GSC AC current waveforms
(f) GSC AC current FFT results

Fig. 7.8 Steady-state waveforms and FFT results of voltages and currents of the stator and GSC AC side

Figure 7.10 shows the waveforms and FFT results of DC voltage at the steady-state operating point. It can be seen that it only contains DC component.

Based on the FFT results, the steady-state components of the stator and GSC AC side can be arranged into the following order.

$$[-f_1, 0, f_1]^{\mathrm{T}} \tag{7.35}$$

The steady-state components of the rotor and RSC AC side can be arranged into the following order.

$$[-(f_1 - f_r), 0, (f_1 - f_r)]^{\mathrm{T}} \tag{7.36}$$

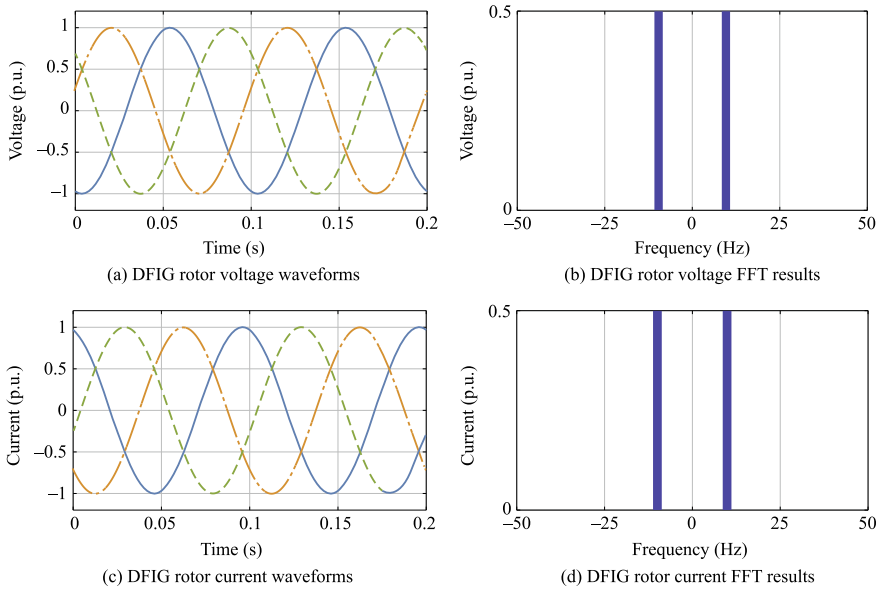

(a) DFIG rotor voltage waveforms
(b) DFIG rotor voltage FFT results
(c) DFIG rotor current waveforms
(d) DFIG rotor current FFT results

Fig. 7.9 Steady-state waveforms and FFT results of voltages and currents of the rotor and RSC AC side

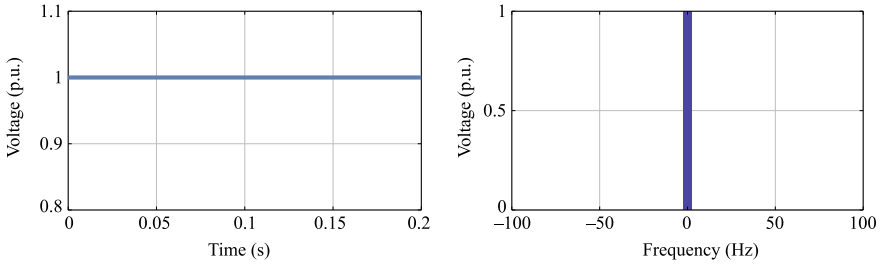

(a) DC bus voltage waveforms
(b) DC bus voltage FFT results

Fig. 7.10 Steady-state waveforms and FFT results of DC voltage

If the SCF is used as the reference coordinate frame, the steady-state components of the rotor and RSC AC side is consistent with the stator and GSC AC side, which is

$$[-f_1, 0, f_1]^{\mathrm{T}} \tag{7.37}$$

Take phase a as an example, the steady-state vectors of the stator and GSC in frequency domain can be expressed as

$$\begin{cases} \boldsymbol{V}_{\mathrm{a}} = [\boldsymbol{V}_1^*, 0, \boldsymbol{V}_1]^{\mathrm{T}} \\ \boldsymbol{I}_{\mathrm{sa}} = [\boldsymbol{I}_{\mathrm{s1}}^*, 0, \boldsymbol{I}_{\mathrm{s1}}]^{\mathrm{T}} \\ \boldsymbol{I}_{\mathrm{ga}} = [\boldsymbol{I}_{\mathrm{g1}}^*, 0, \boldsymbol{I}_{\mathrm{g1}}]^{\mathrm{T}} \\ \boldsymbol{M}_{\mathrm{ga}} = [\boldsymbol{M}_{\mathrm{g1}}^*, 0, \boldsymbol{M}_{\mathrm{g1}}]^{\mathrm{T}} \end{cases} \tag{7.38}$$

The steady-state vectors of the rotor and RSC in frequency domain can be expressed as

$$\begin{cases} \boldsymbol{V}_{\mathrm{ra}} = [\boldsymbol{V}_{\mathrm{r1}}^*, 0, \boldsymbol{V}_{\mathrm{r1}}]^{\mathrm{T}} \\ \boldsymbol{I}_{\mathrm{ra}} = [\boldsymbol{I}_{\mathrm{r1}}^*, 0, \boldsymbol{I}_{\mathrm{r1}}]^{\mathrm{T}} \\ \boldsymbol{M}_{\mathrm{ra}} = [\boldsymbol{M}_{\mathrm{r1}}^*, 0, \boldsymbol{M}_{\mathrm{r1}}]^{\mathrm{T}} \end{cases} \tag{7.39}$$

where

$\boldsymbol{V}_{\mathrm{a}}$ is the steady-state vector of the stator and GSC AC voltage.
$\boldsymbol{I}_{\mathrm{sa}}$ is the steady-state vector of the stator current.
$\boldsymbol{I}_{\mathrm{ga}}$ is the steady-state vector of GSC AC current.
$\boldsymbol{M}_{\mathrm{ga}}$ is the steady-state vector of GSC modulation signal.
$\boldsymbol{V}_{\mathrm{ra}}$ is the steady-state vector of the rotor and RSC AC voltage.
$\boldsymbol{I}_{\mathrm{ra}}$ is the steady-state vector of the rotor and RSC AC current.
$\boldsymbol{M}_{\mathrm{ra}}$ is the steady-state vector of RSC modulation signal.

Each element in the vector is expressed in the form of column complex vector, $\boldsymbol{V}_1 = V_1 \mathrm{e}^{\mathrm{j}\varphi_{\mathrm{v1}}}/2$, $\boldsymbol{I}_{\mathrm{s1}} = I_{\mathrm{s1}} \mathrm{e}^{\mathrm{j}\varphi_{\mathrm{is1}}}/2$, $\boldsymbol{I}_{\mathrm{g1}} = I_{\mathrm{g1}} \mathrm{e}^{\mathrm{j}\varphi_{\mathrm{ig1}}}/2$, $\boldsymbol{M}_{\mathrm{g1}} = M_{\mathrm{g1}} \mathrm{e}^{\mathrm{j}\varphi_{\mathrm{mg1}}}/2$, $\boldsymbol{V}_{\mathrm{r1}} = V_{\mathrm{r1}} \mathrm{e}^{\mathrm{j}\varphi_{\mathrm{vr1}}}/2$, $\boldsymbol{I}_{\mathrm{r1}} = I_{\mathrm{r1}} \mathrm{e}^{\mathrm{j}\varphi_{\mathrm{ir1}}}/2$, $\boldsymbol{M}_{\mathrm{r1}} = M_{\mathrm{r1}} \mathrm{e}^{\mathrm{j}\varphi_{\mathrm{mr1}}}/2$, indicating the amplitude and phase of the steady-state components at their corresponding frequency. And the negative-frequency component is equal to the conjugate of the positive-frequency component, which is indicated by the superscript "*".

The components at f_1 and $f_1 - f_{\mathrm{r}}$ are in positive sequence, and the corresponding ones lag $2\pi/3$ in turn in the three-phase vectors. The components at $-f_1$ and $-(f_1 - f_{\mathrm{r}})$ are in negative sequence, and the corresponding ones lead $2\pi/3$ in turn in the three-phase vectors. In addition, the middle component is in zero sequence. According to the three-phase symmetrical relationship, the steady-state vectors of phase b and phase c can be described as follows

$$\begin{cases} \boldsymbol{V}_{\mathrm{b}} = \boldsymbol{D}\boldsymbol{V}_{\mathrm{a}}, \boldsymbol{I}_{\mathrm{sb}} = \boldsymbol{D}\boldsymbol{I}_{\mathrm{sa}}, \boldsymbol{M}_{\mathrm{gb}} = \boldsymbol{D}\boldsymbol{M}_{\mathrm{ga}}, \boldsymbol{I}_{\mathrm{gb}} = \boldsymbol{D}\boldsymbol{I}_{\mathrm{ga}} \\ \boldsymbol{V}_{\mathrm{rb}} = \boldsymbol{D}\boldsymbol{V}_{\mathrm{ra}}, \boldsymbol{I}_{\mathrm{rb}} = \boldsymbol{D}\boldsymbol{I}_{\mathrm{ra}}, \boldsymbol{M}_{\mathrm{rb}} = \boldsymbol{D}\boldsymbol{M}_{\mathrm{ra}} \end{cases} \tag{7.40}$$

$$\begin{cases} \boldsymbol{V}_{\mathrm{c}} = \boldsymbol{D}^*\boldsymbol{V}_{\mathrm{a}}, \boldsymbol{I}_{\mathrm{sc}} = \boldsymbol{D}^*\boldsymbol{I}_{\mathrm{sa}}, \boldsymbol{M}_{\mathrm{gc}} = \boldsymbol{D}^*\boldsymbol{M}_{\mathrm{ga}}, \boldsymbol{I}_{\mathrm{gc}} = \boldsymbol{D}^*\boldsymbol{I}_{\mathrm{ga}} \\ \boldsymbol{V}_{\mathrm{rc}} = \boldsymbol{D}^*\boldsymbol{V}_{\mathrm{ra}}, \boldsymbol{I}_{\mathrm{rc}} = \boldsymbol{D}^*\boldsymbol{I}_{\mathrm{ra}}, \boldsymbol{M}_{\mathrm{rc}} = \boldsymbol{D}^*\boldsymbol{M}_{\mathrm{ra}} \end{cases} \tag{7.41}$$

where $\boldsymbol{D}$ is the phase-sequence coefficient matrix, expressed as

$$\boldsymbol{D} = \mathrm{diag}[\{\mathrm{e}^{-\mathrm{j}2k\pi/3}\}\big|_{k=-1,0,1}] \tag{7.42}$$

In the above expression, the steady-state vectors of the rotor and RSC AC side are all based on the SCF and are all converted to the stator side.

7.2.2 Frequency-Domain Steady-State Model of Main Circuit

7.2.2.1 Steady-State Model of DFIG

Transform DFIG time-domain model shown in Eqs. (7.24) and (7.25) to frequency domain, there is the steady-state model of DFIG as follows

$$\begin{cases} \boldsymbol{V}_{sl} = (R_\mathrm{s} + s_0 L_\mathrm{s})\boldsymbol{I}_{sl} + s_0 L_\mathrm{m}\boldsymbol{I}_{rl} \\ \boldsymbol{V}_{rl} = \left[R_\mathrm{r} + (s_0 - \mathrm{j}\omega_\mathrm{r})L_\mathrm{r}\right]\boldsymbol{I}_{rl} + (s_0 - \mathrm{j}\omega_\mathrm{r})L_\mathrm{m}\boldsymbol{I}_{sl} \end{cases} \tag{7.43}$$

where $s_0 = 2\pi f_1$.

7.2.2.2 Steady-State Model of DC Bus

Transform the time-domain model of DC bus shown in Eq. (7.34) to frequency domain, there is the steady-state model of DC bus as follows

$$0 = -\sum_{l=\mathrm{a,b,c}} \boldsymbol{V}_{rl} \otimes \boldsymbol{I}_{rl} - \sum_{l=\mathrm{a,b,c}} \boldsymbol{V}_{gl} \otimes \boldsymbol{I}_{gl} \tag{7.44}$$

where $\boldsymbol{V}_{rl}$ and $\boldsymbol{I}_{rl}$ are the three-phase steady-state vectors of RSC modulation voltages and AC currents respectively; $\boldsymbol{V}_{gl}$ and $\boldsymbol{I}_{gl}$ are the three-phase steady-state vectors of GSC modulation voltages and AC currents respectively.

7.2.2.3 Steady-State Model of GSC

Transform the time-domain model of GSC shown in Eq. (7.26) to frequency domain, there is the steady-state model of GSC as follows

$$K_\mathrm{m} V_\mathrm{dc} \boldsymbol{M}_{gl} = \boldsymbol{V}_1 + \boldsymbol{Z}_{\mathrm{Lf0}} \boldsymbol{I}_{gl} \tag{7.45}$$

where $\boldsymbol{Z}_{\mathrm{Lf0}}$ is a fifth-order diagonal matrix, representing the impedance of GSC AC filter inductor in the steady-state frequency order, expressed as

$$\boldsymbol{Z}_{\mathrm{Lf0}} = \mathrm{j}2\pi L_\mathrm{f} \cdot \mathrm{diag}[-2f_1, \quad -f_1, \quad 0, \quad f_1, \quad 2f_1]$$

7.2.2.4 Steady-State Model of RSC

Transform the time-domain model of RSC shown in Eq. (7.33) to frequency domain, there is the steady-state model of GSC as follows

$$\boldsymbol{V}_{rl} = K_e K_m V_{dc} \boldsymbol{M}_{rl} \tag{7.46}$$

where $\boldsymbol{M}_{rl}$ is the three-phase steady-state vectors of RSC modulation signals.

7.3 Small-Signal Impedance Modeling in Frequency Domain

In this section, the frequency-domain linearization method is used to establish the small-signal impedance model of DFIG-based wind turbines. First, the AC voltage, AC current, and modulation signals are transformed to the frequency domain to obtain the steady-state operating point. Then, a small-signal perturbation of a specific frequency is added on the AC voltage. Finally, the small-signal impedance model of DFIG-based wind turbines is established by calculating the response of AC current to a small-signal perturbation in AC voltage.

7.3.1 Small-Signal Frequency-Domain Characteristics Analysis

Inject a sinusoidal small-signal perturbation at f_p into the AC voltage of DFIG, the transfer path and frequency distribution of DFIG small signals are shown in Fig. 7.11. As can be seen from the figure, there are two transfer paths for the small signal in DFIG. In path 1, the small signal is first transferred from the stator to the rotor through the air-gap magnetic field, and then to the AC port through RSC, DC bus and GSC. In path 2, the small signal is first transferred to the rotor through GSC, DC bus and RSC, and then to the stator and the AC port through the air-gap magnetic field.

As for path 1, the small-signal $\hat{\boldsymbol{v}}_1$ in the positive sequence (at f_p) is injected to the AC voltage of DFIG at the steady-state operating point. A small-signal response of the stator current $\hat{\boldsymbol{i}}_{sl}$ at f_p will be generated. In addition, according to the analysis of two-level converter small-signal frequency domain characteristics in Sect. 3.3.1, a small-signal response of $\hat{\boldsymbol{i}}_{sl}$ at $f_p - 2f_1$ will also be introduced.

$\hat{\boldsymbol{i}}_{sl}$ at f_p leads to a small-signal response of the stator flux linkage at f_p. As the flux linkage of the stator and rotor remain relatively stationary, the rotor flux linkage will be introduced into a small-signal response at $f_p - f_r$. At this time, RSC AC voltage $\hat{\boldsymbol{v}}_{rl}$ and AC current $\hat{\boldsymbol{i}}_{rl}$ will also contain a small signal at $f_p - f_r$. $\hat{\boldsymbol{v}}_{rl}$ at $f_p - f_r$ multiplying the steady-state component of $\boldsymbol{I}_{rl}$ at $-(f_1 - f_r)$ and $\hat{\boldsymbol{i}}_{rl}$ at $f_p - f_r$ multiplying the

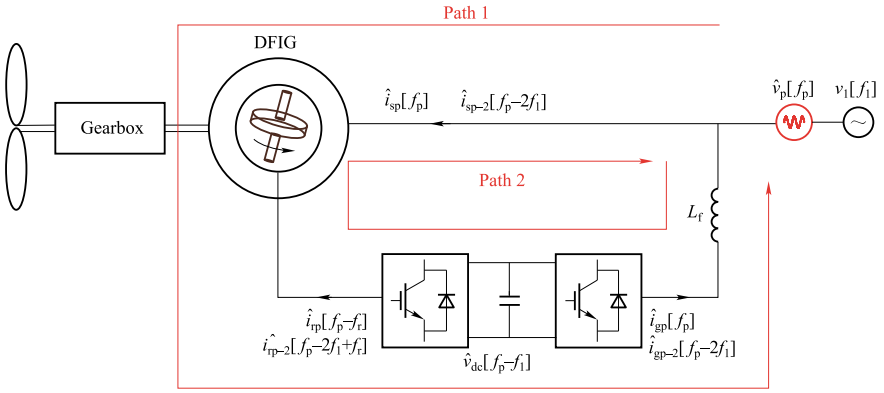

Fig. 7.11 Transfer path and frequency distribution of DFIG small signals

steady-state component of $\boldsymbol{V}_{rl}$ at $-(f_1 - f_r)$ both lead to a small-signal response of active power $\hat{\boldsymbol{p}}_e$ at $f_p - f_1$, thus leading to a small-signal response of DC voltage $\hat{\boldsymbol{v}}_{dc}$ at $f_p - f_1$. $\hat{\boldsymbol{v}}_{dc}$ at $f_p - f_1$ multiplying the steady-state component of GSC modulation signal $\boldsymbol{M}_{gl}$ at f_1 and $-f_1$ lead to small-signal responses of GSC AC current $\hat{\boldsymbol{i}}_{gl}$ at f_p and $f_p - 2f_1$.

$\hat{\boldsymbol{i}}_{sl}$ at $f_p - 2f_1$ further lead to a small-signal response of the stator flux linkage at $f_p - 2f_1$. As the flux linkage of the stator and rotor remain relatively stationary, the rotor flux linkage will be introduced into a small-signal response at $f_p - 2f_1 + f_r$. At this time, $\hat{\boldsymbol{v}}_{rl}$ and $\hat{\boldsymbol{i}}_{rl}$ will also contain a small signal at $f_p - 2f_1 + f_r$. $\hat{\boldsymbol{v}}_{rl}$ at $f_p - 2f_1 + f_r$ multiplying $\boldsymbol{I}_{rl}$ at $f_1 - f_r$ and $\hat{\boldsymbol{i}}_{rl}$ at $f_p - 2f_1 + f_r$ multiplying $\boldsymbol{V}_{rl}$ at $f_1 - f_r$ both lead to a small-signal response of $\hat{\boldsymbol{p}}_e$ at $f_p - f_1$, thus leading to a small-signal response of DC voltage $\hat{\boldsymbol{v}}_{dc}$ at $f_p - f_1$. $\hat{\boldsymbol{v}}_{dc}$ at $f_p - f_1$ multiplying the steady-state component of GSC modulation voltage $\boldsymbol{M}_{gl}$ at f_1 and $-f_1$ lead to small-signal responses of GSC AC current $\hat{\boldsymbol{i}}_{gl}$ at f_p and $f_p - 2f_1$.

As for path 2, $\hat{\boldsymbol{v}}_1$ in the positive sequence (at f_p) is injected to the AC port voltage of DFIG at the steady-state operating point. It is transferred from GSC to RSC through two ways: one is through DC voltage and PWM modulation, and the other is through RSC power controller. Then, $\hat{\boldsymbol{v}}_{rl}$ and $\hat{\boldsymbol{i}}_{rl}$ will be introduced into small-signal responses at $f_p - f_r$ and $f_p - 2f_1 + f_r$. The above small-signal components further lead to small-signal responses of the rotor flux linkage at $f_p - f_r$ and $f_p - 2f_1 + f_r$. As the flux linkage of the stator and rotor remain relatively stationary, the stator flux linkage will be introduced into small-signal responses at f_p and $f_p - 2f_1$, as well as the stator current $\hat{\boldsymbol{i}}_{sl}$.

When the rotor speed is 1.2 p.u., and the injected small signal is at 80 Hz, the waveforms and FFT results of voltage and current of the stator and GSC AC side are shown in Fig. 7.12. It can be seen that the stator and GSC AC voltage contains component at 80 Hz, and the current contains components at 80 and −20 Hz. The waveforms and FFT results of voltage and current of the rotor and RSC AC side are

shown in Fig. 7.13. It can be seen that they both contain components at 20 and 40 Hz. The waveform and FFT result of DC voltage is shown in Fig. 7.14. It can be seen that it only contains component at 30 Hz.

The small-signal frequency relationship of DFIG-based wind turbine is shown in Table 7.1.

In order to describe the frequency domain characteristics of voltages and currents of DFIG-based wind turbines, the small-signal components of the stator and GSC AC side can be arranged into the following order.

$$[f_p - 2f_1, f_p - f_1, f_p, f_p + f_1, f_p + 2f_1]^T \tag{7.47}$$

Take the rotor rotation coordinate frame as the reference coordinate frame, the small-signal components of the stator and GSC AC side can be arranged into the following order.

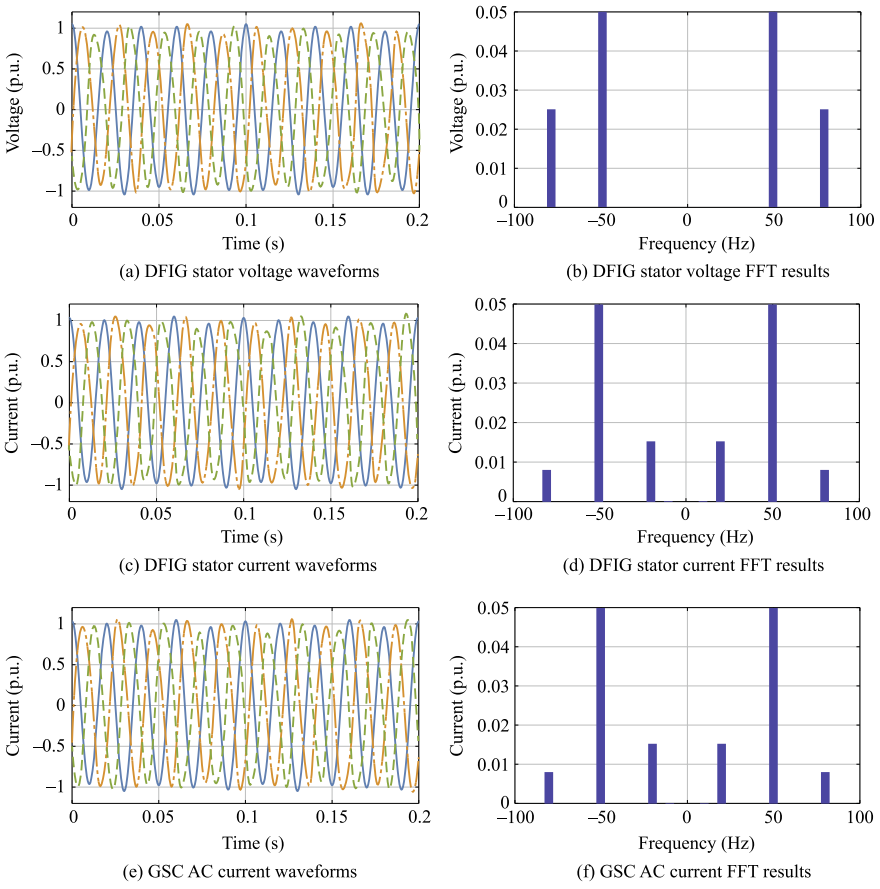

(a) DFIG stator voltage waveforms
(b) DFIG stator voltage FFT results
(c) DFIG stator current waveforms
(d) DFIG stator current FFT results
(e) GSC AC current waveforms
(f) GSC AC current FFT results

Fig. 7.12 Waveforms and FFT results of voltages and currents of the stator and GSC AC side

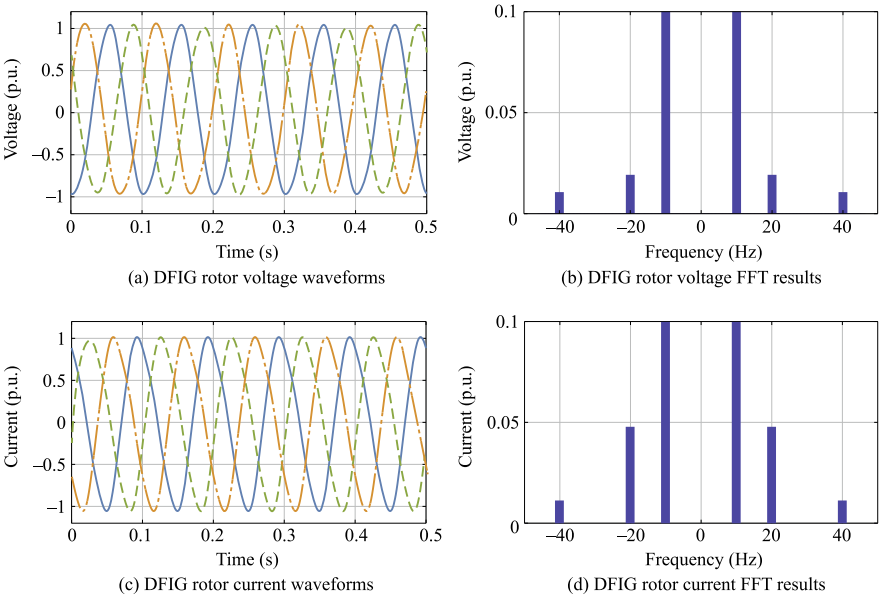

(a) DFIG rotor voltage waveforms
(b) DFIG rotor voltage FFT results
(c) DFIG rotor current waveforms
(d) DFIG rotor current FFT results

Fig. 7.13 Waveforms and FFT results of voltages and currents of the rotor and RSC AC side

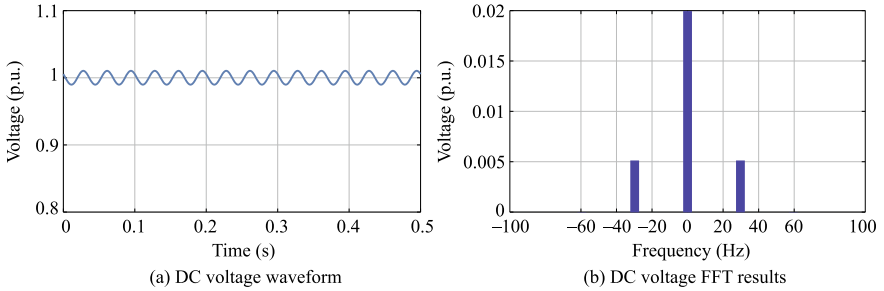

(a) DC voltage waveform
(b) DC voltage FFT results

Fig. 7.14 Waveform and FFT result of DC voltage

$$[f_p - 2f_1 + f_r,\ f_p - f_1,\ f_p - f_r,\ f_p + f_1 - 2f_r,\ f_p + 2f_1 - 3f_r]^T \tag{7.48}$$

In order to achieve the convolution between the steady-state vectors and the small-signal vectors, the steady-state frequency orders in Eqs. (7.35) and (7.36) need to be expanded as follows.

$$\begin{cases} [-2f_1,\ -f_1,\ 0,\ f_1,\ 2f_1]^T \\ [-2(f_1 - f_r),\ -(f_1 - f_r),\ 0,\ (f_1 - f_r),\ 2(f_1 - f_r)]^T \end{cases} \tag{7.49}$$

Table 7.1 The small-signal frequency relationship of DFIG-based wind turbine

DFIG-Based Wind Turbine	Electrical Quantities	Frequency
The stator and GSC	$\hat{\boldsymbol{v}}_{\mathrm{l}}$	f_{p}
	$\hat{\boldsymbol{i}}_{sl}$, $\hat{\boldsymbol{i}}_{gl}$	f_{p}
		$f_{\mathrm{p}} - 2f_{\mathrm{l}}$
	$\hat{\boldsymbol{m}}_{gl}$	f_{p}
		$f_{\mathrm{p}} - 2f_{\mathrm{l}}$
The rotor and RSC	$\hat{\boldsymbol{v}}_{rl}$	$f_{\mathrm{p}} - 2f_{\mathrm{l}} + f_{\mathrm{r}}$
		$f_{\mathrm{p}} - f_{\mathrm{r}}$
	$\hat{\boldsymbol{i}}_{rl}$	$f_{\mathrm{p}} - 2f_{\mathrm{l}} + f_{\mathrm{r}}$
		$f_{\mathrm{p}} - f_{\mathrm{r}}$
	$\hat{\boldsymbol{m}}_{rl}$	$f_{\mathrm{p}} - 2f_{\mathrm{l}} + f_{\mathrm{r}}$
		$f_{\mathrm{p}} - f_{\mathrm{r}}$
DC bus	$\hat{\boldsymbol{v}}_{\mathrm{dc}}$	$f_{\mathrm{p}} - f_{\mathrm{l}}$

Take phase a as an example, the small-signal vectors of the stator and GSC in frequency domain can be expressed as

$$\begin{cases} \hat{\boldsymbol{v}}_{\mathrm{a}} = [\,\hat{\boldsymbol{v}}_{\mathrm{p\text{-}2}},\ 0,\ \hat{\boldsymbol{v}}_{\mathrm{p}},\ 0,\ 0\,]^{\mathrm{T}} \\ \hat{\boldsymbol{i}}_{\mathrm{sa}} = [\,\hat{\boldsymbol{i}}_{\mathrm{sp\text{-}2}},\ 0,\ \hat{\boldsymbol{i}}_{\mathrm{sp}},\ 0,\ 0\,]^{\mathrm{T}} \\ \hat{\boldsymbol{i}}_{\mathrm{ga}} = [\,\hat{\boldsymbol{i}}_{\mathrm{gp\text{-}2}},\ 0,\ \hat{\boldsymbol{i}}_{\mathrm{gp}},\ 0,\ 0\,]^{\mathrm{T}} \\ \hat{\boldsymbol{m}}_{\mathrm{ga}} = [\,\hat{\boldsymbol{m}}_{\mathrm{gp\text{-}2}},\ 0,\ \hat{\boldsymbol{m}}_{\mathrm{gp}},\ 0,\ 0\,]^{\mathrm{T}} \end{cases} \tag{7.50}$$

The small-signal vectors of the rotor and RSC in frequency domain can be expressed as

$$\begin{cases} \hat{\boldsymbol{v}}_{\mathrm{ra}} = [\,\hat{\boldsymbol{v}}_{\mathrm{rp\text{-}2}},\ 0,\ \hat{\boldsymbol{v}}_{\mathrm{rp}},\ 0,\ 0\,]^{\mathrm{T}} \\ \hat{\boldsymbol{i}}_{\mathrm{ra}} = [\,\hat{\boldsymbol{i}}_{\mathrm{rp\text{-}2}},\ 0,\ \hat{\boldsymbol{i}}_{\mathrm{rp}},\ 0,\ 0\,]^{\mathrm{T}} \\ \hat{\boldsymbol{m}}_{\mathrm{ra}} = [\,\hat{\boldsymbol{m}}_{\mathrm{rp\text{-}2}},\ 0,\ \hat{\boldsymbol{m}}_{\mathrm{rp}},\ 0,\ 0\,]^{\mathrm{T}} \end{cases} \tag{7.51}$$

where

$\hat{\boldsymbol{v}}_{\mathrm{a}}$ is the small-signal vector of the stator and GSC AC voltage.
$\hat{\boldsymbol{i}}_{\mathrm{sa}}$ is the small-signal vector of the stator current.
$\hat{\boldsymbol{i}}_{\mathrm{ga}}$ is the small-signal vector of GSC AC current.
$\hat{\boldsymbol{m}}_{\mathrm{ga}}$ is the small-signal vector of GSC modulation signal.
$\hat{\boldsymbol{v}}_{\mathrm{ra}}$ is the small-signal vector of the rotor and RSC AC voltage.
$\hat{\boldsymbol{i}}_{\mathrm{ra}}$ is the small-signal vector of the rotor and RSC AC current.
$\hat{\boldsymbol{m}}_{\mathrm{ra}}$ is the small-signal vector of RSC modulation signal.

Each element in the vector is expressed in the form of column complex vector, $\hat{\boldsymbol{v}}_{\mathrm{p}} = V_{\mathrm{p}}\mathrm{e}^{\mathrm{j}\varphi_{\mathrm{vp}}}/2, \hat{\boldsymbol{v}}_{\mathrm{p\text{-}2}} = V_{\mathrm{p\text{-}2}}\mathrm{e}^{\mathrm{j}\varphi_{\mathrm{vp\text{-}2}}}/2, \hat{\boldsymbol{i}}_{\mathrm{sp}} = I_{\mathrm{sp}}\mathrm{e}^{\mathrm{j}\varphi_{\mathrm{isp}}}/2, \hat{\boldsymbol{i}}_{\mathrm{sp\text{-}2}} = I_{\mathrm{sp\text{-}2}}\mathrm{e}^{\mathrm{j}\varphi_{\mathrm{isp\text{-}2}}}/2, \hat{\boldsymbol{i}}_{\mathrm{gp}} = I_{\mathrm{gp}}\mathrm{e}^{\mathrm{j}\varphi_{\mathrm{igp}}}/2, \hat{\boldsymbol{i}}_{\mathrm{gp\text{-}2}} = I_{\mathrm{gp\text{-}2}}\mathrm{e}^{\mathrm{j}\varphi_{\mathrm{igp\text{-}2}}}/2, \hat{\boldsymbol{m}}_{\mathrm{gp}} = M_{\mathrm{gp}}\mathrm{e}^{\mathrm{j}\varphi_{\mathrm{mgp}}}/2, \hat{\boldsymbol{m}}_{\mathrm{gp\text{-}2}} = M_{\mathrm{gp\text{-}2}}\mathrm{e}^{\mathrm{j}\varphi_{\mathrm{mgp\text{-}2}}}/2, \hat{\boldsymbol{v}}_{\mathrm{rp}} = V_{\mathrm{rp}}\mathrm{e}^{\mathrm{j}\varphi_{\mathrm{vrp}}}/2, \hat{\boldsymbol{v}}_{\mathrm{rp\text{-}2}} = V_{\mathrm{rp\text{-}2}}\mathrm{e}^{\mathrm{j}\varphi_{\mathrm{vrp\text{-}2}}}/2, \hat{\boldsymbol{i}}_{\mathrm{rp}} = I_{\mathrm{rp}}\mathrm{e}^{\mathrm{j}\varphi_{\mathrm{irp}}}/2, \hat{\boldsymbol{i}}_{\mathrm{rp\text{-}2}} = I_{\mathrm{rp\text{-}2}}\mathrm{e}^{\mathrm{j}\varphi_{\mathrm{irp\text{-}2}}}/2, \hat{\boldsymbol{m}}_{\mathrm{rp}} = M_{\mathrm{rp}}\mathrm{e}^{\mathrm{j}\varphi_{\mathrm{mrp}}}/2, \hat{\boldsymbol{m}}_{\mathrm{rp\text{-}2}} = M_{\mathrm{rp\text{-}2}}\mathrm{e}^{\mathrm{j}\varphi_{\mathrm{mrp\text{-}2}}}/2$, indicating the amplitude and phase of the small-signal components at their corresponding frequency. And the negative-frequency component is equal to the conjugate of the positive-frequency component, which is indicated by the superscript "*".

The components at f_{p} are in positive sequence, and the corresponding ones lag $2\pi/3$ in turn in the three-phase vectors. The components at $f_{\mathrm{p}} - 2f_1$ are in negative sequence, and the corresponding ones lead $2\pi/3$ in turn in the three-phase vectors. In addition, the middle component is in zero sequence. According to the three-phase symmetrical relationship, the small-signal vectors of phase b and phase c can be described as

$$\begin{cases} \hat{\boldsymbol{v}}_{\mathrm{b}} = \boldsymbol{D}_{\mathrm{p}}\hat{\boldsymbol{v}}_{\mathrm{a}}, \hat{\boldsymbol{i}}_{\mathrm{sb}} = \boldsymbol{D}_{\mathrm{p}}\hat{\boldsymbol{i}}_{\mathrm{sa}}, \hat{\boldsymbol{m}}_{\mathrm{gb}} = \boldsymbol{D}_{\mathrm{p}}\hat{\boldsymbol{m}}_{\mathrm{ga}}, \hat{\boldsymbol{i}}_{\mathrm{gb}} = \boldsymbol{D}_{\mathrm{p}}\hat{\boldsymbol{i}}_{\mathrm{ga}} \\ \hat{\boldsymbol{v}}_{\mathrm{rb}} = \boldsymbol{D}_{\mathrm{p}}\hat{\boldsymbol{v}}_{\mathrm{ra}}, \hat{\boldsymbol{i}}_{\mathrm{rb}} = \boldsymbol{D}_{\mathrm{p}}\hat{\boldsymbol{i}}_{\mathrm{ra}}, \hat{\boldsymbol{m}}_{\mathrm{rb}} = \boldsymbol{D}_{\mathrm{p}}\hat{\boldsymbol{m}}_{\mathrm{ra}} \end{cases} \tag{7.52}$$

$$\begin{cases} \hat{\boldsymbol{v}}_{\mathrm{c}} = \boldsymbol{D}_{\mathrm{p}}^{*}\hat{\boldsymbol{v}}_{\mathrm{a}}, \hat{\boldsymbol{i}}_{\mathrm{sc}} = \boldsymbol{D}_{\mathrm{p}}^{*}\hat{\boldsymbol{i}}_{\mathrm{sa}}, \hat{\boldsymbol{m}}_{\mathrm{gc}} = \boldsymbol{D}_{\mathrm{p}}^{*}\hat{\boldsymbol{m}}_{\mathrm{ga}}, \hat{\boldsymbol{i}}_{\mathrm{gc}} = \boldsymbol{D}_{\mathrm{p}}^{*}\hat{\boldsymbol{i}}_{\mathrm{ga}} \\ \hat{\boldsymbol{v}}_{\mathrm{rc}} = \boldsymbol{D}_{\mathrm{p}}^{*}\hat{\boldsymbol{v}}_{\mathrm{ra}}, \hat{\boldsymbol{i}}_{\mathrm{rc}} = \boldsymbol{D}_{\mathrm{p}}^{*}\hat{\boldsymbol{i}}_{\mathrm{ra}}, \hat{\boldsymbol{m}}_{\mathrm{rc}} = \boldsymbol{D}_{\mathrm{p}}^{*}\hat{\boldsymbol{m}}_{\mathrm{ra}} \end{cases} \tag{7.53}$$

where $\boldsymbol{D}_{\mathrm{p}}$ is the phase-sequence coefficient matrix, which is expressed as

$$\boldsymbol{D}_{\mathrm{p}} = \mathrm{diag}[\{\mathrm{e}^{-\mathrm{j}2(k+1)\pi/3}\}\big|_{k=-2,-1,0,1,2}] \tag{7.54}$$

7.3.2 Frequency-Domain Small-Signal Model

7.3.2.1 Small-Signal Model of DFIG

Based on Eqs. (7.24) and (7.25), the small-signal frequency-domain model of DFIG at f_{p} is

$$\begin{cases} \hat{\boldsymbol{v}}_{\mathrm{p}} = (R_{\mathrm{s}} + sL_{\mathrm{s}})\hat{\boldsymbol{i}}_{\mathrm{sp}} + sL_{\mathrm{m}}\hat{\boldsymbol{i}}_{\mathrm{rp}} \\ \hat{\boldsymbol{v}}_{\mathrm{rp}} = (s - \mathrm{j}\omega_{\mathrm{r}})L_{\mathrm{m}}\hat{\boldsymbol{i}}_{\mathrm{sp}} + [R_{\mathrm{r}} + (s - \mathrm{j}\omega_{\mathrm{r}})L_{\mathrm{r}}]\hat{\boldsymbol{i}}_{\mathrm{rp}} \end{cases} \tag{7.55}$$

where $s = \mathrm{j}2\pi f_{\mathrm{p}}$.

Similarly, the small-signal frequency-domain model of DFIG at $f_{\mathrm{p}} - 2f_1$ can be obtained as

$$\begin{cases} \hat{\boldsymbol{v}}_{\text{sp-2}} = (R_\text{s} + s_2 L_\text{s})\hat{\boldsymbol{i}}_{\text{sp-2}} + s_2 L_\text{m}\hat{\boldsymbol{i}}_{\text{rp-2}} \\ \hat{\boldsymbol{v}}_{\text{rp-2}} = (s_2 + \text{j}\omega_\text{r})L_\text{m}\hat{\boldsymbol{i}}_{\text{sp-2}} + [R_\text{r} + (s_2 + \text{j}\omega_\text{r})L_\text{r}]\hat{\boldsymbol{i}}_{\text{rp-2}} \end{cases} \tag{7.56}$$

where $s_2 = \text{j}2\pi(f_\text{p} - 2f_1)$.

The small-signal model of DFIG in the SCF can be obtained by associating Eqs. (7.55) and (7.56) as

$$\begin{cases} \hat{\boldsymbol{i}}_{\text{rp}} = \dfrac{1}{sL_\text{m}}\hat{\boldsymbol{v}}_\text{p} - \dfrac{1}{sL_\text{m}}(R_\text{s} + sL_\text{s})\hat{\boldsymbol{i}}_{\text{sp}} \\ \hat{\boldsymbol{i}}_{\text{rp-2}} = \dfrac{1}{s_2 L_\text{m}}\hat{\boldsymbol{v}}_{\text{p-2}} - \dfrac{1}{s_2 L_\text{m}}(R_\text{s} + s_2 L_\text{s})\hat{\boldsymbol{i}}_{\text{sp-2}} \end{cases} \tag{7.57}$$

$$\begin{cases} \hat{\boldsymbol{v}}_{\text{rp}} = \dfrac{1}{sL_\text{m}}[R_\text{r} + (s - \text{j}\omega_\text{r})L_\text{r}]\hat{\boldsymbol{v}}_\text{p} + [(s - \text{j}\omega_\text{r})L_\text{m} \\ \qquad - \dfrac{1}{sL_\text{m}}(R_\text{s} + sL_\text{s})[R_\text{r} + (s - \text{j}\omega_\text{r})L_\text{r}]]\hat{\boldsymbol{i}}_{\text{sp}} \\ \hat{\boldsymbol{v}}_{\text{rp-2}} = \dfrac{1}{s_2 L_\text{m}}[R_\text{r} + (s_2 + \text{j}\omega_\text{r})L_\text{r}]\hat{\boldsymbol{v}}_{\text{p-2}} + [(s_2 + \text{j}\omega_\text{r})L_\text{m} \\ \qquad - \dfrac{1}{s_2 L_\text{m}}(R_\text{s} + s_2 L_\text{s})[R_\text{r} + (s_2 + \text{j}\omega_\text{r})L_\text{r}]]\hat{\boldsymbol{i}}_{\text{sp-2}} \end{cases} \tag{7.58}$$

Further, organize the above model into vector form, there is

$$\begin{cases} \hat{\boldsymbol{i}}_{\text{ra}} = \boldsymbol{G}_{11}\hat{\boldsymbol{v}}_\text{a} + \boldsymbol{G}_{12}\hat{\boldsymbol{i}}_{\text{sa}} \\ \hat{\boldsymbol{v}}_{\text{ra}} = \boldsymbol{G}_{21}\hat{\boldsymbol{v}}_\text{a} + \boldsymbol{G}_{22}\hat{\boldsymbol{i}}_{\text{sa}} \end{cases} \tag{7.59}$$

where $\boldsymbol{G}_{11}$, $\boldsymbol{G}_{12}$, $\boldsymbol{G}_{21}$, $\boldsymbol{G}_{22}$ are fifth-order matrices. All other elements in the matrices are zero except for the following

$$\begin{cases} \boldsymbol{G}_{11}(1,1) = \dfrac{1}{s_2 L_\text{m}} \\ \boldsymbol{G}_{11}(3,3) = \dfrac{1}{sL_\text{m}} \end{cases} \tag{7.60}$$

$$\begin{cases} \boldsymbol{G}_{12}(1,1) = -\dfrac{1}{s_2 L_\text{m}}(R_\text{s} + s_2 L_\text{s}) \\ \boldsymbol{G}_{12}(3,3) = -\dfrac{1}{sL_\text{m}}(R_\text{s} + sL_\text{s}) \end{cases} \tag{7.61}$$

$$\begin{cases} \boldsymbol{G}_{21}(1,1) = \dfrac{1}{s_2 L_\text{m}}[R_\text{r} + (s_2 + \text{j}\omega_\text{r})L_\text{r}] \\ \boldsymbol{G}_{21}(3,3) = \dfrac{1}{sL_\text{m}}[R_\text{r} + (s - \text{j}\omega_\text{r})L_\text{r}] \end{cases} \tag{7.62}$$

$$\begin{cases} \boldsymbol{G}_{22}(1,1) = (s_2 + \mathrm{j}\omega_\mathrm{r})L_\mathrm{m} - \dfrac{1}{s_2 L_\mathrm{m}}(R_\mathrm{s} + s_2 L_\mathrm{s})[R_\mathrm{r} + (s_2 + \mathrm{j}\omega_\mathrm{r})L_\mathrm{r}] \\ \boldsymbol{G}_{22}(3,3) = (s - \mathrm{j}\omega_\mathrm{r})L_\mathrm{m} - \dfrac{1}{s L_\mathrm{m}}(R_\mathrm{s} + s L_\mathrm{s})[R_\mathrm{r} + (s - \mathrm{j}\omega_\mathrm{r})L_\mathrm{r}] \end{cases} \tag{7.63}$$

7.3.2.2 Small-Signal Model of DC Bus

Transforming Eq. (7.34) to frequency domain, the small-signal model of DC bus can be obtained as

$$\begin{aligned} s_1 C_\mathrm{dc} V_\mathrm{dc} \hat{\boldsymbol{v}}_\mathrm{dc} = &- \sum_{l=\mathrm{a,b,c}} (\boldsymbol{I}_{\mathrm{r}l} \otimes \hat{\boldsymbol{v}}_{\mathrm{r}l} + \boldsymbol{V}_{\mathrm{r}l} \otimes \hat{\boldsymbol{i}}_{\mathrm{r}l}) \\ &- \sum_{l=\mathrm{a,b,c}} (\boldsymbol{I}_{\mathrm{g}l} \otimes \hat{\boldsymbol{v}}_{\mathrm{g}l} + \boldsymbol{V}_{\mathrm{g}l} \otimes \hat{\boldsymbol{i}}_{\mathrm{g}l}) \end{aligned} \tag{7.64}$$

After simplification, the small-signal vector of DC voltage can be expressed as

$$\hat{\boldsymbol{v}}_\mathrm{dc} = \boldsymbol{J}_\mathrm{gi} \hat{\boldsymbol{i}}_\mathrm{ga} + \boldsymbol{J}_\mathrm{ri} \hat{\boldsymbol{i}}_\mathrm{ra} + \boldsymbol{J}_\mathrm{gv} \hat{\boldsymbol{v}}_\mathrm{a} + \boldsymbol{J}_\mathrm{rv} \hat{\boldsymbol{v}}_\mathrm{ra} \tag{7.65}$$

where $\boldsymbol{J}_\mathrm{gi}$, $\boldsymbol{J}_\mathrm{ri}$, $\boldsymbol{J}_\mathrm{gv}$, $\boldsymbol{J}_\mathrm{rv}$ are fifth-order matrices. All other elements in the matrices are zero except for the following

$$\begin{cases} \boldsymbol{J}_\mathrm{gi}(2,1) = -\dfrac{3}{C_\mathrm{dc} V_\mathrm{dc} s_1}(\boldsymbol{V}_\mathrm{g1} + s_2 L_\mathrm{f} \boldsymbol{I}_\mathrm{g1}) \\ \boldsymbol{J}_\mathrm{gi}(2,3) = -\dfrac{3}{C_\mathrm{dc} V_\mathrm{dc} s_1}(\boldsymbol{V}_\mathrm{g1}^* + s L_\mathrm{f} \boldsymbol{I}_\mathrm{g1}^*) \end{cases} \tag{7.66}$$

$$\begin{cases} \boldsymbol{J}_\mathrm{ri}(2,1) = -\dfrac{3}{C_\mathrm{dc} V_\mathrm{dc} s_1} \boldsymbol{V}_\mathrm{r1} \\ \boldsymbol{J}_\mathrm{ri}(2,3) = -\dfrac{3}{C_\mathrm{dc} V_\mathrm{dc} s_1} \boldsymbol{V}_\mathrm{r1}^* \end{cases} \tag{7.67}$$

$$\begin{cases} \boldsymbol{J}_\mathrm{gv}(2,1) = -\dfrac{3}{C_\mathrm{dc} V_\mathrm{dc} s_1} \boldsymbol{I}_\mathrm{g1} \\ \boldsymbol{J}_\mathrm{gv}(2,3) = -\dfrac{3}{C_\mathrm{dc} V_\mathrm{dc} s_1} \boldsymbol{I}_\mathrm{g1}^* \end{cases} \tag{7.68}$$

$$\begin{cases} \boldsymbol{J}_\mathrm{rv}(2,1) = -\dfrac{3}{C_\mathrm{dc} V_\mathrm{dc} s_1} \boldsymbol{I}_\mathrm{r1} \\ \boldsymbol{J}_\mathrm{rv}(2,3) = -\dfrac{3}{C_\mathrm{dc} V_\mathrm{dc} s_1} \boldsymbol{I}_\mathrm{r1}^* \end{cases} \tag{7.69}$$

where $s_1 = \mathrm{j}2\pi(f_\mathrm{p} - f_1)$.

7.3.2.3 Small-Signal Model of GSC

The small-signal modeling of GSC can be referred to Chap. 3. As shown in Fig. 7.6, GSC maintains the stability of DC voltage by controlling the d-axis current through the outer DC voltage loop. The small-signal vectors of d- and q-axis current references of GSC can be expressed as

$$\begin{cases} \hat{\boldsymbol{i}}_{\mathrm{gdref}} = H_{\mathrm{vdc}}(s_1)\hat{\boldsymbol{v}}_{\mathrm{dc}} \\ \hat{\boldsymbol{i}}_{\mathrm{gqref}} = 0 \end{cases} \tag{7.70}$$

where $H_{\mathrm{vdc}}(s_1)$ is the transfer function of DC voltage controller, whose expression is $H_{\mathrm{vdc}}(s_1) = K_{\mathrm{vdcp}} + K_{\mathrm{vdci}}/s_1$, K_{vdcp} and K_{vdci} are proportional and integral coefficients respectively.

According to the structure of GSC, the small-signal vector of its modulation signal can be derived as

$$\hat{\boldsymbol{m}}_{\mathrm{ga}} = \boldsymbol{E}_{\mathrm{dc}}\hat{\boldsymbol{v}}_{\mathrm{dc}} + \boldsymbol{E}_{\mathrm{gi}}\hat{\boldsymbol{i}}_{\mathrm{ga}} + \boldsymbol{E}_{\mathrm{gv}}\hat{\boldsymbol{v}}_{\mathrm{a}} \tag{7.71}$$

where $\boldsymbol{E}_{\mathrm{dc}}$, $\boldsymbol{E}_{\mathrm{gi}}$, $\boldsymbol{E}_{\mathrm{gv}}$ are fifth-order matrices. All other elements in the matrices are zero except for the following

$$\begin{cases} \boldsymbol{E}_{\mathrm{dc}}(1,2) = \dfrac{1}{2}H_{\mathrm{gi}}(s_1)H_{\mathrm{vdc}}(s_1) \\ \boldsymbol{E}_{\mathrm{dc}}(3,2) = \dfrac{1}{2}H_{\mathrm{gi}}(s_1)H_{\mathrm{vdc}}(s_1) \end{cases} \tag{7.72}$$

$$\begin{cases} \boldsymbol{E}_{\mathrm{gi}}(1,1) = -H_{\mathrm{gi}}(s_1) - \mathrm{j}K_{\mathrm{gd}} \\ \boldsymbol{E}_{\mathrm{gi}}(3,3) = -H_{\mathrm{gi}}(s_1) + \mathrm{j}K_{\mathrm{gd}} \end{cases} \tag{7.73}$$

$$\begin{cases} \boldsymbol{E}_{\mathrm{gv}}(1,1) = T_{\mathrm{PLL}}(s_1)[(H_{\mathrm{gi}}(s_1) + \mathrm{j}K_{\mathrm{gd}})\boldsymbol{I}_{\mathrm{g1}}^{*} + \boldsymbol{M}_1^{*}] \\ \boldsymbol{E}_{\mathrm{gv}}(1,3) = -T_{\mathrm{PLL}}(s_1)[(H_{\mathrm{gi}}(s_1) + \mathrm{j}K_{\mathrm{gd}})\boldsymbol{I}_{\mathrm{g1}}^{*} + \boldsymbol{M}_1^{*}] \\ \boldsymbol{E}_{\mathrm{gv}}(3,1) = -T_{\mathrm{PLL}}(s_1)[(H_{\mathrm{gi}}(s_1) - \mathrm{j}K_{\mathrm{gd}})\boldsymbol{I}_{\mathrm{g1}} + \boldsymbol{M}_1] \\ \boldsymbol{E}_{\mathrm{gv}}(3,3) = T_{\mathrm{PLL}}(s_1)[(H_{\mathrm{gi}}(s_1) - \mathrm{j}K_{\mathrm{gd}})\boldsymbol{I}_{\mathrm{g1}} + \boldsymbol{M}_1] \end{cases} \tag{7.74}$$

Transforming Eq. (7.26) to frequency domain, the small-signal model of GSC main circuit can be obtained as

$$K_{\mathrm{m}}(V_{\mathrm{dc}}\hat{\boldsymbol{m}}_{\mathrm{ga}} + \boldsymbol{M}_{\mathrm{ga}}\hat{\boldsymbol{v}}_{\mathrm{dc}}) = \hat{\boldsymbol{v}}_{\mathrm{a}} + \boldsymbol{Z}_{\mathrm{Lf}}\hat{\boldsymbol{i}}_{\mathrm{ga}} \tag{7.75}$$

where $\boldsymbol{M}_{\mathrm{ga}}$ is the extended steady-state matrix of GSC modulation signal, whose expression is

$$\boldsymbol{M}_{\mathrm{ga}}=\begin{bmatrix} 0 & \boldsymbol{M}_{\mathrm{g1}}^{*} & 0 & 0 & 0 \\ \boldsymbol{M}_{\mathrm{g1}} & 0 & \boldsymbol{M}_{\mathrm{g1}}^{*} & 0 & 0 \\ 0 & \boldsymbol{M}_{\mathrm{g1}} & 0 & \boldsymbol{M}_{\mathrm{g1}}^{*} & 0 \\ 0 & 0 & \boldsymbol{M}_{\mathrm{g1}} & 0 & \boldsymbol{M}_{\mathrm{g1}}^{*} \\ 0 & 0 & 0 & \boldsymbol{M}_{\mathrm{g1}} & 0 \end{bmatrix}$$

$\boldsymbol{Z}_{\mathrm{Lf}}$ is a fifth-order diagonal matrix, representing the impedance of GSC AC filter inductor in the small-signal frequency order, expressed as

$$\boldsymbol{Z}_{\mathrm{Lf}}=\mathrm{j}2\pi L_{\mathrm{f}}\cdot\mathrm{diag}[f_{\mathrm{p}}-2f_{1},\ f_{\mathrm{p}}-f_{1},\ f_{\mathrm{p}},\ f_{\mathrm{p}}+f_{1},\ f_{\mathrm{p}}+2f_{1}]$$

After simplification, the small-signal model of GSC can be expressed as

$$\hat{\boldsymbol{v}}_{\mathrm{a}}=\boldsymbol{F}_{\mathrm{dc}}\hat{\boldsymbol{v}}_{\mathrm{dc}}+\boldsymbol{F}_{\mathrm{gi}}\hat{\boldsymbol{i}}_{\mathrm{ga}} \tag{7.76}$$

where $\boldsymbol{F}_{\mathrm{dc}}$ and $\boldsymbol{F}_{\mathrm{gi}}$ are fifth-order matrices, whose expression is

$$\begin{cases}\boldsymbol{F}_{\mathrm{dc}}=(\boldsymbol{U}-K_{\mathrm{m}}V_{\mathrm{dc}}\boldsymbol{E}_{\mathrm{gv}})^{-1}(K_{\mathrm{m}}\boldsymbol{M}_{\mathrm{ga}}+K_{\mathrm{m}}V_{\mathrm{dc}}\boldsymbol{E}_{\mathrm{dc}}) \\ \boldsymbol{F}_{\mathrm{gi}}=(\boldsymbol{U}-K_{\mathrm{m}}V_{\mathrm{dc}}\boldsymbol{E}_{\mathrm{gv}})^{-1}(K_{\mathrm{m}}V_{\mathrm{dc}}\boldsymbol{E}_{\mathrm{gi}}-\boldsymbol{Z}_{\mathrm{Lf}})\end{cases} \tag{7.77}$$

$\boldsymbol{U}$ is fifth-order identity matrix.

7.3.2.4 Small-Signal Model of RSC

According to the typical control strategy of RSC in Fig. 7.7, the d-axis current reference of RSC is obtained from the outer active power loop, and the q-axis current reference of RSC is obtained from the outer reactive power loop. The small-signal vectors of d- and q-axis current references of RSC can be expressed as

$$\begin{cases}\hat{\boldsymbol{i}}_{\mathrm{rdref}}=-\dfrac{1}{1-s_{\mathrm{n}}}H_{\mathrm{p}}(s_{1})\hat{\boldsymbol{p}}_{\mathrm{e}} \\ \hat{\boldsymbol{i}}_{\mathrm{rqref}}=-H_{\mathrm{q}}(s_{1})\hat{\boldsymbol{q}}_{\mathrm{e}}\end{cases} \tag{7.78}$$

where $H_{\mathrm{p}}(s_1)$ is the transfer function of active power controller, whose expression is $H_{\mathrm{p}}(s_1)=K_{\mathrm{pep}}+K_{\mathrm{pei}}/s_1$, K_{pep} and K_{pei} are its proportional and integral coefficients respectively. $H_{\mathrm{q}}(s_1)$ is the transfer function of active power controller, whose expression is $H_{\mathrm{q}}(s_1)=K_{\mathrm{qep}}+K_{\mathrm{qei}}/s_1$, K_{qep} and K_{qei} are its proportional and integral coefficients respectively.

The small-signal vectors of DFIG output power can be calculated by

$$\begin{cases}\hat{\boldsymbol{p}}_{\mathrm{e}}=\boldsymbol{P}_{\mathrm{si}}\hat{\boldsymbol{i}}_{\mathrm{sa}}+\boldsymbol{P}_{\mathrm{gi}}\hat{\boldsymbol{i}}_{\mathrm{ga}}+\boldsymbol{P}_{\mathrm{v}}\hat{\boldsymbol{v}}_{\mathrm{a}} \\ \hat{\boldsymbol{q}}_{\mathrm{e}}=\boldsymbol{Q}_{\mathrm{si}}\hat{\boldsymbol{i}}_{\mathrm{sa}}+\boldsymbol{Q}_{\mathrm{gi}}\hat{\boldsymbol{i}}_{\mathrm{ga}}+\boldsymbol{Q}_{\mathrm{v}}\hat{\boldsymbol{v}}_{\mathrm{a}}\end{cases} \tag{7.79}$$

where $\boldsymbol{P}_{\mathrm{si}}$, $\boldsymbol{P}_{\mathrm{gi}}$, $\boldsymbol{P}_{\mathrm{v}}$, $\boldsymbol{Q}_{\mathrm{si}}$, $\boldsymbol{Q}_{\mathrm{gi}}$, $\boldsymbol{Q}_{\mathrm{v}}$ are fifth-order matrices. All other elements in the matrices are zero except for the following

$$\begin{cases} \boldsymbol{P}_{\mathrm{si}}(2,1) = -3\boldsymbol{V}_1 \\ \boldsymbol{P}_{\mathrm{si}}(2,3) = -3\boldsymbol{V}_1^* \end{cases} \tag{7.80}$$

$$\begin{cases} \boldsymbol{P}_{\mathrm{gi}}(2,1) = 3\boldsymbol{V}_1 \\ \boldsymbol{P}_{\mathrm{gi}}(2,3) = 3\boldsymbol{V}_1^* \end{cases} \tag{7.81}$$

$$\begin{cases} \boldsymbol{P}_{\mathrm{v}}(2,1) = 3(\boldsymbol{I}_{\mathrm{g1}} - \boldsymbol{I}_{\mathrm{s1}}) \\ \boldsymbol{P}_{\mathrm{v}}(2,3) = 3(\boldsymbol{I}_{\mathrm{g1}}^* - \boldsymbol{I}_{\mathrm{s1}}^*) \end{cases} \tag{7.82}$$

$$\begin{cases} \boldsymbol{Q}_{\mathrm{si}}(2,1) = \mathrm{j}3\boldsymbol{V}_1 \\ \boldsymbol{Q}_{\mathrm{si}}(2,3) = -\mathrm{j}3\boldsymbol{V}_1^* \end{cases} \tag{7.83}$$

$$\begin{cases} \boldsymbol{Q}_{\mathrm{gi}}(2,1) = -\mathrm{j}3\boldsymbol{V}_1 \\ \boldsymbol{Q}_{\mathrm{gi}}(2,3) = \mathrm{j}3\boldsymbol{V}_1^* \end{cases} \tag{7.84}$$

$$\begin{cases} \boldsymbol{Q}_{\mathrm{v}}(2,1) = \mathrm{j}3(\boldsymbol{I}_{\mathrm{g1}} - \boldsymbol{I}_{\mathrm{s1}}) \\ \boldsymbol{Q}_{\mathrm{v}}(2,3) = -\mathrm{j}3(\boldsymbol{I}_{\mathrm{g1}}^* - \boldsymbol{I}_{\mathrm{s1}}^*) \end{cases} \tag{7.85}$$

According to the structure of RSC, the small-signal vector of its modulation signal can be derived as

$$\hat{\boldsymbol{m}}_{\mathrm{ra}} = \boldsymbol{E}_{\mathrm{rgi}}\hat{\boldsymbol{i}}_{\mathrm{ga}} + \boldsymbol{E}_{\mathrm{rsi}}\hat{\boldsymbol{i}}_{\mathrm{sa}} + \boldsymbol{E}_{\mathrm{rri}}\hat{\boldsymbol{i}}_{\mathrm{ra}} + \boldsymbol{E}_{\mathrm{rv}}\hat{\boldsymbol{v}}_{\mathrm{a}} \tag{7.86}$$

where $\boldsymbol{E}_{\mathrm{rgi}}$, $\boldsymbol{E}_{\mathrm{rsi}}$, $\boldsymbol{E}_{\mathrm{rri}}$, $\boldsymbol{E}_{\mathrm{rv}}$ are fifth-order matrices. All other elements in the matrices are zero except for the following

$$\begin{cases} \boldsymbol{E}_{\mathrm{rgi}}(1,1) = \dfrac{3}{2}H_{\mathrm{ri}}(s_1)\left(-\dfrac{1}{1-s_{\mathrm{n}}}H_{\mathrm{p}}(s_1) + H_{\mathrm{q}}(s_1)\right)\boldsymbol{V}_1 \\ \boldsymbol{E}_{\mathrm{rgi}}(1,3) = \dfrac{3}{2}H_{\mathrm{ri}}(s_1)\left(-\dfrac{1}{1-s_{\mathrm{n}}}H_{\mathrm{p}}(s_1) - H_{\mathrm{q}}(s_1)\right)\boldsymbol{V}_1^* \\ \boldsymbol{E}_{\mathrm{rgi}}(3,1) = \dfrac{3}{2}H_{\mathrm{ri}}(s_1)\left(-\dfrac{1}{1-s_{\mathrm{n}}}H_{\mathrm{p}}(s_1) - H_{\mathrm{q}}(s_1)\right)\boldsymbol{V}_1 \\ \boldsymbol{E}_{\mathrm{rgi}}(3,3) = \dfrac{3}{2}H_{\mathrm{ri}}(s_1)\left(-\dfrac{1}{1-s_{\mathrm{n}}}H_{\mathrm{p}}(s_1) + H_{\mathrm{q}}(s_1)\right)\boldsymbol{V}_1^* \end{cases} \tag{7.87}$$

$$\begin{cases} \boldsymbol{E}_{\mathrm{rsi}}(1,1) = -\boldsymbol{E}_{\mathrm{rgi}}(1,1) \\ \boldsymbol{E}_{\mathrm{rsi}}(1,3) = -\boldsymbol{E}_{\mathrm{rgi}}(1,3) \\ \boldsymbol{E}_{\mathrm{rsi}}(3,1) = -\boldsymbol{E}_{\mathrm{rgi}}(3,1) \\ \boldsymbol{E}_{\mathrm{rsi}}(3,3) = -\boldsymbol{E}_{\mathrm{rgi}}(3,3) \end{cases} \tag{7.88}$$

$$\begin{cases} \boldsymbol{E}_{\mathrm{rri}}(1,1) = -K_{\mathrm{e}}(H_{\mathrm{ri}}(s_1) + \mathrm{j}K_{\mathrm{rd}}) \\ \boldsymbol{E}_{\mathrm{rri}}(3,3) = -K_{\mathrm{e}}(H_{\mathrm{ri}}(s_1) - \mathrm{j}K_{\mathrm{rd}}) \end{cases} \tag{7.89}$$

$$\begin{cases} \boldsymbol{E}_{\mathrm{rv}}(1,1) = \dfrac{3}{2}H_{\mathrm{ri}}(s_1)\left(-\dfrac{1}{1-s_{\mathrm{n}}}H_{\mathrm{p}}(s_1) - H_{\mathrm{q}}(s_1)\right)(\boldsymbol{I}_{\mathrm{g1}} - \boldsymbol{I}_{\mathrm{s1}}) \\ \qquad\qquad + T_{\mathrm{PLL}}(s_1)[K_{\mathrm{e}}(H_{\mathrm{ri}}(s_1) + \mathrm{j}K_{\mathrm{rd}})\boldsymbol{I}_{\mathrm{r1}}^* + \boldsymbol{M}_{\mathrm{r1}}^*] \\ \boldsymbol{E}_{\mathrm{rv}}(1,3) = \dfrac{3}{2}H_{\mathrm{ri}}(s_1)\left(-\dfrac{1}{1-s_{\mathrm{n}}}H_{\mathrm{p}}(s_1) + H_{\mathrm{q}}(s_1)\right)(\boldsymbol{I}_{\mathrm{g1}}^* - \boldsymbol{I}_{\mathrm{s1}}^*) \\ \qquad\qquad + T_{\mathrm{PLL}}(s_1)[-K_{\mathrm{e}}(H_{\mathrm{ri}}(s_1) + \mathrm{j}K_{\mathrm{rd}})\boldsymbol{I}_{\mathrm{r1}}^* - \boldsymbol{M}_{\mathrm{r1}}^*] \\ \boldsymbol{E}_{\mathrm{rv}}(3,1) = \dfrac{3}{2}H_{\mathrm{ri}}(s_1)\left(-\dfrac{1}{1-s_{\mathrm{n}}}H_{\mathrm{p}}(s_1) + H_{\mathrm{q}}(s_1)\right)(\boldsymbol{I}_{\mathrm{g1}} - \boldsymbol{I}_{\mathrm{s1}}) \\ \qquad\qquad + T_{\mathrm{PLL}}(s_1)[-K_{\mathrm{e}}(H_{\mathrm{ri}}(s_1) - \mathrm{j}K_{\mathrm{rd}})\boldsymbol{I}_{\mathrm{r1}} - \boldsymbol{M}_{\mathrm{r1}}] \\ \boldsymbol{E}_{\mathrm{rv}}(3,3) = \dfrac{3}{2}H_{\mathrm{ri}}(s_1)\left(-\dfrac{1}{1-s_{\mathrm{n}}}H_{\mathrm{p}}(s_1) - H_{\mathrm{q}}(s_1)\right)(\boldsymbol{I}_{\mathrm{g1}}^* - \boldsymbol{I}_{\mathrm{s1}}^*) \\ \qquad\qquad + T_{\mathrm{PLL}}(s_1)[K_{\mathrm{e}}(H_{\mathrm{ri}}(s_1) - \mathrm{j}K_{\mathrm{rd}})\boldsymbol{I}_{\mathrm{r1}} + \boldsymbol{M}_{\mathrm{r1}}] \end{cases} \tag{7.90}$$

Transforming Eq. (7.33) to frequency domain, the small-signal model of RSC main circuit can be obtained as

$$\hat{\boldsymbol{v}}_{\mathrm{ra}} = K_{\mathrm{e}}K_{\mathrm{m}}(V_{\mathrm{dc}}\hat{\boldsymbol{m}}_{\mathrm{ra}} + \boldsymbol{M}_{\mathrm{ra}}\hat{\boldsymbol{v}}_{\mathrm{dc}}) \tag{7.91}$$

After simplification, the small-signal model of RSC can be expressed as

$$\hat{\boldsymbol{v}}_{\mathrm{ra}} = \boldsymbol{B}_{\mathrm{dc}}\hat{\boldsymbol{v}}_{\mathrm{dc}} + \boldsymbol{B}_{\mathrm{rgi}}\hat{\boldsymbol{i}}_{\mathrm{ga}} + \boldsymbol{B}_{\mathrm{rsi}}\hat{\boldsymbol{i}}_{\mathrm{sa}} + \boldsymbol{B}_{\mathrm{rri}}\hat{\boldsymbol{i}}_{\mathrm{ra}} + \boldsymbol{B}_{\mathrm{rv}}\hat{\boldsymbol{v}}_{\mathrm{a}} \tag{7.92}$$

where $\boldsymbol{B}_{\mathrm{dc}}$, $\boldsymbol{B}_{\mathrm{rgi}}$, $\boldsymbol{B}_{\mathrm{rsi}}$, $\boldsymbol{B}_{\mathrm{rri}}$, $\boldsymbol{B}_{\mathrm{rv}}$ are fifth-order matrices, whose expression is

$$\begin{cases} \boldsymbol{B}_{\mathrm{dc}} = K_{\mathrm{e}}K_{\mathrm{m}}\boldsymbol{M}_{\mathrm{ra}} \\ \boldsymbol{B}_{\mathrm{rgi}} = K_{\mathrm{e}}K_{\mathrm{m}}V_{\mathrm{dc}}\boldsymbol{E}_{\mathrm{rgi}} \\ \boldsymbol{B}_{\mathrm{rsi}} = K_{\mathrm{e}}K_{\mathrm{m}}V_{\mathrm{dc}}\boldsymbol{E}_{\mathrm{rsi}} \\ \boldsymbol{B}_{\mathrm{rri}} = K_{\mathrm{e}}K_{\mathrm{m}}V_{\mathrm{dc}}\boldsymbol{E}_{\mathrm{rri}} \\ \boldsymbol{B}_{\mathrm{rv}} = K_{\mathrm{e}}K_{\mathrm{m}}V_{\mathrm{dc}}\boldsymbol{E}_{\mathrm{rv}} \end{cases} \tag{7.93}$$

$\boldsymbol{M}_{\mathrm{ra}}$ is the extended steady-state matrix of RSC modulation signal, whose expression is

$$\boldsymbol{M}_{\mathrm{ra}} = \begin{bmatrix} 0 & \boldsymbol{M}_{\mathrm{r1}}^* & 0 & 0 & 0 \\ \boldsymbol{M}_{\mathrm{r1}} & 0 & \boldsymbol{M}_{\mathrm{r1}}^* & 0 & 0 \\ 0 & \boldsymbol{M}_{\mathrm{r1}} & 0 & \boldsymbol{M}_{\mathrm{r1}}^* & 0 \\ 0 & 0 & \boldsymbol{M}_{\mathrm{r1}} & 0 & \boldsymbol{M}_{\mathrm{r1}}^* \\ 0 & 0 & 0 & \boldsymbol{M}_{\mathrm{r1}} & 0 \end{bmatrix}$$

7.3.3 AC Port Impedance Model

The AC port admittance of DFIG-based wind turbines can be obtained from the ratio of the total input current small signal and voltage small signal at the AC port, namely

$$\boldsymbol{Y}_{\mathrm{DFIG}} = -\frac{\hat{\boldsymbol{i}}_{\mathrm{a}}}{\hat{\boldsymbol{v}}_{\mathrm{a}}} \tag{7.94}$$

$\hat{\boldsymbol{i}}_{\mathrm{a}}$ is the total output current of DFIG-based wind turbine at its AC port, which can be calculated by

$$\hat{\boldsymbol{i}}_{\mathrm{a}} = \hat{\boldsymbol{i}}_{\mathrm{ga}} - \hat{\boldsymbol{i}}_{\mathrm{sa}} \tag{7.95}$$

Based on Eqs. (7.59), (7.65), (7.76) and (7.92), the relationship of each small-signal vector can be derived

$$\begin{cases} \boldsymbol{G}_{\mathrm{gg}}\hat{\boldsymbol{i}}_{\mathrm{ga}} + \boldsymbol{G}_{\mathrm{gs}}\hat{\boldsymbol{i}}_{\mathrm{sa}} + \boldsymbol{G}_{\mathrm{gv}}\hat{\boldsymbol{v}}_{\mathrm{a}} = 0 \\ \boldsymbol{G}_{\mathrm{rg}}\hat{\boldsymbol{i}}_{\mathrm{ga}} + \boldsymbol{G}_{\mathrm{rs}}\hat{\boldsymbol{i}}_{\mathrm{sa}} + \boldsymbol{G}_{\mathrm{rv}}\hat{\boldsymbol{v}}_{\mathrm{a}} = 0 \end{cases} \tag{7.96}$$

where

$$\begin{cases} \boldsymbol{G}_{\mathrm{gg}} = \boldsymbol{F}_{\mathrm{dc}}\boldsymbol{J}_{\mathrm{gi}} + \boldsymbol{F}_{\mathrm{gi}} \\ \boldsymbol{G}_{\mathrm{gs}} = \boldsymbol{F}_{\mathrm{dc}}\boldsymbol{J}_{\mathrm{ri}}\boldsymbol{G}_{12} + \boldsymbol{F}_{\mathrm{dc}}\boldsymbol{J}_{\mathrm{rv}}\boldsymbol{G}_{22} \\ \boldsymbol{G}_{\mathrm{gv}} = \boldsymbol{F}_{\mathrm{dc}}\boldsymbol{J}_{\mathrm{ri}}\boldsymbol{G}_{11} + \boldsymbol{F}_{\mathrm{dc}}\boldsymbol{J}_{\mathrm{gv}} + \boldsymbol{F}_{\mathrm{dc}}\boldsymbol{J}_{\mathrm{rv}}\boldsymbol{G}_{21} - \boldsymbol{U} \\ \boldsymbol{G}_{\mathrm{rg}} = \boldsymbol{B}_{\mathrm{dc}}\boldsymbol{J}_{\mathrm{gi}} + \boldsymbol{B}_{\mathrm{rgi}} \\ \boldsymbol{G}_{\mathrm{rs}} = (\boldsymbol{B}_{\mathrm{dc}}\boldsymbol{J}_{\mathrm{ri}} + \boldsymbol{B}_{\mathrm{rri}})\boldsymbol{G}_{12} + (\boldsymbol{B}_{\mathrm{dc}}\boldsymbol{J}_{\mathrm{rv}} - \boldsymbol{U})\boldsymbol{G}_{22} + \boldsymbol{B}_{\mathrm{rsi}} \\ \boldsymbol{G}_{\mathrm{rv}} = (\boldsymbol{B}_{\mathrm{dc}}\boldsymbol{J}_{\mathrm{ri}} + \boldsymbol{B}_{\mathrm{rri}})\boldsymbol{G}_{11} + (\boldsymbol{B}_{\mathrm{dc}}\boldsymbol{J}_{\mathrm{gv}} + \boldsymbol{B}_{\mathrm{rv}}) + (\boldsymbol{B}_{\mathrm{dc}}\boldsymbol{J}_{\mathrm{rv}} - \boldsymbol{U})\boldsymbol{G}_{21} \end{cases} \tag{7.97}$$

Simultaneous solving Eq.(7.95) and (7.96), there is

$$\begin{aligned} \hat{\boldsymbol{i}}_{\mathrm{a}} = -\Big[&(\boldsymbol{G}_{\mathrm{gg}}^{-1}\boldsymbol{G}_{\mathrm{gs}} + \boldsymbol{U})(\boldsymbol{G}_{\mathrm{rg}}\boldsymbol{G}_{\mathrm{gg}}^{-1}\boldsymbol{G}_{\mathrm{gs}} - \boldsymbol{G}_{\mathrm{rs}})^{-1}(-\boldsymbol{G}_{\mathrm{rg}}\boldsymbol{G}_{\mathrm{gg}}^{-1}\boldsymbol{G}_{\mathrm{gv}} + \boldsymbol{G}_{\mathrm{rv}}) \\ &+ \boldsymbol{G}_{\mathrm{gg}}^{-1}\boldsymbol{G}_{\mathrm{gv}}\Big]\hat{\boldsymbol{v}}_{\mathrm{a}} \end{aligned} \tag{7.98}$$

According to Eqs. (7.94) and (7.98), the AC port admittance of DFIG-based wind turbine can be obtained as

$$\boldsymbol{Y}_{\mathrm{DFIG}} = \boldsymbol{G}_{\mathrm{gg}}^{-1}\boldsymbol{G}_{\mathrm{gv}} + (\boldsymbol{U} + \boldsymbol{G}_{\mathrm{gg}}^{-1}\boldsymbol{G}_{\mathrm{gs}})(\boldsymbol{G}_{\mathrm{rg}}\boldsymbol{G}_{\mathrm{gg}}^{-1}\boldsymbol{G}_{\mathrm{gs}} - \boldsymbol{G}_{\mathrm{rs}})^{-1}(\boldsymbol{G}_{\mathrm{rv}} - \boldsymbol{G}_{\mathrm{rg}}\boldsymbol{G}_{\mathrm{gg}}^{-1}\boldsymbol{G}_{\mathrm{gv}}) \tag{7.99}$$

Since there are only components at f_{p} and $f_{\mathrm{p}} - 2f_1$ in small-signal vectors of AC voltage and AC current of DFIG-based wind turbine, only relevant elements at these

two frequencies are extracted, and the AC port admittance shown in Eq. (7.99) are rearranged as the following 2 × 2 matrix.

$$\begin{bmatrix} \boldsymbol{Y}_{\mathrm{DFIG}}^{\mathrm{pp}} & \boldsymbol{Y}_{\mathrm{DFIG}}^{\mathrm{np}} \\ \boldsymbol{Y}_{\mathrm{DFIG}}^{\mathrm{pn}} & \boldsymbol{Y}_{\mathrm{DFIG}}^{\mathrm{nn}} \end{bmatrix} = \begin{bmatrix} \boldsymbol{Y}_{\mathrm{DFIG}}(3,3) & \boldsymbol{Y}_{\mathrm{DFIG}}(3,1) \\ \boldsymbol{Y}_{\mathrm{DFIG}}(1,3) & \boldsymbol{Y}_{\mathrm{DFIG}}(1,1) \end{bmatrix} \tag{7.100}$$

where

$\boldsymbol{Y}_{\mathrm{DFIG}}(3,3)$ is the element in the third row and the third column of $\boldsymbol{Y}_{\mathrm{DFIG}}$;
$\boldsymbol{Y}_{\mathrm{DFIG}}(3,1)$ is the element in the third row and the first column of $\boldsymbol{Y}_{\mathrm{DFIG}}$;
$\boldsymbol{Y}_{\mathrm{DFIG}}(1,3)$ is the element in the first row and the third column of $\boldsymbol{Y}_{\mathrm{DFIG}}$;
$\boldsymbol{Y}_{\mathrm{DFIG}}(1,1)$ is the element in the first row and the first column of $\boldsymbol{Y}_{\mathrm{DFIG}}$.

The relationship between the small-signal components of AC voltage and AC current at the perturbation frequency and coupling frequency meets

$$\begin{bmatrix} -\hat{\boldsymbol{i}}_{\mathrm{p}} \\ -\hat{\boldsymbol{i}}_{\mathrm{p\text{-}2}} \end{bmatrix} = \begin{bmatrix} \boldsymbol{Y}_{\mathrm{DFIG}}^{\mathrm{pp}} & \boldsymbol{Y}_{\mathrm{DFIG}}^{\mathrm{np}} \\ \boldsymbol{Y}_{\mathrm{DFIG}}^{\mathrm{pn}} & \boldsymbol{Y}_{\mathrm{DFIG}}^{\mathrm{nn}} \end{bmatrix} \begin{bmatrix} \hat{\boldsymbol{v}}_{\mathrm{p}} \\ \hat{\boldsymbol{v}}_{\mathrm{p\text{-}2}} \end{bmatrix} \tag{7.101}$$

where $\boldsymbol{Y}_{\mathrm{DFIG}}^{\mathrm{pp}}$ is the positive-sequence admittance of DFIG-based wind turbines, representing the small-signal response of AC current at f_{p} in positive sequence under per unit small-signal perturbation of AC voltage at f_{p} in positive sequence.

$\boldsymbol{Y}_{\mathrm{DFIG}}^{\mathrm{pn}}$ is the positive-sequence coupling admittance of DFIG-based wind turbines, representing the small-signal response of AC current at $f_{\mathrm{p}}-2f_1$ in negative sequence under per unit small-signal perturbation of AC voltage at f_{p} in positive sequence.

$\boldsymbol{Y}_{\mathrm{DFIG}}^{\mathrm{nn}}$ is the negative-sequence admittance of DFIG-based wind turbines, representing the small-signal response of AC current at $f_{\mathrm{p}}-2f_1$ in negative sequence under per unit small-signal perturbation of AC voltage at $f_{\mathrm{p}}-2f_1$ in negative sequence.

$\boldsymbol{Y}_{\mathrm{DFIG}}^{\mathrm{np}}$ is the negative-sequence coupling admittance of DFIG-based wind turbines, representing the small-signal response of AC current at f_{p} in positive sequence under per unit small-signal perturbation of AC voltage at $f_{\mathrm{p}}-2f_1$ in negative sequence.

The AC port impedance of DFIG-based wind turbine can be obtained by calculating the inverse matrix of the AC port admittance as

$$\begin{bmatrix} \boldsymbol{Z}_{\mathrm{DFIG}}^{\mathrm{pp}} & \boldsymbol{Z}_{\mathrm{DFIG}}^{\mathrm{pn}} \\ \boldsymbol{Z}_{\mathrm{DFIG}}^{\mathrm{np}} & \boldsymbol{Z}_{\mathrm{DFIG}}^{\mathrm{nn}} \end{bmatrix} = \begin{bmatrix} \boldsymbol{Y}_{\mathrm{DFIG}}^{\mathrm{pp}} & \boldsymbol{Y}_{\mathrm{DFIG}}^{\mathrm{np}} \\ \boldsymbol{Y}_{\mathrm{DFIG}}^{\mathrm{pn}} & \boldsymbol{Y}_{\mathrm{DFIG}}^{\mathrm{nn}} \end{bmatrix}^{-1} \tag{7.102}$$

$\boldsymbol{Z}_{\mathrm{DFIG}}^{\mathrm{pp}}$ represents the positive-sequence impedance of DFIG-based wind turbines, which is the element in the first row and the first column of the AC port admittance inverse matrix.

$\boldsymbol{Z}_{\mathrm{DFIG}}^{\mathrm{pn}}$represents the positive-sequence coupling impedance of DFIG-based wind turbines, which is the element in the first row and the second column of the AC port admittance inverse matrix.

$\boldsymbol{Z}_{\mathrm{DFIG}}^{\mathrm{nn}}$ represents the negative-sequence impedance of DFIG-based wind turbines, which is the element in the second row and the second column of the AC port admittance inverse matrix.

$\boldsymbol{Z}_{\mathrm{DFIG}}^{\mathrm{np}}$ represents the negative-sequence coupling impedance of DFIG-based wind turbines, which is the element in the second row and the first column of the AC port admittance inverse matrix.

In addition, the frequency-domain relationship between the negative-sequence impedance and the positive-sequence impedance satisfies $\boldsymbol{Z}_{\mathrm{DFIG}}^{\mathrm{nn}} = \boldsymbol{Z}_{\mathrm{DFIG}}^{\mathrm{pp}^*}(\mathrm{j}2\omega_1 - s)$, and the frequency-domain relationship between the negative-sequence coupling impedance and the positive-sequence coupling impedance satisfies $\boldsymbol{Z}_{\mathrm{DFIG}}^{\mathrm{np}} = \boldsymbol{Z}_{\mathrm{DFIG}}^{\mathrm{pn}^*}(\mathrm{j}2\omega_1 - s)$.

Table 7.2 lists the main circuit and controller parameters of DFIG-based wind turbines. Figure 7.15 shows the comparison between analytical impedance (in solid line) and scanning impedance (in discrete points). As seen from the figure, all the discrete points fall on the solid lines, which verify the accuracy of the derived impedance model of DFIG-based wind turbines.

7.4 Analysis of Broadband Impedance Characteristics

In this section, based on the impedance model of DFIG-based wind turbines, the stator-GSC small-signal decoupling equivalent model will be established first. The dominant factors of impedance characteristics in different frequency bands are analyzed, and the frequency-band division method of DFIG-based wind turbines is proposed. Then, the frequency-band overlapping effects of multiple controllers are clarified and the negative damping characteristics of each frequency band are analyzed. Finally, based on CHIL impedance scanning results of different types of DFIG-based wind turbines, typical values of frequency band division are given.

7.4.1 Stator-GSC Decoupling Model

The outer power loop and DC bus provide a coupling path for RSC-GSC, which leads to dynamic coupling between the stator-side impedance and GSC-side impedance. In this section, the stator-GSC small-signal decoupling equivalent model is established to independently analyse the stator and GSC impedance characteristics.

According to Eq. (7.96), the small-signal vectors of the stator and GSC AC side satisfy the following relationship

Table 7.2 The main circuit and controller parameters of DFIG-based wind turbines

Parameter	Definition	Value
P_N	Rated power	1.5 MW
V_N	Rated AC voltage	563 V
f_1	Rated frequency	50 Hz
R_s , R_r	Stator and rotor resistance	0.0022, 0.0027 Ω
L_{1s}, L_{1r}	Stator and rotor leakage inductance	1.4×10^{-4} H, 1.1×10^{-4} H
L_m	Stator and rotor mutual inductance	0.0041 H
L_f	GSC AC filter inductance	0.0007 H
V_{dc}	Steady-state value of the DC voltage	1200 V
K_e	Turn ratio of stator and rotor windings	3
K_{pp}, K_{pi}	Proportional and integral coefficients of PLL controller	0.0788, 4.954
K_{gip}, K_{gii}	Proportional and integral coefficients of GSC AC current controller	0.0016, 3.7600
K_{rip}, K_{rii}	Proportional and integral coefficients of RSC AC current controller	1.4000×10^{-4}, 3.6000×10^{-4}
K_{pep}, K_{pei}	Proportional and integral coefficients of active power controller	0.0006, 0.0020
K_{qep}, K_{qei}	Proportional and integral coefficients of reactive power controller	0.0006, 0.0020
K_{vdcp}, K_{vdci}	Proportional and integral coefficients of DC voltage controller	1.1000
K_{gd}	Decoupling coefficient of GSC AC current control	3.3000×10^{-5}
K_{rd}	Decoupling coefficient of RSC AC current control	3.2667×10^{-6}

$$\begin{cases} \hat{\boldsymbol{v}}_a + \boldsymbol{\Psi}_1 \hat{\boldsymbol{i}}_{ga} = \boldsymbol{Z}_1 \hat{\boldsymbol{i}}_{sa} \\ \hat{\boldsymbol{v}}_a + \boldsymbol{\Psi}_2 \hat{\boldsymbol{i}}_{sa} = -\boldsymbol{Z}_2 \hat{\boldsymbol{i}}_{ga} \end{cases} \tag{7.103}$$

where

$$\begin{cases} \boldsymbol{\Psi}_1 = \boldsymbol{G}_{rv}^{-1} \boldsymbol{G}_{rg} \\ \boldsymbol{\Psi}_2 = \boldsymbol{G}_{gv}^{-1} \boldsymbol{G}_{gs} \end{cases} \tag{7.104}$$

$$\begin{cases} \boldsymbol{Z}_1 = -\boldsymbol{G}_{rv}^{-1} \boldsymbol{G}_{rs} \\ \boldsymbol{Z}_2 = \boldsymbol{G}_{gv}^{-1} \boldsymbol{G}_{gg} \end{cases} \tag{7.105}$$

The stator-GSC coupling equivalent model can be obtained from Eq. (7.103) as shown in Fig. (7.16). It can be seen that the small-signal vector of GSC AC current $\hat{\boldsymbol{i}}_{ga}$ is coupled to the stator, equivalent to a controlled voltage source $\boldsymbol{\Psi}_1 \hat{\boldsymbol{i}}_{ga}$; the small-signal vector of the stator current $\hat{\boldsymbol{i}}_{sa}$ is coupled to the stator, equivalent to a controlled voltage source $\boldsymbol{\Psi}_2 \hat{\boldsymbol{i}}_{sa}$.

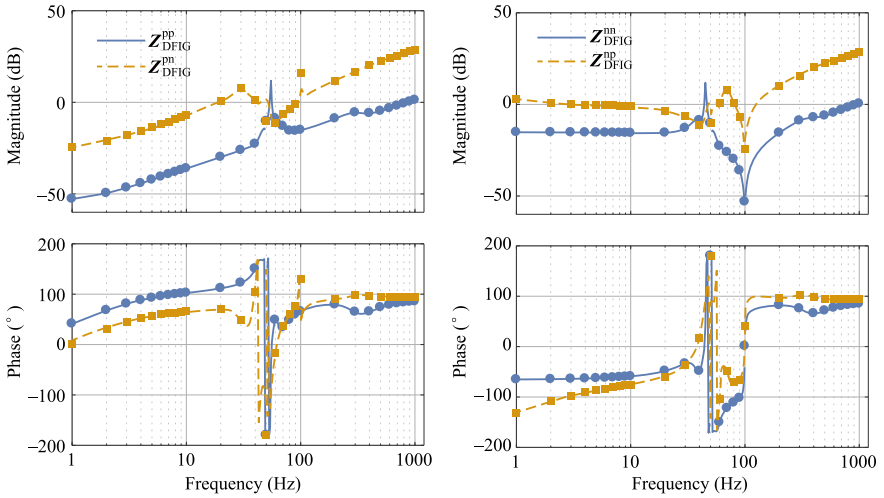

(a) Positive-sequence impedance and positive-sequence coupling impedance

(b) Negative-sequence impedance and negative-sequence coupling impedance

Fig. 7.15 Analytical and scanning results of DFIG-based wind turbines impedance

In order to reduce the complexity brought by the coupling, the impedance model of DFIG-based wind turbines can be equivalent to the stator-side impedance and GSC-side impedance connected in parallel, thus realizing the decoupling of the stator and GSC.

Define the stator-side impedance as $\boldsymbol{Z}_{\text{stator}}$ and GSC-side impedance as $\boldsymbol{Z}_{\text{GSC}}$. Equation (7.103) can be expressed as

$$\begin{cases} \hat{\boldsymbol{v}}_{\text{a}} = \boldsymbol{Z}_{\text{stator}} \hat{\boldsymbol{i}}_{\text{sa}} \\ \hat{\boldsymbol{v}}_{\text{a}} = -\boldsymbol{Z}_{\text{GSC}} \hat{\boldsymbol{i}}_{\text{ga}} \end{cases} \tag{7.106}$$

where

$$\boldsymbol{Z}_{\text{stator}} = \frac{\hat{\boldsymbol{v}}_{\text{a}}}{\hat{\boldsymbol{i}}_{\text{sa}}} = (-\boldsymbol{G}_{\text{rg}}\boldsymbol{G}_{\text{gg}}^{-1}\boldsymbol{G}_{\text{gv}} + \boldsymbol{G}_{\text{rv}})^{-1}(\boldsymbol{G}_{\text{rg}}\boldsymbol{G}_{\text{gg}}^{-1}\boldsymbol{G}_{\text{gs}} - \boldsymbol{G}_{\text{rs}}) \tag{7.107}$$

$$\boldsymbol{Z}_{\text{GSC}} = -\frac{\hat{\boldsymbol{v}}_{\text{a}}}{\hat{\boldsymbol{i}}_{\text{ga}}} = (\boldsymbol{G}_{\text{gs}}\boldsymbol{G}_{\text{rs}}^{-1}\boldsymbol{G}_{\text{rv}} - \boldsymbol{G}_{\text{gv}})^{-1}(\boldsymbol{G}_{\text{gs}}\boldsymbol{G}_{\text{rs}}^{-1}\boldsymbol{G}_{\text{rg}} - \boldsymbol{G}_{\text{gg}}) \tag{7.108}$$

According to Eqs. (7.107) and (7.108), the model in Fig. 7.16 can be decoupled into the stator-GSC decoupling equivalent model shown in Fig. 7.17.

Based on the above decoupling equivalent model, the stator-side equivalent positive-sequence impedance $\boldsymbol{Z}^{\text{pp}}_{\text{stator}}$ and the GSC-side equivalent positive- sequence impedance $\boldsymbol{Z}^{\text{pp}}_{\text{GSC}}$ can be obtained. $\boldsymbol{Z}^{\text{pp}}_{\text{stator}}$ and $\boldsymbol{Z}^{\text{pp}}_{\text{GSC}}$ connected in parallel can obtain the impedance of DFIG-based wind turbines $\boldsymbol{Z}^{\text{pp}}_{\text{stator}} || \boldsymbol{Z}^{\text{pp}}_{\text{GSC}}$. Figure 7.18 shows the

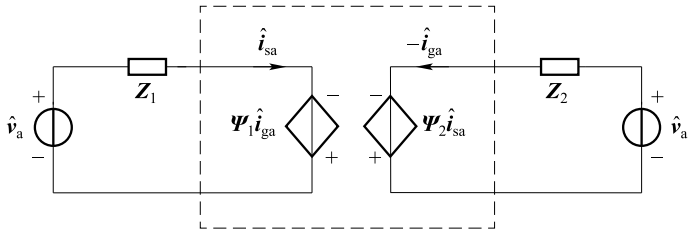

Fig. 7.16 The stator-GSC coupling equivalent model

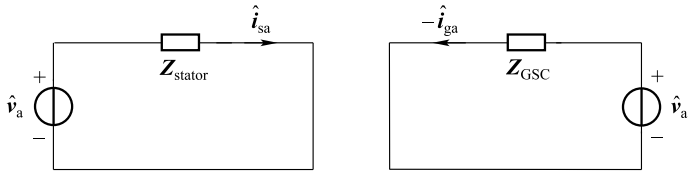

Fig. 7.17 The stator-GSC decoupling equivalent model

comparison between the actual impedance model $\boldsymbol{Z}_{\mathrm{DFIG}}^{\mathrm{pp}}$(in solid line) and the decoupling equivalent model $\boldsymbol{Z}_{\mathrm{stator}}^{\mathrm{pp}}||\boldsymbol{Z}_{\mathrm{GSC}}^{\mathrm{pp}}$(in discrete line) of DFIG-based wind turbines. As seen from the figure, all the discrete points fall on the solid lines, which verifies the accuracy of the decoupled equivalent model of DFIG-based wind turbines.

Figure 7.19 shows the comparison between $\boldsymbol{Z}_{\mathrm{DFIG}}^{\mathrm{pp}}$, $\boldsymbol{Z}_{\mathrm{stator}}^{\mathrm{pp}}$ and $\boldsymbol{Z}_{\mathrm{GSC}}^{\mathrm{pp}}$, and the following characteristics can be summarized.

1. Subsynchronous frequency band: the magnitude of $\boldsymbol{Z}_{\mathrm{stator}}^{\mathrm{pp}}$ is smaller than the magnitude of $\boldsymbol{Z}_{\mathrm{GSC}}^{\mathrm{pp}}$, and the impedance characteristics of $\boldsymbol{Z}_{\mathrm{DFIG}}^{\mathrm{pp}}$ is dominated by $\boldsymbol{Z}_{\mathrm{stator}}^{\mathrm{pp}}$.
2. Super-synchronous frequency band: the impedance characteristics of $\boldsymbol{Z}_{\mathrm{DFIG}}^{\mathrm{pp}}$ is dominated by $\boldsymbol{Z}_{\mathrm{stator}}^{\mathrm{pp}}$. However, at the cut-off frequency of GSC AC current loop, the magnitude of $\boldsymbol{Z}_{\mathrm{stator}}^{\mathrm{pp}}$ is close to the magnitude of $\boldsymbol{Z}_{\mathrm{GSC}}^{\mathrm{pp}}$, and the magnitude of $\boldsymbol{Z}_{\mathrm{DFIG}}^{\mathrm{pp}}$ has a resonant peak. At this time, $\boldsymbol{Z}_{\mathrm{DFIG}}^{\mathrm{pp}}$ is simultaneously affected by $\boldsymbol{Z}_{\mathrm{stator}}^{\mathrm{pp}}$ and $\boldsymbol{Z}_{\mathrm{GSC}}^{\mathrm{pp}}$.
3. High-frequency band: the impedance characteristics of $\boldsymbol{Z}_{\mathrm{DFIG}}^{\mathrm{pp}}$ is dominated by the LC filter.

7.4.2 Frequency-Band Division of Broadband Impedance

In this section, the dominant factors of DFIG-based wind turbines impedance characteristics in each frequency band are analyzed based on the decoupling equivalent model, and the frequency-band division method is proposed.

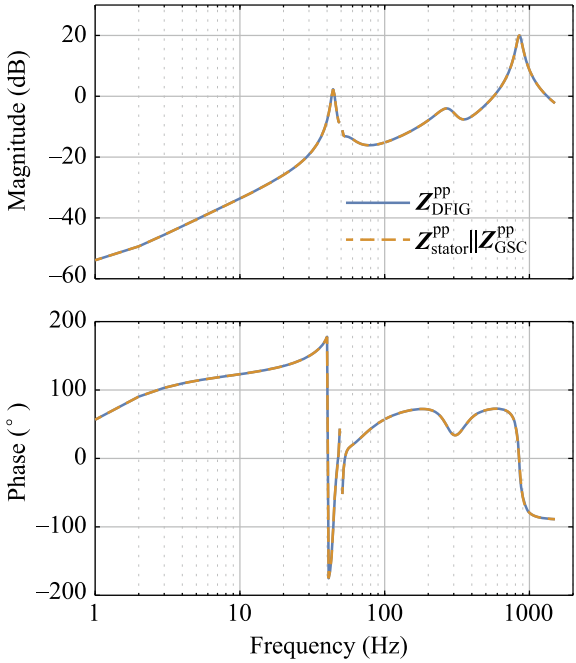

Fig. 7.18 Comparison between Z^{pp}_{DFIG} and $Z^{pp}_{stator}||Z^{pp}_{GSC}$

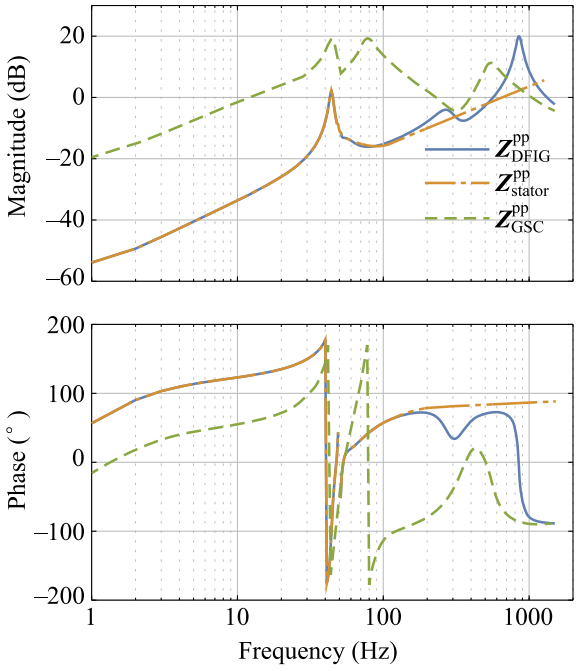

Fig. 7.19 Comparison between Z^{pp}_{DFIG}, Z^{pp}_{stator} and Z^{pp}_{GSC}

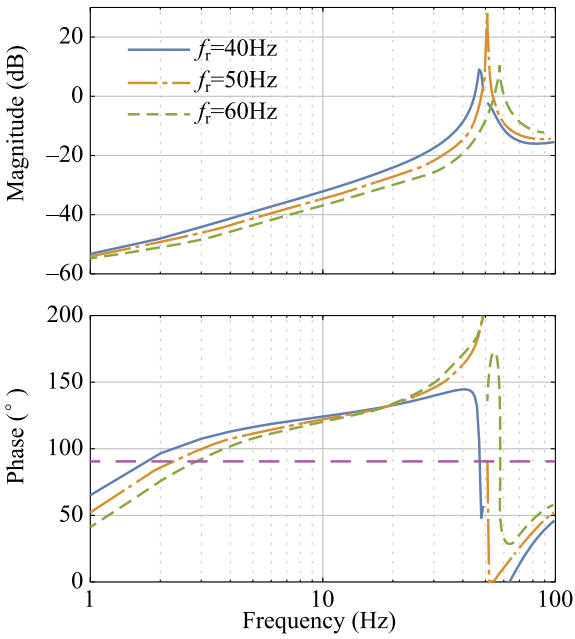

Fig. 7.20 Influence of rotor electrical frequency on impedance characteristics

7.4.2.1 Influence of Rotor Electrical Frequency on Impedance Characteristics

The impedance of DFIG-based wind turbines in the subsynchronous frequency band ($f < f_r$) are dominated by $\boldsymbol{Z}_{\text{stator}}^{\text{pp}}$. According to Eq. (7.107), $\boldsymbol{Z}_{\text{stator}}^{\text{pp}}$ is closely related to the rotor electrical frequency f_r. Figure 7.20 shows the impedance curves of DFIG-based wind turbines when f_r is taken as 40, 50 and 60 Hz respectively. It can be seen from the figure that in the frequency band $f < f_r$, the impedance presents inductive negative damping characteristics (the phase of the impedance more than 90°), and with the increase of f_r, the level of negative damping characteristics increases.

7.4.2.2 Influence of GSC AC Current Loop on Impedance Characteristics

The impedance of DFIG-based wind turbines in the super-synchronous frequency band is dominated by $\boldsymbol{Z}_{\text{stator}}^{\text{pp}}$ while being affected by $\boldsymbol{Z}_{\text{GSC}}^{\text{pp}}$. The influence of GSC AC current loop on impedance characteristics is shown in Fig. 7.21. The block diagram and parameter calculation method of GSC AC current loop can be found in Sect. 6.4.1.2. On the one hand, the influence of GSC AC current loop bandwidth can be obtained by setting f_{gic} to 100, 200 and 300 Hz respectively with a constant PM of 10°. On the other hand, the influence of GSC AC current loop PM can be obtained by setting θ_{gic} to 10°, 45°and 80° respectively with a constant bandwidth of 300 Hz.

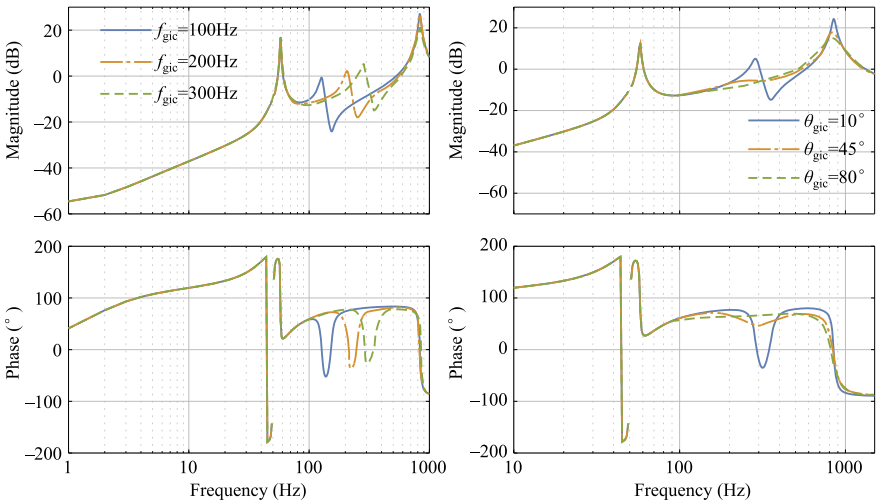

(a) Different GSC AC current loop bandwidths (b) Different GSC AC current loop PMs

Fig. 7.21 Influence of GSC AC current loop on impedance characteristics

As shown in Fig. 7.21, near the bandwidth of GSC current loop $f_1 + f_{gic}$ (in SCF), the magnitudes of $\boldsymbol{Z}_{GSC}^{pp}$ and $\boldsymbol{Z}_{stator}^{pp}$ are close, which leads to a resonance peak in the magnitude of $\boldsymbol{Z}_{DFIG}^{pp}$. Meanwhile, the phase of $\boldsymbol{Z}_{DFIG}^{pp}$ decreases within the frequency range of the resonant peak.

7.4.2.3 Influence of LC Filter on Impedance Characteristics

The impedance of DFIG-based wind turbines in the high frequency band ($f > f_1 + f_{gic}$) is dominated by the LC filter. Since the damping effect of the stator and rotor windings is weak, the stator and rotor resistances can be ignored, and the resonant frequency of DFIG-based wind turbines in the high frequency band can be approximated as

$$f_h = \frac{1}{2\pi\sqrt{((L_{1s} + L_{1r})||L_f)C_f}} \tag{7.109}$$

The influence of LC filter on impedance characteristics is shown in Fig. 7.22. The influence of the filter capacitor C_f is obtained by setting C_f to 0.1, 0.2 and 0.3 mF respectively with a constant filter inductance of 0.7 mF. It can be seen from the figure that the filter capacitor mainly affects the impedance characteristics in the high-frequency band of DFIG-based wind turbines. The magnitude of $\boldsymbol{Z}_{DFIG}^{pp}$ exhibits resonance peak at f_h, and the phase of $\boldsymbol{Z}_{DFIG}^{pp}$ changes from inductive to capacitive characteristics at f_h.

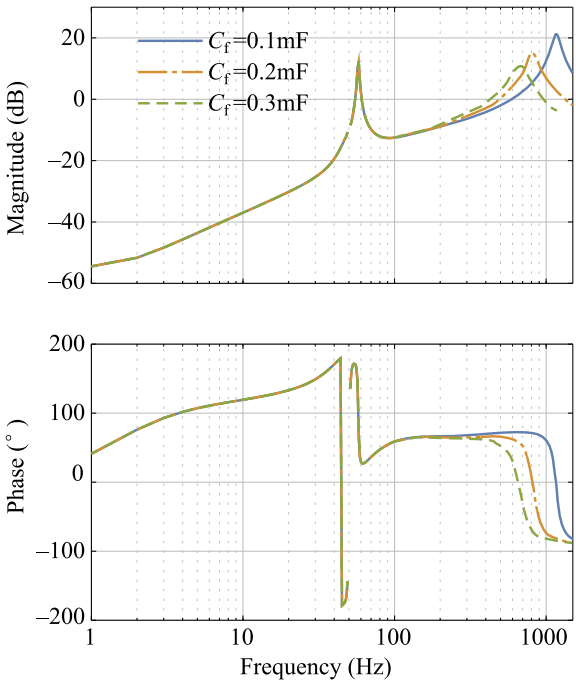

Fig. 7.22 Influence of LC filter on impedance characteristics

7.4.2.4 Influence of the Steady-State Operating Point on Impedance Characteristics

The impedance model of DFIG-based wind turbines is obtained by small-signal linearization based on the steady-state operating point. During the operation of DFIG-based wind turbines, the change of wind speed will lead to the variation of rotor frequency and active power, and the impedance characteristics will change accordingly. Figure 7.23 shows the three-dimensional bode diagram of the influence of the steady-state operating point (active power) on impedance characteristics. It can be seen from the figure that the change of the steady-state operating point mainly affects the impedance characteristics near f_r.

7.4.2.5 Frequency-Band Division Principle of Broadband Impedance

According to the analysis of dominant factors of DFIG-based wind turbines impedance characteristics in each frequency band, the following frequency bands can be divided:

1. Band I_{DFIG} ($f < f_r$): The impedance is dominated by $\boldsymbol{Z}_{stator}^{pp}$. It exhibits inductive negative damping characteristics, and is affected by the steady-state operating point.

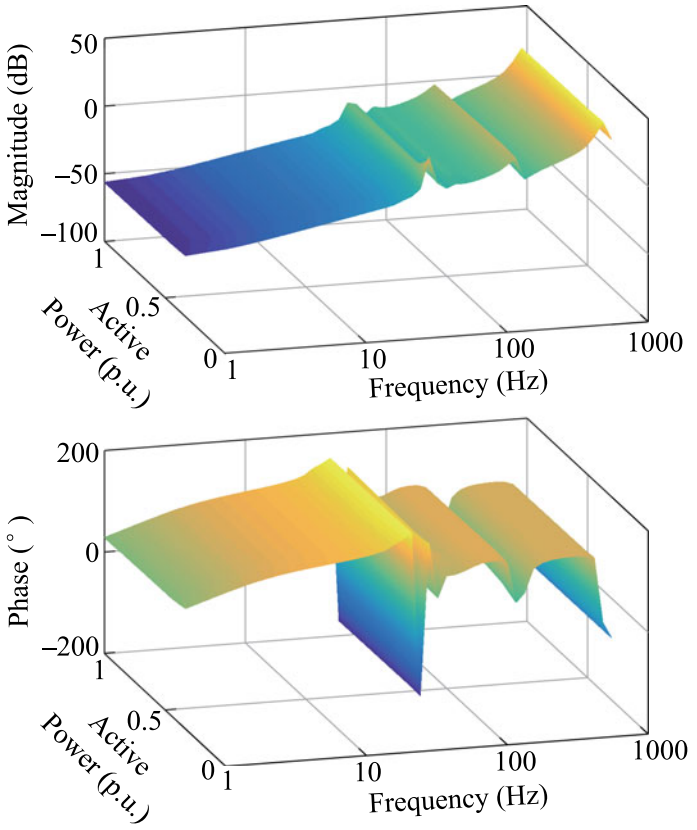

Fig. 7.23 Influence of the steady-state operating point on impedance characteristics

2. Band II_{DFIG} ($f_{\text{r}} < f < f_1 + f_{\text{gic}}$): The impedance is dominated by $\boldsymbol{Z}^{\text{pp}}_{\text{stator}}$ and affected by $\boldsymbol{Z}^{\text{pp}}_{\text{GSC}}$. The magnitude of $\boldsymbol{Z}^{\text{pp}}_{\text{DFIG}}$ exhibits a resonance peak at about $f_1 + f_{\text{gic}}$ and the phase of $\boldsymbol{Z}^{\text{pp}}_{\text{DFIG}}$ represents capacitance characteristics.
3. Band III_{DFIG} ($f > f_1 + f_{\text{gic}}$): The impedance is dominated by the LC filter. The phase of $\boldsymbol{Z}^{\text{pp}}_{\text{DFIG}}$ changes from inductive to capacitive characteristics at LC resonant frequency.

Impedance scanning is carried out based on CHIL platform of different types of DFIG-based wind turbines, and the scanning results are shown in Figs. 7.24, 7.25 and 7.26. It can be seen from the figure that the frequency range of band I_{DFIG} is around $f < 60$ Hz, the frequency range of band II_{DFIG} is around 60 Hz $< f <$ 250 Hz, and the frequency range of band III_{DFIG} is around $f > 250$ Hz.

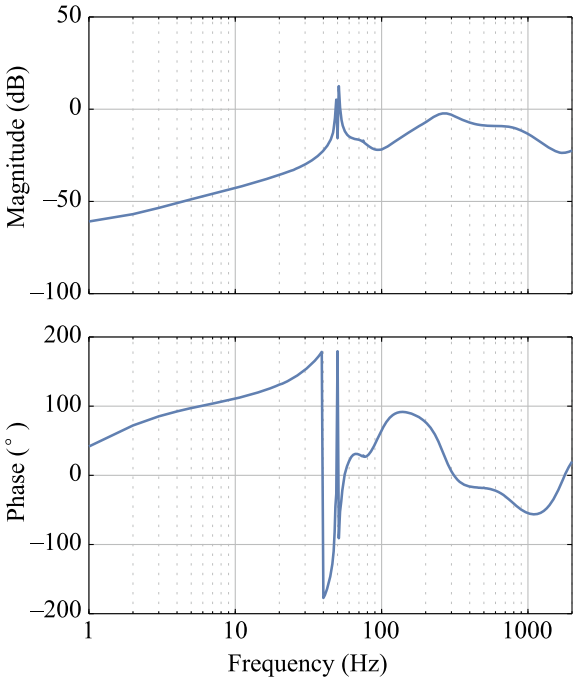

Fig. 7.24 Impedance of a 3.0 MW DFIG-based wind turbine (Type A)

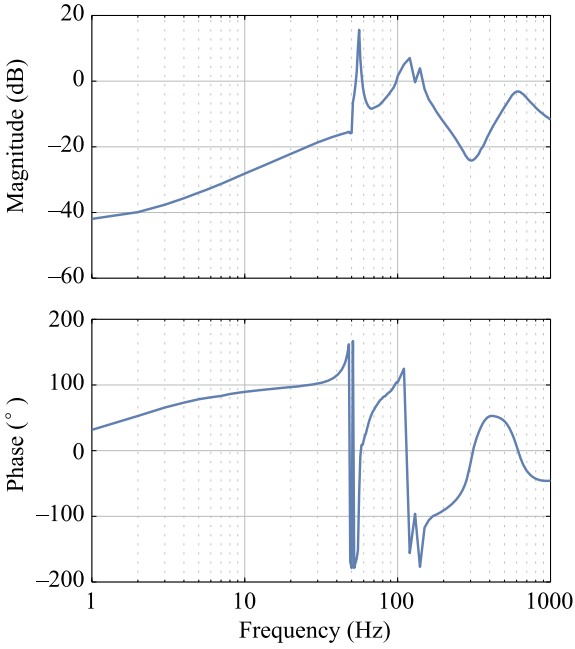

Fig. 7.25 Impedance of a 3.0 MW DFIG-based wind turbine (Type B)

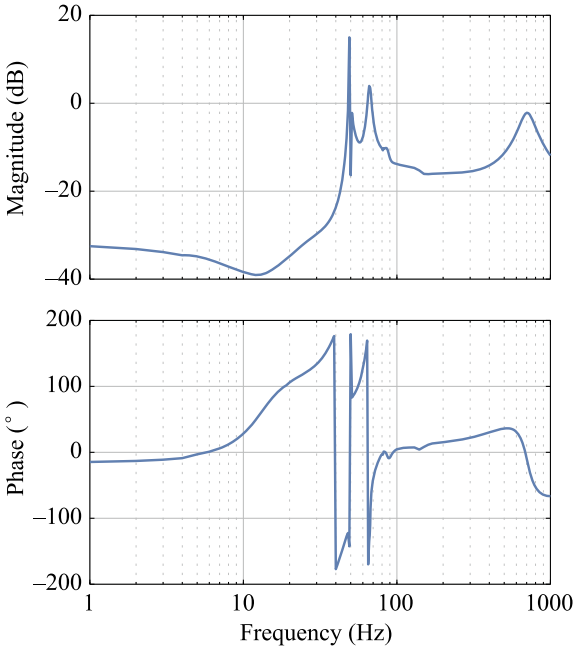

Fig. 7.26 Impedance of a 3.3 MW DFIG-based wind turbine (Type C)

7.4.3 Analysis of Negative Damping Characteristics

The frequency-band division principle of broadband impedance of DFIG-based wind turbines is proposed through the analysis in Sect. 7.4.2. Considering the control system of DFIG-based wind turbines involves the coordination of multiple controllers, the impedance characteristics in each frequency band are affected not only by the dominant factors, but also by the frequency-band overlapping effects of other controllers. In this section, the frequency-band overlapping effects of RSC AC current loop, power loop, rotor electrical frequency, DC voltage loop and time delay will be analyzed to reveal the mechanism of the negative damping characteristics in each frequency band.

7.4.3.1 Analysis of Negative Damping Characteristics in Band $\mathbf{I_{DFIG}}$

In Band I_{DFIG}, the impedance of DFIG-based wind turbines is dominated by $\boldsymbol{Z}_{\text{stator}}^{\text{pp}}$ and affected by the rotor electrical frequency, outer power loop and AC current loop of RSC.

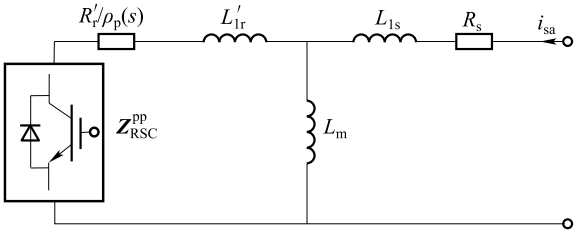

Fig. 7.27 The equivalent circuit of the stator port

Considering the above factors, their influence on the negative damping characteristics in Band I_{DFIG} will be analyzed next.

1. Influence of Rotor Electrical Frequency on Negative Damping Characteristics

The equivalent circuit of DFIG-based wind turbines stator port is shown in Fig. 7.27. First, analyze the influence of the rotor electrical frequency f_r on the damping characteristics of ideal stator-side impedance. Here, assume that the ideal excitation current is applied directly to the DFIG rotor winding, i.e., the external impedance of the rotor winding brought by RSC is neglected. According to DFIG small-signal frequency-domain model shown in Eq. (7.59), the ideal stator-side impedance can be obtained as

$$\boldsymbol{Z}_{\text{stator}}^{\text{pp}*} = R_s + sL_s - \frac{s^2 L_m^2 \rho_p(s)}{R_r' + s\rho_p(s)L_r} \tag{7.110}$$

where $\rho_p(s)$ is the slip conversion factor, and its expression is

$$\rho_p(s) = \frac{s - j\omega_r}{s} \tag{7.111}$$

The ideal stator-side impedance $\boldsymbol{Z}_{\text{stator}}^{\text{pp}*}$ is not only related to the parameters of the stator and rotor windings, but also related to $\rho_p(s)$, that is, related to the rotor electrical frequency f_r.

By setting f_r to 40, 50, and 60 Hz respectively, the influence of f_r on the damping characteristics of the ideal stator-side impedance $\boldsymbol{Z}_{\text{stator}}^{\text{pp}*}$ is shown in Fig. 7.28. It can be seen that $\boldsymbol{Z}_{\text{stator}}^{\text{pp}*}$ exhibits inductive characteristics in general, and the resonance peak appears at f_r. Especially near f_r, $\boldsymbol{Z}_{\text{stator}}^{\text{pp}*}$ presents negative damping characteristics. Define f^* as the frequency at which the impedance phase curve crosses 90°, when f_r increases, f^* will also increase.

According to the above analysis, the influence of f_r on Band I_{DFIG} impedance damping characteristics is mainly reflected in three aspects:

1. Upper limit of the negative damping frequency range. The negative damping mainly occurs near f_r, and f_r will affect the upper limit of the negative damping frequency.

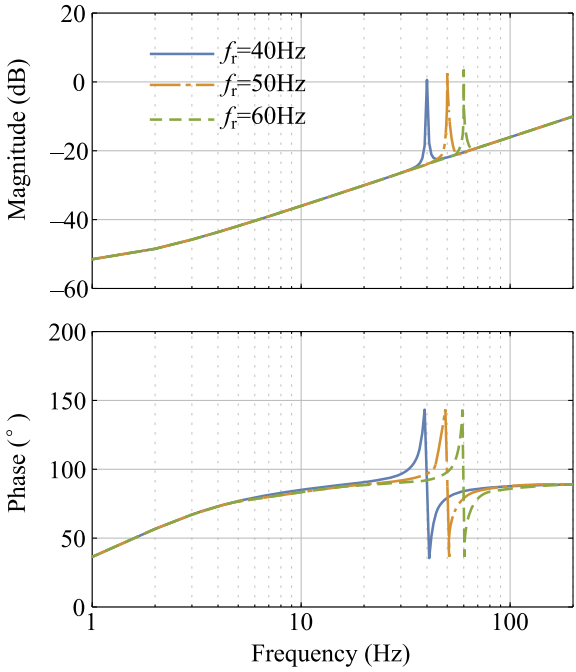

Fig. 7.28 Influence of f_r on the damping characteristics of ideal stator-side impedance

2. Lower limit of the negative damping frequency range. The phase of $\boldsymbol{Z}_{\text{stator}}^{\text{pp}*}$ changes from positive damping to negative damping at f^*. f^* reflects the lower limit of the negative damping range and varies with f_r.
3. The negative damping level. f_r affects the real part and imaginary part of $\boldsymbol{Z}_{\text{stator}}^{\text{pp}*}$, thus affecting the negative damping level.

Since the excitation current of DFIG-based wind turbines is provided by RSC, RSC also has an effect on $\boldsymbol{Z}_{\text{stator}}^{\text{pp}}$, thus affects the damping characteristics of $\boldsymbol{Z}_{\text{DFIG}}^{\text{pp}}$. By setting f_r to 40, 50, and 60 Hz, respectively, the influence of f_r on the damping characteristics of $\boldsymbol{Z}_{\text{DFIG}}^{\text{pp}}$ is shown in Fig. 7.29. As shown in the figure, when f_r changes, both the lower and the upper limit of the negative damping frequency range change, resulting in a change of the range (f^*, f_r). In addition, the level of inductive negative damping characteristics of $\boldsymbol{Z}_{\text{DFIG}}^{\text{pp}}$ varies with the change of f_r.

2. Influence of RSC AC Current Loop on Negative Damping Characteristics

The block diagam of RSC AC current loop is shown in Fig. 7.30, and the open-loop transfer function is shown in Eq. (7.112).

$$G_{\text{ri}}(s) = H_{\text{ri}}(s)\frac{K_{\text{m}}V_{\text{dc}}}{R_{\text{r}} + s\sigma L_{\text{r}}} \tag{7.112}$$

where $H_{\text{ri}}(s)$ is the transfer function of RSC current controller; σ is the leakage coefficient, $\sigma = 1 - L_{\text{m}}^2/L_{\text{r}}L_{\text{s}}$.

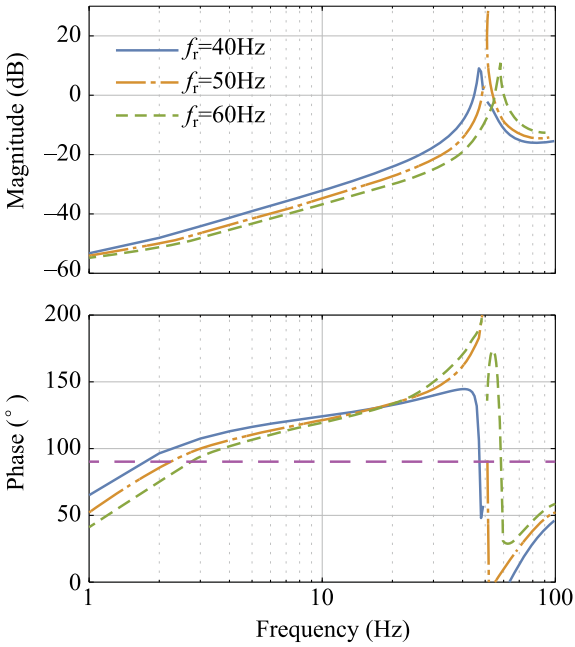

Fig. 7.29 Influence of f_r on the damping characteristics in Band I_{DFIG}

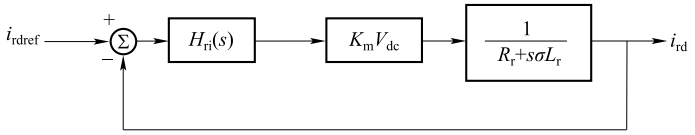

Fig. 7.30 Block diagram of RSC AC current loop

Given RSC AC current loop bandwidth f_{ric} and PM θ_{ric}, the PI coefficients can be solved from Eq. (7.113).

$$\begin{cases} \left| H_{ri}(s) \dfrac{K_m V_{dc}}{R_r + s\sigma L_r} \right|_{s=j2\pi f_{ric}} = 1 \\ \angle\left(H_{ri}(s) \dfrac{K_m V_{dc}}{R_r + s\sigma L_r} \right)_{s=j2\pi f_{ric}} = \theta_{ric} - 180^\circ \end{cases} \tag{7.113}$$

where the open-loop gain is 1 at f_{ric}, the corresponding PM is θ_{ric}.

The influence of RSC AC current loop on the damping characteristics in Band I_{DFIG} is shown in Fig. 7.31. On the one hand, the influence of RSC AC current loop bandwidth can be obtained by setting f_{ric} to 5, 15 and 30 Hz respectively with a constant PM of 45°. On the other hand, the influence of RSC AC current loop PM can be obtained by setting θ_{ric} to 10°, 45°and 80°respectively with a constant bandwidth of 15 Hz.

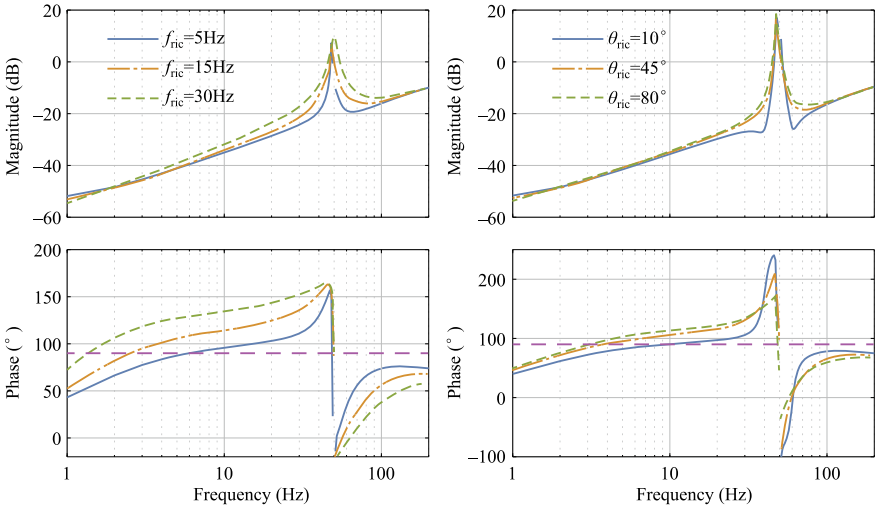

(a) Different RSC AC current loop bandwidth (b) Different RSC AC current loop PM

Fig. 7.31 Influence of RSC current loop on the damping characteristics in Band I_{DFIG}

As shown in Fig. 7.31, the lower limit f^* of negative damping frequency range varies with the change of RSC AC current loop bandwidth f_{ric} and PM θ_{ric}. And the level of inductive negative damping characteristics deepens with the increase of f_{ric} and θ_{ric}.

3. Influence of Power Loop on Negative Damping Characteristics

The block diagram of power loop is shown in Fig. 7.32, and the open-loop transfer function is shown in Eq. (7.114).

$$G_p(s) = \frac{3L_m V_1}{2L_s} H_p(s) \tag{7.114}$$

Given the power loop bandwidth f_{pc} and PM θ_{pc}, the PI coefficients can be solved from Eq. (7.115).

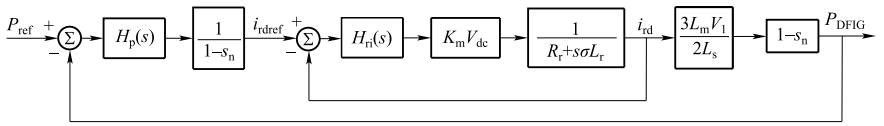

Fig. 7.32 Block diagram of power loop

$$\begin{cases} \left| \dfrac{3L_m V_1}{2L_s} H_p(s) \right|_{s=j2\pi f_{pc}} = 1 \\ \angle\left(\dfrac{3L_m V_1}{2L_s} H_p(s) \right)_{s=j2\pi f_{pc}} = \theta_{pc} - 180^\circ \end{cases} \tag{7.115}$$

where the open-loop gain is 1 at f_{pc}, the corresponding PM is θ_{pc}. In the same way, the PI coefficients of reactive power controller can be obtained.

The influence of power loop on the damping characteristics in Band I_{DFIG} is shown in Fig. 7.33. On the one hand, the influence of power loop bandwidth can be obtained by setting f_{pc} to 0.1, 1 and 10 Hz respectively with a constant PM of 135°. On the other hand, the influence of power loop PM can be obtained by setting θ_{pc} to 100°, 135° and 170° respectively with a constant bandwidth of 1 Hz.

As shown in Fig. 7.33, the level of negative damping characteristics deepens slightly with the increase of the power loop bandwidth f_{pc}. The lower limit f^* of negative damping frequency range decreases with the increase of the power loop PM θ_{pc}.

4. Influence of PLL on Negative Damping Characteristics

The block diagram and parameter calculation method of PLL can be found in Sect. 5.4.1.1. The influence of PLL on the damping characteristics in Band I_{DFIG} is shown in Fig. 7.34. On the one hand, the influence of PLL bandwidth can be obtained by setting f_{tc} to 5, 10 and 30 Hz respectively with a constant PM of 45°. On the other hand, the influence of PLL PM can be obtained by setting θ_{tc} to 10°, 45° and 80° respectively with a constant bandwidth of 10 Hz.

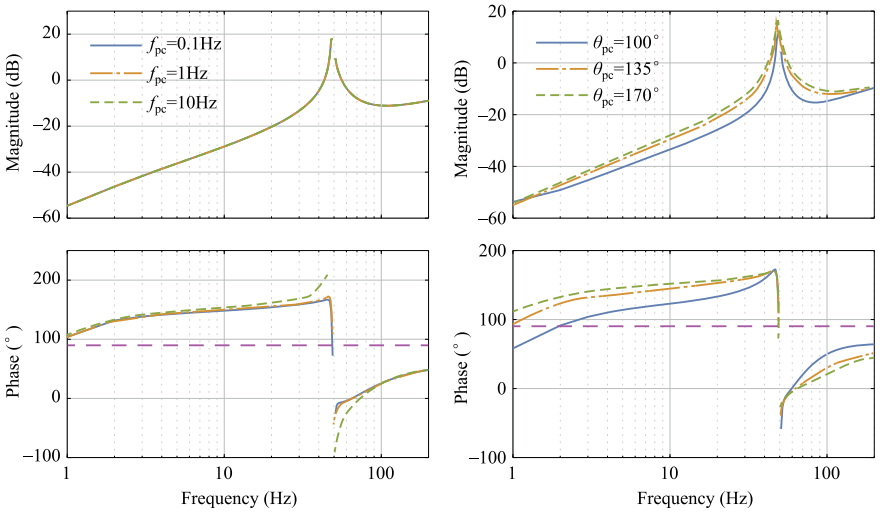

(a) Different power loop bandwidths (b) Different power loop PMs

Fig. 7.33 Influence of power loop on the damping characteristics in Band I_{DFIG}

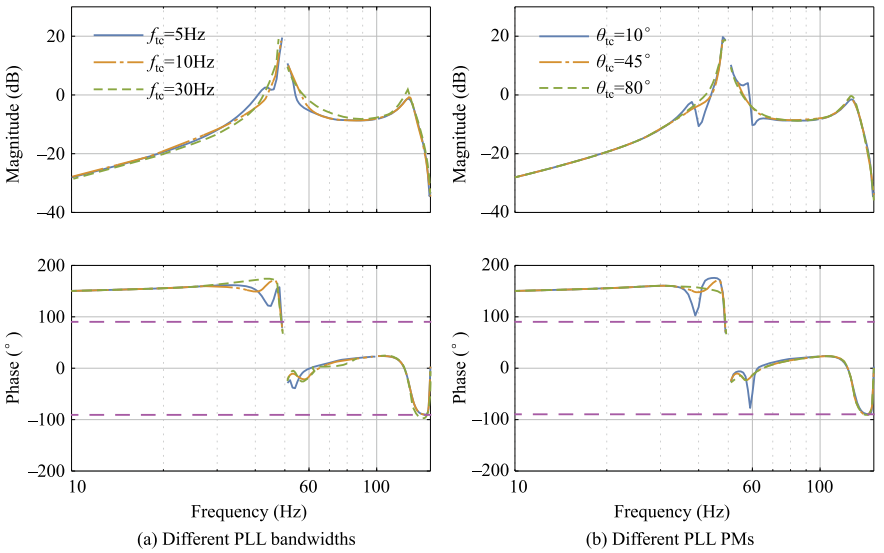

Fig. 7.34 Influence of PLL on the damping characteristics in Band I_{DFIG}

As shown in Fig. 7.34, the resonance peak appears at f_{tc}. As f_{tc} and θ_{tc} increases, the resonance peak becomes less pronounced and the level of inductive negative damping characteristics deepens.

5. Influence of the Steady-State Operating Point on Negative Damping Characteristics

As the wind speed increases, firstly, DFIG-based wind turbines operate in the MPPT zone, the rotor electrical frequency f_r and active power both increase. At this time, the impedance characteristics are mainly affected by f_r. Then, DFIG-based wind turbines enter the constant speed zone, the rotor electrical frequency remains unchanged and the active power continues to increase. The impedance characteristics are mainly affected by the active power. Finally, DFIG-based wind turbines enter the constant power zone, the rotor electrical frequency and active power both remain unchanged, and the steady-state operating point remains unchanged, which has no effect on the impedance characteristics.

According to the above analysis, as the steady-state active power increases, the influence of the steady-state operating point on the damping characteristics will gradually decrease. Figure 7.35 shows the influence of the steady-state operating point on the damping characteristics in Band I_{DFIG} when the active power changes from 0.3, 0.7 to 1.0 p.u.

As shown in the figure, when the active power increases from 0.3 to 0.7 p.u. (from MPPT zone to constant speed zone), f_r increases, the location of the resonant peak and the negative damping frequency range change accordingly. When the active power changes from 0.7 to 1 p.u. (from the constant speed zone to the constant power

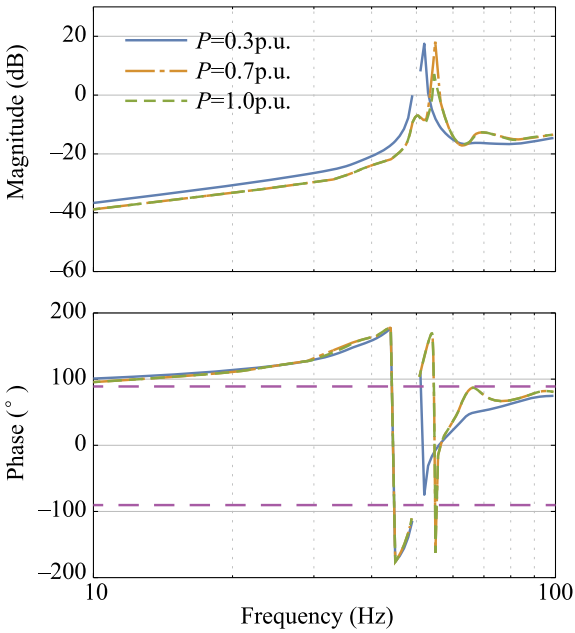

Fig. 7.35 Influence of the steady-state operating point on the damping characteristics in Band $\mathrm{I_{DFIG}}$

zone), f_r and the location of the resonant peak remains unchanged, and the degree of negative damping changes slightly.

7.4.3.2 Analysis of Negative Damping Characteristics in Band $\mathrm{II_{DFIG}}$

The impedance of DFIG-based wind turbines in Band $\mathrm{II_{DFIG}}$ is dominated by $\boldsymbol{Z}_{\mathrm{stator}}^{\mathrm{pp}}$ while being affected by GSC AC current loop and DC voltage loop. At GSC AC current loop bandwidth $f_1 + f_{\mathrm{gic}}$ (in SCF), the magnitude of $\boldsymbol{Z}_{\mathrm{GSC}}^{\mathrm{pp}}$ and $\boldsymbol{Z}_{\mathrm{stator}}^{\mathrm{pp}}$is close to each other, resulting in a resonant peak in the magnitude of the impedance and a capacitive decrease in the phase of the impedance. The RSC outer power loop as a coupling path introduces the GSC AC current into the RSC modulating voltage, resulting in the interaction of the power loop, RSC AC current loop, GSC AC current loop and DC voltage loop. Therefore, the impedance characteristics in Band $\mathrm{II_{DFIG}}$ are jointly affected by the power loop, RSC AC current loop, GSC AC current loop and DC voltage loop.

1. Influence of RSC AC Current Loop on Negative Damping Characteristics

The influence of RSC current loop on the damping characteristics in Band $\mathrm{II_{DFIG}}$ is shown in Fig. 7.36. On the one hand, the influence of RSC AC current loop bandwidth can be obtained by setting f_{ric} to 30, 60 and 90 Hz respectively with a constant PM of 45°. On the other hand, the influence of RSC AC current loop PM can be obtained by setting θ_{ric} to 10°, 45°and 80°respectively with a constant bandwidth of 15 Hz.

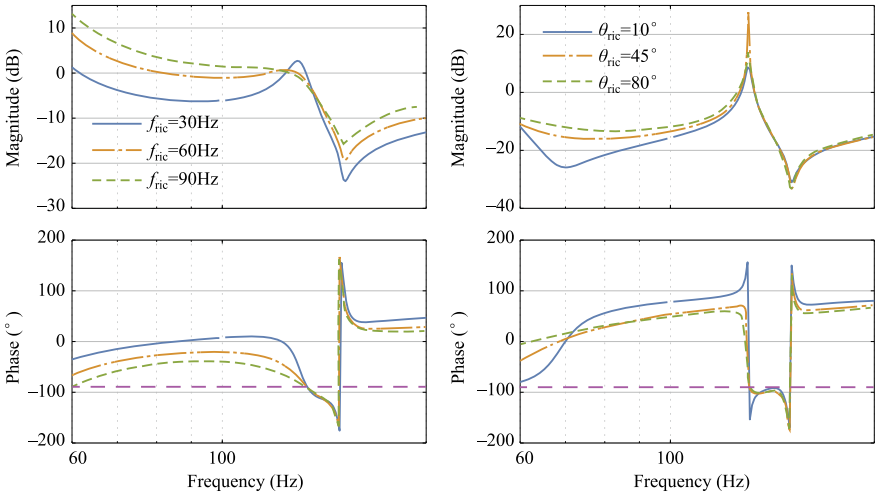

(a) Different RSC AC current loop bandwidths (b) Different RSC AC current loop PMs

Fig. 7.36 Influence of RSC AC current loop on the damping characteristics in Band $\mathrm{II}_{\mathrm{DFIG}}$

As shown in Fig. 7.36, the level of negative capacitive damping (the phase of the impedance less than −90°) deepens as RSC current bandwidth increases and PM decreases.

2. Influence of Power Loop on Negative Damping Characteristics

The influence of power loop on the damping characteristics in Band $\mathrm{II}_{\mathrm{DFIG}}$ is shown in Fig. 7.37. On the one hand, the influence of power loop bandwidth can be obtained by setting f_{pc} to 0.1, 1 and 10 Hz respectively with a constant PM of 135°. On the other hand, the influence of power loop PM can be obtained by setting θ_{pc} to 100°, 135° and 170° respectively with a constant bandwidth of 1 Hz.

As shown in Fig. 7.37, there is a frequency-band overlapping effect between the outer power loop and GSC AC current loop, resulting in capacitive negative damping characteristics in Band $\mathrm{II}_{\mathrm{DFIG}}$. The increase of the outer power loop PM will aggravate the negative damping in Band $\mathrm{II}_{\mathrm{DFIG}}$.

3. Influence of DC Voltage Loop on Negative Damping Characteristics

The influence of DC voltage loop on the damping characteristics in Band $\mathrm{II}_{\mathrm{DFIG}}$ is shown in Fig. 7.38. On the one hand, the influence of DC voltage loop bandwidth can be obtained by setting f_{vdc} to 10, 20 and 30 Hz respectively with a constant PM of 45°. On the other hand, the influence of DC voltage loop PM can be obtained by setting θ_{vdc} to 10°, 45° and 80° respectively with a constant bandwidth of 10 Hz.

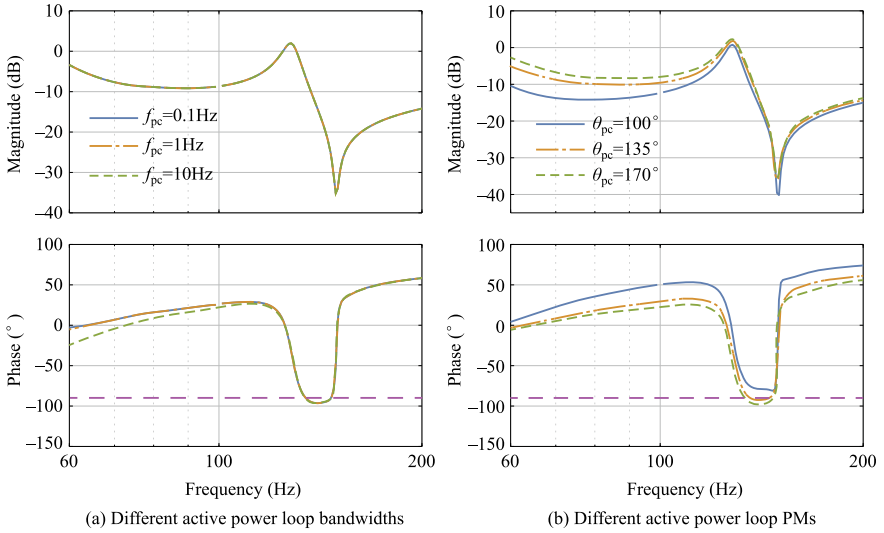

(a) Different active power loop bandwidths (b) Different active power loop PMs

Fig. 7.37 Influence of power loop on the damping characteristics in Band $\mathrm{II}_{\mathrm{DFIG}}$

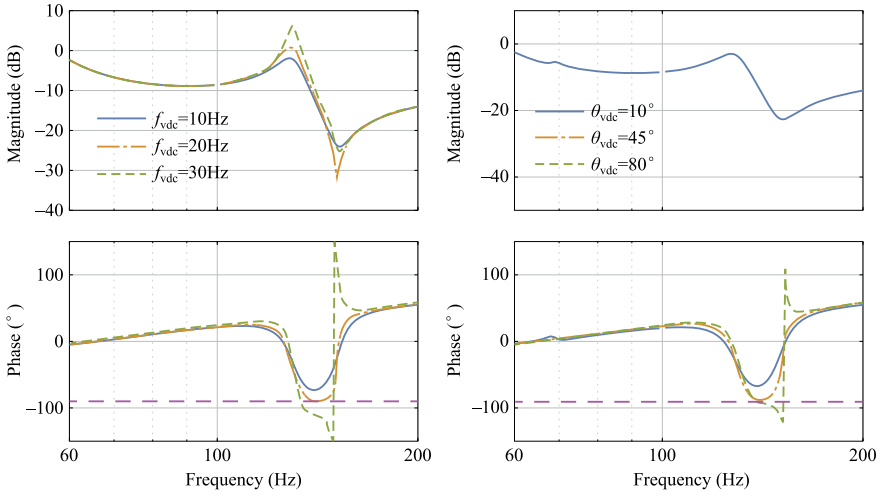

(a) Different GSC DC voltage loop bandwidths (b) Different GSC DC voltage loop PMs

Fig. 7.38 Influence of power loop on the damping characteristics in Band $\mathrm{II}_{\mathrm{DFIG}}$

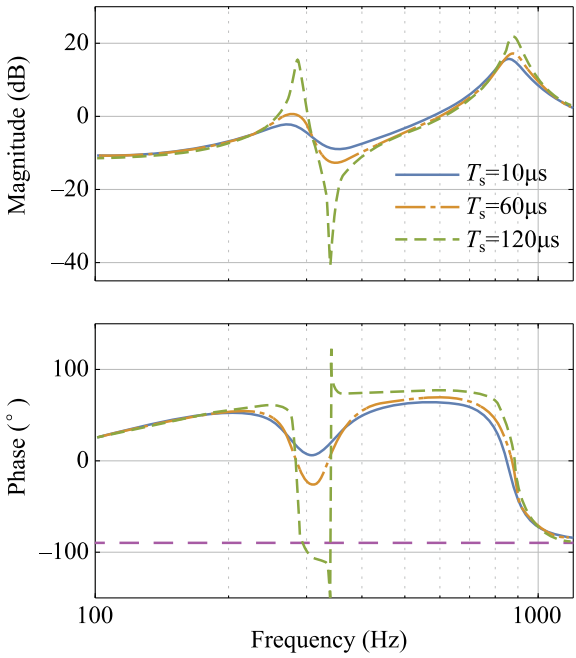

Fig. 7.39 Influence of time delay on the damping characteristics in Band $\mathrm{II}_{\mathrm{DFIG}}$

As shown in Fig. 7.38, the level of the capacitive negative damping characteristics at the resonant frequency in Band $\mathrm{II}_{\mathrm{DFIG}}$ deepens with the increase of the DC voltage loop bandwidth and PM.

4. Influence of Time Delay on Negative Damping Characteristics

The influence of time delay on the damping characteristics in Band $\mathrm{II}_{\mathrm{DFIG}}$ is shown in Fig. 7.39. The influence of time delay can be obtained by changing it to 10, 60 and 120 μs respectively with constant control parameters of the GSC AC current loop. As shown in Fig. 7.39, the frequency-band overlapping effect of time delay and GSC AC current loop leads to negative damping characteristics in Band $\mathrm{II}_{\mathrm{DFIG}}$. In addition, with the increase of time delay, the degree of negative damping becomes more severe.

7.4.3.3 Analysis of Negative Damping Characteristics in Band $\mathrm{III}_{\mathrm{DFIG}}$

The negative damping characteristics of DFIG-based wind turbines in Band $\mathrm{III}_{\mathrm{DFIG}}$ are mainly affected by time delay. The influence of time delay on the damping characteristics in Band $\mathrm{III}_{\mathrm{DFIG}}$ is shown in Fig. 7.40. The influence of time delay can be obtained by changing it to 10, 100 and 200 μs respectively with constant LC filter parameters. As shown in Fig. 7.40, the frequency-band overlapping effect of

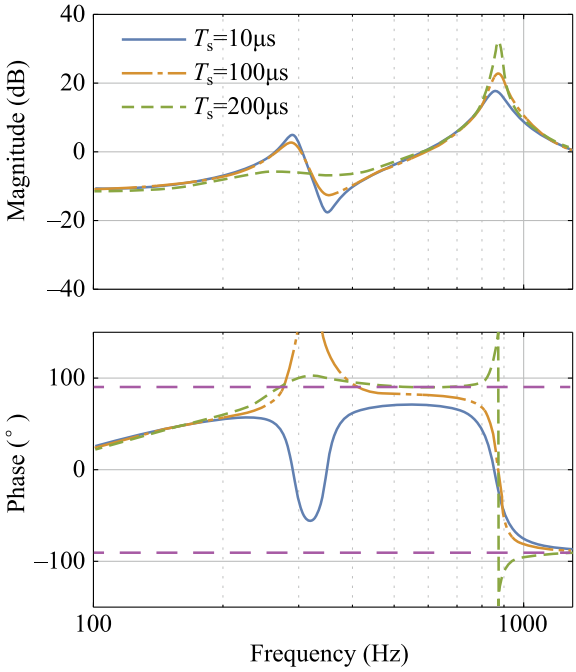

Fig. 7.40 Influence of time delay on the damping characteristics in Band III_{DFIG}

time delay and LC filter leads to negative damping characteristics in Band III_{DFIG}. In addition, with the increase of time delay, the degree of negative damping becomes more severe.

7.4.3.4 Summary of Negative Damping Characteristics in Each Frequency Band

Based on the analysis above, the following conclusions are obtained:

1. Band I_{DFIG}: The impedance characteristics of DFIG-based wind turbines are dominated by the stator-side impedance, exhibiting inductive damping characteristics, and affected by the rotor electrical frequency as well as steady-state operating point. The negative damping frequency range is related to the rotor electrical frequency, the outer power loop, RSC AC current loop and PLL. The upper limit of the negative damping range is determined by the rotor electrical frequency. The lower limit of the negative damping range is determined by the rotor electrical frequency, the outer power loop, and RSC AC current loop. The level of negative damping is jointly affected by the outer power loop, RSC AC current loop and PLL.
2. Band II_{DFIG}: The impedance characteristics of DFIG-based wind turbines are dominated by the stator-side impedance while being affected by the GSC-side

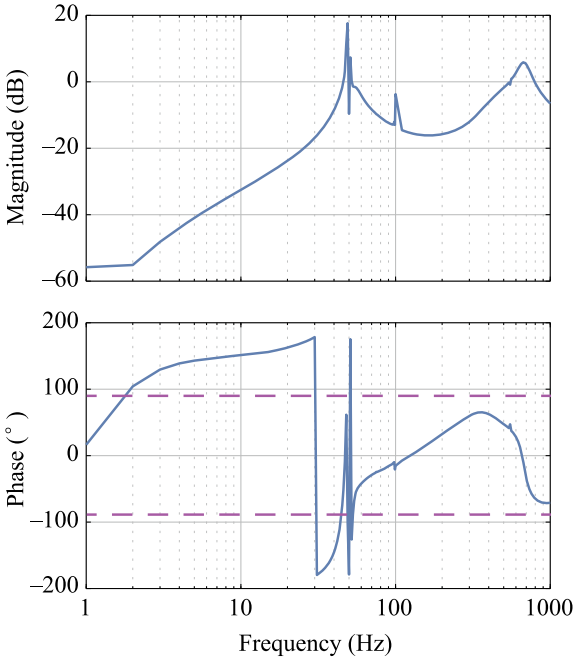

Fig. 7.41 Damping characteristics of a 1.6 MW DFIG-based wind turbine (Type D)

impedance. The frequency-band overlapping effect of the DC voltage loop and the GSC AC current loop leads to the negative damping characteristic, and the negative damping level of the impedance at the resonant peak is affected by the DC voltage loop. The power loop introduces the GSC AC current into the RSC modulation, resulting in the interaction between the power loop, RSC AC current loop, and the GSC AC current loop. Both the power loop and RSC AC current loop affect the degree of negative damping. The frequency-band overlapping effect of time delay and GSC AC current loop affects the degree of capacitive negative damping.

3. Band III_{DFIG}: The impedance characteristics are dominated by LC filter. The frequency-band overlapping effect of time delay and LC filter leads to negative damping characteristics. The degree of negative damping becomes more severe with the increase of time delay constant.

Impedance scanning is carried out based on CHIL platform of different types of DFIG-based wind turbines, and the scanning results are shown in Figs. 7.41 and 7.42. It can be seen from the figure that the impedances of DFIG-based wind turbines present inductive or capacitive negative damping characteristics respectively in different frequency bands.

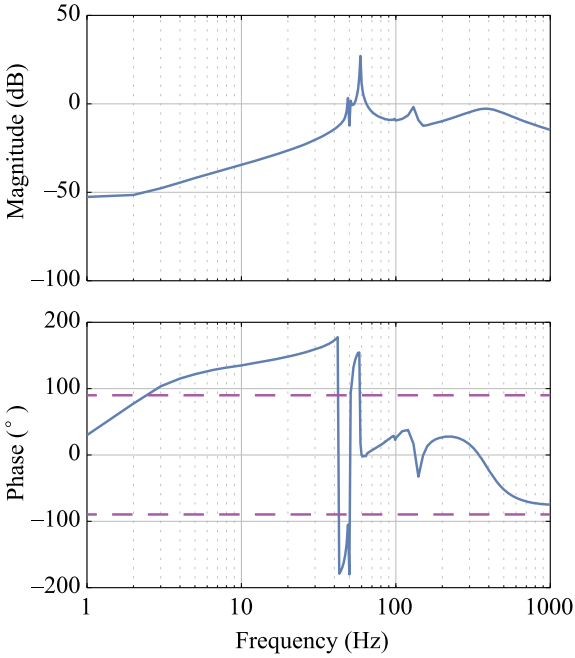

Fig. 7.42 Damping characteristics of a 2.0 MW DFIG-based wind turbine (Type E)

References

1. YANG S Y, ZHOU T B, CHANG L C, et al. Analytical method for DFIG transients during voltage dips [J]. IEEE Transactions on Power Electronics, 2017, 32(9): 6863–6881.
2. LI G H, WANG W S, ZHANG X, et al. Modeling and suppression method of sub/super-synchronous oscillation of grid-connected DFIG wind farms (Part I): sequence impedance modeling and analysis of dfig wind turbines considering power loop [J]. Proceedings of the CSEE, 2022, 47(7): 2438–2449. (Chinese)
3. LI G H, WANG W S, ZHANG X, et al. Modeling and mechanism analysis of sub/super-synchronous oscillation of grid-connected DFIG wind farms (Part II): analysis of impedance characteristic and oscillation mechanism [J]. Proceedings of the CSEE, 2022, 42(10): 3614–3627. (Chinese)

Chapter 8
Impedance Model and Characteristic Analysis of PV Unit

PV array is the power supply of PV unit. The changes in irradiance and temperature will affect the output voltage and current of PV array. As DC bus provides a coupling path between PV array and the inverter[1], operation conditions have significant impacts on the broadband impedance characteristics of PV unit.

In this chapter, first, the impedance model of PV unit is established and verified. The main circuit includes PV array, DC bus, and grid-connected inverter. The control loops include PLL, current loop, and DC voltage loop. Then, the dominant factors of impedance characteristics in different frequency bands are analyzed. Moreover, the influence of irradiance and temperature on the broadband impedance of PV units is analyzed. Finally, based on CHIL platform, the broadband impedances of several types of PV units are scanned, and the typical values of frequency band division are given.

8.1 Operation Principle and Time-Domain Model

8.1.1 Operation Principle

The single-stage PV unit is mainly composed of PV array and grid-connected inverter, and its topology is shown in Fig.8.1. The PV array consists of PV modules connected in series and parallel, converting solar energy into electric energy through photovoltaic effect. The core of PV modules is the photovoltaic conversion devices,

[1] According to the types of grid-connected inverters, PV units are mainly divided into centralized type, string type, and distributed type. This chapter takes the centralized PV unit as an example of impedance modeling and characteristic analysis. The impedance modeling and characteristic analysis of the other two types of PV units can refer to this chapter.

© China Electric Power Press 2023

W. Wang et al., *Analysis and Mitigation of Broadband Oscillation in Renewable Energy Generation and AC/DC Transmission Systems*,
https://doi.org/10.1007/978-981-99-1568-2_8

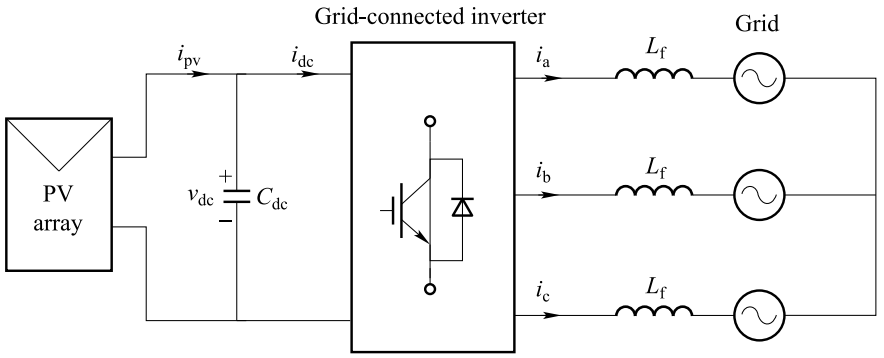

Fig. 8.1 Topology of the single-stage the PV unit

mainly silicon photovoltaic cells which include monocrystalline silicon, polycrystalline silicon, amorphous silicon and other kinds of cells. The DC power generated by the PV array is converted into AC power through a grid-connected inverter for grid-connected power generation.

The typical control structure of the grid-connected inverter is shown in Fig. 8.2, including MPPT control, DC voltage control and AC current control. First, the DC voltage reference V_{dcref} is obtained by MPPT algorithm. As the DC voltage depends on the active power balance between AC and DC ports, it can be kept stable by controlling the active power. Therefore, the DC voltage regulation can be achieved by controlling the d-axis AC current i_{d}. The power factor control can be achieved by adjusting the q-axis AC current i_{q}. Finally, the three-phase modulation signal m_l can be obtained by inverse Park transformation.

PV manufacturers usually provide users with short circuit current I_{sc}, open circuit voltage V_{oc}, maximum power point output power P_{m}, maximum power point voltage V_{m} and maximum power point current I_{m} under the standard condition (irradiance 1000 W/m^2, temperature 25 °C). The output current of PV module under the standard condition is

$$i_{\text{pv}} = I_{\text{sc}}[1 - C_1(\text{e}^{v_{\text{dc}}/C_2 V_{\text{oc}}} - 1)] \tag{8.1}$$

where the expression of C_1 and C_2 is

$$\begin{cases} C_1 = \left(1 - \dfrac{I_{\text{m}}}{I_{\text{sc}}}\right)\text{e}^{\frac{-V_{\text{m}}}{C_2 V_{\text{oc}}}} \\ C_2 = \left(\dfrac{V_{\text{m}}}{V_{\text{oc}}} - 1\right)\left[\ln\left(1 - \dfrac{I_{\text{m}}}{I_{\text{sc}}}\right)\right]^{-1} \end{cases} \tag{8.2}$$

According to Eqs. (8.1) and (8.2), the characteristic curve $i_{\text{pv}} - v_{\text{dc}}$ of PV modules under the standard condition can be obtained. However, irradiance and temperature are not necessarily at the standard condition, and the characteristic curve for the

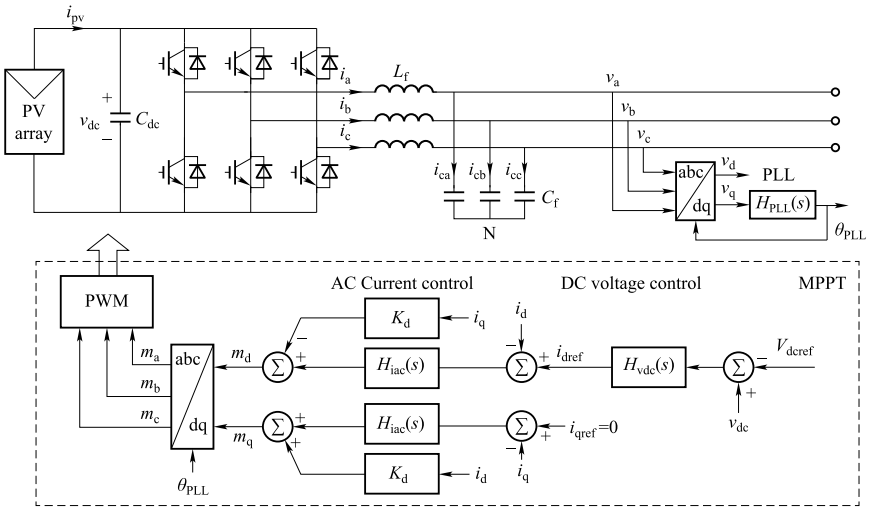

Fig. 8.2 Typical control structure of the grid-connected inverter

standard condition needs to be modified to apply to other operating conditions. The method can be used is to derive I'_{sc}, V'_{oc}, P'_m, V'_m and I'_m under the non-standard condition from I_{sc}, V_{oc}, P_m, V_m and I_m under the standard condition, and then substitute into Eqs. (8.1) and (8.2) to calculate the output characteristic curve under the non-standard condition.

Define the temperature difference ΔT and relative irradiance ΔS between the non-standard and standard conditions as

$$\begin{cases} \Delta T = T - T_{ref} \\ \Delta S = \dfrac{S}{S_{ref}} - 1 \end{cases} \tag{8.3}$$

where T and S are the temperature and irradiance under the non-standard condition respectively. T_{ref} and S_{ref} are the temperature and irradiance under the standard condition respectively.

I'_{sc}, V'_{oc}, I'_m and V'_m under the non-standard condition can be calculated as

$$\begin{cases} I'_{sc} = I_{sc}\dfrac{S}{S_{ref}}(1 + \alpha\Delta T) \\ V'_{oc} = V_{oc}(1 - \gamma\Delta T)\ln(e + \beta\Delta S) \\ I'_m = I_m\dfrac{S}{S_{ref}}(1 + \alpha\Delta T) \\ V'_m = V_m(1 - \gamma\Delta T)\ln(e + \beta\Delta S) \end{cases} \tag{8.4}$$

where α, β, γ are conversion coefficients, whose typical values are $\alpha = 0.0025/\,^{\circ}\mathrm{C}$, $\beta = 0.5$, $\gamma = 0.00288/^{\circ}\mathrm{C}$.

By substituting Eq. (8.4) into Eqs. (8.1) and (8.2), the characteristic curves of PV modules under non-standard conditions can be obtained.

For a PV array consisting of N_{ser} PV modules connected in series and N_{par} PV modules connected in parallel, the output current can be expressed as

$$i_{\mathrm{pv}} = N_{\mathrm{par}} I'_{\mathrm{sc}} \left[1 - C_1 \left(\mathrm{e}^{\frac{v_{\mathrm{dc}}}{N_{\mathrm{ser}} C_2 V'_{\mathrm{oc}}}} - 1 \right) \right] \tag{8.5}$$

where $C_1 = \left(1 - \frac{I'_{\mathrm{m}}}{I'_{\mathrm{sc}}}\right) \mathrm{e}^{\frac{-V'_{\mathrm{m}}}{C_2 V'_{\mathrm{oc}}}}$, $C_2 = \left(\frac{V'_{\mathrm{m}}}{V'_{\mathrm{oc}}} - 1 \right) \left[\ln\left(1 - \frac{I'_{\mathrm{m}}}{I'_{\mathrm{sc}}}\right) \right]^{-1}$.

8.1.2 *Time-Domain Model*

The difference between the three-phase modulation voltage and the voltage at the AC port drops on the filter inductor L_{f} to generate the output current. Accordingly, the time-domain model of the main circuit can be expressed as

$$K_{\mathrm{m}} v_{\mathrm{dc}} m_l = v_l + s L_{\mathrm{f}} i_l \tag{8.6}$$

where K_{m} is the modulation gain, v_{dc} is the DC voltage, m_l is the three-phase modulation signals, v_l is the three-phase AC voltages, and i_l is the three-phase AC currents.

According to the active power balance of AC and DC sides, there is its analytical time-domain model as

$$C_{\mathrm{dc}} \frac{\mathrm{d}v_{\mathrm{dc}}}{\mathrm{d}t} v_{\mathrm{dc}} = v_{\mathrm{dc}} i_{\mathrm{pv}} - \sum_{l=\mathrm{a,b,c}} v_l i_l \tag{8.7}$$

where C_{dc} is the DC bus capacitance.

8.2 Frequency-Domain Modeling of Steady-State Operation

8.2.1 *Frequency-Domain Characteristic Analysis of Steady-State Operating Point*

At the steady-state operating point of PV unit, the AC voltage, current and modulation signal are at the rated frequency f_1. The output voltage and current of PV array only

contain DC component. The steady-state waveforms and FFT results of PV unit are shown in Fig. 8.3.

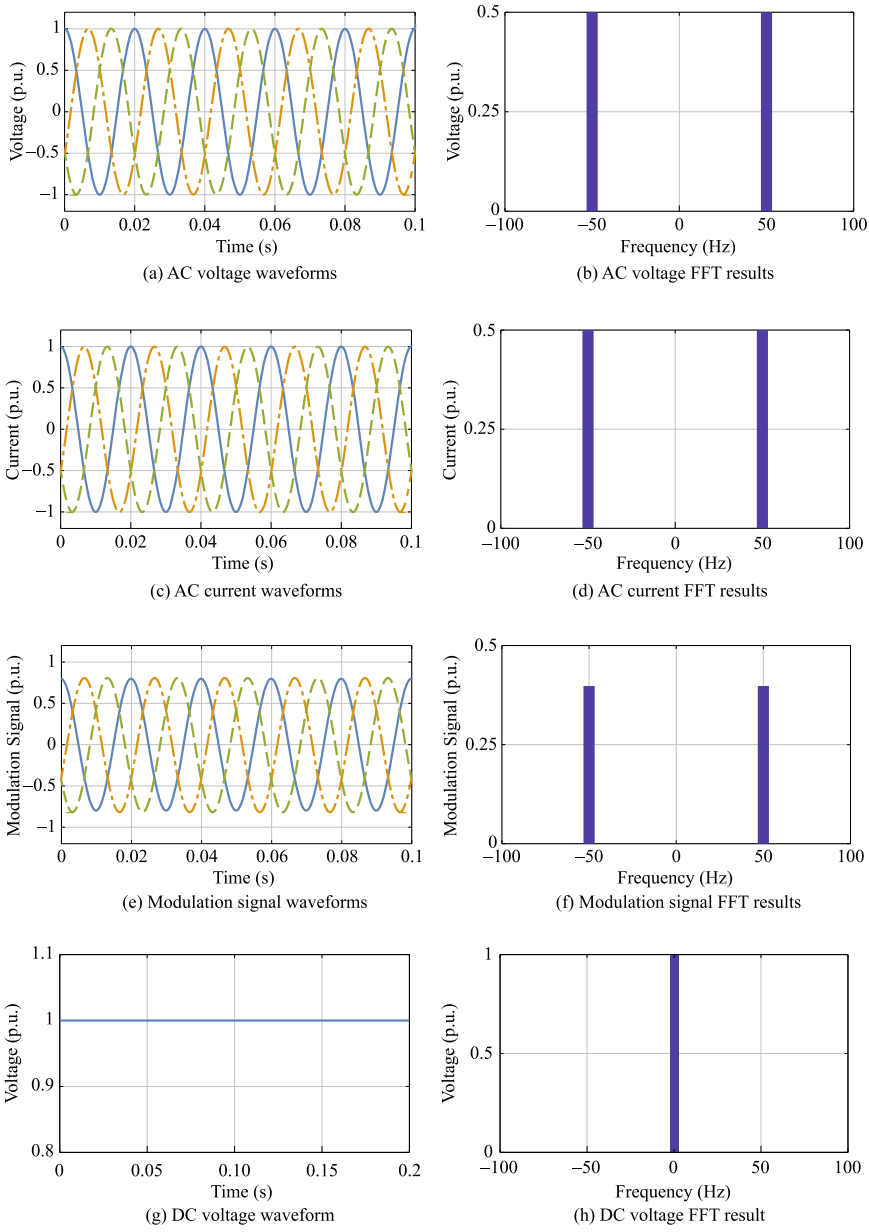

Fig. 8.3 Steady-state waveforms and FFT results of PV unit

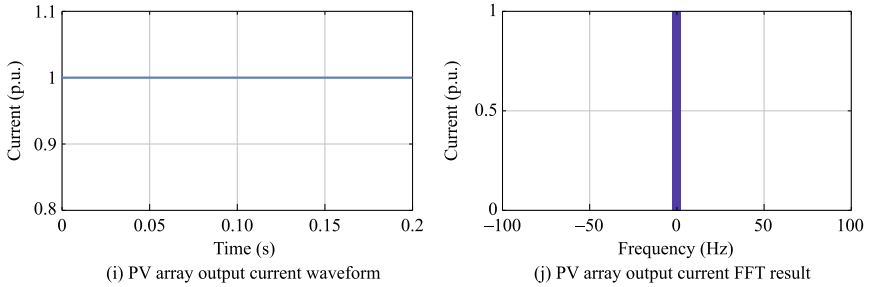

(i) PV array output current waveform (j) PV array output current FFT result

Fig. 8.3 (continued)

Based on the FFT results, the steady-state components can be arranged into the following order.

$$[-f_1,\ 0,\ f_1\,]^{\mathrm{T}} \tag{8.8}$$

Take phase a as an example, the steady-state vectors in frequency domain can be expressed as

$$\begin{cases} \boldsymbol{V}_{\mathrm{a}} = [\,\boldsymbol{V}_1^*,\ 0,\ \boldsymbol{V}_1\,]^{\mathrm{T}} \\ \boldsymbol{I}_{\mathrm{a}} = [\,\boldsymbol{I}_1^*,\ 0,\ \boldsymbol{I}_1\,]^{\mathrm{T}} \\ \boldsymbol{M}_{\mathrm{a}} = [\,\boldsymbol{M}_1^*,\ 0,\ \boldsymbol{M}_1\,]^{\mathrm{T}} \end{cases} \tag{8.9}$$

where $\boldsymbol{V}_{\mathrm{a}}$ is the steady-state vector of AC voltage, $\boldsymbol{I}_{\mathrm{a}}$ is the steady-state vector of AC current, $\boldsymbol{M}_{\mathrm{a}}$ is the steady-state vector of the modulation signal. Each element in the vector is expressed in the form of column complex vector, $\boldsymbol{V}_1 = V_1 \mathrm{e}^{\mathrm{j}\varphi_{\mathrm{v1}}}/2$, $\boldsymbol{I}_1 = I_1 \mathrm{e}^{\mathrm{j}\varphi_{\mathrm{i1}}}/2$, $\boldsymbol{M}_1 = M_1 \mathrm{e}^{\mathrm{j}\varphi_{\mathrm{m1}}}/2$, indicating the amplitude and phase of the steady-state components at their corresponding frequency. And the negative-frequency component is equal to the conjugate of the positive-frequency component, which is indicated by the superscript "*".

The components at f_1 is in positive sequence, and the corresponding ones lag $2\pi/3$ in turn in the three-phase vectors. The components at $-f_1$ are in negative sequence, and the corresponding ones lead $2\pi/3$ in turn in the three-phase vectors. In addition, the middle component is in zero sequence. According to the three-phase symmetrical relationship, the steady-state vectors of phase b and phase c can be described as

$$\begin{cases} \boldsymbol{V}_{\mathrm{b}} = \boldsymbol{D}\boldsymbol{V}_{\mathrm{a}} \\ \boldsymbol{I}_{\mathrm{b}} = \boldsymbol{D}\boldsymbol{I}_{\mathrm{a}} \\ \boldsymbol{M}_{\mathrm{b}} = \boldsymbol{D}\boldsymbol{M}_{\mathrm{a}} \end{cases} \tag{8.10}$$

$$\begin{cases} \boldsymbol{V}_{\mathrm{c}} = \boldsymbol{D}^{*}\boldsymbol{V}_{\mathrm{a}} \\ \boldsymbol{I}_{\mathrm{c}} = \boldsymbol{D}^{*}\boldsymbol{I}_{\mathrm{a}} \\ \boldsymbol{M}_{\mathrm{c}} = \boldsymbol{D}^{*}\boldsymbol{M}_{\mathrm{a}} \end{cases} \tag{8.11}$$

where $\boldsymbol{D}$ is the phase-sequence coefficient matrix in the steady-state frequency order, expressed as

$$\boldsymbol{D} = \mathrm{diag}[\,\{\mathrm{e}^{-\mathrm{j}2k\pi/3}\}\big|_{k=-1,0,1}\,] \tag{8.12}$$

8.2.2 Frequency-Domain Steady-State Model of Main Circuit

8.2.2.1 Steady-State Model of PV Array

By transforming Eq. (8.5) into the frequency domain, the steady-state model of PV array can be obtained as

$$\boldsymbol{I}_{\mathrm{pv}} = N_{\mathrm{par}} I'_{\mathrm{sc}} \left[1 - C_1 \left(\mathrm{e}^{\frac{V_{\mathrm{dc}}}{N_{\mathrm{ser}} C_2 V'_{\mathrm{oc}}}} - 1 \right) \right] \tag{8.13}$$

where $\boldsymbol{I}_{\mathrm{pv}}$, $\boldsymbol{V}_{\mathrm{dc}}$ are the steady-state vectors of PV array output current and voltage respectively.

8.2.2.2 Steady-State Model of Grid-Connected Inverter

By transforming the time-domain model of the grid-connected inverter shown in Eq. (8.6) to frequency domain, there is the steady-state model as follows

$$K_{\mathrm{m}} V_{\mathrm{dc}} \boldsymbol{M}_l = \boldsymbol{V}_l + \boldsymbol{Z}_{\mathrm{Lf0}} \boldsymbol{I}_l \tag{8.14}$$

where V_{dc} is the steady-state DC voltage. $\boldsymbol{Z}_{\mathrm{Lf0}}$ is a fifth-order diagonal matrix, representing the impedance of the filter inductor in the steady-state frequency order, expressed as $\boldsymbol{Z}_{\mathrm{Lf0}} = \mathrm{j}2\pi L_{\mathrm{f}} \cdot \mathrm{diag}[\,-2f_1,\ -f_1,\ 0,\ f_1,\ 2f_1\,]$.

8.2.2.3 DC Bus Steady-State Model

By transforming Eq. (8.7) into the frequency domain, the steady-state model of DC bus can be obtained as

$$0 = V_{\mathrm{dc}} I_{\mathrm{pv}} - \sum_{l=\mathrm{a,b,c}} \boldsymbol{V}_{\mathrm{i}l} \otimes \boldsymbol{I}_l \tag{8.15}$$

where $\boldsymbol{V}_{il}$ and $\boldsymbol{I}_l$ are the three-phase steady-state vectors of the modulation voltages and AC currents respectively.

8.3 Small-Signal Impedance Modeling in Frequency Domain

In this section, the frequency-domain linearization method is used to establish the small-signal impedance model of PV units. First, the AC voltage AC current and modulation signals are transformed to the frequency domain to obtain the steady-state operating point. Then, a small-signal perturbation of a specific frequency is added on the AC voltage. Finally, the small-signal impedance model of PV units is established by calculating the response of AC current to a small-signal perturbation in AC voltage.

8.3.1 Small-Signal Frequency-Domain Characteristic Analysis

Inject a sinusoidal small-signal perturbation at f_p into the AC voltage of PV units, the transfer path and frequency distribution of PV unit small signals are shown in Fig. 8.4.

Take phase a as an example, the small-signal $\hat{\boldsymbol{v}}_l$ in the positive sequence (at f_p) is injected to the AC voltage of PV unit at the steady-state operating point. A small-signal response of AC port power at $f_\mathrm{p} - f_1$ will be generated since $\hat{\boldsymbol{v}}_l$ at f_p multiplies the steady-state vector of AC current $\boldsymbol{I}_l$ at $-f_1$. According to the instantaneous power balance, a small-signal power at $f_\mathrm{p} - f_1$ will be responded in the DC port. Meanwhile,

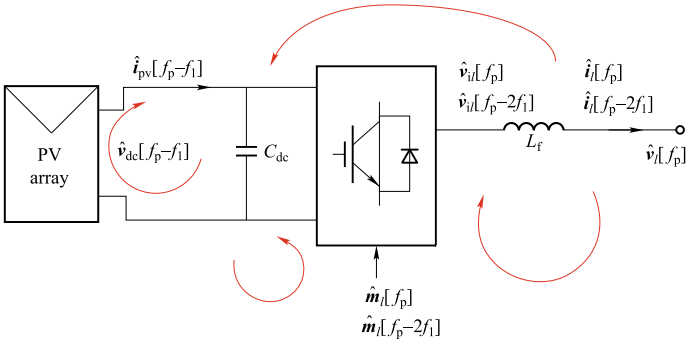

Fig. 8.4 Transfer path and frequency distribution of PV unit small signals

a small-signal DC voltage $\hat{\boldsymbol{v}}_{\mathrm{dc}}$ at $f_{\mathrm{p}} - f_1$ will also be responded. $\hat{\boldsymbol{v}}_{\mathrm{dc}}$ at $f_{\mathrm{p}} - f_1$ acts on PV array, causing PV array to output a small-signal current $\hat{\boldsymbol{i}}_{\mathrm{pv}}$ at $f_{\mathrm{p}} - f_1$.

$\hat{\boldsymbol{v}}_{\mathrm{dc}}$ at $f_{\mathrm{p}} - f_1$ multiplying the steady-state component of the modulation signal $\boldsymbol{M}_l$ at f_1 will lead to a small-signal response of the modulation voltage $\hat{\boldsymbol{v}}_{il}$ at f_{p}. $\hat{\boldsymbol{v}}_{\mathrm{dc}}$ at $f_{\mathrm{p}} - f_1$ multiplying the steady-state component of the modulation signal $\boldsymbol{M}_l$ at $-f_1$ will lead to a small-signal response of the modulation voltage $\hat{\boldsymbol{v}}_{il}$ at $f_{\mathrm{p}} - 2f_1$.

Since $\hat{\boldsymbol{v}}_l$ only contains the small-signal component at f_{p} while $\hat{\boldsymbol{v}}_{il}$ contains the small-signal components both at f_{p} and $f_{\mathrm{p}} - 2f_1$, the difference between $\hat{\boldsymbol{v}}_{il}$ and $\hat{\boldsymbol{v}}_l$ on the filter inductor L_{f} leads to small-signal responses of $\hat{\boldsymbol{i}}_l$ at f_{p} and $f_{\mathrm{p}} - 2f_1$.

When the injected small signal is at 80 Hz, the waveforms and FFT results of the PV unit are shown in Fig. 8.5. It can be seen that the AC voltage contains component at 80 Hz, the AC current and modulation signal contain components at 80 Hz and − 20 Hz. The DC voltage contains component at 30 Hz.

The small-signal frequency relationship of the PV unit is shown in Table 8.1.

In order to describe the frequency domain characteristics of voltages and currents of PV units, the small-signal components can be arranged into the following order.

$$[\, f_{\mathrm{p}} - 2f_1,\ f_{\mathrm{p}} - f_1,\ f_{\mathrm{p}},\ f_{\mathrm{p}} + f_1,\ f_{\mathrm{p}} + 2f_1 \,]^{\mathrm{T}} \tag{8.16}$$

In order to achieve the convolution between the steady-state vectors and the small-signal vectors, the steady-state frequency orders in Eq. (8.8) need to be expanded as follows.

$$[\, -2f_1,\ -f_1,\ 0,\ f_1,\ 2f_1 \,]^{\mathrm{T}} \tag{8.17}$$

In Eq. (8.17), the steady-state components at $\pm 2f_1$ are zero.

Take phase a as an example, the small-signal vectors in frequency domain can be expressed as

$$\begin{cases} \hat{\boldsymbol{v}}_{\mathrm{a}} = [\, \hat{\boldsymbol{v}}_{\mathrm{p\text{-}2}},\ 0,\ \hat{\boldsymbol{v}}_{\mathrm{p}},\ 0,\ 0 \,]^{\mathrm{T}} \\ \hat{\boldsymbol{i}}_{\mathrm{a}} = [\, \hat{\boldsymbol{i}}_{\mathrm{p\text{-}2}},\ 0,\ \hat{\boldsymbol{i}}_{\mathrm{p}},\ 0,\ 0 \,]^{\mathrm{T}} \\ \hat{\boldsymbol{m}}_{\mathrm{a}} = [\, \hat{\boldsymbol{m}}_{\mathrm{p\text{-}2}},\ 0,\ \hat{\boldsymbol{m}}_{\mathrm{p}},\ 0,\ 0 \,]^{\mathrm{T}} \end{cases} \tag{8.18}$$

where $\hat{\boldsymbol{v}}_{\mathrm{a}}$ is the small-signal vector of AC voltage, $\hat{\boldsymbol{i}}_{\mathrm{a}}$ is the small-signal vector of AC current, and $\hat{\boldsymbol{m}}_{\mathrm{a}}$ is the small-signal vector of the modulation signal. Each element in the vector is expressed in the form of column complex vector, $\hat{\boldsymbol{v}}_{\mathrm{p}} = V_{\mathrm{p}} \mathrm{e}^{\mathrm{j}\varphi_{\mathrm{vp}}}/2$, $\hat{\boldsymbol{v}}_{\mathrm{p\text{-}2}} = V_{\mathrm{p\text{-}2}} \mathrm{e}^{\mathrm{j}\varphi_{\mathrm{vp\text{-}2}}}/2$, $\hat{\boldsymbol{i}}_{\mathrm{p}} = I_{\mathrm{p}} \mathrm{e}^{\mathrm{j}\varphi_{\mathrm{ip}}}/2$, $\hat{\boldsymbol{i}}_{\mathrm{p\text{-}2}} = I_{\mathrm{p\text{-}2}} \mathrm{e}^{\mathrm{j}\varphi_{\mathrm{ip\text{-}2}}}/2$, $\hat{\boldsymbol{m}}_{\mathrm{p}} = M_{\mathrm{p}} \mathrm{e}^{\mathrm{j}\varphi_{\mathrm{mp}}}/2$, $\hat{\boldsymbol{m}}_{\mathrm{p\text{-}2}} = M_{\mathrm{p\text{-}2}} \mathrm{e}^{\mathrm{j}\varphi_{\mathrm{mp\text{-}2}}}/2$, indicating the amplitude and phase of the small-signal components at their corresponding frequency. And the negative-frequency component is equal to the conjugate of the positive-frequency component, which is indicated by the superscript "*".

The components at f_{p} are in positive sequence, and the corresponding ones lag $2\pi/3$ in turn in the three-phase vectors. The components at $f_{\mathrm{p}} - 2f_1$ are in negative

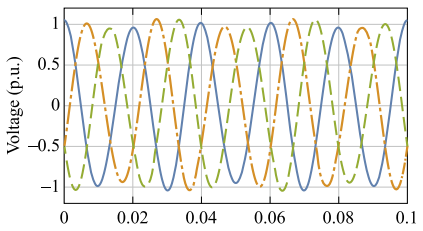

(a) AC voltage waveforms

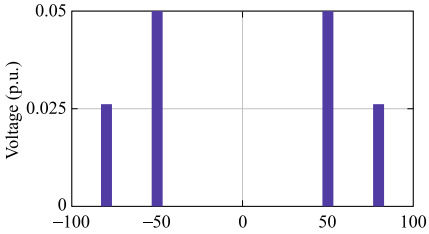

(b) AC voltage FFT results

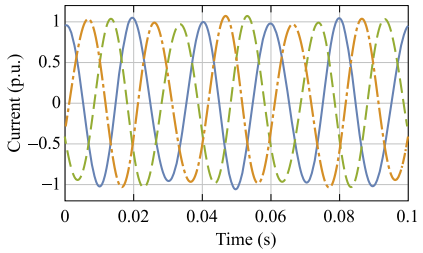

(c) AC current waveforms

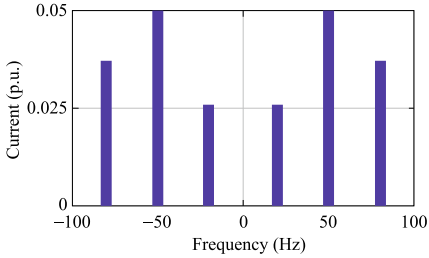

(d) AC current FFT results

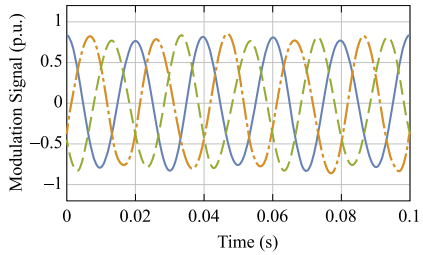

(e) Modulation signal waveforms

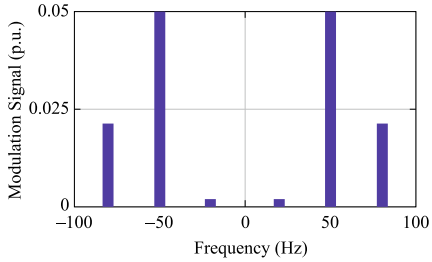

(f) Modulation signal FFT results

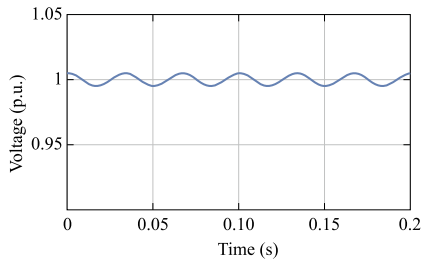

(g) DC bus voltage waveform

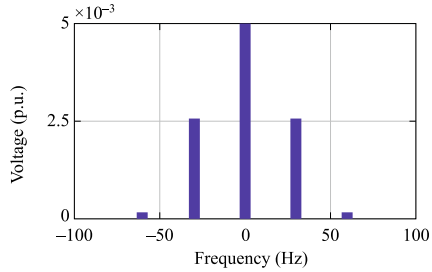

(h) DC bus voltage FFT result

Fig. 8.5 Waveforms and FFT results of the PV unit

Table 8.1 The small-signal frequency relationship of the PV unit

PV Unit	Small-Signal Vector	Frequency
Grid-connected inverter	$\hat{\boldsymbol{v}}_l$	f_p
	$\hat{\boldsymbol{i}}_l$	f_p
		$f_\mathrm{p} - 2f_1$
PV Array and DC bus	$\hat{\boldsymbol{v}}_\mathrm{dc}$	$f_\mathrm{p} - f_1$
	$\hat{\boldsymbol{i}}_\mathrm{pv}$	$f_\mathrm{p} - f_1$

sequence, and the corresponding ones lead $2\pi/3$ in turn in the three-phase vectors. In addition, the middle component is in zero sequence. According to the three-phase symmetrical relationship, the small-signal vectors of phase b and phase c can be described as follows

$$\begin{cases} \hat{\boldsymbol{v}}_\mathrm{b} = \boldsymbol{D}_\mathrm{p}\hat{\boldsymbol{v}}_\mathrm{a} \\ \hat{\boldsymbol{i}}_\mathrm{b} = \boldsymbol{D}_\mathrm{p}\hat{\boldsymbol{i}}_\mathrm{a} \\ \hat{\boldsymbol{m}}_\mathrm{b} = \boldsymbol{D}_\mathrm{p}\hat{\boldsymbol{m}}_\mathrm{a} \end{cases} \tag{8.19}$$

$$\begin{cases} \hat{\boldsymbol{v}}_\mathrm{c} = \boldsymbol{D}_\mathrm{p}^*\hat{\boldsymbol{v}}_\mathrm{a} \\ \hat{\boldsymbol{i}}_\mathrm{c} = \boldsymbol{D}_\mathrm{p}^*\hat{\boldsymbol{i}}_\mathrm{c} \\ \hat{\boldsymbol{m}}_\mathrm{c} = \boldsymbol{D}_\mathrm{p}^*\hat{\boldsymbol{m}}_\mathrm{c} \end{cases} \tag{8.20}$$

$\boldsymbol{D}_\mathrm{p}$ is the phase-sequence coefficient matrix in the small-signal frequency order, expressed as

$$\boldsymbol{D}_\mathrm{p} = \mathrm{diag}[\{\mathrm{e}^{-\mathrm{j}2(k+1)\pi/3}\}\big|_{k=-2,-1,0,1,2}] \tag{8.21}$$

8.3.2 Frequency-Domain Small-Signal Model

8.3.2.1 Small-Signal Model of PV Array

According to the model of PV array shown in Eq. (8.5), the relationship between the small-signal vector of output current $\hat{\boldsymbol{i}}_\mathrm{pv}$ and the small-signal vector of DC voltage $\hat{\boldsymbol{v}}_\mathrm{dc}$ is

$$\hat{\boldsymbol{i}}_\mathrm{pv} = -\frac{N_\mathrm{par} I'_\mathrm{sc} C_1}{N_\mathrm{ser} C_2 V'_\mathrm{oc}} \mathrm{e}^{\frac{V_\mathrm{dc}}{N_\mathrm{ser} C_2 V'_\mathrm{oc}}} \hat{\boldsymbol{v}}_\mathrm{dc} \tag{8.22}$$

From the above equation, it can be seen that $\hat{\boldsymbol{i}}_\mathrm{pv}$ and $\hat{\boldsymbol{v}}_\mathrm{dc}$ are proportional to each other, and the impedance of PV array $\boldsymbol{Z}_\mathrm{array}$ can be expressed as

$$\boldsymbol{Z}_{\text{array}} = -\frac{\hat{\boldsymbol{v}}_{\text{dc}}}{\hat{\boldsymbol{i}}_{\text{pv}}} = \frac{N_{\text{ser}} C_2 V'_{\text{oc}}}{N_{\text{par}} I'_{\text{sc}} C_1 \text{e}^{\frac{V_{\text{dc}}}{N_{\text{ser}} C_2 V'_{\text{oc}}}}} \tag{8.23}$$

$\boldsymbol{Z}_{\text{array}}$ is related to irradiance and temperature according to Eq. (8.23).

8.3.2.2 Small-Signal Model of Grid-Connected Inverter

The grid-connected inverter controls the d-axis current through the outer DC voltage loop to maintain the stability of DC voltage. The small-signal vectors of d- and q-axis current reference can be expressed as

$$\begin{cases} \hat{\boldsymbol{i}}_{\text{dref}} = H_{\text{vdc}}(s_1)\hat{\boldsymbol{v}}_{\text{dc}} \\ \hat{\boldsymbol{i}}_{\text{qref}} = 0 \end{cases} \tag{8.24}$$

where $s_1 = \text{j}2\pi(f_\text{p} - f_1)$, $H_{\text{vdc}}(s_1)$ is the transfer function of DC voltage controller, whose expression is $H_{\text{vdc}}(s_1) = K_{\text{vdcp}} + K_{\text{vdci}}/s_1$, K_{vdcp} and K_{vdci} are proportional and integral coefficients respectively.

According to the control structure of the grid-connected inverter, the small-signal vector of its modulation signal can be derived as

$$\hat{\boldsymbol{m}}_\text{a} = \boldsymbol{E}_{\text{dc}}\hat{\boldsymbol{v}}_{\text{dc}} + \boldsymbol{E}_\text{i}\hat{\boldsymbol{i}}_\text{a} + \boldsymbol{E}_\text{v}\hat{\boldsymbol{v}}_\text{a} \tag{8.25}$$

where $\boldsymbol{E}_{\text{dc}}$, $\boldsymbol{E}_\text{i}$ and $\boldsymbol{E}_\text{v}$ are fifth-order matrices. All other elements in the matrices are zero except for the following

$$\begin{cases} \boldsymbol{E}_{\text{dc}}(1,2) = \dfrac{1}{2}H_{\text{iac}}(s_1)H_{\text{vdc}}(s_1) \\ \boldsymbol{E}_{\text{dc}}(3,2) = \dfrac{1}{2}H_{\text{iac}}(s_1)H_{\text{vdc}}(s_1) \end{cases} \tag{8.26}$$

$$\begin{cases} \boldsymbol{E}_\text{i}(1,1) = -H_{\text{iac}}(s_1) - \text{j}K_\text{d} \\ \boldsymbol{E}_\text{i}(3,3) = -H_{\text{iac}}(s_1) + \text{j}K_\text{d} \end{cases} \tag{8.27}$$

$$\begin{cases} \boldsymbol{E}_\text{v}(1,1) = T_{\text{PLL}}(s_1)[(H_{\text{iac}}(s_1) + \text{j}K_\text{d})\boldsymbol{I}_1^* + \boldsymbol{M}_1^*] \\ \boldsymbol{E}_\text{v}(1,3) = -T_{\text{PLL}}(s_1)[(H_{\text{iac}}(s_1) + \text{j}K_\text{d})\boldsymbol{I}_1^* + \boldsymbol{M}_1^*] \\ \boldsymbol{E}_\text{v}(3,1) = -T_{\text{PLL}}(s_1)[(H_{\text{iac}}(s_1) - \text{j}K_\text{d})\boldsymbol{I}_1 + \boldsymbol{M}_1] \\ \boldsymbol{E}_\text{v}(3,3) = T_{\text{PLL}}(s_1)[(H_{\text{iac}}(s_1) - \text{j}K_\text{d})\boldsymbol{I}_1 + \boldsymbol{M}_1] \end{cases} \tag{8.28}$$

By transforming Eq. (8.6) to frequency domain, the small-signal model of the main circuit can be obtained as

$$K_\text{m}(V_{\text{dc}}\hat{\boldsymbol{m}}_\text{a} + \boldsymbol{M}_\text{a}\hat{\boldsymbol{v}}_{\text{dc}}) = \hat{\boldsymbol{v}}_\text{a} + \boldsymbol{Z}_\text{f}\hat{\boldsymbol{i}}_\text{a} \tag{8.29}$$

where $\boldsymbol{M}_{\mathrm{a}}$ is the extended steady-state matrix of the modulation signal, whose expression is

$$\boldsymbol{M}_{\mathrm{a}} = \begin{bmatrix} 0 & \boldsymbol{M}_1^* & 0 & 0 & 0 \\ \boldsymbol{M}_1 & 0 & \boldsymbol{M}_1^* & 0 & 0 \\ 0 & \boldsymbol{M}_1 & 0 & \boldsymbol{M}_1^* & 0 \\ 0 & 0 & \boldsymbol{M}_1 & 0 & \boldsymbol{M}_1^* \\ 0 & 0 & 0 & \boldsymbol{M}_1 & 0 \end{bmatrix}$$

$\boldsymbol{Z}_{\mathrm{f}}$ is a fifth-order diagonal matrix, representing the filter inductor impedance in the small-signal frequency order, expressed as

$$\boldsymbol{Z}_{\mathrm{f}} = \mathrm{j}2\pi L_{\mathrm{f}} \cdot \mathrm{diag}[\, f_{\mathrm{p}} - 2f_1,\ f_{\mathrm{p}} - f_1,\ f_{\mathrm{p}},\ f_{\mathrm{p}} + f_1,\ f_{\mathrm{p}} + 2f_1\,]$$

After simplification, the small-signal model of the grid-connected inverter can be expressed as

$$\hat{\boldsymbol{v}}_{\mathrm{a}} = \boldsymbol{F}_{\mathrm{dc}}\hat{\boldsymbol{v}}_{\mathrm{dc}} + \boldsymbol{F}_{\mathrm{i}}\hat{\boldsymbol{i}}_{\mathrm{a}} \tag{8.30}$$

where $\boldsymbol{F}_{\mathrm{dc}}$, $\boldsymbol{F}_{\mathrm{i}}$ are fifth-order matrices, whose expression is

$$\begin{cases} \boldsymbol{F}_{\mathrm{dc}} = (\boldsymbol{U} - K_{\mathrm{m}} V_{\mathrm{dc}} \boldsymbol{E}_{\mathrm{v}})^{-1}(K_{\mathrm{m}} \boldsymbol{M}_{\mathrm{a}} + K_{\mathrm{m}} V_{\mathrm{dc}} \boldsymbol{E}_{\mathrm{dc}}) \\ \boldsymbol{F}_{\mathrm{i}} = (\boldsymbol{U} - K_{\mathrm{m}} V_{\mathrm{dc}} \boldsymbol{E}_{\mathrm{v}})^{-1}(K_{\mathrm{m}} V_{\mathrm{dc}} \boldsymbol{E}_{\mathrm{i}} - \boldsymbol{Z}_{\mathrm{f}}) \end{cases} \tag{8.31}$$

$\boldsymbol{U}$ is fifth-order identity matrix.

8.3.2.3 Small-Signal Model of DC Bus

Transforming Eq. (8.7) to frequency domain, the small-signal model of DC bus can be obtained as

$$\begin{aligned} s_1 C_{\mathrm{dc}} V_{\mathrm{dc}} \hat{\boldsymbol{v}}_{\mathrm{dc}} = {} & (\boldsymbol{I}_{\mathrm{pv}} \otimes \hat{\boldsymbol{v}}_{\mathrm{dc}} + \boldsymbol{V}_{\mathrm{dc}} \otimes \hat{\boldsymbol{i}}_{\mathrm{pv}}) \\ & - \sum_{l=\mathrm{a,b,c}} (\boldsymbol{I}_l \otimes \hat{\boldsymbol{v}}_{il} + \boldsymbol{V}_{il} \otimes \hat{\boldsymbol{i}}_l) \end{aligned} \tag{8.32}$$

After simplification, the small-signal vector of DC voltage can be expressed as

$$\hat{\boldsymbol{v}}_{\mathrm{dc}} = \boldsymbol{J}_{\mathrm{i}}\hat{\boldsymbol{i}}_{\mathrm{a}} + \boldsymbol{J}_{\mathrm{v}}\hat{\boldsymbol{v}}_{\mathrm{a}} + \boldsymbol{J}_{\mathrm{pv}}\hat{\boldsymbol{i}}_{\mathrm{pv}} \tag{8.33}$$

where $\boldsymbol{J}_{\mathrm{i}}$, $\boldsymbol{J}_{\mathrm{v}}$ and $\boldsymbol{J}_{\mathrm{pv}}$ are fifth-order matrices. All other elements in the matrices are zero except for the following

$$\begin{cases} \boldsymbol{J}_{\mathrm{i}}(2,1) = -\dfrac{3}{C_{\mathrm{dc}}V_{\mathrm{dc}}s_1 - I_{\mathrm{pv}}}(\boldsymbol{V}_1 + s_2 L_{\mathrm{f}}\boldsymbol{I}_1) \\ \boldsymbol{J}_{\mathrm{i}}(2,3) = -\dfrac{3}{C_{\mathrm{dc}}V_{\mathrm{dc}}s_1 - I_{\mathrm{pv}}}(\boldsymbol{V}_1^* + sL_{\mathrm{f}}\boldsymbol{I}_1^*) \end{cases} \tag{8.34}$$

$$\begin{cases} \boldsymbol{J}_{\mathrm{v}}(2,1) = -\dfrac{3}{C_{\mathrm{dc}}V_{\mathrm{dc}}s_1 - I_{\mathrm{pv}}}\boldsymbol{I}_1 \\ \boldsymbol{J}_{\mathrm{v}}(2,3) = -\dfrac{3}{C_{\mathrm{dc}}V_{\mathrm{dc}}s_1 - I_{\mathrm{pv}}}\boldsymbol{I}_1^* \end{cases} \tag{8.35}$$

$$\boldsymbol{J}_{\mathrm{pv}}(2,2) = \frac{V_{\mathrm{dc}}}{C_{\mathrm{dc}}V_{\mathrm{dc}}s_1 - I_{\mathrm{pv}}} \tag{8.36}$$

8.3.3 AC Port Impedance Model

The AC port admittance of PV unit can be obtained from the ratio of the input current small signal and voltage small signal at the AC port, namely

$$\boldsymbol{Y}_{\mathrm{PV}} = -\frac{\hat{\boldsymbol{i}}_{\mathrm{a}}}{\hat{\boldsymbol{v}}_{\mathrm{a}}} \tag{8.37}$$

By solving Eqs. (8.22), (8.30) and (8.33), there is

$$\begin{aligned} \hat{\boldsymbol{i}}_{\mathrm{a}} = &-[\boldsymbol{F}_{\mathrm{dc}}(\boldsymbol{U} + \boldsymbol{J}_{\mathrm{pv}}/\boldsymbol{Z}_{\mathrm{array}})^{-1}\boldsymbol{J}_{\mathrm{i}} + \boldsymbol{F}_{\mathrm{i}}]^{-1} \\ &\cdot [\boldsymbol{F}_{\mathrm{dc}}(\boldsymbol{U} + \boldsymbol{J}_{\mathrm{pv}}/\boldsymbol{Z}_{\mathrm{array}})^{-1}\boldsymbol{J}_{\mathrm{v}} - \boldsymbol{U}]\hat{\boldsymbol{v}}_{\mathrm{a}} \end{aligned} \tag{8.38}$$

So, the AC port admittance of PV unit can be obtained as

$$\begin{aligned} \boldsymbol{Y}_{\mathrm{PV}} = &[\boldsymbol{F}_{\mathrm{dc}}(\boldsymbol{U} + \boldsymbol{J}_{\mathrm{pv}}/\boldsymbol{Z}_{\mathrm{array}})^{-1}\boldsymbol{J}_{\mathrm{i}} + \boldsymbol{F}_{\mathrm{i}}]^{-1} \\ &\cdot [\boldsymbol{F}_{\mathrm{dc}}(\boldsymbol{U} + \boldsymbol{J}_{\mathrm{pv}}/\boldsymbol{Z}_{\mathrm{array}})^{-1}\boldsymbol{J}_{\mathrm{v}} - \boldsymbol{U}] \end{aligned} \tag{8.39}$$

Since there are only components at f_{p} and $f_{\mathrm{p}} - 2f_1$ in small-signal vectors of AC voltage and AC current of PV unit, only relevant elements at these two frequencies are extracted, and the AC port admittance shown in Eq. (8.39) are rearranged as the following 2×2 matrix.

$$\begin{bmatrix} \boldsymbol{Y}_{\mathrm{PV}}^{\mathrm{pp}} & \boldsymbol{Y}_{\mathrm{PV}}^{\mathrm{np}} \\ \boldsymbol{Y}_{\mathrm{PV}}^{\mathrm{pn}} & \boldsymbol{Y}_{\mathrm{PV}}^{\mathrm{nn}} \end{bmatrix} = \begin{bmatrix} \boldsymbol{Y}_{\mathrm{PV}}(3,3) & \boldsymbol{Y}_{\mathrm{PV}}(3,1) \\ \boldsymbol{Y}_{\mathrm{PV}}(1,3) & \boldsymbol{Y}_{\mathrm{PV}}(1,1) \end{bmatrix} \tag{8.40}$$

where

$\boldsymbol{Y}_{\mathrm{PV}}(3, 3)$ is the element in the third row and the third column of $\boldsymbol{Y}_{\mathrm{PV}}$;
$\boldsymbol{Y}_{\mathrm{PV}}(3, 1)$ is the element in the third row and the first column of $\boldsymbol{Y}_{\mathrm{PV}}$;
$\boldsymbol{Y}_{\mathrm{PV}}(1, 3)$ is the element in the first row and the third column of $\boldsymbol{Y}_{\mathrm{PV}}$;
$\boldsymbol{Y}_{\mathrm{PV}}(1, 1)$ is the element in the first row and the first column of $\boldsymbol{Y}_{\mathrm{PV}}$.

The relationship between the small-signal components of AC voltage and AC current at the disturbance frequency and coupling frequency meets

$$\begin{bmatrix} -\hat{\boldsymbol{i}}_{\mathrm{p}} \\ -\hat{\boldsymbol{i}}_{\mathrm{p\text{-}2}} \end{bmatrix} = \begin{bmatrix} \boldsymbol{Y}_{\mathrm{PV}}^{\mathrm{pp}} & \boldsymbol{Y}_{\mathrm{PV}}^{\mathrm{np}} \\ \boldsymbol{Y}_{\mathrm{PV}}^{\mathrm{pn}} & \boldsymbol{Y}_{\mathrm{PV}}^{\mathrm{nn}} \end{bmatrix} \begin{bmatrix} \hat{\boldsymbol{v}}_{\mathrm{p}} \\ \hat{\boldsymbol{v}}_{\mathrm{p\text{-}2}} \end{bmatrix} \tag{8.41}$$

where $\boldsymbol{Y}_{\mathrm{PV}}^{\mathrm{pp}}$ is the positive-sequence admittance of PV units, representing the small-signal response of AC current at f_{p} in positive sequence under per unit small-signal perturbation of AC voltage at f_{p} in positive sequence.

$\boldsymbol{Y}_{\mathrm{PV}}^{\mathrm{pn}}$ is the positive-sequence coupled admittance of PV units, representing the small-signal response of AC current at $f_{\mathrm{p}} - 2f_1$ in negative sequence under per unit small-signal perturbation of AC voltage at f_{p} in positive sequence.
$\boldsymbol{Y}_{\mathrm{PV}}^{\mathrm{nn}}$ is the negative-sequence admittance of PV units, representing the small-signal response of AC current at $f_{\mathrm{p}} - 2f_1$ in negative sequence under per unit small-signal perturbation of AC voltage at $f_{\mathrm{p}} - 2f_1$ in negative sequence.
$\boldsymbol{Y}_{\mathrm{PV}}^{\mathrm{np}}$ is the negative-sequence coupled admittance of PV units, representing the small-signal response of AC current at f_{p} in positive sequence under per unit small-signal perturbation of AC voltage at $f_{\mathrm{p}} - 2f_1$ in negative sequence.

The AC port impedance of PV unit can be obtained by calculating the inverse matrix of the AC port admittance as

$$\begin{bmatrix} \boldsymbol{Z}_{\mathrm{PV}}^{\mathrm{pp}} & \boldsymbol{Z}_{\mathrm{PV}}^{\mathrm{pn}} \\ \boldsymbol{Z}_{\mathrm{PV}}^{\mathrm{np}} & \boldsymbol{Z}_{\mathrm{PV}}^{\mathrm{nn}} \end{bmatrix} = \begin{bmatrix} \boldsymbol{Y}_{\mathrm{PV}}^{\mathrm{pp}} & \boldsymbol{Y}_{\mathrm{PV}}^{\mathrm{np}} \\ \boldsymbol{Y}_{\mathrm{PV}}^{\mathrm{pn}} & \boldsymbol{Y}_{\mathrm{PV}}^{\mathrm{nn}} \end{bmatrix}^{-1} \tag{8.42}$$

$\boldsymbol{Z}_{\mathrm{PV}}^{\mathrm{pp}}$ represents the positive-sequence impedance of PV units, which is the element in the first row and the first column of the AC port admittance inverse matrix;
$\boldsymbol{Z}_{\mathrm{PV}}^{\mathrm{pn}}$ represents the positive-sequence coupled impedance of PV units, which is the element in the first row and the second column of the AC port admittance inverse matrix;
$\boldsymbol{Z}_{\mathrm{PV}}^{\mathrm{nn}}$ represents the negative-sequence impedance of PV units, which is the element in the second row and the second column of the AC port admittance inverse matrix;
$\boldsymbol{Z}_{\mathrm{PV}}^{\mathrm{np}}$ represents the negative-sequence coupled impedance of PV units, which is the element in the second row and the first column of the AC port admittance inverse matrix;

Table 8.2 The main circuit and controller parameters of PV units

Parameter	Definition	Value
P_N	Rated power	500 kW
V_N	Rated voltage	311 V
f_1	Rated frequency	50 Hz
L_f	Filter inductance	0.105 mH
C_f	Filter capacitance	0.6 mF
V_{dc}	DC voltage	780 V
C_{dc}	DC capacitance	15.12mF
K_{pp}, K_{pi}	Proportional and integral coefficients of PLL controller	0.5247, 57
K_{iacp}, K_{iaci}	Proportional and integral coefficients of AC current controller	4.3950×10^{-4}, 0.4783
K_{vdcp}, K_{vdci}	Proportional and integral coefficients of DC voltage controller	5.9680, 546
K_d	Decoupling coefficient of AC current control	8.4580×10^{-4}

In addition, the frequency-domain relationship between the negative-sequence impedance and the positive-sequence impedance satisfies $\boldsymbol{Z}_{PV}^{nn} = \boldsymbol{Z}_{PV}^{pp*}(j2\omega_1 - s)$, and the frequency-domain relationship between the negative-sequence coupling impedance and the positive-sequence coupling impedance satisfies $\boldsymbol{Z}_{PV}^{np} = \boldsymbol{Z}_{PV}^{pn*}(j2\omega_1 - s)$.

Table 8.2 lists the main circuit and controller parameters of PV units. Figure 8.6 shows the comparison between the analytical impedance (in solid lines) and scanning impedance (in discrete points). As seen from the figure, all the discrete points fall on the solid lines, which verify the the accuracy of the established impedance model of PV units.

8.4 Analysis of Broadband Impedance Characteristics

In this section, based on the impedance model of PV unit, the dominant factors of impedance characteristics in different frequency bands are analyzed, and the frequency-band division method of PV unit impedance is proposed. Then, the frequency-band overlapping effects of multiple controllers are clarified and the negative damping characteristics of each frequency band are analysed. Fanally, based on CHIL impedance scanning results of different types of PV units, typical values of frequency band division are given.

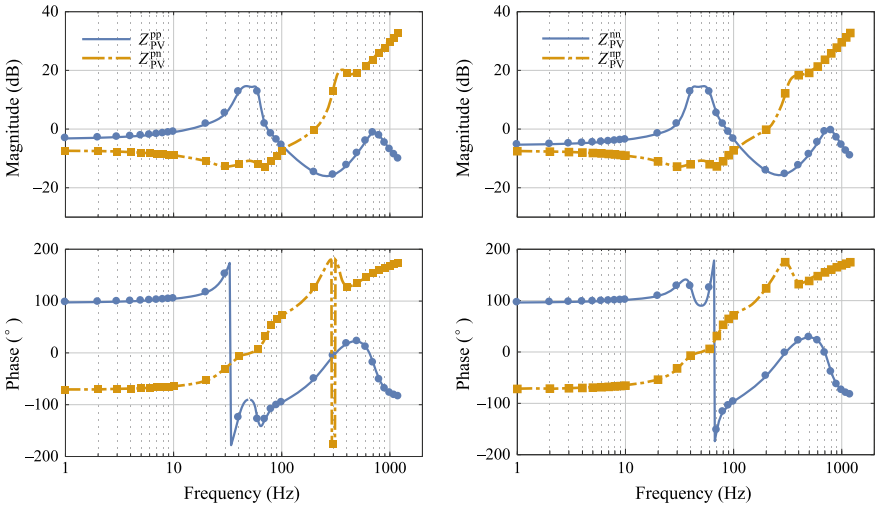

(a) Positive-sequence impedance and positive-sequence coupling impedance

(b) Negative-sequence impedance and negative-sequence coupling impedance

Fig. 8.6 Analytical and scanning results of PV unit impedance

8.4.1 Frequency-Band Division of Broadband Impedance

According to the impedance model of PV unit, it is known that the impedance characteristics are affected by PLL, AC current loop, DC voltage loop, time delay, and LC filter. In this section, the dominant factors of PV unit impedance characteristics in each frequency band are analyzed, and the impedance frequency-band division method is proposed.

8.4.1.1 Influence of PLL on Impedance Characteristics

The block diagram and parameter calculation method of PLL can be found in Sect. 5.4.1.1. The influence of PLL on impedance characteristics is shown in Fig. 8.7. On the one hand, the influence of PLL bandwidth can be obtained by setting f_{tc} to 5, 20 and 30 Hz respectively with a constant PM of 45°. On the other hand, the influence of PLL PM can be obtained by setting θ_{tc} to 10°, 45° and 80° respectively with a constant bandwidth of 5 Hz.

As shown in Fig. 8.7, the bandwidth f_{tc} of PLL mainly affects the frequency of the impedance resonance peak $f_1 - f_{tc}$ and $f_1 + f_{tc}$. With the increase of f_{tc}, the difference between the resonance peak frequency and the fundamental frequency increases. At the frequency of the resonance peak, the phase of the impedance represents capacitive negative damping characteristics (the phase of the impedance less than $-90°$). The PM θ_{tc} of PLL mainly affects the impedance magnitude and phase at the frequency of the impedance resonance peak $f_1 - f_{tc}$ and $f_1 + f_{tc}$. With the increase of θ_{tc},

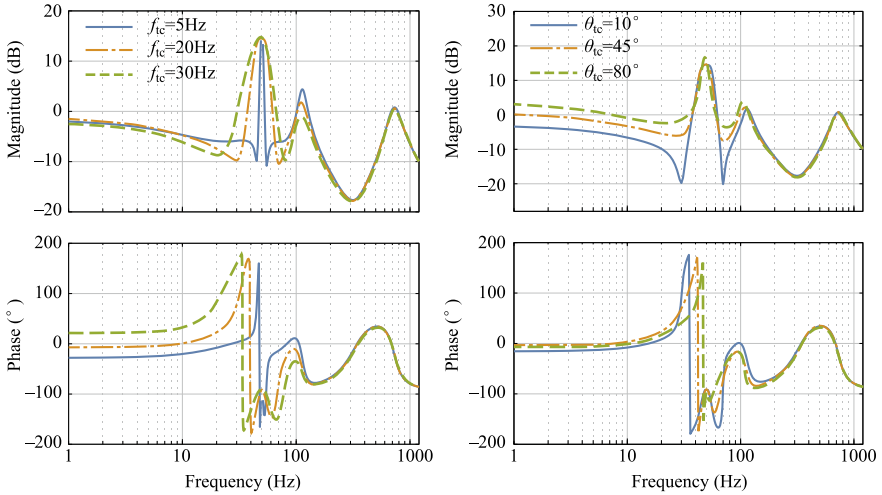

(a) Different PLL bandwidths (b) Different PLL PMs

Fig. 8.7 Influence of PLL on impedance characteristics

the level of the capacitive negative damping decreases. In conclusion, PLL mainly affects the impedance characteristics in $f_1 - f_{tc} < f < f_1 + f_{tc}$.

8.4.1.2 Influence of AC Current Loop on Impedance Characteristics

The block diagram and parameter calculation method of AC current loop can be found in Sect. 5.4.1.1. The influence of AC current loop on impedance characteristics is shown in Fig. 8.8. On the one hand, the influence of AC current loop bandwidth can be obtained by setting f_{iac} to 100, 200 and 300 Hz respectively with a constant PM of 45°. On the other hand, the influence of AC current loop PM can be obtained by setting θ_{iac} to 10°, 45° and 80° respectively with a constant bandwidth of 300Hz.

As shown in Fig. 8.8, the AC current loop mainly affects the impedance characteristics in $f < f_1 - f_{tc}$ and $f_1 + f_{tc} < f < f_1 + f_{iac}$. At the AC current loop bandwidth $f_1 + f_{iac}$ (in SCF), the magnitude of the impedance exhibits a resonant peak, the phase of the impedance changes from capacitive to inductive. With the increase of f_{iac}, the frequency of resonant peak increases. In addition, as the AC current loop PM θ_{iac} decreases, the resonant peak becomes steeper, the phase change becomes more intense, and the level of damping decreases.

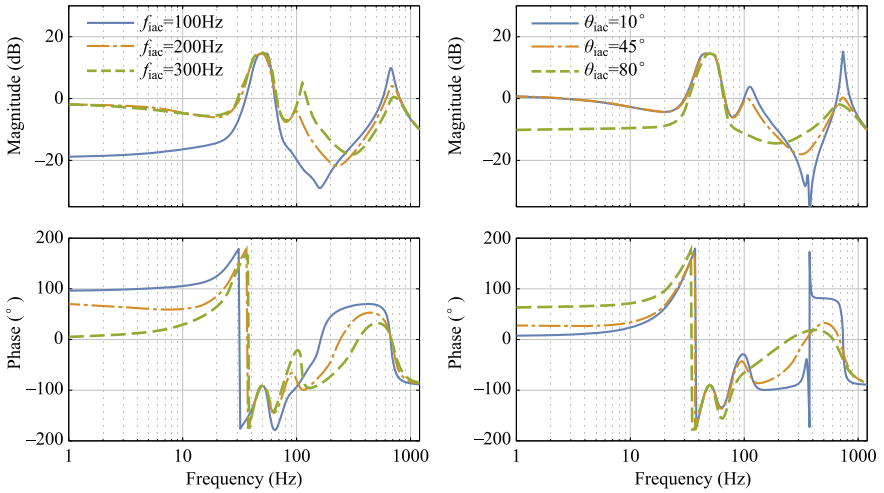

Fig. 8.8 Influence of AC current loop on impedance characteristics

8.4.1.3 Influence of LC Filter on Impedance Characteristics

According to the influence of AC current loop on the impedance characteristics, when the frequency reaches AC current loop bandwidth, the impedance characteristics change from capacitive to inductive. As the frequency further increases to the LC resonant frequency, the impedance characteristic changes from inductive to capacitive. The LC resonant frequency is related to the filter parameters. The influence of LC filter on impedance characteristics is shown in Fig. 8.9. The influence of the filter capacitor C_f is obtained by setting C_f to 0.4, 0.6 and 0.8 mF respectively with fixed filter inductance.

As shown in Fig. 8.9, LC filter mainly affects the impedance characteristics in $f > f_1 + f_{iac}$. The impedance is inductive at first, and at the LC resonant frequency, the phase changes from inductive to capacitive.

8.4.1.4 Influence of the Steady-State Operating Point on Impedance Characteristics

The impedance model of PV units is obtained by small-signal linearization based on the steady-state operating point. During the operation of PV units, the change of irradiance and temperature will lead to the variation of the steady-state operating point. By Changing the irradiance from 0.2 kW/m^2 to 1.2 kW/m^2 with a constant temperature of 25 °C, the influence of irradiance on impedance characteristics is shown in Fig. 8.10(a). By Changing the temperature from 0 °C to 50 °C with a constant irradiance of 1 kW/m^2, the influence of temperature on impedance characteristics is shown in Fig. 8.10.

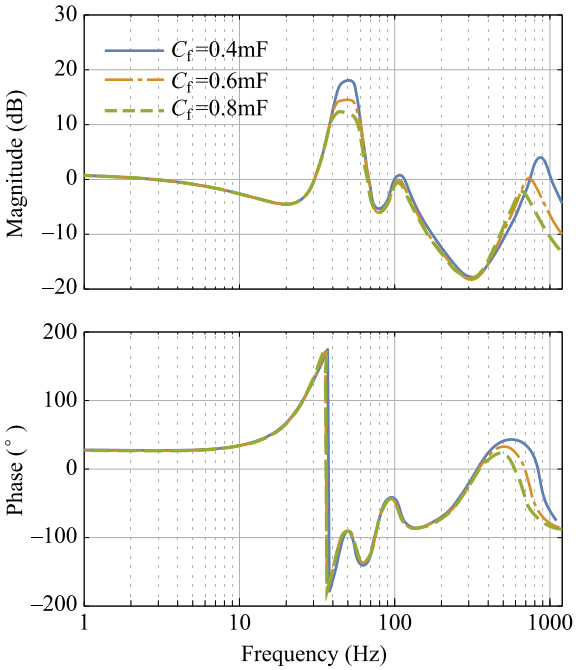

Fig. 8.9 Influence of LC filter on impedance characteristics

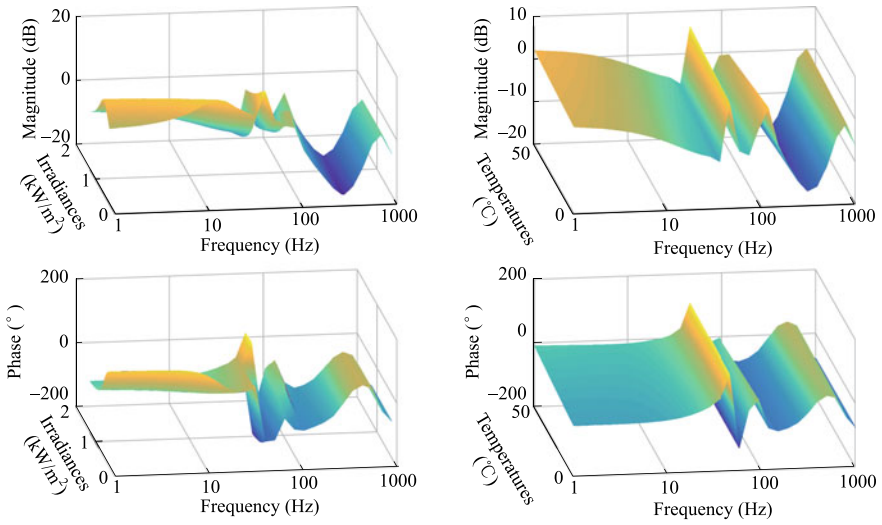

(a) Different irradiances (b) Different temperatures

Fig. 8.10 Influence of irradiance and temperature on impedance characteristics

As shown in Fig. 8.10, the irradiance and temperature mainly affects the impedance characteristics in $f < f_1 + f_{iac}$. For $f > f_1 + f_{iac}$, the impedance characteristics are mainly determined by LC filter, and the influence of irradiance and temperature can be ignored.

8.4.1.5 Frequency-Band Division Principle of Broadband Impedance

According to the dominant factors of PV unit impedance characteristics in each frequency band, the following frequency bands can be divided:

(1) Band I_{PV} ($f < f_1 - f_{tc}$): There is no dominant factors of PV unit impedance characteristics. PLL, the AC current loop, and the steady-state operating point all have an influence on the impedance characteristics in this band.
(2) Band II_{PV} ($f_1 - f_{tc} < f < f_1 + f_{tc}$): The impedance characteristics of PV unit are dominated by PLL. As the bandwidth f_{tc} of PLL increases, the frequency range of band II_{PV} expands. As the PM θ_{tc} of PLL increases, the level of capacitive negative damping decreases. In addition, the steady-state operating point have an effect on the impedance characteristics.
(3) Band III_{PV} ($f_1 + f_{tc} < f < f_1 + f_{iac}$): The impedance characteristics of PV unit are dominated by the AC current loop. With the increase of the bandwidth f_{iac}, the frequency range in which the impedance represents capacitive characteristics increases. With the increase of the PM θ_{iac}, the level of capacitive damping weakens. In addition, the steady-state operating point has effect on the impedance characteristics in this band.
(4) Band IV_{PV} ($f > f_1 + f_{iac}$): The impedance characteristics of PV unit are dominated by LC filter. As the frequency increases, the impedance changes from inductive to capacitive, and the resonance frequency is related to the main circuit LC filter parameters.

Impedance scanning is carried out based on CHIL platform of different types of PV units, and the scanning results are shown in Figs. 8.11, 8.12 and 8.13. It can be seen from the figure that the frequency range of band I_{PV} is around $f < 40$ Hz, the frequency range of band II_{PV} is around 40 Hz $< f <$ 60 Hz, the frequency range of band III_{PV} is around 60 Hz $< f <$ 200 Hz, and the frequency range of band IV_{PV} is around $f > 200$ Hz.

8.4.2 Analysis of Negative Damping Characteristics

The frequency-band division principle of PV unit impedance is proposed in Sect. 8.4.1. Considering the control system of PV unit involves the coordination of multiple controllers, the impedance characteristics in each frequency band are affected not only by the dominant factors, but also by the frequency-band overlapping effects of other controllers. In this section, the frequency-band overlapping

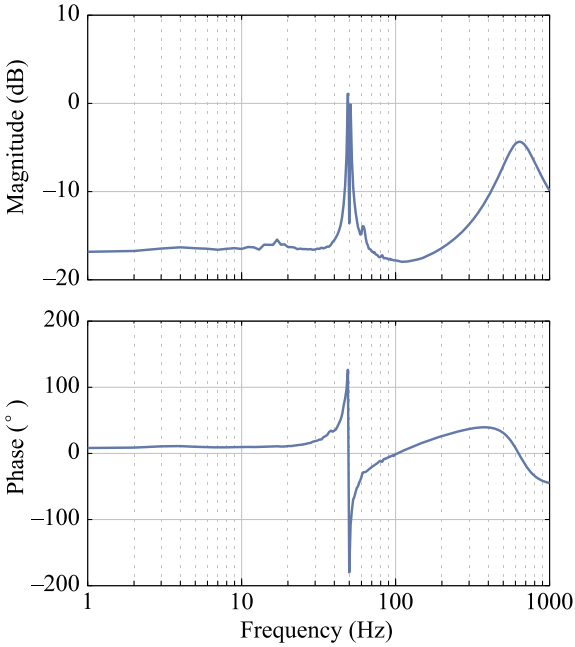

Fig. 8.11 Impedance of a 0.5 MW PV unit (Type A)

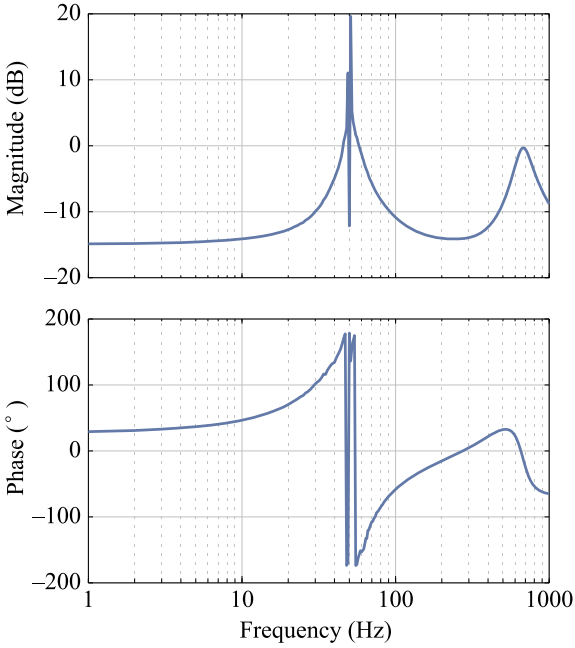

Fig. 8.12 Impedance of a 1.0 MW PV unit (Type B)

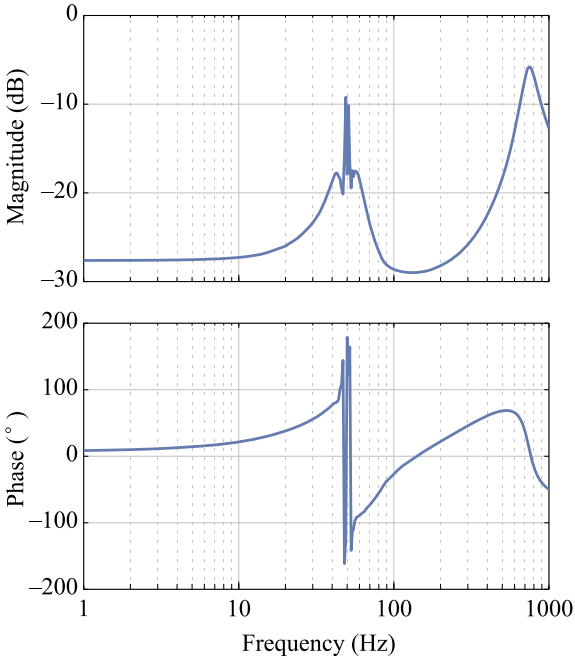

Fig. 8.13 Impedance of a 3.15 MW PV unit (Type C)

effects of DC voltage loop and time delay will be analyzed to reveal the mechanism of the negative damping characteristics in each frequency band.

8.4.2.1 Analysis of Negative Damping Characteristics in Band $\mathrm{II_{PV}}$

In Band $\mathrm{II_{PV}}$, the impedance characteristics of PV unit are dominated by PLL. In addition, the impedance characteristics are also affected by DC voltage loop and the steady-state operating point. In this section, the effects of DC voltage loop and the steady-state operating point on the negative damping characteristics in Band $\mathrm{II_{PV}}$ are analyzed.

1. Influence of DC Voltage Loop on Negative Damping Characteristics

The block diagram and parameter calculation method of DC voltage loop can be found. The influence of DC voltage loop on impedance characteristics is shown in Fig. 8.14. Firstly, the PLL bandwidth f_{tc} is set to 30Hz, and the PM of the PLL θ_{tc} is set to 45°. On the one hand, the influence of DC voltage loop bandwidth can be obtained by setting f_{vdc} to 5, 15 and 25 Hz respectively with a constant PM of 45°. On the other hand, the influence of DC voltage loop PM can be obtained by setting θ_{vdc} to 10°, 45° and 80° respectively with a constant bandwidth of 15 Hz.

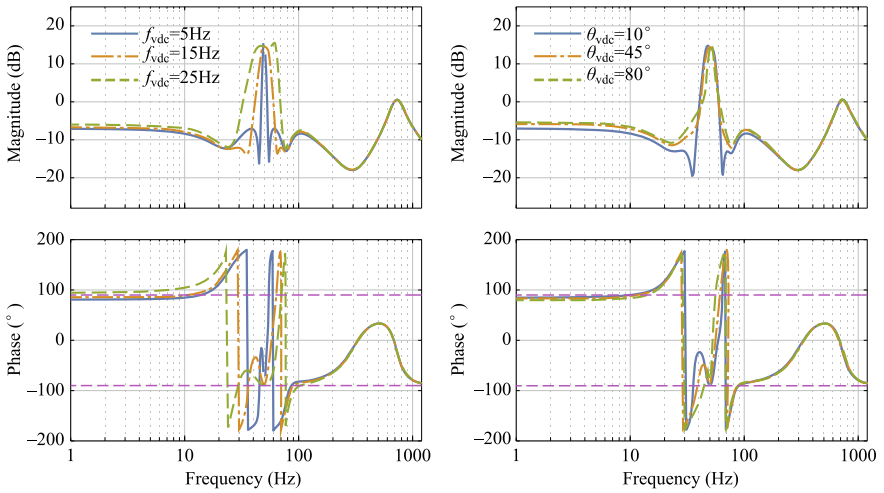

(a) Different DC voltage loop bandwidths (b) Different DC voltage loop PMs

Fig. 8.14 Influence of DC voltage loop on the damping characteristics in band $\mathrm{II_{PV}}$

As shown in Fig. 8.14, the frequency-band overlapping effect of PLL and DC voltage loop results in negative damping characteristics in this band. The PM of DC-voltage loop affects the level of negative damping.

2. Influence of the Steady-State Operating Point on Negative Damping Characteristics

Figure 8.15 shows the influence of the steady-state operating point on the damping characteristics in band $\mathrm{II_{PV}}$. On the one hand, the influence of irradiance can be obtained by changing it to 0.3, 0.6, and 1 kW/m^2 respectively with a constant temperature of 25 °C. On the other hand, the influence of temperature can be obtained by setting it to 0, 25, 50 °C respectively with a constant irradiance of 1 kW/m^2.

As shown in Fig. 8.15, with the increase of irradiance, the magnitude of the impedance decreases and the level of negative damping deepens. Temperature has no significant effect on impedance characteristics.

8.4.2.2 Analysis of Negative Damping Characteristics in Band $\mathrm{III_{PV}}$

In band $\mathrm{III_{PV}}$, the impedance characteristics of PV unit are dominated by the current loop. The impedance characteristics in the first half band are also affected by DC voltage loop. The impedance characteristics in the second half band are also affected by time delay.

1. Influence of DC Voltage Loop on Negative Damping Characteristics

The influence of DC voltage loop on the damping characteristics in Band $\mathrm{III_{PV}}$ is shown in Fig. 8.16. Firstly, the PLL bandwidth f_{tc} is set to 5 Hz, and the PM of the

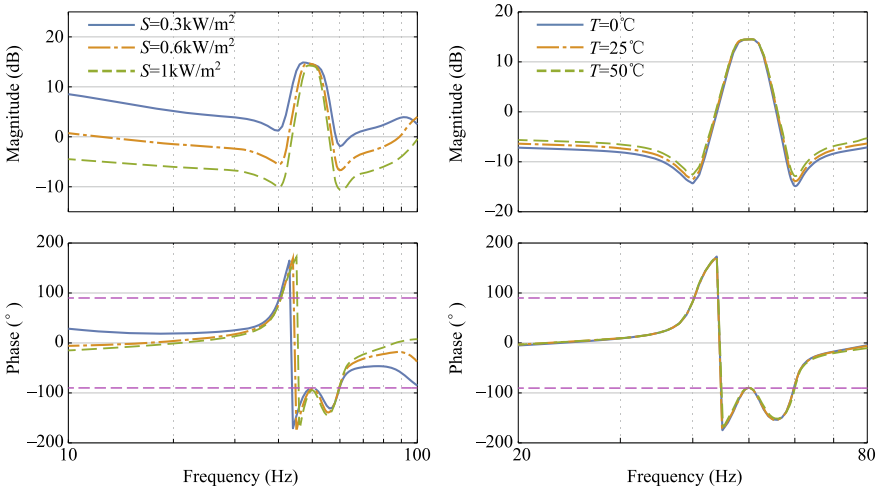

(a) Different irradiances (b) Different temperatures

Fig. 8.15 Influence of the steady-state operating point on the damping characteristics in band $\mathrm{II_{PV}}$

PLL is set to 45°. On the one hand, the influence of DC voltage loop bandwidth can be obtained by setting f_{vdc} to 40, 60 and 80 Hz respectively with a constant PM of 60°. On the other hand, the influence of power loop PM can be obtained by setting θ_{vdc} to 10°, 45° and 80° respectively with a constant bandwidth of 70 Hz.

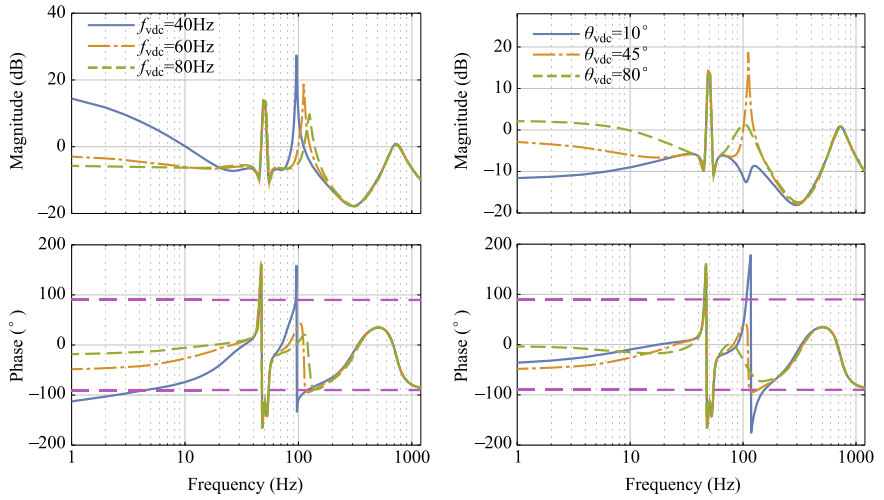

(a) Different DC voltage loop bandwidths (b) Different DC voltage loop PMs

Fig. 8.16 Influence of DC voltage loop on the damping characteristics in Band $\mathrm{III_{PV}}$

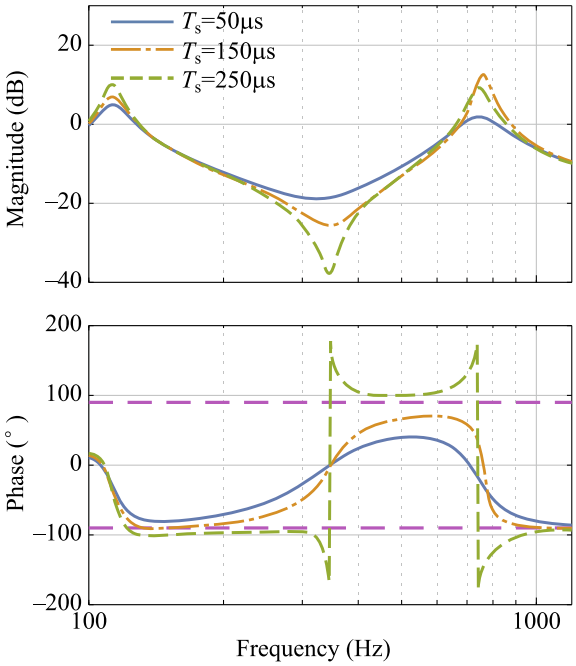

Fig. 8.17 Influence of time delay on the damping characteristics in Band III_{PV}

As shown in Fig. 8.16, the frequency-band overlapping effect of the current loop and DC voltage loop results in negative damping characteristics in this band. As the bandwidth and PM of DC-voltage loop decreases, the level of negative damping deepens.

2. Influence of Time Delay on Negative Damping Characteristics

The influence of time delay on the damping characteristics in Band III_{PV} is shown in Fig. 8.17. Firstly, the AC current control bandwidth f_{iac} is set to 300Hz, and the PM of the AC current control θ_{iac} is set to 45°. The influence of time delay can be obtained by changing it to 50, 150 and 250 μs respectively with constant LC filter parameters. As shown in Fig. 8.17, the frequency-band overlapping effect of time delay and the current loop leads to negative damping characteristics in Band III_{PV}. In addition, with the increase of time delay, the level of negative damping deepens.

3. Influence of the Steady-State Operating Point on Negative Damping Characteristics

Figure 8.18 shows the influence of the steady-state operating point on the damping characteristics in Band III_{PV}. On the one hand, the influence of irradiance can be

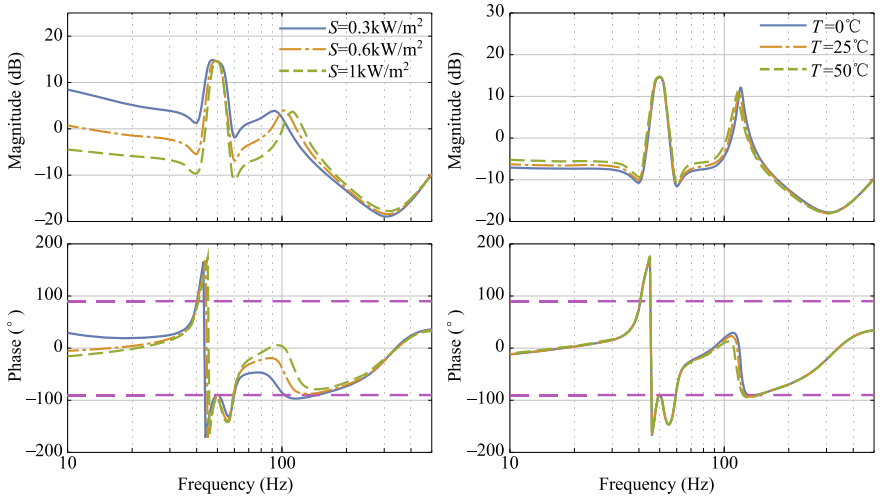

(a) Different irradiances (b) Different temperatures

Fig. 8.18 Influence of the steady-state operating point on the damping characteristics in Band II_{PV}

obtained by changing it to 0.3, 0.6, 1 kW/m^2 respectively with a constant temperature of 25 °C. On the other hand, the influence of temperature can be obtained by setting it to 0 °C, 25 °C, 50 °C respectively with a constant irradiance of 1 kW/m^2.

As shown in Fig. 8.18, with the decrease of irradiance, the level of negative damping deepens. Temperature has little effect on impedance characteristics in this band.

8.4.2.3 Analysis of Negative Damping Characteristics in Band IV_{PV}

In Band IV_{PV}, the impedance characteristics of PV unit are dominated by LC filter and affected by time delay. The influence of time delay on the damping characteristics in Band IV_{PV} is shown in Fig. 8.19. The influence of time delay can be obtained by changing it from 10, 100 to 200 μs respectively with constant LC filter parameters. As shown in Fig. 8.19, the frequency-band overlapping effect of time delay and LC filter leads to negative damping characteristics in Band IV_{PV}. In addition, with the increase of time delay, the level of negative damping deepens.

8.4.2.4 Summary of Negative Damping Characteristics in Each Frequency Band

Based on the analysis above, the following conclusions are obtained:

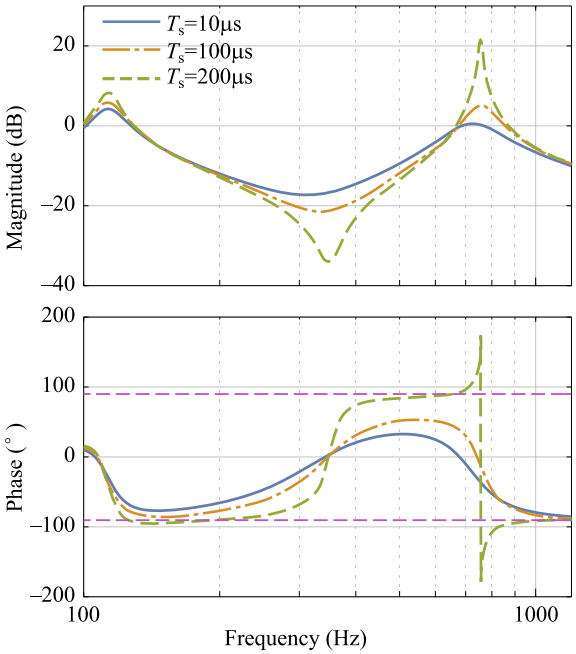

Fig. 8.19 Influence of time delay on the damping characteristics in Band IV_{PV}

(1) In Band II_{PV}: The impedance characteristics are dominated by the PLL and affected by DC voltage loop and the steady-state operating point. When the bandwidth of DC voltage loop is lower than PLL, there is a frequency-band overlapping effect of DC voltage loop and PLL, resulting in negative damping characteristics in this band. In addition, the level of the negative damping deepens with the increase of irradiance.

(2) In Band III_{PV}: The impedance characteristics are dominated by the current loop and affected by DC voltage loop and time delay. In the first half band of III_{PV}, there is frequency-band overlapping effect of the current loop and DC voltage loop. The level of the negative damping deepens with the decrease of DC voltage loop PM. In the second half band of Band III_{PV}, the frequency-band overlapping effect of the current loop and time delay leads to negative damping characteristics near the bandwidth of the current loop, and the increase of time delay will aggravate the negative damping characteristics. Besides, the level of the negative damping deepens with the decrease of irradiance.

(3) In Band IV_{PV}: The impedance characteristics are dominated by LC filter. The frequency-band overlapping effect of time delay and LC filter leads to negative damping characteristics. The level of negative damping deepens with the increase of time delay.

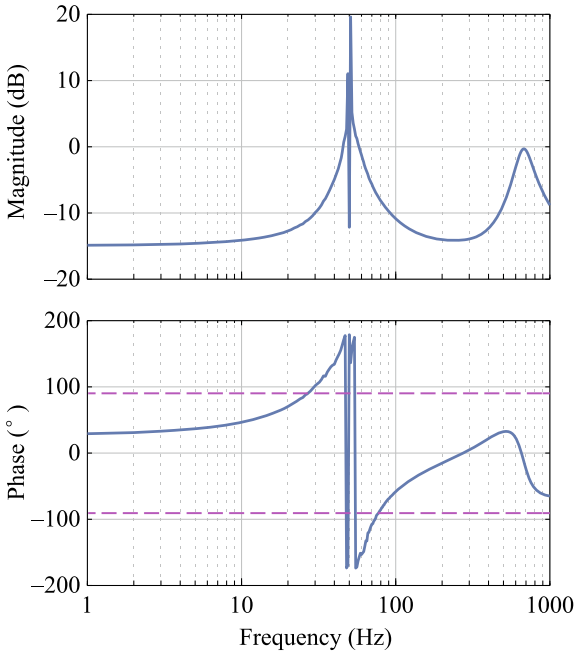

Fig. 8.20 Damping characteristics of a 1.0 MWPV unit (Type D)

Impedance scanning is carried out based on CHIL platform of different types of PV units, and the scanning results are shown in Fig. 8.20 and Fig. 8.21. It can be seen that the impedance represents capacitive negative damping characteristics in Band $\mathrm{III}_{\mathrm{PV}}$.

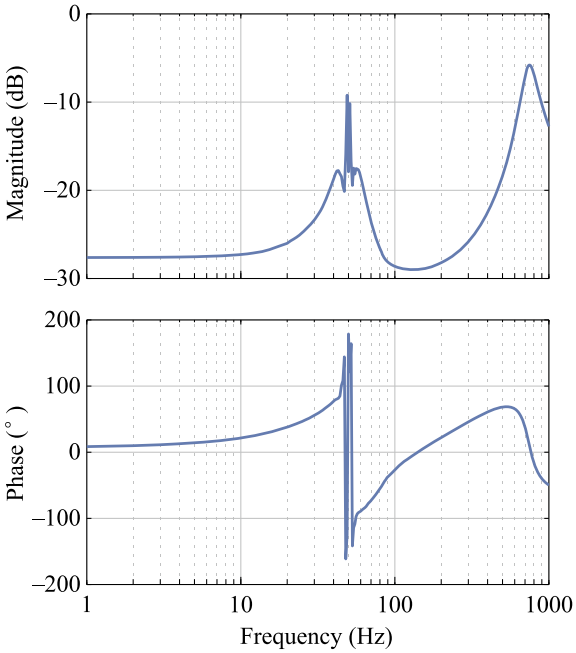

Fig. 8.21 Damping characteristics of a 3.15 MW PV uniy (Type E)

Chapter 9
Impedance Model and Characteristic Analysis of SVG

The cascaded H-bridge topology (star connection) is commonly used for medium- and high-voltage SVGs. Compared with the MMC topology (double-star connection) introduced in Chap. 4, the arm circulating current and circulating current control are not included in the SVG (star-connection MMC). According to different operation requirements, SVG will operate in various modes, such as reactive power control mode and AC voltage control mode, which leads to the difference of the control strategies in SVG and MMC.

In this chapter, first, the operation principle and control strategies of SVG are introduced. Then, based on the frequency-domain steady-state operating point and considering the reactive power control mode and AC voltage control mode, the AC port impedance model of SVG is established. Moreover, the dominant factors of the impedance characteristics in different frequency bands under two operation modes are analyzed separately, and the frequency band division method of SVG is proposed. The frequency-band overlapping effect of multiple control loops and the negative damping characteristics of each frequency band are clarified. Finally, based on the CHIL simulation platform, the broadband impedances of different types of SVGs are scanned, and the typical values of each frequency band are given.

9.1 Operation Principle and Control Strategy

9.1.1 Topology

Compared with the delta-connected configuration, as mentioned in Chap. 4, the star-connected configuration possesses a higher output voltage level for the same number of submodules (SMs) in each arm. The star-connected configuration is thus mainly used in SVG, as shown in Fig. 9.1.

© China Electric Power Press 2023

W. Wang et al., *Analysis and Mitigation of Broadband Oscillation in Renewable Energy Generation and AC/DC Transmission Systems*,
https://doi.org/10.1007/978-981-99-1568-2_9

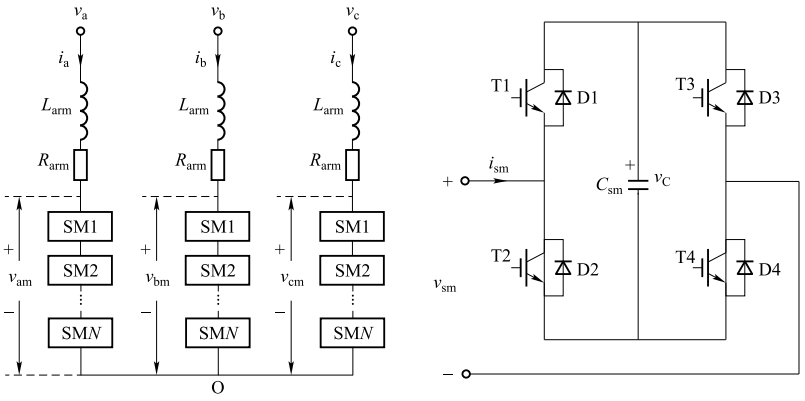

Fig. 9.1 The typical topology of SVG

In Fig. 9.1(a), v_l, i_l ($l = \mathrm{a}, \mathrm{b}, \mathrm{c}$) are the three-phase AC voltages and currents respectively. $v_{l\mathrm{m}}$ are the three-phase arm voltages. L_{arm}, R_{arm} are the arm inductor and resistor respectively. N is the number of SMs in each arm. The full-bridge submodule (FBSM), as shown in Fig. 9.1(b), is applied in SVG, which can output three voltage levels: v_{C}, 0, $-v_{\mathrm{C}}$.

9.1.2 *Operation Principle*

The operating principle of each arm in SVG is similar to MMC in Chap. 4. The SM capacitor voltage balancing algorithm is utilized to maintain voltage balancing between each SM, i.e., the SM capacitor voltages in the same arm can be considered equal. According to Chap. 4, an equivalent SM can be used to replace N SMs in each arm, and then the averaged model of SVG is established, as shown in Fig. 9.2.

In Fig. 9.2, each arm consists of a controlled voltage source, a controlled current source, and an arm capacitor. C_{eq} is the arm capacitor in the averaged model, and the capacitance is equal to $1/N$ of that of the SM capacitor C_{sm}, i.e., $C_{\mathrm{eq}} = C_{\mathrm{sm}}/N$. The three-phase arm capacitor voltages $v_{Cl\mathrm{m}}$ are equal to N times the single SM capacitor voltage in the corresponding arm, respectively. The controlled current source represents the arm capacitor current, which is equal to the AC current multiplied by the arm modulation signal, i.e., $m_{l\mathrm{m}}i_l$. The controlled voltage source represents the arm voltage, which is equal to the arm capacitor voltage multiplied by the arm modulation signal, i.e., $m_{l\mathrm{m}}v_{Cl\mathrm{m}}$.

The three-phase arm capacitor voltages $v_{Cl\mathrm{m}}$ and arm capacitor currents $m_{l\mathrm{m}}i_l$ satisfy

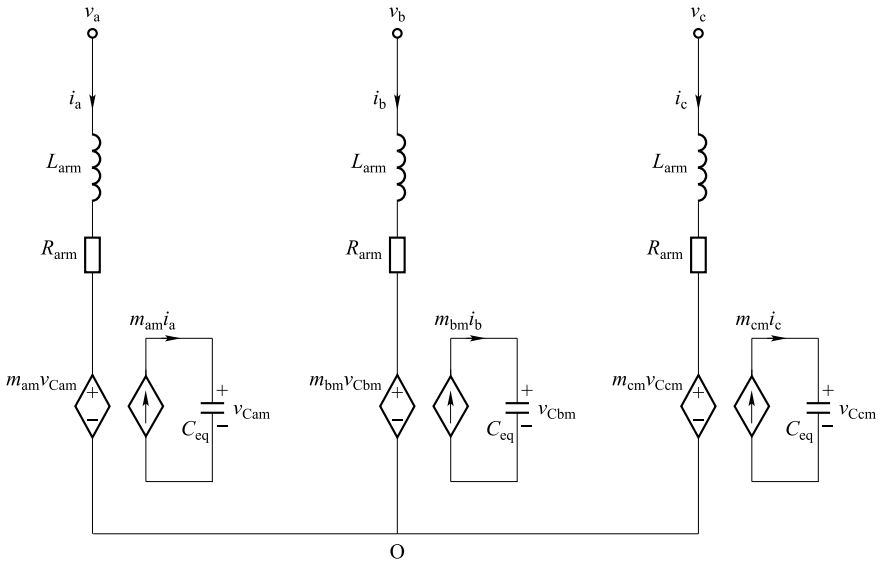

Fig. 9.2 The averaged model of SVG

$$C_{\text{eq}}\frac{\mathrm{d}v_{Cl\text{m}}}{\mathrm{d}t} = m_{l\text{m}}i_l \tag{9.1}$$

According to the relationship between $m_{l\text{m}}v_{Cl\text{m}}$ and there-phase AC current i_l, the time-domain model of the three-phase arm circuits can be expressed as

$$m_{l\text{m}}v_{Cl\text{m}} + L_{\text{arm}}\frac{\mathrm{d}i_l}{\mathrm{d}t} + R_{\text{arm}}i_l = v_l - v_{\text{O}} \tag{9.2}$$

where v_{O} is the AC neutral voltage, expressed as

$$v_{\text{O}} = -\frac{1}{3}\sum_{l=\text{a,b,c}} m_{l\text{m}}v_{Cl\text{m}} \tag{9.3}$$

It can be seen that v_{O} is the zero sequence component of the three-phase arm voltages.

9.1.3 Control Strategy

The function of SVG is to compensate for reactive power and support the grid voltage. The PLL is used in SVG to track the voltage phase of the AC grid. The reactive power control or AC voltage control is applied as the outer-loop control strategy, and the AC

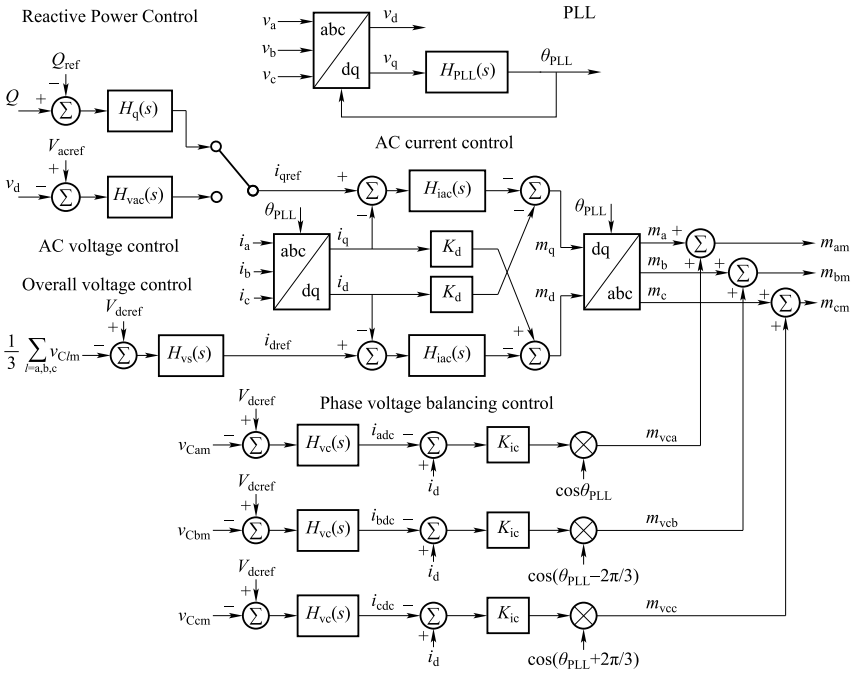

Fig. 9.3 The typical control diagram of SVG

current control is adopted in the inner-loop control strategy. In addition, the overall voltage control is used to regulate the overall capacitor voltages in SVG around their rated values, and the phase (clustered) voltage balancing control is used to maintain the capacitor voltage balancing among three-phase arms. The typical control diagram is shown in Fig. 9.3.

As seen in Fig. 9.3, the reactive power control or AC voltage control, overall voltage control, and AC current control are performed in SCF, and the PLL output angle θ_{PLL} provides the rotation reference angle for the Park transformation and inverse Park transformation.

SVG can operate in reactive power control mode and AC voltage control mode according to different operation requirements. In reactive power control mode, SVG supplies reactive power to the grid according to the reference. The reactive power Q and its reference Q_{ref} are fed into the reactive power controller to generate the q-axis current reference i_{qref}. Alternatively, in AC voltage control mode, SVG regulates the grid voltage according to the reference. The d-axis voltage v_{d} and the AC voltage reference V_{acref} are fed into the AC voltage controller to generate the q-axis current reference i_{qref}. In addition, the overall voltage controller regulates the average value of the three-phase arm capacitor voltages v_{Clm} to track the DC voltage reference V_{dcref}, and generates the d-axis current reference i_{dref}. In the figure, $H_{\mathrm{q}}(s)$ is the transfer function of the reactive power controller, expressed as $H_{\mathrm{q}}(s) = K_{\mathrm{qep}} + K_{\mathrm{qei}}/s.K_{\mathrm{qep}}$,

K_{qei} are the corresponding proportional and integral coefficients respectively. $H_{\mathrm{vac}}(s)$ is the transfer function of the AC voltage controller, expressed as $H_{\mathrm{vac}}(s) = K_{\mathrm{vacp}} + K_{\mathrm{vaci}}/s$. K_{vacp}, K_{vaci} are the corresponding proportional and integral coefficients respectively. $H_{\mathrm{vs}}(s)$ is the transfer function of the overall voltage controller, expressed as $H_{\mathrm{vs}}(s) = K_{\mathrm{vsp}} + K_{\mathrm{vsi}}/s$. K_{vsp}, K_{vsi} are the corresponding proportional and integral coefficients respectively. V_{dcref} is equal to the sum of the rated capacitor voltages of the N SMs in one arm.

Then, the dq-axis currents i_{d}, i_{q} and their references i_{dref}, i_{qref} are fed into the AC current controller to generate the dq-axis modulation signal m_{d}, m_{q}. After the inverse Park transformation, the three-phase AC modulation signals m_l are generated. In the figure, $H_{\mathrm{iac}}(s)$ is the transfer function of the AC current controller, expressed as $H_{\mathrm{iac}}(s) = K_{\mathrm{iacp}} + K_{\mathrm{iaci}}/s$. K_{iacp}, K_{iaci} are the corresponding proportional and integral coefficients respectively. K_{d} is the decoupling coefficient of the AC current control.

Besides, the phase voltage balancing controller regulates the arm capacitor voltage $v_{Cl\mathrm{m}}$ in each phase to track the DC voltage reference V_{dcref} separately, generating the current compensation quantity $i_{l\mathrm{dc}}$. The differences between i_{d} and three-phase current compensation quantities $i_{l\mathrm{dc}}$ are first multiplied by the current proportional factor K_{ic}, and then multiplied by $\cos\theta_{\mathrm{PLL}}$, $\cos(\theta_{\mathrm{PLL}} - 2\pi/3)$, $\cos(\theta_{\mathrm{PLL}} + 2\pi/3)$, respectively, generating the three-phase voltage balancing modulation signals $m_{\mathrm{vc}l}$. In the figure, $H_{\mathrm{vc}}(s)$ is the transfer function of the phase voltage balancing controller, expressed as $H_{\mathrm{vc}}(s) = K_{\mathrm{vcp}} + K_{\mathrm{vci}}/s$. K_{vcp}, K_{vci} are the corresponding proportional and integral coefficients respectively.

Finally, the sum of the three-phase AC modulation signals m_l and voltage balancing modulation signals $m_{\mathrm{vc}l}$ forms the three-phase arm modulation signals $m_{l\mathrm{m}}$, which can be expressed as

$$m_{l\mathrm{m}} = m_l + m_{\mathrm{vc}l} \tag{9.4}$$

9.2 Frequency-Domain Modeling of Steady-State Operation

This section analyzes the steady-state harmonic characteristics of SVG, and establishes the frequency-domain steady-state model of the main circuit.

9.2.1 Frequency-Domain Characteristic Analysis of Steady-State Operating Point

Compared with MMC as mentioned in Chap. 4, only one arm per phase is used in SVG, and the arm current is the AC current i_l without the circulating current among three phases. In addition, the arm voltage $m_{l\mathrm{m}}v_{Cl\mathrm{m}}$ is directly connected to the AC circuit, so the modulation signal $m_{l\mathrm{m}}$ contains a fundamental component without the DC and second harmonic components.

The fundamental component of i_l multiplying the fundamental component of $m_{l\mathrm{m}}$ leads to a second harmonic component in the arm capacitor voltage $v_{Cl\mathrm{m}}$, apart from the DC component. The second harmonic component of $v_{Cl\mathrm{m}}$ multiplying the fundamental component of $m_{l\mathrm{m}}$ leads to a third harmonic component (zero sequence) in the arm voltage $m_{l\mathrm{m}}v_{Cl\mathrm{m}}$. Since three is no zero-sequence current path in SVG (star connection), the third harmonic component of the arm voltage is canceled by the AC neutral voltage. The third harmonic component will not be introduced into the AC current, arm capacitor voltage, and arm modulation signal, so SVG does not contain higher-order harmonic components than the third.

Without loss of generality, the steady-state harmonic components within $\pm 3f_1$ in the AC current, arm capacitor voltage, and arm modulation signal are considered. The steady-state harmonic components of the SVG quantities are arranged in the following steady-state frequency order

$$\left[-3f_1,\ -2f_1,\ -f_1,\ 0,\ f_1,\ 2f_1,\ 3f_1\right]^{\mathrm{T}} \tag{9.5}$$

Taking the phase-a as an example, the steady-state vectors of the AC current, arm capacitor voltage, and arm modulation signal can be expressed as

$$\begin{cases} \boldsymbol{I}_{\mathrm{a}} = \left[0,\ 0,\ \boldsymbol{I}_1^*,\ 0,\ \boldsymbol{I}_1,\ 0,\ 0\right]^{\mathrm{T}} \\ \boldsymbol{V}_{\mathrm{Cam}} = \left[0,\ \boldsymbol{V}_{\mathrm{Cam2}}^*,\ 0,\ \boldsymbol{V}_{\mathrm{Cam0}},\ 0,\ \boldsymbol{V}_{\mathrm{Cam2}},\ 0\right]^{\mathrm{T}} \\ \boldsymbol{M}_{\mathrm{am}} = \left[0,\ 0,\ \boldsymbol{M}_{\mathrm{am1}}^*,\ 0,\ \boldsymbol{M}_{\mathrm{am1}},\ 0,\ 0\right]^{\mathrm{T}} \end{cases} \tag{9.6}$$

where $\boldsymbol{I}_k = I_k \mathrm{e}^{\mathrm{j}\varphi_{ik}}$, $\boldsymbol{V}_{\mathrm{Cam}k} = V_k \mathrm{e}^{\mathrm{j}\varphi_{\mathrm{v}k}}$, $\boldsymbol{M}_{\mathrm{am}k} = M_k \mathrm{e}^{\mathrm{j}\varphi_{\mathrm{m}k}}$ are the steady-state harmonic components at kf_1 ($k = 0, \pm 1, \pm 2, \pm 3$). The component at $-kf_1$ is equal to the conjugate of the component at kf_1, i.e., $\boldsymbol{I}_{(-k)} = \boldsymbol{I}_k^*$, $\boldsymbol{V}_{\mathrm{Cam}(-k)} = \boldsymbol{V}_{\mathrm{Cam}k}^*$, and $\boldsymbol{M}_{\mathrm{am}(-k)} = \boldsymbol{M}_{\mathrm{am}k}^*$.

The phase-sequence relationship of the steady-state quantities among three phases can be expressed by defining the following modulo-3 function

$$\mathrm{mod}(k, 3) = \begin{cases} +1, & k = 3n+1 \\ -1, & k = 3n+2 \\ 0, & k = 3n \end{cases} \quad (n = 0, \pm 1) \tag{9.7}$$

where +1 indicates positive sequence, i.e., the component at $(3n+1)f_1$ is in positive sequence. −1 indicates negative sequence, i.e., the component at $(3n+2)f_1$ is in negative sequence. 0 indicates zero sequence, i.e., the component at $3nf_1$ is in zero sequence.

According to the phase-sequence relationship, the steady-state vectors of the arm currents, capacitor voltages, and modulation signals in each arm of phase b and phase c can be obtained.

$$\begin{cases} \boldsymbol{I}_{\mathrm{b}} = \boldsymbol{D}\boldsymbol{I}_{\mathrm{a}},\ \boldsymbol{V}_{\mathrm{Cbm}} = \boldsymbol{D}\boldsymbol{V}_{\mathrm{Cam}},\ \boldsymbol{M}_{\mathrm{bm}} = \boldsymbol{D}\boldsymbol{M}_{\mathrm{am}} \\ \boldsymbol{I}_{\mathrm{c}} = \boldsymbol{D}^{*}\boldsymbol{I}_{\mathrm{a}},\ \boldsymbol{V}_{\mathrm{Ccm}} = \boldsymbol{D}^{*}\boldsymbol{V}_{\mathrm{Cam}},\ \boldsymbol{M}_{\mathrm{cm}} = \boldsymbol{D}^{*}\boldsymbol{M}_{\mathrm{am}} \end{cases} \tag{9.8}$$

where $\boldsymbol{D}$ is the phase-sequence coefficient matrix of the steady-state vectors, expressed as

$$\boldsymbol{D} = \mathrm{diag}\left[\{\mathrm{e}^{-\mathrm{j}2k\pi/3}\}\big|_{k=-3\sim 3} \right] \tag{9.9}$$

9.2.2 Frequency-Domain Steady-State Model of Main Circuit

Based on the steady-state vectors of the AC current, arm capacitor voltage, and arm modulation signal of SVG, the frequency-domain steady-state model of the arm circuit can be obtained by transforming Eqs. (9.1) and (9.2) to the frequency domain.

$$\boldsymbol{Y}_{\mathrm{Ceq0}}\boldsymbol{V}_{Cl\mathrm{m}} = \boldsymbol{M}_{l\mathrm{m}} \otimes \boldsymbol{I}_{l} \tag{9.10}$$

$$\boldsymbol{Z}_{\mathrm{Larm0}}\boldsymbol{I}_{l} = \boldsymbol{V}_{l} - \boldsymbol{V}_{\mathrm{O}} - \boldsymbol{M}_{l\mathrm{m}} \otimes \boldsymbol{V}_{Cl\mathrm{m}} \tag{9.11}$$

where $\boldsymbol{V}_{\mathrm{O}}$ is the steady-state vector of the AC neural voltage, canceling the zero-sequence third harmonic component of the arm voltage $\boldsymbol{M}_{l\mathrm{m}} \otimes \boldsymbol{V}_{Cl\mathrm{m}}$.

$\boldsymbol{V}_{l}$ are the steady-state vectors of the three-phase AC voltages. Taking phase a as an example, and the expression of $\boldsymbol{V}_{\mathrm{a}}$ is given as

$$\boldsymbol{V}_{\mathrm{a}} = \left[0,\ 0,\ V_1/2,\ 0,\ V_1/2,\ 0,\ 0\right]^{\mathrm{T}} \tag{9.12}$$

where V_1 is the amplitude of the fundamental component of AC voltage.

$\boldsymbol{Z}_{\mathrm{Larm0}}$ and $\boldsymbol{Y}_{\mathrm{Ceq0}}$ are the impedance of the arm inductor and the admittance of the arm capacitor in the steady-state frequency order respectively, which are

$$\boldsymbol{Z}_{\mathrm{Larm0}} = R_{\mathrm{arm}}\boldsymbol{U} + \mathrm{j}2\pi L_{\mathrm{arm}} \cdot \mathrm{diag}\left[-3f_1,\ -2f_1,\ -f_1,\ 0,\ f_1,\ 2f_1,\ 3f_1\right] \tag{9.13}$$

$$\boldsymbol{Y}_{\mathrm{Ceq0}} = \mathrm{j}2\pi C_{\mathrm{eq}} \cdot \mathrm{diag}\left[-3f_1,\ -2f_1,\ -f_1,\ 0,\ f_1,\ 2f_1,\ 3f_1\right] \tag{9.14}$$

Table 9.1 The frequency-domain characteristics of the steady-state vectors in SVG

Steady-State Vectors	Frequency
$\boldsymbol{I}_l$	$\pm f_1$
$\boldsymbol{V}_{\mathrm{C}l\mathrm{m}}$	DC
	$\pm 2f_1$
$\boldsymbol{M}_{l\mathrm{m}}$	$\pm f_1$

In order to use the scalar product instead of convolution in Eqs. (9.10) and (9.11), the steady-state vectors of the three-phase arm modulation signals need to be expanded into matrices. Using the vector $\boldsymbol{M}_{\mathrm{am}}$ as an example, the expression of the expanded steady-state matrix is given as

$$\boldsymbol{M}_{\mathrm{am}} = \begin{bmatrix} 0 & \boldsymbol{M}^*_{\mathrm{am1}} & 0 & 0 & 0 & 0 & 0 \\ \boldsymbol{M}_{\mathrm{am1}} & 0 & \boldsymbol{M}^*_{\mathrm{am1}} & 0 & 0 & 0 & 0 \\ 0 & \boldsymbol{M}_{\mathrm{am1}} & 0 & \boldsymbol{M}^*_{\mathrm{am1}} & 0 & 0 & 0 \\ 0 & 0 & \boldsymbol{M}_{\mathrm{am1}} & 0 & \boldsymbol{M}^*_{\mathrm{am1}} & 0 & 0 \\ 0 & 0 & 0 & \boldsymbol{M}_{\mathrm{am1}} & 0 & \boldsymbol{M}^*_{\mathrm{am1}} & 0 \\ 0 & 0 & 0 & 0 & \boldsymbol{M}_{\mathrm{am1}} & 0 & \boldsymbol{M}^*_{\mathrm{am1}} \\ 0 & 0 & 0 & 0 & 0 & \boldsymbol{M}_{\mathrm{am1}} & 0 \end{bmatrix} \tag{9.15}$$

To sum up, the frequency-domain characteristics of the steady-state vectors in SVG are listed in Table 9.1. The steady-state vectors of the AC currents and arm modulation signals contain the components at $\pm f_1$. The steady-state vectors of the arm capacitor voltages contain the components at dc and $\pm 2f_1$.

9.3 Small-Signal Impedance Modeling in Frequency Domain

This section carries out the small-signal impedance modeling of SVG in the frequency domain. First, a small-signal perturbation is superimposed on the AC voltage at the steady-state operating point, and the frequency-domain distribution characteristics of the voltage, current, and modulation signal are elaborated. Then, the frequency-domain small-signal models of the main circuit and control loops are developed, respectively. Finally, the small-signal impedance model of SVG is established by calculating the response of the AC current to the AC voltage perturbation.

9.3.1 Small-Signal Frequency-Domain Characteristic Analysis

After injecting a small-signal perturbation at the steady-state operating point, the multiplication between the AC current or arm capacitor voltage and the arm modulation signal will produce small-signal responses at the sidebands around steady-state harmonic frequencies. The small-signal transfer path and frequency response relationship of SVG are shown in Fig. 9.4.

The positive-sequence small-signal perturbation at f_p is superimposed on the AC voltage at the steady-state operating point. The difference between the small-signal component of the AC voltage $\hat{\boldsymbol{v}}_l$ at f_p and the arm voltage drops on the arm inductor, which leads to a small-signal response of the AC current $\hat{\boldsymbol{i}}_l$ at f_p. The small-signal component of $\hat{\boldsymbol{i}}_l$ at f_p multiplying the steady-state components of the arm modulation signal $\boldsymbol{M}_{l\mathrm{m}}$ at $\pm f_1$ leads to small-signal responses of the arm capacitor voltage $\hat{\boldsymbol{v}}_{Cl\mathrm{m}}$ at $f_\mathrm{p} \pm f_1$. The small-signal components of $\hat{\boldsymbol{v}}_{Cl\mathrm{m}}$ at $f_\mathrm{p} \pm f_1$ multiplying the steady-state components of $\boldsymbol{M}_{l\mathrm{m}}$ at $\pm f_1$ leads to small-signal responses of the arm voltage at f_p and $f_\mathrm{p} \pm 2f_1$.

The difference between $\hat{\boldsymbol{v}}_l$ and the small-signal components of the arm voltage dropping on the arm inductor leads to small-signal responses of $\hat{\boldsymbol{i}}_l$ at f_p and $f_\mathrm{p} - 2f_1$. Since there is no zero-sequence current path in SVG, the small-signal component of $\hat{\boldsymbol{i}}_l$ at $f_\mathrm{p} + 2f_1$ will not be produced by the small-signal component of the arm voltage at $f_\mathrm{p} + 2f_1$.

The small-signal component of $\hat{\boldsymbol{i}}_l$ at $f_\mathrm{p} - 2f_1$ multiplying the steady-state components of $\boldsymbol{M}_{l\mathrm{m}}$ at $\pm f_1$ leads to small-signal responses of $\hat{\boldsymbol{v}}_{Cl\mathrm{m}}$ at $f_\mathrm{p} - f_1$ and $f_\mathrm{p} - 3f_1$. The small-signal components of $\hat{\boldsymbol{v}}_{Cl\mathrm{m}}$ at $f_\mathrm{p} - 3f_1$ again multiplying the steady-state components of $\boldsymbol{M}_{l\mathrm{m}}$ at $\pm f_1$ leads to a small-signal response of the arm voltage at $f_\mathrm{p} - 4f_1$. The small-signal component of the arm voltage at $f_\mathrm{p} - 4f_1$ is in zero sequence, so the small-signal component of $\hat{\boldsymbol{i}}_l$ at $f_\mathrm{p} - 4f_1$ will not be produced. In conclusion, no higher-frequency small-signal components will be produced in SVG.

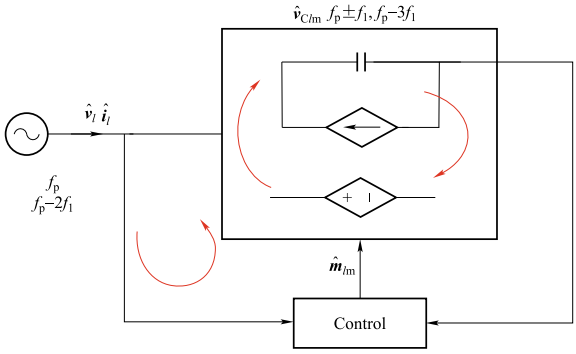

Fig. 9.4 The small-signal transfer path and frequency response relationship of SVG

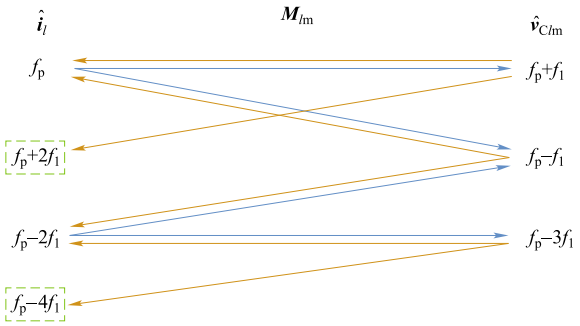

Fig. 9.5 The small-signal transfer path and frequency response relationship of SVG

The production process of the small-signal components at each frequency in SVG is shown in Fig. 9.5. The blue arrows represent the multiplication between the small-signal component of $\hat{\boldsymbol{i}}_l$ and the steady-state components of $\boldsymbol{M}_{l\mathrm{m}}$ at $\pm f_1$. The yellow arrows represent the multiplication between the small-signal component of $\hat{\boldsymbol{v}}_{C\mathrm{m}}$ and the steady-state components of $\boldsymbol{M}_{l\mathrm{m}}$ at $\pm f_1$. The AC current does not contain the zero-sequence component at $f_\mathrm{p}+2f_1$ and $f_\mathrm{p}-4f_1$.

Furthermore, in the effect of the control loops, the small-signal components of the modulation signal $\hat{\boldsymbol{m}}_{l\mathrm{m}}$ at f_p and $f_\mathrm{p}-2f_1$ are produced. The multiplication between $\hat{\boldsymbol{m}}_{l\mathrm{m}}$ and the steady-state components of the arm capacitor voltage $\boldsymbol{V}_{C\mathrm{m}}$ or the AC current $\boldsymbol{I}_l$ leads to small-signal responses of the AC current $\hat{\boldsymbol{i}}_l$ or arm capacitor voltage $\hat{\boldsymbol{v}}_{C\mathrm{m}}$ as well. The balance will be finally achieved after repeating the above process.

In summary, the frequency-domain characteristics of the small-signal vectors in SVG are listed in Table 9.2. The small-signal vectors of the arm currents and modulation signals contain the components at f_p and $f_\mathrm{p}-2f_1$. The small-signal vectors of the arm capacitor voltages contain the components at $f_\mathrm{p}\pm f_1$ and $f_\mathrm{p}-3f_1$.

In order to describe the frequency-domain small-signal characteristics, the small-signal components of SVG quantities are arranged in the following small-signal frequency order.

$$\left[\, f_\mathrm{p}-3f_1,\ f_\mathrm{p}-2f_1,\ f_\mathrm{p}-f_1,\ f_\mathrm{p},\ f_\mathrm{p}+f_1,\ f_\mathrm{p}+2f_1,\ f_\mathrm{p}+3f_1 \,\right]^\mathrm{T} \tag{9.16}$$

Table 9.2 The frequency-domain characteristics of the small-signal vectors in SVG

Small-Signal Vectors	Frequency
$\hat{\boldsymbol{i}}_l$	f_p
	$f_\mathrm{p}-2f_1$
$\hat{\boldsymbol{v}}_{C\mathrm{m}}$	$f_\mathrm{p}+f_1$
	$f_\mathrm{p}-f_1$
	$f_\mathrm{p}-3f_1$
$\hat{\boldsymbol{m}}_{l\mathrm{m}}$	f_p
	$f_\mathrm{p}-2f_1$

Taking the phase-a as an example, the small-signal vectors of the AC current, arm capacitor voltage, and arm modulation signal can be expressed as

$$\begin{cases} \hat{\boldsymbol{i}}_{\mathrm{a}} = \left[0,\ \hat{\boldsymbol{i}}_{\mathrm{p\text{-}2}},\ 0,\ \hat{\boldsymbol{i}}_{\mathrm{p}},\ 0,\ 0,\ 0\right]^{\mathrm{T}} \\ \hat{\boldsymbol{v}}_{\mathrm{Cam}} = \left[\hat{\boldsymbol{v}}_{\mathrm{Cam\text{-}3}},\ 0,\ \hat{\boldsymbol{v}}_{\mathrm{Cam\text{-}1}},\ 0,\ \hat{\boldsymbol{v}}_{\mathrm{Cam+1}},\ 0,\ 0\right]^{\mathrm{T}} \\ \hat{\boldsymbol{m}}_{\mathrm{am}} = \left[0,\ \hat{\boldsymbol{m}}_{\mathrm{am\text{-}2}},\ 0,\ \hat{\boldsymbol{m}}_{\mathrm{am0}},\ 0,\ 0,\ 0\right]^{\mathrm{T}} \end{cases} \tag{9.17}$$

where each component $\hat{\boldsymbol{i}}_{\mathrm{p}k}$, $\hat{\boldsymbol{v}}_{\mathrm{Cam}k}$, $\hat{\boldsymbol{m}}_{\mathrm{am}k}$ $(k = 0, \pm1, \pm2, \pm3)$ represents the small-signal component at $f_{\mathrm{p}} + kf_1$.

For the positive-sequence perturbation at f_{p}, this angle is delayed by $2\pi/3$ among three phases. Combined with the phases of the steady-state components at kf_1, the phase-sequence relationship of a small-signal component at $f_{\mathrm{p}} + kf_1$ changes, which can be expressed by defining the following modulo-3 function

$$\mathrm{mod}(k+1, 3) = \begin{cases} +1, & k = 3n \\ -1, & k = 3n+1 \\ 0, & k = 3n+2 \end{cases} \quad (n = 0, \pm1) \tag{9.18}$$

The small-signal component at $f_{\mathrm{p}} + 3nf_1$ is in positive sequence, the small-signal component at $f_{\mathrm{p}} + (3n+1)f_1$ is in negative sequence, and the small-signal component at $f_{\mathrm{p}} + (3n+2)f_1$ is in zero sequence.

According to the phase-sequence relationship, the small-signal vectors of the AC currents, arm capacitor voltages, and arm modulation signals in phase b and phase c can be obtained.

$$\begin{cases} \hat{\boldsymbol{i}}_{\mathrm{b}} = \boldsymbol{D}_{\mathrm{p}}\hat{\boldsymbol{i}}_{\mathrm{a}},\ \hat{\boldsymbol{v}}_{\mathrm{Cbm}} = \boldsymbol{D}_{\mathrm{p}}\hat{\boldsymbol{v}}_{\mathrm{Cam}},\ \hat{\boldsymbol{m}}_{\mathrm{bm}} = \boldsymbol{D}_{\mathrm{p}}\hat{\boldsymbol{m}}_{\mathrm{am}} \\ \hat{\boldsymbol{i}}_{\mathrm{c}} = \boldsymbol{D}_{\mathrm{p}}^{*}\hat{\boldsymbol{i}}_{\mathrm{a}},\ \hat{\boldsymbol{v}}_{\mathrm{Ccm}} = \boldsymbol{D}_{\mathrm{p}}^{*}\hat{\boldsymbol{v}}_{\mathrm{Cam}},\ \hat{\boldsymbol{m}}_{\mathrm{cm}} = \boldsymbol{D}_{\mathrm{p}}^{*}\hat{\boldsymbol{m}}_{\mathrm{am}} \end{cases} \tag{9.19}$$

where $\boldsymbol{D}_{\mathrm{p}}$ is the phase-sequence coefficient matrix of the small-signal vectors, expressed as

$$\boldsymbol{D}_{\mathrm{p}} = \mathrm{diag}\left[\left\{\mathrm{e}^{-\mathrm{j}2(k+1)\pi/3}\right\}\Big|_{k=-3\sim3}\right] \tag{9.20}$$

9.3.2 Frequency-Domain Small-Signal Model

9.3.2.1 Small-Signal Model of Main Circuit

In the following of this chapter, $\boldsymbol{I}_l$, $\boldsymbol{V}_{Cl\mathrm{m}}$, $\boldsymbol{M}_{l\mathrm{m}}$ represent the steady-state matrices, and the convolution is replaced with the scalar product. By transforming Eqs. (9.1)

and (9.2) to the frequency domain, the small-signal model of the main circuit can be obtained.

$$\hat{\boldsymbol{v}}_{Cl\mathrm{m}} = \boldsymbol{Z}_{\mathrm{Ceq}}\left(\boldsymbol{I}_l\hat{\boldsymbol{m}}_{l\mathrm{m}} + \boldsymbol{M}_{l\mathrm{m}}\hat{\boldsymbol{i}}_l\right) \tag{9.21}$$

$$\hat{\boldsymbol{i}}_l = -\boldsymbol{Y}_{\mathrm{Larm}}\left(\boldsymbol{V}_{Cl\mathrm{m}}\hat{\boldsymbol{m}}_{l\mathrm{m}} + \boldsymbol{M}_{l\mathrm{m}}\hat{\boldsymbol{v}}_{Cl\mathrm{m}} - \hat{\boldsymbol{v}}_l\right) \tag{9.22}$$

where $\hat{\boldsymbol{v}}_l$ are the small-signal vectors of the three-phase AC voltages, expressed as

$$\hat{\boldsymbol{v}}_l = \left[0,\ \hat{\boldsymbol{v}}_{\mathrm{p\text{-}2}},\ 0,\ \hat{\boldsymbol{v}}_{\mathrm{p}},\ 0,\ 0,\ 0\right]^{\mathrm{T}} \tag{9.23}$$

where $\hat{\boldsymbol{v}}_{\mathrm{p}}$ and $\hat{\boldsymbol{v}}_{\mathrm{p\text{-}2}}$ are the small-signal components of AC voltage at f_{p} and $f_{\mathrm{p}}-2f_1$ respectively.

$\boldsymbol{Z}_{\mathrm{Ceq}}$ is the admittance of the arm capacitor in the small-signal frequency order, expressed as

$$\begin{aligned}\boldsymbol{Z}_{\mathrm{Ceq}} = \frac{1}{\mathrm{j}2\pi C_{\mathrm{eq}}}\cdot\mathrm{diag}\Bigg[&\frac{1}{f_{\mathrm{p}}-3f_1},\ \frac{1}{f_{\mathrm{p}}-2f_1},\ \frac{1}{f_{\mathrm{p}}-f_1},\ \frac{1}{f_{\mathrm{p}}},\\ &\frac{1}{f_{\mathrm{p}}+f_1},\ \frac{1}{f_{\mathrm{p}}+2f_1},\ \frac{1}{f_{\mathrm{p}}+3f_1}\Bigg]\end{aligned} \tag{9.24}$$

$\boldsymbol{Y}_{\mathrm{Larm}}$ is the admittance of the arm inductor in the small-signal frequency order. The diagonal elements at $f_{\mathrm{p}}-f_1$ and $f_{\mathrm{p}}+2f_1$ are zero, indicating there is no zero-sequence current path on the AC side of SVG. The function of the small-signal vector of AC neutral voltage $\hat{\boldsymbol{v}}_{\mathrm{O}}$ can be replaced by $\boldsymbol{Y}_{\mathrm{Larm}}$, which has been dropped from Eq. (9.22). The expression of $\boldsymbol{Y}_{\mathrm{Larm}}$ is given as

$$\begin{aligned}\boldsymbol{Y}_{\mathrm{Larm}} = \mathrm{diag}\Bigg[&\frac{1}{R_{\mathrm{arm}}+\mathrm{j}2\pi(f_{\mathrm{p}}-3f_1)L_{\mathrm{arm}}},\ \frac{1}{R_{\mathrm{arm}}+\mathrm{j}2\pi(f_{\mathrm{p}}-2f_1)L_{\mathrm{arm}}},\ 0,\\ &\frac{1}{R_{\mathrm{arm}}+\mathrm{j}2\pi f_{\mathrm{p}}L_{\mathrm{arm}}},\ \frac{1}{R_{\mathrm{arm}}+\mathrm{j}2\pi(f_{\mathrm{p}}+f_1)L_{\mathrm{arm}}},\\ &0,\ \frac{1}{R_{\mathrm{arm}}+\mathrm{j}2\pi(f_{\mathrm{p}}+3f_1)L_{\mathrm{arm}}}\Bigg]\end{aligned} \tag{9.25}$$

9.3.2.2 Small-Signal Model of Control Loops

SVG can operate in reactive power control mode and AC voltage control mode. Figure 9.3 shows the typical control diagram of SVG. The small-signal model of the control loops is established, taking into account the two operation modes respectively.

1. **Reactive Power Control Mode**

Firstly, after injecting the positive-sequence perturbation on the AC voltage, the small-signal vector of the reactive power $\hat{\boldsymbol{q}}$ is produced. The small-signal response of the q-axis current reference $\hat{\boldsymbol{i}}_{\text{qref}}$ is introduced by the reactive power controller $H_{\text{q}}(s)$, and the small-signal response of the d-axis current reference $\hat{\boldsymbol{i}}_{\text{dref}}$ is introduced by the overall voltage controller $H_{\text{vs}}(s)$. Next, the small-signal vectors of the three-phase AC currents $\hat{\boldsymbol{i}}_l$ and PLL output angle $\hat{\boldsymbol{\theta}}_{\text{PLL}}$ lead to small-signal responses of the dq-axis currents $\hat{\boldsymbol{i}}_{\text{d}}$, $\hat{\boldsymbol{i}}_{\text{q}}$. Then, $\hat{\boldsymbol{i}}_{\text{d}}$, $\hat{\boldsymbol{i}}_{\text{q}}$ and their references $\hat{\boldsymbol{i}}_{\text{dref}}$, $\hat{\boldsymbol{i}}_{\text{qref}}$ are fed into the AC current controller $H_{\text{iac}}(s)$, leading to small-signal responses of the dq-axis modulation signal $\hat{\boldsymbol{m}}_{\text{d}}$, $\hat{\boldsymbol{m}}_{\text{q}}$. Finally, the small-signal vectors of the three-phase AC modulation signals $\hat{\boldsymbol{m}}_l$ are generated after the inverse Park transformation. Taking phase a as an example, the expression of $\hat{\boldsymbol{m}}_{\text{a}}$ is

$$\hat{\boldsymbol{m}}_{\text{a}} = \boldsymbol{G}_1\boldsymbol{D}_1\hat{\boldsymbol{i}}_{\text{a}} + \boldsymbol{G}_2\boldsymbol{D}_2\hat{\boldsymbol{v}}_{\text{a}} + \boldsymbol{G}_3\boldsymbol{D}_3\hat{\boldsymbol{v}}_{\text{Cam}} \tag{9.26}$$

where $\boldsymbol{G}_1$, $\boldsymbol{G}_2$, $\boldsymbol{G}_3$ are 7×7 matrices, and all other elements in the matrices are zero except for Eqs. (9.27) to (9.29).

$$\begin{cases} \boldsymbol{G}_1(2,2) = H_{\text{iac}}[\text{j}2\pi(f_{\text{p}} - f_1)]\left\{3V_1H_{\text{q}}[\text{j}2\pi(f_{\text{p}} - f_1)]/2 + 1\right\} + \text{j}K_{\text{d}} \\ \boldsymbol{G}_1(2,4) = -3V_1H_{\text{q}}(s)H_{\text{iac}}(s)/2 \\ \boldsymbol{G}_1(4,2) = -3V_1H_{\text{q}}(s)H_{\text{iac}}(s)/2 \\ \boldsymbol{G}_1(4,4) = H_{\text{iac}}[\text{j}2\pi(f_{\text{p}} - f_1)]\left\{3V_1H_{\text{q}}[\text{j}2\pi(f_{\text{p}} - f_1)]/2 + 1\right\} - \text{j}K_{\text{d}} \end{cases} \tag{9.27}$$

$$\begin{cases} \boldsymbol{G}_2(2,2) = -T_{\text{PLL}}[\text{j}2\pi(f_{\text{p}} - f_1)]\left[\left\{H_{\text{iac}}[\text{j}2\pi(f_{\text{p}} - f_1)] + \text{j}K_{\text{d}}\right\}\boldsymbol{I}_1^* + \boldsymbol{M}_{\text{am1}}^*\right] \\ \qquad\qquad - 3H_{\text{q}}[\text{j}2\pi(f_{\text{p}} - f_1)]H_{\text{iac}}[\text{j}2\pi(f_{\text{p}} - f_1)] \cdot \boldsymbol{I}_1/2 \\ \boldsymbol{G}_2(2,4) = T_{\text{PLL}}[\text{j}2\pi(f_{\text{p}} - f_1)]\left[\left\{H_{\text{iac}}[\text{j}2\pi(f_{\text{p}} - f_1)] + \text{j}K_{\text{d}}\right\}\boldsymbol{I}_1^* + \boldsymbol{M}_{\text{am1}}^*\right] \\ \qquad\qquad + 3H_{\text{q}}[\text{j}2\pi(f_{\text{p}} - f_1)]H_{\text{iac}}[\text{j}2\pi(f_{\text{p}} - f_1)] \cdot \boldsymbol{I}_1^*/2 \\ \boldsymbol{G}_2(4,2) = T_{\text{PLL}}[\text{j}2\pi(f_{\text{p}} - f_1)]\left[\left\{H_{\text{iac}}[\text{j}2\pi(f_{\text{p}} - f_1)] - \text{j}K_{\text{d}}\right\}\boldsymbol{I}_1 + \boldsymbol{M}_{\text{am1}}\right] \\ \qquad\qquad + 3H_{\text{q}}[\text{j}2\pi(f_{\text{p}} - f_1)]H_{\text{iac}}[\text{j}2\pi(f_{\text{p}} - f_1)] \cdot \boldsymbol{I}_1/2 \\ \boldsymbol{G}_2(4,4) = -T_{\text{PLL}}[\text{j}2\pi(f_{\text{p}} - f_1)]\left[\left\{H_{\text{iac}}[\text{j}2\pi(f_{\text{p}} - f_1)] - \text{j}K_{\text{d}}\right\}\boldsymbol{I}_1 + \boldsymbol{M}_{\text{am1}}\right] \\ \qquad\qquad - 3H_{\text{q}}[\text{j}2\pi(f_{\text{p}} - f_1)]H_{\text{iac}}[\text{j}2\pi(f_{\text{p}} - f_1)] \cdot \boldsymbol{I}_1^*/2 \end{cases} \tag{9.28}$$

$$\boldsymbol{G}_3(2,3) = \boldsymbol{G}_3(4,3) = H_{\text{vs}}[\text{j}2\pi(f_{\text{p}} - f_1)]H_{\text{iac}}[\text{j}2\pi(f_{\text{p}} - f_1)]/2 \tag{9.29}$$

$\boldsymbol{D}_1$, $\boldsymbol{D}_2$, $\boldsymbol{D}_3$ in Eq. (9.26) are the time delay transfer function matrices of the AC current control, PLL control, and overall voltage control respectively, which are $7\times$ 7 matrices can be expressed as

$$\boldsymbol{D}_1 = \mathrm{diag}\left[\left\{\mathrm{e}^{-\mathrm{j}2\pi(f_\mathrm{p}+kf_1)T_\mathrm{c}}\frac{1-\mathrm{e}^{-\mathrm{j}2\pi(f_\mathrm{p}+kf_1)T_\mathrm{c}}}{\mathrm{j}2\pi(f_\mathrm{p}+kf_1)T_\mathrm{c}}\frac{1}{1+\mathrm{j}2\pi(f_\mathrm{p}+kf_1)T_\mathrm{iac}}\right\}\Big|_{k=-3\sim3}\right] \tag{9.30}$$

$$\boldsymbol{D}_2 = \mathrm{diag}\left[\left\{\mathrm{e}^{-\mathrm{j}2\pi(f_\mathrm{p}+kf_1)T_\mathrm{c}}\frac{1-\mathrm{e}^{-\mathrm{j}2\pi(f_\mathrm{p}+kf_1)T_\mathrm{c}}}{\mathrm{j}2\pi(f_\mathrm{p}+kf_1)T_\mathrm{c}}\frac{1}{1+\mathrm{j}2\pi(f_\mathrm{p}+kf_1)T_\mathrm{vac}}\right\}\Big|_{k=-3\sim3}\right] \tag{9.31}$$

$$\boldsymbol{D}_3 = \mathrm{diag}\left[\left\{\mathrm{e}^{-\mathrm{j}2\pi(f_\mathrm{p}+kf_1)T_\mathrm{c}}\frac{1-\mathrm{e}^{-\mathrm{j}2\pi(f_\mathrm{p}+kf_1)T_\mathrm{c}}}{\mathrm{j}2\pi(f_\mathrm{p}+kf_1)T_\mathrm{c}}\frac{1}{1+\mathrm{j}2\pi(f_\mathrm{p}+kf_1)T_\mathrm{vc}}\right\}\Big|_{k=-3\sim3}\right] \tag{9.32}$$

where T_c is the control period of SVG. T_iac, T_vac, T_vc are the filter time delay of the AC current, AC voltage, and arm capacitor voltage, respectively.

The phase voltage balancing control is performed in SCF. The small-signal vectors of the three-phase arm capacitor voltages $\hat{\boldsymbol{v}}_{C\mathrm{m}}$ and their references are fed into the phase voltage balancing controllers $H_\mathrm{vc}(s)$ respectively, leading to small-signal responses of the three-phase current compensation quantities $\hat{\boldsymbol{i}}_{l\mathrm{dc}}$. The differences between the small-signal vector of the d-axis current $\hat{\boldsymbol{i}}_\mathrm{d}$ and $\hat{\boldsymbol{i}}_{l\mathrm{dc}}$ are first multiplied by the current proportional factor K_ic, and then multiplied by $\cos\theta_\mathrm{PLL}$, $\cos(\theta_\mathrm{PLL}-2\pi/3)$, $\cos(\theta_\mathrm{PLL}+2\pi/3)$ respectively, leading to small-signal responses of the three-phase voltage balancing modulation signals $\hat{\boldsymbol{m}}_{\mathrm{vc}l}$. Taking phase a as an example, the expression of $\hat{\boldsymbol{m}}_\mathrm{vca}$ is

$$\hat{\boldsymbol{m}}_\mathrm{vca} = \boldsymbol{G}_4\boldsymbol{D}_1\hat{\boldsymbol{i}}_\mathrm{a} + \boldsymbol{G}_5\boldsymbol{D}_2\hat{\boldsymbol{v}}_\mathrm{a} + \boldsymbol{G}_6\boldsymbol{D}_3\hat{\boldsymbol{v}}_\mathrm{Cam} \tag{9.33}$$

where $\boldsymbol{G}_4$, $\boldsymbol{G}_5$, $\boldsymbol{G}_6$ are 7×7 matrices, and all other elements in the matrices are zero except for Eqs. (9.34)to (9.36).

$$\boldsymbol{G}_4(2,2) = \boldsymbol{G}_4(2,4) = \boldsymbol{G}_4(4,2) = \boldsymbol{G}_4(4,4) = K_\mathrm{ic}/2 \tag{9.34}$$

$$\begin{cases} \boldsymbol{G}_5(2,2) = \boldsymbol{G}_5(4,2) = T_\mathrm{PLL}[\mathrm{j}2\pi(f_\mathrm{p}-f_1)]\cdot K_\mathrm{ic}(\boldsymbol{I}_1-\boldsymbol{I}_1^*)/2 \\ \boldsymbol{G}_5(2,4) = \boldsymbol{G}_5(4,4) = -T_\mathrm{PLL}[\mathrm{j}2\pi(f_\mathrm{p}-f_1)]\cdot K_\mathrm{ic}(\boldsymbol{I}_1-\boldsymbol{I}_1^*)/2 \end{cases} \tag{9.35}$$

$$\begin{cases} \boldsymbol{G}_6(2,1) = K_\mathrm{ic}H_\mathrm{vc}[\mathrm{j}2\pi(f_\mathrm{p}-3f_1)]/2 \\ \boldsymbol{G}_6(2,3) = \boldsymbol{G}_6(4,3) = K_\mathrm{ic}H_\mathrm{vc}[\mathrm{j}2\pi(f_\mathrm{p}-f_1)]/2 \\ \boldsymbol{G}_6(6,5) = K_\mathrm{ic}H_\mathrm{vc}[\mathrm{j}2\pi(f_\mathrm{p}+f_1)]/2 \end{cases} \tag{9.36}$$

Based on Eqs. (9.4), (9.26) and (9.33), the small-signal vector of the phase-a arm modulation signal $\hat{\boldsymbol{m}}_\mathrm{am}$ can be obtained.

$$\hat{\boldsymbol{m}}_\mathrm{am} = \boldsymbol{G}_\mathrm{i}\hat{\boldsymbol{i}}_\mathrm{a} + \boldsymbol{G}_\mathrm{v1}\hat{\boldsymbol{v}}_\mathrm{a} + \boldsymbol{G}_\mathrm{v2}\hat{\boldsymbol{v}}_\mathrm{Cam} \tag{9.37}$$

where $\boldsymbol{G}_{\mathrm{i}}$, $\boldsymbol{G}_{\mathrm{v1}}$, $\boldsymbol{G}_{\mathrm{v2}}$ are express as

$$\begin{cases} \boldsymbol{G}_{\mathrm{i}} = (\boldsymbol{G}_1 + \boldsymbol{G}_4)\boldsymbol{D}_1 \\ \boldsymbol{G}_{\mathrm{v1}} = (\boldsymbol{G}_2 + \boldsymbol{G}_5)\boldsymbol{D}_2 \\ \boldsymbol{G}_{\mathrm{v2}} = (\boldsymbol{G}_3 + \boldsymbol{G}_6)\boldsymbol{D}_3 \end{cases} \tag{9.38}$$

Based on the phase-sequence relationship among there-phase small-signal vectors shown in Eq. (9.19), the small-signal vectors of the arm modulation signals in phase b and phase c can also be obtained according to $\hat{\boldsymbol{m}}_{\mathrm{am}}$.

2. **AC Voltages Mode**

After injecting the positive-sequence perturbation on the AC voltage, the small-signal vector of the d-axis voltage $\hat{\boldsymbol{v}}_{\mathrm{d}}$ is produced. $\hat{\boldsymbol{v}}_{\mathrm{d}}$ and its references are fed into the AC voltage controller $H_{\mathrm{vac}}(s)$, leading to small-signal responses of the q-axis current reference $\hat{\boldsymbol{i}}_{\mathrm{qref}}$. The control structures of the overall voltage control and AC current control are the same as that of reactive power control mode. Similarly, the small-signal vectors of the three-phase AC modulation signals $\hat{\boldsymbol{m}}_l$ can be obtained. Taking phase a as an example, the expression of $\hat{\boldsymbol{m}}_{\mathrm{a}}$ is

$$\hat{\boldsymbol{m}}_{\mathrm{a}} = \Delta\boldsymbol{G}_1\boldsymbol{D}_1\hat{\boldsymbol{i}}_{\mathrm{a}} + \Delta\boldsymbol{G}_2\boldsymbol{D}_2\hat{\boldsymbol{v}}_{\mathrm{a}} + \boldsymbol{G}_3\boldsymbol{D}_3\hat{\boldsymbol{v}}_{\mathrm{Cam}} \tag{9.39}$$

where the expression of $\boldsymbol{G}_3$ is shown in Eq. (9.29). $\Delta\boldsymbol{G}_1$, $\Delta\boldsymbol{G}_2$ are 7×7 matrices, and all other elements in the matrices are zero except for Eqs. (9.40)to (9.41).

$$\begin{cases} \Delta\boldsymbol{G}_1(2,2) = H_{\mathrm{iac}}[\mathrm{j}2\pi(f_{\mathrm{p}} - f_1)] + \mathrm{j}K_{\mathrm{d}} \\ \Delta\boldsymbol{G}_1(4,4) = H_{\mathrm{iac}}[\mathrm{j}2\pi(f_{\mathrm{p}} - f_1)] - \mathrm{j}K_{\mathrm{d}} \end{cases} \tag{9.40}$$

$$\begin{cases} \Delta\boldsymbol{G}_2(2,2) = -T_{\mathrm{PLL}}[\mathrm{j}2\pi(f_{\mathrm{p}} - f_1)]\Big[\big\{H_{\mathrm{iac}}[\mathrm{j}2\pi(f_{\mathrm{p}} - f_1)] + \mathrm{j}K_{\mathrm{d}}\big\}\boldsymbol{I}_1^* + \boldsymbol{M}_{\mathrm{am1}}^*\Big] \\ \qquad\qquad - \mathrm{j}H_{\mathrm{vac}}[\mathrm{j}2\pi(f_{\mathrm{p}} - f_1)]H_{\mathrm{iac}}[\mathrm{j}2\pi(f_{\mathrm{p}} - f_1)]/2 \\ \Delta\boldsymbol{G}_2(2,4) = T_{\mathrm{PLL}}[\mathrm{j}2\pi(f_{\mathrm{p}} - f_1)]\Big[\big\{H_{\mathrm{iac}}[\mathrm{j}2\pi(f_{\mathrm{p}} - f_1)] + \mathrm{j}K_{\mathrm{d}}\big\}\boldsymbol{I}_1^* + \boldsymbol{M}_{\mathrm{am1}}^*\Big] \\ \qquad\qquad - \mathrm{j}H_{\mathrm{vac}}[\mathrm{j}2\pi(f_{\mathrm{p}} - f_1)]H_{\mathrm{iac}}[\mathrm{j}2\pi(f_{\mathrm{p}} - f_1)]/2 \\ \Delta\boldsymbol{G}_2(4,2) = T_{\mathrm{PLL}}[\mathrm{j}2\pi(f_{\mathrm{p}} - f_1)]\Big[\big\{H_{\mathrm{iac}}[\mathrm{j}2\pi(f_{\mathrm{p}} - f_1)] - \mathrm{j}K_{\mathrm{d}}\big\}\boldsymbol{I}_1 + \boldsymbol{M}_{\mathrm{am1}}\Big] \\ \qquad\qquad + \mathrm{j}H_{\mathrm{vac}}[\mathrm{j}2\pi(f_{\mathrm{p}} - f_1)]H_{\mathrm{iac}}[\mathrm{j}2\pi(f_{\mathrm{p}} - f_1)]/2 \\ \Delta\boldsymbol{G}_2(4,4) = -T_{\mathrm{PLL}}[\mathrm{j}2\pi(f_{\mathrm{p}} - f_1)]\Big[\big\{H_{\mathrm{iac}}[\mathrm{j}2\pi(f_{\mathrm{p}} - f_1)] - \mathrm{j}K_{\mathrm{d}}\big\}\boldsymbol{I}_1 + \boldsymbol{M}_{\mathrm{am1}}\Big] \\ \qquad\qquad + \mathrm{j}H_{\mathrm{vac}}[\mathrm{j}2\pi(f_{\mathrm{p}} - f_1)] \cdot H_{\mathrm{iac}}[\mathrm{j}2\pi(f_{\mathrm{p}} - f_1)]/2 \end{cases} \tag{9.41}$$

Besides, the control structure of the phase voltage balancing control in AC voltage control mode is the same as that of reactive power control mode. The small-signal vector of the voltage balancing modulation signal in AC voltage control mode remains unchanged, as shown in Eq. (9.33).

It is only necessary to replace $\boldsymbol{G}_1$, $\boldsymbol{G}_2$ in Eq. (9.38) with $\Delta\boldsymbol{G}_1$, $\Delta\boldsymbol{G}_2$ respectively, so that the small-signal vector of the phase-a arm modulation signal $\hat{\boldsymbol{m}}_{\mathrm{am}}$ can be

obtained.

$$\hat{\boldsymbol{m}}_{\mathrm{am}} = \boldsymbol{G}_{\mathrm{i}}\hat{\boldsymbol{i}}_{\mathrm{a}} + \boldsymbol{G}_{\mathrm{v1}}\hat{\boldsymbol{v}}_{\mathrm{a}} + \boldsymbol{G}_{\mathrm{v2}}\hat{\boldsymbol{v}}_{\mathrm{Cam}} \tag{9.42}$$

where the expression of $\boldsymbol{G}_{\mathrm{v2}}$ is shown in Eq. (9.38). $\boldsymbol{G}_{\mathrm{i}}$, $\boldsymbol{G}_{\mathrm{v1}}$ in AC voltage control mode are given as

$$\begin{cases} \boldsymbol{G}_{\mathrm{i}} = (\Delta\boldsymbol{G}_1 + \boldsymbol{G}_4)\boldsymbol{D}_1 \\ \boldsymbol{G}_{\mathrm{v1}} = (\Delta\boldsymbol{G}_2 + \boldsymbol{G}_5)\boldsymbol{D}_2 \end{cases} \tag{9.43}$$

9.3.3 AC Port Impedance Model

The AC port admittance of SVG can be obtained by calculating the ratio of the small-signal vectors of the three-phase AC currents and voltages, namely

$$\boldsymbol{Y}_{\mathrm{SVG}} = \frac{\hat{\boldsymbol{i}}_l}{\hat{\boldsymbol{v}}_l} \tag{9.44}$$

According to the small-signal models of the main circuit and control loops, combining Eqs. (9.21), (9.22), (9.37), and (9.38), the AC port admittance of SVG in reactive power control mode can be obtained.

$$\begin{aligned} \boldsymbol{Y}_{\mathrm{SVG}} = -[&\boldsymbol{Z}_{\mathrm{Larm}} + \boldsymbol{V}_{Cl\mathrm{m}}\boldsymbol{G}_{\mathrm{i}} \\ &+ (\boldsymbol{V}_{Cl\mathrm{m}}\boldsymbol{G}_{\mathrm{v2}} + \boldsymbol{M}_{l\mathrm{m}})\left(\boldsymbol{Y}_{\mathrm{Ceq}} - \boldsymbol{I}_l\boldsymbol{G}_{\mathrm{v2}}\right)^{-1}(\boldsymbol{I}_l\boldsymbol{G}_{\mathrm{i}} + \boldsymbol{M}_{l\mathrm{m}})\Big]^{-1} \\ &\cdot\Big[(\boldsymbol{V}_{Cl\mathrm{m}}\boldsymbol{G}_{\mathrm{v2}} + \boldsymbol{M}_{l\mathrm{m}})\left(\boldsymbol{Y}_{\mathrm{Ceq}} - \boldsymbol{I}_l\boldsymbol{G}_{\mathrm{v2}}\right)^{-1}\boldsymbol{I}_l\boldsymbol{G}_{\mathrm{v1}} + \boldsymbol{V}_{Cl\mathrm{m}}\boldsymbol{G}_{\mathrm{v1}} - \boldsymbol{U}\Big] \end{aligned} \tag{9.45}$$

Besides, replacing $\boldsymbol{G}_{\mathrm{i}}$, $\boldsymbol{G}_{\mathrm{v1}}$ in Eq. (9.45) with that in Eq. (9.43), the AC port admittance of SVG in AC voltage control mode can be obtained.

The small-signal components at f_{p} and $f_{\mathrm{p}} - 2f_1$ are the main components in the small-signal vectors of the AC voltage and current of SVG, while the amplitudes of the other components are relatively small. The characteristics of the AC port impedance or admittance at f_{p} and $f_{\mathrm{p}} - 2f_1$ are more significant. Only relevant elements at these two frequencies are extracted, and the relationship between the small-signal vectors of the AC voltage and current and AC port admittance is reformulated as

$$\begin{bmatrix} \hat{\boldsymbol{i}}_{\mathrm{p}} \\ \hat{\boldsymbol{i}}_{\mathrm{p\text{-}2}} \end{bmatrix} = \begin{bmatrix} \boldsymbol{Y}_{\mathrm{SVG}}^{\mathrm{pp}} & \boldsymbol{Y}_{\mathrm{SVG}}^{\mathrm{np}} \\ \boldsymbol{Y}_{\mathrm{SVG}}^{\mathrm{pn}} & \boldsymbol{Y}_{\mathrm{SVG}}^{\mathrm{nn}} \end{bmatrix} \begin{bmatrix} \hat{\boldsymbol{v}}_{\mathrm{p}} \\ \hat{\boldsymbol{v}}_{\mathrm{p\text{-}2}} \end{bmatrix} \tag{9.46}$$

where the expression of the 2×2 AC port admittance matrix is

$$\begin{bmatrix} \boldsymbol{Y}_{\mathrm{SVG}}^{\mathrm{pp}} & \boldsymbol{Y}_{\mathrm{SVG}}^{\mathrm{np}} \\ \boldsymbol{Y}_{\mathrm{SVG}}^{\mathrm{pn}} & \boldsymbol{Y}_{\mathrm{SVG}}^{\mathrm{nn}} \end{bmatrix} = \begin{bmatrix} \boldsymbol{Y}_{\mathrm{SVG}}(4,4) & \boldsymbol{Y}_{\mathrm{SVG}}(4,2) \\ \boldsymbol{Y}_{\mathrm{SVG}}(2,4) & \boldsymbol{Y}_{\mathrm{SVG}}(2,2) \end{bmatrix}$$

where

$\boldsymbol{Y}_{\mathrm{SVG}}^{\mathrm{pp}}$ is the positive-sequence admittance of SVG, representing the small-signal response of AC current at f_{p} in positive sequence under per unit small-signal perturbation of AC voltage at f_{p} in positive sequence.
$\boldsymbol{Y}_{\mathrm{SVG}}^{\mathrm{pn}}$ is the positive-sequence coupled admittance of SVG, representing the small-signal response of AC current at $f_{\mathrm{p}} - 2f_1$ in negative sequence under per unit small-signal perturbation of AC voltage at f_{p} in positive sequence.
$\boldsymbol{Y}_{\mathrm{SVG}}^{\mathrm{nn}}$ is the negative-sequence admittance of SVG, representing the small-signal response of AC current at $f_{\mathrm{p}} - 2f_1$ in negative sequence under per unit small-signal perturbation of AC voltage at $f_{\mathrm{p}} - 2f_1$ in negative sequence.
$\boldsymbol{Y}_{\mathrm{SVG}}^{\mathrm{np}}$ is the negative-sequence admittance of SVG, representing the small-signal response of AC current at f_{p} in positive sequence under per unit small-signal perturbation of AC voltage at $f_{\mathrm{p}} - 2f_1$ in negative sequence.
$\boldsymbol{Y}_{\mathrm{SVG}}(4,4)$ is the element in the 4th row and the 4th column of $\boldsymbol{Y}_{\mathrm{SVG}}$.
$\boldsymbol{Y}_{\mathrm{SVG}}(4,2)$ is the element in the 4th row and the 2nd column of $\boldsymbol{Y}_{\mathrm{SVG}}$.
$\boldsymbol{Y}_{\mathrm{SVG}}(2,4)$ is the element in the 2nd row and the 4th column of $\boldsymbol{Y}_{\mathrm{SVG}}$.
$\boldsymbol{Y}_{\mathrm{SVG}}(2,2)$ is the element in the 2nd row and the 2nd column of $\boldsymbol{Y}_{\mathrm{SVG}}$.

The AC port impedance of SVG can be obtained by calculating the inverse matrix of the AC port admittance as

$$\begin{bmatrix} \boldsymbol{Z}_{\mathrm{SVG}}^{\mathrm{pp}} & \boldsymbol{Z}_{\mathrm{SVG}}^{\mathrm{pn}} \\ \boldsymbol{Z}_{\mathrm{SVG}}^{\mathrm{np}} & \boldsymbol{Z}_{\mathrm{SVG}}^{\mathrm{nn}} \end{bmatrix} = \begin{bmatrix} \boldsymbol{Y}_{\mathrm{SVG}}^{\mathrm{pp}} & \boldsymbol{Y}_{\mathrm{SVG}}^{\mathrm{np}} \\ \boldsymbol{Y}_{\mathrm{SVG}}^{\mathrm{pn}} & \boldsymbol{Y}_{\mathrm{SVG}}^{\mathrm{nn}} \end{bmatrix}^{-1} \tag{9.47}$$

where

$\boldsymbol{Z}_{\mathrm{SVG}}^{\mathrm{pp}}$ represents the positive-sequence impedance of SVG.
$\boldsymbol{Z}_{\mathrm{SVG}}^{\mathrm{pn}}$ represents the positive-sequence coupled impedance of SVG.
$\boldsymbol{Z}_{\mathrm{SVG}}^{\mathrm{nn}}$ represents the negative-sequence impedance of SVG.
$\boldsymbol{Z}_{\mathrm{SVG}}^{\mathrm{np}}$ represents the negative-sequence coupled impedance of SVG.

Besides, both in passive islanding mode and grid-connected mode, the frequency-domain relationship between the negative-sequence impedance and the positive-sequence impedance satisfies $\boldsymbol{Z}_{\mathrm{SVG}}^{\mathrm{nn}} = \boldsymbol{Z}_{\mathrm{SVG}}^{\mathrm{pp}*}(\mathrm{j}2\omega_1 - s)$, and the frequency-domain relationship between the negative-sequence coupled impedance and the positive-sequence coupled impedance satisfies $\boldsymbol{Z}_{\mathrm{SVG}}^{\mathrm{np}} = \boldsymbol{Z}_{\mathrm{SVG}}^{\mathrm{pn}*}(\mathrm{j}2\omega_1 - s)$.

Table 9.3 Main circuit and controller parameters of SVG

Parameter	Definition	Value
Q_{ref}	Reactive power references	10 Mvar
V_1	Amplitude of the fundamental component of the AC voltage	28.58 kV
N	Arm SM number	36
V_C	Rated SM capacitor voltage	1 kV
C_{sm}	SM capacitance	1.5 mF
L_{arm}	Arm inductance	30 mH
K_{pp}, K_{pi}	Proportional and integral coefficients of the PLL controller	7.7730×10^{-4}, 0.0244
K_{qep}, K_{qei}	Proportional and integral coefficients of the reactive power controller	1.6500×10^{-5}, 0.0013
K_{vsp}, K_{vsi}	Proportional and integral coefficients of the overall voltage controller	0.0140, 2.6375
K_{iacp}, K_{iaci}	Proportional and integral coefficients of the AC current controller	7.4050×10^{-4}, 0.9305
K_d	Decoupling coefficients of the AC current control	2.6180×10^{-4}
K_{vcp}, K_{vci}	Proportional and integral coefficients of the phase voltage balancing controller	7.7730×10^{-5}, 2.4421×10^{-4}
K_{ic}	Current proportional factor	1×10^{-6}

The main circuit and controller parameters of SVG are listed in Table 9.3. Figure 9.6 shows the analytical (in solid lines) and scanning (in discrete points) results of the AC port impedance of SVG in reactive power control mode. As seen from the figure, all the discrete points fall on the solid lines, which verifies the accuracy of the established impedance model of SVG in reactive power control mode.

In AC voltage control mode, the proportional and integral coefficients of the AC voltage controller are 0.0100 and 0.5000 respectively, and other main circuit and controller parameters of SVG are consistent with Table 9.3. Figure 9.7 shows the analytical (in solid lines) and scanning (in discrete points) results of the AC port impedance of SVG in AC voltage control mode. As seen from the figure, all the discrete points fall on the solid lines, which verifies the accuracy of the established impedance model of SVG in AC voltage control mode.

9.4 Impedance Characteristic Analysis of Reactive Power Control Mode SVG

Based on the established impedance model of SVG in reactive power control mode, this section first analyzes the dominant factors of the impedance characteristics in different frequency bands, and proposes the frequency band division method of SVG.

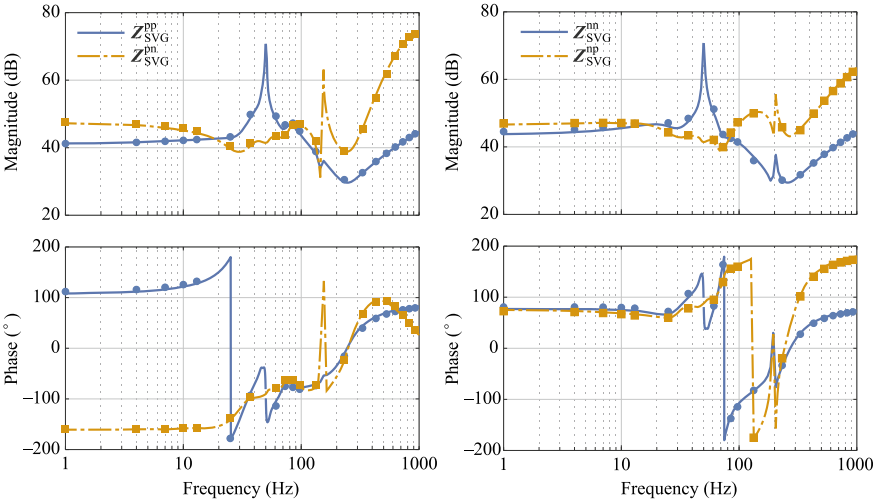

(a) Positive-sequence impedance and positive-sequence coupling impedance

(b) Negative-sequence impedance and negative-sequence coupling impedance

Fig. 9.6 The analytical and scanning results of the AC port impedance of SVG (in reactive power control mode)

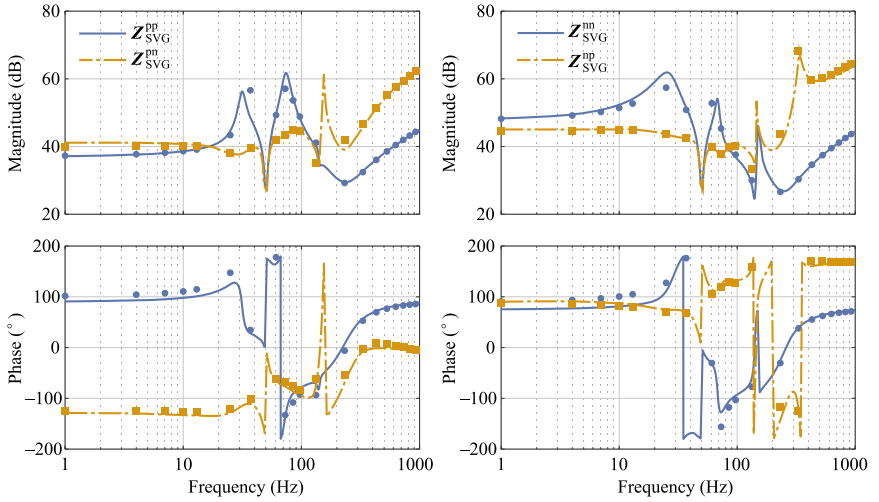

(a) Positive-sequence impedance and positive-sequence coupling impedance

(b) Negative-sequence impedance and negative-sequence coupling impedance

Fig. 9.7 The analytical and scanning results of the AC port impedance of SVG (in AC voltage control mode)

Then, the frequency-band overlapping effect of the multiple control loops or links and the negative damping characteristics in each frequency band are clarified. Finally, based on the CHIL scanning results of SVG impedance, the typical values of each frequency band are given.

9.4.1 *Frequency-Band Division of Broadband Impedance*

The impedance characteristics of SVG are influenced by the multiple control loops or links. This section establishes the frequency-domain relationship between the impedance characteristics, control loop bandwidth and PM in reactive power control mode. The dominant factor of the impedance characteristics in each frequency band is clarified, and the frequency band division method is proposed.

9.4.1.1 Influence of PLL on Impedance Characteristics

The influence of PLL on the impedance characteristics of SVG (in reactive power control mode) is shown in Fig. 9.8. On the one hand, the influence of PLL bandwidth can be obtained by changing f_{tc} to 5, 10 and 20 Hz respectively with a constant PM of 45°. On the other hand, the influence of PLL PM can be obtained by changing θ_{tc} to 20°, 45° and 70° respectively with a constant bandwidth of 5 Hz.

As shown in Fig. 9.8, with the increase of PLL bandwidth f_{tc}, the impedance characteristics change from inductive negative damping (the phase

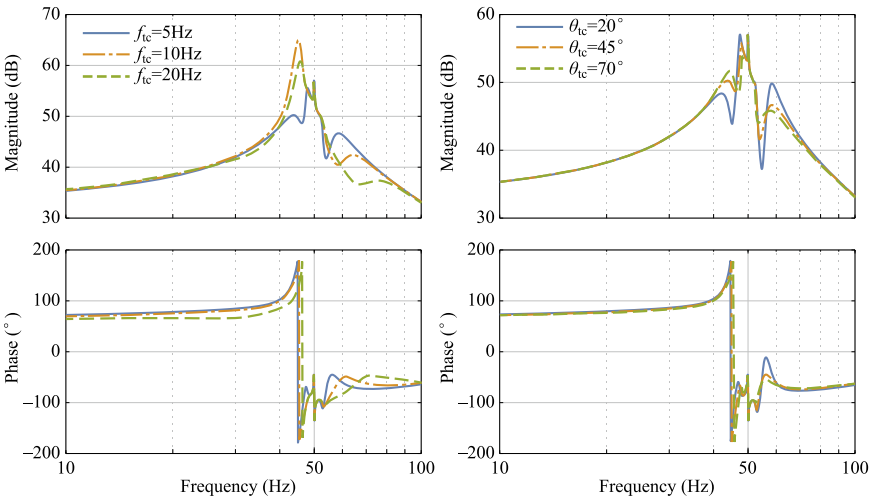

Fig. 9.8 The influence of PLL on the impedance characteristics (in reactive power control mode)

of the impedance more than 90°) to capacitive negative damping (the phase of the impedance phase less than −90°) around $f_1 - f_{tc}$. The impedance characteristics change from capacitive negative damping to capacitive positive damping around $f_1 + f_{tc}$. The change of the PLL PM θ_{tc} mainly influences the damping characteristics around $f_1 - f_{tc}$ and $f_1 + f_{tc}$. With the increase of θ_{tc}, the damping characteristics around $f_1 - f_{tc}$ and $f_1 + f_{tc}$ are enhanced, and the dipping in impedance magnitude is attenuated. Therefore, PLL mainly influences the impedance characteristics within the frequency band of $f_1 - f_{tc} < f < f_1 + f_{tc}$.

9.4.1.2 Influence of AC Current Loop on Impedance Characteristics

The influence of the AC current control on the AC port impedance of SVG is analyzed as follows. The block diagram of the AC current loop is shown in Fig. 9.9.

Given the bandwidth and PM of the AC current loop f_{iac}, θ_{iac} in SRF, the coefficients of the AC current controller can be solved from the following equation

$$\begin{cases} \left| H_{iac}(s) \dfrac{V_{dcref}}{R_{arm} + sL_{arm}} \right|_{s=j2\pi f_{iac}} = 1 \\ \angle \left(H_{iac}(s) \dfrac{V_{dcref}}{R_{arm} + sL_{arm}} \right)_{s=j2\pi f_{iac}} = \theta_{iac} - \pi \end{cases} \tag{9.48}$$

where the open-loop gain is 1 at f_{iac}, and the corresponding PM is θ_{iac}.

The influence of the AC current loop on the impedance characteristics of SVG is shown in Fig. 9.10. On the one hand, the influence of AC current loop bandwidth can be obtained by changing f_{iac} to 100, 150 and 200 Hz respectively with a constant PM of 45°. On the other hand, the influence of AC current loop PM can be obtained by changing θ_{iac} to 20°, 45° and 70° respectively with a constant bandwidth of 100 Hz.

As shown in Fig. 9.10, the AC current loop bandwidth f_{iac} mainly influences the impedance characteristics within the frequency bands of $f < f_1 - f_{tc}$ and $f_1 + f_{tc} < f < f_1 + f_{iac}$. With the increase of f_{iac}, the impedance magnitudes within the two frequency bands increase. Besides, the impedance magnitude exhibits an anti-resonant peak around the AC current loop bandwidth in SCF, i.e., $f_1 + f_{iac}$, and the impedance characteristics transition from capacitive (the phase of the impedance less than 0°) to inductive (the phase of the impedance more than 0°) around $f_1 + f_{iac}$. The resonant frequency is further away from the fundamental frequency. The AC current

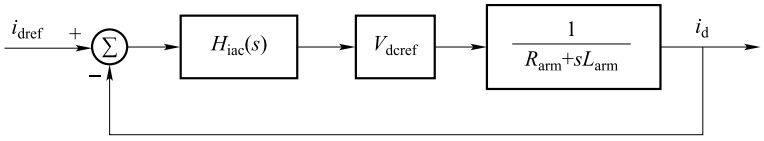

Fig. 9.9 The block diagram of the AC current loop

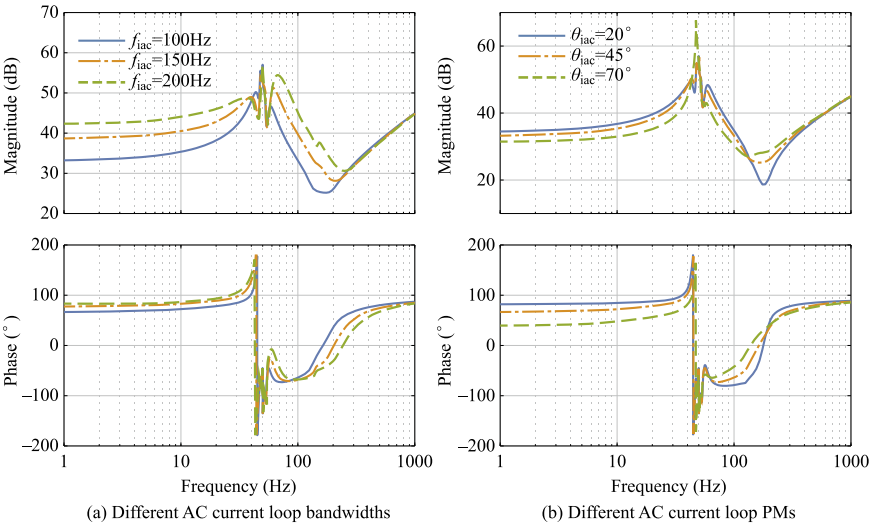

(a) Different AC current loop bandwidths (b) Different AC current loop PMs

Fig. 9.10 The influence of AC current loop on the impedance characteristics

loop PM θ_{iac} has an influence on the impedance characteristics in both $f < f_1 - f_{tc}$ and $f_1 + f_{tc} < f < f_1 + f_{iac}$. With the increase of θ_{iac}, the damping characteristics are enhanced around $f_1 + f_{iac}$, presenting that the dipping in impedance magnitude is attenuated and the impedance phase changes more flatly.

9.4.1.3 Influence of Arm Inductor on Impedance Characteristics

With the arm inductor L_{arm} equivalent to 20, 30 and 40 mH, the influence of the arm inductor on the impedance characteristics (in reactive power control mode) is shown in Fig. 9.11.

As shown in Fig. 9.11, the arm inductor mainly influences the impedance characteristics in the frequency band of $f > f_1 + f_{iac}$. With the increase of L_{arm}, the impedance magnitude and phase in the frequency band of $f > f_1 + f_{iac}$ increases.

9.4.1.4 Influence of SM Capacitor on Impedance Characteristics

With the SM capacitor C_{sm} equivalent to 2, 4 and 6 mF, the influence of the SM capacitor on the impedance characteristics (in reactive power control mode) is shown in Fig. 9.12.

As shown in Fig. 9.12, the SM capacitor mainly influences the impedance characteristics within the frequency band of $f < f_1 - f_{tc}$. With the increase of C_{sm}, the impedance magnitude decreases.

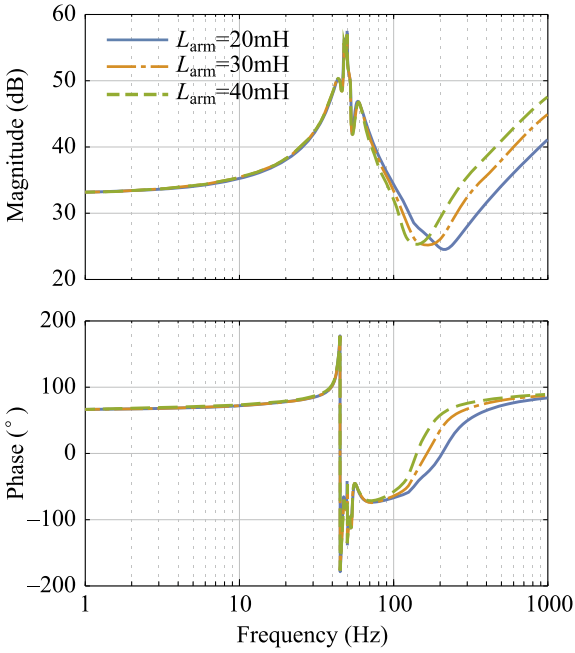

Fig. 9.11 The influence of the arm inductor on the impedance characteristics (in reactive power control mode)

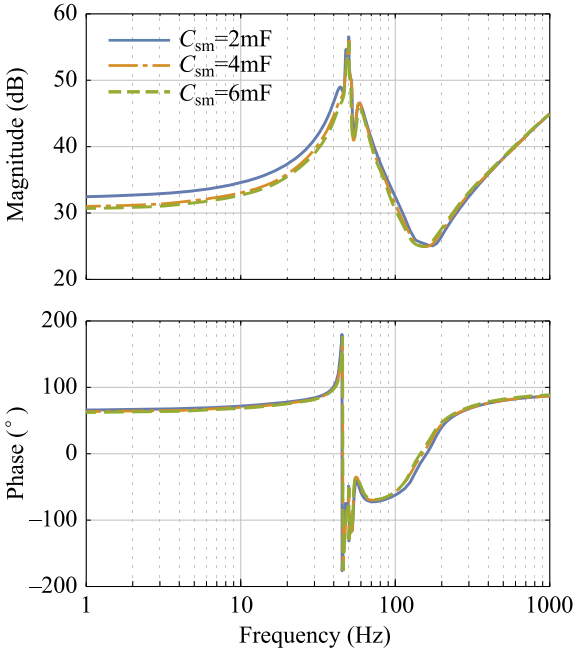

Fig. 9.12 The influence of the SM capacitor on the impedance characteristics (in reactive power control mode)

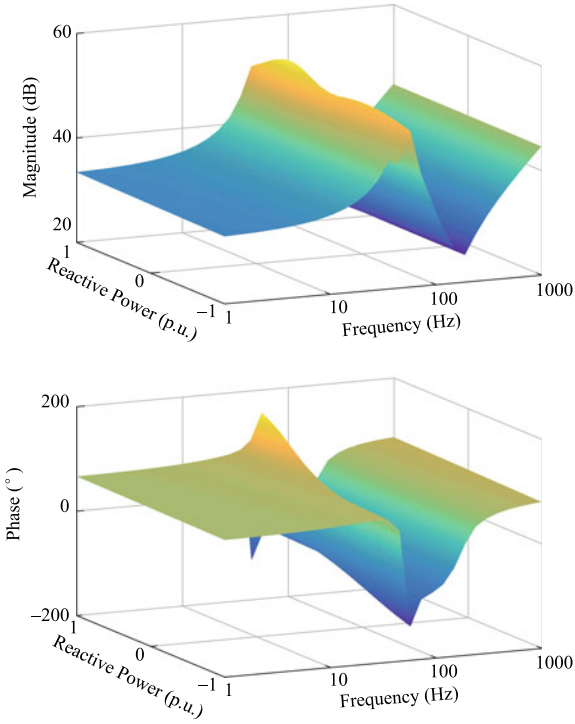

Fig. 9.13 The influence of the reactive power on the impedance characteristics (in reactive power control mode)

9.4.1.5 Influence of Steady-State Operating Point

Since the impedance model of SVG is established based on the linearization method at the steady-state operating point, the impedance characteristics of SVG vary with the steady-state operating point, such as the power change. The influence of the reactive power changing from −1.0 to 1.0 p.u. on the impedance characteristics of SVG (in reactive power control mode) is shown in Fig. 9.13.

As shown in Fig. 9.13, the change of the active power mainly influences the impedance characteristics around the fundamental frequency with little influence in other frequency bands. When the reactive power changes from −1.0 to 1.0 p.u., the trends of the broadband impedance curves with frequency are similar. The negative reactive power means SVG outputs inductive reactive power, and the positive reactive power means SVG outputs capacitive reactive power.

9.4.1.6 Frequency-Band Division of Broadband Impedance

According to the analysis of the dominant factors of SVG impedance characteristics in each frequency band (in reactive power control mode), the following frequency bands can be divided.

(1) Band I_{SVG} ($f < f_1 - f_{tc}$): The impedance characteristics are influenced by the AC current loop and SM capacitor.
(2) Band II_{SVG} ($f_1 - f_{tc} < f < f_1 + f_{tc}$): The impedance characteristics are dominated by PLL. The impedance magnitude and phase in this frequency band changes with the PLL bandwidth and PM. Besides, the reactive power has an impact on the impedance characteristics in this frequency band as well.
(3) Band III_{SVG} ($f_1 + f_{tc} < f < f_1 + f_{iac}$): The impedance characteristics are dominated by the AC current loop. The impedance magnitude exhibits an anti-resonant peak around $f_1 + f_{fiac}$, and the impedance characteristics transition from capacitive to inductive around $f_1 + f_{fiac}$. With the increase of AC current loop bandwidth, the impedance magnitude in this frequency band increases. With the increase of AC current loop PM, the impedance magnitude and phase change more flatly.
(4) Band IV_{SVG} ($f > f_1 + f_{iac}$): The impedance characteristics are dominated by the arm inductor. With the increase of the arm inductor, the impedance magnitude and phase in this frequency band increases, tending to be inductive.

Impedance scanning is carried out based on the CHIL platform of different types of SVGs, and the scanning results in reactive power control mode are shown in Fig. 9.14. It can be seen from the figure that the frequency range of Band I_{SVG} is around $f < 30$ Hz, the frequency range of Band II_{SVG} is around 30 Hz $< f <$ 70 Hz, the frequency range of Band III_{SVG} is around 70 Hz $< f <$ 100 Hz, and the frequency range of Band IV_{SVG} is around $f >$ 100 Hz.

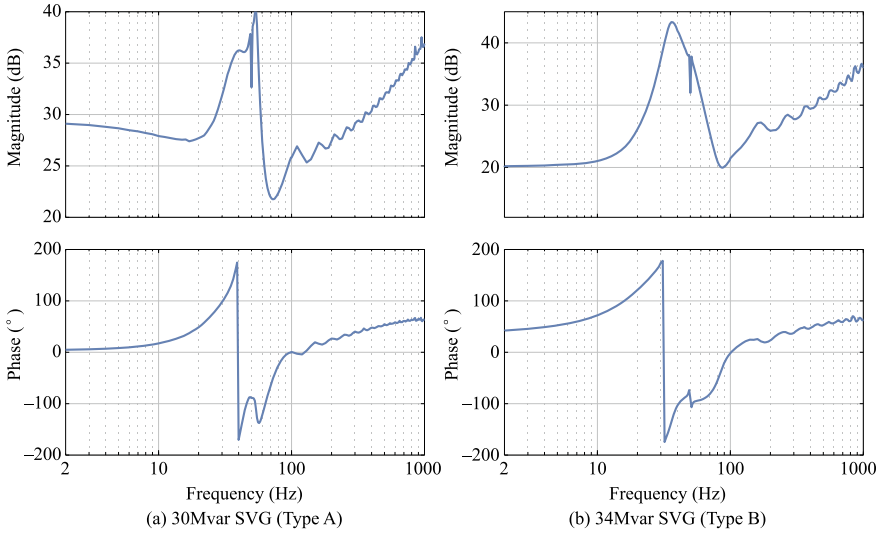

Fig. 9.14 The scanning impedance of SVG based on CHIL platform (in reactive power control mode)

9.4.2 Analysis of Negative Damping Characteristics

The frequency-band division method of the broadband impedance of SVG in reactive power control mode has been proposed according to the analysis in Sect. 9.4.1. The impedance characteristics in each frequency band are influenced not only by the dominant factors, but also by the frequency-band overlapping effects of the other controllers or links. In this section, the frequency-band overlapping effects of multiple control loops or links in reactive power control mode will be analyzed to reveal the mechanism of the negative damping characteristics in each frequency band.

9.4.2.1 Negative Damping Characteristics in Band I_{SVG}

The influence of the overall voltage control on the damping characteristics of SVG in Band I_{SVG} is analyzed as follows. The block diagram of the overall voltage loop is shown in Fig. 9.15.

Given the bandwidth and PM of the overall voltage loop f_{vs}, θ_{vs} in SRF, the coefficients of the overall voltage controller can be solved from the following equation

$$\begin{cases} \left| H_{vs}(s) \dfrac{3V_l}{2V_{dcref}} \dfrac{1}{s \cdot 3C_{eq}} \right|_{s=j2\pi f_{vs}} = 1 \\ \angle \left(H_{vs}(s) \dfrac{3V_l}{2V_{dcref}} \dfrac{1}{s \cdot 3C_{eq}} \right)_{s=j2\pi f_{vs}} = \theta_{vs} - \pi \end{cases} \tag{9.49}$$

where the open-loop gain is 1 at f_{vs}, and the corresponding PM is θ_{vs}.

The influence of the overall voltage loop on the damping characteristics of SVG in Band I_{SVG} (in reactive power control mode) is shown in Fig. 9.16. On the one hand, the influence of overall voltage loop bandwidth can be obtained by changing f_{vs} to 20, 30 and 40 Hz respectively with a constant PM of 45°. On the other hand, the influence of overall voltage loop PM can be obtained by changing θ_{vs} to 20°, 45° and 70° respectively with a constant bandwidth of 40 Hz.

As shown in Fig. 9.16, both the bandwidth and PM of the overall voltage loop have an influence on the damping characteristics in Band I_{SVG}. With the increase of f_{vs} and decrease of θ_{vs}, the degree of the negative damping is deepened, and the frequency of the transition from inductive negative damping to capacitive negative damping is reduced.

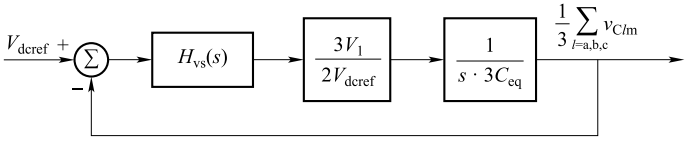

Fig. 9.15 The block diagram of the overall voltage loop

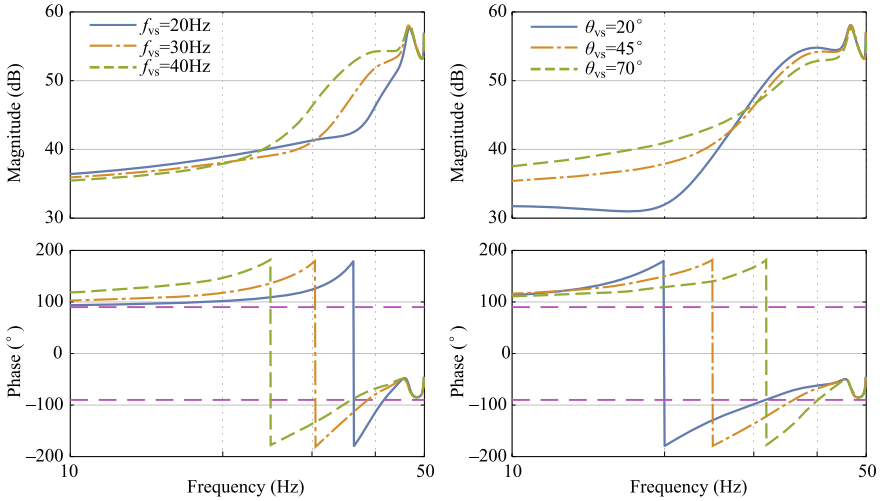

(a) Different overall voltage loop bandwidths (b) Different overall voltage loop PMs

Fig. 9.16 The influence of the overall voltage loop on the damping characteristics in Band I_{SVG} (in reactive power control mode)

9.4.2.2 Negative Damping Characteristics in Band II_{SVG}

The impedance characteristics in Band II_{SVG} are dominated by PLL, and present negative damping characteristics at $f_1 + f_{tc}$ and $f_1 - f_{tc}$. Based on this, the influence of the reactive power operating point on the damping characteristics of SVG in Band II_{SVG} is analyzed as follows.

With the reactive power equivalent to −1.0, −0.5, 0.5 and 1.0 p.u., the influence of the reactive power operating point on the impedance characteristics in Band II_{SVG} is shown in Fig. 9.17.

As shown in Fig. 9.17, when the reactive power changes from −1.0 to 1.0 p.u., the frequency of the transition from inductive negative damping to capacitive negative damping is reduced. The transition frequency is above the fundamental frequency as SVG outputs inductive reactive power, while the transition frequency is below the fundamental frequency as SVG outputs capacitive reactive power.

9.4.2.3 Negative Damping Characteristics in Band III_{SVG}

The impedance characteristics in Band III_{SVG} are dominated by the AC current control, and simultaneously influenced by the overall voltage control, reactive power control, and time delay introduced from communication, sampling, filtering, digital control, and so on. The influence of these factors on the damping characteristics are analyzed as follows.

1. **Influence of Overall Voltage Loop**

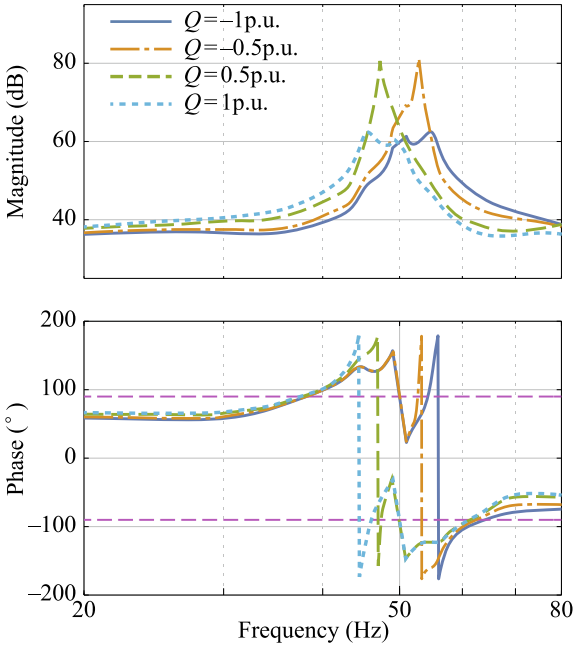

Fig. 9.17 The influence of the reactive power operating point on the impedance characteristics

The influence of the overall voltage loop on the damping characteristics of SVG in Band $\mathrm{III}_{\mathrm{SVG}}$ (in reactive power control mode) is shown in Fig. 9.18. On the one hand, the influence of overall voltage loop bandwidth can be obtained by changing f_{vs} to 20, 30 and 40 Hz respectively with a constant PM of 45°. On the other hand, the influence of overall voltage loop PM can be obtained by changing θ_{vs} to 20°, 45° and 70° respectively with a constant bandwidth of 40 Hz.

As shown in Fig. 9.18, both the bandwidth and PM of the overall voltage loop have an influence on the damping characteristics in Band $\mathrm{III}_{\mathrm{SVG}}$. With the increase of f_{vs}, the impedance gradually changes from capacitive positive damping to capacitive negative damping, and the negative damping characteristics are deepened. With the increase of θ_{vs}, the degree of the negative damping is attenuated below 100 Hz, but deepened above 100 Hz.

2. **Influence of Reactive Power Loop**

The influence of the reactive power control on the damping characteristics of SVG in Band $\mathrm{III}_{\mathrm{SVG}}$ is analyzed as follows. The block diagram of the reactive power loop is shown in Fig. 9.19.

Given the bandwidth and PM of the reactive power loop f_{qc}, θ_{qc} in SRF, the coefficients of the reactive power controller can be solved from the following equation

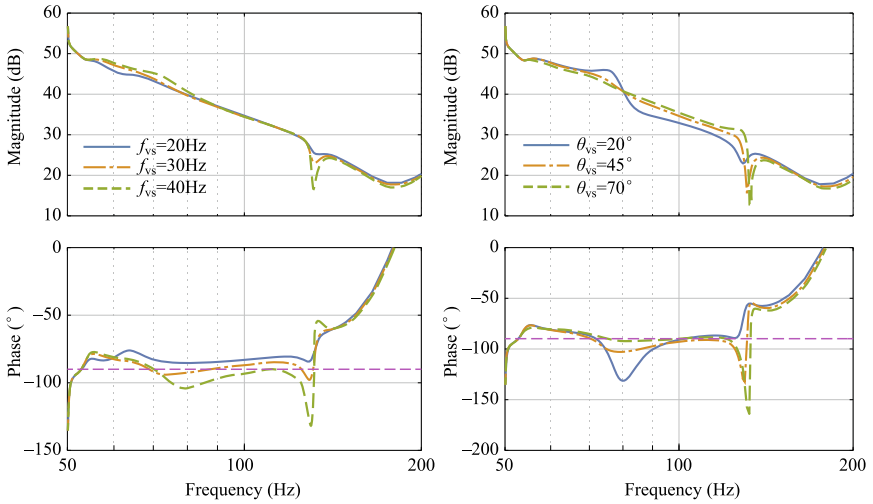

(a) Different overall voltage loop bandwidths (b) Different overall voltage loop PMs

Fig. 9.18 The influence of the overall voltage loop on the damping characteristics in Band $\mathrm{III}_{\mathrm{SVG}}$ (in reactive power control mode)

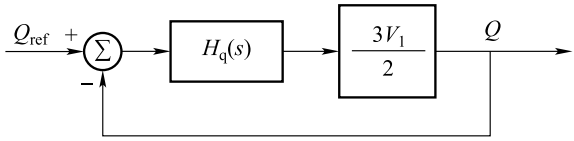

Fig. 9.19 The block diagram of the reactive power loop

$$\begin{cases} \left| H_{\mathrm{q}}(s)\dfrac{3V_1}{2} \right|_{s=\mathrm{j}2\pi f_{\mathrm{qc}}} = 1 \\ \angle\left(H_{\mathrm{q}}(s)\dfrac{3V_1}{2} \right)_{s=\mathrm{j}2\pi f_{\mathrm{qc}}} = \theta_{\mathrm{qc}} - \pi \end{cases} \tag{9.50}$$

where the open-loop gain is 1 at f_{qc}, and the corresponding PM is θ_{qc}.

With θ_{qc} equivalent to 10°, 45° and 80° and keeping a constant bandwidth ($f_{\mathrm{qc}} =$ 30 Hz), the influence of the reactive power loop on the damping characteristics of SVG in Band $\mathrm{III}_{\mathrm{SVG}}$ is shown in Fig. 9.20.

As shown in Fig. 9.20, with the decrease of θ_{qc}, the degree of the negative damping is deepened in Band $\mathrm{III}_{\mathrm{SVG}}$.

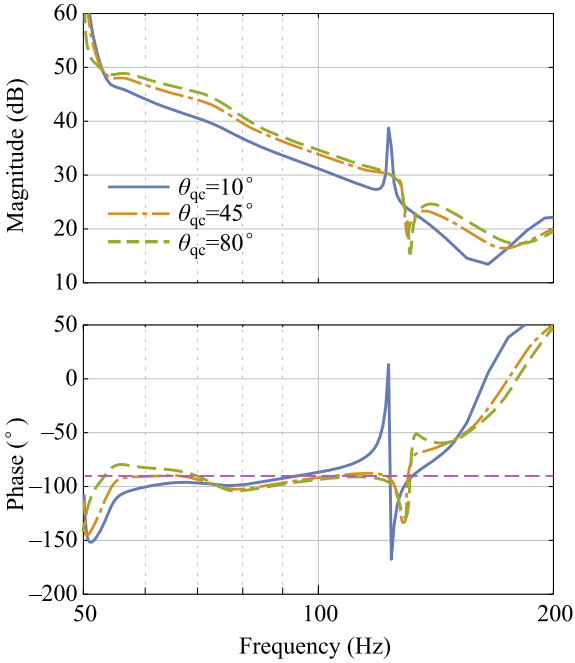

Fig. 9.20 The influence of the reactive power loop on the damping characteristics in Band III_{SVG}

3. **Influence of Time Delay**

The impedance characteristics are dominated by the AC current loop, and also influenced by the time delay. This section analyzes the influence of the time delay on the damping characteristics of SVG in Band III_{SVG}.

Setting the AC current loop bandwidth f_{iac} to 200 Hz and phase margin θ_{iac} to 15°, the influence of the time delay T_s equivalent to 0, 100, and 200 μs on the damping characteristics of SVG in Band III_{SVG} is shown in Fig. 9.21.

As shown in Fig. 9.21, the time delay mainly influences the impedance characteristics around the AC current loop bandwidth in SCF, i.e., $f_1 + f_{iac}$. With the increase of the time delay, the impedance presents the capacitive and inductive negative damping around $f_1 + f_{iac}$, and the degree of the negative damping is deepened. The frequency-band overlapping effect of time delay and AC current loop leads to negative damping characteristics in band III_{SVG}.

9.4.2.4 Negative Damping Characteristics in Band IV_{SVG}

The impedance characteristics are dominated by the arm inductor and also influenced by the time delay. Keeping the arm inductor constant, the influence of the time delay T_s equivalent to 0, 100, and 200 μs on the damping characteristics of SVG in Band IV_{SVG} is shown in Fig. 9.22.

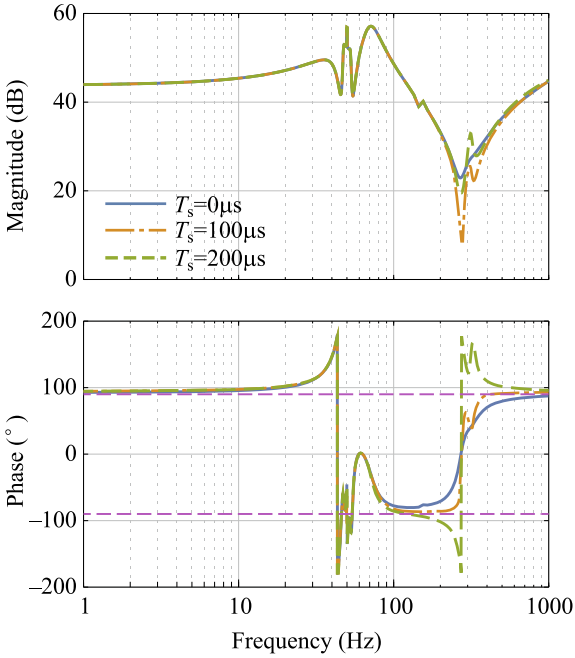

Fig. 9.21 The influence of the time delay on the damping characteristics in Band III_{SCG} (in grid-connected mode)

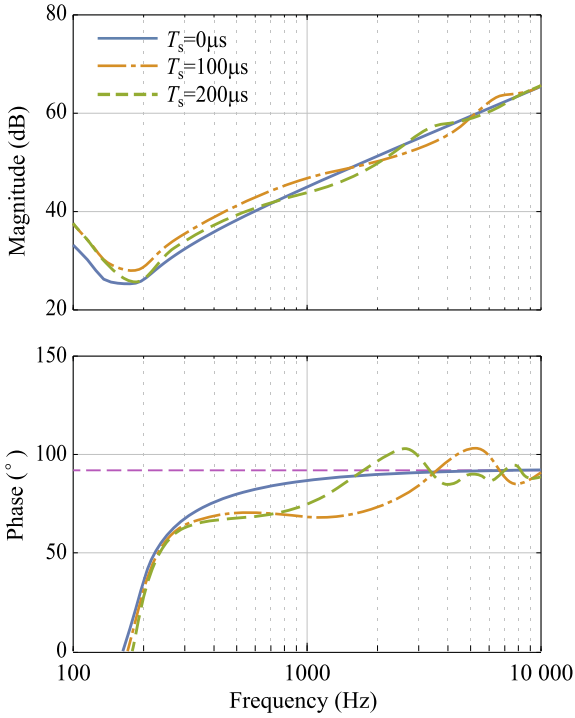

Fig. 9.22 The influence of the time delay on the damping characteristics in Band IV_{SVG}

As shown in Fig. 9.22, the degree of the inductive negative damping is deepened with the increase of the time delay. The frequency-band overlapping effect of time delay and AC current loop leads to negative damping characteristics in band $\mathrm{III}_{\mathrm{SVG}}$.

9.4.2.5 Summary of Negative Damping Characteristics in Each Frequency Band

According to the analysis of the negative damping characteristics of SVG in reactive power control mode, the following conclusions are obtained.

(1) Band $\mathrm{I}_{\mathrm{SVG}}$ ($f < f_1 - f_{\mathrm{tc}}$): The impedance characteristics are influenced by the AC current loop, SM capacitor, and the overall voltage loop. The frequency-band overlapping effect of the overall voltage loop, AC current loop, and SM capacitor leads to negative damping in this frequency band. With the increase of overall voltage loop bandwidth or the decrease of overall voltage loop PM, the negative damping degree is deepened.

(2) Band $\mathrm{II}_{\mathrm{SVG}}$ ($f_1 - f_{\mathrm{tc}} < f < f_1 + f_{\mathrm{tc}}$): The impedance characteristics are dominated by PLL, and also influenced by the reactive power operating point. The transition frequency is above the fundamental frequency as SVG outputs inductive reactive power, while the transition frequency is below the fundamental frequency as SVG outputs capacitive reactive power.

(3) Band $\mathrm{III}_{\mathrm{SVG}}$ ($f_1 + f_{\mathrm{tc}} < f < f_1 + f_{\mathrm{iac}}$): The impedance characteristics are dominated by the AC current loop. The frequency-band overlapping effect between the overall voltage loop, reactive power loop, time delay and the AC current loop leads to negative damping in this frequency band. The increase of the overall voltage loop bandwidth and time delay, or the decrease of the reactive power loop PM, leads to the increased degree of the negative damping.

(4) Band $\mathrm{IV}_{\mathrm{SVG}}$ ($f > f_1 + f_{\mathrm{iac}}$): The impedance characteristics are dominated by the arm inductor. The frequency-band overlapping effect of the time delay and arm inductor leads to inductive negative damping periodically presenting in this frequency band. With the increase of the time delay, the degree of the inductive negative damping is deepened.

Impedance scanning is carried out based on the CHIL platform of different types of SVGs, and the scanning results in reactive power control mode are shown in Fig. 9.23. It can be seen from the figure that the impedances of SVGs present inductive or capacitive negative damping characteristics respectively in different frequency bands.

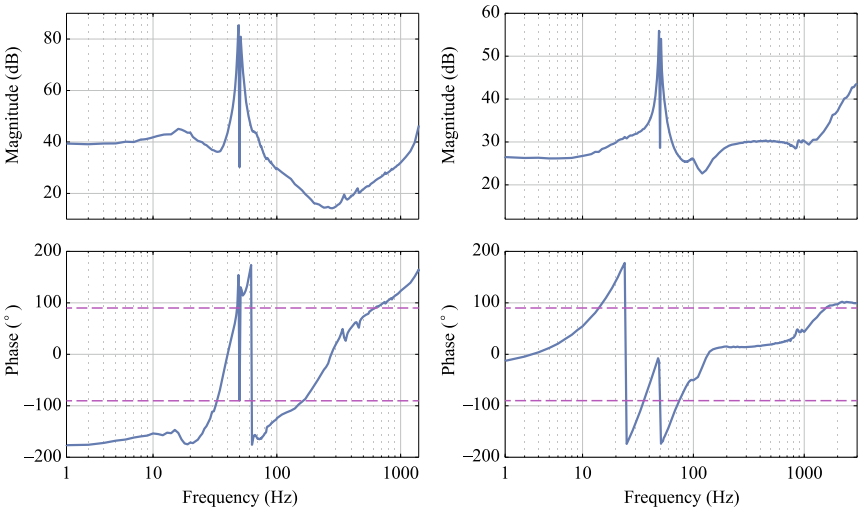

Fig. 9.23 The scanning damping characteristics of SVG based on CHIL platform (in reactive power control mode)

9.5 Impedance Characteristic Analysis of AC Voltage Control Mode SVG

Based on the established impedance model of SVG in AC voltage control mode, this section first analyzes the dominant factors of the impedance characteristics in different frequency bands, and proposes the frequency band division method of SVG. Then, the frequency-band overlapping effect of the multiple control loops or links and the negative damping characteristics in each frequency band are clarified. Finally, based on the CHIL scanning results of SVG impedance, the typical values of each frequency band are given.

9.5.1 Frequency-Band Division of Broadband Impedance

The difference of the impedance characteristics between the AC voltage control mode and reactive power control mode is analysed first, as shown in Fig. 9.24. In the figure, $\boldsymbol{Z}_{\mathrm{SVG}}^{\mathrm{V}}$, $\boldsymbol{Z}_{\mathrm{SVG}}^{\mathrm{Q}}$are the impedances of SVG in AC voltage control mode and reactive power control mode respectively. The main circuit and controller parameters are the same in the two modes, except for the AC voltage controller and reactive power controller.

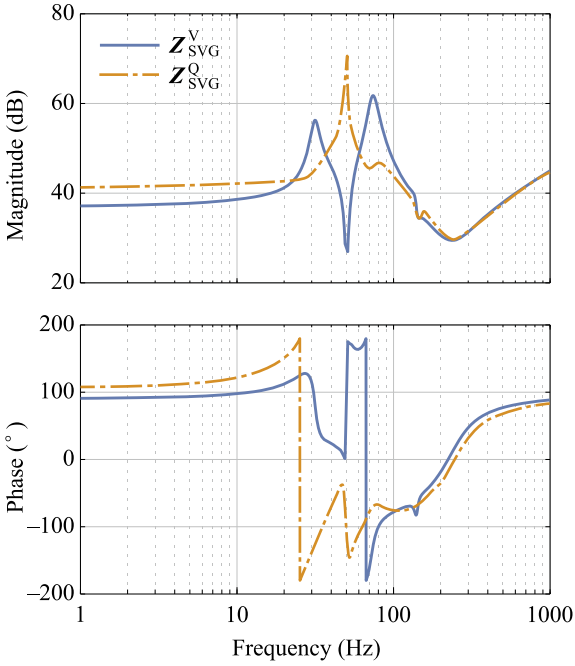

Fig. 9.24 Difference of the impedance characteristics between the AC voltage control mode and reactive power control mode

Since the impedance characteristics in the medium- and high- frequency bands are dominated by the AC current controller and arm inductor, the impedance characteristics between the two modes are almost identical. The main differences of the impedance characteristics are in the subsynchronous and super-synchronous frequency bands.

In this section, the impedance characteristics of SVG in AC voltage control mode within Band I_{SVG} and Band II_{SVG} are analyzed as follows.

9.5.1.1 Influence of AC Voltage Loop on Impedance Characteristics

The influence of AC voltage loop on the impedance characteristics of SVG is shown in Fig. 9.25. On the one hand, the influence of AC voltage loop bandwidth can be obtained by changing f_{vac} to 5, 10 and 20 Hz respectively with a constant PM of 45°. On the other hand, the influence of AC voltage loop PM can be obtained by changing θ_{vac} to 20°, 45° and 70° respectively with a constant bandwidth of 10 Hz.

As shown in Fig. 9.25, two resonant peaks appear in the impedance magnitude around $f_1 - f_{vac}$ and $f_1 + f_{vac}$. With the increase of AC voltage loop bandwidth f_{vac}, the two resonant frequencies are further away from the fundamental frequency. The change of the AC voltage loop PM PM θ_{vac} mainly influences the damping characteristics at the resonant frequencies. With the increase of θ_{vac}, the damping characteristics are enhanced, and the impedance magnitude and phase change more

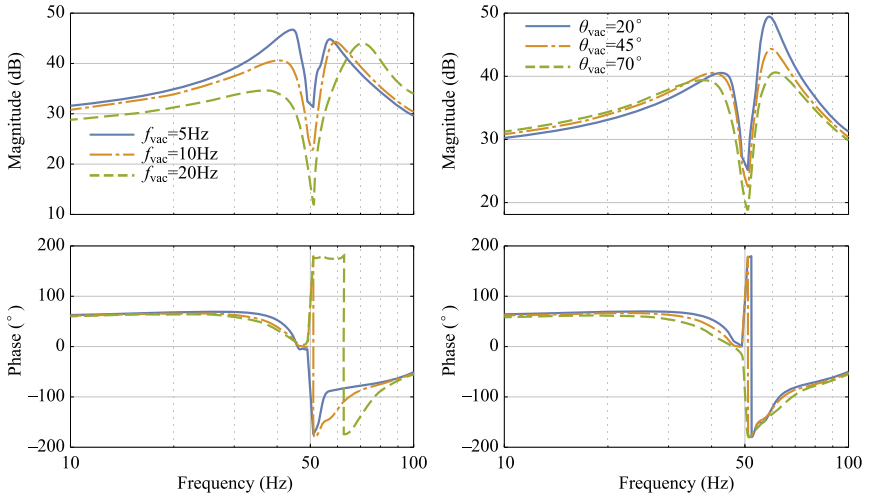

(a) Different AC voltage loop bandwidths (b) Different AC voltage loop PMs

Fig. 9.25 The influence of AC voltage loop on the impedance characteristics

flatly. The impedance presents capacitive negative damping above the fundamental frequency within this frequency band. Therefore, AC voltage loop mainly influences the impedance characteristics within the frequency band of $f_1 - f_{vac} < f < f_1 + f_{vac}$.

9.5.1.2 Influence of PLL on Impedance Characteristics

The influence of PLL on the impedance characteristics of SVG (in AC voltage control mode) is shown in Fig. 9.26. On the one hand, the influence of PLL bandwidth can be obtained by changing f_{tc} to 5, 10 and 20 Hz respectively with a constant PM of 45°. On the other hand, the influence of PLL PM can be obtained by changing θ_{tc} to 20°, 45° and 70° respectively with a constant bandwidth of 5 Hz.

As shown in Fig. 9.26, PLL mainly influences the damping characteristics at the resonant peaks around $f_1 - f_{vac}$ and $f_1 + f_{vac}$. With the increase of f_{tc} and θ_{tc}, the damping characteristics at the resonant peaks are enhanced. The impedance magnitude decreases, and the impedance phase changes more flatly within the frequency band of $f_1 - f_{vac} < f < f_1 + f_{vac}$.

9.5.1.3 Influence of SM Capacitor on Impedance Characteristics

With the SM capacitor C_{sm} equivalent to 2, 4 and 6 mF, the influence of the SM capacitor on the impedance characteristics (in AC voltage control mode) is shown in Fig. 9.27.

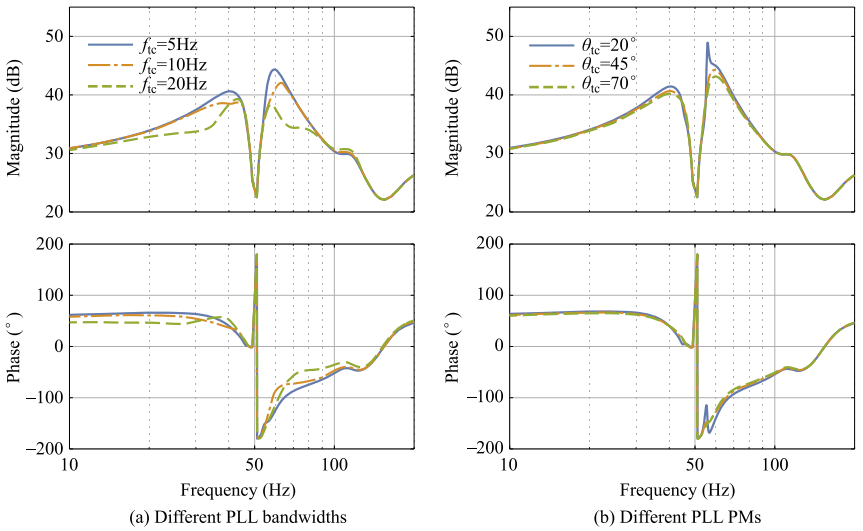

Fig. 9.26 The influence of PLL on the impedance characteristics (in AC voltage control mode)

Fig. 9.27 The influence of the SM capacitor on the impedance characteristics (in AC voltage control mode)

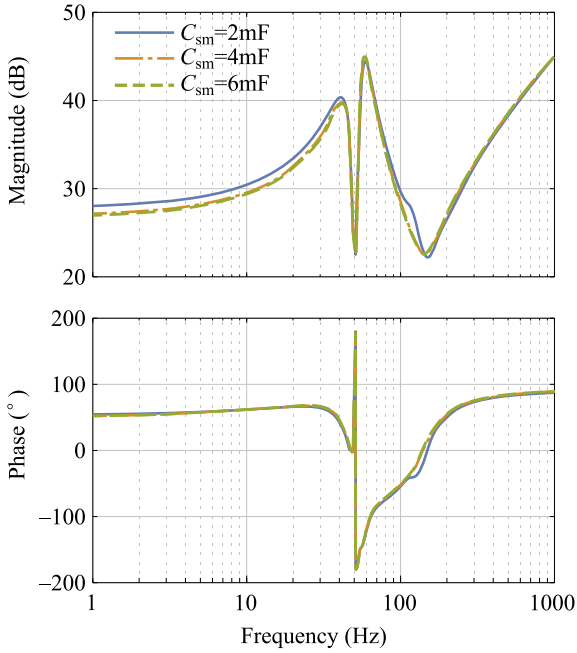

As shown in Fig. 9.12, the SM capacitor mainly influences the impedance characteristics within the frequency band of $f_1 - f_{vac}$. With the increase of C_{sm}, the impedance magnitude decreases.

9.5.1.4 Frequency-Band Division of Broadband Impedance

According to the analysis of the dominant factors of SVG impedance characteristics in each frequency band (in AC voltage control mode), the following frequency bands can be divided.

(1) Band I_{SVG} ($f < f_1 - f_{vac}$): The impedance characteristics are influenced by the AC current loop and SM capacitor.
(2) Band II_{SVG} ($f_1 - f_{vac} < f < f_1 + f_{vac}$): The impedance characteristics are dominated by the AC voltage loop. With the increase of AC voltage loop bandwidth, the frequencies of the resonant peaks in the impedance are further away from the fundamental frequency. With the increase of AC voltage loop PM, the impedance magnitude and phase change more flatly. Besides, PLL also has an influence on the damping characteristics in this frequency band.
(3) Band III_{SVG} ($f_1 + f_{vac} < f < f_1 + f_{iac}$): The impedance characteristics are dominated by the AC current loop. The impedance characteristics in AC voltage control mode are almost consistent with reactive power control mode within this frequency band.
(4) Band IV_{SVG} ($f > f_1 + f_{iac}$): The impedance characteristics are dominated by the arm inductor. The impedance characteristics in AC voltage control mode are almost consistent with reactive power control mode within this frequency band.

Impedance scanning is carried out based on the CHIL platform of different types of SVGs, and the scanning results in AC voltage control mode are shown in Fig. 9.28. It can be seen from the figure that the frequency range of Band I_{SVG} is around $f <$ 30 Hz, the frequency range of Band II_{SVG} is around 30 Hz $< f <$ 70 Hz, the frequency range of Band III_{SVG} is around 70 Hz $< f <$ 100 Hz, and the frequency range of Band IV_{SVG} is around $f >$ 100 Hz.

9.5.2 Analysis of Negative Damping Characteristics

The frequency-band division method of the broadband impedance of SVG in AC voltage control mode has been proposed in Sect. 9.5.1. The impedance characteristics in each frequency band are influenced not only by the dominant factors, but also by the frequency-band overlapping effects of the other controllers or links. Since the dominant factors of the impedance characteristics in the medium- and high-frequency bands are the same in AC voltage control mode and reactive power control mode, the mechanism of the negative damping in Band III_{SVG} (AC current loop and time

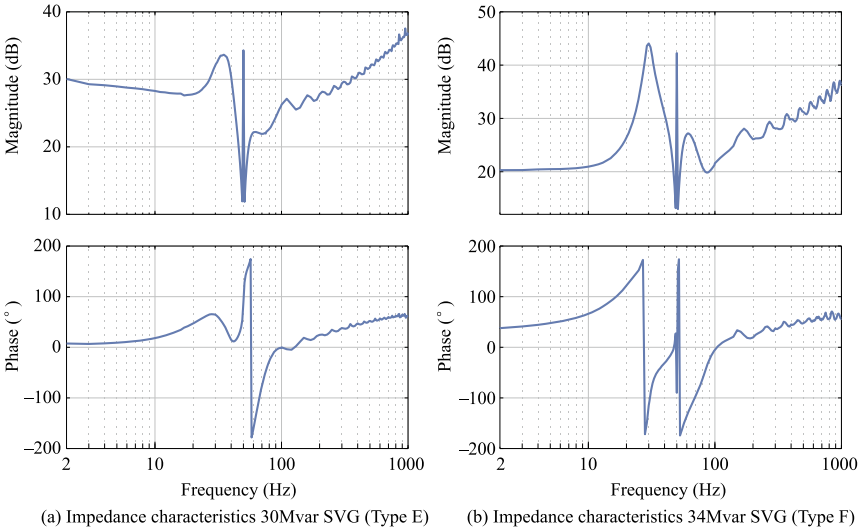

(a) Impedance characteristics 30Mvar SVG (Type E) (b) Impedance characteristics 34Mvar SVG (Type F)

Fig. 9.28 The scanning impedance of SVG based on CHIL platform (in AC voltage control mode)

delay) and Band IV_{SVG} (arm inductor and time delay) under AC voltage control mode is consistent with that in reactive power control mode. In addition, the damping characteristics in Band II_{SVG} under AC voltage control mode are mainly influenced by the AC voltage loop and PLL according to Sects. 9.5.1.1 and 9.5.1.2. In this section, the negative damping characteristics in Band I_{SVG} and Band III_{SVG} under AC voltage control mode are further analyzed.

9.5.2.1 Negative Damping Characteristics in Band I_{SVG}

The impedance characteristics are influenced by the AC current loop and SM capacitor in Band I_{SVG}. The AC current control bandwidth f_{iac} is set to 100Hz, and the PM of the AC current control θ_{iac} is set to 30° firstly. Based on this, the frequency-band overlapping effect between the overall voltage loop with the AC current loop and SM capacitor in this frequency band under AC voltage control mode is analyzed as follows.

The influence of the overall voltage loop on the damping characteristics in Band I_{SVG} (in AC voltage control mode) is shown in Fig. 9.29. Firstly, the AC current control bandwidth f_{iac} is set to 100 Hz, and the PM of the AC current control θ is set to 30°. On the one hand, the influence of overall voltage loop bandwidth can be obtained by changing f_{vs} to 20, 30 and 40 Hz respectively with a constant PM of 45°. On the other hand, the influence of overall voltage loop PM can be obtained by changing θ_{vs} to 20°, 45° and 70° respectively with a constant bandwidth of 40 Hz.

As shown in Fig. 9.29, both the bandwidth and PM of the overall voltage loop have an influence on the damping characteristics in Band I_{SVG}. With the increase of f_{vs},

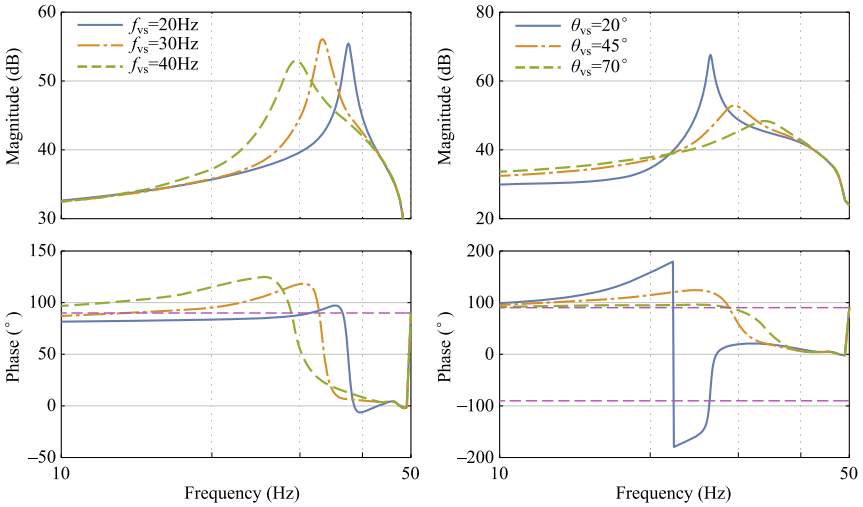

(a) Different overall voltage loop bandwidths (b) Different overall voltage loop PMs

Fig. 9.29 The influence of the overall voltage loop on the damping characteristics in Band I_{SVG} (in AC voltage control mode)

the degree of the negative damping is deepened, and the frequency of the impedance presenting negative damping is further away from the fundamental frequency. With the decrease of θ_{vs}, the damping characteristics are weakened, and the impedance even presents capacitive negative damping from inductive negative damping.

9.5.2.2 Negative Damping Characteristics in Band III_{SVG}

The impedance characteristics are influenced by the AC current loop in Band III_{SVG}. The influence of the overall voltage loop on the damping characteristics in this frequency band (in AC voltage control mode) is shown in Fig. 9.30. Firstly, the AC current control bandwidth f_{iac} is set to 100 Hz, and the PM of the AC current control θ_{iac} is set to 30°. On the one hand, the influence of overall voltage loop bandwidth can be obtained by changing f_{vs} to 20, 30 and 40 Hz respectively with a constant PM of 45°. On the other hand, the influence of overall voltage loop PM can be obtained by changing θ_{vs} to 20°, 45° and 70° respectively with a constant bandwidth of 40 Hz.

As shown in Fig. 9.30, a resonant peak appears in the impedance magnitude, and the impedance presents capacitive negative damping around the resonant frequency. With the increase of f_{vs}, the degree of the capacitive negative damping is deepened. With the increase of θ_{vs}, the degree of the capacitive negative damping is also deepened, and the impedance even presents the inductive negative damping.

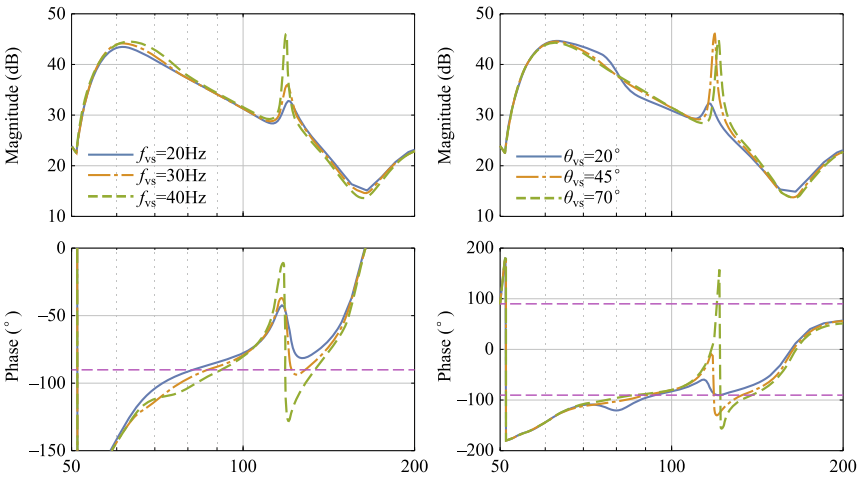

(a) Different overall voltage loop bandwidths (b) Different overall voltage loop PMs

Fig. 9.30 The influence of the overall voltage loop on the damping characteristics in Band $\mathrm{III_{SVG}}$ (in AC voltage control mode)

9.5.2.3 Summary of Negative Damping Characteristics in Each Frequency Band

According to the analysis of the negative damping characteristics of SVG in AC voltage control mode, the following conclusions are obtained.

(1) Band $\mathrm{I_{SVG}}$ ($f < f_1 - f_{vac}$): The impedance characteristics are influenced by the AC current loop, SM capacitor, and overall voltage loop. The frequency-band overlapping effect of the overall voltage loop, AC current loop, and SM capacitor leads to inductive negative damping in this frequency band. The negative damping degree is deepened with the increase of overall voltage loop bandwidth or the decrease of overall voltage loop PM.

(2) Band $\mathrm{II_{SVG}}$ ($f_1 - f_{vac} < f < f_1 + f_{vac}$): The impedance characteristics are dominated by the AC voltage loop, and the impedance presents capacitive negative damping above the fundamental frequency. Besides, PLL also has an influence on the negative damping characteristics. With the increase of PLL bandwidth and PM, the damping characteristics at the resonant peaks are enhanced.

(3) Band $\mathrm{III_{SVG}}$ ($f_1 + f_{vac} < f < f_1 + f_{iac}$): The impedance characteristics are dominated by the AC current loop. The frequency-band overlapping effect between the overall voltage loop or time delay and the AC current loop leads to negative damping in this frequency band. With the increase of the overall voltage loop bandwidth, PM, and time delay, the degree of the negative damping is deepened.

(4) Band $\mathrm{IV_{SVG}}$ ($f > f_1 + f_{iac}$): The impedance characteristics are dominated by the arm inductor. The frequency-band overlapping effect of the time delay and

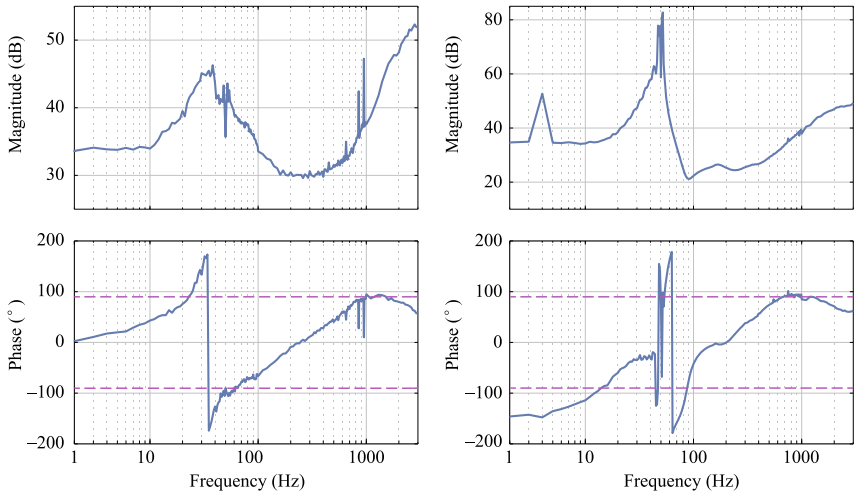

(a) Damping characteristics 19Mvar SVG (Type G) (b) Damping characteristics 26Mvar SVG (Type H)

Fig. 9.31 The scanning damping characteristics of SVG based on CHIL platform (in AC voltage control mode)

arm inductor leads to inductive negative damping periodically presenting in this frequency band. The negative damping characteristics in AC voltage control mode are consistent with reactive power control mode within this frequency band.

Impedance scanning is carried out based on the CHIL platform of different types of SVGs, and the scanning results in AC voltage control mode are shown in Fig. 9.31. It can be seen from the figure that the impedances of SVGs present inductive or capacitive negative damping characteristics, respectively, in different frequency bands.

Chapter 10
Impedance Model and Characteristic Analysis of LCC-HVDC

For the LCC-HVDC transmission system, the sending-end converter station commonly operates in DC current control mode, and the receiving-end converter station operates in DC voltage control mode. The DC transmission lines of LCC-HVDC exhibit non-ideal voltage source characteristics due to the relatively long length of the transmission lines. The converter control and AC grid strength at the receiving end will also influence the impedance characteristics of LCC-HVDC at the sending end via the DC transmission lines.

In this chapter, first, the operating principle and control strategies of the sending-end and receiving-end converter stations in LCC-HVDC are introduced. Then, based on the frequency-domain steady-state operating point, the AC port impedance model of LCC-HVDC at the sending end is established with the sending-end and receiving-end converter control, AC grid strength at the receiving end, and DC transmission lines are taken into account [1]. Moreover, the dominant factors of the impedance characteristics in different frequency bands are analyzed, and the frequency band division method of LCC-HVDC is proposed. The frequency-band overlapping effect and negative damping characteristics are clarified. Finally, based on the CHIL simulation platform, the broadband impedance of LCC-HVDC is scanned, and the typical values of each frequency band are given.

10.1 Operation Principle and Control Strategy

10.1.1 Topology

The LCC-HVDC transmission system can be classified into two-terminal LCC-HVDC transmission and multi-terminal LCC-HVDC transmission. The two-terminal LCC-HVDC transmission system consists of a rectifier station (sending-end

© China Electric Power Press 2023

W. Wang et al., *Analysis and Mitigation of Broadband Oscillation in Renewable Energy Generation and AC/DC Transmission Systems*,
https://doi.org/10.1007/978-981-99-1568-2_10

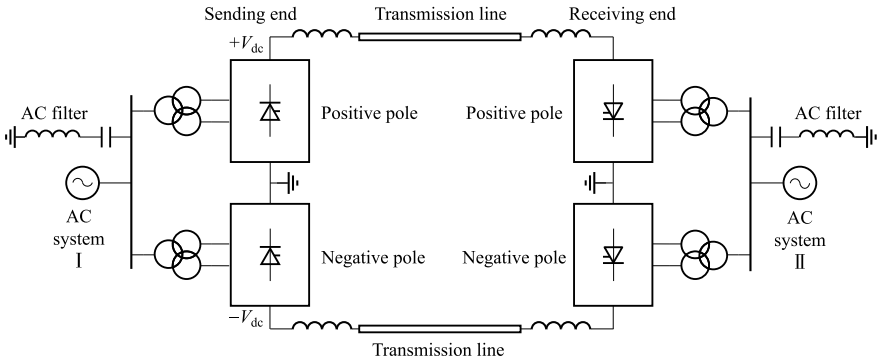

Fig. 10.1 The topology of the two-terminal bipolar LCC-HVDC

converter station), an inverter station (receiving-end converter station), and DC transmission lines, which allows power transmission between two regional AC grids.The multi-terminal LCC-HVDC transmission system consists of three or more converter stations, which realize the interconnection and power transmission between multiple regional AC grids. The multi-terminal LCC-HVDC transmission system can contain multiple rectifier and inverter stations due to the different power flow directions.

The topology of the two-terminal bipolar LCC-HVDC transmission system is shown in Fig. 10.1. The sending-end converter station is a rectifier station, and the receiving-end converter station is an inverter station. The sending-end and receiving-end converter stations are connected by the DC transmission lines to realize the power transmission from the sending-end AC grid (I) to the receiving-end AC grid (II). The bipolar configuration is used in LCC-HVDC, and each converter station consists of a positive-polar converter unit and a negative-polar converter unit. The DC neutral buses at both the sending-end and receiving-end converter stations are grounded. If one DC transmission line or one-polar converter unit fails, the two-terminal LCC-HVDC transmission system can be converted to mono-polar operation with ground earth return.

Since the circuit structure and operation principle of the positive- and negative-polar converter units are symmetrical, the positive-polar converter unit is taken as an example in this chapter. The topology of the two-terminal mono-polar LCC-HVDC transmission system is shown in Fig. 10.2. Both the sending-end and receiving-end converter stations use a 12-pulse converter unit. Each 12-pulse converter unit consists of two 6-pulse thyristor converters, as mentioned in Chap. 5 by connecting the AC port in parallel and the DC port in series. The AC ports of the two 6-pulse thyristor converters are connected to the AC grid via a three-winding transformer or two two-winding transformers.The valve sides of the transformer are star-connected and delta-connected respectively, i.e., Yd1 or Yd11, so that the AC input voltages between the two 6-pulse thyristor converters differ by $\pi/6$. The 6-pulse thyristor converter at the star-connected valve side is marked as Converter I, and the 6-pulse thyristor converter at the delta-connected valve side is marked as Converter II.

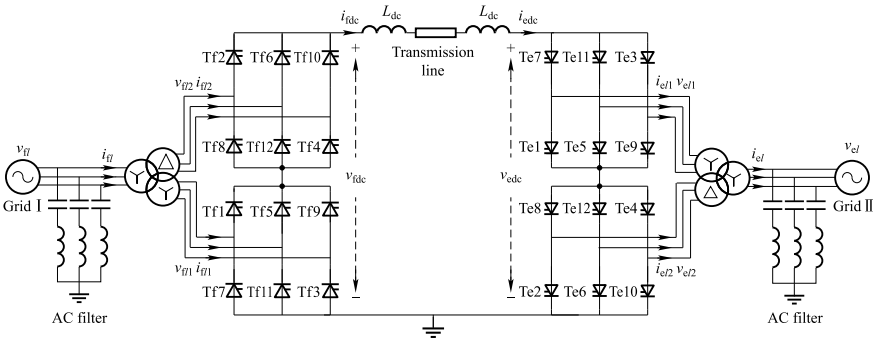

Fig. 10.2 The topology of the two-terminal mono-polar LCC-HVDC

In addition, AC filters are usually equipped to improve the harmonic performances and compensate for the reactive power consumption of the converters.

In Fig. 10.2, the subscript "f " indicates the variable at the sending side, and the subscript "e" indicates the variable at the receiving side. l refers to phases a, b, c. v_{fl}, i_{fl} are the sending-end three-phase AC voltages and currents respectively. v_{fl1}, i_{fl1} are the three-phase AC voltages and currents of Converter I in the sending-end line commutated converter (LCC) respectively. v_{fl2}, i_{fl2} are the three-phase AC voltages and currents of Converter II in the sending-end LCC respectively. v_{fdc}, i_{fdc} are the DC voltage and current of the sending-end LCC respectively. v_{edc}, i_{edc} are the DC voltage and current of the receiving-end LCC respectively. v_{el}, i_{el} are the receiving-end three-phase AC voltages and currents respectively. v_{el1}, i_{el1} are the three-phase AC voltages and currents of Converter I in the receiving-end LCC respectively. v_{el2}, i_{el2} are the three-phase AC voltages and currents of Converter II in the receiving-end LCC respectively. Tfh, Teh ($h = 1$–12) are the hth thyristor of the sending-end and receiving-end LCCs respectively. L_{dc} is a DC smoothing reactor.

10.1.2 Operation Principle

The operation principles of the sending-end and receiving-end LCCs are different and will be introduced in this section respectively.

10.1.2.1 Operation Principle of Sending-end LCC

According to the operation principle of 6-pulse thyristor converter in Chap. 5, the operation principle of the sending-end LCC is analyzed as follows.

Each thyristor is triggered by delaying a trigger angle αf ($\alpha f \leq \pi/2$) at the six natural commutation points in a 6-pulse thyristor converter. Then each thyristor will turn on at $\pi/3$ intervals, and the converter will produce 6-pulse DC voltage

For Converter I in the sending-end LCC, the thyristors are turned on and off in the order of Tf1-Tf3-Tf5-Tf7-Tf9-Tf11. For Converter II in the sending-end LCC, the thyristors are turned on and off in the order of Tf2-Tf4-Tf6-Tf8-Tf10-Tf12.

Because the transformer valve side windings are Yd1 and Yd11 connections respectively, the phase difference of the input voltages of the two thyristor converter is $\pi/6$. The transformer with the Yd1 connection is taken as an example in this section. Each thyristor in Converter I is triggered ahead $\pi/6$ of the corresponding thyristor in Converter II. The twelve thyristors are turned on and off in the order of Tf1~Tf12. The twelve pulses exist in the DC voltage within a fundamental period, so Converter I and Converter II together are called a 12-pulse thyristor converter.

The waveforms of the AC/DC voltages and currents in the sending-end LCC are shown in Fig. 10.3. The AC currents of Converter I i_{fl1} are $\pi/6$ ahead of those of Converter II i_{fl2}. The steady-state values of the DC voltages in Converter I and Converter II are identical, equaling to half of the steady-state value of the DC voltage V_{fdc} in the sending-end LCC. The DC voltage pulses of Converter I are also $\pi/6$ ahead of those of Converter II, leading to the twelve pulses exist in the DC voltage V_{fdc} within a fundamental period. Besides, the transformer leakage inductance introduces the commutation process, resulting in a commutation voltage drop in the DC voltage. α_f is the trigger angle of the sending-end LCC, and μ_f is the overlap angle of the sending-end LCC.

Considering the influence of the transformer leakage inductance, the time-domain model of the AC-side circuit in the sending-end LCC can be obtained with the valve-side leakage inductance referred to the line side.

$$v_{fTl} = v_{fl} - L_{fT}\frac{di_{fl}}{dt} \tag{10.1}$$

where v_{fTl} are the line-side three-phase AC voltages at the sending end. L_{fT} is the transformer leakage inductance at the sending end.

According to the voltage conversion relationship of the transformer, the three-phase AC voltages of Converter I and Converter II in the sending-end LCC can be derived as

$$\begin{cases} v_{fl1}(t) = \dfrac{1}{k_{fT}} v_{fTl}(t) \\ v_{fl2}(t) = \dfrac{1}{k_{fT}} v_{fTl}\left(t - \dfrac{1}{12 f_1}\right) \end{cases} \tag{10.2}$$

where k_{fT} is the transformer voltage ratio at the sending end.

According to the voltage switching function in Chap. 5, the relationship of the AC/DC voltages in the sending-end LCC is given as

$$v_{fdc} = \sum_{l=a,b,c} s_{fl1} v_{fl1} + \sum_{l=a,b,c} s_{fl2} v_{fl2} \tag{10.3}$$

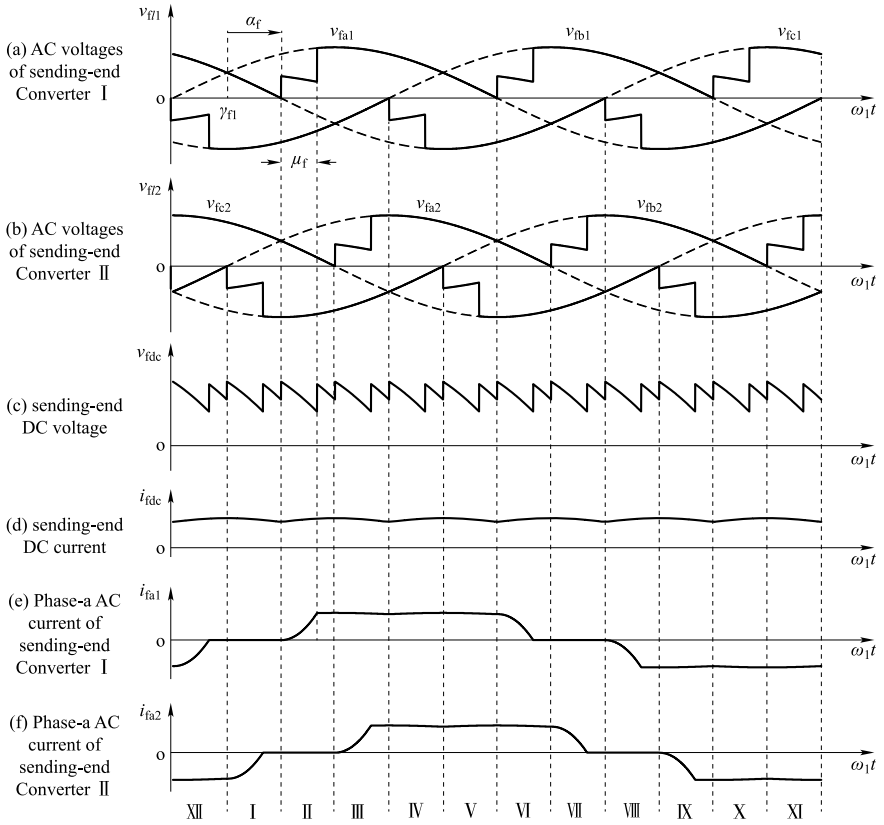

Fig. 10.3 The AC/DC voltages and currents in the sending-end LCC

where s_{fl1}, s_{fl2} are the three-phase switching functions of Converter I and Converter II in the sending-end LCC, respectively.

The definition of the switching functions of Converter I is consistent with Chap. 5. The switching functions of Converter II can be expressed by the switching functions of Converter I, which are

$$s_{fl2}(t) = s_{fl1}\left(t - \frac{1}{12 f_1}\right) \tag{10.4}$$

The relationship of the AC/DC currents in the sending-end LCC satisfies

$$\begin{cases} i_{fl1} = s_{fl1} i_{fdc} \\ i_{fl2} = s_{fl2} i_{fdc} \end{cases} \tag{10.5}$$

According to Eq. (10.5), the sending-end three-phase AC currents can be obtained.

$$\begin{cases} i_{\mathrm{fa}} = \dfrac{1}{k_{\mathrm{fT}}} i_{\mathrm{fa1}} + \dfrac{1}{\sqrt{3}k_{\mathrm{fT}}}(i_{\mathrm{fa2}} - i_{\mathrm{fb2}}) \\ i_{\mathrm{fb}} = \dfrac{1}{k_{\mathrm{fT}}} i_{\mathrm{fb1}} + \dfrac{1}{\sqrt{3}k_{\mathrm{fT}}}(i_{\mathrm{fb2}} - i_{\mathrm{fc2}}) \\ i_{\mathrm{fc}} = \dfrac{1}{k_{\mathrm{fT}}} i_{\mathrm{fc1}} + \dfrac{1}{\sqrt{3}k_{\mathrm{fT}}}(i_{\mathrm{fc2}} - i_{\mathrm{fa2}}) \end{cases} \tag{10.6}$$

10.1.2.2 Operating Principle of Receiving-End LCC

Similarly, the operating principle of the receiving-end LCC is introduced as follows.

The twelve thyristors are turned on and off in the order of Te1~Te12, and Each thyristor in Converter I is triggered $\pi/6$ ahead of the corresponding thyristor in Converter II for the receiving-end LCC. The value range of the trigger angle of the receiving-end LCC α_{e} ($\geq \pi/2$) is different from that of the sending-end LCC α_{f} ($< \pi/2$). Besides, the potential at the common anode of the thyristors is higher than that of the common cathode in the sending-end LCC, so the DC positive and negative pole connection of the receiving-end LCC is opposite to that of the sending-end LCC.

The waveforms of the AC/DC voltages and currents in the sending-end LCC are shown in Fig. 10.4. Taking the natural commutation point γ_{e1} as the reference point, Te1 of Converter I is triggerd in Interval I ($\gamma_{\mathrm{e1}} + \alpha_{\mathrm{e}} \sim \gamma_{\mathrm{e1}} + \alpha_{\mathrm{e}} + \pi/6$), realizing the commutation from Te9 to Te1. Te11 maintains conduction in this interval. During the commutation period, the AC current i_{ea1} in phase a, where Te1 locates, gradually decreases from zero to $-i_{\mathrm{edc}}$. The DC voltage of Converter I in the receiving-end LCC is equal to $v_{\mathrm{eb1}} - v_{\mathrm{ea1}}$. Comparatively, the DC voltage of Converter I in the sending-end LCC is equal to $v_{\mathrm{fa1}} - v_{\mathrm{fb1}}$. In other intervals, the operation states of Converter I and Converter II can be obtained similarly. Therefore, the DC voltages of Converter I and Converter II in the receiving-end LCC are opposite to those of the sending-end LCCμ_{e} is the overlap angle of the receiving-end LCC.

Considering the influence of the transformer leakage inductance,the time-domain model of the AC-side circuit in the receiving-end LCC can be obtained with the valve-side leakage inductance referred to the line side.

$$v_{\mathrm{eT}l} = v_{\mathrm{e}l} + L_{\mathrm{eT}} \frac{\mathrm{d}i_{\mathrm{e}l}}{\mathrm{d}t} \tag{10.7}$$

where $v_{\mathrm{eT}l}$ are the line-side three-phase AC voltages at the receiving end. L_{eT} is the transformer leakage inductance at the receiving end.

According to the voltage conversion relationship of the transformer, the three-phase AC voltages of Converter I and Converter II in the receiving-end LCC can be derived as

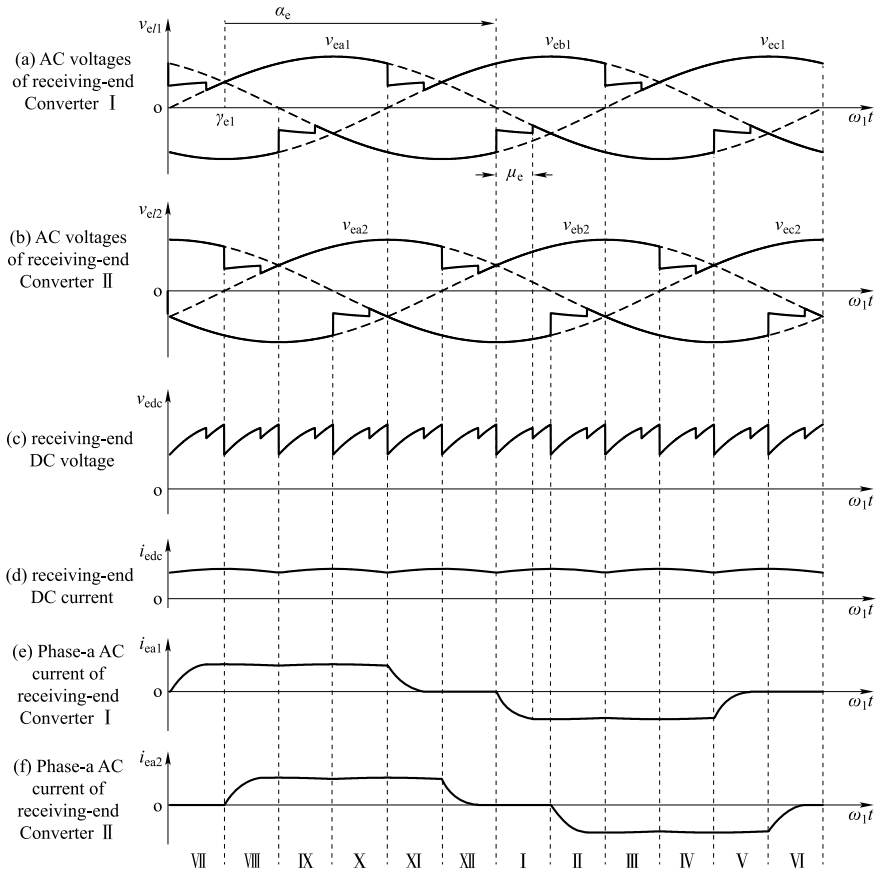

Fig. 10.4 The AC/DC voltages and currents in the receiving-end LCC

$$\begin{cases} v_{el1}(t) = \dfrac{1}{k_{eT}} v_{eTl}(t) \\ v_{el2}(t) = \dfrac{1}{k_{eT}} v_{eTl}\left(t - \dfrac{1}{12 f_1}\right) \end{cases} \tag{10.8}$$

where k_{eT} is the transformer voltage ratio at the receiving end.

Since the DC pole connection of the sending-end and receiving-end LCCs is opposite, the AC/DC voltage conversion relationship is also opposite. To simplify the analysis, the definition of the switching functions in the receiving-end LCC is consistent with the sending-end LCC. The relationship of the AC/DC voltages in the receiving-end LCC can be expressed as

$$v_{edc} = -\left(\sum_{l=a,b,c} s_{el1} v_{el1} + \sum_{l=a,b,c} s_{el2} v_{el2}\right) \tag{10.9}$$

where s_{el1}, s_{el2} are the three-phase switching functions of Converter I and Converter II in the receiving-end LCC respectively.

Since each thyristor in Converter I is triggered $\pi/6$ ahead of the corresponding thyristor in Converter II, the switching functions of Converter II can be expressed by the switching functions of Converter I, which are

$$s_{el2}(t) = s_{el1}\left(t - \frac{1}{12f_1}\right) \tag{10.10}$$

According to the reference direction of the receiving-end AC currents shown in Fig. 10.2, the relationship of the AC/DC currents in the receiving-end LCC satisfies

$$\begin{cases} i_{el1} = -s_{el1} i_{edc} \\ i_{el2} = -s_{el2} i_{edc} \end{cases} \tag{10.11}$$

According to Eq. (10.11), the receiving-end three-phase AC currents can be obtained.

$$\begin{cases} i_{ea} = \dfrac{1}{k_{eT}} i_{ea1} + \dfrac{1}{\sqrt{3}k_{eT}}(i_{ea2} - i_{eb2}) \\ i_{eb} = \dfrac{1}{k_{eT}} i_{eb1} + \dfrac{1}{\sqrt{3}k_{eT}}(i_{eb2} - i_{ec2}) \\ i_{ec} = \dfrac{1}{k_{eT}} i_{ec1} + \dfrac{1}{\sqrt{3}k_{eT}}(i_{ec2} - i_{ea2}) \end{cases} \tag{10.12}$$

10.1.3 Control Strategy

The power transmission of LCC-HVDC is achieved by the coordination control of both the sending-end and receiving-end LCCs. The principle of the coordination control is: one converter station establishes the DC voltage for the HVDC system by adopting constant DC voltage control, constant trigger angle control, or constant extinction angle control (only used in the receiving-end LCC); the other converter station adopts constant DC current control to achieve power transmission. The typical control of the LCC-HVDC transmission system is that the sending-end converter station operates in DC current control mode, and the receiving-end converter station operates in DC voltage control mode.

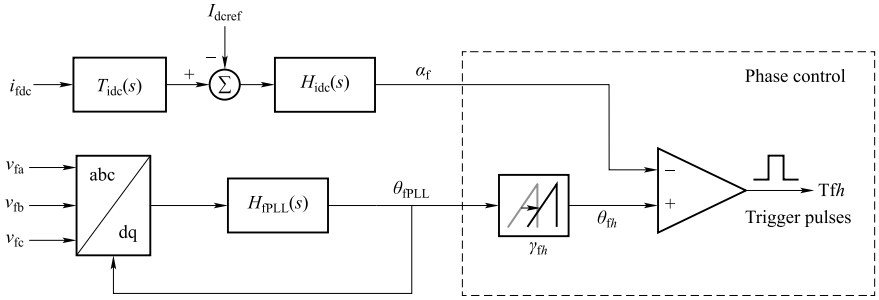

Fig. 10.5 The typical control diagram of the sending-end LCC

10.1.3.1 Control Strategy of Sending-End LCC

The sending-end converter station operates in DC current control mode, and the typical control diagram is shown in Fig. 10.5. The instant when each thyristor is triggered is determined by the PLL output angle θ_{fPLL} and trigger angle α_f of the sending-end LCC together.

First, θ_{fPLL} is obtained by the PLL control, and α_f is obtained by the DC current control. The DC current of the sending-end LCC is filtered and fed into the DC current controller with its reference I_{dcref}, producing α_f. $H_{fPLL}(s)$ is the transfer function of the PLL controller in the sending-end LCC, expressed as $H_{fPLL}(s) = K_{fpp} + K_{fpi}/s$. K_{fpp}, K_{fpi} are the corresponding proportional and integral coefficients respectively. $T_{idc}(s)$ is the transfer function of the DC current filter, expressed as $T_{idc}(s) = 1/(1 + T_{idcf}s)$. T_{idcf} is the corresponding filter time delay. $H_{idc}(s)$ is the transfer function of the DC current controller, expressed as $H_{idc}(s) = K_{idcp} + K_{idci}/s$. K_{idcp}, K_{idci} are the corresponding proportional and integral coefficients respectively.

Then, the phase control function receives θ_{fPLL} and α_f. θ_{fPLL} is equally delayed to produce the reference angle of each thyristor in the sending-end LCC θ_{fh}, which is expressed as

$$\theta_{fh} = \theta_{fPLL} - \gamma_{fh},\ h = 1, 2, \ldots, 12 \tag{10.13}$$

where $\gamma_{fh} = (h - 2)\pi/6$. h corresponds to each thyristor number. γ_{fh} are the phase-shift angles of the twelve natural commutation points in the sending-end LCC respectively, and the difference between two adjacent phase-shift angles is $\pi/6$.

Finally, the firing pulse of each thyristor is triggered by comparing θ_{fh} and α_f.

10.1.3.2 Control Strategy of Receiving-End LCC

The receiving-end converter station operates in DC voltage control mode, and the typical control diagram is shown in Fig. 10.6.

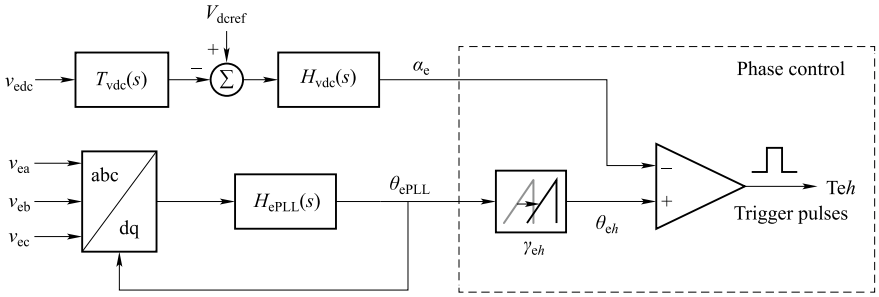

Fig. 10.6 The typical control diagram of the receiving-end LCC

First, the PLL output angle of the receiving-end LCC θ_{ePLL} is produced by the PLL control. Then, the DC voltage of the receiving-end LCC is filtered and fed into the DC voltage controller with its reference, producing the trigger angle of the receiving-end LCC α_e. Finally, the phase control function receives θ_{ePLL} and α_e, triggering the firing pulse of each thyristor. $H_{\text{ePLL}}(s)$ is the transfer function of the PLL controller in the receiving-end LCC, expressed as $H_{\text{ePLL}}(s) = K_{\text{epp}} + K_{\text{epi}}/s$. K_{epp}, K_{epi} are the corresponding proportional and integral coefficients respectively. $T_{\text{vdc}}(s)$ is the transfer function of the DC voltage filter, expressed as $T_{\text{vdc}}(s) = 1/(1 + T_{\text{vdcf}}s)$. T_{vdcf} is the corresponding filter time delay. $H_{\text{vdc}}(s)$ is the transfer functions of the DC voltage controller, expressed as $H_{\text{vdc}}(s) = K_{\text{vdcp}} + K_{\text{vdci}}/s$. K_{vdcp}, K_{vdci} are the corresponding proportional and integral coefficients respectively. γ_{eh} are the phase-shift angles of the twelve natural commutation points in the receiving-end LCC respectively.

10.2 Frequency-Domain Modeling of Steady-State Operation

This section analyzes the steady-state harmonic characteristics of both the sending-end and receiving-end LCC-HVDC, and establishes the frequency- domain steady-state model of the main circuit.

10.2.1 Frequency-Domain Characteristic Analysis of Steady-State Operating Point

According to the frequency-domain steady-state characteristics of the thyristor converter, as mentioned in Chap. 5, the AC voltage, AC current, and switching function of the 6-pulse thyristor converter contain the steady-state harmonic components at $(6n \pm 1)f_1$ $(n = 0, \pm 1, \pm 2, \ldots)$, and the DC voltage and current contain

the steady-state harmonic components at $6nf_1$. Notably, the steady-state characteristics of the 6-pulse thyristor converters in the LCC-HVDC transmission system are consistent.

For the steady-state characteristics of LCC-HVDC, the sending-end LCC is taken as an example. The AC voltages of Converter I and Converter II contain the steady-state harmonic components at $(6n \pm 1)f_1$, expressed as $\boldsymbol{V}_{\mathrm{fl}1,6n\pm1}$ and $\boldsymbol{V}_{\mathrm{fl}2,6n\pm1}$ respectively. According to Eq. (10.2), the relationship between the two converter satisfies

$$\begin{cases} \boldsymbol{V}_{\mathrm{fl}2,6n+1} = \boldsymbol{V}_{\mathrm{fl}1,6n+1}\mathrm{e}^{-\mathrm{j}(6n+1)\pi/6} \\ \boldsymbol{V}_{\mathrm{fl}2,6n-1} = \boldsymbol{V}_{\mathrm{fl}1,6n-1}\mathrm{e}^{-\mathrm{j}(6n-1)\pi/6} \end{cases} \tag{10.14}$$

where $\boldsymbol{V}_{\mathrm{fl}1,6n+1}$, $\boldsymbol{V}_{\mathrm{fl}1,6n-1}$ are the steady-state harmonic components of the three-phase AC voltages of Converter I at $(6n+1)f_1$ and $(6n-1)f_1$ in the sending-end LCC respectively; $\boldsymbol{V}_{\mathrm{fl}2,6n+1}$, $\boldsymbol{V}_{\mathrm{fl}2,6n-1}$ are the steady-state harmonic components of the three-phase AC voltages of Converter II at $(6n+1)f_1$ and $(6n-1)f_1$ in the sending-end LCC respectively.

According to Eq. (10.4), the switching functions between Converter I and Converter II satisfy

$$\begin{cases} \boldsymbol{S}_{\mathrm{fl}2,6n+1} = \boldsymbol{S}_{\mathrm{fl}1,6n+1}\mathrm{e}^{-\mathrm{j}(6n+1)\pi/6} \\ \boldsymbol{S}_{\mathrm{fl}2,6n-1} = \boldsymbol{S}_{\mathrm{fl}1,6n-1}\mathrm{e}^{-\mathrm{j}(6n-1)\pi/6} \end{cases} \tag{10.15}$$

where $\boldsymbol{S}_{\mathrm{fl}1,6n+1}$, $\boldsymbol{S}_{\mathrm{fl}1,6n-1}$ are the steady-state components of the three-phase switching functions of Converter I at $(6n+1)f_1$ and $(6n-1)f_1$ in the sending-end LCC respectively; $\boldsymbol{S}_{\mathrm{fl}2,6n+1}$, $\boldsymbol{S}_{\mathrm{fl}2,6n-1}$ are the steady-state components of the three-phase switching functions of Converter II at $(6n+1)f_1$ and $(6n-1)f_1$ in the sending-end LCC respectively.

For Converter I, the multiplications between $\boldsymbol{S}_{\mathrm{fl}1,6n_1+1}$ with $\boldsymbol{V}_{\mathrm{fl}1,6n_2-1}$, $\boldsymbol{S}_{\mathrm{fl}1,6n_1-1}$ with $\boldsymbol{V}_{\mathrm{fl}1,6n_2+1}$, $\boldsymbol{S}_{\mathrm{fl}1,6n_2+1}$ with $\boldsymbol{V}_{\mathrm{fl}1,6n_1-1}$, and $\boldsymbol{S}_{\mathrm{fl}1,6n_2-1}$ with $\boldsymbol{V}_{\mathrm{fl}1,6n_1+1}$ lead to the steady-state harmonic components of the DC voltage at $6(n_1+n_2)f_1$ $(n_1, n_2 = 0, \pm1, \pm2, \ldots)$. Similarly, the steady-state harmonic components of the DC voltage of Converter 2 can also be analyzed.

The relationship of the AC/DC voltages in the sending-end LCC can be derived by transforming Eq. (10.3) to the frequency domain.

$$\begin{aligned} \boldsymbol{V}_{\mathrm{fdc},6(n_1+n_2)} = & \sum_{l=\mathrm{a,b,c}} \boldsymbol{S}_{\mathrm{fl}1,6n_1+1}\boldsymbol{V}_{\mathrm{fl}1,6n_2-1} + \sum_{l=\mathrm{a,b,c}} \boldsymbol{S}_{\mathrm{fl}1,6n_1-1}\boldsymbol{V}_{\mathrm{fl}1,6n_2+1} \\ & + \sum_{l=\mathrm{a,b,c}} \boldsymbol{S}_{\mathrm{fl}1,6n_2+1}\boldsymbol{V}_{\mathrm{fl}1,6n_1-1} + \sum_{l=\mathrm{a,b,c}} \boldsymbol{S}_{\mathrm{fl}1,6n_2-1}\boldsymbol{V}_{\mathrm{fl}1,6n_1+1} \\ & + \sum_{l=\mathrm{a,b,c}} \boldsymbol{S}_{\mathrm{fl}2,6n_1+1}\boldsymbol{V}_{\mathrm{fl}2,6n_2-1} + \sum_{l=\mathrm{a,b,c}} \boldsymbol{S}_{\mathrm{fl}2,6n_1-1}\boldsymbol{V}_{\mathrm{fl}2,6n_2+1} \end{aligned}$$

$$+\sum_{l=\mathrm{a,b,c}} \boldsymbol{S}_{\mathrm{f}l2,6n_2+1}\boldsymbol{V}_{\mathrm{f}l2,6n_1-1}+\sum_{l=\mathrm{a,b,c}} \boldsymbol{S}_{\mathrm{f}l2,6n_2-1}\boldsymbol{V}_{\mathrm{f}l2,6n_1+1} \tag{10.16}$$

where $\boldsymbol{V}_{\mathrm{fdc},6(n_1+n_2)}$ are the steady-state harmonic components of the DC voltage at $6(n_1+n_2)f_1$ in the sending-end LCC.

Substituting Eqs. (10.14) and (10.15) into Eq. (10.16), the steady-state harmonic components of the DC voltage in the sending-end LCC can be simplified to

$$\boldsymbol{V}_{\mathrm{fdc},6(n_1+n_2)}=\boldsymbol{V}_{\mathrm{fdc1},6(n_1+n_2)}+\boldsymbol{V}_{\mathrm{fdc2},6(n_1+n_2)} \tag{10.17}$$

where $\boldsymbol{V}_{\mathrm{fdc1},6(n_1+n_2)}$, $\boldsymbol{V}_{\mathrm{fdc2},6(n_1+n_2)}$ are the steady-state harmonic components of the DC voltages of Converter I and Converter II at $6(n_1+n_2)f_1$ in the sending-end LCC respectively. The expressions of $\boldsymbol{V}_{\mathrm{fdc1},6(n_1+n_2)}$ and $\boldsymbol{V}_{\mathrm{fdc2},6(n_1+n_2)}$ are

$$\begin{cases} \boldsymbol{V}_{\mathrm{fdc1},6(n_1+n_2)}=\displaystyle\sum_{l=\mathrm{a,b,c}} (\boldsymbol{S}_{\mathrm{f}l1,6n_1+1}\boldsymbol{V}_{\mathrm{f}l1,6n_2-1}+\boldsymbol{S}_{\mathrm{f}l1,6n_1-1}\boldsymbol{V}_{\mathrm{f}l1,6n_2+1} \\ \qquad\qquad +\boldsymbol{S}_{\mathrm{f}l1,6n_2+1}\boldsymbol{V}_{\mathrm{f}l1,6n_1-1}+\boldsymbol{S}_{\mathrm{f}l1,6n_2-1}\boldsymbol{V}_{\mathrm{f}l1,6n_1+1}) \\ \boldsymbol{V}_{\mathrm{fdc2},6(n_1+n_2)}=\boldsymbol{V}_{\mathrm{fdc1},6(n_1+n_2)}\mathrm{e}^{-\mathrm{j}(n_1+n_2)\pi} \end{cases}$$

Besides, the following relationship is satisfied

$$\mathrm{e}^{-\mathrm{j}(n_1+n_2)\pi}=\begin{cases} -1, & \text{if } n_1+n_2 \text{ is odd} \\ 1, & \text{if } n_1+n_2 \text{ is even} \end{cases} \tag{10.18}$$

As seen in Eq. (10.18), if n_1+n_2 is odd, the steady-state harmonic components of the DC voltages of Converter I and Converter II at $6(n_1+n_2)f_1$ have the same amplitude but opposite phase. If n_1+n_2 is even, the steady-state harmonic components of the DC voltages of Converter I and Converter II at $6(n_1+n_2)f_1$ have the same amplitude and phase. The steady-state harmonic components of the DC voltages of Converter I and Converter II at $6(2n+1)f_1$ are canceled by each other. In comparison, the steady-state harmonic components of the DC voltages of Converter I and Converter II at $12nf_1$ are superimposed on each other. Therefore, the frequencies of the steady-state harmonic components of the DC voltage in the sending-end LCC are increased to $12nf_1$. Similarly, it can be obtained that the DC voltages and currents of the sending-end and receiving-end LCCs contain steady-state harmonic components at $12nf_1$.

Transforming Eqs. (10.5) and (10.6) to the frequency domain, and substituting Eq. (10.15), the steady-state harmonic components of the AC currents can be derived as

$$\boldsymbol{I}_{\mathrm{f}l,6n_1\pm1+12n_2}=\boldsymbol{I}_{\mathrm{f}l1,6n_1\pm1+12n_2}+\boldsymbol{I}_{\mathrm{f}l2,6n_1\pm1+12n_2} \tag{10.19}$$

where $\boldsymbol{I}_{\mathrm{f}l,6n_1\pm1+12n_2}$ are the steady-state harmonic components of the sending-end three-phase AC currents at $(6n_1\pm1+12n_2)f_1$ respectively; $\boldsymbol{I}_{\mathrm{f}l1,6n_1\pm1+12n_2}$,

$\boldsymbol{I}_{\mathrm{fl}2,6n_1\pm1+12n_2}$ are the steady-state harmonic components of the three-phase AC currents of Converter I and Converter II at $(6n_1 \pm 1 + 12n_2)f_1$ in the sending-end LCC respectively. The expressions of $\boldsymbol{I}_{\mathrm{fl}1,6n_1\pm1+12n_2}$ and $\boldsymbol{I}_{\mathrm{fl}2,6n_1\pm1+12n_2}$ are

$$\begin{cases} \boldsymbol{I}_{\mathrm{fl}1,6n_1\pm1+12n_2} = \dfrac{1}{k_{\mathrm{fT}}}\boldsymbol{S}_{\mathrm{fl}1,6n_1\pm1}\boldsymbol{I}_{\mathrm{fdc},12n_2} \\ \boldsymbol{I}_{\mathrm{fl}2,6n_1\pm1+12n_2} = \boldsymbol{I}_{\mathrm{fl}1,6n_1\pm1+12n_2}\mathrm{e}^{-\mathrm{j}n_1\pi} \end{cases}$$

where $\boldsymbol{I}_{\mathrm{fdc},12n_2}$ are the steady-state harmonic components of the DC current in the sending-end LCC at $12n_2 f_1$.

In Eq. (10.19), $\mathrm{e}^{-\mathrm{j}n_1\pi} = -1$ as n_1 is odd, and $\mathrm{e}^{-\mathrm{j}n_1\pi} = 1$ as n_1 is even. This indicates that the steady-state harmonic components of the AC currents of Converter I and Converter II at $[6(2n+1) \pm 1]f_1$, referred to the line side, are canceled by each other. In comparison, the steady-state harmonic components of the AC currents of Converter I and Converter II at $(12n \pm 1)f_1$ are superimposed on each other. It can be obtained that the sending-end and receiving-end AC voltages and currents contain steady-state harmonic components at $(12n \pm 1)f_1$.

Since the AC- and DC-side harmonic frequencies of LCC-HVDC are $(12n \pm 1)f_1$ and $12nf_1$ respectively, only the steady-state harmonic components at $(12n \pm 1)f_1$ in the switching functions should be considered.

In order to describe the steady-state harmonic characteristics, the steady-state harmonic components of LCC-HVDC quantities are arranged in the following steady-state frequency order.

$$[\,(-12g-1)f_1,\ \ldots,\ -2f_1,\ -f_1,\ 0,\ f_1,\ 2f_1,\ \ldots,\ (12g+1)f_1\,]^{\mathrm{T}} \tag{10.20}$$

where the frequency order is from $-(12g+1)f_1$ to $(12g+1)f_1$ ($24g+3$ in total).

The AC voltages and currents contain the steady-state harmonic components at $(12n \pm 1)f_1$. Taking phase a as an example, the steady-state vectors of the sending-end AC voltage and current can be expressed as

$$\begin{cases} \boldsymbol{V}_{\mathrm{fa}} = [\ldots,\ \boldsymbol{V}^*_{\mathrm{f}13},\ 0,\ \boldsymbol{V}^*_{\mathrm{f}11},\ 0,\ 0,\ 0,\ 0,\ 0,\ 0,\ 0,\ 0,\ 0,\ \boldsymbol{V}^*_{\mathrm{f}1},\ 0, \\ \qquad \boldsymbol{V}_{\mathrm{f}1},\ 0,\ 0,\ 0,\ 0,\ 0,\ 0,\ 0,\ 0,\ 0,\ \boldsymbol{V}_{\mathrm{f}11},\ 0,\ \boldsymbol{V}_{\mathrm{f}13},\ \ldots]^{\mathrm{T}} \\ \boldsymbol{I}_{\mathrm{fa}} = [\ldots,\ \boldsymbol{I}^*_{\mathrm{f}13},\ 0,\ \boldsymbol{I}^*_{\mathrm{f}11},\ 0,\ 0,\ 0,\ 0,\ 0,\ 0,\ 0,\ 0,\ 0,\ \boldsymbol{I}^*_{\mathrm{f}1},\ 0, \\ \qquad \boldsymbol{I}_{\mathrm{f}1},\ 0,\ 0,\ 0,\ 0,\ 0,\ 0,\ 0,\ 0,\ 0,\ \boldsymbol{I}_{\mathrm{f}11},\ 0,\ \boldsymbol{I}_{\mathrm{f}13},\ \ldots]^{\mathrm{T}} \end{cases} \tag{10.21}$$

where each component is represented in the form of complex vector, such as $\boldsymbol{V}_{\mathrm{f}k} = V_{\mathrm{f}k}\mathrm{e}^{\mathrm{j}\varphi_{\mathrm{f}vk}}$, $\boldsymbol{I}_{\mathrm{f}k} = I_{\mathrm{f}k}\mathrm{e}^{\mathrm{j}\varphi_{\mathrm{f}ik}}$. The subscript number $k = 0, \pm1, \pm2, \ldots, \pm(12g+1)$ indicates the harmonic order, corresponding to the frequency kf_1. The component at $-kf_1$ is equal to the conjugate of the component at kf_1, such as $\boldsymbol{V}_{-\mathrm{f}k} = \boldsymbol{V}^*_{\mathrm{f}k}$, $\boldsymbol{I}_{-\mathrm{f}k} = \boldsymbol{I}^*_{\mathrm{f}k}$. The amplitude of the harmonic component at kf_1 or $-kf_1$ is equal to half of each actual harmonic component at frequency kf_1. For the AC voltage and current, and the components are non-zero if and only if $k = 12n \pm 1$.

Considering the influence of the commutation, the steady-state vectors of the phase-a voltage and current switching functions in the sending-end LCC can be expressed as

$$\begin{cases} \boldsymbol{S}_{\mathrm{fva}} = [\ldots, \boldsymbol{S}^*_{\mathrm{fv13}}, 0, \boldsymbol{S}^*_{\mathrm{fv11}}, 0, 0, 0, 0, 0, 0, 0, 0, 0, \boldsymbol{S}^*_{\mathrm{fv1}}, 0, \\ \qquad \boldsymbol{S}_{\mathrm{fv1}}, 0, 0, 0, 0, 0, 0, 0, 0, 0, \boldsymbol{S}_{\mathrm{fv11}}, 0, \boldsymbol{S}_{\mathrm{fv13}}, \ldots]^{\mathrm{T}} \\ \boldsymbol{S}_{\mathrm{fia}} = [\ldots, \boldsymbol{S}^*_{\mathrm{fi13}}, 0, \boldsymbol{S}^*_{\mathrm{fi11}}, 0, 0, 0, 0, 0, 0, 0, 0, 0, \boldsymbol{S}^*_{\mathrm{fi1}}, 0, \\ \qquad \boldsymbol{S}_{\mathrm{fi1}}, 0, 0, 0, 0, 0, 0, 0, 0, 0, \boldsymbol{S}_{\mathrm{fi11}}, 0, \boldsymbol{S}_{\mathrm{fi13}}, \ldots]^{\mathrm{T}} \end{cases} \tag{10.22}$$

where $\boldsymbol{S}_{\mathrm{fv}k}$ or $\boldsymbol{S}_{\mathrm{fi}k}$ is the steady-state component at the frequency kf_1; the element is non-zero if and only if $k = 12n \pm 1$.

According to the steady-state model of the switching functions in Chapter 5, the element $\boldsymbol{S}_{\mathrm{fv}k}$ at kf_1 $(k = 12n \pm 1)$ in the steady-state vector of the voltage switching function can be expressed as

$$\boldsymbol{S}_{\mathrm{fv}k} = \frac{\sin(k\pi/3)\left(1 - \mathrm{e}^{-\mathrm{j}k\pi}\right)\left(1 + \mathrm{e}^{-\mathrm{j}k\mu_{\mathrm{f}}}\right)}{2k\pi} \mathrm{e}^{-\mathrm{j}k\alpha_{\mathrm{f0}}} \mathrm{e}^{\mathrm{j}k\varphi_{\mathrm{fv1}}} \tag{10.23}$$

where μ_{f} and α_{f0} are the overlap angle and steady-state trigger angle of the sending-end LCC respectively; φ_{fv1} is the phase of the fundamental component of the sending-end AC voltage.

The element $\boldsymbol{S}_{\mathrm{fi}k}$ at $kf_1 (k = 12n \pm 1)$ in the steady-state vector of the current switching function can be expressed as

$$\boldsymbol{S}_{\mathrm{fi}k} = \mathrm{j}\frac{\sin(k\pi/3)\left(1 - \mathrm{e}^{-\mathrm{j}k\pi}\right)\left(\mathrm{e}^{-\mathrm{j}k\mu_{\mathrm{fi}}} - 1\right)}{k^2\pi\mu_{\mathrm{fi}}} \mathrm{e}^{-\mathrm{j}k\alpha_{\mathrm{f0}}} \mathrm{e}^{\mathrm{j}k\varphi_{\mathrm{fv1}}} \tag{10.24}$$

where μ_{fi} is the equivalent current overlap angle of the sending-end LCC.

Based on the phase-sequence relationship of the steady-state component at each frequency, the steady-state vectors of the sending-end AC voltages, AC currents, and voltage and current switching functions in phase b and phase c can be obtained according to Eqs. (10.22) and (10.23).

$$\begin{cases} \boldsymbol{V}_{\mathrm{fb}} = \boldsymbol{D}\boldsymbol{V}_{\mathrm{fa}}, \quad \boldsymbol{I}_{\mathrm{fb}} = \boldsymbol{D}\boldsymbol{I}_{\mathrm{fa}}, \quad \boldsymbol{S}_{\mathrm{fvb}} = \boldsymbol{D}\boldsymbol{S}_{\mathrm{fva}}, \quad \boldsymbol{S}_{\mathrm{fib}} = \boldsymbol{D}\boldsymbol{S}_{\mathrm{fia}} \\ \boldsymbol{V}_{\mathrm{fc}} = \boldsymbol{D}^*\boldsymbol{V}_{\mathrm{fa}}, \quad \boldsymbol{I}_{\mathrm{fc}} = \boldsymbol{D}^*\boldsymbol{I}_{\mathrm{fa}}, \quad \boldsymbol{S}_{\mathrm{fvc}} = \boldsymbol{D}^*\boldsymbol{S}_{\mathrm{fva}}, \quad \boldsymbol{S}_{\mathrm{fic}} = \boldsymbol{D}^*\boldsymbol{S}_{\mathrm{fia}} \end{cases} \tag{10.25}$$

where $\boldsymbol{D}$ is the phase-sequence coefficient matrix of the steady-state vectors, expressed as

$$\boldsymbol{D} = \mathrm{diag}\left[\left\{\mathrm{e}^{-\mathrm{j}2k\pi/3}\right\}\Big|_{k=-12g-1,\ldots,0,\ldots,12g+1}\right] \tag{10.26}$$

The DC voltages and currents contain the steady-state harmonic components at $(12n \pm 1)f_1$. The steady-state vectors of the DC voltage and current in the sending-end LCC can be expressed as

$$\begin{cases} \boldsymbol{V}_{\mathrm{fdc}} = [\ldots, 0, \boldsymbol{V}^*_{\mathrm{fdc12}}, 0, 0, 0, 0, 0, 0, 0, 0, 0, 0, 0, 0, \boldsymbol{V}_{\mathrm{fdc0}}, \\ \qquad 0, 0, 0, 0, 0, 0, 0, 0, 0, 0, 0, \boldsymbol{V}_{\mathrm{fdc12}}, 0, \ldots]^{\mathrm{T}} \\ \boldsymbol{I}_{\mathrm{fdc}} = [\ldots, 0, \boldsymbol{I}^*_{\mathrm{fdc12}}, 0, 0, 0, 0, 0, 0, 0, 0, 0, 0, 0, 0, \boldsymbol{I}_{\mathrm{fdc0}}, \\ \qquad 0, 0, 0, 0, 0, 0, 0, 0, 0, 0, 0, \boldsymbol{I}_{\mathrm{fdc12}}, 0, \ldots]^{\mathrm{T}} \end{cases} \tag{10.27}$$

Similarly, the steady-state vectors of the receiving-end phase-a AC voltage and current can be expressed as

$$\begin{cases} \boldsymbol{V}_{\mathrm{ea}} = [\ldots, \boldsymbol{V}^*_{\mathrm{e13}}, 0, \boldsymbol{V}^*_{\mathrm{e11}}, 0, 0, 0, 0, 0, 0, 0, 0, 0, 0, \boldsymbol{V}^*_{\mathrm{e1}}, 0, \\ \qquad \boldsymbol{V}_{\mathrm{e1}}, 0, 0, 0, 0, 0, 0, 0, 0, 0, 0, \boldsymbol{V}_{\mathrm{e11}}, 0, \boldsymbol{V}_{\mathrm{e13}}, \ldots]^{\mathrm{T}} \\ \boldsymbol{I}_{\mathrm{ea}} = [\ldots, \boldsymbol{I}^*_{\mathrm{e13}}, 0, \boldsymbol{I}^*_{\mathrm{e11}}, 0, 0, 0, 0, 0, 0, 0, 0, 0, 0, \boldsymbol{I}^*_{\mathrm{e1}}, 0, \\ \qquad \boldsymbol{I}_{\mathrm{e1}}, 0, 0, 0, 0, 0, 0, 0, 0, 0, 0, \boldsymbol{I}_{\mathrm{e11}}, 0, \boldsymbol{I}_{\mathrm{e13}}, \ldots]^{\mathrm{T}} \end{cases} \tag{10.28}$$

The steady-state vectors of the phase-a voltage and current switching functions in the receiving-end LCC can be expressed as

$$\begin{cases} \boldsymbol{S}_{\mathrm{eva}} = [\ldots, \boldsymbol{S}^*_{\mathrm{ev13}}, 0, \boldsymbol{S}^*_{\mathrm{ev11}}, 0, 0, 0, 0, 0, 0, 0, 0, 0, 0, \boldsymbol{S}^*_{\mathrm{ev1}}, 0, \\ \qquad \boldsymbol{S}_{\mathrm{ev1}}, 0, 0, 0, 0, 0, 0, 0, 0, 0, 0, \boldsymbol{S}_{\mathrm{ev11}}, 0, \boldsymbol{S}_{\mathrm{ev13}}, \ldots]^{\mathrm{T}} \\ \boldsymbol{S}_{\mathrm{eia}} = [\ldots, \boldsymbol{S}^*_{\mathrm{ei13}}, 0, \boldsymbol{S}^*_{\mathrm{ei11}}, 0, 0, 0, 0, 0, 0, 0, 0, 0, 0, \boldsymbol{S}^*_{\mathrm{ei1}}, 0, \\ \qquad \boldsymbol{S}_{\mathrm{ei1}}, 0, 0, 0, 0, 0, 0, 0, 0, 0, 0, \boldsymbol{S}_{\mathrm{ei11}}, 0, \boldsymbol{S}_{\mathrm{ei13}}, \ldots]^{\mathrm{T}} \end{cases} \tag{10.29}$$

where the expressions of the elements are consistent with Eqs. (10.23) and (10.24) with the subscript "f" replaced with "e".

Based on the phase-sequence relationship of the steady-state component at each frequency, the steady-state vectors of the receiving-end AC voltages, AC currents, and voltage and current switching functions in phase b and phase c can be obtained according to Eqs. (10.28) and (10.29).

$$\begin{cases} \boldsymbol{V}_{\mathrm{eb}} = \boldsymbol{D}\boldsymbol{V}_{\mathrm{ea}}, \ \boldsymbol{I}_{\mathrm{eb}} = \boldsymbol{D}\boldsymbol{I}_{\mathrm{ea}}, \ \boldsymbol{S}_{\mathrm{evb}} = \boldsymbol{D}\boldsymbol{S}_{\mathrm{eva}}, \ \boldsymbol{S}_{\mathrm{eib}} = \boldsymbol{D}\boldsymbol{S}_{\mathrm{eia}} \\ \boldsymbol{V}_{\mathrm{ec}} = \boldsymbol{D}^*\boldsymbol{V}_{\mathrm{ea}}, \ \boldsymbol{I}_{\mathrm{ec}} = \boldsymbol{D}^*\boldsymbol{I}_{\mathrm{ea}}, \ \boldsymbol{S}_{\mathrm{evc}} = \boldsymbol{D}^*\boldsymbol{S}_{\mathrm{eva}}, \ \boldsymbol{S}_{\mathrm{eic}} = \boldsymbol{D}^*\boldsymbol{S}_{\mathrm{eia}} \end{cases} \tag{10.30}$$

The steady-state vectors of the DC voltage and current in the receiving-end LCC can be expressed as

$$\begin{cases} \boldsymbol{V}_{\mathrm{edc}} = [\ldots, 0, \boldsymbol{V}^*_{\mathrm{edc12}}, 0, 0, 0, 0, 0, 0, 0, 0, 0, 0, 0, 0, \boldsymbol{V}_{\mathrm{edc0}}, \\ \qquad 0, 0, 0, 0, 0, 0, 0, 0, 0, 0, 0, \boldsymbol{V}_{\mathrm{edc12}}, 0, \ldots]^{\mathrm{T}} \\ \boldsymbol{I}_{\mathrm{edc}} = [\ldots, 0, \boldsymbol{I}^*_{\mathrm{edc12}}, 0, 0, 0, 0, 0, 0, 0, 0, 0, 0, 0, 0, \boldsymbol{I}_{\mathrm{edc0}}, \\ \qquad 0, 0, 0, 0, 0, 0, 0, 0, 0, 0, 0, \boldsymbol{I}_{\mathrm{edc12}}, 0, \ldots]^{\mathrm{T}} \end{cases} \tag{10.31}$$

To sum up, the frequency-domain characteristics of the steady-state vectors in the sending-end and receiving-end LCCs are listed in Table 10.1. The frequency-domain distribution characteristics of the corresponding steady-state vectors in the sending-end and receiving-end LCCs are the same.

Table 10.1 The frequency-domain characteristics of the steady-state vectors in LCC-HVDC

Steady-State Vectors	Frequency
$\boldsymbol{V}_{\mathrm{f}l}$, $\boldsymbol{V}_{\mathrm{e}l}$, $\boldsymbol{I}_{\mathrm{f}l}$, $\boldsymbol{I}_{\mathrm{e}l}$	$(12n+1)f_1$
	$(12n-1)f_1$
$\boldsymbol{S}_{\mathrm{fv}l}$, $\boldsymbol{S}_{\mathrm{ev}l}$, $\boldsymbol{S}_{\mathrm{fi}l}$, $\boldsymbol{S}_{\mathrm{ei}l}$	$(12n+1)f_1$
	$(12n-1)f_1$
$\boldsymbol{V}_{\mathrm{fdc}}$, $\boldsymbol{V}_{\mathrm{edc}}$, $\boldsymbol{I}_{\mathrm{fdc}}$, $\boldsymbol{I}_{\mathrm{edc}}$	$12nf_1$

10.2.2 Frequency-Domain Steady-State Model of Main Circuit

Based on the steady-state vectors of the AC/DC voltages and currents in the sending-end and receiving-end LCCs, the frequency-domain steady-state model of the main circuit is established in this section.

The steady-state model of the AC-side circuit in the sending-end LCC can be obtained by transforming Eq. (10.1) to the frequency domain.

$$\boldsymbol{V}_{\mathrm{fT}l} = \boldsymbol{V}_{\mathrm{f}l} - \boldsymbol{Z}_{\mathrm{fT0}}\boldsymbol{I}_{\mathrm{f}l} \tag{10.32}$$

where $\boldsymbol{V}_{\mathrm{fT}l}$ are the steady-state vectors of the line-side three-phase AC voltages at the sending end respectively; $\boldsymbol{Z}_{\mathrm{fT0}}$ is the impedance of the transformer leakage inductance at the sending end in the steady-state frequency order, expressed as

$$\begin{aligned}\boldsymbol{Z}_{\mathrm{fT0}} = \mathrm{j}2\pi L_{\mathrm{fT}} \cdot \mathrm{diag}[&(-12g-1)f_1, \ldots, -2f_1, -f_1, 0,\\ &f_1, 2f_1, \ldots, (12g+1)f_1]\end{aligned} \tag{10.33}$$

The frequency-domain relationship of the AC/DC voltage in the sending-end LCC can be developed by transforming Eqs. (10.2) and (10.3) to the frequency domain.

$$\boldsymbol{V}_{\mathrm{fdc}} = \frac{2}{k_{\mathrm{fT}}} \sum_{l=\mathrm{a,b,c}} \boldsymbol{S}_{\mathrm{fv}l}\boldsymbol{V}_{\mathrm{fT}l} \tag{10.34}$$

where $\boldsymbol{S}_{\mathrm{fv}l}$ are the expanded steady-state matrices of the three-phase voltage switching functions in the sending-end LCC, and the convolution is replaced by the scalar product.

The frequency-domain relationship of the AC/DC currents in the sending-end LCC can be developed by transforming Eqs. (10.5) and (10.6) to the frequency domain.

$$\boldsymbol{I}_{\mathrm{f}l} = \frac{2}{k_{\mathrm{fT}}}\boldsymbol{S}_{\mathrm{fi}l}\boldsymbol{I}_{\mathrm{fdc}} \tag{10.35}$$

where $\boldsymbol{S}_{\mathrm{fl}l}$ are the expanded steady-state matrices of the three-phase voltage switching functions in the sending-end LCC.

The steady-state model of the AC-side circuit in the receiving-end LCC can be obtained by transforming Eq. (10.7) to the frequency domain.

$$\boldsymbol{V}_{\mathrm{eT}l} = \boldsymbol{V}_{\mathrm{e}l} + \boldsymbol{Z}_{\mathrm{eT0}}\boldsymbol{I}_{\mathrm{e}l} \tag{10.36}$$

where $\boldsymbol{V}_{\mathrm{eT}l}$ are the steady-state vectors of the line-side three-phase AC voltages at the receiving end respectively; $\boldsymbol{Z}_{\mathrm{eT0}}$ is the impedance of the transformer leakage inductance at the receiving end in the steady-state frequency order; the expression is consistent with Eq. (10.33) with the subscript "f" replaced with "e".

The DC pole connection of the sending-end and receiving-end LCCs is opposite, and the reference directions of the ending-end and receiving-end AC currents are also opposite. According to Eqs. (10.34) and (10.35), the frequency-domain relationships of the AC/DC voltages and currents in the receiving-end LCC can be expressed as

$$\begin{cases} \boldsymbol{V}_{\mathrm{edc}} = -\dfrac{2}{k_{\mathrm{eT}}}\displaystyle\sum_{l=\mathrm{a,b,c}} \boldsymbol{S}_{\mathrm{ev}l}\boldsymbol{V}_{\mathrm{eT}l} \\ \boldsymbol{I}_{\mathrm{e}l} = -\dfrac{2}{k_{\mathrm{eT}}}\boldsymbol{S}_{\mathrm{ei}l}\boldsymbol{I}_{\mathrm{edc}} \end{cases} \tag{10.37}$$

where $\boldsymbol{S}_{\mathrm{ev}l}$, $\boldsymbol{S}_{\mathrm{ei}l}$ are the expanded steady-state matrices of the three-phase voltage and current switching functions in the receiving-end LCC respectively.

10.3 Small-Signal Impedance Modeling in Frequency Domain

In this section, the LCC-HVDC impedance model, including the sending-end and receiving-end LCCs and the DC transmission lines, established based on the operation principle and control strategy of LCC-HVDC.

10.3.1 Small-Signal Frequency-Domain Characteristic Analysis

In order to establish the impedance model of LCC-HVDC, first, a small-signal perturbation is superimposed on the AC voltage of the sending-end LCC at the steady-state operating point. The frequency-domain distribution characteristics of the voltage, current, and switching function are elaborated. Then, the frequency-domain small-signal model of the main circuit and control loops in LCC-HVDC is developed, respectively. Finally, the small-signal impedance model of LCC-HVDC

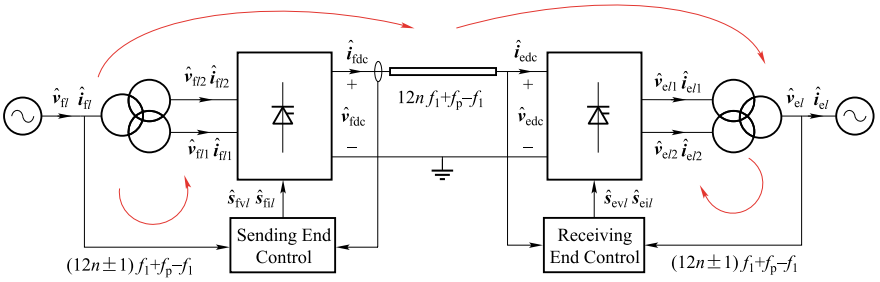

Fig. 10.7 The small-signal transfer path and frequency response relationship of LCC-HVDC

at the sending end is established by calculating the response of the AC current to the AC voltage perturbation. The small-signal transfer path and frequency response relationship of LCC-HVDC are shown in Fig. 10.7.

Initially, a positive-sequence small-signal perturbation at f_p is superimposed on the sending-end AC voltage at the steady-state operating point. The small-signal components are produced in the sending-end AC current $\hat{\boldsymbol{i}}_{fl}$, the AC voltage $\hat{\boldsymbol{v}}_{fl1}$ and current $\hat{\boldsymbol{i}}_{fl1}$ of Converter I, and the AC voltage $\hat{\boldsymbol{v}}_{fl2}$ and current $\hat{\boldsymbol{i}}_{fl2}$ of Converter II. The small-signal components of the AC voltages $\hat{\boldsymbol{v}}_{fl1}$, $\hat{\boldsymbol{v}}_{fl2}$ at f_p multiplying the steady-state components of the voltage switching function $\boldsymbol{S}_{fvl}$ at $(12n-1)f_1$ leads to the small-signal response of the DC voltage $\hat{\boldsymbol{v}}_{fdc}$ at $f_p - f_1 + 12nf_1$ in the sending-end LCC.

The difference between $\hat{\boldsymbol{v}}_{fdc}$ at $f_p - f_1 + 12nf_1$ and the DC voltage of the receiving-end LCC drops on the DC smoothing reactor and transmission lines, which leads to the small-signal response of the DC current $\hat{\boldsymbol{i}}_{edc}$ at $f_p - f_1 + 12nf_1$ in the receiving-end LCC. The small-signal components $\hat{\boldsymbol{i}}_{edc}$ at $f_p - f_1 + 12nf_1$ multiplying the steady-state components of the current switching function $\boldsymbol{S}_{eil}$ at $(12n \pm 1)f_1$ leads to the small-signal responses of the receiving-end AC current $\hat{\boldsymbol{i}}_{el}$ and currents of Converter I and Converter II $\hat{\boldsymbol{i}}_{el1}$, $\hat{\boldsymbol{i}}_{el2}$ at $f_p - f_1 + (12n \pm 1)f_1$. $\hat{\boldsymbol{i}}_{el}$ flows through the impedances of the receiving-end AC grid and filters, leading to small-signal responses of the receiving-end AC voltage $\hat{\boldsymbol{v}}_{el}$. Similarly, the small-signal components at $f_p - f_1 + (12n \pm 1)f_1$ are also introduced into the AC voltages $\hat{\boldsymbol{v}}_{el1}$, $\hat{\boldsymbol{v}}_{el2}$ of Converter I and Converter II in the receiving-end LCC.

The small-signal components of the AC voltages $\hat{\boldsymbol{v}}_{el1}$, $\hat{\boldsymbol{v}}_{el2}$ at $f_p - f_1 + (12n \pm 1)f_1$ multiplying the steady-state components of the voltage switching function $\boldsymbol{S}_{evl}$ at $(12n \pm 1)f_1$ leads to the small-signal response of the DC voltage $\hat{\boldsymbol{v}}_{edc}$ at $f_p - f_1 + 12nf_1$ in the receiving-end LCC. The difference between $\hat{\boldsymbol{v}}_{edc}$ at $f_p - f_1 + 12nf_1$ and the DC voltage of the sending-end LCC drops on the DC smoothing reactor and transmission lines, which leads to the small-signal response of the DC current $\hat{\boldsymbol{i}}_{fdc}$ at $f_p - f_1 + 12nf_1$ in the sending-end LCC. The small-signal components $\hat{\boldsymbol{i}}_{fdc}$ at $f_p - f_1 + 12nf_1$ multiplying the steady-state components of the current switching function $\boldsymbol{S}_{fil}$ at $(12n \pm 1)f_1$ leads to the small-signal responses of the sending-end AC current $\hat{\boldsymbol{i}}_{fl}$ and currents of Converter I and Converter II $\hat{\boldsymbol{i}}_{fl1}$, $\hat{\boldsymbol{i}}_{fl2}$ at $f_p - f_1 + (12n \pm 1)f_1$.

Table 10.2 The frequency-domain characteristics of the small-signal vectors in LCC-HVDC

Steady-State Vectors	Frequency
$\hat{\boldsymbol{v}}_{\mathrm{fl}}, \hat{\boldsymbol{v}}_{\mathrm{el}}, \hat{\boldsymbol{i}}_{\mathrm{fl}}, \hat{\boldsymbol{i}}_{\mathrm{el}}$	$f_\mathrm{p} - f_1 + (12n+1)f_1$
	$f_\mathrm{p} - f_1 + (12n-1)f_1$
$\hat{\boldsymbol{s}}_{\mathrm{fvl}}, \hat{\boldsymbol{s}}_{\mathrm{evl}}, \hat{\boldsymbol{s}}_{\mathrm{fil}}, \hat{\boldsymbol{s}}_{\mathrm{eil}}$	$f_\mathrm{p} - f_1 + (12n+1)f_1$
	$f_\mathrm{p} - f_1 + (12n-1)f_1$
$\hat{\boldsymbol{v}}_{\mathrm{fdc}}, \hat{\boldsymbol{v}}_{\mathrm{edc}}, \hat{\boldsymbol{i}}_{\mathrm{fdc}}, \hat{\boldsymbol{i}}_{\mathrm{edc}}$	$f_\mathrm{p} - f_1 + 12nf_1$

Furthermore, the small-signal components at $f_\mathrm{p} - f_1 + (12n \pm 1)f_1$ are also introduced into the voltage and current switching functions $\hat{\boldsymbol{s}}_{\mathrm{fv}l}$, $\hat{\boldsymbol{s}}_{\mathrm{fi}l}$, $\hat{\boldsymbol{s}}_{\mathrm{ev}l}$, $\hat{\boldsymbol{s}}_{\mathrm{ei}l}$ in the sending-end and receiving-end LCCs due to the converter control loops.

For the sending-end LCC, the small-signal components of $\hat{\boldsymbol{s}}_{\mathrm{fv}l}$ at $f_\mathrm{p} - f_1 + (12n \pm 1)f_1$ multiplying the steady-state components of the AC voltages of Converter I and Converter II $\boldsymbol{V}_{\mathrm{f}l1}$, $\boldsymbol{V}_{\mathrm{f}l2}$ at $(12n \pm 1)f_1$ leads to small-signal responses of $\hat{\boldsymbol{v}}_{\mathrm{fdc}}$ at $f_\mathrm{p} - f_1 + 12nf_1$. The small-signal component of $\hat{\boldsymbol{s}}_{\mathrm{fi}l}$ at $f_\mathrm{p} - f_1 + (12n \pm 1)f_1$ multiplying the steady-state components of the DC current $\boldsymbol{I}_{\mathrm{fdc}}$ at $12nf_1$ leads to small-signal responses of $\hat{\boldsymbol{i}}_{\mathrm{f}l}$ at $f_\mathrm{p} - f_1 + (12n \pm 1)f_1$.

For the receiving-end LCC, the small-signal components of $\hat{\boldsymbol{s}}_{\mathrm{ev}l}$ at $f_\mathrm{p} - f_1 + (12n \pm 1)f_1$ multiplying the steady-state components of the AC voltages of Converter I and Converter II $\boldsymbol{V}_{\mathrm{e}l1}$, $\boldsymbol{V}_{\mathrm{e}l2}$ at $(12n \pm 1)f_1$ leads to small-signal responses of $\hat{\boldsymbol{v}}_{\mathrm{edc}}$ at $f_\mathrm{p} - f_1 + 12nf_1$. The small-signal component of $\hat{\boldsymbol{s}}_{\mathrm{ei}l}$ at $f_\mathrm{p} - f_1 + (12n \pm 1)f_1$ multiplying the steady-state components of the DC current $\boldsymbol{I}_{\mathrm{edc}}$ at $12nf_1$ leads to small-signal responses of $\hat{\boldsymbol{i}}_{\mathrm{e}l}$ at $f_\mathrm{p} - f_1 + (12n \pm 1)f_1$.

The balance of the small-signal production in LCC-HVDC will be finally achieved after repeating the above process.

To sum up, the frequency-domain characteristics of the small-signal vectors in the sending-end and receiving-end LCCs are listed in Table 10.2. The frequency-domain distribution characteristics of the corresponding small-signal vectors in the sending-end and receiving-end LCCs are the same.

In order to describe the frequency-domain small-signal characteristics, the small-signal components of LCC-HVDC quantities are arranged in the following small-signal frequency order.

$$\begin{aligned}[\quad & f_\mathrm{p} - (12g+2)f_1,\ f_\mathrm{p} - (12g+1)f_1,\ f_\mathrm{p} - 12gf_1,\ \ldots, \\ \ldots, \quad & f_\mathrm{p} - 2f_1, \qquad f_\mathrm{p} - f_1, \qquad f_\mathrm{p}, \qquad \ldots, \\ \ldots, \ & f_\mathrm{p} + (12g-2)f_1,\ f_\mathrm{p} + (12g-1)f_1,\ f_\mathrm{p} + 12gf_1 \quad]^\mathrm{T}\end{aligned} \tag{10.38}$$

where the frequency order is from $f_\mathrm{p} - f_1 - (12g+1)f_1$ to $f_\mathrm{p} - f_1 + (12g+1)f_1$ ($24g+3$ in total).

The AC voltages and currents contain the small-signal components at $f_\mathrm{p} - f_1 + (12n \pm 1)f_1$. Taking phase-a as an example, the small-signal vectors of the sending-end AC voltage and current can be expressed as

$$\begin{cases} \hat{\boldsymbol{v}}_{\mathrm{fa}} = [\ldots, \hat{\boldsymbol{v}}_{\mathrm{f\text{-}14}}, 0, \hat{\boldsymbol{v}}_{\mathrm{f\text{-}12}}, 0, 0, 0, 0, 0, 0, \quad 0, \quad 0, \quad 0, \quad \hat{\boldsymbol{v}}_{\mathrm{f\text{-}2}}, 0, \\ \qquad \hat{\boldsymbol{v}}_{\mathrm{f}}, \quad 0, \quad 0, \quad 0, \quad 0, 0, 0, 0, 0, 0, \hat{\boldsymbol{v}}_{\mathrm{f+10}}, 0, \hat{\boldsymbol{v}}_{\mathrm{f+12}}, \ldots]^{\mathrm{T}} \\ \hat{\boldsymbol{i}}_{\mathrm{fa}} = [\ldots, \hat{\boldsymbol{i}}_{\mathrm{f\text{-}14}}, 0, \hat{\boldsymbol{i}}_{\mathrm{f\text{-}12}}, 0, 0, 0, 0, 0, 0, \quad 0, \quad 0, \quad 0, \quad \hat{\boldsymbol{i}}_{\mathrm{f\text{-}2}}, 0, \\ \qquad \hat{\boldsymbol{i}}_{\mathrm{f}}, \quad 0, \quad 0, \quad 0, \quad 0, 0, 0, 0, 0, 0, \hat{\boldsymbol{i}}_{\mathrm{f+10}}, 0, \hat{\boldsymbol{i}}_{\mathrm{f+12}}, \ldots]^{\mathrm{T}} \end{cases} \tag{10.39}$$

where $\hat{\boldsymbol{v}}_{\mathrm{f}+k-1}$ or $\hat{\boldsymbol{i}}_{\mathrm{f}+k-1}$ is the small-signal component at the frequency $f_{\mathrm{p}}+(k-1)f_1$; the element is non-zero if and only if $k = 12n \pm 1$.

The frequencies of the small-signal components of the voltage and current switching functions are the same as the AC voltage and current. The small-signal vectors of the voltage and current switching functions in the sending-end LCC can be expressed as

$$\begin{cases} \hat{\boldsymbol{s}}_{\mathrm{fva}} = [\ldots, \hat{\boldsymbol{s}}_{\mathrm{fv\text{-}14}}, 0, \hat{\boldsymbol{s}}_{\mathrm{fv\text{-}12}}, 0, 0, 0, 0, 0, 0, \quad 0, \quad 0, \quad 0, \quad \hat{\boldsymbol{s}}_{\mathrm{fv\text{-}2}}, 0, \\ \qquad \hat{\boldsymbol{s}}_{\mathrm{fv}}, \quad 0, \quad 0, \quad 0, \quad 0, 0, 0, 0, 0, 0, \hat{\boldsymbol{s}}_{\mathrm{fv+10}}, 0, \hat{\boldsymbol{s}}_{\mathrm{fv+12}}, \ldots]^{\mathrm{T}} \\ \hat{\boldsymbol{s}}_{\mathrm{fia}} = \ldots, \hat{\boldsymbol{s}}_{\mathrm{fi\text{-}14}}, 0, \hat{\boldsymbol{s}}_{\mathrm{fi\text{-}12}}, 0, 0, 0, 0, 0, 0, \quad 0, \quad 0, \quad 0, \quad \hat{\boldsymbol{s}}_{\mathrm{fi\text{-}2}}, 0, \\ \qquad \hat{\boldsymbol{s}}_{\mathrm{fi}}, \quad 0, \quad 0, \quad 0, \quad 0, 0, 0, 0, 0, 0, \hat{\boldsymbol{s}}_{\mathrm{fi+10}}, 0, \hat{\boldsymbol{s}}_{\mathrm{fi+12}}, \ldots]^{\mathrm{T}} \end{cases} \tag{10.40}$$

where $\hat{\boldsymbol{s}}_{\mathrm{fv}+k-1}$ or $\hat{\boldsymbol{s}}_{\mathrm{fi}+k-1}$ is the small-signal component at the frequency $f_{\mathrm{p}} + (k-1)f_1$; the element is non-zero if and only if $k = 12n \pm 1$.

Based on the phase-sequence relationship of the small-signal component at each frequency, the small-signal vectors of the sending-end AC voltages, AC currents, and voltage and current switching functions in phase b and phase c can be obtained according to Eqs. (10.39) and (10.40).

$$\begin{cases} \hat{\boldsymbol{v}}_{\mathrm{fb}} = \boldsymbol{D}_{\mathrm{p}}\hat{\boldsymbol{v}}_{\mathrm{fa}}, \ \hat{\boldsymbol{i}}_{\mathrm{fb}} = \boldsymbol{D}_{\mathrm{p}}\hat{\boldsymbol{i}}_{\mathrm{fa}}, \ \hat{\boldsymbol{s}}_{\mathrm{fvb}} = \boldsymbol{D}_{\mathrm{p}}\hat{\boldsymbol{s}}_{\mathrm{fva}}, \ \hat{\boldsymbol{s}}_{\mathrm{fib}} = \boldsymbol{D}_{\mathrm{p}}\hat{\boldsymbol{s}}_{\mathrm{fia}} \\ \hat{\boldsymbol{v}}_{\mathrm{fc}} = \boldsymbol{D}_{\mathrm{p}}^{*}\hat{\boldsymbol{v}}_{\mathrm{fa}}, \ \hat{\boldsymbol{i}}_{\mathrm{fc}} = \boldsymbol{D}_{\mathrm{p}}^{*}\hat{\boldsymbol{i}}_{\mathrm{fa}}, \ \hat{\boldsymbol{s}}_{\mathrm{fvc}} = \boldsymbol{D}_{\mathrm{p}}^{*}\hat{\boldsymbol{s}}_{\mathrm{fva}}, \ \hat{\boldsymbol{s}}_{\mathrm{fic}} = \boldsymbol{D}_{\mathrm{p}}^{*}\hat{\boldsymbol{s}}_{\mathrm{fia}} \end{cases} \tag{10.41}$$

where $\boldsymbol{D}_{\mathrm{p}}$ is the phase-sequence coefficient matrix of the small-signal vectors, and $\boldsymbol{D}_{\mathrm{p}} = \boldsymbol{D}$.

The DC voltage and current contain the small-signal components at $f_{\mathrm{p}} - f_1 + 12nf_1$, and the corresponding small-signal vectors can be expressed as

$$\begin{cases} \hat{\boldsymbol{v}}_{\mathrm{fdc}} = [\ldots, 0, \hat{\boldsymbol{v}}_{\mathrm{fdc\text{-}13}}, 0, 0, 0, 0, 0, 0, 0, 0, \quad 0, \quad 0, \quad 0, \quad \hat{\boldsymbol{v}}_{\mathrm{fdc\text{-}1}}, \\ \qquad 0, \quad 0, \quad 0, \quad 0, 0, 0, 0, 0, 0, 0, 0, \hat{\boldsymbol{v}}_{\mathrm{fdc+11}}, 0, \ldots]^{\mathrm{T}} \\ \hat{\boldsymbol{i}}_{\mathrm{fdc}} = [\ldots, 0, \hat{\boldsymbol{i}}_{\mathrm{fdc\text{-}13}}, 0, 0, 0, 0, 0, 0, 0, 0, \quad 0, \quad 0, \quad 0, \quad \hat{\boldsymbol{i}}_{\mathrm{fdc\text{-}1}}, \\ \qquad 0, \quad 0, \quad 0, \quad 0, 0, 0, 0, 0, 0, 0, 0, \hat{\boldsymbol{i}}_{\mathrm{fdc+11}}, 0, \ldots]^{\mathrm{T}} \end{cases} \tag{10.42}$$

Similarly, the small-signal vectors of the receiving-end phase-a AC voltage and current can be expressed as

$$\begin{cases} \hat{\boldsymbol{v}}_{\mathrm{ea}} = [\ldots, \hat{\boldsymbol{v}}_{\mathrm{e\text{-}14}}, 0, \hat{\boldsymbol{v}}_{\mathrm{e\text{-}12}}, 0, 0, 0, 0, 0, 0, \quad 0, \quad 0, \quad 0, \quad \hat{\boldsymbol{v}}_{\mathrm{e\text{-}2}}, 0, \\ \qquad \hat{\boldsymbol{v}}_{\mathrm{e}}, \quad 0, \quad 0, \quad 0, \quad 0, 0, 0, 0, 0, 0, \hat{\boldsymbol{v}}_{\mathrm{e+10}}, 0, \hat{\boldsymbol{v}}_{\mathrm{e+12}}, \ldots]^{\mathrm{T}} \\ \hat{\boldsymbol{i}}_{\mathrm{ea}} = [\ldots, \hat{\boldsymbol{i}}_{\mathrm{e\text{-}14}}, 0, \hat{\boldsymbol{i}}_{\mathrm{e\text{-}12}}, 0, 0, 0, 0, 0, 0, \quad 0, \quad 0, \quad 0, \quad \hat{\boldsymbol{i}}_{\mathrm{e\text{-}2}}, 0, \\ \qquad \hat{\boldsymbol{i}}_{\mathrm{e}}, \quad 0, \quad 0, \quad 0, \quad 0, 0, 0, 0, 0, 0, \hat{\boldsymbol{i}}_{\mathrm{e+10}}, 0, \hat{\boldsymbol{i}}_{\mathrm{e+12}}, \ldots]^{\mathrm{T}} \end{cases} \tag{10.43}$$

The small-signal vectors of the phase-a voltage and current switching functions in the receiving-end LCC can be expressed as

$$\begin{cases} \hat{\boldsymbol{s}}_{\mathrm{eva}} = [\ldots, \hat{\boldsymbol{s}}_{\mathrm{ev\text{-}14}}, 0, \hat{\boldsymbol{s}}_{\mathrm{ev\text{-}12}}, 0, 0, 0, 0, 0, 0, \quad 0, \quad 0, \quad 0, \quad \hat{\boldsymbol{s}}_{\mathrm{ev\text{-}2}}, 0, \\ \qquad \hat{\boldsymbol{s}}_{\mathrm{ev}}, \quad 0, \quad 0, \quad 0, \quad 0, 0, 0, 0, 0, 0, \hat{\boldsymbol{s}}_{\mathrm{ev+10}}, 0, \hat{\boldsymbol{s}}_{\mathrm{ev+12}}, \ldots]^{\mathrm{T}} \\ \hat{\boldsymbol{s}}_{\mathrm{eia}} = [\ldots, \hat{\boldsymbol{s}}_{\mathrm{ei\text{-}14}}, 0, \hat{\boldsymbol{s}}_{\mathrm{ei\text{-}12}}, 0, 0, 0, 0, 0, 0, \quad 0, \quad 0, \quad 0, \quad \hat{\boldsymbol{s}}_{\mathrm{ei\text{-}2}}, 0, \\ \qquad \hat{\boldsymbol{s}}_{\mathrm{ei}}, \quad 0, \quad 0, \quad 0, \quad 0, 0, 0, 0, 0, 0, \hat{\boldsymbol{s}}_{\mathrm{ei+10}}, 0, \hat{\boldsymbol{s}}_{\mathrm{ei+12}}, \ldots]^{\mathrm{T}} \end{cases} \tag{10.44}$$

Based on the phase-sequence relationship of the small-signal component at each frequency, the small-signal vectors of the receiving-end AC voltages, AC currents, and voltage and current switching functions in phase b and phase c can be obtained according to Eqs. (10.43) and (10.44).

$$\begin{cases} \hat{\boldsymbol{v}}_{\mathrm{eb}} = \boldsymbol{D}_{\mathrm{p}}\hat{\boldsymbol{v}}_{\mathrm{ea}}, \ \hat{\boldsymbol{i}}_{\mathrm{eb}} = \boldsymbol{D}_{\mathrm{p}}\hat{\boldsymbol{i}}_{\mathrm{ea}}, \ \hat{\boldsymbol{s}}_{\mathrm{evb}} = \boldsymbol{D}_{\mathrm{p}}\hat{\boldsymbol{s}}_{\mathrm{eva}}, \ \hat{\boldsymbol{s}}_{\mathrm{eib}} = \boldsymbol{D}_{\mathrm{p}}\hat{\boldsymbol{s}}_{\mathrm{eia}} \\ \hat{\boldsymbol{v}}_{\mathrm{ec}} = \boldsymbol{D}_{\mathrm{p}}^{*}\hat{\boldsymbol{v}}_{\mathrm{ea}}, \ \hat{\boldsymbol{i}}_{\mathrm{ec}} = \boldsymbol{D}_{\mathrm{p}}^{*}\hat{\boldsymbol{i}}_{\mathrm{ea}}, \ \hat{\boldsymbol{s}}_{\mathrm{evc}} = \boldsymbol{D}_{\mathrm{p}}^{*}\hat{\boldsymbol{s}}_{\mathrm{eva}}, \ \hat{\boldsymbol{s}}_{\mathrm{eic}} = \boldsymbol{D}_{\mathrm{p}}^{*}\hat{\boldsymbol{s}}_{\mathrm{eia}} \end{cases} \tag{10.45}$$

The small-signal vectors of the DC voltage and current in the receiving-end LCC can be expressed as

$$\begin{cases} \hat{\boldsymbol{v}}_{\mathrm{edc}} = [\ldots, 0, \hat{\boldsymbol{v}}_{\mathrm{edc\text{-}13}}, 0, 0, 0, 0, 0, 0, 0, 0, \quad 0, \quad 0, \quad 0, \quad \hat{\boldsymbol{v}}_{\mathrm{edc\text{-}1}}, \\ \qquad 0, \quad 0, \quad 0, \quad 0, 0, 0, 0, 0, 0, 0, 0, \hat{\boldsymbol{v}}_{\mathrm{edc+11}}, 0, \ldots]^{\mathrm{T}} \\ \hat{\boldsymbol{i}}_{\mathrm{edc}} = [\ldots, 0, \hat{\boldsymbol{i}}_{\mathrm{edc\text{-}13}}, 0, 0, 0, 0, 0, 0, 0, 0, \quad 0, \quad 0, \quad 0, \quad \hat{\boldsymbol{i}}_{\mathrm{edc\text{-}1}}, \\ \qquad 0, \quad 0, \quad 0, \quad 0, 0, 0, 0, 0, 0, 0, 0, \hat{\boldsymbol{i}}_{\mathrm{edc+11}}, 0, \ldots]^{\mathrm{T}} \end{cases} \tag{10.46}$$

10.3.2 Frequency-Domain Small-Signal Model

Based on the small-signal vectors of the AC/DC voltages, currents, and switching functions, this section establishes the frequency-domain small-signal model, including the main circuits and control loops of the sending-end and receiving-end LCCs as well as the DC transmission lines.

10.3.2.1 Small-Signal Model of Sending-End LCC

The small-signal modeling of the main circuit and control loops in the sending-end LCC is carried out as follows.

1. **Small-Signal Model of Main Circuit**

The small-signal model of the AC-side circuit in the sending-end LCC can be obtained by transforming Eq. (10.1) to the frequency domain.

$$\hat{\boldsymbol{v}}_{\mathrm{fT}l} = \hat{\boldsymbol{v}}_{\mathrm{f}l} - \boldsymbol{Z}_{\mathrm{fT}}\hat{\boldsymbol{i}}_{\mathrm{f}l} \tag{10.47}$$

where $\hat{\boldsymbol{v}}_{\mathrm{fT}l}$ are the small-signal vectors of the line-side three-phase AC voltages at the sending end respectively; $\boldsymbol{Z}_{\mathrm{fT}}$ is the impedance of the transformer leakage inductance at the sending end in the small-signal frequency order, expressed as

$$\boldsymbol{Z}_{\mathrm{fT}} = \mathrm{j}2\pi L_{\mathrm{fT}} \cdot \mathrm{diag}[f_{\mathrm{p}} - (12g+2)f_1, \ldots, f_{\mathrm{p}} - f_1, \ldots, f_{\mathrm{p}} + 12gf_1] \tag{10.48}$$

According to Eqs. (10.34) and (10.35), the relationships of the small-signal vectors of the AC/DC voltages and currents in the sending-end LCC can be expressed as

$$\begin{cases} \hat{\boldsymbol{v}}_{\mathrm{fdc}} = \dfrac{2}{k_{\mathrm{fT}}}\boldsymbol{D}_{\mathrm{ad}}\left(\boldsymbol{V}_{\mathrm{fTa}}\hat{\boldsymbol{s}}_{\mathrm{fva}} + \boldsymbol{S}_{\mathrm{fva}}\hat{\boldsymbol{v}}_{\mathrm{fTa}}\right) \\ \hat{\boldsymbol{i}}_{\mathrm{f}l} = \dfrac{2}{k_{\mathrm{fT}}}\left(\boldsymbol{I}_{\mathrm{fdc}}\hat{\boldsymbol{s}}_{\mathrm{fi}l} + \boldsymbol{S}_{\mathrm{fi}l}\hat{\boldsymbol{i}}_{\mathrm{fdc}}\right) \end{cases} \tag{10.49}$$

where $\boldsymbol{V}_{\mathrm{fTa}}$ is the expanded steady-state matrix of the line-side phase-a AC voltages at the sending end; $\boldsymbol{I}_{\mathrm{fdc}}$ is the expanded steady-state matrix of the DC current in the sending-end LCC; $\boldsymbol{S}_{\mathrm{fva}}$, $\boldsymbol{S}_{\mathrm{fi}l}$ are the expanded steady-state matrices of the three-phase voltage and current switching functions in the sending-end LCCrespectively; $\boldsymbol{D}_{\mathrm{ad}}$ is the AC/DC conversion matrix, expressed as

$$\boldsymbol{D}_{\mathrm{ad}} = 3 \cdot \mathrm{diag}\left[\{1 - |\mathrm{mod}(k,3)|\}|_{k=-12g-1,\ldots,0,\ldots,12g+1}\right] \tag{10.50}$$

2. **Small-Signal Model of Control Loops**

The sending-end LCC operates in DC current control mode, and the typical control diagram is shown in Fig. 10.5. Since $\hat{\boldsymbol{i}}_{\mathrm{fdc}}$ contains the small-signal components at $f_{\mathrm{p}} - f_1 + 12nf_1$, the small-signal responses of the trigger angle $\hat{\boldsymbol{\alpha}}_{\mathrm{f}}$ at $f_{\mathrm{p}} - f_1 + 12nf_1$ are produced in the sending-end LCC, under the effect of the DC current filter $T_{\mathrm{idc}}(s)$ and DC current controller $H_{\mathrm{idc}}(s)$. Besides, the small-signal components of the sending-end AC voltage $\hat{\boldsymbol{v}}_{\mathrm{f}l}$ lead to the small-signal responses of the PLL output angle $\hat{\boldsymbol{\theta}}_{\mathrm{fPLL}}$ at $f_{\mathrm{p}} - f_1 + 12nf_1$ in the sending-end LCC.

The phase control receives $\hat{\boldsymbol{\alpha}}_{\mathrm{f}}$ and $\hat{\boldsymbol{\theta}}_{\mathrm{fPLL}}$, producing the small-signal components of the combined angle $\hat{\boldsymbol{\delta}}_{\mathrm{f}}$ at $f_{\mathrm{p}} - f_1 + 12nf_1$ in the sending-end LCC. The expression of $\hat{\boldsymbol{\delta}}_{\mathrm{f}}$ is given as

$$\hat{\boldsymbol{\delta}}_{\mathrm{f}} = \boldsymbol{Q}_{\mathrm{f}}\hat{\boldsymbol{i}}_{\mathrm{fdc}} + \boldsymbol{E}_{\mathrm{f}}\hat{\boldsymbol{v}}_{\mathrm{fa}} \tag{10.51}$$

where $\boldsymbol{Q}_{\mathrm{f}}$, $\boldsymbol{E}_{\mathrm{f}}$ are $(24g+3)\times(24g+3)$ matrices; all other elements in the matrices are zero except for Eq. (10.52).

$$\begin{cases} \boldsymbol{Q}_{\mathrm{f}}(12g+2, 12g+2) = T_{\mathrm{idc}}\left[\mathrm{j}2\pi\left(f_{\mathrm{p}} - f_{\mathrm{l}}\right)\right]H_{\mathrm{idc}}\left[\mathrm{j}2\pi\left(f_{\mathrm{p}} - f_{\mathrm{l}}\right)\right] \\ \boldsymbol{E}_{\mathrm{f}}(12g+2, 12g+1) = -\mathrm{j}T_{\mathrm{fPLL}}\left[\mathrm{j}2\pi\left(f_{\mathrm{p}} - f_{\mathrm{l}}\right)\right] \\ \boldsymbol{E}_{\mathrm{f}}(12g+2, 12g+3) = \mathrm{j}T_{\mathrm{fPLL}}\left[\mathrm{j}2\pi\left(f_{\mathrm{p}} - f_{\mathrm{l}}\right)\right] \end{cases} \tag{10.52}$$

According to the switching function modeling in Chap. 5, the relationships between $\hat{\boldsymbol{s}}_{\mathrm{fv}l}$, $\hat{\boldsymbol{s}}_{\mathrm{fi}l}$ with $\hat{\boldsymbol{\delta}}_{\mathrm{f}}$ satisfy

$$\begin{cases} \hat{\boldsymbol{s}}_{\mathrm{fv}l} = \boldsymbol{C}\boldsymbol{S}_{\mathrm{fv}l}\hat{\boldsymbol{\delta}}_{\mathrm{f}} \\ \hat{\boldsymbol{s}}_{\mathrm{fi}l} = \boldsymbol{C}\boldsymbol{S}_{\mathrm{fi}l}\hat{\boldsymbol{\delta}}_{\mathrm{f}} \end{cases} \tag{10.53}$$

where $\boldsymbol{C}$ is the transformation coefficient matrix of the switching functions, expressed as

$$\boldsymbol{C} = -\mathrm{j}\cdot\mathrm{diag}[-12g-1, \ldots, 0 \ldots, 12g+1] \tag{10.54}$$

10.3.2.2 Small-Signal Model of Receiving-End LCC

The small-signal modeling of the main circuit and control loops in the receiving-end LCC is carried out as follows.

1. **Small-Signal Model of Main Circuit**

The small-signal model of the AC-side circuit in the receiving-end LCC can be obtained by transforming Eq. (10.7) to the frequency domain.

$$\hat{\boldsymbol{v}}_{\mathrm{eT}l} = \hat{\boldsymbol{v}}_{\mathrm{e}l} + \boldsymbol{Z}_{\mathrm{eT}}\hat{\boldsymbol{i}}_{\mathrm{e}l} \tag{10.55}$$

where $\hat{\boldsymbol{v}}_{\mathrm{eT}l}$ are the small-signal vectors of the line-side three-phase AC voltages at the receiving end respectively; $\boldsymbol{Z}_{\mathrm{eT}}$ is the impedance of the transformer leakage inductance at the receiving end in the small-signal frequency order, and the expression is consistent with Eq. (10.48) with the subscript "f" replaced with "e".

$\hat{\boldsymbol{i}}_{\mathrm{e}l}$ flows through the AC filters and receiving-end AC grid inductors, leading to small-signal responses of the receiving-end AC voltages $\hat{\boldsymbol{v}}_{\mathrm{e}l}$, which satisfies

$$\hat{\boldsymbol{v}}_{\mathrm{e}l} = \boldsymbol{Z}_{\mathrm{eac}}\hat{\boldsymbol{i}}_{\mathrm{e}l} \tag{10.56}$$

where $\boldsymbol{Z}_{\mathrm{eac}}$ is the AC-side impedance at the receiving end, and composed of the parallel connection of the receiving-end AC grid impedance and filter impedance,

expressed as

$$\boldsymbol{Z}_{\text{eac}} = \boldsymbol{Z}_{\text{eg}} || \boldsymbol{Z}_{\text{eflt}} \tag{10.57}$$

where "||" represents the parallel operation. $\boldsymbol{Z}_{\text{eg}}$, $\boldsymbol{Z}_{\text{eflt}}$ are the receiving-end AC grid impedance and filter impedance in the small-signal frequency order.

According to Eq. (10.37), the relationships of the small-signal vectors of the AC/DC voltages and currents in the sending-end LCC can be expressed as

$$\begin{cases} \hat{\boldsymbol{v}}_{\text{edc}} = -\dfrac{2}{k_{\text{eT}}} \boldsymbol{D}_{\text{ad}} \left(\boldsymbol{V}_{\text{eTa}} \hat{\boldsymbol{s}}_{\text{eva}} + \boldsymbol{S}_{\text{eva}} \hat{\boldsymbol{v}}_{\text{eTa}} \right) \\ \hat{\boldsymbol{i}}_{\text{e}l} = -\dfrac{2}{k_{\text{eT}}} \left(\boldsymbol{I}_{\text{edc}} \hat{\boldsymbol{s}}_{\text{ei}l} + \boldsymbol{S}_{\text{ei}l} \hat{\boldsymbol{i}}_{\text{edc}} \right) \end{cases} \tag{10.58}$$

where $\boldsymbol{V}_{\text{eTa}}$ is the expanded steady-state matrix of the line-side phase-a AC voltages at the receiving end; $\boldsymbol{I}_{\text{edc}}$ is the expanded steady-state matrix of the DC current in the receiving-end LCC; $\boldsymbol{S}_{\text{ev}l}$, $\boldsymbol{S}_{\text{ei}l}$ are the expanded steady-state matrices of the three-phase voltage and current switching functions in the receiving-end LCC respectively.

2. **Small-Signal Model of Control Loops**

The receiving-end LCC operates in DC voltage control mode, and the typical control diagram is shown in Fig. 10.6. Since $\hat{\boldsymbol{v}}_{\text{edc}}$ contains the small-signal components at $f_{\text{p}} - f_1 + 12nf_1$, the small-signal responses of the trigger angle $\hat{\boldsymbol{\alpha}}_{\text{e}}$ at $f_{\text{p}} - f_1 + 12nf_1$ are produced in the receiving-end LCC, under the effect of the DC voltage filter $T_{\text{vdc}}(s)$ and DC voltage controller $H_{\text{vdc}}(s)$. Besides, the small-signal components of the receiving-end AC voltage $\hat{\boldsymbol{v}}_{\text{e}l}$ at $f_{\text{p}} - f_1 + (12n \pm 1)f_1$ lead to the small-signal responses of the PLL output angle $\hat{\boldsymbol{\theta}}_{\text{ePLL}}$ at $f_{\text{p}} - f_1 + 12nf_1$ in the receiving-end LCC.

The phase control receives $\hat{\boldsymbol{\alpha}}_{\text{e}}$ and $\hat{\boldsymbol{\theta}}_{\text{ePLL}}$, producing the small-signal components of the combined angle $\hat{\boldsymbol{\delta}}_{\text{e}}$ at $f_{\text{p}} - f_1 + 12nf_1$ in the receiving-end LCC. The expression of $\hat{\boldsymbol{\delta}}_{\text{e}}$ is given as

$$\hat{\boldsymbol{\delta}}_{\text{e}} = \boldsymbol{Q}_{\text{e}} \hat{\boldsymbol{v}}_{\text{edc}} + \boldsymbol{E}_{\text{e}} \hat{\boldsymbol{v}}_{\text{ea}} \tag{10.59}$$

where $\boldsymbol{Q}_{\text{e}}$, $\boldsymbol{E}_{\text{e}}$ are $(24g + 3) \times (24g + 3)$ matrices respectively; all other elements in the matrices are zero except for Eq. (10.60).

$$\begin{cases} \boldsymbol{Q}_{\text{e}}(12g + 2, 12g + 2) = -T_{\text{vdc}}\left[\text{j}2\pi\left(f_{\text{p}} - f_1\right)\right] H_{\text{vdc}}\left[\text{j}2\pi\left(f_{\text{p}} - f_1\right)\right] \\ \boldsymbol{E}_{\text{e}}(12g + 2, 12g + 1) = -\text{j}T_{\text{ePLL}}\left[\text{j}2\pi\left(f_{\text{p}} - f_1\right)\right] \\ \boldsymbol{E}_{\text{e}}(12g + 2, 12g + 3) = \text{j}T_{\text{ePLL}}\left[\text{j}2\pi\left(f_{\text{p}} - f_1\right)\right] \end{cases} \tag{10.60}$$

Futhermore, the relationships between $\hat{\boldsymbol{s}}_{\text{ev}l}$, $\hat{\boldsymbol{s}}_{\text{ei}l}$ with $\hat{\boldsymbol{\delta}}_{\text{e}}$ satisfy

$$\begin{cases} \hat{\boldsymbol{s}}_{evl} = \boldsymbol{C}\boldsymbol{S}_{evl}\hat{\boldsymbol{\delta}}_{e} \\ \hat{\boldsymbol{s}}_{eil} = \boldsymbol{C}\boldsymbol{S}_{eil}\hat{\boldsymbol{\delta}}_{e} \end{cases} \tag{10.61}$$

10.3.2.3 Small-Signal Model of DC Transmission Lines

DC transmission lines provide the coupling path for the sending-end and receiving-end LCCs, and the receiving-end LCC will influence the operating characteristics of the sending-end LCC via the DC transmission lines. The equivalent model of the DC transmission lines is shown in Fig. 10.8.

In Fig. 10.8, the DC transmission lines are represented by n Π-line segments. R_{dcL}, L_{dcL}, C_{dcL} are line resistor, line inductor, and line capacitor in a single Π-line segment respectively. The DC transmission line length is l_{line}. According to the equivalent model, the frequency-domain small-signal model of the DC transmission lines can be expressed as

$$\begin{cases} \hat{\boldsymbol{v}}_{\mathrm{edc}} = \boldsymbol{Z}_{\mathrm{edc}}\hat{\boldsymbol{i}}_{\mathrm{edc}} \\ \hat{\boldsymbol{v}}_{\mathrm{fdc}} = \boldsymbol{Z}_{\mathrm{fdc}}\hat{\boldsymbol{i}}_{\mathrm{fdc}} \end{cases} \tag{10.62}$$

where $\boldsymbol{Z}_{\mathrm{edc}}$ is the DC port impedance of the receiving-end LCC; $\boldsymbol{Z}_{\mathrm{fdc}}$ is the DC-side impedance of the sending-end LCC, seen from the DC port of the sending-end LCC to the receiving-end LCC.

The expression of $\boldsymbol{Z}_{\mathrm{fdc}}$ can be derived according to the following equation

$$\boldsymbol{Z}_{\mathrm{fdc}} = \boldsymbol{Z}_{n} + \boldsymbol{Z}_{\mathrm{Ldc}} \tag{10.63}$$

where $\boldsymbol{Z}_{n}$ represents the equivalent impedance of the Π-line segments with the receiving-end LCC considered; The subscript "n" denotes the number of the Π-line segments; $\boldsymbol{Z}_{\mathrm{Ldc}}$ is the impedance of the DC smoothing reactor. The expressions of $\boldsymbol{Z}_{\mathrm{Ldc}}$ and $\boldsymbol{Z}_{n}$ are

$$\boldsymbol{Z}_{\mathrm{Ldc}} = \mathrm{j}2\pi L_{\mathrm{dc}} \cdot \mathrm{diag}[f_{\mathrm{p}} - (12g+2)f_1, \ldots, f_{\mathrm{p}} - f_1, \ldots, f_{\mathrm{p}} + 12gf_1] \tag{10.64}$$

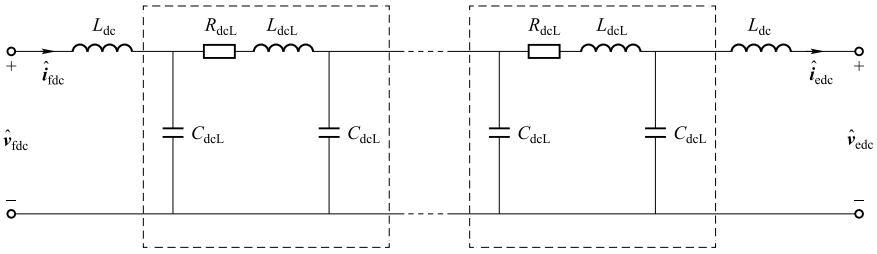

Fig. 10.8 The equivalent model of the DC transmission lines

$$\begin{cases} \boldsymbol{Z}_0 = \boldsymbol{Z}_{\text{edc}} + \boldsymbol{Z}_{\text{Ldc}} \\ \boldsymbol{Z}_n = \left[(\boldsymbol{Z}_{n-1} \| \boldsymbol{Z}_{\text{CdcL}}) + \boldsymbol{Z}_{\text{LdcL}} + \boldsymbol{Z}_{\text{RdcL}} \right] \| \boldsymbol{Z}_{\text{CdcL}} \end{cases} \tag{10.65}$$

where $\boldsymbol{Z}_0$ is the initial item of $\boldsymbol{Z}_n$; $\boldsymbol{Z}_{\text{RdcL}}$, $\boldsymbol{Z}_{\text{LdcL}}$,$\boldsymbol{Z}_{\text{LdcL}}$ are the impedance of the line resistor, line inductor, and line capacitor in a single Π-line segment respectively, expressed as

$$\begin{cases} \boldsymbol{Z}_{\text{RdcL}} = R_{\text{dcL}} \boldsymbol{U} \\ \boldsymbol{Z}_{\text{LdcL}} = \text{j}2\pi L_{\text{dcL}} \cdot \text{diag}[f_{\text{p}} - (12g+2) f_1, \ldots, f_{\text{p}} - f_1, \ldots, f_{\text{p}} + 12g f_1] \\ \boldsymbol{Z}_{\text{CdcL}} = \dfrac{1}{\text{j}2\pi C_{\text{dcL}}} \cdot \text{diag}\left[\dfrac{1}{f_{\text{p}} - (12g+2) f_1}, \ldots, \dfrac{1}{f_{\text{p}} - f_1}, \ldots, \dfrac{1}{f_{\text{p}} + 12g f_1} \right] \end{cases} \tag{10.66}$$

10.3.3 AC Port Impedance Model

The AC port admittance $\boldsymbol{Y}_{\text{LCC}}$ of LCC-HVDC at the sending end is obtained by the sending-end LCC admittance $\boldsymbol{Y}_{\text{self}}$ and AC filter admittance, which is expressed as

$$\begin{cases} \boldsymbol{Y}_{\text{self}} = \dfrac{\hat{\boldsymbol{i}}_{fl}}{\hat{\boldsymbol{v}}_{fl}} \\ \boldsymbol{Y}_{\text{LCC}} = \boldsymbol{Y}_{\text{self}} + \boldsymbol{Z}_{\text{fflt}}^{-1} \end{cases} \tag{10.67}$$

where $\boldsymbol{Z}_{\text{fflt}}$ is the sending-end AC filter impedance.

The AC port admittance of LCC-HVDC at the sending end is related to the sending-end and receiving-end LCCs. According to the small-signal models of the main circuit and control loops in the receiving-end LCC, the DC port impedance of the receiving-end LCC is obtained by combining Eqs. (10.55), (10.56), (10.58), (10.59), and (10.61).

$$\boldsymbol{Z}_{\text{edc}} = \frac{\hat{\boldsymbol{v}}_{\text{edc}}}{\hat{\boldsymbol{i}}_{\text{edc}}} = \left[(\boldsymbol{\Gamma}_1 + \boldsymbol{\Gamma}_7)(\boldsymbol{\Gamma}_2 + \boldsymbol{\Gamma}_6 \boldsymbol{\Gamma}_7)^{-1} \boldsymbol{\Gamma}_3 - \boldsymbol{\Gamma}_4 \right]^{-1} \boldsymbol{\Gamma}_5 \tag{10.68}$$

where $\boldsymbol{\Gamma}_1$, $\boldsymbol{\Gamma}_2$ are the transfer function matrices related to the PLL control of the receiving-end LCC respectively; $\boldsymbol{\Gamma}_3$, $\boldsymbol{\Gamma}_4$ are the transfer function matrices related to the DC voltage control of the receiving-end LCC respectively; $\boldsymbol{\Gamma}_5$ is the transfer function matrix related to the current switching function of the receiving-end LCC; $\boldsymbol{\Gamma}_6$ is the transfer function matrix related to the receiving-end transformer leakage inductance; $\boldsymbol{\Gamma}_7$ is the transfer function matrix related to the receiving-end AC grid impedance. $\boldsymbol{\Gamma}_1 \sim \boldsymbol{\Gamma}_7$ are $(24g+3) \times (24g+3)$ matrices, and their expressions are

$$\begin{cases} \boldsymbol{\Gamma}_1 = 2/k_{\mathrm{eT}} \cdot \boldsymbol{I}_{\mathrm{edc}} \boldsymbol{C} \boldsymbol{S}_{\mathrm{eia}} \boldsymbol{E}_{\mathrm{e}} \\ \boldsymbol{\Gamma}_2 = 2/k_{\mathrm{eT}} \cdot \boldsymbol{D}_{\mathrm{ad}} (\boldsymbol{V}_{\mathrm{eTa}} \boldsymbol{C} \boldsymbol{S}_{\mathrm{eva}} \boldsymbol{E}_{\mathrm{e}} + \boldsymbol{S}_{\mathrm{eva}}) \\ \boldsymbol{\Gamma}_3 = 2/k_{\mathrm{eT}} \cdot \boldsymbol{D}_{\mathrm{ad}} \left(\boldsymbol{V}_{\mathrm{eTa}} \boldsymbol{C} \boldsymbol{S}_{\mathrm{eva}} \boldsymbol{Q}_{\mathrm{e}} + \boldsymbol{U} \right) \\ \boldsymbol{\Gamma}_4 = 2/k_{\mathrm{eT}} \cdot \boldsymbol{I}_{\mathrm{edc}} \boldsymbol{C} \boldsymbol{S}_{\mathrm{eia}} \boldsymbol{Q}_{\mathrm{e}} \\ \boldsymbol{\Gamma}_5 = 2/k_{\mathrm{eT}} \cdot \boldsymbol{S}_{\mathrm{eia}} \\ \boldsymbol{\Gamma}_6 = 2/k_{\mathrm{eT}} \cdot \boldsymbol{D}_{\mathrm{ad}} \boldsymbol{S}_{\mathrm{eva}} \boldsymbol{Z}_{\mathrm{eT}} \\ \boldsymbol{\Gamma}_7 = \boldsymbol{Z}_{\mathrm{eac}}^{-1} \end{cases} \tag{10.69}$$

According to the small-signal model of the DC transmission lines, the DC-side impedance of the sending-end LCC $\boldsymbol{Z}_{\mathrm{fdc}}$ can be obtained by substituting $\boldsymbol{Z}_{\mathrm{edc}}$ in Eq. (10.68) into Eq. (10.63).

According to the small-signal model of the sending-end LCC, combining Eqs. (10.47), (10.49), (10.51), (10.53), and $\boldsymbol{Z}_{\mathrm{fdc}}$, the AC port admittance of LCC-HVDC at the sending end can be derived as

$$\boldsymbol{Y}_{\mathrm{LCC}} = \left[\boldsymbol{U} + \boldsymbol{\Lambda}_1 (\boldsymbol{Z}_{\mathrm{fdc}} - \boldsymbol{\Lambda}_2)^{-1} \boldsymbol{\Lambda}_5 \right]^{-1} \left[\boldsymbol{\Lambda}_1 (\boldsymbol{Z}_{\mathrm{fdc}} - \boldsymbol{\Lambda}_2)^{-1} \boldsymbol{\Lambda}_3 + \boldsymbol{\Lambda}_4 \right] + \boldsymbol{\Lambda}_6 \tag{10.70}$$

where $\boldsymbol{\Lambda}_1$, $\boldsymbol{\Lambda}_2$ are the transfer function matrices related to the DC current control of the sending-end LCC respectively; $\boldsymbol{\Lambda}_3$, $\boldsymbol{\Lambda}_4$ are the transfer function matrices related to the PLL control of the sending-end LCC respectively; $\boldsymbol{\Lambda}_5$ is the transfer function matrix related to the sending-end transformer leakage inductance; $\boldsymbol{\Lambda}_6$ is the transfer function matrix related to the sending-end AC filter admittance. $\boldsymbol{\Lambda}_1 \sim \boldsymbol{\Lambda}_6$ are $(24g + 3) \times (24g + 3)$ matrices, and their expressions are

$$\begin{cases} \boldsymbol{\Lambda}_1 = 2/k_{\mathrm{fT}} \cdot \left(\boldsymbol{I}_{\mathrm{fdc}} \boldsymbol{C} \boldsymbol{S}_{\mathrm{fia}} \boldsymbol{Q}_{\mathrm{f}} + \boldsymbol{S}_{\mathrm{fia}} \right) \\ \boldsymbol{\Lambda}_2 = 2/k_{\mathrm{fT}} \cdot \boldsymbol{D}_{\mathrm{ad}} \boldsymbol{V}_{\mathrm{fTa}} \boldsymbol{C} \boldsymbol{S}_{\mathrm{fva}} \boldsymbol{Q}_{\mathrm{f}} \\ \boldsymbol{\Lambda}_3 = 2/k_{\mathrm{fT}} \cdot \boldsymbol{D}_{\mathrm{ad}} (\boldsymbol{V}_{\mathrm{fTa}} \boldsymbol{C} \boldsymbol{S}_{\mathrm{fva}} \boldsymbol{E}_{\mathrm{f}} + \boldsymbol{S}_{\mathrm{fva}}) \\ \boldsymbol{\Lambda}_4 = 2/k_{\mathrm{fT}} \cdot \boldsymbol{I}_{\mathrm{fdc}} \boldsymbol{C} \boldsymbol{S}_{\mathrm{fia}} \boldsymbol{E}_{\mathrm{f}} \\ \boldsymbol{\Lambda}_5 = 2/k_{\mathrm{fT}} \cdot \boldsymbol{D}_{\mathrm{ad}} \boldsymbol{S}_{\mathrm{fva}} \boldsymbol{Z}_{\mathrm{fT}} \\ \boldsymbol{\Lambda}_6 = \boldsymbol{Z}_{\mathrm{fflt}}^{-1} \end{cases} \tag{10.71}$$

The small-signal components at f_{p} and $f_{\mathrm{p}} - 2f_1$ are the main components in the small-signal vectors of the AC voltage and current of LCC-HVDC, while the amplitudes of the other components are relatively small. The characteristics of the AC port impedance or admittance at f_{p} and $f_{\mathrm{p}} - 2f_1$ are more significant. Only relevant elements at these two frequencies are extracted, and the relationship between the small-signal vectors of the AC voltage and current and AC port admittance is reformulated as

$$\begin{bmatrix} \hat{\boldsymbol{i}}_{\mathrm{f}} \\ \hat{\boldsymbol{i}}_{\mathrm{f\text{-}2}} \end{bmatrix} = \begin{bmatrix} \boldsymbol{Y}_{\mathrm{LCC}}^{\mathrm{pp}} & \boldsymbol{Y}_{\mathrm{LCC}}^{\mathrm{np}} \\ \boldsymbol{Y}_{\mathrm{LCC}}^{\mathrm{pn}} & \boldsymbol{Y}_{\mathrm{LCC}}^{\mathrm{nn}} \end{bmatrix} \begin{bmatrix} \hat{\boldsymbol{v}}_{\mathrm{f}} \\ \hat{\boldsymbol{v}}_{\mathrm{f\text{-}2}} \end{bmatrix} \tag{10.72}$$

where $\hat{\boldsymbol{v}}_{\mathrm{f}}$, $\hat{\boldsymbol{v}}_{\mathrm{f}-2}$ are the small-signal components of the sending-end AC voltage at f_{p} and $f_{\mathrm{p}}-2f_{\mathrm{l}}$ respectively; $\hat{\boldsymbol{i}}_{\mathrm{f}}$, $\hat{\boldsymbol{i}}_{\mathrm{f}-2}$ are the small-signal components of the sending-end AC current at f_{p} and $f_{\mathrm{p}}-2f_{\mathrm{l}}$ respectively. The expression of the 2×2 AC port admittance matrix is

$$\begin{bmatrix} \boldsymbol{Y}_{\mathrm{LCC}}^{\mathrm{pp}} & \boldsymbol{Y}_{\mathrm{LCC}}^{\mathrm{np}} \\ \boldsymbol{Y}_{\mathrm{LCC}}^{\mathrm{pn}} & \boldsymbol{Y}_{\mathrm{LCC}}^{\mathrm{nn}} \end{bmatrix} = \begin{bmatrix} \boldsymbol{Y}_{\mathrm{LCC}}(12g+3,12g+3) & \boldsymbol{Y}_{\mathrm{LCC}}(12g+3,12g+1) \\ \boldsymbol{Y}_{\mathrm{LCC}}(12g+1,12g+3) & \boldsymbol{Y}_{\mathrm{LCC}}(12g+1,12g+1) \end{bmatrix}$$

in which

$\boldsymbol{Y}_{\mathrm{LCC}}^{\mathrm{pp}}$ is the positive-sequence admittance of LCC-HVDC at the sending end, representing the small-signal response of AC current at f_{p} in positive sequence under per unit small-signal perturbation of AC voltage at f_{p} in positive sequence.
$\boldsymbol{Y}_{\mathrm{LCC}}^{\mathrm{pn}}$ is the positive-sequence coupled admittance of LCC-HVDC at the sending end, representing the small-signal response of AC current at $f_{\mathrm{p}}-2f_{\mathrm{l}}$ in negative sequence under per unit small-signal perturbation of AC voltage at f_{p} in positive sequence.
$\boldsymbol{Y}_{\mathrm{LCC}}^{\mathrm{nn}}$ is the negative-sequence admittance of LCC-HVDC at the sending end, representing the small-signal response of AC current at $f_{\mathrm{p}}-2f_{\mathrm{l}}$ in negative sequence under per unit small-signal perturbation of AC voltage at $f_{\mathrm{p}}-2f_{\mathrm{l}}$ in negative sequence.
$\boldsymbol{Y}_{\mathrm{LCC}}^{\mathrm{np}}$ is the negative-sequence coupled admittance of LCC-HVDC at the sending end, representing the small-signal response of AC current at f_{p} in positive sequence under per unit small-signal perturbation of AC voltage at $f_{\mathrm{p}}-2f_{\mathrm{l}}$ in negative sequence.
$\boldsymbol{Y}_{\mathrm{LCC}}(12g+3,12g+3)$ is the element in the $(12g+3)$ th row and the $(12g+3)$ th column of $\boldsymbol{Y}_{\mathrm{LCC}}$.
$\boldsymbol{Y}_{\mathrm{LCC}}(12g+3,12g+1)$ is the element in the $(12g+3)$ th row and the $(12g+1)$ th column of $\boldsymbol{Y}_{\mathrm{LCC}}$.
$\boldsymbol{Y}_{\mathrm{LCC}}(12g+1,12g+3)$ is the element in the $(12g+1)$ th row and the $(12g+3)$ th column of $\boldsymbol{Y}_{\mathrm{LCC}}$.
$\boldsymbol{Y}_{\mathrm{LCC}}(12g+1,12g+1)$ is the element in the $(12g+1)$ th row and the $(12g+1)$ th column of $\boldsymbol{Y}_{\mathrm{LCC}}$.

The AC port impedance of the thyristor can be obtained by calculating the inverse matrix of the AC port admittance as

$$\begin{bmatrix} \boldsymbol{Z}_{\mathrm{LCC}}^{\mathrm{pp}} & \boldsymbol{Z}_{\mathrm{LCC}}^{\mathrm{pn}} \\ \boldsymbol{Z}_{\mathrm{LCC}}^{\mathrm{np}} & \boldsymbol{Z}_{\mathrm{LCC}}^{\mathrm{nn}} \end{bmatrix} = \begin{bmatrix} \boldsymbol{Y}_{\mathrm{LCC}}^{\mathrm{pp}} & \boldsymbol{Y}_{\mathrm{LCC}}^{\mathrm{np}} \\ \boldsymbol{Y}_{\mathrm{LCC}}^{\mathrm{pn}} & \boldsymbol{Y}_{\mathrm{LCC}}^{\mathrm{nn}} \end{bmatrix}^{-1} \tag{10.73}$$

where

$\boldsymbol{Z}_{\mathrm{LCC}}^{\mathrm{pp}}$ represents the positive-sequence impedance and is the element in the first row and the first column of the AC port admittance inverse matrix.

$\boldsymbol{Z}_{\mathrm{LCC}}^{\mathrm{pn}}$ represents the positive-sequence coupled impedance and is the element in the first row and the second column of the AC port admittance inverse matrix.
$\boldsymbol{Z}_{\mathrm{LCC}}^{\mathrm{nn}}$ represents the negative-sequence impedance and is the element in the second row and the second column of the AC port admittance inverse matrix.
$\boldsymbol{Z}_{\mathrm{LCC}}^{\mathrm{np}}$ represents the negative-sequence coupled impedance and is the element in the second row and the first column of the AC port admittance inverse matrix.

In addition, the frequency-domain relationship between the negative-sequence impedance and the positive-sequence impedance satisfies $\boldsymbol{Z}_{\mathrm{LCC}}^{\mathrm{nn}} = \boldsymbol{Z}_{\mathrm{LCC}}^{\mathrm{pp}*}(\mathrm{j}2\omega_1 - s)$, and the frequency-domain relationship between the negative-sequence coupled impedance and the positive-sequence coupling impedance satisfies $\boldsymbol{Z}_{\mathrm{LCC}}^{\mathrm{np}} = \boldsymbol{Z}_{\mathrm{LCC}}^{\mathrm{pn}*}(\mathrm{j}2\omega_1 - s)$.

The main circuit and controller parameters of LCC-HVDC are listed in Table 10.3. The short circuit ratio (SCR) of the receiving end power grid is set to 3.0, which represents the power grid strength. Figure 10.9 shows the analytical (in solid lines) and scanning (in discrete points) results of the AC port impedance of LCC-HVDC at the sending end. As seen from the figure, all the discrete points fall on the solid lines, which verifies the accuracy of the established impedance model of LCC-HVDC.

10.4 Analysis of Broadband Impedance Characteristics

Based on the established impedance model of LCC-HVDC, this section first analyzes the dominant factors of the impedance characteristics in different frequency bands, and proposes the frequency band division method of LCC-HVDC. Then, the frequency-band overlapping effect of the multiple control loops or links and the negative damping characteristics in each frequency band are clarified. Finally, based on the CHIL scanning result of LCC-HVDC impedance, the typical values of each frequency band are given.

10.4.1 Frequency-Band Division of Broadband Impedance

Based on the established analytical impedance model of LCC-HVDC, the AC port impedance at the sending end is influenced by the sending-end AC filters, the control characteristics of the sending-end and receiving-end LCCs, receiving-end AC grid strength, and DC transmission lines. Based on the frequency-domain relationship between the impedance characteristics with controllers or links, the dominant factor of the impedance characteristics in each frequency band is clarified, and the frequency band division method is proposed.

Table 10.3 Main circuit and controller parameters of LCC-HVDC

Parameter	Definition	Value
P_N	Rated Power	2000 MW
V_{dcref}	DC voltage reference	400 kV
I_{dcref}	DC current reference	5000 A
k_{fT}	Transformer voltage ratio at the sending end	530 kV/172 kV
L_{fT}	Transformer leakage inductance at the sending end	37.3 mH
k_{eT}	Transformer voltage ratio at the receiving end	530 kV/165 kV
L_{eT}	Transformer leakage inductance at the receiving end	46.6 mH
L_{dc}	DC smoothing reactance	150 mH
l_{line}	DC transmission line length	1000 km
R_{dcL}	Line resistance in a single Π-line segment	0.0033 Ω/km
L_{dcL}	Line inductance in a single Π-line segment	0.2 mH/km
C_{dcL}	Line capacitance in a single Π-line segment	0.015 μF/km
K_{fpp}, K_{fpi}	Proportional and integral coefficients of the PLL controller in the sending-end LCC	1.7110×10^{-5}, 1.7900×10^{-4}
K_{idcp}, K_{idci}	Proportional and integral coefficients of the DC current controller	0.0350, 0.2857
T_{idcf}	DC current filter time delay	0.0003 s
K_{epp}, K_{epi}	Proportional and integral coefficients of the PLL controller in the receiving-end LCC	1.0267×10^{-4}, 0.0065
K_{vdcp}, K_{vdci}	Proportional and integral coefficients of the DC voltage controller	1.2500×10^{-6}, 0.0015
T_{vdcf}	DC voltage filter time delay	0.0160 s

10.4.1.1 Influence of Sending-End AC Filters

The AC port impedance of LCC-HVDC at the sending end $\boldsymbol{Z}_{LCC}$ consists of the sending-end LCC impedance $\boldsymbol{Z}_{self}$ and AC filter impedance $\boldsymbol{Z}_{fflt}$ in parallel, as shown in (10.67). The influence of $\boldsymbol{Z}_{self}$ and $\boldsymbol{Z}_{fflt}$ on the impedance characteristics of $\boldsymbol{Z}_{LCC}$ is shown in Fig. 10.10.

As shown in Fig. 10.10, the magnitude of $\boldsymbol{Z}_{fflt}$ is larger than that of $\boldsymbol{Z}_{self}$ in the subsynchronous frequency band. According to the parallel relationship of $\boldsymbol{Z}_{fflt}$ and $\boldsymbol{Z}_{self}$, the impedance characteristics of $\boldsymbol{Z}_{LCC}$ are dominated by $\boldsymbol{Z}_{self}$ in this frequency band. The magnitude of $\boldsymbol{Z}_{fflt}$ declines as the frequency increases. When the magnitudes of $\boldsymbol{Z}_{fflt}$ and $\boldsymbol{Z}_{self}$ are close around the fundamental frequency, $\boldsymbol{Z}_{LCC}$ are determined by both $\boldsymbol{Z}_{fflt}$ and $\boldsymbol{Z}_{self}$. As the frequency continues to increase, the magnitude of $\boldsymbol{Z}_{fflt}$ is further reduced. $\boldsymbol{Z}_{LCC}$ is dominated by $\boldsymbol{Z}_{fflt}$ when the magnitude of $\boldsymbol{Z}_{fflt}$ is lower than that of $\boldsymbol{Z}_{self}$ in the medium- and high-frequency bands. In this case, $\boldsymbol{Z}_{LCC}$ presents capacitive.

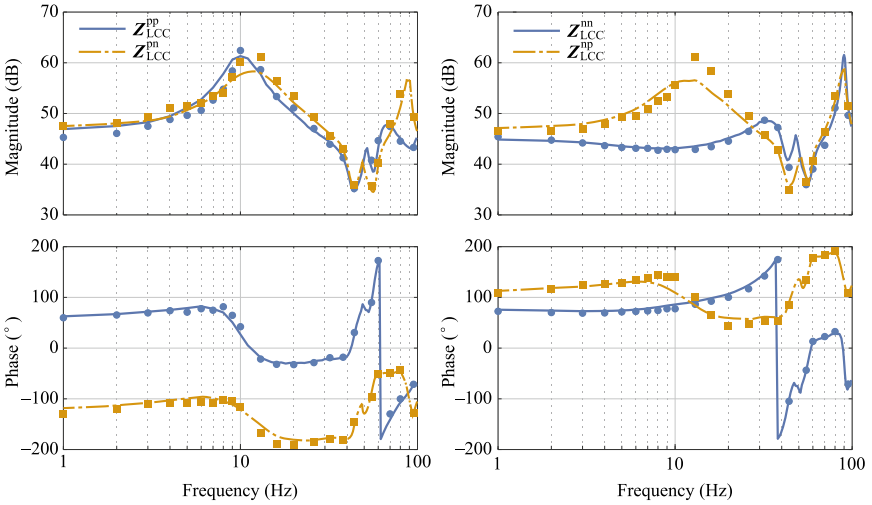

(a) Positive-sequence impedance and positive-sequence coupling impedance

(b) Negative-sequence impedance and negative-sequence coupling impedance

Fig. 10.9 The analytical and scanning results of the AC port impedance of LCC-HVDC at the sending end

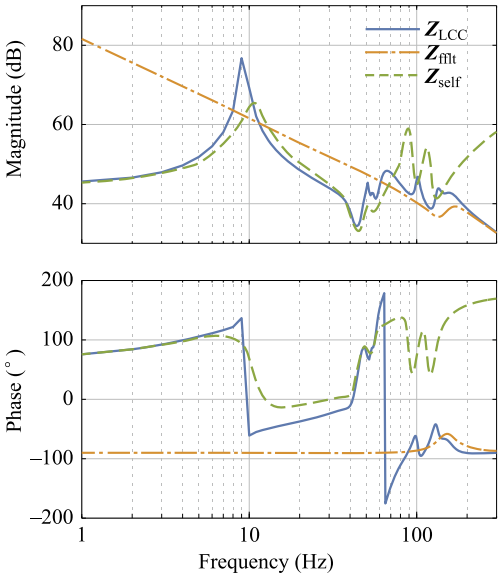

Fig. 10.10 The influence of sending-end LCC impedance and AC filter impedance on the impedance characteristics

Since $\boldsymbol{Z}_{\mathrm{LCC}}$ is dominated by $\boldsymbol{Z}_{\mathrm{fflt}}$ in the medium- and high-frequency bands, the impedance characteristics of LCC-HVDC at the sending end can be obtained according to the passive filter parameters. Therefore, for the impedance analysis of LCC-HVDC, the impedance characteristics in the subsynchronous and super-synchronous frequency bands are focused on in this chapter. The influences of the other factors on the impedance characteristics will be analyzed below based on the impedance model of $\boldsymbol{Z}_{\mathrm{self}}$.

10.4.1.2 Influence of DC-Side Impedance of Sending-End LCC

According to Eq. (10.70), ignoring the sending-end AC filters and transformer leakage inductance, the impedance model can be simplified as

$$\boldsymbol{Y}_{\mathrm{self}} = \boldsymbol{\Lambda}_1(\boldsymbol{Z}_{\mathrm{fdc}} - \boldsymbol{\Lambda}_2)^{-1}\boldsymbol{\Lambda}_3 + \boldsymbol{\Lambda}_4 \tag{10.74}$$

According to Eq. (10.74), the DC-side impedance of the sending-end LCC $\boldsymbol{Z}_{\mathrm{fdc}}$ has a coupling effect on $\boldsymbol{Z}_{\mathrm{self}}$.

The AC voltages and currents contain the small-signal components at $f_{\mathrm{p}} - f_1 + (12n \pm 1)f_1$, while the DC voltage and current contain the small-signal components at $f_{\mathrm{p}} - f_1 + 12nf_1$. The small-signal components at f_{p} and $f_{\mathrm{p}} - 2f_1$ are the main components for the AC voltages and currents, while the small-signal components at $f_{\mathrm{p}} - f_1$ are the main components for the DC voltage and current. The frequency difference of the small-signal components of the AC/DC quantities is f_1, $\boldsymbol{Z}_{\mathrm{fdc}}[j2\pi(f_{\mathrm{p}} - f_1)]$ has an influence on $\boldsymbol{Z}_{\mathrm{self}}(j2\pi f_{\mathrm{p}})$.

With the DC transmission line length l_{line} equivalent to 1000, 1500 and 2000 km, the influences of l_{line} on the impedance characteristics of $\boldsymbol{Z}_{\mathrm{fdc}}$ and $\boldsymbol{Z}_{\mathrm{self}}$ are shown in Fig. 10.11. In the figure, the DC-side impedance shows the curves of $\boldsymbol{Z}_{\mathrm{fdc}}[j2\pi(f_{\mathrm{p}} - f_1)]$.

As shown in Fig. 10.11, $\boldsymbol{Z}_{\mathrm{fdc}}$ is symmetrical about the fundamental frequency, i.e., the amplitude is equal and the phase is opposite about the fundamental frequency. $\boldsymbol{Z}_{\mathrm{fdc}}$ has multiple resonant peaks in the subsynchronous and super-synchronous frequency bands, and the impedance characteristics change from inductive to capacitive, or from capacitive to inductive, around the resonant frequencies. With the increase of the DC transmission line length, the magnitudes of the resonant peaks increase, and the resonant frequencices are closer to the fundamental frequency. Besides, $\boldsymbol{Z}_{\mathrm{fdc}}$ presents inductive above the resonant frequencies in the medium- and high-frequency bands.

Comparing the curves of $\boldsymbol{Z}_{\mathrm{fdc}}$ and $\boldsymbol{Z}_{\mathrm{self}}$, the trend of the impedance variations with frequency are similar except around the fundamental frequency, and the resonant frequencies are identical. With the increase of the DC transmission line length, the magnitudes of the resonant peaks in $\boldsymbol{Z}_{\mathrm{self}}$ also increase, and the resonant frequencices are closer to the fundamental frequency, indicating that $\boldsymbol{Z}_{\mathrm{self}}$ is dominated by $\boldsymbol{Z}_{\mathrm{fdc}}$. The main difference is that $\boldsymbol{Z}_{\mathrm{self}}$ has a larger phase than $\boldsymbol{Z}_{\mathrm{fdc}}$ in general. There is an inductive bias in $\boldsymbol{Z}_{\mathrm{self}}$, which presents inductive characteristics above the fundamental frequency.

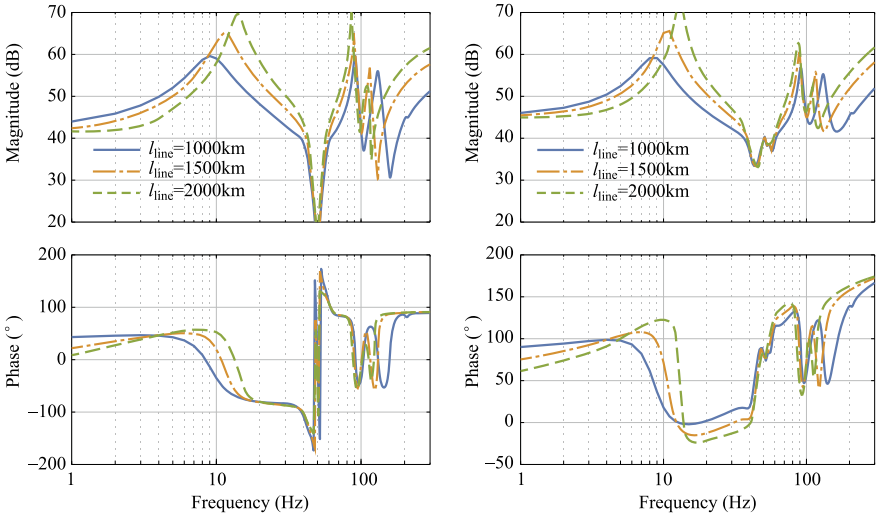

(a) DC-side impedance of sending-end LCC (b) Sending-end LCC impedance

Fig. 10.11 The influence of the DC transmission line length on the impedance characteristics

10.4.1.3 Influence of DC Current Loop in Sending-End LCC

The difference between $\boldsymbol{Z}_{\text{self}}$ and $\boldsymbol{Z}_{\text{fdc}}$ is mainly influenced by the control characteristics of the sending-end LCC. According to Eq. (10.74), the DC current control in the sending-end LCC has an influence on $\boldsymbol{Z}_{\text{self}}$ in two aspects. On the one hand, $\boldsymbol{\Lambda}_2$ is in series with $\boldsymbol{Z}_{\text{fdc}}$, and the effect of $\boldsymbol{\Lambda}_2$ is equivalent to changing $\boldsymbol{Z}_{\text{fdc}}$. On the other hand, $\boldsymbol{\Lambda}_1$ is multiplied by $\left(\boldsymbol{Z}_{\text{fdc}} - \boldsymbol{\Lambda}_2\right)^{-1}$, and the effect of $\boldsymbol{\Lambda}_1$ is equivalent to adjust the gain of $\boldsymbol{Z}_{\text{fdc}}$. The DC current control affects the coupling degree of the AC- and DC-side impedances in the sending-end LCC.

The influence of the DC current loop in the sending-end LCC on $\boldsymbol{Z}_{\text{self}}$ is shown in Fig. 10.12. On the one hand, the influence of DC current loop bandwidth f_{idc} can be obtained by changing f_{idc} to 5, 10 and 20 Hz respectively with a constant PM of 45°. On the other hand, the influence of DC current loop PM θ_{idc} can be obtained by changing θ_{idc} to 20°, 45° and 70° respectively with a constant bandwidth of 10 Hz.

As shown in Fig. 10.12, two anti-resonant peaks appear in $\boldsymbol{Z}_{\text{self}}$ around $f_1 - f_{\text{idc}}$ and $f_1 + f_{\text{idc}}$. With the increase of f_{idc}, the two resonant frequencies are further away from the fundamental frequency. The change of θ_{idc} mainly influences the impedance magnitude and phase at each resonant peaks in $\boldsymbol{Z}_{\text{self}}$. With the increase of θ_{idc}, the impedance magnitude and phase change more flatly around the resonant frequencies. Besides, the influence of $\boldsymbol{Z}_{\text{fdc}}$ on $\boldsymbol{Z}_{\text{self}}$ is attenuated by the DC current control. With the increase of f_{idc} and θ_{idc}, the magnitude of $\boldsymbol{Z}_{\text{self}}$ is reduced in the subsynchronous and super-synchronous frequency bands.

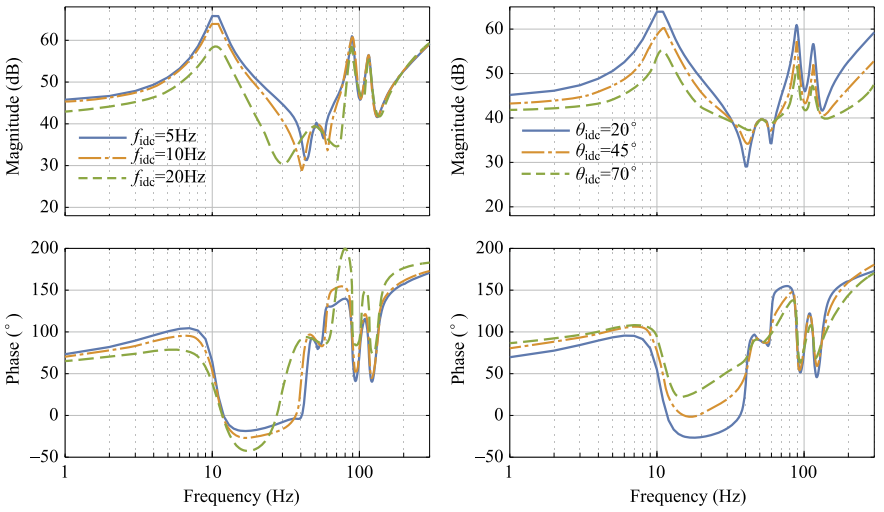

(a) Different DC current loop bandwidths (b) Different DC current loop PMs

Fig. 10.12 The influence of the DC current loop in the sending-end LCC on the impedance characteristics

10.4.1.4 Influence of PLL in Sending-End LCC

According to Eq. (10.74), the PLL control in the sending-end LCC has an influence on $\boldsymbol{Z}_{\text{self}}$ in two aspects. On the one hand, the effect of $\boldsymbol{\Lambda}_3$ is equivalent to adjust the gain of $\boldsymbol{Z}_{\text{fdc}}$, affecting the coupling degree of the AC- and DC-side impedances. On the other hand, the inverse matrix of $\boldsymbol{\Lambda}_4$ is equivalent to connect $\boldsymbol{Z}_{\text{fdc}}$ in parallel, constituting the part of $\boldsymbol{Z}_{\text{self}}$.

The influence of the PLL in the sending-end LCC on $\boldsymbol{Z}_{\text{self}}$ is shown in Fig. 10.13. On the one hand, the influence of PLL bandwidth f_{ftc} can be obtained by changing f_{ftc} to 5, 10 and 20 Hz respectively with a constant PM of 45°. On the other hand, the influence of DC current loop PM θ_{ftc} can be obtained by changing θ_{ftc} to 20°, 45° and 70° respectively with a constant bandwidth of 10 Hz.

As shown in Fig. 10.13, $\boldsymbol{Z}_{\text{self}}$ has two anti-resonant peaks around $f_1 - f_{\text{ftc}}$ and $f_1 + f_{\text{ftc}}$. With the increase of f_{ftc}, the resonant frequencies are further away from the fundamental frequency. The change of θ_{ftc} has little influence on $\boldsymbol{Z}_{\text{self}}$. The PLL control mainly influences the impedance characteristics at the resonant peaks in the subsynchronous and super synchronous frequency bands.

10.4.1.5 Frequency-Band Division of Broadband Impedance

According to the analysis of the dominant factors of LCC-HVDC impedance characteristics in each frequency band, the following frequency bands can be divided.

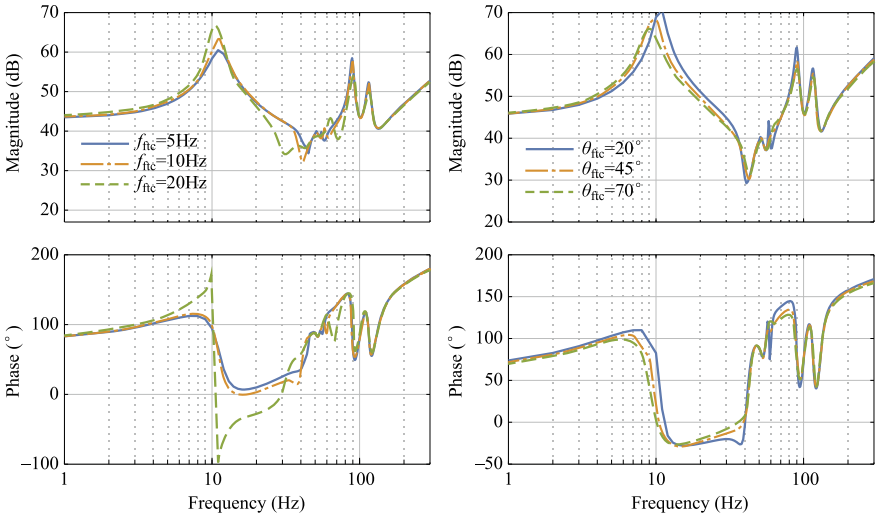

(a) Different sending-end LCC PLL bandwidths (b) Different sending-end LCC PLL PMs

Fig. 10.13 The influence of the PLL in the sending-end LCC on the impedance characteristics

(1) Band I_{LCC} ($f < f_1 + f_{\text{idc}}$): The AC port impedance of LCC-HVDC at the sending end $\boldsymbol{Z}_{\text{LCC}}$ is dominated by the DC-side impedance of the sending-end LCC $\boldsymbol{Z}_{\text{fdc}}$. Multiple resonant peaks exist in $\boldsymbol{Z}_{\text{LCC}}$. With the increase of the DC transmission line length, the impedance magnitudes at the resonant peaks increase, and the resonant frequencices are closer to the fundamental frequency.
(2) Band II_{LCC} ($f > f_1 + f_{\text{idc}}$): The AC port impedance of LCC-HVDC at the sending end $\boldsymbol{Z}_{\text{LCC}}$ is dominated by the sending-end AC filter $\boldsymbol{Z}_{\text{fflt}}$. As the frequency continues to increase, the impedance magnitude declines, and impedance characteristics presents capacitive.

The DC current control and PLL control mainly influence the impedance characteristics in the subsynchronous and super synchronous frequency bands, i.e., Band I_{LCC} and the former segment of Band II_{LCC}. With the increase of bandwidths of the DC current loop and PLL, the frequencies of the resonant peaks in impedance magnitude are further away from the fundamental frequency. With the increase of DC current loop PM, the impedance magnitude and phase change more flatly around the resonant frequencies.

Impedance scanning is carried out based on the CHIL platform of LCC-HVDC, and the scanning result is shown in Fig. 10.14. It can be seen from the figure that the frequency range of Band I_{LCC} is around $f < 70$ Hz, and the frequency range of Band II_{LCC} is around $f > 70$ Hz.

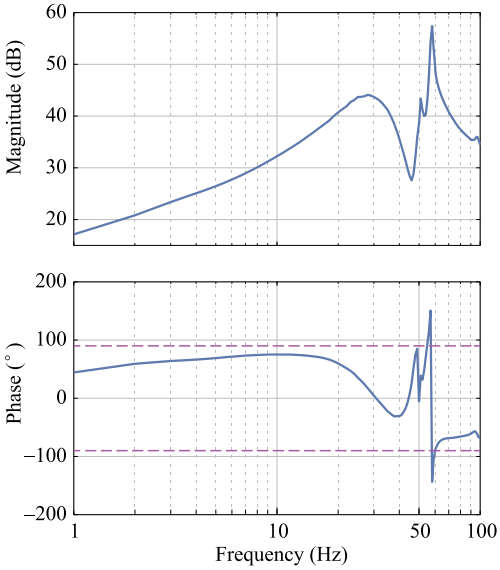

Fig. 10.14 The scanning impedance of LCC-HVDC based on CHIL platform

10.4.2 Analysis of Negative Damping Characteristics

The frequency-band division method of the broadband impedance of LCC-HVDC has been proposed according to the analysis in Sect. 10.4.1. Considering the LCC-HVDC control system involves the coordination of the multiple controllers in the sending-end and receiving-end LCCs, the impedance characteristics in each frequency band are influenced not only by the dominant factors, but also by the frequency-band overlapping effects of the other controllers or links. In this section, the frequency-band overlapping effects of multiple control loops or links will be analyzed to reveal the mechanism of the negative damping characteristics in each frequency band.

10.4.2.1 Influence of Sending-End LCC Control on Negative Damping Characteristics

The DC-side impedance of the sending-end LCC has an influence on the AC port impedance characteristics of LCC-HVDC at the sending end through the DC current control and PLL control. Based on this, this section analyzes the influence of the DC current loop and PLL of the sending-end LCC on the damping characteristics of LCC-HVDC at the sending end.

1. **Influence of DC Current Loop in Sending-End LCC**

The influence of the DC current loop on the damping characteristics of LCC-HVDC at the sending end is shown in Fig. 10.15. On the one hand, the influence of DC current

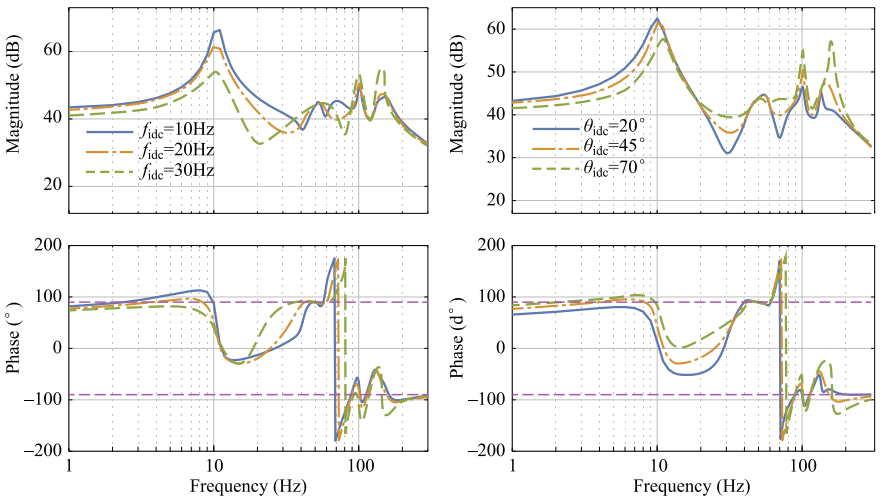

Fig. 10.15 The influence of DC current loop in the sending-end LCC on the damping characteristics

loop bandwidth can be obtained by changing f_{idc} to 10, 20 and 30 Hz respectively with a constant PM of 45°. On the other hand, the influence of DC current loop PM can be obtained by changing θ_{idc} to 20°, 45° and 70° respectively with a constant bandwidth of 20 Hz.

As shown in Fig. 10.15, the AC port impedance of LCC-HVDC at the sending end $\boldsymbol{Z}_{\text{LCC}}$ presents inductive negative damping in Band I_{LCC} (impedance phase above 90°). At the junction of Band I_{LCC} and Band II_{LCC}, i.e., around the DC current control bandwidth in SCF ($f_1 + f_{\text{idc}}$), $\boldsymbol{Z}_{\text{LCC}}$ changes from inductive negative damping to capacitive negative damping (impedance phase below $-90°$). With the increase of f_{idc}, the damping characteristicsare improved at the resonant peak (around 10 Hz), but the capacitive negative damping degree is deepened around $f_1 + f_{\text{idc}}$. Besides, the negative damping degree is also deepened with the increase of θ_{idc}. The results indicate that the frequency-band overlapping effect between the DC current loop and the DC-side impedance of the sending-end LCC leads to the negative damping in the AC port impedance of LCC-HVDC at the sending-end LCC.

2. Influence of PLL in Sending-End LCC

The influence of the PLL on the damping characteristics of LCC-HVDC at the sending end is shown in Fig. 10.16. On the one hand, the influence of PLL bandwidth can be obtained by changing f_{ftc} to 5, 20 and 40 Hz respectively with a constant PM of 45°. On the other hand, the influence of PLL PM can be obtained by changing θ_{ftc} to 20°, 45° and 70° respectively with a constant bandwidth of 20Hz.

As shown in Fig. 10.16, the PLL control in the sending-end LCC mainly influences the impedance magnitude and phase at the resonant peak in Band I_{LCC}. With the decrease of f_{ftc} and θ_{ftc}, the negative damping degree is deepened in this frequency

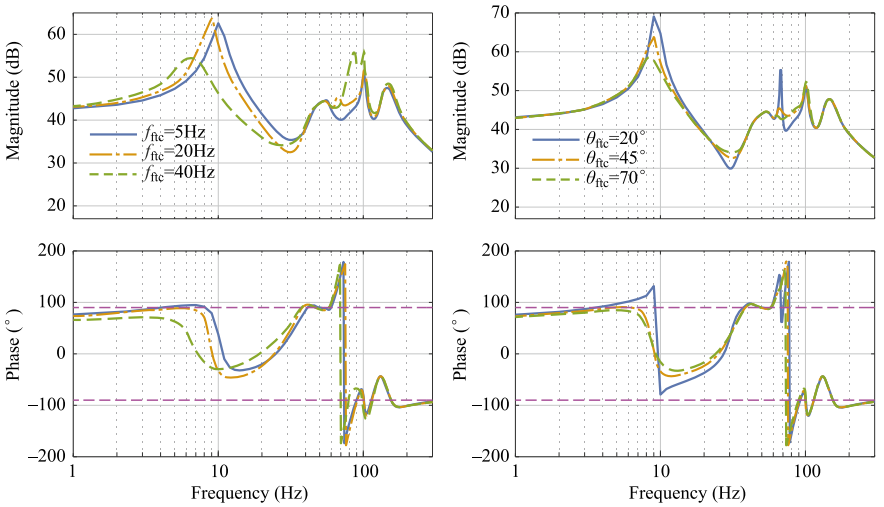

(a) Different sending-end PLL bandwidths (b) Different sending-end PLL PMs

Fig. 10.16 The influence of PLL in the sending-end LCC on the damping characteristics

band. The PLL control has little influence on the damping characteristics in Band II_{LCC}.

10.4.2.2 Influence of Receiving-End LCC on Negative Damping Characteristics

Based on the established impedance model of LCC-HVDC, the DC-side impedance of the sending-end LCC $\boldsymbol{Z}_{\text{fdc}}$ consists of the DC transmission line impedance and the DC port impedance of the receiving-end LCC $\boldsymbol{Z}_{\text{edc}}$. The receiving-end LCC has a coupling effect on the AC port impedance of LCC-HVDC at the sending end $\boldsymbol{Z}_{\text{LCC}}$. The influences of the receiving-end AC grid strength and the receiving-end LCC control on the damping characteristics of LCC-HVDC at the sending end are analyzed as follows.

1. **Influence of SCR at Receiving End**

The influence of the receiving-end AC grid strength on the damping characteristics of LCC-HVDC at the sending end is analyzed as follows. With the short circuit ratio (SCR) at the receiving end equivalent to 2.0, 3.0 and 5.0, the influence of the SCR at the receiving end on the damping characteristics is shown in Fig. 10.17.

As shown in Fig. 10.17, with the decrease of the SCR at the receiving end, the impedance of the receiving-end AC grid is increased, the coupling effect of the receiving-end AC grid strength on the damping characteristics of LCC-HVDC at the sending end is more significant. The resonant peaks in the impedance magnitude are closer to the fundamental frequency, and the negative damping degrees are deepened

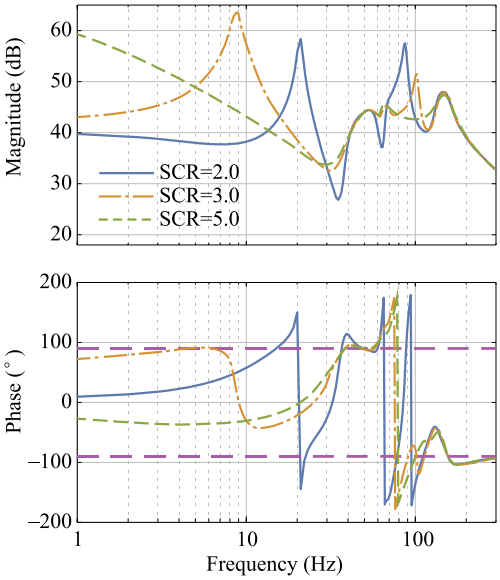

Fig. 10.17 The influence of SCR at the receiving end on the damping characteristics

around the resonant peaks in Band $\mathrm{I}_{\mathrm{LCC}}$ and $f_1 + f_{\mathrm{idc}}$. The receiving-end AC grid strength has little influence on the damping characteristics in the latter segment of Band $\mathrm{II}_{\mathrm{LCC}}$.

2. **Influence of PLL in Receiving-End LCC**

The influence of the PLL in the receiving-end LCC on the damping characteristics of LCC-HVDC at the sending end is shown in Fig. 10.18. On the one hand, the influence of PLL bandwidth can be obtained by changing f_{etc} to 5, 10, and 20 Hz respectively with a constant PM of 45°. On the other hand, the influence of PLL PM can be obtained by changing θ_{etc} to 20°, 45° and 70° respectively with a constant bandwidth of 10 Hz.

As shown in Fig. 10.18, with the increase of f_{etc} and θ_{etc}, the negative damping degree at the resonant peak in Band $\mathrm{I}_{\mathrm{LCC}}$ is deepened. The PLL in the receiving-end LCC has little influence on the damping characteristics in Band $\mathrm{II}_{\mathrm{LCC}}$.

3. **Influence of DC Voltage Loop in Receiving-End LCC**

The influence of the DC voltage loop in the receiving-end LCC on the damping characteristics of LCC-HVDC at the sending end is shown in Fig. 10.19. On the one hand, the influence of DC voltage loop bandwidth can be obtained by changing f_{vdc} to 10, 20 and 30 Hz respectively with a constant PM of 45°. On the other hand, the influence of DC voltage loop PM can be obtained by changing θ_{vdc} to 20°, 45° and 70° respectively with a constant bandwidth of 20 Hz.

As shown in Fig. 10.19, with the increase of f_{vdc} or θ_{vdc}, the negative damping degree at the resonant peak in Band $\mathrm{I}_{\mathrm{LCC}}$ is deepened, and the impedance changes

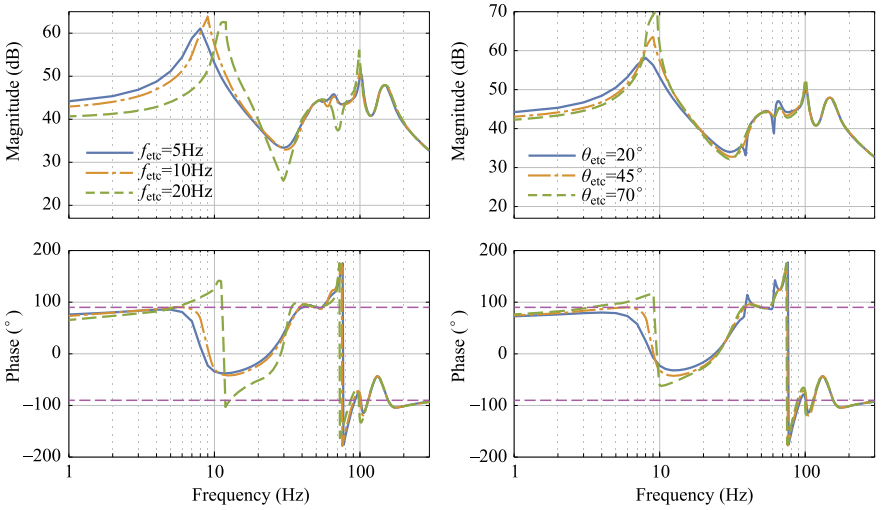

(a) Different receiving-end PLL bandwidths (b) Different receiving-end PLL PMs

Fig. 10.18 The influence of PLL in the receiving-end LCC on the damping characteristics

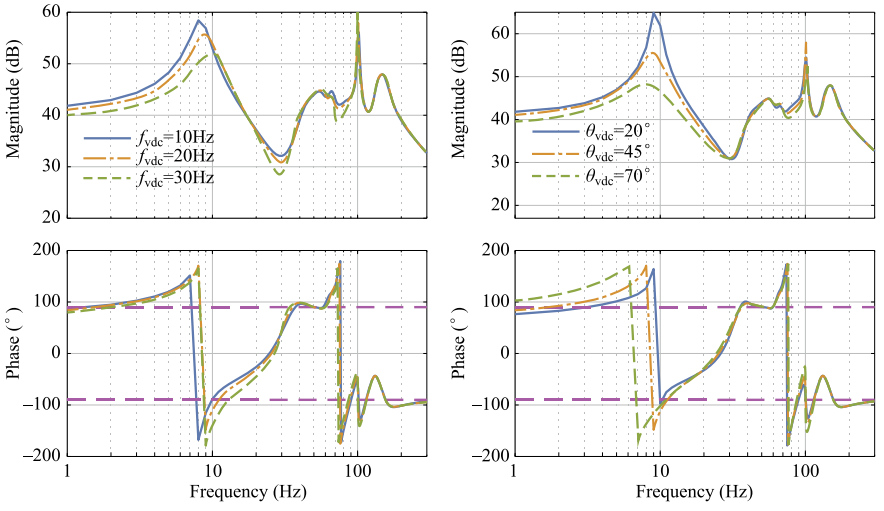

(a) Different DC voltage loop bandwidths (b) Different DC voltage loop PMs

Fig. 10.19 The influence of DC voltage loop in the receiving-end LCC on the damping characteristics

from inductive negative damping to capacitive negative damping. The DC voltage control in the receiving-end LCC has little influence on the damping characteristics in Band $\mathrm{II}_{\mathrm{LCC}}$.

10.4.2.3 Summary of Negative Damping Characteristics in Each Frequency Band

According to the analysis of the negative damping characteristics of LCC-HVDC at the sending end, the following conclusions are obtained.

(1) Band $\mathrm{I}_{\mathrm{LCC}}$ ($f < f_1 + f_{\mathrm{idc}}$): The AC port impedance of LCC-HVDC at the sending end $\boldsymbol{Z}_{\mathrm{LCC}}$ is dominated by the DC-side impedance of the sending-end LCC $\boldsymbol{Z}_{\mathrm{fdc}}$. The frequency-band overlapping effect of the DC current loop and DC-side impedance of the sending-end LCC leads toinductive negative damping in this frequency band. With the decrease of receiving-end AC grid strength, or the increase of bandwidths and PMs of PLL and DC voltage loop in the receiving-end LCC, the negative damping degree at the resonant peak in this frequency band is deepened. The impedance changes from inductive negative damping to capacitive negative damping around the resonant peak.

(2) Band $\mathrm{II}_{\mathrm{LCC}}$ ($f > f_1 + f_{\mathrm{idc}}$): The AC port impedance of LCC-HVDC at the sending end $\boldsymbol{Z}_{\mathrm{LCC}}$ is dominated by the sending-end AC filter $\boldsymbol{Z}_{\mathrm{fflt}}$. $\boldsymbol{Z}_{\mathrm{LCC}}$ changes from inductive negative damping to capacitive negative damping in this frequency band under the effective of $\boldsymbol{Z}_{\mathrm{fflt}}$.

Reference

1. XIAO Yuntao, LI Guanghui, WANG Weisheng, et al. Oscillation Mechanism Analysis and Suppression Strategy of Renewable Energy Base Connected into LCC-HVDC (Part I): Impedance Modeling with the Consideration of Receiving-end Influence[J]. Proceedings of the CSEE, 2023, 43(2): 427–441 (in Chinese).

Chapter 11
Impedance Model and Characteristic Analysis of MMC-HVDC

MMC-HVDC can operate in passive islanding mode and grid-connected mode for power transmission, according to different outer-loop control strategies. The impedance characteristics of MMC-HVDC are different in the two operation modes. Besides, since the DC transmission lines of MMC-HVDC exhibit non-ideal voltage source characteristics, the converter control loops and AC grid strength at the receiving side also influence the impedance characteristics of MMC-HVDC at the sending end.

In this chapter, first, the operating principle and control strategies of the sending-end and receiving-end converter stations in MMC-HVDC are introduced. Then, based on the frequency-domain steady-state operating point and considering the passive islanding and grid-connected operation modes, the AC port impedance model of MMC-HVDC at the sending end is established with the sending- and receiving-end converter control, AC grid strength at the receiving end, and DC transmission lines taken into account. Moreover, the dominant factors of the impedance characteristics in different frequency bands under two operation modes are analyzed separately, and the frequency band division method of MMC-HVDC is proposed [1]. The frequency-band overlapping effect of multiple control loops and the negative damping characteristics of each frequency band are clarified. Finally, based on the CHIL simulation platform, the broadband impedance of MMC-HVDC is scanned, and the typical values of each frequency band are given.

© China Electric Power Press 2023

W. Wang et al., *Analysis and Mitigation of Broadband Oscillation in Renewable Energy Generation and AC/DC Transmission Systems*,
https://doi.org/10.1007/978-981-99-1568-2_11

11.1 Operation Principle and Control Strategy

11.1.1 Topology

MMC-HVDC transmission system can be classified into two-terminal MMC-HVDC transmission and multi-terminal MMC-HVDC transmission. The two-terminal MMC-HVDC transmission system consists of a rectifier station (sending-end converter station), an inverter station (receiving-end converter station), and DC transmission lines, which allows power transmission between two regional AC grids. The multi-terminal MMC-HVDC transmission system consists of three or more converter stations, which realize the interconnection and power transmission between multiple regional AC grids.

MMC-HVDC can operate not only in grid-connected mode, but also in passive islanding mode, independently establishing AC voltage and frequency for the passive islanding system interconnected with other regional AC grids.

MMC-HVDC has three main configurations: symmetrical mono-polar, asymmetrical mono-polar, and bipolar, as shown in Fig. 11.1. The positive polar voltage is $V_{\mathrm{dc}}/2$ and the negative polar voltage is $-V_{\mathrm{dc}}/2$ in the symmetrical mono-polar MMC-HVDC. In the asymmetrical mono-polar MMC-HVDC, a return path with ground/sea electrodes is used, and the positive polar voltage is V_{dc}, while the negative pole is grounded. Bipolar MMC-HVDC consists of two asymmetrical mono-polar MMC-HVDCs, and the positive and negative polar voltages are V_{dc} and $-V_{\mathrm{dc}}$, respectively.

In this chapter, the symmetric mono-polar MMC-HVDC is analyzed as an example, and the topology is shown in Fig. 11.2. The double-star connection is adopted in the sending- and receiving-end MMCs, and the SMs can be half-bridge submodules (HBSMs) or FBSMs, as mentioned in Chap. 4. In the figure, the subscript "f" indicates the variable at the sending side, and the subscript "e" indicates the variable at the receiving side. N_{f}, N_{e} are the numbers of SMs in each arm of the sending-end and receiving-end MMCs respectively. L_{farm}, R_{farm} are the arm inductor and resistor of the sending-end MMC respectively. L_{earm}, R_{earm} are the arm inductor and resistor of the receiving-end MMC respectively. $v_{\mathrm{f}l}$, $i_{\mathrm{f}l}$ are the sending-end three-phase AC voltages and currents respectively. $v_{\mathrm{e}l}$, $i_{\mathrm{e}l}$ are the receiving-end three-phase AC voltages and currents respectively. v_{fdc}, i_{fdc} are the DC voltage and current of the sending-end MMC respectively. v_{edc}, i_{edc} are the DC voltage and current of the receiving-end MMC respectively. $i_{\mathrm{f}l\mathrm{u}}$, $i_{\mathrm{f}l\mathrm{v}}$ are the three-phase upper and lower arm currents of the sending-end MMC respectively. $i_{\mathrm{e}l\mathrm{u}}$, $i_{\mathrm{e}l\mathrm{v}}$ are the three-phase upper and lower arm currents of the receiving-end MMC respectively. l refers to phases a, b, c.

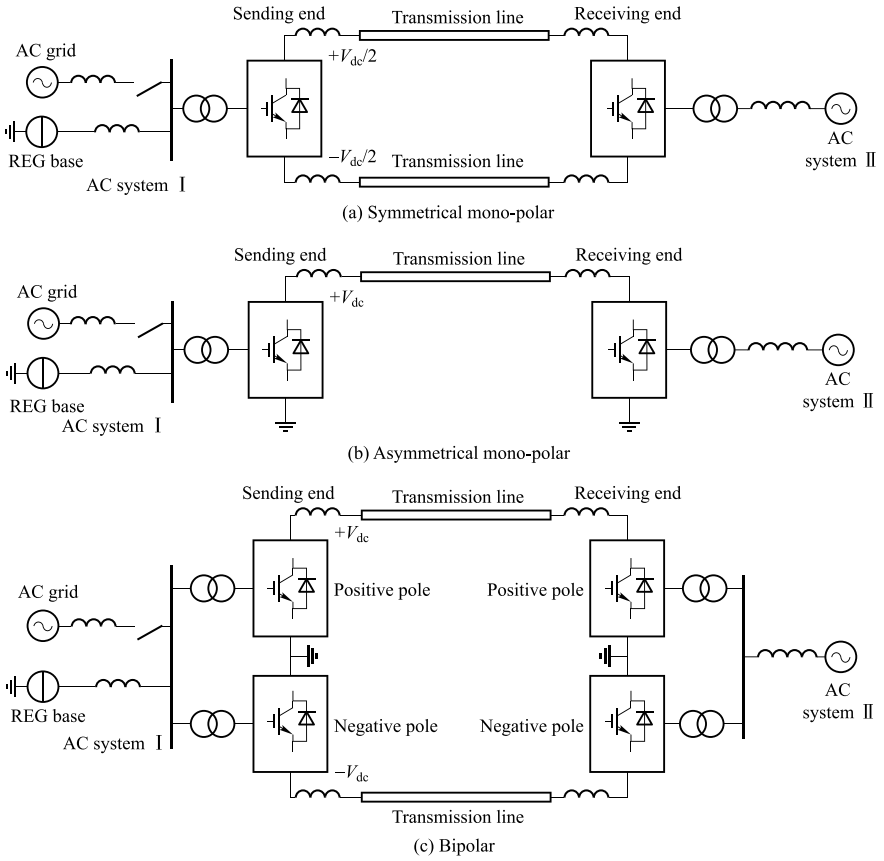

Fig. 11.1 The main configurations of MMC-HVDC

11.1.2 Operation Principle

The operation principle of the sending-end and receiving-end MMCs is reviewed in brief, according to Chap. 4.

11.1.2.1 Operation Principle of Sending-End MMC

The SM capacitor voltage balancing algorithm is utilized to maintain voltage balancing between each SM, i.e., the SM capacitor voltages in each arm can be considered equal. According to Chap. 4, an equivalent SM can be used to replace N_f SMs in the same arm, and then the averaged model of the sending-end MMC is established, as shown in Fig. 11.3.

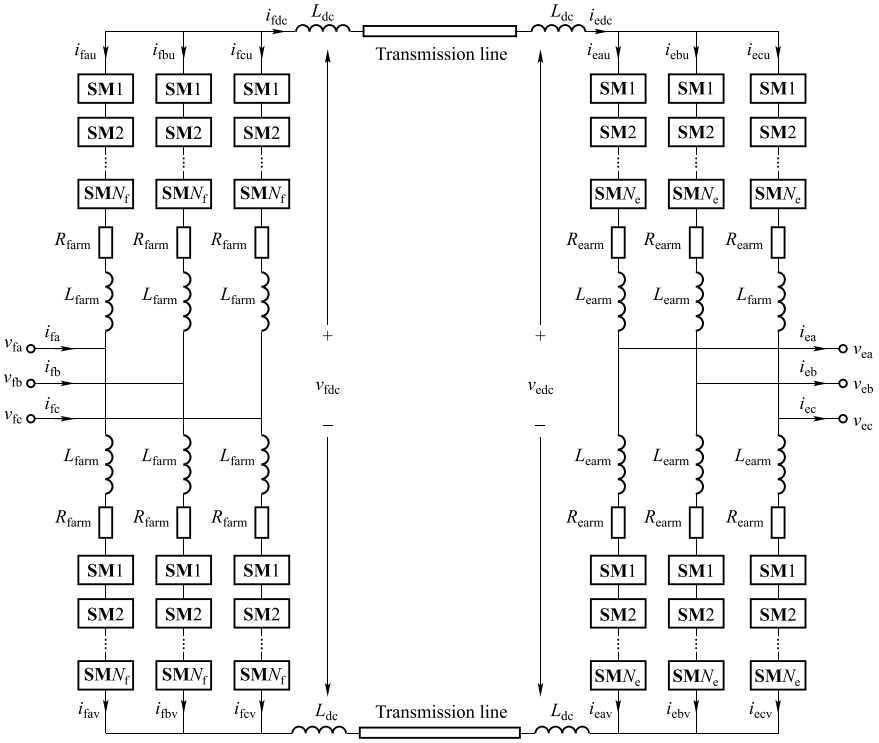

Fig. 11.2 The main configurations of symmetric mono-polar MMC-HVDC

In Fig. 11.3, each arm consists of a controlled voltage source, a controlled current source, and an arm capacitor. C_{feq} is the arm capacitor of the sending-end MMC, and the capacitance is equal to $1/N_{\mathrm{f}}$ of that of the SM capacitor C_{fsm}, i.e., $C_{\mathrm{feq}} = C_{\mathrm{fsm}}/N_{\mathrm{f}}$. The three-phase upper and lower arm capacitor voltages of the sending-end MMC $v_{\mathrm{fC}l\mathrm{u}}$, $v_{\mathrm{fC}l\mathrm{v}}$ operate around the DC voltage v_{fdc}, and are equal to N_{f} times the single SM capacitor voltage in the corresponding arm, respectively. The controlled current source represents the arm capacitor current, which is equal to the arm current multiplied by the arm modulation signal, i.e., $m_{\mathrm{f}l\mathrm{u}}i_{\mathrm{f}l\mathrm{u}}$, $m_{\mathrm{f}l\mathrm{v}}i_{\mathrm{f}l\mathrm{v}}$. The controlled voltage source represents the arm voltage, which is equal to the arm capacitor voltage multiplied by the arm modulation signal, i.e., $m_{\mathrm{f}l\mathrm{u}}v_{\mathrm{fC}l\mathrm{u}}$, $m_{\mathrm{e/v}}v_{\mathrm{eC/v}}$.

The arm capacitor voltage $v_{\mathrm{fC}l\mathrm{u}}$, $v_{\mathrm{fC}l\mathrm{v}}$ and the arm capacitor current $m_{\mathrm{f}l\mathrm{u}}i_{\mathrm{f}l\mathrm{u}}$, $m_{\mathrm{f}l\mathrm{v}}i_{\mathrm{f}l\mathrm{v}}$ satisfy

$$\begin{cases} C_{\mathrm{feq}}\dfrac{\mathrm{d}v_{\mathrm{fC}l\mathrm{u}}}{\mathrm{d}t} = m_{\mathrm{f}l\mathrm{u}}i_{\mathrm{f}l\mathrm{u}} \\ C_{\mathrm{feq}}\dfrac{\mathrm{d}v_{\mathrm{fC}l\mathrm{v}}}{\mathrm{d}t} = m_{\mathrm{f}l\mathrm{v}}i_{\mathrm{f}l\mathrm{v}} \end{cases} \tag{11.1}$$

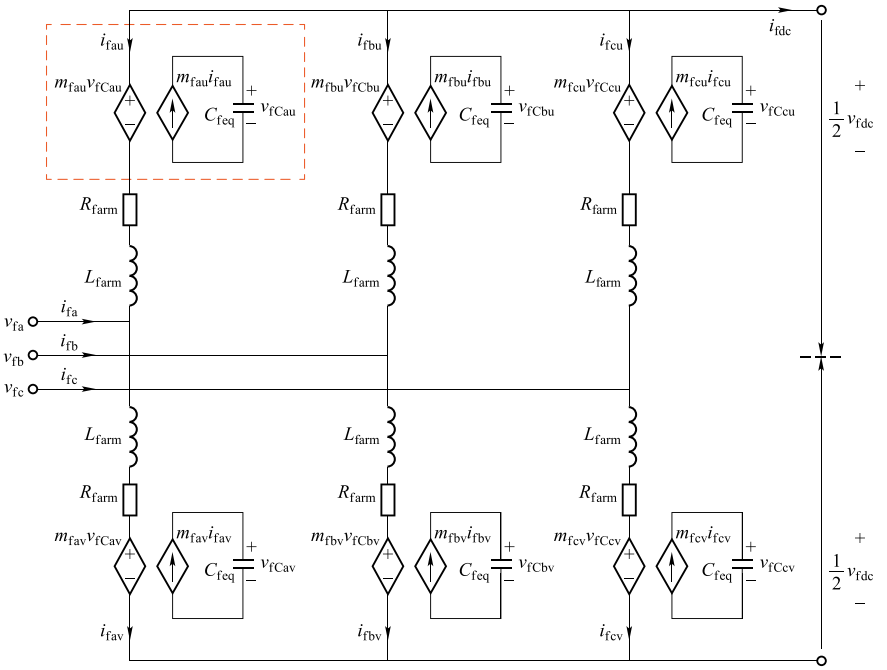

Fig. 11.3 The averaged model of the sending-end MMC

According to the relationship between $m_{fl\mathrm{u}}v_{\mathrm{fC}l\mathrm{u}}$, $m_{fl\mathrm{v}}v_{\mathrm{fC}l\mathrm{v}}$ and the arm current $i_{fl\mathrm{u}}$, $i_{fl\mathrm{v}}$, the time-domain model of the three-phase upper and lower arm circuits can be expressed as

$$\begin{cases} m_{fl\mathrm{u}}v_{\mathrm{fC}l\mathrm{u}} + L_{\mathrm{farm}}\dfrac{\mathrm{d}i_{fl\mathrm{u}}}{\mathrm{d}t} + R_{\mathrm{farm}}i_{fl\mathrm{u}} = \dfrac{v_{\mathrm{fdc}}}{2} - v_{fl} - v_{\mathrm{fO}} \\ m_{fl\mathrm{v}}v_{\mathrm{fC}l\mathrm{v}} + L_{\mathrm{farm}}\dfrac{\mathrm{d}i_{fl\mathrm{v}}}{\mathrm{d}t} + R_{\mathrm{farm}}i_{fl\mathrm{v}} = \dfrac{v_{\mathrm{fdc}}}{2} + v_{fl} + v_{\mathrm{fO}} \end{cases} \tag{11.2}$$

where v_{fO} is the sending-end AC neutral voltage.

The relationship between the three-phase AC currents i_{fl}, DC current i_{fdc}, and three-phase upper and lower arm currents $i_{fl\mathrm{u}}$, $i_{fl\mathrm{v}}$ satisfies

$$\begin{cases} i_{fl} = -(i_{fl\mathrm{u}} - i_{fl\mathrm{v}}) \\ i_{\mathrm{fdc}} = -\sum\limits_{l=\mathrm{a,b,c}} i_{fl\mathrm{u}} = -\sum\limits_{l=\mathrm{a,b,c}} i_{fl\mathrm{v}} \end{cases} \tag{11.3}$$

Based on the DM and CM characteristics of the three-phase upper and lower arm currents, the relationship between i_{fl} and the three-phase arm DM currents of the sending-end MMC $i_{\mathrm{fdif}l}$, and the relationship between i_{fdc} and the three-phase arm CM currents of the sending-end MMC $i_{\mathrm{fcom}l}$ can be obtained, respectively.

$$\begin{cases} i_{\mathrm{f}l} = -2i_{\mathrm{fdif}l} \\ i_{\mathrm{fdc}} = -\sum\limits_{l=\mathrm{a,b,c}} i_{\mathrm{fcom}l} \end{cases} \tag{11.4}$$

The expressions of $i_{\mathrm{fdif}l}$, $i_{\mathrm{fcom}l}$ are given as

$$\begin{cases} i_{\mathrm{fdif}l} = \dfrac{i_{\mathrm{f}l\mathrm{u}} - i_{\mathrm{f}l\mathrm{v}}}{2} \\ i_{\mathrm{fcom}l} = \dfrac{i_{\mathrm{f}l\mathrm{u}} + i_{\mathrm{f}l\mathrm{v}}}{2} \end{cases} \tag{11.5}$$

The expressions of three-phase arm DM and CM voltages of the sending-end MMC $v_{\mathrm{fdif}l}$, $v_{\mathrm{fcom}l}$ are given as

$$\begin{cases} v_{\mathrm{fdif}l} = \dfrac{v_{\mathrm{f}l\mathrm{u}} - v_{\mathrm{f}l\mathrm{v}}}{2} \\ v_{\mathrm{fcom}l} = \dfrac{v_{\mathrm{f}l\mathrm{u}} + v_{\mathrm{f}l\mathrm{v}}}{2} \end{cases} \tag{11.6}$$

where $v_{\mathrm{f}l\mathrm{u}}$, $v_{\mathrm{f}l\mathrm{v}}$ are the three-phase upper and lower arm voltages of the sending-end MMC respectively, satisfying $v_{\mathrm{f}l\mathrm{u}} = m_{\mathrm{f}l\mathrm{u}} v_{\mathrm{fC}l\mathrm{u}}$ and $v_{\mathrm{f}l\mathrm{v}} = m_{\mathrm{f}l\mathrm{v}} v_{\mathrm{fC}l\mathrm{v}}$.

The sending-end AC neutral voltage v_{fO} can be expressed as

$$v_{\mathrm{fO}} = -\frac{1}{6} \sum_{l=\mathrm{a,b,c}} \left(m_{\mathrm{f}l\mathrm{u}} v_{\mathrm{fC}l\mathrm{u}} - m_{\mathrm{f}l\mathrm{v}} v_{\mathrm{fC}l\mathrm{v}} \right) \tag{11.7}$$

11.1.2.2 Operating Principle of Receiving-End MMC

Similarly, the averaged model of the receiving-end MMC is established, as shown in Fig. 11.4. Notably, the positive reference direction of the AC current and DC current of the receiving-end MMC is opposite to that of the sending-end MMC.

As shown in Fig. 11.4, each arm consists of a controlled voltage source, a controlled current source, and an arm capacitor. C_{eeq} is the arm capacitor of the receiving-end MMC, and the capacitance is equal to $1/N_{\mathrm{e}}$ of that of the SM capacitor C_{esm}, i.e., $C_{\mathrm{eeq}} = C_{\mathrm{esm}}/N_{\mathrm{e}}$. The three-phase upper and lower arm capacitor voltages of the receiving-end MMC $v_{\mathrm{eC}l\mathrm{u}}$, $v_{\mathrm{eC}l\mathrm{v}}$ operate around the DC voltage v_{edc}, and are equal to N_{e} times the single SM capacitor voltage in the corresponding arm, respectively. The controlled current source represents the arm capacitor current, which is equal to the arm current multiplied by the arm modulation signal, i.e., $m_{\mathrm{e}l\mathrm{u}} i_{\mathrm{e}l\mathrm{u}}$, $m_{\mathrm{e}l\mathrm{v}} i_{\mathrm{e}l\mathrm{v}}$. The controlled voltage source represents the arm voltage, which is equal to the arm capacitor voltage multiplied by the arm modulation signal, i.e., $m_{\mathrm{e}l\mathrm{u}} v_{\mathrm{eC}l\mathrm{u}}$, $m_{\mathrm{e}l\mathrm{v}} v_{\mathrm{eC}l\mathrm{v}}$.

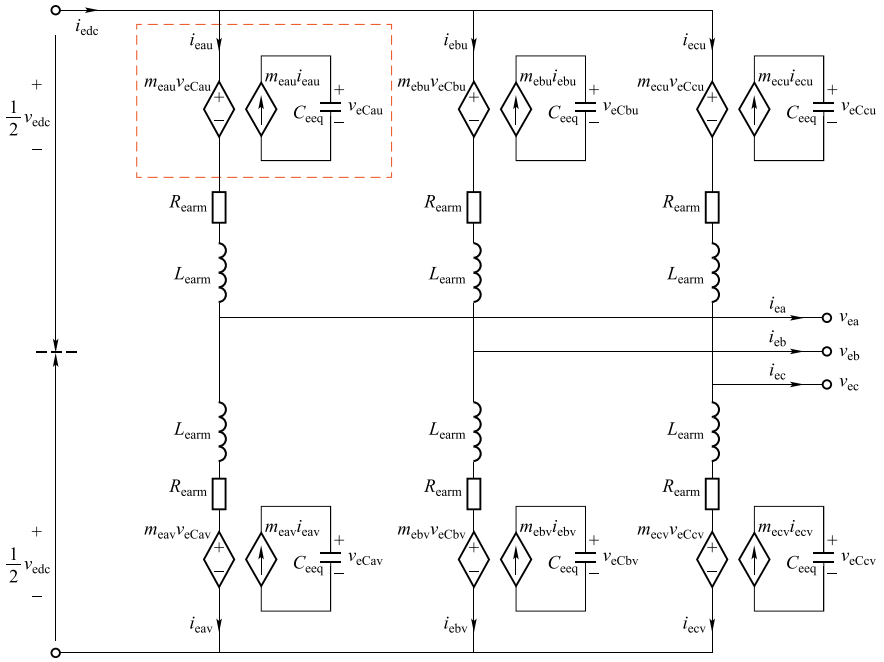

Fig. 11.4 The averaged model of the receiving-end MMC

The arm capacitor voltage $v_{eCl\mathrm{u}}$, $v_{eCl\mathrm{v}}$ and the arm capacitor current $m_{el\mathrm{u}}i_{el\mathrm{u}}$, $m_{el\mathrm{v}}i_{el\mathrm{v}}$ satisfy

$$\begin{cases} C_{\mathrm{eeq}}\dfrac{\mathrm{d}v_{eCl\mathrm{u}}}{\mathrm{d}t} = m_{el\mathrm{u}}i_{el\mathrm{u}} \\ C_{\mathrm{eeq}}\dfrac{\mathrm{d}v_{eCl\mathrm{v}}}{\mathrm{d}t} = m_{el\mathrm{v}}i_{el\mathrm{v}} \end{cases} \tag{11.8}$$

According to the relationship between $m_{el\mathrm{u}}v_{eCl\mathrm{u}}$, $m_{el\mathrm{v}}v_{eCl\mathrm{v}}$ and the arm current $i_{el\mathrm{u}}$, $i_{el\mathrm{v}}$, the time-domain model of the three-phase upper and lower arm circuits can be expressed as

$$\begin{cases} m_{el\mathrm{u}}v_{eCl\mathrm{u}} + L_{\mathrm{earm}}\dfrac{\mathrm{d}i_{el\mathrm{u}}}{\mathrm{d}t} + R_{\mathrm{earm}}i_{el\mathrm{u}} = \dfrac{v_{\mathrm{edc}}}{2} - v_{el} - v_{\mathrm{eO}} \\ m_{el\mathrm{v}}v_{eCl\mathrm{v}} + L_{\mathrm{earm}}\dfrac{\mathrm{d}i_{el\mathrm{v}}}{\mathrm{d}t} + R_{\mathrm{earm}}i_{el\mathrm{v}} = \dfrac{v_{\mathrm{edc}}}{2} + v_{el} + v_{\mathrm{eO}} \end{cases} \tag{11.9}$$

where v_{eO} is the receiving-end AC neutral voltage.

The relationship between the three-phase AC currents i_{el}, DC current i_{edc}, and three-phase upper and lower arm currents i_{elu}, i_{elv} satisfies

$$\begin{cases} i_{el} = i_{elu} - i_{elv} \\ i_{edc} = \sum\limits_{l=a,b,c} i_{elu} = \sum\limits_{l=a,b,c} i_{elv} \end{cases} \tag{11.10}$$

Based on the DM and CM characteristics of the three-phase upper and lower arm currents, the relationship between i_{el} and the three-phase arm DM currents i_{edifl}, and between i_{edc} and the three-phase arm CM currents i_{ecoml} can be obtained, respectively.

$$\begin{cases} i_{el} = -2i_{edifl} \\ i_{edc} = -\sum\limits_{l=a,b,c} i_{ecoml} \end{cases} \tag{11.11}$$

The expressions of i_{edifl}, i_{ecoml} are given as

$$\begin{cases} i_{edifl} = \dfrac{i_{elu} - i_{elv}}{2} \\ i_{ecoml} = \dfrac{i_{elu} + i_{elv}}{2} \end{cases} \tag{11.12}$$

The expressions of three-phase DM and CM voltages of the receiving-end MMC v_{edifl}, v_{ecoml} are given as

$$\begin{cases} v_{edifl} = \dfrac{v_{elu} - v_{elv}}{2} \\ v_{ecoml} = \dfrac{v_{elu} + v_{elv}}{2} \end{cases} \tag{11.13}$$

where v_{elu}, v_{elv} are the three-phase upper and lower arm voltages of the receiving-end MMC respectively, satisfying $v_{elu} = m_{elu}v_{eCl u}$ and $v_{elv} = m_{elv}v_{eCl v}$.

The receiving-end AC neutral voltage v_{eO} can be expressed as

$$v_{eO} = -\frac{1}{6}\sum_{l=a,b,c}(m_{elu}v_{eCl u} - m_{elv}v_{eCl v}) \tag{11.14}$$

The three-phase upper and lower arm currents, voltages, and capacitor voltages contain DC, fundamental, second harmonic, third harmonic, and even higher-order harmonic components. Among these harmonic components, the odd-order components have the same amplitude but opposite phase, corresponding to the DM components, while the even-order components have the same amplitude and phase, corresponding to the CM components. The arm DM current i_{fdifl} or i_{edifl} in each phase

constitutes half of the AC current, while the arm CM current $i_{\text{fcom}l}$ or $i_{\text{ecom}l}$ in each phase constitutes the arm circulating current.

11.1.3 Control Strategy

The power transmission of MMC-HVDC is achieved by the coordination control of both the sending-end and receiving-end MMCs. Compared with the control strategy introduced in Chap. 4, the outer-loop control strategies are also adopted in the sending-end and receiving-end MMCs, in addition to the inner-loop control strategies, including AC current control and circulating current control.

For the sending-end MMC, the AC voltage control is adopted for establishing AC voltage and frequency in passive islanding mode, while the outer-loop power control and PLL are adopted in grid-connected mode.

The receiving-end MMC only operates in grid-connected mode. PLL is used to track the voltage phase of the AC grid at the receiving end, and the DC voltage control is adopted to establish the DC voltage for MMC-HVDC transmission system.

11.1.3.1 Control Strategy of Sending-End MMC

The sending-end MMC can operate in passive islanding mode and grid-connected mode, and the typical control diagram is shown in Fig. 11.5.

As seen from Fig. 11.5(a), in the passive islanding mode, the fundamental frequency is directly given as f_1, and the rotation reference angle of the sending-end MMC is $\theta_{\text{f}} = 2\pi f_1 t$. The AC voltage control is performed in SRF rotating with θ_{f}. $H_{\text{vac}}(s)$ is the transfer function of the AC voltage controller, expressed as $H_{\text{vac}}(s) = K_{\text{vacp}} + K_{\text{vaci}}/s$. K_{vacp}, K_{vaci} are the corresponding proportional and integral coefficients respectively; v_{fd}, v_{fq} are the dq-axis voltages of the sending-end MMC respectively; i_{fdref}, i_{fqref} are the dq-axis current references of the sending-end MMC respectively, which are the outputs of AC voltage controllers; V_{f1} is the amplitude of the fundamental frequency component of the sending-end AC voltage, as the d-axis voltage reference.

As seen from Fig. 11.5(b), in the grid-connected mode, the PLL output angle of the sending-end MMC θ_{fPLL} provides the rotation reference angle for the sending-end MMC. The active and reactive power control is performed in SRF to generate the dq-axis current references i_{fdref}, i_{fqref}. $H_{\text{fPLL}}(s)$ is the transfer function of the PLL controller, expressed as $H_{\text{fPLL}}(s) = K_{\text{fpp}} + K_{\text{fpi}}/s$. K_{fpp}, K_{fpi} are the corresponding proportional and integral coefficients respectively; P_{ref}, Q_{ref} are the active and reactive power references respectively.

The AC current control is similar in both modes. $H_{\text{fiac}}(s)$ is the transfer function of the AC current controller in the sending-end MMC, expressed as $H_{\text{fiac}}(s) = K_{\text{fiacp}} + K_{\text{fiaci}}/s$. K_{fiacp}, K_{fiaci} are the corresponding proportional and integral coefficients respectively. i_{fd}, i_{fq} are the dq-axis currents of the sending-end MMC respectively K_{fd}

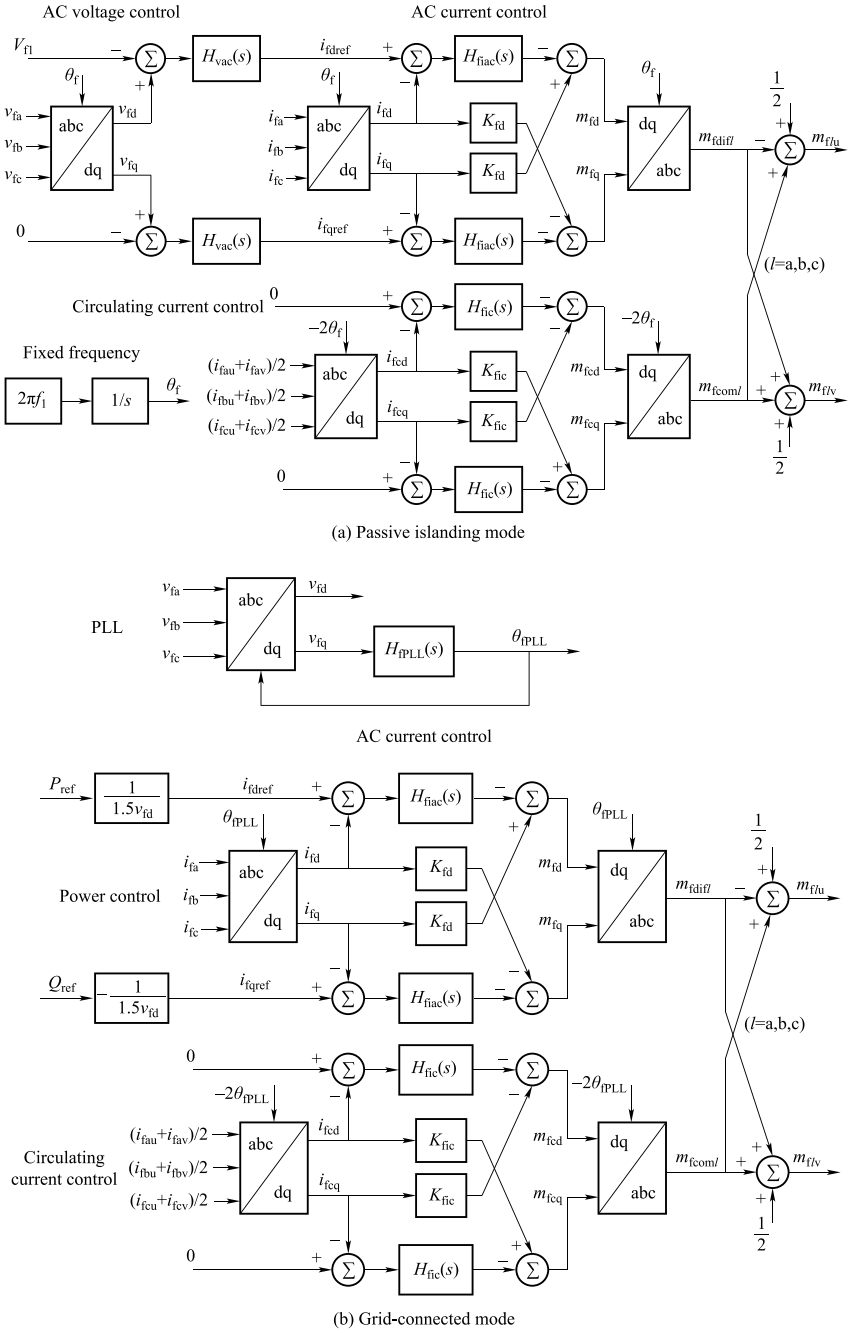

Fig. 11.5 The typical control diagram of the sending-end MMC

is the decoupling coefficient of the AC current control in the sending-end MMC; m_{fd}, m_{fq} are the dq-axis modulation signals of the sending-end MMC respectively, which are the outputs of AC current controllers. $m_{\mathrm{fdif}l}$ are the three-phase arm differential mode (DM) modulation signals of the sending-end MMC generated by the inverse Park transformation.

Besides, the circulating current control is also similar in both modes. The circulating current control is performed in the negative-sequence second-harmonic SRF. $H_{\mathrm{fic}}(s)$ is the transfer function of the circulating current controller in the sending-end MMC, expressed as $H_{\mathrm{fic}}(s) = K_{\mathrm{ficp}} + K_{\mathrm{fici}}/s$. K_{ficp}, K_{fici} are the corresponding proportional and integral coefficients respectively; i_{fcd}, i_{fcq} are the dq-axis circulating currents of the sending-end MMC respectively; K_{fic} is the decoupling coefficient of the circulating current control in the sending-end MMC; m_{fcd}, m_{fcq} are the dq-axis circulating modulation signals of the sending-end MMC respecyively, which are the outputs of circulating current controllers; $m_{\mathrm{fcom}l}$ are the three-phase arm common mode (CM) modulation signals of the sending-end MMC generated by the inverse Park transformation. The dq-axis circulating current references are both zero.

The three-phase upper and lower arm modulation signals of the sending-end MMC can be obtained according to $m_{\mathrm{fdif}l}$ and $m_{\mathrm{fcom}l}$.

$$\begin{cases} m_{fl\mathrm{u}} = \dfrac{1}{2} - m_{\mathrm{fdif}l} + m_{\mathrm{fcom}l} \\ m_{fl\mathrm{v}} = \dfrac{1}{2} + m_{\mathrm{fdif}l} + m_{\mathrm{fcom}l} \end{cases} \tag{11.15}$$

11.1.3.2 Control Strategy of Receiving-End MMC

The receiving-end MMC can operate in grid-connected mode, and the DC voltage control is adopted to establish the DC voltage for MMC-HVDC transmission system. The typical control diagram is shown in Fig. 11.6.

As seen from Fig. 11.6, PLL is used to track the voltage phase of the AC grid at the receiving end, and the PLL output angle of the receiving-end MMC θ_{ePLL} provides the rotation reference angle for the receiving-end MMC. $H_{\mathrm{vdc}}(s)$ is the transfer function of the DC voltage controller, expressed as $H_{\mathrm{vdc}}(s) = K_{\mathrm{vdcp}} + K_{\mathrm{vdci}}/s$. K_{vdcp}, K_{vdci} are the corresponding proportional and integral coefficients respectively. The DC voltage control and reactive power control are performed in SRF to generate the dq-axis current references of the receiving-end MMC i_{edref}, i_{eqref}. V_{dcref}, Q_{ref} are the DC voltage and reactive power references respectively.

The AC current control and circulating current control are also adopted in the receiving-end MMC. $H_{\mathrm{eiac}}(s)$ is the transfer function of the AC current controller in the receiving-end MMC, expressed as $H_{\mathrm{eiac}}(s) = K_{\mathrm{eiacp}} + K_{\mathrm{eiaci}}/s$. K_{eiacp}, K_{eiaci} are the corresponding proportional and integral coefficients respectively; i_{ed}, i_{eq} are the dq-axis currents of the receiving-end MMC respectively; K_{ed} is the decoupling coefficient of the AC current control in the receiving-end MMC. m_{ed}, m_{eq} are the

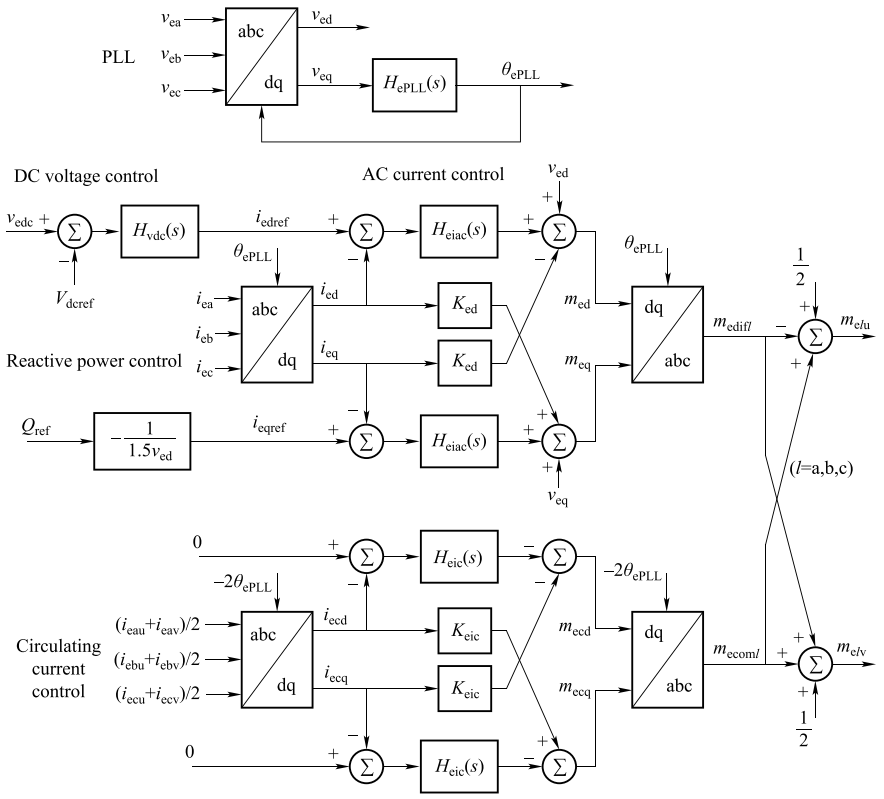

Fig. 11.6 The typical control diagram of the receiving-end MMC

dq-axis modulation signals of the receiving-end MMC respectively, which are the outputs of AC current controllers; m_{edifl} are the three-phase arm DM modulation signals of the receiving-end MMC generated by the inverse Park transformation.

The circulating current control is performed in the negative-sequence second-harmonic SRF rotating with $-2\theta_{ePLL}$. $H_{eic}(s)$ is the transfer function of the circulating current controller in the receiving-end MMC, expressed as $H_{eic}(s) = K_{eicp} + K_{eici}/s$. K_{eicp}, K_{eici} are the corresponding proportional and integral coefficients respectively; i_{ecd}, i_{ecq} are the dq-axis circulating currents of the receiving-end MMC respectively; K_{eic} is the decoupling coefficient of the circulating current control in the receiving-end MMC; m_{ecd}, m_{ecq} are the dq-axis circulating modulation signals of the receiving-end MMC respectively, which are the outputs of circulating current controllers; m_{ecoml} are the three-phase arm CM modulation signals of the receiving-end MMC generated by the inverse Park transformation; the dq-axis circulating current references are both zero.

The three-phase upper and lower arm modulation signals of the receiving-end MMC can be obtained according to m_{edifl} and m_{ecoml}.

$$\begin{cases} m_{\mathrm{elu}} = \dfrac{1}{2} - m_{\mathrm{edif}l} + m_{\mathrm{ecom}l} \\ m_{\mathrm{elv}} = \dfrac{1}{2} + m_{\mathrm{edif}l} + m_{\mathrm{ecom}l} \end{cases} \tag{11.16}$$

11.2 Frequency-Domain Modeling of Steady-State Operation

This section analyzes the steady-state harmonic characteristics of both the sending-end and receiving-end MMCs, and establishes the frequency-domain steady-state model of the main circuit.

11.2.1 Frequency-Domain Characteristic Analysis of Steady-State Operating Point

As mentioned in Chap. 4, the arm current, capacitor voltage, and modulation signal contain an infinite number of steady-state harmonic components. Without loss of generality, the steady-state harmonic components at $kf_1(k = 0, \pm 1, \ldots, \pm g)$ in the arm current, capacitor voltage, and modulation signal of the sending-end and receiving-end MMCs are considered. The steady-state harmonic components of the quantities at kf_1 are arranged in the following steady-state frequency order

$$\left[-gf_1, \ldots, -f_1, 0, f_1, \ldots, gf_1 \right]^{\mathrm{T}} \tag{11.17}$$

For the sending-end MMC, taking the phase-a upper arm as an example, the steady-state vectors of the arm current, capacitor voltage, and modulation signal can be expressed as

$$\begin{cases} \boldsymbol{I}_{\mathrm{fau}} = [\ldots, \boldsymbol{I}^*_{\mathrm{fau3}}, \boldsymbol{I}^*_{\mathrm{fau2}}, \boldsymbol{I}^*_{\mathrm{fau1}}, \boldsymbol{I}_{\mathrm{fau0}}, \boldsymbol{I}_{\mathrm{fau1}}, \boldsymbol{I}_{\mathrm{fau2}}, \boldsymbol{I}_{\mathrm{fau3}}, \ldots]^{\mathrm{T}} \\ \boldsymbol{V}_{\mathrm{fCau}} = [\ldots, \boldsymbol{V}^*_{\mathrm{fCau3}}, \boldsymbol{V}^*_{\mathrm{fCau2}}, \boldsymbol{V}^*_{\mathrm{fCau1}}, \boldsymbol{V}_{\mathrm{fCau0}}, \boldsymbol{V}_{\mathrm{fCau1}}, \boldsymbol{V}_{\mathrm{fCau2}}, \boldsymbol{V}_{\mathrm{fCau3}}, \ldots]^{\mathrm{T}} \\ \boldsymbol{M}_{\mathrm{fau}} = [\ldots \boldsymbol{M}^*_{\mathrm{fau3}}, \boldsymbol{M}^*_{\mathrm{fau2}}, \boldsymbol{M}^*_{\mathrm{fau1}}, \boldsymbol{M}_{\mathrm{fau0}}, \boldsymbol{M}_{\mathrm{fau1}}, \boldsymbol{M}_{\mathrm{fau2}}, \boldsymbol{M}_{\mathrm{fau3}}, \ldots]^{\mathrm{T}} \end{cases} \tag{11.18}$$

where $\boldsymbol{I}_{\mathrm{fau}k}$, $\boldsymbol{V}_{\mathrm{fCau}k}$, $\boldsymbol{M}_{\mathrm{fau}k}$ are the steady-state harmonic components at kf_1 respectively; the component at $-kf_1$ is equal to the conjugate of the component at kf_1, i.e., $\boldsymbol{I}_{\mathrm{fau}(-k)} = \boldsymbol{I}^*_{\mathrm{fau}k}$, $\boldsymbol{V}_{\mathrm{fau}(-k)} = \boldsymbol{V}^*_{\mathrm{fau}k}$, and $\boldsymbol{M}_{\mathrm{fau}(-k)} = \boldsymbol{M}^*_{\mathrm{fau}k}$.

The odd-order harmonic components of the quantities in the three-phase upper and lower arms are the DM components, while the even-order harmonic components are the CM components. According to Eq. (11.5), the steady-state vectors of the

phase-a AC current and arm circulating current in the sending-end MMC can be expressed as

$$\begin{cases} \boldsymbol{I}_{\mathrm{fa}} = -2\boldsymbol{A}_{\mathrm{d}}\boldsymbol{I}_{\mathrm{fau}} \\ \boldsymbol{I}_{\mathrm{fcoma}} = \boldsymbol{A}_{\mathrm{c}}\boldsymbol{I}_{\mathrm{fau}} \end{cases} \tag{11.19}$$

where $\boldsymbol{A}_{\mathrm{d}}$ is the DM matrix of the arm steady-state vectors; $\boldsymbol{A}_{\mathrm{c}}$ is the CM matrix of the arm steady-state vectors. Their expressions are

$$\begin{cases} \boldsymbol{A}_{\mathrm{d}} = \dfrac{1}{2}\mathrm{diag}\left[\left.\{1-(-1)^k\}\right|_{k=-g,\ldots,0,\ldots,g}\right] \\ \boldsymbol{A}_{\mathrm{c}} = \dfrac{1}{2}\mathrm{diag}\left[\left.\{1+(-1)^k\}\right|_{k=-g,\ldots,0,\ldots,g}\right] \end{cases} \tag{11.20}$$

According to the DM and CM relationship shown in Eq. (11.19), the steady-state vectors of the phase-a lower arm current, capacitor voltage, and modulation signal can be obtained.

$$\begin{cases} \boldsymbol{I}_{\mathrm{fav}} = \boldsymbol{A}\boldsymbol{I}_{\mathrm{fau}} \\ \boldsymbol{V}_{\mathrm{fCav}} = \boldsymbol{A}\boldsymbol{V}_{\mathrm{fCau}} \\ \boldsymbol{M}_{\mathrm{fav}} = \boldsymbol{A}\boldsymbol{M}_{\mathrm{fau}} \end{cases} \tag{11.21}$$

where $\boldsymbol{A}$ is the transformation matrix of the arm steady-state vectors, expressed as

$$\boldsymbol{A} = \mathrm{diag}\left[\left.\{(-1)^k\}\right|_{k=-g,\ldots,0,\ldots,g}\right] \tag{11.22}$$

The phase-sequence relationship of the steady-state quantities among three phases can be expressed by defining the following modulo-3 function

$$\mathrm{mod}(k,3) = \begin{cases} +1, & k = 3n+1 \\ -1, & k = 3n+2 \\ 0, & k = 3n \end{cases} \quad (n = 0, \pm 1, \pm 2, \ldots) \tag{11.23}$$

where $+1$ indicates positive sequence, i.e., the component at $(3n+1)f_1$ is in positive sequence. -1 indicates negative sequence, i.e., the component at $(3n+2)f_1$ is in negative sequence. 0 indicates zero sequence, i.e., the component at $3nf_1$ is in zero sequence.

According to the phase-sequence relationship, the steady-state vectors of the arm currents, capacitor voltages, and modulation signals in each arm of phase b and phase c can be obtained.

$$\begin{cases} \boldsymbol{I}_{\mathrm{fbu}} = \boldsymbol{D}\boldsymbol{I}_{\mathrm{fau}}, & \boldsymbol{V}_{\mathrm{fCbu}} = \boldsymbol{D}\boldsymbol{V}_{\mathrm{fCau}}, & \boldsymbol{M}_{\mathrm{fbu}} = \boldsymbol{D}\boldsymbol{M}_{\mathrm{fau}} \\ \boldsymbol{I}_{\mathrm{fbv}} = \boldsymbol{D}\boldsymbol{A}\boldsymbol{I}_{\mathrm{fau}}, & \boldsymbol{V}_{\mathrm{fCbv}} = \boldsymbol{D}\boldsymbol{A}\boldsymbol{V}_{\mathrm{fCau}}, & \boldsymbol{M}_{\mathrm{fbv}} = \boldsymbol{D}\boldsymbol{A}\boldsymbol{M}_{\mathrm{fau}} \end{cases} \tag{11.24}$$

$$\begin{cases} \boldsymbol{I}_{\mathrm{fcu}} = \boldsymbol{D}^{*}\boldsymbol{I}_{\mathrm{fau}}, \quad \boldsymbol{V}_{\mathrm{fCcu}} = \boldsymbol{D}^{*}\boldsymbol{V}_{\mathrm{fCau}}, \quad \boldsymbol{M}_{\mathrm{fcu}} = \boldsymbol{D}^{*}\boldsymbol{M}_{\mathrm{fau}} \\ \boldsymbol{I}_{\mathrm{fcv}} = \boldsymbol{D}^{*}\boldsymbol{A}\boldsymbol{I}_{\mathrm{fau}}, \ \boldsymbol{V}_{\mathrm{fCcv}} = \boldsymbol{D}^{*}\boldsymbol{A}\boldsymbol{V}_{\mathrm{fCau}}, \ \boldsymbol{M}_{\mathrm{fcv}} = \boldsymbol{D}^{*}\boldsymbol{A}\boldsymbol{M}_{\mathrm{fau}} \end{cases} \tag{11.25}$$

where $\boldsymbol{D}$ is the phase-sequence coefficient matrix of the steady-state vectors, expressed as

$$\boldsymbol{D} = \mathrm{diag}\left[\{\mathrm{e}^{-\mathrm{j}2k\pi/3}\}\big|_{k=-g,\ldots,0,\ldots,g} \right] \tag{11.26}$$

For the receiving-end MMC, the steady-state vectors of the phase-a arm current, capacitor voltage, and modulation signal can be expressed as

$$\begin{cases} \boldsymbol{I}_{\mathrm{eau}} = [\ldots, \boldsymbol{I}^{*}_{\mathrm{eau3}}, \boldsymbol{I}^{*}_{\mathrm{eau2}}, \boldsymbol{I}^{*}_{\mathrm{eau1}}, \boldsymbol{I}_{\mathrm{eau0}}, \boldsymbol{I}_{\mathrm{eau1}}, \boldsymbol{I}_{\mathrm{eau2}}, \boldsymbol{I}_{\mathrm{eau3}}, \ldots]^{\mathrm{T}} \\ \boldsymbol{V}_{\mathrm{eCau}} = [\ldots, \boldsymbol{V}^{*}_{\mathrm{eCau3}}, \boldsymbol{V}^{*}_{\mathrm{eCau2}}, \boldsymbol{V}^{*}_{\mathrm{eCau1}}, \boldsymbol{V}_{\mathrm{eCau0}}, \boldsymbol{V}_{\mathrm{eCau1}}, \boldsymbol{V}_{\mathrm{eCau2}}, \boldsymbol{V}_{\mathrm{eCau3}}, \ldots]^{\mathrm{T}} \\ \boldsymbol{M}_{\mathrm{eau}} = [\ldots, \boldsymbol{M}^{*}_{\mathrm{eau3}}, \boldsymbol{M}^{*}_{\mathrm{eau2}}, \boldsymbol{M}^{*}_{\mathrm{eau1}}, \boldsymbol{M}_{\mathrm{eau0}}, \boldsymbol{M}_{\mathrm{eau1}}, \boldsymbol{M}_{\mathrm{eau2}}, \boldsymbol{M}_{\mathrm{eau3}}, \ldots]^{\mathrm{T}} \end{cases} \tag{11.27}$$

According to the DM and CM relationship of the quantities in the upper and lower arms, the steady-state vectors of the phase-a AC current and arm circulating current in the receiving-end MMC can be obtained.

$$\begin{cases} \boldsymbol{I}_{\mathrm{ea}} = 2\boldsymbol{A}_{\mathrm{d}}\boldsymbol{I}_{\mathrm{eau}} \\ \boldsymbol{I}_{\mathrm{ecoma}} = \boldsymbol{A}_{\mathrm{c}}\boldsymbol{I}_{\mathrm{eau}} \end{cases} \tag{11.28}$$

The steady-state vectors of the phase-a lower arm current, capacitor voltage, and modulation signal are expressed as

$$\begin{cases} \boldsymbol{I}_{\mathrm{eav}} = \boldsymbol{A}\boldsymbol{I}_{\mathrm{eau}} \\ \boldsymbol{V}_{\mathrm{eCav}} = \boldsymbol{A}\boldsymbol{V}_{\mathrm{eCau}} \\ \boldsymbol{M}_{\mathrm{eav}} = \boldsymbol{A}\boldsymbol{M}_{\mathrm{eau}} \end{cases} \tag{11.29}$$

According to the phase-sequence relationship, the steady-state vectors of the arm currents, capacitor voltages, and modulation signals in each arm of phase b and phase c can be obtained.

$$\begin{cases} \boldsymbol{I}_{\mathrm{ebu}} = \boldsymbol{D}\boldsymbol{I}_{\mathrm{eau}}, \quad \boldsymbol{V}_{\mathrm{eCbu}} = \boldsymbol{D}\boldsymbol{V}_{\mathrm{eCau}}, \quad \boldsymbol{M}_{\mathrm{ebu}} = \boldsymbol{D}\boldsymbol{M}_{\mathrm{eau}} \\ \boldsymbol{I}_{\mathrm{ebv}} = \boldsymbol{D}\boldsymbol{A}\boldsymbol{I}_{\mathrm{eau}}, \ \boldsymbol{V}_{\mathrm{eCbv}} = \boldsymbol{D}\boldsymbol{A}\boldsymbol{V}_{\mathrm{eCau}}, \ \boldsymbol{M}_{\mathrm{ebv}} = \boldsymbol{D}\boldsymbol{A}\boldsymbol{M}_{\mathrm{eau}} \end{cases} \tag{11.30}$$

$$\begin{cases} \boldsymbol{I}_{\mathrm{ecu}} = \boldsymbol{D}^{*}\boldsymbol{I}_{\mathrm{eau}}, \quad \boldsymbol{V}_{\mathrm{eCcu}} = \boldsymbol{D}^{*}\boldsymbol{V}_{\mathrm{eCau}}, \quad \boldsymbol{M}_{\mathrm{ecu}} = \boldsymbol{D}^{*}\boldsymbol{M}_{\mathrm{eau}} \\ \boldsymbol{I}_{\mathrm{ecv}} = \boldsymbol{D}^{*}\boldsymbol{A}\boldsymbol{I}_{\mathrm{eau}}, \ \boldsymbol{V}_{\mathrm{eCcv}} = \boldsymbol{D}^{*}\boldsymbol{A}\boldsymbol{V}_{\mathrm{eCau}}, \ \boldsymbol{M}_{\mathrm{ecv}} = \boldsymbol{D}^{*}\boldsymbol{A}\boldsymbol{M}_{\mathrm{eau}} \end{cases} \tag{11.31}$$

11.2.2 Frequency-Domain Steady-State Model of Main Circuit

11.2.2.1 Frequency-Domain Steady-State Model of Sending-End MMC

Based on the steady-state vectors of the arm current, capacitor voltage, and modulation signal of the sending-end MMC, the frequency-domain steady-state model of the arm circuit can be obtained by transforming Eqs. (11.1) and (11.2) to the frequency domain.

$$\boldsymbol{Y}_{\mathrm{Cfeq0}}\boldsymbol{V}_{\mathrm{fCau}} = \boldsymbol{M}_{\mathrm{fau}} \otimes \boldsymbol{I}_{\mathrm{fau}} \tag{11.32}$$

$$\boldsymbol{Z}_{\mathrm{Lfarm0}}\boldsymbol{I}_{\mathrm{fau}} = \frac{1}{2}\boldsymbol{V}_{\mathrm{fdc}} - \boldsymbol{V}_{\mathrm{fa}} - \boldsymbol{M}_{\mathrm{fau}} \otimes \boldsymbol{V}_{\mathrm{fCau}} - \boldsymbol{V}_{\mathrm{fO}} \tag{11.33}$$

where $\boldsymbol{V}_{\mathrm{fdc}}$ and $\boldsymbol{V}_{\mathrm{fa}}$ are the steady-state vectors of the DC voltage and phase-a AC voltage in the sending-end MMC respectively, and the expressions are given as

$$\begin{cases} \boldsymbol{V}_{\mathrm{fdc}} = \left[\ldots, 0, \ldots, 0, V_{\mathrm{fdc}}, 0, \ldots, 0, \ldots\right]^{\mathrm{T}} \\ \boldsymbol{V}_{\mathrm{fa}} = \left[\ldots, 0, \ldots, V_{\mathrm{f1}}/2, 0, V_{\mathrm{f1}}/2, \ldots, 0, \ldots\right]^{\mathrm{T}} \end{cases} \tag{11.34}$$

where V_{fdc} is steady-state value of the DC voltage in the sending-end MMC.

$\boldsymbol{Z}_{\mathrm{Lfarm0}}$ and $\boldsymbol{Y}_{\mathrm{Cfeq0}}$ are the impedance of the arm inductor and the admittance of the arm capacitor of the sending-end MMC in the steady-state frequency order respectively, which are

$$\boldsymbol{Z}_{\mathrm{Lfarm0}} = R_{\mathrm{farm}}\boldsymbol{U} + \mathrm{j}2\pi L_{\mathrm{farm}} \cdot \mathrm{diag}\left[-gf_1, \ldots, -f_1, 0, f_1, \ldots, gf_1\right] \tag{11.35}$$

$$\boldsymbol{Y}_{\mathrm{Cfeq0}} = \mathrm{j}2\pi C_{\mathrm{feq}} \cdot \mathrm{diag}\left[-gf_1, \ldots, -f_1, 0, f_1, \ldots, gf_1\right] \tag{11.36}$$

$\boldsymbol{V}_{\mathrm{fO}}$ is the steady-state vector of the sending-end AC neutral voltage, and can be obtained by transforming Eq. (11.7) to the frequency domain.

$$\boldsymbol{V}_{\mathrm{fO}} = -\frac{1}{6}\sum_{l=\mathrm{a,b,c}} \left(\boldsymbol{M}_{\mathrm{f}l\mathrm{u}} \otimes \boldsymbol{V}_{\mathrm{fC}l\mathrm{u}} - \boldsymbol{M}_{\mathrm{f}l\mathrm{v}} \otimes \boldsymbol{V}_{\mathrm{fC}l\mathrm{v}}\right) \tag{11.37}$$

As known from Eq. (11.37), the AC neutral voltage is the zero-sequence DM component of the three-phase upper and lower arm voltages. $\boldsymbol{V}_{\mathrm{fO}}$ cancels the zero-sequence DM voltage of the three-phase upper and lower arms in Eq. (11.33), so the corresponding zero-sequence DM current is zero, i.e., there is no zero-sequence current path on the AC side of the sending-end MMC.

Besides, the zero-sequence CM component of the three-phase upper or lower arm currents constitutes the DC current. The steady-state vector of the DC current in the sending-end MMC can be obtained by transforming Eq. (11.4) to the frequency domain.

$$\boldsymbol{I}_{\mathrm{fdc}} = -3\boldsymbol{A}_{\mathrm{c0}}\boldsymbol{I}_{\mathrm{fau}} \tag{11.38}$$

where $\boldsymbol{A}_{\mathrm{c0}}$ is the zero-sequence CM matrix of the arm steady-state vectors, expressed as

$$\boldsymbol{A}_{\mathrm{c0}} = \mathrm{diag}\left[\left\{\frac{1+(-1)^k}{2}\cdot(1-|\mathrm{mod}(k,3)|)\right\}_{k=-g,\ldots,0,\ldots,g}\right] \tag{11.39}$$

11.2.2.2 Frequency-Domain Steady-State Model of Receiving-End MMC

Based on the steady-state vectors of the arm current, capacitor voltage, and modulation signal of the receiving-end MMC, the frequency-domain steady-state model of the arm circuit can be obtained by transforming Eqs. (11.8) and (11.9) to the frequency domain.

$$\boldsymbol{Y}_{\mathrm{Ceeq0}}\boldsymbol{V}_{\mathrm{eCau}} = \boldsymbol{M}_{\mathrm{eau}} \otimes \boldsymbol{I}_{\mathrm{eau}} \tag{11.40}$$

$$\boldsymbol{Z}_{\mathrm{Learm0}}\boldsymbol{I}_{\mathrm{eau}} = \boldsymbol{V}_{\mathrm{edc}} - \boldsymbol{V}_{\mathrm{ea}} - \boldsymbol{M}_{\mathrm{eau}} \otimes \boldsymbol{V}_{\mathrm{eCau}} - \boldsymbol{V}_{\mathrm{eO}} \tag{11.41}$$

where $\boldsymbol{Z}_{\mathrm{Learm0}}$ and $\boldsymbol{Y}_{\mathrm{Ceeq0}}$ are the impedance of the arm inductor and the admittance of the arm capacitor of the receiving-end MMC in the steady-state frequency order respectively. Their expressions can be obtained by replacing the subscript "f" with "e" in Eqs. (11.35) and (11.36). $\boldsymbol{V}_{\mathrm{edc}}$ and $\boldsymbol{V}_{\mathrm{ea}}$ are the steady-state vectors of the DC voltage and phase-a AC voltage in the receiving-end MMC respectively, and the expressions are given as

$$\begin{cases} \boldsymbol{V}_{\mathrm{edc}} = \left[\ldots, 0, \ldots, 0, V_{\mathrm{edc}}, 0, \ldots, 0, \ldots\right]^{\mathrm{T}} \\ \boldsymbol{V}_{\mathrm{ea}} = \left[\ldots, 0, \ldots, V_{\mathrm{e1}}/2, 0, V_{\mathrm{e1}}/2, \ldots, 0, \ldots\right]^{\mathrm{T}} \end{cases} \tag{11.42}$$

where V_{edc} is steady-state value of the DC voltage. V_{e1} is the amplitude of the fundamental frequency component of the sending-end AC voltage.

$\boldsymbol{V}_{\mathrm{eO}}$ is the steady-state vector of the sending-end AC neutral voltage, and can be obtained by transforming Eq. (11.14) to the frequency domain.

$$\boldsymbol{V}_{\mathrm{eO}} = -\frac{1}{6}\sum_{l=\mathrm{a,b,c}} (\boldsymbol{M}_{\mathrm{e}l\mathrm{u}} \otimes \boldsymbol{V}_{\mathrm{eC}l\mathrm{u}} - \boldsymbol{M}_{\mathrm{e}l\mathrm{v}} \otimes \boldsymbol{V}_{\mathrm{eC}l\mathrm{v}}) \tag{11.43}$$

$\boldsymbol{V}_{\mathrm{eO}}$ cancels the zero-sequence DM voltage of the three-phase upper and lower arms in Eq. (11.41), so that the corresponding zero-sequence DM current is zero.

Besides, the zero-sequence CM component of the three-phase upper or lower arm currents constitutes the DC current. The steady-state vector of the DC current of the receiving-end MMC can be obtained by transforming Eq. (11.11) to the frequency domain.

$$\boldsymbol{I}_{\mathrm{edc}} = 3\boldsymbol{A}_{\mathrm{c0}}\boldsymbol{I}_{\mathrm{eau}} \tag{11.44}$$

In order to use the scalar product instead of convolution in Eqs. (11.32), (11.33), (11.40), and (11.41), the steady-state vectors of the quantities of the sending-end and receiving-end MMCs can be expanded into matrices. In the following of this chapter, $\boldsymbol{I}_{\mathrm{f}l\mathrm{u}}$, $\boldsymbol{V}_{\mathrm{fC}l\mathrm{u}}$, $\boldsymbol{M}_{\mathrm{f}l\mathrm{u}}$, $\boldsymbol{I}_{\mathrm{e}l\mathrm{u}}$, $\boldsymbol{V}_{\mathrm{eC}l\mathrm{u}}$, $\boldsymbol{M}_{\mathrm{e}l\mathrm{u}}$ represent the steady-state matrices, and the convolution is replaced with the scalar product.

To sum up, the frequency-domain characteristics of the steady-state vectors in the sending-end and receiving-end MMCs are listed in Table 11.1. The frequency-domain distribution characteristics of the corresponding steady-state vectors in the sending-end and receiving-end MMCs are the same. The steady-state vectors of the arm capacitor voltages contain infinite number of steady-state harmonic components at kf_1 ($k = 0, \pm1, \pm2, \ldots$). The steady-state vectors of the arm currents and modulation signals contain all harmonic components at kf_1 ($k \neq 6n+3$, $n = 0, \pm1, \pm2, \ldots$), with the zero-sequence DM components excluded. The steady-state vectors of the AC currents contain the DM harmonic components at $(6n+1)f_1$ and $(6n+5)f_1$, with the zero sequence excluded. The steady-state vectors of the arm circulating currents contain the CM components at $6nf_1$, $(6n+2)f_1$, and $(6n+4)f_1$.

Table 11.1 The frequency-domain characteristics of the steady-state vectors in MMC-HVDC

Steady-State Vectors	Frequency
$\boldsymbol{V}_{\mathrm{fC}l\mathrm{u}}$, $\boldsymbol{V}_{\mathrm{fC}l\mathrm{v}}$, $\boldsymbol{V}_{\mathrm{eC}l\mathrm{u}}$, $\boldsymbol{V}_{\mathrm{eC}l\mathrm{v}}$	kf_1
$\boldsymbol{I}_{\mathrm{f}l\mathrm{u}}$, $\boldsymbol{I}_{\mathrm{f}l\mathrm{v}}$, $\boldsymbol{I}_{\mathrm{e}l\mathrm{u}}$, $\boldsymbol{I}_{\mathrm{e}l\mathrm{v}}$	kf_1 ($k \neq 6n+3$)
$\boldsymbol{M}_{\mathrm{f}l\mathrm{u}}$, $\boldsymbol{M}_{\mathrm{f}l\mathrm{v}}$, $\boldsymbol{M}_{\mathrm{e}l\mathrm{u}}$, $\boldsymbol{M}_{\mathrm{e}l\mathrm{v}}$	kf_1 ($k \neq 6n+3$)
$\boldsymbol{I}_{\mathrm{f}l}$, $\boldsymbol{I}_{\mathrm{e}l}$	$(6n+1)f_1$
	$(6n+5)f_1$
$\boldsymbol{I}_{\mathrm{fcom}l}$, $\boldsymbol{I}_{\mathrm{ecom}l}$	$6nf_1$
	$(6n+2)f_1$
	$(6n+4)f_1$
$\boldsymbol{I}_{\mathrm{fdc}}$, $\boldsymbol{I}_{\mathrm{edc}}$	$6nf_1$

11.3 Small-Signal Impedance Modeling in Frequency Domain

In this section, the MMC-HVDC impedance model, including the sending-end and receiving-end MMCs and the DC transmission lines, is established based on the operation principle and control strategy of MMC-HVDC.

11.3.1 Small-Signal Frequency-Domain Characteristic Analysis

In order to establish the impedance model of MMC-HVDC, first, a small-signal perturbation is superimposed on the AC voltage of the sending-end MMC at the steady-state operating point. The frequency-domain distribution characteristics of the voltage, current, and modulation signal are elaborated. Then, the frequency-domain small-signal model of the main circuit and control loops in MMC-HVDC is developed, respectively. Finally, the small-signal impedance model of MMC-HVDC at the sending end is established by calculating the response of the AC current to the AC voltage perturbation. The small-signal transfer path and frequency response relationship of MMC-HVDC are shown in Fig. 11.7.

The small-signal transfer path and frequency response relationship of the sending-end MMC is analyzed as follows. The positive-sequence small-signal perturbation at f_p is superimposed on the sending-end AC voltage at the steady-state operating point. The difference between the small-signal component of the sending-end AC voltage $\hat{\boldsymbol{v}}_{\mathrm{fl}}$ at f_p and the arm DM voltage drops on the arm inductor, which leads to a small-signal response of the sending-end AC current $\hat{\boldsymbol{i}}_{\mathrm{fl}}$ at f_p. Subsequently, the small-signal responses of the arm current $\hat{\boldsymbol{i}}_{\mathrm{flu}}$, $\hat{\boldsymbol{i}}_{\mathrm{flv}}$ at f_p are produced. The small-signal responses of $\hat{\boldsymbol{i}}_{\mathrm{flu}}$, $\hat{\boldsymbol{i}}_{\mathrm{flv}}$ at f_p multiplying the steady-state components of the arm modulation signal $\boldsymbol{M}_{\mathrm{flu}}$, $\boldsymbol{M}_{\mathrm{flv}}$ at kf_1 ($k = 0, \pm1, \ldots, \pm g$) leads to small-signal

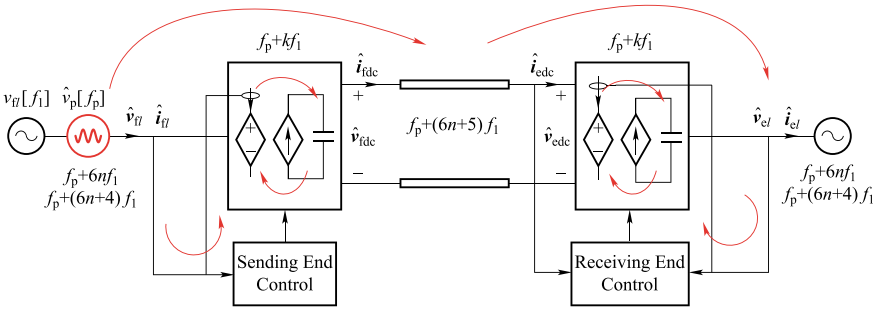

Fig. 11.7 The small-signal transfer path and frequency response relationship of MMC-HVDC

responses of the arm capacitor voltage $\hat{\boldsymbol{v}}_{\mathrm{fC}l\mathrm{u}}$, $\hat{\boldsymbol{v}}_{\mathrm{fC}l\mathrm{v}}$ at $f_\mathrm{p}+kf_1$. The small-signal components of $\hat{\boldsymbol{v}}_{\mathrm{fC}l\mathrm{u}}$, $\hat{\boldsymbol{v}}_{\mathrm{fC}l\mathrm{v}}$ at $f_\mathrm{p}+kf_1$ multiplying the steady-state components of $\boldsymbol{M}_{\mathrm{f}l\mathrm{u}}$, $\boldsymbol{M}_{\mathrm{f}l\mathrm{v}}$ at kf_1 leads to small-signal responses of the arm voltage at $f_\mathrm{p}+kf_1$. The difference between the small-signal components of the arm voltage and the AC voltage or DC voltage dropping on the arm inductor leads to small-signal responses of $\hat{\boldsymbol{i}}_{\mathrm{f}l\mathrm{u}}$, $\hat{\boldsymbol{i}}_{\mathrm{f}l\mathrm{v}}$ at $f_\mathrm{p}+kf_1$.

The DM components of $\hat{\boldsymbol{i}}_{\mathrm{f}l\mathrm{u}}$, $\hat{\boldsymbol{i}}_{\mathrm{f}l\mathrm{v}}$, except for the zero sequence, constitute the small-signal components of the sending-end AC current $\hat{\boldsymbol{i}}_{\mathrm{f}l}$, corresponding to the components at $f_\mathrm{p}+6nf_1$ and $f_\mathrm{p}+(6n+4)f_1$. The CM components $\hat{\boldsymbol{i}}_{\mathrm{fcom}l}$ constitute the small-signal components of the arm circulating current, corresponding to the components at $f_\mathrm{p}+(6n+1)f_1$, $f_\mathrm{p}+(6n+3)f_1$, and $f_\mathrm{p}+(6n+5)f_1$. In addition, the zero-sequence CM components flow into the DC side, leading to the small-signal responses of the DC current of the sending-end MMC $\hat{\boldsymbol{i}}_{\mathrm{fdc}}$ at $f_\mathrm{p}+(6n+5)f_1$.

Then, the small-signal transfer path and frequency response relationship of the receiving-end MMC is analyzed. The small-signal component of $\hat{\boldsymbol{i}}_{\mathrm{fdc}}$ at $f_\mathrm{p}+(6n+5)f_1$ is transmitted to the receiving-end MMC via the DC transmission line, leading to small-signal components at $f_\mathrm{p}+(6n+5)f_1$ in the DC current and voltage of the receiving-end MMC $\hat{\boldsymbol{i}}_{\mathrm{edc}}$, $\hat{\boldsymbol{v}}_{\mathrm{edc}}$. Along with $\hat{\boldsymbol{i}}_{\mathrm{edc}}$ flowing into the receiving-end MMC, the small-signal components at $f_\mathrm{p}+(6n+5)f_1$ are produced in the arm current $\hat{\boldsymbol{i}}_{\mathrm{e}l\mathrm{u}}$, $\hat{\boldsymbol{i}}_{\mathrm{e}l\mathrm{v}}$. The small-signal components of $\hat{\boldsymbol{i}}_{\mathrm{e}l\mathrm{u}}$, $\hat{\boldsymbol{i}}_{\mathrm{e}l\mathrm{v}}$ multiplying the steady-state components of $\boldsymbol{M}_{\mathrm{e}l\mathrm{u}}$, $\boldsymbol{M}_{\mathrm{e}l\mathrm{v}}$ at kf_1 leads to small-signal responses of the arm capacitor voltage at $f_\mathrm{p}+kf_1$. The difference between the small-signal components of the arm voltage dropping on the arm inductor leads to small-signal responses of $\hat{\boldsymbol{i}}_{\mathrm{e}l\mathrm{u}}$, $\hat{\boldsymbol{i}}_{\mathrm{e}l\mathrm{v}}$ at $f_\mathrm{p}+kf_1$.

The DM components of $\hat{\boldsymbol{i}}_{\mathrm{e}l\mathrm{u}}$, $\hat{\boldsymbol{i}}_{\mathrm{e}l\mathrm{v}}$, except for the zero sequence, constitute the small-signal components of the receiving-end AC current $\hat{\boldsymbol{i}}_{\mathrm{e}l}$, corresponding to the components at $f_\mathrm{p}+6nf_1$ and $f_\mathrm{p}+(6n+4)f_1$. $\hat{\boldsymbol{i}}_{\mathrm{e}l}$ flows through the impedance of the receiving-end AC grid, leading to small-signal responses of the receiving-end AC voltage $\hat{\boldsymbol{v}}_{\mathrm{e}l}$ at $f_\mathrm{p}+6nf_1$ and $f_\mathrm{p}+(6n+4)f_1$. Similarly, the small-signal components of $\hat{\boldsymbol{v}}_{\mathrm{e}l}$, $\hat{\boldsymbol{i}}_{\mathrm{e}l}$ also lead to the small-signal responses in the sending-end MMC via the DC transmission lines. Besides, under the control of the sending-end and receiving-end MMCs, the small-signal components at $f_\mathrm{p}+kf_1$ are produced in the arm modulation signals $\hat{\boldsymbol{m}}_{\mathrm{f}l\mathrm{u}}$, $\hat{\boldsymbol{m}}_{\mathrm{f}l\mathrm{v}}$, $\hat{\boldsymbol{m}}_{\mathrm{e}l\mathrm{u}}$, $\hat{\boldsymbol{m}}_{\mathrm{e}l\mathrm{v}}$. The balance will be finally achieved after repeating the above process.

In summary, the frequency-domain characteristics of the small-signal vectors in MMC-HVDC are listed in Table 11.2. The frequency-domain distribution characteristics of the corresponding small-signal vectors in the sending-end and receiving-end MMCs are the same. The small-signal vectors of the arm capacitor voltages contain infinite number of small-signal components at $f_\mathrm{p}+kf_1$ ($k=0,\pm1,\pm2,\ldots$). The small-signal vectors of the arm currents and modulation signals contain all components at $f_\mathrm{p}+kf_1$ ($k\neq 6n+2$, $n=0,\pm1,\pm2,\ldots$), with the zero-sequence DM components excluded. The small-signal vectors of the AC currents contain the DM components at $f_\mathrm{p}+6nf_1$ and $f_\mathrm{p}+(6n+4)f_1$, with the zero sequence excluded. The

Table 11.2 The frequency-domain characteristics of the small-signal vectors in MMC-HVDC

Small-Signal Vectors	Frequency
$\hat{\boldsymbol{v}}_{\mathrm{fC}l\mathrm{u}}, \hat{\boldsymbol{v}}_{\mathrm{fC}l\mathrm{v}}, \hat{\boldsymbol{v}}_{\mathrm{eC}l\mathrm{u}}, \hat{\boldsymbol{v}}_{\mathrm{eC}l\mathrm{v}}$	$f_\mathrm{p} + kf_1$
$\hat{\boldsymbol{i}}_{\mathrm{f}l\mathrm{u}}, \hat{\boldsymbol{i}}_{\mathrm{f}l\mathrm{v}}, \hat{\boldsymbol{i}}_{\mathrm{e}l\mathrm{u}}, \hat{\boldsymbol{i}}_{\mathrm{e}l\mathrm{v}}$	$f_\mathrm{p} + kf_1$ $(k \neq 6n+2)$
$\hat{\boldsymbol{m}}_{\mathrm{f}l\mathrm{u}}, \hat{\boldsymbol{m}}_{\mathrm{f}l\mathrm{v}}, \hat{\boldsymbol{m}}_{\mathrm{e}l\mathrm{u}}, \hat{\boldsymbol{m}}_{\mathrm{e}l\mathrm{v}}$	$f_\mathrm{p} + kf_1$ $(k \neq 6n+2)$
$\hat{\boldsymbol{i}}_{\mathrm{f}l}, \hat{\boldsymbol{i}}_{\mathrm{e}l}$	$f_\mathrm{p} + 6nf_1$
	$f_\mathrm{p} + (6n+4)f_1$
$\hat{\boldsymbol{i}}_{\mathrm{fcom}l}, \hat{\boldsymbol{i}}_{\mathrm{ecom}l}$	$f_\mathrm{p} + (6n+1)f_1$
	$f_\mathrm{p} + (6n+3)f_1$
	$f_\mathrm{p} + (6n+5)f_1$
$\hat{\boldsymbol{i}}_{\mathrm{fdc}}, \hat{\boldsymbol{i}}_{\mathrm{edc}}$	$f_\mathrm{p} + (6n+5)f_1$

small-signal vectors of the arm circulating currents contain the CM components at $f_\mathrm{p} + (6n+1)f_1$, $f_\mathrm{p} + (6n+3)f_1$, and $f_\mathrm{p} + (6n+5)f_1$.

In order to describe the frequency-domain small-signal characteristics, the small-signal components of MMC-HVDC quantities at $f_\mathrm{p} + kf_1$ $(k = 0, \pm1, \pm2, \ldots)$ are arranged in the following small-signal frequency order.

$$\left[f_\mathrm{p} - gf_1,\ \ldots,\ f_\mathrm{p} - f_1,\ f_\mathrm{p},\ f_\mathrm{p} + f_1,\ \ldots,\ f_\mathrm{p} + gf_1 \right]^\mathrm{T} \tag{11.45}$$

Taking the phase-a upper arm of the sending-end MMC as an example, the small-signal vectors of the arm current, capacitor voltage, and modulation signal can be expressed as

$$\begin{cases} \hat{\boldsymbol{i}}_{\mathrm{fau}} = [\ldots, \hat{\boldsymbol{i}}_{\mathrm{fau\text{-}3}}, \hat{\boldsymbol{i}}_{\mathrm{fau\text{-}2}}, \hat{\boldsymbol{i}}_{\mathrm{fau\text{-}1}}, \hat{\boldsymbol{i}}_{\mathrm{fau0}}, \hat{\boldsymbol{i}}_{\mathrm{fau+1}}, \hat{\boldsymbol{i}}_{\mathrm{fau+2}}, \hat{\boldsymbol{i}}_{\mathrm{fau+3}}, \ldots]^\mathrm{T} \\ \hat{\boldsymbol{v}}_{\mathrm{fCau}} = [\ldots, \hat{\boldsymbol{v}}_{\mathrm{fCau\text{-}3}}, \hat{\boldsymbol{v}}_{\mathrm{fCau\text{-}2}}, \hat{\boldsymbol{v}}_{\mathrm{fCau\text{-}1}}, \hat{\boldsymbol{v}}_{\mathrm{fCau0}}, \hat{\boldsymbol{v}}_{\mathrm{fCau+1}}, \hat{\boldsymbol{v}}_{\mathrm{fCau+2}}, \hat{\boldsymbol{v}}_{\mathrm{fCau+3}}, \ldots]^\mathrm{T} \\ \hat{\boldsymbol{m}}_{\mathrm{fau}} = [\ldots, \hat{\boldsymbol{m}}_{\mathrm{fau\text{-}3}}, \hat{\boldsymbol{m}}_{\mathrm{fau\text{-}2}}, \hat{\boldsymbol{m}}_{\mathrm{fau\text{-}1}}, \hat{\boldsymbol{m}}_{\mathrm{fau0}}, \hat{\boldsymbol{m}}_{\mathrm{fau+1}}, \hat{\boldsymbol{m}}_{\mathrm{fau+2}}, \hat{\boldsymbol{m}}_{\mathrm{fau+3}}, \ldots]^\mathrm{T} \end{cases} \tag{11.46}$$

where each component $\hat{\boldsymbol{i}}_{\mathrm{fau}k}$, $\hat{\boldsymbol{v}}_{\mathrm{fCau}k}$, $\hat{\boldsymbol{m}}_{\mathrm{fau}k}$ $(k = 0,\pm1,\pm2,...)$ represents the small-signal component at $f_\mathrm{p} + kf_1$.

For the positive-sequence perturbation at f_p, this angle is delayed by $2\pi/3$ among three phases. Combined with the phases of the steady-state components at kf_1, the phase-sequence relationship of a small-signal component at $f_\mathrm{p} + kf_1$ changes, which can be expressed by defining the following modulo-3 function

$$\mathrm{mod}(k+1, 3) = \begin{cases} +1, & k = 3n \\ -1, & k = 3n+1 \\ 0, & k = 3n+2 \end{cases} \quad (n = 0, \pm1, \pm2, \ldots) \tag{11.47}$$

The small-signal component at $f_p + 3nf_1$ is in positive sequence, the small-signal component at $f_p + (3n+1)f_1$ is in negative sequence, and the small-signal component at $f_p + (3n+2)f_1$ is in zero sequence.

According to the phase-sequence relationship shown in Eq. (11.47), the small-signal vectors of the arm currents, capacitor voltages, and modulation signals in the upper arms of phase b and phase c can be obtained.

$$\begin{cases} \hat{\boldsymbol{i}}_{\mathrm{fbu}} = \boldsymbol{D}_{\mathrm{p}}\hat{\boldsymbol{i}}_{\mathrm{fau}},\ \hat{\boldsymbol{v}}_{\mathrm{fCbu}} = \boldsymbol{D}_{\mathrm{p}}\hat{\boldsymbol{v}}_{\mathrm{fCau}},\ \hat{\boldsymbol{m}}_{\mathrm{fbu}} = \boldsymbol{D}_{\mathrm{p}}\hat{\boldsymbol{m}}_{\mathrm{fau}} \\ \hat{\boldsymbol{i}}_{\mathrm{fcu}} = \boldsymbol{D}_{\mathrm{p}}^{*}\hat{\boldsymbol{i}}_{\mathrm{fau}},\ \hat{\boldsymbol{v}}_{\mathrm{fCcu}} = \boldsymbol{D}_{\mathrm{p}}^{*}\hat{\boldsymbol{v}}_{\mathrm{fCau}},\ \hat{\boldsymbol{m}}_{\mathrm{fcu}} = \boldsymbol{D}_{\mathrm{p}}^{*}\hat{\boldsymbol{m}}_{\mathrm{fau}} \end{cases} \tag{11.48}$$

where $\boldsymbol{D}_{\mathrm{p}}$ is the phase-sequence coefficient matrix of the small-signal vectors, expressed as

$$\boldsymbol{D}_{\mathrm{p}} = \mathrm{diag}\left[\{\mathrm{e}^{-\mathrm{j}2(k+1)\pi/3}\}\big|_{k=-g,\ldots,0,\ldots,g} \right] \tag{11.49}$$

After injecting the positive-sequence perturbation, the DM and CM characteristics of the small-signal components at $f_p + kf_1$ in the upper and lower arms satisfy the following relationship. If $k = 2n$, i.e., $\mathrm{mod}(k+1, 2) = 1$, the small-signal component at $f_p + 2nf_1$ is the DM component. If $k = 2n+1$, i.e., $\mathrm{mod}(k+1, 2) = 0$, the small-signal component at $f_p + (2n+1)f_1$ is the CM component.

Based on the DM and CM relationships of the small-signal components, the small-signal vectors of the arm currents, capacitor voltages, and modulation signals in the three-phase lower arms can be obtained according to Eqs. (11.46) and (11.48).

$$\begin{cases} \hat{\boldsymbol{i}}_{\mathrm{fav}} = \boldsymbol{A}_{\mathrm{p}}\hat{\boldsymbol{i}}_{\mathrm{fau}}, & \hat{\boldsymbol{v}}_{\mathrm{fCav}} = \boldsymbol{A}_{\mathrm{p}}\hat{\boldsymbol{v}}_{\mathrm{fCau}}, & \hat{\boldsymbol{m}}_{\mathrm{fav}} = \boldsymbol{A}_{\mathrm{p}}\hat{\boldsymbol{m}}_{\mathrm{fau}} \\ \hat{\boldsymbol{i}}_{\mathrm{fbv}} = \boldsymbol{D}_{\mathrm{p}}\boldsymbol{A}_{\mathrm{p}}\hat{\boldsymbol{i}}_{\mathrm{fau}}, & \hat{\boldsymbol{v}}_{\mathrm{fCbv}} = \boldsymbol{D}_{\mathrm{p}}\boldsymbol{A}_{\mathrm{p}}\hat{\boldsymbol{v}}_{\mathrm{fCau}}, & \hat{\boldsymbol{m}}_{\mathrm{fbv}} = \boldsymbol{D}_{\mathrm{p}}\boldsymbol{A}_{\mathrm{p}}\hat{\boldsymbol{m}}_{\mathrm{fau}} \\ \hat{\boldsymbol{i}}_{\mathrm{fcv}} = \boldsymbol{D}_{\mathrm{p}}^{*}\boldsymbol{A}_{\mathrm{p}}\hat{\boldsymbol{i}}_{\mathrm{fau}}, & \hat{\boldsymbol{v}}_{\mathrm{fCcv}} = \boldsymbol{D}_{\mathrm{p}}^{*}\boldsymbol{A}_{\mathrm{p}}\hat{\boldsymbol{v}}_{\mathrm{fCau}}, & \hat{\boldsymbol{m}}_{\mathrm{fcv}} = \boldsymbol{D}_{\mathrm{p}}^{*}\boldsymbol{A}_{\mathrm{p}}\hat{\boldsymbol{m}}_{\mathrm{fau}} \end{cases} \tag{11.50}$$

where $\boldsymbol{A}_{\mathrm{p}}$ is the transformation matrix of the arm small-signal vectors, expressed as

$$\boldsymbol{A}_{\mathrm{p}} = \mathrm{diag}\left[\{(-1)^{k+1}\}\big|_{k=-g,\ldots,0,\ldots,g} \right] \tag{11.51}$$

The small-signal vectors of the receiving-end MMC can be obtained by replacing the subscript "f" with "e" in the small-signal vectors of the sending-end MMC, such as $\hat{\boldsymbol{i}}_{el\mathrm{u}}$, $\hat{\boldsymbol{i}}_{el\mathrm{v}}$, $\hat{\boldsymbol{v}}_{\mathrm{eC}l\mathrm{u}}$, $\hat{\boldsymbol{v}}_{\mathrm{eC}l\mathrm{v}}$, $\hat{\boldsymbol{m}}_{el\mathrm{u}}$, $\hat{\boldsymbol{m}}_{el\mathrm{v}}$.

11.3.2 Frequency-Domain Small-Signal Model

Based on the small-signal vectors of the voltage, current, and modulation signal, this section establishes the frequency-domain small-signal model, including the main

circuits and control loops of the sending-end and receiving-end MMCs as well as the DC transmission lines.

11.3.2.1 Small-Signal Model of Sending-End MMC

The small-signal modeling of the main circuit and control loops in the sending-end MMC is carried out as follows.

1. **Small-Signal Model of Main Circuit**

By transforming Eqs. (11.1) and (11.2) to the frequency domain, the small-signal model of the arm circuit in the phase-a upper arm can be obtained.

$$\hat{\boldsymbol{v}}_{\mathrm{fCau}} = \boldsymbol{Z}_{\mathrm{Cfeq}}\left(\boldsymbol{I}_{\mathrm{fau}}\hat{\boldsymbol{m}}_{\mathrm{fau}} + \boldsymbol{M}_{\mathrm{fau}}\hat{\boldsymbol{i}}_{\mathrm{fau}}\right) \tag{11.52}$$

$$\hat{\boldsymbol{i}}_{\mathrm{fau}} = -\boldsymbol{Y}_{\mathrm{Lfarm}}\left(\boldsymbol{V}_{\mathrm{fCau}}\hat{\boldsymbol{m}}_{\mathrm{fau}} + \boldsymbol{M}_{\mathrm{fau}}\hat{\boldsymbol{v}}_{\mathrm{fCau}} + \hat{\boldsymbol{v}}_{\mathrm{fa}} + \hat{\boldsymbol{v}}_{\mathrm{fO}} - \frac{1}{2}\hat{\boldsymbol{v}}_{\mathrm{fdc}}\right) \tag{11.53}$$

where $\hat{\boldsymbol{v}}_{\mathrm{fa}}$ is the small-signal vector of the sending-end phase-a AC voltage, expressed as

$$\hat{\boldsymbol{v}}_{\mathrm{fa}} = [\ldots, 0, \hat{\boldsymbol{v}}_{\mathrm{f\text{-}2}}, 0, \hat{\boldsymbol{v}}_{\mathrm{f}}, 0, 0, 0, \ldots]^{\mathrm{T}} \tag{11.54}$$

Correspondingly, $\hat{\boldsymbol{v}}_{\mathrm{f}}$ and $\hat{\boldsymbol{v}}_{\mathrm{f\text{-}2}}$ are the small-signal components of AC voltages at f_{p} and $f_{\mathrm{p}} - 2f_1$.

$\boldsymbol{Z}_{\mathrm{Cfeq}}$ is the admittance of the arm capacitor of the sending-end MMC in the small-signal frequency order, expressed as

$$\boldsymbol{Z}_{\mathrm{Cfeq}} = \frac{1}{\mathrm{j}2\pi C_{\mathrm{feq}}} \cdot \mathrm{diag}\left[\frac{1}{f_{\mathrm{p}} - gf_1}, \ldots, \frac{1}{f_{\mathrm{p}} - f_1}, \frac{1}{f_{\mathrm{p}}}, \frac{1}{f_{\mathrm{p}} + f_1}, \ldots, \frac{1}{f_{\mathrm{p}} + gf_1}\right] \tag{11.55}$$

The small-signal vector of sending-end AC neutral voltage $\hat{\boldsymbol{v}}_{\mathrm{fO}}$ cancels the zero-sequence DM components of the three-phase upper and lower arm voltages in Eq. (11.53), so the small-signal vectors of the corresponding arm currents exclude the zero-sequence DM components, i.e., there is no zero-sequence current path on the AC side. The function of $\hat{\boldsymbol{v}}_{\mathrm{fO}}$ can be replaced by defining the admittance of the arm inductor of the sending-end MMC in the small-signal frequency order as

$$\boldsymbol{Y}_{\mathrm{Lfarm}} = \boldsymbol{A}_{\mathrm{pd0}} \cdot \mathrm{diag}\left[\frac{1}{R_{\mathrm{farm}} + \mathrm{j}2\pi(f_{\mathrm{p}} - gf_1)L_{\mathrm{farm}}}, \ldots, \right.$$
$$\left. \frac{1}{R_{\mathrm{farm}} + \mathrm{j}2\pi(f_{\mathrm{p}} - f_1)L_{\mathrm{farm}}}, \frac{1}{R_{\mathrm{farm}} + \mathrm{j}2\pi f_{\mathrm{p}}L_{\mathrm{farm}}},\right.$$

$$\left.\frac{1}{R_{\text{farm}}+\text{j}2\pi(f_{\text{p}}+f_{\text{l}})L_{\text{farm}}},\ldots,\frac{1}{R_{\text{farm}}+\text{j}2\pi(f_{\text{p}}+gf_{\text{l}})L_{\text{farm}}}\right] \tag{11.56}$$

where $\boldsymbol{A}_{\text{pd0}}$ is the modified admittance matrix of arm inductor. If and only if mod $(k+1,3)=0$ and mod $(k+1,2)=1$, corresponding to $k=6n+2$, the diagonal element in $\boldsymbol{A}_{\text{pd0}}$ is 0; otherwise, the diagonal element is 1.

The modified $\boldsymbol{Y}_{\text{Lfarm}}$ forces the zero-sequence DM components of the arm currents to be zero, such that $\hat{\boldsymbol{v}}_{\text{fO}}$ can be dropped from Eq. (11.53).

The DM components of the upper and lower arm currents in each phase constitute half of the AC current, and the CM components constitute the arm circulating current. The small-signal vectors of the three-phase AC currents and arm circulating currents in the sending-end MMC can be obtained.

$$\begin{cases}\hat{\boldsymbol{i}}_{\text{f}l}=-2\boldsymbol{A}_{\text{pd}}\hat{\boldsymbol{i}}_{\text{f/u}}\\ \hat{\boldsymbol{i}}_{\text{fcom}l}=\boldsymbol{A}_{\text{pc}}\hat{\boldsymbol{i}}_{\text{f/u}}\end{cases} \tag{11.57}$$

where $\boldsymbol{A}_{\text{pd}}$ is the DM matrix of the arm small-signal vectors, and $\boldsymbol{A}_{\text{pc}}$ is the CM matrix of the arm small-signal vectors. Their expressions are

$$\begin{cases}\boldsymbol{A}_{\text{pd}}=\dfrac{1}{2}\text{diag}\left[\{1+(-1)^k\}\big|_{k=-g,\ldots,0,\cdots,g}\right]\\ \boldsymbol{A}_{\text{pc}}=\dfrac{1}{2}\text{diag}\left[\{1-(-1)^k\}\big|_{k=-g,\ldots,0,\cdots,g}\right]\end{cases} \tag{11.58}$$

Besides, the zero-sequence CM component of the three-phase upper or lower arm currents constitutes the DC current. The small-signal vector of the DC current in the sending-end MMC can be obtained by transforming Eq. (11.4) to the frequency domain.

$$\hat{\boldsymbol{i}}_{\text{fdc}}=-3\boldsymbol{A}_{\text{pc0}}\hat{\boldsymbol{i}}_{\text{fau}} \tag{11.59}$$

where $\boldsymbol{A}_{\text{pc0}}$ is the zero-sequence CM matrix of the arm small-signal vectors, expressed as

$$\boldsymbol{A}_{\text{pc0}}=\text{diag}\left[\left\{\frac{1-(-1)^k}{2}\cdot(1-|\text{mod}(k+1,3)|)\right\}_{k=-g,\ldots,0,\ldots,g}\right] \tag{11.60}$$

2. **Small-Signal Model of Control Loops**

According to the frequency-domain small-signal model of the arm circuit, both the arm current and the arm capacitor voltage are related to the arm modulation signal. In this section, based on the control strategy of sending-end MMC, the small-signal

model of the control loops is derived, taking into account the passive islanding mode and grid-connected mode respectively.

(1) **Passive Islanding Mode**. The control diagram of the sending-end MMC in passive islanding mode is shown in Fig. 11.5a. The AC voltage control is adopted in the outer loop, and the AC current control and circulating current control are adopted in the inner loop.

AC Voltage Control and AC Current Control Firstly, after injecting the positive-sequence perturbation on the sending-end AC voltage, the small-signal vectors of the dq-axis voltages in the sending-end MMC $\hat{\boldsymbol{v}}_{\mathrm{fd}}$, $\hat{\boldsymbol{v}}_{\mathrm{fq}}$ are produced. In the effect of the AC voltage controller $H_{\mathrm{vac}}(s)$, the small-signal responses of the dq-axis current references in the sending-end MMC $\hat{\boldsymbol{i}}_{\mathrm{fdref}}$, $\hat{\boldsymbol{i}}_{\mathrm{fqref}}$ are generated. Then, the small-signal vectors of the dq-axis currents in the sending-end MMC $\hat{\boldsymbol{i}}_{\mathrm{fd}}$, $\hat{\boldsymbol{i}}_{\mathrm{fq}}$ and their references $\hat{\boldsymbol{i}}_{\mathrm{fdref}}$, $\hat{\boldsymbol{i}}_{\mathrm{fqref}}$ are fed into the AC current controller $H_{\mathrm{fiac}}(s)$, leading to small-signal responses of the dq-axis modulation signal in the sending-end MMC $\hat{\boldsymbol{m}}_{\mathrm{fd}}$, $\hat{\boldsymbol{m}}_{\mathrm{fq}}$. Finally, the small-signal vectors of the three-phase arm DM modulation signals in the sending-end MMC $\hat{\boldsymbol{m}}_{\mathrm{fdif}l}$ are generated after the inverse Park transformation. Taking phase a as an example, the expression of $\hat{\boldsymbol{m}}_{\mathrm{fdifa}}$ is

$$\hat{\boldsymbol{m}}_{\mathrm{fdifa}} = \boldsymbol{G}_{\mathrm{f1}}\boldsymbol{D}_{\mathrm{f1}}\hat{\boldsymbol{i}}_{\mathrm{fau}} + \boldsymbol{G}_{\mathrm{f2}}\boldsymbol{D}_{\mathrm{f2}}\hat{\boldsymbol{v}}_{\mathrm{fa}} \tag{11.61}$$

where $\boldsymbol{G}_{\mathrm{f1}}$, $\boldsymbol{G}_{\mathrm{f2}}$ are $(2g+1)\times(2g+1)$ matrices, and all other elements in the matrices are zero except for Eqs. (11.62) and (11.63).

$$\begin{aligned}\boldsymbol{G}_{\mathrm{f1}}(g+k+1, g+k+1) = {} & |\mathrm{mod}(k+1,3)|\cdot[1+(-1)^k] \\ & \cdot\left\{-H_{\mathrm{fiac}}[\mathrm{j}2\pi(f_{\mathrm{p}}+kf_1-\mathrm{mod}(k+1,3)f_1)]\right. \\ & \left.+\ \mathrm{mod}(k+1,3)\mathrm{j}K_{\mathrm{fd}}\right\}\end{aligned} \tag{11.62}$$

$$\begin{aligned}\boldsymbol{G}_{\mathrm{f2}}(g-1, g-1) &= \boldsymbol{G}_{\mathrm{f2}}(g+1, g+1) \\ &= -H_{\mathrm{vac}}[\mathrm{j}2\pi(f_{\mathrm{p}}-f_1)]H_{\mathrm{fiac}}[\mathrm{j}2\pi(f_{\mathrm{p}}-f_1)]\end{aligned} \tag{11.63}$$

Since the AC current control and AC voltage control are implemented in the MMC-HVDC system pole control, $\boldsymbol{D}_{\mathrm{f1}}$, $\boldsymbol{D}_{\mathrm{f2}}$ in Eq. (11.61) are the time delay transfer function matrices of the AC current control and AC voltage control in the sending-end MMC respectively, expressed as

$$\begin{aligned}&\boldsymbol{D}_{\mathrm{f1}} \\ &= \mathrm{diag}\left[\left\{\mathrm{e}^{-\mathrm{j}2\pi(f_{\mathrm{p}}+kf_1)T_{\mathrm{fpol}}}\frac{1-\mathrm{e}^{-\mathrm{j}2\pi(f_{\mathrm{p}}+kf_1)T_{\mathrm{fpol}}}}{\mathrm{j}2\pi(f_{\mathrm{p}}+kf_1)T_{\mathrm{fpol}}}\frac{1}{1+\mathrm{j}2\pi(f_{\mathrm{p}}+kf_1)T_{\mathrm{fiac}}}\right\}\Bigg|_{k=-g,\ldots,0,\ldots,g}\right]\end{aligned} \tag{11.64}$$

$$\boldsymbol{D}_{\mathrm{f2}} = \mathrm{diag}\left[\left\{\mathrm{e}^{-\mathrm{j}2\pi(f_{\mathrm{p}}+kf_1)T_{\mathrm{fpol}}}\frac{1-\mathrm{e}^{-\mathrm{j}2\pi(f_{\mathrm{p}}+kf_1)T_{\mathrm{fpol}}}}{\mathrm{j}2\pi(f_{\mathrm{p}}+kf_1)T_{\mathrm{fpol}}}\frac{1}{1+\mathrm{j}2\pi(f_{\mathrm{p}}+kf_1)T_{\mathrm{fvac}}}\right\}\Big|_{k=-g,\ldots,0,\ldots,g}\right] \tag{11.65}$$

where T_{fpol} is the control period of the sending-end MMC pole control. T_{fiac}, T_{fvac} are the filter time delay of the AC current and voltage in the sending-end MMC, respectively.

Circulating Current Control Firstly, after the negative-sequence second-harmonic Park transformation to the three-phase arm circulating currents, the small-signal vectors of the dq-axis circulating currents in the sending-end MMC $\hat{\boldsymbol{i}}_{\mathrm{fcd}}$, $\hat{\boldsymbol{i}}_{\mathrm{fcq}}$ are produced. Then, in the effect of the circulating current controller $H_{\mathrm{fic}}(s)$, the small-signal responses of the dq-axis circulating modulation signals in the sending-end MMC $\hat{\boldsymbol{m}}_{\mathrm{fcd}}$, $\hat{\boldsymbol{m}}_{\mathrm{fcq}}$ are generated. Finally, the small-signal vectors of the three-phase arm CM modulation signals in the sending-end MMC $\hat{\boldsymbol{m}}_{\mathrm{fcom}l}$ are generated after the corresponding inverse Park transformation. Taking phase a as an example, the expression of $\hat{\boldsymbol{m}}_{\mathrm{fcoma}}$ is

$$\hat{\boldsymbol{m}}_{\mathrm{fcoma}} = \boldsymbol{G}_{\mathrm{f3}}\boldsymbol{D}_{\mathrm{f3}}\hat{\boldsymbol{i}}_{\mathrm{au}} \tag{11.66}$$

where $\boldsymbol{G}_{\mathrm{f3}}$ are $(2g+1)\times(2g+1)$ matrices, and all other elements in the matrices are zero except for Eq. (11.67).

$$\begin{aligned}\boldsymbol{G}_{\mathrm{f3}}(g+k+1, g+k+1) = {} & \frac{1-(-1)^k}{2}\cdot|\mathrm{mod}(k+1,3)| \\ & \cdot\left\{H_{\mathrm{fic}}[\mathrm{j}2\pi(f_{\mathrm{p}}+kf_1+\mathrm{mod}(k+1,3)\cdot 2f_1)]\right. \\ & \left.-\ \mathrm{mod}\ (k+1,3)\mathrm{j}K_{\mathrm{fic}}\right\}\end{aligned} \tag{11.67}$$

Since the circulating current control is implemented in the MMC-HVDC system valve control, $\boldsymbol{D}_{\mathrm{f3}}$ in Eq. (11.66) is the time delay transfer function matrix of the circulating current control in the sending-end MMC, expressed as

$$\boldsymbol{D}_{\mathrm{f3}} = \mathrm{diag}\left[\left\{\mathrm{e}^{-\mathrm{j}2\pi(f_{\mathrm{p}}+kf_1)T_{\mathrm{fval}}}\frac{1-\mathrm{e}^{-\mathrm{j}2\pi(f_{\mathrm{p}}+kf_1)T_{\mathrm{fval}}}}{\mathrm{j}2\pi(f_{\mathrm{p}}+kf_1)T_{\mathrm{fval}}}\frac{1}{1+\mathrm{j}2\pi(f_{\mathrm{p}}+kf_1)T_{\mathrm{fic}}}\right\}\Big|_{k=-g,\ldots,0,\ldots,g}\right] \tag{11.68}$$

where T_{fval} is the control period of the sending-end MMC valve control. T_{fic} is the filter time delay of the circulating current in the sending-end MMC.

Arm Modulation Signal Based on Eqs. (11.61) and (11.66), the small-signal vector of the phase-a upper arm modulation signal $\hat{\boldsymbol{m}}_{\mathrm{fau}}$ in passive islanding mode can be obtained.

$$\hat{\boldsymbol{m}}_{\mathrm{fau}} = \boldsymbol{G}_{\mathrm{fi}}\hat{\boldsymbol{i}}_{\mathrm{fau}} + \boldsymbol{G}_{\mathrm{fv}}\hat{\boldsymbol{v}}_{\mathrm{fa}} \tag{11.69}$$

where $\boldsymbol{G}_{\mathrm{fi}}$, $\boldsymbol{G}_{\mathrm{fv}}$ in passive islanding mode are

$$\begin{cases} \boldsymbol{G}_{\mathrm{fi}} = -\boldsymbol{G}_{\mathrm{f1}}\boldsymbol{D}_{\mathrm{f1}} + \boldsymbol{G}_{\mathrm{f3}}\boldsymbol{D}_{\mathrm{f3}} \\ \boldsymbol{G}_{\mathrm{fv}} = -\boldsymbol{G}_{\mathrm{f2}}\boldsymbol{D}_{\mathrm{f2}} \end{cases} \tag{11.70}$$

According to the DM, CM, and phase-sequence relationships between the small-signal vectors shown in Eqs. (11.48) and (11.50), the small-signal vectors of the other arm modulation signals in the sending-end MMC can also be obtained according to $\hat{\boldsymbol{m}}_{\mathrm{fau}}$.

(2) **Grid-connected Mode**. The control diagram of the sending-end MMC in grid-connected mode is shown in Fig. 11.5b. The power control is adopted in the outer loop, and the AC current control and circulating current control are adopted in the inner loop. Besides, PLL is used to track the voltage phase of the AC grid.

Power Control and AC Current Control Firstly, after injecting the positive-sequence perturbation on the sending-end AC voltage, the small-signal vectors of the dq-axis voltages $\hat{\boldsymbol{v}}_{\mathrm{fd}}$, $\hat{\boldsymbol{v}}_{\mathrm{fq}}$ and PLL output angle $\hat{\boldsymbol{\theta}}_{\mathrm{fPLL}}$ in the sending-end MMC are produced. In the effect of the active and reactive power control, the small-signal responses of the dq-axis current references $\hat{\boldsymbol{i}}_{\mathrm{fdref}}$, $\hat{\boldsymbol{i}}_{\mathrm{fqref}}$ in the sending-end MMC are generated. Next, the small-signal vectors of the three-phase AC currents $\hat{\boldsymbol{i}}_{\mathrm{f}l}$ and PLL output angle $\hat{\boldsymbol{\theta}}_{\mathrm{fPLL}}$ lead to small-signal responses of the dq-axis currents $\hat{\boldsymbol{i}}_{\mathrm{fd}}$, $\hat{\boldsymbol{i}}_{\mathrm{fq}}$ in the sending-end MMC. Then, $\hat{\boldsymbol{i}}_{\mathrm{fd}}$, $\hat{\boldsymbol{i}}_{\mathrm{fq}}$ and their references $\hat{\boldsymbol{i}}_{\mathrm{fdref}}$, $\hat{\boldsymbol{i}}_{\mathrm{fqref}}$ are fed into the AC current controller $H_{\mathrm{fiac}}(s)$, leading to small-signal responses of the dq-axis modulation signal $\hat{\boldsymbol{m}}_{\mathrm{fd}}$, $\hat{\boldsymbol{m}}_{\mathrm{fq}}$ in the sending-end MMC. Finally, the small-signal vectors of the three-phase arm DM modulation signals $\hat{\boldsymbol{m}}_{\mathrm{fdif}l}$ in the sending-end MMC are generated after the inverse Park transformation. Taking phase a as an example, the expression of $\hat{\boldsymbol{m}}_{\mathrm{fdifa}}$ is

$$\hat{\boldsymbol{m}}_{\mathrm{fdifa}} = \boldsymbol{G}_{\mathrm{f1}}\boldsymbol{D}_{\mathrm{f1}}\hat{\boldsymbol{i}}_{\mathrm{fau}} + \Delta\boldsymbol{G}_{\mathrm{f2}}\boldsymbol{D}_{\mathrm{f2}}\hat{\boldsymbol{v}}_{\mathrm{fa}} \tag{11.71}$$

where the expressions of $\boldsymbol{G}_{\mathrm{f1}}$, $\boldsymbol{D}_{\mathrm{f1}}$, $\boldsymbol{D}_{\mathrm{f2}}$ are shown in Eqs. (11.62), (11.64), and (11.65). $\Delta\boldsymbol{G}_{\mathrm{f2}}$ is a $(2g+1)\times(2g+1)$ matrix, and all other elements in the matrix are zero except for Eq. (11.72).

$$\begin{cases}
\Delta \boldsymbol{G}_{\mathrm{f2}}(g-1,g-1) = T_{\mathrm{fPLL}}[\mathrm{j}2\pi(f_{\mathrm{p}}-f_1)] \cdot \left[2\left\{H_{\mathrm{fiac}}[\mathrm{j}2\pi(f_{\mathrm{p}}-f_1)] + \mathrm{j}K_{\mathrm{fd}}\right\}\right. \\
\qquad\qquad \left. \cdot \boldsymbol{I}^*_{\mathrm{fau1}} - \boldsymbol{M}^*_{\mathrm{fau1}} - k_{\mathrm{fv}} V_{\mathrm{f1}}\right] - H_{\mathrm{fiac}}[\mathrm{j}2\pi(f_{\mathrm{p}}-f_1)] \\
\qquad\qquad \cdot (P_{\mathrm{ref}} - \mathrm{j}Q_{\mathrm{ref}})/(3V_{\mathrm{f1}}^2) + k_{\mathrm{fv}} \\
\Delta \boldsymbol{G}_{\mathrm{f2}}(g-1,g+1) = -T_{\mathrm{fPLL}}[\mathrm{j}2\pi(f_{\mathrm{p}}-f_1)] \cdot \left[2\left\{H_{\mathrm{fiac}}[\mathrm{j}2\pi(f_{\mathrm{p}}-f_1)] + \mathrm{j}K_{\mathrm{fd}}\right\}\right. \\
\qquad\qquad \left. \cdot \boldsymbol{I}^*_{\mathrm{fau1}} - \boldsymbol{M}^*_{\mathrm{fau1}} - k_{\mathrm{fv}} V_{\mathrm{f1}}\right] - H_{\mathrm{fiac}}[\mathrm{j}2\pi(f_{\mathrm{p}}-f_1)] \\
\qquad\qquad \cdot (P_{\mathrm{ref}} - \mathrm{j}Q_{\mathrm{ref}})/(3V_{\mathrm{f1}}^2) \\
\Delta \boldsymbol{G}_{\mathrm{f2}}(g+1,g-1) = -T_{\mathrm{fPLL}}[\mathrm{j}2\pi(f_{\mathrm{p}}-f_1)] \cdot \left[2\left\{H_{\mathrm{fiac}}[\mathrm{j}2\pi(f_{\mathrm{p}}-f_1)] - \mathrm{j}K_{\mathrm{fd}}\right\}\right. \\
\qquad\qquad \left. \cdot \boldsymbol{I}_{\mathrm{fau1}} - \boldsymbol{M}_{\mathrm{fau1}} - k_{\mathrm{fv}} V_{\mathrm{f1}}\right] - H_{\mathrm{fiac}}[\mathrm{j}2\pi(f_{\mathrm{p}}-f_1)] \\
\qquad\qquad \cdot (P_{\mathrm{ref}} + \mathrm{j}Q_{\mathrm{ref}})/(3V_{\mathrm{f1}}^2) \\
\Delta \boldsymbol{G}_{\mathrm{f2}}(g+1,g+1) = T_{\mathrm{fPLL}}[\mathrm{j}2\pi(f_{\mathrm{p}}-f_1)] \cdot \left[2\left\{H_{\mathrm{fiac}}[\mathrm{j}2\pi(f_{\mathrm{p}}-f_1)] - \mathrm{j}K_{\mathrm{fd}}\right\}\right. \\
\qquad\qquad \left. \cdot \boldsymbol{I}_{\mathrm{fau1}} - \boldsymbol{M}_{\mathrm{fau1}} - k_{\mathrm{fv}} V_{\mathrm{f1}}\right] - H_{\mathrm{fiac}}[\mathrm{j}2\pi(f_{\mathrm{p}}-f_1)] \\
\qquad\qquad \cdot (P_{\mathrm{ref}} + \mathrm{j}Q_{\mathrm{ref}})/(3V_{\mathrm{f1}}^2) + k_{\mathrm{fv}}
\end{cases} \tag{11.72}$$

in which voltage feedforward coefficient of the sending-end MMC k_{fv} is equal to 1.

Circulating Current Control Firstly, after the negative-sequence second-harmonic Park transformation to the three-phase arm circulating currents, the small-signal vectors of the dq-axis circulating currents $\hat{\boldsymbol{i}}_{\mathrm{fcd}}$, $\hat{\boldsymbol{i}}_{\mathrm{fcq}}$ in the sending-end MMC are produced. Then, in the effect of the circulating current controller $H_{\mathrm{fic}}(s)$, the small-signal responses of the dq-axis circulating modulation signals $\hat{\boldsymbol{m}}_{\mathrm{fcd}}$, $\hat{\boldsymbol{m}}_{\mathrm{fcq}}$ in the sending-end MMC are generated. Finally, the small-signal vectors of the three-phase arm CM modulation signals $\hat{\boldsymbol{m}}_{\mathrm{fcom}l}$ in the sending-end MMC are generated after the corresponding inverse Park transformation. Taking phase a as an example, the expression of $\hat{\boldsymbol{m}}_{\mathrm{fcoma}}$ is

$$\hat{\boldsymbol{m}}_{\mathrm{fcoma}} = \boldsymbol{G}_{\mathrm{f3}} \boldsymbol{D}_{\mathrm{f3}} \hat{\boldsymbol{i}}_{\mathrm{au}} + \Delta \boldsymbol{G}_{\mathrm{f4}} \boldsymbol{D}_{\mathrm{f4}} \hat{\boldsymbol{v}}_{\mathrm{fa}} \tag{11.73}$$

where the expressions of $\boldsymbol{G}_{\mathrm{f3}}$, $\boldsymbol{D}_{\mathrm{f3}}$ are shown in Eqs. (11.67) and (11.68). $\Delta \boldsymbol{G}_{\mathrm{f4}}$ is a $(2g+1) \times (2g+1)$ matrix; all other elements in the matrix are zero except for Eq. (11.74).

$$\begin{cases}
\Delta \boldsymbol{G}_{\mathrm{f4}}(g-2,g-1) = -\Delta \boldsymbol{G}_{\mathrm{f4}}(g-2,g+1) \\
\qquad\qquad = 2T_{\mathrm{fPLL}}[\mathrm{j}2\pi(f_{\mathrm{p}}-f_1)] \\
\qquad\qquad \cdot \left[\left\{-H_{\mathrm{fic}}[\mathrm{j}2\pi(f_{\mathrm{p}}-f_1)] + \mathrm{j}K_{\mathrm{fic}}\right\} \boldsymbol{I}^*_{\mathrm{fau2}} + \boldsymbol{M}^*_{\mathrm{fau2}}\right] \\
\Delta \boldsymbol{G}_{\mathrm{f4}}(g+2,g-1) = -\Delta \boldsymbol{G}_{\mathrm{f4}}(g+2,g+1) \\
\qquad\qquad = 2T_{\mathrm{fPLL}}[\mathrm{j}2\pi(f_{\mathrm{p}}-f_1)] \\
\qquad\qquad \cdot \left[\left\{H_{\mathrm{fic}}[\mathrm{j}2\pi(f_{\mathrm{p}}-f_1)] + \mathrm{j}K_{\mathrm{fic}}\right\} \boldsymbol{I}_{\mathrm{fau2}} - \boldsymbol{M}_{\mathrm{fau2}}\right]
\end{cases} \tag{11.74}$$

In Eq. (11.73), $\boldsymbol{D}_{\mathrm{f4}}$ is the time delay transfer function matrix of the circulating current control and PLL control in the sending-end MMC, expressed as

$$\boldsymbol{D}_{\mathrm{f4}} = \mathrm{diag}\left[\left\{\mathrm{e}^{-\mathrm{j}2\pi(f_{\mathrm{p}}+kf_1)T_{\mathrm{fval}}}\frac{1-\mathrm{e}^{-\mathrm{j}2\pi(f_{\mathrm{p}}+kf_1)T_{\mathrm{fval}}}}{\mathrm{j}2\pi(f_{\mathrm{p}}+kf_1)T_{\mathrm{fval}}}\frac{1}{1+\mathrm{j}2\pi(f_{\mathrm{p}}+kf_1)T_{\mathrm{fvac}}}\right\}\Big|_{k=-g,\ldots,0,\ldots,g}\right] \tag{11.75}$$

Arm Modulation Signal Based on Eqs. (11.71) and (11.73), the small-signal vector of the phase-a upper arm modulation signal $\hat{\boldsymbol{m}}_{\mathrm{fau}}$ in grid-connected mode can be obtained.

$$\hat{\boldsymbol{m}}_{\mathrm{fau}} = \boldsymbol{G}_{\mathrm{fi}}\hat{\boldsymbol{i}}_{\mathrm{fau}} + \boldsymbol{G}_{\mathrm{fv}}\hat{\boldsymbol{v}}_{\mathrm{fa}} \tag{11.76}$$

where $\boldsymbol{G}_{\mathrm{fi}}$, $\boldsymbol{G}_{\mathrm{fv}}$ in grid-connected mode are

$$\begin{cases} \boldsymbol{G}_{\mathrm{fi}} = -\boldsymbol{G}_{\mathrm{f1}}\boldsymbol{D}_{\mathrm{f1}} + \boldsymbol{G}_{\mathrm{f3}}\boldsymbol{D}_{\mathrm{f3}} \\ \boldsymbol{G}_{\mathrm{fv}} = -\Delta\boldsymbol{G}_{\mathrm{f2}}\boldsymbol{D}_{\mathrm{f2}} + \Delta\boldsymbol{G}_{\mathrm{f4}}\boldsymbol{D}_{\mathrm{f4}} \end{cases} \tag{11.77}$$

Based on the DM, CM, and phase-sequence relationships between the small-signal vectors shown in Eqs. (11.48) and (11.50), the small-signal vectors of the other arm modulation signals in the sending-end MMC can also be obtained according to $\hat{\boldsymbol{m}}_{\mathrm{fau}}$.

11.3.2.2 Small-Signal Model of Receiving-End MMC

The small-signal modeling of the main circuit and control loops in the receiving-end MMC is carried out as follows.

1. **Small-Signal Model of Main Circuit**

By transforming Eqs. (11.8) and (11.9) to the frequency domain, the small-signal model of the arm circuit in the phase-a upper arm can be obtained.

$$\hat{\boldsymbol{v}}_{\mathrm{eCau}} = \boldsymbol{Z}_{\mathrm{Ceeq}}\left(\boldsymbol{I}_{\mathrm{eau}}\hat{\boldsymbol{m}}_{\mathrm{eau}} + \boldsymbol{M}_{\mathrm{eau}}\hat{\boldsymbol{i}}_{\mathrm{eau}}\right) \tag{11.78}$$

$$\hat{\boldsymbol{i}}_{\mathrm{eau}} = -\boldsymbol{Y}_{\mathrm{Learm}}\left(\boldsymbol{V}_{\mathrm{eCau}}\hat{\boldsymbol{m}}_{\mathrm{eau}} + \boldsymbol{M}_{\mathrm{eau}}\hat{\boldsymbol{v}}_{\mathrm{eCau}} + \hat{\boldsymbol{v}}_{\mathrm{ea}} - \frac{1}{2}\hat{\boldsymbol{v}}_{\mathrm{edc}}\right) \tag{11.79}$$

where $\boldsymbol{Z}_{\text{Ceeq}}$ and $\boldsymbol{Y}_{\text{Learm}}$ are the impedance of the arm capacitor and the admittance of the arm capacitor of the receiving-end MMC in the small-signal frequency order respectively. Their expressions can be obtained by replacing the subscript "f" with "e" in Eqs. (11.55) and (11.56).

The small-signal vectors of the three-phase AC currents and arm circulating currents in the receiving-end MMC can be obtained by transforming Eq. (11.12) to the frequency domain.

$$\begin{cases} \hat{\boldsymbol{i}}_{el} = 2\boldsymbol{A}_{\text{pd}}\hat{\boldsymbol{i}}_{el\text{u}} \\ \hat{\boldsymbol{i}}_{\text{ecom}l} = \boldsymbol{A}_{\text{pc}}\hat{\boldsymbol{i}}_{el\text{u}} \end{cases} \tag{11.80}$$

Based on the DM, CM, and phase-sequence relationships of the arm currents, the small-signal vector of the DC current in the receiving-end MMC can be obtained by transforming Eq. (11.11) to the frequency domain.

$$\hat{\boldsymbol{i}}_{\text{edc}} = 3\boldsymbol{A}_{\text{pc0}}\hat{\boldsymbol{i}}_{\text{eau}} \tag{11.81}$$

The small-signal vectors of the receiving-end three-phase AC currents $\hat{\boldsymbol{i}}_{el}$ flow through the impedance of the receiving-end AC grid, and the small-signal vectors of the receiving-end three-phase AC voltages are produced, which satisfies

$$\hat{\boldsymbol{v}}_{el} = \boldsymbol{Z}_{\text{eg}}\hat{\boldsymbol{i}}_{el} \tag{11.82}$$

where $\boldsymbol{Z}_{\text{eg}}$ is the receiving-end AC grid impedance in small-signal frequency order, expressed as

$$\boldsymbol{Z}_{\text{eg}} = \text{j}2\pi L_{\text{eg}} \cdot \text{diag}\left[f_{\text{p}} - gf_1,\ \ldots,\ f_{\text{p}} - f_1,\ f_{\text{p}},\ f_{\text{p}} + f_1,\ \ldots,\ f_{\text{p}} + gf_1 \right] \tag{11.83}$$

where L_{eg} is the inductance of the receiving-end AC grid.

2. **Small-Signal Model of Control Loops**

The control diagram of the receiving-end MMC is shown in Fig. 11.6. The receiving-end MMC operates in grid-connected mode with the PLL adopted to track the voltage phase of the receiving-end AC grid. The DC voltage control is adopted to generate the d-axis current reference, while the reactive power control is adopted to generate the q-axis current reference.

DC Voltage, Reactive Power and AC Current Control Firstly, in the effect of the DC voltage control, the small-signal vector of the DC voltage in the receiving-end MMC $\hat{\boldsymbol{v}}_{\text{edc}}$ leads to a small-signal response of the d-axis current reference in

the receiving-end MMC $\hat{\boldsymbol{i}}_{\text{edref}}$. The reactive power control leads to a small-signal response of the receiving-end q-axis current reference in the receiving-end MMC $\hat{\boldsymbol{i}}_{\text{eqref}}$. Next, the small-signal vectors of the three-phase AC currents $\hat{\boldsymbol{i}}_{el}$ and PLL output angle $\hat{\boldsymbol{\theta}}_{\text{ePLL}}$ in the receiving-end MMC lead to small-signal responses of the dq-axis currents in the receiving-end MMC $\hat{\boldsymbol{i}}_{\text{ed}}, \hat{\boldsymbol{i}}_{\text{eq}}$. Then, $\hat{\boldsymbol{i}}_{\text{ed}}, \hat{\boldsymbol{i}}_{\text{eq}}$ and their references $\hat{\boldsymbol{i}}_{\text{edref}}, \hat{\boldsymbol{i}}_{\text{eqref}}$ are fed into the AC current controller $H_{\text{eiac}}(s)$, leading to small-signal responses of the dq-axis modulation signal in the receiving-end MMC $\hat{\boldsymbol{m}}_{\text{ed}}, \hat{\boldsymbol{m}}_{\text{eq}}$. Finally, the small-signal vectors of the three-phase arm DM modulation signals in the receiving-end MMC $\hat{\boldsymbol{m}}_{\text{edif}l}$ are generated after the inverse Park transformation. Taking phase a as an example, the expression of $\hat{\boldsymbol{m}}_{\text{edifa}}$ is

$$\hat{\boldsymbol{m}}_{\text{edifa}} = \boldsymbol{G}_{\text{e1}}\boldsymbol{D}_{\text{e1}}\hat{\boldsymbol{i}}_{\text{eau}} + \boldsymbol{G}_{\text{e2}}\boldsymbol{D}_{\text{e2}}\hat{\boldsymbol{v}}_{\text{ea}} + \boldsymbol{G}_{\text{e3}}\boldsymbol{D}_{\text{e3}}\hat{\boldsymbol{v}}_{\text{edc}} \tag{11.84}$$

where $\boldsymbol{G}_{\text{e1}}, \boldsymbol{G}_{\text{e2}}, \boldsymbol{G}_{\text{e3}}$ are $(2g+1)\times(2g+1)$ matrices, and all other elements in the matrices are zero except for Eqs. (11.85)–(11.87).

$$\begin{aligned}\boldsymbol{G}_{\text{e1}}(g+k+1, g+k+1) = {} & |\text{mod}(k+1,3)| \cdot [1+(-1)^k] \\ & \cdot \left\{-H_{\text{eiac}}[\text{j}2\pi(f_{\text{p}}+kf_1-\text{mod}(k+1,3)f_1)]\right. \\ & \left. +\ \text{mod}(k+1,3)\text{j}K_{\text{ed}}\right\}\end{aligned} \tag{11.85}$$

$$\begin{cases}\boldsymbol{G}_{\text{e2}}(g-1, g-1) = T_{\text{ePLL}}[\text{j}2\pi(f_{\text{p}}-f_1)] \cdot \left[2\left\{H_{\text{eiac}}[\text{j}2\pi(f_{\text{p}}-f_1)]+\text{j}K_{\text{ed}}\right\}\right. \\ \qquad\qquad \left. \cdot \boldsymbol{I}^*_{\text{eau1}} - \boldsymbol{M}^*_{\text{eau1}} - k_{\text{ev}}V_{\text{e1}}\right] + \text{j}H_{\text{eiac}}[\text{j}2\pi(f_{\text{p}}-f_1)] \\ \qquad\qquad \cdot Q_{\text{ref}}/(3V_{\text{e1}}^2) + k_{\text{ev}} \\ \boldsymbol{G}_{\text{e2}}(g-1, g+1) = -T_{\text{ePLL}}[\text{j}2\pi(f_{\text{p}}-f_1)] \cdot \left[2\left\{H_{\text{eiac}}[\text{j}2\pi(f_{\text{p}}-f_1)]+\text{j}K_{\text{ed}}\right\}\right. \\ \qquad\qquad \left. \cdot \boldsymbol{I}^*_{\text{eau1}} - \boldsymbol{M}^*_{\text{eau1}} - k_{\text{ev}}V_{\text{e1}}\right] + \text{j}H_{\text{eiac}}[\text{j}2\pi(f_{\text{p}}-f_1)] \\ \qquad\qquad \cdot Q_{\text{ref}}/(3V_{\text{e1}}^2) \\ \boldsymbol{G}_{\text{e2}}(g+1, g-1) = -T_{\text{ePLL}}[\text{j}2\pi(f_{\text{p}}-f_1)] \cdot \left[2\left\{H_{\text{eiac}}[\text{j}2\pi(f_{\text{p}}-f_1)]-\text{j}K_{\text{ed}}\right\}\right. \\ \qquad\qquad \left. \cdot \boldsymbol{I}_{\text{eau1}} - \boldsymbol{M}_{\text{eau1}} - k_{\text{ev}}V_{\text{e1}}\right] - \text{j}H_{\text{eiac}}[\text{j}2\pi(f_{\text{p}}-f_1)] \\ \qquad\qquad \cdot Q_{\text{ref}}/(3V_{\text{e1}}^2) \\ \boldsymbol{G}_{\text{e2}}(g+1, g+1) = T_{\text{ePLL}}[\text{j}2\pi(f_{\text{p}}-f_1)] \cdot \left[2\left\{H_{\text{eiac}}[\text{j}2\pi(f_{\text{p}}-f_1)]-\text{j}K_{\text{ed}}\right\}\right. \\ \qquad\qquad \left. \cdot \boldsymbol{I}_{\text{eau1}} - \boldsymbol{M}_{\text{eau1}} - k_{\text{ev}}V_{\text{e1}}\right] - \text{j}H_{\text{eiac}}[\text{j}2\pi(f_{\text{p}}-f_1)] \\ \qquad\qquad \cdot Q_{\text{ref}}/(3V_{\text{e1}}^2) + k_{\text{ev}}\end{cases} \tag{11.86}$$

$$\begin{aligned}\boldsymbol{G}_{\text{e3}}(g+k+1, g+k) &= \boldsymbol{G}_{\text{e3}}(g+k-1, g+k) \\ &= |\text{mod}(k+1,3)| \cdot \frac{1+(-1)^k}{4} \\ &\quad \cdot H_{\text{vdc}}[\text{j}2\pi(f_{\text{p}}+kf_1-\text{mod}(k+1,3)f_1)]\end{aligned}$$

$$\cdot H_{\text{eiac}}[\text{j}2\pi(f_\text{p} + kf_1 - \text{mod}(k+1,3)f_1)] \tag{11.87}$$

where voltage feedforward coefficient k_{ev} is equal to 1.

Since the AC current control, PLL control, and DC voltage control are implemented in the MMC-HVDC system pole control, $\boldsymbol{D}_{\text{e1}}$, $\boldsymbol{D}_{\text{e2}}$, $\boldsymbol{D}_{\text{e3}}$ in Eq. (11.61) are the time delay transfer function matrices of the AC current control, PLL control, and DC voltage control in the receiving-end MMC respectively, which can be expressed as

$$\boldsymbol{D}_{\text{e1}} = \text{diag}\left[\left\{\text{e}^{-\text{j}2\pi(f_\text{p}+kf_1)T_{\text{epol}}}\frac{1-\text{e}^{-\text{j}2\pi(f_\text{p}+kf_1)T_{\text{epol}}}}{\text{j}2\pi(f_\text{p}+kf_1)T_{\text{epol}}}\frac{1}{1+\text{j}2\pi(f_\text{p}+kf_1)T_{\text{eiac}}}\right\}\Big|_{k=-g,\ldots,0,\ldots,g}\right] \tag{11.88}$$

$$\boldsymbol{D}_{\text{e2}} = \text{diag}\left[\left\{\text{e}^{-\text{j}2\pi(f_\text{p}+kf_1)T_{\text{epol}}}\frac{1-\text{e}^{-\text{j}2\pi(f_\text{p}+kf_1)T_{\text{epol}}}}{\text{j}2\pi(f_\text{p}+kf_1)T_{\text{epol}}}\frac{1}{1+\text{j}2\pi(f_\text{p}+kf_1)T_{\text{evac}}}\right\}\Big|_{k=-g,\ldots,0,\ldots,g}\right] \tag{11.89}$$

$$\boldsymbol{D}_{\text{e3}} = \text{diag}\left[\left\{\text{e}^{-\text{j}2\pi(f_\text{p}+kf_1)T_{\text{epol}}}\frac{1-\text{e}^{-\text{j}2\pi(f_\text{p}+kf_1)T_{\text{epol}}}}{\text{j}2\pi(f_\text{p}+kf_1)T_{\text{epol}}}\frac{1}{1+\text{j}2\pi(f_\text{p}+kf_1)T_{\text{evdc}}}\right\}\Big|_{k=-g,\ldots,0,\ldots,g}\right] \tag{11.90}$$

where T_{epol} is the control period of the receiving-end MMC pole control. T_{eiac}, T_{evac}, T_{evdc} are the filter time delay of the AC current, AC voltage, and DC voltage in the receiving-end MMC, respectively.

Circulating Current Control Firstly, after the negative-sequence second-harmonic Park transformation to the three-phase arm circulating currents, the small-signal vectors of the dq-axis circulating currents $\hat{\boldsymbol{i}}_{\text{ecd}}$, $\hat{\boldsymbol{i}}_{\text{ecq}}$ in the sending-end MMC are produced. Then, in the effect of the circulating current controller $H_{\text{eic}}(s)$, the small-signal responses of the dq-axis circulating modulation signals $\hat{\boldsymbol{m}}_{\text{ecd}}$, $\hat{\boldsymbol{m}}_{\text{ecq}}$ in the sending-end MMC are generated. Finally, the small-signal vectors of the three-phase arm CM modulation signals $\hat{\boldsymbol{m}}_{\text{ecom}l}$ in the sending-end MMC are generated after the corresponding inverse Park transformation. Taking phase a as an example, the expression of $\hat{\boldsymbol{m}}_{\text{ecoma}}$ is

$$\hat{\boldsymbol{m}}_{\text{ecoma}} = \boldsymbol{G}_{\text{e4}}\boldsymbol{D}_{\text{e4}}\hat{\boldsymbol{i}}_{\text{eau}} + \boldsymbol{G}_{\text{e5}}\boldsymbol{D}_{\text{e2}}\hat{\boldsymbol{v}}_{\text{ea}} \tag{11.91}$$

where $\boldsymbol{G}_{\text{e4}}$, $\boldsymbol{G}_{\text{e5}}$ are $(2g+1)\times(2g+1)$ matrices; all other elements in the matrices are zero except for Eqs. (11.92) and (11.93).

$$\begin{aligned}\boldsymbol{G}_{\mathrm{e4}}(g+k+1,g+k+1)=&\frac{1-(-1)^k}{2}\cdot|\mathrm{mod}(k+1,3)|\\&\cdot\{H_{\mathrm{eic}}[\mathrm{j}2\pi(f_{\mathrm{p}}+kf_1+\mathrm{mod}(k+1,3)\cdot 2f_1)]\\&-\mathrm{mod}(k+1,3)\mathrm{j}K_{\mathrm{eic}}\}\end{aligned}\tag{11.92}$$

$$\begin{cases}\boldsymbol{G}_{\mathrm{e5}}(g-2,g-1)=-\boldsymbol{G}_{\mathrm{e5}}(g-2,g+1)\\\qquad\qquad=2T_{\mathrm{ePLL}}[\mathrm{j}2\pi(f_{\mathrm{p}}-f_1)]\\\qquad\qquad\cdot\left[\left\{-H_{\mathrm{eic}}[\mathrm{j}2\pi(f_{\mathrm{p}}-f_1)]+\mathrm{j}K_{\mathrm{eic}}\right\}\boldsymbol{I}^*_{\mathrm{eau2}}+\boldsymbol{M}^*_{\mathrm{eau2}}\right]\\\boldsymbol{G}_{\mathrm{e5}}(g+2,g-1)=-\boldsymbol{G}_{\mathrm{e5}}(g+2,g+1)\\\qquad\qquad=2T_{\mathrm{ePLL}}[\mathrm{j}2\pi(f_{\mathrm{p}}-f_1)]\\\qquad\qquad\cdot\left[\left\{H_{\mathrm{eic}}[\mathrm{j}2\pi(f_{\mathrm{p}}-f_1)]+\mathrm{j}K_{\mathrm{eic}}\right\}\boldsymbol{I}_{\mathrm{eau2}}-\boldsymbol{M}_{\mathrm{eau2}}\right]\end{cases}\tag{11.93}$$

Since the circulating current control is implemented in the MMC-HVDC system valve control, $\boldsymbol{D}_{\mathrm{e4}}$ in Eq. (11.91) is the time delay transfer function matrix of the circulating current control in the receiving-end MMC, expressed as

$$\begin{aligned}&\boldsymbol{D}_{\mathrm{e4}}\\&=\mathrm{diag}\left[\left\{\mathrm{e}^{-\mathrm{j}2\pi(f_{\mathrm{p}}+kf_1)T_{\mathrm{eval}}}\frac{1-\mathrm{e}^{-\mathrm{j}2\pi(f_{\mathrm{p}}+kf_1)T_{\mathrm{eval}}}}{\mathrm{j}2\pi(f_{\mathrm{p}}+kf_1)T_{\mathrm{eval}}}\frac{1}{1+\mathrm{j}2\pi(f_{\mathrm{p}}+kf_1)T_{\mathrm{eic}}}\right\}\Big|_{k=-g,\ldots,0,\ldots,g}\right]\end{aligned}\tag{11.94}$$

where T_{eval} is the control period of the receiving-end MMC valve control. T_{eic} is the filter time delay of the circulating current in the receiving-end MMC.

Arm Modulation Signal Based on Eqs. (11.84) and (11.91), the small-signal vector of the phase-a upper arm modulation signal of the receiving-end MMC $\hat{\boldsymbol{m}}_{\mathrm{eau}}$ can be obtained.

$$\hat{\boldsymbol{m}}_{\mathrm{eau}}=\boldsymbol{G}_{\mathrm{ei}}\hat{\boldsymbol{i}}_{\mathrm{eau}}+\boldsymbol{G}_{\mathrm{ev1}}\hat{\boldsymbol{v}}_{\mathrm{ea}}+\boldsymbol{G}_{\mathrm{ev2}}\hat{\boldsymbol{v}}_{\mathrm{edc}}\tag{11.95}$$

where $\boldsymbol{G}_{\mathrm{ei}}$, $\boldsymbol{G}_{\mathrm{ev1}}$, $\boldsymbol{G}_{\mathrm{ev2}}$ are

$$\begin{cases}\boldsymbol{G}_{\mathrm{ei}}=-\boldsymbol{G}_{\mathrm{e1}}\boldsymbol{D}_{\mathrm{e1}}+\boldsymbol{G}_{\mathrm{e4}}\boldsymbol{D}_{\mathrm{e4}}\\\boldsymbol{G}_{\mathrm{ev1}}=-(\boldsymbol{G}_{\mathrm{e2}}+\boldsymbol{G}_{\mathrm{e5}})\boldsymbol{D}_{\mathrm{e2}}\\\boldsymbol{G}_{\mathrm{ev2}}=-\boldsymbol{G}_{\mathrm{e3}}\boldsymbol{D}_{\mathrm{e3}}\end{cases}\tag{11.96}$$

Based on the DM, CM, and phase-sequence relationships between the small-signal vectors, the small-signal vectors of the other arm modulation signals in the receiving-end MMC can also be obtained according to $\hat{\boldsymbol{m}}_{\mathrm{eau}}$.

11.3.2.3 Small-Signal Model of DC Transmission Lines

DC transmission lines provide the coupling path for the sending-end and receiving-end MMCs, and the receiving-end MMC will influence the operating characteristics of the sending-end MMC via the DC transmission lines. The equivalent model of the DC transmission lines is shown in Fig. 11.8.

In Fig. 11.8, the DC transmission lines are represented by n Π-line segments. R_{dcL}, L_{dcL}, C_{dcL} are line resistor, line inductor, and line capacitor in a single Π-line segment respectively. The DC transmission line length is l_{line}. According to the equivalent model, the frequency-domain small-signal model of the DC transmission lines can be expressed as

$$\begin{cases} \hat{\boldsymbol{v}}_{\mathrm{edc}} = \boldsymbol{Z}_{\mathrm{edc}} \hat{\boldsymbol{i}}_{\mathrm{edc}} \\ \hat{\boldsymbol{v}}_{\mathrm{fdc}} = \boldsymbol{Z}_{\mathrm{fdc}} \hat{\boldsymbol{i}}_{\mathrm{fdc}} \end{cases} \tag{11.97}$$

where $\boldsymbol{Z}_{\mathrm{edc}}$ is the DC port impedance of the receiving-end MMC, and $\boldsymbol{Z}_{\mathrm{fdc}}$ is the DC-side impedance of the sending-end MMC, seen from the DC port of the sending-end MMC to the receiving-end MMC.

The expression of $\boldsymbol{Z}_{\mathrm{fdc}}$ can be derived according to the following equation

$$\boldsymbol{Z}_{\mathrm{fdc}} = \boldsymbol{Z}_n + \boldsymbol{Z}_{\mathrm{Ldc}} \tag{11.98}$$

where $\boldsymbol{Z}_n$ represents the equivalent impedance of the Π-line segments with the receiving-end MMC considered. The subscript "n" denotes the number of the Π-line segments. $\boldsymbol{Z}_{\mathrm{Ldc}}$ is the impedance of the DC smoothing reactor. The expressions of $\boldsymbol{Z}_{\mathrm{Ldc}}$ and $\boldsymbol{Z}_n$ are

$$\boldsymbol{Z}_{\mathrm{Ldc}} = \mathrm{j}2\pi L_{\mathrm{dc}} \cdot \mathrm{diag}\left[f_{\mathrm{p}} - gf_1, \ldots, f_{\mathrm{p}} - f_1, f_{\mathrm{p}}, f_{\mathrm{p}} + f_1, \ldots, f_{\mathrm{p}} + gf_1 \right] \tag{11.99}$$

$$\begin{cases} \boldsymbol{Z}_0 = \boldsymbol{Z}_{\mathrm{edc}} + \boldsymbol{Z}_{\mathrm{Ldc}} \\ \boldsymbol{Z}_n = \left[(\boldsymbol{Z}_{n-1} \| \boldsymbol{Z}_{\mathrm{CdcL}}) + \boldsymbol{Z}_{\mathrm{LdcL}} + \boldsymbol{Z}_{\mathrm{RdcL}} \right] \| \boldsymbol{Z}_{\mathrm{CdcL}} \end{cases} \tag{11.100}$$

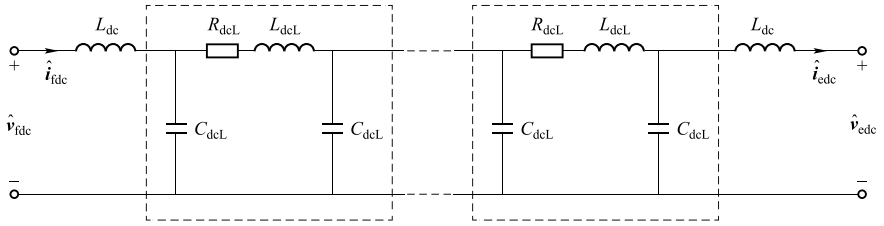

Fig. 11.8 The equivalent model of the DC transmission lines

where "||" represents the parallel operation. $\boldsymbol{Z}_0$ is the initial item of $\boldsymbol{Z}_n$. $\boldsymbol{Z}_{\mathrm{RdcL}}$, $\boldsymbol{Z}_{\mathrm{LdcL}}$, $\boldsymbol{Z}_{\mathrm{LdcL}}$ are the impedance of the line resistor, inductor, and capacitor in a single Π-line segment respectively, expressed as

$$\begin{cases} \boldsymbol{Z}_{\mathrm{RdcL}} = R_{\mathrm{dcL}}\boldsymbol{U} \\ \boldsymbol{Z}_{\mathrm{LdcL}} = \mathrm{j}2\pi L_{\mathrm{dcL}} \cdot \mathrm{diag}[f_{\mathrm{p}} - gf_1, \ldots, f_{\mathrm{p}} - f_1, f_{\mathrm{p}}, f_{\mathrm{p}} + f_1, \ldots, f_{\mathrm{p}} + gf_1] \\ \boldsymbol{Z}_{\mathrm{CdcL}} = \dfrac{1}{\mathrm{j}2\pi C_{\mathrm{dcL}}} \cdot \mathrm{diag}\left[\dfrac{1}{f_{\mathrm{p}} - gf_1}, \ldots, \dfrac{1}{f_{\mathrm{p}} - f_1}, \dfrac{1}{f_{\mathrm{p}}}, \dfrac{1}{f_{\mathrm{p}} + f_1}, \ldots, \dfrac{1}{f_{\mathrm{p}} + gf_1}\right] \end{cases} \tag{11.101}$$

11.3.3 AC Port Impedance Model

The AC port admittance of MMC-HVDC at the sending end can be obtained by calculating the ratio of the small-signal vectors of the sending-end three-phase AC currents and voltages, namely

$$\boldsymbol{Y}_{\mathrm{MMC}} = \frac{\hat{\boldsymbol{i}}_{fl}}{\hat{\boldsymbol{v}}_{fl}} \tag{11.102}$$

The AC port admittance of MMC-HVDC at the sending end is related to the sending-end and receiving-end MMCs. According to the small-signal models of the main circuit and control loops in the receiving-end MMC, the DC port admittance of the receiving-end MMC is obtained by combining Eqs. (11.78)–(11.82) and (11.95).

$$\boldsymbol{Y}_{\mathrm{edc}} = \frac{\hat{\boldsymbol{i}}_{\mathrm{edc}}}{\hat{\boldsymbol{v}}_{\mathrm{edc}}} = \boldsymbol{\Gamma}_6(\boldsymbol{\Gamma}_1 + \boldsymbol{\Gamma}_2\boldsymbol{\Gamma}_5 + \boldsymbol{\Gamma}_4)^{-1}\boldsymbol{\Gamma}_3 \tag{11.103}$$

where $\boldsymbol{\Gamma}_1$ is the transfer function matrix related to the AC current control and circulating current control of the receiving-end MMC. $\boldsymbol{\Gamma}_2$ is the transfer function matrix related to the PLL and AC current control of the receiving-end MMC. $\boldsymbol{\Gamma}_3$ is the transfer function matrix related to the DC voltage control and AC current control of the receiving-end MMC. $\boldsymbol{\Gamma}_4$ is the transfer function matrix related to the steady-state operating point at the receiving end. $\boldsymbol{\Gamma}_5$ is the transfer function matrix related to the receiving-end AC grid impedance. $\boldsymbol{\Gamma}_6$ is the transformation matrix of the zero-sequence CM vector. $\boldsymbol{\Gamma}_1$~$\boldsymbol{\Gamma}_6$ are $(2g+1) \times (2g+1)$ matrices, and their expressions are

$$\begin{cases} \boldsymbol{\Gamma}_1 = \left(\boldsymbol{V}_{\text{eCau}} + \boldsymbol{M}_{\text{eau}}\boldsymbol{Z}_{\text{Ceeq}}\boldsymbol{I}_{\text{eau}}\right)\boldsymbol{G}_{\text{ei}} \\ \boldsymbol{\Gamma}_2 = \left(\boldsymbol{V}_{\text{eCau}} + \boldsymbol{M}_{\text{eau}}\boldsymbol{Z}_{\text{Ceeq}}\boldsymbol{I}_{\text{eau}}\right)\boldsymbol{G}_{\text{ev1}} + \boldsymbol{U} \\ \boldsymbol{\Gamma}_3 = \left(\boldsymbol{V}_{\text{eCau}} + \boldsymbol{M}_{\text{eau}}\boldsymbol{Z}_{\text{Ceeq}}\boldsymbol{I}_{\text{eau}}\right)\boldsymbol{G}_{\text{ev2}} - \dfrac{1}{2}\boldsymbol{U} \\ \boldsymbol{\Gamma}_4 = \boldsymbol{M}_{\text{eau}}\boldsymbol{Z}_{\text{Ceeq}}\boldsymbol{M}_{\text{eau}} + \boldsymbol{Z}_{\text{Learm}} \\ \boldsymbol{\Gamma}_5 = 2\boldsymbol{Z}_{\text{eg}}\boldsymbol{A}_{\text{pd}} \\ \boldsymbol{\Gamma}_6 = -3\boldsymbol{A}_{\text{pc0}} \end{cases} \tag{11.104}$$

The DC port impedance of the receiving-end MMC is equal to the inverse of the DC port admittance, i.e., $\boldsymbol{Z}_{\text{edc}} = \boldsymbol{Y}_{\text{edc}}^{-1}$. According to the small-signal model of the DC transmission lines, the DC-side impedance of the sending-end MMC $\boldsymbol{Z}_{\text{fdc}}$ can be obtained by substituting $\boldsymbol{Z}_{\text{edc}}$ in Eq. (11.103) into Eq. (11.98).

According to the small-signal model of the sending-end MMC, combining Eqs. (11.52), (11.53), (11.57), (11.59), (11.69) and $\boldsymbol{Z}_{\text{fdc}}$, the AC port admittance of MMC-HVDC at the sending end can be derived as

$$\boldsymbol{Y}_{\text{MMC}} = \boldsymbol{\Lambda}_5(\boldsymbol{\Lambda}_1 + \boldsymbol{\Lambda}_3 + \boldsymbol{\Lambda}_4)^{-1}\boldsymbol{\Lambda}_2 \tag{11.105}$$

where $\boldsymbol{\Lambda}_1$ is the transfer function matrix related to the AC current control and circulating current control of the sending-end MMC. $\boldsymbol{\Lambda}_2$ is the transfer function matrix related to the AC voltage control (in passive islanding mode) or power control (in grid-connected mode) of the sending-end MMC. $\boldsymbol{\Lambda}_3$ is the transfer function matrix related to the steady-state operating point at the sending end. $\boldsymbol{\Lambda}_4$ is the transfer function matrix related to the DC-side impedance of the sending-end MMC. $\boldsymbol{\Lambda}_5$ is the transformation matrix of the DM vector. $\boldsymbol{\Lambda}_1 \sim \boldsymbol{\Lambda}_5$ are $(2g+1) \times (2g+1)$ matrices, and their expressions are

$$\begin{cases} \boldsymbol{\Lambda}_1 = \left(\boldsymbol{V}_{\text{fCau}} + \boldsymbol{M}_{\text{fau}}\boldsymbol{Z}_{\text{Cfeq}}\boldsymbol{I}_{\text{fau}}\right)\boldsymbol{G}_{\text{fi}} \\ \boldsymbol{\Lambda}_2 = \left(\boldsymbol{V}_{\text{fCau}} + \boldsymbol{M}_{\text{fau}}\boldsymbol{Z}_{\text{Cfeq}}\boldsymbol{I}_{\text{fau}}\right)\boldsymbol{G}_{\text{fv}} + \boldsymbol{U} \\ \boldsymbol{\Lambda}_3 = \boldsymbol{M}_{\text{fau}}\boldsymbol{Z}_{\text{Cfeq}}\boldsymbol{M}_{\text{fau}} + \boldsymbol{Z}_{\text{Lfarm}} \\ \boldsymbol{\Lambda}_4 = \dfrac{3}{2}\boldsymbol{Z}_{\text{fdc}}\boldsymbol{A}_{\text{pc0}} \\ \boldsymbol{\Lambda}_5 = 2\boldsymbol{A}_{\text{pd}} \end{cases} \tag{11.106}$$

According to the small-signal model of the control loops in the sending-end MMC as shown in Eqs. (11.70) and (11.77), substituting $\boldsymbol{G}_{\text{fi}}$, $\boldsymbol{G}_{\text{fv}}$ into Eq. (11.105), the AC port admittance of MMC-HVDC at the sending end in passive islanding mode and grid-connected mode can be developed, respectively.

The small-signal components at f_{p} and $f_{\text{p}} - 2f_1$ are the main components in the small-signal vectors of the AC voltage and current of MMC-HVDC, while the amplitudes of the other components are relatively small. The characteristics of the AC port impedance or admittance at f_{p} and $f_{\text{p}} - 2f_1$ are more significant.

First, the AC port impedance or admittance of the MMC-HVDC at the sending end in passive islanding mode is analyzed. The relationship between the small-signal vectors of the AC voltage and current and AC port impedance at f_p and $f_\mathrm{p} - 2f_\mathrm{l}$ is reformulated as

$$\begin{bmatrix} \hat{\boldsymbol{v}}_\mathrm{f} \\ \hat{\boldsymbol{v}}_\mathrm{f\text{-}2} \end{bmatrix} = \begin{bmatrix} \boldsymbol{Z}_\mathrm{MMC}^\mathrm{pp} & \boldsymbol{Z}_\mathrm{MMC}^\mathrm{np} \\ \boldsymbol{Z}_\mathrm{MMC}^\mathrm{pn} & \boldsymbol{Z}_\mathrm{MMC}^\mathrm{nn} \end{bmatrix} \begin{bmatrix} \hat{\boldsymbol{i}}_\mathrm{f} \\ \hat{\boldsymbol{i}}_\mathrm{f\text{-}2} \end{bmatrix} \tag{11.107}$$

where $\hat{\boldsymbol{v}}_\mathrm{f}$ and $\hat{\boldsymbol{v}}_\mathrm{f\text{-}2}$ are the small-signal components of sending-end AC voltages at f_p and $f_\mathrm{p} - 2f_\mathrm{l}$ resepectively. $\hat{\boldsymbol{i}}_\mathrm{f}$ and $\hat{\boldsymbol{i}}_\mathrm{f\text{-}2}$ are the small-signal components of sending-end AC currents at f_p and $f_\mathrm{p} - 2f_\mathrm{l}$ resepectively. The expression of the 2×2 AC port impedance matrix in passive islanding mode is

$$\begin{bmatrix} \boldsymbol{Z}_\mathrm{MMC}^\mathrm{pp} & \boldsymbol{Z}_\mathrm{MMC}^\mathrm{np} \\ \boldsymbol{Z}_\mathrm{MMC}^\mathrm{pn} & \boldsymbol{Z}_\mathrm{MMC}^\mathrm{nn} \end{bmatrix} = \begin{bmatrix} \boldsymbol{Y}_\mathrm{MMC}(g+1, g+1) & \boldsymbol{Y}_\mathrm{MMC}(g+1, g-1) \\ \boldsymbol{Y}_\mathrm{MMC}(g-1, g+1) & \boldsymbol{Y}_\mathrm{MMC}(g-1, g-1) \end{bmatrix}^{-1}$$

in which

$\boldsymbol{Z}_\mathrm{MMC}^\mathrm{pp}$ is the positive-sequence impedance of MMC-HVDC at the sending end, representing the small-signal response of AC voltage at f_p in positive sequence under per unit small-signal perturbation of AC current at f_p in positive sequence.
$\boldsymbol{Z}_\mathrm{MMC}^\mathrm{pn}$ is the positive-sequence coupled impedance of MMC-HVDC at the sending end, representing the small-signal response of AC voltage at $f_\mathrm{p} - 2f_\mathrm{l}$ in negative sequence under per unit small-signal perturbation of AC current at f_p in positive sequence.
$\boldsymbol{Z}_\mathrm{MMC}^\mathrm{nn}$ is the negative-sequence impedance of MMC-HVDC at the sending end, representing the small-signal response of AC voltage at $f_\mathrm{p} - 2f_\mathrm{l}$ in negative sequence under per unit small-signal perturbation of AC current at $f_\mathrm{p} - 2f_\mathrm{l}$ in negative sequence.
$\boldsymbol{Z}_\mathrm{MMC}^\mathrm{np}$ is the negative-sequence coupled impedance of MMC-HVDC at the sending end, representing the small-signal response of AC voltage at f_p in positive sequence under per unit small-signal perturbation of AC current at $f_\mathrm{p} - 2f_\mathrm{l}$ in negative sequence.
$\boldsymbol{Y}_\mathrm{MMC}(g+1, g+1)$ is the element in the $(g+1)$th row and the $(g+1)$th column of $\boldsymbol{Y}_\mathrm{MMC}$.
$\boldsymbol{Y}_\mathrm{MMC}(g+1, g-1)$ is the element in the $(g+1)$th row and the $(g-1)$th column of $\boldsymbol{Y}_\mathrm{MMC}$.
$\boldsymbol{Y}_\mathrm{MMC}(g-1, g+1)$ is the element in the $(g-1)$th row and the $(g+1)$th column of $\boldsymbol{Y}_\mathrm{MMC}$.
$\boldsymbol{Y}_\mathrm{MMC}(g-1, g-1)$ is the element in the $(g-1)$th row and the $(g-1)$th column of $\boldsymbol{Y}_\mathrm{MMC}$.

Then, the AC port impedance or admittance of the MMC-HVDC at the sending end in grid-connected mode is analyzed. The relationship between the small-signal vectors of the AC voltage and current and AC port admittance at f_p and $f_\mathrm{p} - 2f_\mathrm{l}$ is

reformulated as

$$\begin{bmatrix} \hat{\boldsymbol{i}}_{\mathrm{f}} \\ \hat{\boldsymbol{i}}_{\mathrm{f\text{-}2}} \end{bmatrix} = \begin{bmatrix} \boldsymbol{Y}_{\mathrm{MMC}}^{\mathrm{pp}} & \boldsymbol{Y}_{\mathrm{MMC}}^{\mathrm{np}} \\ \boldsymbol{Y}_{\mathrm{MMC}}^{\mathrm{pn}} & \boldsymbol{Y}_{\mathrm{MMC}}^{\mathrm{nn}} \end{bmatrix} \begin{bmatrix} \hat{\boldsymbol{v}}_{\mathrm{f}} \\ \hat{\boldsymbol{v}}_{\mathrm{f\text{-}2}} \end{bmatrix} \tag{11.108}$$

where the expression of the 2×2 AC port admittance matrix in grid-connected mode is

$$\begin{bmatrix} \boldsymbol{Y}_{\mathrm{MMC}}^{\mathrm{pp}} & \boldsymbol{Y}_{\mathrm{MMC}}^{\mathrm{np}} \\ \boldsymbol{Y}_{\mathrm{MMC}}^{\mathrm{pn}} & \boldsymbol{Y}_{\mathrm{MMC}}^{\mathrm{nn}} \end{bmatrix} = \begin{bmatrix} \boldsymbol{Y}_{\mathrm{MMC}}(g+1, g+1) & \boldsymbol{Y}_{\mathrm{MMC}}(g+1, g-1) \\ \boldsymbol{Y}_{\mathrm{MMC}}(g-1, g+1) & \boldsymbol{Y}_{\mathrm{MMC}}(g-1, g-1) \end{bmatrix}$$

where

$\boldsymbol{Y}_{\mathrm{MMC}}^{\mathrm{pp}}$ is the positive-sequence admittance of MMC-HVDC at the sending end, representing the small-signal response of AC current at f_{p} in positive sequence under per unit small-signal perturbation of AC voltage at f_{p} in positive sequence.
$\boldsymbol{Y}_{\mathrm{MMC}}^{\mathrm{pn}}$ is the positive-sequence coupled admittance of MMC-HVDC at the sending end, representing the small-signal response of AC current at $f_{\mathrm{p}} - 2f_1$ in negative sequence under per unit small-signal perturbation of AC voltage at f_{p} in positive sequence.
$\boldsymbol{Y}_{\mathrm{MMC}}^{\mathrm{nn}}$ is the negative-sequence admittance of MMC-HVDC at the sending end, representing the small-signal response of AC current at $f_{\mathrm{p}} - 2f_1$ in negative sequence under per unit small-signal perturbation of AC voltage at $f_{\mathrm{p}} - 2f_1$ in negative sequence.
$\boldsymbol{Y}_{\mathrm{MMC}}^{\mathrm{np}}$ is the negative-sequence coupled admittance of MMC-HVDC at the sending end, representing the small-signal response of AC current at f_{p} in positive sequence under per unit small-signal perturbation of AC voltage at $f_{\mathrm{p}} - 2f_1$ in negative sequence.

The AC port impedance of MMC-HVDC at the sending end in grid-connected mode can be obtained by calculating the inverse matrix of the AC port admittance as

$$\begin{bmatrix} \boldsymbol{Z}_{\mathrm{MMC}}^{\mathrm{pp}} & \boldsymbol{Z}_{\mathrm{MMC}}^{\mathrm{pn}} \\ \boldsymbol{Z}_{\mathrm{MMC}}^{\mathrm{np}} & \boldsymbol{Z}_{\mathrm{MMC}}^{\mathrm{nn}} \end{bmatrix} = \begin{bmatrix} \boldsymbol{Y}_{\mathrm{MMC}}^{\mathrm{pp}} & \boldsymbol{Y}_{\mathrm{MMC}}^{\mathrm{np}} \\ \boldsymbol{Y}_{\mathrm{MMC}}^{\mathrm{pn}} & \boldsymbol{Y}_{\mathrm{MMC}}^{\mathrm{nn}} \end{bmatrix}^{-1}$$

where

$\boldsymbol{Z}_{\mathrm{MMC}}^{\mathrm{pp}}$ represents the positive-sequence impedance of MMC-HVDC at the sending end and is the element in the first row and the first column of the AC port admittance inverse matrix.
$\boldsymbol{Z}_{\mathrm{MMC}}^{\mathrm{pn}}$ represents the positive-sequence coupled impedance of MMC-HVDC at the sending end and is the element in the first row and the second column of the AC port admittance inverse matrix.

$\boldsymbol{Z}_{\mathrm{MMC}}^{\mathrm{nn}}$ represents the negative-sequence impedance of MMC-HVDC at the sending end and is the element in the second row and the second column of the AC port admittance inverse matrix.
$\boldsymbol{Z}_{\mathrm{MMC}}^{\mathrm{np}}$ represents the negative-sequence coupled impedance of MMC-HVDC at the sending end and is the element in the second row and the first column of the AC port admittance inverse matrix.

Besides, both in passive islanding mode and grid-connected mode, the frequency-domain relationship between the negative-sequence impedance and the positive-sequence impedance satisfies $\boldsymbol{Z}_{\mathrm{MMC}}^{\mathrm{nn}} = \boldsymbol{Z}_{\mathrm{MMC}}^{\mathrm{pp*}}(\mathrm{j}2\omega_1 - s)$, and the frequency-domain relationship between the negative-sequence coupling impedance and the positive-sequence coupled impedance satisfies $\boldsymbol{Z}_{\mathrm{MMC}}^{\mathrm{np}} = \boldsymbol{Z}_{\mathrm{MMC}}^{\mathrm{pn*}}(\mathrm{j}2\omega_1 - s)$.

The main circuit and controller parameters of MMC-HVDC are listed in Table 11.3. Fig. 11.9 shows the analytical (in solid lines) and scanning (in discrete points) results of the AC port impedance of MMC-HVDC at the sending end in passive islanding mode. As seen from the figure, all the discrete points fall on the solid lines, which verifies the accuracy of the established impedance model of MMC-HVDC in passive islanding mode.

Different from the passive islanding mode, the PLL control, not AC voltage control, is adopted in grid-connected mode. The proportional and integral coefficients of the PLL controller in the sending-end MMC are 3.51×10^{-4} and 0.0441 respectively. The proportional and integral coefficients of the AC current controller in the sending-end MMC are 3.47×10^{-5} and 0.0436 respectively. The other main circuit and controller parameters of MMC-HVDC are consistent with Table 11.3. Fig. 11.10 shows the analytical (in solid lines) and scanning (in discrete points) results of the AC port impedance of MMC-HVDC at the sending end in grid-connected mode. As seen from the figure, all the discrete points fall on the solid lines, which verifies the accuracy of the established impedance model of MMC-HVDC in grid-connected mode.

11.4 Impedance Characteristic Analysis of Passive Islanding Mode MMC-HVDC

Based on the established impedance model of MMC-HVDC in passive islanding mode, this section first analyzes the dominant factors of the impedance characteristics in different frequency bands, and proposes the frequency band division method of MMC-HVDC. Then, the frequency-band overlapping effect of the multiple control loops or links and the negative damping characteristics in each frequency band are clarified. Finally, based on the CHIL scanning result of MMC-HVDC impedance, the typical values of each frequency band are given.

Table 11.3 Main circuit and controller parameters of MMC-HVDC

Parameter	Definition	Value
P_N	Rated Power	1000 MW
V_{dcref}	DC voltage reference	640 kV
V_{f1}, V_{e1}	Amplitude of the fundamental component of the AC voltage of the sending-end and receiving-end MMC	310 kV
N_f, N_e	Arm SM number of the sending-end and receiving-end MMC	256
C_{fsm}, C_{esm}	SM capacitance of the sending-end and receiving-end MMC	8 mF
L_{farm}, L_{earm}	Arm inductance of the sending-end and receiving-end MMC	46.6 mH
SCR	Short circuit ratio at the receiving end	3.0
L_{dc}	DC smoothing reactance	25 mH
l_{line}	DC transmission line length	200 km
R_{dcL}	Line resistance in a single Π-line segment	0.0033 Ω/km
L_{dcL}	Line inductance in a single Π-line segment	0.2 mH/km
C_{dcL}	Line capacitance in a single Π-line segment	0.015 μF/km
K_{vacp}, K_{vaci}	Proportional and integral coefficients of the AC voltage controller	0.1000, 1
K_{fiacp}, K_{fiaci}	Proportional and integral coefficients of the AC current controller in the sending-end MMC	1.0600×10^{-5}, 0.0019
K_{ficp}, K_{fici}	Proportional and integral coefficients of the circulating current controller in the sending-end MMC	2.0800×10^{-5}, 0.0079
K_{epp}, K_{epi}	Proportional and integral coefficients of the PLL controller in the receiving-end MMC	3.5100×10^{-4}, 0.0441
K_{vdcp}, K_{vdci}	Proportional and integral coefficients of the DC voltage controller	0.0001, 10
K_{eiacp}, K_{eiaci}	Proportional and integral coefficients of the AC current controller in the receiving-end MMC	2.6030×10^{-5}, 0.0245
K_{eicp}, K_{eici}	Proportional and integral coefficients of the circulating current controller in the receiving-end MMC	1.3880×10^{-5}, 0.0035

11.4.1 Frequency-Band Division of Broadband Impedance

The impedance characteristics of MMC-HVDC at the sending end are influenced by the multiple control loops or links of the sending-end and receiving-end MMCs. This section establishes the frequency-domain relationship between the impedance characteristics, control loop bandwidth and PM in passive islanding mode. The dominant factor of the impedance characteristics in each frequency band is clarified, and the frequency band division method is proposed.

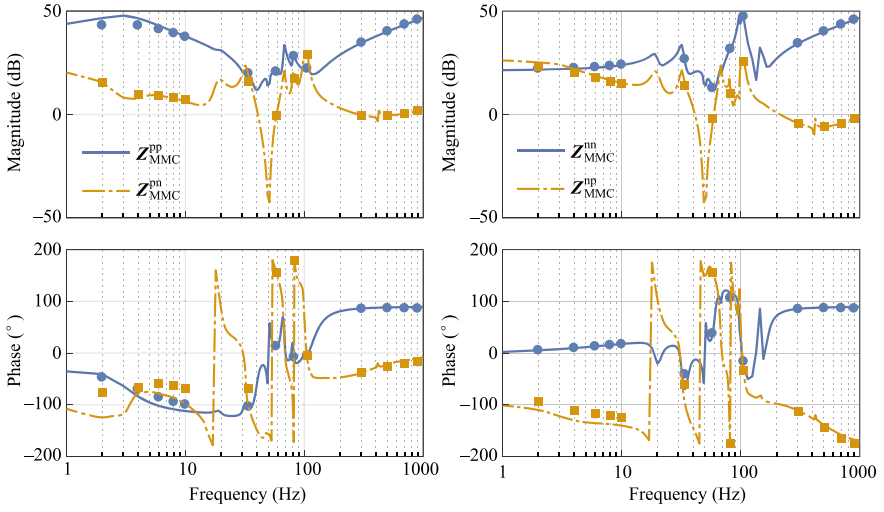

(a) Positive-sequence impedance and positive-sequence coupling impedance

(b) Negative-sequence impedance and negative-sequence coupling impedance

Fig. 11.9 The analytical and scanning results of the AC port impedance of MMC-HVDC at the sending end (in passive islanding mode)

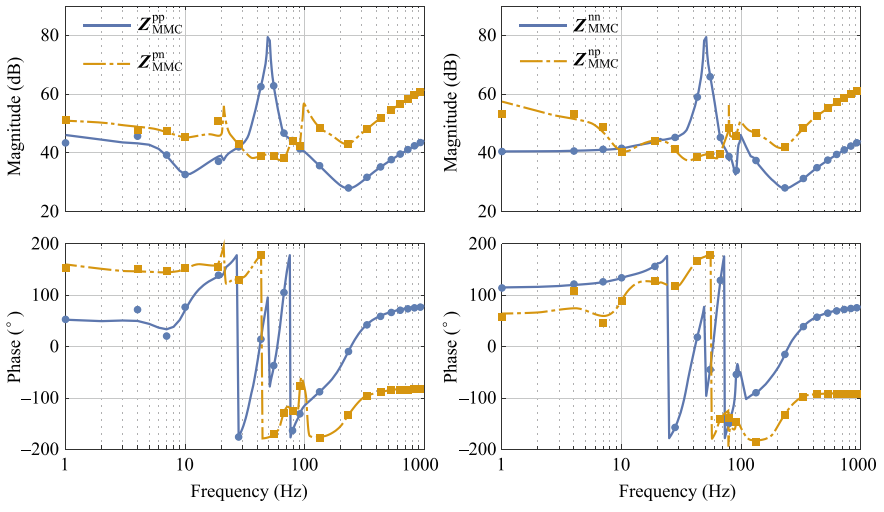

(a) Positive-sequence impedance and positive-sequence coupling impedance

(b) Negative-sequence impedance and negative-sequence coupling impedance

Fig. 11.10 The analytical and scanning results of the AC port impedance of MMC-HVDC at the sending end (in grid-connected mode)

11.4.1.1 Influence of AC Voltage Loop in Sending-End MMC

The influence of the AC voltage control in the sending-end MMC on the AC port impedance at the sending end is analyzed as follows. The block diagram of the AC voltage loop (in passive islanding mode) is shown in Fig. 11.11a.

In the figure, $Z_{\text{load}}(s)$ is the sending-end AC load impedance, considering the influence of the REG plants. Since $Z_{\text{load}}(s)$ varies along with the output power and grid-connected units of REG, the influence of $Z_{\text{load}}(s)$ on the performance of the AC voltage control is complicated. The AC current loop is regarded as a unit gain function to simplify the block diagram of the AC voltage loop, as shown in Fig. 11.11b. Besides, the fundamental-frequency impedance is used to replace the AC load impedance in the broadband range, which can be expressed as

$$Z_{\text{load}}(s) = \frac{V_{\text{fl}}^2}{P_{\text{load}} - \text{j}Q_{\text{load}}} \tag{11.109}$$

where P_{load}, Q_{load} are the active and reactive power of the sending-end MMC respectively.

According to Fig. 11.11b, given the bandwidth and PM of the AC voltage loop f_{vac}, θ_{vac} in SRF, the coefficients of the AC voltage controller can be solved from the following equation

$$\begin{cases} |H_{\text{vac}}(s)Z_{\text{load}}(s)|_{s=\text{j}2\pi f_{\text{vac}}} = 1 \\ \angle(H_{\text{vac}}(s)Z_{\text{load}}(s))_{s=\text{j}2\pi f_{\text{vac}}} = \theta_{\text{vac}} - \pi \end{cases} \tag{11.110}$$

where the open-loop gain is 1 at f_{vac}, and the corresponding PM is θ_{vac}.

If the sending-end MMC operates at the unit power factor, $Z_{\text{load}}(s)$ is regarded as the resistive load. In this case, the numerator and denominator of the open-loop transfer function of the AC voltage loop are first order. With θ_{vac} equivalent to 20°, 45° and 70°, the variation of the open-loop transfer function of the AC voltage loop is shown in Fig. 11.12.

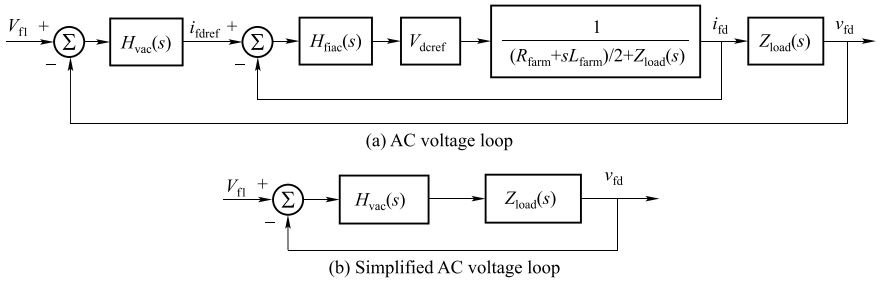

Fig. 11.11 The block diagram of the AC voltage loop (in passive islanding mode)

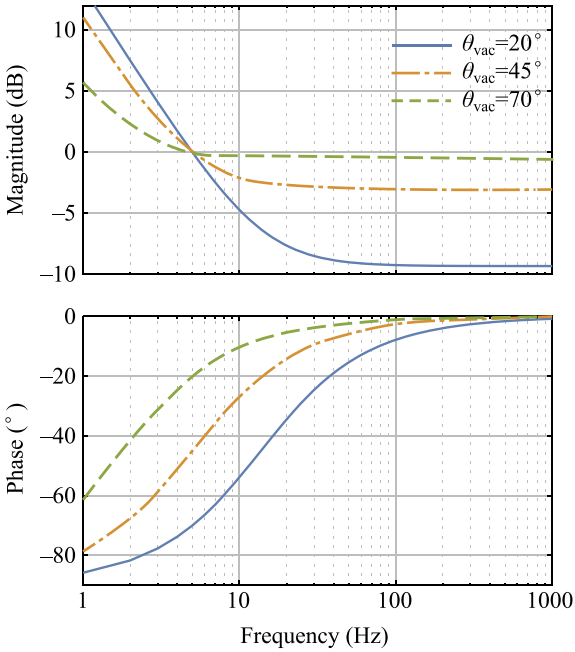

Fig. 11.12 The influence of the AC voltage loop PM on the open-loop transfer function

As seen from Fig. 11.12, θ_{vac} influences the characteristics of the open-loop transfer function of the AC voltage loop, especially in the high-frequency band. Furthermore, the broadband impedance characteristics of MMC-HVDC at the sending end will be influenced by the variation of θ_{vac}.

Assuming $Z_{load}(s)$ is regarded as the resistive and capacitive load, the influence of the AC voltage control on the impedance characteristics of MMC-HVDC at the sending is analyzed as follows. The influence of the AC voltage loop on the impedance characteristics (in passive islanding mode) is shown in Fig. 11.13. On the one hand, the influence of AC voltage loop bandwidth can be obtained by changing f_{vac} to 5, 10 and 15 Hz respectively with a constant PM of 45°. On the other hand, the influence of AC voltage loop PM can be obtained by changing θ_{vac} to 20°, 45° and 70° respectively with a constant bandwidth of 5 Hz.

As shown in Fig. 11.13, two resonant peaks appear in the impedance of MMC-HVDC at the sending end around $f_1 - f_{vac}$ and $f_1 + f_{vac}$. The change of the AC voltage loop bandwidth f_{vac} mainly influences the resonant frequencies. With the increase of f_{vac}, the two resonant frequencies are further away from the fundamental frequency. The change of the AC voltage loop PM θ_{vac} mainly influences the magnitudes and phases of the resonant peaks. With the increase of θ_{vac}, the impedance magnitude and phase change more flatly within the frequency band of $f_1 - f_{vac} < f < f_1 + f_{vac}$.

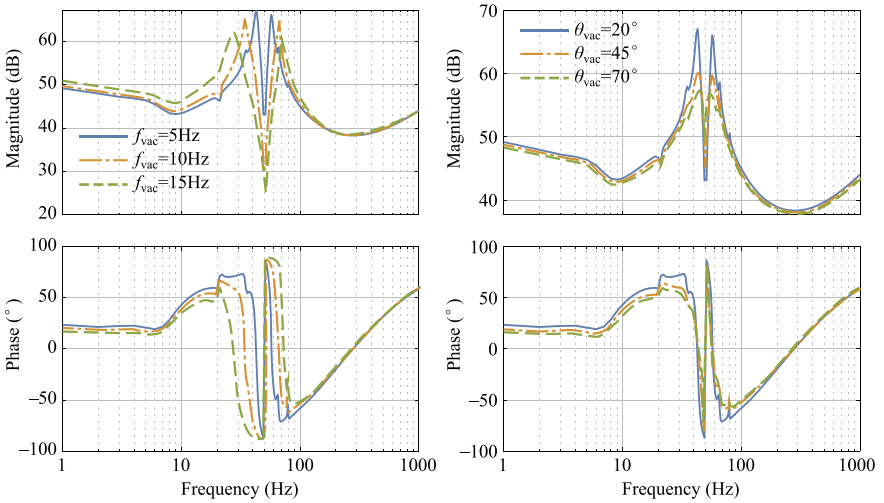

(a) Different AC voltage loop bandwidths (b) Different AC voltage loop PMs

Fig. 11.13 The influence of AC voltage loop in the sending-end MMC on the impedance characteristics (in passive islanding mode)

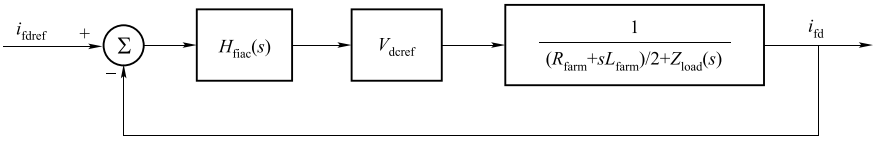

Fig. 11.14 The block diagram of the AC current loop (in passive islanding mode)

11.4.1.2 Influence of AC Current Loop in Sending-End MMC

The influence of the AC current control in the sending-end MMC on the AC port impedance at the sending end is analyzed as follows. The block diagram of the AC current loop (in passive islanding mode) is shown in Fig. 11.14.

Given the bandwidth and PM of the AC current loop f_{fiac}, θ_{fiac} in the sending-end MMC (in SRF), the coefficients of the AC current controller can be solved from the following equation

$$\begin{cases} \left| H_{fiac}(s) \dfrac{V_{dcref}}{(R_{farm}+sL_{farm})/2+Z_{load}(s)} \right|_{s=j2\pi f_{fiac}} = 1 \\ \angle\left(H_{fiac}(s) \dfrac{V_{dcref}}{(R_{farm}+sL_{farm})/2+Z_{load}(s)} \right)_{s=j2\pi f_{fiac}} = \theta_{fiac} - \pi \end{cases} \tag{11.111}$$

where the open-loop gain is 1 at f_{fiac}, and the corresponding PM is θ_{fiac}.

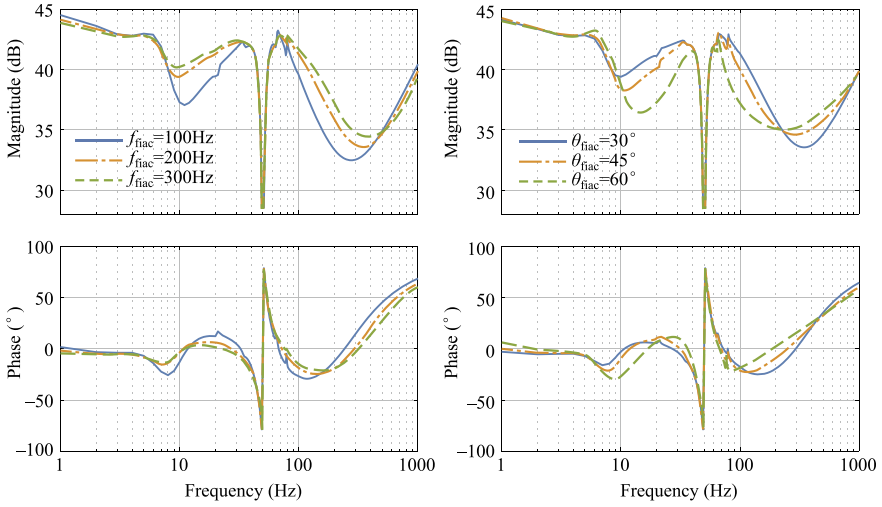

(a) Different AC current loop bandwidths (b) Different AC current loop PMs

Fig. 11.15 The influence of AC current loop in the sending-end MMC on the impedance characteristics (in passive islanding mode)

The influence of the AC current loop on the impedance characteristics of MMC-HVDC at the sending end (in passive islanding mode) is shown in Fig. 11.15. On the one hand, the influence of AC current loop bandwidth can be obtained by changing f_{fiac} to 100, 200 and 300 Hz respectively with a constant PM of 45°. On the other hand, the influence of AC current loop PM can be obtained by changing θ_{fiac} to 30°, 45° and 60° respectively with a constant bandwidth of 200 Hz.

As shown in Fig. 11.15, the AC current loop bandwidth f_{fiac} mainly influences the impedance characteristics within the frequency bands of $f < f_1 - f_{\text{vac}}$ and $f_1 + f_{\text{vac}} < f < f_1 + f_{\text{fiac}}$. With the increase of f_{fiac}, the impedance magnitudes within the two frequency bands increase. The AC voltage loop PM θ_{fiac} has an influence on the impedance characteristics in both $f < f_1 - f_{\text{vac}}$ and $f_1 + f_{\text{vac}} < f < f_1 + f_{\text{fiac}}$. With the increase of θ_{fiac}, the impedance magnitude and phase change more flatly within the two frequency bands.

11.4.1.3 Influence of Arm Inductor in Sending-End MMC

With the arm inductor of the sending-end MMC L_{farm} equivalent to 40, 50 and 60mH, the influence of the arm inductor on the impedance characteristics of MMC-HVDC at the sending end (in passive islanding mode) is shown in Fig. 11.16.

As shown in Fig. 11.16, the arm inductor of the sending-end MMC mainly influences the impedance characteristics in the frequency bands of $f < f_1 - f_{\text{vac}}$ and $f > f_1 + f_{\text{fiac}}$. With the increase of L_{farm}, the impedance magnitude and phase in

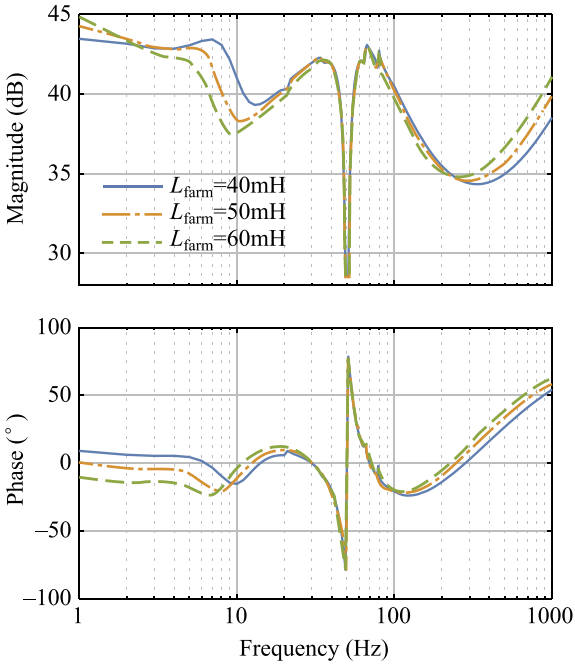

Fig. 11.16 The influence of the arm inductor in the sending-end MMC on the impedance characteristics (in passive islanding mode)

the frequency band of $f > f_1 + f_{fiac}$ increase, indicating that the impedance characteristics of MMC-HVDC at the sending end are dominated by the arm inductor of the sending-end MMC in the high-frequency band.

11.4.1.4 Influence of SM Capacitor in Sending-End MMC

With the arm number of sending-end MMC $N_f = 256$, and SM capacitor of the sending-end MMC C_{fsm} equivalent to 6, 8 and 10mF, the influence of the SM capacitor on the impedance characteristics of MMC-HVDC at the sending end (in passive islanding mode) is shown in Fig. 11.17.

As shown in Fig. 11.17, the SM capacitor of the sending-end MMC mainly influences the impedance characteristics within the frequency band of $f < f_1 - f_{vac}$. The SM capacitor and arm inductor form a passive resonant circuit, and the impedance magnitude exhibits a resonant peak in this frequency band. With the increase of C_{fsm}, the resonant frequency is reduced, and there are apparent changes in the impedance magnitude and phase.

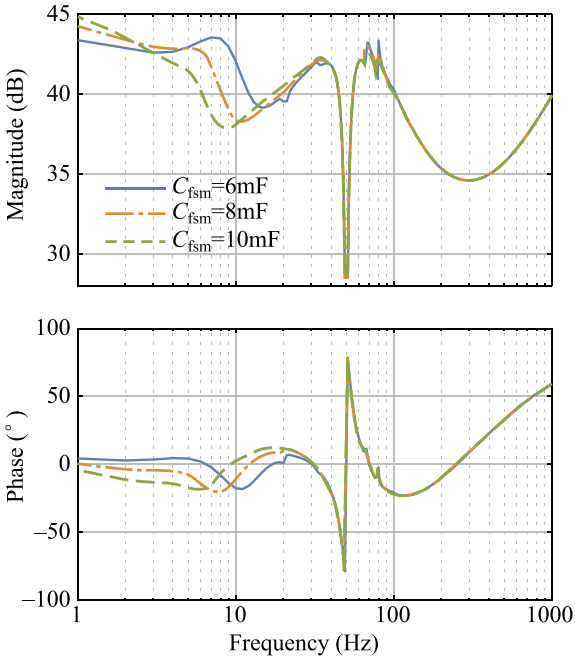

Fig. 11.17 The influence of the SM capacitor in the sending-end MMC on the impedance characteristics (in passive islanding mode)

11.4.1.5 Influence of Receiving-End MMC

The influence of the receiving-end MMC on the impedance characteristics of MMC-HVDC at the sending is analyzed as follows. First, without considering the impedance of the DC transmission lines and receiving-end MMC ($\boldsymbol{Z}_{\text{fdc}} = 0$), the impedance characteristics of MMC-HVDC at the sending are analyzed. Then, the influence of the DC transmission lines is taken into account, while the influence of receiving-end MMC is not considered ($\boldsymbol{Z}_{\text{edc}} = 0$). Finally, the influence of both the DC transmission lines and receiving-end MMC is considered ($\boldsymbol{Z}_{\text{fdc}} \neq 0$). The variation of the impedance curves of MMC-HVDC at the sending end in the three cases (in passive islanding mode) is shown in Fig. 11.18.

As shown in Fig. 11.18, the DC transmission lines and the receiving-end MMC mainly influence the impedance characteristics within the frequency band of $f < f_1 - f_{\text{vac}}$. If the impedance characteristics and oscillation risk evaluation above the fundamental frequency are concerned, the influence of the DC transmission lines and the receiving-end MMC can be ignored. If the impedance characteristics and oscillation risk evaluation below the fundamental frequency are concerned, the influence of the DC transmission lines and the receiving-end MMC should be considered.

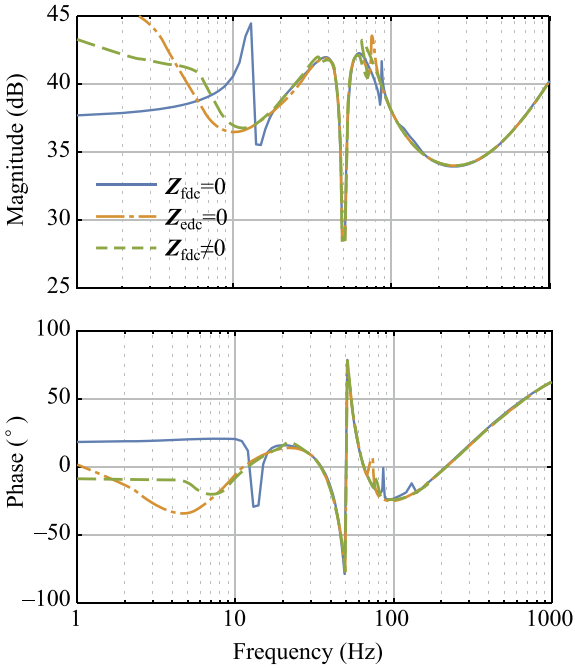

Fig. 11.18 The influence of the DC transmission lines and receiving-end MMC on the impedance characteristics (in passive islanding mode)

11.4.1.6 Influence of Steady-State Operating Point

Since the impedance model of MMC-HVDC is established based on the linearization method at the steady-state operating point, the impedance characteristics of MMC-HVDC will vary with the steady-state operating point, such as the power change. The influence of the active power changing from 0 to 1.0 p.u. on the impedance characteristics of MMC-HVDC at the sending (in passive islanding mode) is shown in Fig. 11.19.

As shown in Fig. 11.19, the change of the active power mainly influences the impedance characteristics below the fundamental frequency with little influence on the impedance characteristics above the fundamental frequency. When the active power changes from 0 to 1.0 p.u., the trends of the broadband impedance curves with frequency are similar, indicating that the steady-state operating point has little influence on the boundary of each frequency band.

11.4.1.7 Frequency-Band Division of Broadband Impedance

According to the analysis of the dominant factors of MMC-HVDC impedance characteristics in each frequency band (in passive islanding mode), the following frequency bands can be divided.

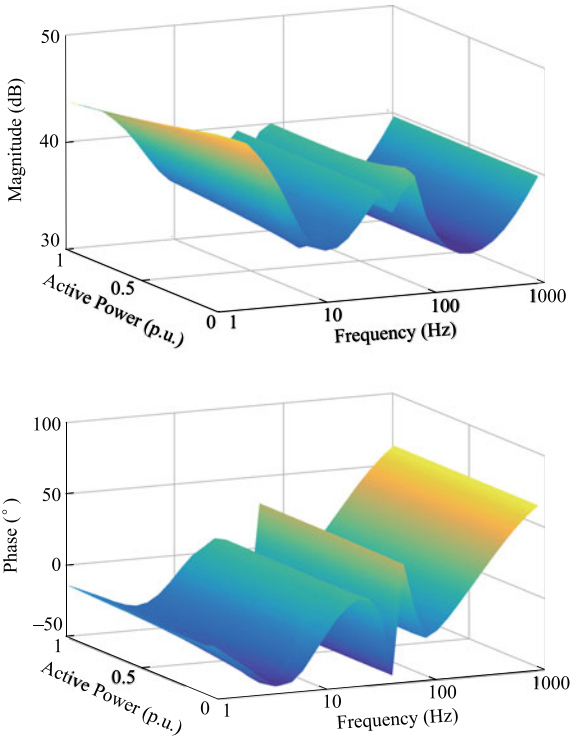

Fig. 11.19 The influence of the active power on the impedance characteristics (in passive islanding mode)

(1) Band $\mathrm{I}_{\mathrm{MMC}}$ ($f < f_1 - f_{\mathrm{vac}}$): The impedance characteristics are influenced by the AC current loop, arm inductor, and SM capacitor of the sending-end MMC, as well as the DC transmission lines, receiving-end MMC, and steady-state operating point.

(2) Band $\mathrm{II}_{\mathrm{MMC}}$ ($f_1 - f_{\mathrm{vac}} < f < f_1 + f_{\mathrm{vac}}$): The impedance characteristics are dominated by the AC voltage loop of the sending-end MMC. There exist resonant peaks at $f_1 - f_{\mathrm{vac}}$ and $f_1 + f_{\mathrm{vac}}$. With the increase of the AC voltage loop bandwidth, the resonant frequencies are further away from the fundamental frequency. With the increase of AC voltage loop PM, the impedance magnitude and phase change more flatly in this frequency band.

(3) Band $\mathrm{III}_{\mathrm{MMC}}$ ($f_1 + f_{\mathrm{vac}} < f < f_1 + f_{\mathrm{fiac}}$): The impedance characteristics are dominated by the AC current loop of the sending-end MMC. With the increase of AC current loop bandwidth, the impedance magnitude in this frequency band increases. With the increase of AC current loop PM, the impedance magnitude and phase change more flatly in this frequency band.

(4) Band $\mathrm{IV}_{\mathrm{MMC}}$ ($f > f_1 + f_{\mathrm{fiac}}$): The impedance characteristics are dominated by the arm inductor of the sending-end MMC. With the increase of the arm inductor, the impedance magnitudes and phases in this frequency band increase, tending to be inductive.

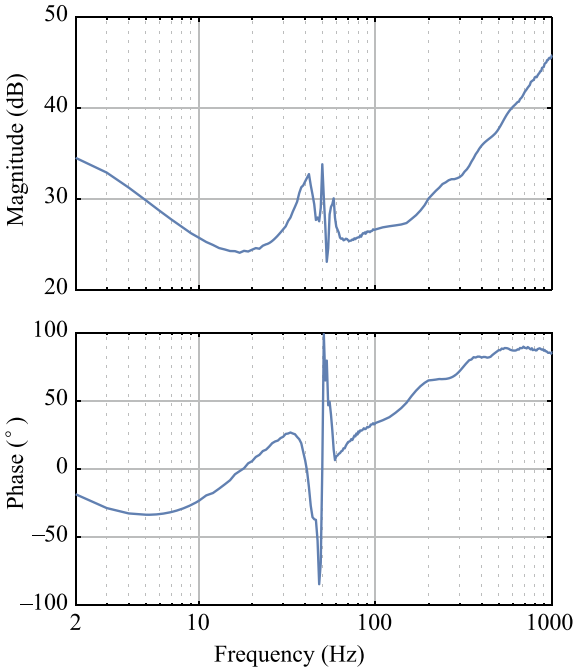

Fig. 11.20 The scanning impedance of MMC-HVDC based on CHIL platform (in passive islanding mode)

Impedance scanning is carried out based on the CHIL platform of MMC-HVDC, and the scanning result is shown in Fig. 11.20. It can be seen from the figure that the frequency range of Band I_{MMC} is around $f < 30$ Hz, the frequency range of Band II_{MMC} is around 30 Hz $< f <$ 70 Hz, the frequency range of Band III_{MMC} is around 70 Hz $< f <$ 300 Hz, and the frequency range of Band IV_{MMC} is around $f > 300$ Hz.

11.4.2 Analysis of Negative Damping Characteristics

The frequency-band division method of the broadband impedance of MMC-HVDC in passive islanding mode has been proposed according to the analysis in Sect. 11.4.1. Considering the MMC-HVDC control system involves the coordination of the multiple controllers in the sending-end and receiving-end MMCs, the impedance characteristics in each frequency band are influenced not only by the dominant factors, but also by the frequency-band overlapping effects of the other controllers or links. In this section, the frequency-band overlapping effects of multiple control loops or links in passive islanding mode will be analyzed to reveal the mechanism of the negative damping characteristics in each frequency band.

11.4.2.1 Negative Damping Characteristics in Band I_{MMC}

The impedance characteristics are influenced by the AC current control, arm inductor, and SM capacitor of the sending-end MMC, as well as the DC transmission lines, receiving-end MMC, and steady-state operating point. Based on these results, this section analyzes the influence of the circulating current control of the sending-end MMC and each control of the receiving-end MMC on the damping characteristics in Band I_{MMC}.

1. **Influence of Circulating Current Loop in Sending-End MMC**

The influence of the circulating current control in the sending-end MMC on the damping characteristics of MMC-HVDC at the sending end in Band I_{MMC} is analyzed as follows. The block diagram of the circulating current loop (in passive islanding mode) is shown in Fig. 11.21.

Given the bandwidth and PM of the circulating current loop f_{fic}, θ_{fic} in the sending-end MMC (in SRF), the coefficients of the circulating current controller can be solved from the following equation

$$\begin{cases} \left| H_{fic}(s) \dfrac{V_{dcref}}{R_{farm} + sL_{farm}} \right|_{s=j2\pi f_{fic}} = 1 \\ \angle \left(H_{fic}(s) \dfrac{V_{dcref}}{R_{farm} + sL_{farm}} \right)_{s=j2\pi f_{fic}} = \theta_{fic} - \pi \end{cases} \tag{11.112}$$

where the open-loop gain is 1 at f_{fic}; the corresponding PM is θ_{fic}.

The influence of the circulating current loop on the damping characteristics of MMC-HVDC at the sending end (in passive islanding mode) is shown in Fig. 11.22. On the one hand, the influence of circulating current loop bandwidth can be obtained by changing f_{fic} to 10, 30 and 50 Hz respectively with a constant PM of 10°. On the other hand, the influence of circulating current loop PM can be obtained by changing θ_{fic} to 10°, 45° and 80° respectively with a constant bandwidth of 30 Hz.

As shown in Fig. 11.22, both the bandwidth and PM of the circulating current loop have an influence on the damping characteristics in Band I_{MMC}. The frequency-band overlapping effect of the circulating current loop, AC current loop, and the main circuit components (including arm inductor and SM capacitor) in Band I_{MMC} leads to capacitive negative damping (impedance phase below −90°) in this frequency band. With the decrease of f_{fic} and θ_{fic}, the degree of the capacitive negative damping is deepened.

2. **Influence of DC Voltage Loop in Receiving-End MMC**

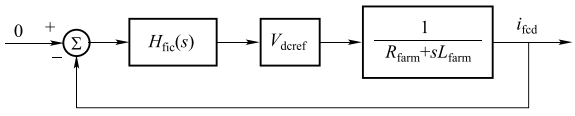

Fig. 11.21 The block diagram of the circulating current loop (in passive islanding mode)

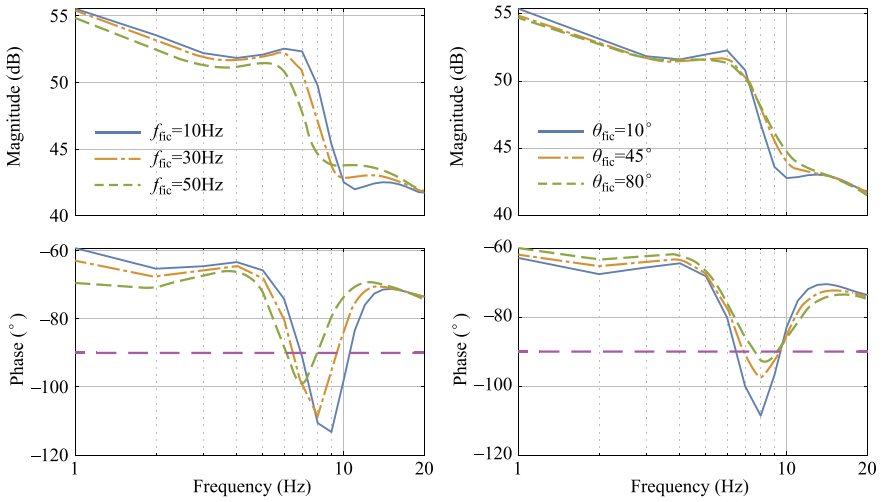

(a) Different circulating current loop bandwidths (b) Different circulating current loop PMs

Fig. 11.22 The influence of circulating current loop in the sending-end MMC on the damping characteristics in Band I_{MMC} (in passive islanding mode)

The influence of the DC voltage control in the receiving-end MMC on the damping characteristics of MMC-HVDC at the sending end in Band I_{MMC} is analyzed as follows. The influence of the DC voltage loop on the damping characteristics (in passive islanding mode) is shown in Fig. 11.23. On the one hand, the influence of DC voltage loop bandwidth can be obtained by changing f_{vdc} to 20, 30 and 40 Hz respectively with a constant PM of 45°. On the other hand, the influence of DC voltage loop PM can be obtained by changing θ_{vdc} to 20°, 45° and 70° respectively with a constant bandwidth of 30 Hz.

As shown in Fig. 11.23, with the increase of f_{vdc}, the degree of the capacitive negative damping in Band I_{MMC} is deepened. With the increase of θ_{vdc}, the frequency range of the negative damping in Band I_{MMC} is increased, and the negative damping degree is also deepened. The results indicate that the coupling effect of the receiving-end MMC to the damping characteristics of MMC-HVDC at the sending end is more pronounced with the increase of f_{vdc} and θ_{vdc}.

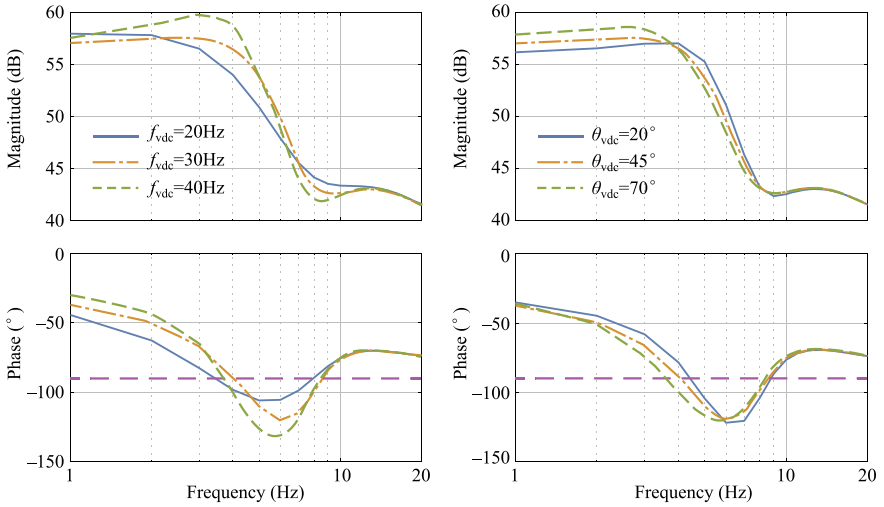

(a) Different DC voltage loop bandwidths (b) Different DC voltage loop PMs

Fig. 11.23 The influence of DC voltage loop in the receiving-end MMC on the damping characteristics in Band I_{MMC} (in passive islanding mode)

3. Influence of AC current Loop in Receiving-End MMC

The influence of the AC current control in the receiving-end MMC on the damping characteristics of MMC-HVDC at the sending end in Band I_{MMC} is analyzed as follows. The influence of the AC current loop on the damping characteristics (in passive islanding mode) is shown in Fig. 11.24. On the one hand, the influence of AC current loop bandwidth can be obtained by changing f_{eiac} to 100, 150 and 200 Hz respectively with a constant PM of 45°. On the other hand, the influence of AC current loop PM can be obtained by changing θ_{eiac} to 20°, 45° and 70° respectively with a constant bandwidth of 200 Hz.

As shown in Fig. 11.24, with the increase of f_{eiac} or the decrease of θ_{eiac}, the degree of the capacitive negative damping in Band I_{MMC} is deepened. The results indicate that the coupling effect of the receiving-end MMC to the damping characteristics of MMC-HVDC at the sending end is more pronounced with the increase of f_{eiac} or the decrease of θ_{eiac}.

4. Influence of PLL in Receiving-End MMC

The influence of the PLL control in the receiving-end MMC on the damping characteristics of MMC-HVDC at the sending end in Band I_{MMC} is analyzed as follows. The influence of the PLL on the damping characteristics (in passive islanding mode) is shown in Fig. 11.25. On the one hand, the influence of PLL bandwidth can be obtained by changing f_{etc} to 10, 15 and 20 Hz respectively with a constant PM of

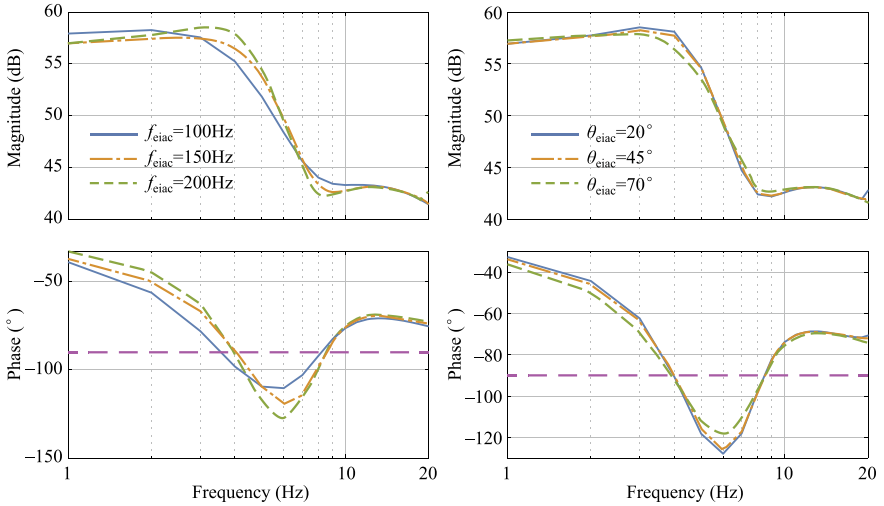

(a) Different AC current loop bandwidths (b) Different AC current loop PMs

Fig. 11.24 The influence of AC current loop in the receiving-end MMC on the damping characteristics in Band I_{MMC} (in passive islanding mode)

45°. On the other hand, the influence of PLL PM can be obtained by changing θ_{etc} to 20°, 45° and 70° respectively with a constant bandwidth of 20 Hz.

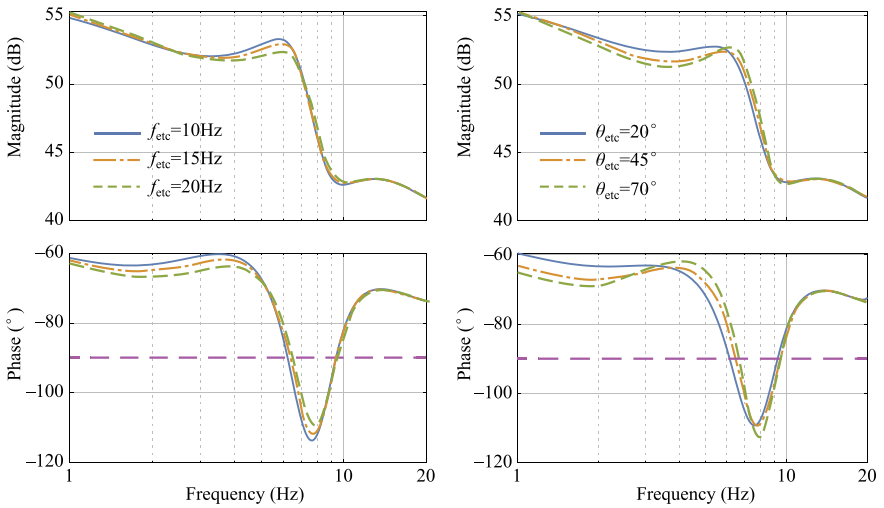

(a) Different PLL bandwidths (b) Different PLL PMs

Fig. 11.25 The influence of PLL in the receiving-end MMC on the damping characteristics in Band I_{MMC} (in passive islanding mode)

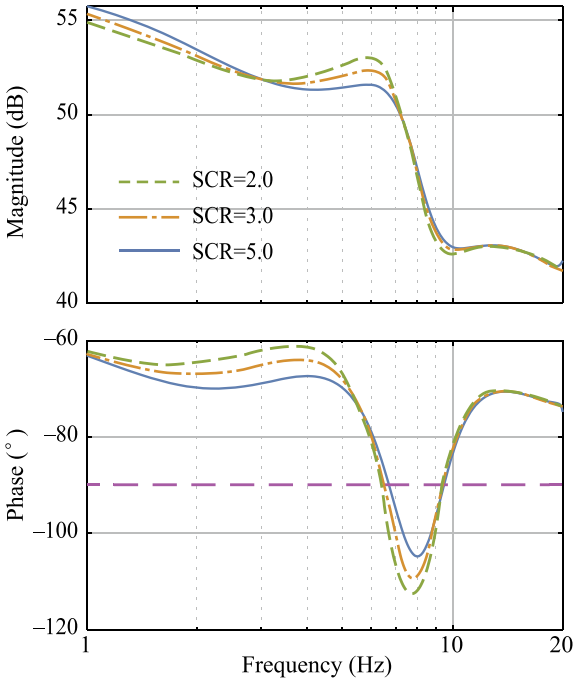

Fig. 11.26 The influence of SCR at the receiving end on the damping characteristics in Band I_{MMC} (in passive islanding mode)

As shown in Fig. 11.25, with the decrease of f_{etc} or the increase of θ_{etc}, the degree of the capacitive negative damping in Band I_{MMC} is deepened to some extent.

5. **Influence of SCR at Receiving End**

The influence of the receiving-end AC grid strength on the damping characteristics of MMC-HVDC at the sending end in Band I_{MMC} is analyzed as follows. With the SCR at the receiving end equivalent to 2.0, 3.0 and 5.0, the influence of the SCR at the receiving end on the impedance characteristics of MMC-HVDC at the sending end (in passive islanding mode) is shown in Fig. 11.26.

As shown in Fig. 11.26, with the decrease of the SCR at the receiving end, the impedance of the receiving-end AC grid is increased, and the negative damping degree in Band I_{MMC} is deepened. The results indicate that the receiving-end AC grid strength has a certain influence on the damping characteristics of MMC-HVDC at the sending end.

11.4.2.2 Negative Damping Characteristics in Band III_{MMC}

The impedance characteristics are dominated by the AC current loop of the sending-end MMC, and also influenced by the time delay introduced from communication, sampling, filtering, digital control, and so on. This section analyzes the influence of

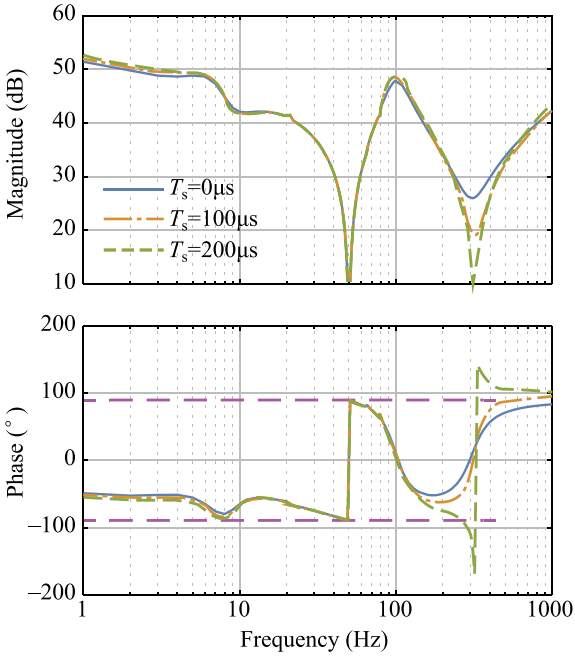

Fig. 11.27 The influence of the time delay on the damping characteristics in Band III_{MMC} (in passive islanding mode)

the time delay on the damping characteristics of MMC-HVDC at the sending end in Band III_{MMC}.

Setting the AC current loop bandwidth f_{fiac} to 300 Hz and PM θ_{fiac} to 10° in the sending-end MMC, the influence of the time delay T_s equivalent to 0, 100, and 200 μs on the damping characteristics of MMC-HVDC at the sending end in Band III_{MMC} (in passive islanding mode) is shown in Fig. 11.27.

As shown in Fig. 11.27, the time delay mainly influences the impedance characteristics around the AC current loop bandwidth of the sending-end MMC in SCF, i.e., $f_1 + f_{\text{fiac}}$. There exists the frequency-band overlapping effect of the time delay and AC current loop of the sending-end MMC in Band III_{MMC}. With the increase of the time delay, the impedance presents capacitive negative damping and inductive negative damping (impedance phase above 90°) around $f_1 + f_{\text{fiac}}$. Besides, the negative damping degree is deepened with the increase of the time delay.

11.4.2.3 Negative Damping Characteristics in Band IV_{MMC}

The impedance characteristics are dominated by the arm inductor of the sending-end MMC, and also influenced by the time delay. This section analyzes the influence of the time delay on the damping characteristics of MMC-HVDC at the sending end in Band IV_{MMC}.

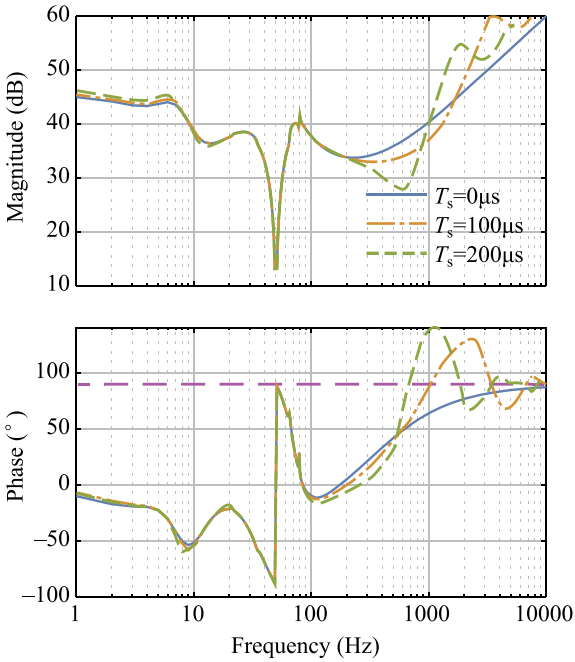

Fig. 11.28 The influence of the time delay on the damping characteristics in Band IV_{MMC} (in passive islanding mode)

Keeping the arm inductor of the sending-end MMC constant, the influence of the time delay T_s equivalent to 0, 100, and 200 μs on the damping characteristics of MMC-HVDC at the sending end in Band IV_{MMC} (in passive islanding mode) is shown in Fig. 11.28.

As shown in Fig. 11.28, there exists the frequency-band overlapping effect of the time delay and arm inductor of the sending-end MMC in Band IV_{MMC}, leading to inductive negative damping periodically presenting in this frequency band. Besides, the degree of the inductive negative damping is deepened with the increase of the time delay.

Impedance scanning is carried out based on the CHIL platform of MMC-HVDC, and the scanning result is shown in Fig. 11.29. It can be seen from the figure that the impedance of MMC-HVDC at the sending end presents inductive negative damping characteristics above 400 Hz (in Band IV_{MMC}).

11.4.2.4 Summary of Negative Damping Characteristics in Each Frequency Band

According to the analysis of the negative damping characteristics of MMC-HVDC in passive islanding mode, the following conclusions are obtained.

(1) Band I_{MMC} ($f < f_1 - f_{vac}$): The impedance characteristics are influenced by the AC current loop, arm inductor, SM capacitor as well as the circulating current

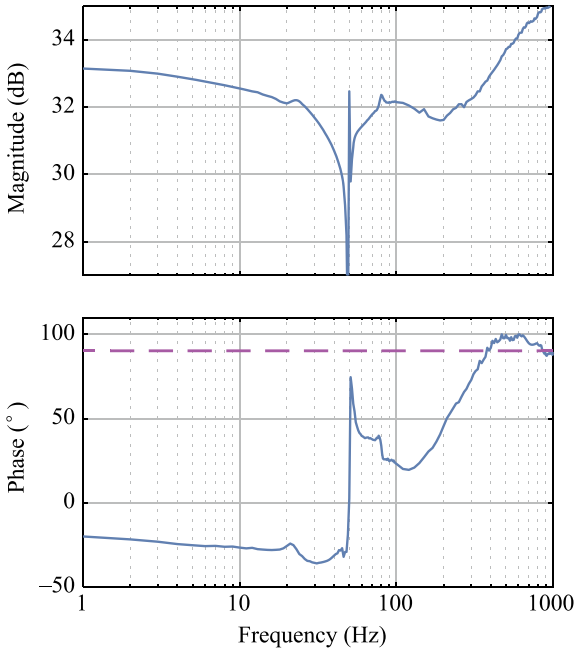

Fig. 11.29 The scanning damping characteristics of MMC-HVDC based on CHIL platform (in passive islanding mode)

control of the sending-end MMC. The frequency-band overlapping effect of the circulating current loop, AC current loop, and main circuit components leads to the capacitive negative damping in this frequency band. With the increase of circulating current loop bandwidth or PM, the negative damping degree is deepened. Besides, the damping characteristics are also influenced by the receiving-end MMC. With the increase of the bandwidths of the DC voltage loop and AC current loop of the receiving-end MMC, the negative damping degree is further deepened.

(2) Band III_{MMC} ($f_1 + f_{\text{vac}} < f < f_1 + f_{\text{fiac}}$): The impedance characteristics are dominated by the AC current loop of the sending-end MMC. The frequency-band overlapping effect of the time delay and AC current loop leads to the capacitive and inductive negative damping around the AC current loop bandwidth of the sending-end MMC in SCF, i.e., $f_1 + f_{\text{fiac}}$. With the increase of the time delay, the negative damping degree is deepened.

(3) Band IV_{MMC} ($f > f_1 + f_{\text{fiac}}$): The impedance characteristics are dominated by the arm inductor of the sending-end MMC. The frequency-band overlapping effect of the time delay and arm inductor leads to the inductive negative damping in this frequency band. With the increase of the time delay, the degree of the inductive negative damping is deepened.

11.5 Impedance Characteristic Analysis of Grid-Connected Mode MMC-HVDC

Based on the established impedance model of MMC-HVDC in grid-connected mode, this section first analyzes the dominant factors of the impedance characteristics in different frequency bands, and proposes the frequency band division method of MMC-HVDC. Then, the frequency-band overlapping effect of multiple control loops or links and the negative damping characteristics of each frequency band are clarified. Finally, based on the CHIL scanning result of MMC-HVDC impedance, the typical values of each frequency band are given.

11.5.1 Frequency-Band Division of Broadband Impedance

This section establishes the frequency-domain relationship between the impedance characteristics, control loop bandwidth and PM in grid-connected mode. The dominant factor of the impedance characteristics in each frequency band is clarified, and the frequency band division method is proposed.

11.5.1.1 Influence of PLL in Sending-End MMC

The influence of the PLL in the sending-end MMC on the impedance characteristics of MMC-HVDC at the sending end is analyzed as follows. The influence of PLL on the impedance characteristics (in grid-connected mode) is shown in Fig. 11.30. On the one hand, the influence of PLL bandwidth can be obtained by changing f_{ftc} to 5, 10 and 15 Hz respectively with a constant PM of 45°. On the other hand, the influence of PLL PM can be obtained by changing θ_{ftc} to 20°, 45° and 70° respectively with a constant bandwidth of 5 Hz.

As shown in Fig. 11.30, two anti-resonant peaks appear in the impedance of MMC-HVDC at the sending end around $f_1 - f_{\text{ftc}}$ and $f_1 + f_{\text{ftc}}$. The change of the PLL bandwidth f_{ftc} mainly influences the resonant frequencies. With the increase of f_{ftc}, the two resonant frequencies are further away from the fundamental frequency, and the impedance magnitudes increase within the frequency band of $f_1 - f_{\text{ftc}} < f < f_1 + f_{\text{ftc}}$. Besides, the impedance presents negative damping characteristics around the resonant frequencies, changing from inductive negative damping to capacitive negative damping at $f_1 - f_{\text{ftc}}$ and $f_1 + f_{\text{ftc}}$. The change of the PLL PM θ_{ftc} mainly influences the damping characteristics within $f_1 - f_{\text{ftc}} < f < f_1 + f_{\text{ftc}}$. With the increase of θ_{ftc}, the damping characteristics at the anti-resonant peaks are enhanced, and the impedance magnitude changes more flatly. Therefore, PLL mainly influences the impedance characteristics within the frequency band of $f_1 - f_{\text{ftc}} < f < f_1 + f_{\text{ftc}}$.

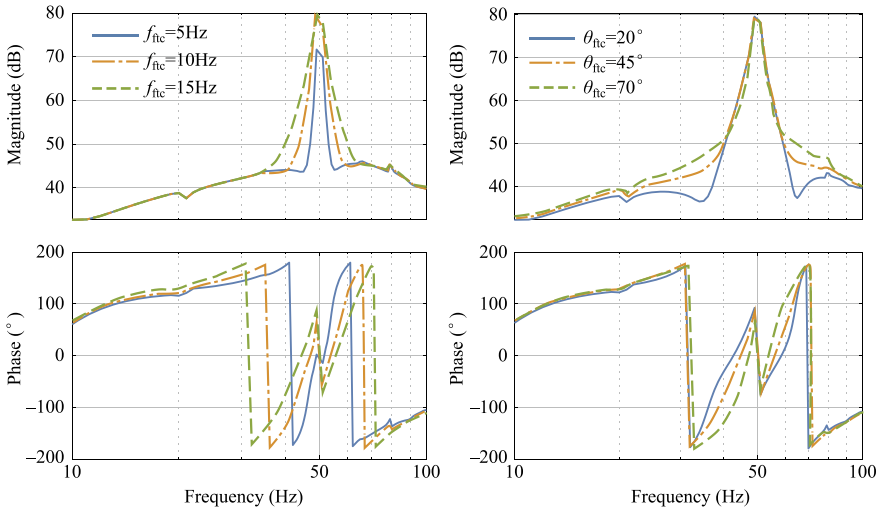

(a) Different PLL bandwidths (b) Different PLL PMs

Fig. 11.30 The influence of PLL in the sending-end MMC on the impedance characteristics (in grid-connected mode)

11.5.1.2 Influence of AC Current Loop in Sending-End MMC

Different from the passive islanding mode, the plant of the AC current loop of the sending-end MMC in grid-connected mode is mainly the arm inductor. The block diagram of the AC current loop (in grid-connected mode) is shown in Fig. 11.31.

Given the bandwidth and PM of the AC current loop f_{fiac}, θ_{fiac} in sending-end MMC (in SRF), the coefficients of the AC current controller can be solved from the following equation

$$\begin{cases} \left| H_{\text{fiac}}(s) \dfrac{2V_{\text{dcref}}}{R_{\text{farm}} + sL_{\text{farm}}} \right|_{s=\text{j}2\pi f_{\text{fiac}}} = 1 \\ \angle\left(H_{\text{fiac}}(s) \dfrac{2V_{\text{dcref}}}{R_{\text{farm}} + sL_{\text{farm}}} \right)_{s=\text{j}2\pi f_{\text{fiac}}} = \theta_{\text{fiac}} - \pi \end{cases} \tag{11.113}$$

where the open-loop gain is 1 at f_{fiac}, and the corresponding PM is θ_{fiac}.

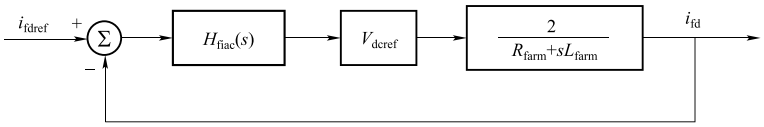

Fig. 11.31 The block diagram of the AC current loop (in grid-connected mode)

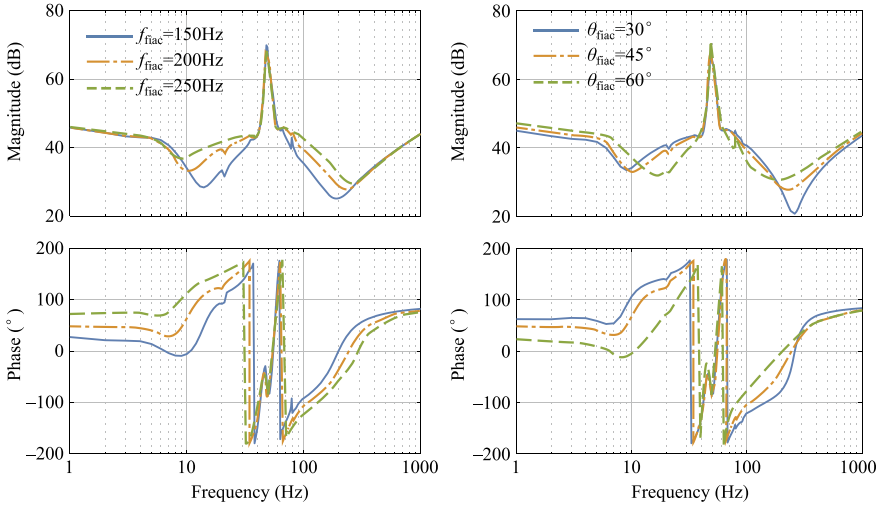

(a) Different AC current loop bandwidths (b) Different AC current loop PMs

Fig. 11.32 The influence of AC current loop in the sending-end MMC on the impedance characteristics (in grid-connected mode)

The influence of the AC current loop of the sending-end MMC on the impedance characteristics of MMC-HVDC at the sending end (in grid-connected mode) is shown in Fig. 11.32. On the one hand, the influence of the AC current loop bandwidth can be obtained by changing f_{fiac} to 150, 200 and 250 Hz respectively with a constant PM of 45°. On the other hand, the influence of the AC current loop PM can be obtained by changing θ_{fiac} to 30°, 45° and 60° respectively with a constant bandwidth of 200 Hz.

As shown in Fig. 11.32, the AC current loop bandwidth f_{fiac} mainly influences the impedance characteristics within the frequency bands of $f < f_1 - f_{\text{ftc}}$ and $f_1 + f_{\text{ftc}} < f < f_1 + f_{\text{fiac}}$. With the increase of f_{fiac}, the impedance magnitudes within the two frequency bands increase. Besides, the impedance magnitude exhibits an anti-resonant peak around the AC current loop bandwidth of the sending-end MMC in SCF, i.e., $f_1 + f_{\text{fiac}}$. The impedance characteristics transition from capacitive to inductive around $f_1 + f_{\text{fiac}}$. The AC voltage loop PM θ_{fiac} has an influence on the impedance characteristics in both $f < f_1 - f_{\text{ftc}}$ and $f_1 + f_{\text{ftc}} < f < f_1 + f_{\text{fiac}}$. With the increase of θ_{fiac}, the damping characteristics around $f_1 + f_{\text{fiac}}$ are enhanced.

11.5.1.3 Influence of Arm Inductor in Sending-End MMC

With the arm inductor of the sending-end MMC L_{farm} equivalent to 40, 50 and 60 mH, the influence of the arm inductor on the impedance characteristics of MMC-HVDC at the sending end (in grid-connected mode) is shown in Fig. 11.33.

As shown in Fig. 11.33, the arm inductor of the sending-end MMC mainly influences the impedance characteristics in the frequency bands of $f < f_1 - f_{\text{ftc}}$

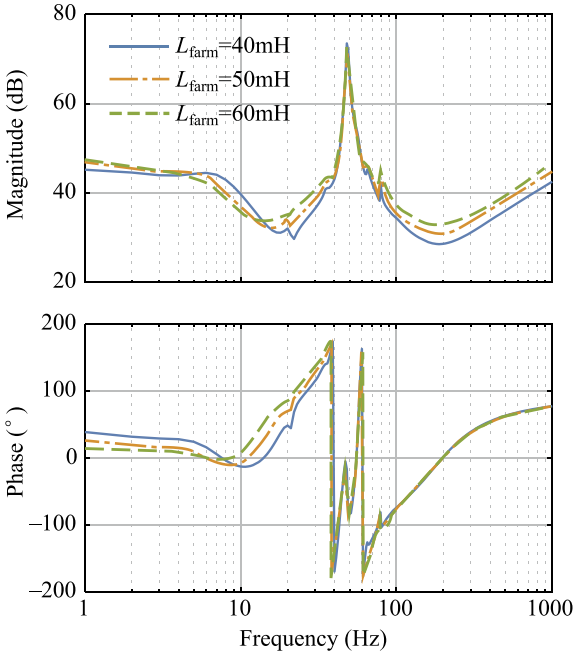

Fig. 11.33 The influence of the arm inductor in the sending-end MMC on the impedance characteristics (in grid-connected mode)

and $f > f_1 + f_{fiac}$. With the increase of L_{farm}, the impedance magnitude in the frequency band of $f > f_1 + f_{fiac}$ increases, indicating that the impedance characteristics of MMC-HVDC at the sending end are dominated by the arm inductor of the sending-end MMC in the high-frequency band.

11.5.1.4 Influence of SM Capacitor in Sending-End MMC

With the SM capacitor of the sending-end MMC C_{fsm} equivalent to 6, 8 and 10 mF, the influence of the SM capacitor on the impedance characteristics of MMC-HVDC at the sending end (in grid-connected mode) is shown in Fig. 11.34.

As shown in Fig. 11.34, the SM capacitor of the sending-end MMC mainly influences the impedance characteristics within the frequency band of $f < f_1 - f_{ftc}$. The SM capacitor and arm inductor form a passive resonant circuit, and the impedance magnitude exhibits a resonant peak in this frequency band. With the increase of C_{fsm}, the resonant frequency is reduced, and there are apparent changes in the impedance magnitude and phase.

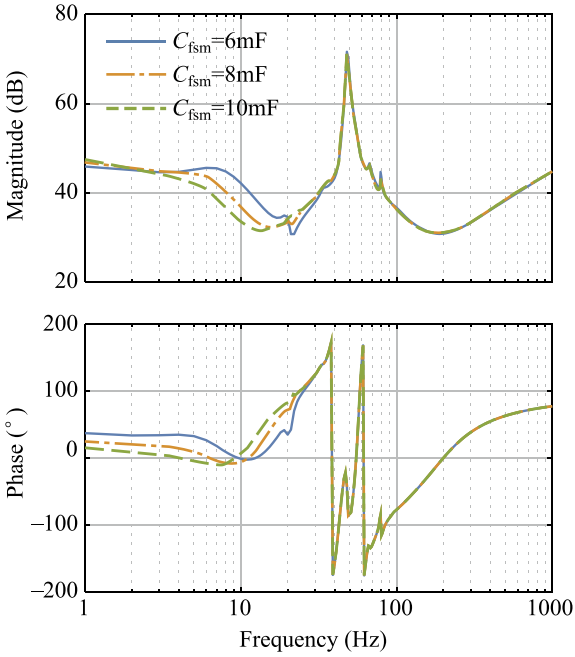

Fig. 11.34 The influence of the SM capacitor in the sending-end MMC on the impedance characteristics (in grid-connected mode)

11.5.1.5 Influence of Receiving-End MMC

The influence of the receiving-end MMC on the impedance characteristics of MMC-HVDC at the sending is analyzed as follows. First, without considering the impedance of the DC transmission lines and receiving-end MMC ($\boldsymbol{Z}_{\text{fdc}} = 0$), the impedance characteristics of MMC-HVDC at the sending are analyzed. Then, the influence of the DC transmission lines is taken into account, while the influence of receiving-end MMC is not considered ($\boldsymbol{Z}_{\text{edc}} = 0$). Finally, the influence of both the DC transmission lines and receiving-end MMC is considered ($\boldsymbol{Z}_{\text{fdc}} \neq 0$). The variation of the impedance curves of MMC-HVDC at the sending end in the three cases (in grid-connected mode) is shown in Fig. 11.35.

As shown in Fig. 11.35, the DC transmission lines and the receiving-end MMC mainly influence the impedance characteristics within the frequency band of $f < f_1 - f_{\text{ftc}}$. If the impedance characteristics and oscillation risk evaluation above the fundamental frequency are concerned, the influence of the DC transmission lines and the receiving-end MMC can be ignored. If the impedance characteristics and oscillation risk evaluation below the fundamental frequency are concerned, the influence of the DC transmission lines and the receiving-end MMC should be considered.

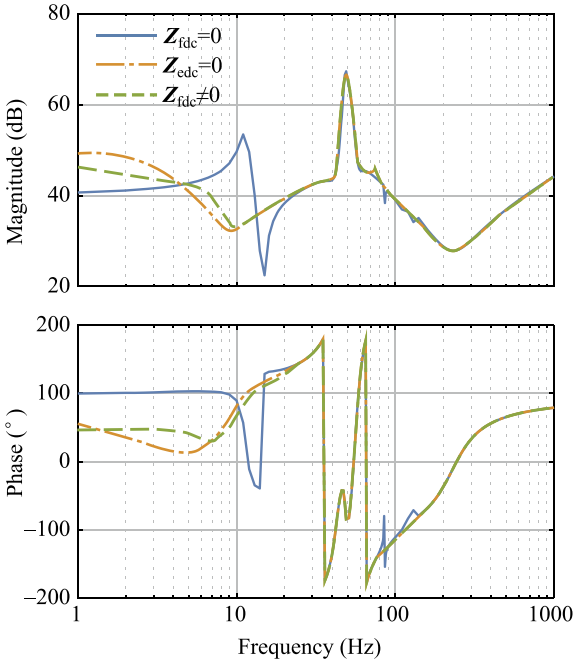

Fig. 11.35 The influence of the DC transmission lines and receiving-end MMC on the impedance characteristics (in grid-connected mode)

11.5.1.6 Influence of Steady-State Operating Point

The impedance characteristics of MMC-HVDC vary with the steady-state operating point, such as the power change. The influence of the active power changing from 0 to 1.0 p.u. on the impedance characteristics of MMC-HVDC at the sending (in grid-connected mode) is shown in Fig. 11.36.

As shown in Fig. 11.36, the change of the active power mainly influences the impedance characteristics below the fundamental frequency with little influence on the impedance characteristics above the fundamental frequency. When the active power changes from 0 to 1.0 p.u., the trends of the broadband impedance curves with frequency are similar, indicating that the steady-state operating point has little influence on the boundary of each frequency band.

11.5.1.7 Frequency-Band Division of Broadband Impedance

According to the analysis of the dominant factors of MMC-HVDC impedance characteristics in each frequency band (in grid-connected mode), the following frequency bands can be divided.

(1) Band I_{MMC} ($f < f_1 - f_{ftc}$): The impedance characteristics are influenced by the AC current loop, arm inductor, and SM capacitor of the sending-end MMC,

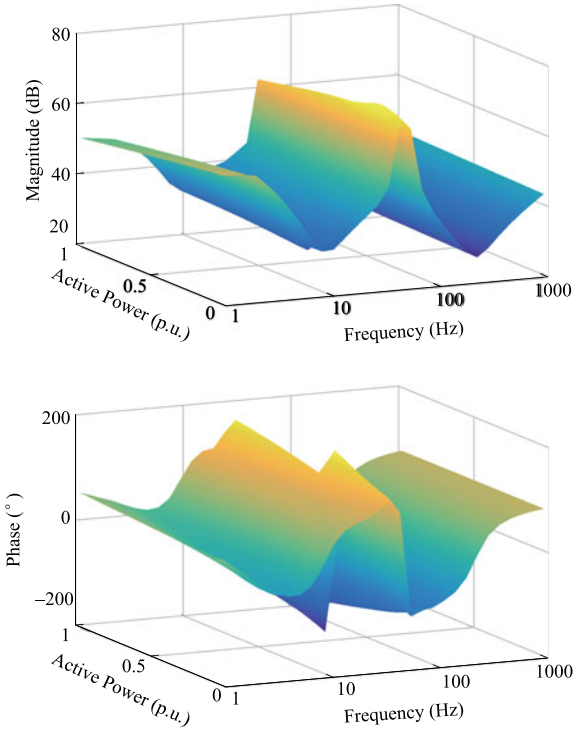

Fig. 11.36 The influence of the active power on the impedance characteristics (in grid-connected mode)

as well as the DC transmission lines, receiving-end MMC, and steady-state operating point.

(2) Band II_{MMC} ($f_1 - f_{\text{ftc}} < f < f_1 + f_{\text{ftc}}$): The impedance characteristics are dominated by the PLL of the sending-end MMC. There exist anti-resonant peaks at $f_1 - f_{\text{ftc}}$ and $f_1 + f_{\text{ftc}}$. With the increase of the PLL bandwidth, the resonant frequencies are further away from the fundamental frequency. With the increase of PLL PM, the damping characteristics at the anti-resonant peaks are enhanced, and the impedance magnitude changes more flatly.

(3) Band III_{MMC} ($f_1 + f_{\text{ftc}} < f < f_1 + f_{\text{fiac}}$): The impedance characteristics are dominated by the AC current loop of the sending-end MMC. With the increase of AC current loop bandwidth, the impedance magnitude in this frequency band increases. The impedance characteristics transition from capacitive to inductive around $f_1 + f_{\text{fiac}}$.

(4) Band IV_{MMC} ($f > f_1 + f_{\text{fiac}}$): The impedance characteristics are dominated by the arm inductor of the sending-end MMC. With the increase of the arm inductor L_{farm}, the impedance magnitude in this frequency band increases, tending to be inductive.

Comparing the impedance characteristics of MMC-HVDC in passive islanding mode and grid-connected mode, the difference between the impedance characteristics of the two modes is mainly in Band II_{MMC}. The impedance characteristics are dominated by the AC voltage loop, but by the PLL in grid-connected mode.

11.5.2 Analysis of Negative Damping Characteristics

The frequency-band division method of the broadband impedance of MMC-HVDC in grid-connected mode has been proposed according to the analysis in Sect. 11.4.1. Considering the MMC-HVDC control system involves the coordination of the multiple controllers in the sending-end and receiving-end MMCs, the impedance characteristics in each frequency band are influenced not only by the dominant factors, but also by the frequency-band overlapping effects of the other controllers or links. In this section, the frequency-band overlapping effects of multiple control loops or links in grid-connected mode will be analyzed to reveal the mechanism of the negative damping characteristics in each frequency band.

11.5.2.1 Negative Damping Characteristics in Band I_{MMC}

The impedance characteristics are influenced by the AC current loop, arm inductor, and SM capacitor of the sending-end MMC, as well as the DC transmission lines, receiving-end MMC, and steady-state operating point. Based on these results, this section analyzes the influence of the circulating current loop in the sending-end MMC and the multiple control loops in the receiving-end MMC on the damping characteristics in Band I_{MMC}.

1. **Influence of Circulating Current Loop in Sending-End MMC**

The influence of the circulating current control in the sending-end MMC on the damping characteristics of MMC-HVDC at the sending end in Band I_{MMC} is analyzed as follows. The influence of the circulating current loop on the damping characteristics of MMC-HVDC at the sending end (in grid-connected mode) is shown in Fig. 11.37. On the one hand, the influence of circulating current loop bandwidth can be obtained by changing f_{fic} to 20, 40 and 60 Hz respectively with a constant PM of 10°. On the other hand, the influence of circulating current loop PM can be obtained by changing θ_{fic} to 10°, 45° and 80° respectively with a constant bandwidth of 60 Hz.

As shown in Fig. 11.37, both the bandwidth and PM of the circulating current loop have an influence on the damping characteristics in Band I_{MMC}. The frequency-band overlapping effect of the circulating current loop, AC current loop, and the

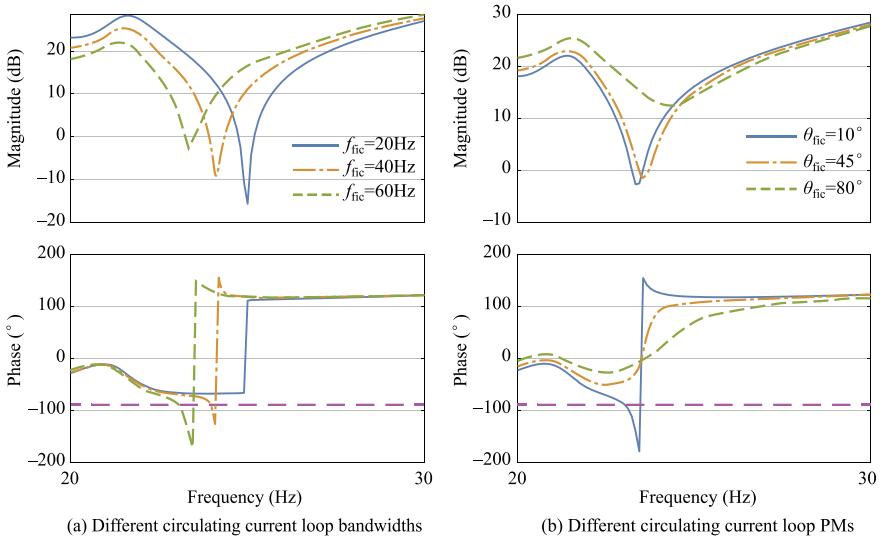

(a) Different circulating current loop bandwidths (b) Different circulating current loop PMs

Fig. 11.37 The influence of circulating current loop in the sending-end MMC on the damping characteristics in Band I_{MMC} (in grid-connected mode)

main circuit components in Band I_{MMC} leads to capacitive and inductive negative damping in this frequency band. With the increase of f_{fic}, the negative damping degree is deepened, and the frequency at which the impedance starts to present negative damping is reduced. With the decrease of θ_{fic}, the negative damping degree is also deepened.

2. Influence of DC Voltage Loop in Receiving-End MMC

The influence of the DC voltage control in the receiving-end MMC on the damping characteristics of MMC-HVDC at the sending end in Band I_{MMC} is analyzed as follows. The influence of the DC voltage loop on the damping characteristics (in grid-connected mode) is shown in Fig. 11.38. On the one hand, the influence of DC voltage loop bandwidth can be obtained by changing f_{vdc} to 10, 20 and 30 Hz respectively with a constant PM of 45°. On the other hand, the influence of DC voltage loop PM can be obtained by changing θ_{vdc} to 20°, 45° and 70° respectively with a constant bandwidth of 30 Hz.

As shown in Fig. 11.38, with the increase of f_{vdc}, the frequency at which the impedance starts to present negative damping is reduced. Besides, with the increase of f_{vdc} or the decrease of θ_{vdc}, the negative damping degree is deepened. The results indicate the coupling effect of the receiving-end MMC to the damping characteristics

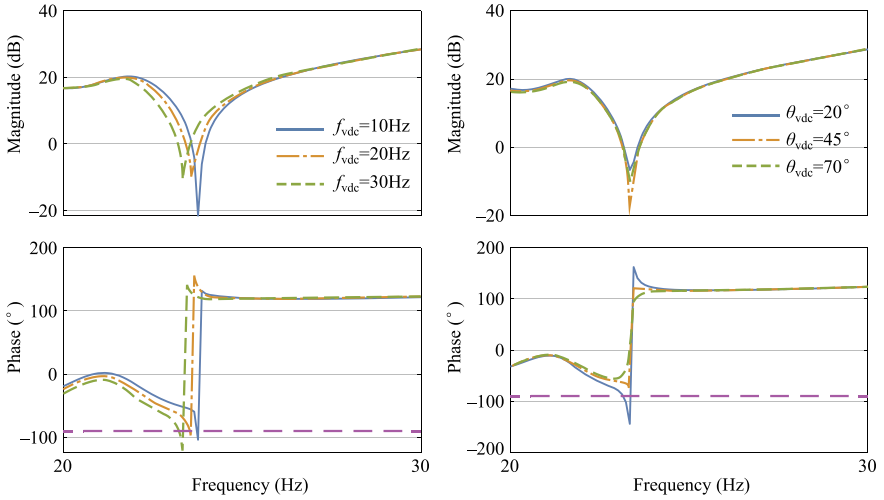

(a) Different DC voltage loop bandwidths (b) Different DC voltage loop PMs

Fig. 11.38 The influence of DC voltage loop in the receiving-end MMC on the damping characteristics in Band I_{MMC} (in grid-connected mode)

of MMC-HVDC at the sending end is more pronounced with the increase of f_{vdc} or the decrease of θ_{vdc}.

3. Influence of AC Current Loop in Receiving-End MMC

The influence of the AC current control in the receiving-end MMC on the damping characteristics of MMC-HVDC at the sending end in Band I_{MMC} is analyzed as follows. The influence of the AC current loop on the damping characteristics (in grid-connected mode) is shown in Fig. 11.39. On the one hand, the influence of AC current loop bandwidth can be obtained by changing f_{eiac} to 100, 150 and 200 Hz respectively with a constant PM of 45°. On the other hand, the influence of AC current loop PM can be obtained by changing θ_{eiac} to 20°, 45° and 70° respectively with a constant bandwidth of 200 Hz.

As shown in Fig. 11.39, with the increase of f_{eiac} or the decrease of θ_{eiac}, the negative damping degree in Band I_{MMC} is deepened. The results indicate that the coupling effect of the receiving-end MMC to the damping characteristics of MMC-HVDC at the sending end is more pronounced with the increase of f_{eiac} or the decrease of θ_{eiac}.

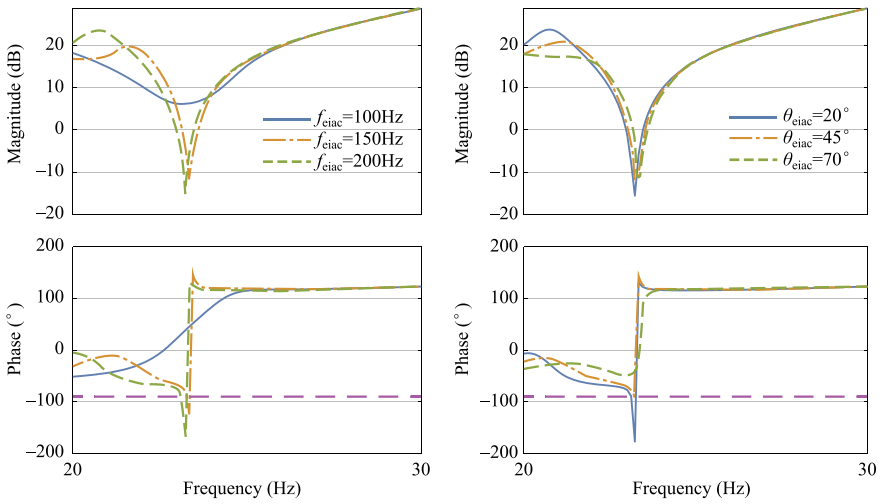

(a) Different AC current loop bandwidths (b) Different AC current loop PMs

Fig. 11.39 The influence of AC current loop in the receiving-end MMC on the damping characteristics in Band I_{MMC} (in grid-connected mode)

4. Influence of PLL in Receiving-End MMC

The influence of the PLL control in the receiving-end MMC on the damping characteristics of MMC-HVDC at the sending end in Band I_{MMC} is analyzed as follows. The influence of the PLL on the damping characteristics (in grid-connected mode) is shown in Fig. 11.40. On the one hand, the influence of PLL bandwidth can be obtained by changing f_{etc} to 10, 15 and 20 Hz respectively with a constant PM of 45°. On the other hand, the influence of PLL PM can be obtained by changing θ_{etc} to 20°, 45° and 70° respectively with a constant bandwidth of 20 Hz.

As shown in Fig. 11.40, with the decrease of f_{etc}, the frequency range of the negative damping is increased, and the negative damping degree is deepened. With the decrease of θ_{etc}, the negative damping degree in Band I_{MMC} is further deepened.

5. Influence of SCR at Receiving End

The influence of the receiving-end AC grid strength on the damping characteristics of MMC-HVDC at the sending end in Band I_{MMC} is analyzed as follows. With the SCR at the receiving end equivalent to 2.0, 3.0 and 5.0, the influence of the SCR at the receiving end on the impedance characteristics of MMC-HVDC at the sending end (in grid-connected mode) is shown in Fig. 11.41.

As shown in Fig. 11.41, with the decrease of the SCR at the receiving end, the impedance of the receiving-end AC grid is increased, and the frequency at which the impedance starts to present negative damping is slightly reduced. The results indicate that the receiving-end AC grid strength has a certain influence on the damping characteristics of MMC-HVDC at the sending end.

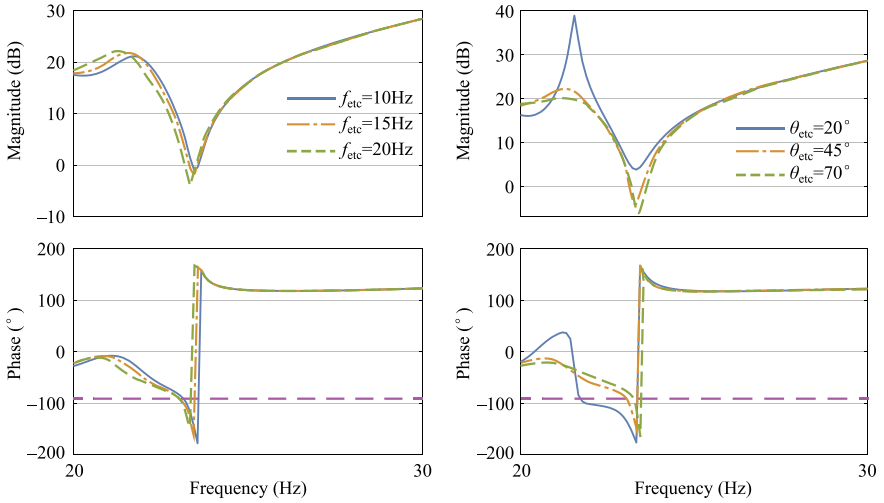

Fig. 11.40 The influence of PLL in the receiving-end MMC on the damping characteristics in Band I_{MMC} (in grid-connected mode)

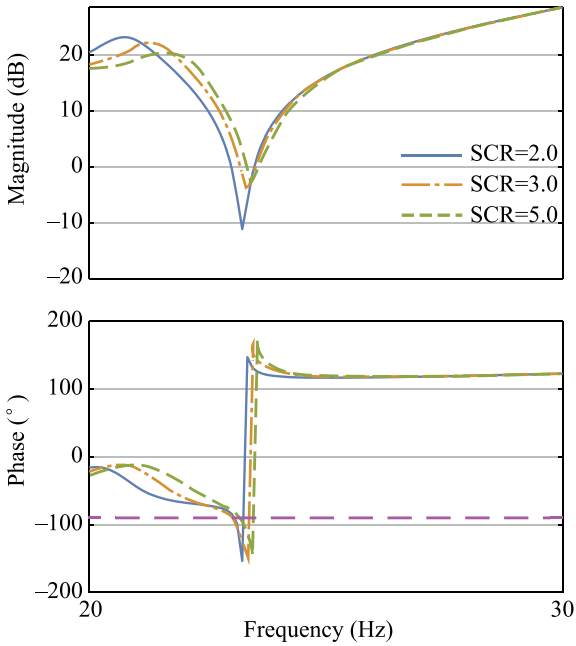

Fig. 11.41 The influence of SCR at the receiving end on the damping characteristics in Band I_{MMC} (in grid-connected mode)

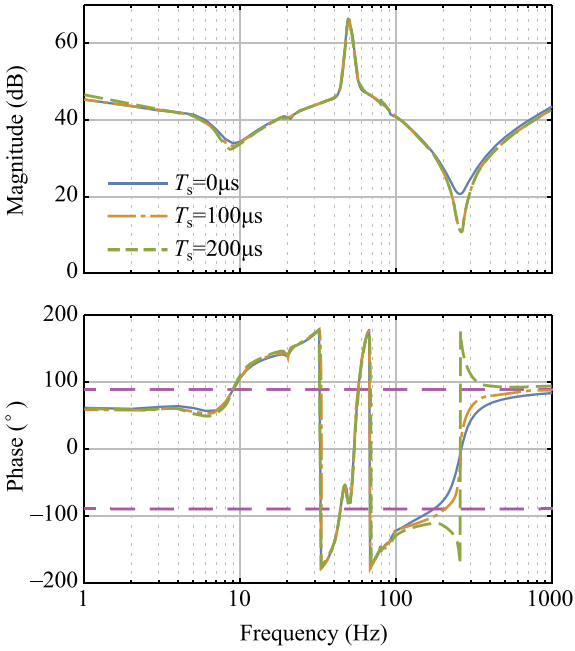

Fig. 11.42 The influence of the time delay on the damping characteristics in Band III_{MMC} (in grid-connected mode)

11.5.2.2 Negative Damping Characteristics in Band III_{MMC}

The impedance characteristics are dominated by the AC current loop of the sending-end MMC, and also influenced by the time delay. This section analyzes the influence of the time delay on the damping characteristics of MMC-HVDC at the sending end in Band III_{MMC}.

Setting the AC current loop bandwidth f_{fiac} to 200Hz and PM θ_{fiac} to 20° in the sending-end MMC, the influence of the time delay T_s equivalent to 0, 100, and 200 μs on the damping characteristics of MMC-HVDC at the sending end in Band III_{MMC} (in grid-connected mode) is shown in Fig. 11.42.

As shown in Fig. 11.42, the time delay mainly influences the impedance characteristics around the AC current loop bandwidth of the sending-end MMC in SCF, i.e., $f_1 + f_{fiac}$. There exists the frequency-band overlapping effect of the time delay and AC current loop of the sending-end MMC in Band III_{MMC}, leading to capacitive negative damping and inductive negative damping around $f_1 + f_{fiac}$. With the increase of the time delay, the negative damping degree is deepened.

11.5.2.3 Negative Damping Characteristics in Band IV_{MMC}

The impedance characteristics are dominated by the arm inductor of the sending-end MMC, and also influenced by the time delay. This section analyzes the influence of

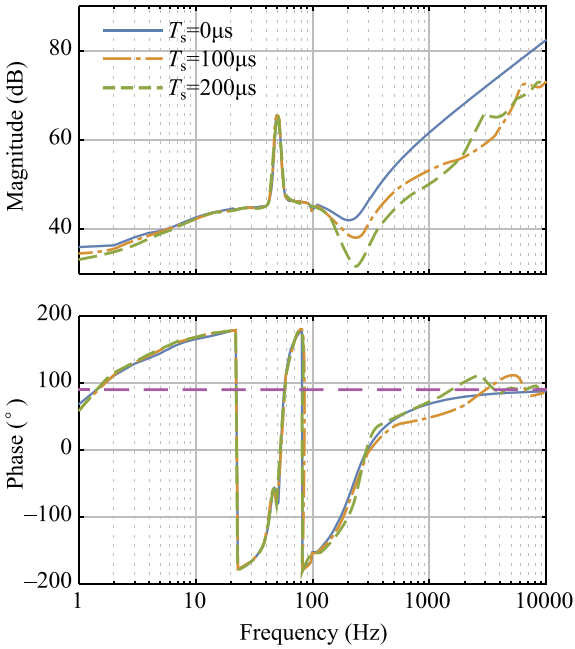

Fig. 11.43 The influence of the time delay on the damping characteristics in Band IV_{MMC} (in grid-connected mode)

the time delay on the damping characteristics of MMC-HVDC at the sending end in Band IV_{MMC}.

Keeping the arm inductor of the sending-end MMC constant, the influence of the time delay T_s equivalent to 0, 100, and 200 μs on the damping characteristics of MMC-HVDC at the sending end in Band IV_{MMC} (in grid-connected mode) is shown in Fig. 11.43.

As shown in Fig. 11.43, there exists the frequency-band overlapping effect of the time delay and arm inductor of the sending-end MMC in Band IV_{MMC}, leading to inductive negative damping periodically presenting in this frequency band. Besides, the degree of the inductive negative damping is deepened with the increase of the time delay.

11.5.2.4 Summary of Negative Damping Characteristics in Each Frequency Band

According to the analysis of the negative damping characteristics of MMC-HVDC in grid-connected mode, the following conclusions are obtained.

(1) Band I_{MMC} ($f < f_1 - f_{ftc}$): The impedance characteristics are influenced by the AC current loop, arm inductor, SM capacitor, as well as the circulating current loop of the sending-end MMC. The frequency-band overlapping effect of the circulating current loop, AC current loop, and main circuit components leads

to the capacitive and inductive negative damping in this frequency band. With the increase of circulating current loop bandwidth or the decrease of circulating current loop PM, the negative damping degree is deepened. Besides, the damping characteristics are also influenced by the receiving-end MMC. With the increase of the bandwidths of the DC voltage loop and AC current loop of the receiving-end MMC, the negative damping degree is further deepened.

(2) Band $\mathrm{III}_{\mathrm{MMC}}$ ($f_1 + f_{\mathrm{ftc}} < f < f_1 + f_{\mathrm{fiac}}$): The impedance characteristics are dominated by the AC current loop of the sending-end MMC. The frequency-band overlapping effect of the time delay and AC current loop leads to the capacitive and inductive negative damping around the AC current loop bandwidth of the sending-end MMC in SCF, i.e., $f_1 + f_{\mathrm{fiac}}$. With the increase of the time delay, the negative damping degree is deepened.

(3) Band $\mathrm{IV}_{\mathrm{MMC}}$ ($f > f_1 + f_{\mathrm{fiac}}$): The impedance characteristics are dominated by the arm inductor of the sending-end MMC. The frequency-band overlapping effect of the time delay and arm inductor leads to the inductive negative damping in this frequency band. With the increase of the time delay, the degree of the inductive negative damping is deepened.

Reference

1. LI G H. Research on Broadband Oscillation Mechanism and Suppression Strategy for Wind Farm Connected into MMC-HVDC System [D]. Hefei: Hefei Polytechnic University, 2022. (Chinese)

Part III
Broadband Oscillation Analysis of REG and AC/DC Transmission System

Renewable energy generation (REG) can be connected into the power grid in alternating current (AC) or direct current (DC) mode. The AC mode includes the pure AC transmission line and series-compensation transmission line. The DC mode includes line commutated converter-based high voltage direct current (LCC-HVDC) and modular multilevel converter-based high voltage direct current (MMC-HVDC). In order to address the issues of multiple coupling frequencies, difficulty in determining the dominant oscillation factors, and unclear oscillation mechanism of the REG grid-connected system [1–5], this part proposes a method to determine the dominant oscillation factors and reveals the broadband oscillation mechanism [6–9]. This part includes the following chapters:

Chapter 12: Impedance Modeling and Analysis for REG Plant. Based on the typical structure, the REG plant impedance network model is established, which considers the collecting lines, transformers, and other devices. Moreover, the influencing factors of the impedance characteristics of the REG plant are analyzed.

Chapter 13: Analysis of Broadband Oscillation for REG Connected into HVAC System. Based on the analytical impedance models of the REG plant, AC weak grid, and series compensation, the frequency-band division method for different REG connected into the AC transmission system is proposed. The dominant factors in different frequency bands causing oscillation are illustrated, and the oscillation mechanism is revealed.

Chapter 14: Analysis of Broadband Oscillation for REG Connected into HVDC System. Based on the impedance model of RPG plants and HVDC transmission systems, a method for dividing the frequency bands for system impedance is proposed considering different scenarios of RPG connected into LCC-HVDC and MMC-HVDC. The dominant factors of system oscillation in different frequency bands are analyzed, and the broadband oscillation mechanism is revealed.

References

1. TAYLOR C W. Power system voltage stability [M]. WANG W S, Translate. Beijing: China Electric Power Press, 2002. (Chinese)
2. CHENG S J, CAO Y J, JIANG Q Y. Theory and method of subsynchronous oscillation in power system [M]. Beijing: Science Press, 2009. (Chinese)
3. YUAN X M. Overview of problems in large-scale wind integrations [J]. Journal of Modern Power Systems and Clean Energy, 2013, 1(1): 22-25.
4. YUAN X M, ZHANG M Q, CHI Y N, et al. Basic challenges of and technical roadmap to power-electronized power system dynamics issues [J]. Proceedings of the CSEE, 2022, 42(5): 1904-1917. (Chinese)
5. XIE X R, LIU H K, HE J B, et al. On new oscillation issues of power systems [J]. Proceedings of the CSEE, 2018, 38(10): 2821-2828+3133. (Chinese)
6. WANG W S, LIN W F, HE G Q, et al. Enlightenment of 2021 Texas blackout to the renewable energy development in China [J]. Proceedings of the CSEE, 2021, 41(12): 4033-4043. (Chinese)
7. WANG W S, ZHANG C, HE G Q, et al. Overview of research on subsynchronous oscillations in large-scale wind farm integrated system [J]. Power System Technology, 2017, 41(4): 1050-1060. (Chinese)
8. HE G Q. Analysis and suppression for broadband oscillations of large-scale wind power cluster [D].Beijing: China Electric Power Research Institute, 2021. (Chinese)
9. HOU C C, ZHU M, LIU C, et al. Harmonic amplification mechanism and application of grid-tied VSI [J]. Proceedings of the CSEE, 2022, 42(17): 6398-6410. (Chinese)

Chapter 12
Impedance Modeling and Analysis of REG Plant

REG plants usually include dozens to thousands of units, as well as overhead transmission lines or cables, unit box transformers, station step-up transformers and other collecting network elements [1–3]. In the previous literature on the oscillation analysis of REG plant grid-connected system, the REG units of same type are usually equivalent to a single unit with enlarged capacity, and the collecting lines and transformers are equivalent to an aggregation impedance. However, the interaction between different devices through the collection network, especially the frequency coupling effect in the sub/super synchronous band, is ignored.

This chapter first introduces the typical structure of the REG plant, and presents the impedance model of collecting elements, which are modeled as consistent with the structure of REG unit impedance [4–8]. Secondly, the characterization method based on voltage controlled current source (VCCS) is proposed for the frequency coupling effect of REG unit, and the frequency-coupling impedance network model is presented for REG plant. Then, the analytic expression of equivalent impedance for REG plant and the practical calculation method are proposed. Finally, based on the typical plant configuration and time-domain simulation model, the factors affecting the impedance characteristics of REG plants are analyzed.

12.1 Structure of REG Plant and Model of Collecting Network

12.1.1 Typical Structure of REG Plant

The typical composition and structure of wind and photovoltaic (PV) plant are shown in Figs. 12.1 and 12.2, respectively, generally including wind turbines/PV units, step-up transformers, collecting lines, reactive power compensation device, etc. Several

© China Electric Power Press 2023

W. Wang et al., *Analysis and Mitigation of Broadband Oscillation in Renewable Energy Generation and AC/DC Transmission Systems*,
https://doi.org/10.1007/978-981-99-1568-2_12

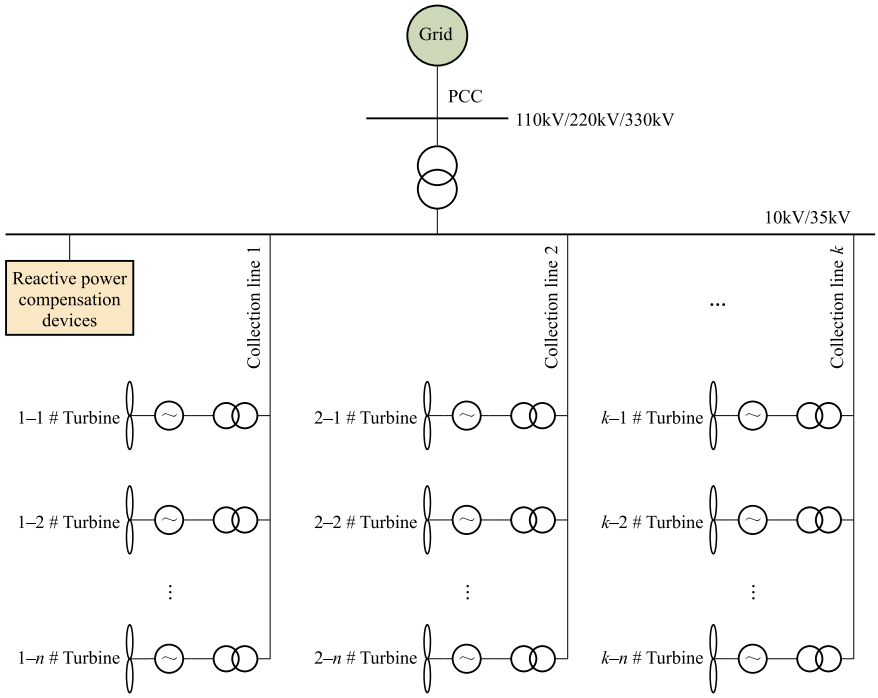

Fig. 12.1 Typical composition and structure of wind plant

wind turbines/PV units connect to a 10 kV/35 kV medium voltage collecting line through the step-up transformers in series. Several collecting lines connect to the medium voltage bus of plant, and then step up to 110 kV/220 kV/330 kV through the main transformer to connect to the grid.

For larger-scale REG plants, the structure with multiple main transformers and multiple collecting buses in parallel would be used. The step-up stations of REG plants undertaking collecting function would use three-winding transformers, as shown in Fig. 12.3. The high-voltage side is generally 220 kV/330 kV, the medium voltage side is generally 110 kV, which collects other REG plants, and the low-voltage side is generally 35 kV, which collects the REG units and reactive power compensation devices of the plant.

With reference to the definition of the impedance characteristics of REG unit and other devices, the impedance of REG plant is defined as the disturbance response relationship between the small-signal voltage and current with the PCC of plant as the port. Clearly, the impedance of the plant is not only related to the REG units, but also to other devices or elements in the plant, such as the reactive power compensation devices and collecting elements.

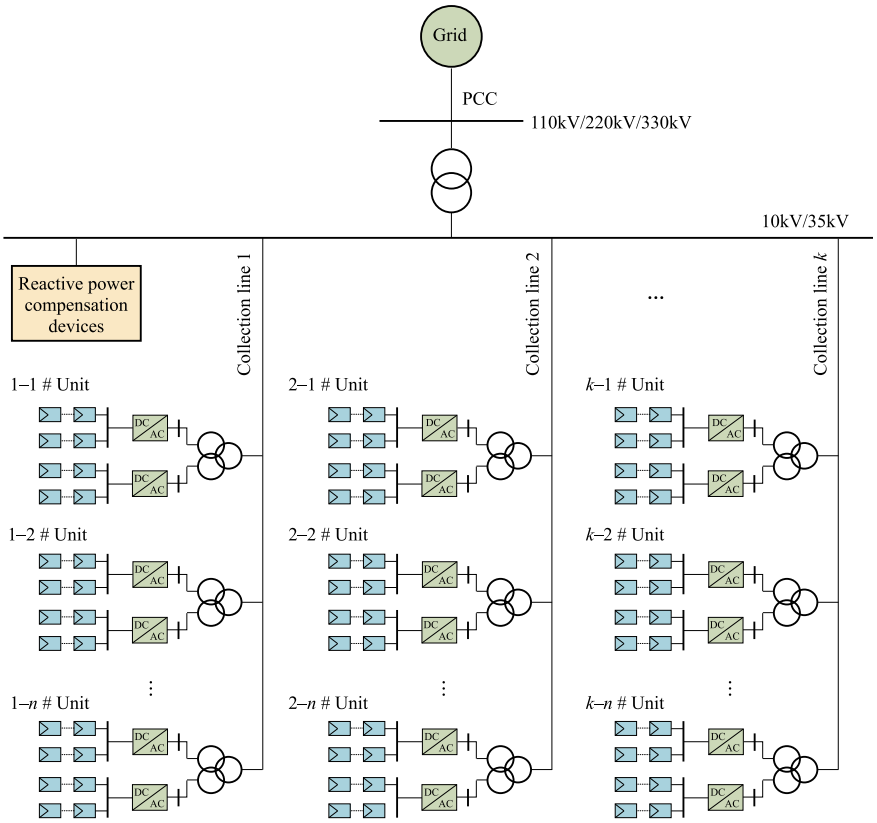

Fig. 12.2 Typical composition and structure of PV plant

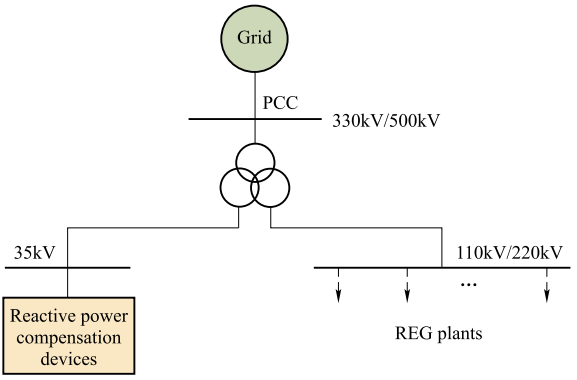

Fig. 12.3 Structure of REG plants undertaking collecting function

12.1.2 Collecting Line Model

Overhead lines or cables are generally used as the collecting lines for REG plants. The parameters of overhead lines and cables mainly depend on their manufacturing standard specifications, and are related to external factors such as erection and laying conditions. In practice, the parameters of lines and cables can be obtained through theoretical calculations or actual measurements. This section takes overhead lines as an example, introduces the models and parameters applied to impedance modeling and analysis.

Suppose an overhead line of length l, of which the parameters are uniformly distributed along the line. The impedance and conductance per unit length are $\boldsymbol{Z}_0 = r_0 + \mathrm{j}\omega L_0$ and $\boldsymbol{Y}_0 = g_0 + \mathrm{j}\omega C_0$, respectively, in which r_0, L_0, g_0 and C_0 are the resistance, inductance, conductance and capacitance per unit length, respectively. A microsegment $\mathrm{d}x$ is taken at the point distance x from the end, and the equivalent circuit is shown in Fig. 12.4.

The differential equation for the line is established and solved, providing the following relationship between the voltage and current at the beginning of the line and the voltage and current at the end.

$$\begin{cases} \boldsymbol{V}_{\mathrm{L1}} = \boldsymbol{V}_{\mathrm{L2}} \cosh(\boldsymbol{\gamma} l) + \boldsymbol{I}_{\mathrm{L2}} \boldsymbol{Z}_{\mathrm{C}} \sinh(\boldsymbol{\gamma} l) \\ \boldsymbol{I}_{\mathrm{L1}} = \dfrac{\boldsymbol{V}_{\mathrm{L2}}}{\boldsymbol{Z}_{\mathrm{C}}} \sinh(\boldsymbol{\gamma} l) + \boldsymbol{I}_{\mathrm{L2}} \cosh(\boldsymbol{\gamma} l) \end{cases} \tag{12.1}$$

where $\boldsymbol{\gamma}$ is the propagation characteristic of the line and $\boldsymbol{Z}_{\mathrm{C}}$ is the characteristic impedance, both of which are frequency-dependent parameters.

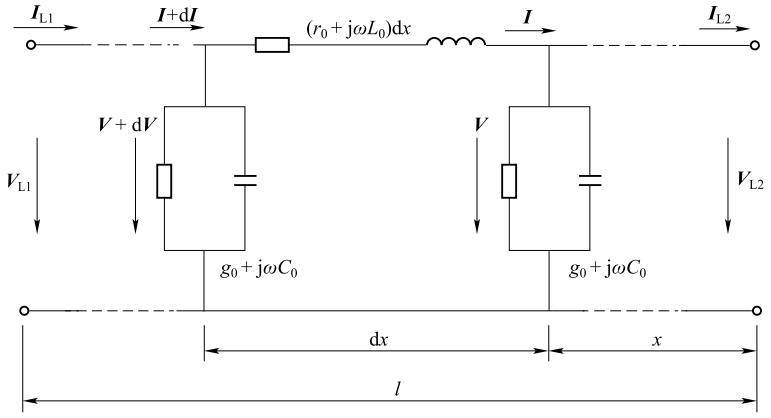

Fig. 12.4 Equivalent circuit of overhead transmission line

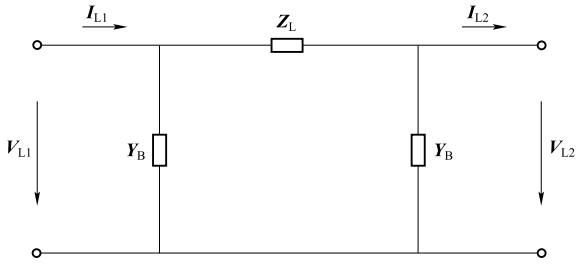

Fig. 12.5 Lumped parameter equivalent circuit of Π-type for overhead transmission line

$$\boldsymbol{Z}_{\mathrm{C}}(f)=\sqrt{\frac{r_0+\mathrm{j}2\pi f L_0}{g_0+\mathrm{j}2\pi f C_0}} \tag{12.2}$$

$$\boldsymbol{\gamma}(f)=\sqrt{(g_0+\mathrm{j}2\pi f C_0)(r_0+\mathrm{j}2\pi f L_0)} \tag{12.3}$$

From Eq. (12.1), the lumped parameter equivalent circuit of type Π for the line can be built as shown in Fig. 12.5.

where $\boldsymbol{Z}_{\mathrm{L}}$ and $\boldsymbol{Y}_{\mathrm{B}}$ are impedance and admittance of the Π-type equivalent circuit for overhead line, which can be expressed as

$$\boldsymbol{Z}_{\mathrm{L}}=\boldsymbol{Z}_{\mathrm{C}}\sinh(\boldsymbol{\gamma}l) \tag{12.4}$$

$$\boldsymbol{Y}_{\mathrm{B}}=\frac{\cosh(\boldsymbol{\gamma}l)-1}{\boldsymbol{Z}_{\mathrm{C}}\sinh(\boldsymbol{\gamma}l)} \tag{12.5}$$

Thus, Eq. (12.1) can be rewritten as

$$\begin{cases}\boldsymbol{V}_{\mathrm{L1}}=(1+\boldsymbol{Z}_{\mathrm{L}}\boldsymbol{Y}_{\mathrm{B}})\boldsymbol{V}_{\mathrm{L2}}+\boldsymbol{Z}_{\mathrm{L}}\boldsymbol{I}_{\mathrm{L2}}\\ \boldsymbol{I}_{\mathrm{L1}}=(2\boldsymbol{Y}_{\mathrm{B}}+\boldsymbol{Y}_{\mathrm{B}}\boldsymbol{Z}_{\mathrm{L}}\boldsymbol{Y}_{\mathrm{B}})\boldsymbol{V}_{\mathrm{L2}}+(1+\boldsymbol{Y}_{\mathrm{B}}\boldsymbol{Z}_{\mathrm{L}})\boldsymbol{I}_{\mathrm{L2}}\end{cases} \tag{12.6}$$

Transmission lines are generally three-phase symmetrical passive components, such that both their positive- and negative-sequence equivalent circuit models can be captured by the circuit shown in Fig. 12.5, and there are no control-induced frequency coupling effect as described previously. However, to ensure consistency in the model structure for system analysis, the impedance matrix $\boldsymbol{Z}_{\mathrm{Lpn}}$ and the conductance matrix $\boldsymbol{Y}_{\mathrm{Bpn}}$ of the line are defined with reference to the impedance models of REG units and other devices as

$$\boldsymbol{Z}_{\mathrm{Lpn}}=\begin{bmatrix}\boldsymbol{Z}_{\mathrm{L}}^{\mathrm{pp}} & \boldsymbol{Z}_{\mathrm{L}}^{\mathrm{np}}\\ \boldsymbol{Z}_{\mathrm{L}}^{\mathrm{pn}} & \boldsymbol{Z}_{\mathrm{L}}^{\mathrm{nn}}\end{bmatrix} \tag{12.7}$$

$$\boldsymbol{Y}_{\mathrm{Bpn}}=\begin{bmatrix}\boldsymbol{Y}_{\mathrm{B}}^{\mathrm{pp}} & \boldsymbol{Y}_{\mathrm{B}}^{\mathrm{np}}\\ \boldsymbol{Y}_{\mathrm{B}}^{\mathrm{pn}} & \boldsymbol{Y}_{\mathrm{B}}^{\mathrm{nn}}\end{bmatrix} \tag{12.8}$$

where $\boldsymbol{Z}_{\mathrm{L}}^{\mathrm{pp}}$ is the positive-sequence impedance of the line at frequency f_{p} and $\boldsymbol{Z}_{\mathrm{L}}^{\mathrm{nn}}$ is the negative-sequence impedance at frequency $f_{\mathrm{p}} - 2f_1$, which can be calculated according to Eq. (12.4); $\boldsymbol{Z}_{\mathrm{L}}^{\mathrm{pn}}$ and $\boldsymbol{Z}_{\mathrm{L}}^{\mathrm{np}}$ are the coupling impedances between the frequency f_{p} of positive-sequence and the frequency $f_{\mathrm{p}} - 2f_1$ of negative-sequence; $\boldsymbol{Y}_{\mathrm{B}}^{\mathrm{pp}}$ and $\boldsymbol{Y}_{\mathrm{B}}^{\mathrm{nn}}$ are the positive- and negative-sequence admittance to ground at frequency f_{p} and $f_{\mathrm{p}} - 2f_1$, respectively, which can be calculated according to Eq. (12.5); $\boldsymbol{Y}_{\mathrm{B}}^{\mathrm{pn}}$ and $\boldsymbol{Y}_{\mathrm{B}}^{\mathrm{np}}$ are the coupling admittance to ground between the frequency f_{p} of positive-sequence and the frequency $f_{\mathrm{p}} - 2f_1$ of negative-sequence.

Thus, the relationship between the small-signal voltage and current at the beginning and end of the line can be described as

$$\begin{cases} \hat{\boldsymbol{v}}_{\mathrm{L1}} = \left(\boldsymbol{U} + \boldsymbol{Z}_{\mathrm{Lpn}}\boldsymbol{Y}_{\mathrm{Bpn}}\right)\hat{\boldsymbol{v}}_{\mathrm{L2}} + \boldsymbol{Z}_{\mathrm{Lpn}}\hat{\boldsymbol{i}}_{\mathrm{L2}} \\ \hat{\boldsymbol{i}}_{\mathrm{L1}} = \left(2\boldsymbol{Y}_{\mathrm{Bpn}} + \boldsymbol{Y}_{\mathrm{Bpn}}\boldsymbol{Z}_{\mathrm{Lpn}}\boldsymbol{Y}_{\mathrm{Bpn}}\right)\hat{\boldsymbol{v}}_{\mathrm{L2}} + \left(\boldsymbol{U} + \boldsymbol{Y}_{\mathrm{Bpn}}\boldsymbol{Z}_{\mathrm{Lpn}}\right)\hat{\boldsymbol{i}}_{\mathrm{L2}} \end{cases} \tag{12.9}$$

where $\hat{\boldsymbol{v}}_{\mathrm{L1}} = \left[\hat{\boldsymbol{v}}_{1\mathrm{p}}, \hat{\boldsymbol{v}}_{1\mathrm{n}}\right]^{\mathrm{T}}$ and $\hat{\boldsymbol{v}}_{\mathrm{L2}} = \left[\hat{\boldsymbol{v}}_{2\mathrm{p}}, \hat{\boldsymbol{v}}_{2\mathrm{n}}\right]^{\mathrm{T}}$ are the small-signal voltage vectors at the beginning and end of the line, respectively, in which $\hat{\boldsymbol{v}}_{1\mathrm{p}}$ and $\hat{\boldsymbol{v}}_{2\mathrm{p}}$ are the positive-sequence small-signal voltage components at frequency f_{p}, respectively; $\hat{\boldsymbol{v}}_{1\mathrm{n}}$ and $\hat{\boldsymbol{v}}_{2\mathrm{n}}$ are the negative-sequence small-signal voltage components at frequency $f_{\mathrm{p}} - 2f_1$, respectively; $\hat{\boldsymbol{i}}_{\mathrm{L1}} = \left[\hat{\boldsymbol{i}}_{1\mathrm{p}}, \hat{\boldsymbol{i}}_{1\mathrm{n}}\right]^{\mathrm{T}}$ and $\hat{\boldsymbol{i}}_{\mathrm{L2}} = \left[\hat{\boldsymbol{i}}_{2\mathrm{p}}, \hat{\boldsymbol{i}}_{2\mathrm{n}}\right]^{\mathrm{T}}$ are the small-signal current vectors at the beginning and end of the line.

To verify the above model, electromagnetic transient (EMT) simulation model is established as shown in Fig. 12.6. The impedance characteristics of the 35 kV overhead lines commonly used in REG plants are scanned for verification, and the line parameters used are presented in Table 12.1. The beginning of the line is connected to a 35 kV ideal voltage source in series with a small-signal disturbance source, and the end of the line is connected to a load impedance $\boldsymbol{Z}_{\mathrm{o}}$, which is equal to 10 Ω, and Eq. (12.10) can be obtained.

$$\begin{aligned} \hat{\boldsymbol{v}}_{\mathrm{L1}} = &\left[\left(\boldsymbol{U} + \boldsymbol{Z}_{\mathrm{Lpn}}\boldsymbol{Y}_{\mathrm{Bpn}}\right)\boldsymbol{Z}_{\mathrm{o}} + \boldsymbol{Z}_{\mathrm{Lpn}}\right] \\ &\cdot \left[\left(2\boldsymbol{Y}_{\mathrm{Bpn}} + \boldsymbol{Y}_{\mathrm{Bpn}}\boldsymbol{Z}_{\mathrm{Lpn}}\boldsymbol{Y}_{\mathrm{Bpn}}\right)\boldsymbol{Z}_{\mathrm{o}} + \left(\boldsymbol{U} + \boldsymbol{Y}_{\mathrm{Bpn}}\boldsymbol{Z}_{\mathrm{Lpn}}\right)\right]^{-1}\hat{\boldsymbol{i}}_{\mathrm{L1}} \end{aligned} \tag{12.10}$$

Let $\boldsymbol{Z}_{1\mathrm{pn}}$ be the port impedance at the beginning of the line.

$$\boldsymbol{Z}_{1\mathrm{pn}} = \begin{bmatrix} \boldsymbol{Z}_1^{\mathrm{pp}} & \boldsymbol{Z}_1^{\mathrm{np}} \\ \boldsymbol{Z}_1^{\mathrm{pn}} & \boldsymbol{Z}_1^{\mathrm{nn}} \end{bmatrix} \tag{12.11}$$

$$\hat{\boldsymbol{v}}_{\mathrm{L1}} = \boldsymbol{Z}_{1\mathrm{pn}}\hat{\boldsymbol{i}}_{\mathrm{L1}} \tag{12.12}$$

That is, the elements of the impedance matrix $\boldsymbol{Z}_{1\mathrm{pn}}$ are scanned for verification.

The calculated and scanned results of the impedance of collecting line are shown in Fig. 12.7. Figure 12.7(a) presents the calculated (lines) and scanned (dots) results of the positive-sequence impedance $\boldsymbol{Z}_1^{\mathrm{pp}}$ and negative-sequence impedance $\boldsymbol{Z}_1^{\mathrm{nn}}$. The calculated and scanned are basically equal. In the frequency band below 100 Hz,

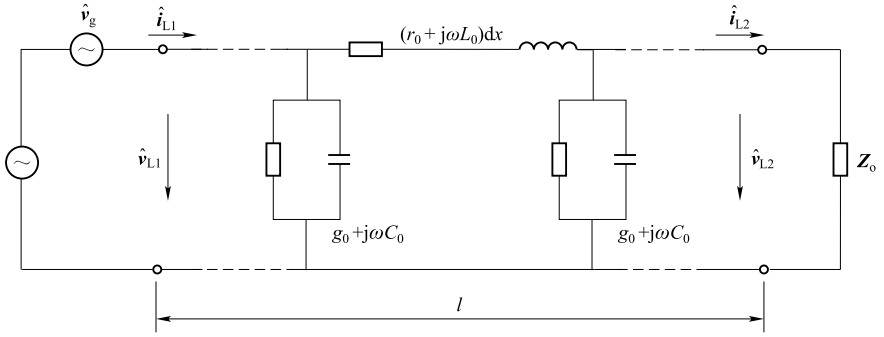

Fig. 12.6 Schematic diagram of impedance simulation scanning model of 35 kV transmission line

Table 12.1 Simulation parameters of LGJ-120/20 model collecting line of REG plant

Simulation parameter	Value
Nominal cross-sectional area (mm^2)	134.49
Electrical resistivity ($\Omega \cdot mm^2/km$)	31.2
Phase spacing (m)	2.0
Conductor height (m)	15.0
Line length (km)	20.0

the impedance of the 35 kV collecting line mainly shows resistive inductance. With increasing frequency, the inductance characteristic gradually increases, and the resonance frequency of the line is approximately 3700 Hz. Figure 12.7(b) shows the simulation scanned results of the coupling impedance $\boldsymbol{Z}_1^{\mathrm{pn}}$ and $\boldsymbol{Z}_1^{\mathrm{np}}$. It can be seen that the amplitude of the coupling impedance is much smaller than the positive- and negative-sequence impedance, therefore, the coupling effect of the impedance of collecting line can be neglected.

Therefore, the impedance and admittance matrix models shown in Eqs. (12.7) and (12.8) can be simplified to

$$\boldsymbol{Z}_{\mathrm{Lpn}} = \begin{bmatrix} \boldsymbol{Z}_{\mathrm{L}}^{\mathrm{pp}} & 0 \\ 0 & \boldsymbol{Z}_{\mathrm{L}}^{\mathrm{nn}} \end{bmatrix} \tag{12.13}$$

$$\boldsymbol{Y}_{\mathrm{Bpn}} = \begin{bmatrix} \boldsymbol{Y}_{\mathrm{B}}^{\mathrm{pp}} & 0 \\ 0 & \boldsymbol{Y}_{\mathrm{B}}^{\mathrm{nn}} \end{bmatrix} \tag{12.14}$$

To facilitate network computing, this book describes line impedance in derivative form

$$\boldsymbol{Y}_{\mathrm{Lpn}} = \boldsymbol{Z}_{\mathrm{Lpn}}^{-1} = \begin{bmatrix} \boldsymbol{Y}_{\mathrm{L}}^{\mathrm{pp}} & 0 \\ 0 & \boldsymbol{Y}_{\mathrm{L}}^{\mathrm{nn}} \end{bmatrix} \tag{12.15}$$

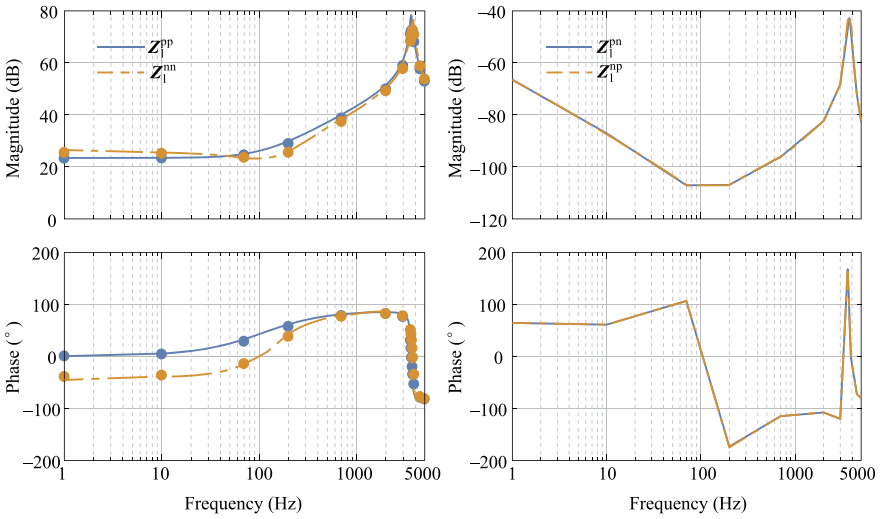

(a) Positive- and negative- sequence impedances Z_l^{pp} and Z_l^{nn} (b) Coupling impedances Z_l^{pn} and Z_l^{np}

Fig. 12.7 The calculated and scanned results of the impedance of collecting line

For medium- and low-voltage overhead lines of short distances, the impedance and the conductance to ground can be modeled using a Π-type circuit equivalent with lumped parameters

$$\boldsymbol{Z}_{\mathrm{L}} = (r_0 + \mathrm{j}2\pi f L_0) \cdot l \tag{12.16}$$

$$\boldsymbol{Y}_{\mathrm{B}} = \frac{(g_0 + \mathrm{j}2\pi f C_0) \cdot l}{2} \tag{12.17}$$

Otherwise, the ground admittance $\boldsymbol{Y}_{\mathrm{B}}$ can be neglected. Figure 12.8 shows the results of the comparison between the detailed model and the simplified model, and it can be seen that the simplified model can accurately describe the impedance characteristics of the 35 kV collecting line of REG plant in the frequency band below 2000 Hz.

12.1.3 Transformer Model

The transformers in the REG plant mainly include the box type transformers of units and the main transformers of the plant. The box type transformer of the wind turbine usually adopts the double winding transformer. The box type transformer of the PV unit and the main transformer of the plant adopt both the double winding and three winding transformers according to the different capacities and connection modes.

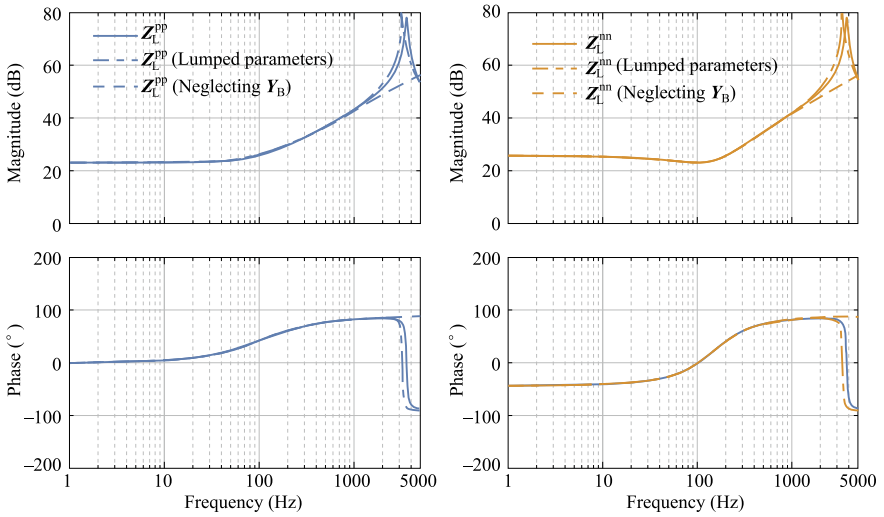

Fig. 12.8 Detail model and simplified model of collecting line

This section introduces the models and parameters applied to impedance modeling and analysis by taking a double winding transformer as an example.

The equivalent circuit of double winding transformer generally converts the resistance and leakage reactance of the secondary winding to the primary winding side and combines them with the resistance and leakage reactance of the primary winding, which is represented by the equivalent impedance $R_T + jX_T$, and converts the excitation branch to the primary winding side, which is represented by the equivalent admittance $G_T - jB_T$, as shown in Fig. 12.9.

The equivalent circuit parameters of transformer generally include resistance R_T, reactance X_T, conductance G_T and susceptance B_T. These parameters can be calculated from the four test data on the factory nameplate, including short circuit loss ΔP_S, short circuit voltage $V_S\%$, open circuit loss ΔP_0, and open circuit current $I_0\%$. The first two data are obtained from the short circuit test to determine R_T and X_T, and the last two data are obtained from the open circuit to determine G_T and B_T. The

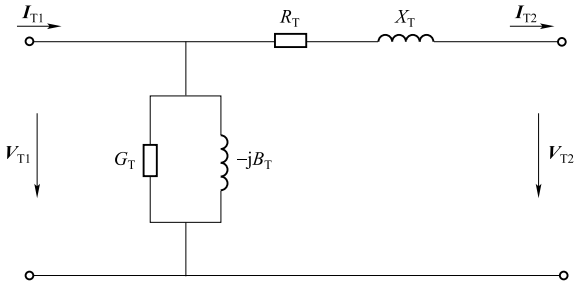

Fig. 12.9 Equivalent circuit of double winding transformer

specific calculation formula is

$$R_{\mathrm{T}} = \frac{\Delta P_{\mathrm{S}} V_{\mathrm{N}}^2}{S_{\mathrm{N}}^2} \times 10^3 \tag{12.18}$$

$$X_{\mathrm{T}} = \frac{V_{\mathrm{S}}\%}{100} \times \frac{V_{\mathrm{N}}^2}{S_{\mathrm{N}}} \times 10^3 \tag{12.19}$$

$$G_{\mathrm{T}} = \frac{\Delta P_0}{V_{\mathrm{N}}^2} \times 10^{-3} \tag{12.20}$$

$$B_{\mathrm{T}} = \frac{I_0\%}{100} \times \frac{S_{\mathrm{N}}}{V_{\mathrm{N}}^2} \times 10^{-3} \tag{12.21}$$

where, S_{N} is the three-phase rated capacity of the transformer, kVA; V_{N} is the rated line voltage of transformer, kV; ΔP_{S} and ΔP_0 are short-circuit loss and open-circuit loss respectively, kW; R_{T} and X_{T} are resistance and reactance respectively, Ω; G_{T} and B_{T} are conductance and susceptance respectively, S.

If the magnetization saturation characteristic of the iron core is ignored, the equivalent circuit of the transformer can be represented as a Γ-type equivalent circuit as shown in Fig. 12.10, in which $\boldsymbol{Z}_{\mathrm{T}} = R_{\mathrm{T}} + \mathrm{j}\omega L_{\mathrm{T}}$, $\boldsymbol{Y}_{\mathrm{T}} = G_{\mathrm{T}} - \mathrm{j}\omega C_{\mathrm{T}}$, $L_{\mathrm{T}} = X_{\mathrm{T}}/\omega_1$, $C_{\mathrm{T}} = B_{\mathrm{T}}/\omega_1$.

Referring to the impedance model expression of transmission line, the impedance matrix $\boldsymbol{Z}_{\mathrm{Tpn}}$ and admittance matrix $\boldsymbol{Y}_{\mathrm{Tpn}}$ of double winding transformer are respectively expressed as

$$\boldsymbol{Z}_{\mathrm{Tpn}} = \begin{bmatrix} \boldsymbol{Z}_{\mathrm{T}}^{\mathrm{pp}} & \boldsymbol{Z}_{\mathrm{T}}^{\mathrm{np}} \\ \boldsymbol{Z}_{\mathrm{T}}^{\mathrm{pn}} & \boldsymbol{Z}_{\mathrm{T}}^{\mathrm{nn}} \end{bmatrix} \tag{12.22}$$

$$\boldsymbol{Y}_{\mathrm{Tpn}} = \begin{bmatrix} \boldsymbol{Y}_{\mathrm{T}}^{\mathrm{pp}} & \boldsymbol{Y}_{\mathrm{T}}^{\mathrm{np}} \\ \boldsymbol{Y}_{\mathrm{T}}^{\mathrm{pn}} & \boldsymbol{Y}_{\mathrm{T}}^{\mathrm{nn}} \end{bmatrix} \tag{12.23}$$

where $\boldsymbol{Z}_{\mathrm{T}}^{\mathrm{pp}}$ is the positive-sequence impedance of the transformer at frequency f_{p}, $\boldsymbol{Z}_{\mathrm{T}}^{\mathrm{nn}}$ is the negative-sequence impedance at frequency $f_{\mathrm{p}} - 2f_1$; $\boldsymbol{Z}_{\mathrm{T}}^{\mathrm{pn}}$ and $\boldsymbol{Z}_{\mathrm{T}}^{\mathrm{np}}$ are

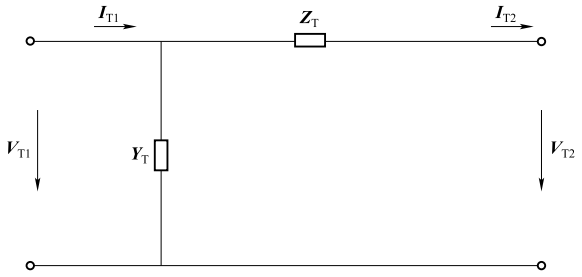

Fig. 12.10 Γ-type equivalent circuit of double winding transformer

the coupling impedances between the frequency f_p of positive-sequence and the frequency $f_p - 2f_1$ of negative-sequence; $\boldsymbol{Y}_T^{pp}$ and $\boldsymbol{Y}_T^{nn}$ are the positive- and negative-sequence admittance to ground at frequency f_p and $f_p - 2f_1$, respectively; $\boldsymbol{Y}_T^{pn}$ and $\boldsymbol{Y}_T^{np}$ are the coupling admittance to ground between the frequency f_p of positive-sequence and the frequency $f_p - 2f_1$ of negative-sequence.

The relationship between small-signal voltage and current at the primary and secondary sides of the transformer can be described as

$$\begin{cases} \hat{\boldsymbol{v}}_{T1} = \hat{\boldsymbol{v}}_{T2} + \boldsymbol{Z}_{Tpn}\hat{\boldsymbol{i}}_{T2} \\ \hat{\boldsymbol{i}}_{T1} = \boldsymbol{Y}_{Tpn}\hat{\boldsymbol{v}}_{T2} + \left(\boldsymbol{Y}_{Tpn}\boldsymbol{Z}_{Tpn} + \boldsymbol{U}\right)\hat{\boldsymbol{i}}_{T2} \end{cases} \tag{12.24}$$

where $\hat{\boldsymbol{v}}_{T1} = \left[\hat{\boldsymbol{v}}_{1p}, \hat{\boldsymbol{v}}_{1n}\right]^T$ and $\hat{\boldsymbol{v}}_{T2} = \left[\hat{\boldsymbol{v}}_{2p}, \hat{\boldsymbol{v}}_{2n}\right]^T$ are the small-signal voltage vectors at the primary and secondary sides of the transformer, respectively, in which $\hat{\boldsymbol{v}}_{1p}$ and $\hat{\boldsymbol{v}}_{2p}$ are the positive-sequence small-signal voltage components at frequency f_p, respectively $\hat{\boldsymbol{v}}_{1n}$ and $\hat{\boldsymbol{v}}_{2n}$ are the negative-sequence small-signal voltage components at frequency $f_p - 2f_1$, respectively; $\hat{\boldsymbol{i}}_{T1} = \left[\hat{\boldsymbol{i}}_{1p}, \hat{\boldsymbol{i}}_{1n}\right]^T$ and $\hat{\boldsymbol{i}}_{T2} = \left[\hat{\boldsymbol{i}}_{2p}, \hat{\boldsymbol{i}}_{2n}\right]^T$ are the small-signal current vectors at the primary and secondary sides of the transformer.

In order to verify the effectiveness of the above models, an EMT simulation model as shown in Fig. 12.11 is established to scan the impedance characteristics of 220 kV/35 kV double winding transformer commonly used in REG plant. Transformer parameters are shown in Table 12.2. The primary side is connected to the 220 kV ideal voltage source, the small-signal voltage disturbance source is connected in series, and the secondary side is connected to the load impedance. It can be obtained by solving Eq. (12.24),

$$\hat{\boldsymbol{v}}_{T1} = \left(\boldsymbol{Z}_o + \boldsymbol{Z}_{Tpn}\right)\left(\boldsymbol{Z}_o\boldsymbol{Y}_{Tpn} + \boldsymbol{Y}_{Tpn}\boldsymbol{Z}_{Tpn} + \boldsymbol{U}\right)^{-1}\hat{\boldsymbol{i}}_{T1} \tag{12.25}$$

Let $\boldsymbol{Z}_{1pn}$ be the port impedance at the primary side.

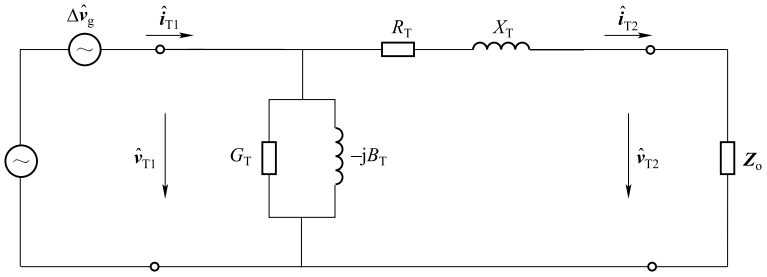

Fig. 12.11 Schematic diagram of impedance simulation scanning model of double winding transformer

Table 12.2 Simulation parameters of 220 kV/35 kV double winding transformer of REG plant

Simulation Parameter	Value
Rated capacity (MVA)	100
Rated frequency (Hz)	50
Rated frequency of primary side (kV)	230
Rated frequency of secondary side (kV)	37.5
Short-circuit loss (kW)	285
Short-circuit voltage (%)	13
Open-circuit loss (kW)	65
Open-circuit current (%)	0.11

$$\boldsymbol{Z}_{1\mathrm{pn}} = \begin{bmatrix} \boldsymbol{Z}_1^{\mathrm{pp}} & \boldsymbol{Z}_1^{\mathrm{np}} \\ \boldsymbol{Z}_1^{\mathrm{pn}} & \boldsymbol{Z}_1^{\mathrm{nn}} \end{bmatrix} \tag{12.26}$$

$$\hat{\boldsymbol{v}}_{\mathrm{T1}} = \boldsymbol{Z}_{1\mathrm{pn}} \hat{\boldsymbol{i}}_{\mathrm{T1}} \tag{12.27}$$

That is, the elements of the impedance matrix $\boldsymbol{Z}_{1\mathrm{pn}}$ are scanned for verification.

The calculated and scanned results of the impedance of double winding transformer are shown in Fig. 12.12. Figure 12.12(a) presents the calculated (lines) and scanned (dots) results of the positive- and negative- sequence impedances $\boldsymbol{Z}_1^{\mathrm{pp}}$ and $\boldsymbol{Z}_1^{\mathrm{nn}}$. The calculated and scanned are basically equal. In the frequency band below 100 Hz, the impedance of the transformer mainly shows resistive inductance. With increasing frequency, the inductance characteristic gradually increases. Figure 12.12(b) shows the simulation scanned results of the coupling impedance $\boldsymbol{Z}_1^{\mathrm{pn}}$ and $\boldsymbol{Z}_1^{\mathrm{np}}$. It can be seen that the amplitude of the coupling impedance is much smaller than the positive- and negative-sequence impedances, therefore, the coupling effect of the impedance of transformer can be neglected.

The impedance and admittance matrix models shown in Eqs. (12.22) and (12.23) can be simplified to

$$\boldsymbol{Z}_{\mathrm{Tpn}} = \begin{bmatrix} \boldsymbol{Z}_{\mathrm{T}}^{\mathrm{pp}} & 0 \\ 0 & \boldsymbol{Z}_{\mathrm{T}}^{\mathrm{nn}} \end{bmatrix} \tag{12.28}$$

$$\boldsymbol{Y}_{\mathrm{Tpn}} = \begin{bmatrix} \boldsymbol{Y}_{\mathrm{T}}^{\mathrm{pp}} & 0 \\ 0 & \boldsymbol{Y}_{\mathrm{T}}^{\mathrm{nn}} \end{bmatrix} \tag{12.29}$$

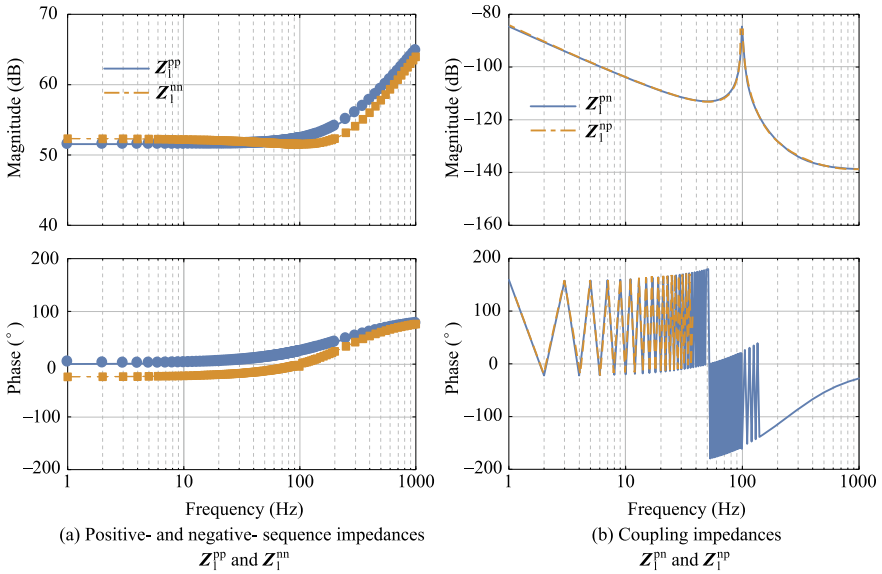

Fig. 12.12 The calculated and scanned results of the impedance of double winding transformer

12.2 Impedance Modeling of REG Plant

12.2.1 Small-Signal Circuit Model Involving Frequency Coupling Effect

With the consideration of frequency coupling effect, the impedance models of wind turbine, PV units inverter, SVG and other devices can all be described by the transfer function matrix models shown in Eqs. (12.30)–(12.32).

$$\hat{\boldsymbol{i}} = \boldsymbol{Y}_{\mathrm{dev}}\hat{\boldsymbol{v}} \tag{12.30}$$

$$\hat{\boldsymbol{v}} = \boldsymbol{Z}_{\mathrm{dev}}\hat{\boldsymbol{i}} \tag{12.31}$$

$$\boldsymbol{Z}_{\mathrm{dev}} = \boldsymbol{Y}_{\mathrm{dev}}^{-1} \tag{12.32}$$

where $\hat{\boldsymbol{v}} = \left[\hat{\boldsymbol{v}}^{\mathrm{p}}, \hat{\boldsymbol{v}}^{\mathrm{n}}\right]^{\mathrm{T}}$ is the small-signal voltage vector of the device port, in which $\hat{\boldsymbol{v}}^{\mathrm{p}}$ is the positive-sequence component at frequency f_{p}, $\hat{\boldsymbol{v}}^{\mathrm{n}}$ is the negative-sequence component at frequency $f_{\mathrm{p}} - 2f_{\mathrm{l}}$; $\hat{\boldsymbol{i}} = \left[\hat{\boldsymbol{i}}^{\mathrm{p}}, \hat{\boldsymbol{i}}^{\mathrm{n}}\right]^{\mathrm{T}}$ is the corresponding small-signal current vector; $\boldsymbol{Y}_{\mathrm{dev}}$ and $\boldsymbol{Z}_{\mathrm{dev}}$ are the admittance and impedance matrix models of the device respectively, with dimensions of 2×2, and are inverse matrices of each other.

Suppose the conductance model $\boldsymbol{Y}_{\text{dev}}$ as shown in Eq. (12.33).

$$\boldsymbol{Y}_{\text{dev}} = \begin{bmatrix} \boldsymbol{Y}^{\text{pp}} & \boldsymbol{Y}^{\text{np}} \\ \boldsymbol{Y}^{\text{pn}} & \boldsymbol{Y}^{\text{nn}} \end{bmatrix} \tag{12.33}$$

Then, the transitive and coupling relationship between the small-signal voltage $\hat{\boldsymbol{v}}$ and the small-signal current $\hat{\boldsymbol{i}}$ at the device port can be expressed as

$$\begin{cases} \hat{\boldsymbol{i}}^{\text{p}} = \boldsymbol{Y}^{\text{pp}}\hat{\boldsymbol{v}}^{\text{p}} + \boldsymbol{Y}^{\text{np}}\hat{\boldsymbol{v}}^{\text{n}} \\ \hat{\boldsymbol{i}}^{\text{n}} = \boldsymbol{Y}^{\text{pn}}\hat{\boldsymbol{v}}^{\text{p}} + \boldsymbol{Y}^{\text{nn}}\hat{\boldsymbol{v}}^{\text{n}} \end{cases} \tag{12.34}$$

That is, the positive-sequence small-signal current at frequency f_{p} includes not only the response component generated by the positive-sequence small-signal voltage $\hat{\boldsymbol{v}}^{\text{p}}$ at the same frequency via the positive-sequence conductor $\boldsymbol{Y}^{\text{pp}}$, but also the response component generated by the negative-sequence small-signal voltage $\hat{\boldsymbol{v}}^{\text{n}}$ at frequency $f_{\text{p}} - 2f_1$ via the coupling admittance $\boldsymbol{Y}^{\text{np}}$; the same is true for the components of the negative-sequence small-signal current $\hat{\boldsymbol{i}}^{\text{n}}$ at frequency $f_{\text{p}} - 2f_1$.

Based on the above analysis, the small-signal impedance model of wind turbine, PV units, SVG and other devices can be captured as two impedance circuits that are mutually coupled, as shown in Fig. 12.13.

In the figure, the controlled current sources $\hat{\boldsymbol{i}}^{\text{np}}$ and $\hat{\boldsymbol{i}}^{\text{pn}}$ represent the coupling effect between the two circuits, as shown in Eq. (12.35), in which $\hat{\boldsymbol{i}}^{\text{np}}$ represents the positive-sequence current response due to the negative-sequence voltage perturbation $\hat{\boldsymbol{v}}^{\text{n}}$, and $\hat{\boldsymbol{i}}^{\text{pn}}$ represents the negative-sequence current response due to the positive-sequence voltage perturbation $\hat{\boldsymbol{v}}^{\text{p}}$.

$$\begin{cases} \hat{\boldsymbol{i}}^{\text{np}} = \boldsymbol{Y}^{\text{np}}\hat{\boldsymbol{v}}^{\text{n}} \\ \hat{\boldsymbol{i}}^{\text{pn}} = \boldsymbol{Y}^{\text{pn}}\hat{\boldsymbol{v}}^{\text{p}} \end{cases} \tag{12.35}$$

When connected to the ideal power grid, the frequency coupling effect of device only exists inside the device, that is, the negative-sequence current $\hat{\boldsymbol{i}}^{\text{pn}}$ generated

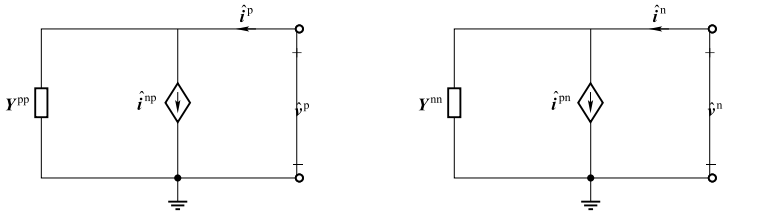

(a) Positive-sequence impedance circuit at f_{p} (b) Negative-sequence impedance circuit at f_{p}–$2f_1$

Fig. 12.13 Small-signal impedance circuit model of device

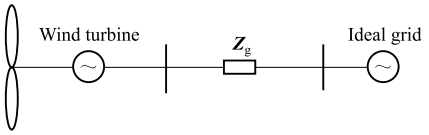

Fig. 12.14 Schematic diagram of single wind turbine grid-connected system

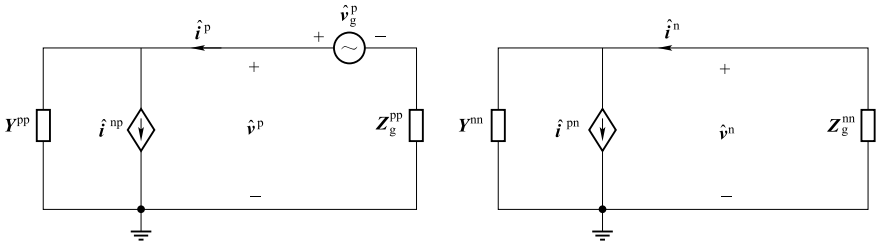

(a) Positive-sequence impedance circuit at f_p (b) Negative-sequence impedance circuit at f_p–$2f_1$

Fig. 12.15 Small-signal impedance circuit model of single wind turbine grid-connected system

by the positive-sequence voltage $\hat{\boldsymbol{v}}^p$ would not further induce or contribute to the negative-sequence voltage $\hat{\boldsymbol{v}}^n$. However, the frequency coupling effect will cause interactions between the device and the grid when the device is connected to nonideal grid conditions. Figure 12.14 shows a schematic diagram of single wind turbine grid-connected system, where $\boldsymbol{Z}_g$ is the grid impedance. The small-signal impedance circuit model of this system is developed and shown in Fig. 12.15, where $\boldsymbol{Z}_g^{pp}$ is the positive-sequence grid impedance at frequency f_p and $\boldsymbol{Z}_g^{nn}$ is the negative-sequence grid impedance at frequency $f_p - 2f_1$.

Assuming a positive-sequence voltage perturbation $\hat{\boldsymbol{v}}_g^p$ at frequency f_p is injected in series between the wind turbine and the grid, as shown in Fig. 12.15(a), the induced positive-sequence voltage component $\hat{\boldsymbol{v}}^p$ will produce a coupling current response $\hat{\boldsymbol{i}}^{pn}$ in the negative-sequence impedance circuit, meanwhile, due to the existence of negative-sequence grid impedance $\boldsymbol{Z}_g^{nn}$, $\hat{\boldsymbol{i}}^{pn}$ will induce a voltage response $\hat{\boldsymbol{v}}^n$, which would produce a current response $\hat{\boldsymbol{i}}^{np}$ in the positive-sequence impedance circuit. The above process forms a feedback to the positive-sequence current $\hat{\boldsymbol{i}}^p$ and voltage $\hat{\boldsymbol{v}}^p$.

A 1.5 MW permanent magnet synchronous generators (PMSG) -based wind turbine connected to power grid with short circuit ratio (SCR) of 5 is used as an example to verify the validity of the above model. Supposing the amplitude of the positive-sequence voltage perturbation $\hat{\boldsymbol{v}}_g^p$ is 0.1 p.u. of fundamental voltage, and the frequency is 70Hz. With the impedance circuit model presented in Fig. 12.15, the positive and negative-sequence voltage and current components $\hat{\boldsymbol{v}}^p$ and $\hat{\boldsymbol{v}}^n$, $\hat{\boldsymbol{i}}^p$ and $\hat{\boldsymbol{i}}^n$ at the wind turbine port are calculated, the comparison between the calculation and EMT simulation results are presented in Fig. 12.16. It can be seen that, the magnitude and phase of the calculation and simulation voltage and current components are basically

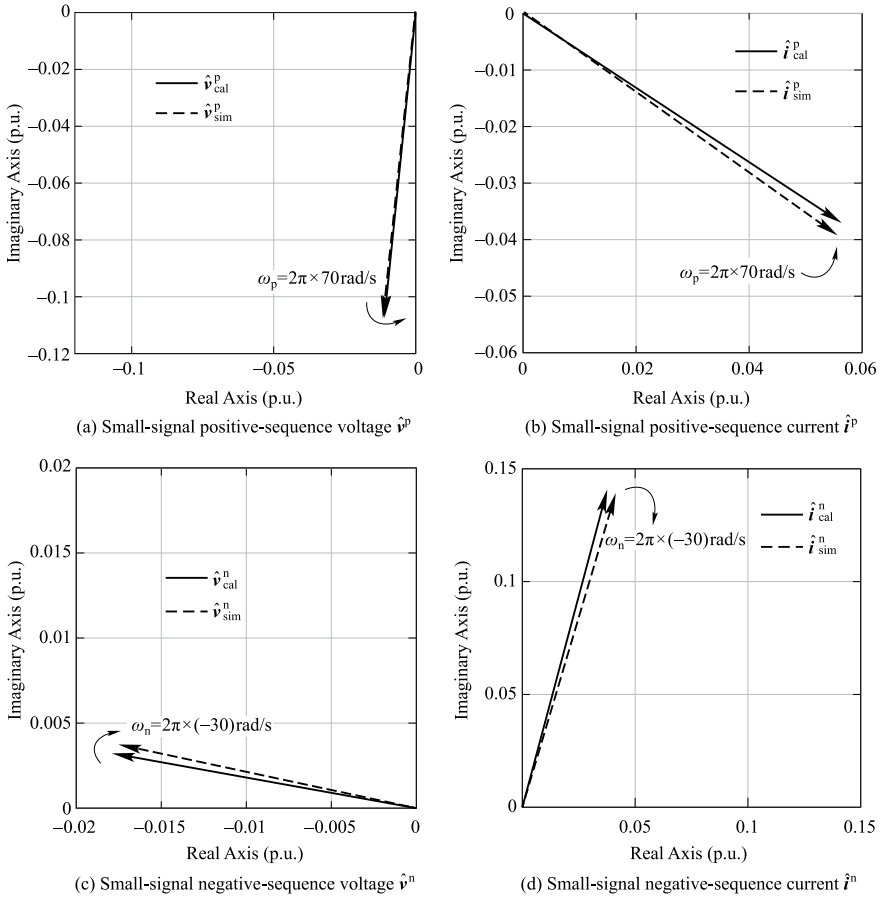

Fig. 12.16 Simulation and verification of small-signal impedance circuit model for single wind turbine grid-connected system

consistent. In addition to the positive-sequence voltage and current components at 70Hz, there are also negative-sequence voltage and current components at –30Hz, which are mathematically equivalent to the conjugate of the positive-sequence components at 30Hz.

12.2.2 Impedance Network Model of Multi-Unit System Involving Frequency Coupling Effect

For the wind plant and PV plant shown in Figs. 12.1 and 12.2, dozens or even hundreds of REG units are connected to the medium voltage bus through box transformers and

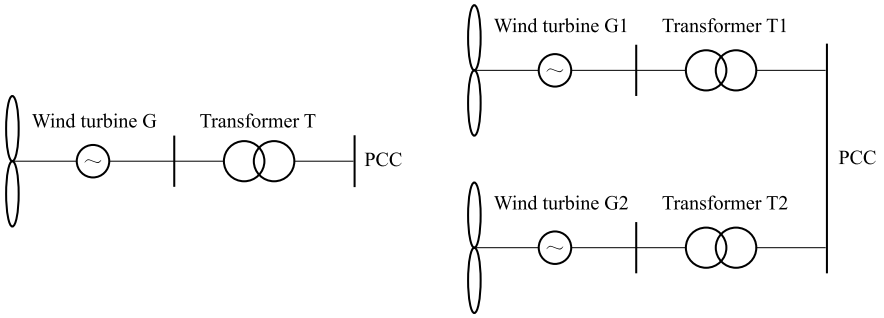

(a) Single wind turbine system (b) Two paralleled wind turbines system

Fig. 12.17 Single wind turbine and two paralleled wind turbines grid-connected system

collecting lines, and together with reactive power compensation devices, connected to the power grid through the main transformer. The overall impedance characteristics of the wind plant or PV plant are jointly determined by the REG units, reactive power compensation devices, and the collecting network. Meanwhile, the frequency coupling effects of the devices would cause complex interactions between the devices and the collecting network. In order to establish the impedance model of the plant, the series and parallel connection laws of the small-signal impedance models considering frequency coupling effect are first discussed, based on the simple systems shown in Fig. 12.17.

The single wind turbine system shown in Fig. 12.17(a) can be captured as the small-signal impedance circuit model shown in Fig. 12.18, where $\boldsymbol{Y}_{\mathrm{W}}$ is the small-signal admittance matrix of the wind turbine, $\boldsymbol{Y}_{\mathrm{T}}$ is the small-signal admittance matrix of the transformer, $\hat{\boldsymbol{v}}_{\mathrm{PCC}}$ and $\hat{\boldsymbol{i}}_{\mathrm{PCC}}$ are the small-signal voltage and current vectors at the point of common coupling (PCC) point respectively, $\hat{\boldsymbol{v}}_{\mathrm{W}}$ and $\hat{\boldsymbol{i}}_{\mathrm{W}}$ are the small-signal voltage and current vectors at the wind turbine port respectively.

The circuit equations of the model shown in Fig. 12.18 can be represented as Eqs. (12.36)–(12.38).

$$\hat{\boldsymbol{i}}_{\mathrm{W}} = \boldsymbol{Y}_{\mathrm{W}}\hat{\boldsymbol{v}}_{\mathrm{W}} \tag{12.36}$$

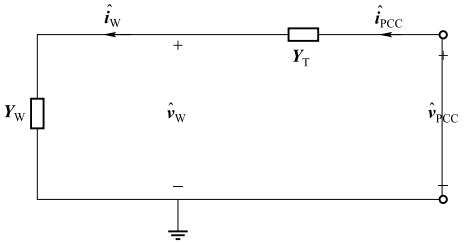

Fig. 12.18 Small-signal impedance circuit model of single wind turbine with transformer

$$\hat{\boldsymbol{i}}_{\mathrm{PCC}} = \boldsymbol{Y}_{\mathrm{T}}\left[\hat{\boldsymbol{v}}_{\mathrm{PCC}} - \hat{\boldsymbol{v}}_{\mathrm{W}}\right] \tag{12.37}$$

$$\hat{\boldsymbol{i}}_{\mathrm{W}} = \hat{\boldsymbol{i}}_{\mathrm{PCC}} \tag{12.38}$$

Solving the simultaneous Eqs. (12.36)–(12.38), the following can be obtained.

$$\hat{\boldsymbol{i}}_{\mathrm{PCC}} = \boldsymbol{Y}_{\mathrm{W}}[\boldsymbol{Y}_{\mathrm{W}} + \boldsymbol{Y}_{\mathrm{T}}]^{-1}\boldsymbol{Y}_{\mathrm{T}}\hat{\boldsymbol{v}}_{\mathrm{PCC}} = \left[\boldsymbol{Y}_{\mathrm{W}}^{-1} + \boldsymbol{Y}_{\mathrm{T}}^{-1}\right]^{-1}\hat{\boldsymbol{v}}_{\mathrm{PCC}} \tag{12.39}$$

Therefore, the overall admittance model of the wind turbine in series with the transformer is

$$\boldsymbol{Y}_{\mathrm{W\text{-}T}} = \left[\boldsymbol{Y}_{\mathrm{W}}^{-1} + \boldsymbol{Y}_{\mathrm{T}}^{-1}\right]^{-1} \tag{12.40}$$

Let $\boldsymbol{Z}_{\mathrm{W\text{-}T}} = \boldsymbol{Y}_{\mathrm{W\text{-}T}}^{-1}$, $\boldsymbol{Z}_{\mathrm{W}} = \boldsymbol{Y}_{\mathrm{W}}^{-1}$, and $\boldsymbol{Z}_{\mathrm{T}} = \boldsymbol{Y}_{\mathrm{T}}^{-1}$, the following can be obtained.

$$\boldsymbol{Z}_{\mathrm{W\text{-}T}} = \boldsymbol{Z}_{\mathrm{W}} + \boldsymbol{Z}_{\mathrm{T}} \tag{12.41}$$

Thus, combining Eqs. (12.40) and (12.41), it can be seen that the small-signal admittance and impedance matrix models satisfy the generalized series law, i.e., the impedance matrix models add up to obtain the overall impedance matrix model of the series system.

Similarly, the two paralleled wind turbines system shown in Fig. 12.17 can be captured by the equivalent circuit model presented in Fig. 12.19, where $\boldsymbol{Y}_{\mathrm{W\text{-}T1}}$ and $\boldsymbol{Y}_{\mathrm{W\text{-}T2}}$ are the admittance models of the two pairs of turbine and transformer in series respectively, and the small-signal current vectors at the high-voltage side of the transformers are $\hat{\boldsymbol{i}}_{\mathrm{W\text{-}T1}}$ and $\hat{\boldsymbol{i}}_{\mathrm{W\text{-}T2}}$ respectively.

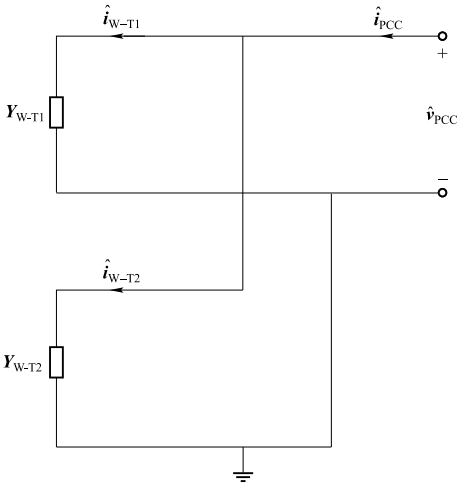

Fig. 12.19 Small-signal impedance circuit model of two paralleled wind turbines with transformers

Derive and reorganize the circuit equations of the model shown in Fig. 12.19, the overall admittance and impedance model of the parallel system can be written as

$$\boldsymbol{Y}_{\mathrm{W//W}} = \boldsymbol{Y}_{\mathrm{W\text{-}T1}} + \boldsymbol{Y}_{\mathrm{W\text{-}T2}} \tag{12.42}$$

$$\boldsymbol{Z}_{\mathrm{W//W}} = \left[\boldsymbol{Z}_{\mathrm{W\text{-}T1}}^{-1} + \boldsymbol{Z}_{\mathrm{W\text{-}T2}}^{-1}\right]^{-1} \tag{12.43}$$

It can be seen that, the small-signal admittance and impedance matrix models satisfy the generalized parallel law, i.e., the admittance models are summed to obtain the overall admittance model of the parallel system.

The structures of the two simple systems shown in Fig. 12.17 are of general significance, and the REG plant is a combination of these two structures. As shown in Fig. 12.20, an impedance network model that is consistent with the topology of wind plant can be pictured by connecting the impedance models of wind turbines, reactive power compensation devices (e.g., SVG), transformers, and collecting lines. In the Fig. 12.20, $\boldsymbol{Y}_{\mathrm{W}ij}$ is the admittance matrix of the turbine j of collecting line i, $\boldsymbol{Y}_{\mathrm{T}ij}$ is the admittance matrix of the box transformer of this turbine, $\boldsymbol{Y}_{\mathrm{L}ij}$ is the admittance matrix of the collecting line of this turbine, $\boldsymbol{Y}_{\mathrm{SVG}}$ is the admittance matrix of the SVG, and $\boldsymbol{Y}_{\mathrm{MT}}$ is the admittance matrix model of the main transformer of the wind plant. It is important to note that the admittances to ground of the collecting line and transformer are ignored in the figure for simplicity of representation. Therefore, based on the series and parallel laws shown in Eqs. (12.40)–(12.43), the overall impedance model of the farm can be obtained by aggregating them step by step in order, from the end of the collecting lines to the beginning, and from the low-voltage level to the high-voltage level.

12.2.3 Equivalent Impedance Model of REG Plant Involving Frequency Coupling Effect

The impedance network proposed in the previous section has two shortcomings when applied to the port impedance equivalence of REG plant. First, for REG plants with different topologies, the path and order of impedance aggregation step by step are different, and there is a lack of unified method. Second, the complex frequency coupling effect between devices through the collecting network cannot be clearly described. Therefore, a more general impedance network model involving frequency coupling effect and impedance equivalence method for REG plant are proposed below.

Taking the wind plant shown in Fig. 12.1 as an example, the impedance network model involving frequency coupling is shown in Fig. 12.21. Figure 12.21(a) shows the positive-sequence impedance network at frequency f_{p} (hereafter referred to as the positive-sequence network), and Fig. 12.21(b) shows the negative-sequence

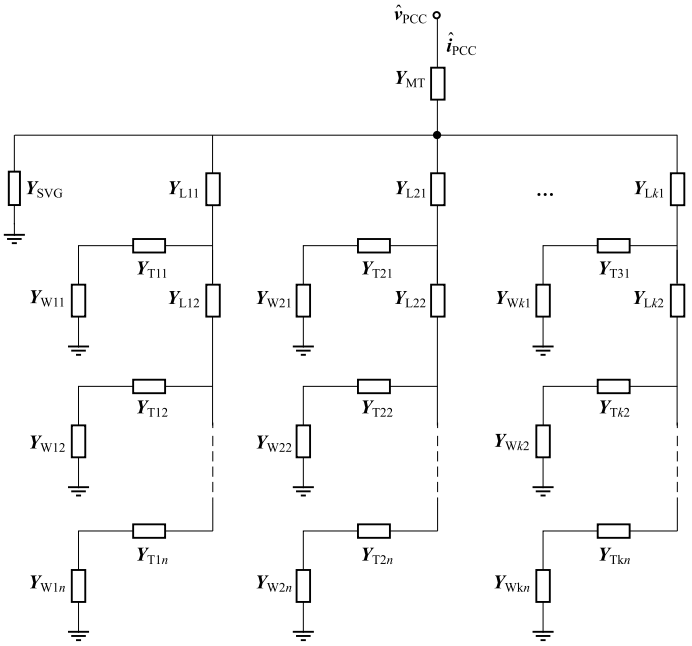

Fig. 12.20 Impedance network model of wind plant

impedance network at frequency $f_{\mathrm{p}} - 2f_1$ (hereafter referred to as the negative-sequence network). For a clear description, the PCC of wind farm is numbered as #0, the internal nodes are numbered #1~#N, where $N = 2kn + 1$, and only the 1st and kth collecting lines, as well as the SVG branch, are drawn. The box transformer high- and low-voltage sides of the n turbines of the 1st collecting line are numbered #1~#2n, and the box transformer high- and low-voltage sides of the n turbines of the kth collecting line are numbered #$m + 1$~#$m + 2n$, where $m = 2n(k - 1)$.

Each wind turbine is described as a pair of admittance and controlled current source in each of the two coupling networks, e.g., turbine #1-1 is described as a pair of positive-sequence admittance $\boldsymbol{Y}_{\mathrm{W11}}^{\mathrm{pp}}$ and controlled current source $\hat{\boldsymbol{i}}_{\mathrm{W11}}^{\mathrm{np}}$ in the positive-sequence network, with Eq. (12.44), it can be seen that $\hat{\boldsymbol{i}}_{\mathrm{W11}}^{\mathrm{np}}$ is related to the coupling admittance $\boldsymbol{Y}_{\mathrm{W11}}^{\mathrm{np}}$ of turbine #1-1 and the voltage $\hat{\boldsymbol{v}}_{n+1}^{\mathrm{n}}$ in the negative-sequence network of node #$n + 1$ that turbine #1-1 is connected, and vice versa.

$$\begin{cases} \hat{\boldsymbol{i}}_{\mathrm{W11}}^{\mathrm{np}} = \boldsymbol{Y}_{\mathrm{W11}}^{\mathrm{np}} \hat{\boldsymbol{v}}_{n+1}^{\mathrm{n}} \\ \hat{\boldsymbol{i}}_{\mathrm{W11}}^{\mathrm{pn}} = \boldsymbol{Y}_{\mathrm{W11}}^{\mathrm{pn}} \hat{\boldsymbol{v}}_{n+1}^{\mathrm{p}} \end{cases} \tag{12.44}$$

Transformers and collecting lines are described as connecting admittances between nodes in the impedance networks, e.g., the box transformer of turbine #i–j

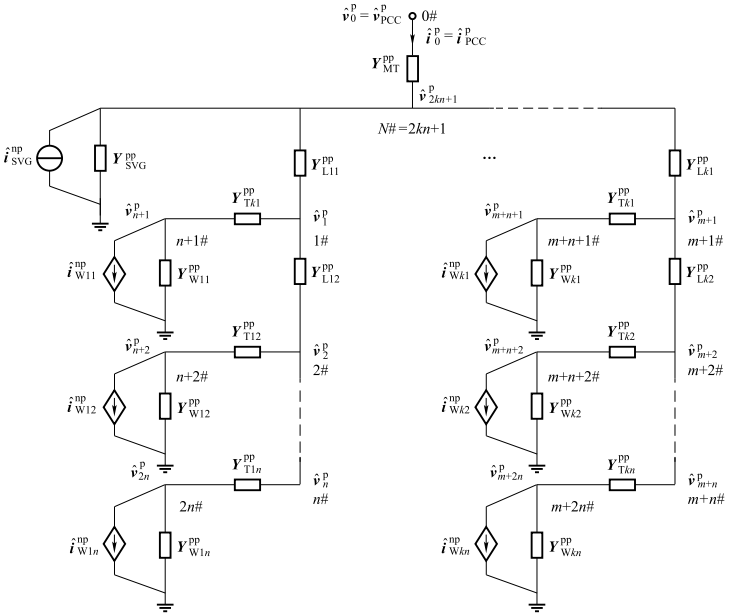

(a) Positive-sequence impedance network of wind farm at f_p

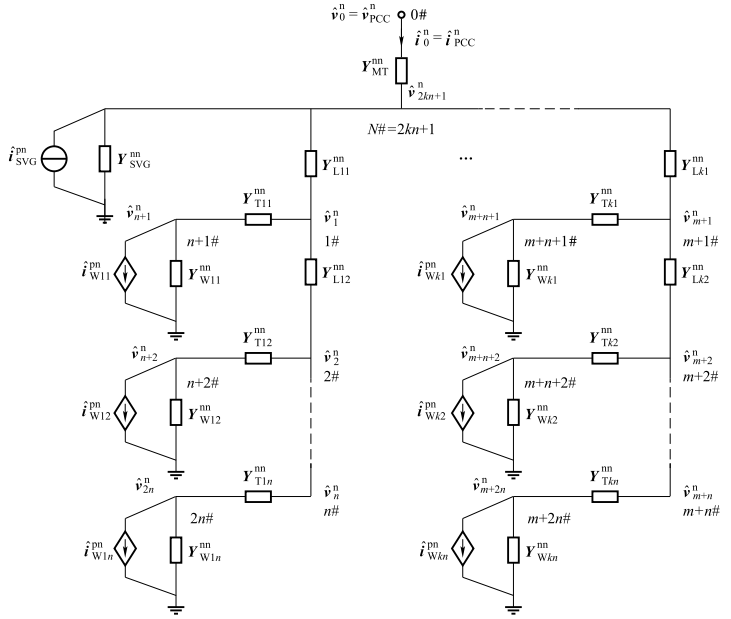

(b) Positive-sequence impedance network of wind farm at f_p-2f_1

Fig. 12.21 Frequency coupling impedance network model of wind plant

is described as connecting admittances $\boldsymbol{Y}_{\mathrm{T}ij}^{\mathrm{pp}}$ and $\boldsymbol{Y}_{\mathrm{T}ij}^{\mathrm{nn}}$ in the positive- and negative-sequence networks respectively, and the collecting line of turbine #*i*–*j* is described as connecting admittances $\boldsymbol{Y}_{\mathrm{L}ij}^{\mathrm{pp}}$ and $\boldsymbol{Y}_{\mathrm{L}ij}^{\mathrm{nn}}$ respectively.

With reference to the form of the admittance matrix model of the device, the aggregation equivalent impedance model of REG plant is defined by Eq. (12.45).

$$\boldsymbol{Y}_{\mathrm{WF}} = \begin{bmatrix} \boldsymbol{Y}_{\mathrm{WF}}^{\mathrm{pp}} & \boldsymbol{Y}_{\mathrm{WF}}^{\mathrm{np}} \\ \boldsymbol{Y}_{\mathrm{WF}}^{\mathrm{pn}} & \boldsymbol{Y}_{\mathrm{WF}}^{\mathrm{nn}} \end{bmatrix} \tag{12.45}$$

Therefore,

$$\begin{bmatrix} \hat{\boldsymbol{i}}_0^{\mathrm{p}} \\ \hat{\boldsymbol{i}}_0^{\mathrm{n}} \end{bmatrix} = \begin{bmatrix} \boldsymbol{Y}_{\mathrm{WF}}^{\mathrm{pp}} & \boldsymbol{Y}_{\mathrm{WF}}^{\mathrm{np}} \\ \boldsymbol{Y}_{\mathrm{WF}}^{\mathrm{pn}} & \boldsymbol{Y}_{\mathrm{WF}}^{\mathrm{nn}} \end{bmatrix} \begin{bmatrix} \hat{\boldsymbol{v}}_0^{\mathrm{p}} \\ \hat{\boldsymbol{v}}_0^{\mathrm{n}} \end{bmatrix} \tag{12.46}$$

That is, the small-signal impedance of REG plant is modeled as a transfer function matrix with positive- and negative-sequence small-signal voltages $\hat{\boldsymbol{v}}_0^{\mathrm{p}}$ and $\hat{\boldsymbol{v}}_0^{\mathrm{n}}$ as inputs and current responses $\hat{\boldsymbol{i}}_0^{\mathrm{p}}$ and $\hat{\boldsymbol{i}}_0^{\mathrm{n}}$ as outputs.

In the following, the expressions of the four elements in the model are derived. First, based on electrical network theory, the nodal voltage equations for both positive- and negative-sequence networks are listed as Eqs. (12.47) and (12.48) respectively.

$$\boldsymbol{Y}_{\mathrm{N}}^{\mathrm{pp}} \hat{\boldsymbol{v}}^{\mathrm{p}} + \hat{\boldsymbol{i}}^{\mathrm{np}} = \hat{\boldsymbol{v}}_0^{\mathrm{p}} \boldsymbol{y}_0^{\mathrm{p}} \tag{12.47}$$

$$\boldsymbol{Y}_{\mathrm{N}}^{\mathrm{nn}} \hat{\boldsymbol{v}}^{\mathrm{n}} + \hat{\boldsymbol{i}}^{\mathrm{pn}} = \hat{\boldsymbol{v}}_0^{\mathrm{n}} \boldsymbol{y}_0^{\mathrm{n}} \tag{12.48}$$

where, $\boldsymbol{Y}_{\mathrm{N}}^{\mathrm{pp}}$ and $\boldsymbol{Y}_{\mathrm{N}}^{\mathrm{nn}}$ are the nodal admittance matrices of the positive- and negative-sequence networks (excluding the PCC #0) respectively, with dimensions of $N \times N$; $\hat{\boldsymbol{v}}^{\mathrm{p}}$ and $\hat{\boldsymbol{v}}^{\mathrm{n}}$ are the small-signal nodal voltage vectors of the two networks respectively, with dimensions of $N \times 1$. $\boldsymbol{y}_0^{\mathrm{p}}$ and $\boldsymbol{y}_0^{\mathrm{n}}$ are the connecting admittance vectors between the internal nodes of the wind plant and the PCC #0, with dimensions of $N \times 1$.

$$\boldsymbol{y}_0^{\mathrm{p}} = \left[\boldsymbol{Y}_{0i}^{\mathrm{pp}} |_{i=1,2,\ldots,N} \right]^T \tag{12.49}$$

$$\boldsymbol{y}_0^{\mathrm{n}} = \left[\boldsymbol{Y}_{0i}^{\mathrm{nn}} |_{i=1,2,\ldots,N} \right]^T \tag{12.50}$$

For the impedance network shown in Fig. 12.21, only node #*N* at the low-voltage side of the main transformer is connected to PCC #0, so the elements of *N*th row in $\boldsymbol{y}_0^{\mathrm{p}}$ and $\boldsymbol{y}_0^{\mathrm{n}}$ equal to $\boldsymbol{Y}_{\mathrm{MT}}^{\mathrm{pp}}$ and $\boldsymbol{Y}_{\mathrm{MT}}^{\mathrm{nn}}$, respectively, and all other elements are 0.

$\hat{\boldsymbol{i}}^{\mathrm{np}}$ and $\hat{\boldsymbol{i}}^{\mathrm{pn}}$ are the controlled current source vectors in the positive- and negative-sequence networks respectively, with dimension of $N \times 1$.

$$\hat{\boldsymbol{i}}^{\mathrm{np}} = \boldsymbol{Y}_{\mathrm{N}}^{\mathrm{np}} \hat{\boldsymbol{v}}^{\mathrm{n}} \tag{12.51}$$

$$\hat{\boldsymbol{i}}^{\mathrm{pn}} = \boldsymbol{Y}_{\mathrm{N}}^{\mathrm{pn}} \hat{\boldsymbol{v}}^{\mathrm{p}} \tag{12.52}$$

where $\boldsymbol{Y}_{\mathrm{N}}^{\mathrm{np}}$ and $\boldsymbol{Y}_{\mathrm{N}}^{\mathrm{pn}}$ are the diagonal matrices composed of the coupling admittances of each turbine respectively, with dimensions of $N \times N$.

$$\boldsymbol{Y}_{\mathrm{N}}^{\mathrm{np}} = \mathrm{diag}\left\{ \underbrace{0, ..., 0,}_{1\sim n} \underbrace{\boldsymbol{Y}_{\mathrm{W11}}^{\mathrm{np}}, \boldsymbol{Y}_{\mathrm{W12}}^{\mathrm{np}}, ..., \boldsymbol{Y}_{\mathrm{W1}n}^{\mathrm{np}}}_{n+1\sim 2n}, ... \right\} \tag{12.53}$$

$$\boldsymbol{Y}_{\mathrm{N}}^{\mathrm{pn}} = \mathrm{diag}\left\{ \underbrace{0, ..., 0,}_{1\sim n} \underbrace{\boldsymbol{Y}_{\mathrm{W11}}^{\mathrm{pn}}, \boldsymbol{Y}_{\mathrm{W12}}^{\mathrm{pn}}, ..., \boldsymbol{Y}_{\mathrm{W1}n}^{\mathrm{pn}}}_{n+1\sim 2n}, ... \right\} \tag{12.54}$$

Applying the KCL theorem to PCC #0 of the two impedance networks yields,

$$\hat{\boldsymbol{v}}_0^{\mathrm{p}} \sum_{i=1}^{N} \boldsymbol{Y}_{0i}^{\mathrm{pp}} - \left[\boldsymbol{y}_0^{\mathrm{p}}\right]^{\mathrm{T}} \hat{\boldsymbol{v}}^{\mathrm{p}} = \hat{\boldsymbol{i}}_0^{\mathrm{p}} \tag{12.55}$$

$$\hat{\boldsymbol{v}}_0^{\mathrm{n}} \sum_{i=1}^{N} \boldsymbol{Y}_{0i}^{\mathrm{nn}} - \left[\boldsymbol{y}_0^{\mathrm{n}}\right]^{\mathrm{T}} \hat{\boldsymbol{v}}^{\mathrm{n}} = \hat{\boldsymbol{i}}_0^{\mathrm{n}} \tag{12.56}$$

Solving the simultaneous Eqs. (12.47)–(12.56) yields the REG plant equivalent admittance model expressions in Eqs. (12.57)–(12.60)

$$\boldsymbol{Y}_{\mathrm{WF}}^{\mathrm{pp}} = \sum_{i=1}^{N} \boldsymbol{Y}_{0i}^{\mathrm{pp}} - \left[\boldsymbol{y}_0^{\mathrm{p}}\right]^{\mathrm{T}} \left\{ \boldsymbol{Y}_{\mathrm{N}}^{\mathrm{pp}} - \boldsymbol{Y}_{\mathrm{N}}^{\mathrm{np}} \left[\boldsymbol{Y}_{\mathrm{N}}^{\mathrm{nn}}\right]^{-1} \boldsymbol{Y}_{\mathrm{N}}^{\mathrm{pn}} \right\}^{-1} \boldsymbol{y}_0^{\mathrm{p}} \tag{12.57}$$

$$\boldsymbol{Y}_{\mathrm{WF}}^{\mathrm{nn}} = \sum_{i=1}^{N} \boldsymbol{Y}_{0i}^{\mathrm{nn}} - \left[\boldsymbol{y}_0^{\mathrm{n}}\right]^{\mathrm{T}} \left\{ \boldsymbol{Y}_{\mathrm{N}}^{\mathrm{nn}} - \boldsymbol{Y}_{\mathrm{N}}^{\mathrm{pn}} \left[\boldsymbol{Y}_{\mathrm{N}}^{\mathrm{pp}}\right]^{-1} \boldsymbol{Y}_{\mathrm{N}}^{\mathrm{np}} \right\}^{-1} \boldsymbol{y}_0^{\mathrm{n}} \tag{12.58}$$

$$\boldsymbol{Y}_{\mathrm{WF}}^{\mathrm{pn}} = \left[\boldsymbol{y}_0^{\mathrm{n}}\right]^{\mathrm{T}} \left\{ \boldsymbol{Y}_{\mathrm{N}}^{\mathrm{nn}} - \boldsymbol{Y}_{\mathrm{N}}^{\mathrm{pn}} \left[\boldsymbol{Y}_{\mathrm{N}}^{\mathrm{pp}}\right]^{-1} \boldsymbol{Y}_{\mathrm{N}}^{\mathrm{np}} \right\}^{-1} \boldsymbol{Y}_{\mathrm{N}}^{\mathrm{pn}} \left[\boldsymbol{Y}_{\mathrm{N}}^{\mathrm{pp}}\right]^{-1} \boldsymbol{y}_0^{\mathrm{p}} \tag{12.59}$$

$$\boldsymbol{Y}_{\mathrm{WF}}^{\mathrm{np}} = \left[\boldsymbol{y}_0^{\mathrm{p}}\right]^{\mathrm{T}} \left\{ \boldsymbol{Y}_{\mathrm{N}}^{\mathrm{pp}} - \boldsymbol{Y}_{\mathrm{N}}^{\mathrm{np}} \left[\boldsymbol{Y}_{\mathrm{N}}^{\mathrm{nn}}\right]^{-1} \boldsymbol{Y}_{\mathrm{N}}^{\mathrm{pn}} \right\}^{-1} \boldsymbol{Y}_{\mathrm{N}}^{\mathrm{np}} \left[\boldsymbol{Y}_{\mathrm{N}}^{\mathrm{nn}}\right]^{-1} \boldsymbol{y}_0^{\mathrm{n}} \tag{12.60}$$

A wind farm consisting of 33 1.5 MWPMSG-based wind turbines is taken as an example to verify the validity of the above equivalence model. Supposing the wind plant contain three collecting lines, each of which is connected to 11 turbines, and the distance between two adjacent turbine is 0.5 km. Based on the EMT simulation model of wind plant connected to the ideal grid, the impedance is scanned at the PCC, and the

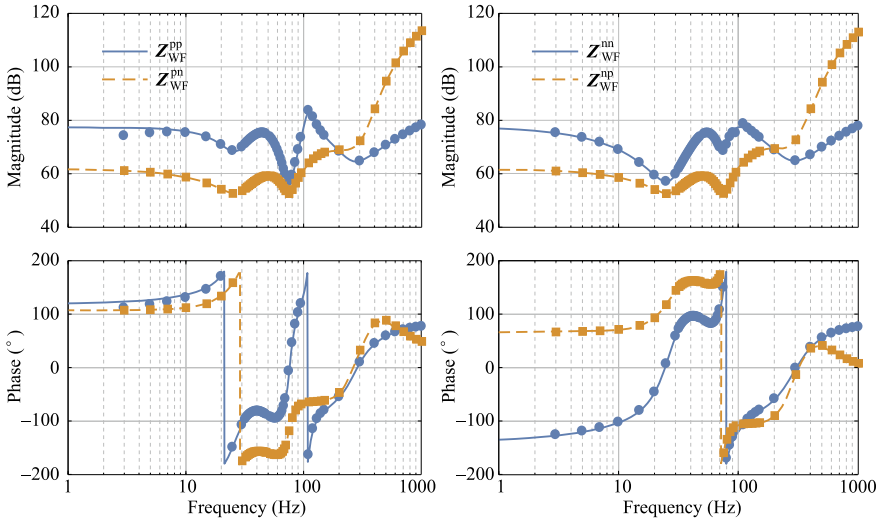

Fig. 12.22 Comparison between analytical model and simulation scan of wind plant impedance characteristics

results are compared with the calculation impedance based on Eqs. (12.57)–(12.60). As shown in Fig. 12.22, the calculation results are consistent with the simulation results.

12.2.4 Calculation of Equivalent Impedance of REG Plant

An equivalent impedance model applicable to REG plants with arbitrary structure is proposed in the previous section, and its basic construction ideas and methods are consistent with the electric network theory and have the conditions for practical large-scale system application. Meanwhile, the impedance characteristics of REG units are related to their operating points, due to the influence of wind speed, light intensity, location distribution and other factors, the operating points of each unit in the plant are different. Therefore, the calculation of equivalent impedance of REG plant needs to consider the operating points of each unit and device in the plant under different operating conditions.

Table 12.3 shows the component parameters used to calculate the equivalent impedance of REG plant, including nodes, collecting lines, transformers, REG units, SVG, and other devices, as follows:

Table 12.3 Element parameters used to calculate equivalent impedance of REG plant

Elements	Parameters
Nodes	Node number; rated voltage; voltage amplitude and phase
Collecting lines	The node number of the beginning and end; line length; line unit length parameter (resistance, inductance, capacitance)
Double winding transformer	Node numbers of the primary and secondary sides; rated voltage of primary side and secondary side; rated capacity; short-circuit voltage, short-circuit loss
Three winding transformer	Node number of primary side, secondary side and tertiary side, rated voltage and rated capacity of primary side, secondary side and tertiary side, short-circuit voltage and short-circuit loss
REG units	Number of the node connected; the number of connected units; rated voltage and rated capacity; on and off state; active power and reactive power output; node voltage amplitude and phase, output current amplitude and phase; model/type of REG unit
SVG	Number of the node connected; rated voltage and rated capacity; on and off state; reactive power output; node voltage amplitude and phase, output current amplitude and phase; model/type of SVG
Other reactive compensations	Number of the node connected; capacitive reactive power capacity; inductive reactive power capacity

(1) The structure information of the plant is described by the number of nodes, the collecting lines, transformers and the nodes they connect with, the REG units and the nodes they connect to.
(2) The operating conditions of the plant are described by the voltage amplitude and phase of the node inside the plant, as well as the start-up and shut-down status, the output active and reactive power of the REG units and SVG.
(3) The impedance models of elements such as collecting lines, transformers and reactive power compensation devices can be calculated by their electric parameters. The impedance models of REG units and SVG can be designed as calculation functions and called according to their types.

Based on the structure information and element parameters of the plant, the equivalent impedance calculation of the station includes the following steps:

(1) Establish the parameter library of the plant including the structure information, element parameters, as well as the operating conditions. The flow chart of the process is shown in Fig. 12.23. First, import or define the structure information and element parameters of REG plant, mainly including the parameters and variables irrelevant to the operating point; secondly, set the reference capacity and reference voltage of the modeling, obtain the per-unit values of the relevant parameters of capacity, voltage, impedance and others in the library; then, set the operation conditions of the plant and the voltage of PCC point, and execute the power flow calculation of the grid-connected system of the plant, PCC point is set as the slack bus in the power flow calculation; finally, the power flow results

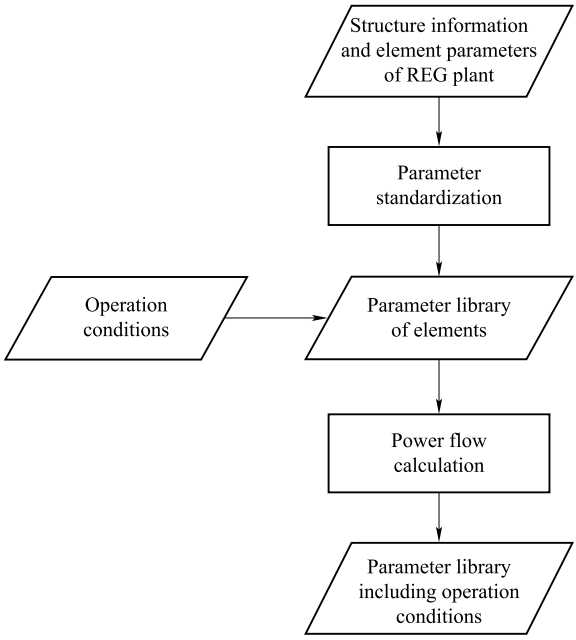

Fig. 12.23 Flow chart of station structure information and elements parameter library establishment including operation conditions

are input into the parameter library to form the basic parameters for impedance calculation.

(2) Calculate the equivalent impedance of plant under the set operating condition. Based on the parameter library involving the operating conditions, the equivalent impedance can be calculated with the process shown in Fig. 12.24. For the frequencies $f_\mathrm{p} = 1, 2, \ldots, f_\mathrm{max}$, the vectors $\boldsymbol{y}_0^\mathrm{p}$ and $\boldsymbol{y}_0^\mathrm{n}$ of the connection admittances between the nodes inside the plant and the PCC in the positive- and negative-sequence networks, the nodal admittance matrices $\boldsymbol{Y}_\mathrm{N}^\mathrm{pp}$ and $\boldsymbol{Y}_\mathrm{N}^\mathrm{nn}$ of the positive- and negative-sequence networks, and the diagonal matrices $\boldsymbol{Y}_\mathrm{N}^\mathrm{np}$ and $\boldsymbol{Y}_\mathrm{N}^\mathrm{pn}$ composed of the coupling admittances of each REG unit and SVG are calculated in turn, and the equivalent admittance of the plant at frequency f_p are obtained after the full-band calculation with Eqs. (12.57)–(12.60).

Since the proposed modeling method is consistent with the electrical network theory, the integration of REG unit, SVG and other device is equivalent as the addition of grounded admittance at the connecting nodes. The general method for constructing nodal admittance matrix is not be repeated.

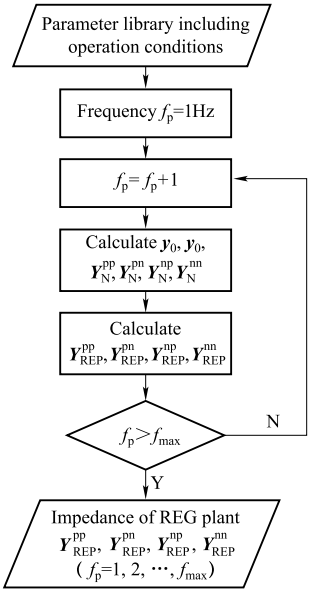

Fig. 12.24 Calculation flow chart of station equivalent impedance model

12.3 Impedance Characteristic Analysis of REG Plant

12.3.1 Influence of Collecting Lines on the Impedance Characteristics

The length of collecting lines in REG plant is mainly determined by the development region and environment. In concentrated large-scale development regions such as northwest China, the length of collecting line between the adjacent wind turbines or PV units generally does not exceed 1 km, while in the mountainous south-central region, the length of the collecting line between the adjacent units may exceed 2 km. In Fig. 12.25, the impedance characteristics of the PMSG-based wind farm described in Sect. 12.2.3 are given for different collecting line lengths, and the output active power of the wind farm is 1.0 p.u. It can be seen that, the length of the collecting line mainly affects the characteristics in the sub-synchronous frequency band of the positive-sequence impedance. With increasing length of collecting line, the magnitude is reduced and the negative damping characteristic is moved closer to the fundamental frequency. Since the impedance of collecting line does not involve frequency coupling effect, it has little influence on coupling impedance of the farm. A Nyquist analysis for the PMSG-based wind plant connected to the grid with a SCR of 2 is presented in Fig. 12.26, and it can be seen that, with the increasing length of collection line, the Nyquist curve gradually encircles the point (−1, j0), and the risk of system oscillation increases.

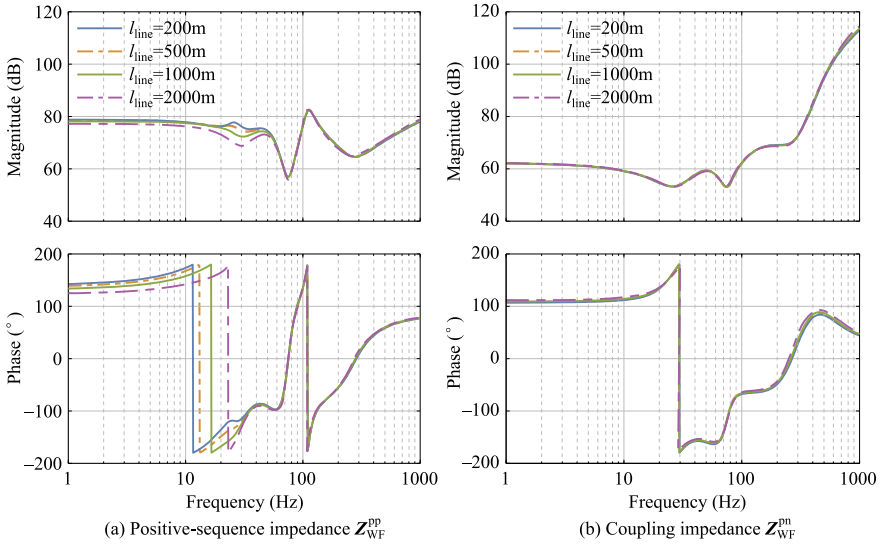

Fig. 12.25 Impedance characteristics of PMSG-based wind plants with different lengths of collecting lines

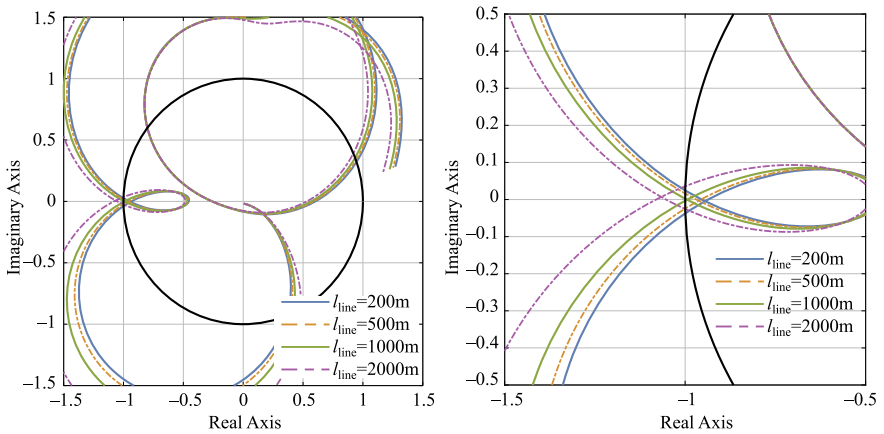

Fig. 12.26 Nyquist curves of PMSG-based wind plants grid-connected system with different lengths of collecting lines

12.3.2 *Influence of Transformer Levels on the Impedance Characteristics*

With the development of large-scale REG clusters, the transmission system voltage of the REG plant gradually increases. Therefore, the voltage step-up stages of the plants developed in different periods may be different. Figure 12.27 shows the impedance characteristics of the PMSG-based wind plant with two-stage (0.69 kV/35 kV/220 kV) and three-stage (0.69 kV/35 kV/110 kV/220 kV) step-up configurations. The active power output of the wind plant is 1.0 p.u. Similar to the collecting line, the number of voltage step-up stages mainly affects the characteristics in the sub-synchronous frequency band of the positive-sequence impedance. With more step-up stages, the magnitude is reduced and the negative damping characteristic is moved closer to the fundamental frequency. Since the impedance of transformer does not involve frequency coupling effect, it has little influence on coupling impedance of the farm. A Nyquist analysis for the PMSG-based wind plant connected to the grid with a short-circuit ratio (SCR) of 2 is presented in Fig. 12.28, and it can be seen that, with the increasing step-up stages of voltage, the Nyquist curve gradually encircles the point (−1, j0), and the risk of system oscillation increases.

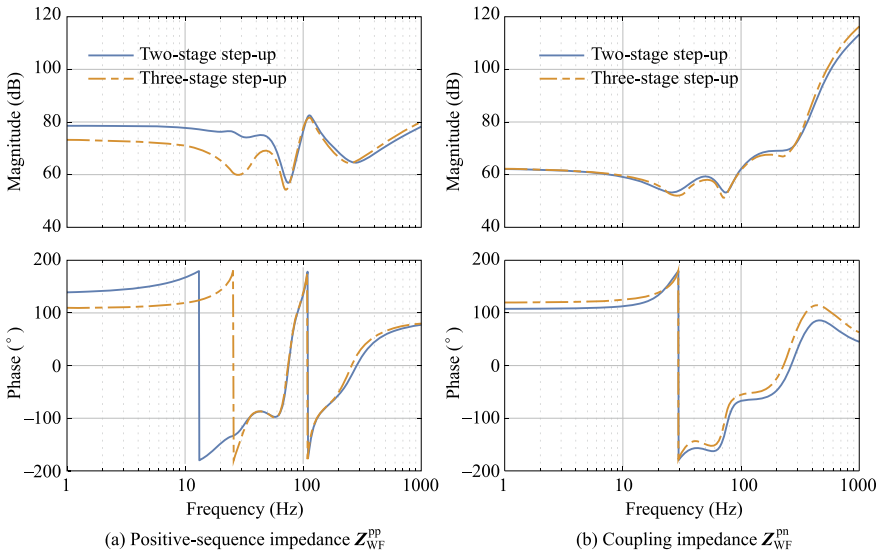

Fig. 12.27 Impedance characteristics of PMSG-based wind plants with different number of voltage step-up stages

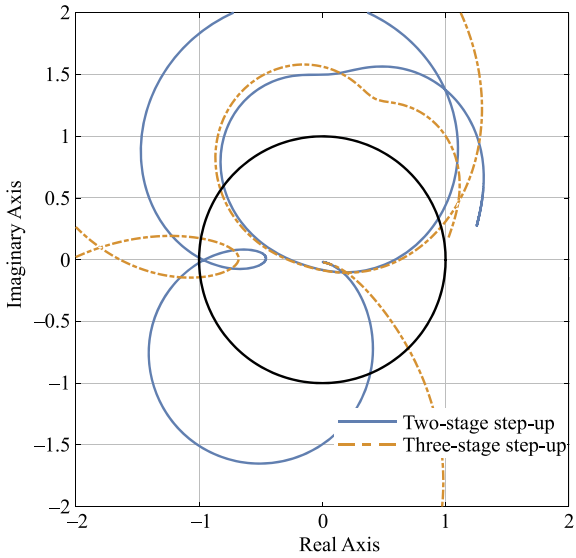

Fig. 12.28 Nyquist curves of PMSG-based wind plants grid-connected system with different number of voltage step-up stages

12.3.3 Influence of Operation Mode on Impedance Characteristics

In the power system with high oscillation risk, the REG plants usually need to curtail part of their output power according to the constraint of system stability. Meanwhile, with the limited power order of the plant, the startup status and operation modes of REG units will affect the impedance characteristics and system stability. Figure 12.29 presents the impedance characteristics of the wind plants under different operation modes. Mode 1 is when all turbines are startup with output active power of 0.5 p.u. Mode 2 is when half of the turbines close to the head end of each collecting line are shutdown, and half of the turbines close to the end output full active power. Mode 3 is opposite to Mode 2. It can be seen that, the operation mode mainly affects the characteristics in the sub-synchronous frequency band of the positive-sequence impedance. Figure 12.30 presents the Nyquist analysis of the PMSG-based wind plants with difference operation modes and connected to the grid with a short-circuit ratio (SCR) of 2. It can be seen that, the Nyquist curve is relatively far from the (−1, j0) point and the system is more stable under Mode 1, that is the output power of each turbine is average; and comparing Mode 2 and Mode 3, shutting down the turbines near the end of collecting line is better for the system stability.

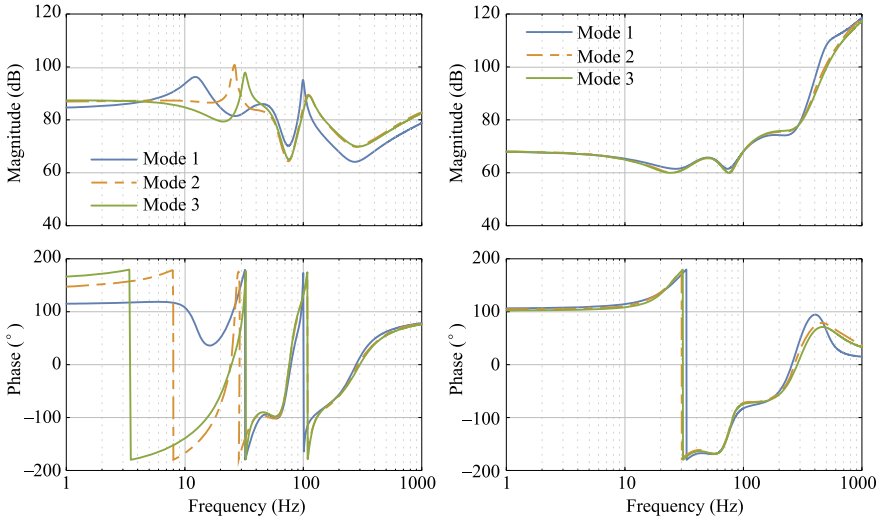

(a) Positive-sequence impedance $\boldsymbol{Z}_{\mathrm{WF}}^{\mathrm{pp}}$ (b) Coupling impedance $\boldsymbol{Z}_{\mathrm{WF}}^{\mathrm{pn}}$

Fig. 12.29 Impedance characteristics of PMSG-based wind plants with different operation modes

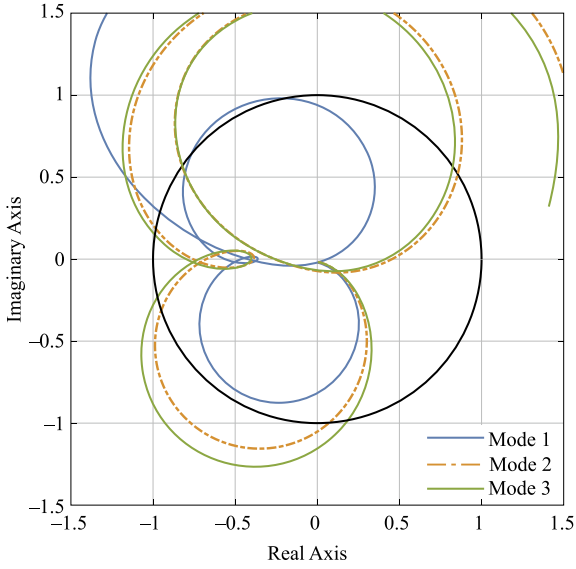

Fig. 12.30 Nyquist curves of PMSG-based wind plants grid-connected system with different operation modes

References

1. BI T S, LI J Y. Risk screening of SSO induced in large-scale wind farms based on aggregated short circuit ratio [J]. Power System Protection and Control, 2019, 47(5): 52-59. (Chinese)
2. ZHANG D H, CHEN X, ZHANG Y, et al. Stability analysis and resonance participation risk assessment of wind farm based on active node sequence impedance model [J/OL]. Proceedings of the CSEE, [2022-09-26]. (Chinese)

3. LI M J, YU Z, XU T, et al. Study of complex oscillation caused by renewable energy integration and its solution [J]. Power System Technology, 2017, 41(4): 1035-1042. (Chinese)
4. WANG H J, VIETO I, SUN J. A method to aggregate turbine and network impedances for wind farm system resonance analysis: 2018 IEEE 19th Workshop on Control and Modeling for Power Electronics (COMPEL), Padua, Italy, June 25–28, 2018 [C]. Piscataway, NJ: IEEE, 2018.
5. ZHU L Z, QU L N, LIU C, et al. Improved calculation method of equivalent short-circuit ratio for power generation cluster of renewable energy [J]. Automation of Electric Power Systems, 2021, 45(22): 74-82. (Chinese)
6. WANG H J, SUN J. Impedance-based stability modeling and analysis of networked converter systems: 2019 IEEE 20th Workshop on Control and Modeling for Power Electronics (COMPEL), Toronto, ON, Canada, June 17–20, 2019 [C]. Piscataway, NJ: IEEE, 2019.
7. WANG H J, BUCHHAGEN C, SUN J. Methods to aggregate turbine and network impedance for wind farm resonance analysis [J]. IET Renewable Power Generation, 2020, 14(8): 1304-1311.
8. WANG H J, HE G Q, LIU C, et al. Equivalent method for sequence impedance model of wind farms considering frequency coupling and colleting network [J]. Automation of Electric Power Systems, 2019, 43(15): 87-92. (Chinese)

Chapter 13
Analysis of Broadband Oscillation for REG Connected into HVAC System

At the sending end of HVAC transmission, thousands of REG units are integrated into AC grid through multiple step-up transformers. Besides, series capacitive compensators are widely used in HVAC to improve transmission capacity and enhance system stability. However, the broadband oscillation incidents caused by the interaction between the REG plants and the AC grid occur occasionally [1–5], threatening safe and stable operation of the power system.

In this chapter, the oscillation analysis for REG plants connected into the HVAC system is implemented. Firstly, this system is equivalent to a two-port network [6–9], and the stability criteria are proposed based on the extended Nyquist criterion. Then, the frequency-band division method is proposed based on the analytical impedance models of the REG plants. The dominant factors in different frequency bands causing oscillation for various REG plants connected into AC grid is illustrated. Hence, the oscillation mechanism is revealed and verified based on the full electromagnetic transient (EMT) simulation platform and the test platform for REG and AC/DC transmission systems.

13.1 Stability Criteria

In this section, the equivalent model is first established for REG plants connected into HVAC system. Then the necessary and sufficient conditions for the system stability are proposed. Finally, the Nyquist criterion of maximum peak value is elaborated for the stability analysis.

In practice, REG units usually employ maximum power point tracking (MPPT) control or active/reactive power control, according to the dispatch instructions to rapidly and precisely adjust the amplitude and phase of grid-connected currents. In accordance with the current control mode, REG units can be seen as current sources in parallel with their output impedance. Since REG plants are consisted of hundreds

© China Electric Power Press 2023

W. Wang et al., *Analysis and Mitigation of Broadband Oscillation in Renewable Energy Generation and AC/DC Transmission Systems*,
https://doi.org/10.1007/978-981-99-1568-2_13

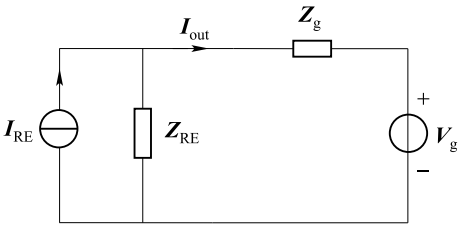

Fig. 13.1 Equivalent model for the sending side system of HVAC

to thousands of REG units in current control model, they can also be equivalent as non-ideal current sources.

Hence, the sending side system of HVAC can be equivalent to a two-port network shown in Fig. 13.1, where $\boldsymbol{I}_{\text{out}}$ is the current of REG port. In this model, the output of REG can be equivalent to an ideal current source $\boldsymbol{I}_{\text{RE}}$ in parallel with its port impedance $\boldsymbol{Z}_{\text{RE}}$, which can be derived by the REG plants modeling method in Chap. 12. And the AC grid is an ideal voltage source $\boldsymbol{V}_{\text{g}}$ in series with its impedance $\boldsymbol{Z}_{\text{g}}$. Generally, $\boldsymbol{Z}_{\text{g}}$ is composed of the inductance of transformers and the short-circuit impedance of the AC grid. Particularly, it will include the series capacitance if the series capacitive compensators are used.

According to this model, $\boldsymbol{I}_{\text{out}}$ can be expressed as follows

$$\boldsymbol{I}_{\text{out}} = \left(\boldsymbol{I}_{\text{RE}} - \frac{\boldsymbol{V}_{\text{g}}}{\boldsymbol{Z}_{\text{RE}}}\right) \cdot \frac{1}{1 + \boldsymbol{Z}_{\text{g}}/\boldsymbol{Z}_{\text{RE}}} \tag{13.1}$$

Equation (13.1) can be seen as the multiplication of two closed-loop transfer functions, denoted as

$$\begin{cases} TF_1 = \boldsymbol{I}_{\text{RE}} - \dfrac{\boldsymbol{V}_{\text{g}}}{\boldsymbol{Z}_{\text{RE}}} \\ TF_2 = \dfrac{1}{1 + \boldsymbol{Z}_{\text{g}}/\boldsymbol{Z}_{\text{RE}}} \end{cases} \tag{13.2}$$

As the stability for this equivalent system is determined by TF_1 and TF_2, this system is stable if, and only if the poles of TF_1 and TF_2 are all in the left-half-plane.

On one hand, the equivalent circuit of TF_1 is shown in Fig. 13.2(a), where $\boldsymbol{I}_{\text{ideal}}$ is the current of REG port connected into ideal AC grid. Since the REG plants are practically stable when connected to ideal AC grid, TF_1 can be claimed not to have any right-half-plane poles. System stability only depends on TF_2.

On the other hand, TF_2 can be reformulated to fit a feedback loop with a open-loop gain of $\boldsymbol{Z}_{\text{g}}/\boldsymbol{Z}_{\text{RE}}$, as shown in Fig. 13.2b. All the poles of TF_2 should be in the left-half-plane, that is, this system is stable if and only if the impedance ratio $\boldsymbol{Z}_{\text{g}}/\boldsymbol{Z}_{\text{RE}}$ conforms with Nyquist criterion.

Based on the classical Nyquist criterion, the stability of this system can be determined by checking the encirclement of the $(-1, \text{j}0)$ point by the loop gain. This system is unstable if and only if the stability margin equals to zero. However, this condition

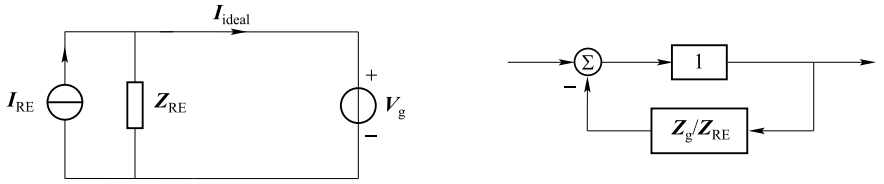

(a) Equivalent circuit of TF_1 (b) Equivalent feedback loop of TF_2

Fig. 13.2 Equivalent circuit and feedback loop of the closed-loop transfer functions

is too strict for practical use. Since the operating points change constantly with the control modes and operation modes of the power electronic devices, a system with small stability margin is vulnerable to external disturbance and oscillation incidents may occur in practice.

Therefore, the stability criterion is expended to the Nyquist criterion of maximum peak value, where the $(-1, j0)$ point is expended to a forbidden area with radius R_{min}. The forbidden area in Fig. 13.3 can be obtained by

$$R_{min} = \max\left\{2\sin\left(\frac{PM}{2}\right), 1 - \frac{1}{GM}\right\} \tag{13.3}$$

where gain margin (GM) is the reciprocal of the distance from the intersection point of the Nyquist curve and the negative real axis to the origin point; phase margin (PM) is the angle from the intersection point of the Nyquist curve and unit circle to the negative real axis.

According to the this criterion, if the Nyquist curve of $\mathbf{Z}_g/\mathbf{Z}_{RE}$ crosses in the forbidden area, the gain margin or phase margin (GM/PM) of the system is insufficient, indicating oscillation risk. Otherwise, the system is stable with no oscillation risk.

Particularly, the forbidden area of R_{min} can cover the requirements of both GM and PM of the system in Fig. 13.3. The stability criteria can be more flexible as different R_{min} can be chosen for different grid-connected scenarios. Besides, thanks to the definition of the forbidden area, the vulnerable frequency range can be figured out in the oscillation risk evaluation.

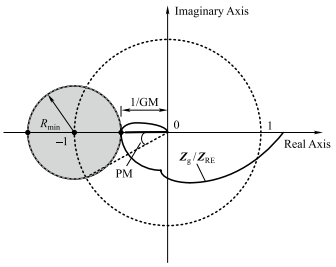

Fig. 13.3 Forbidden area of the Nyquist criterion of maximum peak value

13.2 Frequency-Band Division and Oscillation Analysis

In this section, based on the impedance characteristics analysis of permanent magnet synchronous generators (PMSG), doubly-fed induction generator (DFIG) and PV plants, the frequency-band division method is proposed and the dominant factors in different frequency bands causing oscillation for various REG plants connected into AC grid is illustrated.

13.2.1 Frequency-Band Division

The sending side system of HVAC involves multiple power electronic devices including PMSG, DFIG PV plants. The dynamics of these devices in the power system mainly depend on the multi-loop control characteristics. Under the coordination of multi-loop control of multiple devices, the control bandwidth of the power system can cover from several Hertz to hundreds of Hertz, appearing broadband characteristics. Hence, it is important to determine the dominant device and the dominant control loop causing oscillation for the analysis and mitigation of oscillation.

According to the analysis of REG impedance characteristics mentioned in Part II, the working frequency ranges of the main circuit filters and multiple control loops of PMSG, DFIG and PV plants are clear. Since the impedance characteristics of PV plants are almost the same as those of PMSG-based wind plants, they can be classified as the same type of device in frequency band division. Generally, the frequency band of impedance characteristics are divided into Band I, Band II, Band III and Band IV. The dominant control loops and impedance characteristics of PMSG, DFIG, PV plants and the AC grid in each frequency band are illustrated in Fig. 13.4.

As seen from the figure, the dominant factors in the same frequency band differs from various devices because of the inherent difference of their topology and control principle. In some frequency bands, the impedance of REG plants may represent negative damping characteristics due to the frequency-band overlapping effect, and the frequency range of negative damping also differs from various devices.

For the two-port network of REG connected into AC grid, there will be oscillation risk, if the impedance of one port represents negative damping characteristics and the GM/PM of this system is insufficient. Moreover, there may be oscillation risk in broadband from several Hertz to hundreds of Hertz, as the difference of the frequency range of negative damping characteristics for various REG devices.

13.2.2 Oscillation Risk Evaluation for PMSG/PV Plant Connected into Weak Grid

The oscillation risk evaluation and the dominant factors for PMSG-based wind plants or PV plants connected into AC grid in each frequency band is summarized as follows.

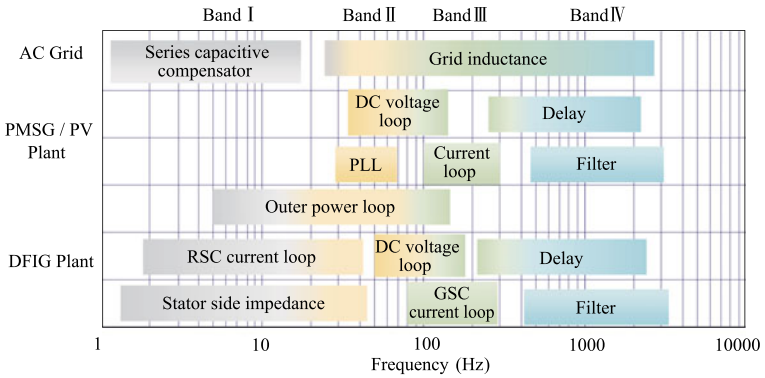

(a) Dominant control loops of REG and the AC grid in each frequency-band

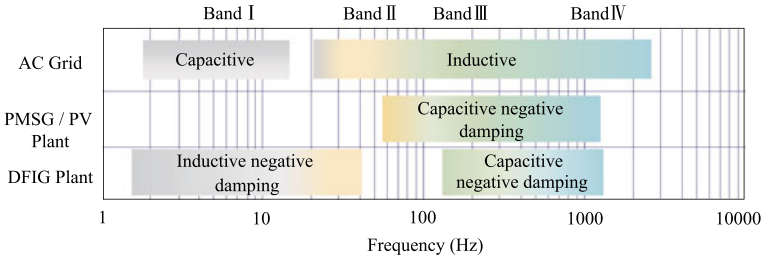

(b) Impedance characteristics of REG and the AC grid in each frequency-band

Fig. 13.4 Dominant factors and impedance characteristics of REG and the AC grid

1. **Band I** (around $f < 37$ Hz)

Since the impedance of PMSG/PV plants doesn't exhibit negative damping characteristics, there is no oscillation risk for PMSG/PV plants connected into HVAC system.

2. **Band II** (around 37 Hz $< f <$ 63 Hz)

The impedance of AC grid represents inductance characteristics in this frequency range. However, the impedance of PMSG/PV plants represents capacitive characteristics, as it is dominated by the PLL control in this frequency range. Moreover, it may represent capacitive negative damping characteristics due to the frequency-band overlapping effect of the DC voltage loop.

Hence, there will be oscillation risk for PMSG/PV plants connected into AC grid in this frequency range, if the magnitudes of the impedance curves intersect and the PM of the intersection point is insufficient.

3. **Band III** (around 63 Hz $< f <$ 420 Hz)

The impedance of AC grid remains inductance characteristics. However, the impedance of PMSG/PV plants represents capacitive characteristics, as it is dominated by the AC current control in this frequency range. Moreover, it may represent

capacitive negative damping characteristics due to the frequency-band overlapping effect of the DC voltage loop in the former frequency range of Band III, or due to that of the time delay in the latter frequency range.

Hence, there will be oscillation risk for PMSG/PV plants connected into AC grid in this frequency range, if the magnitudes of the impedance curves intersect and the PM of the intersection point is insufficient.

4. **Band IV** (around $f > 420$ Hz)

The impedance of AC grid remains inductance characteristics. However, the impedance of PMSG-based wind plants changes from inductive to capacitive characteristics in this frequency range, as it is determined by LC filter. Furthermore, when it represents capacitive characteristics, it may represent capacitive negative damping characteristics due to the frequency-band overlapping effect of the time delay.

Hence, there will be oscillation risk for PMSG/PV plants connected into AC grid in this frequency range, if the magnitudes of the impedance curves intersect and the PM of the intersection point is insufficient.

13.2.3 Oscillation Risk Evaluation for DFIG Plant Connected into Weak Grid

The oscillation risk evaluation and the dominant factors for DFIG-based wind plants connected into AC grid in each frequency band is summarized as follows.

1. **Band I** (around $f < 37$ Hz)

The impedance of AC grid may represent capacitive characteristics if the series capacitive compensators are used. However, the impedance of DFIG-based wind plants represents inductive negative damping characteristics, as it is determined by the stator side impedance and affected by the rotor electrical frequency and the steady-state operating points.

Hence, there will be oscillation risk for DFIG-based wind plants connected into AC grid in this frequency range, if the magnitudes of the impedance curves intersect and the PM of the intersection point is insufficient.

2. **Band II** (around $37 \text{ Hz} < f < 63$ Hz)

The impedance of AC grid represents inductive characteristics. The impedance of DFIG-based wind plants remains inductive negative damping characteristics as that of Band I.

Based on the phase ranges, there is no oscillation risk for DFIG-based wind plants connected into AC grid in this frequency range.

3. **Band III** (around $63 \text{ Hz} < f < 420$ Hz)

The impedance of AC grid remains inductive characteristics. On the other hand, the impedance of DFIG-based wind plants represents capacitive negative damping

characteristics, as it is determined by stator side and GSC impedance, and also affected by the frequency-band overlapping of DC voltage loop and AC current loop or that of the time delay and AC current loop.

Hence, there will be oscillation risk for DFIG-based wind plants connected into AC grid in this frequency range, if the magnitudes of the impedance curves intersect and the PM of the intersection point is insufficient.

4. **Band IV** (around $f > 420$ Hz)

The impedance of AC grid remains inductive characteristics. However, the impedance of DFIG-based wind plants changes from inductive to capacitive characteristics, as it is determined by the LC filter. Furthermore, when it represents capacitive characteristics, it may represent capactive negative damping characteristics due to the frequency-band overlapping effect of the time delay.

Hence, there will be oscillation risk for DFIG-based wind plants connected into AC grid in this frequency range, if the magnitudes of the impedance curves intersect and the PM of the intersection point is insufficient.

13.3 Frequency Coupling Effect Analysis

In this section, the frequency coupling effect of multiple frequency oscillation induced by single dominant oscillation frequency is explained in detail, based on the analysis of oscillation risk in each frequency band.

Specifically, according to the conclusion in Sects. 13.1 and 13.2, there will be oscillation risk for REG plants connected into AC grid at f_{osc}, if the REG port impedance $\boldsymbol{Z}_{\text{RE}}$ represents capacitive negative damping characteristics and the GM/PM between $\boldsymbol{Z}_{\text{RE}}$ and the AC grid impedance $\boldsymbol{Z}_{\text{g}}$ at f_{osc} is insufficient.

Generally, the oscillation risk for one REG plant may induce the oscillation of multiple REG plants at multiple frequency. The oscillation propagation process with the frequency coupling effect for PMSG, DFIG and PV plants connected into AC grid is shown in Fig. 13.5.

It is assumed that there is only oscillation risk for the PMSG-based wind plant connected into AC grid at positive-sequence oscillation frequency f_{osc}, and no oscillation risk for the DFIG-based wind plant or the PV plant connected into AC grid.

At the beginning, the PMSG-based wind plant oscillates with the AC grid. Thus, there will be a small-signal component of AC voltage of the PMSG-based wind plant at f_{osc}, denoted by $\hat{\boldsymbol{v}}_{\text{PMSG}}$. According to the conclusion in Part II, it will lead to a small-signal response of the AC current at f_{osc}, denoted by $\hat{\boldsymbol{i}}_{\text{PMSG}}$, due to the positive-sequence admittance $\boldsymbol{Y}_{\text{PMSG}}^{\text{pp}}$. Meanwhile, it will lead to another small-signal response of the AC current at $f_{\text{osc}} - 2f_1$, denoted by $\hat{\boldsymbol{i}}_{\text{PMSG2}}$, due to the positive-sequence coupled admittance $\boldsymbol{Y}_{\text{PMSG}}^{\text{pn}}$. This process is shown by the Process ① in Fig. 13.5.

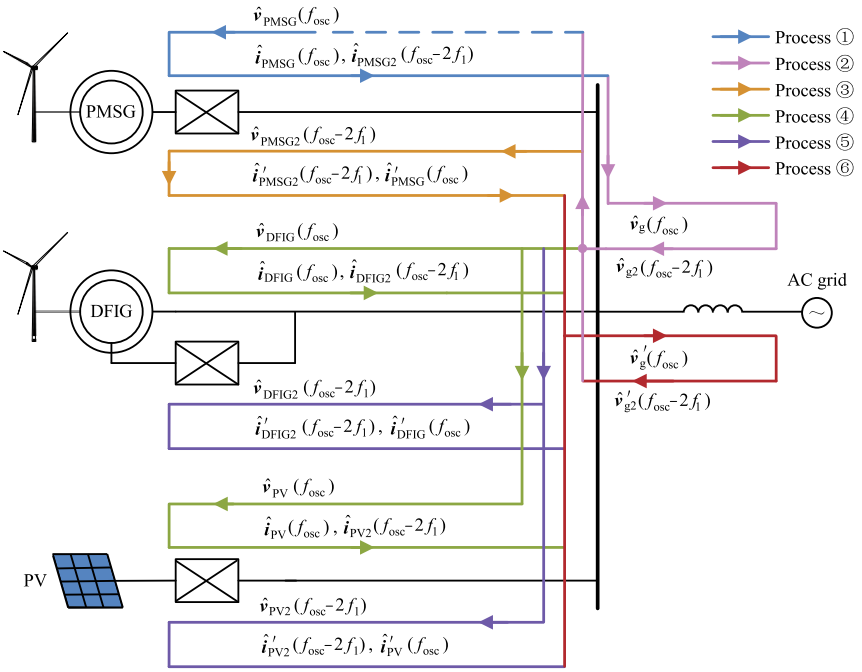

Fig. 13.5 Oscillation propagation process with the frequency coupling effect for multiple REG plants connected into AC grid

Then, as shown by the Process ②, small-signal components of the AC grid voltage at f_{osc} and $f_{\text{osc}} - 2f_1$ will be generated, denoted by $\hat{\boldsymbol{v}}_{\text{g}}$ and $\hat{\boldsymbol{v}}_{\text{g2}}$, as the response of AC grid impedance to $\hat{\boldsymbol{i}}_{\text{PMSG}}$ and $\hat{\boldsymbol{i}}_{\text{PMSG2}}$.

Accordingly, as shown by the Process ③, $\hat{\boldsymbol{v}}_{\text{g2}}$ will lead to a small-signal response of the AC current at $f_{\text{osc}} - 2f_1$, denoted by $\hat{\boldsymbol{i}}'_{\text{PMSG2}}$, due to the negative-sequence admittance $\boldsymbol{Y}^{\text{nn}}_{\text{PMSG}}$. Meanwhile, it will lead to another small-signal response of the AC current at f_{osc}, denoted by $\hat{\boldsymbol{i}}'_{\text{PMSG}}$, due to the negative-sequence coupled admittance $\boldsymbol{Y}^{\text{np}}_{\text{PMSG}}$. To sum up, $\hat{\boldsymbol{i}}_{\text{PMSG}}$ and $\hat{\boldsymbol{i}}'_{\text{PMSG}}$ are the positive-sequence small-signal components of the AC current, $\hat{\boldsymbol{i}}_{\text{PMSG2}}$ and $\hat{\boldsymbol{i}}'_{\text{PMSG2}}$ are the negative-sequence small-signal components.

Besides, for the DFIG-based wind plant and the PV plant, $\hat{\boldsymbol{v}}_{\text{g}}$ will lead to $\hat{\boldsymbol{i}}_{\text{DFIG}}$ and $\hat{\boldsymbol{i}}_{\text{PV}}$ at f_{osc} due to their positive-sequence admittance, and $\hat{\boldsymbol{i}}_{\text{DFIG2}}$ and $\hat{\boldsymbol{i}}_{\text{PV2}}$ at $f_{\text{osc}} - 2f_1$ due to their positive-sequence coupled admittance, as shown by the Process ④. Meanwhile, $\hat{\boldsymbol{v}}_{\text{g2}}$ will lead to $\hat{\boldsymbol{i}}'_{\text{DFIG2}}$ and $\hat{\boldsymbol{i}}'_{\text{PV2}}$ at $f_{\text{osc}} - 2f_1$ due to their negative-sequence admittance, and $\hat{\boldsymbol{i}}'_{\text{DFIG}}$ and $\hat{\boldsymbol{i}}'_{\text{PV}}$ at f_{osc} due to their negative-sequence coupled admittance, as shown by the Process ⑤.

Next, as shown by Process ⑥, $\hat{\boldsymbol{i}}_{\text{DFIG}}$, $\hat{\boldsymbol{i}}'_{\text{DFIG}}$, $\hat{\boldsymbol{i}}_{\text{PV}}$, $\hat{\boldsymbol{i}}'_{\text{PV}}$, $\hat{\boldsymbol{i}}_{\text{DFIG2}}$, $\hat{\boldsymbol{i}}'_{\text{DFIG2}}$, $\hat{\boldsymbol{i}}_{\text{PV2}}$, and $\hat{\boldsymbol{i}}'_{\text{PV2}}$ will lead to small-signal components of the AC grid voltage at f_{osc} and $f_{\text{osc}} - 2f_1$.

Table 13.1 Frequency relationship for the frequency coupling effect of oscillation

Input Oscillation Frequency	Output Oscillation Frequency	Output Coupling Oscillation Frequency
$f_{osc}(< 2f_1)$ (positive-sequence)	f_{osc} (positive-sequence)	$2f_1 - f_{osc}$ (positive-sequence)
$f_{osc}(> 2f_1)$ (positive-sequence)	f_{osc} (positive-sequence)	$f_{osc} - 2f_1$ (negative-sequence)
f_{osc} (negative-sequence)	f_{osc} (negative-sequence)	$f_{osc} + 2f_1$ (positive-sequence)

Additionally, they will also lead to small-signal components of the AC voltage of the PMSG-based wind plant at f_{osc} and $f_{osc} - 2f_1$.

Finally, the oscillation of this system will reach a dynamic balance through multiple interactions of the aforementioned processes.

In conclusion, the oscillation risk for one REG plant at one dominate frequency will induce the oscillation of multiple REG plants at multiple frequency, which is called the frequency coupling effect of oscillation. The positive-sequence oscillation of one REG plant at f_{osc} will induce the positive-sequence oscillation of the system at f_{osc} and the negative-sequence coupling oscillation of the system at $f_{osc} - 2f_1$. Similarly, the negative-sequence oscillation of one REG plant at f_{osc} will induce the negative-sequence oscillation of the system at f_{osc} and the positive-sequence coupling oscillation of the system at $f_{osc} + 2f_1$. The frequency relationship is summarized in Table 13.1. In the table, the negative-sequence coupling oscillation components at $f_{osc} - 2f_1(f_{osc} < 2f_1)$ correspond to the positive-sequence coupling oscillation components at $2f_1 - f_{osc}$.

13.4 Simulation Verification

In this section, the impedance scanning of various types of REG plants are first implemented based on the full EMT simulation platform for REG and AC/DC transmission systems. Then, based on the Nyquist criterion of maximum peak value, the oscillation risk evaluation for various REG plants connected into different AC grids can be implemented.

13.4.1 Oscillation Verification for PMSG/PV Plant Connected into Weak Grid

In this section, three different PMSG-based wind plants are selected respectively to conduct frequency-domain analysis and time-domain simulation on the risk of broadband oscillation when they are connected to weak grids of different strengths.

The three wind plants are respectively composed of Type 1, Type 2 and Type 3 PMSG-based wind turbines.

13.4.1.1 Band II

Based on full EMT simulation, frequency-domain analysis and time-domain simulation of oscillation risk is carried out to verify the correctness of oscillation risk analysis of Band II. The total capacity of the PMSG-based wind plant (Type 1) is 150 MW and composed of 100 identical units. The simulation parameters of a PMSG-based wind turbine are listed in Table 13.2. The SCR of AC grid is 1.6. Based on these parameters, Fig. 13.6 shows the evaluation results of the oscillation risk for the PMSG-based wind plant connected into AC grid.

As seen from the figure, the phase of the PMSG impedance $\boldsymbol{Z}_{\mathrm{PMSG}}$ represents capacitive negative damping characteristics in Band II. The magnitudes of $\boldsymbol{Z}_{\mathrm{PMSG}}$ curve and $\boldsymbol{Z}_{\mathrm{g}}$ curve intersect at Point A (77 Hz), and the PM is 0.5°. The GM/PM is insufficient, indicating oscillation risk in the system.

In addition, in Fig. 13.6(b), a forbidden area with radius $R_{\min}$ of 0.1 is drawn based on the Nyquist criterion of maximum peak value. The Nyquist curve of $\boldsymbol{Z}_{\mathrm{g}}/\boldsymbol{Z}_{\mathrm{PMSG}}$ around Point A (77 Hz) is in the forbidden area. Therefore, the system stability margin is insufficient, also indicating oscillation risk at 77 Hz as in the Bode plot.

Meanwhile, the time-domain simulation of oscillation recurrence for the above system is carried out base on the full EMT simulation platform. The oscillation waveforms and the fast Fourier transform (FFT) results are shown in Fig. 13.7.

As seen from the figure, this system oscillates at 77 Hz, corresponding with the Point A in the forbidden area in Fig. 13.6. There is also an oscillation harmonics at 23 Hz in Fig. 13.7. It results from the frequency coupling effect of the oscillation at 77 Hz. Coincidentally, the simulation results in time domain and in frequency domain are almost the same. Thus, the oscillation mechanism for PMSG-based wind plants connected into AC grid in Band II is verified by the simulation results.

Table 13.2 PMSG wind turbine (Type 1) simulation parameters

Parameter	Definition	Value
N_{PMSG}	Number of PMSG-based wind turbines	100
P_{N}	Rated power	1.5 MW
V_{dc}	Steady-state value of DC voltage	1100 V
V_{1}	Amplitude of the fundamental frequency component of AC voltage	690 V
k_{T}	Transformer voltage ratio	0.69 kV/35 kV
C_{dc}	DC filter capacitance	13.6 mF
L_{f}	AC filter inductance	0.3 mH
C_{f}	AC filter capacitance	0.5 mF

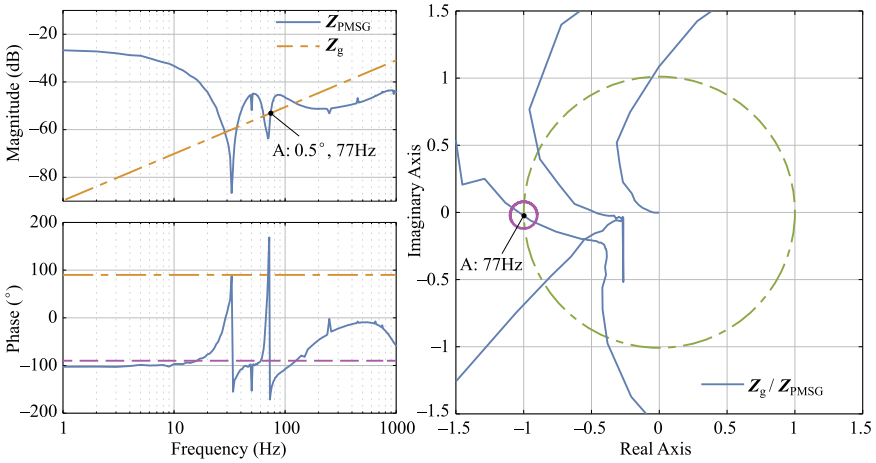

(a) System impedance Bode plot (b) System Nyquist plot

Fig. 13.6 The evaluation results of oscillation risk for PMSG-based wind plant (Type 1) connected into AC grid

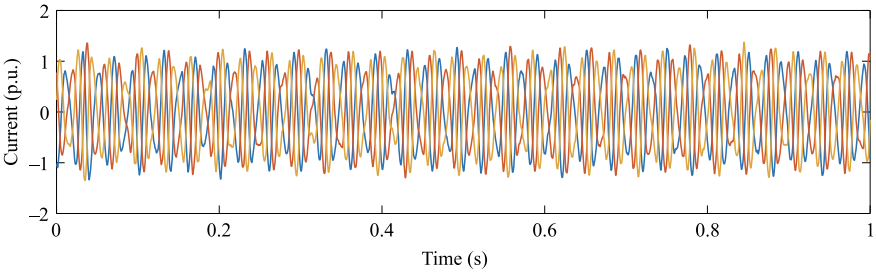

(a) PMSG-based wind plant AC currents

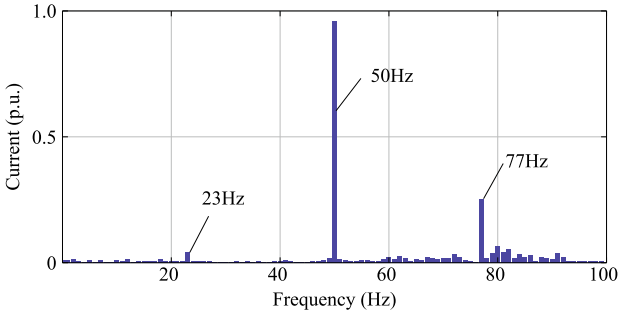

(b) FFT results of PMSG-based wind plant AC current

Fig. 13.7 Oscillation waveforms and the FFT results for PMSG-based wind plant (Type 1) connected into AC grid

13.4.1.2 Band III

Based on full EMT simulation, frequency-domain analysis and time-domain simulation of oscillation risk are carried out to verify the correctness of oscillation risk analysis of Band III. The total capacity of the PMSG-based wind plant (Type 2) is 150 MW and composed of 100 identical units. The simulation parameters of a PMSG-based wind turbine are listed in Table 13.3. The SCR of AC grid is 1.6. Based on these parameters, Fig. 13.8 shows the evaluation results of the oscillation risk for the PMSG-based wind plant connected into AC grid.

As seen from the figure, the phase of $\boldsymbol{Z}_{\mathrm{PMSG}}$ represents capacitive negative damping characteristics in Band III. The magnitudes of $\boldsymbol{Z}_{\mathrm{PMSG}}$ curve and $\boldsymbol{Z}_{\mathrm{g}}$ curve

Table 13.3 PMSG wind turbine (Type 2) simulation parameters

Parameter	Definition	Value
N_{PMSG}	Number of PMSG-based wind turbines	100
P_{N}	Rated power	1.5 MW
V_{dc}	Steady-state value of DC voltage	1500 V
V_1	Amplitude of the fundamental frequency component of AC voltage	620 V
k_{T}	Transformer voltage ratio	0.62 kV/35 kV
C_{dc}	DC capacitance	13 mF
L_{f}	AC filter inductance	0.075 mH
C_{f}	AC filter capacitance	0.67 mF

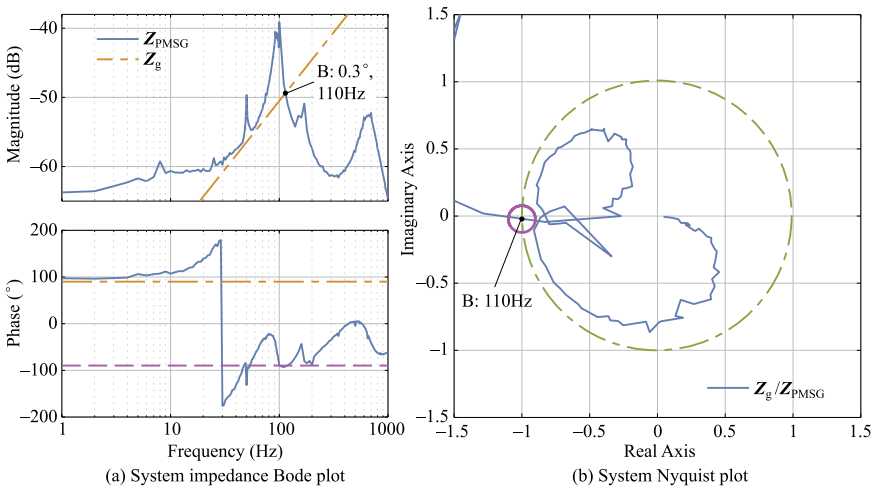

Fig. 13.8 The evaluation results of oscillation risk for PMSG-based wind plant (Type 2) connected into AC grid

intersect at Point B (110 Hz), and the PM is 0.3°. The GM/PM is insufficient, indicating oscillation risk in the system.

In addition, in Fig. 13.8(b), a forbidden area with radius $R_{\min}$ of 0.1 is drawn based on the Nyquist criterion of maximum peak value. The Nyquist curve of $\boldsymbol{Z}_{\mathrm{g}}/\boldsymbol{Z}_{\mathrm{PMSG}}$ around Point B (110 Hz) is in the forbidden area. Therefore, the system stability margin is insufficient, also indicating oscillation risk at 110 Hz as in the Bode plot.

Meanwhile, the time-domain simulation of oscillation recurrence for the above system is carried out base on the full EMT simulation platform. The oscillation waveforms and the FFT results are shown in Fig. 13.9.

As seen from the figure, this system oscillates at 110 Hz, corresponding with the Point B in the forbidden area in Fig. 13.8. There is also a oscillation harmonics at 10 Hz in Fig. 13.9. It results from the frequency coupling effect of the oscillation at 110 Hz. Coincidentally, the simulation results in time domain and in frequency domain are almost the same. Thus, the oscillation mechanism for PMSG-based wind plants connected into AC grid in Band III is verified by the simulation results.

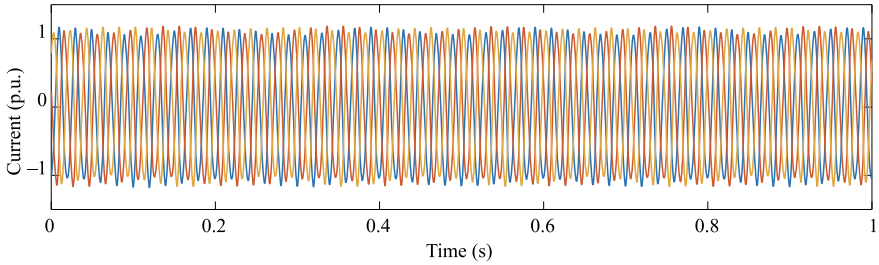

(a) PMSG-based wind plant AC currents

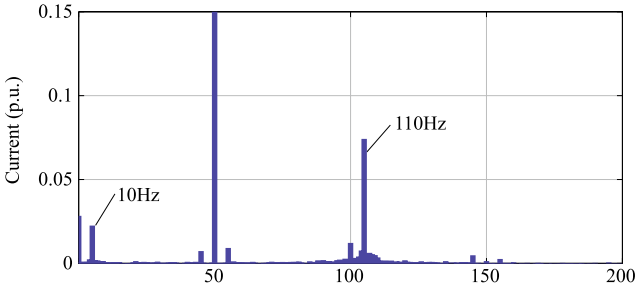

(b) FFT results of PMSG-based wind plant AC currents

Fig. 13.9 Oscillation waveforms and the FFT results for PMSG-based wind plant (Type 2) connected into AC grid

13.4.1.3 Band IV

Based on full EMT simulation, frequency-domain analysis and time-domain simulation of oscillation risk are carried out to verify the correctness of oscillation risk analysis of Band IV. The total capacity of the PMSG-based wind plant (Type 3) is 200 MW and composed of 100 identical units. The simulation parameters of a PMSG-based wind turbine are listed in Table 13.4. The SCR of AC grid is 1.7. Based on these parameters, Fig. 13.10 shows the evaluation results of the oscillation risk for the PMSG-based wind plant connected into AC grid.

As seen from the figure, the phase of $\boldsymbol{Z}_{\mathrm{PMSG}}$ represents capacitive negative damping characteristics in Band IV. The magnitudes of $\boldsymbol{Z}_{\mathrm{PMSG}}$ curve and $\boldsymbol{Z}_{\mathrm{g}}$ curve

Table 13.4 PMSG wind turbine (Type 3) simulation parameters

Parameter	Definition	Value
N_{PMSG}	Number of PMSG-based wind turbines	100
P_{N}	Rated power	2 MW
V_{dc}	Steady-state value of DC voltage	1080 V
V_1	Amplitude of the fundamental frequency component of AC voltage	650 V
k_{T}	Transformer voltage ratio	0.65 kV/35 kV
C_{dc}	DC capacitance	38 mF
L_{f}	AC filter inductance	0.075 mH
C_{f}	AC filter capacitance	0.67 mF

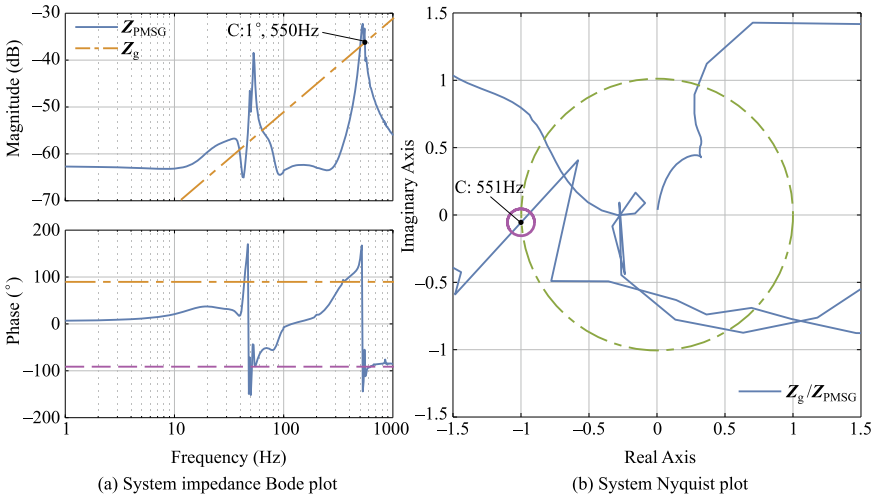

(a) System impedance Bode plot (b) System Nyquist plot

Fig. 13.10 The evaluation results of oscillation risk for PMSG-based wind plant (Type 3) connected into AC grid

intersect at Point C (551 Hz), and the PM is 1°. The GM/PM is insufficient, indicating oscillation risk in the system.

In addition, in Fig. 13.10(b), a forbidden area with radius $R_{\min}$ of 0.1 is drawn based on the Nyquist criterion of maximum peak value. The Nyquist curve of $\boldsymbol{Z}_{\mathrm{g}}/\boldsymbol{Z}_{\mathrm{PMSG}}$ around Point C (551 Hz) is in the forbidden area. Therefore, the system stability margin is insufficient, also indicating oscillation risk at 551 Hz as in the Bode plot.

Meanwhile, the time-domain simulation of oscillation recurrence for the above system is carried out base on the full EMT simulation platform. The oscillation waveforms and the FFT results are shown in Fig. 13.11.

As seen from the figure, this system oscillates at 551 Hz, corresponding with the Point B in the forbidden area in Fig. 13.10. Coincidentally, the simulation results in time domain and in frequency domain are almost the same. Thus, the oscillation mechanism for PMSG-based wind plants connected into AC grid in Band IV is verified by the simulation results.

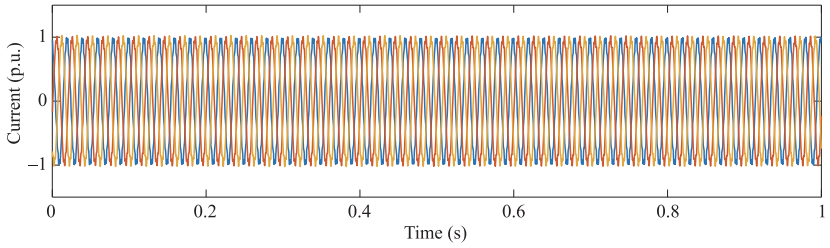

(a) PMSG-based wind plant AC currents

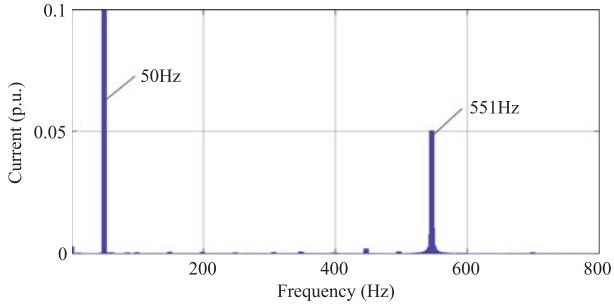

(b) FFT results of PMSG-based wind plant AC current

Fig. 13.11 Oscillation waveforms and the FFT results for PMSG-based wind plant (Type 3) connected into AC grid

13.4.2 Oscillation Verification for DFIG Plant Connected into Weak Grid

In this section, two different DFIG-based wind plants are selected to conduct frequency-domain analysis and time-domain simulation on the risk of broadband oscillation when they are connected to weak grids of different strengths. The two wind plants are respectively composed of Type 1 and Type 2 DFIG-based wind turbines.

13.4.2.1 Band I

Based on full EMT simulation, frequency-domain analysis and time domain simulation of oscillation risk is carried out to verify the correctness of oscillation risk analysis of Band I. The total capacity of the DFIG-based wind plant (Type 1) is 200 MW and composed of 100 identical units. The simulation parameters of a DFIG-based wind turbine are listed in Table 13.5. The SCR of AC grid is 1.6 and the series-complement degree is 0.4. Based on these parameters, Fig. 13.12 shows the evaluation results of the oscillation risk for the DFIG-based wind plant connected into AC grid with series capacitive compensators.

As seen from the figure, when the rotor electrical angular frequency ω_r is 1.2 p.u., the phase of the DFIG impedance $\boldsymbol{Z}_{\mathrm{DFIG}}$ represents inductive negative damping characteristics in Band I. And the phase of the AC grid impedance $\boldsymbol{Z}_g$ represents capacitive characteristics. The magnitudes of $\boldsymbol{Z}_{\mathrm{DFIG}}$ curve and $\boldsymbol{Z}_g$ curve intersect at Point D (7 Hz) and the PM is 1.5°. The GM/PM is insufficient, indicating oscillation risk in the system.

In addition, in Fig. 13.12(b), a forbidden area with radius $R_{\min}$ of 0.1 is drawn based on the Nyquist criterion of maximum peak value. The Nyquist curve of $\boldsymbol{Z}_g/\boldsymbol{Z}_{\mathrm{DFIG}}$ around Point D (7 Hz) is in the forbidden area. Therefore, the system stability margin is insufficient, also indicating oscillation risk at 7 Hz as in the Bode plot.

When the rotor electrical angular frequency ω_r is 0.9 p.u., the phase of $\boldsymbol{Z}_{\mathrm{DFIG}}$ remains inductive negative damping characteristics. The magnitudes of $\boldsymbol{Z}_{\mathrm{DFIG}}$ curve

Table 13.5 DFIG wind turbine (Type 1) simulation parameters

Parameter	Definition	Value
N_{DFIG}	Number of DFIG-based wind turbines	100
P_N	Rated power	2 MW
V_{dc}	Steady-state value of DC voltage	1050 V
V_1	Amplitude of the fundamental frequency component of AC voltage	690 V
k_T	Transformer voltage ratio	0.69 kV/35 kV
L_f	AC filter inductance	0.04 mH
C_f	AC filter capacitance	0.167 mF

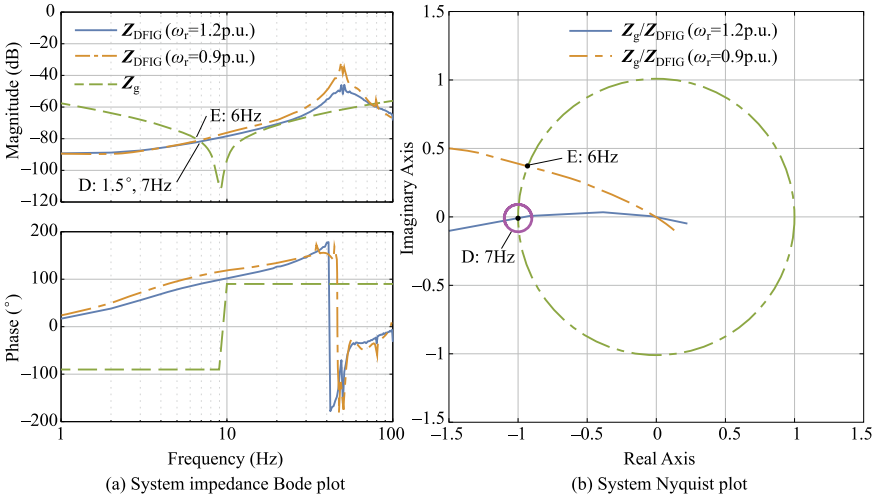

(a) System impedance Bode plot (b) System Nyquist plot

Fig. 13.12 The evaluation results of oscillation risk for DFIG-based wind plant (Type 1) connected into AC grid with series capacitive compensators

and the AC grid impedance $\boldsymbol{Z}_g$ curve intersect at Point E (6 Hz). However, the Nyquist curve of $\boldsymbol{Z}_g/\boldsymbol{Z}_{DFIG}$ around Point E (6 Hz) isn't in the forbidden area. Therefore, the system stability margin is sufficient, indicating no oscillation risk.

Meanwhile, the time-domain simulation of oscillation recurrence for the above system is carried out base on the full EMT simulation platform. The oscillation waveforms and the FFT results are shown in Fig. 13.13.

As seen from the Fig. 13.13, this system oscillates at 7 Hz, corresponding with the Point E in the forbidden area in Fig. 13.12. Coincidentally, the simulation results in time domain and in frequency domain are almost the same. Thus, the oscillation mechanism for DFIG-based wind plants connected into AC grid with series capacitive compensators in Band I is verified by the simulation results.

13.4.2.2 Band III

Based on full EMT simulation, frequency-domain analysis and time domain simulation of oscillion risk is carried out to verify the correctness of oslillation risk analysis of Band III. The total capacity of the DFIG-based wind plant (Type 2) is 210 MW and composed of 100 identical units. The simulation parameters of a DFIG-based wind turbine are listed in Table 13.6. The SCR of AC grid is 1.6. Based on these parameters, Fig. 13.14 shows the evaluation results of the oscillation risk for the DFIG-based wind plant connected into AC grid.

As seen from the figure, the phase of $\boldsymbol{Z}_{DFIG}$ represents capacitive negative damping characteristics in Band III. The magnitudes of $\boldsymbol{Z}_{DFIG}$ curve and $\boldsymbol{Z}_g$ curve intersect at

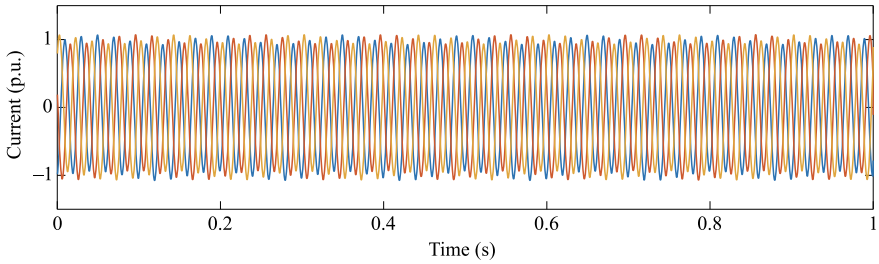

(a) DFIG-based wind plant AC currents

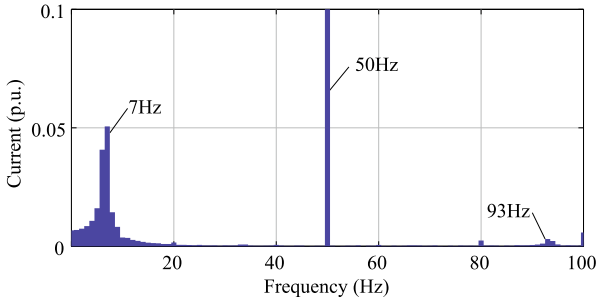

(b) FFT results of DFIG-based wind plant AC current

Fig. 13.13 Oscillation waveforms and the FFT results for DFIG-based wind plant (Type 1) connected into AC grid

Table 13.6 DFIG wind turbine (Type 2) simulation parameters

Parameter	Definition	Value
N_{DFIG}	Number of DFIG-based wind turbines	100
P_{N}	Rated power	2.1 MW
V_{dc}	Steady-state value of DC voltage	1050 V
V_1	Amplitude of the fundamental frequency component of AC voltage	690 V
k_{T}	Transformer voltage ratio	0.69 kV/35 kV
L_{f}	AC filter inductance	3 mH
C_{f}	AC filter capacitance	0.5 mF

Point F (63 Hz) and the PM is 2.1°. The GM/PM is insufficient, indicating oscillation risk in the system.

In addition, in Fig. 13.14(b), a forbidden area with radius $R_{\min}$ of 0.1 is drawn based on the Nyquist criterion of maximum peak value. The Nyquist curve of $\boldsymbol{Z}_{\mathrm{g}}/\boldsymbol{Z}_{\mathrm{DFIG}}$ around Point F (63 Hz) is in the forbidden area. Therefore, the system stability margin is insufficient, also indicating oscillation risk at 63 Hz as in the Bode plot.

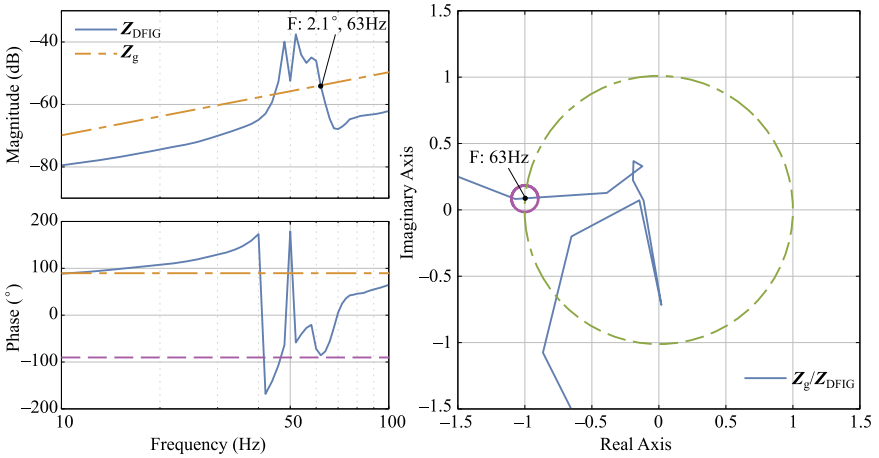

Fig. 13.14 The evaluation results of oscillation risk for DFIG-based wind plant (Type 2) connected into AC grid

Meanwhile, the time-domain simulation of oscillation recurrence for the above system is carried out base on the full EMT simulation platform. The oscillation waveforms and the FFT results are shown in Fig. 13.15.

As seen from the figure, this system oscillates at 63 Hz, corresponding with the Point B in the forbidden area in Fig. 13.14. There is also a oscillation harmonics at 37 Hz in Fig. 13.15. It results from the frequency coupling effect of the oscillation at 63 Hz. Coincidentally, the simulation results in time domain and in frequency domain are almost the same. Thus, the oscillation mechanism for DFIG-based wind plants connected into AC grid in Band III is verified by the simulation results.

13.5 Field Test Verification

In this section, the field test of oscillation recurrence for various REG units connected into AC grid are accomplished in the test and experimental verification platform for REG and AC/DC transmission systems and the analysis of oscillation mechanism can be then verified.

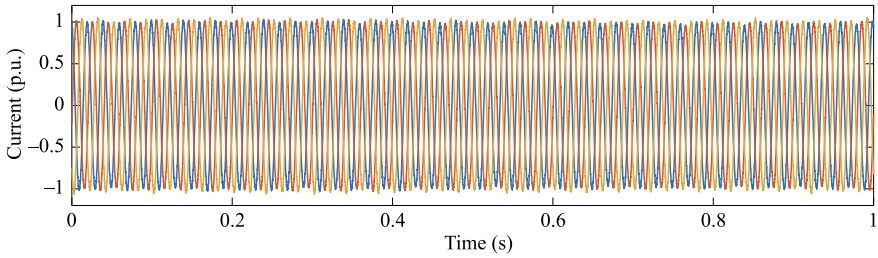

(a) DFIG-based wind plant AC currents

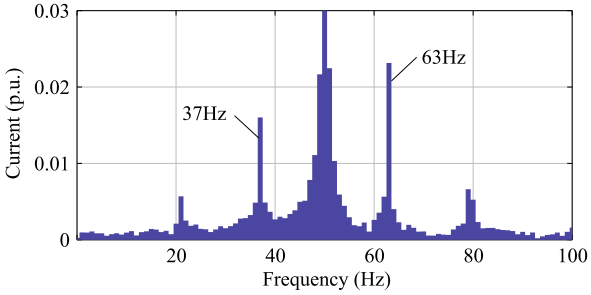

(b) FFT results of DFIG-based wind plant AC current

Fig. 13.15 Oscillation waveforms and the FFT results for DFIG-based wind plant (Type 2) connected into AC grid

13.5.1 Oscillation Verification for PMSG/PV Plant Connected into Weak Grid

13.5.1.1 Experimental System

The field test of oscillation recurrence for PMSG-based wind turbine connected into AC grid will be carried out on the No. 9 wind turbine in Zhangbei Test Base. The parameters of this wind turbine is given in Table 13.7. Te experimental system is shown in Fig. 13.16, where the wind turbine is integrated to the test bus through an adjustable impedance. Different grid strength of the AC grid can be realized by changing the adjustable impedance.

13.5.1.2 Oscillation Risk Evaluation

Based on the above parameters, an equivalent simulation model is firstly built on the CHIL simulation platform. Then, the frequency-domain impedance scanning can be carried out for PMSG-based wind turbine connected into AC grid.

For field implementation, the active power of the PMSG-base wind turbine is set to 0.4 p.u. based on the practical wind speed in Zhangbei Test Base. Besides, the

SCR of the AC grid is set to 1.3 by the adjustable impedance. Figure 13.17 shows the evaluation results of the oscillation risk for the PMSG-based wind turbine connected into AC grid.

Table 13.7 PMSG wind turbine parameters

Parameter	Definition	Value
P_N	Rated power	3.2 MW
V_1	Amplitude of the fundamental frequency component of AC voltage	690 V
k_T	Transformer voltage ratio	0.69 kV/35 kV
L_f	AC filter inductance	0.05 mH
C_f	AC filter capacitance	0.668 mF

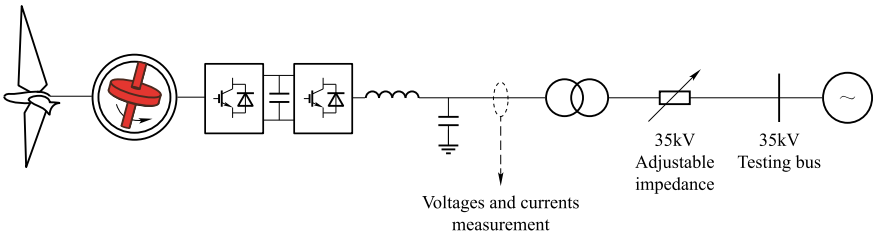

Fig. 13.16 Experimental system of PMSG-based wind turbine connected into AC grid

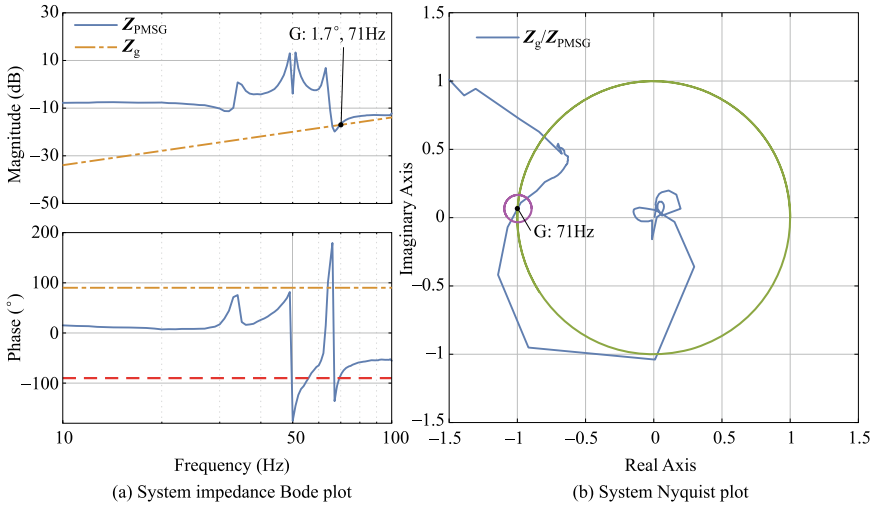

(a) System impedance Bode plot (b) System Nyquist plot

Fig. 13.17 The evaluation results of oscillation risk for PMSG-based wind turbine connected into AC grid

As seen from the figure, the phase of $\boldsymbol{Z}_{\mathrm{PMSG}}$ represents capacitive negative damping characteristics in Band III. The magnitudes of $\boldsymbol{Z}_{\mathrm{PMSG}}$ curve and $\boldsymbol{Z}_{\mathrm{g}}$ curve intersect at Point G (71 Hz) and the PM is 1.7°. The GM/PM is insufficient, indicating oscillation risk in the system.

In addition, in Fig. 13.17(b), a forbidden area with radius $R_{\min}$ of 0.1 is drawn based on the Nyquist criterion of maximum peak value. The Nyquist curve of $\boldsymbol{Z}_{\mathrm{g}}/\boldsymbol{Z}_{\mathrm{PMSG}}$ around Point G (71 Hz) is in the forbidden area. Therefore, the system stability margin is insufficient, also indicating oscillation risk at 71 Hz as in the Bode plot.

13.5.1.3 Field Test

Based on the test and experimental verification platform, the field test of oscillation recurrence for PMSG-based wind turbine connected into AC grid based on the same parameters in Sect. 13.5.1.1. Firstly, the adjustable impedance is set to 300 Ω to realize SCR = 1.3. Then the active power reaches 0.4 p.u. by setting the power instruction and control parameters. Finally, the oscillation waveforms and the FFT results are shown in Fig. 13.18.

As seen from the figure, this system oscillates at 29 and 71 Hz, same as the evaluation results in Fig. 13.17. Thus, the oscillation mechanism for PMSG-based wind turbines connected into AC grid is verified by the field test results.

13.5.2 Oscillation Verification for DFIG Plant Connected into Weak Grid

13.5.2.1 Experimental System

The field test of oscillation recurrence for DFIG-based wind turbine connected into AC grid will be carried out on the No. 22 wind turbine in Zhangbei Test Base. The parameters of this wind turbine is given in Table 13.8. The experimental system is shown in Fig. 13.19, where the wind turbine is integrated to the test bus through an adjustable impedance. Different grid strength of the AC grid can be realized by changing the adjustable impedance.

13.5.2.2 CHIL Simulation

Based on the above parameters, an equivalent simulation model is firstly built on the CHIL simulation platform. Then, the frequency-domain impedance scanning can be carried out for DFIG-based wind turbine connected into AC grid.

For field implementation, the active power of the DFIG-base wind turbine is set to 0.4 p.u. based on the practical wind speed in Zhangbei Test Base. Besides, the

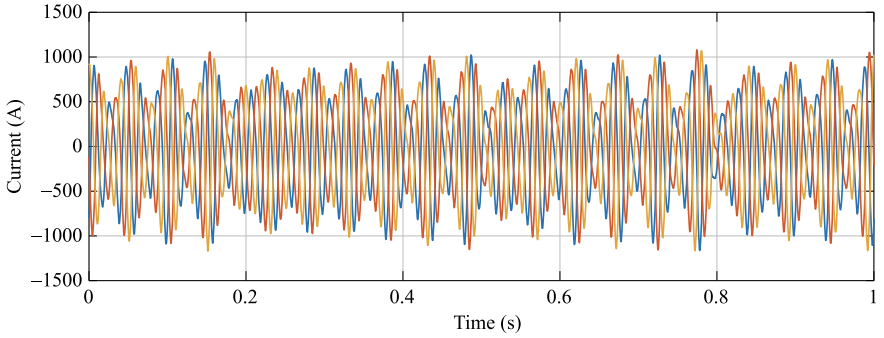

(a) PMSG-based wind turbine AC currents

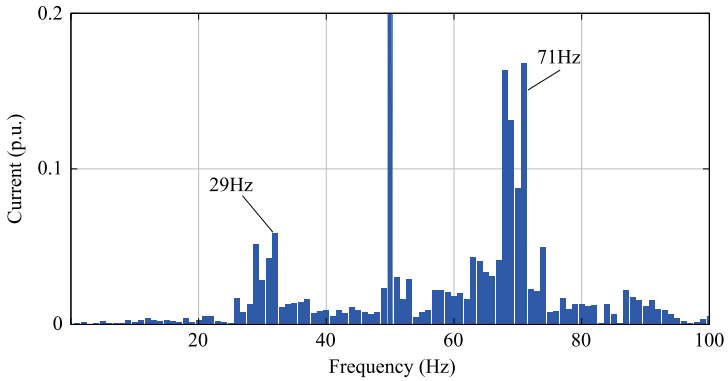

(b) FFT results of PMSG-based wind turbine AC current

Fig. 13.18 Oscillation waveforms and the FFT results for PMSG-based wind turbine connected into AC grid

Table 13.8 DFIG wind turbine parameters

Parameter	Definition	Value
P_N	Rated power	2 MW
V_1	Amplitude of the fundamental frequency component of AC voltage	690 V
k_T	Transformer voltage ratio	0.69 kV/35 kV
L_f	AC filter inductance	0.3 mH
C_f	AC filter capacitance	0.2228 mF

SCR of the AC grid is set to 1.9 by the adjustable impedance. Figure 13.20 shows the evaluation results of the oscillation risk for the DFIG-based wind turbine connected into AC grid.

As seen from the figure, the phase of $\boldsymbol{Z}_{\mathrm{DFIG}}$ represents capacitive negative damping characteristics in Band II. The magnitudes of $\boldsymbol{Z}_{\mathrm{DFIG}}$ curve and $\boldsymbol{Z}_{\mathrm{g}}$ curve intersect at

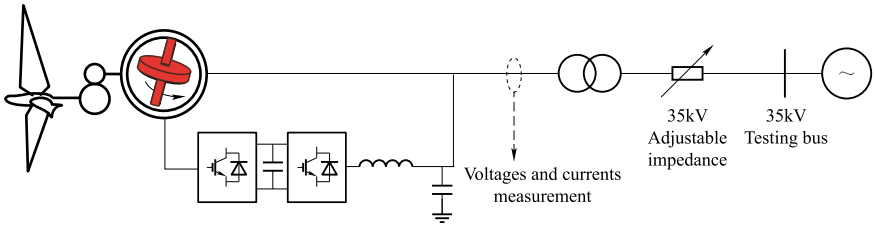

Fig. 13.19 Experimental system of DFIG-based wind turbine connected into AC grid

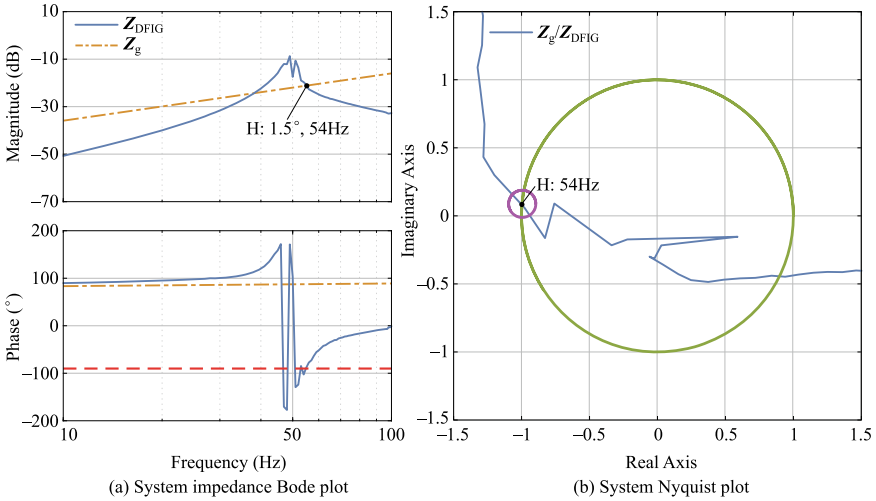

(a) System impedance Bode plot (b) System Nyquist plot

Fig. 13.20 The evaluation results of oscillation risk for DFIG-based wind turbine connected into AC grid

Point H (55 Hz) and the PM is 1.5°. The GM/PM is insufficient, indicating oscillation risk in the system.

In addition, in Fig. 13.20(b), a forbidden area with radius $R_{\min}$ of 0.1 is drawn based on the Nyquist criterion of maximum peak value. The Nyquist curve of $\boldsymbol{Z}_g/\boldsymbol{Z}_{DFIG}$ around Point H (54 Hz) is in the forbidden area. Therefore, the system stability margin is insufficient, also indicating oscillation risk at 54 Hz as in the Bode plot.

13.5.2.3 Field Test

Based on the test and experimental verification platform, the field test of oscillation recurrence for DFIG-based wind turbine connected into AC grid based on the same parameters in Sect. 13.5.2.1. Firstly, the adjustable impedance is set to 325 Ω to realize SCR = 1.9. Then the active power reaches 0.4 p.u. by setting the power

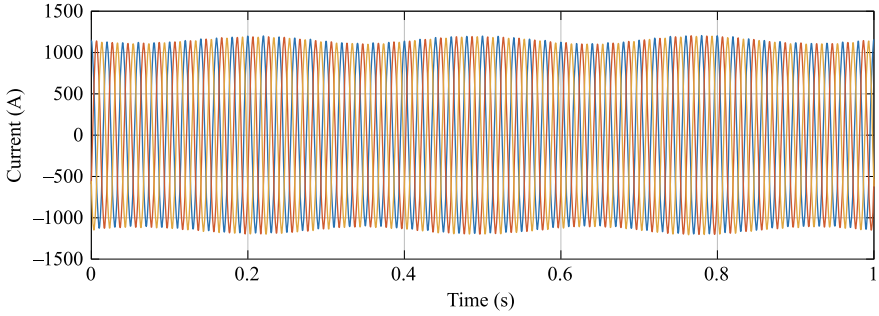

(a) DFIG-based wind turbine AC currents

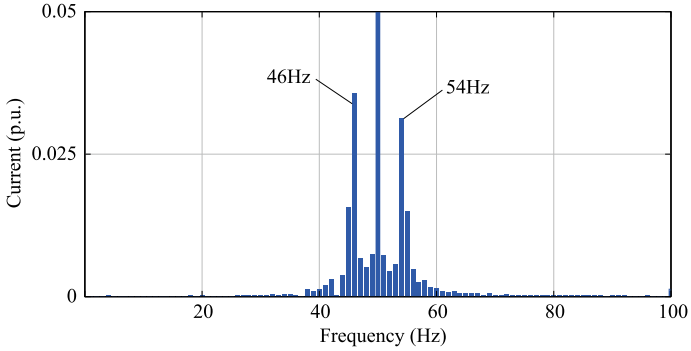

(b) FFT results of DFIG-based wind turbine AC current

Fig. 13.21 Oscillation waveforms and the FFT results for DFIG-based wind turbine connected into AC grid

instruction and control parameters. Finally, the oscillation waveforms and the FFT results are shown in Fig. 13.21.

As seen from the figure, this system oscillates at 46 and 54 Hz, the same as the evaluation results in Fig. 13.20. Thus, the oscillation mechanism for DFIG-based wind turbines connected into AC grid is verified by the field test results.

References

1. CHEN X, WANG Y C, GONG C Y, et al. Overview of stability research for grid-connected inverters based on impedance analysis method [J]. Proceedings of the CSEE, 2018, 38(7): 2082–2094+2223 (Chinese).
2. LIU H K, XIE X R, HE G Q, et al. Synchronous reference frame based impedance model and stability criterion for grid-connected renewable energy generation systems [J]. Proceedings of the CSEE, 2017, 37(14): 4002–4007+4278 (Chinese).
3. WANG X F, BLAABJERG F, WU W M. Modeling and analysis of harmonic stability in an AC power-electronics-based power system [J]. IEEE Transactions on Power Electronics, 2014, 29(12): 6421–6432.
4. WANG X F, BLAABJERG F. Harmonic stability in power electronic-based power systems: concept, modeling and analysis [J]. IEEE Transactions on Smart Grid, 2019, 10(3): 2858–2870.
5. WANG Y B, WANG X F, BLAABJERG F, et al. Harmonic instability assessment using state-space modeling and participation analysis in inverter-fed power systems [J]. IEEE Transactions on Industrial Electronics, 2017, 64(1): 806–816.
6. SUN J. Impedance-based stability criterion for grid-connected inverters [J]. IEEE Transactions on Power Electronics, 2011, 26(11): 3075–3078.
7. SUN J, WANG G N, DU X, et al. A theory for harmonics created by resonance in converter-grid systems [J]. IEEE Transactions on Power Electronics, 2019, 34(4): 3025–3029.
8. SUN J. Frequency-domain stability criteria for converter-based power systems [J]. IEEE Open Journal of Power Electronics, 2022, 3: 222–254.
9. CHOU S, WANG X F, BLAABJERG F. Two-port network modeling and stability analysis of grid-connected current-controlled VSCs [J]. IEEE Transactions on Power Electronics, 2020, 35(4): 3519–3529.

Chapter 14
Analysis of Broadband Oscillation for REG Connected into HVDC System

At the sending side of HVDC transmission, both LCC-HVDC system and MMC-HVDC system can be used for REG connection. For LCC-HVDC system, as an external AC grid is necessary to provide the synchronous voltage, this system can be equivalent to a three-port network. Due to the voltage support capability of MMC-HVDC system, it can be equivalent to a three-port network or a two-port network according to its grid-connected mode or passive islanding mode. With the scanned impedances of REG plants, LCC-HVDC and MMC-HVDC, the Nyquist stability criterion can be applied to evaluate the oscillation risk of the sending end system. However, this method is difficult to illustrate which control loop causes the oscillation and needs to be optimized, since the analysis of internal control loops is omitted.

In this chapter, the broadband oscillations for REG connected into LCC-HVDC and MMC-HVDC are analyzed in detail [1]. Firstly, for the LCC-HVDC system, the stability criteria for three-port network are proposed based on the analytical impedance models of the REG plants, and the LCC-HVDC. Additionally, the dominant factors of oscillations in different frequency bands for various REG plants connected into LCC-HVDC system are discovered. Based on the results, the mechanism of sub- and super-synchronous oscillation for REG connected into LCC-HVDC system is revealed. Secondly, the stability criteria for three-port network in grid-connected mode and for two-port network in passive islanding mode of MMC-HVDC system are proposed respectively. Similarly, the dominant factors in different frequency bands and the mechanism of broadband oscillation for REG connected into MMC-HVDC are revealed.

© China Electric Power Press 2023

W. Wang et al., *Analysis and Mitigation of Broadband Oscillation in Renewable Energy Generation and AC/DC Transmission Systems*,
https://doi.org/10.1007/978-981-99-1568-2_14

14.1 Analysis of Oscillation for REG Connected into LCC-HVDC System

In order to analysis the stability issues of the sending side system of LCC-HVDC, the three-port network model is first derived and the stability criteria are then proposed. Besides, the working frequency range of the control loops are clarified. The frequency-band division methods for the impedance characteristics of REG and LCC-HVDC are then illustrated. Base on these, the dominant oscillation factors in different frequency-band are figured out. Finally, the oscillation mechanism is revealed based on the negative damping characteristics of REG impedance and that of LCC-HVDC impedance.

14.1.1 Stability Criteria

The sending side system of LCC-HVDC can be equivalent to a three-port network composed of the REG, the AC grid and the LCC-HVDC, as shown in Fig. 14.1, where $\boldsymbol{I}_{\text{out}}$ is the current of REG port, $\boldsymbol{I}_{\text{g}}$ is the current of AC grid and $\boldsymbol{I}_{\text{trans}}$ is the current of LCC-HVDC. Since the LCC-HVDC usually employs power control mode, it can be seen as non-ideal current sources. In this model, the LCC-HVDC port can be equivalent to an ideal current source $\boldsymbol{I}_{\text{LCC}}$ in parallel with its port impedance $\boldsymbol{Z}_{\text{LCC}}$. According to Chap. 13, the output of REG can be equivalent to an ideal current source $\boldsymbol{I}_{\text{RE}}$ in parallel with its port impedance $\boldsymbol{Z}_{\text{RE}}$. Moreover, the REG port is in series with equivalent inductance of transformers $\boldsymbol{Z}_{\text{CN}}$, as the REG plants are grid-connected through multiple step-up transformers. And the AC grid is an ideal voltage source $\boldsymbol{V}_{\text{g}}$ in series with its impedance $\boldsymbol{Z}_{\text{g}}$.

According to this model, $\boldsymbol{I}_{\text{out}}$ can be expressed as follows

$$\boldsymbol{I}_{\text{out}} = \left(\boldsymbol{I}_{\text{RE}} - \frac{\boldsymbol{V}_{\text{sys}}}{\boldsymbol{Z}_{\text{RE}}}\right) \cdot \frac{1}{1 + \boldsymbol{Z}_{\text{sys}}/\boldsymbol{Z}_{\text{RE}}} \tag{14.1}$$

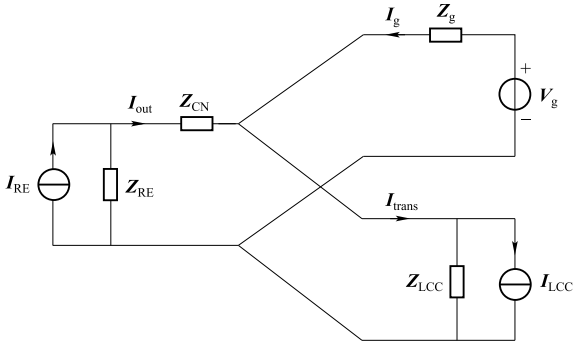

Fig. 14.1 Equivalent model for the sending side system of LCC-HVDC

where $\boldsymbol{V}_{\text{sys}}$ and $\boldsymbol{Z}_{\text{sys}}$ can be expressed as

$$\boldsymbol{V}_{\text{sys}} = \frac{1}{1 + \boldsymbol{Z}_{\text{g}}/\boldsymbol{Z}_{\text{LCC}}}\left(\boldsymbol{V}_{\text{g}} - \boldsymbol{I}_{\text{LCC}}\boldsymbol{Z}_{\text{g}}\right) \tag{14.2}$$

$$\boldsymbol{Z}_{\text{sys}} = \frac{\boldsymbol{Z}_{\text{LCC}}\boldsymbol{Z}_{\text{g}}}{\boldsymbol{Z}_{\text{LCC}} + \boldsymbol{Z}_{\text{g}}} + \boldsymbol{Z}_{\text{CN}} \tag{14.3}$$

Equation (14.1) can be seen as the multiplication of two closed-loop transfer functions, denoted as

$$\begin{cases} TF_1 = \boldsymbol{I}_{\text{RE}} - \dfrac{\boldsymbol{V}_{\text{sys}}}{\boldsymbol{Z}_{\text{RE}}} \\ TF_2 = \dfrac{1}{1 + \boldsymbol{Z}_{\text{sys}}/\boldsymbol{Z}_{\text{RE}}} \end{cases} \tag{14.4}$$

As the stability for this equivalent system is determined by TF_1 and TF_2, this system is stable if, and only if the poles of TF_1 and TF_2 are all in the left-half-plane.

On one hand, the distribution of poles for TF_1 is analyzed. Based on the conclusion in Chap. 13, all the poles of $\boldsymbol{I}_{\text{RE}} - 1/\boldsymbol{Z}_{\text{RE}}$ are all in the left-half-plane, since the REG plants are practically stable when connected to ideal AC grid. The stability of TF_1 is then determined by $\boldsymbol{V}_{\text{sys}}$. Therefore, all the poles of TF_1 are in the left-half-plane if and only of $\boldsymbol{V}_{\text{sys}}$ doesn't have any right-half-plane poles.

According to Eq. (14.2), $\boldsymbol{V}_{\text{sys}}$ is the open-circuit voltage of the REG port, and the equivalent circuit of LCC-HVDC connected into AC grid is shown in Fig. 14.2. Besides, $\boldsymbol{Z}_{\text{sys}}$ in Eq. (14.3) is the system impedance seen from REG plants at the PCC.

The system in Fig. 14.2 can be seen as typical current source connected into voltage source system. Since the LCC-HVDC is practically stable when connected to ideal AC grid, the stability of $\boldsymbol{V}_{\text{sys}}$ only depends on $\boldsymbol{Z}_{\text{g}}/\boldsymbol{Z}_{\text{LCC}}$. Therefore, $\boldsymbol{V}_{\text{sys}}$ can be claimed not to have any right-half-plane poles and all the poles of TF_1 are in the left-half-plane if, and only if

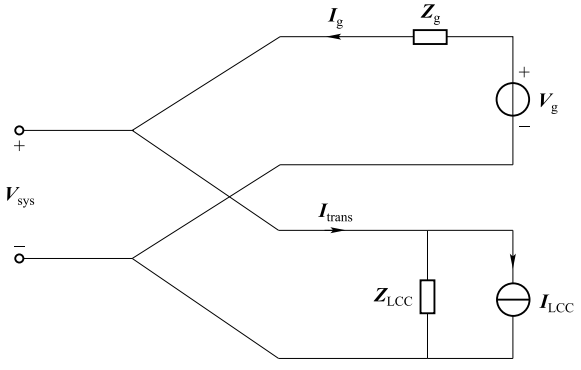

Fig. 14.2 Equivalent circuit of LCC-HVDC connected into AC grid

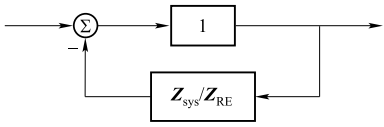

Fig. 14.3 Equivalent feedback loop of TF_2

- The impedance ratio $\boldsymbol{Z}_g/\boldsymbol{Z}_{LCC}$ conforms with Nyquist criterion.

On the other hand, TF_2 can be reformulated to fit a feedback loop with a open-loop gain of $\boldsymbol{Z}_{sys}/\boldsymbol{Z}_{RE}$, as shown in Fig. 14.3. All the poles of TF_2 should be in the left-half-plane, that is, this system is stable if, and only if

- The impedance ratio $\boldsymbol{Z}_{sys}/\boldsymbol{Z}_{RE}$ conforms with Nyquist criterion.

In conclusion, the REG plants connected into LCC-HVDC system is stable if and only if the following two conditions are satisfied.

① The LCC-HVDC is stable when connected into AC grid, that is, the impedance ratio $\boldsymbol{Z}_g/\boldsymbol{Z}_{LCC}$ conforms with Nyquist criterion.
② The impedance ratio $\boldsymbol{Z}_{sys}/\boldsymbol{Z}_{RE}$ conforms with Nyquist criterion.

When $\boldsymbol{I}_{LCC} = 0$, $\boldsymbol{Z}_{LCC} = \infty$ and $\boldsymbol{Z}_{CN} = 0$, that is, the REG plants are connected into the AC grid without LCC-HVDC, the output current of REG port can be simplified as follows

$$\boldsymbol{I}_{out} = \left(\boldsymbol{I}_{RE} - \frac{\boldsymbol{V}_g}{\boldsymbol{Z}_{RE}}\right) \cdot \frac{1}{1 + \boldsymbol{Z}_g/\boldsymbol{Z}_{RE}} \tag{14.5}$$

Apparently, the expression in Eq. (14.5) is the same as that of two-port network in Chap. 13. Therefore, the essential of the stability criteria for multi-port system is consistent with that of the two-port system.

14.1.2 Frequency-Band Division and Oscillation Analysis

In this section, the stability of LCC-HVDC connected into AC grid is first analyzed, and the influence of LCC-HVDC on the system impedance seen from REG plants is introduced. Then, based on the impedance characteristics analysis of PMSG, DFIG and PV plants, the frequency-band division method is proposed and the dominant factors in different frequency bands causing oscillation for various REG plants connected into LCC-HVDC system is illustrated.

14.1.2.1 System Impedance Characteristics

According to the aforementioned three-port network stability criteria, the oscillation risk between the LCC-HVDC and the AC gird should be first evaluated based on

the impedance characteristics of $\boldsymbol{Z}_{\mathrm{LCC}}$ and $\boldsymbol{Z}_{\mathrm{g}}$. Figure 14.4 shows the impedance characteristics under certain $\boldsymbol{Z}_{\mathrm{g}}$ (SCR = 1.5) and different $\boldsymbol{Z}_{\mathrm{LCC}}$. It can be seen that there is no oscillation risk with the transmission power of LCC-HVDC varying from 0.6 to 1.0 p.u.. Significantly, condition ① in Sect. 14.1.1 is conformed in this system.

According to condition ②, the influence of LCC-HVDC on the system impedance seen from REG plants will be elaborated. The impact of $\boldsymbol{Z}_{\mathrm{LCC}}$, $\boldsymbol{Z}_{\mathrm{g}}$ on $\boldsymbol{Z}_{\mathrm{sys}}$ is shown in Fig. 14.5.

The system impedance seen from REG plants represents inductance characteristics without the connection of LCC-HVDC. The system impedance changes with the connection of LCC-HVDC. As seen from the figure, within 1–30 Hz frequency range, since the magnitude of $\boldsymbol{Z}_{\mathrm{LCC}}$ is much higher than that of $\boldsymbol{Z}_{\mathrm{g}}$, the impact of $\boldsymbol{Z}_{\mathrm{LCC}}$ can be ignored. $\boldsymbol{Z}_{\mathrm{sys}}$ is close to $\boldsymbol{Z}_{\mathrm{g}} + \boldsymbol{Z}_{\mathrm{CN}}$ and shows as inductance. However, within 30–100 Hz frequency range, $\boldsymbol{Z}_{\mathrm{sys}}$ depends on $\boldsymbol{Z}_{\mathrm{LCC}}$, $\boldsymbol{Z}_{\mathrm{g}}$ and $\boldsymbol{Z}_{\mathrm{CN}}$, since the magnitude of them are close.

In 30–50 Hz (subsynchronous frequency range), the magnitude of $\boldsymbol{Z}_{\mathrm{LCC}}$ exhibits resonance peak and the phase represents capacitance characteristics. This effect makes the magnitude of $\boldsymbol{Z}_{\mathrm{sys}}$ also represent small resonance peak and its phase be slightly lower than 90° in this range.

In 50–100 Hz (supersynchronous frequency range), $\boldsymbol{Z}_{\mathrm{LCC}}$ represents inductive negative damping characteristics due to the frequency-band overlapping effect of the DC current loop and DC impedance. In consequence, $\boldsymbol{Z}_{\mathrm{sys}}$ also exhibits inductive negative damping characteristics in this frequency range.

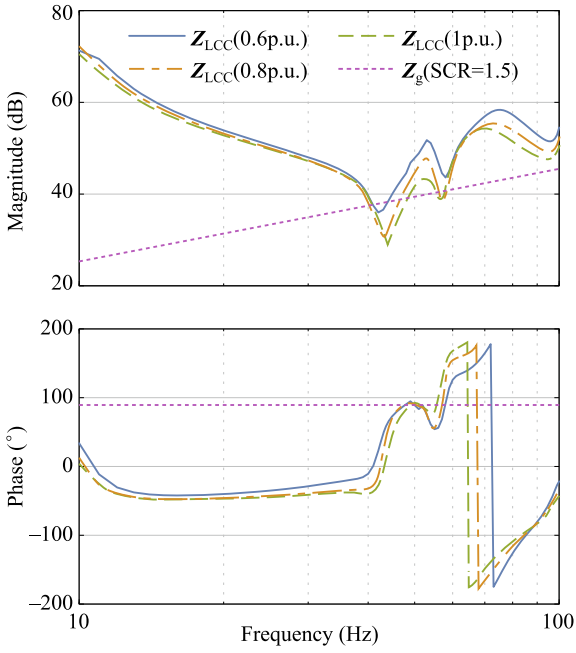

Fig. 14.4 Impedance characteristics of LCC-HVDC and AC grid

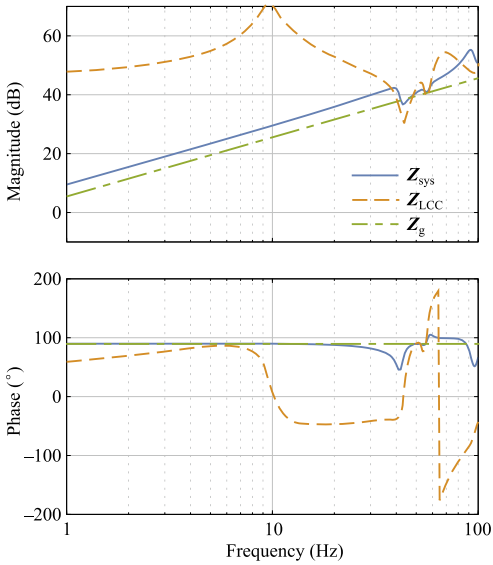

Fig. 14.5 Impedance characteristics of the connected system

To sum up, there is no oscillation risk for LCC-HVDC connected into AC grid, that is, condition ① is conformed. The following analysis will then focus on condition ②. The oscillation risk for REG plants connected into this LCC-HVDC system will be evaluated based on the impedance characteristics of $\boldsymbol{Z}_{\mathrm{RE}}$ and $\boldsymbol{Z}_{\mathrm{sys}}$.

14.1.2.2 Frequency-Band Division Method

According to the analysis of REG and LCC-HVDC impedance characteristics mentioned in Part II, the dominant factors in the same frequency range differs from various devices because of the inherent difference of their topology and control principle.

Generally, the frequency band within 1–100 Hz are divided into Band I, Band II and Band III according to the impedance characteristics of REG plants. Since the impedance characteristics of PV plants are almost the same as those of PMSG-based wind plants, they can be classified as the same type of device in frequency band division. To sum up, the dominant control loops and the impedance characteristics of PMSG, DFIG, PV plants and the connected system in each frequency band are illustrated in Fig. 14.6.

In conclusion, the dominant factors causing oscillation of REG connected into LCC-HVDC in each frequency band is summarized as:

1. **Band I** (around $f < 30\,\mathrm{Hz}$)

The impedance of the connected system shows inductance characteristics as seen from REG plants at the PCC. However, the impedance of PMSG-based wind plants

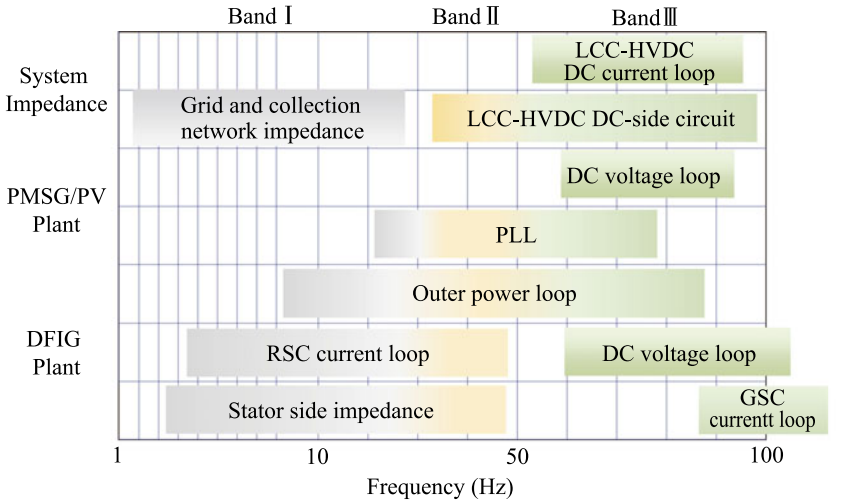

(a) Dominant control loops of REG and the connected system in each frequency-band

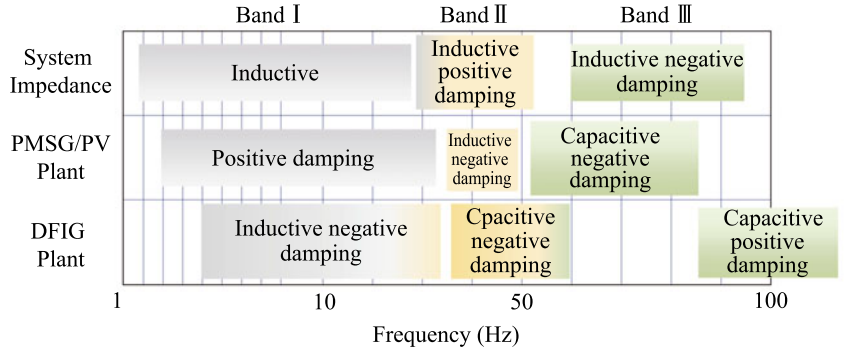

(b) Impedance characteristics of REG and the connected system in each frequency-band

Fig. 14.6 Dominant factors and impedance characteristics of REG and the connected system

represents positive damping characteristics, as it is impacted by multiple control loops of GSC and MSC in this frequency range. The impedance of DFIG-based wind plants represents inductive negative damping characteristics, as it is dominated by the stator side impedance and affected by the rotor electrical frequency in this frequency range.

Based on the phase ranges of these impedances, there is no oscillation risk for PMSG-based wind plants or DFIG-based wind plants connected into LCC-HVDC system in this frequency range.

2. **Band II** (around 30 Hz $< f <$ 50 Hz)

The impedance of the connected system represents inductive positive damping characteristics as seen from REG plants at the PCC. However, the impedance of PMSG-based wind plants represents inductive negative damping characteristics, as the control of PLL dominated in this frequency range. The impedance of DFIG-based wind plants represents capacitive negative damping characteristics, as it is dominated by the stator side impedance and affected by the rotor electrical frequency, outer power loop and MSC AC current loop in this frequency range.

Based on the phase ranges of these impedances, there is no oscillation risk for PMSG-based wind plants connected into LCC-HVDC system. However, there will be oscillation risk for DFIG-based wind plants connected into LCC-HVDC system in this frequency range, if the magnitudes of the impedance curves intersect and the PM of the intersection point is insufficient.

3. **Band III** (around 50 Hz $< f <$ 100 Hz)

The impedance of the connected system represents inductive negative damping characteristics as seen from REG plants at the PCC, as the frequency-band overlapping effect of DC-side main circuit and DC voltage loop of the LCC-HVDC. However, the impedance of PMSG-based wind plants represents capacitive negative damping characteristics, as the influence of PLL and DC voltage loop. The impedance of DFIG-based wind plants represents inductive positive damping characteristics, as the influence of the stator side impedance and GSC impedance.

Based on the phase ranges of these impedances, there is no oscillation risk for DFIG-based wind plants connected into LCC-HVDC system. However, there will be oscillation risk for PMSG-based wind plants connected into LCC-HVDC system in this frequency range, if the magnitudes of the impedance curves intersect and the PM of the intersection point is insufficient.

14.1.3 Simulation Verification

In this section, the impedance scanning of various REG plants is first implemented based on the full EMT simulation platform for REG and AC/DC transmission systems. Then, through the analysis of the results, the oscillation mechanisms for various REG plants connected into LCC-HVDC system can be figured out.

14.1.3.1 Oscillation Recurrence of PMSG-Based Wind Plant

The simulation parameters of the PMSG and the LCC-HVDC are listed in Tables 14.1 and 14.2 respectively. The SCR of sending-end AC grid is 1.9. Based on these parameters, Fig. 14.7 shows the evaluation results of the oscillation risk for the PMSG-based wind plant connected into LCC-HVDC system.

Table 14.1 PMSG wind plant simulation parameters

Parameter	Definition	Value
N_{PMSG}	Number of PMSG-based wind turbines	2960
P_{N}	Unit rated power	4.5 MW
P_{ref}	Active power	0.6 p.u.
V_{dc}	Steady-state value of DC voltage	1200 V
V_1	Amplitude of the fundamental frequency component of AC voltage	690 V
f_1	Fundamental frequency	50 Hz
k_{T}	Transformer voltage ratio	0.69 kV/35 kV
R_{s}	Stator resistance	0.0091 Ω
L_{sd}, L_{sq}	PMSG stator dq-axis inductance	2.794 mH, 2.715 mH
L_{f}	GSC AC filter inductance	0.0370 mH
C_{f}	AC filter capacitance	1 mF
C_{dc}	DC bus capacitance	28.86 mF

Table 14.2 LCC-HVDC simulation parameters

Parameter	Definition	Value
P_{N}	Rated power	8000 MW
V_{dc}	Steady-state value of DC voltage	±800 kV
V_{f1}	Amplitude of the fundamental frequency component of AC voltage at the sending side	750 kV
V_{e1}	Amplitude of the fundamental frequency component of AC voltage at the receiving side	530 kV
L_{dc}	DC smoothing reactor	300 mH
l_{line}	DC line length	1578.5 km

As seen from the figure, the phase of the PMSG impedance $\boldsymbol{Z}_{\mathrm{PMSG}}$ represents capacitive negative damping characteristics, and the phase of the system impedance $\boldsymbol{Z}_{\mathrm{sys}}$ represents inductive characteristics in Band III. The magnitudes of $\boldsymbol{Z}_{\mathrm{PMSG}}$ curve and $\boldsymbol{Z}_{\mathrm{sys}}$ curve intersect at Point A (64 Hz) and the PM is 7°. The GM/PM is insufficient, indicating oscillation risk in the system.

In addition, in Fig. 14.7(b), a forbidden area with radius R_{min} of 0.2 is drawn based on the Nyquist criterion of maximum peak value. The Nyquist curve of $\boldsymbol{Z}_{\mathrm{sys}}/\boldsymbol{Z}_{\mathrm{PMSG}}$ around Point A (64 Hz) is in the forbidden area. Therefore, the system stability margin is insufficient, also indicating oscillation risk at 64 Hz as in the Bode plot.

Meanwhile, the time-domain simulation of oscillation recurrence for the above system is carried out base on the full EMT simulation platform. The oscillation waveforms and the FFT results are shown in Fig. 14.8.

As seen from the figure, this system oscillates at 60 Hz, corresponding with the Point A in the forbidden area in Fig. 14.7. There is also a oscillation harmonics at 40 Hz in Fig. 14.8. It results from the frequency coupling effect of the oscillation at 60 Hz. The simulation results in time domain and in frequency domain are almost

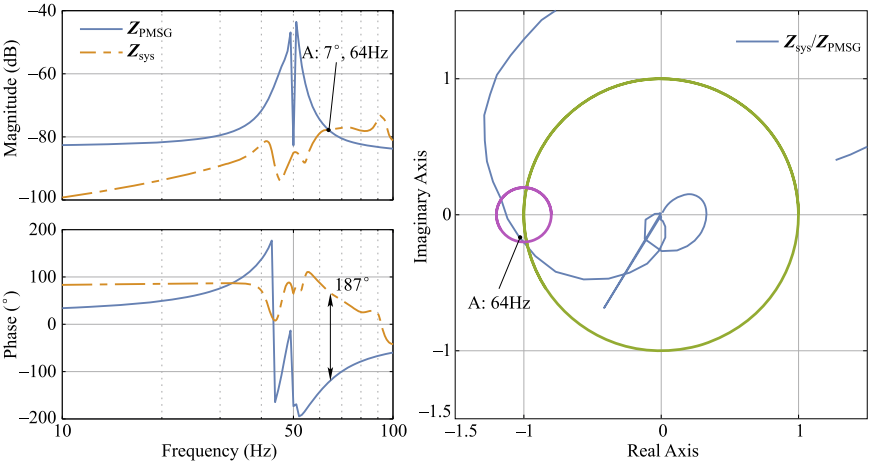

(a) System impedance Bode plot (b) System Nyquist plot

Fig. 14.7 The evaluation results of oscillation risk for PMSG-based wind plant connected into LCC-HVDC system

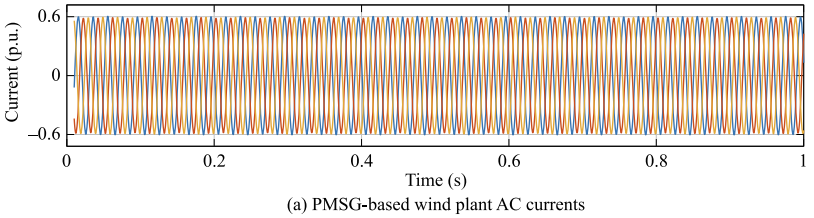

(a) PMSG-based wind plant AC currents

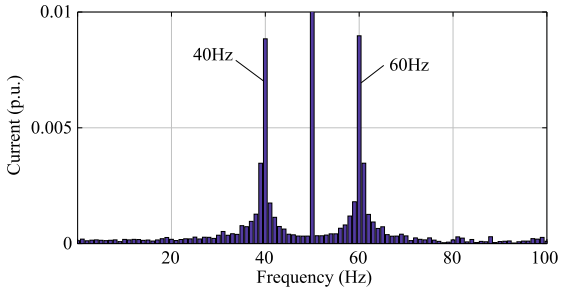

(b) FFT results of PMSG-based wind plant AC current

Fig. 14.8 Oscillation waveforms and the FFT results for PMSG-based wind plant connected into LCC-HVDC system

Table 14.3 Stability margin of different PMSG-based wind plants connected to the LCC-HVDC system

Product Type	Unit Rated Power (MW)	SCR of Sending-End AC Grid	Intersection Frequency (Hz)
Type 1	3	1.9	71
Type 2	3.4	1.6	54
Type 3	4	1.7	57

the same. Thus, the oscillation mechanism for PMSG-based wind plants connected into LCC-HVDC system is verified by the simulation results.

Similarly, the oscillation risk evaluations for different types of PMSG-based wind plants are accomplished, namely Type 1, Type 2 and Type 3. Each wind plant is composed of 296 identical units and the active power is 0.6 p.u.. The simulation parameters of LCC-HVDC remains as Table 14.2. The intersection frequency and the PM at this frequency are summarized in Table 14.3. From these results, there are oscillation risk for the three types PMSG-based wind plants connected into LCC-HVDC system in the supersynchronous frequency band.

14.1.3.2 Oscillation Recurrence of DFIG-Based Wind Plant

The simulation parameters of the DFIG are listed in Table 14.4 and that of the LCC-HVDC remains as Table 14.2. The SCR of sending-end AC grid remains 1.9. Based on these parameters, Fig. 14.9 shows the evaluation results of the oscillation risk for the DFIG-based wind plant connected into LCC-HVDC system.

As seen from the figure, the phase of the DFIG impedance $\boldsymbol{Z}_{\mathrm{DFIG}}$ represents capacitive negative damping characteristics, and the phase of the system impedance $\boldsymbol{Z}_{\mathrm{sys}}$ represents inductive positive damping in Band II. The magnitudes of $\boldsymbol{Z}_{\mathrm{DFIG}}$ curve and $\boldsymbol{Z}_{\mathrm{sys}}$ curve intersect at Point B (43 Hz) and the PM is 6°. The GM/PM is insufficient, indicating oscillation risk in the system.

In addition, in Fig. 14.9(b), a forbidden area with radius $R_{\min}$ of 0.2 is drawn based on the Nyquist criterion of maximum peak value. The Nyquist curve of $\boldsymbol{Z}_{\mathrm{sys}}/\boldsymbol{Z}_{\mathrm{DFIG}}$ around Point B (43 Hz) is in the forbidden area. Therefore, the system stability margin is insufficient, also indicating oscillation risk at 43 Hz as in the Bode plot.

Meanwhile, the time-domain simulation of oscillation recurrence for the above system is carried out base on the full EMT simulation platform. The oscillation waveforms and the FFT results are shown in Fig. 14.10.

As seen from the figure, this system oscillates at 43 Hz, corresponding with the Point B in the forbidden area in Fig. 14.9. There is also a oscillation harmonic at 43 Hz in Fig. 14.10. It results from the frequency coupling effect of the oscillation at 57 Hz, which can be deduced from the conclusions in Chap. 13. The simulation

Table 14.4 DFIG wind plant simulation parameters

Parameter	Definition	Value
N_{DFIG}	Number of DFIG-based wind turbines	5320
P_{N}	Unit rated power	2.5 MW
P_{ref}	Active power	0.6 p.u.
V_{dc}	Steady-state value of DC voltage	1200 V
V_1	Amplitude of the fundamental frequency component of AC voltage	690 V
f_1	Fundamental frequency	50 Hz
k_{T}	Transformer voltage ratio	0.69 kV/35 kV
R_{s}, R_r	Stator/Rotor resistance	0.0032 Ω, 0.0023 Ω
L_{1s}, L_{1r}	DFIG sator/rotor inductance	0.0425 mH, 0.0903 mH
L_{ms}, L_{mr}	DFIG stator/rotor mutual inductance	1.844 mH
K_{e}	Stator turns ratio	3
L_{f}	GSC AC filter inductance	0.3500 mH
C_{f}	AC filter capacitance	1 mF
C_{dc}	DC bus capacitance	9.6 mF

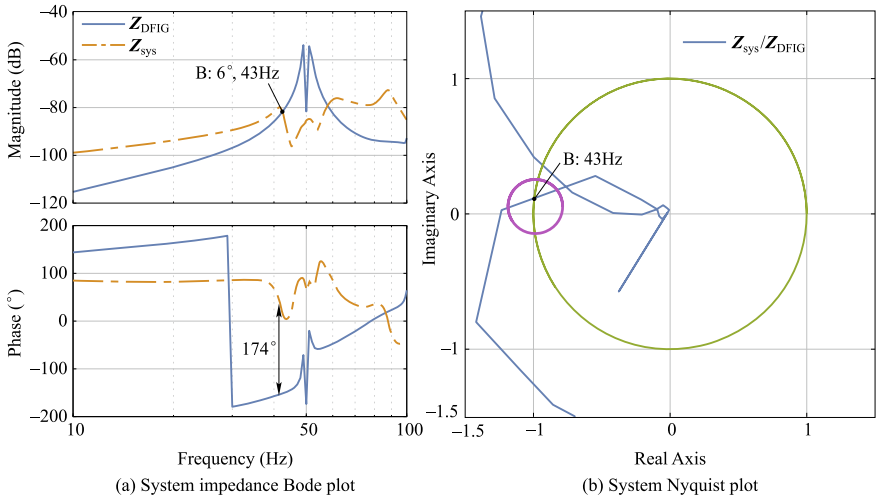

(a) System impedance Bode plot (b) System Nyquist plot

Fig. 14.9 The evaluation results of oscillation risk for DFIG-based wind plant connected into LCC-HVDC system

results in time domain and in frequency domain are almost the same. Thus, the oscillation mechanism for DFIG-based wind plants connected into LCC-HVDC system is verified by the simulation results.

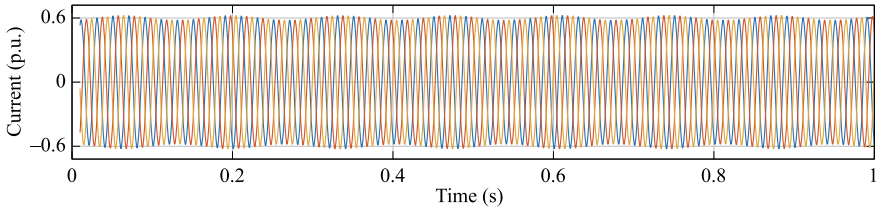

(a) DFIG-based wind plant AC currents

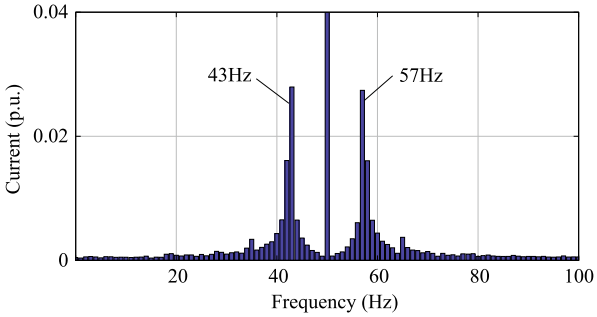

(b) FFT results of DFIG-based wind plant AC current

Fig. 14.10 Oscillation waveforms and the FFT results for DFIG-based wind plant connected into LCC-HVDC system

Table 14.5 Stability margin of different DFIG-based wind plants connected to the LCC-HVDC system

Product Type	Unit Rated Power (MW)	SCR of Sending-End AC Grid	Intersection Frequency (Hz)
Type 1	2	1.9	43
Type 2	3	1.9	41
Type 3	3.3	1.8	44

The intersection frequency and the PM at this frequency are summarized in Table 14.5. From these results, there are oscillation risk for the three types DFIG-based wind plants connected into LCC-HVDC system in the subsynchronous frequency band.

14.1.3.3 Oscillation Recurrence of PV Plant

The simulation parameters of the PV plant are listed in Table 14.6 and that of the LCC-HVDC remains as Table 14.2. The SCR of sending-end AC grid remains 1.9. Based on these parameters, Fig. 14.11 shows the evaluation results of the oscillation risk for the PV plant connected into LCC-HVDC system.

Table 14.6 PV plant simulation parameters

Parameter	Definition	Value
N_{PV}	Number of PV units	4260
P_N	Unit rated power	3.125 MW
P_{ref}	Active power	0.6 p.u.
V_{dc}	Steady-state value of DC voltage	1500 V
V_1	Amplitude of the fundamental frequency component of AC voltage	600 V
f_1	Fundamental frequency	50 Hz
L_f	AC filter inductance	0.035 mH
C_f	AC filter capacitance	0.446 mF
C_{dc}	DC bus capacitance	12 mF

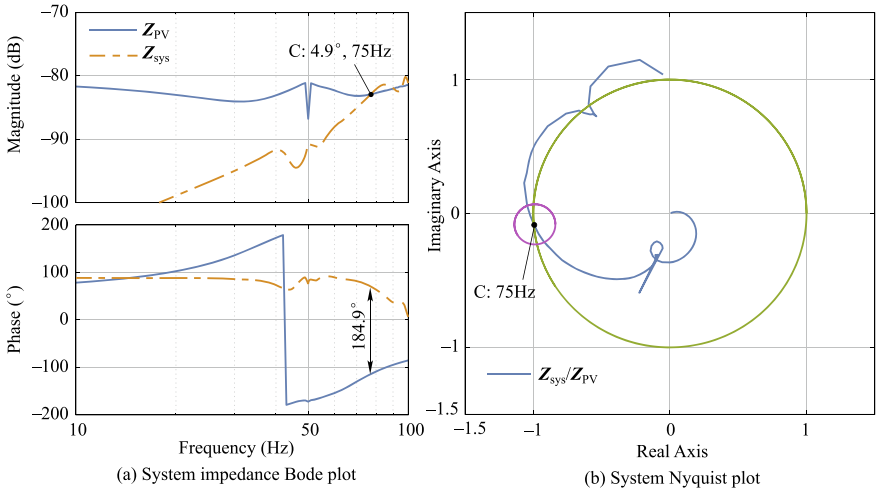

(a) System impedance Bode plot (b) System Nyquist plot

Fig. 14.11 The evaluation results of oscillation risk for PV plant connected into LCC-HVDC system

As seen from the figure, the phase of the PV plant impedance $\boldsymbol{Z}_{PV}$ represents capacitive negative damping characteristics, and the phase of the system impedance $\boldsymbol{Z}_{sys}$ represents inductive characteristics in Band III. The magnitudes of $\boldsymbol{Z}_{PV}$ curve and $\boldsymbol{Z}_{sys}$ curve intersect at Point C (75 Hz) and the PM is 4.9°. The GM/PM is insufficient, indicating oscillation risk in the system.

In addition, in Fig. 14.11(b), a forbidden area with radius R_{min} of 0.15 is drawn based on the Nyquist criterion of maximum peak value. The Nyquist curve of $\boldsymbol{Z}_{sys}/\boldsymbol{Z}_{PV}$ around Point C (75 Hz) is in the forbidden area. Therefore, the system stability margin is insufficient, also indicating oscillation risk at 75 Hz as in the Bode plot.

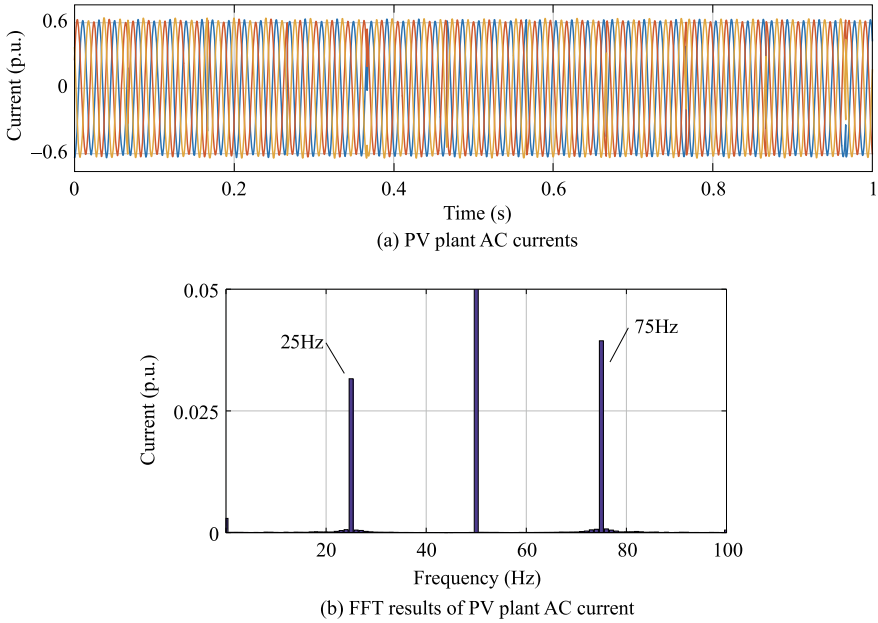

Fig. 14.12 Oscillation waveforms and the FFT results for PV plant connected into LCC-HVDC system

Meanwhile, the time-domain simulation of oscillation recurrence for the above system is carried out base on the full EMT simulation platform. The oscillation waveforms and the FFT results are shown in Fig. 14.12.

As seen from the figure, this system oscillates at 75 Hz, corresponding with the Point C in the forbidden area in Fig. 14.11. There is also a oscillation harmonics at 25 Hz in Fig. 14.12. It results from the frequency coupling effect of the oscillation at 75 Hz. The simulation results in time domain and in frequency domain are almost the same. Thus, the oscillation mechanism for PV plants connected into LCC-HVDC system is verified by the simulation results.

Similarly, the oscillation risk evaluations for different types of PV plants are accomplished, namely Type 1, Type 2 and Type 3. Each PV plant is composed of 426 identical units and the active power is 0.6 p.u.. The simulation parameters of LCC-HVDC remains as Table 14.2. The intersection frequency and the PM at this frequency are summarized in Table 14.7. From these results, there are oscillation risk for the three types PV plants connected into LCC-HVDC system in the supersynchronous frequency band.

Table 14.7 Stability margin of different PV plants connected to the LCC-HVDC system

Product Type	Unit Rated Power (MW)	SCR of Sending-End AC Grid	Intersection Frequency (Hz)
Type 1	0.125	1.9	76
Type 2	0.175	1.8	76
Type 3	1.25	1.9	54

14.2 Analysis of Oscillation for REG Connected into MMC-HVDC System

In order to analysis the stability issues of REG connected into MMC-HVDC system, firstly, the three-port network model in grid-connected mode and the two-port network model in passive islanding mode for MMC-HVDC are derived. The stability criteria are then proposed respectively. Besides, the frequency-band division methods for impedance characteristics of REG and MMC-HVDC, and the oscillation dominant factors in different frequency-bands are illustrated. Finally, the oscillation mechanism is revealed based on the negative damping characteristics of REG impedance and that of MMC-HVDC impedance.

14.2.1 Stability Criteria

According to whether there is a synchronous power grid, there are two different control modes for MMC-HVDC at the sending side, grid-connected mode and passive islanding mode. Hence, different port network model will be established respectively to analyze the stability issues.

14.2.1.1 Stability Criteria in Passive Islanding Mode

The sending side system of MMC-HVDC in passive islanding mode can be equivalent to a two-port network composed of the REG and the MMC-HVDC, as shown in Fig. 14.13, where $\boldsymbol{I}_{\text{out}}$ is the current of REG port. Since the MMC-HVDC usually employs voltage control mode and provides the synchronous voltage, it can be equivalent to a voltage source $\boldsymbol{V}_{\text{MMC}}$ in series with its port impedance $\boldsymbol{Z}_{\text{MMC}}$. According to Chap. 13, the output of REG can be equivalent to an ideal current source $\boldsymbol{I}_{\text{RE}}$ in parallel with its port impedance $\boldsymbol{Z}_{\text{RE}}$. Moreover, the REG port is in series with equivalent inductance of transformers $\boldsymbol{Z}_{\text{CN}}$, as the REG plants are grid-connected through multiple step-up transformers.

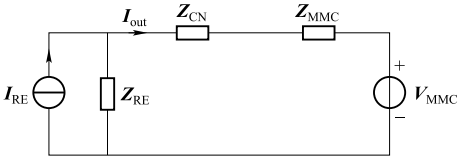

Fig. 14.13 Equivalent model for the sending side system of MMC-HVDC in passive islanding mode

According to this model, $\boldsymbol{I}_{\text{out}}$ can be expressed as follows

$$\boldsymbol{I}_1 = \left(\boldsymbol{I}_{\text{RE}} - \frac{\boldsymbol{V}_{\text{MMC}}}{\boldsymbol{Z}_{\text{RE}}}\right) \cdot \frac{1}{1 + \boldsymbol{Z}_{\text{sys}}/\boldsymbol{Z}_{\text{RE}}} \tag{14.6}$$

where $\boldsymbol{Z}_{\text{sys}}$ is the system impedance seen from REG plants at the PCC, expressed as

$$\boldsymbol{Z}_{\text{sys}} = \boldsymbol{Z}_{\text{MMC}} + \boldsymbol{Z}_{\text{CN}} \tag{14.7}$$

Equation (14.6) can be seen as the multiplication of two closed-loop transfer functions, denoted as

$$\begin{cases} TF_1 = \boldsymbol{I}_{\text{RE}} - \dfrac{\boldsymbol{V}_{\text{MMC}}}{\boldsymbol{Z}_{\text{RE}}} \\ TF_2 = \dfrac{1}{1 + \boldsymbol{Z}_{\text{sys}}/\boldsymbol{Z}_{\text{RE}}} \end{cases} \tag{14.8}$$

As the stability for this equivalent system is determined by TF_1 and TF_2, this system is stable if, and only if the poles of TF_1 and TF_2 are all in the left-half-plane.

On one hand, the distribution of poles for TF_1 is analyzed. Based on the conclusion in Chap. 13, all the poles of $\boldsymbol{I}_{\text{RE}} - 1/\boldsymbol{Z}_{\text{RE}}$ are all in the left-half-plane, since the REG plants are practically stable when connected to ideal AC grid. Besides, $\boldsymbol{V}_{\text{MMC}}$ can be claimed not to have any right-half-plane poles, since the MMC-HVDC is practically stable in no-load operation mode. Thus, TF_1 can be claimed not to have any right-half-plane poles. System stability only depends on TF_2.

On the other hand, all the poles of TF_2 should be in the left-half-plane, that is, this system is stable if, and only if

- The impedance ratio $\boldsymbol{Z}_{\text{sys}}/\boldsymbol{Z}_{\text{RE}}$ conforms with Nyquist criterion.

14.2.1.2 Stability Criteria in Grid-Connected Mode

The sending side system of MMC-HVDC in grid-connected mode can be equivalent to a three-port network composed of the REG, the AC grid and the MMC-HVDC, as shown in Fig. 14.14, where $\boldsymbol{I}_{\text{out}}$ is the current of REG port, $\boldsymbol{I}_{\text{g}}$ is the current of AC grid and $\boldsymbol{I}_{\text{trans}}$ is the current of MMC-HVDC. Since the MMC-HVDC usually employs power control mode, it can be seen as non-ideal current sources. In this model, the MMC-HVDC port can be equivalent to an ideal current source $\boldsymbol{I}_{\text{MMC}}$ in parallel with its port impedance $\boldsymbol{Z}_{\text{MMC}}$. According to Chap. 13, the output of REG can be equivalent to an ideal current source $\boldsymbol{I}_{\text{RE}}$ in parallel with its port impedance

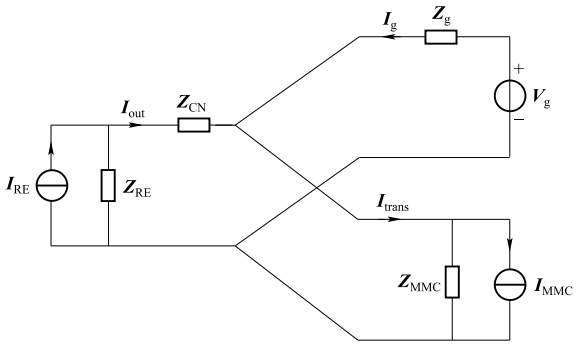

Fig. 14.14 Equivalent model for the sending side of MMC-HVDC in grid-connected mode

$\boldsymbol{Z}_{RE}$. Moreover, the REG port is in series with equivalent inductance of transformers $\boldsymbol{Z}_{CN}$, as the REG plants are grid-connected through multiple step-up transformers. And the AC grid is an ideal voltage source $\boldsymbol{V}_g$ in series with its impedance $\boldsymbol{Z}_g$.

According to this model, $\boldsymbol{I}_{out}$ can be expressed as follows

$$\boldsymbol{I}_{out} = \left(\boldsymbol{I}_{RE} - \frac{\boldsymbol{V}_{sys}}{\boldsymbol{Z}_{RE}}\right) \cdot \frac{1}{1 + \boldsymbol{Z}_{sys}/\boldsymbol{Z}_{RE}} \tag{14.9}$$

where $\boldsymbol{V}_{sys}$ and $\boldsymbol{Z}_{sys}$ can be expressed as

$$\boldsymbol{V}_{sys} = \frac{1}{1 + \boldsymbol{Z}_g/\boldsymbol{Z}_{MMC}}\left(\boldsymbol{V}_g - \boldsymbol{I}_{MMC}\boldsymbol{Z}_g\right) \tag{14.10}$$

$$\boldsymbol{Z}_{sys} = \frac{\boldsymbol{Z}_{MMC}\boldsymbol{Z}_g}{\boldsymbol{Z}_{MMC} + \boldsymbol{Z}_g} + \boldsymbol{Z}_{CN} \tag{14.11}$$

Equation (14.9) can be seen as the multiplication of two closed-loop transfer functions, denoted as

$$\begin{cases} TF_1 = \boldsymbol{I}_{RE} - \dfrac{\boldsymbol{V}_{sys}}{\boldsymbol{Z}_{RE}} \\ TF_2 = \dfrac{1}{1 + \boldsymbol{Z}_{sys}/\boldsymbol{Z}_{RE}} \end{cases} \tag{14.12}$$

As the stability for this equivalent system is determined by TF_1 and TF_2, this system is stable if, and only if the poles of TF_1 and TF_2 are all in the left-half-plane.

On one hand, the distribution of poles for TF_1 is analyzed. Based on the conclusion in Chap. 13, all the poles of $\boldsymbol{I}_{RE} - 1/\boldsymbol{Z}_{RE}$ are all in the left-half-plane, since the REG plants are practically stable when connected to ideal AC grid. The stability of TF_1 is then determined by $\boldsymbol{V}_{sys}$. Therefore, all the poles of TF_1 are in the left-half-plane if and only of $\boldsymbol{V}_{sys}$ doesn't have any right-half-plane poles.

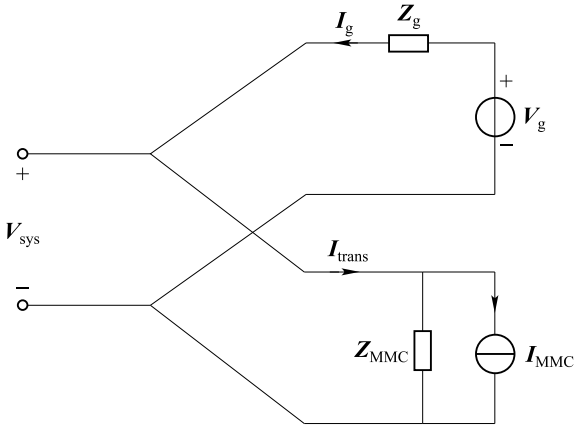

Fig. 14.15 Equivalent circuit of MMC-HVDC connected into AC grid

According to Eq. (14.10), $\boldsymbol{V}_{sys}$ is the open-circuit voltage of the REG port, and the equivalent circuit of MMC-HVDC connected into AC grid is shown in Fig. 14.15. Besides, $\boldsymbol{Z}_{sys}$ in Eq. (14.3) is the system impedance seen from REG plants at the PCC.

The system in Fig. 14.15 can be seen as typical current source connected into voltage source system. Since the MMC-HVDC are practically stable when connected to ideal AC grid, the stability of $\boldsymbol{V}_{sys}$ only depends on $\boldsymbol{Z}_g/\boldsymbol{Z}_{MMC}$. Therefore, $\boldsymbol{V}_{sys}$ can be claimed not to have any right-half-plane poles and all the poles of TF_1 are in the left-half-plane if, and only if

- The impedance ratio $\boldsymbol{Z}_g/\boldsymbol{Z}_{MMC}$ conforms with Nyquist criterion.

On the other hand, TF_2 can be reformulated to fit a feedback loop with a open-loop gain of $\boldsymbol{Z}_{sys}/\boldsymbol{Z}_{RE}$, as shown in Fig. 14.16. All the poles of TF_2 should be in the left-half-plane, that is, this system is stable if, and only if

- The impedance ratio $\boldsymbol{Z}_{sys}/\boldsymbol{Z}_{RE}$ conforms with Nyquist criterion.

In conclusion, the REG plants connected into MMC-HVDC system is stable if and only if the following two conditions are satisfied.

① The MMC-HVDC is stable when connected into AC grid, that is, the impedance ratio $\boldsymbol{Z}_g/\boldsymbol{Z}_{MMC}$ conforms with Nyquist criterion.
② The impedance ratio $\boldsymbol{Z}_{sys}/\boldsymbol{Z}_{RE}$ conforms with Nyquist criterion.

When $\boldsymbol{I}_{MMC} = 0$, $\boldsymbol{Z}_{MMC} = \infty$ and $\boldsymbol{Z}_{CN} = 0$, that is, the REG plants are connected into the AC grid without MMC-HVDC, the output current of REG port can be

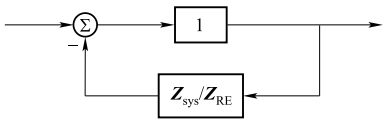

Fig. 14.16 Equivalent feedback loop of TF_2

simplified as follows

$$\boldsymbol{I}_{\text{out}} = \left(\boldsymbol{I}_{\text{RE}} - \frac{\boldsymbol{V}_{\text{g}}}{\boldsymbol{Z}_{\text{RE}}}\right) \cdot \frac{1}{1 + \boldsymbol{Z}_{\text{g}}/\boldsymbol{Z}_{\text{RE}}} \tag{14.13}$$

Apparently, the expression in Eq. (14.13) is the same as that of two-port network in Chap. 13. Therefore, these results indicates again that the essential of the stability criteria for multi-port system is consistent with that of the two-port system.

14.2.2 Frequency-Band Division and Oscillation Analysis

The sending side system of MMC-HVDC involves multiple power electronic devices including PMSG, DFIG, PV plants and MMC-HVDC. The dynamics of these devices in the power system mainly depend on the multi-loop control characteristics. Under the coordination of multi-loop control of multiple devices, the control bandwidth of the system covers from several Hertz to hundreds of Hertz, appearing broadband characteristics.

According to the analysis of REG and MMC-HVDC impedance characteristics mentioned in Part II, the dominant factors in the frequency ranges differ from various devices because of the inherent difference of their topology and control principle. Generally, the frequency band of impedance characteristics are divided into Band I, Band II, Band III and Band IV. Since the impedance characteristics of PV plants are almost the same as those of PMSG-based wind plants, they can be classified as the same type of device in frequency band division. The dominant control loops and the impedance characteristics of PMSG, DFIG, PV plants and MMC-HVDC in each frequency band are illustrated in Fig. 14.17.

In conclusion, the dominant factors causing oscillation for different REG connected into MMC-HVDC in each frequency band is summarized as follows.

1. **For PMSG-based wind plants connected into MMC-HVDC system**

According to Part II, in the range of 1–50 Hz, the impedance of PMSG-based wind plants and MMC-HVDC may represent various phase characteristics, as they are affected by multiple control loops. Hence, the analysis of oscillation risk for this system should be carried out specifically based on the practical conditions. Thus, the following analysis mainly focus on the oscillation above 50 Hz.

(a) **Band II** (around 50 Hz $< f <$ 70 Hz)

The impedance of MMC-HVDC represents inductance characteristics, as it is dominated by the AC voltage control in this frequency range. On the other hand, the impedance of PMSG-based wind plants represents capacitive negative damping characteristics, as it is determined by the PLL control and affected by the frequency-band overlapping effect of the DC voltage loop in this frequency range.

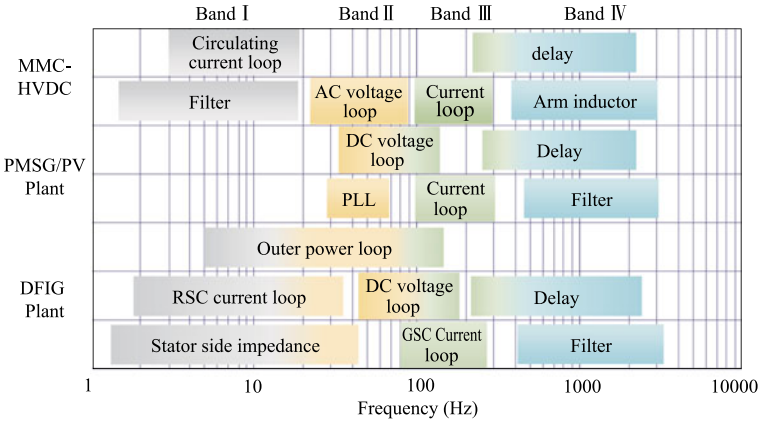

(a) Dominant control loops of REG and MMC-HVDC in each frequency-band

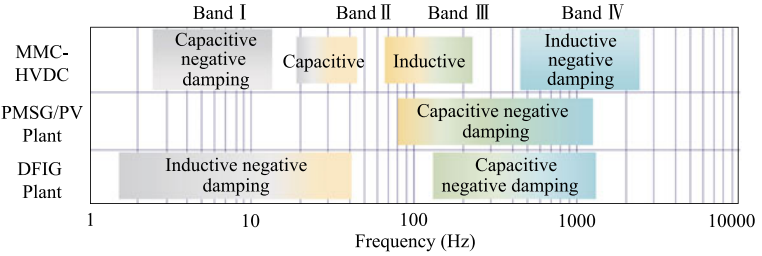

(b) Impedance characteristics of REG and MMC-HVDC in each frequency-band

Fig. 14.17 Dominant factors and impedance characteristics of REG and MMC-HVDC

Hence, there will be oscillation risk for PMSG-based wind plants connected into MMC-HVDC system in this frequency range if the magnitudes of the impedance curves intersect and the PM of the intersection point is insufficient.

(b) **Band III** (around 70 Hz $< f <$ 300 Hz)

The impedance of MMC-HVDC under AC voltage control mode represents inductance characteristics, as it is dominated by AC current loop control in this frequency range. On the other hand, the impedance of PMSG-based wind plants represents capacitive characteristics, as it is determined by the AC current control. It may represent capacitive negative damping characteristics due to the frequency-band overlapping effect of the DC voltage loop in the former frequency range of Band III, or due to that of the time delay in the latter frequency range.

Hence, there will be oscillation risk for PMSG-based wind plants connected into MMC-HVDC system in this frequency range, if the magnitudes of the impedance curves intersect and the PM of the intersection point is insufficient.

(c) **Band IV** (around $f > 300$ Hz)

The impedance of MMC-HVDC represents inductance characteristics, as it is dominated by the arm inductor in this frequency range. Moreover, it may represent inductance negative damping characteristics due to the frequency-band overlapping effect of the time delay. On the other hand, the impedance of PMSG-based wind plants changes from inductive to capacitive characteristics in this frequency range, as it is determined by LC filter. Furthermore, when it represents capacitive characteristics, it may represent capactive negative damping characteristics due to the frequency-band overlapping effect of the time delay.

Hence, there will be oscillation risk for PMSG-based wind plants connected into MMC-HVDC system in this frequency range, if the magnitudes of the impedance curves intersect and the PM of the intersection point is insufficient.

2. **For DFIG-based wind plants connected into MMC-HVDC system**

(a) **Band I** (around $f < 30$ Hz)

The impedance of MMC-HVDC is affected by SM capacitor, arm inductor and AC current control in this frequency range. It represents capacitive negative damping characteristics due to the frequency-band overlapping effect of the circuiting current control loop. On the other hand, the impedance of DFIG-based wind plants represents inductive negative damping characteristics, as it is determined by the stator side impedance and and affected by the rotor electrical frequency in this frequency range.

Hence, there will be oscillation risk for DFIG-based wind plants connected into MMC-HVDC system in this frequency range, if the magnitudes of the impedance curves intersect and the PM of the intersection point is insufficient.

(b) **Band II** (around $30\,\text{Hz} < f < 70\,\text{Hz}$)

The impedance of MMC-HVDC represents capacitive characteristics in 30–50 Hz and inductive characteristics in 50–70 Hz, as it is dominated by AC voltage control. On the other hand, the impedance of DFIG-based wind plants remains inductive negative damping characteristics as that of Band I.

Hence, there will be oscillation risk for DFIG-based wind plants connected into MMC-HVDC system in this frequency range, if the magnitudes of the impedance curves intersect and the PM of the intersection point is insufficient.

(c) **Band III** (around $70\,\text{Hz} < f < 300\,\text{Hz}$)

The impedance of MMC-HVDC represents inductive characteristics, as it is dominated by AC current control in this frequency range. On the other hand, the impedance of DFIG-based wind plants represents capacitive negative damping characteristics, as it is determined by stator side and GSC impedance, and also affected by the frequency-band overlapping of DC voltage loop and AC current loop or that of the time delay and AC current loop.

Hence, there will be oscillation risk for DFIG-based wind plants connected into MMC-HVDC system in this frequency range, if the magnitudes of the impedance curves intersect and the PM of the intersection point is insufficient.

(d) **Band IV** (around $f > 300$ Hz)

The impedance of MMC-HVDC represents inductive characteristics, as it is dominated by arm inductor in this frequency range. It may represent inductive negative damping characteristics due to the frequency-band overlapping of the time delay. On the other hand, the impedance of DFIG-based wind plants changes from inductive to capacitive characteristics, as it is determined by the LC filter. Furthermore, when it represents capacitive characteristics, it may represent capactive negative damping characteristics due to the frequency-band overlapping effect of the time delay.

Hence, there will be oscillation risk for DFIG-based wind plants connected into MMC-HVDC system in this frequency range, if the magnitudes of the impedance curves intersect and the PM of the intersection point is insufficient.

In a word, the impedance characteristics of various devices or systems are mainly affected by the dominant control in the relevant frequency band. Moreover, the negative damping characteristics are easily caused by the frequency-band overlapping effect of different control loops in a certain frequency band. If the stability margin of the system is insufficient, there will be oscillation risk in REG plants connected into MMC-HVDC system.

14.2.3 Simulation Verification

In this section, the impedance scanning of various types of REG plants and MMC-HVDC are first implemented based on the full EMT simulation platform. Then, through the analysis of the results, the oscillation mechanisms for the REG plants connected into MMC-HVDC system can be figured out.

14.2.3.1 Oscillation Recurrence of PMSG-Based Wind Plant

The simulation parameters of the PMSG and the MMC-HVDC are listed in Tables 14.8 and 14.9 respectively. Based on these parameters, Fig. 14.18 shows the evaluation results of the oscillation risk in the PMSG-based wind plant connected into MMC-HVDC system.

As seen from the figure, the magnitudes of the PMSG impedance $\boldsymbol{Z}_{\mathrm{PMSG}}$ curve and the MMC-HVDC impedance $\boldsymbol{Z}_{\mathrm{MMC}}$ curve intersect at several points in a broadband frequency band. In Band II, the phase of $\boldsymbol{Z}_{\mathrm{PMSG}}$ first represents inductive characteristics and then changes to capacitive characteristics. However, the phase of $\boldsymbol{Z}_{\mathrm{MMC}}$ first represents capacitive characteristics and then changes to inductive characteristics. The magnitudes of $\boldsymbol{Z}_{\mathrm{PMSG}}$ and $\boldsymbol{Z}_{\mathrm{MMC}}$ curves intersect at Point D (33 Hz) and Point E (67 Hz) and the PMs are 6° and 9°. The GM/PM is insufficient, indicating oscillation risk in the system. Besides, in Band IV, the phase of $\boldsymbol{Z}_{\mathrm{PMSG}}$ represents capacitive

Table 14.8 PMSG wind plant simulation parameters

Parameter	Definition	Value
N_{PMSG}	Number of PMSG-based wind turbines	50
P_{N}	Unit rated power	2 MW
P_{ref}	Active power	0.9 p.u.
V_1	Amplitude of the fundamental frequency component of AC voltage	690 V
f_1	Fundamental frequency	50 Hz
k_{T}	Transformer voltage ratio	0.69 kV/35 kV

Table 14.9 MMC-HVDC simulation parameters

Parameter	Definition	Value
P_{N}	Rated power	100 MW
V_{dc}	Steady-state value of DC voltage	±200 kV
V_1	Amplitude of the fundamental frequency component of AC voltage at the sending side	110 kV
N	SM modules	250
L_{arm}	DC smoothing reactor	350 mH
C_{sm}	SM capacitor	3 mF

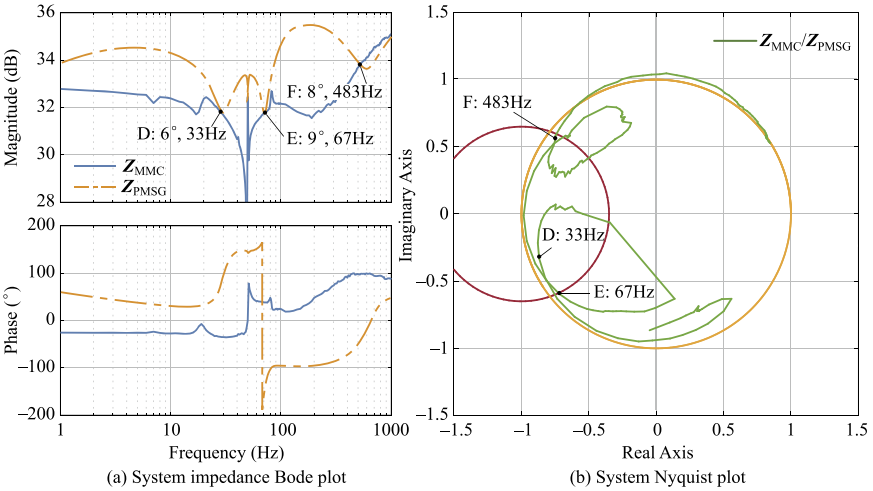

(a) System impedance Bode plot (b) System Nyquist plot

Fig. 14.18 The evaluation results of oscillation risk for PMSG-based wind plant connected into MMC-HVDC system

characteristics and the phase of $\boldsymbol{Z}_{\mathrm{MMC}}$ represents inductive negative damping characteristics. The magnitudes of $\boldsymbol{Z}_{\mathrm{PMSG}}$ and $\boldsymbol{Z}_{\mathrm{MMC}}$ curves intersect at Point F (483 Hz) and the PM is 8°. The GM/PM is insufficient, indicating oscillation risk in the system.

In addition, in Fig. 14.18(b), a forbidden area with radius $R_{\min}$ of 0.65 is drawn based on the Nyquist criterion of maximum peak value. The Nyquist curve of $\boldsymbol{Z}_{\mathrm{MMC}}/\boldsymbol{Z}_{\mathrm{PMSG}}$ around Point D (33 Hz), Point E (67 Hz) and Point F (483 Hz) are in the forbidden area. Therefore, the system stability margin is insufficient, also indicating oscillation risk in these frequency bands as in the Bode plot.

Meanwhile, the time-domain simulation of oscillation recurrence for a PMSG-based wind plant connected into MMC-HVDC is carried out base on the full EMT simulation platform. The FFT results of the oscillation currents are shown in Fig. 14.19.

As seen from the figure, there are oscillation harmonics at 33, 67 and 483 Hz, corresponding with the Point D, Point E and Point F in the forbidden area in Fig. 14.18. Coincidentally, the simulation results in time domain and in frequency domain are almost the same. Thus, the oscillation mechanism for PMSG-based wind plants connected into MMC-HVDC system is verified by the simulation results.

14.2.3.2 Oscillation Recurrence of DFIG-Based Wind Plant

The simulation parameters of DFIG are listed in Table 14.10 and that of MMC-HVDC remains the same as Table 14.9. Based on these parameters, Fig. 14.20 shows the evaluation results of the oscillation risk for DFIG-based wind plant connected into MMC-HVDC system.

As seen from the figure, the magnitudes of the DFIG impedance $\boldsymbol{Z}_{\mathrm{MMC}}$ curve and the MMC-HVDC impedance $\boldsymbol{Z}_{\mathrm{MMC}}$ curve intersect at several points in a broadband frequency band. The phase of $\boldsymbol{Z}_{\mathrm{DFIG}}$ represents inductive negative damping characteristics, and the phase of $\boldsymbol{Z}_{\mathrm{MMC}}$ represents capacitive characteristics in Band II. The magnitudes of $\boldsymbol{Z}_{\mathrm{DFIG}}$ and $\boldsymbol{Z}_{\mathrm{MMC}}$ curvers intersect at Point G (36 Hz) and the PM is 7°. The GM/PM is insufficient, indicating oscillation risk. Besides, the phase of $\boldsymbol{Z}_{\mathrm{DFIG}}$ represents capacitive characteristics and the phase of $\boldsymbol{Z}_{\mathrm{MMC}}$ represents inductive negative damping characteristics in Band IV. The magnitudes of $\boldsymbol{Z}_{\mathrm{DFIG}}$ and $\boldsymbol{Z}_{\mathrm{MMC}}$ curvers intersect at Point H (717 Hz) and the PM is 5°. Apparently, the GM/PM is insufficient, indicating oscillation risk.

In addition, in Fig. 14.20(b), a forbidden area with radius $R_{\min}$ of 0.65 is drawn based on the Nyquist criterion of maximum peak value. The Nyquist curve of $\boldsymbol{Z}_{\mathrm{MMC}}/\boldsymbol{Z}_{\mathrm{DFIG}}$ around Point G (36 Hz), and Point H (717 Hz) is in the forbidden area. Therefore, the system stability margin is insufficient, also indicating oscillation risk in these frequency bands.

Meanwhile, the time-domain simulation of oscillation recurrence for a DFIG-based wind plant connected into MMC-HVDC is carried out base on the full EMT simulation platform. The FFT results of the oscillation currents are shown in Fig. 14.21.

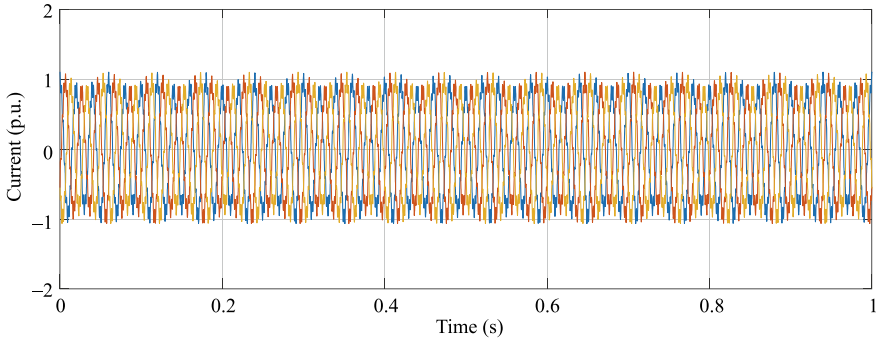

(a) PMSG-based wind plant AC currents

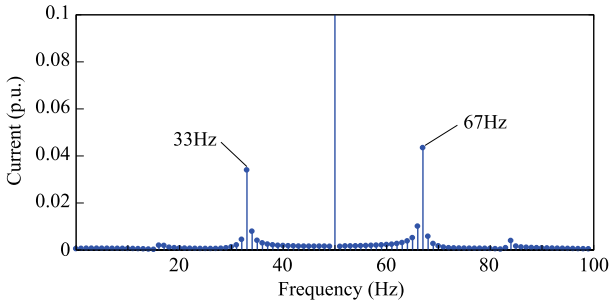

(b) FFT results of PMSG-based wind plant AC current in 1~100Hz

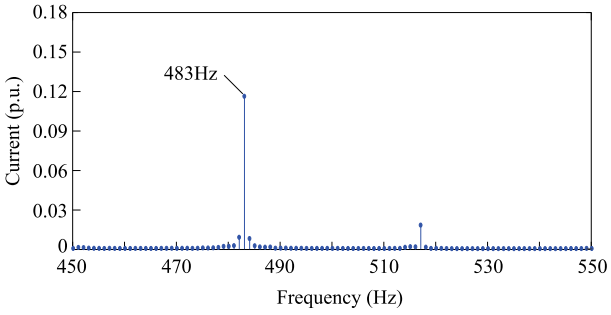

(c) FFT results of PMSG-based wind plant AC current in 450~550Hz

Fig. 14.19 FFT results of oscillation currents for a PMSG-based wind plant connected into MMC-HVDC system

As seen from the figure, there are oscillation harmonics at 36 and 717 Hz, corresponding with the Point G and Point H in the forbidden area in Fig. 14.20. Coincidentally, the simulation results in time domain and in frequency domain are almost the same. Thus, the oscillation mechanism for DFIG-based wind plants connected into MMC-HVDC system is also verified by the simulation results.

Table 14.10 DFIG wind plant simulation parameters

Parameter	Definition	Value
N_{DFIG}	Number of DFIG-based wind turbines	50
P_{N}	Unit rated power	2 MW
P_{ref}	Active power	0.9 p.u.
V_1	Amplitude of the fundamental frequency component of AC voltage	690 V
f_1	Fundamental frequency	50 Hz
k_{T}	Transformer voltage ratio	0.69 kV/35 kV

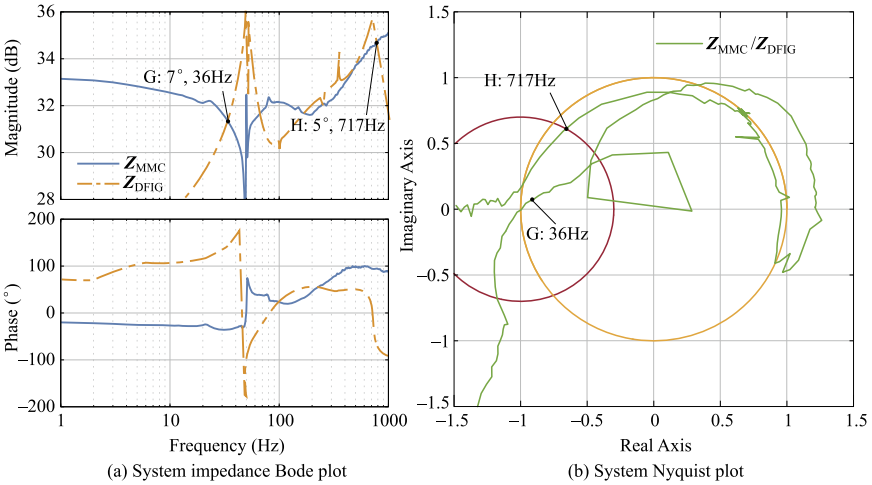

Fig. 14.20 The evaluation results of oscillation risk for DFIG-based wind plant connected into MMC-HVDC system

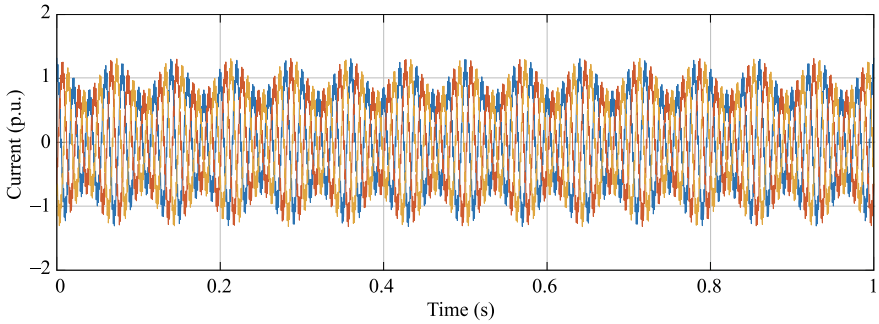

(a) DFIG-based wind plant AC currents

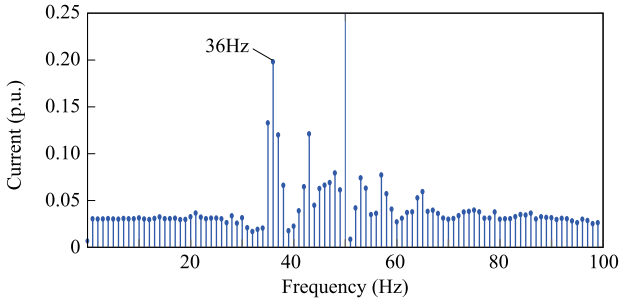

(b) FFT results of DFIG-based wind plant AC current in 1~100Hz

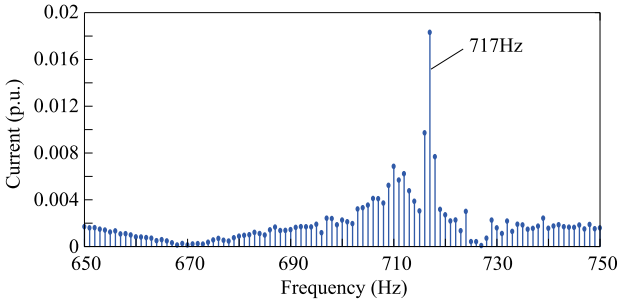

(c) FFT results of DFIG-based wind plant AC current in 650~750Hz

Fig. 14.21 FFT results of oscillation currents for DFIG-based wind plant connected into MMC-HVDC system

Reference

1. Li G H, Wang W S, Guo J B, et al. Broadband oscillation mechanism and analysis for wind farm Integration through MMC-HVDC system [J]. Proceedings of the CSEE, 2019, 39(18): 5281–5297+5575. (Chinese)

Part IV
Broadband Oscillation Mitigation of REG and AC/DC Transmission Systems

It is indicated in Part III when either renewable energy generation (REG)-side devices such as wind plants, photovoltaic (PV) plants, or system-side devices such as series compensation, line commutated converter-based high voltage direct current (LCC-HVDC), and modular multilevel converter-based high voltage direct current (MMC-HVDC) presents negative damping characteristics, and the REG-side and system-side form a series resonant circuit, broadband oscillation will occur in the system. Since the control structures and parameters in wind turbines, PV units, static var generator (SVG), LCC-HVDC, MMC-HVDC, and other power electronic devices are different, the impedances of these devices will present negative damping characteristics in some frequency bands, which bring potential risks of the system broadband oscillation.

This part will fully excavate the impedance plasticity of the power electronic device to carry out broadband oscillation suppression, based on impedance reshaping of both the REG-side devices, such as wind turbine, PV unit, SVG, and system-side devices, such as LCC-HVDC, MMC-HVDC, and finally achieve engineering applications. This part includes the following chapters:

Chapter 15: Oscillation Mitigation Based on Impedance Reshaping of REG Unit. In this chapter, impedance reshaping of the REG plant and system oscillation suppression is realized through impedance reshaping of REG units. The broadband impedance reshaping methods for permanent magnet synchronous generator (PMSG) and doubly-fed induction generator (DFIG)-based wind turbines based on the combination of control strategy improvement and control parameter optimization is proposed. Considering the frequency-band overlapping effect, the iterative optimization method of control parameters in different frequency bands is further proposed.

Chapter 16: Oscillation Mitigation Based on Impedance Reshaping of SVG. In this chapter, impedance reshaping of the REG plant and system oscillation suppression is realized through the impedance reshaping of SVG. This chapter proposes the SVG broadband impedance reshaping strategy and establishes the analytical impedance model of the SVG after impedance reshaping. The control parameter optimization of the proposed strategy is carried out to mitigate the negative damping characteristics of the REG plant in different frequency bands.

Chapter 17: Oscillation Mitigation Based on Impedance Reshaping of LCC-HVDC. In this chapter, the oscillation mitigation of RPG connected into LCC-HVDC system oscillation mitigation is realized through the impedance reshaping of LCC-HVDC. The impedance reshaping strategy based on the combination of control strategy improvement and control parameter optimization is proposed. Finally, impedance reshaping in sub-/super- synchronous frequency band of LCC-HVDC and system oscillation mitigation are realized.

Chapter 18: Oscillation Mitigation Based on Impedance Reshaping of MMC-HVDC. In this chapter, the oscillation mitigation of RPG connected into MMC-HVDC system is realized through the impedance reshaping of MMC-HVDC. The MMC-HVDC impedance reshaping strategy based on circulating current active damping control and filtering capacitor current active damping control is proposed. Based on the optimization of control parameters, impedance reshaping in different frequency bands is realized, and broadband oscillation mitigation of RPG connected into MMC-HVDC system is effectively realized.

Chapter 19: Project Cases of REG and AC/DC Transmission System Oscillation. This chapter focuses on the oscillation events that occurred in China, including Hami of Xinjiang, Zhangbei of Hebei, and Ximeng of Inner Mongolia. Based on the full electromagnetic (EMT) transient simulation platform for REG and alternating current (AC)/direct current (DC) transmission systems, the oscillation mechanism is analyzed, the dominant oscillation equipment is determined, the oscillation mitigation strategy is proposed, and the field test of oscillation mitigation is carried out, effectively solving the oscillation problem of the above projects.

References

1. ZHOU L M, LUO A, CHEN Y D, et al. A robust grid-current-feedback-active-damping method for LCL-type grid-connected inverters [J]. Proceedings of the CSEE, 2016, 36(10): 2742-2752. (Chinese)
2. WANG X F, BLAABJERG F, LOH P C. Grid-current-feedback active damping for LCL resonance in grid-connected voltage-source converters [J]. IEEE Transactions on Power Electronics, 31(1): 213-223.
3. BERES R N, WANG X F, LISERRE M, et al. A review of passive power filters for three-phase grid-connected voltage-source converters [J]. Journal of Emerging and Selected Topics in Power Electronics, 2016, 4(1): 54-69.

Chapter 15
Oscillation Mitigation Based on Impedance Reshaping of REG Unit

Impedance reshaping of PMSG- and DFIG-based wind turbines based on control parameter optimization or control strategy improvement is an effective measure to mitigate the oscillation in power system [1–3]. Compared with control strategy improvement, control parameter optimization is simpler and has been widely used in practice. However, for specific frequency bands, if it is hard to achieve the impedance reshaping by control parameter optimization, control strategy improvement is required.

According to the analysis of broadband impedance characteristics in Part II, it is known that for PMSG- and DFIG-based wind turbines, frequency-band overlapping effects may occur between different controllers. In this case, the impedance reshaping method designed for a specific frequency band will affect the impedance characteristics in other frequency bands. This may cause the impedance characteristics which are originally stable to become unstable, thus triggering new oscillations in other frequency bands. In addition, the existing impedance reshaping technology is mainly to optimize the control parameters or improve the control strategy according to the oscillation frequency when the incident happens. However, in the development stage of REG Unit, there is still a lack of unified design method for impedance reshaping that covers a broadband frequency range and takes into account the characteristics and needs of complex power grids.

In this chapter, the broadband impedance reshaping methods for PMSG- and DFIG-based wind turbines based on the combination of control strategy improvement and control parameter optimization are proposed [4–6]. For PMSG-based wind turbines, a broadband impedance reshaping control strategy based on the combination of grid-side converter (GSC) active damping control and GSC virtual admittance control is proposed. For DFIG-based wind turbines, a broadband impedance reshaping control strategy based on the combination of GSC active damping control and rotor-side converter (RSC) virtual impedance control is proposed. Considering the frequency-band overlapping effect, the iterative optimization method of control parameters in different frequency bands is further proposed. Finally, based on the

© China Electric Power Press 2023

W. Wang et al., *Analysis and Mitigation of Broadband Oscillation in Renewable Energy Generation and AC/DC Transmission Systems*,
https://doi.org/10.1007/978-981-99-1568-2_15

full EMT simulation platform of REG and AC/DC transmission system the simulation and field test of the system oscillation mitigation is carried out to verify the effectiveness of the relevant research in this chapter.

15.1 Impedance Reshaping of PMSG-Based Wind Turbine

The dominant factors of impedance characteristics and the causes of the negative damping in each frequency band are different. Therefore, the impedance reshaping strategy is different for each frequency band. In this section, a broadband impedance reshaping strategy for PMSG-based wind turbines based on the combination of control strategy improvement and control parameter optimization is proposed. By the phase compensation of the impedance in different frequency bands, the damping characteristics are improved and the broadband oscillation is mitigated. Finally, the oscillation mitigation strategy based on PMSG-based wind turbine impedance reshaping is verified by simulations and field tests.

15.1.1 Impedance Reshaping Strategy

Based on the typical control structure of PMSG-based wind turbines, active damping control and virtual admittance control are added to GSC control to achieve the impedance reshaping in Band $\mathrm{II}_{\mathrm{PMSG}}$, $\mathrm{III}_{\mathrm{PMSG}}$ and $\mathrm{IV}_{\mathrm{PMSG}}$. The GSC control structure considering impedance reshaping is shown in Fig. 15.1.

As shown in Fig. 15.1, the impedance reshaping control includes virtual admittance control and active damping control. Virtual admittance control: the d- and q-axis voltages v_{d} and v_{q} are taken as input signals superposed to the d- and q-axis

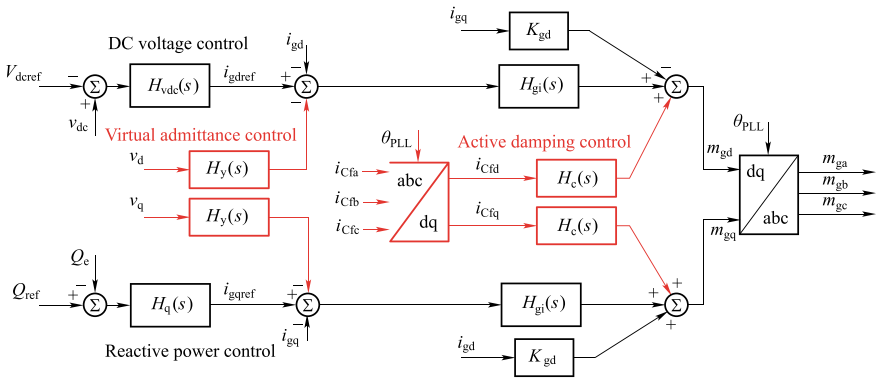

Fig. 15.1 GSC control structure considering impedance reshaping

current references i_{gdref} and i_{gqref} via the virtual admittance controller $H_{\mathrm{y}}(s)$. Active damping control: the d- and q-axis capacitor currents i_{Cfd} and i_{Cfq} are taken as input signals superposed to GSC d- and q-axis modulation signals m_{gd} and m_{gq} via the active damping controller $H_{\mathrm{c}}(s)$.

15.1.1.1 Impedance Reshaping Strategy in Band $\mathrm{II}_{\mathrm{PMSG}}$

The capacitive negative damping characteristics of PMSG-based wind turbines in Band $\mathrm{II}_{\mathrm{PMSG}}$ are mainly determined by phase lock loop (PLL). By reasonably adjusting PLL parameters, the impedance in Band $\mathrm{II}_{\mathrm{PMSG}}$ can be reshaped. Considering PLL bandwidth has great impact on the fault ride-through performance, the principle of impedance reshaping in Band $\mathrm{II}_{\mathrm{PMSG}}$ is: first determine PLL bandwidth, then adjust the PM of PLL to eliminate the negative damping in Band $\mathrm{II}_{\mathrm{PMSG}}$ on the premise of taking into account the fault ride-through control performance of PMSG-based wind turbines.

15.1.1.2 Impedance Reshaping Strategy in Band $\mathrm{III}_{\mathrm{PMSG}}$

In the first half of Band $\mathrm{III}_{\mathrm{PMSG}}$, the frequency-band overlapping effect of the DC voltage loop and GSC AC current loop leads to capacitive negative damping characteristics in the impedance. The capacitive negative damping in the first half of Band $\mathrm{III}_{\mathrm{PMSG}}$ can be eliminated by optimizing DC voltage control parameters. In the second half of Band $\mathrm{III}_{\mathrm{PMSG}}$, the frequency-band overlapping effect of time delay and GSC AC current loop leads to capacitive negative damping characteristics near GSC AC current loop bandwidth. Since the time delay is an inherent characteristic of PMSG-based wind turbines, it is difficult to optimize its parameter. Therefore, the virtual admittance control is proposed, as shown in Fig. 15.1. Through the additional controller, the impedance phase compensation in Band $\mathrm{III}_{\mathrm{PMSG}}$ is realized to improve the negative damping characteristics.

In the virtual admittance control, v_{d} and v_{q} are taken as input signals superposed to the GSC d- and q-axis current references i_{gdref} and i_{gqref} via the virtual admittance controller $H_{\mathrm{y}}(s)$, so as to achieve impedance reshaping in the second half of Band $\mathrm{III}_{\mathrm{PMSG}}$. In order to reduce the influence on impedance characteristics in other frequency bands, bandpass filter is adopted, and its expression is

$$H_{\mathrm{y}}(s) = \frac{k_{\mathrm{y}}}{\omega_{\mathrm{y1}}} \frac{s}{(s/\omega_{\mathrm{y1}} + 1)(s/\omega_{\mathrm{y2}} + 1)} \tag{15.1}$$

where k_{y} is the virtual admittance coefficient,which can be designed to adjust the damping characteristics in Band $\mathrm{III}_{\mathrm{PMSG}}$, ω_{y1} and ω_{y2} are the lower and upper limits of the angular frequency for the virtual admittance control respectively, which can be designed to adjust the effective frequency range of the compensator.

15.1.1.3 Impedance Reshaping Strategy in Band IV_{PMSG}

The frequency-band overlapping effect of time delay and the LC filter results in capacitive negative damping characteristics in Band IV_{PMSG}. As the filter capacitance and time delay are inherent parameters of PMSG-based wind turbines, it is difficult to adjust. Therefore, the active damping control based on the filter capacitor current feedforward is proposed, as shown in Fig. 15.1. Through the additional controller, the impedance phase compensation in Band IV_{PMSG} is realized to improve the negative damping characteristics.

In order to avoid the influence on the impedance characteristics in other frequency bands, the active damping control utilizes a lead-lag compensator to improve the impedance phase, whose transfer function is

$$H_c(s) = k_c \cdot \frac{s/\omega_{c1} + 1}{s/\omega_{c2} + 1} \tag{15.2}$$

where $k_c$is the active damping coefficient and can be designed to adjust the damping characteristics in Band IV_{PMSG}. ω_{c1} and ω_{c2} are the lower and upper limits of the angular frequency for the active damping control respectively, which can be designed to adjust the effective frequency range of the compensator.

To sum up, the impedance reshaping principle for PMSG-based wind turbines can be summarized as follows:

1. Band II_{PMSG}: the impedance reshaping strategy based on PLL parameter optimization is adopted. On the premise of considering the fault ride-through control performance, eliminate the capacitive negative damping in this band.
2. Band III_{PMSG}: the impedance reshaping strategy combining DC voltage control parameter optimization and virtual admittance control is adopted. The virtual admittance control is used to compensate for the impedance phase to improve the damping characteristics.
3. Band IV_{PMSG}: the active damping control strategy based on filter capacitor current feedforward is adopted to eliminate the capacitive negative damping in this band.

15.1.2 Reshaped Impedance Model

Based on the active damping control and virtual admittance control, the analytical impedance model of PMSG-based wind turbines with impedance reshaping control strategy is established in this section.

According to Fig. 15.1, the small-signal vectors of GSC d- and q-axis modulation signals $\hat{\boldsymbol{m}}_{gd}$, $\hat{\boldsymbol{m}}_{gq}$ are expressed as

$$\begin{cases} \hat{\boldsymbol{m}}_{\mathrm{gd}} = \left[H_{\mathrm{vdc}}(s_1)\hat{\boldsymbol{v}}_{\mathrm{dc}} - \hat{\boldsymbol{i}}_{\mathrm{gd}}\right]H_{\mathrm{gi}}(s_1) - K_{\mathrm{gd}}\hat{\boldsymbol{i}}_{\mathrm{gq}} \\ \qquad\quad + \left[-H_{\mathrm{y}}(s_1)H_{\mathrm{gi}}(s_1)\hat{\boldsymbol{v}}_{\mathrm{d}} + H_{\mathrm{c}}(s_1)\hat{\boldsymbol{i}}_{\mathrm{Cfd}}\right] \\ \hat{\boldsymbol{m}}_{\mathrm{gq}} = \left[H_{\mathrm{q}}(s_1)(\boldsymbol{Q}_{\mathrm{i}}\hat{\boldsymbol{i}}_{\mathrm{ga}} + \boldsymbol{Q}_{\mathrm{v}}\hat{\boldsymbol{v}}_{\mathrm{a}}) - \hat{\boldsymbol{i}}_{\mathrm{gq}}\right]H_{\mathrm{gi}}(s_1) + K_{\mathrm{gd}}\hat{\boldsymbol{i}}_{\mathrm{gd}} \\ \qquad\quad + \left[-H_{\mathrm{y}}(s_1)H_{\mathrm{gi}}(s_1)\hat{\boldsymbol{v}}_{\mathrm{q}}H_{\mathrm{c}}(s_1)\hat{\boldsymbol{i}}_{\mathrm{Cfq}}\right] \end{cases} \tag{15.3}$$

Transform $\hat{\boldsymbol{m}}_{\mathrm{gd}}$, $\hat{\boldsymbol{m}}_{\mathrm{gq}}$ to the stationary coordinate frame (SCF) through inverse Park transformation, the phase-a small-signal vector of the GSC modulation signal can be obtained as

$$\hat{\boldsymbol{m}}_{\mathrm{ga}} = \boldsymbol{E}_{\mathrm{dc}} \cdot \hat{\boldsymbol{v}}_{\mathrm{dc}} + \boldsymbol{E}_{\mathrm{gi}} \cdot \hat{\boldsymbol{i}}_{\mathrm{ga}} + (\boldsymbol{E}_{\mathrm{gv}} + \Delta\boldsymbol{E}_{\mathrm{gv}}) \cdot \hat{\boldsymbol{v}}_{\mathrm{a}} \tag{15.4}$$

where $\Delta\boldsymbol{E}_{\mathrm{gv}}$ is the coefficient matrix introduced by impedance reshaping; other coefficient matrices can refer to Chap. 6. The expression of $\Delta\boldsymbol{E}_{\mathrm{gv}}$ is

$$\Delta\boldsymbol{E}_{\mathrm{gv}} = \begin{bmatrix} \begin{matrix} -H_{\mathrm{gi}}(s_1)H_{\mathrm{y}}(s_1)[1 - T_{\mathrm{PLL}}(s_1)\boldsymbol{V}_1^*] \\ +H_{\mathrm{c}}(s_1)[C_{\mathrm{f}}s_2 - T_{\mathrm{PLL}}(s_1)\boldsymbol{I}_{\mathrm{Cf1}}^*] \end{matrix} & 0 & \begin{matrix} -H_{\mathrm{gi}}(s_1)H_{\mathrm{y}}(s_1)T_{\mathrm{PLL}}(s_1)\boldsymbol{V}_1^* \\ +H_{\mathrm{c}}(s_1)T_{\mathrm{PLL}}(s_1)\boldsymbol{I}_{\mathrm{Cf1}}^* \end{matrix} & 0\ 0 \\ 0 & 0 & 0 & 0\ 0 \\ \begin{matrix} -H_{\mathrm{gi}}(s_1)H_{\mathrm{y}}(s_1)T_{\mathrm{PLL}}(s_1)\boldsymbol{V}_1 \\ +H_{\mathrm{c}}(s_1)T_{\mathrm{PLL}}(s_1)\boldsymbol{I}_{\mathrm{Cf1}} \end{matrix} & 0 & \begin{matrix} -H_{\mathrm{gi}}(s_1)H_{\mathrm{y}}(s_1)[1 - T_{\mathrm{PLL}}(s_1)\boldsymbol{V}_1] \\ +H_{\mathrm{c}}(s_1)[C_{\mathrm{f}}s - T_{\mathrm{PLL}}(s_1)\boldsymbol{I}_{\mathrm{Cf1}}] \end{matrix} & 0\ 0 \\ 0 & 0 & 0 & 0\ 0 \\ 0 & 0 & 0 & 0\ 0 \end{bmatrix}$$

The small-signal model of GSC can be obtained as

$$\hat{\boldsymbol{v}}_{\mathrm{a}} = \boldsymbol{F}'_{\mathrm{dc}}\hat{\boldsymbol{v}}_{\mathrm{dc}} + \boldsymbol{F}'_{\mathrm{gi}}\hat{\boldsymbol{i}}_{\mathrm{ga}} \tag{15.5}$$

where $\boldsymbol{F}'_{\mathrm{dc}}$ and $\boldsymbol{F}'_{\mathrm{gi}}$ are the voltage coefficient matrices of GSC after impedance reshaping, and their expressions are

$$\begin{cases} \boldsymbol{F}'_{\mathrm{dc}} = [\boldsymbol{U} - K_{\mathrm{m}}V_{\mathrm{dc}}(\boldsymbol{E}_{\mathrm{gv}} + \Delta\boldsymbol{E}_{\mathrm{gv}})]^{-1}(K_{\mathrm{m}}\boldsymbol{M}_{\mathrm{ga}} + K_{\mathrm{m}}V_{\mathrm{dc}}\boldsymbol{E}_{\mathrm{dc}}) \\ \boldsymbol{F}'_{\mathrm{gi}} = [\boldsymbol{U} - K_{\mathrm{m}}V_{\mathrm{dc}}(\boldsymbol{E}_{\mathrm{gv}} + \Delta\boldsymbol{E}_{\mathrm{gv}})]^{-1}(K_{\mathrm{m}}V_{\mathrm{dc}}\boldsymbol{E}_{\mathrm{gi}} - \boldsymbol{Z}_{\mathrm{Lf}}) \end{cases}$$

By substituting Eq. (15.5) into the small-signal model of the machine-side converter (MSC) in Chap. 6 the analytical impedance model of PMSG-based wind turbines considering impedance reshaping strategy can be obtained.

15.1.3 Impedance Reshaping Design

Due to the frequency-band overlapping effect of multiple controllers, the impedance reshaping in Band II_{PMSG} and Band IV_{PMSG} will affect the impedance characteristics in Band III_{PMSG}. By reasonably choosing the virtual admittance cut-off frequency, the influence of impedance reshaping in Band III_{PMSG} on the impedance characteristics in Band II_{PMSG} and Band IV_{PMSG} can be reduced. In this section, impedance reshaping will be carried out in the order of Band II_{PMSG}, IV_{PMSG}, III_{PMSG}.

First, based on the optimization of PLL parameters, the impedance in Band $\text{II}_{\text{PMSG}}$is reshaped to eliminate the negative damping in this band. Considering that PLL also affects fault ride-through characteristics of PMSG-based wind turbines, PLL parameter optimization is verified by the fault ride-through test.

Then, based on the active damping control, the impedance in Band IV_{PMSG} is reshaped to eliminate the negative damping and meet the stability requirements.

Finally, the impedance in Band III_{PMSG} is reshaped. The negative damping characteristic in the first half of Band III_{PMSG} is eliminated by optimizing the PM of the DC voltage control. The negative damping characteristic in the second half of Band III_{PMSG} is eliminated by combining GSC AC current control parameter optimization with the virtual admittance control.

Taking a certain type of PMSG-based wind turbine as an example, the impedance characteristics before reshaping are shown in Fig. 15.2. It can be seen from the figure that negative damping characteristics exist in Band II_{PMSG}, III_{PMSG} and IV_{PMSG}.

15.1.3.1 Impedance Reshaping Design in Band II_{PMSG}

The impedance characteristics in Band II_{PMSG} are dominated by PLL, which control parameters affect the level of the capacitive negative damping. In the following, the impedance reshaping in Band II_{PMSG} is realized by optimizing PLL parameters under the premise of considering fault ride-through performance.

The influence of PLL on impedance characteristics is shown in Fig. 15.3. On the one hand, the influence of PLL bandwidth can be obtained by changing f_{tc} to 5, 10, 20 Hz respectively with a constant PM of 10°. On the other hand, the influence of the PLL PM can be obtained by changing θ_{tc} to 10°, 45° and 80° respectively with a constant bandwidth of 20 Hz.

As shown in Fig. 15.3 with the decrease of PLL bandwidth f_{tc}, the difference between the resonance peak frequency and the fundamental frequency decreases and the frequency range of negative damping decreases. With the increase of PLL PM θ_{tc}, the difference between the resonance peak frequency and the fundamental frequency remains unchanged, while the level of negative damping reduces. On the premise of meeting the requirements of fault ride-through performance, lower PLL bandwidth and PM should be chosen.

The influence of PLL bandwidth on fault ride-through performance is verified by time-domain simulation, as shown in Fig. 15.4. In the figure, when grid voltage phase

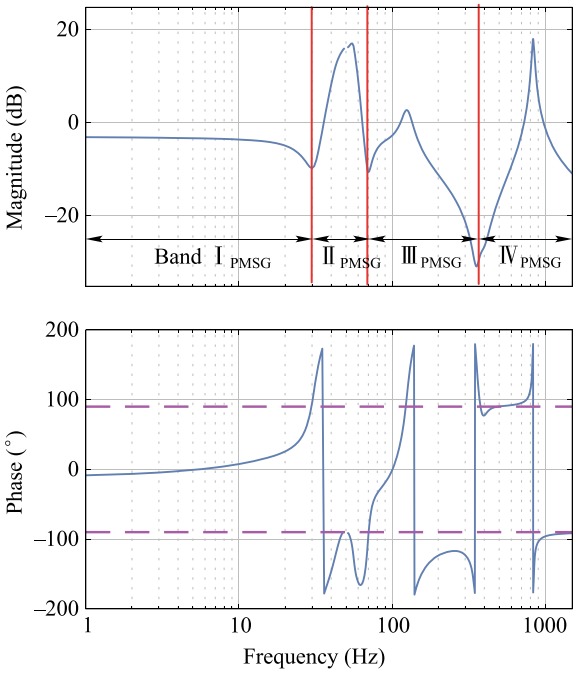

Fig. 15.2 Impedance characteristics of PMSG-based wind turbine before reshaping

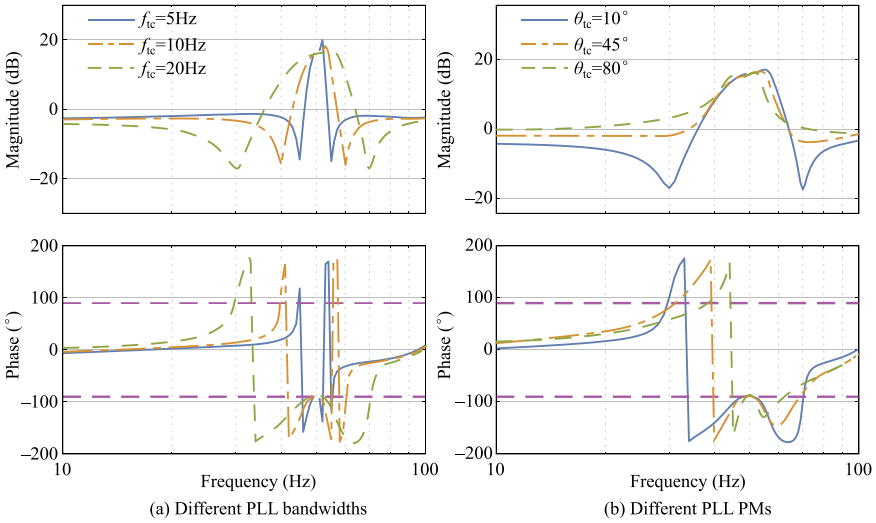

Fig. 15.3 Influence of PLL on impedance characteristics in Band II_{PMSG}

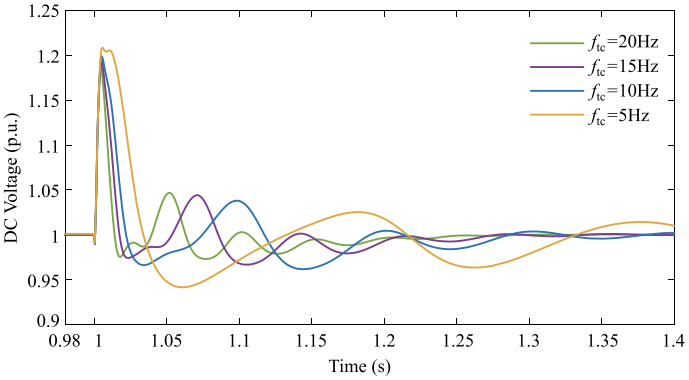

Fig. 15.4 Influence of PLL bandwidth on fault ride-through performance

steps 60° at $t = 1$ s, DC voltage responses are overshot. As PLL bandwidth decreases, the DC voltage response speed decreases, and the overshot duration increases. When the PLL bandwidth decreases to 5Hz, DC voltage significantly overshoots, which easily leads to the overvoltage protection of PMSG-based wind turbines.

15.1.3.2 Impedance Reshaping Design in Band $\mathrm{IV_{PMSG}}$

The impedance characteristics of $\mathrm{IV_{PMSG}}$ is dominated by LC filter and change from inductive to capacitive. The frequency-band overlapping effect of time delay and LC filter results in capacitive negative damping in Band $\mathrm{IV_{PMSG}}$. By reasonably choosing the active damping coefficient and the upper and lower limits of the angular frequency of the active damping control, the impedance phase can be compensated to eliminate the negative damping in Band $\mathrm{IV_{PMSG}}$. The amplitude-frequency characteristics of the active damping controller are shown in Fig. 15.5.

The influence of the active damping coefficient k_c on damping characteristics in Band $\mathrm{IV_{PMSG}}$ is shown in Fig. 15.6 when k_c changes from -0.0001 to 0. It can be seen that $H_c(s)$ can effectively eliminate the negative damping in Band $\mathrm{IV_{PMSG}}$. With the increase of k_c, the negative damping characteristics in Band $\mathrm{IV_{PMSG}}$ are finally eliminated. However, the value of k_c should not be too large, otherwise, it will affect the damping characteristics in Band $\mathrm{III_{PMSG}}$. The design of $H_c(s)$ should take into account the needs of Band $\mathrm{III_{PMSG}}$ and $\mathrm{IV_{PMSG}}$.

15.1.3.3 Impedance Reshaping Design in Band $\mathrm{III_{PMSG}}$

Theimpedance characteristics in Band $\mathrm{III_{PMSG}}$ are dominated by the AC current loop and present capacitive characteristics.

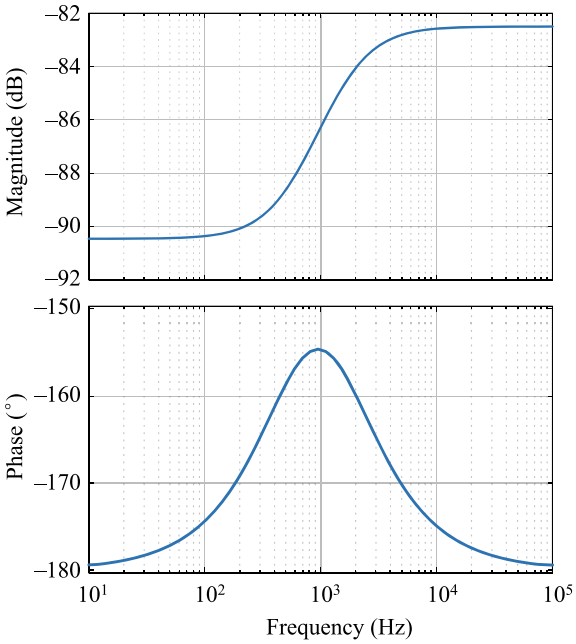

Fig. 15.5 Amplitude-frequency characteristics of the active damping controller

Fig. 15.6 Influence of the active damping coefficient on damping characteristics in Band IV_{PMSG}

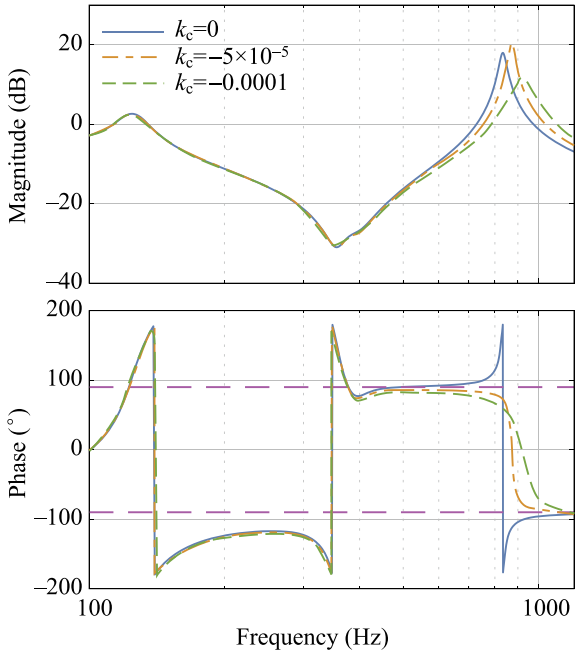

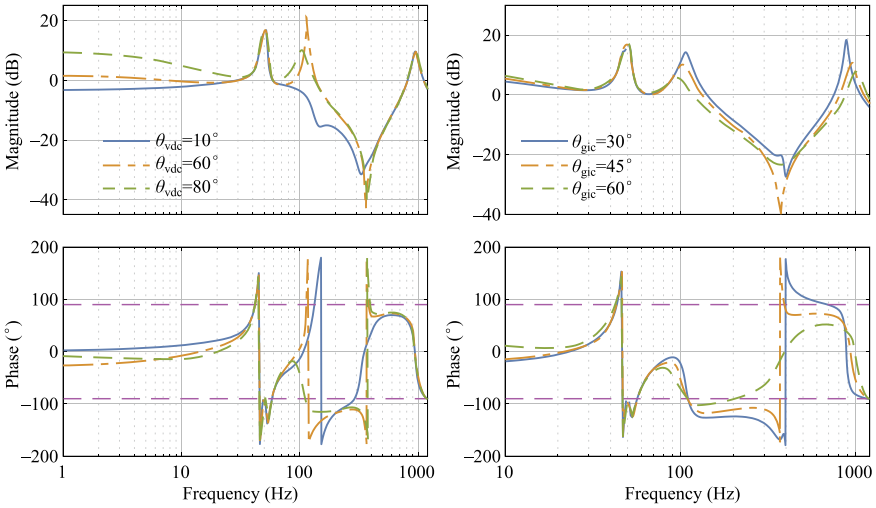

(a) Different DC voltage loop PMs (b) Different GSC AC Current loop PMs

Fig. 15.7 Influence of control parameter optimization on damping characteristics in Band $\mathrm{III}_{\mathrm{PMSG}}$

In the first half of Band $\mathrm{III}_{\mathrm{PMSG}}$, the frequency-band overlapping effect of DC voltage and GSC AC current loop leads to negative damping characteristics. The impedance can be reshaped by optimizing DC voltage loop parameters.

The influence of DC voltage loop on damping characteristics is shown in Fig. 15.7(a) when the PM θ_{vdc} changes from 10° to 80° with a constant bandwidth. It can be seen that the negative damping in the first half of Band $\mathrm{III}_{\mathrm{PMSG}}$ is eliminated with the increase of DC voltage loop PM θ_{vdc}.

In the second half of Band $\mathrm{III}_{\mathrm{PMSG}}$, the frequency-band overlapping effect of time delay and GSC AC current loop leads to negative damping characteristics near GSC AC current loop bandwidth f_{gic}. A combination of GSC AC current control parameter improvement and virtual admittance control is used to eliminate the negative damping.

The influence of GSC AC current loop on damping characteristics is shown in Fig. 15.7(b) when the GSC AC current loop PM θ_{vdc} changes from 30° to 60° with a constant bandwidth. It can be seen that the negative damping in the second half of Band $\mathrm{III}_{\mathrm{PMSG}}$ is eliminated with the increase of GSC AC current loop PM.

According to Eq. (15.1), the virtual admittance controller is a bandpass filter, and its amplitude-frequency characteristics are shown in Fig. 15.8. In order to reduce the influence of virtual admittance controller $H_{\mathrm{y}}(s)$ on the impedance characteristics in Band $\mathrm{II}_{\mathrm{PMSG}}$ and $\mathrm{IV}_{\mathrm{PMSG}}$, the control effect is limited to Band $\mathrm{III}_{\mathrm{PMSG}}$, namely $\omega_{\mathrm{y1}} = 2\pi f_{\mathrm{tc}}$, $\omega_{\mathrm{y2}} = 2\pi f_{\mathrm{gic}}$. By reasonably choosing the virtual admittance coefficient k_{y}, the damping characteristics in Band $\mathrm{III}_{\mathrm{PMSG}}$ can be eliminated.

The influence of the virtual admittance coefficient k_{y} on damping characteristics in Band $\mathrm{III}_{\mathrm{PMSG}}$ is shown in Fig. 15.9 when it changes from 0 to 2. It can be seen that $H_{\mathrm{y}}(s)$ can effectively eliminate the negative damping in this band. With the increase

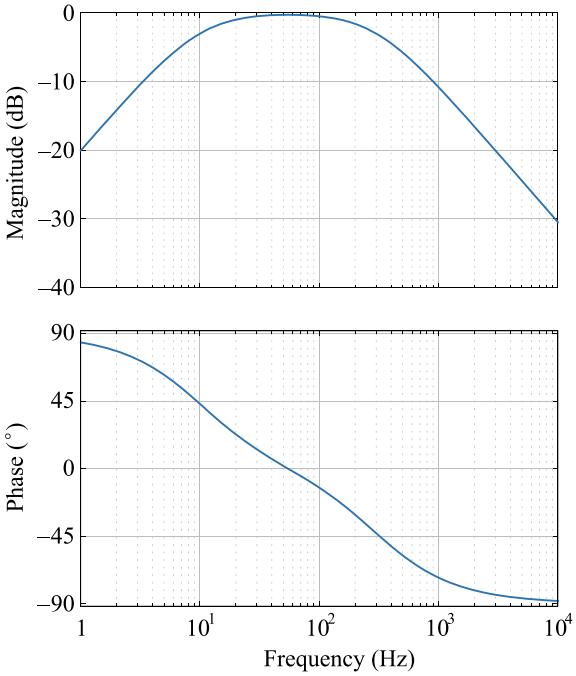

Fig. 15.8 Amplitude-frequency characteristics of the virtual admittance controller

of k_y, the negative damping characteristics in Band III_{PMSG} are finally eliminated. However, the value of k_y should not be too large, otherwise, it will affect the damping characteristics in Band II_{PMSG} and IV_{PMSG}. So the design of $H_y(s)$ should consider the needs of Band III_{PMSG}, II_{PMSG} and IV_{PMSG}.

In summary, the impedance reshaping in the order of Band II_{PMSG}, IV_{PMSG} and III_{PMSG} can effectively eliminate the negative damping of PMSG-based wind turbines, and the comparison of impedance characteristics before and after impedance reshaping is shown in Fig. 15.10.

The impedance of PMSG-based wind turbines is related to the steady-state operating point, and it needs to be verified under different operation conditions to ensure that the reshaped impedance characteristics meet the requirements of multiple operation conditions. The three-dimensional Bode diagram of the reshaped impedance characteristics is shown in Fig. 15.11. In the figure, as the active power varies from 0.2 p.u. to 1 p.u. the negative damping characteristics are improved in the frequency range from 1 to 1000 Hz.

The chart of the impedance reshaping for PMSG-based wind turbines is shown in Fig. 15.12.

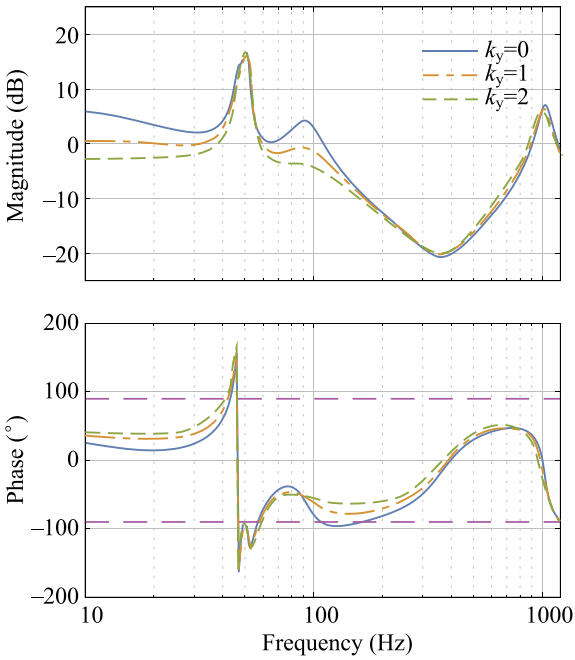

Fig. 15.9 Influence of the virtual admittance coefficient on damping characteristics in Band $\mathrm{III}_{\mathrm{PMSG}}$

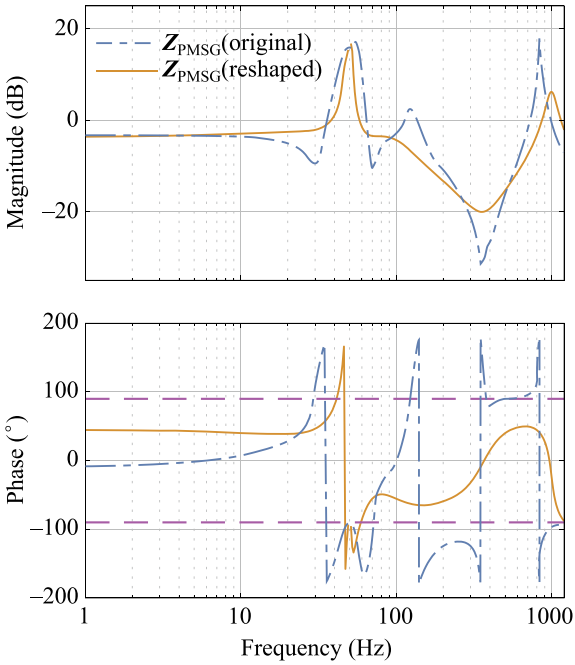

Fig. 15.10 Comparison of PMSG-based wind turbine impedance characteristics before and after impedance reshaping

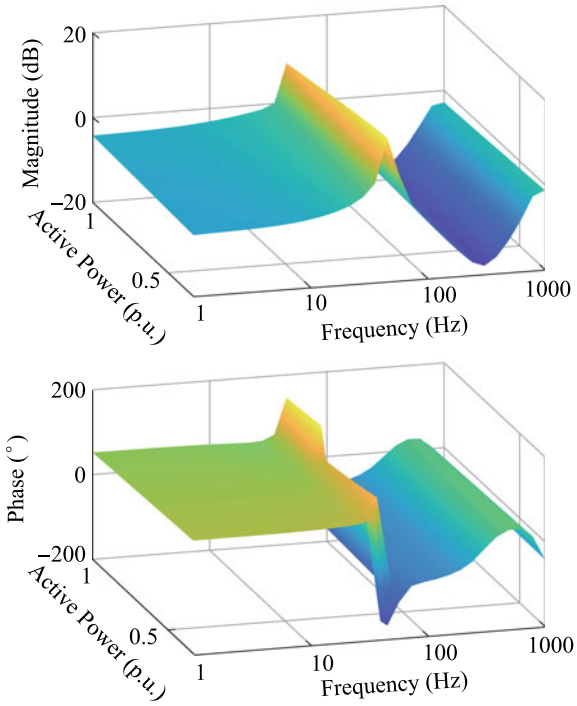

Fig. 15.11 Three-dimensional Bode diagram of the reshaped PMSG-based wind turbines impedance characteristics

15.1.4 Simulation Verification

Based on the full EMT simulation platform, taking the PMSG-based wind plant connected into weak AC grid as an example, frequency-domain analysis and time-domain simulation of oscillation mitigation based on PMSG-based wind turbines impedance reshaping are carried out to verify the effectiveness of the impedance reshaping strategy mentioned above. The EMT simulation parameters of PMSG-based wind plants are listed in Table 15.1. Figure 15.13 shows the evaluation results of oscillation risk for the PMSG-based wind plant connected into weak AC grid before and after impedance reshaping.

As seen from Fig. 15.13(a), the magnitude curves of the PMSG-based wind plant impedance $\boldsymbol{Z}_{\mathrm{PMSG}}$ and AC grid impedance $\boldsymbol{Z}_{\mathrm{g}}$ intersect at Point A (102 Hz), and the PM is only 1.4° before the impedance reshaping. The gain margin (GM)/phase margin (PM) is insufficient, indicating oscillation risk in the system. After the impedance reshaping, the intersection point of the magnitude curves shifts from Point A to Point B (132 Hz), and the PM is increased to 39.1°. The stability margin is thus improved and the oscillation risk is eliminated.

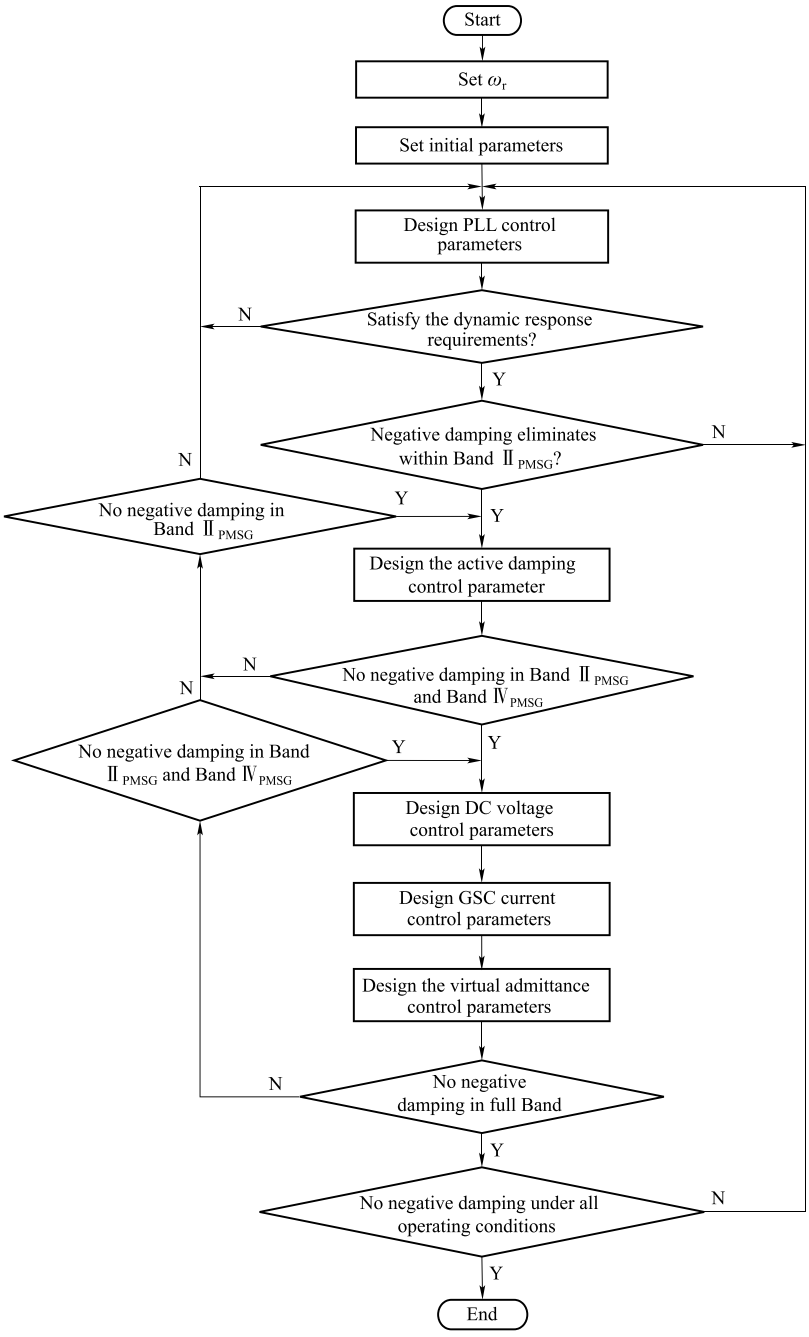

Fig. 15.12 Flow chart of impedance reshaping for PMSG-based wind turbines

Table 15.1 EMT simulation parameters of the PMSG-based wind plant

Parameter	Definition	Value
N_{PMSG}	Number of PMSG-based wind turbines	100
P_N	Rated power	1.5 MW
V_N	Rated voltage	690 V
f_1	Rated frequency	50 Hz
k_T	Transformer voltage ratio	0.69/35 kV
R_s	Stator resistance	0.001 Ω
L_{sd}, L_{sq}	d- and q-axis inductance of the stator	0.2699 mH, 0.2830 mH
L_f	GSC filter inductance	0.1000 mH
V_{dc}	DC voltage	1500 V
K_{pp}, K_{ip}	Proportional and integral coefficients of PLL controller	0.1099, 1.2176
K_{gip}, K_{gii}	Proportional and integral coefficients of GSC AC current controller	1.5350×10^{-4}, 0.0899
K_{sip}, K_{sii}	Proportional and integral coefficients of MSC AC current controller	1.3685×10^{-5}, 0.0091×10^{-5}
K_{pep}, K_{pei}	Proportional and integral coefficients of active power controller	0.0084, 0.0152
K_{qep}, K_{qei}	Proportional and integral coefficients of reactive power controller	5.9207×10^{-4}, 0.0322
K_{vdcp}, K_{vdci}	Proportional and integral coefficients of DC voltage controller	12.8195, 1278.2
k_c	Active damping coefficient	−0.00008
ω_{c1}, ω_{c2}	The lower and upper limits of the angular frequency for the active damping control	3.7699×10^3, 8.7965×10^3
k_y	Virtual admittance coefficient	2
ω_{y1}, ω_{y2}	The lower and upper limits of the angular frequency for the virtual admittance control	62.8319, 1.8850×10^3
K_{sd}	Decoupling coefficient of MSC AC current control	2.3160×10^{-5}
K_{gd}	Decoupling coefficient of GSC AC current control	4.2341×10^{-4}

As seen from Fig. 15.13(b), the original Nyquist curve around Point A (102 Hz) is in the forbidden area, indicating oscillation risk. After the impedance reshaping, the optimized Nyquist curve is outside the forbidden area, indicating that the impedance reshaping of PMSG-based wind turbines effectively eliminates the oscillation risk of the system.

The time-domain simulation of the PMSG-based wind plant connected to weak AC grid is conducted based on the EMT simulation platform. The current waveforms and fast fourier transform (FFT) results of the PMSG-based wind plant before and after the impedance reshaping are shown in Fig. 15.14.

As seen from Fig. 15.14 initially, there is a super-synchronous oscillation component at 102 Hz and a coupling sub-synchronous oscillation component at 2 Hz

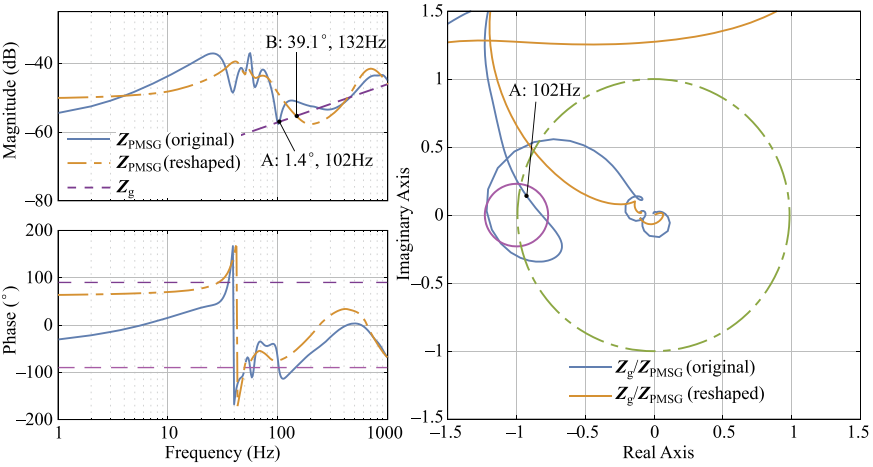

(a) System impedance Bode plot (b) System Nyquist plot

Fig. 15.13 The evaluation results of oscillation risk for PMSG-based wind plants connected into weak AC grid before and after impedance reshaping

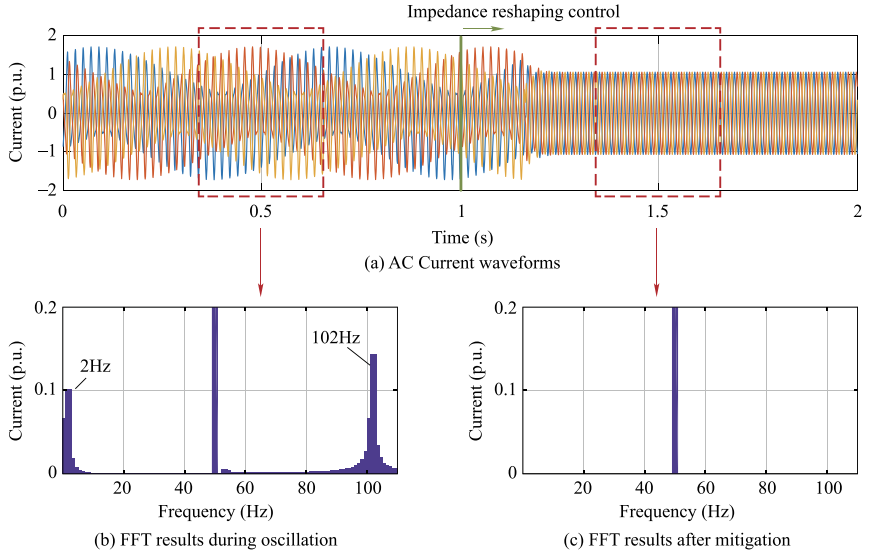

(a) AC Current waveforms

(b) FFT results during oscillation (c) FFT results after mitigation

Fig. 15.14 The current waveforms and FFT results of the PMSG-based wind plant before and after impedance reshaping

according to the FFT results of the AC currents. After the impedance reshaping of PMSG-based wind turbines is enabled at $t = 1$ s, the oscillation of the AC currents is mitigated, and the sub-/super- synchronous oscillation components are eliminated as shown in the corresponding FFT analysis. The simulation results verify the effectiveness of oscillation mitigation strategy based on the proposed impedance reshaping of PMSG-based wind turbines.

15.1.5 Field Test Verification

Based on the test and experimental verification platform of REG and AC/DC transmission system, taking PMSG-based wind turbine connected to weak AC grid as an example, the field test of oscillation mitigation was carried out to verify the effectiveness of the impedance reshaping strategy. The system structure and parameters are the same as Sect. 13.4. The oscillation risk analysis of PMSG-based wind turbine connected to weak AC grid is shown in Fig. 15.15.

As seen from Fig. 15.15(a), the magnitude curves of the PMSG-based wind turbine impedance $\boldsymbol{Z}_{\text{PMSG}}$ and AC grid impedance $\boldsymbol{Z}_{\text{g}}$ intersect at Point C (71 Hz), and the PM is only 1.7° before impedance reshaping. The GM/PM is insufficient, indicating oscillation risk in the system. After impedance reshaping, the intersection point of the magnitude curves shifts from Point C to Point D (95 Hz), and the PM is increased to 20°. The stability margin is thus improved and the oscillation risk is eliminated.

As seen from Fig. 15.15(b), the original Nyquist curve around Point C (71 Hz) is in the forbidden area, indicating oscillation risk. After impedance reshaping, the optimized Nyquist curve is outside the forbidden area, indicating that the impedance

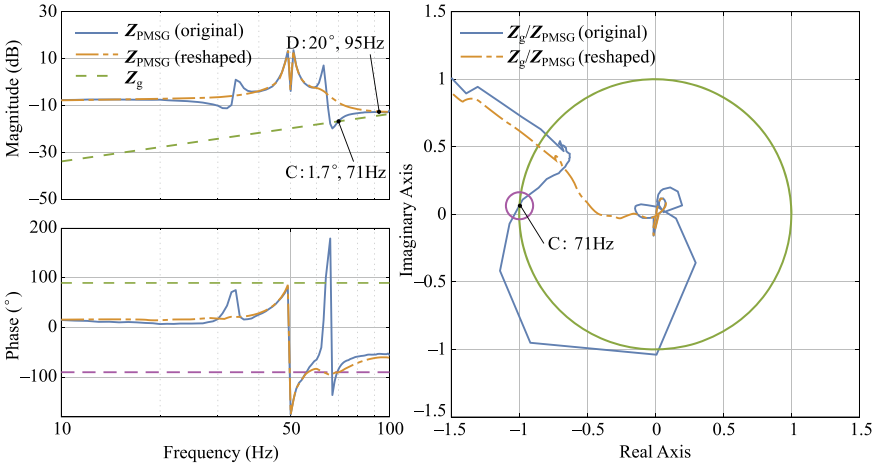

Fig. 15.15 The oscillation risk of the PMSG-based wind turbine connected to weak AC grid

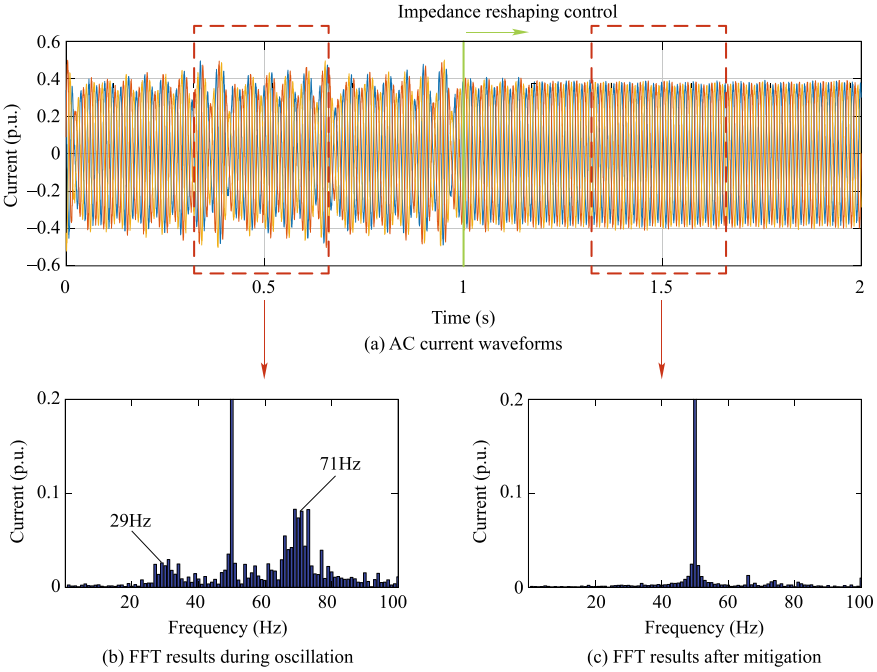

Fig. 15.16 The field test result of PMSG-based wind turbine connected to weak AC grid

reshaping of the PMSG-based wind turbine effectively eliminates the oscillation risk of the system.

The field test of the PMSG-based wind turbine connected into weak AC grid is conducted and its result is shown in Fig. 15.16. In the figure, initially, thereis a super-synchronous oscillation component at 71 Hz and a coupling sub-synchronous oscillation component at 29 Hz according to the FFT results of the AC currents. After the impedance reshaping of PMSG-based wind turbines is enabled at $t = 1$ s, the oscillation of the current waveforms is mitigated, and the sub-/super- synchronous oscillation components are eliminated as shown in the corresponding FFT analysis. The field test results verify the effectiveness of the oscillation mitigation strategy based on the proposed impedance reshaping of the PMSG-based wind turbine.

15.2 Impedance Reshaping of DFIG-Based Wind Turbine

In this section, a broadband impedance reshaping strategy for DFIG-based wind turbines based on the combination of control strategy improvement and control parameter optimization is proposed. First, the impedance reshaping control strategy for DFIG-based wind turbines is proposed. Then, the impedance model considering

impedance reshaping is established and the optimized control parameters are given. Finally, the simulation verification of the oscillation mitigation strategy based on the impedance reshaping is carried out.

15.2.1 Impedance Reshaping Strategy

Based on the typical control of DFIG-based wind turbines, the active damping control is introduced to GSC to realize the impedance reshaping in Band $\mathrm{II_{DFIG}}$ and $\mathrm{III_{DFIG}}$; The virtual impedance control is introduced to RSC to realize the impedance reshaping in Band $\mathrm{I_{DFIG}}$. The control structure of DFIG-based wind turbine considering impedance reshaping is shown in Fig. 15.17.

15.2.1.1 Impedance Reshaping Design in Band $\mathrm{I_{DFIG}}$

The impedance characteristics of DFIG-based wind turbines in Band $\mathrm{I_{DFIG}}$ are dominated by the stator impedance, which is inductive. Due to the existence of the slip, the impedance represents inductive negative damping characteristics. The inductive negative damping level and its frequency range are related to the rotor electrical frequency, active power loop, RSC AC current loop and PLL in Band $\mathrm{I_{DFIG}}$. By reasonably choosing the above control parameters and introducing virtual impedance control, the impedance in Band $\mathrm{I_{DFIG}}$ can be reshaped.

The virtual impedance controller $H_\mathrm{d}(s)$ utilizes a bandpass filter, which expression is

$$H_\mathrm{d}(s) = k_\mathrm{d}\frac{Q_\mathrm{d}^{-1}\omega_{\mathrm{d}0}s}{s^2 + Q_\mathrm{d}^{-1}\omega_{\mathrm{d}0}s + \omega_{\mathrm{d}0}^2} \tag{15.6}$$

where $\omega_{\mathrm{d}0}$ is the center angular frequency of the bandpass filter, $\omega_{\mathrm{d}0} = \sqrt{\omega_{\mathrm{dh}}\omega_{\mathrm{dl}}}$. ω_{dh} and ω_{dl} are the upper and lower limits of the bandpass filter angular frequency respectively; Q_d is the quality factor of the bandpass filter, $Q_\mathrm{d} = \omega_{\mathrm{d}0}/B_\mathrm{d}$; B_d is the bandwidth of the bandpass filter, $B_\mathrm{d} = \omega_\mathrm{h} - \omega_\mathrm{l}$; k_d is the virtual impedance coefficient, and it can be calculated as

$$k_\mathrm{d} = K_\mathrm{r}\left(\frac{R_\mathrm{r}}{V_\mathrm{dc}} + K_\mathrm{rip}\right) \tag{15.7}$$

K_r is the virtual impedance gain.

15.2.1.2 Impedance Reshaping Design in Band $\mathrm{II_{DFIG}}$

The impedance of DFIG-based wind turbines in Band $\mathrm{II_{DFIG}}$ are jointly dominated by the stator impedance and GSC impedance. The frequency-band overlapping effect

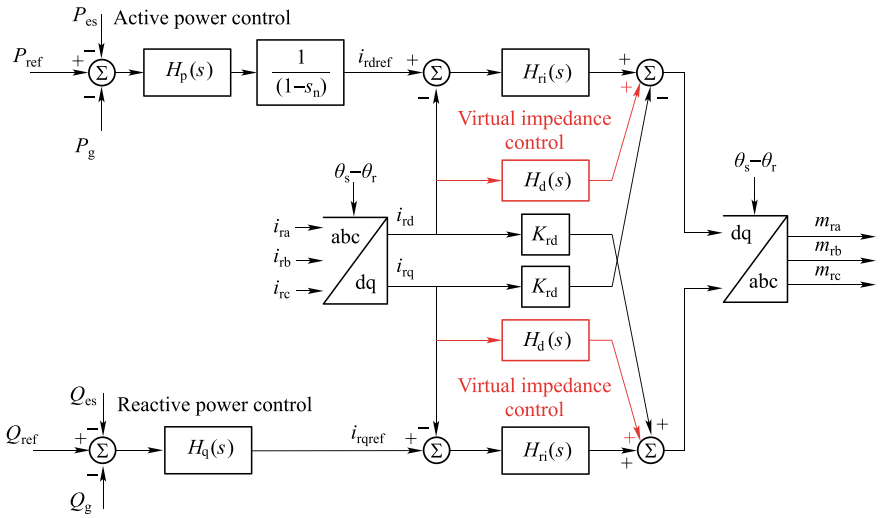

(a) Block diagram of RSC control

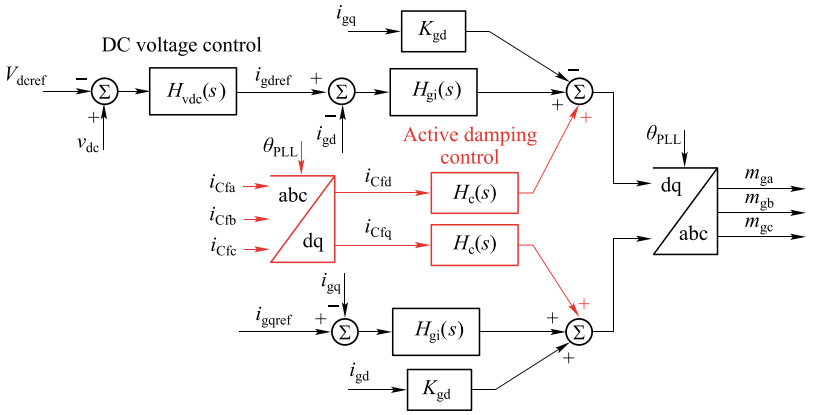

(b) Block diagram of GSC control

Fig. 15.17 Control structure of DFIG-based wind turbines considering impedance reshaping

of DC voltage loop and GSC AC current loop leads to capacitive negative damping characteristics in this band. At the same time, the power loop provides a coupling path for RSC-GSC, further deepening the level of capacitive negative damping. In Band $\mathrm{II}_{\mathrm{DFIG}}$, GSC AC current control and DC voltage control parameters are optimized to eliminate capacitive negative damping characteristics.

15.2.1.3 Impedance Reshaping Design in Band $\mathrm{III}_{\mathrm{DFIG}}$

The impedance characteristics of DFIG-based wind turbine in Band $\mathrm{III}_{\mathrm{DFIG}}$ are dominated by the LC filter, and the negative damping is generated due to the frequency-band overlapping effect of time delay and LC filter. The impedance reshaping strategy of DFIG-based wind turbine in this band is the same as that of the PMSG-based wind turbine in Band $\mathrm{IV}_{\mathrm{PMSG}}$, that is, the active damping controller shown in Eq. (15.2) is used to achieve the phase compensation.

To sum up, the impedance reshaping principle for DFIG-based wind turbines can be summarized as follows:

1. Band $\mathrm{I}_{\mathrm{DFIG}}$: the impedance reshaping strategy based on the combination of control parameter improvement and virtual impedance control is adopted. The inductive negative damping is eliminated by adding the virtual impedance controller $H_{\mathrm{d}}(s)$.
2. Band $\mathrm{II}_{\mathrm{DFIG}}$: the impedance reshaping strategy based on GSC AC current control and DC voltage control parameter optimization is adopted to improve the negative damping characteristics.
3. Band $\mathrm{III}_{\mathrm{DFIG}}$: the active damping control strategy based on filter capacitor current feedforward is adopted to achieve impedance reshaping, and the negative damping characteristics are improved by reasonably choosing the damping coefficient. The working frequency band of active damping is adjusted by reasonably choosing the active damping cut-off frequency to avoid affecting the impedance characteristics in other frequency bands.

15.2.2 Reshaped Impedance Model

On the basis of the small-signal model of DFIG-based wind turbine in Chap. 7, adding GSC active damping control and RSC virtual impedance control, the impedance model of DFIG-based wind turbine considering impedance reshaping is established in this section.

As shown in Fig. 15.17, the small-signal vectors of GSC d- and q-axis modulation signals $\hat{\boldsymbol{m}}_{\mathrm{gd}}$, $\hat{\boldsymbol{m}}_{\mathrm{gq}}$ are expressed as

$$\begin{cases} \hat{\boldsymbol{m}}_{\mathrm{gd}} = \left[H_{\mathrm{vdc}}(s_1)\hat{\boldsymbol{v}}_{\mathrm{dc}} - \hat{\boldsymbol{i}}_{\mathrm{gd}}\right]H_{\mathrm{gi}}(s_1) - K_{\mathrm{gd}}\hat{\boldsymbol{i}}_{\mathrm{gq}} + H_{\mathrm{c}}(s_1)\hat{\boldsymbol{i}}_{\mathrm{Cfd}} \\ \hat{\boldsymbol{m}}_{\mathrm{gq}} = -H_{\mathrm{gi}}(s_1)\hat{\boldsymbol{i}}_{\mathrm{gq}} + K_{\mathrm{gd}}\hat{\boldsymbol{i}}_{\mathrm{gd}} + H_{\mathrm{c}}(s_1)\hat{\boldsymbol{i}}_{\mathrm{Cfq}} \end{cases} \tag{15.8}$$

Transform $\hat{\boldsymbol{m}}_{\mathrm{gd}}$, $\hat{\boldsymbol{m}}_{\mathrm{gq}}$ to the SCF through inverse Park transformation, the small-signal vector of GSC modulation signal can be obtained as

$$\hat{\boldsymbol{m}}_{\mathrm{ga}} = \boldsymbol{E}_{\mathrm{dc}} \cdot \hat{\boldsymbol{v}}_{\mathrm{dc}} + \boldsymbol{E}_{\mathrm{gi}} \cdot \hat{\boldsymbol{i}}_{\mathrm{ga}} + (\boldsymbol{E}_{\mathrm{gv}} + \Delta\boldsymbol{E}_{\mathrm{gv}}) \cdot \hat{\boldsymbol{v}}_{\mathrm{a}} \tag{15.9}$$

where $\Delta\boldsymbol{E}_{\mathrm{gv}}$ is the coefficient matrix introduced by the impedance reshaping strategy; other coefficient matrices can refer to Chap. 7. The expression of $\Delta\boldsymbol{E}_{\mathrm{gv}}$ can be

expressed as

$$\Delta \boldsymbol{E}_{\mathrm{gv}} = \begin{bmatrix} H_{\mathrm{c}}(s_1)[C_{\mathrm{f}}s_2 - T_{\mathrm{PLL}}(s_1)\boldsymbol{I}^*_{\mathrm{Cf1}}] & 0 & H_{\mathrm{c}}(s_1)T_{\mathrm{PLL}}(s_1)\boldsymbol{I}^*_{\mathrm{Cf1}} & 0\ 0 \\ 0 & 0 & 0 & 0\ 0 \\ H_{\mathrm{c}}(s_1)T_{\mathrm{PLL}}(s_1)\boldsymbol{I}_{\mathrm{Cf1}} & 0 & H_{\mathrm{c}}(s_1)[C_{\mathrm{f}}s - T_{\mathrm{PLL}}(s_1)\boldsymbol{I}_{\mathrm{Cf1}}] & 0\ 0 \\ 0 & 0 & 0 & 0\ 0 \\ 0 & 0 & 0 & 0\ 0 \end{bmatrix}$$

Therefore, the small-signal model of GSC can be obtained as

$$\hat{\boldsymbol{v}}_{\mathrm{a}} = \boldsymbol{F}'_{\mathrm{dc}}\hat{\boldsymbol{v}}_{\mathrm{dc}} + \boldsymbol{F}'_{\mathrm{gi}}\hat{\boldsymbol{i}}_{\mathrm{ga}} \tag{15.10}$$

where $\boldsymbol{F}'_{\mathrm{dc}}$ and $\boldsymbol{F}'_{\mathrm{gi}}$ are the voltage coefficient matrices of GSC after impedance reshaping, and their expression are

$$\begin{cases} \boldsymbol{F}'_{\mathrm{dc}} = \left[\boldsymbol{U} - K_{\mathrm{m}}V_{\mathrm{dc}}(\boldsymbol{E}_{\mathrm{gv}} + \Delta\boldsymbol{E}_{\mathrm{gv}})\right]^{-1}(K_{\mathrm{m}}\boldsymbol{M}_{\mathrm{ga}} + K_{\mathrm{m}}V_{\mathrm{dc}}\boldsymbol{E}_{\mathrm{dc}}) \\ \boldsymbol{F}'_{\mathrm{gi}} = \left[\boldsymbol{U} - K_{\mathrm{m}}V_{\mathrm{dc}}(\boldsymbol{E}_{\mathrm{gv}} + \Delta\boldsymbol{E}_{\mathrm{gv}})\right]^{-1}(K_{\mathrm{m}}V_{\mathrm{dc}}\boldsymbol{E}_{\mathrm{gi}} - \boldsymbol{Z}_{\mathrm{f}}) \end{cases}$$

The small-signal vectors of RSC d- and q-axis modulation signals $\hat{\boldsymbol{m}}_{\mathrm{rd}}$, $\hat{\boldsymbol{m}}_{\mathrm{rq}}$ can be expressed as

$$\begin{cases} \hat{\boldsymbol{m}}_{\mathrm{rd}} = H_{\mathrm{ri}}(s_1)\left[-\dfrac{1}{1-s_{\mathrm{n}}}H_{\mathrm{p}}(s_1)\hat{\boldsymbol{p}}_{\mathrm{e}} - K_{\mathrm{e}}\hat{\boldsymbol{i}}_{\mathrm{rd}}\right] - K_{\mathrm{rd}}K_{\mathrm{e}}\hat{\boldsymbol{i}}_{\mathrm{rq}} + H_{\mathrm{d}}(s_1)\hat{\boldsymbol{i}}_{\mathrm{rd}} \\ \hat{\boldsymbol{m}}_{\mathrm{rq}} = H_{\mathrm{ri}}(s_1)\left[-H_{\mathrm{q}}(s_1)\hat{\boldsymbol{q}}_{\mathrm{e}} - K_{\mathrm{e}}\hat{\boldsymbol{i}}_{\mathrm{rq}}\right] + K_{\mathrm{rd}}K_{\mathrm{e}}\hat{\boldsymbol{i}}_{\mathrm{rd}} + H_{\mathrm{d}}(s_1)\hat{\boldsymbol{i}}_{\mathrm{rq}} \end{cases} \tag{15.11}$$

By transforming $\hat{\boldsymbol{m}}_{\mathrm{rd}}$, $\hat{\boldsymbol{m}}_{\mathrm{rq}}$ to the SCF through inverse Park transformation, the small-signal vector of the RSC modulation signal can be obtained as

$$\hat{\boldsymbol{m}}_{\mathrm{ra}} = \boldsymbol{E}_{\mathrm{rgi}}\hat{\boldsymbol{i}}_{\mathrm{ga}} + \boldsymbol{E}_{\mathrm{rsi}}\hat{\boldsymbol{i}}_{\mathrm{sa}} + (\boldsymbol{E}_{\mathrm{rri}} + \Delta\boldsymbol{E}_{\mathrm{rri}})\hat{\boldsymbol{i}}_{\mathrm{ra}} + (\boldsymbol{E}_{\mathrm{rv}} + \Delta\boldsymbol{E}_{\mathrm{rv}})\hat{\boldsymbol{v}}_{\mathrm{a}} \tag{15.12}$$

where $\Delta\boldsymbol{E}_{\mathrm{rri}}$, $\Delta\boldsymbol{E}_{\mathrm{rv}}$ are the coefficient matrix introduced by the impedance reshaping strategy respectively; other coefficient matrices can refer to Chap. 7. $\Delta\boldsymbol{E}_{\mathrm{rri}}$, $\Delta\boldsymbol{E}_{\mathrm{rv}}$ are fifth-order matrices; all other elements in the matrices are zero except for the following

$$\begin{cases} \Delta\boldsymbol{E}_{\mathrm{rri}}(1,1) = K_{\mathrm{e}}H_{\mathrm{d}}(s_1) \\ \Delta\boldsymbol{E}_{\mathrm{rri}}(3,3) = K_{\mathrm{e}}H_{\mathrm{d}}(s_1) \end{cases} \tag{15.13}$$

$$\begin{cases} \Delta\boldsymbol{E}_{\mathrm{rv}}(1,1) = -K_{\mathrm{e}}H_{\mathrm{d}}(s_1)T_{\mathrm{PLL}}(s_1)\boldsymbol{I}^*_{\mathrm{rl}} \\ \Delta\boldsymbol{E}_{\mathrm{rv}}(1,3) = K_{\mathrm{e}}H_{\mathrm{d}}(s_1)T_{\mathrm{PLL}}(s_1)\boldsymbol{I}^*_{\mathrm{rl}} \\ \Delta\boldsymbol{E}_{\mathrm{rv}}(3,1) = K_{\mathrm{e}}H_{\mathrm{d}}(s_1)T_{\mathrm{PLL}}(s_1)\boldsymbol{I}_{\mathrm{rl}} \\ \Delta\boldsymbol{E}_{\mathrm{rv}}(3,3) = -K_{\mathrm{e}}H_{\mathrm{d}}(s_1)T_{\mathrm{PLL}}(s_1)\boldsymbol{I}_{\mathrm{rl}} \end{cases} \tag{15.14}$$

Therefore, the small-signal model of RSC can be obtained as

$$\hat{\boldsymbol{v}}_{\mathrm{ra}} = \boldsymbol{B}_{\mathrm{dc}}\hat{\boldsymbol{v}}_{\mathrm{dc}} + \boldsymbol{B}_{\mathrm{rgi}}\hat{\boldsymbol{i}}_{\mathrm{ga}} + \boldsymbol{B}_{\mathrm{rsi}}\hat{\boldsymbol{i}}_{\mathrm{sa}} + \boldsymbol{B}'_{\mathrm{rri}}\hat{\boldsymbol{i}}_{\mathrm{ra}} + \boldsymbol{B}'_{\mathrm{rv}}\hat{\boldsymbol{v}}_{\mathrm{a}} \tag{15.15}$$

where $\boldsymbol{B}'_{\mathrm{rri}}$, $\boldsymbol{B}'_{\mathrm{rv}}$ are the voltage coefficient matrices of RSC after impedance reshaping, and their expression are

$$\begin{cases} \boldsymbol{B}'_{\mathrm{rri}} = K_{\mathrm{e}}K_{\mathrm{m}}V_{\mathrm{dc}}(\boldsymbol{E}_{\mathrm{rri}} + \Delta\boldsymbol{E}_{\mathrm{rri}}) \\ \boldsymbol{B}'_{\mathrm{rv}} = K_{\mathrm{e}}K_{\mathrm{m}}V_{\mathrm{dc}}(\boldsymbol{E}_{\mathrm{rv}} + \Delta\boldsymbol{E}_{\mathrm{rv}}) \end{cases} \tag{15.16}$$

By substituting Eqs. (15.10) and (15.15) into the small-signal model ininto the small-signal model in Chap. 7, the analytical impedance model of DFIG-based wind turbine considering impedance reshaping strategy can be obtained.

15.2.3 Impedance Reshaping Design

Due to the frequency-band overlapping effect of multiple controllers, the impedance reshaping in Band $\mathrm{I}_{\mathrm{DFIG}}$ and $\mathrm{III}_{\mathrm{DFIG}}$ will affect the impedance characteristics in Band $\mathrm{II}_{\mathrm{DFIG}}$. In this section, impedance reshaping will be carried out in the order of Band $\mathrm{I}_{\mathrm{DFIG}}$, $\mathrm{III}_{\mathrm{DFIG}}$ and $\mathrm{II}_{\mathrm{DFIG}}$.

First, for the inductive negative damping in Band $\mathrm{I}_{\mathrm{DFIG}}$, virtual impedance control is introduced to RSC. The center angle frequency ω_{d0} and bandwidth B_{d} of the bandpass filter are chosen according to the frequency range of negative damping in this band. By reasonably choosing the virtual impedance coefficient, the inductive negative damping in the first half of Band $\mathrm{I}_{\mathrm{DFIG}}$ is eliminated. Then, by optimizing the parameters of active power control, RSC AC current control and PLL, the impedance characteristics in the second half of Band $\mathrm{I}_{\mathrm{DFIG}}$ are reshaped.

Then, for the negative damping in Band $\mathrm{III}_{\mathrm{DFIG}}$, active damping control is introduced to GSC. By reasonably choosing the active damping coefficient, the impedance is reshaped and the negative damping is eliminated in this band.

Finally, for the negative damping in Band $\mathrm{II}_{\mathrm{DFIG}}$, by optimizing the parameters of GSC AC current control and DC voltage control, the impedance is reshaped and the negative damping is eliminated in this band.

Taking a certain type of DFIG-based wind turbine as an example, the impedance characteristics before reshaping are shown in Fig. 15.18. As shown in the figure, negative damping characteristics exist in Band $\mathrm{I}_{\mathrm{DFIG}}$ and $\mathrm{II}_{\mathrm{DFIG}}$, which introduces potential oscillation risk to the system.

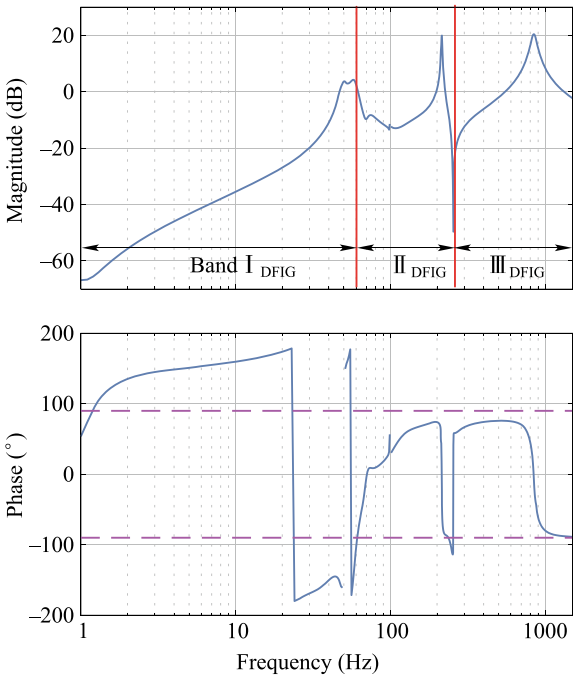

Fig. 15.18 Impedance characteristics of DFIG-based wind turbine before reshaping

15.2.3.1 Impedance Reshaping Design in Band I_{DFIG}

The impedance of DFIG-based wind turbine in Band I_{DFIG} is dominated by the stator impedance, and affected by power loop, RSC AC current loop and PLL, which results in inductive negative damping in the first half of Band I_{DFIG}. By reasonably choosing RSC AC current control parameters and introducing a virtual impedance controller $H_d(s)$, the inductive negative damping in this Band is eliminated. At the same time, affected by PLL parameters, in the second half of Band I_{DFIG}, the impedance characteristics will change from inductive to capacitive negative damping characteristics. By reasonably optimizing the parameters of active power control and PLL, the capacitive negative damping is eliminated.

The influence of RSC current loop on impedance characteristics is shown in Fig. 15.19. On the one hand, the influence of RSC AC current loop bandwidth can be obtained by changing f_{ric} to 5, 15 and 30 Hz respectively with a constant PM of 45°. On the other hand, the influence of RSC AC current loop PM can be obtained by changing θ_{ric} to 10°, 45° and 80° respectively with a constant bandwidth of 15 Hz.

As shown in Fig. 15.19 with the increase of RSC AC current loop bandwidth f_{ric} and PM θ_{ric}, the frequency range of inductive negative damping increases. On the premise of ensuring RSC AC current fault ride-through performance, lower bandwidth and PM can reduce the frequency range of inductive negative damping in Band I_{DFIG}.

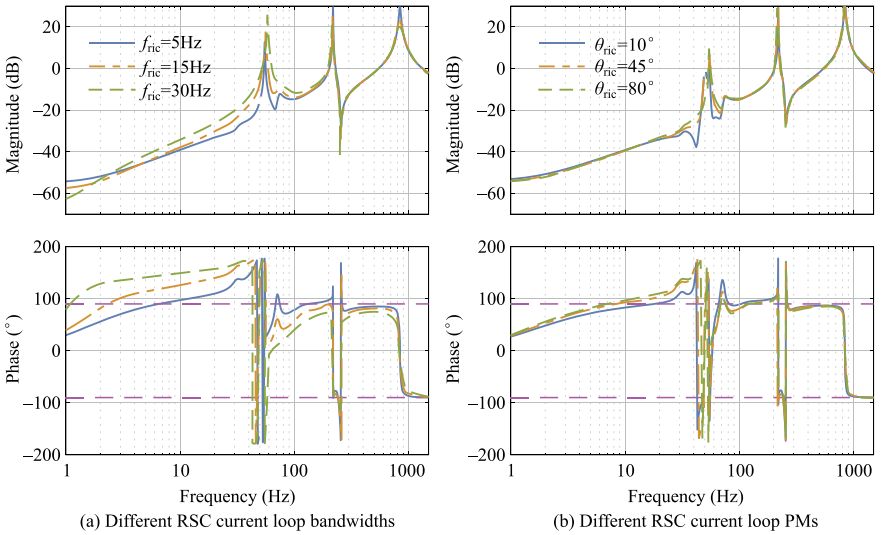

(a) Different RSC current loop bandwidths (b) Different RSC current loop PMs

Fig. 15.19 Influence of RSC current loop on damping characteristics in Band $\mathrm{I}_{\mathrm{DFIG}}$

The amplitude-frequency characteristics of the virtual impedance controller are shown in Fig. 15.20. By reasonably choosing the virtual impedance coefficient k_{d}, the center angular frequency ω_{d0} and bandwidth B_{d} of the bandpass filter, the inductive negative damping in the first half of Band $\mathrm{I}_{\mathrm{DFIG}}$ can be further eliminated. k_{d} can be calculated as

$$k_{\mathrm{d}} = K_{\mathrm{r}}\left(\frac{R_{\mathrm{r}}}{K_{\mathrm{m}} V_{\mathrm{dc}}} + K_{\mathrm{rip}}\right) \tag{15.17}$$

where K_{r} is the virtual impedance gain.

With RSC AC current loop bandwidth f_{ric} of 10 Hz and PM θ_{ric} of 20°, different virtual impedance gains are chosen to achieve impedance reshaping in the first half of Band $\mathrm{I}_{\mathrm{DFIG}}$, as shown in Fig. 15.21. In the figure, the virtual impedance gain K_{r} is increased from 0 to 6.

As shown in Fig. 15.21, the damping characteristics in Band $\mathrm{I}_{\mathrm{DFIG}}$ are eliminated by adding the virtual impedance controller $H_{\mathrm{d}}(s)$. In addition, with the increase of K_{r}, the virtual impedance control will affect the impedance characteristics in Band $\mathrm{II}_{\mathrm{DFIG}}$. So it needs to consider the damping characteristics both in Band $\mathrm{I}_{\mathrm{DFIG}}$ and $\mathrm{II}_{\mathrm{DFIG}}$.

For the capacitive negative damping in the second half of Band $\mathrm{I}_{\mathrm{DFIG}}$, it can be eliminated by reasonably choosing the parameters of active power control and PLL.

The influence of active power loop on damping characteristics in the second half of Band $\mathrm{I}_{\mathrm{DFIG}}$ is shown in Fig. 15.22. On the one hand, the influence of active power loop bandwidth can be obtained by setting f_{pc} to 0.1, 1 and 10 Hz respectively with a constant PM of 135°. On the other hand, the influence of active power loop PM

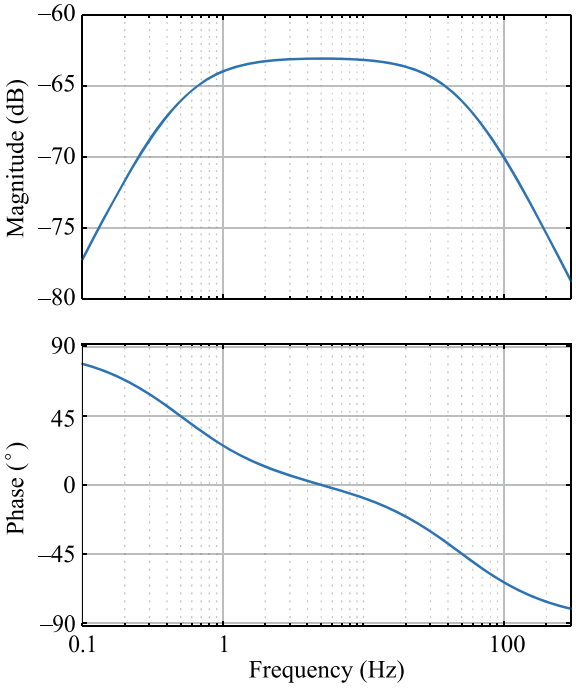

Fig. 15.20 Amplitude-frequency characteristics of the virtual impedance controller

can be obtained by setting θ_{pc} to 100°, 135° and 170° respectively with a constant bandwidth of 1 Hz.

As shown in Fig. 15.22, with the increase of the active power loop bandwidth f_{pc} and PM θ_{pc}, the negative damping characteristics in the second half of Band I_{DFIG} are improved. Therefore, higher active power control bandwidth and PM can be adopted on the premise of ensuring fault ride-through performance.

With active power loop bandwidth f_{pc} of 1 Hz and PM θ_{pc} of 170°, the influence of PLL on the damping characteristics in Band I_{DFIG} is shown in Fig. 15.23. On the one hand, the influence of PLL bandwidth can be obtained by setting f_{tc} to 5, 10 and 20 Hz respectively with a constant PM of 45°. On the other hand, the influence of PLL PM can be obtained by setting θ_{tc} to 10°, 45° and 80° respectively with a constant bandwidth of 5 Hz.

As shown in Fig. 15.23, with the decrease of PLL bandwidth f_{tc} and PM θ_{pc}, the negative damping characteristics in the second half of Band I_{DFIG} can be improved. On the basis of ensuring PLL fault ride-through performance, lower PLL bandwidth and PM can be adopted.

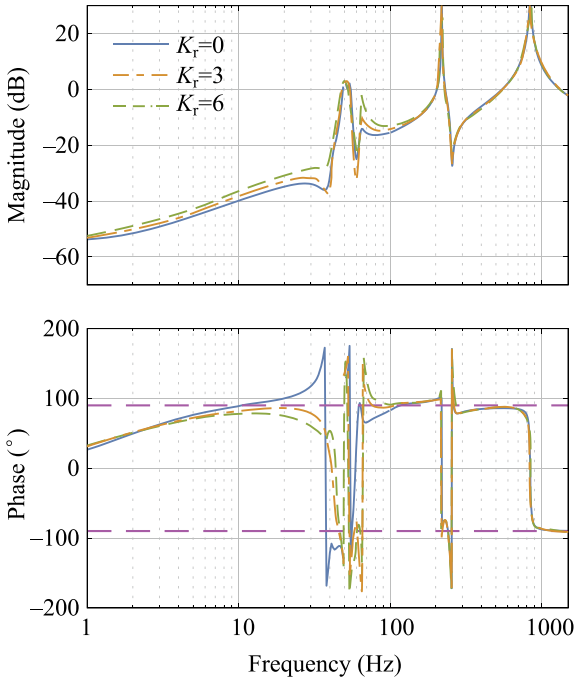

Fig. 15.21 Influence of the virtual impedance coefficient on damping characteristics in Band I_{DFIG}

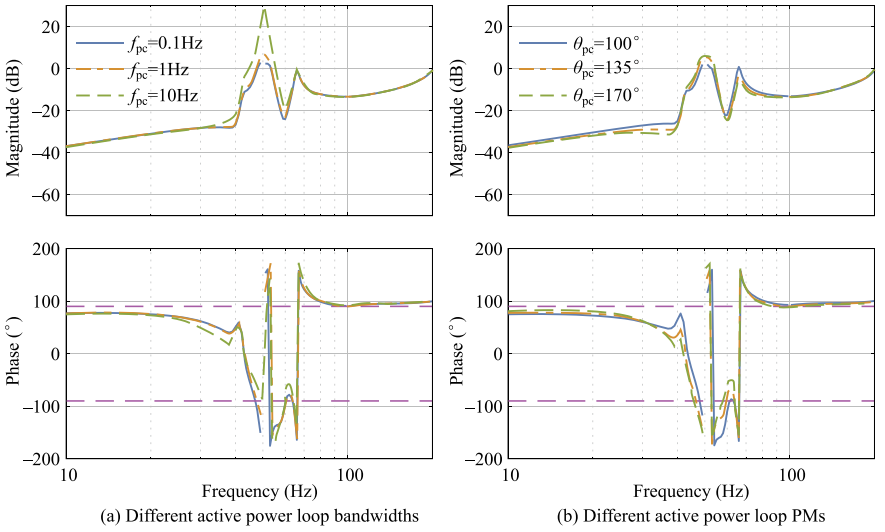

Fig. 15.22 Influence of active power loop on damping characteristics in the second half of Band I_{DFIG}

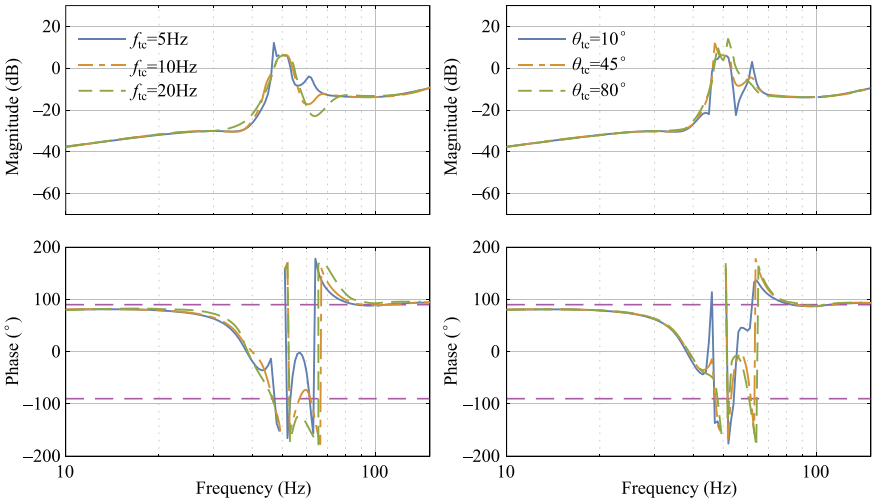

Fig. 15.23 Influence of PLL on damping characteristics in the second half of Band $\mathrm{I_{DFIG}}$

15.2.3.2 Impedance Reshaping Design in Band $\mathrm{III_{DFIG}}$

The impedance characteristics of DFIG-based wind turbines in Band $\mathrm{III_{DFIG}}$ are dominated by LC filter. When the time delay is large, the frequency-band overlapping effect of time delay and LC filter results in the capacitive negative damping characteristics in Band $\mathrm{III_{DFIG}}$. To reshape the impedance in Band $\mathrm{III_{DFIG}}$, the active damping controller $H_c(s)$ is introduced.

Different active damping coefficients k_c are chosen to realize the impedance reshaping in Band $\mathrm{III_{DFIG}}$, and the influence on damping characteristics is shown in Fig. 15.24. In the figure, k_c is reduced from 0 to −0.0006.

As shown in Fig. 15.24, the negative damping characteristics in Band $\mathrm{III_{DFIG}}$ $H_c(s)$.

15.2.3.3 Impedance Reshaping Design in Band $\mathrm{II_{DFIG}}$

The impedance of DFIG-based wind turbine is dominated by the stator impedance and affected by GSC AC current loop and DC voltage loop in Band $\mathrm{II_{DFIG}}$.

The influence of DC voltage loop on damping characteristics in Band $\mathrm{II_{DFIG}}$ is shown in Fig. 15.25. On the one hand, the influence of DC voltage loop bandwidth can be obtained by setting f_{vdc} to 30, 50 and 70 Hz respectively with a constant PM of $\theta_{vdc} = 45°$. On the other hand, the influence of DC voltage loop PM can be obtained by setting θ_{vdc} to 10°, 45° and 80° respectively with a constant bandwidth of 60 Hz.

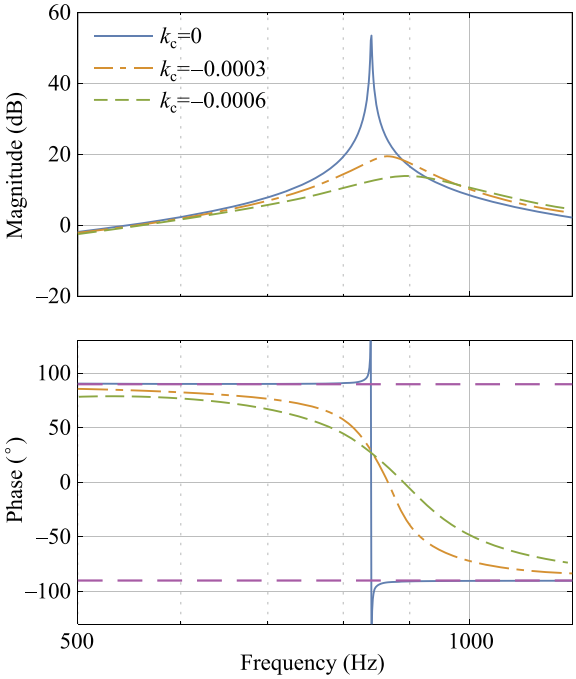

Fig. 15.24 Influence of time delay on damping characteristics in Band III_{DFIG}

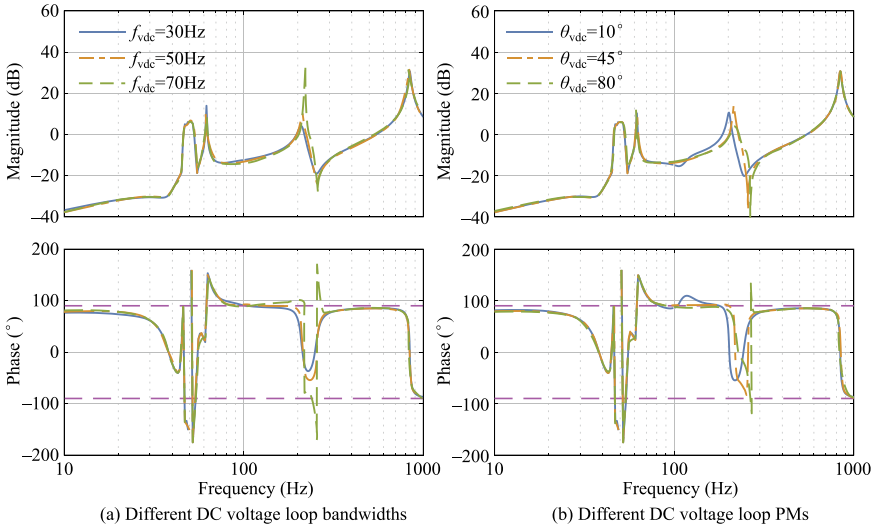

Fig. 15.25 Influence of DC voltage loop on damping characteristics in Band II_{DFIG}

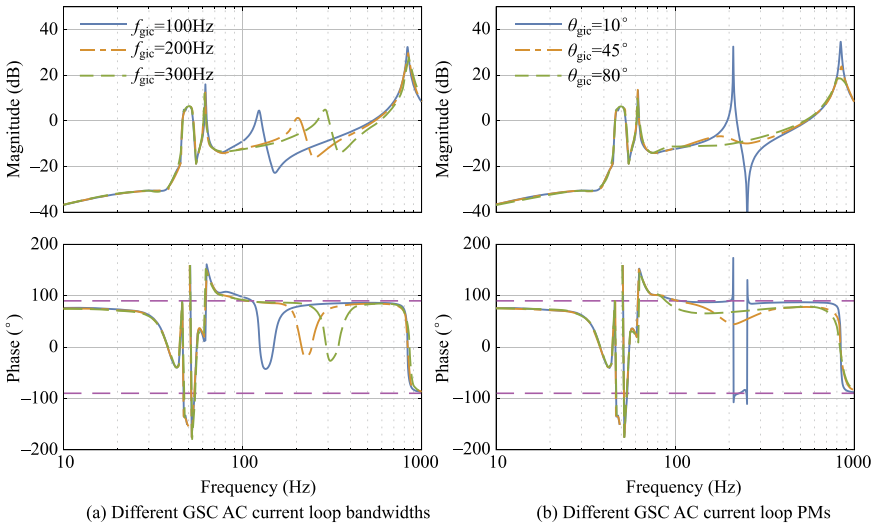

Fig. 15.26 Influence of GSC AC current loop on damping characteristics in Band II_{DFIG}

As shown in Fig. 15.25, with the decrease of DC voltage loop bandwidth f_{vdc} and PM θ_{vdc}, the negative damping characteristics in Band II_{DFIG} can be improved. On the basis of ensuring fault ride-through performance, lower DC voltage loop bandwidth and PM can be adopted.

With DC voltage loop bandwidth f_{vdc} of 30 Hz and PM θ_{vdc} of 30°, the influence of GSC AC current loop on damping characteristics in Band II_{DFIG} is shown in Fig. 15.26. On the one hand, the influence of GSC AC current loop bandwidth can be obtained by setting f_{gic} to 100, 200 and 300 Hz respectively with a constant PM of $\theta_{\text{gic}} = 20°$. On the other hand, the influence of GSC AC current loop PM can be obtained by setting θ_{gic} to 10°, 45° and 80° respectively with a constant bandwidth of 200 Hz.

As shown in Fig. 15.26, GSC AC current loop bandwidth f_{gic} mainly affects the frequency of the phase decrease near the resonant peak. With the increase of f_{gic}, the impedance becomes less capacitive. GSC AC current loop PM θ_{gic} mainly affects the level of the phase decrease near the resonant peak. With the increase of θ_{gic}, the impedance becomes less capacitive. Therefore, the negative damping characteristics in Band II_{DFIG} can be eliminated by increasing GSC AC current loop bandwidth and PM while ensuring the stability.

In summary, the impedance reshaping in the order of Band I_{DFIG}, III_{DFIG} and II_{DFIG} can effectively eliminate the negative damping of DFIG-based wind turbines, and the comparison of impedance characteristics before and after impedance reshaping is shown in Fig. 15.27.

The impedance of DFIG-based wind turbines is closely related to the steady-state operating point, and it needs to be verified under different operation conditions to ensure that the reshaped impedance characteristics meet the requirements of

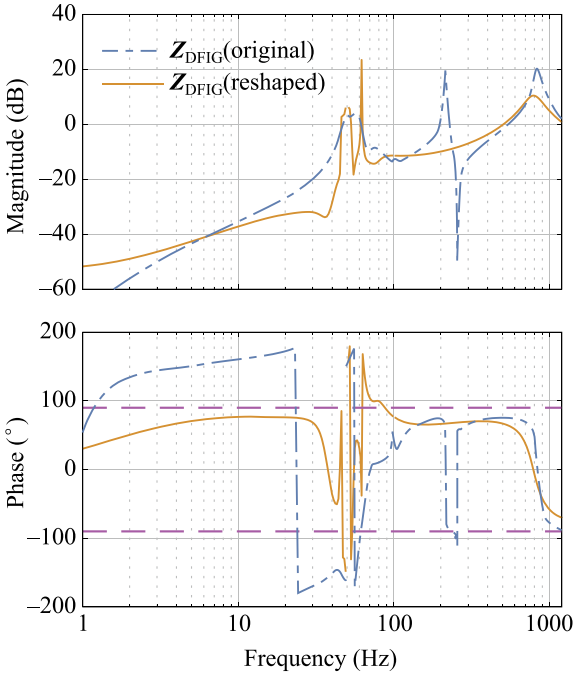

Fig. 15.27 Comparison of DFIG-based wind turbine impedance characteristics before and after impedance reshaping

multiple operation conditions. The three-dimensional Bode diagram of the reshaped impedance characteristics is shown in Fig. 15.28. In the figure, as the active power varies from 0.2 p.u. to 1 p.u., the negative damping characteristics are improved in the frequency range from 1 to 1000 Hz.

The flow chart of impedance reshaping for DFIG-based wind turbine is shown in Fig. 15.29.

15.2.4 Simulation Verification

Based on the full EMT simulation platform, taking the DFIG-based wind plant connected into AC grid with series capacitive compensators as an example, frequency-domain analysis and time-domain simulation of oscillation mitigation based on DFIG-based wind turbines impedance reshaping are carried out to verify the effectiveness of the impedance reshaping strategy mentioned above. The EMT simulation parameters of the DFIG-based wind plant are listed in Table 15.2. Figure 15.30 shows the evaluation results of oscillation risk for the DFIG-based wind plant connected into AC grid with series capacitive compensators before and after impedance reshaping.

As seen from Fig. 15.30(a), the magnitude curves of the DFIG-based wind plant impedance $\boldsymbol{Z}_{\mathrm{DFIG}}$ and AC grid impedance $\boldsymbol{Z}_{\mathrm{g}}$ intersect at Point A (5 Hz) and the PM

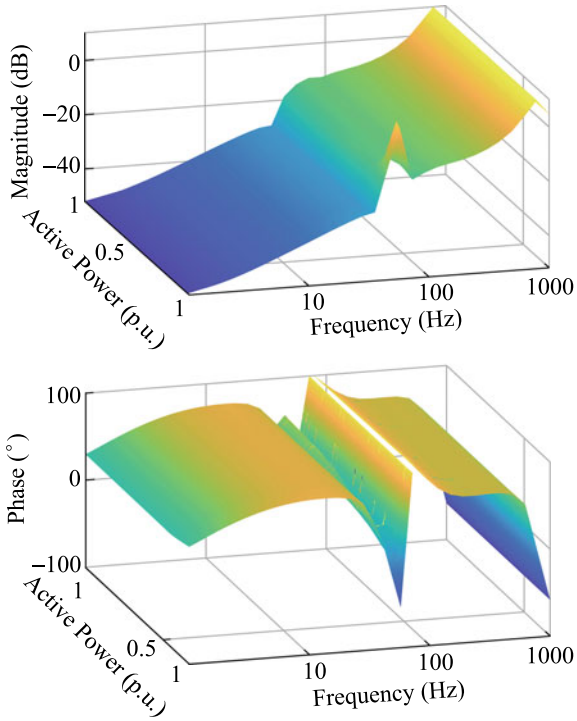

Fig. 15.28 Three-dimensional Bode diagram of the reshaped DFIG-based wind turbine impedance characteristics

is 0.3°. The GM/PM is insufficient, indicating oscillation risk in the system. After the impedance reshaping, the intersection point of the magnitude curves shifts from Point A to Point B (5 Hz), and the PM is increased to 19.4°. The stability margin is thus improved and the oscillation risk is eliminated.

As seen from Fig. 15.30(b), the original Nyquist curve around Point A (5 Hz) is in the forbidden area, indicating oscillation risk. After the impedance reshaping, the optimized Nyquist curve is outside the forbidden area, indicating that the impedance reshaping of DFIG-based wind turbine effectively eliminates the oscillation risk of the system.

The time-domain simulation of DFIG-based wind plants connected into AC grid with series capacitive compensators is conducted based on the full EMT simulation platform. The current waveforms and FFT results of the DFIG-based wind plant before and after the impedance reshaping are shown in Fig. 15.31.

As seen from Fig. 15.31, initially, there is a sub-synchronous oscillation component at 5 Hz and a coupling sub-synchronous oscillation component at 95 Hz according to the FFT results of the currents. After the impedance reshaping of DFIG-based wind turbines is enabled at $t = 1$ s, the oscillation of the current waveforms is mitigated, and the sub-/super- synchronous oscillation components are eliminated as

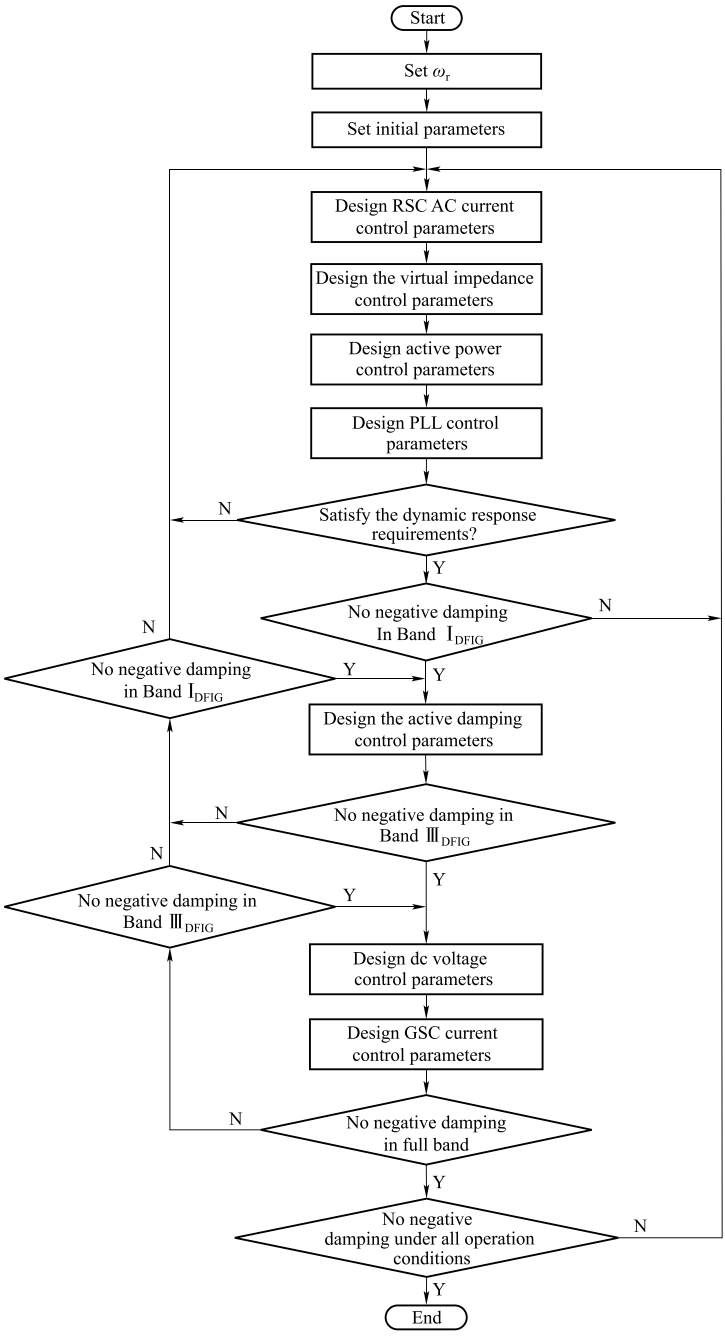

Fig. 15.29 Flow chart of impedance reshaping for DFIG-based wind turbine

Table 15.2 EMT simulation parameters of DFIG-based wind plant

Parameter	Definition	Value
N_{DFIG}	Number of DFIG-based wind turbines	100
P_{N}	Rated power	1.5 MW
V_N	Rated voltage	690 V
f_1	Rated frequency	50 Hz
k_{T}	Transformer voltage ratio	0.69/35 kV
R_{s}, R_{r}	Stator and rotor resistance	0.0022, 0.0027 Ω
$L_{1\mathrm{s}}$, $L_{1\mathrm{r}}$	Stator and rotor leakage inductance	1.4437×10^{-4}, 1.0913×10^{-4} H
L_{m}	Stator and rotor mutual inductance	0.0041 H
L_{f}	Filter inductance	0.7 mH
V_{dc}	DC voltage	1200 V
K_{e}	Turn ratio of stator and rotor windings	3
K_{pp}, K_{pi}	Proportional and integral coefficients of PLL controller	0.0144, 1.6922
K_{gip}, K_{gii}	Proportional and integral coefficients of GSC current controller	0.0012, 0.2559
K_{rip}, K_{rii}	Proportional and integral coefficients of RSC current controller	5.1286×10^{-5}, 0.0071×10^{-5}
K_{pep}, K_{pei}	Proportional and integral coefficients of active power controller	0.0012, 0.0013
K_{qep}, K_{qei}	Proportional and integral coefficients of reactive power controller	0.0012, 0.0013
K_{vdcp}, K_{vdci}	Proportional and integral coefficients of DC voltage controller	2.0075, 655.4064
K_{r}	Virtual admittance coefficient	5
ω_{d0}	Center angular frequency of the virtual admittance control	18.8496
B_{d}	Bandwidth of the the virtual admittance control	251.3274 ara>
k_{c}	Active damping coefficient	−0.0006
ω_{c1}, ω_{c2}	The lower and upper limits of the angular frequency for the active damping control	3.1416×10^3, 9.4248×10^3
K_{gd}	Decoupling coefficient of RSC current control	3.3×10^{-5}
K_{rd}	Decoupling coefficient of GSC current control	1.8744×10^{-4}

shown in the corresponding FFT analysis. The simulation results verify the effectiveness of oscillation mitigation strategy based on the proposed impedance reshaping of DFIG-based wind turbines.

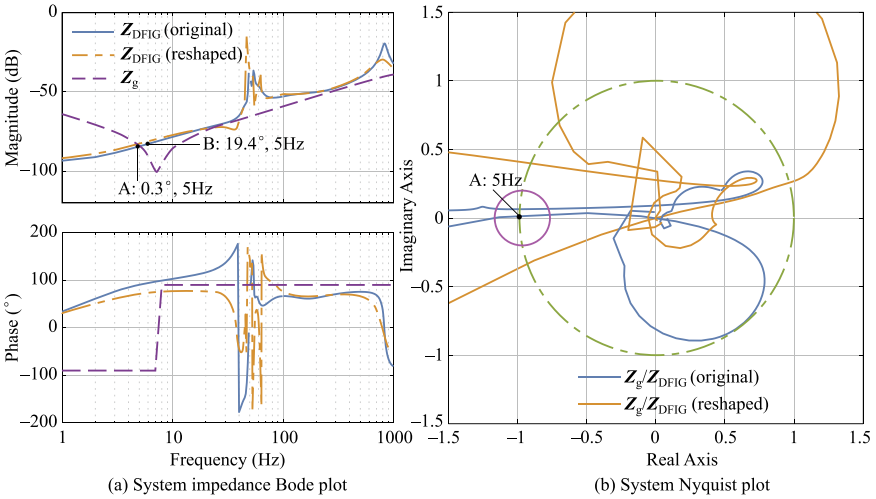

Fig. 15.30 The evaluation results of oscillation risk for the DFIG-based wind plant connected into AC grid with series capacitive compensators before and after impedance reshaping

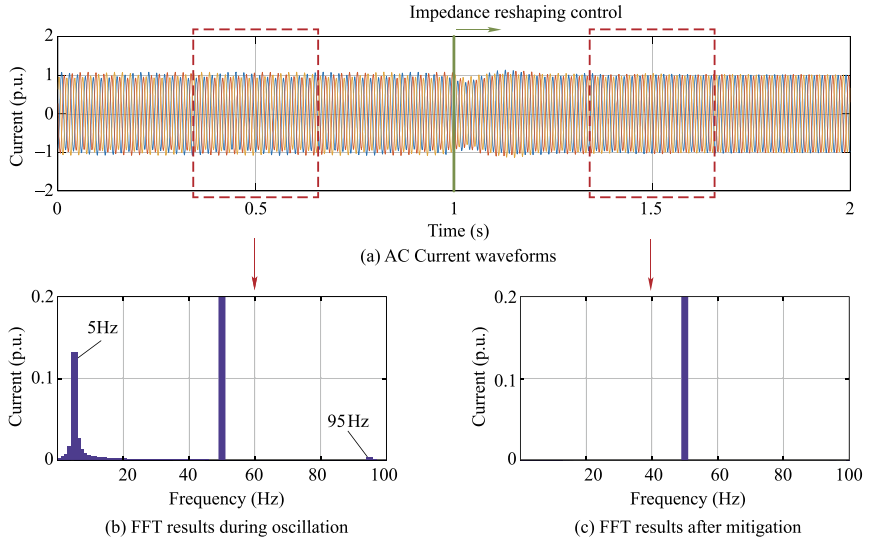

Fig. 15.31 The current waveforms and FFT results of the DFIG-based wind plant before and after impedance reshaping

15.2.5 Field Test Verification

Based on the test and experimental verification platform of REG and AC/DC transmission system, taking DFIG-based wind turbine connected to weak AC grid as an

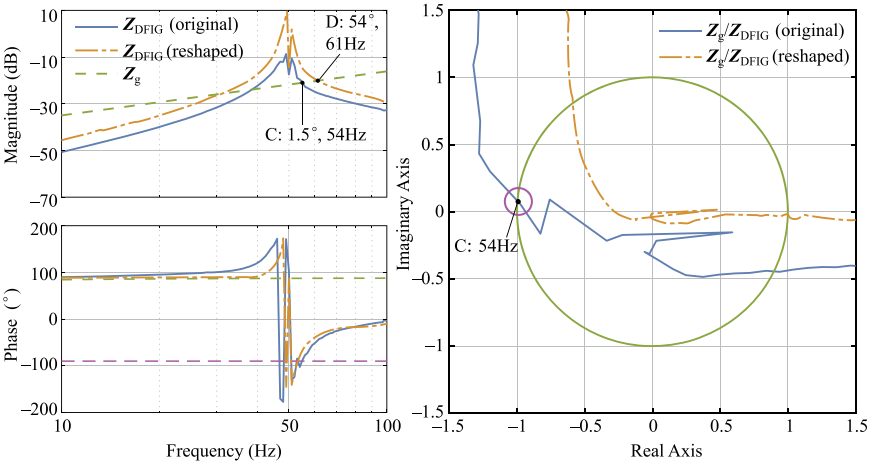

(a) System impedance Bode plot (b) System Nyquist plot

Fig. 15.32 The oscillation risk analysis of the DFIG-based wind turbine connected into weak AC grid

example, the field test of oscillation mitigation was carried out to verify the effectiveness of the impedance reshaping strategy. The system structure and parameters are the same as Sect. 13.4. The oscillation risk analysis of the DFIG-based wind turbine connected into weak AC grid is shown in Fig. 15.32.

As seen from Fig. 15.32(a), the magnitude curves of the DFIG-based wind turbine impedance $\boldsymbol{Z}_{\text{DFIG}}$ and AC grid impedance $\boldsymbol{Z}_{\text{g}}$ intersect at Point C (55 Hz), and the PM is only 1.5° before the impedance reshaping. The GM/PM is insufficient, indicating oscillation risk in the system. After the impedance reshaping, the intersection point of the magnitude curves shifts from Point C to Point D (61 Hz), and the PM is increased to 54°. The stability margin is thus improved and the oscillation risk is eliminated.

As seen from Fig. 15.32(b), the original Nyquist curve around Point C (55 Hz) is in the forbidden area, indicating oscillation risk. After the impedance reshaping, the optimized Nyquist curve is outside the forbidden area, indicating that the impedance reshaping of the DFIG-based wind turbine effectively eliminates the oscillation risk of the system.

The field test of the DFIG-based wind turbine connected into weak AC grid is conducted and its result is shown in Fig. 15.33. In the figure, initially, there is a super-synchronous oscillation component at 54 Hz and a coupling sub-synchronous oscillation component at 46 Hz according to the FFT results of the currents. After the impedance reshaping of DFIG-based wind turbine is enabled at $t = 1$s, the oscillation of the currents is mitigated, and the sub-/super- synchronous oscillation components are eliminated as shown in the corresponding FFT analysis. The field test results verify the effectiveness of oscillation mitigation strategy based on the proposed impedance reshaping of DFIG-based wind turbines.

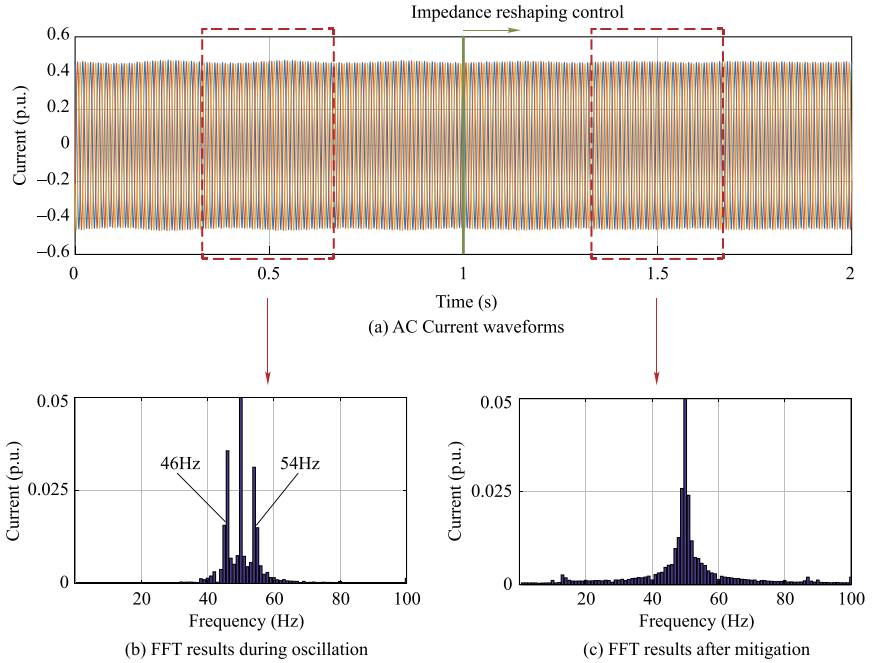

Fig. 15.33 The field test result of DFIG-based wind turbines connected into weak AC grid

References

1. WANG X F, BLAABJERG F, LOH P C. Passivity-based stability analysis and damping injection for multiparalleled VSCs with LCL filters [J]. IEEE Transactions on Power Electronics, 32(11): 8922–8935.
2. WANG X F, LI Y W, BLAABJERG F, et al. Virtual-impedance-based control for voltage-source and current-source converters [J]. IEEE Transactions on Power Electronics, 2015, 30(12): 7019–7037.
3. WANG X F, BLAABJERG F, LISERRE M, et al. An active damper for stabilizing power-electronics-based AC systems [J]. IEEE Transactions on Power Electronics, 2014, 29(7): 3318–3329.
4. LI G H, WANG W S, LIU C, et al. Mechanism analysis and suppression method of wideband oscillation of PMSG wind farms connected to weak grid (Part II): suppression method of wide-band oscillation based on impedance reshaping [J]. Proceedings of the CSEE, 2019, 39(23): 6908–6920+7104. (Chinese)
5. HE G Q, WANG W S, WANG H J. Coordination control method for multi-wind farm systems to prevent sub/super- synchronous oscillations [J/OL]. CSEE Journal of Power and Energy Systems, [2022–11–20]. https://ieeexplore.ieee.org/document/9606953/.
6. WANG H J, LIU C. Active control strategy for wind farm systems to prevent sub/super-synchronous oscillations: 2021 3rd Asia Energy and Electrical Engineering Symposium (AEEES), Chengdu, China, March 26–29, 2021 [C]. Piscataway, NJ: IEEE, 2021.

Chapter 16
Oscillation Mitigation Based on the Impedance Reshaping of SVG

In Chap. 15, the impedance reshaping of REG units based on control strategy improvement and control parameter optimization is proposed to mitigate the broadband oscillation of REG plants. Since REG plants contain plenty of units, including PV units, PMSG- and DFIG-based wind turbines from different manufacturers, there are some difficulties in implementing the impedance reshaping of the REG units. The impedance reshaping of SVG in the plants can also be utilized to achieve the broadband impedance reshaping and oscillation mitigation of the REG plants.

The impedance reshaping of REG plants in each frequency band. This chapter first proposes SVG's broadband impedance reshaping strategy based on voltage feedforward control and active damping control for PMSG-based wind plants. For DFIG-based wind plants, the broadband impedance reshaping strategy of SVG combining two types of voltage feedforward control and active damping control is proposed. Then, the control parameter optimization of the proposed strategy of SVG is carried out to mitigate the negative damping characteristics of REG plants in different frequency bands. Finally, the oscillation mitigation strategy is verified based on the full EMT simulation platform for a REG connected into AC grid system.

16.1 Impedance Reshaping of PMSG-Based Wind Plants

According to the analysis of the impedance characteristics of REG plants, the negative damping characteristics of PMSG-based wind plants and PV plants are generally the same. PMSG-based wind plants are taken as an example in this section, and the impedance reshaping and oscillation mitigation of PMSG-based wind plants is achieved by optimizing the impedance characteristics of SVG in the plants.

© China Electric Power Press 2023

W. Wang et al., *Analysis and Mitigation of Broadband Oscillation in Renewable Energy Generation and AC/DC Transmission Systems*,
https://doi.org/10.1007/978-981-99-1568-2_16

16.1.1 Impedance Reshaping Strategy of SVG

Figure 16.1 shows the impedance characteristics of a PMSG-based wind plant in the frequency range of 1~2000Hz. $\boldsymbol{Z}_{\mathrm{WF}}$ is the impedance of the wind plant. As seen from the figure, the negative damping characteristics of the wind plant impedance may occur in Band $\mathrm{II}_{\mathrm{PMSG}}$, $\mathrm{III}_{\mathrm{PMSG}}$ and $\mathrm{IV}_{\mathrm{PMSG}}$.

According to Chap. 15, the negative damping characteristics of PMSG-based wind plants in Band $\mathrm{II}_{\mathrm{PMSG}}$ are eliminated by the optimization of PLL. Since PLL is used in both PMSG-based wind units and SVG, the optimization of the impedance characteristics in this frequency band can be referred to Chap. 15, which is not expounded in this section. In view of the negative damping characteristics of the wind plants in Band $\mathrm{III}_{\mathrm{PMSG}}$ and $\mathrm{IV}_{\mathrm{PMSG}}$, this section will utilize the impedance reshaping of SVG based on control strategy improvement to optimize the impedance characteristics of the wind plants.

According to Chap. 9, the impedance characteristics of SVG under reactive power control mode in Band $\mathrm{III}_{\mathrm{PMSG}}$ and $\mathrm{IV}_{\mathrm{PMSG}}$ are consistent with those under AC voltage control mode. Therefore, the reactive power control mode is taken as an example for analysis. The impedance reshaping strategy based on voltage feedforward control and active damping control is introduced to achieve impedance reshaping in Band $\mathrm{III}_{\mathrm{PMSG}}$ and $\mathrm{IV}_{\mathrm{PMSG}}$. The main circuit and control diagram of SVG considering the impedance reshaping of PMSG-based wind plants are shown in Fig. 16.2.

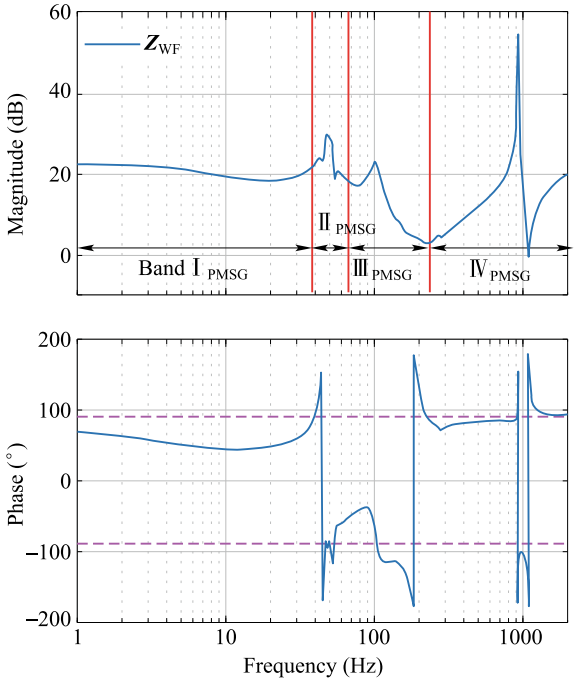

Fig. 16.1 The impedance characteristics of a PMSG-based wind plant

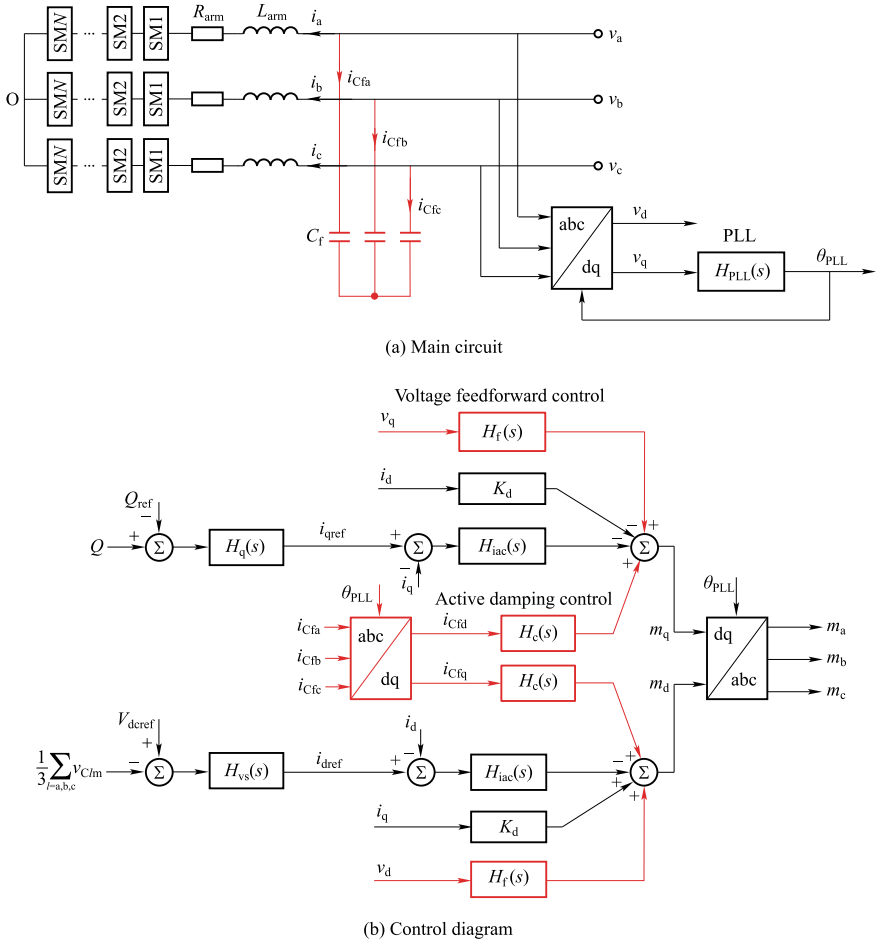

Fig. 16.2 The main circuit and control diagram of SVG considering the impedance reshaping of PMSG-based wind plants

16.1.1.1 Impedance Reshaping Method in Band $\mathrm{III}_{\mathrm{PMSG}}$

The voltage feedforward control shown in Fig. 16.2 is utilized to eliminate the negative damping characteristics of the PMSG-based wind plants in Band $\mathrm{III}_{\mathrm{PMSG}}$. Specifically, the outputs of voltage feedforward controllers $H_{\mathrm{f}}(s)$ are superimposed to the d- and q-axis modulation signals m_{d}, m_{q} respectively, after the controllers receive the d- and q-axis voltages v_{d}, v_{q}.

In order to reduce the influence of the voltage feedforward controller on the impedance characteristics in other frequency bands, a band-pass filter is adopted in the voltage feedforward controller, and the expression is

$$H_{\mathrm{f}}(s) = \left(k_{\mathrm{f}} \frac{Q_{\mathrm{f}}^{-1} \omega_{\mathrm{f0}} s}{s^2 + Q_{\mathrm{f}}^{-1} \omega_{\mathrm{f0}} s + \omega_{\mathrm{f0}}^2} \right)^* \tag{16.1}$$

where k_{f} is the voltage feedforward coefficient and can be designed to adjust the impedance characteristics in Band $\mathrm{III}_{\mathrm{PMSG}}$. ω_{f0} and Q_{f} are the center angular frequency and quality factor of the band-pass filter in the voltage feedforward control respectively. The value of ω_{f0} is designed to adjust the center frequency of the voltage feedforward controller $H_{\mathrm{f}}(s)$, and the value of Q_{f} is designed to adjust the working frequency range of $H_{\mathrm{f}}(s)$, covering the negative damping frequency range in Band $\mathrm{III}_{\mathrm{PMSG}}$.

16.1.1.2 Impedance Reshaping Method in Band $\mathrm{IV}_{\mathrm{PMSG}}$

The active damping control shown in Fig. 16.2 is utilized to eliminate the negative damping characteristics of the PMSG-based wind plants in Band $\mathrm{IV}_{\mathrm{PMSG}}$. First, additional AC filter capacitors are required in parallel to the AC port of SVG. Then, the capacitor currents can be introduced in a feedforward path for the proposed active damping control. Finally, the outputs of active damping controllers $H_{\mathrm{c}}(s)$ are superimposed to m_{d}, m_{q} respectively, after the controllers receive the d- and q-axis components i_{Cfd}, i_{Cfq} of the capacitor currents. The impedance phase in Band $\mathrm{IV}_{\mathrm{PMSG}}$ can thus be compensated.

In order to reduce the influence of the active damping controller on the impedance characteristics in other frequency bands, the band-pass filter shown in Eq. (16.1) can be also adopted in the active damping controller. Its expression is restated as Eq. (16.2) due to different parameter values.

$$H_{\mathrm{c}}(s) = \left(k_{\mathrm{c}} \frac{Q_{\mathrm{c}}^{-1} \omega_{\mathrm{c0}} s}{s^2 + Q_{\mathrm{c}}^{-1} \omega_{\mathrm{c0}} s + \omega_{\mathrm{c0}}^2} \right)^* \tag{16.2}$$

where k_{c} is the active damping coefficient and can be designed to adjust the impedance characteristics in Band IVPMSG. ω_{c0} and Q_{c} are the center angular frequency and quality factor of the band-pass filter in the active damping control respectively. The value of ω_{c0} is designed to adjust the center frequency of the active damping controller $H_{\mathrm{c}}(s)$, and the value of Q_{c} Q_{c} is designed to adjust the working frequency range of $H_{\mathrm{c}}(s)$, covering the negative damping frequency range in Band $\mathrm{IV}_{\mathrm{PMSG}}$.

16.1.2 Reshaped Impedance Model of SVG

Based on the small-signal modeling of the control loops of SVG in reactive power control mode, with the voltage feedforward control and active damping control in Sect. 16.1.1, the small-signal vector of the AC modulation signal in phase a is given as

$$\hat{\boldsymbol{m}}_{\mathrm{a}} = \boldsymbol{G}_1\boldsymbol{D}_1\hat{\boldsymbol{i}}_{\mathrm{a}} + (\boldsymbol{G}_2 + \Delta\boldsymbol{G}_2)\boldsymbol{D}_2\hat{\boldsymbol{v}}_{\mathrm{a}} + \boldsymbol{G}_3\boldsymbol{D}_3\hat{\boldsymbol{v}}_{\mathrm{Cam}} \tag{16.3}$$

where $\Delta\boldsymbol{G}_2$ is the transfer function matrix introduced by the voltage feedforward control and active damping control, and all other elements in the matrix are zero except for Eq. (16.4). The expressions of the other matrices in Eq. (16.3) can be referred to Chap. 9.

$$\begin{cases} \Delta\boldsymbol{G}_2(2,2) = -T_{\mathrm{PLL}}[\mathrm{j}2\pi(f_{\mathrm{p}} - f_1)] \cdot \left[H_{\mathrm{f}}[\mathrm{j}2\pi(f_{\mathrm{p}} - f_1)] \cdot V_1 \right. \\ \qquad\qquad \left. + H_{\mathrm{c}}[\mathrm{j}2\pi(f_{\mathrm{p}} - f_1)] \cdot \boldsymbol{I}^*_{\mathrm{Cf1}}\right] + H_{\mathrm{f}}[\mathrm{j}2\pi(f_{\mathrm{p}} - f_1)] \\ \qquad\qquad + \mathrm{j}2\pi(f_{\mathrm{p}} - 2f_1)C_{\mathrm{f}} \cdot H_{\mathrm{c}}[\mathrm{j}2\pi(f_{\mathrm{p}} - f_1)] \\ \Delta\boldsymbol{G}_2(2,4) = T_{\mathrm{PLL}}[\mathrm{j}2\pi(f_{\mathrm{p}} - f_1)] \cdot \left[H_{\mathrm{f}}[\mathrm{j}2\pi(f_{\mathrm{p}} - f_1)] \cdot V_1 \right. \\ \qquad\qquad \left. + H_{\mathrm{c}}[\mathrm{j}2\pi(f_{\mathrm{p}} - f_1)] \cdot \boldsymbol{I}^*_{\mathrm{Cf1}}\right] \\ \Delta\boldsymbol{G}_2(4,2) = T_{\mathrm{PLL}}[\mathrm{j}2\pi(f_{\mathrm{p}} - f_1)] \cdot \left[H_{\mathrm{f}}[\mathrm{j}2\pi(f_{\mathrm{p}} - f_1)] \cdot V_1 \right. \\ \qquad\qquad \left. + H_{\mathrm{c}}[\mathrm{j}2\pi(f_{\mathrm{p}} - f_1)] \cdot \boldsymbol{I}_{\mathrm{Cf1}}\right] \\ \Delta\boldsymbol{G}_2(4,4) = -T_{\mathrm{PLL}}[\mathrm{j}2\pi(f_{\mathrm{p}} - f_1)] \cdot \left[H_{\mathrm{f}}[\mathrm{j}2\pi(f_{\mathrm{p}} - f_1)] \cdot V_1 \right. \\ \qquad\qquad \left. + H_{\mathrm{c}}[\mathrm{j}2\pi(f_{\mathrm{p}} - f_1)] \cdot \boldsymbol{I}_{\mathrm{Cf1}}\right] + H_{\mathrm{f}}[\mathrm{j}2\pi(f_{\mathrm{p}} - f_1)] \\ \qquad\qquad + \mathrm{j}2\pi\ f_{\mathrm{p}}C_{\mathrm{f}} \cdot H_{\mathrm{c}}[\mathrm{j}2\pi(f_{\mathrm{p}} - f_1)] \end{cases} \tag{16.4}$$

where $\boldsymbol{I}_{\mathrm{Cf1}}$ is the steady-state fundamental component of the AC currents of the filter capacitors.

By substituting Eq. (16.3) into the small-signal model of the main circuit in Chap. 9, the analytical impedance model of SVG with the impedance reshaping strategy can be derived. Furthermore, the impedance model of PMSG-based wind plants can be obtained after the analytical impedance model of SVG is substituted.

16.1.3 Impedance Reshaping Design

Based on the impedance reshaping strategy of SVG, the design of the impedance reshaping of PMSG-based wind plants in Band $\mathrm{III}_{\mathrm{PMSG}}$ and $\mathrm{IV}_{\mathrm{PMSG}}$ is performed successively to eliminate the negative damping characteristics. Since the impedance characteristics between adjacent frequency bands are influenced by each other, the control parameters of the proposed impedance reshaping strategy should be adjusted, which meets the requirements of the negative damping optimization in both two frequency bands.

16.1.3.1 Impedance Reshaping Design in Band $\mathrm{III}_{\mathrm{PMSG}}$

As shown in Fig. 16.1, the frequency range of the negative damping characteristics in Band $\mathrm{III}_{\mathrm{PMSG}}$ is approximately 100Hz in SCF, and the center frequency is around 200Hz in SCF. According to the results, the value of ω_{f0} is set as $2\pi \times 150$ (in SRF), and the value of Q_{f} is designed to let the voltage feedforward controller $H_{\mathrm{f}}(s)$ cover the frequency range of negative damping in Band $\mathrm{III}_{\mathrm{PMSG}}$. The amplitude-frequency and phase-frequency characteristics of $H_{\mathrm{f}}(s)$ are shown in Fig. 16.3. The value of k_{f} is set as 1.0 here for the analysis of the amplitude-frequency characteristics.

According to the impedance reshaping model in Sect. 16.1.2, the voltage feedforward controller $H_{\mathrm{f}}(s)$ is located in the denominator of the analytical impedance model. The influence of $H_{\mathrm{f}}(s)$ on the impedance characteristics of SVG is opposite to its amplitude-frequency and phase-frequency characteristics. By adopting $H_{\mathrm{f}}(s)$, the impedance magnitude of SVG in the specific range of Band $\mathrm{III}_{\mathrm{PMSG}}$ can be reduced, so that the impedance characteristics of PMSG- based wind plants can be dominated by SVG. Furthermore, the phase compensation of $H_{\mathrm{f}}(s)$ can contribute to the increase of the impedance phase below ω_{f0} and the decrease of the impedance phase above ω_{f0}. The negative damping characteristics of the PMSG-based wind plants in Band $\mathrm{III}_{\mathrm{PMSG}}$, such as Fig. 16.1, can thus be improved.

The value of the voltage feedforward coefficient k_{f} is refined to reshape the impedance curve in Band $\mathrm{III}_{\mathrm{PMSG}}$. With k_{f} equivalent to 0, 5×10^{-5}, and 1×10^{-4}, the

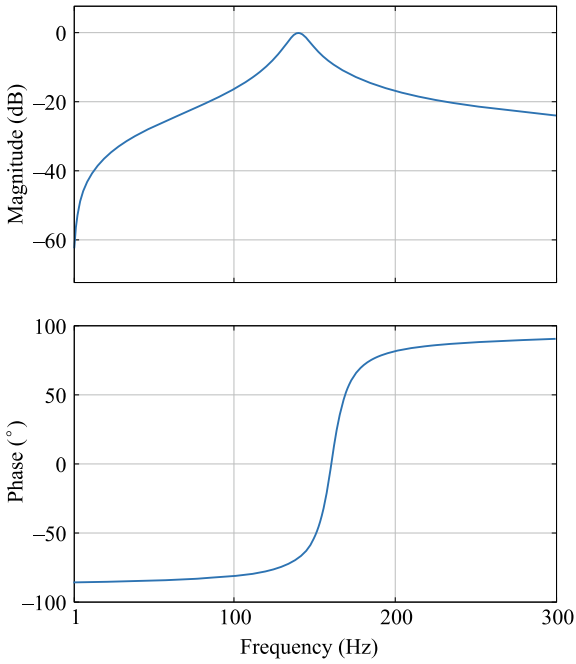

Fig. 16.3 The amplitude-frequency and phase-frequency characteristics of the voltage feedforward controller

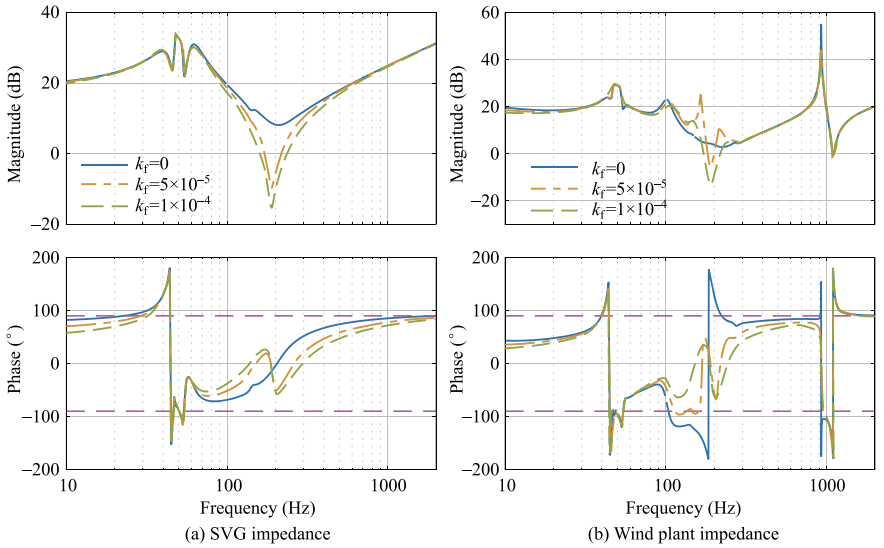

Fig. 16.4 The influence of the voltage feedforward coefficient on impedance characteristics of SVG and PMSG-based wind plants

variation of the impedance curves of SVG and PMSG-based wind plants is shown in Fig. 16.4.

As seen from Fig. 16.4, with the increase of k_f, the magnitude curve of SVG impedance decreases near 200 Hz (in Band III_{PMSG}), and the impedance phase increases below 200 Hz and decreases above 200 Hz. The impedance characteristics of the PMSG-based wind plants near 200 Hz are thus dominated by SVG. Besides, with the increase of k_f, the impedance magnitude of the wind plants near 200 Hz also decreases, and the capacitive negative damping (impedance phase below −90°) below 200 Hz and the inductive negative damping (impedance phase above 90°) above 200 Hz are gradually eliminated. Moreover, the voltage feedforward controller $H_f(s)$ has little influence on the impedance characteristics in the other frequency bands. The proposed voltage feedforward controller can effectively eliminate the negative damping characteristics of the PMSG-based wind plants in Band III_{PMSG}.

16.1.3.2 Impedance Reshaping Design in Band IV_{PMSG}

In order to achieve the impedance reshaping of the wind plants in Band IV_{PMSG}, additional AC filter capacitors are in parallel to the AC port of SVG. Figure 16.5 shows the influence of the shunt capacitor on the impedance characteristics of SVG and PMSG-based wind plants. The original impedance of the wind plants without the capacitor in Band VI_{PMSG} presents capacitive negative damping and inductive

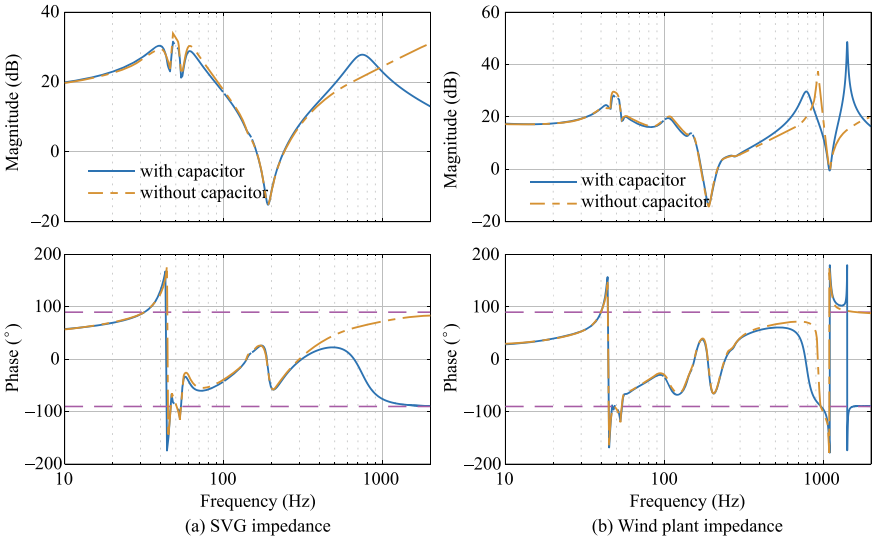

Fig. 16.5 The influence of shunt capacitor on impedance characteristics of SVG and PMSG-based wind plants

negative damping. With the shunt capacitor, the impedance characteristics of SVG in Band VI_{PMSG} change from inductive to capacitive. Correspondingly, the inductive negative damping of the wind plants in the high-frequency band becomes capacitive negative damping. Moreover, the shunt capacitor does not affect the frequency range of the negative damping in Band VI_{PMSG}.

After the filter capacitors are connected, the active damping control based on capacitor current feedforward can be used to optimize the impedance characteristics of the wind plants in Band VI_{PMSG}. Firstly, ω_{c0} and Q_{c} are designed for the active damping controller $H_{\text{c}}(s)$ covering the frequency range of negative damping in Band VI_{PMSG}. Then, impedance reshaping in this frequency band is achieved by optimizing the active damping coefficient k_{c}. With k_{c} equivalent to 0, -0.005 and -0.02, the variation of the impedance curves of SVG and PMSG-based wind plants is shown in Fig. 16.6.

As seen from Fig. 16.6, with the increase of k_{c}, the magnitude curve of SVG impedance in Band IV_{PMSG} decreases, and the impedance characteristics of the wind plants are dominated by SVG. The impedance phase of the wind plants below ω_{c0} increases, while the impedance phase above ω_{c0} decreases. As a result, the negative damping characteristics of the wind plants in Band IV_{PMSG} are gradually eliminated. Moreover, the active damping controller $H_{\text{c}}(s)$ has little influence on the impedance characteristics in the other frequency bands. The proposed active damping controller effectively eliminates the negative damping characteristics of the PMSG-based wind plants in Band IV_{PMSG}.

With the overall impedance reshaping, the optimized impedance characteristics of the PMSG-based wind plants are shown in Fig. 16.7. As seen from the figure, the

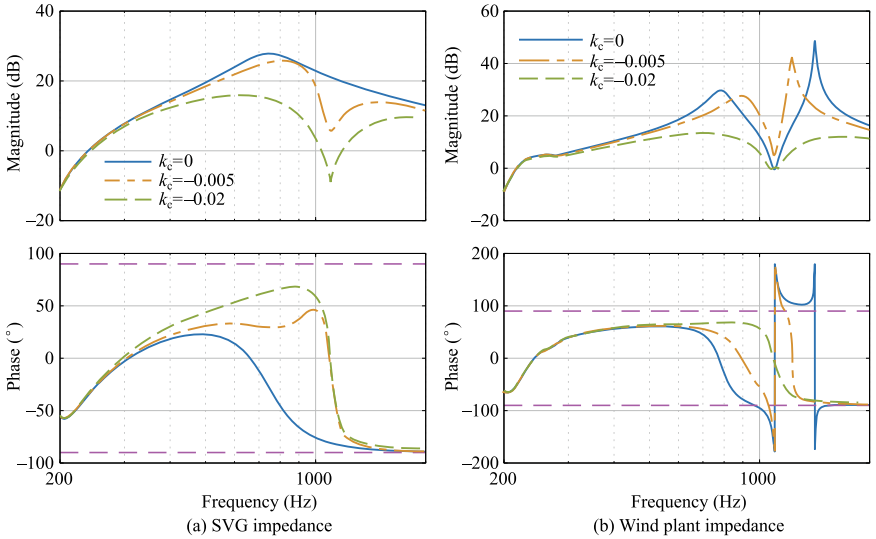

Fig. 16.6 The influence of the active damping coefficient on impedance characteristics of SVG and PMSG-based wind plants

negative damping characteristics of the wind plants in Band III_{PMSG} and IV_{PMSG} are eliminated after the impedance reshaping of SVG.

16.1.4 Simulation Verification

The EMT simulation parameters of the PMSG-based wind plants and the SVG are listed in Tables 16.1 and 16.2 respectively, and short circuit ratio (SCR) of AC grid is 2.0. Figure 16.8 shows the evaluation results of oscillation risk for PMSG-based wind plants connected into AC grid system before and after the impedance reshaping of SVG.

As seen from Fig. 16.8(a), the magnitude curves of wind plant impedance $\boldsymbol{Z}_{\text{WF}}$ and AC grid impedance $\boldsymbol{Z}_{\text{g}}$ intersect at Point A (118 Hz), and the PM is only 1.8° before SVG impedance reshaping. The GM/PM is insufficient, indicating oscillation risk in the system. After the impedance reshaping, the intersection point of the two impedance magnitude curves shifts from Point A to Point B (110 Hz), and the PM is increased to 19.8°. The stability margin is thus improved.

As seen from Fig. 16.8(b), the original Nyquist curve around Point A (118 Hz) is in the forbidden area, indicating oscillation risk. After the impedance reshaping, the optimized Nyquist curve is always outside the forbidden area, indicating that the impedance reshaping of SVG effectively eliminates the oscillation risk of the system.

The time-domain simulation of PMSG-based wind plants connected into AC grid system is conducted based on the full EMT simulation platform. The current

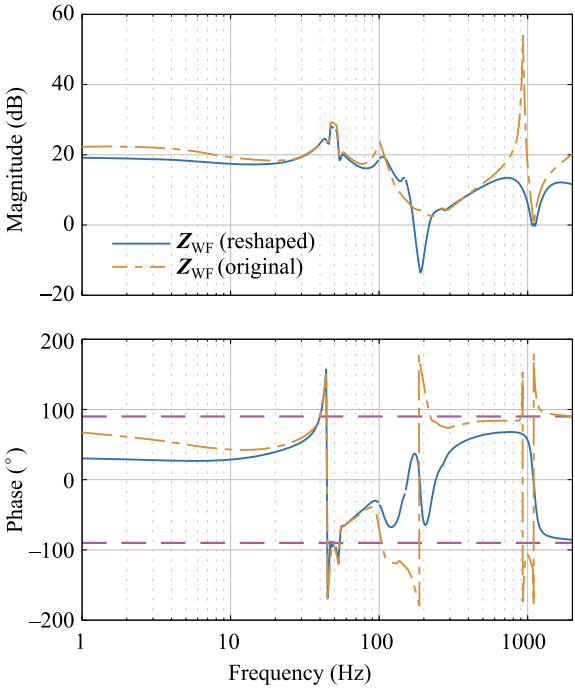

Fig. 16.7 The impedance characteristics of PMSG-based wind plants before and after the impedance reshaping of SVG

waveforms of the wind plants and the corresponding FFT results before and after the impedance reshaping of SVG are shown in Fig. 16.9.

As seen from Fig. 16.9, initially, there is a oscillation component at 118 Hz and a coupling oscillation component at 18 Hz according to the FFT results of the wind plant currents. After the impedance reshaping control of SVG is enabled at $t = 2$ s, the oscillation of the current waveforms is mitigated, and the oscillation components are eliminated as shown in the corresponding FFT analysis. The simulation results verify the effectiveness of oscillation mitigation strategy based on the proposed impedance reshaping of SVG.

16.2 Impedance Reshaping of DFIG-Based Wind Plant

In this section, DFIG-based wind plants are taken as an example, and the impedance reshaping and oscillation mitigation of DFIG-based wind plants are achieved by optimizing the impedance characteristics of SVG in the plants.

Table 16.1 EMT simulation parameters of PMSG-based wind plants

Parameter	Definition	Value
N_{PMSG}	Number of PMSG-based wind turbines	200
P_{N}	Rated power	1.5 MW
V_1	Fundametal component amplitude of AC voltage	690 V
f_1	Fundamental frequency	50 Hz
k_{T}	AC transformer ratio	0.69 kV/35 kV
R_{s}	Stator resistance	0.001 Ω
L_{sd}, L_{sq}	D- and q-axis inductance of the stator	0.2699 mH, 0.283 mH
L_{f}	GSC filter inductance	0.1 mH
V_{dc}	Steady-state value of DC voltage	1500 V
K_{pp}, K_{pi}	Proportional and integral coefficients of PLL controller	0.2198, 4.8706
K_{gip}, K_{gii}	Proportional and integral coefficients of GSC current controller	8.3993×10^{-5}, 0.4205
K_{sip}, K_{sii}	Proportional and integral coefficients of machine-side converter (MSC) current controller	1.1404×10^{-5}, 6.3172×10^{-5}
K_{pep}, K_{pei}	Proportional and integral coefficients of active power controller	5×10^{-6}, 0.0200
K_{qep}, K_{qei}	Proportional and integral coefficients of reactive power controller	5.9207×10^{-4}, 0.0322
K_{vdcp}, K_{vdci}	Proportional and integral coefficients of DC voltage controller	4.0774, 279.7374
K_{sd}	Decoupling coefficient of MSC current control	2.3160×10^{-5}
K_{gd}	Decoupling coefficient of GSC current control	4.2341×10^{-4}

16.2.1 Impedance Reshaping Strategy of SVG

Figure 16.10 shows the impedance characteristics of a DFIG-based wind plant in the frequency range of 1~2000 Hz. As seen from the figure, the negative damping characteristics of the wind plant impedance may occur in Band $\mathrm{I}_{\mathrm{DFIG}}$, $\mathrm{II}_{\mathrm{DFIG}}$ and $\mathrm{III}_{\mathrm{DFIG}}$.

In view of the broadband negative damping characteristics of the DFIG-based wind plants, this section will utilize the impedance reshaping of SVG based on control strategy improvement to optimize the impedance characteristics of the wind plants.

The impedance reshaping of SVG in reactive power control mode is taken as an example for analysis. The impedance reshaping strategy combining two types of voltage feedforward control and active damping control is introduced to achieve

Table 16.2 EMT simulation parameters of SVG

Parameter	Definition	Value
S_{SVG}	Rated capacity	100 Mvar
V_1	Amplitude of the fundamental component of the AC voltage	35 kV
V_{dc}	Steady-state value of DC voltage	36 kV
N	Arm SM number	36
V_C	Rated SM capacitor voltage	1 kV
C_{sm}	SM capacitor	1.5 mF
L_{arm}	Arm inductor	30 mH
K_{pp}, K_{pi}	Proportional and integral coefficients of the PLL controller	7.7734×10^{-4}, 0.0244
K_{qep}, K_{qei}	Proportional and integral coefficients of the reactive power controller	2.1922×10^{-5}, 3.9894×10^{-5}
K_{vsp}, K_{vsi}	Proportional and integral coefficients of the overall voltage controller	0.0023, 0.0733
K_{iacp}, K_{iaci}	Proportional and integral coefficients of the AC current controller	5.5536×10^{-4}, 0.5234
K_d	Decoupling coefficients of the AC current control	2.6180×10^{-4}
K_{vcp}, K_{vci}	Proportional and integral coefficients of the phase voltage balancing controller	7.7734×10^{-5}, 2.4421×10^{-4}
K_{ic}	Current proportional factor	1×10^{-6}

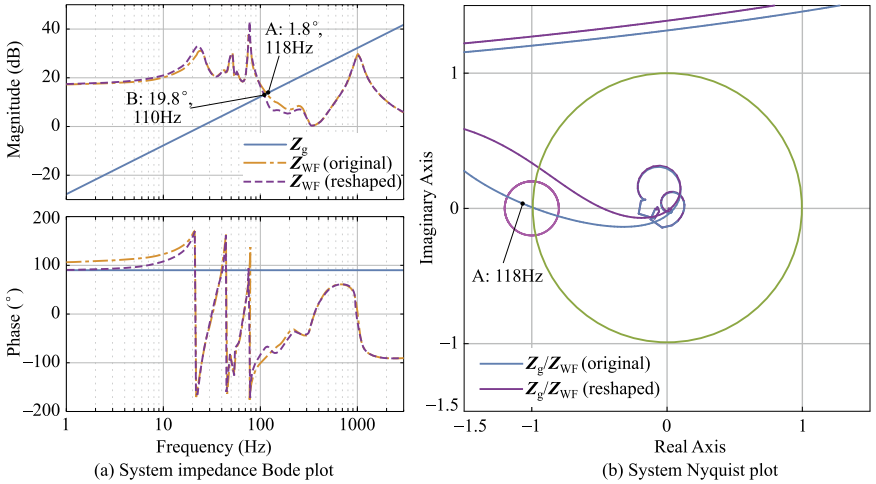

Fig. 16.8 The evaluation results of oscillation risk for PMSG-based wind plants connected into AC grid system before and after the impedance reshaping of SVG

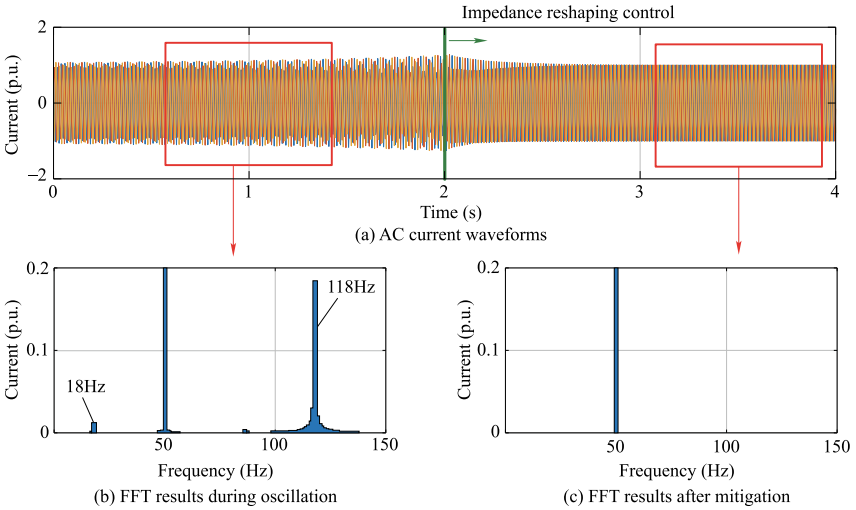

Fig. 16.9 The evaluation results of oscillation risk for PMSG-based wind plants connected into AC grid system before and after the impedance reshaping of SVG

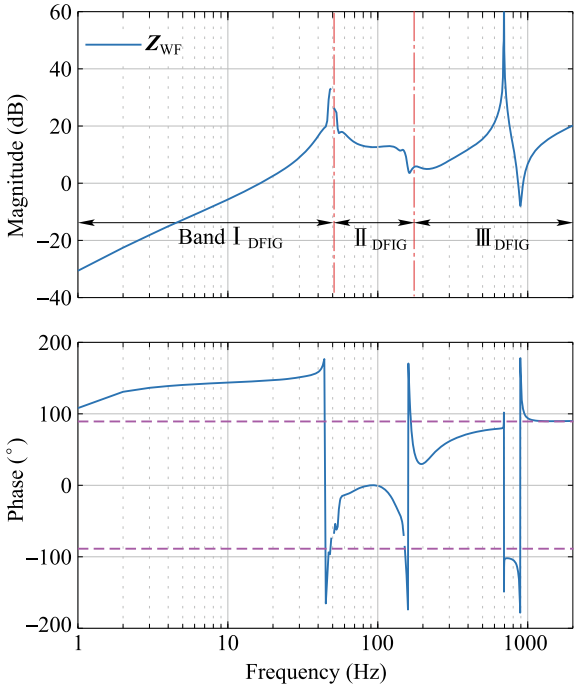

Fig. 16.10 The impedance characteristics of a DFIG-based wind plant

impedance reshaping in Band I_{DFIG}, II_{DFIG} and III_{DFIG}. The main circuit and control diagram of SVG considering the impedance reshaping of DFIG-based wind plants are shown in Fig. 16.11. In the figure, the voltage feedforward control and active damping control in the SRF are consistent with those in Sect. 16.1, in order to optimize the impedance characteristics of the wind plants in Band II_{DFIG} and III_{DFIG}. Besides, the Type-S voltage feedforward control in the SCF is adopted to optimize the impedance characteristics in Band I_{DFIG}.

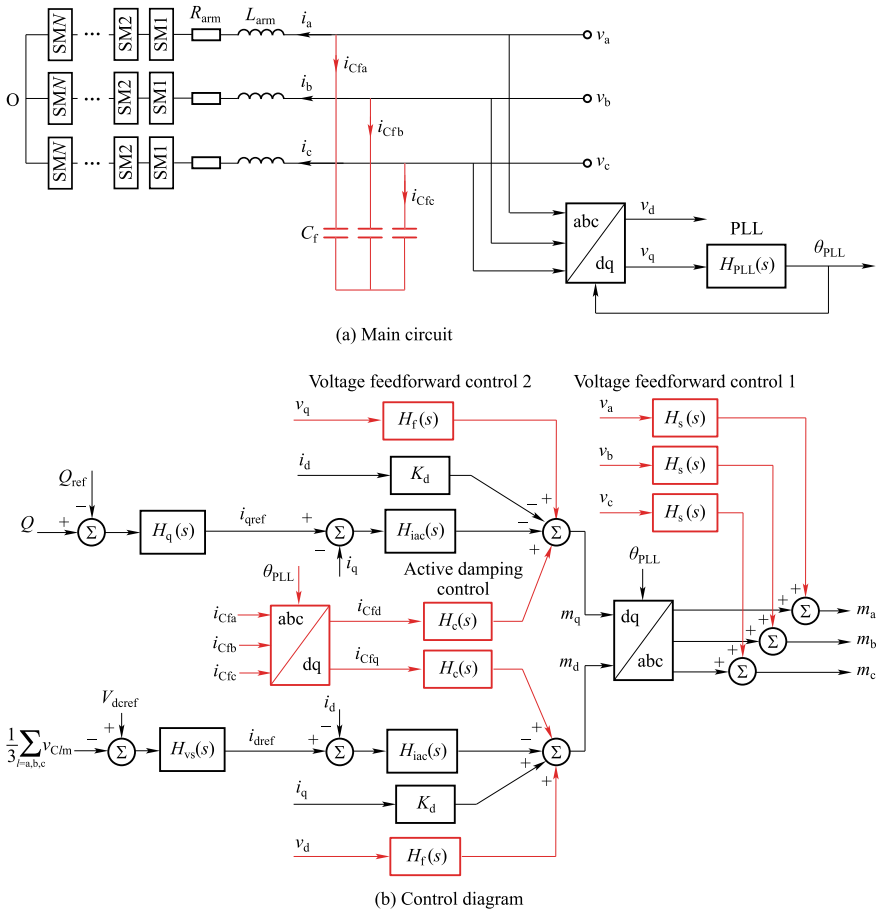

Fig. 16.11 The main circuit and control diagram of SVG considering the impedance reshaping of DFIG-based wind plants

16.2.1.1 Impedance Reshaping Method in Band $\mathrm{I_{DFIG}}$

The Type-S voltage feedforward control in the stationary coordinate frame (SCF) is utilized to eliminate the negative damping characteristics of the DFIG-based wind plants in Band $\mathrm{I_{DFIG}}$, as shown in Fig. 16.11. Specifically, the outputs of the Type-S voltage feedforward controller $H_\mathrm{s}(s)$ are superimposed to the three-phase AC modulation signals m_a, m_b, m_c respectively, after the controllers receive the three-phase AC voltages of SVG.

In order to reduce the influence of the Type-S voltage feedforward controller on the impedance characteristics of other frequency bands, its transfer function is designed as a low-pass filter, as shown in Eq. (16.5).

$$H_\mathrm{s}(s) = \left(k_\mathrm{s}\frac{Q_\mathrm{s}^{-1}\omega_{\mathrm{s}0}s}{s^2 + Q_\mathrm{s}^{-1}\omega_{\mathrm{s}0}s + \omega_{\mathrm{s}0}^2}\right)^*\left(\frac{1}{1+s/\omega_{\mathrm{s}1}}\right)^2 \tag{16.5}$$

where k_s is the voltage feedforward coefficient in SCF and can be designed to adjust the impedance characteristics in Band $\mathrm{I_{DFIG}}$. $\omega_{\mathrm{s}0}$ and Q_s are the center angular frequency and quality factor of the low-pass filter in the Type-S voltage feedforward control respectively. The value of $\omega_{\mathrm{s}0}$ is designed to adjust the center frequency of the controller $H_\mathrm{s}(s)$, and the value of Q_s is designed to adjust the working frequency range of $H_\mathrm{s}(s)$, covering the negative damping frequency range in Band $\mathrm{I_{DFIG}}$.

Moreover, a second-order low-pass filter is added in the controller, which increases the attenuation rate of $H_\mathrm{s}(s)$ outside the frequency range in Band $\mathrm{I_{DFIG}}$. $\omega_{\mathrm{s}1}$ is the corresponding cut-off angular frequency.

16.2.1.2 Impedance Reshaping Method in Band $\mathrm{II_{DFIG}}$

The generation mechanism of the negative damping of DFIG-based wind plants in Band $\mathrm{II_{DFIG}}$ is similar to that of PMSG-based wind plants in Band $\mathrm{III_{PMSG}}$. The impedance reshaping method of SVG in Band $\mathrm{II_{DFIG}}$ can be referred to that in Band $\mathrm{III_{PMSG}}$, as mentioned in Sect. 16.1.1.1. Similarly, the voltage feedforward control in the SRF is utilized to eliminate the negative damping characteristics of the DFIG-based wind plants in Band $\mathrm{II_{DFIG}}$, as shown in Fig. 16.11. The transfer function of the voltage feedforward controller $H_\mathrm{f}(s)$ is also designed as Eq. (16.1), while the specific values of the parameters are different.

16.2.1.3 Impedance Reshaping Method in Band $\mathrm{III_{DFIG}}$

The generation mechanism of the negative damping of DFIG-based wind plants in Band $\mathrm{III_{DFIG}}$ is similar to that of PMSG-based wind plants in Band $\mathrm{IV_{PMSG}}$. The impedance reshaping method of SVG in Band $\mathrm{III_{DFIG}}$ can be referred to that in Band $\mathrm{IV_{PMSG}}$, as mentioned in Sect. 16.1.1.2. Similarly, additional AC filter capacitors

are in parallel to the AC port of SVG first. Then, the capacitor currents can be introduced in a feedforward path for the proposed active damping control, as shown in Fig. 16.11. The transfer function of the active damping controller $H_c(s)$ is also designed as Eq. (16.2), while the specific values of the parameters are different.

16.2.2 Reshaped Impedance Model of SVG

Based on the small-signal modeling of the control loops of SVG in reactive power control mode, with the two types of voltage feedforward control and active damping control in Sect. 16.2.1, the small-signal vector of the AC modulation signal in phase a is given as

$$\hat{\boldsymbol{m}}_a = \boldsymbol{G}_1\boldsymbol{D}_1\hat{\boldsymbol{i}}_a + (\boldsymbol{G}_2 + \Delta\boldsymbol{G}_2)\boldsymbol{D}_2\hat{\boldsymbol{v}}_a + \boldsymbol{G}_3\boldsymbol{D}_3\hat{\boldsymbol{v}}_{Cam} \tag{16.6}$$

where $\Delta\boldsymbol{G}_2$ is the transfer function matrix introduced by the two types of voltage feedforward control and active damping control, and all other elements in the matrix are zero except for Eq. (16.7). The expressions of the other matrices in Eq. (16.6) can be referred to Chap. 9.

$$\begin{cases} \Delta\boldsymbol{G}_2(2,2) = -T_{PLL}[\mathrm{j}2\pi(f_p - f_1)] \cdot \big[H_f[\mathrm{j}2\pi(f_p - f_1)] \cdot V_1 \\ \qquad\qquad +H_c[\mathrm{j}2\pi(f_p - f_1)] \cdot \boldsymbol{I}^*_{Cf1}\big] + H_s[\mathrm{j}2\pi(f_p - 2f_1)] \\ \qquad\qquad +H_f[\mathrm{j}2\pi(f_p - f_1)] + \mathrm{j}2\pi(f_p - 2f_1)C_f \cdot H_c[\mathrm{j}2\pi(f_p - f_1)] \\ \Delta\boldsymbol{G}_2(2,4) = T_{PLL}[\mathrm{j}2\pi(f_p - f_1)] \cdot \big[H_f[\mathrm{j}2\pi(f_p - f_1)] \cdot V_1 \\ \qquad\qquad +H_c[\mathrm{j}2\pi(f_p - f_1)] \cdot \boldsymbol{I}^*_{Cf1}\big] \\ \Delta\boldsymbol{G}_2(4,2) = T_{PLL}[\mathrm{j}2\pi(f_p - f_1)] \cdot \big[H_f[\mathrm{j}2\pi(f_p - f_1)] \cdot V_1 \\ \qquad\qquad +H_c[\mathrm{j}2\pi(f_p - f_1)] \cdot \boldsymbol{I}_{Cf1}\big] \\ \Delta\boldsymbol{G}_2(4,4) = -T_{PLL}[\mathrm{j}2\pi(f_p - f_1)] \cdot \big[H_f[\mathrm{j}2\pi(f_p - f_1)] \cdot V_1 \\ \qquad\qquad +H_c[\mathrm{j}2\pi(f_p - f_1)] \cdot \boldsymbol{I}_{Cf1}\big] + H_s[\mathrm{j}2\pi f_p] \\ \qquad\qquad + H_f[\mathrm{j}2\pi(f_p - f_1)] + \mathrm{j}2\pi f_p C_f \cdot H_c[\mathrm{j}2\pi(f_p - f_1)] \end{cases} \tag{16.7}$$

By substituting Eq. (16.6) into the small-signal model of the main circuit in Chap. 9, the analytical impedance model of SVG with the impedance reshaping strategy can be derived. Furthermore, the impedance model of DFIG-based wind plants can be obtained after the analytical impedance model of SVG is substituted.

16.2.3 Impedance Reshaping Design

Based on the impedance reshaping strategy of SVG, the design of the impedance reshaping of DFIG-based wind plants is performed in the order of Band $\mathrm{I}_{\mathrm{DFIG}}$, $\mathrm{II}_{\mathrm{DFIG}}$ and $\mathrm{III}_{\mathrm{DFIG}}$ to eliminate the negative damping characteristics. Since the impedance characteristics between adjacent frequency bands are influenced by each other, the control parameters of the proposed impedance reshaping strategy should be adjusted, which meets the requirements of the negative damping optimization in these three frequency bands, simultaneously.

16.2.3.1 Impedance Reshaping Design in Band $\mathrm{I}_{\mathrm{DFIG}}$

In order to reduce the negative damping characteristics in Band $\mathrm{I}_{\mathrm{DFIG}}$, the value of ω_{s0} is set as 0.2π rad/s, which is approached to zero, the value of Q_s is set as 0.2, and the value of ω_{s1} is set as $2\pi \times 50$ rad/s in Eq. (16.5). The amplitude-frequency and phase-frequency characteristics of the Type-S voltage feedforward controller in the SCF are shown in Fig. 16.12. The value of k_s is set as 1.0 here for the analysis of the amplitude-frequency characteristics.

As seen from Fig. 16.12, after adding a second-order low-pass filter into the Type-S voltage feedforward controller $H_s(s)$, the attenuation rate of the control effect of

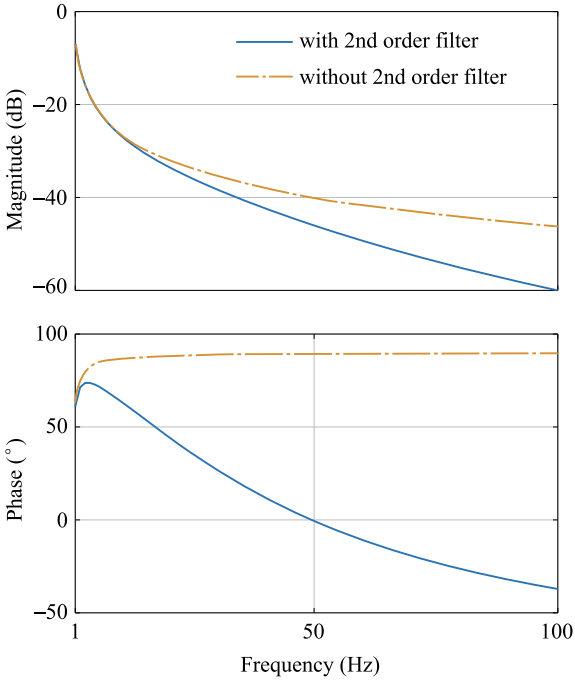

Fig. 16.12 The amplitude-frequency and phase-frequency characteristics of the Type-S voltage feedforward controller in the SRF

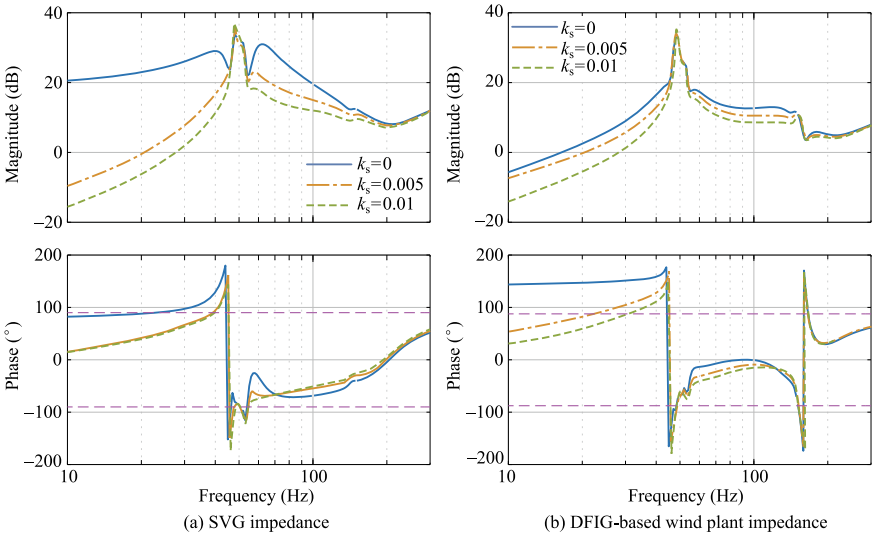

Fig. 16.13 The influence of the voltage feedforward coefficient in SCF on impedance characteristics of SVG and DFIG-based wind plants

$H_s(s)$ increases outside the frequency range of Band $\mathrm{I_{DFIG}}$, which can mitigate the influence of $H_s(s)$ on the impedance characteristics in the other frequency bands.

The value of the voltage feedforward coefficient k_s in SCF is refined to reshape the impedance curve in Band $\mathrm{I_{DFIG}}$. With k_s equivalent to 0, 0.005, and 0.01, the variation of the impedance curves of SVG and DFIG-based wind plants is shown in Fig. 16.13.

As seen from Fig. 16.13, with the increase of k_s, the magnitude curve of SVG impedance decreases in Band $\mathrm{I_{DFIG}}$. Thus, the impedance characteristics of the DFIG-based wind plants are dominated by SVG in this frequency band. Compared with the impedance curve when $k_s = 0$, the magnitude curve of the impedance of the wind plants decreases, and the frequency range of the inductive negative damping in Band $\mathrm{I_{DFIG}}$ is reduced accordingly. The proposed Type-S voltage feedforward control in SCF effectively optimizes the damping characteristics in Band $\mathrm{I_{DFIG}}$.

16.2.3.2 Impedance Reshaping Design in Band $\mathrm{II_{DFIG}}$

Similar to Sect. 16.1.3.1, the values of ω_{f0} and Q_f are designed for the voltage feedforward controller $H_f(s)$ covering the frequency range of negative damping in Band $\mathrm{II_{DFIG}}$. The impedance reshaping in this frequency band is achieved by the design of the voltage feedforward coefficient k_f. With k_f equivalent to 0, 1×10^{-5} and 5×10^{-5}, the variation of the impedance curves of SVG and DFIG-based wind plants is shown in Fig. 16.14.

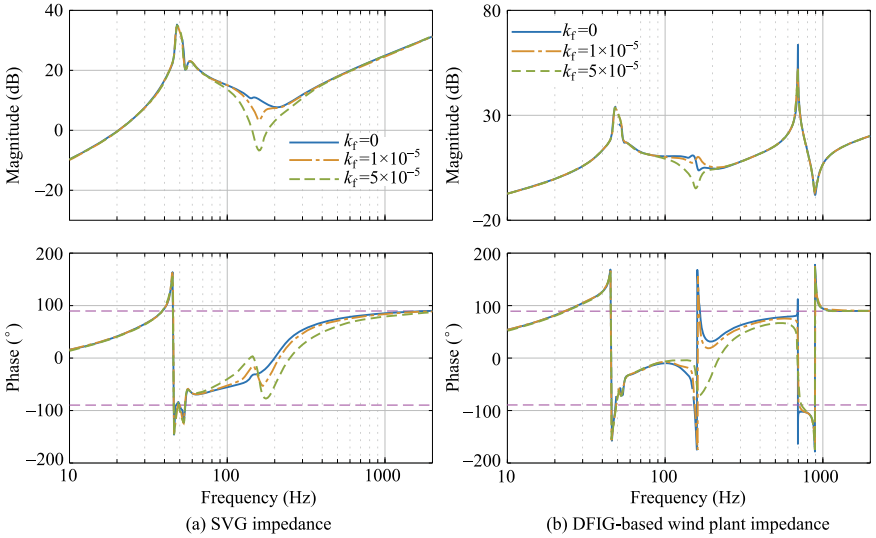

Fig. 16.14 The influence of the voltage feedforward coefficient in SRF on impedance characteristics of SVG and DFIG-based wind plants

As seen from Fig. 16.14, with the increase of k_f, the magnitude curve of SVG impedance decreases in Band II_{DFIG}. The impedance characteristics of the DFIG-based wind plants are dominated by SVG in this frequency band. Furthermore, the magnitude curve of the impedance of the wind plants decreases, and both the inductive and capacitive negative damping characteristics in Band II_{DFIG} are gradually eliminated. Besides, the voltage feedforward controller $H_f(s)$ has little influence on the impedance characteristics in the other frequency bands. The proposed voltage feedforward control in SRF effectively improves the damping characteristics in Band II_{DFIG}.

16.2.3.3 Impedance Reshaping Design in Band III_{DFIG}

In order to achieve the impedance reshaping of the wind plants in Band III_{DFIG}, additional AC filter capacitors are in parallel to the AC port of SVG. Figure 16.15 shows the influence of the shunt capacitor on the impedance characteristics of SVG and DFIG-based wind plants. The original impedance of the wind plants in Band III_{DFIG} without the capacitor presents capacitive negative damping and inductive negative damping. With the shunt capacitor, the impedance characteristics of SVG in Band III_{DFIG} change from inductive to capacitive. Correspondingly, the inductive negative damping of the wind plants in the high-frequency band becomes capacitive negative damping. Moreover, the shunt capacitor does not affect the frequency range of the negative damping in Band III_{DFIG}.

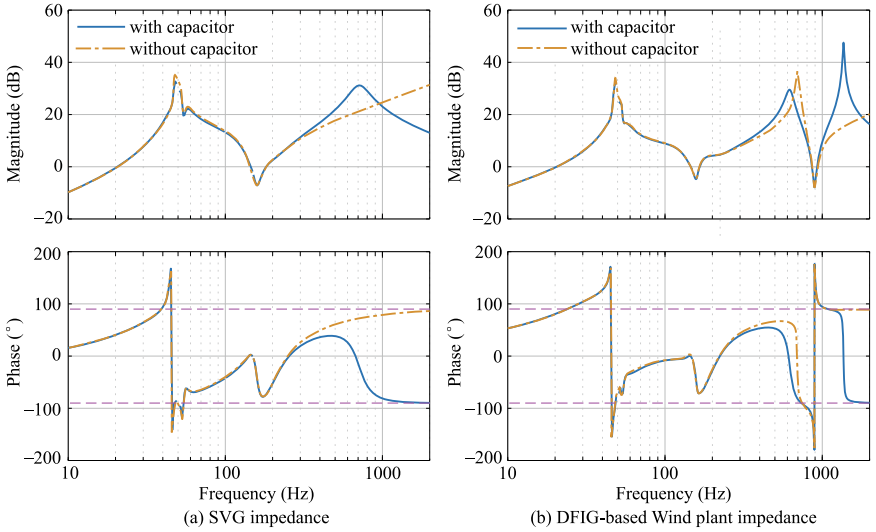

Fig. 16.15 The influence of shunt capacitor on impedance characteristics of SVG and DFIG-based wind plants

After the filter capacitors are connected, the active damping control based on capacitor current feedforward can be used to optimize the impedance characteristics in Band $\mathrm{III}_{\mathrm{DFIG}}$. Firstly, ω_{c0} and Q_c are designed for the active damping controller $H_c(s)$ covering the frequency range of the negative damping in this frequency band. Then, impedance reshaping in Band $\mathrm{III}_{\mathrm{DFIG}}$ is achieved by optimizing the active damping coefficient k_c. With k_c equivalent to 0, -0.02, and -0.05, the variation of the impedance curves of SVG and DFIG-based wind plants is shown in Fig. 16.16.

As seen from Fig. 16.16, the magnitude curves of SVG impedance and the wind plants in Band $\mathrm{III}_{\mathrm{DFIG}}$ decrease with the increase of k_c. The impedance phase of the wind plants below 900 Hz (around ω_{c0}) increases, while the impedance phase above 900 Hz decreases. As a result, both the inductive and capacitive negative damping characteristics of the wind plants in Band $\mathrm{III}_{\mathrm{DFIG}}$ are gradually eliminated. Besides, the active damping controller $H_c(s)$ has little influence on the impedance characteristics in the other frequency bands. The proposed active damping control effectively improves the damping characteristics of the DFIG-based wind plants in Band $\mathrm{III}_{\mathrm{DFIG}}$.

With the overall impedance reshaping, the optimized impedance characteristics of the DFIG-based wind plants are shown in Fig. 16.17. As seen from the figure, the negative damping characteristics of the wind plants in Band $\mathrm{I}_{\mathrm{DFIG}}$, $\mathrm{II}_{\mathrm{DFIG}}$ and $\mathrm{III}_{\mathrm{DFIG}}$ are eliminated after the impedance reshaping of SVG.

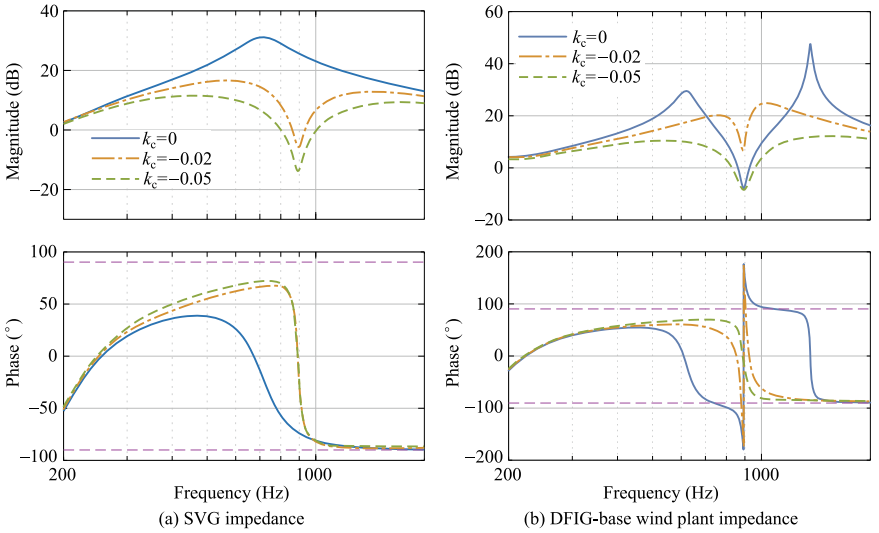

Fig. 16.16 The influence of the active damping coefficient on impedance characteristics of SVG and DFIG-based wind plants

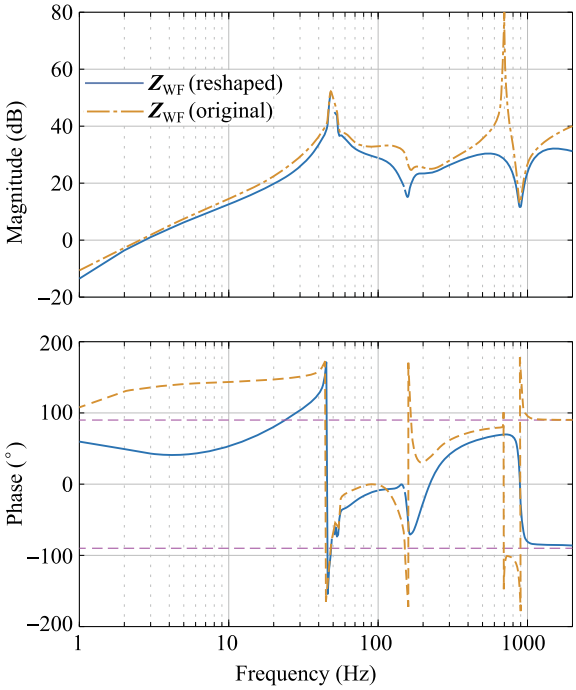

Fig. 16.17 The impedance characteristics of DFIG-based wind plants before and after the impedance reshaping of SVG

16.2.4 Simulation Verification

The EMT simulation parameters of the DFIG-based wind plants and the SVG are listed in Tables 16.2 and 16.3 respectively. SCR of AC grid is 2.0, and the degree of series compensation is 1%. Figure 16.18 shows the evaluation results of oscillation risk for DFIG-based wind plants connected into series compensation transmission lines before and after the impedance reshaping of SVG.

As seen from Fig. 16.18(a), the magnitude curves of wind plant impedance $\boldsymbol{Z}_{\mathrm{WT}}$ and impedance of series compensation transmission lines $\boldsymbol{Z}_{\mathrm{g}}$ intersect at Point C (21 Hz), and the PM is only 0.2° before SVG impedance reshaping. The GM/PM is insufficient, indicating oscillation risk in the system. After the impedance reshaping,

Table 16.3 EMT simulation parameters of DFIG-based wind plants

Variables	Definition	Value
N_{DFIG}	Number of DFIG-based wind turbines	200
P_{N}	Rated power	1.5 MW
V_1	Rated voltage	690 V
f_1	Rated frequency	50 Hz
k_{T}	AC transformer ratio	0.69 kV/35 kV
R_{s}, R_{r}	Stator and rotor resistance	0.0022, 0.0027
$L_{1\mathrm{s}}$, $L_{1\mathrm{r}}$	Stator and rotor leakage inductance	1.4437×10^{-4}, 1.0913×10^{-4}
L_{ms}, L_{mr}	Stator and rotor mutual inductance	0.0041 mH
L_{f}	Filter inductance	0.7 mH
V_{dc}	DC voltage	1500 V
K_{e}	Turn ratio of stator and rotor windings	3
K_{pp}, K_{pi}	Proportional and integral coefficients of PLL controller	0.1048, 2.3967
K_{gip}, K_{gii}	Proportional and integral coefficients of GSC current controller	0.0016, 3.7600
K_{rip}, K_{rii}	Proportional and integral coefficients of RSC current controller	1.4359×10^{-5}, 7.5702×10^{-5}
K_{pep}, K_{pei}	Proportional and integral coefficients of active power controller	6×10^{-4}, 0.0020
K_{qep}, K_{qei}	Proportional and integral coefficients of reactive power controller	6×10^{-4}, 0.0020
K_{vdcp}, K_{vdci}	Proportional and integral coefficients of DC voltage controller	3.9301, 155
K_{gd}	Decoupling coefficient of GSC current control	3.3000×10^{-5}
K_{rd}	Decoupling coefficient of RSC current control	1.8744×10^{-4}

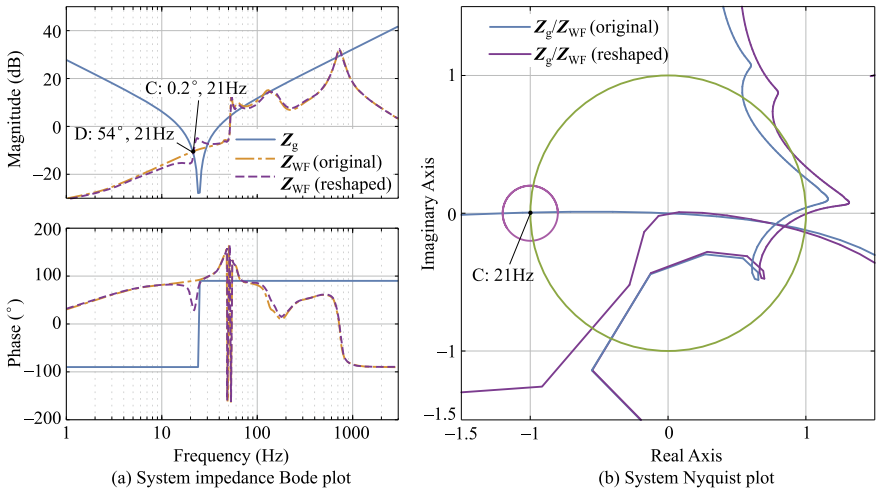

Fig. 16.18 The evaluation results of oscillation risk for DFIG-based wind plants connected into series compensation transmission lines before and after the impedance reshaping of SVG

the intersection point of the two impedance magnitude curves is still at 21 Hz, while the PM is increased to 54° (Point D). The stability margin is thus improved.

As seen from Fig. 16.18(b), the original Nyquist curve around Point C (21 Hz) is in the forbidden area, indicating oscillation risk. After the impedance reshaping, the optimized Nyquist curve is always outside the forbidden area, indicating that the impedance reshaping of SVG effectively eliminates the oscillation risk of the system.

The time-domain simulation of DFIG-based wind plants connected into AC series compensation system is conducted based on the full EMT simulation platform. The current waveforms of the wind plants and the corresponding FFT results before and after the impedance reshaping of SVG are shown in Fig. 16.19.

As seen from Fig. 16.19, initially, there is a sub-synchronous oscillation component at 21 Hz and a coupling super-synchronous oscillation component at 79 Hz according to the FFT results of the wind plant currents. After the impedance reshaping control of SVG is enabled at $t = 2$ s, the oscillation of the current waveforms is mitigated, and the sub-/super- synchronous oscillation components are eliminated as shown in the corresponding FFT analysis. The simulation results verify the effectiveness of oscillation mitigation strategy based on the proposed impedance reshaping of SVG.

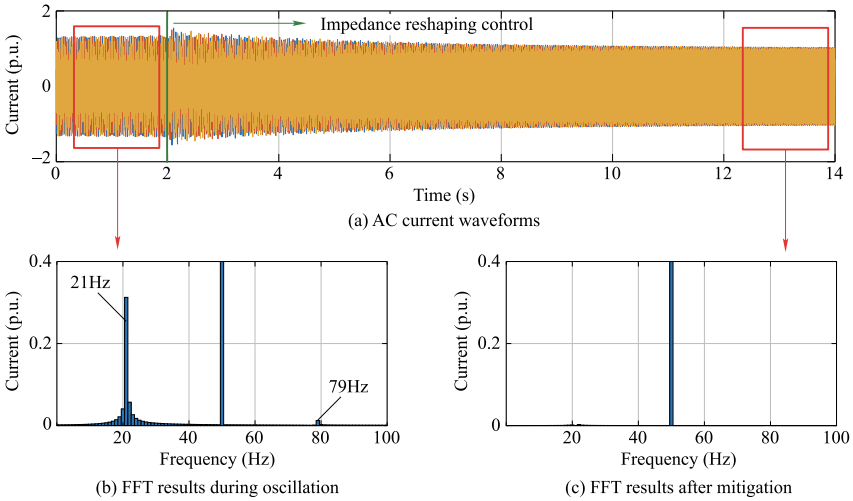

Fig. 16.19 The evaluation results of oscillation risk for DFIG-based wind plants connected into series compensation transmission lines before and after the impedance reshaping of SVG

Chapter 17
Oscillation Mitigation Based on Impedance Reshaping of LCC-HVDC

In Chaps. 15 and 16, the impedance reshaping of REG units and SVG is respectively utilized to optimize the impedance characteristics of REG plants and mitigate the oscillation risk of the system. For the oscillation of REG connected into the LCC-HVDC system, the oscillation mitigation can also be achieved by the impedance reshaping of LCC-HVDC.

In this chapter, the impedance reshaping strategy of LCC-HVDC is first proposed, and the analytical impedance model is refined and verified. Then, the design of the impedance reshaping of LCC-HVDC in the sub-/super-synchronous frequency band is realized by the impedance reshaping strategy and control parameter optimization. Finally, the oscillation mitigation strategy is verified based on the full EMT simulation platform for REG and AC/DC transmission systems.

17.1 Impedance Reshaping Strategy of LCC-HVDC

According to Chap. 10, the sending-end line commutated converter (LCC) operates in DC current control mode and the receiving-end LCC operates in DC voltage control mode for LCC-HVDC transmission system. The basic control characteristics of DC voltage and DC current are shown in Fig. 17.1. The operating point is M1. The overlapping effect of the DC current control and DC-side impedance of the sending-end LCC leads to the negative damping characteristics in the AC port impedance of LCC-HVDC at the sending end.

In order to eliminate the potential oscillation risk caused by negative damping characteristics, the impedance reshaping strategy of LCC-HVDC is proposed, with trigger angle control adopted in the sending-end LCC and DC current control adopted in the receiving-end LCC. Under the effect of the control characteristics shown in Fig. 17.1, the operation mode of the receiving-end LCC will be automatically adjusted from constant DC voltage control mode to constant DC current control mode, along

© China Electric Power Press 2023

W. Wang et al., *Analysis and Mitigation of Broadband Oscillation in Renewable Energy Generation and AC/DC Transmission Systems*,
https://doi.org/10.1007/978-981-99-1568-2_17

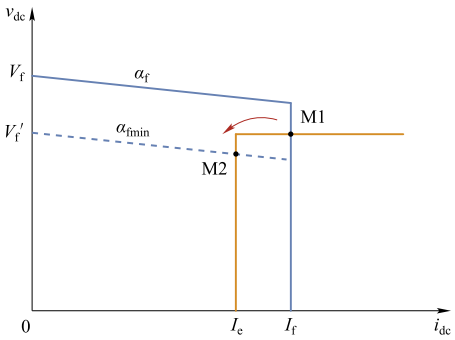

Fig. 17.1 LCC-HVDC basic control characteristics of DC voltage and DC current

with the adjustment of the operation mode in the sending-end LCC. The operating point shifts from Point M1 to Point M2.

With the impedance reshaping strategy, the sending-end LCC operates in constant trigger angle control mode with a fixed minimum value α_{fmin}. The phase control receives the sending-end phase-locked angle θ_{fPLL} and the trigger angle α_{fmin}, and then generates the trigger pulses to turn on the thyristors in the sending-end LCC. The control diagram is shown in Fig. 17.2(a), in which v_{fl} (l = a,b,c) are sending-end three-phase AC voltages. Tfh is the hth thyristor of the sending-end LCC. θ_{fh} is the reference angle of Tfh. γ_{fh} is the phase-shift angle of Tfh.

The receiving-end LCC operates in constant DC current control mode with the DC current reference I_{dcref}. The DC current is filtered by $T_{\text{idc}}(s)$ and fed back into the DC current controller $H_{\text{idc}}(s)$ to generate the firing angle α_{e}. The phase control receives the receiving-end phase-locked angle θ_{ePLL} and the trigger angle α_{e}, and then generates the trigger pulses to turn on the thyristors in the sending-end LCC. The control diagram is shown in Fig. 17.2b, in which v_{el} (l = a, b, c) are receiving-end three-phase AC voltages. Teh is the hth thyristor of the receiving-end LCC. θ_{eh} is the reference angle of Teh. γ_{eh} is the phase-shift angle of Teh.

17.2 Reshaped Impedance Model of LCC-HVDC

With the proposed impedance reshaping strategy, the effect of DC current control and PLL leads to small-signal responses in the combined angle $\hat{\boldsymbol{\delta}}_{\text{e}}$ in the receiving-end LCC. The expression of $\hat{\boldsymbol{\delta}}_{\text{e}}$ is

$$\hat{\boldsymbol{\delta}}_{\text{e}} = \boldsymbol{Q}_{\text{e}}\hat{\boldsymbol{i}}_{\text{edc}} + \boldsymbol{E}_{\text{e}}\hat{\boldsymbol{v}}_{\text{ea}} \tag{17.1}$$

where $\boldsymbol{Q}_{\text{e}}$ and $\boldsymbol{E}_{\text{e}}$ are the transfer function matrixes of $(24g + 3) \times (24g + 3)$ introduced by DC current control and PLL respectively, and all other elements are zero except for

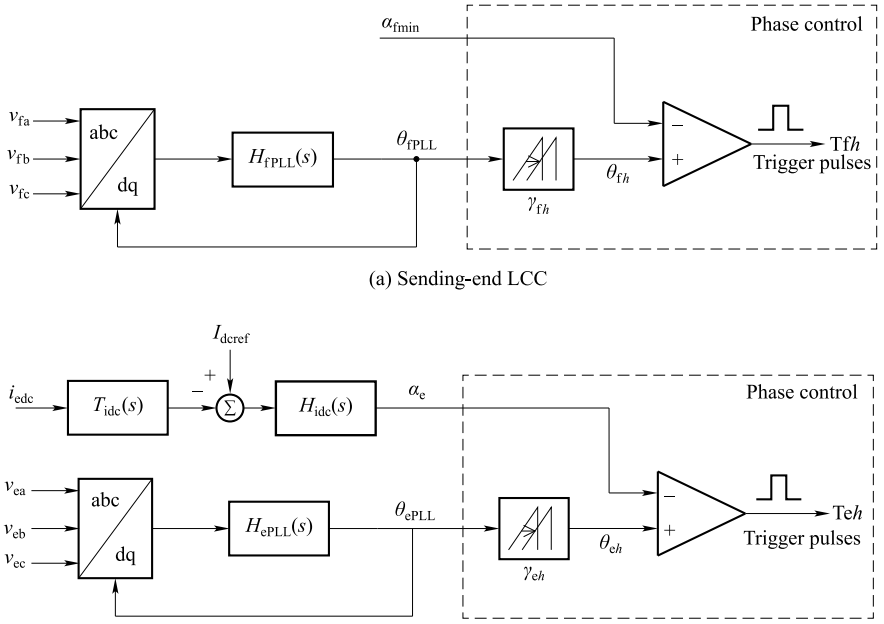

Fig. 17.2 The control diagram of LCC-HVDC considering impedance reshaping

$$\begin{cases} \boldsymbol{Q}_{\mathrm{e}}(12g+2, 12g+2) = T_{\mathrm{idc}}\left[\mathrm{j}2\pi\left(f_{\mathrm{p}} - f_1\right)\right] H_{\mathrm{idc}}\left[\mathrm{j}2\pi\left(f_{\mathrm{p}} - f_1\right)\right] \\ \boldsymbol{E}_{\mathrm{e}}(12g+2, 12g+1) = -\mathrm{j}T_{\mathrm{ePLL}}\left[\mathrm{j}2\pi\left(f_{\mathrm{p}} - f_1\right)\right] \\ \boldsymbol{E}_{\mathrm{e}}(12g+2, 12g+3) = \mathrm{j}T_{\mathrm{ePLL}}\left[\mathrm{j}2\pi\left(f_{\mathrm{p}} - f_1\right)\right] \end{cases} \tag{17.2}$$

where $T_{\mathrm{idc}}(s)$, $H_{\mathrm{idc}}(s)$ and $T_{\mathrm{ePLL}}(s)$ are the transfer functions of DC current filter, DC current control, and PLL of the receiving-end LCC respectively, referring to Chap. 10.

The frequency-domain relationship between the small-signal vectors of the switching function and combined angle satisfies

$$\begin{cases} \hat{\boldsymbol{s}}_{\mathrm{ev}l} = \boldsymbol{C}\boldsymbol{S}_{\mathrm{ev}l}\hat{\boldsymbol{\delta}}_{\mathrm{e}} \\ \hat{\boldsymbol{s}}_{\mathrm{ei}l} = \boldsymbol{C}\boldsymbol{S}_{\mathrm{ei}l}\hat{\boldsymbol{\delta}}_{\mathrm{e}} \end{cases} \tag{17.3}$$

where $\hat{\boldsymbol{s}}_{\mathrm{ev}l}$ and $\hat{\boldsymbol{s}}_{\mathrm{ei}l}$ (l = a, b, c) are the small-signal vectors of the voltage and current switching functions of the receiving-end LCC, respectively; $\boldsymbol{S}_{\mathrm{ev}l}$ and $\boldsymbol{S}_{\mathrm{ei}l}$ are the steady-state vectors of voltage and current switching functions of the receiving-end LCC, respectively; $\boldsymbol{C}$ is the characteristic-frequency coefficient matrix of switching function. These detailed expressions have been given in Chap. 10.

By substituting Eqs. (17.1) and (17.3) into the small-signal model of the main circuit of the receiving-end LCC in Chap. 10, the DC port admittance of the receiving-end LCC after impedance reshaping can be derived as

$$\boldsymbol{Z}'_{\mathrm{edc}} = (\boldsymbol{\Gamma}_2 + \boldsymbol{\Gamma}_6\boldsymbol{\Gamma}_7)(\boldsymbol{\Gamma}_1 + \boldsymbol{\Gamma}_7)^{-1}\left(\boldsymbol{\Gamma}'_4 + \boldsymbol{\Gamma}_5\right) - \boldsymbol{\Gamma}'_3 \tag{17.4}$$

where $\boldsymbol{\Gamma}'_3$ and $\boldsymbol{\Gamma}'_4$ are the transfer function matrixes introduced by DC current control, and the expressions are

$$\begin{cases} \boldsymbol{\Gamma}'_3 = (2/k_{\mathrm{eT}}) \cdot \boldsymbol{D}_{\mathrm{ad}} \boldsymbol{V}_{\mathrm{eTa}} \boldsymbol{C} \boldsymbol{S}_{\mathrm{eva}} \boldsymbol{Q}_{\mathrm{e}} \\ \boldsymbol{\Gamma}'_4 = (2/k_{\mathrm{eT}}) \cdot \boldsymbol{I}_{\mathrm{edc}} \boldsymbol{C} \boldsymbol{S}_{\mathrm{eia}} \boldsymbol{Q}_{\mathrm{e}} \end{cases} \tag{17.5}$$

where $\boldsymbol{D}_{\mathrm{ad}}$ is the transformation matrix of AC and DC voltages; $\boldsymbol{V}_{\mathrm{eTa}}$ is the steady-state vector of the grid-side voltage of the transformer in the receiving-end LCC; $\boldsymbol{I}_{\mathrm{edc}}$ is the steady-state vector of DC current in the receiving-end LCC; The detailed expressions of $\boldsymbol{\Gamma}_1$, $\boldsymbol{\Gamma}_2$, $\boldsymbol{\Gamma}_5$, $\boldsymbol{\Gamma}_6$, and $\boldsymbol{\Gamma}_7$ can be referred to Chap. 10.

Since the operation of the sending-end LCC is adjusted to trigger angle control mode from DC current control mode, the transfer function matrix $\boldsymbol{Q}_{\mathrm{f}}$, relevant to DC current control, in the original AC port admittance in the sending-end LCC should be set to zero. Combined with Eq. (17.4), the AC port admittance of LCC-HVDC at the sending end after the impedance reshaping can be derived as

$$\boldsymbol{Y}'_{\mathrm{LCC}} = \left[\boldsymbol{U} + \boldsymbol{\Lambda}'_1 \cdot \left(\boldsymbol{Z}'_{\mathrm{fdc}}\right)^{-1} \cdot \boldsymbol{\Lambda}_5\right]^{-1}\left[\boldsymbol{\Lambda}'_1 \cdot \left(\boldsymbol{Z}'_{\mathrm{fdc}}\right)^{-1} \cdot \boldsymbol{\Lambda}_3 + \boldsymbol{\Lambda}_4\right] + \boldsymbol{\Lambda}_6 \tag{17.6}$$

where $\boldsymbol{Z}'_{\mathrm{fdc}}$ is the DC-side impedance of sending-end converter station after the impedance reshaping; $\boldsymbol{\Lambda}'_1$ is the transfer function matrixes introduced by the proposed impedance reshaping strategy. The expressions of $\boldsymbol{Z}'_{\mathrm{fdc}}$ and $\boldsymbol{\Lambda}'_1$ are

$$\begin{cases} \boldsymbol{\Lambda}'_1 = (2/k_{\mathrm{fT}}) \cdot \boldsymbol{S}_{\mathrm{fia}} \\ \boldsymbol{Z}'_{\mathrm{fdc}} = \boldsymbol{Z}'_n + \boldsymbol{Z}_{\mathrm{Ldc}} \end{cases} \tag{17.7}$$

The detailed expressions of the quantities in Eqs. (17.6) and (17.7) can be referred to Chap. 10.

The f_{p} and $f_{\mathrm{p}} - 2f_1$ are the main components in the small-signal vectors of the AC voltage and current of LCC-HVDC, while the amplitudes of the other components are relatively small. The characteristics of the AC port impedance or admittance at f_{p} and $f_{\mathrm{p}} - 2f_1$ are more significant. Only relevant elements at these two frequencies are extracted, and the relationship between the small-signal vectors of the AC voltage and current and AC port admittance is reformulated as

$$\begin{bmatrix} \hat{\boldsymbol{i}}_{\mathrm{f}} \\ \hat{\boldsymbol{i}}_{\mathrm{f-2}} \end{bmatrix} = \begin{bmatrix} \boldsymbol{Y}^{\mathrm{pp}}_{\mathrm{LCC}} & \boldsymbol{Y}^{\mathrm{np}}_{\mathrm{LCC}} \\ \boldsymbol{Y}^{\mathrm{pn}}_{\mathrm{LCC}} & \boldsymbol{Y}^{\mathrm{nn}}_{\mathrm{LCC}} \end{bmatrix} \begin{bmatrix} \hat{\boldsymbol{v}}_{\mathrm{f}} \\ \hat{\boldsymbol{v}}_{\mathrm{f-2}} \end{bmatrix} \tag{17.8}$$

After impedance reshaping, the expression of the 2×2 AC port admittance matrix is

$$\begin{bmatrix} \boldsymbol{Y}_{\mathrm{LCC}}^{\mathrm{pp}} & \boldsymbol{Y}_{\mathrm{LCC}}^{\mathrm{np}} \\ \boldsymbol{Y}_{\mathrm{LCC}}^{\mathrm{pn}} & \boldsymbol{Y}_{\mathrm{LCC}}^{\mathrm{nn}} \end{bmatrix} = \begin{bmatrix} \boldsymbol{Y}'_{\mathrm{LCC}}(12g+3, 12g+3) & \boldsymbol{Y}'_{\mathrm{LCC}}(12g+3, 12g+1) \\ \boldsymbol{Y}'_{\mathrm{LCC}}(12g+1, 12g+3) & \boldsymbol{Y}'_{\mathrm{LCC}}(12g+1, 12g+1) \end{bmatrix}$$

where

$\boldsymbol{Y}_{\mathrm{LCC}}^{\mathrm{pp}}$ is the positive-sequence admittance of LCC-HVDC at the sending end, representing the small-signal response of AC current at f_{p} in positive sequence under per unit small-signal perturbation of AC voltage at f_{p} in positive sequence.

$\boldsymbol{Y}_{\mathrm{LCC}}^{\mathrm{pn}}$ is the positive-sequence coupling admittance of LCC-HVDC at the sending end, representing the small-signal response of AC current at $f_{\mathrm{p}} - 2f_1$ in negative sequence under per unit small-signal perturbation of AC voltage at f_{p} in positive sequence.

$\boldsymbol{Y}_{\mathrm{LCC}}^{\mathrm{nn}}$ is the negative-sequence admittance of LCC-HVDC at the sending end, representing the small-signal response of AC current at $f_{\mathrm{p}} - 2f_1$ in negative sequence under per unit small-signal perturbation of AC voltage at $f_{\mathrm{p}} - 2f_1$ in negative sequence.

$\boldsymbol{Y}_{\mathrm{LCC}}^{\mathrm{np}}$ is the negative-sequence coupling admittance of LCC-HVDC at the sending end, representing the small-signal response of AC current at f_{p} in positive sequence under per unit small-signal perturbation of AC voltage at $f_{\mathrm{p}} - 2f_1$ in negative sequence.

$$\begin{bmatrix} \boldsymbol{Z}_{\mathrm{LCC}}^{\mathrm{pp}} & \boldsymbol{Z}_{\mathrm{LCC}}^{\mathrm{pn}} \\ \boldsymbol{Z}_{\mathrm{LCC}}^{\mathrm{np}} & \boldsymbol{Z}_{\mathrm{LCC}}^{\mathrm{nn}} \end{bmatrix} = \begin{bmatrix} \boldsymbol{Y}_{\mathrm{LCC}}^{\mathrm{pp}} & \boldsymbol{Y}_{\mathrm{LCC}}^{\mathrm{np}} \\ \boldsymbol{Y}_{\mathrm{LCC}}^{\mathrm{pn}} & \boldsymbol{Y}_{\mathrm{LCC}}^{\mathrm{nn}} \end{bmatrix}^{-1} \tag{17.9}$$

where

$\boldsymbol{Z}_{\mathrm{LCC}}^{\mathrm{pp}}$ represents the positive-sequence impedance and is the element in the first row and the first column of the AC port admittance inverse matrix.

$\boldsymbol{Z}_{\mathrm{LCC}}^{\mathrm{pn}}$ represents the positive-sequence coupling impedance and is the element in the first row and the second column of the AC port admittance inverse matrix.

$\boldsymbol{Z}_{\mathrm{LCC}}^{\mathrm{nn}}$ represents the negative-sequence impedance and is the element in the second row and the second column of the AC port admittance inverse matrix.

$\boldsymbol{Z}_{\mathrm{LCC}}^{\mathrm{np}}$ represents the negative-sequence coupling impedance and is the element in the second row and the first column of the AC port admittance inverse matrix.

In addition, the frequency-domain relationship between the negative-sequence impedance and the positive-sequence impedance satisfies $\boldsymbol{Z}_{\mathrm{LCC}}^{\mathrm{nn}} = \boldsymbol{Z}_{\mathrm{LCC}}^{\mathrm{pp}*}(\mathrm{j}2\omega_1 - s)$, and the frequency-domain relationship between the negative- sequence coupling impedance and the positive-sequence coupling impedance satisfies $\boldsymbol{Z}_{\mathrm{LCC}}^{\mathrm{np}} = \boldsymbol{Z}_{\mathrm{LCC}}^{\mathrm{pn}*}(\mathrm{j}2\omega_1 - s)$.

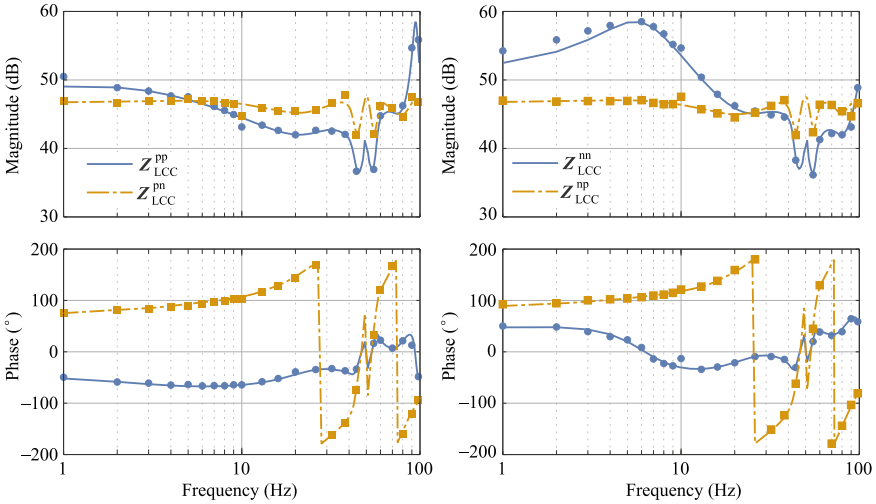

(a) Positive-sequence impedance and positive-sequence coupling impedance

(b) Negative-sequence impedance and negative-sequence coupling impedance

Fig. 17.3 Comparison of the analytical impedance model and simulation scanning results after the impedance reshaping of LCC-HVDC

Figure 17.3 shows the comparison of the analytical impedance model and simulation scanning results after the impedance reshaping of LCC-HVDC. The analytical model matches the scanning results well, which verifies the correctness of the analytical model after LCC-HVDC impedance reshaping. The analytical model is depicted in a solid line and the scanning results are marked in discrete points. The voltage ratio of the transformer in the sending-end LCC is 530kV/164kV, the minimum firing angle α_{fmin} is 5°, and the other main circuit parameters of LCC-HVDC are consistent with Table 10.3.

17.3 Impedance Reshaping Design of LCC-HVDC

The comparison of the impedance curves of LCC-HVDC before and after impedance reshaping is shown in Fig. 17.4. In the figure, the negative damping characteristics in the super-synchronous frequency band are eliminated after the impedance reshaping, which verifies the effectiveness of the impedance reshaping strategy.

Furthermore, according to the impedance reshaping model of LCC-HVDC, the influences of PLL in the sending-end LCC, control loops in the receiving-end LCC, and main circuit parameters influence on the impedance characteristics is analyzed as follows.

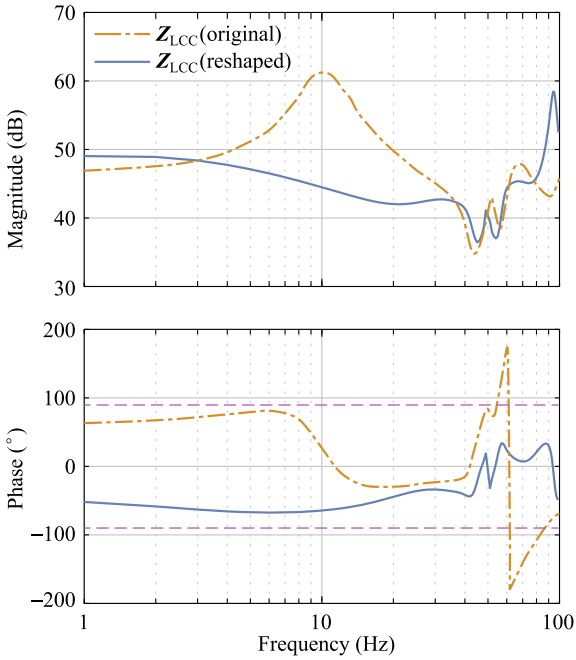

Fig. 17.4 Comparison of LCC-HVDC impedance characteristics before and after impedance reshaping

17.3.1 Influence of PLL of the Sending-End LCC on Impedance Characteristics

According to Eq. (17.6), the AC port impedance of LCC-HVDC is influenced by PLL in the sending-end LCC via the matrixes of $\boldsymbol{\Lambda}_3$ and $\boldsymbol{\Lambda}_4$. The influence of PLL on the impedance characteristics is shown in Fig. 17.5. On the one hand, the influence of PLL bandwidth can be obtained by changing f_{ftc} to 10, 20 and 30 Hz respectively with a constant PM of 60°. On the other hand, the influence of PLL PM can be obtained by changing θ_{ftc} to 30°, 45° and 60° respectively with a constant bandwidth of 30 Hz.

As shown in Fig. 17.5, with the increase of PLL bandwidth, the impedance magnitude decreases, and the impedance phase in the sub-/super- synchronous frequency band is further away from ±90°. This indicates that the damping characteristics of LCC-HVDC are effectively improved. Besides, with the increase of PLL PM, the damping characteristics at the impedance resonance peak are enhanced, which changes from negative damping to positive damping. In consequence, increasing the bandwidth and PM of the PLL in the sending-end LCC can optimize the impedance characteristics of LCC-HVDC.

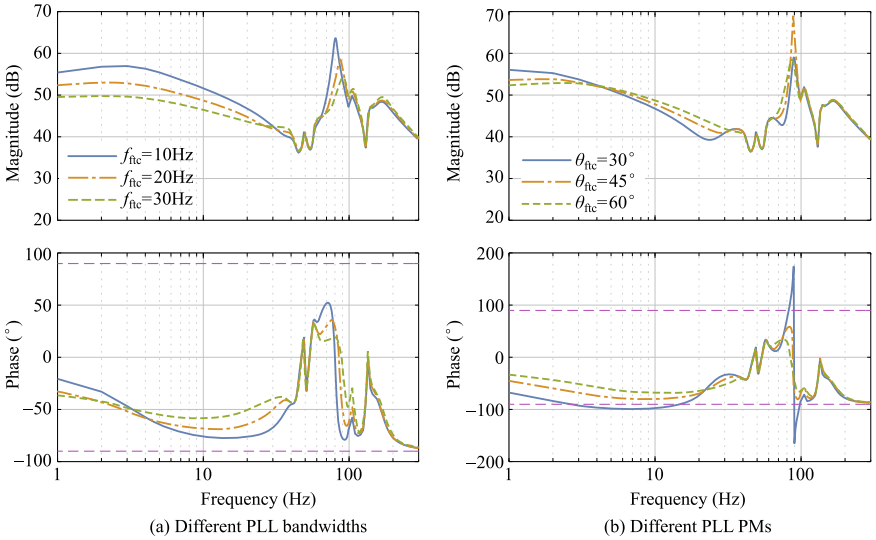

(a) Different PLL bandwidths (b) Different PLL PMs

Fig. 17.5 The influence of PLL in the sending-end LCC on impedance characteristics of LCC-HVDC

17.3.2 Influence of Control Loops of the Receiving-End LCC on Impedance Characteristics

According to Eqs. (17.6) and (17.7), the AC port impedance of LCC-HVDC is influenced by the receiving-end LCC $\boldsymbol{Z}'_{\text{edc}}$. In addition, $\boldsymbol{Z}'_{\text{edc}}$ is influenced by both DC current control and PLL in the receiving-end LCC via the matrixes of $\boldsymbol{\Gamma}'_3$, $\boldsymbol{\Gamma}'_4$, $\boldsymbol{\Gamma}_1$ and $\boldsymbol{\Gamma}_2$ according to Eq. (17.4).

The influence of the DC current control on the impedance characteristics is shown in Fig. 17.6. Firstly, set the PLL bandwidth of the sending-end LCC f_{idc} to 30Hz, and set the PLL PM of the sending-end LCC θ_{idc} to 60°. On the one hand, the influence of the bandwidth of DC current control loop can be obtained by changing f_{idc} to 10, 20 and 30Hz respectively with a constant PM of 45°. On the other hand, the influence of the PM of DC current control loop can be obtained by changing θ_{idc} to 30°, 45° and 60° with a constant bandwidth of 40Hz.

As shown in Fig. 17.6, with the increase of the bandwidth of DC current control loop f_{idc}, the damping characteristics of Z_{LCC} in the subsynchronous frequency band are enhanced, and the impedance magnitude and phase variations become smoother. The change of the PM of DC current control loop θ_{idc} has little influence on the impedance characteristics of Z_{LCC}. Therefore, the impedance characteristics of LCC-HVDC can be optimized by appropriately increasing the bandwidth of DC current control loop in the receiving-end LCC.

The influence of PLL in the receiving-end LCC on the impedance characteristics is shown in Fig. 17.7. On the one hand, the influence of PLL bandwidth can be

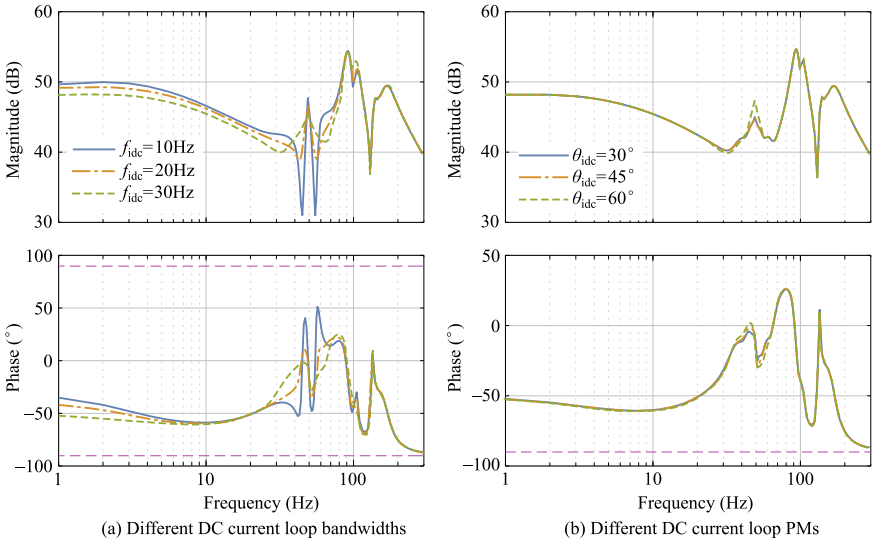

Fig. 17.6 The influence of DC current control in the receiving-end LCC on impedance characteristics of LCC-HVDC

obtained by changing f_{etc} to 10, 20 and 30Hz respectively with a constant PM of 45°. On the other hand, the influence of PLL PM can be obtained by changing θ_{etc} to 30°, 45° and 60° respectively with a constant bandwidth of 10 Hz.

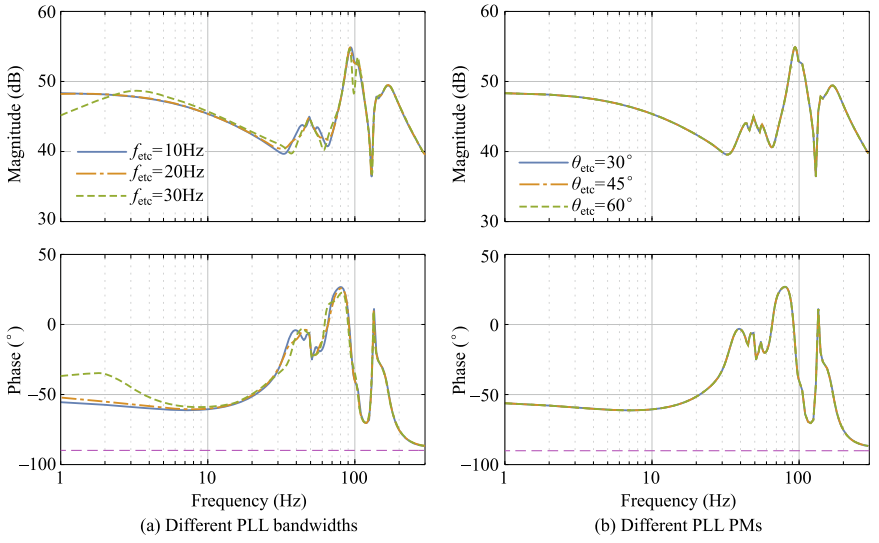

Fig. 17.7 The influence of PLL in the receiving-end LCC on impedance characteristics of LCC-HVDC

As shown in Fig. 17.7, the changes of the bandwidth and PM of PLL in the receiving-end LCC have relatively little influence on the impedance characteristics of Z_{LCC}.

17.3.3 *Influence of Main Circuit Parameters on Impedance Characteristics*

Based on the control parameter optimization in Sects. 17.3.1 and 17.3.2, the influence of the DC transmission line length and SCR at the receiving end on the AC port impedance of LCC-HVDC at the sending end will be analyzed.

By changing DC transmission line length l_{line} to 1000, 1500, and 2000 km respectively with a constant SCR at the receiving end of 3.0, the variation of LCC-HVDC impedance curves is shown in Fig. 17.8(a). By changing the SCR at the receiving end to 2.0, 3.0, and 5.0 respectively with a constant DC transmission line length of 1000 km, the variation of LCC-HVDC impedance curves is shown in Fig. 17.8(b).

As shown in Fig. 17.8, the influence of the SCR at the receiving end and DC transmission line length on the impedance characteristics of LCC-HVDC is similar. With the decrease of SCR at the receiving end,the AC grid impedance increases, and its coupling influence on the DC port impedance of the receiving-end LCC becomes more apparent, which leads to the increase of the DC port impedance. Furthermore, the DC port impedance and DC transmission line impedance together comprise the DC-side impedance of the sending-end LCC. As SCR at the receiving end decreases

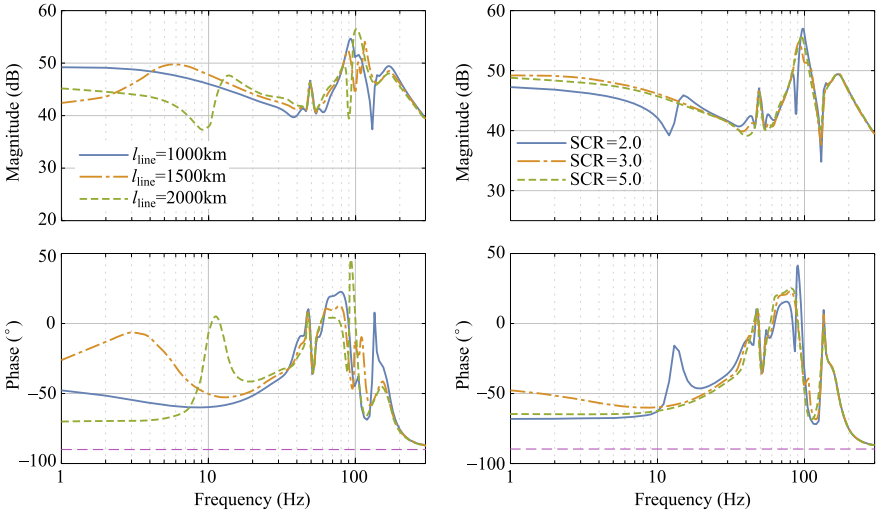

Fig. 17.8 The influence of main circuit parameters on impedance characteristics of LCC-HVDC

and DC transmission line length increases, the DC-side impedance of the sending-end LCC increases, and its coupling influence on the AC port impedance of the sending-end LCC is more apparent. The frequency at the resonance peak of the AC port impedance becomes closer to the fundamental frequency. In addition, there is no negative damping of LCC-HVDC impedance when the DC transmission line length and SCR at the receiving end change, which verifies the effectiveness of the impedance reshaping of LCC-HVDC.

17.4 Simulation Verification

In this section, the time-domain simulation and frequency-domain analysis of a REG connected into the LCC-HVDC system are carried out on the full EMT simulation platform. The effectiveness of the proposed oscillation mitigation strategy based on the impedance reshaping of LCC-HVDC is verified.

17.4.1 Oscillation Mitigation of PMSG-Based Wind Plants Connected into LCC-HVDC System

The EMT simulation parameters of the PMSG-based wind plants and the LCC-HVDC are listed in Tables 14.1 and 14.2, respectively. Figure 17.9 shows the evaluation results of oscillation risk for PMSG-based wind plants connected into LCC-HVDC system.

As seen from Fig. 17.9(a), the magnitude curves of wind plant impedance $\boldsymbol{Z}_{\mathrm{PMSG}}$ and the system impedance $\boldsymbol{Z}_{\mathrm{sys}}$ intersect at Point A (64Hz), and the PM is only 7° before LCC-HVDC impedance reshaping. The GM/PM is insufficient, indicating oscillation risk in the system. After the impedance reshaping, the intersection point of the magnitude curves shifts from Point A to Point B (77Hz), and the PM is increased to 48.7°. The stability margin is thus improved and the oscillation risk is eliminated.

As seen from Fig. 17.9(b), the original Nyquist curve around Point A (64Hz) is in the forbidden area with $R_{\min} = 0.2$, indicating oscillation risk. After the impedance reshaping, the optimized Nyquist curve is always outside the forbidden area, indicating that the impedance reshaping of LCC-HVDC effectively eliminates the oscillation risk of the system.

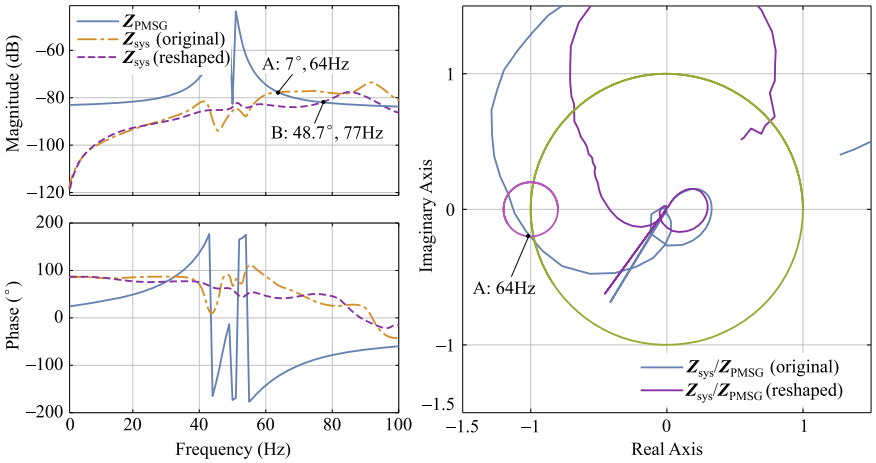

Fig. 17.9 The evaluation results of oscillation risk for PMSG-based wind plants connected into LCC-HVDC system

17.4.2 Oscillation Mitigation of DFIG-Based Wind Plants Connected into LCC-HVDC System

The EMT simulation parameters of the DFIG-based wind plants and the LCC-HVDC are listed in Tables 14.2 and 14.4, respectively. Figure 17.10 shows the evaluation results of oscillation risk for DFIG-based wind plants connected into LCC-HVDC system.

As seen from Fig. 17.10(a), the magnitude curves of wind plant impedance $\boldsymbol{Z}_{\mathrm{DFIG}}$ and the system impedance $\boldsymbol{Z}_{\mathrm{sys}}$ intersect at Point C (43Hz), and the PM is only 6° before LCC-HVDC impedance reshaping. The GM/PM is insufficient, indicating oscillation risk in the system. After the impedance reshaping, the intersection point of the magnitude curves shifts from Point C to Point D (40Hz), and the PM is increased to 53.2°. The stability margin is thus improved and the oscillation risk is eliminated.

As seen from Fig. 17.10(b), the original Nyquist curve around Point C (43Hz) is in the forbidden area with $R_{\min} = 0.2$, indicating oscillation risk. After the impedance reshaping, the optimized Nyquist curve is always outside the forbidden area, indicating that the impedance reshaping of LCC-HVDC effectively eliminates the oscillation risk of the system.

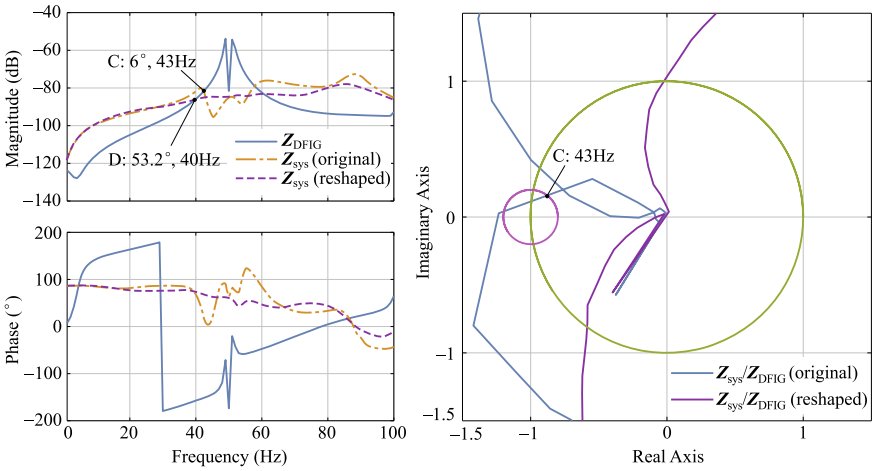

(a) System impedance Bode plot (b) System Nyquist plot

Fig. 17.10 The evaluation results of oscillation risk for DFIG-based wind plants connected into LCC-HVDC system

17.4.3 Oscillation Mitigation of PV Plants Connected into LCC-HVDC System

The EMT simulation parameters of the PV plants and the LCC-HVDC are listed in Tables 14.2 and 14.6, respectively. Figure 17.11 shows the evaluation results of oscillation risk for PV plants connected into LCCHVDC system.

As seen from Fig. 17.11(a), the magnitude curves of PV plant impedance $\boldsymbol{Z}_{PV}$ and the system impedance $\boldsymbol{Z}_{sys}$ intersect at Point E (75Hz), and the PM is only 4.9° before LCC-HVDC impedance reshaping. The GM/PM is insufficient, indicating oscillation risk in the system. After the impedance reshaping, the intersection point of the magnitude curves shifts from Point E to Point F (90Hz), and the PM is increased to 32.3°. The stability margin is thus improved and the oscillation risk is eliminated.

As seen from Fig. 17.11(b), the original Nyquist curve around Point E (75 Hz) is in the forbidden area with $R_{min} = 0.15$, indicating oscillation risk. After the impedance reshaping, the optimized Nyquist curve is always outside the forbidden area, indicating that the impedance reshaping of LCC-HVDC effectively eliminates the oscillation risk of the system.

The time-domain simulation of PV plants connected into MMC-HVDC system is conducted based on the full simulation platform. The current waveforms of PV plants and the corresponding FFT results are shown in Fig. 17.12.

As seen from Fig. 17.12, there is a super-synchronous oscillation component at 75 Hz and a coupling super-synchronous oscillation component at 25Hz according to the FFT results of the PV plant currents. After the impedance reshaping control of LCC-HVDC is enabled at t = 1.2 s, the oscillations of voltage amplitude and

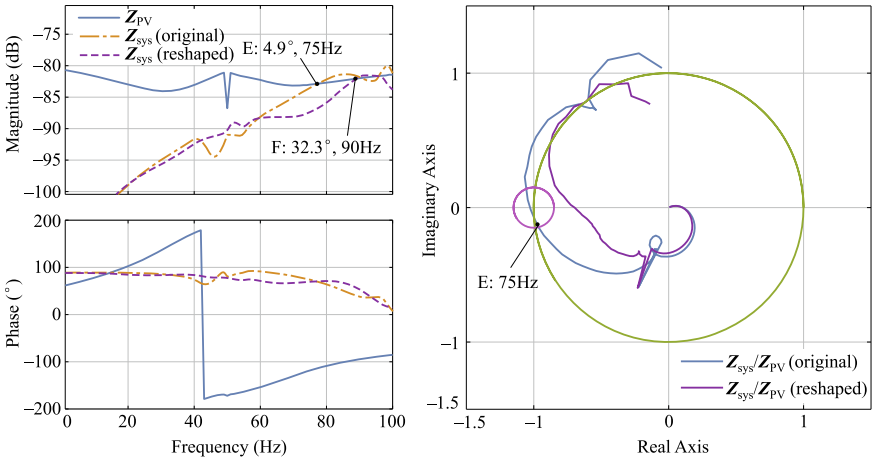

(a) System impedance Bode plot (b) System Nyquist plot

Fig. 17.11 The evaluation results of oscillation risk for PV plants connected into LCC-HVDC system

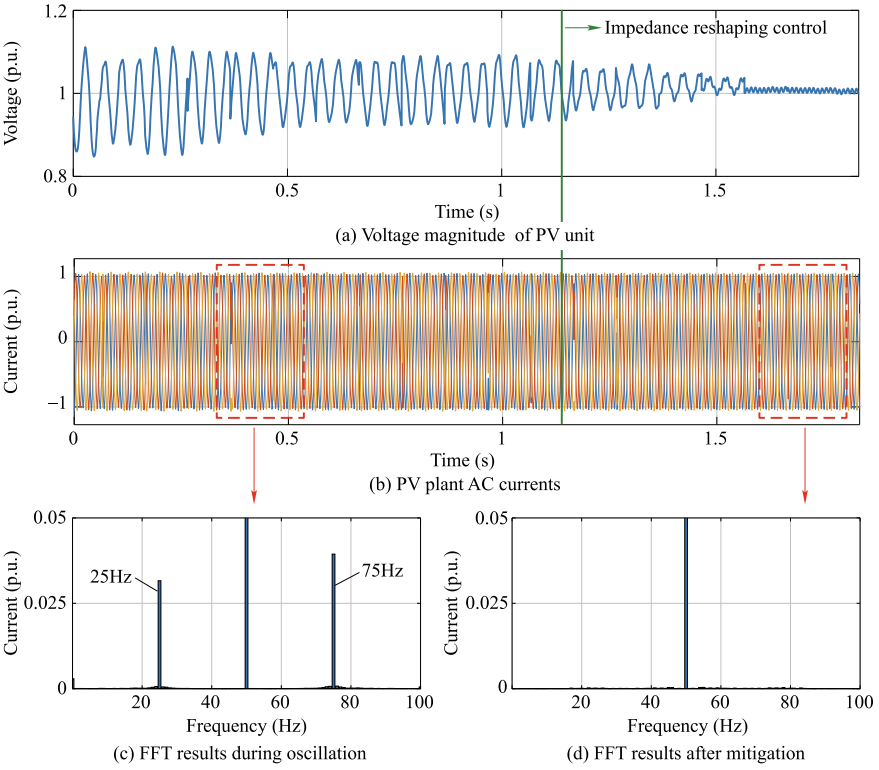

(a) Voltage magnitude of PV unit

(b) PV plant AC currents

(c) FFT results during oscillation (d) FFT results after mitigation

Fig. 17.12 The current waveforms and FFT results of PV plants

current waveforms of the PV plants are gradually mitigated, and the sub- and super-synchronous oscillation components are eliminated as shown in the corresponding FFT analysis.The simulation results verify the effectiveness of oscillation mitigation strategy based on the proposed impedance reshaping of LCC-HVDC.

Chapter 18
Oscillation Mitigation Based on Impedance Reshaping of MMC-HVDC

Compared with LCC-HVDC, the improvement of control strategy for MMC-HVDC is more flexible due to the multiple control loops and wider control bandwidth. For the oscillation of REG connected into MMC-HVDC system, the oscillation mitigation can be achieved by the impedance reshaping of MMC-HVDC in a wider frequency range [1, 2].

In this chapter, the control strategy of broadband impedance reshaping for MMC-HVDC is first illustrated, and the impedance model is refined with the consideration of the control strategy. Then, the design of the MMC-HVDC impedance based on control strategy improvement and control parameter optimization is presented, in which the control interactions between different frequency bands are taken into account. The negative damping characteristics of each frequency band are eliminated by the impedance reshaping of MMC-HVDC. Finally, the oscillation mitigation strategy is verified based on the full EMT simulation platform for a REG connected into MMC-HVDC system.

18.1 Impedance Reshaping Strategy of MMC-HVDC

The broadband negative damping characteristics of MMC-HVDC are caused by the frequency-band overlapping effect of different control loops and main circuit. The mitigation of negative damping can be achieved by impedance reshaping based on the control strategy improvement and control parameter optimization.

© China Electric Power Press 2023

W. Wang et al., *Analysis and Mitigation of Broadband Oscillation in Renewable Energy Generation and AC/DC Transmission Systems*,
https://doi.org/10.1007/978-981-99-1568-2_18

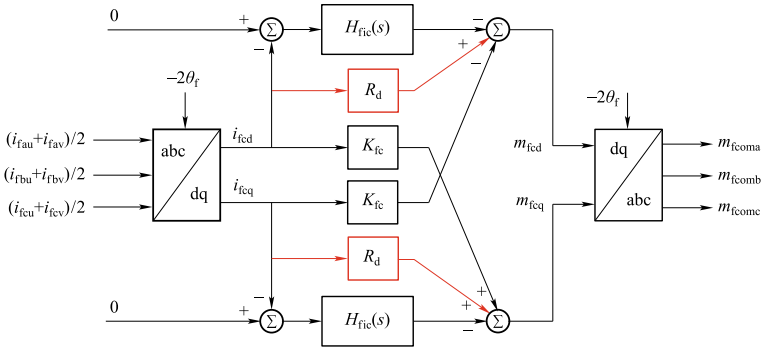

Fig. 18.1 The block diagram of the virtual resistance control based on circulating current feedforward

18.1.1 Impedance Reshaping Method of Band I_{MMC}

The frequency-band overlapping effect of the circulating current control loop and main circuit leads to the negative damping characteristics in Band I_{MMC}. With the virtual resistance control based on circulating current feedforward, the negative damping characteristics in Band I_{MMC} can be eliminated. The block diagram of the virtual resistance control based on circulating current feedforward is shown in Fig. 18.1, where R_d is the virtual resistance.

18.1.2 Impedance Reshaping Method of Band III_{MMC}

As mentioned in Chap. 11, if the PM of AC current control loop is relatively small, the frequency-band overlapping effect of the time delay and the AC current control loop causes capacitive negative damping in Band III_{MMC}. The negative damping in Band III_{MMC} can be eliminated by optimizing the PM of the AC current control loop.

18.1.3 Impedance Reshaping Method of Band IV_{MMC}

The negative damping characteristics in Band IV_{MMC} are caused by the frequency-band overlapping effect of the time delay and the main circuit, which is similar to that of REG. First, AC filter capacitors are additionally required in parallel to the AC port of MMC-HVDC. Then, the capacitor current can be introduced in a feedforward path to compensate for the impedance phase in Band IV_{MMC}, which is the proposed active damping control method. The block diagram of the proposed active damping control is shown in Fig. 18.2.

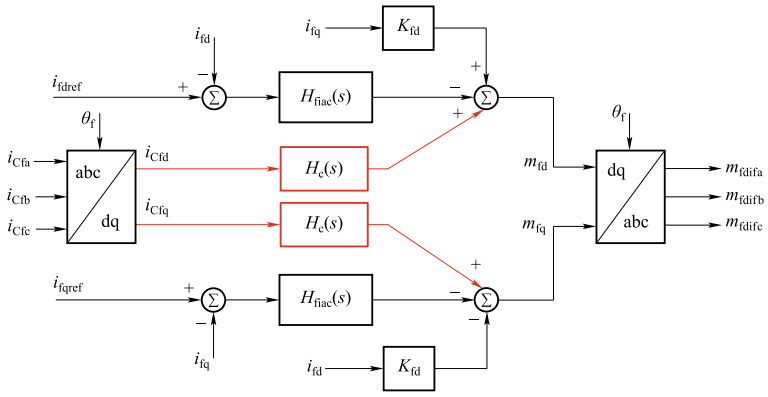

Fig. 18.2 The block diagram of the active damping control based on capacitor current feedforward

In Fig. 18.2, i_{Cfa}, i_{Cfb} and i_{Cfc} are the three-phase AC currents of the filter capacitors, and i_{Cfd}, i_{Cfq} are the d- and q-axis components of the capacitor currents. The active damping control utilizes a lead-lag compensator to improve the impedance phase, whose transfer function is

$$H_c(s) = k_c \cdot \frac{s/\omega_{c1} + 1}{s/\omega_{c2} + 1} \tag{18.1}$$

where k_c is the active damping coefficient and can be designed to adjust the damping characteristics in Band IV_{MMC}. ω_{c1} and ω_{c2} are the lower and upper limits of the angular frequency for the active damping control respectively, which can be designed to adjust the working frequency range of the compensator.

18.2 Reshaped Impedance Model of MMC-HVDC

With the virtual resistance control in Sect. 18.1.1, the small-signal vector of the arm common mode (CM) modulation signal of MMC-HVDC is given as

$$\hat{\boldsymbol{m}}_{\text{fcoma}} = (\boldsymbol{G}_{\text{f3}} + \Delta\boldsymbol{G}_{\text{f3}})\boldsymbol{D}_{\text{f3}}\hat{\boldsymbol{i}}_{\text{au}} \tag{18.2}$$

where $\Delta\boldsymbol{G}_{\text{f3}}$ is the transfer function matrix introduced by the virtual resistance control, and all other elements in the matrix are zero except for Eq. (18.3).

$$\Delta\boldsymbol{G}_{\text{f3}}(g+k+1, g+k+1) = \frac{1-(-1)^k}{2} \cdot |\text{mod}(k+1, 3)| \cdot R_{\text{d}} \tag{18.3}$$

With the active damping control in Sect. 18.1.3, the small-signal vector of the arm differential mode (DM) modulation signal is given as

$$\hat{\boldsymbol{m}}_{\text{fdifa}} = \boldsymbol{G}_{\text{f1}} \boldsymbol{D}_{\text{f1}} \hat{\boldsymbol{i}}_{\text{fau}} + \left(\boldsymbol{G}_{\text{f2}} + \Delta \boldsymbol{G}'_{\text{f2}}\right) \boldsymbol{D}_{\text{f2}} \hat{\boldsymbol{v}}_{\text{fa}} \tag{18.4}$$

where $\Delta \boldsymbol{G}'_{\text{f2}}$ is the transfer function matrix introduced by the active damping control, and all other elements in the matrix are zero except for Eq. (18.5).

$$\begin{cases} \Delta \boldsymbol{G}'_{\text{f2}}(g-1, g-1) = \text{j}2\pi(f_{\text{p}} - 2f_1) C_{\text{f}} \cdot H_{\text{c}}[\text{j}2\pi(f_{\text{p}} - f_1)] \\ \Delta \boldsymbol{G}'_{\text{f2}}(g+1, g+1) = \text{j}2\pi f_{\text{p}} C_{\text{f}} \cdot H_{\text{c}}[\text{j}2\pi(f_{\text{p}} - f_1)] \end{cases} \tag{18.5}$$

By substituting Eqs. (18.2) and (18.4) into the small-signal model of the main circuit, the impedance analytical model of MMC-HVDC including impedance reshaping strategy can be obtained.

18.3 Impedance Reshaping Design of MMC-HVDC

The negative damping characteristics of MMC-HVDC impedance may occur in Band I_{MMC}, III_{MMC} and IV_{MMC}, as shown in Fig. 18.3. As seen from the figure, the negative damping characteristics present capacitive (impedance phase below $-90°$) in Band I_{MMC} and III_{MMC}, and inductive (impedance phase above 90°) in Band IV_{MMC}.

According to Sect. 18.1, the design of impedance reshaping is performed in the order of Band I_{MMC}, III_{MMC} and IV_{MMC} to eliminate the broadband negative damping characteristics. First, the virtual resistance R_{d} is optimized to enhance the damping characteristics in Band I_{MMC}. Then, the impedance phase in Band III_{MMC} is compensated by increasing the PM of the AC current control loop. Finally, the active damping coefficient k_{c} is designed to improve the damping characteristics in Band IV_{MMC}.

18.3.1 Impedance Reshaping Design of Band I_{MMC}

As mentioned in Sect. 18.1.1, the virtual resistance control based on circulating current feedforward can be adopted to eliminate the negative damping characteristics in Band I_{MMC}. The value of the virtual resistance R_{d} is refined to reshape the impedance curve in Band I_{MMC}. With R_{d} equivalent to 0, 3.125×10^{-5} and 3.125×10^{-4}, the variation of the impedance curves of MMC-HVDC in Band I_{MMC} is shown in Fig. 18.4.

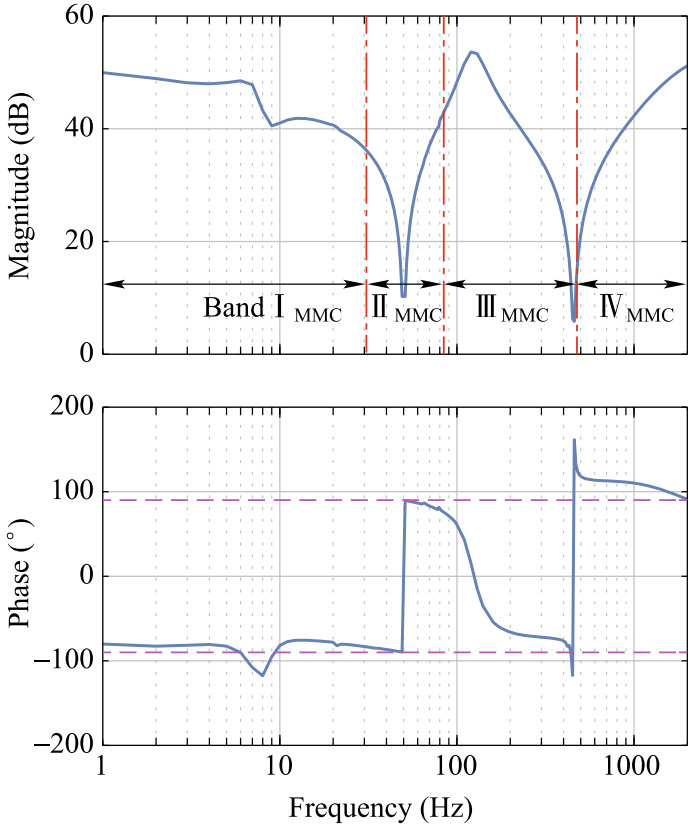

Fig. 18.3 Broadband negative damping characteristics before impedance reshaping

As shown in Fig. 18.4, compared with the impedance curve when $R_d = 0$, the proposed virtual resistance control can effectively enhance the damping characteristics in Band I_{MMC}. With the increase of R_d, the negative damping characteristics are gradually improved in this band, where the capacitive negative damping turns into the capacitive positive damping. The virtual resistance control is to compensate the circulating current control in Band IMMC, which mainly influences the impedance characteristics in this band. Based on plenty of research results and practical experience, the proposed virtual resistance control can eliminate the negative damping characteristics in Band I_{MMC} without impact on other frequency bands.

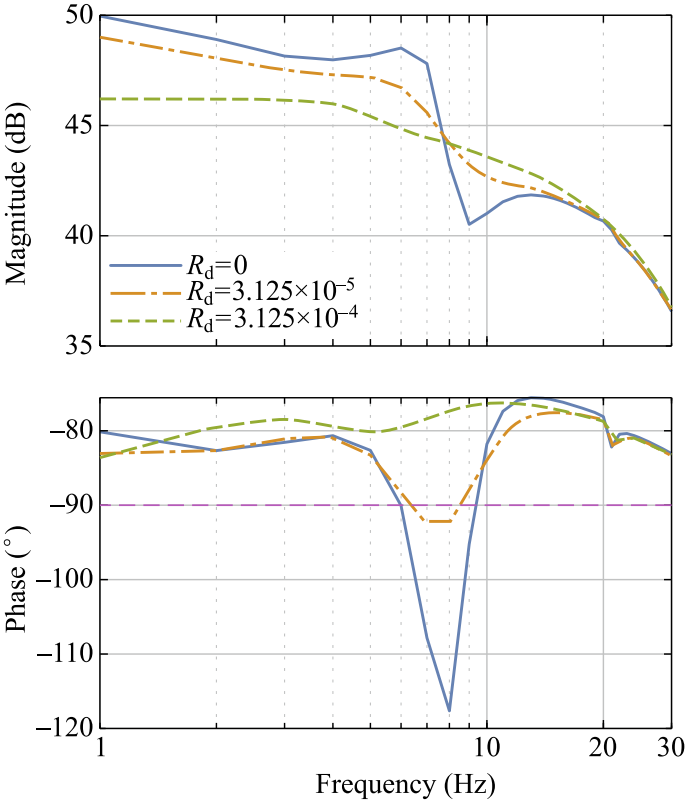

Fig. 18.4 The influence of the virtual resistance R_d on impedance characteristics of MMC-HVDC

18.3.2 Impedance Reshaping Design of Band III$_{MMC}$

The impedance characteristics of Band III are dominated by the AC current loop at the sending-end MMC. When the PM θ_{fiac} of the sending-end MMC AC current loop is in sufficient, the frequency band overlap effect with time delay results in the negative damping characteristics in the AC port impedance of the MMC-HVDC. As mentioned in Sect. 18.1.2, the PM of the AC current control loop can be optimized to compensate for the impedance phase of MMC-HVDC to eliminate the negative damping characteristics in Band III$_{MMC}$. By changing the PM of the AC current control loop θ_{fiac} to 10°, 20° and 45° respectively with a constant control loop bandwidth f_{fiac}, of 300 Hz, the variation of the impedance curves is shown in Fig. 18.5.

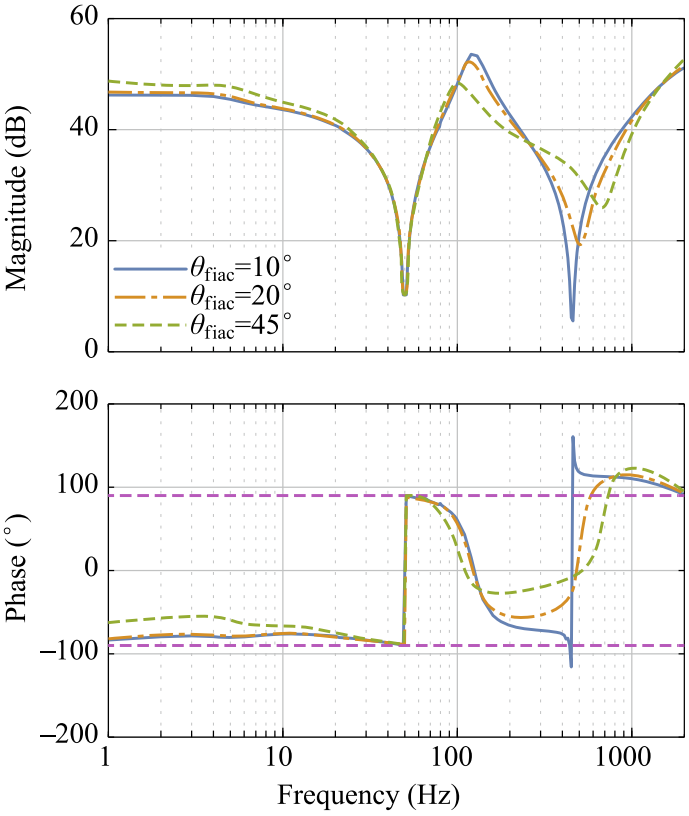

Fig. 18.5 The influence of AC current control optimization on impedance characteristics of MMC-HVDC

As shown in Fig. 18.5, the negative damping characteristics in Band III_{MMC} are eliminated with the increase of the PM. In addition, the AC current control also influences the impedance characteristics in Band I_{MMC}. With the increase of the PM of the AC current control loop, the impedance phase in Band I_{MMC} is also optimized. Therefore, the optimization of AC current control can not only eliminate the negative damping characteristics in Band III_{MMC}, but also further improve the damping characteristics in Band I_{MMC}.

18.3.3 Impedance Reshaping Design of Band IV_{MMC}

As mentioned in Sect. 18.1.3, additional control is necessarily adopted for eliminating the negative damping characteristics in Band IV_{MMC}, since the arm inductor is settled in practical projects and the time delay is difficult to decrease.

Figure 18.6 shows the influence of shunt capacitor on the impedance characteristics of MMC-HVDC. With the shunt capacitor, the impedance of MMC-HVDC exhibits a resonance peak at 1300 Hz (in Band IV_{MMC}). The negative damping characteristics change from inductive type to capacitive type when the frequency exceeds the resonance frequency. Moreover, the shunt capacitor does not affect the frequency range of negative damping in Band IV_{MMC}.

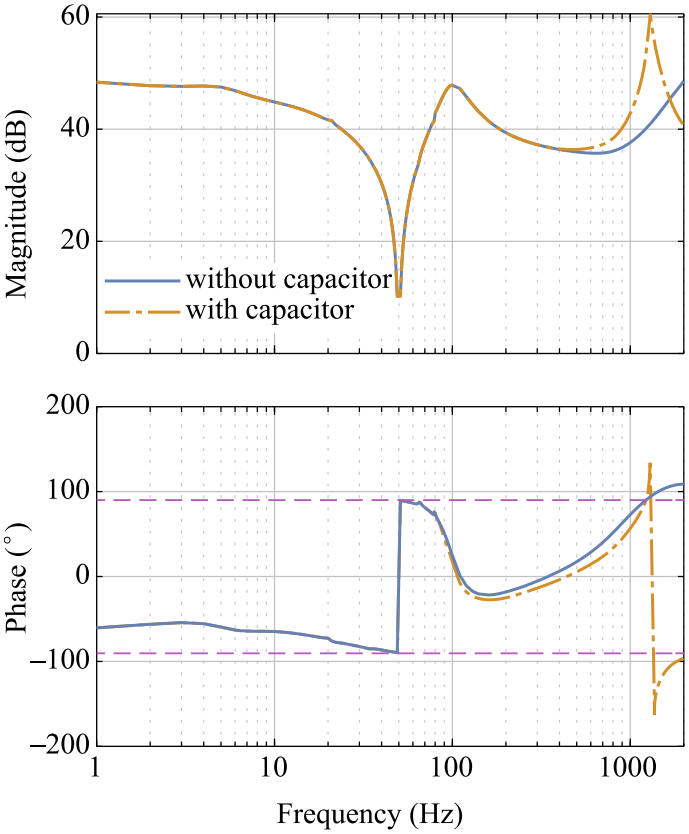

Fig. 18.6 The influence of shunt capacitor on the impedance characteristics of MMC-HVDC

According to Eq. (18.1), ω_{c1}, ω_{c2} of active damping control are firstly designed to set the center frequency of the controller near the resonance frequency. Then, impedance reshaping in Band IV_{MMC} is achieved by selecting different active damping coefficients. With k_c equivalent to 0, -2.3×10^{-5} and -4.6×10^{-5}, the variation of the impedance curves of MMC-HVDC is shown in Fig. 18.7.

As shown in Fig. 18.7, compared with the impedance curve when $k_c = 0$, the proposed active damping control can improve the damping characteristics in Band IV_{MMC}. With the increase k_c, the negative damping characteristics in Band

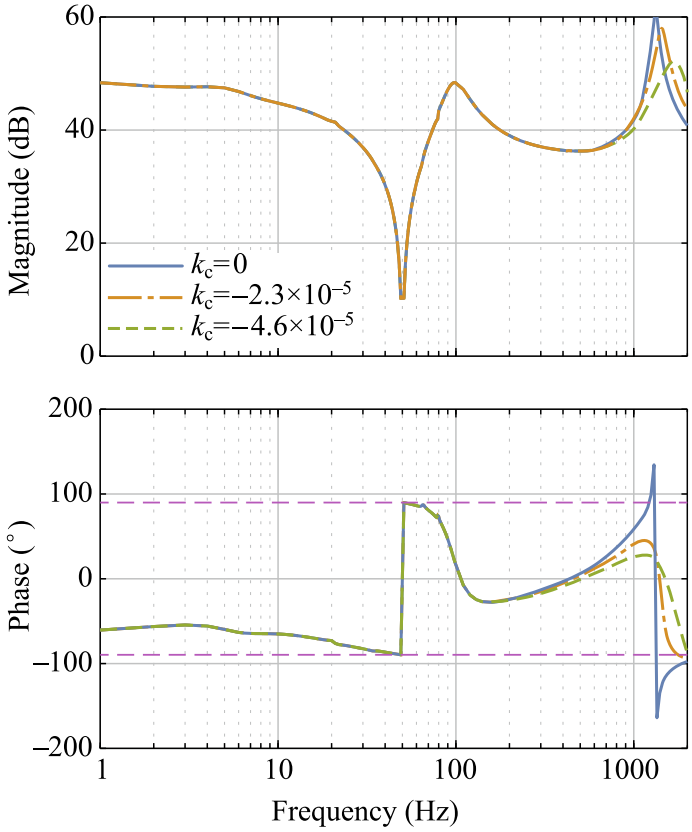

Fig. 18.7 The influence of active damping coefficient k_c on the impedance characteristics of MMC-HVDC

IV_{MMC} are eliminated, verifying the effectiveness of the active damping control. With the overall impedance reshaping strategy in Band I_{MMC}, III_{MMC} and IV_{MMC}, the optimized impedance characteristics of MMC-HVDC are shown in Fig. 18.8. As seen from the figure, the damping characteristics of the impedance is much better after the reshaping.

18.4 Simulation Verification

In this section, the time-domain simulation and frequency-domain analysis of a REG connected into the MMC-HVDC system are carried out on the full EMT simulation platform. The effectiveness of the proposed oscillation mitigation strategy based on the impedance reshaping of MMC-HVDC will be verified.

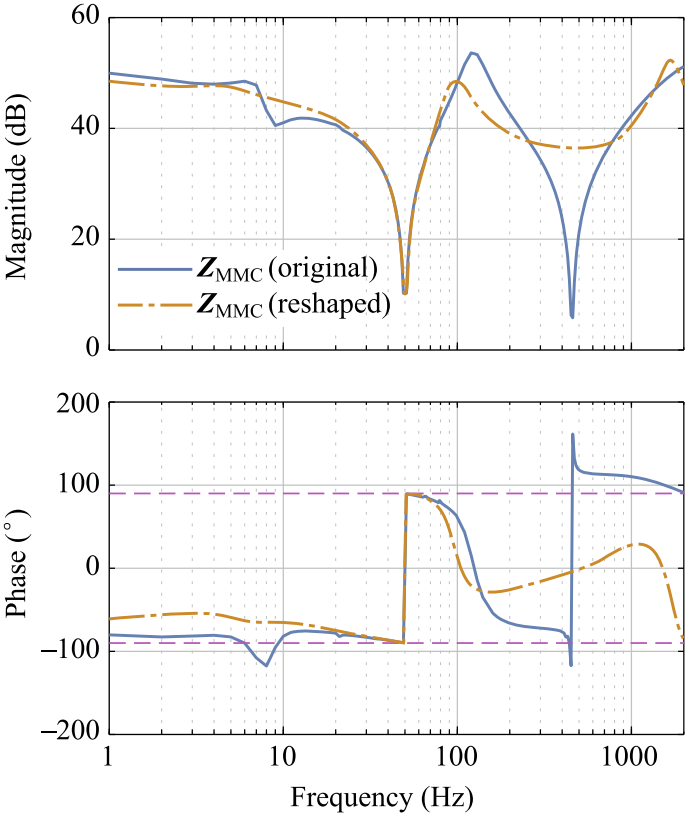

Fig. 18.8 Comparison of impedance characteristics before and after impedance reshaping

18.4.1 Oscillation Mitigation of PMSG-Based Wind Plants Connected into MMC-HVDC System

The EMT simulation parameters of the PMSG-based wind plants and the MMC-HVDC are listed in Tables 18.1 and 18.2 respectively. Fig. 18.9 shows the evaluation results of oscillation risk for PMSG-based wind plants connected into MMC-HVDC system before and after impedance reshaping.

As seen from Fig. 18.9(a), the magnitude curves of MMC-HVDC impedance $\boldsymbol{Z}_{\mathrm{MMC}}$ and wind plant impedance $\boldsymbol{Z}_{\mathrm{PMSG}}$ intersect at Point A (17 Hz), and the PM is only 9° before MMC-HVDC impedance reshaping. The GM/PM is insufficient, indicating oscillation risk in the system. After the impedance reshaping, the intersection point of the magnitude curves shifts from Point A to Point B (2 Hz), and the PM is increased to 50.5°. The stability margin is thus improved.

As seen from Fig. 18.9(b), the original Nyquist curve around Point A (17 Hz) is in the forbidden area with R = 0.2, indicating oscillation risk. The positive-sequence oscillation of 17 Hz with a coupled positive-sequence component of 83 Hz will occur

Table 18.1 EMT simulation parameters of PMSG-based wind plants

Parameter	Definition	Value
N_{PMSG}	Number of PMSG-based wind turbines	1250
P_{N}	Rated power	1.5 MW
P_{ref}	Active power reference	0.5 p.u.
V_{l}	Fundamental component amplitude of AC voltage	690 V
f_{l}	Fundamental frequency	50 Hz
k_{T}	AC transformer ratio	0.69/35 kV
R_{s}	Stator resistance	0.001 Ω
L_{sd}, L_{sq}	d- and q-axis inductance of the stator	0.2699, 0.283 mH
L_{f}	GSC filter inductance	0.1 mH
V_{dc}	Steady-state value of DC voltage	1500 V
K_{pp}, K_{pi}	Proportional and integral coefficients of PLL controller	0.2198, 4.8706
K_{gip}, K_{gii}	Proportional and integral coefficients of GSC current controller	8.5442×10^{-5}, 0.4351
K_{sip}, K_{sii}	Proportional and integral coefficients of MSC current controller	1.1404×10^{-5}, 6.3172×10^{-5}
K_{pep}, K_{pei}	Proportional and integral coefficients of active power controller	5×10^{-6}, 0.0200
K_{qep}, K_{qei}	Proportional and integral coefficients of reactive power controller	5.9207×10^{-4}, 0.0322
K_{vdcp}, K_{vdci}	Proportional and integral coefficients of DC voltage controller	1.3591, 31
K_{sd}	Decoupling coefficient of MSC current control	2.3160×10^{-5}
K_{gd}	Decoupling coefficient of GSC current control	4.2341×10^{-4}

in the system. After the impedance reshaping, the optimized Nyquist curve is always outside the forbidden area, indicating that the impedance reshaping of MMC-HVDC effectively eliminates the oscillation risk of the system.

The time-domain simulation of PMSG-based wind plants connected into MMC-HVDC system is conducted based on the full EMT simulation platform. The current waveforms of wind plants and the corresponding FFT results before and after the impedance reshaping of MMC-HVDC are shown in Fig. 18.10.

Table 18.2 EMT simulation parameters of MMC-HVDC

Parameter	Definition	Value
P_{N}	Rated power	1000 MW
V_{dcref}	DC voltage reference	640 kV
V_{f1}, V_{e1}	Amplitude of the fundamental component of the AC voltage	230 kV
k_{T}	AC transformer ratio	230/310 kV
N_{f}, N_{e}	Arm SM number	256
C_{fsm}, C_{esm}	SM capacitance	8 mF
L_{farm}, L_{earm}	Arm inductance	46.6 mH
SCR	Short circuit ratio at the receiving end	3.0
l_{line}	DC transmission line length	200 km
R_{dcL}	Line resistance in a single Π-line segment	0.005 Ω/km
L_{dcL}	Line inductance in a single Π-line segment	0.45 mH/km
C_{dcL}	Line capacitance in a single Π-line segment	0.015 μF/km
K_{vacp}, K_{vaci}	Proportional and integral coefficients of the AC voltage controller	0.0500, 4
K_{fiacp}, K_{fiaci}	Proportional and integral coefficients of the AC current controller in the sending-end MMC	1.2085×10^{-5}, 6.6947×10^{-4}
K_{ficp}, K_{fici}	Proportional and integral coefficients of the circulating current controller in the sending-end MMC	2.0800×10^{-5}, 0.0079
K_{epp}, K_{epi}	Proportional and integral coefficients of the PLL controller in the receiving-end MMC	3.2247×10^{-4}, 0.0175
K_{vdcp}, K_{vdci}	Proportional and integral coefficients of the DC voltage controller	0.0100, 0.0300
K_{eiacp}, K_{eiaci}	Proportional and integral coefficients of the AC current controller in the receiving-end MMC	3.4595×10^{-5}, 0.0119
K_{eicp}, K_{eici}	Proportional and integral coefficients of the circulating current controller in the receiving-end MMC	1.5625×10^{-4}, 0.0079

As seen from Fig. 18.10, initially, there is a sub-synchronous oscillation component at 17 Hz and a coupled super-synchronous oscillation component at 83 Hz according to the FFT results of the wind plant currents. After the impedance reshaping control of MMC-HVDC is enabled at $t = 2$ s, the oscillation of the current waveforms is mitigated, and the sub- and super- synchronous oscillation components are eliminated as shown in the corresponding FFT analysis. The simulation results verify

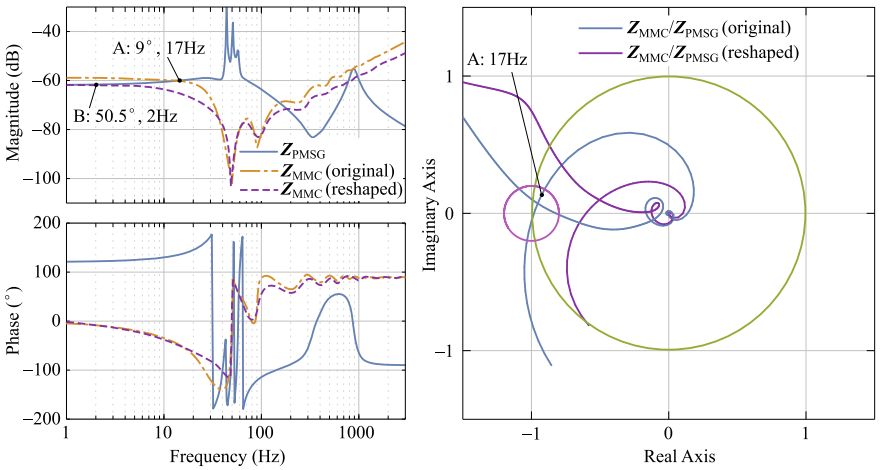

Fig. 18.9 The evaluation results of oscillation risk for PMSG-based wind plants connected into MMC-HVDC system before and after impedance reshaping

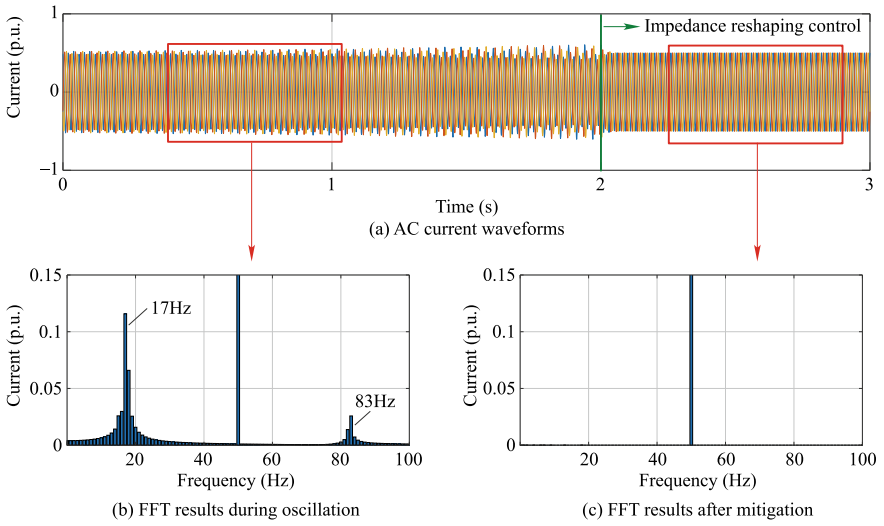

Fig. 18.10 The current waveforms and FFT results of PMSG-based wind plants before and after the impedance reshaping of MMC-HVDC

the effectiveness of oscillation mitigation strategy based on the proposed impedance reshaping of MMC-HVDC.

18.4.2 Oscillation Mitigation of DFIG-Based Wind Plants Connected into MMC-HVDC System

The EMT simulation parameters of the MMC-HVDC and DFIG-based wind plants are listed in Tables 18.2 and 18.3 respectively.

As seen from Fig. 18.11(a), the magnitude curves of MMC-HVDC impedance $\boldsymbol{Z}_{\mathrm{MMC}}$ and wind farm impedance $\boldsymbol{Z}_{\mathrm{DFIG}}$ intersect at Point C (29 Hz), and the PM is only 4.7° before MMC-HVDC impedance reshaping. The GM/PM is insufficient, indicating oscillation risk in the system. After the impedance reshaping, the intersection point of the magnitude curves shifts from Point C to Point D (44 Hz), and the PM is increased to 25.6°. The stability margin is thus improved and the oscillation risk is eliminated.

Table 18.3 EMT simulation parameters of DFIG-based wind plants

Variables Parameter	Definition	Value
N_{DFIG}	Number of DFIG-based wind turbines	420
P_{N}	Rated power	1.5 MW
V_{1}	Fundamental component amplitude of AC voltage	690 V
f_{1}	Fundamental frequency	50 Hz
k_{T}	AC transformer ratio	0.69/35 kV
R_{s}, R_{r}	Stator and rotor resistance	0.0022, 0.0027
L_{1s}, L_{1r}	Stator and rotor leakage inductance	1.4437×10^{-4}, 1.0913×10^{-4}
L_{ms}, L_{mr}	Stator and rotor mutual inductance	0.0041
L_{f}	GSC filter inductance	0.7 mH
V_{dc}	Steady-state value of DC voltage	1500 V
K_{e}	Turn ratio of stator and rotor windings	3
K_{pp}, K_{pi}	Proportional and integral coefficients of PLL controller	0.1048, 2.3967
K_{gip}, K_{gii}	Proportional and integral coefficients of GSC current controller	0.0016, 3.7600
K_{rip}, K_{rii}	Proportional and integral coefficients of RSC current controller	1.4359×10^{-5}, 7.5702×10^{-5}
K_{pep}, K_{pei}	Proportional and integral coefficients of active power controller	6×10^{-4}, 0.0020
K_{qep}, K_{qei}	Proportional and integral coefficients of reactive power controller	6×10^{-4}, 0.0020
K_{vdcp}, K_{vdci}	Proportional and integral coefficients of DC voltage controller	3.9301, 155
K_{gd}	Decoupling coefficient of GSC current control	3.300×10^{-5}
K_{rd}	Decoupling coefficient of RSC current control	1.8744×10^{-4}

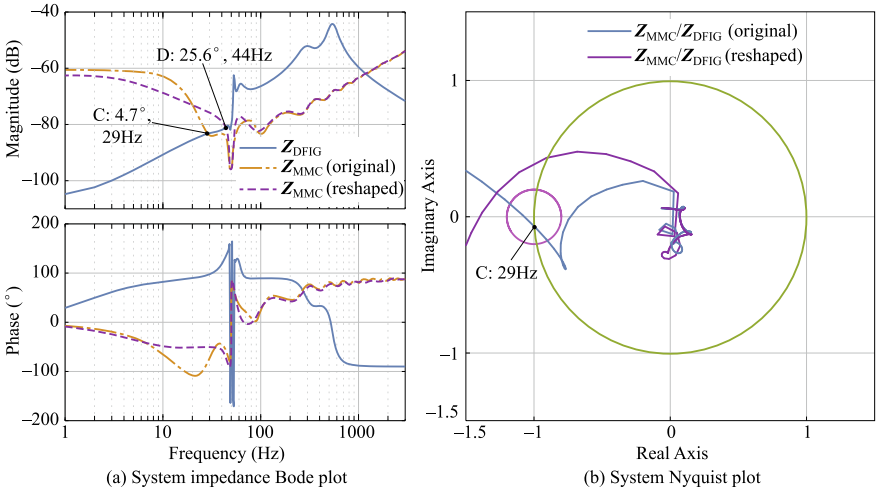

Fig. 18.11 The evaluation results of oscillation risk for DFIG-based wind plants connected into MMC-HVDC system before and after impedance reshaping

As seen from Fig. 18.11(b), the original Nyquist curve around Point C (29 Hz) is in the forbidden area with $R_{min} = 0.2$, indicating oscillation risk. The positive-sequence oscillation of 29 Hz with a coupling positive-sequence oscillation of 71 Hz will occur in the system. After the impedance reshaping, the optimized Nyquist curve is always

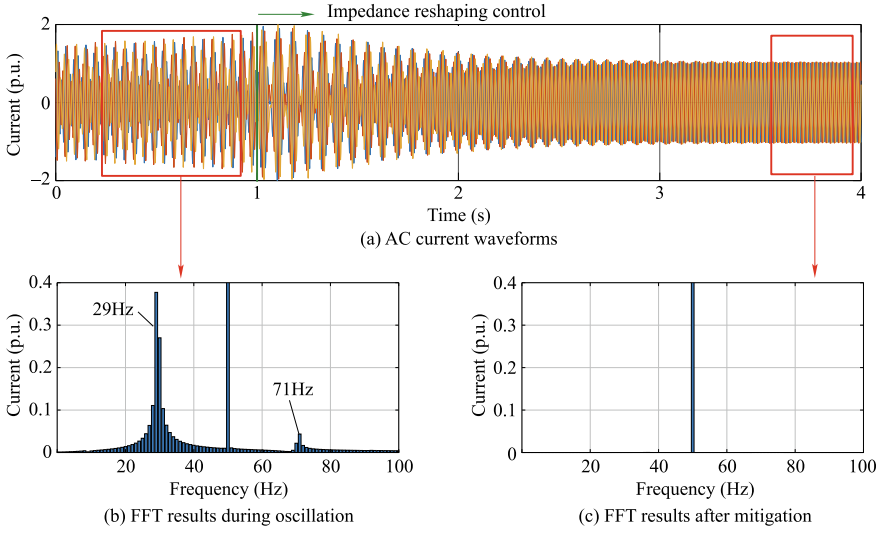

Fig. 18.12 The current waveforms and FFT results of DFIG-based wind plants before and after the impedance reshaping of MMC-HVDC

outside the forbidden area, indicating that the impedance reshaping of MMC-HVDC effectively eliminates the oscillation risk of the system.

The time-domain simulation of DFIG-based wind plants connected into MMC-HVDC system is conducted based on the full EMT simulation platform. The current waveforms of wind plants and the corresponding FFT results before and after the impedance reshaping of MMC-HVDC are shown in Fig. 18.12.

As seen from Fig. 18.12, initially, there is a subsynchronous oscillation component at 29 Hz and a coupling super-synchronous oscillation component at 71 Hz according to the FFT results of wind plant currents. After the impedance reshaping control of MMC-HVDC is enabled at $t = 1$ s, the oscillation of the current waveforms is gradually mitigated, and the sub- and super- synchronous oscillation components are eliminated as shown in the corresponding FFT analysis. The simulation results verify the effectiveness of oscillation mitigation strategy based on the proposed impedance reshaping of MMC-HVDC.

18.4.3 Oscillation Mitigation of Overhead Lines Connected into MMC-HVDC System

Taking the overheadline connected into MMC-HVDC system as an example, the frequency-domain analysis and time-domain simulation of the oscillation suppression based on MMC-HVDC reshaping is conducted. The EMT simulation parameters of the MMC-HVDC and the overhead lines are listed in Tables 18.2 and 18.4 respectively. Figure 18.13 shows the evaluation results of oscillation risk for AC overhead lines connected into MMC-HVDC system before and after impedance reshaping.

As seen from Fig. 18.13(a), the magnitude curves of MMC-HVDC impedance $\boldsymbol{Z}_{\mathrm{MMC}}$ and AC overhead line impedance $\boldsymbol{Z}_{\mathrm{L}}$ intersect at Point E (1080 Hz), and the PM is only 7.8° before MMC-HVDC impedance reshaping. The GM/PM is insufficient, indicating oscillation risk in the system. After the impedance reshaping, the intersection point of the two impedance magnitude curves shifts from Point E to Point F (850 Hz), and the PM is increased to 15.5°. The stability margin is thus improved and the oscillation risk is eliminated.

As seen from Fig. 18.13(b), the original Nyquist curve around Point E (1080 Hz) is in the forbidden area with $R_{\min} = 0.2$, indicating oscillation risk. The positive-sequence oscillation of 1080 Hz with a coupling negative-sequence oscillation of

Table 18.4 EMT Simulation parameters of AC overhead lines

Serial number	Parameter	Value
1	Distributed resistance	1 mΩ/km
2	Distributed inductance	0.1 mH/km
3	Distributed capacitance	0.18 μF/km
4	Line length	5 km

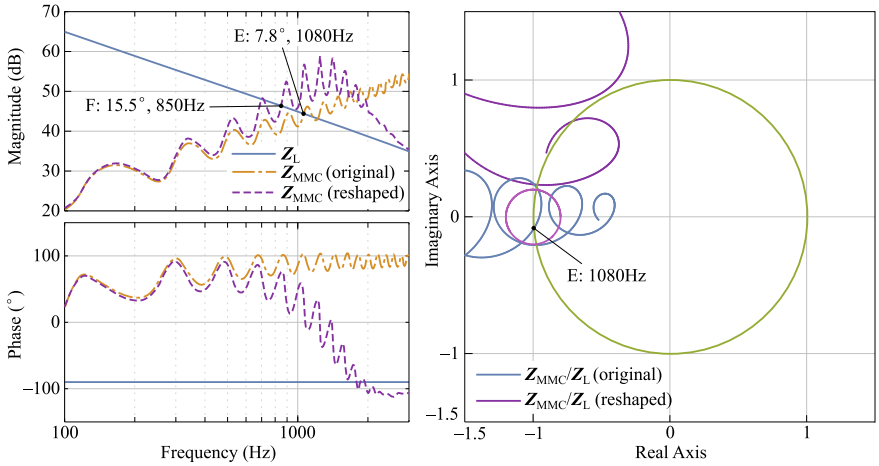

(a) System impedance Bode plot (b) System Nyquist plot

Fig. 18.13 The evaluation results of oscillation risk for AC overhead lines connected into MMC-HVDC system before and after impedance reshaping

980 Hz will occur in the system. After the impedance reshaping, the optimized Nyquist curve is always outside the forbidden area, indicating that the impedance reshaping of MMC-HVDC effectively eliminates the oscillation risk of the system.

The time-domain simulation of AC overhead lines connected into MMC-HVDC system is conducted based on the full EMT simulation platform. The current waveforms of MMC-HVDC and the corresponding FFT results before and after impedance reshaping are shown in Fig. 18.14.

Initially, there are high-frequency oscillation components at 1080 Hz in the positive-sequence domain and 980 Hz in the negative-sequence domain. According to the FFT results of MMC-HVDC currents. After the impedance reshaping control of MMC-HVDC is enabled at t = 2 s, the oscillation of the current waveforms is mitigated, and the high-frequency oscillation component is eliminated as shown in the corresponding FFT analysis. The simulation results verify the effectiveness of oscillation mitigation strategy based on the proposed impedance reshaping of MMC-HVDC.

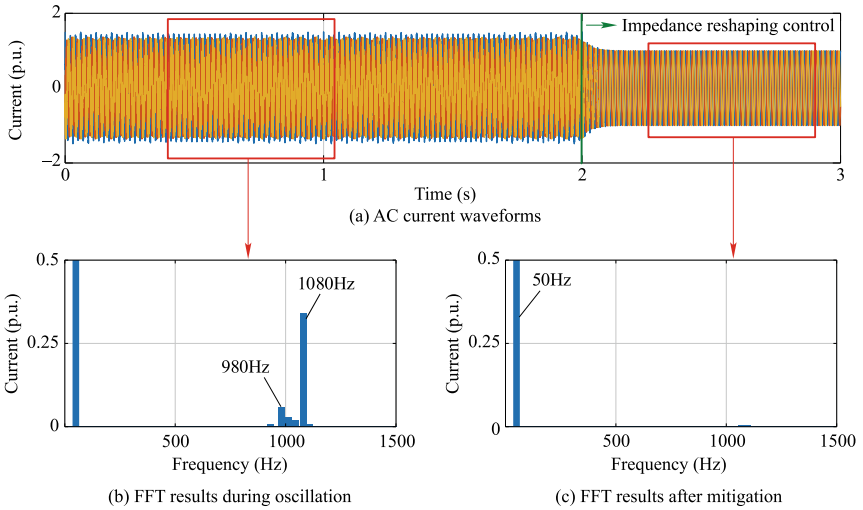

Fig. 18.14 The current waveforms and FFT results of MMC-HVDC before and after impedance reshaping

References

1. LI Y F, TANG G F, HE Z Y, et al. Damping control strategy research for MMC Based HVDC system [J]. Proceedings of the CSEE, 2016, 36(20): 5492-5503. (Chinese)
2. PENG Y, GUO C Y, DU D Y. Research on medium and high frequency oscillation suppression approach based on impedance tuning in flexible HVDC system [J]. Proceedings of the CSEE, 2022, 42(22): 8053-8062. (Chinese)

Chapter 19
Project Cases of REG and AC/DC Transmission System Oscillation

Since 2009, broadband oscillations in REG and AC/DC transmission systems have occurred in Texas of the USA, the North Sea of Germany, Hami of Xinjiang, Guyuan of Hebei, Tongyu of Jilin, and other regions. The oscillation frequency ranges from several to hundreds Hertz. The oscillations resulted in the large-scale tripping-off of REG and thermal power generating units, the decrease of the system transmission capacity, the increase of wind and PV curtailments, and even the damage to the transmission and substation equipment.

This chapter focuses on the oscillations that occurred in China, including the subsynchronous and super-synchronous oscillations in Hami of Xinjiang, the super-synchronous and the high-frequency oscillations in Zhangbei of Hebei, and the broadband oscillations in Ximeng of Inner Mongolia.

Based on the full electromagnetic transient simulation platform for REG and AC/DC transmission systems, the oscillation mechanism is analyzed, the dominant oscillation equipment is determined, the oscillation mitigation strategy is proposed, and the field test of oscillation mitigation is carried out, effectively solving the oscillation problem of the above major projects.

19.1 Sub- and Super-Synchronous Oscillations of PMSG-Based Wind Plants Connected into Weak Grid

In this section, subsynchronous and super-synchronous oscillations of large- scale PMSG-based wind plants in northern area of Hami in 2016 are first introduced. Then, based on full electromagnetic transient simulation platform, the system oscillation risk analysis is carried out to determine the dominant oscillation equipment. Finally,

© China Electric Power Press 2023

W. Wang et al., *Analysis and Mitigation of Broadband Oscillation in Renewable Energy Generation and AC/DC Transmission Systems*,
https://doi.org/10.1007/978-981-99-1568-2_19

the oscillation mitigation strategy based on the impedance reshaping of PMSG units is proposed, effectively solving the subsynchronous and super-synchronous oscillation problems.

19.1.1 Project Overview

The South Hami-Zhengzhou project is an ultra high voltage direct current (UHVDC) project for large-scale thermal, wind, and solar power bundled transmission in China.

The project starts in Hami of Xinjiang and ends in Zhengzhou of Henan. The total length of DC transmission line is 2210 km, the nominal DC voltage is ±800 kV, and the transmission capacity is 8 GW. Three thermal power plants of 2 × 660 MW are connected to the Tianshan converter station at the sending side. The project was put into operation in January 2014.

The installed wind power in Hami is mainly located in northern, eastern, central and western regions and northeast regions. The power grid adopts a radial structure. The wind power is delivered after multi-stage boosting and collection. Up to the end of April 2016, 20 wind plants had been connected into the assembly substations in Hami northern area with a total capacity of 1989 MW, in which the capacity of PMSG-based wind plants is 1567 MW, and the capacity of DFIG-based wind plants is 422 MW. Each wind plant is connected to a 220 kV assembly substations via 110 kV line, and then connected to a 750 kV Santang Lake assembly substation via 220 kV line. The Santang Lake assembly substation is finally connected to Tianshan converter station via long distance (about 300 km) line and Hami assembly substation. The topology of the Hami grid connected with wind plants is shown in Fig. 19.1.

From July 2015 to April 2016, more than 100 oscillation incidents occurred in the northern area of Hami. One oscillation caused large-scale tripping-off of the wind turbine generator systems (WTGS) and three 660 MW thermal power generating units. The DC power was reduced by 1.5 GW in an emergency, and the grid voltage fluctuated significantly. The oscillation incidents seriously affect the safe operation of the grid.

For the oscillation on April 25, 2016, the parameters of wind plants in the northern area of Hami are shown in Table 19.1.

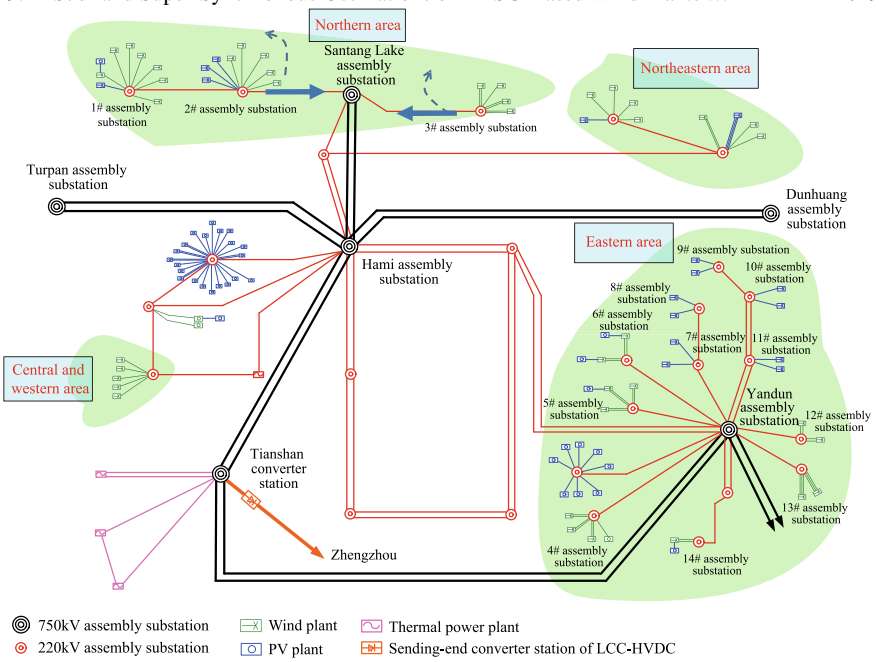

Fig. 19.1 Topolgy of the Hami grid connected with wind plants

19.1.2 Oscillation Analysis

In this section, the frequency-domain characteristics of oscillation current based on field waveform records are first analyzed. Then the equivalent SCRs of each wind plant's grid connection point are calculated based on Hami grid parameters, and the impedance of WTGS is scanned based on controller hardware in the loop (CHIL) simulation platform. Finally, the wind plant's grid connection point is taken as analysis port, the frequency domain analysis of the system oscillation risk is carried out, and the dominant oscillation equipment is determined.

19.1.2.1 Time-Domain Analysis

FFT analysis is applied to the field waveform records of the oscillation occurred on April 25, 2016 to obtain the frequency characteristics of the oscillation current of each assembly substation in northern area of Hami, as shown in Table 19.2. It can be seen that the positive-sequence oscillations of 23/77 Hz occurred in the system. In which the oscillation current component of 3# assembly substation in the northern area is the highest.

According to Table 19.2, it can be inferred that the system oscillation is mainly caused by 3# assembly substation in northern area of Hami. The field oscillation

Table 19.1 Parameters of wind plants in the northern area of Hami (April 25, 2016)

Assembly Substation Number	Wind Plant Number	Type of WTGS	Installed Capacity (MW)	Active Power (MW)
1#	1#	PMSG	75	309
		DFIG	24	
	2#	PMSG	49.5	
	3#	DFIG	50	
	4#	PMSG	49.5	
	5#	PMSG	49.5	
	6#	DFIG	100	
	7#	PMSG	49.5	
	8#	PMSG	49.5	
2#	9#	PMSG	198	660
	10#	PMSG	99	
	11#	PMSG	198	
	12#	DFIG	49.5	
	13#	DFIG	49.5	
	14#	PMSG	49.5	
	15#	DFIG	49.5	
	16#	DFIG	49.5	
		DFIG	49.5	
3#	17#	PMSG	201	589
	18#	PMSG	99	
	19#	PMSG	201	
	20#	PMSG	199.5	

waveforms and FFT results of 3# assembly substation in northern area of Hami are shown in Fig. 19.2. It can be seen that the positive-sequence oscillation of 23/77 Hz occurred in the system.

19.1.2.2 Frequency-Domain Analysis

Frequency-domain impedance analysis is applied to the wind plants of 3# assembly substation in northern area of Hami. According to the transmission line impedance, transformer impedance, wind plant output power, and other parameters, the equivalent SCRs of grid connection points of each wind plant in 3# assembly substation can be calculated, as shown in Table 19.3.

The 3# assembly substation is composed of PMSG units of the same type. The oscillation risk of the 17# wind plant is analyzed. The CHIL simulation platform is

Table 19.2 Frequency characteristics of the oscillation current of each assembly substation in the northern area of Hami

Assembly Substation/Converter Station	Frequency Characteristics of the Positive–Sequence Oscillation	
	Oscillation Frequency (Hz)	Oscillation Component (%)
1# assembly substation	23/77	0.4/0.6
2# assembly substation	23/77	0.7/1
3# assembly substation	23/77	4.3/4.9
Santang lake assembly substation	23/77	1.8/2
Hami assembly substation	23/77	0.4/0.7
Turpan assembly substation	23/77	0.9/0.8
Dunhuang assembly substation	23/77	1.5/1.6
Tianshan converter station	23/77	0.5/0.7

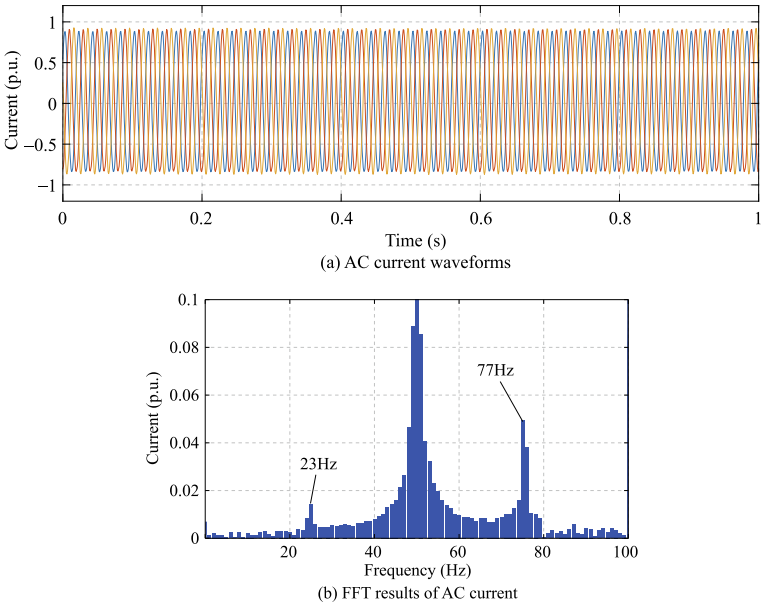

Fig. 19.2 Field oscillation waveforms and FFT results of 3# assembly substation in northern area of Hami

Table 19.3 Equivalent SCRs of each wind plant of 3# assembly substation in northern area of Hami

Wind Plant Number	Type of WTGS	Equivalent SCR
17#	PMSG	1.62
18#	PMSG	1.93
19#	PMSG	1.81
20#	PMSG	1.77

built based on the field PMSG unit controller, and the broadband impedance of the PMSG unit is scanned. The impedance of the 17# PMSG-based wind plant $\boldsymbol{Z}_{\mathrm{PMSG}}$ can be calculated by PMSG unit impedance and wind plant parameters. The AC grid impedance $\boldsymbol{Z}_{\mathrm{g}}$ can be obtained according to the equivalent SCR of grid connection point of the wind plant. The evaluation results of oscillation risk for 17# PMSG-based wind plants are shown in Fig. 19.3.

It can be seen from Fig. 19.3(a) that in super-synchronous frequency band, $\boldsymbol{Z}_{\mathrm{PMSG}}$ presents capacitive negative damping characteristics and $\boldsymbol{Z}_{\mathrm{g}}$ presents inductive characteristics. The magnitude curves of $\boldsymbol{Z}_{\mathrm{PMSG}}$ and $\boldsymbol{Z}_{\mathrm{g}}$ intersect at point A (77 Hz), with a PM of 1°. The GM/PM is insufficient, indicating oscillation risk in the system.

In Fig. 19.3(b), a forbidden area with a radius R_{min} of 0.15 is drawn based on the Nyquist criterion of maximum peak value. The Nyquist plot of $\boldsymbol{Z}_{\mathrm{g}}/\boldsymbol{Z}_{\mathrm{PMSG}}$ crosses point A (77 Hz) in the forbidden area, indicating oscillation risk in the system. The positive-sequence oscillation of 77 Hz with a coupling positive-sequence component of 23 Hz will occur in the system. The frequency-domain analysis results are consistent with the FFT results of the field waveform records in Fig. 19.2.

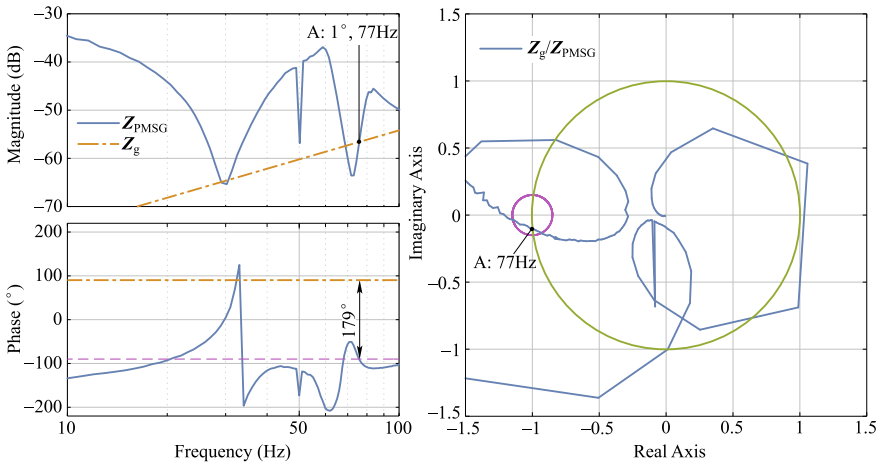

(a) System impedance Bode plot (b) System Nyquist plot

Fig. 19.3 Evaluation results of oscillation risk for 17# PMSG-based wind plants

19.1.3 Oscillation Mitigation

According to Chap. 6, the impedance characteristics of PMSG-based wind plant in super-synchronous frequency band are dominated by PLL and affected by GSC AC current loop. It presents capacitive negative damping characteristics. By optimizing control parameters of PLL and GSC AC current loop, the impedance of PMSG-based wind plants can be reshaped to mitigate the subsynchronous and super-synchronous oscillations. Fig. 19.4 shows the evaluation results of the oscillation risk for 17# PMSG-based wind plant after impedance reshaping.

It can be seen from Fig. 19.4(a) that the magnitude curves of the reshaped PMSG impedance $\boldsymbol{Z}_{\mathrm{PMSG}}$ and $\boldsymbol{Z}_{\mathrm{g}}$ do not intersect.

In Fig. 19.4(b), a forbidden area with a radius $R_{\min}$of 0.15 is drawn based on the Nyquist criterion of maximum peak value. The Nyquist plot of $\boldsymbol{Z}_{\mathrm{g}}/\boldsymbol{Z}_{\mathrm{PMSG}}$ is always outside the forbidden area. By optimizing control parameters of PLL and GSC AC current control, the impedance of 17# PMSG-based wind plant can be reshaped to mitigate the positive-sequence oscillation of 77 Hz with a coupling positive-sequence component of 23 Hz.

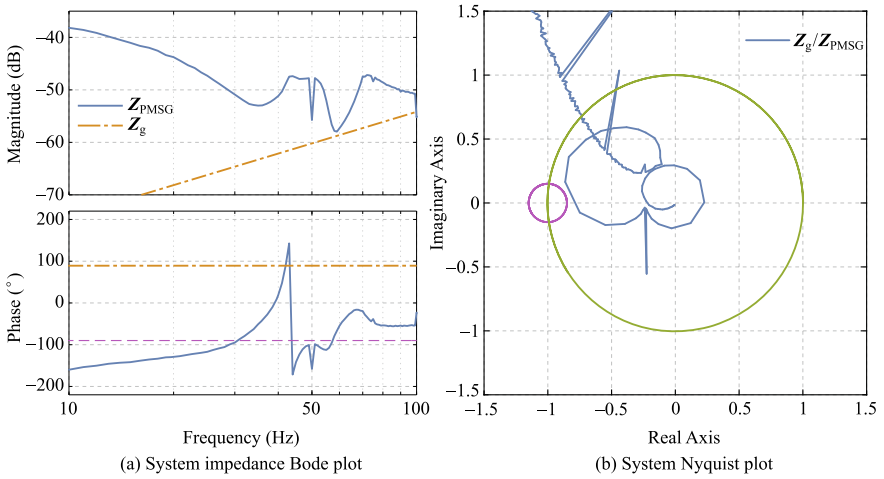

Fig. 19.4 Evaluation results of the oscillation risk for 17# PMSG-based wind plant after impedance reshaping

19.2 Sub- and Super-Synchronous Oscillations of DFIG-Based Wind Plants Connected into Weak Grid

In this section, the subsynchronous and super-synchronous oscillations of large-scale DFIG-based wind plants in eastern area of Hami in 2017 are first introduced. Then, based on full electromagnetic transient simulation platform, the system oscillation risk analysis is carried out to determine the dominant oscillation equipment. Finally, the oscillation mitigation strategy based on impedance reshaping of DFIG units is proposed, effectively solving the subsynchronous and super-synchronous oscillation problems.

19.2.1 Project Overview

Up to the end of August 2017, 23 wind plants had been connected into the assembly substations in Hami eastern area with a total capacity of 5200 MW, in which the capacity of PMSG-based wind plants is 3598 MW, and the capacity of DFIG-based wind plants is 1602 MW. From April to August 2017, many subsynchronous and super-synchronous oscillation incidents occurred in the field, mainly in 13# assembly substation. The topology of the Hami grid connected with wind plants is shown in Fig. 19.1. For the oscillation on August 26, 2017, the parameters of the wind plants in the eastern area of Hami are shown in Table 19.4.

19.2.2 Oscillation Analysis

In this section, frequency-domain characteristics of oscillation current based on the field waveform records are first analyzed. Then the equivalent SCRs of each wind plant grid connection point are calculated based on Hami grid parameters, and the impedance of WTGS is scanned based on CHIL simulation platform. Finally, the wind plant grid connection point is taken as the analysis port, the frequency domain analysis of system oscillation risk is carried out, and the dominant equipment of oscillation is determined.

19.2.2.1 Time-Domain Analysis

The FFT analysis is applied to field waveform records of the oscillation occurred on August 26, 2017, to obtain frequency characteristics of the oscillation current of each assembly substation in eastern area of Hami, as shown in Table 19.5. It can be seen that 37/63 Hz positive-sequence oscillation occurred in the system. In which

Table 19.4 Parameters of wind plants in the eastern area of Hami (August 26, 2017)

Assembly Substation Number	Wind Plant Number	Type of WTGS	Installed Capacity (MW)	Active Power (MW)
4#	21#	PMSG	195	310
		PMSG	1.5	
		PMSG	1.5	
	22#	PMSG	113.9	
		PMSG	85	
	23#	PMSG	193.5	
		PMSG	4.5	
5#	24#	PMSG	200	350
	25#	PMSG	100	
		DFIG	100	
	26#	PMSG	100	
6#	27#	PMSG	201	305
	28#	PMSG	201	
7#	29#	PMSG	200	240
	30#	PMSG	200	
8#	31#	DFIG	201	220
	32#	PMSG	200	
9#	33#	DFIG	201	200
	34#	DFIG	201	
10#	35#	PMSG	200	240
	36#	PMSG	171	
		PMSG	30	
11#	37#	PMSG	200	220
	38#	DFIG	200	
12#	39#	PMSG	199.5	205
	40#	PMSG	201	
13#	41#	DFIG	300	390
	42#	DFIG	300	
14#	43#	PMSG	300	160

the oscillation current component of 13# assembly substation in the eastern area is the highest.

According to Table 19.5, it can be inferred that the system oscillation is mainly caused by the 13# assembly substation in the eastern area of Hami. The field oscillation waveforms and FFT results of the 13# assembly substation in the eastern area

Table 19.5 Frequency characteristics of oscillation current of each assembly substation in the eastern area of Hami

Assembly Substation/Converter Station	Frequency Characteristics of the Positive–Sequence Oscillation	
	Oscillation Frequency (Hz)	Oscillation Component (%)
13# assembly substation	37/63	1.8/3.5
Yandun assembly substation	37/63	0.9/1.5
Hami assembly substation	37/63	0.1/0.3
Turpan assembly substation	37/63	0.05/0.1
Dunhuang assembly substation	37/63	0.04/0.08
Tianshan converter station	37/63	0.02/0.05

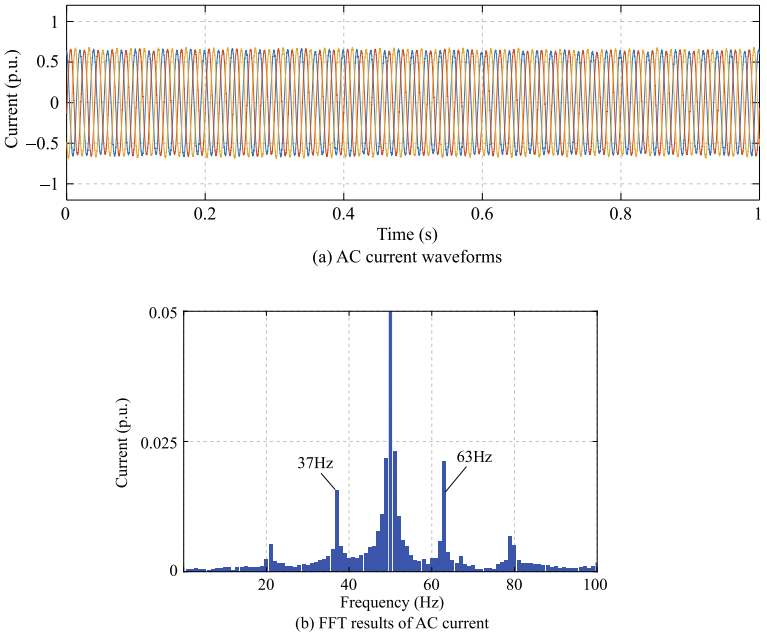

Fig. 19.5 Frequency characteristics of oscillation current of each assembly substation in the eastern area of Hami

of Hami are shown in Fig. 19.5. It can be seen that the positive-sequence oscillation of 37/63 Hz occurred in the system.

19.2.2.2 Frequency-Domain Analysis

The frequency-domain impedance analysis is applied to the wind plants of 13# assembly substation in the eastern area of Hami. According to the transmission line impedance,transformer impedance, wind plant output power, and other parameters, the equivalent SCRs of the grid connection points of each wind plant in 13# assembly substation can be calculated, as shown in Table 19.6.

The 13# assembly substation is composed of DFIG units of the same type. The oscillation risk of the 41# wind plant is analyzed. The CHIL simulation platform is built based on the field DFIG unit controller, and the broadband impedance of the DFIG unit is scanned. The impedance of the 41# DFIG-based wind plant $\boldsymbol{Z}_{\mathrm{DFIG}}$ can be calculated by the DFIG unit impedance and the parameters of the wind plant. The grid impedance $\boldsymbol{Z}_{\mathrm{g}}$ can be obtained according to the equivalent SCR of the grid connection point of the wind plant. The evaluation results of the oscillation risk for the 41# DFIG-based wind plant are shown in Fig. 19.6.

It can be seen from Fig. 19.6(a) in the super-synchronous frequency band, $\boldsymbol{Z}_{\mathrm{DFIG}}$ presents capacitive negative damping characteristics and $\boldsymbol{Z}_{\mathrm{g}}$ presents inductive characteristics. The magnitude curves of $\boldsymbol{Z}_{\mathrm{DFIG}}$ and $\boldsymbol{Z}_{\mathrm{g}}$ intersect at point B (63 Hz), with a PM of 1°. The GM/PM is insufficient, indicating oscillation risk in the system.

Table 19.6 Equivalent SCRs of each wind plant of the 13# assembly substation in the eastern area of Hami

Wind Plant Number	Type of WTGS	Equivalent SCR
41#	DFIG	1.52
42#	DFIG	1.52

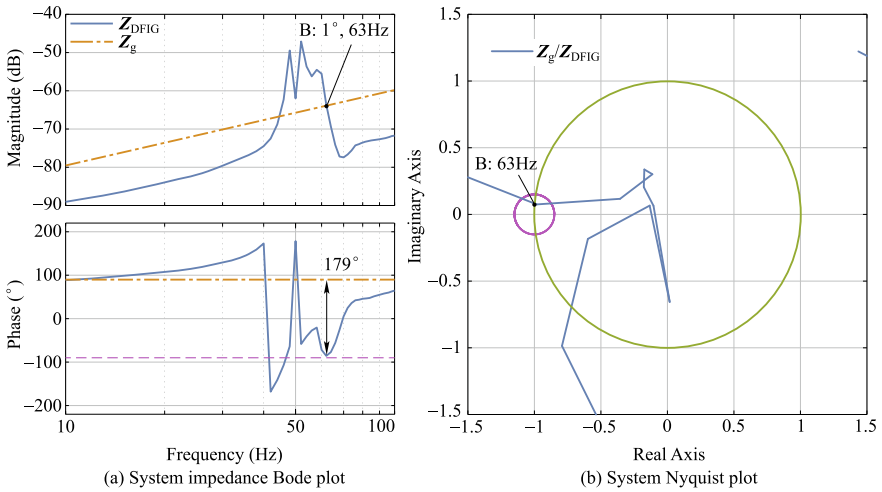

(a) System impedance Bode plot (b) System Nyquist plot

Fig. 19.6 Evaluation results of the oscillation risk for the 41# DFIG-based wind plant

In Fig. 19.6(b), a forbidden area with a radius $R_{\min}$ of 0.15 is drawn based on the Nyquist criterion of maximum peak value. The Nyquist plot of $\boldsymbol{Z}_g/\boldsymbol{Z}_{DFIG}$ crosses point B (63 Hz) in the forbidden area, indicating oscillation risk in the system. The positive-sequence oscillation of 63 Hz with a coupling positive-sequence component of 37 Hz will occur in the system. The frequency-domain analysis results are consistent with the FFT results of the field waveform records in Fig. 19.5.

19.2.3 Oscillation Mitigation

According to Chap. 7, the impedance characteristics of DFIG-based wind plants in super-synchronous frequency band are dominated by stator, and influenced by the active power loop, the GSC AC current loop, and the rotor-side converter (RSC) AC current loop. It presents the capacitive negative damping characteristics. By optimizing control parameters of the active power loop, the impedance of 41# DFIG-based wind plant can be reshaped to mitigate the subsynchronous and super-synchronous oscillation. Figure 19.7 shows the evaluation results of oscillation risk for 41# DFIG-based wind plant after impedance reshaping.

It can be seen from Fig. 19.7(a) that the magnitude curves of the reshaped PMSG impedance $\boldsymbol{Z}_{DFIG}$ and $\boldsymbol{Z}_g$ curve intersect at point B (63 Hz), with the PM increased from 1° to 65°.

In Fig. 19.7(b), a forbidden area with a radius $R_{\min}$ of 0.15 is drawn based on the Nyquist criterion of maximum peak value. The Nyquist plot of $\boldsymbol{Z}_g/\boldsymbol{Z}_{DFIG}$ is always outside the forbidden area. By optimizing the control parameters of the active

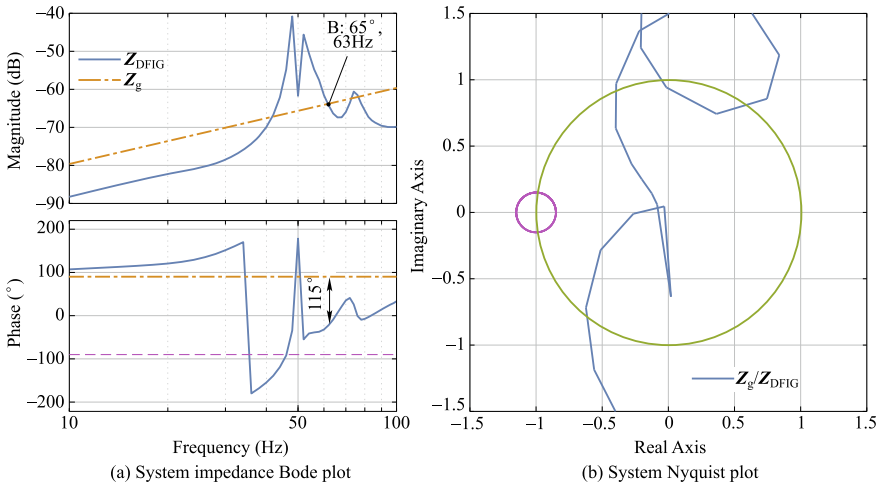

Fig. 19.7 Evaluation results of oscillation risk for 41# DFIG-based wind plant after impedance reshaping

power loop, the impedance of the 41# PMSG-based wind plant can be reshaped to mitigate the positive-sequence oscillation of 63 Hz with a coupling positive-sequence component of 37 Hz.

19.3 High-Frequency Oscillation of REG Connected into MMC-HVDC

In this section, the oscillations of the Zhongdu converter station of REG connected into the Zhangbei MMC-MTDC grid system in 2021 are first introduced. Then, based on the full electromagnetic transient simulation platform, the system oscillation risk analysis is carried out to determine the dominant oscillation equipment. Finally, the oscillation mitigation strategy based on the impedance reshaping of MMC-HVDC is proposed, effectively solving the oscillation problems in the field.

19.3.1 Project Overview

The Zhangbei project is the world's first MMC-MTDC grid project and the MMC-HVDC project with the highest voltage level and the most extensive transmission capacity in the world. The Zhangbei project is a major project for the development of clean and low-carbon energy. For the Zhangbei project, the nominal DC voltage is ±500kV, the overall DC line length is 666km, and four converter stations have been built, which are Zhongdu (3000MW), Kangba Noel (1500MW), Fengning (1500MW), and Beijing (3000MW). The Kangba Noel and Zhongdu converter stations operate in passive islanding control mode, and the Fengning and Beijing converter stations operate in grid-connected control mode. On June 29, 2020, the Zhangbei MMC-MTDC grid project was officially put into operation. The topology of the Zhangbei MMC-MTDC grid is shown in Fig. 19.8.

Since February 2021, with the increasing capacity of grid-connected REG plants, oscillations around 58Hz occurred 24 times in the Zhongdu converter station, causing several times of shutting down of the REG plants.

Up to the end of March 2021, 9 REG plants had been connected into the Zhongdu converter station through a 220kV AC bus with a total capacity of 1408MW, including 4 PV plants and 5 wind plants. The topology of REG plants connected into the Zhongdu converter station is shown in Fig. 19.9.

For the oscillation on March 17, 2021, the Zhongdu converter station was operating in mono-polar mode when the oscillation occurred, and the parameters of the REG plants are shown in Table 19.7.

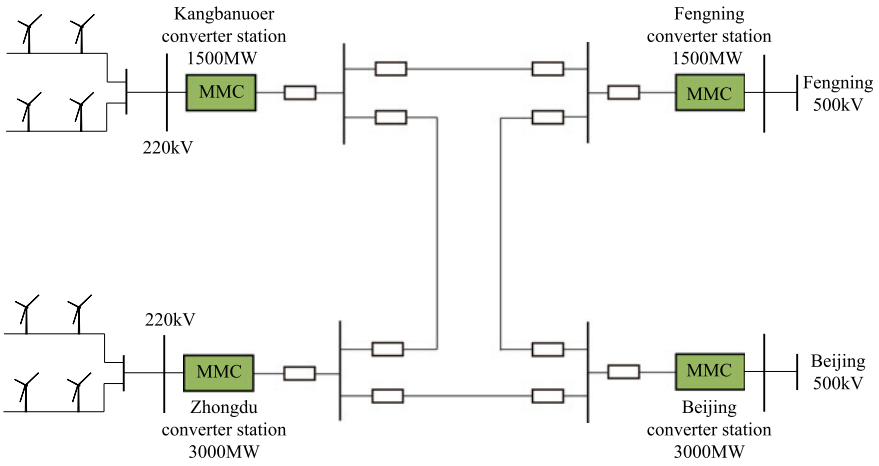

Fig. 19.8 Topology of the Zhangbei MMC-MTDC grid project

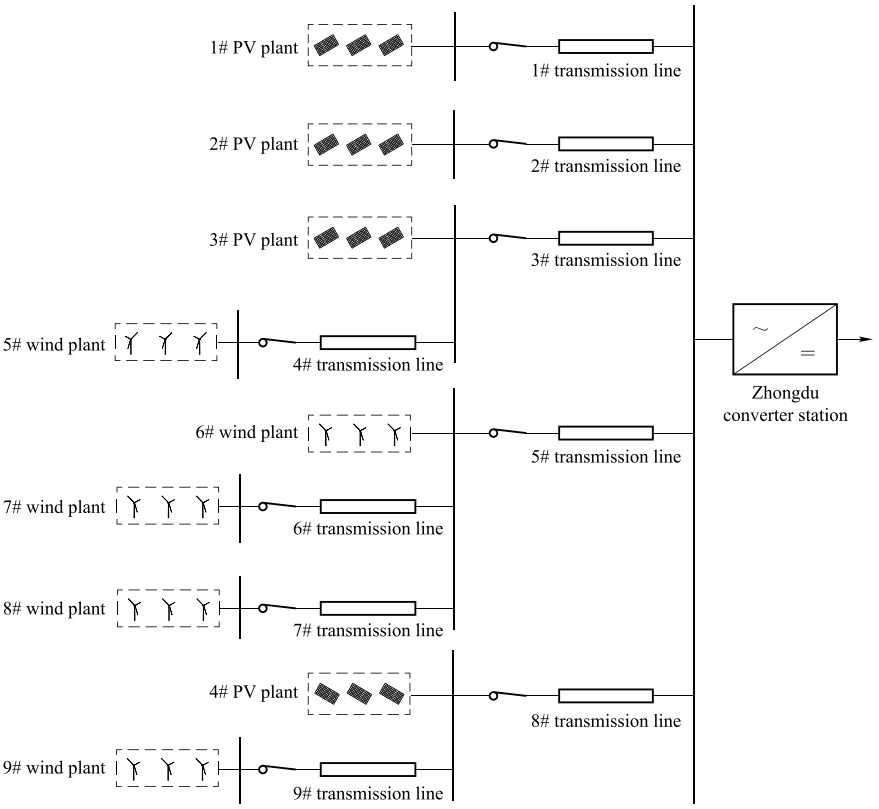

Fig. 19.9 Topology of REG plants connected into the Zhongdu converter station

Table 19.7 Parameters of the REG plants of the Zhongdu converter station (March 17, 2021)

Plant Number	Type of Plant	Installed Capacity (MW)	Active Power (MW)
1#	PV	240	89.53
2#	PV	140	71.86
3#	PV	70	38.18
4#	PV	460	252.09
5#	PMSG	50	0.37
6#	DFIG	99	0
7#	PMSG	49.5	1.94
8#	DFIG	150	4.6
9#	DFIG	150	0.2

19.3.2 Oscillation Analysis

This section, the frequency-domain characteristics of the oscillation current based on the field waveform records are first analyzed. Then, the impedances of the REG plants and the AC port of the Zhongdu converter station are scanned based on the full electromagnetic transient simulation platform. Finally, the AC port of the Zhongdu converter station is taken as the analysis port, the frequency domain analysis of the system oscillation risk is carried out, and the dominant oscillation equipment is determined.

19.3.2.1 Time-Domain Analysis

The FFT analysis is applied to the field waveform records of the oscillation that occurred on March 17, 2021, to obtain the frequency characteristics of the oscillation current of each REG plant of the Zhongdu converter station, as shown in Table 19.8.

According to Table 19.8, it can be inferred that the system oscillation is mainly occurred in the connection port of REG plants to the Zhongdu converter station. The field oscillation waveform records and FFT results of the AC port of the Zhongdu converter station are shown in Fig. 19.10. It can be seen that the negative-sequence oscillation of 58Hz with a coupling positive-sequence component of 158Hz occurred in the system.

19.3.2.2 Frequency-Domain Analysis

Based on the full electromagnetic transient simulation platform, the broadband impedance scanning is applied to the AC port of the Zhongdu converter station and the REG plants to obtain the REG impedance $\boldsymbol{Z}_{\mathrm{RE}}$ (negative sequence) and the AC port impedance of the Zhongdu converter station $\boldsymbol{Z}_{\mathrm{MMC}}$ (negative sequence). The

Table 19.8 Frequency characteristics of the oscillation current of each REG plant of the Zhongdu converter station

Number	Type of Plant	Frequency Characteristics of the Oscillation	
		Oscillation Frequency (Hz)	Oscilltaion Component (%)
1#	PV	58 (negative-sequence)/158 (positive–sequence)	13/1
2#	PV	58 (negative-sequence)/158 (positive–sequence)	5/0.5
3#	PV	58 (negative-sequence)/158 (positive–sequence)	5/0.6
4#	PV	58 (negative-sequence)/158 (positive–sequence)	10/0.8
5#	PMSG	58 (negative-sequence)/158 (positive–sequence)	3/0.3
6#	DFIG	58 (negative-sequence)/158 (positive–sequence)	7/0.6
7#	PMSG	58 (negative-sequence)/158 (positive–sequence)	18/1.3
8#	DFIG	58 (negative-sequence)/158 (positive–sequence)	8/0.6
9#	DFIG	58 (negative-sequence)/158 (positive–sequence)	15/1.0

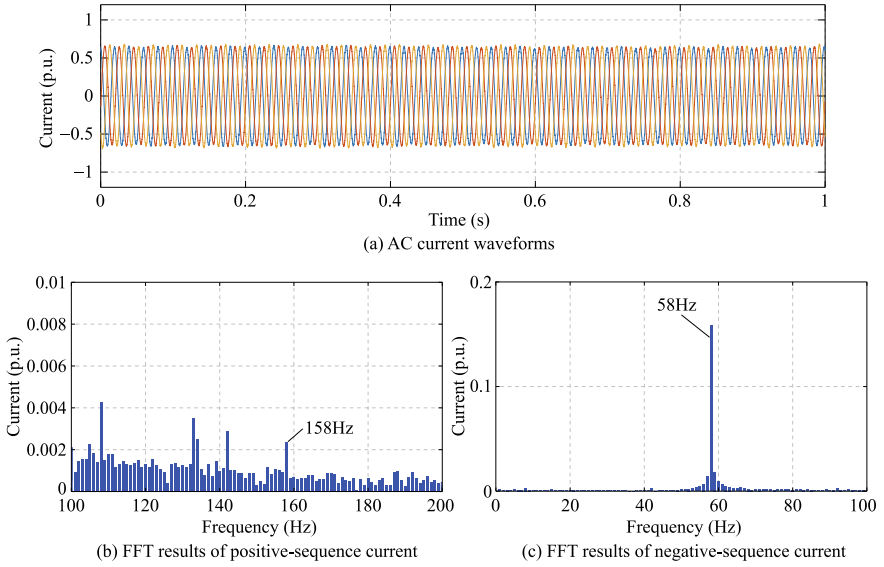

(a) AC current waveforms

(b) FFT results of positive-sequence current

(c) FFT results of negative-sequence current

Fig. 19.10 Field oscillation waveform records and FFT results of the Zhongdu converter station

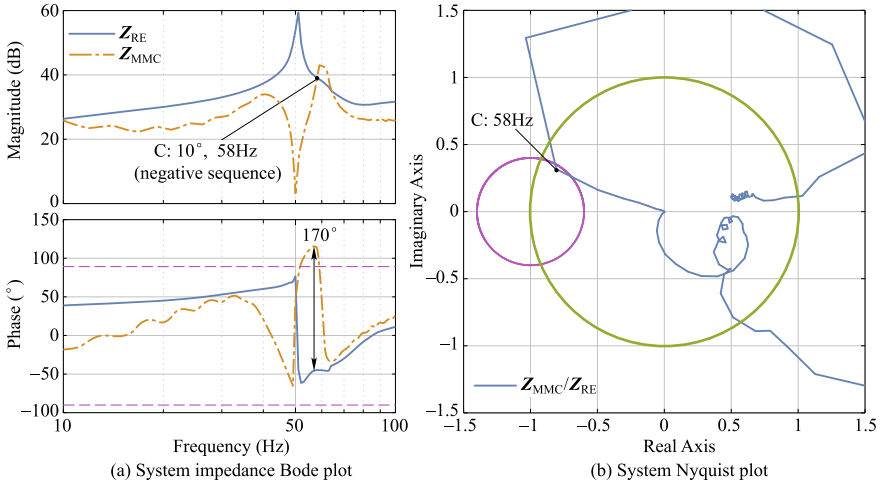

(a) System impedance Bode plot (b) System Nyquist plot

Fig. 19.11 Evaluation results of the oscillation risk for the REG connected into the Zhongdu converter station

evaluation results of the oscillation risk for the REG connected into the Zhongdu converter station are shown in Fig. 19.11.

It can be seen from Fig. 19.11(a) that in the super-synchronous frequency band, $\boldsymbol{Z}_{RE}$ represents the capacitive characteristics and $\boldsymbol{Z}_{MMC}$ represents the inductive negative damping characteristics. The magnitudes of $\boldsymbol{Z}_{RE}$ and $\boldsymbol{Z}_{MMC}$ curves intersect at point C (58Hz), with a PM of 10°. The GM/PM is insufficient, indicating oscillation risk in the system.

In Fig. 19.11(b), a forbidden area with a radius R_{min} of 0.4 is drawn based on the Nyquist criterion of maximum peak value. The Nyquist plot of $\boldsymbol{Z}_{MMC}/\boldsymbol{Z}_{RE}$ crosses point C (58Hz) in the forbidden area, indicating oscillation risk in the system. The negative-sequence oscillation of 58Hz with a coupling positive-sequence component of 158Hz will occur in the system. The frequency-domain analysis results are consistent with the FFT results of the field waveform records in Fig. 19.10.

19.3.3 Oscillation Mitigation

19.3.3.1 Impedance Reshaped Strategy

According to Chap.11 , the impedance characteristics of MMC-HVDC in the super-synchronous frequency band are dominated by AC current loop. By optimizing the control parameters of the AC current loop, the impedance of MMC-HVDC can be reshaped to mitigate the super-synchronous oscillation. By impedance reshaping, the magnitude of the impedance is reduced and the negative damping characteristics are

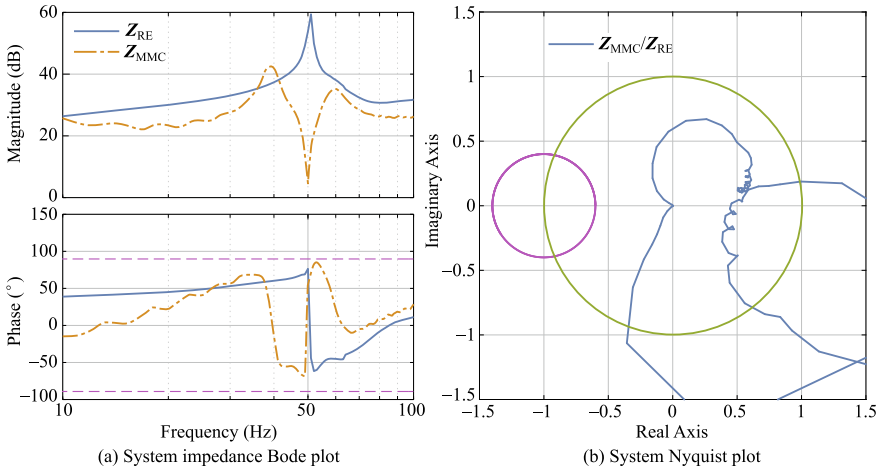

Fig. 19.12 Evaluation results of the oscillation risk for the REG plants connected into the Zhongdu converter station after impedance reshaping

eliminated. Figure 19.12 shows the evaluation results of the oscillation risk for the REG plants connected into the Zhongdu converter station after impedance reshaping.

It can be seen from Fig. 19.12(a) that the magnitudes of the reshaped MMC-HVDC impedance $\boldsymbol{Z}_{\mathrm{MMC}}$ curve and $\boldsymbol{Z}_{\mathrm{RE}}$ curve do not intersect in the super-synchronous frequency band, and the capacitive negative damping characteristics of $\boldsymbol{Z}_{\mathrm{MMC}}$ are eliminated.

In Fig. 19.12(b), a forbidden area with a radius $R_{\min}$ of 0.4 is drawn based on the Nyquist criterion of maximum peak value. The Nyquist plot of $\boldsymbol{Z}_{\mathrm{MMC}}/\boldsymbol{Z}_{\mathrm{RE}}$ is always outside the forbidden area. By optimizing the control parameters of the AC current loop, the impedance of the MMC-HVDC can be reshaped to mitigate the negative-sequence oscillation of 58Hz with a coupling positive-sequence component of 158Hz.

19.3.3.2 Field Test Verification

On July 19, 2021, the filed oscillation recurrence and mitigation test was carried out in the Zhongdu converter station to verify the accuracy of the oscillation mechanism and the effectiveness of the mitigation strategy. In the test, the total active power of REG plants was 465MW. The control of the MMC-HVDC was changed to the oscillation mitigation control when the oscillation was observed. The oscillation recurrence and mitigation field waveform records and the FFT results of the Zhongdu converter station are shown in Fig. 19.13.

Fig. 19.13(a) shows the waveforms of the current, Fig. 19.13(b) shows the FFT results of the negative-sequence oscillation current, and Fig. 19.13(c) shows the FFT results of the negative-sequence current after oscillation mitigation. Fig. 19.13(d)

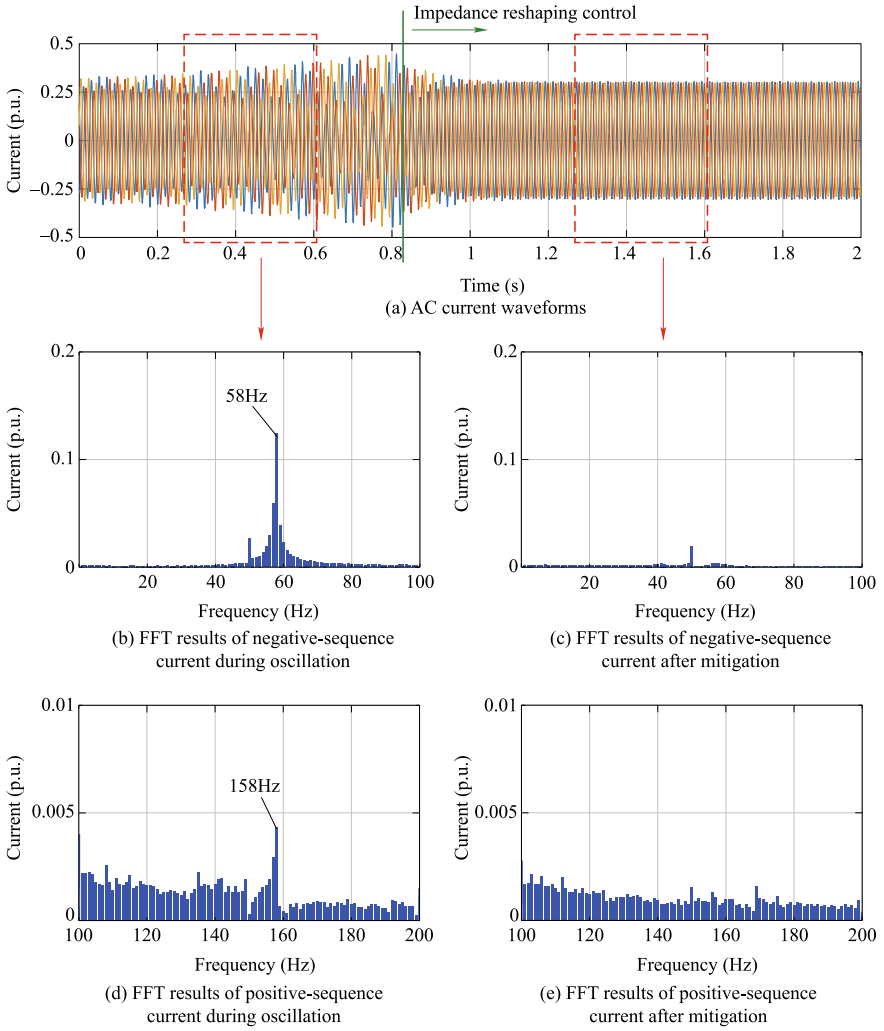

Fig. 19.13 Oscillation recurrence and mitigation field waveform records and FFT results of the Zhongdu converter station

shows the FFT results of the positive-sequence oscillation current, and Fig. 19.13(e) shows the FFT results of the positive-sequence current after oscillation mitigation.

It can be seen that the negative-sequence 58Hz oscillation with a coupling positive-sequence component of 158Hz occurred in the REG connected into the Zhongdu converter station system. The frequency characteristics of the oscillation are the same as the oscillations that have occurred since February 2021, and are consistent with the frequency-domain analysis. About 180ms after the control of the MMC-HVDC was changed to the oscillation mitigation control, both positive and negative

sequence oscillations were eliminated. The above test verified the accuracy of the oscillation analysis and the effectiveness of the mitigation strategy.

19.4 High-Frequency Oscillation of REG Connected into MMC-HVDC

In this section, the oscillations of the Kangba Noel converter station of REG connected into the Zhangbei MMC-MTDC grid are first introduced. Then, based on the full electromagnetic transient simulation platform, the system oscillation risk analysis is carried out to determine the dominant oscillation equipment. Finally, the oscillation mitigation strategy based on the impedance reshaping of MMC-HVDC is proposed, effectively solving the oscillation problems in the field.

19.4.1 Project Overview

From December 2020 to February 2021, several high-frequency oscillations of 650~1550Hz occurred in the Kangba Noel converter station since February 2021. The topology of the REG plants connected into the Kangba Noel converter station is shown in Fig. 19.14.

For the oscillation on February 3, 2021, only the 1# and 2# wind plants were connected into the Kangba Noel converter station through the 1# transmission line,

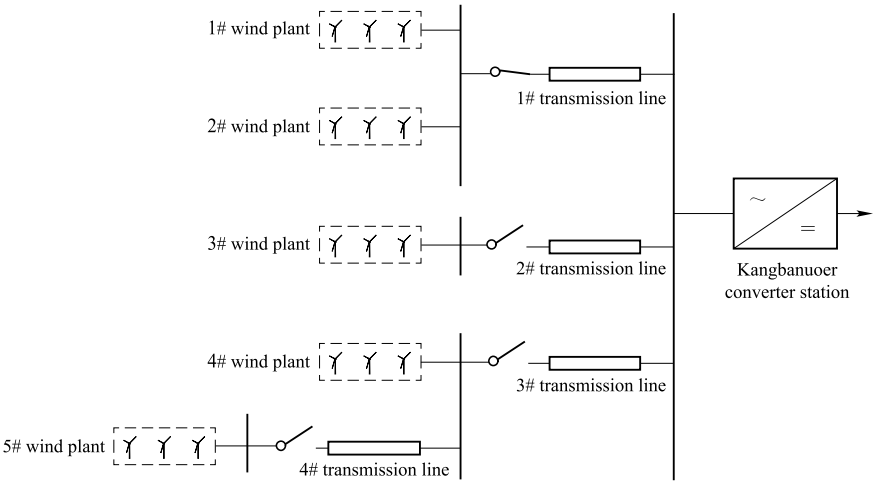

Fig. 19.14 The topology of the REG plants connected into the Kangba Noel converter station

Table 19.9 Parameters of the REG plants of the Kangba Noel converter station (February 3, 2021)

Plant Number	Type of WTGS	Installed Capacity (MW)	Active Power (MW)
1#	DFIG	100	23
2#	PMSG	200	0
3#	PMSG	150	0
4#	DFIG	50	0
5#	PMSG	50	0

and the parameters of the REG plants of the Kangba Noel converter station are shown in Table 19.9.

19.4.2 Oscillation Analysis

In this section, the frequency characteristics of the oscillation current based on the field waveform records are first analyzed. Then, the impedances of the REG plants and the AC port of the Kangbanuoer converter station are scanned based on the full electromagnetic transient simulation platform. Finally, the AC port of the Kangbanuoer converter station is taken as the analysis port, the frequency domain analysis of the system oscillation risk is carried out, and the dominant oscillation equipment is determined.

19.4.2.1 Analysis of the Time-Domain Waveform Records

On February 3, 2021, only the 1# transmission line was connected to the Kangba Noel converter station, and only the 1# wind plant was generating. The field oscillation waveforms and FFT results of the AC port of the Kangba Noel converter station are shown in Fig. 19.15. It can be seen that the positive-sequence oscillation of 750Hz occurred in the system.

19.4.2.2 Frequency-Domain Analysis

Based on the full electromagnetic transient simulation platform, the broadband impedance scanning is applied to the AC port of the Kangbanuoer converter station and the 1# wind plant to obtain the REG impedance $\boldsymbol{Z}_{\mathrm{RE}}$ (including the 1# wind plant and the 1# transmission line) and the AC port impedance of the Kangbanuoer converter station $\boldsymbol{Z}_{\mathrm{MMC}}$. The evaluation results of the oscillation risk for the REG connected into the Kangba Noel converter station are shown in Fig. 19.16.

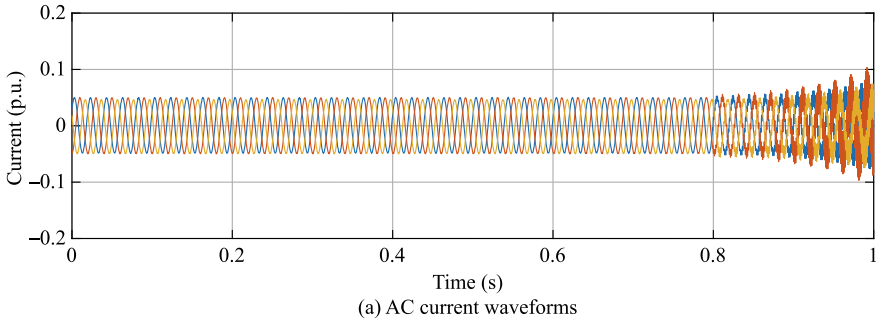

(a) AC current waveforms

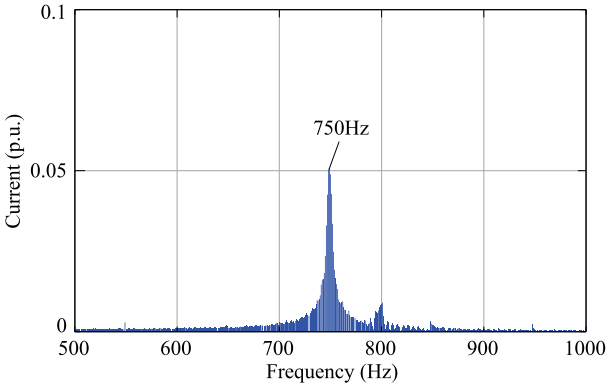

(b) FFT results of AC current

Fig. 19.15 Field oscillation waveforms and FFT results of the AC port of the Kangba Noel converter station

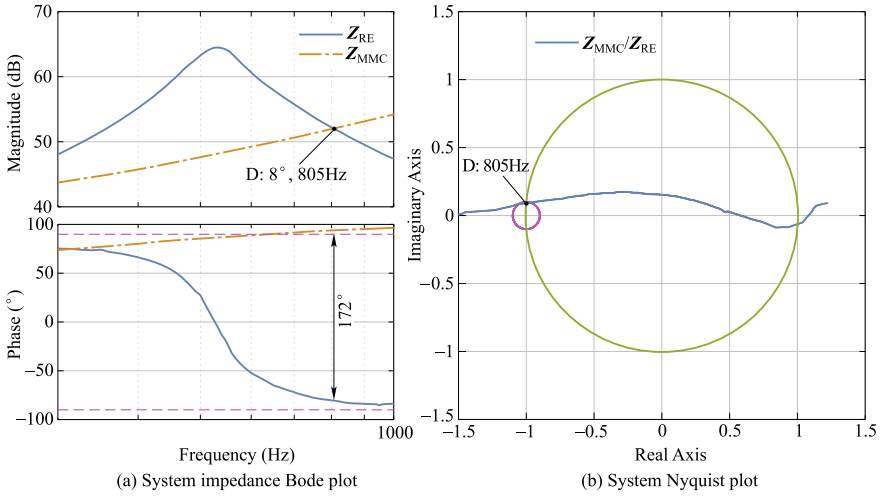

(a) System impedance Bode plot

(b) System Nyquist plot

Fig. 19.16 Evaluation results of the oscillation risk for the REG connected into the Kangba Noel converter station

It can be seen from Fig. 19.16(a) that in the high-frequency band, $\boldsymbol{Z}_{\mathrm{RE}}$ presents capacitive characteristics and $\boldsymbol{Z}_{\mathrm{MMC}}$ presents inductive negative damping characteristics. The magnitudes of $\boldsymbol{Z}_{\mathrm{RE}}$ and $\boldsymbol{Z}_{\mathrm{MMC}}$ curves intersect at point D (805Hz), with a PM of 8°. The GM/PM is insufficient, indicating oscillation risk in the system.

In Fig. 19.16(b), a forbidden area with a radius $R_{\min}$ of 0.1 is drawn based on the Nyquist criterion of maximum peak value. The Nyquist plot of $\boldsymbol{Z}_{\mathrm{MMC}}/\boldsymbol{Z}_{\mathrm{RE}}$ crosses point D (805Hz) in the forbidden area, indicating oscillation risk in the system. The positive-sequence oscillation of 805Hz will occur in the system. The frequency-domain analysis results are consistent with the FFT results of the field waveform records in Fig. 19.15.

19.4.3 Oscillation Mitigation

According to Chap. 11, the impedance characteristics of MMC-HVDC in the high-frequency band are dominated by the arm inductor and affected by the time delay. By introducing active damping control, the impedance of MMC-HVDC can be reshaped to mitigate the high-frequency oscillation. Fig. 19.17 shows the evaluation results of the oscillation risk for the REG plants connected into the Kangba Noel converter station after impedance reshaping.

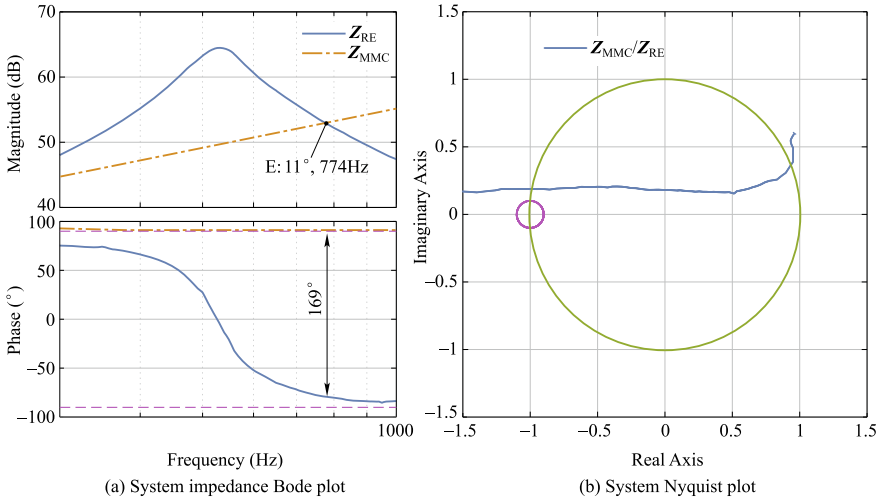

Fig. 19.17 Evaluation results of the oscillation risk for the REG plants connected into the Kangba Noel converter station after impedance reshaping

It can be seen from Fig. 19.17(a) that the magnitudes of the reshaped MMC-HVDC impedance $\boldsymbol{Z}_{\mathrm{MMC}}$ curve and $\boldsymbol{Z}_{\mathrm{RE}}$ curve intersect at point E (774Hz). Compared with point D (805Hz), the PM is increased from 8° to 11°.

In Fig. 19.17(b), a forbidden area with a radius $R_{\min}$ of 0.1 is drawn based on the Nyquist criterion of maximum peak value. The Nyquist plot of $\boldsymbol{Z}_{\mathrm{MMC}}/\boldsymbol{Z}_{\mathrm{RE}}$ is always outside the forbidden area. By introducing active damping control, the impedance of the MMC-HVDC can be reshaped to mitigate the high-frequency oscillation.

19.5 Broadband Oscillation of REG Connected into LCC-HVDC

This section focus on the broadband oscillation risk of large-scale wind plants connected into the sending side of the Ximeng-Taizhou LCC-HVDC system. First, based on the full electromagnetic transient simulation platform, the system oscillation risk analysis is carried out to find the wind plants with oscillation risk. Then, the oscillation mitigation strategy based on the impedance reshaping of the WTGS is proposed. Finally, the improved control parameters are solidified to the field controllers, effectively avoiding the risk of broadband oscillation in the field.

19.5.1 Project Overview

The Ximeng-Taizhou LCC-HVDC project starts in Xilinhot of Inner Mongolia and ends in Taizhou of Jiangsu. The total length of the DC transmission line is 1618km, the nominal DC voltage is ±800kV, and the transmission capacity is 10GW. The project is the first 10GW level UHVDC transmission project in the world and was put into operation in November 2017.

At the sending side grid of the Ximeng-Taizhou LCC-HVDC, the Xilinhot converter station is connected to the 500kV side of the 1000kV Shengli assembly substation through a 500kV triple circuit line, and connected to the Ximeng assembly substation. In this area, 12 thermal power generating units with a total capacity of 7.3GW and 36 wind plants with a total capacity of 7GW are connected to the grid. The wind plants are first connected to five 500kV assembly substations, then to the Shengli assembly substation and Ximeng assembly substation, and finally to the Xilin Hot converter station. The topology of the sending side grid of the Ximeng-Taizhou LCC-HVDC is shown in Fig. 19.18 and the parameters of which are shown in Table 19.10.

There are oscillation risks in the large-scale wind plants connected into the Ximeng-Taizhou LCC-HVDC system, which may lead to the tripping-off of WTGS and thermal power generating units, and even the electrical and mechanical damage to the WTGS, seriously affecting the safe and stable operation of the grid. In order to ensure the safe grid connection and efficient consumption of the wind power at the sending side of the Ximeng-Taizhou project, the frequency-domain analysis and time-domain simulation of the oscillation risk of the wind plants' grid connection are

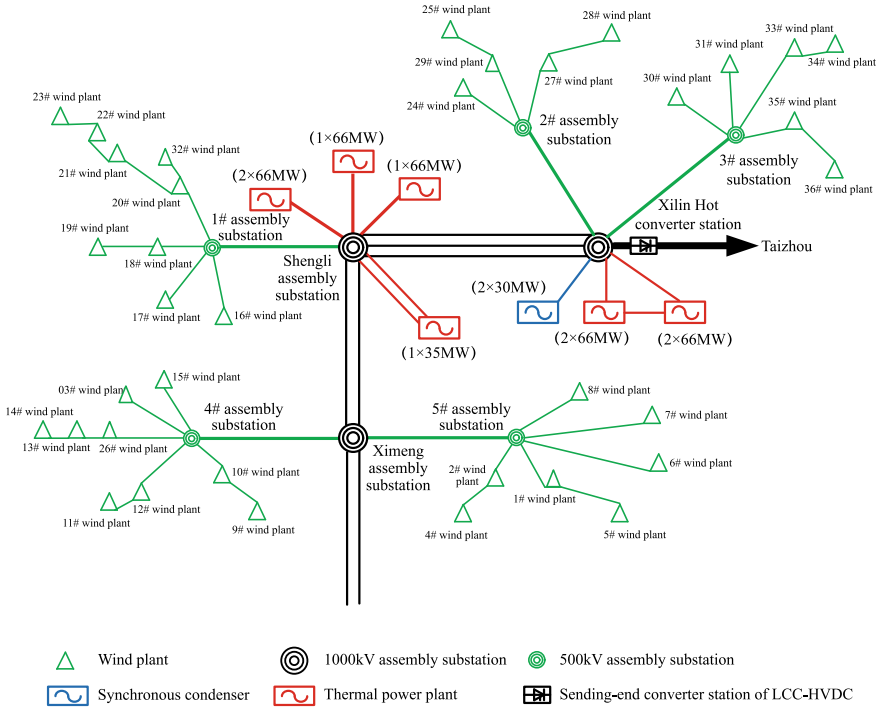

Fig. 19.18 Topology of parameters of the wind plants at the sending side grid of the Ximeng-Taizhou LCC-HVDC

Table 19.10 Parameters of the wind plants at the sending side grid of the Ximeng-Taizhou LCC-HVDC

Assembly Substation Number	Wind Plant Number	Wind Plant Capacity (MW)
1#	9	1300
2#	5	1300
3#	6	1370
4#	9	1800
5#	7	1220

carried out, and the oscillation risks of each wind plant are comprehensively investigated. The parameters of wind plants with oscillation risks are shown in Table 19.11.

19.5.2 Oscillation Analysis

In this section, for the wind plants with oscillation risks, the frequency characteristics of the oscillation current based on the time-domain simulation are first analyzed. The

Table 19.11 Parameters of wind plants with oscillation risks

Plnant Number	Type of WTGS	Installed Capacity (MW)	Active Power (MW)
1#	DFIG	50	10
3#	PMSG	225	45
26#	PMSG	150	90
29#	DFIG	200	40

impedances of the wind plants and their grid connection points are scanned based on the full electromagnetic transient simulation platform. Finally, the grid connection points are taken as the analysis port, the frequency domain analysis of the system oscillation risk is carried out, and the dominant oscillation equipment is determined.

19.5.2.1 Time-Domain Analysis

The FFT analysis is applied to the wind plants with oscillation risks, and the oscillation waveform records and FFT results of the wind plants with oscillation risks are shown in Figs. 19.19, 19.20, 19.21 and 19.22. The frequency characteristics of the oscillation current of the wind plant with oscillation risks are shown in Table 19.12.

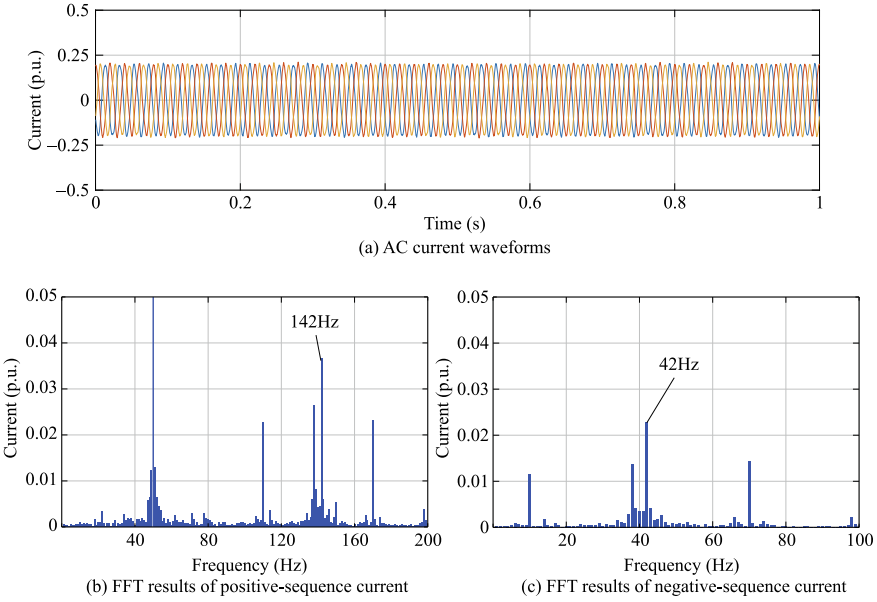

Fig. 19.19 Oscillation waveform records and FFT results of the 1# wind plant at the sending side grid of the Ximeng-Taizhou LCC-HVDC

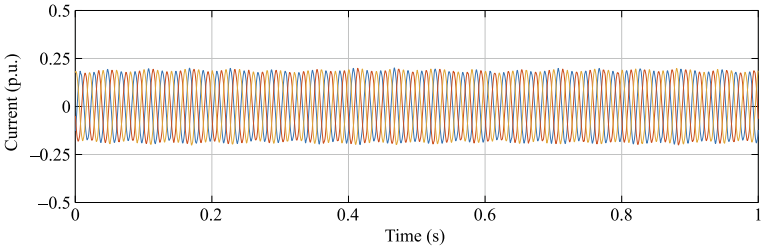

(a) AC current waveforms

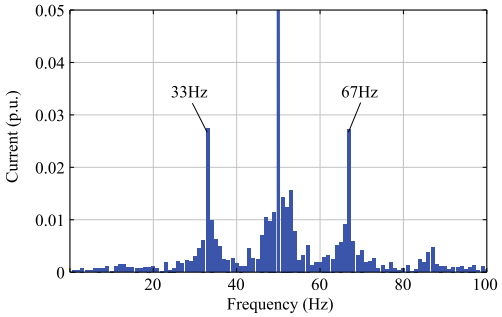

(b) FFT results of AC current

Fig. 19.20 Oscillation waveform records and FFT results of the 3# wind plant at the sending side grid of the Ximeng-Taizhou LCC-HVDC

It can be seen from Table 19.12 that the frequency characteristics of oscillation current in wind plants are different from each other. It can be inferred that the oscillations are caused by the grid connection of each wind plant. Hence, it is necessary to apply frequency-domain analysis for each wind plant.

19.5.2.2 Frequency-Domain Analysis

1. Oscillation risk of the 1# DFIG-based wind plant.

Based on the full electromagnetic transient simulation platform, the broadband impedance scanning is applied to obtain the impedance of the 1# wind plant $\boldsymbol{Z}_{\mathrm{DFIG}}$ and the system impedance at the grid connection point $\boldsymbol{Z}_{\mathrm{g}}$. The evaluation results of the oscillation risk for the 1# wind plant are shown in Fig. 19.23.

It can be seen from Fig. 19.23(a) that $\boldsymbol{Z}_{\mathrm{DFIG}}$ represents the capacitive negative damping characteristics near 142Hz and $\boldsymbol{Z}_{\mathrm{g}}$ represents the inductive characteristics. The magnitudes of $\boldsymbol{Z}_{\mathrm{DFIG}}$ and $\boldsymbol{Z}_{\mathrm{g}}$ curves intersect at point F (142Hz), with a PM of 1°. The GM/PM is insufficient, indicating oscillation risk in the system.

In Fig. 19.23(b), a forbidden area with a radius $R_{\min}$ of 0.15 is drawn based on the Nyquist criterion of maximum peak value. The Nyquist plot of $\boldsymbol{Z}_{\mathrm{g}}/\boldsymbol{Z}_{\mathrm{DFIG}}$ crosses

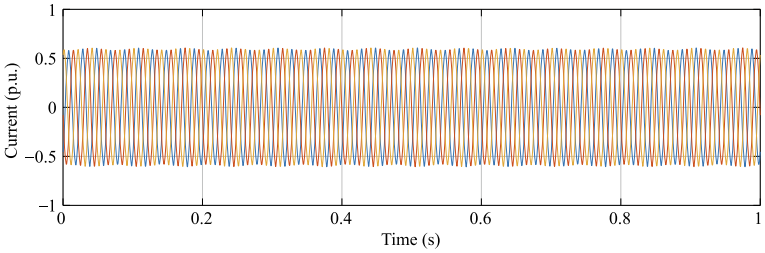

(a) AC current waveforms

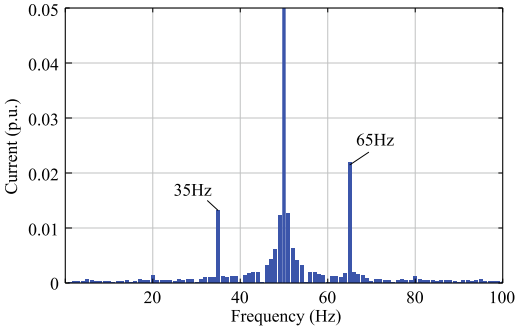

(b) FFT results of current

Fig. 19.21 Oscillation waveform records and FFT results of the 26# wind plant at the sending side grid of the Ximeng-Taizhou LCC-HVDC

point F (142Hz) in the forbidden area, indicating oscillation risk in the system. The positive-sequence oscillation of 142Hz with a coupling negative-sequence component of 42Hz will occur in the system. The frequency-domain analysis results are consistent with the FFT results of the waveform records in Fig. 19.19.

2. Oscillation risk of the 3# PMSG-based wind plant.

Based on the full electromagnetic transient simulation platform, the broadband impedance scanning is applied to obtain the impedance of the 3# wind plant $\boldsymbol{Z}_{\mathrm{PMSG}}$ and the system impedance at the grid connection point $\boldsymbol{Z}_{\mathrm{g}}$. The evaluation results of the oscillation risk for the 3# wind plant are shown in Fig. 19.24.

It can be seen from Fig. 19.24(a) that in the super-synchronous frequency band, $\boldsymbol{Z}_{\mathrm{PMSG}}$ represents the capacitive negative damping characteristics and $\boldsymbol{Z}_{\mathrm{g}}$ represents the inductive characteristics. The magnitudes of $\boldsymbol{Z}_{\mathrm{PMSG}}$ and $\boldsymbol{Z}_{\mathrm{g}}$ curves intersect at point G (67Hz), with a PM of 1°. The GM/PM is insufficient, indicating oscillation risk in the system.

In Fig. 19.24(b), a forbidden area with a radius $R_{\min}$ of 0.15 is drawn based on the Nyquist criterion of maximum peak value. The Nyquist plot of $\boldsymbol{Z}_{\mathrm{g}}/\boldsymbol{Z}_{\mathrm{PMSG}}$ crosses point G (67Hz) in the forbidden area, indicating oscillation risk in the system. The

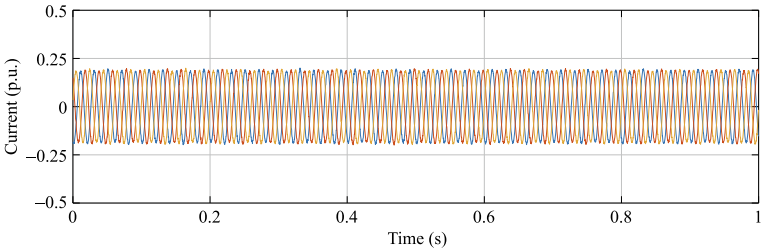

(a) AC current waveforms

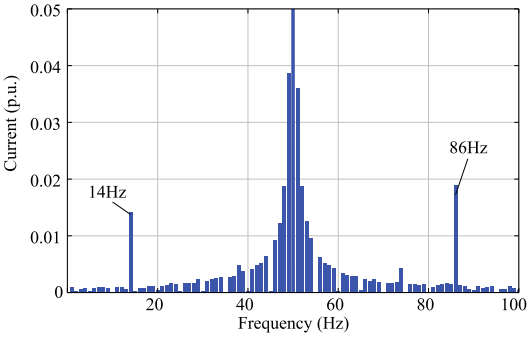

(b) FFT results of AC current

Fig. 19.22 Oscillation waveform records and FFT results of the 29# wind plant at the sending side grid of the Ximeng-Taizhou LCC-HVDC

Table 19.12 Frequency characteristics of oscillation current of the wind plant with oscillation risks

Wind Plant Number	Type of WTGS	Positive-Sequency AC Current	
		Frequency (Hz)	Harmonic Component (%)
1#	DFIG	42 (negative-sequence)/142 (positive-sequence)	2.4/3.7
3#	PMSG	33 (positive-sequence)/ 67 (positive-sequence)	2.7/2.7
26#	PMSG	35 (positive-sequence)/ 65 (positive-sequence)	1.3/2.2
29#	DFIG	14 (positive-sequence)/ 86 (positive-sequence)	1.5/1.9

positive-sequence oscillation of 67Hz with a coupling positive-sequence component of 33Hz will occur in the system. The frequency-domain analysis results are consistent with the FFT results of the waveform records in Fig. 19.20.

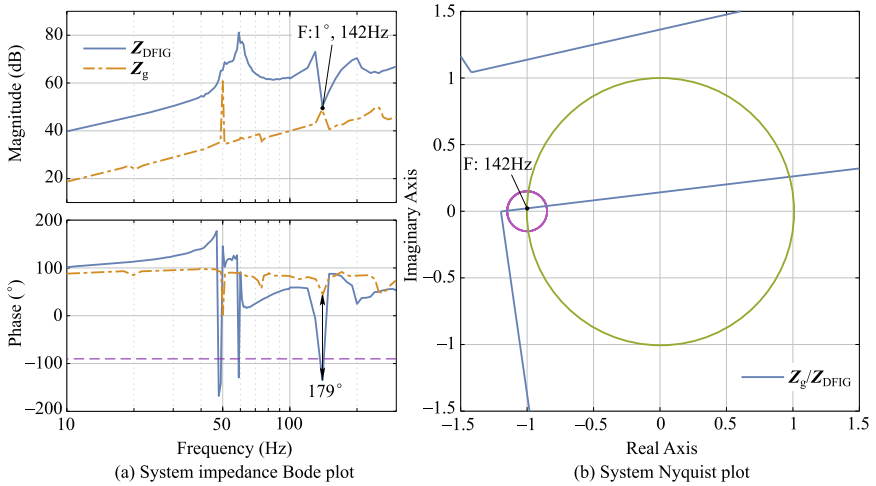

Fig. 19.23 Evaluation results of the oscillation risk for the 1# wind plant

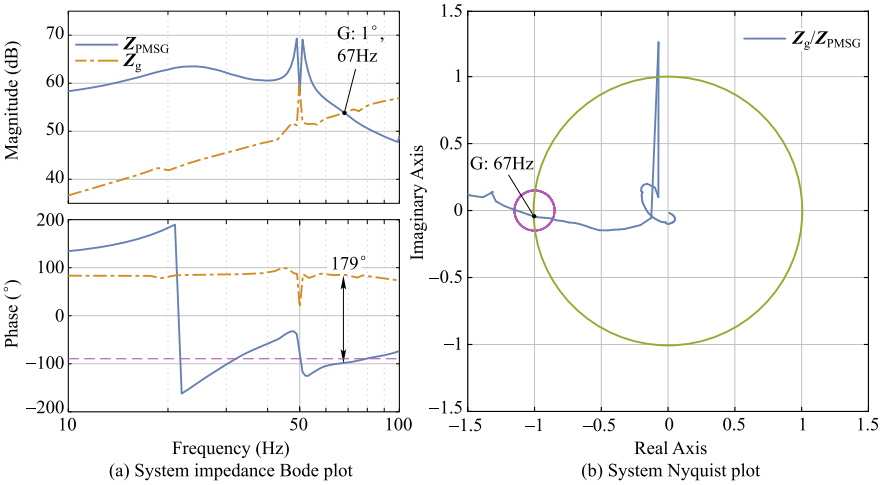

Fig. 19.24 Evaluation results of the oscillation risk for the 3# wind plant

3. Oscillation risk of the 26# PMSG-based wind plant.

Based on the full electromagnetic transient simulation platform, the broadband impedance scanning is applied to obtain the impedance of the 26# wind plant $\boldsymbol{Z}_{\mathrm{PMSG}}$ and the system impedance at the grid connection point $\boldsymbol{Z}_{\mathrm{g}}$. The evaluation results of the oscillation risk for the 26# wind plant are shown in Fig. 19.25.

It can be seen from Fig. 19.25(a) that in the super-synchronous frequency band, $\boldsymbol{Z}_{\mathrm{PMSG}}$ represents the capacitive negative damping characteristics and $\boldsymbol{Z}_{\mathrm{g}}$ represents

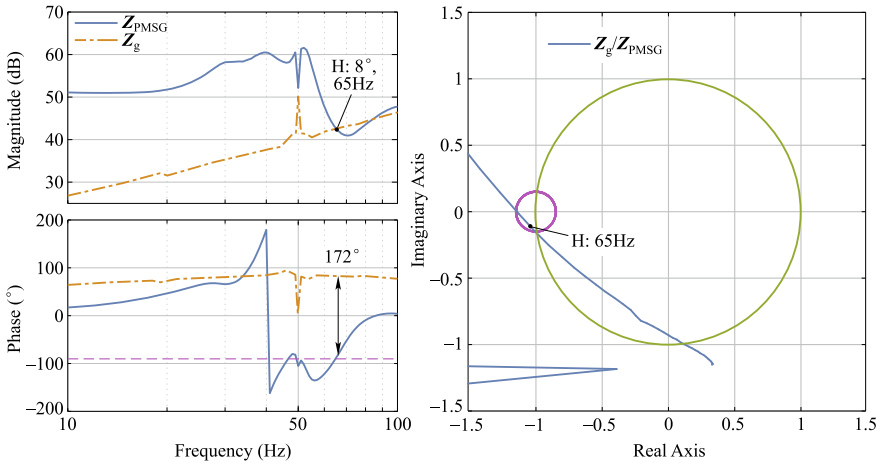

(a) System impedance Bode plot (b) System Nyquist plot

Fig. 19.25 Evaluation results of the oscillation risk for the 26# wind plant

the inductive characteristics. The magnitudes of $\boldsymbol{Z}_{\mathrm{PMSG}}$ and $\boldsymbol{Z}_{\mathrm{g}}$ curves intersect at point H (65Hz), with a PM of 8°. The GM/PM is insufficient, indicating oscillation risk in the system.

In Fig. 19.25(b), a forbidden area with a radius $R_{\min}$ of 0.15 is drawn based on the Nyquist criterion of maximum peak value. The Nyquist plot of $\boldsymbol{Z}_{\mathrm{g}}/\boldsymbol{Z}_{\mathrm{PMSG}}$ crosses point H (65Hz) in the forbidden area, indicating oscillation risk in the system. The positive-sequence oscillation of 65Hz with a coupling positive-sequence component of 35Hz will occur in the system. The frequency-domain analysis results are consistent with the FFT results of the waveform records in Fig. 19.21.

4. Oscillation risk of the 29# DFIG-based wind plant.

Based on the full electromagnetic transient simulation platform, the broadband impedance scanning is applied to obtain the impedance of the 29# wind plant $\boldsymbol{Z}_{\mathrm{DFIG}}$ and the system impedance at the grid connection point $\boldsymbol{Z}_{\mathrm{g}}$. The evaluation results of the oscillation risk for the 29# wind plant are shown in Fig. 19.26.

It can be seen from Fig. 19.26(a) that in the super-synchronous frequency band, $\boldsymbol{Z}_{\mathrm{DFIG}}$ represents the capacitive negative damping characteristics and $\boldsymbol{Z}_{\mathrm{g}}$ represents the inductive characteristics. The magnitudes of $\boldsymbol{Z}_{\mathrm{DFIG}}$ and $\boldsymbol{Z}_{\mathrm{g}}$ curves intersect at point I (86Hz), with a PM of 1°. The GM/PM is insufficient, indicating oscillation risk in the system.

In Fig. 19.26(b), a forbidden area with a radius $R_{\min}$ of 0.15 is drawn based on the Nyquist criterion of maximum peak value. The Nyquist plot of $\boldsymbol{Z}_{\mathrm{g}}/\boldsymbol{Z}_{\mathrm{PMSG}}$ crosses point I (86Hz) in the forbidden area, indicating oscillation risk in the system. The positive-sequence oscillation of 86Hz with a coupling positive-sequence component of 14Hz will occur in the system. The frequency-domain analysis results are consistent with the FFT results of the waveform records in Fig. 19.22.

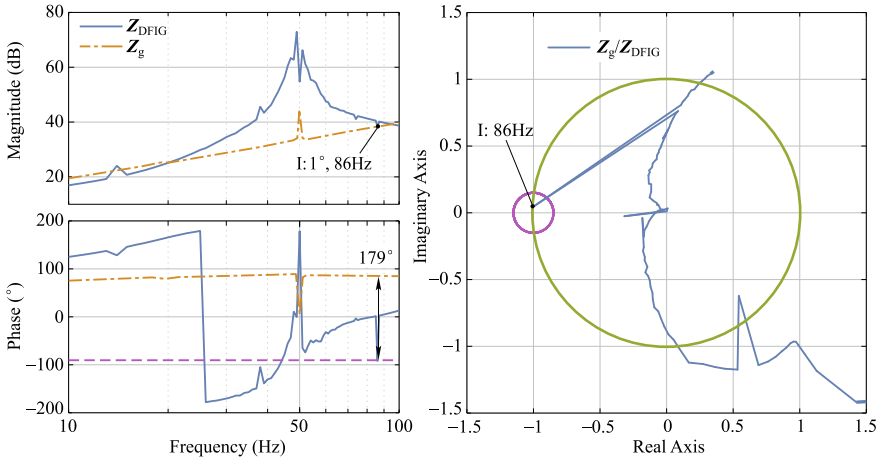

Fig. 19.26 Evaluation results of the oscillation risk for the 29# wind plant

19.5.3 Oscillation Mitigation

1. Impedance reshaping and oscillation mitigation of the 1# DFIG-based wind plant.

According to Chap. 7, the impedance characteristics of DFIG-based wind plants in the 100~200Hz frequency band are dominated by the stator and influenced by the GSC AC current loop. It represents the capacitive negative damping characteristics. By optimizing the control parameters of the GSC and RSC AC current loops, the impedance of the 1# wind plant can be reshaped to mitigate the oscillation. Fig. 19.27 shows the evaluation results of the oscillation risk for the 1# wind plant after impedance reshaping.

It can be seen from Fig. 19.27(a) that the magnitudes of the reshaped wind plant impedance $\boldsymbol{Z}_{\mathrm{DFIG}}$ curve and $\boldsymbol{Z}_{\mathrm{g}}$ curve do not intersect.

In Fig. 19.27(b), a forbidden area with a radius $R_{\min}$ of 0.15 is drawn based on the Nyquist criterion of maximum peak value. The Nyquist plot of $\boldsymbol{Z}_{\mathrm{g}}/\boldsymbol{Z}_{\mathrm{DFIG}}$ is always outside the forbidden area. By optimizing the control parameters of the GSC and RSC current inner loop, the impedance of the 1# wind plant can be reshaped to mitigate the positive-sequence oscillation of 142Hz with a coupling negative-sequence component of 42Hz.

2. Impedance reshaping and oscillation mitigation of the 3# PMSG-based wind plant.

According to Chap. 6, the impedance characteristics of PMSG-based wind plants in the super-synchronous frequency band are dominated by PLL and influenced by the GSC AC current loop. It represents the capacitive negative damping characteristics.

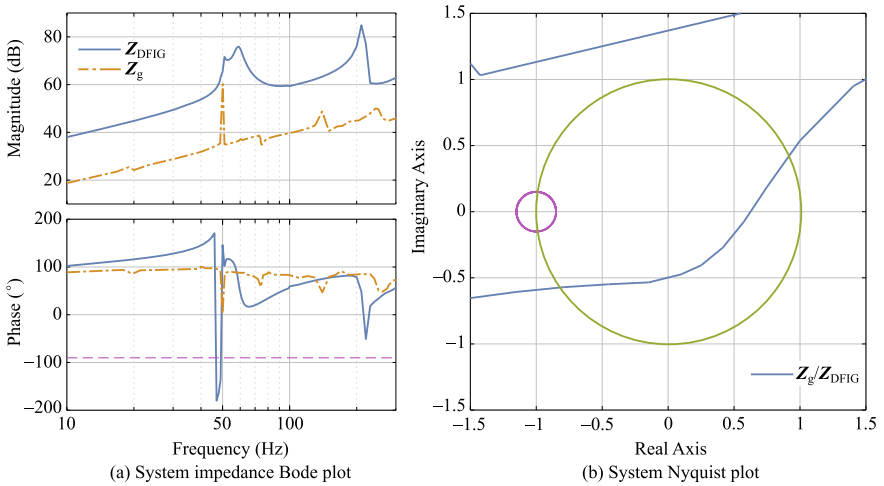

Fig. 19.27 Evaluation results of the oscillation risk for the 1# wind plant after impedance reshaping

By optimizing the control parameters of the PLL and the GSC AC current loop, the impedance of the 3# wind plant can be reshaped to mitigate the oscillation. Fig. 19.28 shows the evaluation results of the oscillation risk for the 3# wind plant after impedance reshaping.

It can be seen from Fig. 19.28(a) that the magnitudes of the reshaped wind plant impedance $\boldsymbol{Z}_{PMSG}$ curve and $\boldsymbol{Z}_g$ curve intersect at point G (67Hz), with the PM increased from 1° to 73°.

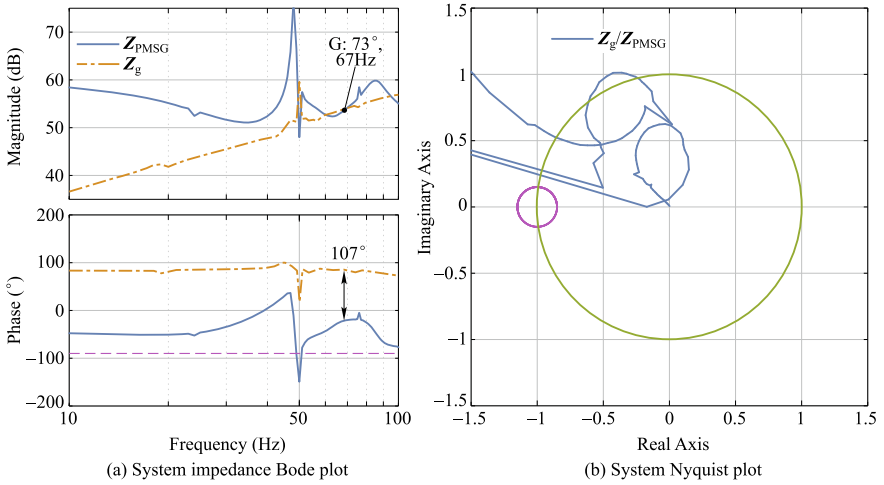

Fig. 19.28 Evaluation results of the oscillation risk for the 3# wind plant after impedance reshaping

In Fig. 19.28(b), a forbidden area with a radius $R_{\min}$ of 0.15 is drawn based on the Nyquist criterion of maximum peak value. The Nyquist plot of $\boldsymbol{Z}_{\mathrm{g}}/\boldsymbol{Z}_{\mathrm{PMSG}}$ is always outside the forbidden area. By optimizing the control parameters of the PLL and the current inner loop, the impedance of the 3# wind plant can be reshaped to mitigate the positive-sequence oscillation of 67Hz with a coupling positive-sequence component of 33Hz.

3. Impedance reshaping and oscillation mitigation of the 26# PMSG-based wind plant.

According to Chap. 6, the impedance characteristics of PMSG-based wind plants in the super-synchronous frequency band are dominated by PLL and influenced by the GSC AC current loop. It represents the capacitive negative damping characteristics. By optimizing the control parameters of the PLL and the GSC AC current loop, the impedance of the 26# wind plant can be reshaped to mitigate the oscillation. Fig. 19.29 shows the evaluation results of the oscillation risk for the 26# wind plant after impedance reshaping.

It can be seen from Fig. 19.29(a) that the magnitudes of the reshaped wind plant impedance $\boldsymbol{Z}_{\mathrm{PMSG}}$ curve and $\boldsymbol{Z}_{\mathrm{g}}$ curve intersect at point H (65Hz), with the PM increased from 8° to 18°.

In Fig. 19.29(b), a forbidden area with a radius $R_{\min}$ of 0.15 is drawn based on the Nyquist criterion of maximum peak value. The Nyquist plot of $\boldsymbol{Z}_{\mathrm{g}}/\boldsymbol{Z}_{\mathrm{PMSG}}$ is always outside the forbidden area. By optimizing the control parameters of the PLL and the GSC AC current loop, the impedance of the 26# wind plant can be reshaped to

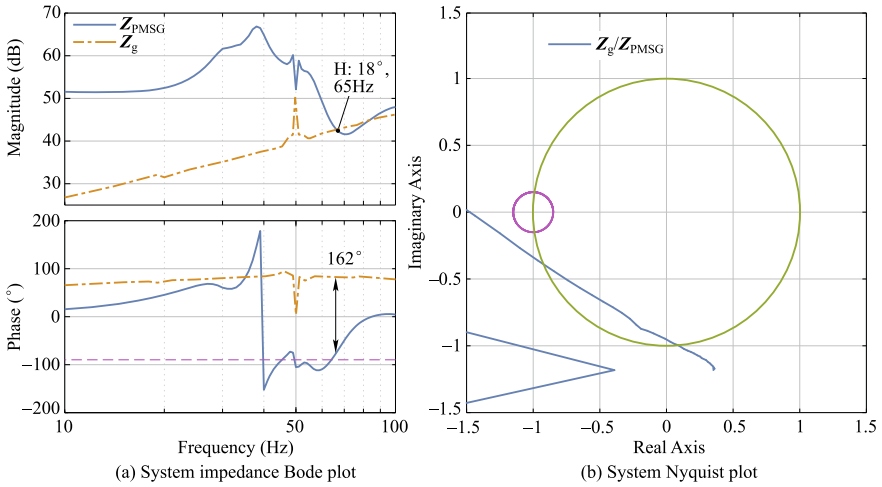

(a) System impedance Bode plot (b) System Nyquist plot

Fig. 19.29 Evaluation results of the oscillation risk for the 26# wind plant after impedance reshaping

mitigate the positive-sequence oscillation of 65Hz with a coupling positive-sequence component of 35Hz.

4. Impedance reshaping and oscillation mitigation of the 29# DFIG-based wind plant.

According to Chap. 7, the impedance characteristics of DFIG-based wind plants in the super-synchronous frequency band are dominated by the stator and influenced by the GSC AC current loop. It represents the capacitive negative damping characteristics. By optimizing the control parameters of the GSC AC current loop, the impedance of the 29# wind plant can be reshaped to mitigate the oscillation. Fig. 19.30 shows the evaluation results of the oscillation risk for the 29# wind plant after impedance reshaping.

It can be seen from Fig. 19.30(a) that the magnitudes of the reshaped wind plant impedance $\boldsymbol{Z}_{\mathrm{DFIG}}$ curve and $\boldsymbol{Z}_{\mathrm{g}}$ curve intersect at point J (72Hz). Compared with point I (86Hz), the PM is increased from 1° to 50°. The damping characteristics of $\boldsymbol{Z}_{\mathrm{DFIG}}$ is increased.

In Fig. 19.30(b), a forbidden area with a radius $R_{\min}$ of 0.15 is drawn based on the Nyquist criterion of maximum peak value. The Nyquist plot of $\boldsymbol{Z}_{\mathrm{g}}/\boldsymbol{Z}_{\mathrm{DFIG}}$ is always outside the forbidden area. By optimizing the control parameters of the GSC AC current loop, the impedance of the 29# wind plant can be reshaped to mitigate the positive-sequence oscillation of 86Hz with a coupling positive-sequence component of 14Hz.

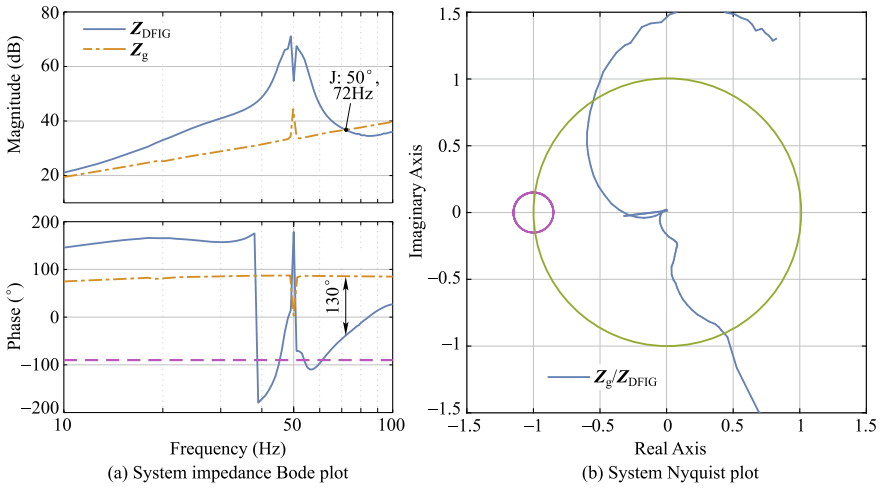

Fig. 19.30 Evaluation results of the oscillation risk for the 29# wind plant after impedance reshaping

Appendix A
Test and Experimental Verification Platform of REG and AC/DC Transmission Systems

The Zhangbei Test Base, an operation and control technology research and test base of large-scale renewable energy generation (REG) and alternating current (AC) /direct current (DC) transmission systems, has been building since 2010. It mainly consists of the test stands of the wind turbine generator system (WTGS), the outdoor test fields of photovoltaic (PV) units, the experimental verification platform for REG collection and transmission systems, and other test facilities. It is the world's largest and the only test base that combines low voltage ride-through (LVRT) test capability, grid adaptability test capability, and wind/solar/energy storage combination test and operation research method. It provides an experimental verification environment and platform for the basic theory and common key technologies of the grid-connected operation of REG.

A.1 Overview of the Zhangbei Test Base

The Zhangbei Test Base covers an area of about 24 km^2. It consists of mainly supporting facilities of 30 test stands of WTGS, one 110 kV substation, 35 km of 35 kV collection line, 4 local distribution rooms, 80 sets of 35 kV metal enclosed switchgear and controlgear. Its plan and aerial view are shown in Figs. A.1 and A.2, respectively.

The research and test on the grid-connection performance of 30 WTGS whose capacity are below 6 MW can be carried out at the same time in the Zhangbei Test Base by using the common foundation of the test stands, the flexible-switching collection system, the high-compatibility and high-speed massive data acquisition and processing system, and other facilities. The core test facilities include the voltage drop generator, grid disturbance generator, integrated test data network, etc.

© China Electric Power Press 2023

W. Wang et al., *Analysis and Mitigation of Broadband Oscillation in Renewable Energy Generation and AC/DC Transmission Systems*,
https://doi.org/10.1007/978-981-99-1568-2

Fig. A.1 Plan view of the Zhangbei Test Base

Fig. A.2 Aerial view of the Zhangbei Test Base

A.2 Research and Development Test Platform of the Grid Connection of REG

The Zhangbei Test Base has 4 WTGS for scientific research and testing, including a 2.5 MW permanent magnet synchronous generator (PMSG)-based wind turbine, a 2.1 MW asynchronous wind turbine, and 2 doubly-fed induction generators (DFIG)-based wind turbines of 1.5 MW and 2.5 MW, as shown in Fig. A.3. The main

(a) 1.5MW DFIG-based wind turbine

(b) 2.5MW DFIG-based wind turbine

(c) 2.1MW asynchronous wind turbine

(d) 2.5MW PMSG-based wind turbine

Fig. A.3 Tested WTGS

Fig. A.4 Voltage drop generator

Fig. A.5 Grid disturbance generator

components of each WTGS are arranged with test measuring points to facilitate the real-time simulation and experimental verification of dynamic characteristics of high-power WTGS.

The Zhangbei Test Base has a fixed type of voltage drop generator of 35 kV/6 MVA, as shown in Fig. A.4. The generator adopts valve control technology. It can telecontrol the switching of the reactor and set voltage drop amplitude and time duration. It can be used for low voltage ride-through (LVRT) and zero voltage ride-through capability test of WTGS, PV inverters and energy storage systems whose capacity are below 6 MW.

The Zhangbei Test Base has a grid disturbance generator of 35 kV/6MVA, as shown in Fig. A.5. It can generate different grid disturbances to test the adaptability of WTGS, PV inverters and energy storage systems whose capacity are below 6 MW to grid voltage deviation, three-phase imbalance, harmonics and other disturbances.

The Zhangbei Test Base has 500 kW fixed bracket PV units, 40 kW dual-axis tracking bracket PV units, 80 kW roof PV units, and 20 kW concentrating PV units. The test fields for 30 kW PV modules and 1.5 MW balance of system have been built to carry out the operation and control study of PV key components and systems,

Fig. A.6 Test fields for PV units

as shown in Fig. A.6. The platform can provide conditions for verification of the autonomous collaborative control theory of distributed REG and energy storage.

A.3 Experimental Verification Platform of REG and AC/DC Transmission Systems

The experimental verification platform is for the stability analysis and experimental verification of the new collection and transmission system of REG. It has 3 WTGS of MW-level, 1.5 MW PV units, 2 synchronous generators, 35 kV AC series adjustable impedances, ±35 kV/5 MW line-commutated converter-based high voltage direct current (LCC-HVDC), ±35 kV/5 MW modular multilevel converter-based high voltage direct current (MMC-HVDC), three ±35 kV/800 V DC/DC converters, and 1Mvar intelligent load. The topology is shown in Fig. A.7. In the future, the renewable energy frequency division power generation and transmission system, the self-synchronous voltage source controlled and synchronous motor interface types of REG will be built in the platform.

The platform can provide the test environment and conditions for different technical verifications, as the technical verification of the DC conversion and DC cascade stability control of REG, the broadband control characteristics and oscillation mitigation of REG, the transient control failure mechanism and stability control of REG, etc.

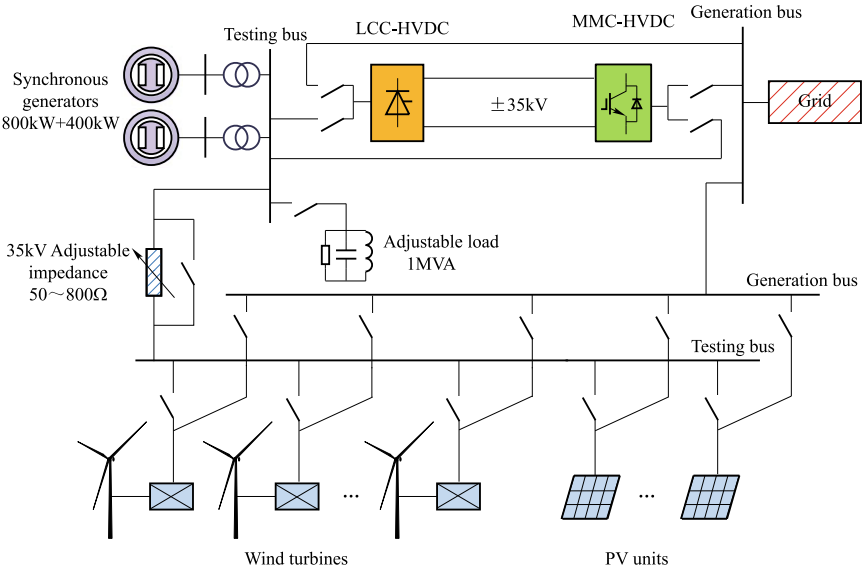

Fig. A.7 Experimental verification platform of REG and AC/DC transmission systems

Appendix B
Full Electromagnetic Transient Simulation Platform for REG and AC/DC Transmission Systems

The full electromagnetic transient (EMT) simulation platform for REG and AC/DC transmission systems is supported by the State Key Laboratory of Operation and Control of Renewable Energy and Storage Systems. The full EMT simulation platform is built by solving the problems of refined modeling of REG units and equivalent modeling of REG plants. The real-time simulation environments for multiple transmission scenarios are built based on the platform, including the REG base connected to the line with series compensation, connected into LCC-HVDC and MMC-HVDC, etc. The field large disturbance test results are accurately recurred by the full EMT simulation platform. It also provides research means for impedance model verification, broadband oscillation mechanism analysis, oscillation mitigation strategy verification, and project cases analysis of REG and AC/DC transmission systems.

Appendix B mainly introduces the basic structure, simulation scale, and model accuracy of the full EMT simulation platform for REG and AC/DC transmission systems.

B.1 Structure of the Full EMT Simulation Platform

The full EMT simulation platform for REG and AC/DC transmission systems mainly consists of the following three parts:

1. EMT modeling of REG unit and static var generator (SVG), which is realized by control hardware-in-the-loop (CHIL) simulation. The controllers of the CHIL simulation platform are the same as the filed controllers.
2. EMT modeling of REG plants, mainly includes REG units, SVG, and AC collection system. The method is realized by equivalent grid division and equivalent multiplication technology of REG units.

© China Electric Power Press 2023

W. Wang et al., *Analysis and Mitigation of Broadband Oscillation in Renewable Energy Generation and AC/DC Transmission Systems*,
https://doi.org/10.1007/978-981-99-1568-2

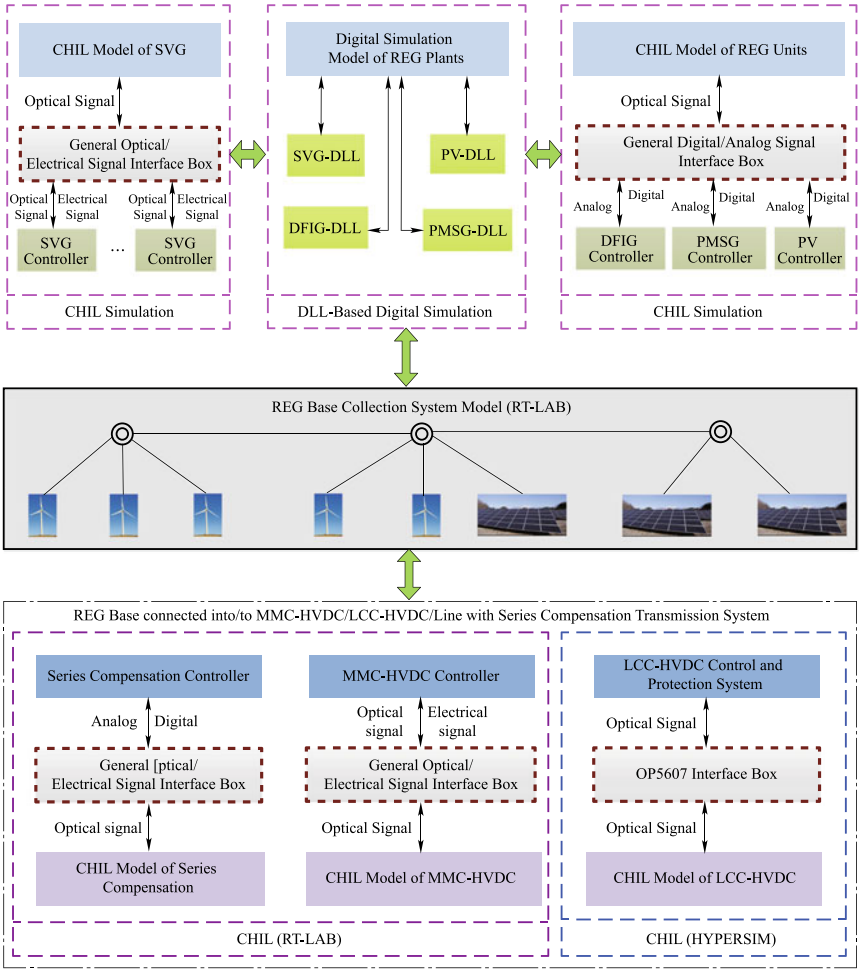

Fig. B.1 Structure of the full EMT simulation platform of REG and AC/DC transmission systems

3. EMT modeling of REG and AC/DC transmission systems, mainly includes REG connected to the line with series compensation, connected into LCC-HVDC and MMC-HVDC. The EMT modeling of the CHIL simulation platform adopts the same control and protection devices as the practical projects.

The structure of the full EMT simulation platform is shown in Fig. B.1.

B.2 Performance of the Full EMT Simulation Platform

1. EMT modeling and model verification of REG units

The grid-connection characteristics of REG units are mainly dominated by the control of the grid-connected converter. The control strategies and parameters of REG units of different manufacturers are different to some extent, leading to the relatively greater difference in the impedance characteristics and fault ride-through characteristics of REG units. The converter control of REG units is the core intellectual property of the manufacturers, which is usually confidential. Hence, it is difficult to obtain the control strategies and control parameters consistent with the actual controller for the EMT modeling of REG units.

The EMT modeling and model verification method named "three approaches mutual verification" is developed to solve the gray box problem of REG controllers of different manufacturers and models, which means testing and verifying the consistency of results of "field type test (FTT)-CHIL simulation-dynamic link library (DLL)". The technical route for the EMT modeling and model verification of REG units is shown in Fig. B.2.

The verification results of the impedance characteristics and transient characteristics of REG units are shown in Fig. B.3. It can be seen that the accuracy of the dynamic link library meets the requirements of the system simulation analysis, for its impedance and transient characteristics are consistent with that of field type test and EMT simulation. The digital models of REG units lay a foundation for the EMT modeling of REG plants.

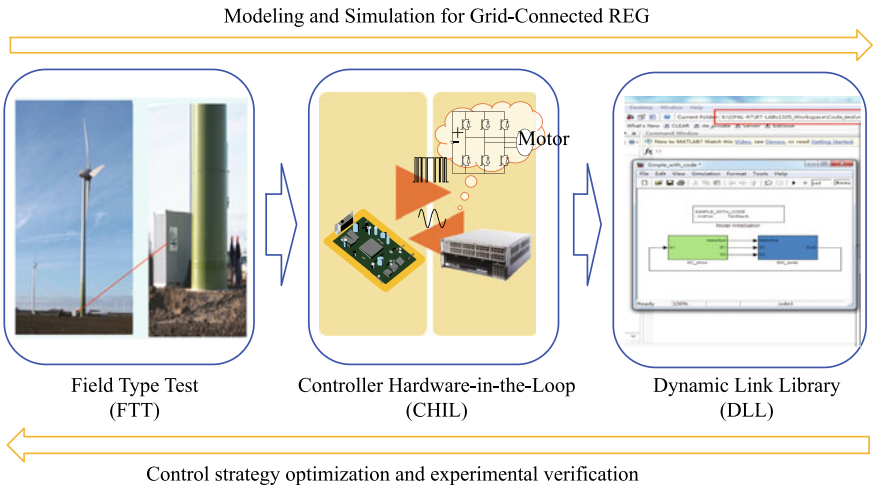

Fig. B.2 Technical route fort the EMT modeling and model verification of REG units

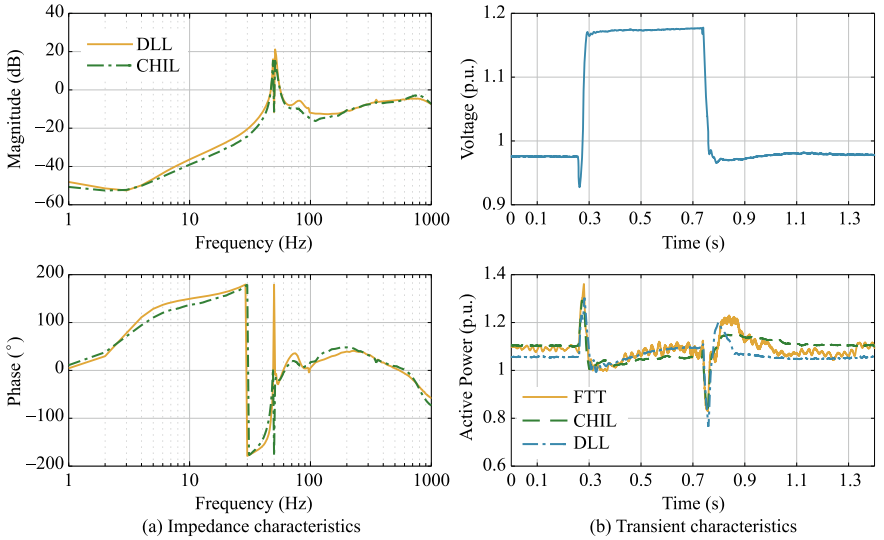

Fig. B.3 Verification results of the impedance characteristics and transient characteristics of REG units

(a) Controllers of REG units

(b) Controllers of SVGs

Fig. B.4 CHIL simulation platform of the REG units and SVGs

At present, the CHIL simulation platform has built a controller model library of 255 REG units and 36 SVGs, covering more than 80% of domestic installed capacity. The CHIL simulation platform for the REG units and SVGs is shown in Fig. B.4.

2. Equivalent EMT modeling of REG plants

Equivalent modeling is necessary for modeling thousands of power electronic devices in REG base. The constraint condition of equivalent modeling is the equivalence of the equivalent model and the detailed model of the collection system impedance. The EMT equivalent grid division model is established based on the constraint condition. An optimized EMT multiplication model is proposed to solve the simulation instability problem caused by the inherent delay of the traditional equivalent multiplication model so that the equivalent EMT modeling of REG plants can be realized.

Figure B.5 shows the equivalent EMT model and the detailed model of REG plants. It compares the broadband impedance and transient characteristics of the equivalent and detailed models. The installed capacity of PV plants is 30 MW, consisting of 48 0.64 MW PV units, and are equivalent to 4 PV units.

The full EMT simulation platform for REG connected into different HVDC projects are built, including South Hami-Zhengzhou, Jiuquan-Hunan, Ximeng-Taizhou, Qinghai-Henan, Shanbei-Hubei, Zhangbei MMC-MTDC grid. In the platform, the EMT model of the REG plants at the DC sending side adopts the actual controllers of REG plants, and is built by the equivalent EMT method. The modeling of LCC-HVDC and MMC-HVDC grids adopt the actual controllers and protection devices consistent with the project. The full EMT simulation platform of REG and AC/DC transmission systems is shown in Fig. B.6. Based on the platform, the field large disturbance test is accurately recurred, and the comparison results are shown in Fig. B.7.

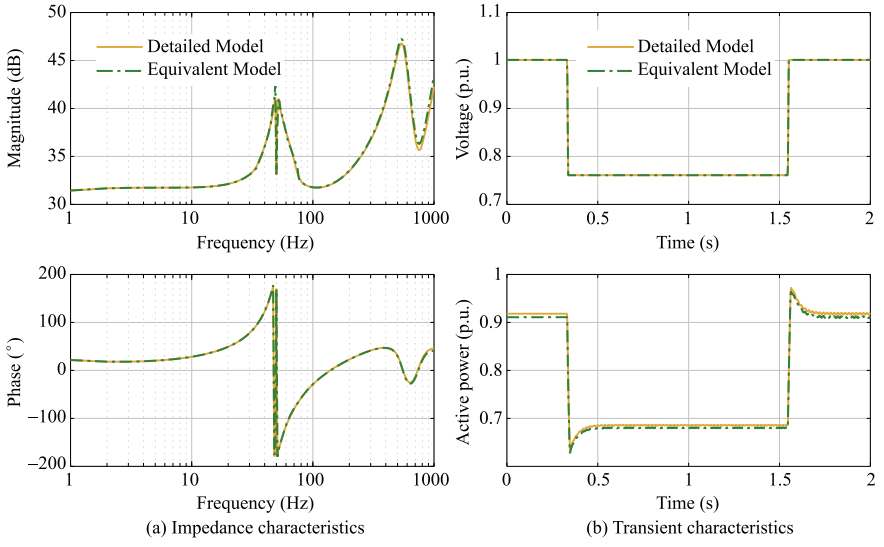

Fig. B.5 Comparison of equivalent and the detailed EMT model of REG plants

Fig. B.6 The full EMT simulation platform of REG and AC/DC transmission systems

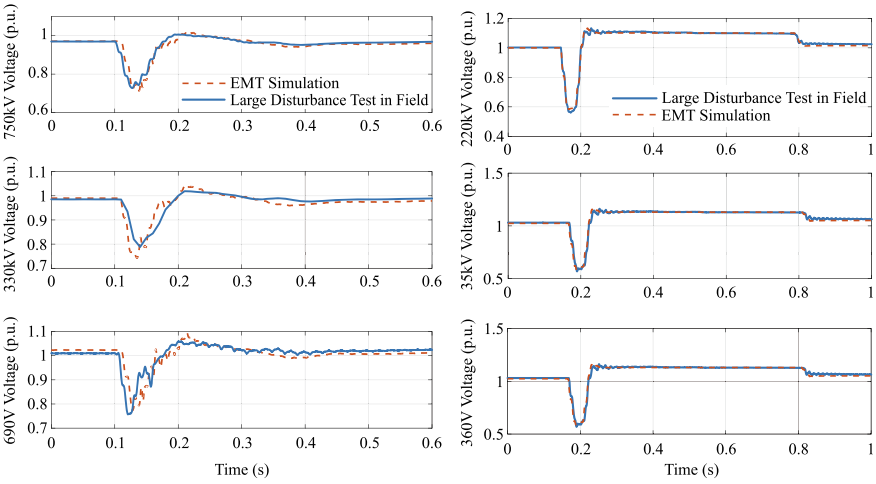

(a) Jiuquan-Hunan LCC-HVDC (b) Zhangbei MMC-MTDC

Fig. B.7 Comparison results of filed large disturbance tests and EMT simulation

Index

A

AC/DC voltages and currents in the receiving-end LCC, 331, 341
AC/DC voltages and currents in the sending-end LCC, 328, 330, 346, 348
AC current loop in grid-connected mode, 426, 434
AC current loop in passive islanding mode, 391, 419
AC port impedance model, 53, 102, 141, 325, 350, 401
AC port impedance model of PV unit, 266
AC port impedance model of SVG, 283, 298
AC port impedance of LCC-HVDC at the sending end, 353–355, 359, 361, 362, 365, 593
AC port impedance of MMC, 103, 104
AC port impedance of the thyristor converter, 144
AC voltage loop in passive islanding mode, 375
Analysis method of the broadband oscillation, 478, 501, 520
Analysis of negative damping characteristics, 182, 184, 192, 239, 246, 273, 308, 319, 416, 432
Analysis of oscillation for REG connected into LCC-HVDC system, 502
Arm equivalent model, 64
Averaged model of receiving-end MMC, 372, 373
Averaged model of sending-end MMC, 369, 371
Averaged model of SVG, 284, 285
Averaged model of the two-level converter, 36
Averaged switching model, 27, 28

B

Block diagram of active power loop, 190
Block diagram of GSC typical control, 207, 208
Block diagram of PLL, 29, 177
Block diagram of PLL controller, 29
Broadband oscillation incidents, 475

C

Calculated results of the impedance of double winding transformer, 454, 455
Calculation flow chart of station equivalent impedance model, 469
Calculation of equivalent impedance of REG plants, 466
CHIL simulation platform, 5, 197, 283, 325, 367, 483, 484, 487, 489, 491, 493, 494, 496, 523, 525, 669, 670, 672
Circulating current control, 59, 74–77, 83, 84, 90, 99, 283, 375, 377, 378, 391–395, 398, 399, 401, 402, 417, 424, 432
Classification of full power converter-based wind turbines, 148

© China Electric Power Press 2023

W. Wang et al., *Analysis and Mitigation of Broadband Oscillation in Renewable Energy Generation and AC/DC Transmission Systems*,
https://doi.org/10.1007/978-981-99-1568-2

Collecting line of the REG plant, 449, 450
Comparison of equivalent and the detailed electromagnetic transient model of REG plant, 673
Complex torque coefficient analysis method, 4
Composition of PV plant, 443, 445
Configurations of symmetrical mono-polar MMC-HVDC, 368
Constant power zone, 198, 245, 246
Constant speed zone, 198, 245
Control diagram of the two-level converter, 37
Controller hardware-in-the-loop simulation, 5
Control strategy of LCC-HVDC, 341
Control strategy of receiving-end LCC, 333
Control strategy of receiving-end MMC, 377
Control strategy of sending-end LCC, 333
Control strategy of sending-end MMC, 375, 390
Control structure of PMSG-based wind turbine, 532
Control structure of the grid-connected inverter, 254, 255, 264
Convolution of frequency-domain vectors, 31

D

DC current control mode, 325, 332, 333, 346
DC voltage control mode, 325, 332, 333, 348
Diagram of the commutation circuit, 111
Dq-axis impedance, 7

E

Eigenvalue analysis method, 4, 5
Electromagnetic transient modeling of REG plant, 669, 671, 673
Equivalent circuit of double winding transformer, 451
Equivalent circuit of overhead transmission line, 446
Equivalent circuit of the closed-loop transfer function, 477
Equivalent impedance model of REG plant, 461, 464
Equivalent model for the REG plants connected into AC grid, 478
Equivalent model of DFIG, 201
Equivalent model of PMSG, 151
Equivalent model of the DC transmission lines, 349, 400
Experimental system of PMSG-based wind turbine connected into AC grid, 495
Experimental verification platform of REG and AC/DC transmission systems, 663, 667, 668

F

Fast Fourier transform, 484
Field test verification for DFIG-based wind plant connected into AC grid, 490, 491
Field test verification for PMSG-based wind plant connected into AC grid, 481, 484, 486, 488
Fixed type of voltage drop generator of 35kV/6 MVA, 666
Flux linkage equation, 200, 202, 203, 207
Frequency-band division method, 177, 229, 232, 268, 269, 308, 319, 416, 432, 475, 478, 502, 504, 506, 516
Frequency-band division method for the REG plants connected into AC grid, 475
Frequency-band division of LCC-HVDC impedance, 358, 506
Frequency-band overlapping effect, 176, 182, 184, 185, 187–190, 192, 193, 197, 229, 239, 247, 249, 251, 268, 273, 275, 276, 278–280, 283, 302, 308, 314, 315, 319, 320, 322, 325, 353, 361, 365, 367, 405, 416, 417, 423–425, 432, 437–439, 478, 479, 481, 505, 508, 520, 522, 523, 531, 533
Frequency coupling impedance network model of wind plant, 463
Frequency distribution characteristics of the small-signal quantities in the thyristor converter, 122
Frequency-domain characteristics of the small-signal vectors in LCC-HVDC, 343
Frequency-domain characteristics of the small-signal vectors in MMC, 86, 87
Frequency-domain characteristics of the small-signal vectors in MMC-HVDC, 386, 387

Frequency-domain characteristics of the small-signal vectors in SVG, 292
Frequency-domain characteristics of the steady-state vectors in LCC-HVDC, 340
Frequency-domain characteristics of the steady-state vectors in MMC, 81
Frequency-domain characteristics of the steady-state vectors in MMC-HVDC, 384
Frequency-domain characteristics of the steady-state vectors in SVG, 290
Frequency-domain linearization, 25, 29, 33
Frequency-domain linearization of the nonlinear system, 16
Frequency-domain model of arm circuit, 73
Frequency-domain results of the current switching function, 138, 140
Frequency-domain small-signal model of main circuit, 48
Frequency-domain small-signal model of the control loops, 90
Frequency-domain steady-state model of receiving-end MMC, 383
Frequency-domain steady-state model of sending-end MMC, 382
Frequency response relationship of the two-level converter, 43

G

Gain margin, 477
Grid-connected inverter, 253, 254, 256, 259, 263, 264
Grid-connected mode, 299, 368, 375, 377, 391, 393, 395, 402–405, 407, 425–430, 432–438, 501, 516–518
Grid disturbance generator of 35kV/6MVA, 666
GSC control strategy, 207

I

Impedance-based analysis method, 4, 6, 8
Impedance characteristics for the REG plants connected into AC grid, 475, 478, 504
Impedance characteristics of DFIG-based wind plant, 480, 481, 507, 508, 522, 523, 579
Impedance characteristics of DFIG-based wind turbine, 197, 215, 217, 227–229, 232, 234–237, 239, 246, 250, 251, 558
Impedance characteristics of LCC-HVDC, 105, 325, 341, 351, 353, 356, 359–363, 365, 502, 504, 505, 593
Impedance characteristics of MMC-HVDC, 367, 385, 402–406, 409, 411, 412, 414, 417–419, 421–425, 427–430, 432, 434, 435, 437, 516, 520–523, 609
Impedance characteristics of MMC-HVDC in passive islanding model, 405, 416, 516, 517
Impedance characteristics of PMSG-based wind plant, 470, 471, 473, 478, 479, 506, 508, 520–522
Impedance characteristics of PMSG-based wind turbine, 176, 177, 182, 184, 187, 193
Impedance characteristics of REG plant, 443, 466, 469, 478, 506, 569, 593, 673
Impedance model of LCC-HVDC, 105, 325, 341, 350, 351, 353, 355, 362, 502, 673
Impedance model of MMC-HVDC, 367, 385, 405, 414, 416, 425
Impedance model of MMC-HVDC in grid-connected model, 367, 377, 402, 403, 405, 425, 427, 429
Impedance model of SVG, 290, 300, 306, 315
Impedance network model of the multi-unit system, 458
Impedance network model of wind farm, 462
Impedance network model of wind plant, 462
Impedance of the AC port of PMSG-based wind turbine, 164
Impedance reshaping design of DFIG-based wind turbine, 549
Impedance reshaping model of PMSG-based wind turbine, 534
Impedance reshaping of DFIG-based wind plant, 579
Impedance reshaping of DFIG-based wind turbine, 548
Impedance reshaping of PMSG-based wind plant, 569
Impedance reshaping of PMSG-based wind turbine, 532

Impedance reshaping strategy of LCC-HVDC, 593
Impedance reshaping strategy of PMSG-based wind turbine, 532
Impedance reshaping strategy of SVG, 569
Impedance scanning, 176, 182, 193, 229, 237, 251, 268, 273, 281, 307, 314, 319, 323, 359, 416, 423, 483, 494, 496, 508, 523
Impedance simulation scanning model of double winding transformer, 453

L

LCC-HVDC basic control characteristics of DC voltage and current, 334, 594
LCC-HVDC project, 1
LCC-HVDC transmission system, 325, 326, 332, 335
Linearization of PLL, 29
Linearization of the nonlinear power electronic system, 16
Linearization of the switching process, 8, 25, 27
Lumped parameter equivalent circuit of type for overhead transmission line, 447

M

Main circuit of the thyristor converter, 106
Maximum power point tracking, 475
MMC averaged model, 65, 66
MMC-HVDC transmission system, 368, 375, 377
Motion equation, 200, 203

N

Negative damping characteristics, 268
Negative damping characteristics of SVG in AC voltage control mode, 298, 300, 315, 319, 322
Nonlinear model, 28, 105, 200, 203
Nyquist criterion of maximum peak value, 475, 477, 483, 484, 487, 489, 490, 492, 496, 498, 509, 511, 514, 525
Nyquist curves of PMSG-based wind plants grid-connected system, 470, 472, 473

O

Offshore wind power, 2
Operating principle of receiving-end LCC, 325, 327, 330, 341
Operating principle of receiving-end MMC, 60, 284, 372
Operating principle of sending-end MMC, 325, 369
Operating states of the HBSM, 64
Operation principle of the wind turbine, 197
Opertation principle of the generator, 666
Oscillation mitigation field test for DFIG-based wind plant connected into AC grid, 491
Oscillation mitigation field test for PMSG-based wind plant connected into AC grid, 481, 484, 488, 508
Oscillation mitigation for DFIG-based wind plant connected into AC grid with series capacitive compensators, 490, 561
Oscillation mitigation for PMSG-based wind plant connected into AC grid, 481, 491, 561
Oscillation mitigation simulation for DFIG-based wind plant connected into AC grid with series capacitive compensators, 491
Oscillation mitigation simulation for PMSG-based wind plant connected into AC grid, 481, 486, 488, 508, 543
Oscillation mitigation simulation verification for DFIG-based wind plant, 491, 562
Oscillation mitigation simulation verification for PMSG-based wind plant, 481, 484
Oscillation propagation process with the frequency coupling effect for REG plants, 482
Oscillation risk evaluation for DFIG-based wind plant connected into AC grid, 480
Oscillation risk evaluation for PMSG-based wind plant connected into AC grid, 478
Oscillation risk of DFIG-based wind plant, 637, 654, 656, 657
Oscillation risk of PMSG-based wind plant, 478, 481, 484–489, 508, 510, 511, 521–525, 654, 656, 658
Oscillation waveforms for DFIG-based wind plant connected into AC grid, 492, 494, 513

Oscillation waveforms for PMSG-based wind plant connected into AC grid, 484, 487, 489, 497

P

Park transformation, 29, 32, 33, 49, 51, 53, 54, 90, 92, 93, 95–98, 100, 101, 130, 132, 202, 203, 254, 286, 287, 295, 377, 378, 391–394, 397, 398
Passive islanding mode, 299, 368, 375, 391–393, 402, 403, 405–407, 409–411, 413, 415–418, 420–424, 426, 432, 501, 516
Permanent magnet synchronous generator, 457, 478, 664
Phase margin, 178, 423, 477
Plan of the Zhangbei Test Base, 664
PLL output angle, 31, 83, 91, 92, 97, 128–132, 286, 295, 333, 334, 346, 348, 375, 377, 393, 397
PMSG-based wind turbine, 149, 150, 159, 164, 170, 173–177, 180, 182–184, 187, 192–194, 465, 484, 486, 488, 494–497, 509, 524, 531–533, 541
Power electronic device, 5, 6, 8, 15, 477, 478, 520, 673
PV array, 253, 254, 256, 259, 261, 263
PV unit, 253, 254, 256, 257, 260–262, 266–269, 271, 273–276, 279, 281, 443, 444, 450, 469, 514, 666, 667, 673

R

REG base, 4, 669, 673
Research and development test platform of the grid connection of REG, 664

S

Schematic diagram of the MMC operating principle, 67
Sequence impedance, 7, 55, 104, 143, 228, 229, 231, 299, 352, 403, 405, 448, 451, 452, 454, 457, 461, 471, 472, 596, 597
Simplified equivalent model of the REG and AC/DC transmission systems, 6
Simulation and verification of small-signal impedance circuit models, 458
Simulation parameters of the double winding transformer of REG plant, 454
Single wind turbine grid-connected system, 457, 458
Small-signal circuit model, 455–457, 459, 460
Small-signal frequency domain characteristics, 43, 215, 260
Small-signal frequency relationship of DFIG-based wind turbine, 217, 219
Small-signal frequency relationship of the PV unit, 261, 263
Small-signal impedance circuit model, 456–460
Small-signal model of AC current control, 50, 92
Small-signal model of arm circuit, 87–90, 102, 389, 390
Small-signal model of DC bus, 47, 168, 222, 265
Small-signal model of DC transmission lines, 349, 400
Small-signal model of DC voltage control, 49
Small-signal model of GSC, 169, 171, 223, 224
Small-signal model of main circuit, 46, 48, 87, 127, 293, 346, 347, 389
Small-signal model of MSC, 172, 173
Small-signal model of PLL, 91
Small-signal model of PV array, 263
Small-signal model of receiving-end LCC, 347
Small-signal model of receiving-end MMC, 396
Small-signal model of RSC, 224, 226
Small-signal model of sending-end LCC, 346
Small-signal model of sending-end MMC, 389
Small-signal model of switching functions, 128, 136
Small-signal model of the control loops, 90, 294, 391, 402
Small-signal model of the grid-connected inverter, 265
Small-signal transfer path and frequency response relationship of SVG, 291, 292
Small-signal transfer path of MMC-HVDC, 385
Small-signal transfer path of SVG, 291, 292
Small-signal transfer path of the thyristor converter, 121

Small-signal transfer path of the two-level converter, 43
Small-signal vector, 22, 43, 44, 46, 47, 50, 51, 53–56, 82, 83, 85–88, 90–103, 124, 126–128, 134, 135, 140–142, 164, 165, 168–170, 172–174, 218–220, 222–225, 227, 229, 261, 263–266, 292–298, 343–346, 348, 351, 386–396, 398, 399, 401–403, 584
Stability criteria in grid-connected mode, 517
Stability criteria in passive islanding mode, 516
Stability criterion, 7, 477, 501
Star-connection MMC circuit, 283
Stator-GSC coupling equivalent model of DFIG, 232
Stator-GSC decoupling model of DFIG, 229
Steady-state frequency order, 41, 47, 76, 80, 115, 118, 214, 218, 259, 261, 288, 289, 337, 340, 341, 379, 382, 383
Steady-state matrix of the modulation signal, 265
Steady-state model of arm circuit, 79
Steady-state model of DC bus, 214, 259
Steady-state model of GSC, 214, 215
Steady-state model of main circuit, 41, 118, 161, 214, 259, 289, 340, 382
Steady-state model of main circuit of the thyristor converter, 105
Steady-state model of MSC, 162
Steady-state model of PV array, 259
Steady-state model of RSC, 162, 215
Steady-state model of the grid-connected inverter, 259
Steady-state operating point, 7, 24, 29–31, 38, 43, 66, 74, 82, 115, 121, 122, 180–182, 187, 190, 192, 210, 211, 215, 216, 236, 237, 245, 246, 250, 256, 260, 271, 273, 275–280, 283, 288, 290, 291, 306, 325, 341, 342, 367, 379, 385, 401, 402, 414, 415, 417, 430–432, 480, 541
Steady-state vector, 39, 41–43, 47, 56, 76–81, 89, 115, 117–120, 134, 138, 140, 158, 162, 212–215, 218, 258–261, 288–290, 337–341, 379–384
Steady-state waveform of DC voltage, 39, 212
Steady-state waveforms of the two-level converter, 40
Structure of REG plants undertaking collecting function, 445
Structure of the CHIL simulation platform, 669, 670
Synchronous generator, 457, 478, 664, 667

T

Thyristor converter, 105–108, 110, 115, 121–123, 128, 129, 141, 142, 144, 326–328, 334, 335
Time-domain model, 73, 74, 105, 109, 110, 114, 162, 200, 203–205, 207, 208, 210, 214, 253, 256, 259, 285, 328, 330, 373
Time-domain model in dq frame, 203
Time-domain model of arm circuit, 73
Time-Domain model of DC bus, 210
Time-domain model of DFIG-based wind turbine, 200
Time-domain simulation analysis method, 4–6
Topology of DFIG-based wind turbine, 198
Topology of MMC-HVDC transmission system, 368
Topology of PMSG-based wind turbine, 198
Topology of the Hami grid connected with wind plants, 629
Topology of the single-stage PV unit, 254
Topology of the three-phase inverter circuit, 28
Topology of the two-level converter, 35, 36
Topology of the two-terminal bipolar LCC-HVDC, 326
Topology of the two-terminal mono-polar LCC-HVDC, 326, 327
Torque equation, 200, 202, 203
Transfer path and frequency distribution of PV unit small signals, 260
Transfer path of DFIG small signals, 215, 216, 291, 342, 385, 386
Transformer model, 450
Trigger angle, 107, 108, 112, 128–132, 328, 330, 338, 346, 348
Trigger angle control mode, 130, 332–334
Type equivalent circuit of double winding transformer, 452
Typical composition of wind plant, 444
Typical control diagram of MMC, 90, 91

Typical control diagram of SVG, 286, 294
Typical control diagram of the thyristor converter, 128, 129
Typical structure of PV plant, 443
Typical structure of REG plant, 443
Typical structure of wind, 443
Typical structure of wind farm, 444
Typical topology of MMC, 60, 61
Typical topology of SM, 61
Typical topology of SVG, 284

V
Verification of the impedance characteristics of REG units, 444
Verification of the transient characteristics of REG units, 671, 672
Voltage equation, 151, 152, 200, 201, 203, 205, 207, 208, 464
Voltage source converter, 35, 207

W
Waveforms of the AC current before and after Park transformation, 52
Waveforms of the dq-axis small-signal vectors of arm circulating currents, 98
Waveforms of the steady-state quantities in the thyristor converter, 116
Waveforms of the switching function of the thyristor converter, 129
Wind turbine, 164, 170, 173, 175–177, 180, 182, 184, 192–194, 197–200, 207, 215, 217, 227–231, 234–239, 241, 245, 251, 443, 450, 455–457, 459, 460, 462, 469, 484, 488, 490, 492, 494–496, 498, 499, 512, 527, 531, 532, 534, 536, 541, 663, 664

X
Ximeng-Taizhou LCC-HVDC, 650

Z
Zhangbei MMC-MTDC project, 3
Zhangbei Test Base, 494, 496, 663, 664, 666